

Pertanika Journal of
**SCIENCE &
TECHNOLOGY**

JST

VOL. 29 (3) JUL. 2021



A scientific journal published by Universiti Putra Malaysia Press

Pertanika Journal of Science & Technology

About the Journal

Overview

Pertanika Journal of Science & Technology (PJST) is the official journal of Universiti Putra Malaysia published by UPM Press. It is an open-access online scientific journal which is free of charge. It publishes the scientific outputs. It neither accepts nor commissions third party content.

Recognized internationally as the leading peer-reviewed interdisciplinary journal devoted to the publication of original papers, it serves as a forum for practical approaches to improving quality in issues pertaining to science and engineering and its related fields.

PJST is a **quarterly** (January, April, July and October) periodical that considers for publication original articles as per its scope. The journal publishes in **English** and it is open to authors around the world regardless of the nationality.

The Journal is available world-wide.

Aims and scope

Pertanika Journal of Science & Technology aims to provide a forum for high quality research related to science and engineering research. Areas relevant to the scope of the journal include: bioinformatics, bioscience, biotechnology and bio-molecular sciences, chemistry, computer science, ecology, engineering, engineering design, environmental control and management, mathematics and statistics, medicine and health sciences, nanotechnology, physics, safety and emergency management, and related fields of study.

History

Pertanika was founded in 1978. A decision was made in 1992 to streamline *Pertanika* into three journals as *Pertanika Journal of Tropical Agricultural Science*, *Pertanika Journal of Science & Technology*, and *Pertanika Journal of Social Sciences & Humanities* to meet the need for specialised journals in areas of study aligned with the interdisciplinary strengths of the university.

After almost 28 years, as an interdisciplinary Journal of Science & Technology, the journal now focuses on research in science and engineering and its related fields.

Goal of *Pertanika*

Our goal is to bring the highest quality research to the widest possible audience.

Quality

We aim for excellence, sustained by a responsible and professional approach to journal publishing. Submissions are guaranteed to receive a decision within 14 weeks. The elapsed time from submission to publication for the articles averages 5-6 months.

Abstracting and indexing of *Pertanika*

The journal is indexed in SCOPUS (Elsevier), Clarivate-Emerging Sources Citation Index [ESCI (Web of Science)], BIOSIS, National Agricultural Science (NAL), Google Scholar, MyCite and ISC.

Future vision

We are continuously improving access to our journal archives, content, and research services. We have the drive to realise exciting new horizons that will benefit not only the academic community, but society itself.

Citing journal articles

The abbreviation for Pertanika Journal of Science & Technology is *Pertanika J. Sci. Technol.*

Publication policy

Pertanika policy prohibits an author from submitting the same manuscript for concurrent consideration by two or more publications. It prohibits as well publication of any manuscript that has already been published either in whole or substantial part elsewhere. It also does not permit publication of manuscript that has been published in full in Proceedings.

Code of Ethics

The *Pertanika* Journals and Universiti Putra Malaysia takes seriously the responsibility of all of its journal publications to reflect the highest in publication ethics. Thus all journals and journal editors are expected to abide by the Journal's codes of ethics. Refer to *Pertanika's Code of Ethics* for full details, or visit the Journal's web link at http://www.pertanika.upm.edu.my/code_of_ethics.php

International Standard Serial Number (ISSN)

An ISSN is an 8-digit code used to identify periodicals such as journals of all kinds and on all media—print and electronic. All *Pertanika* journals have ISSN as well as an e-ISSN.

Pertanika Journal of Science & Technology: ISSN 0128-7680 (*Print*); ISSN 2231-8526 (*Online*).

Lag time

A decision on acceptance or rejection of a manuscript is reached in 3 to 4 months (average 14 weeks). The elapsed time from submission to publication for the articles averages 5-6 months.

Authorship

Authors are not permitted to add or remove any names from the authorship provided at the time of initial submission without the consent of the Journal's Chief Executive Editor.

Manuscript preparation

Refer to *Pertanika's Instructions to Authors* at the back of this journal.

Editorial process

Authors are notified with an acknowledgement containing a *Manuscript ID* on receipt of a manuscript, and upon the editorial decision regarding publication.

Pertanika follows a **double-blind peer-review** process. Manuscripts deemed suitable for publication are usually sent to reviewers. Authors are encouraged to suggest names of at least three potential reviewers at the time of submission of their manuscript to *Pertanika*, but the editors will make the final choice. The editors are not, however, bound by these suggestions.

Notification of the editorial decision is usually provided within ten to fourteen weeks from the receipt of manuscript. Publication of solicited manuscripts is not guaranteed. In most cases, manuscripts are accepted conditionally, pending an author's revision of the material.

The Journal's peer-review

In the peer-review process, three referees independently evaluate the scientific quality of the submitted manuscripts.

Peer reviewers are experts chosen by journal editors to provide written assessment of the **strengths** and **weaknesses** of written research, with the aim of improving the reporting of research and identifying the most appropriate and highest quality material for the journal.

Operating and review process

What happens to a manuscript once it is submitted to *Pertanika*? Typically, there are seven steps to the editorial review process:

1. The Journal's Chief Executive Editor (CEE) and the Editorial Board Members (EBMs) examine the paper to determine whether it is appropriate for the journal and should be reviewed. If not appropriate, the manuscript is rejected outright and the author is informed.
2. The CEE sends the article-identifying information having been removed, to 2 or 3 reviewers who are specialists in the subject matter represented by the article. The CEE requests them to complete the review within 3 weeks.

Comments to authors are about the appropriateness and adequacy of the theoretical or conceptual framework, literature review, method, results and discussion, and conclusions. Reviewers often include suggestions for strengthening of the manuscript. Comments to the editor are in the nature of the significance of the work and its potential contribution to the research field.

3. The Editor-in-Chief (EiC) examines the review reports and decides whether to accept or reject the manuscript, invites the author(s) to revise and resubmit the manuscript, or seek additional review reports. Final acceptance or rejection rests with the CEE and EiC, who reserve the right to refuse any material for publication. In rare instances, the manuscript is accepted with almost no revision. Almost without exception, reviewers' comments (to the author) are forwarded to the author. If a revision is indicated, the editor provides guidelines to the authors for attending to the reviewers' suggestions and perhaps additional advice about revising the manuscript.
4. The authors decide whether and how to address the reviewers' comments and criticisms and the editor's concerns. The authors return a revised version of the paper to the CEE along with specific information describing how they have answered' the concerns of the reviewers and the editor, usually in a tabular form. The author(s) may also submit a rebuttal if there is a need especially when the authors disagree with certain comments provided by reviewer(s).
5. The CEE sends the revised paper out for re-review. Typically, at least 1 of the original reviewers will be asked to examine the article.
6. When the reviewers have completed their work, the EiC examines their comments and decides whether the paper is ready to be published, needs another round of revisions, or should be rejected. If the decision is to accept, the CEE is notified.
7. The CEE reserves the final right to accept or reject any material for publication, if the processing of a particular manuscript is deemed not to be in compliance with the S.O.P. of *Pertanika*. An acceptance letter is sent to all authors.

The editorial office ensures that the manuscript adheres to the correct style (in-text citations, the reference list, and tables are typical areas of concern, clarity, and grammar). The authors are asked to respond to any minor queries by the editorial office. Following these corrections, page proofs are mailed to the corresponding authors for their final approval. At this point, **only essential changes are accepted**. Finally, the manuscript appears in the pages of the journal and is posted online.

Pertanika Journal of

**SCIENCE
& TECHNOLOGY**

Vol. 29 (3) Jul. 2021



A scientific journal published by Universiti Putra Malaysia Press



EDITOR-IN-CHIEF

Luqman Chuah Abdullah
Chemical Engineering

CHIEF EXECUTIVE EDITOR

Mohammad Jawaid
Polymer Composites

UNIVERSITY PUBLICATIONS COMMITTEE

CHAIR

Zulkifli Idrus

EDITORIAL STAFF

Journal Officers:

Kanagamalar Silvarajoo, *ScholarOne*
Siti Zuhaila Abd Wahid, *ScholarOne*
Tee Syin-Ying, *ScholarOne*
Ummi Fairuz Hanapi, *ScholarOne*

Editorial Assistants:

Ku Ida Mastura Ku Baharom
Siti Juridah Mat Arip
Zulinaardawati Kamarudin

PRODUCTION STAFF

Pre-press Officers:

Nur Farrah Dila Ismail
Wong Lih Jiun

WEBMASTER

IT Officer:

Munir Hayat Md Bahrin

EDITORIAL OFFICE

JOURNAL DIVISION

Putra Science Park,
1st Floor, IDEA Tower II
UPM-MTDC Technology Centre
Universiti Putra Malaysia
43400 Serdang, Selangor, Malaysia

General Enquiry

Tel: +603 9769 1622 | 1616

E-mail:

executive_editor.pertanika@upm.edu.my

URL: www.journals-ij.upm.edu.my

PUBLISHER

UPM PRESS

Universiti Putra Malaysia
43400 UPM, Serdang, Selangor, Malaysia.

Tel: +603 9769 8855 | 8854

Fax: +603 9679 6172

E-mail: penerbit@upm.edu.my

URL: <http://penerbit.upm.edu.my>



ASSOCIATE EDITOR

Saidur Rahman

Renewable Energy, Nanofluids, Energy Efficiency, Heat Transfer, Energy Policy
Sunway University, Malaysia

EDITORIAL BOARD 2020-2022

Abdul Latif Ahmad

Chemical Engineering
Universiti Sains Malaysia, Malaysia

Adem Kilicman

Mathematical Sciences
Universiti Putra Malaysia, Malaysia

Ahmad Zaharin Aris

Hydrochemistry, Environmental Chemistry, Environmental Forensics, Heavy Metals
Universiti Putra Malaysia, Malaysia

Azlina Harun@Kamaruddin

Enzyme Technology, Fermentation Technology
Universiti Sains Malaysia, Malaysia

Bassim H. Hameed

Chemical Engineering: Reaction Engineering, Environmental Catalysis & Adsorption
Qatar University, Qatar

Biswajeet Pradhan

Digital image processing, Geographical Information System (GIS), Remote Sensing
University of Technology Sydney, Australia

Daud Ahmad Israf Ali

Cell Biology, Biochemical, Pharmacology
Universiti Putra Malaysia, Malaysia

Hari M. Srivastava

Mathematics and Statistics
University of Victoria, Canada

Ho Yuh-Shan

Water research, Chemical Engineering and Environmental Studies
Asia University, Taiwan

Hsiu-Po Kuo

Chemical Engineering
National Taiwan University, Taiwan

Ivan D. Rukhlenko

Nonlinear Optics, Silicon Photonics, Plasmonics and Nanotechnology
The University of Sydney, Australia

Lee Keat Teong

Energy Environment, Reaction Engineering, Waste Utilization, Renewable Energy
Universiti Sains Malaysia, Malaysia

Mohamed Othman

Communication Technology and Network, Scientific Computing
Universiti Putra Malaysia, Malaysia

Mohd Shukry Abdul Majid

Polymer Composites, Composite Pipes, Natural Fibre Composites, Biodegradable Composites, Bio-Composites
Universiti Malaysia Perlis, Malaysia

Mohd Zulkifly Abdullah

Fluid Mechanics, Heat Transfer, Computational Fluid Dynamics (CFD)
Universiti Sains Malaysia, Malaysia

Mohd. Ali Hassan

Bioprocess Engineering, Environmental Biotechnology
Universiti Putra Malaysia, Malaysia

Mohd Sapuan Salit

Concurrent Engineering and Composite Materials
Universiti Putra Malaysia, Malaysia

Najafpour Darzi Ghasem

Bioprocess Technology, Chemical Engineering, Water and Wastewater Treatment Technology, Biochemical Engineering and Biotechnology, Bioethanol, Biofuel, Biohydrogen, Enzyme and Fermentation Technology
Babol Noshirvani University of Technology, Iran

Nor Azah Yusof

Biosensors, Chemical Sensor, Functional Material
Universiti Putra Malaysia, Malaysia

Norbahiah Misran

Communication Engineering
Universiti Kebangsaan Malaysia, Malaysia

Roslan Abd-Shukur

Physics & Materials Physics, Superconducting Materials
Universiti Kebangsaan Malaysia, Malaysia

Wing Keong Ng

Aquaculture, Aquatic Animal Nutrition, Aqua Feed Technology
Universiti Sains Malaysia, Malaysia

INTERNATIONAL ADVISORY BOARD 2021-2024

CHUNG, Neal Tai-Shung

Polymer Science, Composite and Materials Science
National University of Singapore, Singapore

Mohamed Pourkashanian

Mechanical Engineering, Energy, CFD and Combustion Processes
Sheffield University, United Kingdom

Yulong Ding

Particle Science & Thermal Engineering
University of Birmingham, United Kingdom

Hiroshi Uyama

Polymer Chemistry, Organic Compounds, Coating, Chemical Engineering
Osaka University, Japan

Mohini Sain

Material Science, Biocomposites, Biomaterials
University of Toronto, Canada

ABSTRACTING AND INDEXING OF PERTANIKA JOURNALS

The journal is indexed in SCOPUS (Elsevier), Clarivate-Emerging Sources Citation Index (ESCI), BIOSIS, National Agricultural Science (NAL), Google Scholar, MyCite, ISC. In addition, Pertanika JSSH is recipient of "CREAM" Award conferred by Ministry of Higher Education (MoHE), Malaysia.

The publisher of Pertanika will not be responsible for the statements made by the authors in any articles published in the journal. Under no circumstances will the publisher of this publication be liable for any loss or damage caused by your reliance on the advice, opinion or information obtained either explicitly or implied through the contents of this publication. All rights of reproduction are reserved in respect of all papers, articles, illustrations, etc., published in Pertanika. Pertanika provides free access to the full text of research articles for anyone, web-wide. It does not charge either its authors or author-institution for refereeing/publishing outgoing articles or user-institution for accessing incoming articles.

No material published in Pertanika may be reproduced or stored on microfilm or in electronic, optical or magnetic form without the written authorization of the Publisher.

Copyright © 2020-21 Universiti Putra Malaysia Press. All Rights Reserved.



Pertanika Journal of Science & Technology
Vol. 29 (3) Jul. 2021

Contents

Foreword <i>Mohammad Jawaid</i>	i
Environmental Sciences	
<i>Review article</i>	
Wastewater from Washed Rice Water as Plant Nutrient Source: Current Understanding and Knowledge Gaps <i>Nabayi Abba, Christopher Teh Boon Sung, Tan Ngai Paing and Ali Tan Kee Zuan</i>	1347
Measurement of Thermal Comfort in Urban Public Spaces Semarang, Indonesia <i>Rina Kurniati, Wakhidah Kurniawati, Diah Intan Kusumo Dewi and Mega Febrina Kusumo Astuti</i>	1371
Efficient Solid Waste Management in Prai Industrial Area through GIS using Dijkstra and Travelling Salesman Problem Algorithms <i>Gaeithry Manoharam, Mohd. Tahir Ismail, Ismail Ahmad Abir and Majid Khan Majahar Ali</i>	1397
Traffic Noise Level Assessment in the Residential Area around Different Road Functions in Malang City, East Java, Indonesia <i>Ngudi Tjahjono, Imam Hanafi, Latipun Latipun and Suyadi Suyadi</i>	1419
Factors in Adopting Green Information Technology: A Qualitative Study in Malaysia <i>Siti Aishah Ramli, Boon Cheong Chew and Adi Saptari</i>	1431
Magnesium-Palm Kernel Shell Biochar Composite for Effective Methylene Blue Removal: Optimization via Response Surface Methodology <i>Nur Hanani Hasana, Rafeah Wahi, Yusralina Yusof and Nabisab Mujawar Mubarak</i>	1451
Evaluation and Application of New-Semarang Coastal Resources Management <i>Alin Fithor, Slamet Budi Prayitno, Frida Purwanti and Agus Indarjo</i>	1475
Immobilized Microalgae using Alginate for Wastewater Treatment <i>Amanatuzzakiah Abdul Halim and Wan Nor Atikah Wan Haron</i>	1489

Treat-ability of <i>Manihot esculenta</i> Peel Extract as Coagulant Aid for Stabilised Leachate	1503
<i>Siti Nor Aishah Mohd-Salleh, Nur Shaylinda Mohd-Zin, Norzila Othman, Yashni Gopalakrishnan and Norshila Abu-Bakar</i>	
Sequestration of Pb(II) from Aqueous Environment by Palm Kernel Shell Activated Carbon: Isotherm and Kinetic Analyses	1517
<i>Ekemini Monday Isokise, Abdul Halim Abdullah and Tan Yen Ping</i>	
Rhodamine 6g Removal from Aqueous Solution with Coconut Shell-Derived Nanomagnetic Adsorbent Composite (Cs-Nmac): Isotherm and Kinetic Studies	1535
<i>Palsan Sannasi Abdullah, Lim Kai Wen, Huda Awang and Siti Nuurul Huda Mohammad Azmin</i>	
Length-weight Relationship and Relative Condition Factor of Two Dominant Species (<i>Cyclocheilichthys apogon</i> and <i>Notopterus notopterus</i>) at Subang Lake, Selangor, Malaysia	1557
<i>Xeai Li Chai, Rohasliney Hashim, Muhammad Nur Aiman Rahmat, Mohamad Hamizan Kamaludin, Nur Ain Habullah and Izharuddin Shah Kamaruddin</i>	
Applied Sciences and Technologies	
<i>Review article</i>	
Revisiting Solar Photovoltaic Roadmap of Tropical Malaysia: Past, Present and Future	1567
<i>Hedzlin Zainuddin, Hazman Raziq Salikin, Sulaiman Shaari, Mohamad Zhafran Hussin and Ardin Manja</i>	
Environmental Assessment of Groundwater Quality for Irrigation Purposes: A Case Study of Hillah City In Iraq	1579
<i>Zaid Abed Al-Ridah, Ahmed Samir Naje, Diaan Fliah Hassan and Hussein Ali Mahdi Al-Zubaid</i>	
Designing the Ergonomic Press and Molding Machine of Cassava Chips for Sustainable Development in SMEs	1595
<i>Silviana, Andy Hardianto, Naif Fuhaid and Dadang Hermawan</i>	
Numerical Simulations and Experimental Validation on LBW Bead Profiles of Ti-6Al-4V Alloy	1609
<i>Harish Mooli, Srinivasa Rao Seeram, Satyanarayana Goteti and Nageswara Rao Boggarapu</i>	
Thermal Comfort Performance of Naturally Ventilated Royal Malaysian Police (RMP) Lockup in Hot and Humid Climate of Malaysia	1627
<i>Bismiazan Abd. Razak, Mohd. Farid Mohamed, Wardah Fatimah Mohammad Yusoff and Mohd. Khairul Azhar Mat Sulaiman</i>	

Behavior for Sandwich Plate with Functionally Graded Porous Metal Core <i>Emad Kadum Njim, Sadeq H. Bakhy and Muhannad Al-Waily</i>	1655
Design of Soymilk Product Development from Grobogan Soybean Variety in Indonesia <i>Andita Sayekti, Atris Suyantohadi, Mirwan Ushada and David Yudianto</i>	1683
Engineering Sciences	
<i>Review article</i>	
Contact and Non-contact Heart Beat Rate Measurement Techniques: Challenges and Issues <i>Wei Leong Khong, Muralindran Mariappan and Chee Siang Chong</i>	1707
Application of Cubature Information Filter for Underwater Target Path Estimation <i>Guduru Naga Divya and Sanagapallea Koteswara Rao</i>	1733
Effect of Extraction Time and Temperature on Total Flavanoid Contents of Petai Belalang (<i>Leucaena leucocephala</i>) Seed Pretreated by Enzymatic Hydrolysis <i>Nor Hanimah Hamidi, Nurul Athirah Mohd Alwi, Haishwari Tarmalingam, Siti Sabirah Ani Kutty and Siti Nur Nadzmiah Mohd Nor</i>	1751
Empirical Model of Ground-Borne Vibration Induced by Freight Railway Traffic <i>Mohd Khairul Afzan Mohd Lazi, Muhammad Akram Adnan and Norliana Sulaiman</i>	1763
Development of Mini CNC Machine Design and Building for Making Ceramic Cup and Bowl Prototype <i>Anantakul Intarapadung</i>	1787
Magnetohydrodynamic Flow and Heat Transfer Over an Exponentially Stretching/Shrinking Sheet in Ferrofluids <i>Nurfazila Rasli and Norshafira Ramli</i>	1811
Development of a Fluidized Bed Dryer for Drying of a Sago Bagasse <i>Nur Tantiyani Ali Othman and Ivan Adler Harry</i>	1831
Information, Computer and Communication Technologies	
<i>Review article</i>	
Text Messaging Platforms in Mental Health Computerised-based Therapy: A Review <i>Teh Faradilla Abdul Rahman and Norshita Mat Nayan</i>	1847

<i>Review article</i>	
A Comprehensive Review of Automated Essay Scoring (AES) Research and Development <i>Chun Then Lim, Chih How Bong, Wee Sian Wong and Nung Kion Lee</i>	1875
PRIB-CDS: An Energy Efficient Low Duty Cycle Broadcasting Scheme for Wireless Sensor Network <i>Anubhama Ramasamy and Rajendran Thangavel</i>	1901
Speech Emotion Recognition Using Deep Learning LSTM for Tamil Language <i>Bennilo Fernandes and Kasiprasad Mannepalli</i>	1915
An Analysis of Emotional Speech Recognition for Tamil Language Using Deep Learning Gate Recurrent Unit <i>Bennilo Fernandes and Kasiprasad Mannepalli</i>	1937
Performance Evaluation of Heuristics and Meta-Heuristics Traffic Control Strategies Using the <i>UTNSim</i> Traffic Simulator <i>Ng Kok Mun and Mamun Ibne Reaz</i>	1963
Material Sciences	
Effect of Stick - Slip Phenomena between Human Skin and UHMW Polyethylene <i>Emad Kamil Hussein, Kussay Ahmed Subhi and Tayser Sumer Gaaz</i>	1979
Development of Mini CNC Machine Design and Building for Making Ceramic Cup and Bowl Prototype <i>Anantakul Intarapadung</i>	1991
Synthesis and Characterization of Composite Materials with Enhanced Thermo-Mechanical Properties for Unmanned Aerial Vehicles (Uavs) and Aerospace Technologies <i>Zahid Iqbal Khan, Zurina Mohamad, Abdul Razak Rahmat and Unsia Habib</i>	2003
Electromechanical Characteristics of Core Free Folded Dielectric Electro-active Polymer Soft Actuator <i>Abdul Malek Abdul Wahab, Muhamad Azhan Anuar and Muhamad Sukri Hadi</i>	2017
Medical and Health Sciences	
Methylmercury Detection in Maternal Blood Samples by Liquid Chromatography with Inductively Coupled Plasma Mass Spectrometry <i>Amirah Abedinlah1, Saliza Mohd Elias, Sarva Mangala Praveena, Suhaili Abu Bakar, Zulida Rejali and Juliana Jalaludin</i>	2027

Detection of COVID-19 from Chest X-ray and CT Scan Images using Improved Stacked Sparse Autoencoder <i>Syahril Ramadhan Saufi, Muhd Danial Abu Hasan, Zair Asrar Ahmad, Mohd Salman Leong and Lim Meng Hee</i>	2045
<i>Short communication</i>	
Determination of Antioxidant Compounds, Proximate Compositions and Assessment of Free Radical Scavenging Activities of <i>Nypa Fruticans</i> Wurmmb. Sap <i>Siti Fatimah Roqiah Yahaya, Niza Samsuddin, Suhana Mamat, Rozita Hod, Nor Zamzila Abdullah, Nor Azlina A. Rahman and Siti Zaiton Mat So'Ad</i>	2061
<i>Short communication</i>	
Comparative Analyses on Synthetic Membranes for Artificial Blood Feeding of <i>Aedes aegypti</i> using Digital Thermo Mosquito Blood Feeder (DITMOF) <i>Mohd Farihan Md Yatim, Aishah Hani Azil, Nazarudin Safian, Ahmad Firdaus Mohd Salleh and Mohd Khadri Shahar</i>	2073
Earth Sciences	
The Characteristics of West Season Wind and Wave as well as Their Impacts on Ferry Cruise in The Kalianget-Kangean Cruise Route, Madura, Indonesia <i>Viv Djanat Prasita, Lukman Aulia Zati and Supriyatno Widagdo</i>	2087
Spatial Distribution of Picophytoplankton in Southeastern Coast of Peninsular Malaysia Using Flow Cytometry <i>Roswati Md Amin, Md Suffian Idris, Nurul Asmera Mudiman, Noor Hazwani Mohd Azmi and Hing Lee Siang</i>	2103
Effects of vegetation covers for outdoor thermal improvement: A Case Study at Abubakar Tafawa Balewa University, Bauchi, Nigeria <i>Kabiru Haruna Abdulkarim, Azmiah Abd Ghafar, Lee Yoke Lai and Ismail Said</i>	2125
Mathematical Sciences	
Evaluating the Steady-state Performance of the Synthetic Coefficient of Variation Chart <i>Ming Hui Chew, Wai Chung Yeong, Muzalwana Abdul Talib, Sok Li Lim and Khai Wah Khaw</i>	2149
Assessing the Impacts of Competition and Dispersal on a Multiple Interactions Type Model <i>Murtala Bello Aliyu, Mohd Hafiz Mohd and Mohd Salmi Md. Noorani</i>	2175

Modelling Benign Ovarian Cyst Risk Factors and Symptoms via Log-Linear Model 2199

Siti Zulaikha Mohd Jamaludin, Mohd Tahir Ismail, Mohd Shareduwan Mohd Kasihmuddin, Mohd. Asyraf Mansor, Siti Noor Farwina Mohamad Anwar Antony and Adnin Adawiyah Makhul

Chemical Sciences

In silico Study of Potential Non-oxime Reactivator for Sarin-inhibited Human Acetylcholinesterase 2217

Rauda A. Mohamed, Keat Khim Ong, Norhana Abdul Halim, Noor Azilah Mohd Kasim, Siti Aminah Mohd Noor, Victor Feizal Knight, Rabbani Muhamad and Wan Md Zin Wan Yunus

Foreword

Welcome to the 3rd 2021 issue for the *Pertanika Journal of Science & Technology (PJST)*!

PJST is an open-access journal for studies in Science and Technology published by Universiti Putra Malaysia Press. It is independently owned and managed by the university for the benefit of the world-wide science community.

This issue contains 47 articles; 5 review articles; 2 short communications and the rest are regular articles. The authors of these articles come from different countries namely India, Indonesia, Iran, Iraq, Malaysia, Nigeria, Pakistan, Thailand and Yemen.

Articles submitted for this issue cover various scopes of Science and Technology including: applied sciences and technologies; chemical sciences; earth sciences; engineering sciences; environmental sciences; information, computer and communication technologies; material sciences, mathematical sciences; and medical and health sciences.

The first article selected is on comparative analyses on synthetic membranes for artificial blood feeding of *Aedes aegypti* using digital thermo mosquito blood feeder (DITMOF). In this study, three synthetic membranes were compared (Parafilm-M, Polytetrafluoroethylene tape or PTFE tape and collagen sausage casing) to blood feeding *Aedes aegypti*. The membranes were incorporated with in-house developed device named as DITMOF to heat the cattle blood for mosquito feeding. Results showed that PTFE tape recorded the highest blood feeding rate ($95.00\% \pm 1.67\%$) with significant mean difference ($p < 0.001$) as compared to both Parafilm-M ($72.00\% \pm 2.60\%$) and collagen sausage casing ($71.50\% \pm 3.50\%$). However, there was no difference in term of fecundity for mosquito feed with all three membranes tested ($p=0.292$). Full information on this study is presented on page 2073.

A regular article titled “Spatial distribution of picophytoplankton in southeastern coast of peninsular Malaysia using flowcytometry” was written by Roswati Md Amin and co-researchers from Universiti Malaysia Terengganu. Picophytoplankton has been described as the smallest known autotrophic species; it is of great significance and present in all oceanic provinces. In this study, picophytoplankton was represented by *Synechococcus*, followed by picoeukaryotes and *Prochlorococcus*. The flow cytometry revealed a coastal–offshore gradient dominated by *Synechococcus*, followed by picoeukaryotes and *Prochlorococcus*. *Synechococcus* and picoeukaryote abundance was primarily distributed along the coast and progressively decreased seaward, whereas *Prochlorococcus* abundances showed a slight increasing trend from the middle parts of the study area to the open oceanic waters. The results of canonical correspondence analysis demonstrate that the total chlorophyll, pH, dissolved oxygen, and temperature would favor the abundance of picophytoplankton assemblages in the study areas. Detailed information on this study can be found on page 2103.

Rauda A. Mohamed and co-authors from National Defence University of Malaysia had proposed *in silico* study of potential non-oxime reactivator for sarin-inhibited human acetylcholinesterase (AChE). Fourteen compounds have been screened via *in silico* approach for their potential as sarin-inhibited human acetylcholinesterase poisoning antidotes. A commercially available antidote, 2-PAM was used for the comparison. Results revealed that (*R*)-Boc-nipecotic acid shows shorter nucleophilic attack distance and high binding affinity implying that this compound could be an alternative antidote towards sarin inhibited-hAChE. Despite the commercial charged oxime, 2-PAM, which might present better nucleophilicity towards sarin-inhibited AChE, the uncharged (*R*)-Boc-nipecotic acid is presumed to penetrate the blood-brain barrier and worth to be proven experimentally. Further details of the article are available on page 2217.

We anticipate that you will find the evidence presented in this issue to be intriguing, thought-provoking and useful in reaching new milestones in your own research. Please recommend the journal to your colleagues and students to make this endeavour meaningful.

All the papers published in this edition underwent Pertanika's stringent peer-review process involving a minimum of two reviewers comprising internal as well as external referees. This was to ensure that the quality of the papers justified the high ranking of the journal, which is renowned as a heavily-cited journal not only by authors and researchers in Malaysia but by those in other countries around the world as well.

A special appreciation to all the International Advisory Board of PJST (2018-2020) for serving the journal for the past three years in ensuring Pertanika plays a vital role in shaping the minds of researchers, enriching their lives, and encouraging them to continue their quest for new knowledge. Also, we welcome the new International Advisory Board on board. We hope that their involvement and contributions towards Pertanika would not only improve its quality but also support the development efforts in making it an international journal of good standing.

We would also like to express our gratitude to all the contributors, namely the authors, reviewers, Editor-in-Chief and Editorial Board Members of PJST, who have made this issue possible.

PJST is currently accepting manuscripts for upcoming issues based on original qualitative or quantitative research that opens new areas of inquiry and investigation.

Chief Executive Editor

Dr. Mohammad Jawaid

executive_editor.pertanika@upm.edu.my

Review article

Wastewater from Washed Rice Water as Plant Nutrient Source: Current Understanding and Knowledge Gaps

Nabayi Abba^{1,2}, Christopher Teh Boon Sung^{1*}, Tan Ngai Paing¹ and Ali Tan Kee Zuan¹

¹Department of Land Management, Faculty of Agriculture, Universiti Putra Malaysia, 43400 UPM, Serdang, Selangor, Malaysia

²Department of Soil Science, Faculty of Agriculture, Federal University Dutse, Nigeria. PMB 7156, Ibrahim Aliyu bye-pass Jigawa state, Nigeria

ABSTRACT

A significant wastewater source in every household is washed rice water (WRW) because it contains leached nutrients (from washing the rice prior to cooking) that could be used as fertilizer. The paper reviewed the current understanding of the potential use of WRW as a plant nutrient source. WRW was shown to increase vegetables growth, such as water spinach, pak choy, lettuce, mustard, tomato, and eggplant. Different researchers have used various amounts of WRW, and their results followed a similar trend: the higher the amount of WRW, the higher the plant growth. WRW has also been used for other purposes, such as a source of carbon for microbial growth. WRW from brown rice and white rice had nutrients ranging from 40-150, 43-16306, 51-200, 8-3574, 36-1425, 27-212, and 32-560 mg L⁻¹ of N, P, K, Ca, Mg, S, and vitamin B1 (thiamine), respectively. Proper utilization of WRW could reduce chemical fertilizer use and prevent both surface and groundwater contamination

and environmental pollution. However, only a few of the studies have compared the use of WRW with the use of conventional NPK fertilizer. The major drawback of WRW studies is that they lack depth and scope, such as determining the initial and (or) final soil physico-chemical properties or plant nutrient contents. Considering the rich nutrient content in WRW, it will impact plant growth and soil fertility when used as both irrigation water and plant nutrient source.

ARTICLE INFO

Article history:

Received: 05 December 2020

Accepted: 15 April 2021

Published: 31 July 2021

DOI: <https://doi.org/10.47836/pjst.29.3.11>

E-mail addresses:

abba.nabayi@fud.edu.ng (Nabayi Abba)

chris@upm.edu.my (Christopher Teh Boon Sung)

ngaipaing@upm.edu.my (Tan Ngai Paing)

tkz@upm.edu.my (Ali Tan Kee Zuan)

* Corresponding author

Therefore, it is recommended that studies on WRW effect on soil microbial population, plant, and soil nutrient contents to be carried out to ascertain the sustainability of WRW use as a plant nutrient source.

Keywords: Irrigation, liquid fertilizer, plant growth, soil microbes, wastewater

INTRODUCTION

Washed rice water (WRW) refers to the water used in washing rice before the rice is cooked. Milled rice is washed prior to cooking to remove the bran, dust, and dirt from the rice (Juliano, 1993). But rice washing can remove a significant amount of water-soluble nutrients from the rice. Several studies as reviewed by Juliano (1985) have shown that rice washing can lose up to 7% protein, 65% crude fat, 30% crude fiber, 59% thiamine, 26% riboflavin, 60% niacin, 26% Ca, 47% P, 47% Fe, 11% Zn, 70% Mg, and 41% K via leaching from the rice. Although these losses mean fewer nutrients are available in the rice for human consumption, they also mean the WRW, now enriched by these leached nutrients, could be used as a liquid plant fertilizer and soil amendment. There are many claims on the beneficial effects of WRW as a plant fertilizer, but these claims are very often anecdotal, given without any support of strong scientific evidence.

Unfortunately, rigorous, and in-depth scientific studies on the specific use of WRW as a plant fertilizer are very scarce. Instead, the research focus and interests on WRW are mostly on its potential use for either human or animal health (e.g., use of washed rice water as a health supplement or medical treatment) or cosmetology purposes (e.g., use of washed rice water as a human facial, skin, and hair care). From our search of the literature, most of the research on the potential use of WRW for agriculture purposes appears to be done in Indonesia. Moreover, these studies are often reported in non-English (though some of these reports include abstracts in English). These reports are also not easily available, and they are mostly published in non-cited journals.

But why use WRW when there are conventional fertilizers available? Reusing washed rice water ought to be encouraged because its practice is a part of better water governance. Global freshwater demand is expected to increase by 55% by 2050 (Park, 2013). This increase is mainly due to detrimental climate change and increasing world population, driving the United Nation to advocate for more effective water governance. Wastewater, rather than just being discarded into the environment, is instead reused, treated, or recycled. The AQUASTAT database of the Food and Agriculture Organization of the United Nations (FAO) estimates more than half of the global freshwater withdrawals are simply discarded as wastewater into the environment (WWDR, 2016). Municipal water demand corresponds to 11% of the global freshwater withdrawal, but out of this, only 3% is consumed, with the remaining 8% simply discarded, unused, as wastewater. Used water is being generated by towns and cities, from domestic purposes. These activities represent a waste product

that must be utilized downstream as a resource or otherwise safely disposed. The average volume of wastewater generated daily by human activities depends on the water availability in the house, cultural type, cost of water, and socioeconomic conditions (Kalavrouziotis, 2015). “United Nations Agenda for Sustainable Development 2030” additionally aims to manage and reduce the release of wastes and chemicals into the environment (FAO, 2015).

Amoro et al. (2019) stated that the increase in water scarcity has increased the interest in finding various ways for wastewater reuse. Recently, there is an increase interest in wastewater utilization for irrigation (Khalid et al., 2018). Water scarcity, together with soil erosion, land degradation, and climate change, are the main threats to crop productivity (Roy et al., 2011). The most significant contribution of wastewater reuse in agriculture is to reduce the pressure on freshwater sources (Jaramillo & Restrepo, 2017; Winpenny et al., 2013). The greatest global water user is agriculture, which consumes 70% of available water (Pimentel & Pimentel, 2007). Thus, wastewater reuse contributes to food safety; thereby, increasing agricultural production in regions experiencing water shortages (Corcoran et al., 2010). The reasons for wastewater reuse are two-fold: water for the ever-increasing world population and for agriculture activities (Pescod, 1992), which make it necessary and worth to initiate and support wastewater reuse projects all over the world (Kretschmer et al., 2002). Kretschmer et al. (2002) for instance, reported that wastewater has the potential in improving soil properties and increasing plant yield.

The use of wastewater has been reported to save 45 to 94% of fertilizer needed in alfalfa and wheat production (Balkhair et al., 2013). The effects of wastewater application on the soil nutrient status and nutrient use efficiency are also reported in crop production. It was observed that the yield of marketable fruit was higher with wastewater compared to the use of groundwater (Gatta et al., 2015a; Gatta et al., 2015b). Some other studies (Aghtape et al., 2011; Cirelli et al., 2012; Li & Li, 2009) have also indicated the efficacy and superiority of wastewater irrigation which could be attributed to their enriched nutrients content. The wastewater application on soil also affects the soil microbial activity either directly or indirectly by changing the soil physicochemical properties (Ibekwe et al., 2018; Oliveira & Pampulha, 2006).

Considering that rice is the second most widely grown cereal, and it is eaten by nearly half of the world’s population (GRiSP, 2013), the practice of reusing WRW can potentially lead to considerable savings in water as well as fertilizer use. Consequently, less dependence on energy in today’s environment of detrimental climate change. The use of biofertilizers is, therefore, a part of sustainable agriculture that was proposed to reduce the use of chemical fertilizers (Sairi et al., 2018).

This review has found only 41 papers or studies that specifically used WRW as a plant fertilizer or soil amendment. But only about 10% of these papers were published in indexed journals, and the others: 61% in non-indexed journals and 29% in student research reports. This breakdown of papers indicates a lack of in-depth study on the potential use

of WRW. The objective of the paper was to review these studies to determine our current understanding on WRW and its potential use as organic liquid plant fertilizer, identify the knowledge gaps, and finally recommend future research.

RICE TYPES

There are many rice forms, such as rough rice, brown rice, parboiled rice, regular milled white rice, pre-cooked rice, quick-frozen rice, and crisped, puffed or expanded rice (Kanchanawongkul, 2004). The mineral composition of rice differs according to rice variety, rice fertilization and cultivation, rice processing and cooking, and the soil type on which the rice is grown (Abbas et al., 2011; Roy et al., 2011). The parboiling in rice processing helps to retain some of the nutrients, where milling losses and rice recovery (whole rice kernels after milling) are energy-and labor-intensive activities (Roy et al., 2011). Brown rice is unmilled rice with its bran still intact. It is whole grain rice with an intact bran layer having its inedible outer hull removed (Upadhyay & Karn, 2018). Many researchers have reported that brown rice has a higher nutrients content than white rice (Babu et al., 2009; Pascual et al., 2013). Essential nutrients like iron, manganese, phosphorus, zinc, thiamine, niacin, vitamin E, dietary fiber, protein, and carbohydrate are higher due to the presence of an unremoved bran layer (Babu et al., 2009; Pascual et al., 2013). Red rice is considered as a weed in many countries, such as Greece, Latin America, Spain, and other temperate regions where this rice is grown with white rice (Patindol et al., 2006). However, in some countries, such as Sri Lanka and the Philippines, red rice is grown as a staple rice cultivar (Itani & Ogawa, 2004). Red rice is gaining popularity in Japan as a functional food because of its high polyphenols and anthocyanin content (Itani & Ogawa, 2004; Ling et al., 2001). White rice is known to have a higher glycemic index than other types of staple foods such as brown rice, whole grain, and barley (Helmyati et al., 2020). Black rice is one of the new rice that has a lower patronization rate (Helmyati et al., 2020). Together with brown rice, black rice is higher in fiber and antioxidants than white rice (Hernawan & Meylani, 2016).

WASHED RICE WATER AND WATER GOVERNANCE

Agricultural wastes are abundant in every country, with over 2 billion tons of household wastes generated globally, with more than 60 tons every second in the year 2020 (World Count, 2020). Malaysia produces about 2.6 million tons of agricultural wastes per year (Sreenivasan et al., 2012). It is estimated that about 3 million tonnes of rice are consumed yearly by Malaysians (Bee, 2019). As a conservative estimate, this works out to at least 3 billion L of WRW produced per year by Malaysians, and this amount is unused and simply discarded. So, it would be beneficial if these wastes could instead be utilized to reduce environmental pollution and to increase soil fertility. Different authors have reported an increase in total organic carbon (TOC) and nitrogen due to irrigation using wastewater,

depending on the amount of organic matter in the wastewater (Jaramillo & Restrepo, 2017; Sun et al., 2014).

The indiscriminate disposal of WRW is harmful to the environment (e.g., via N and P pollution) (Siagian, 2018). Based on the reported nutrient content of the WRW in Table 1, it is evident that it is a potential source of contamination of our water sources (He et al., 2016b). Suryana et al. (2017) classified WRW as a waste considered insignificant or unimportant by the Indonesian public. The growing concern about the negative impacts of urban wastewater on the environment to reduce pollution has forced researchers to look for new and effective recycling alternatives (Santos et al., 2017). WRW from the household can serve as organic fertilizer for plant use (Iskarlia, 2017); besides, it can improve and increase soil fertility (Supraptiningsih et al., 2019) and use as an amendment (Brown et al., 2011; Cogger, 2005; Lehmann, 2011).

Many places around the world discharge domestic wastewater into natural waters. Zou et al. (2012) reported about 96% of villages in China would simply discard domestic wastewater, which have contaminated natural water bodies. Winance et al. (2018) reported production of 4 L of WRW by every household in Baomekot Village being thrown every day as waste, which can be utilized as irrigation water. Consequently, a few WRW reuse communal programs have been established, such as in Lambangkuning Village, Indonesia (Supraptiningsih et al., 2019). This village comprised about 30 households, and each of them produced about 5 L of WRW every day, making 150 L per day. The WRW is collected from every household, pooled, and used to irrigate the garden crops in the village and homes. Another communal WRW program is in Polo Geulis, a village in Central Bogor, Indonesia, which practices a centralized water-saving system. WRW is collected from the town citizens, after which the water is used to irrigate and fertilize their neighborhood crops of herbs and vegetables (The Jakarta Post, 2017).

Washed Rice Water as Fertilizer

The global mineral fertilizer demand increases every year because its demand is affected by population and economic growth, agriculture production and governance, and food price (FAO, 2015). Compared with mineral fertilizers, organic fertilizer has a longer-term effect on soils and plants, and it is claimed to be more environmentally friendly (Chandini et al., 2019; Sairi et al., 2018; Shaviv, 2001). However, one of the shortcomings of organic fertilizer is its slower effect on plants than inorganic fertilizers due to the slower release of organic fertilizers' nutrients. Among the organic fertilizers, liquid organic fertilizer is regarded to be better as the nutrients are applied in liquid soluble forms that can easily be absorbed by plants (Duaja et al., 2012). However, the nutrients release rates must match the plant nutrient uptake; otherwise, these nutrients, if not retained in the soils, may be lost via leaching.

Recent researches have shown that WRW can be used as a plant nutrient source as indicated by Bahar (2016), Wardiah and Hafnati (2014), Suryana et al. (2017), Hairudin (2015), Fitriani (2019), Hariyadi (2020), Handiyanto et al. (2013) and Leandro (2009). The presence of carbohydrates, proteins, vitamins, and other minerals at different concentrations in the WRW (Juliano, 1985; Purnami et al., 2014), depends on several factors, such as the rice variety, rice sources, and rice washing intensity (Akib et al., 2015; Purba et al., 2015; Purnami et al., 2014). Gibberellin and auxin are the two most common hormones employed in stimulating plant growth and both are reported to be present in WRW by Leandro (2009). Andrianto (2007) also attributed the increase in *Adenium's* plant roots to the presence of vitamin B1 in the WRW, which stimulated the plant growth into having greater root biomass. Vitamin B1 (Thiamine) applied once every two days combined with KNO_3 fertilizer increased the vegetative growth of *Dendrobium* sp. (orchid) seedlings (Sianipar, 2004).

The use of WRW as a plant nutrient source could reduce chemical fertilizer procurement and pollution. Kalsum et al. (2011) reported that fermented WRW contains numerous nutrients that are essential to plant growth and development. Carbohydrate is the most abundant content in WRW, by up to 300 mg L^{-1} (Kalsum et al., 2011; Nurhasanah et al., 2010). Dini and Salbiah (2019) found WRW have nutrient contents large enough to increase the vegetative and physiological growth of pepper after being fermented with cellulolytic bacteria. Generally, the efficiency of wastewater as a crop nutrient source largely depends on the soil fertility level, type and nutrient requirement of the crop, and the nutrients in the wastewater. The nutrient use efficiency for wastewater is high (Khalid et al., 2018). This is because the nutrients present in wastewater are commonly found in a dissolved form and, therefore, they are readily available for plant uptake (Khalid et al., 2017). Moreover, the wastewater-induced nutrient supply matches the demand of crops because nutrients are supplied with each irrigation, compared to synthetic fertilizers usually applied to crops in splits (Khalid et al., 2017; Sadaf et al., 2017).

An evaluation of WRW on the growth of both tomato and eggplant at different concentrations of the WRW gave a significant higher yield of their test crops such as in plant height, leaf number, and fresh plant weight (Istiqomah, 2012; Ariwibowo, 2012). Likewise, Karlina et al. (2013) compared the growth of spinach using different organic fertilizers and found WRW treatment to have a significant higher plant height than others. Consequently, they attributed the higher growth and yield to the higher nutrient contents of the WRW as well as the presence of a plant growth hormone (auxin).

However, WRW studies are often plagued by common inadequacies such as the absence of an initial and final soil analysis (e.g., Hairudin, 2015; Hariyadi, 2020) and lack of detailed description of the WRW application timings and methodology of the WRW preparation (e.g., Handiyanto et al., 2013; Hikmah, 2015), soil physicochemical and

microbial properties, and the application area (e.g., Ariwibowo, 2012; Fitriani, 2019), as well as lack of comparisons between WRW treatments with conventional fertilizers such as NPK (e.g., Bahar, 2016; Dini & Salbiah, 2019; Ginting et al., 2017; Wulandari et al., 2012).

Washed Rice Water as a Potential Environmental Pollutant

Urban runoff and stormwater can, in some instances, find their way into sewage works (Duncomb et al., 1982). Industrial contamination is a major problem with sewage sludge; however, domestic sewage is also a potential significant contaminant (Naidu et al., 2004). Lack of such wastewater utilization practices will have adverse effects on nearby freshwater ecosystems and groundwater (He et al., 2016b). Moreover, biochemical oxygen demand (BOD) is high in WRW (2715 to 3800 mg L⁻¹) produced from industrial rice washing before use in food processing (He et al., 2016a). Starch, proteins (mainly composed of glutelin), and vitamins are the main solid particles composition of WRW (Watanabe et al., 2013). Malaysian soils are typically low in soil organic matter and have low cation exchange capacity (Shamshuddin, 1989). Consequently, the country's soils have inherently weak retention of nutrients that could increase the risk of large losses of nutrients via leaching. Leaching is a serious problem because large amounts of nutrients being leached out from the soil could pollute the groundwater and other water sources. The nutrient analyses of WRW show that it could be of greater concern due to its P and N content that can cause eutrophication and groundwater contamination, respectively (Table 1), upon their accumulation. The primary causes of groundwater contamination by nitrogenous compounds are landfill leachates (Nooten et al., 2008) and nitrogen-based fertilizer used in agriculture and uncontrolled wastewater discharge (Ghafari et al., 2008).

The treatment of wastewater generally requires a sewage system and a costly wastewater treatment plant (Kretschmer et al., 2002). One reason for this is it requires constant supply of power that may not always be available in some countries (Kretschmer et al., 2002). He et al. (2016a) reported that WRW have NO₃⁻, NO₂⁻, NH₄⁺, total N, and total P in the range of 4.19 to 10.14, 0 to 0.08, 2.57 to 39.72, 51.26 to 84.79, and 23.41 to 58.12 mg L⁻¹, respectively. He et al. (2019) further used WRW for denitrification as a source of carbon for the microorganisms, which has a NO₃⁻, NO₂⁻, NH₄⁺, total N, total P, and total organic carbon 0.63, 0.04, 0.17, 66.82, 33.96 and 495 mg L⁻¹, respectively. The presence of ammonia might be due to the degradation of WRW by microbes as stated by He et al. (2019). Deepa et al. (2008) reported that rice grains contain 7.95-9.52 g of protein 100 g⁻¹ of rice grains, which is second to carbohydrate (72.8-74.1 g 100g⁻¹ of rice grains). The analyses by Deepa et al. (2008) indicated WRW could have a significant amount of protein, and the protein degradation would produce ammonium via ammonification (Jones & Kielland, 2012).

Table 1
Nutrient contents of washed rice water and other commonly utilised organic amendments

References	N	P	K	Ca	Mg	S	Fe	B	Vit. B1	Vit. K	Protein
Brown rice water											
Juliano (1993); Syuhaibah (2017); Wulandari et al. (2012)	47-140	62-14452	78-200	12-3574	66-1328	50-114	257-698	—	431-560	—	—
White rice water											
Wulandari et al. (2012); Syuhaibah (2017); Nurhasanah (2011).	40-150	43-16306	51-200	8-2944	36-1425	27-212	49-427	—	32-430	—	—
Dini and Salbiah (2019)	400	280	1000	—	—	—	—	—	—	—	—
Diana (2016)	70	60	90	—	—	—	10	6	210	10	180
Diana (2016) ++	12000	11000	5000	—	—	—	—	—	—	—	—
Malakar and Banerjee (1959)	440	300	—	2000	—	—	600	—	5000	—	—
Organic amendments (%)											
POME (Madaki & Seng, 2013; Razali et al., 2012; Sakiah & Wahyuni, 2018; Teh, 2016)	0.075-2.5	0.018-0.8	0.227-4	0.43-1.91	0.07-1.2	—	—	—	—	—	—
SS (Schulz & Römheld, 1997; Sommers, 1977)	<0.1-17.6	<0.1-14.3	0.02-2.64	0.1-25	0.03-1.97	0.6-1.5	—	—	—	—	—
EFB (Madaki & Seng, 2013; Moradi et al., 2014)	0.8-0.87	0.05-0.08	1.51-1.89	0.2-0.64	0.07-0.12	—	—	—	—	—	—
Compost (Harrison, 2008; Sullivan et al., 2018)	0.4-3.5	0.2-1.5	0.4-1.5	1.5-3.5	0.27-0.7	0.25-0.8	—	—	—	—	—

Note: ++, biofertilizer using fermented WRW; POME, palm oil mill effluent; SS, sewage sludge; EFB, empty fruit bunch; —, not determined

Washed Rice Water Nutrient Contents and its Effect on Plant Growth

Researchers have tested WRW on several crops which is shown in Table 2. They found that WRW increased the plant height, stem diameter, and yield of several crops such as: tomato (Ariwibowo, 2012; Hariyadi, 2020; Istiqomah, 2012; Leandro, 2009), water spinach (Bahar, 2016; Karlina et al., 2013; Syuhaibah, 2017), eggplant (Bukhari, 2013; Yulianingsih, 2017), and pak choy (Wardiah & Hafnati, 2014). WRW was also reported to have increased the lettuce yield and root weight (Siagian, 2018; Wulandari et al., 2012). It also increased the growth of mushroom (Handiyanto et al., 2013; Kalsum et al., 2011), height and leaf number of Adenium plant (Andrianto, 2007), chili (Sairi et al., 2018), as well as mustard green plants (Hairudin, 2015).

Wulandari et al. (2012) attributed the higher root growth of lettuce to the high sulfur (S) content (270 mg L^{-1}) present in the WRW (Table 2), in which S helps in thiamine synthesis. Thiamine (Vitamin B1) is an essential component of plant stress responses, disease resistance, crop yield, and several non-coenzyme roles of this vitamin are being characterized (Fitzpatrick & Chapman, 2020). As shown in Table 1, when WRW is compared with organic material (OM), particularly liquid OM, WRW is a good plant nutrient source. However, despite lower nutrient contents than compost and sewage sludge, it is at par with EFB and POME for N, P, Ca, and Mg nutrients. This indicated that WRW could make a significant impact when simultaneously used as irrigation water and plant nutrient source (Kalsum et al., 2011; Karlina et al., 2013; Lestari, 2010; Nurhasanah, 2011; Wardiah & Hafnati, 2014).

WRW will ferment over time. The maximum fermentation time tested was 6 days (Akib et al., 2015), where the fermented WRW was found to produce higher ethanol, phosphorus, nitrogen, and sulfur. Dini and Salbiah (2019) reported the nutrient contents of WRW fermented with a cellulolytic bacterial consortium to be 400, 280, and 1000 mg L^{-1} of N, P, and K, respectively. The relatively higher amount of N, P, and K, as compared with Wulandari et al. (2012), Syuhaibah (2017), and Nurhasanah (2011), could be attributed to the presence of the bacteria in the work by Dini and Salbiah (2019). Likewise, presence of bacteria capable of fixing atmospheric N and P, K solubilization could be why it has higher N and P (Table 1) as compared to the domestic waste used by Vermaat and Hanif (1998). Compared with the general nutrients content of other soil amendments such as EFB and compost (Table 1), WRW is a compatible plant nutrient supplement with the others. The commonly used soil amendments are compost and peat moss (Harrison, 2008; Sullivan et al., 2018), which compared with WRW, have higher N content by dry weight (3-1%), but have lower plant available N forms of 0.05 nitrates and 0.01% ammonium (Harrison, 2008).

Diana (2016) recorded high N (1.2%) content in fermented WRW (fermented with sugar and milk) for the development of biofertilizer (Table 1). Significant variability exists more in the N content in the WRW, with some authors reporting as high as 1.2% (Diana,

Table 2
Effect of washed rice water (WRW) on the growth of different crops

Type of WRW	Crop type	Rates	Results	Reference
WR water	<i>Capsicum annuum</i>	10 mL from different rice brand	Higher plant height leaves number and fresh weight, which was at par with liquid NPK fertilizer.	Sairi et al. (2018)
WR water + Goat manure	<i>Brassica nigra</i>	10, 20, and 30 mL of WRW and 5, 10, and 15 g of manure	The interaction was not significant, but higher plant height and leaves number was obtained by using 20 mL + 15g of goat manure	Amalia and Chitra (2018)
WR water + eggshell, WR water + Cassava peels, WR + eggshell + MSG waste and WR water + market waste, WR water + MSG + AC water	<i>Lycopersicon esculentum</i> , <i>Annona muricata</i> , <i>Elaeis guineensis</i> seedlings, <i>Brassica nigra</i> ,	0, 50, 75, and 100 mL of WRW and 0, 10, and 20g of eggshell	Increased leaf number, plant height, stem diameter, and fresh and dry weight resulted in a 9-24% increase compared to control.	Winance et al. (2018); Hikmah (2015); Iskaria (2017); Suryana et al. (2017); Ariwibowo (2012); Hariyadi (2020)
WR and BR water	<i>Phalaenopsis orchid</i> seedlings.	Application frequency of 2, 4, 6, and 8 days	Greater above-ground biomass was obtained at two days application interval with BR water. 11% percent increased BR than WR water was obtained.	Purnami et al. (2014)
WR water, WR + BR water	<i>Brassica rapa</i> , <i>Spinacia oleracea</i> , <i>Lactuca sativa</i>	-	The use of WRW did not increase the growth of pak choy and spinach	Fitriani (2019); Syuhaibah (2017); Wulandari et al. (2012)
BR water	<i>Apium graveolens</i> , <i>Capsicum spp.</i>	0, 100, 200, 300 and 400 mL	The use of BR water increased the growth of their test plants by 7-24%.	Istiqomah (2010); Baniing et al. (2016)
WR water	<i>Lycopersicon esculentum</i> , <i>Solanum melongena</i> , <i>Spinacia oleracea</i> .	0, 0.5, 1 and 1.5 L	Increase the fresh and dry weight with 7-19% relative to the control and increase in plant height, leaves number, leaf length in the range of 22-43%.	Ratnadi et al. (2014); Leandro (2009); Bahar (2016)
WR water	<i>Brassica nigra</i> .	0, 5, 10, 15 and 20 days of fermented WR water	Higher plant height, total chlorophyll, and fresh weight in 0 and 15 days of fermentation. 3-9, 8-11, and 9-16% increase in chlorophyll and fresh weight 0 days more than in 5, 10, and 20 days of fermentation, respectively.	Wijiyanti et al. (2019)

Table 2 (continue)

Type of WRW	Crop type	Rates	Results	Reference
WR water	<i>Brassica nigra</i> .	0, 5, 10, 15 and 20 days of fermented WR water	Higher plant height, total chlorophyll, and fresh weight in 0 and 15 days of fermentation. 3-9, 8-11, and 9-16% increase in chlorophyll and fresh weight 0 days more than in 5, 10, and 20 days of fermentation, respectively.	Wijyaniti et al. (2019)
WR water	<i>Brassica rapa</i> , <i>Brassica nigra</i> , <i>Lycopersicon esculentum</i> , <i>Solanum melongena</i> , <i>Pleurotus ostreatus</i> , <i>Lactuca sativa</i> , and <i>Adenium obesum</i> .	0, 25, 50, 75 and 100 %	12-26% increase in plant growth with a range of 11-23, 9-14, and 6-15% increase in fresh weight, dry weight, and plant height.	Wardiah and Hafnati (2014); Hairudin (2015); Istiqomah (2010); Bukhari (2013); Yulianingsih (2017); Siagian (2018); Kalsum et al. (2011); Handiyanto et al. (2013); Andrianto (2007); Karlina et al. (2013)
WR water	<i>Capsicum spp.</i>	0, 10, and 15 mL of WR water, coconut water, and tofu waste were used.	Higher plant growth in using sole tofu waste at 10 mL concentration. There was a 7% decrease in the chili plant height when compared with the use of WR water at all levels	Dini and Salbiah (2019)

Note: WR, white rice; BR, brown rice; MSG, monosodium glutamate; AC, air conditioner

2016) while others far below 0.01% (Wulandari et al., 2012). These differences could be associated with the inadvertent fermentation of the WRW or differences in the rice washing intensity. When WRW is fermented, the complex compounds are broken down, which could lead to greater nutrient content. Wastewater irrigation in soil altered the ammonia-oxidizing bacterial population making the *Nitrosospira* and *Nitrosomonas* species dominant (Mechri et al., 2008). It is reported that wastewater containing an average concentration of 35 mg L⁻¹ of N, 10 mg L⁻¹ of P, and 30 mg L⁻¹ of K, mostly meets many crops' requirements, particularly vegetables (Kalavrouziotis, 2015). Overall, the results showed that the nutrient content, particularly N, P, and K (Table 1), are within the range expected to impact plant growth and development by Kalavrouziotis (2015).

WRW can either be applied on a sole basis or in combination with other organic wastes with irrigation water. When applied with other organic wastes WRW generally showed significantly higher crop yields, particularly at higher WRW application rates (Table 2). Sairi et al. (2018) used NPK in the growth of chili seedlings and found it to be on par with fermented WRW, which led them to conclude that fermented WRW can be used as NPK replacement. Hariyadi (2020) substantiated it with a recent study that reported that WRW performed better than monosodium glutamate and air conditioner's water on tomato's growth (Table 2).

Comparison between White and Brown Rice Washed Water on Plant Growth

Few studies compared WRW from white (WR) and brown rice (BR) on plant growth. Wulandari et al. (2012) reported WRW from both BR and BR had non-significantly increased the fresh and dry weight of lettuce as compared with just using tap water. Between the two types of WRW, WR water improved the fresh weight of the crop more significantly at an early stage, but at harvest, there was no significant difference than the BR water-treated plants. When WR and BR water were compared with tap water (control), higher roots dry weight was recorded in both WR and BR water, which differed significantly from control. Wulandari et al. (2012) and Syuhaibah (2017) reported no overall significant difference between WRW and tap water in lettuce and spinach growth, respectively (Table 2).

Purnami et al. (2014) evaluated the use of WR and BR water on the growth of *Phalaenopsis* orchid nursery and found the use of BR water once every four days increased the total fresh weight, root length, plant height and higher above-grown biomass more than the WR water. Fitriani (2019) studied the effect of different sources of WRW on the growth of pak choy at different concentrations but found no significant difference between the WRW types on the growth of the plant. This indicates that the WRW had met the nutrients requirement of pak choy enough to support its metabolism and growth. Istiqomah (2010) stated that BR washed water had a significant effect on the increase in plant height and number of leaves of celery plants. The results of Baning et al. (2016) showed the effect of

BR water at different concentrations on the growth of pepper plants and found to increase the number of leaves, fresh and dry weight and recommended its use on the growth of pepper (Table 2).

Effect of WRW on Microbial Growth

Juwarkar et al. (1988) found populations of soil bacteria, fungi, and actinomycetes increased with increasing domestic wastewater applications. An increase in *Azotobacter* soil population was also observed due to the wastewater application (Juwarkar et al., 1988). Other than for fertilizer, WRW has also been studied for its potential use as a growth media for the bacteria *Bacillus thuringiensis* (Blondine & Yuniarti, 2008) and an alternative media carrier for *Pseudomonas fluorescense*. These bacteria help to control rust disease and to stimulate the growth of plants (Nurhasanah et al., 2010). Fermentation of WRW can be aided using microorganisms such as *Rhizopus*, *Aspergillus*., *Mucor*, *Amylomyces*., *Endomycopsis*, *Saccharomyces*, *Pichia anomala*, *Lactobacillus*, and *Acetobacter* (Akib et al., 2015). The fermentation process helps break down the complex structure of carbohydrates into other simpler compounds such as bioethanol and other elemental forms of the compound that could easily be used by the plants. WRW can support the growth of useful microorganisms (bacteria) such as *Rhizobium*, *Azospirillum*, *Azotobacter*, *Pseudomonas*, *Bacillus* for plant growth, and soil fertility increased (Akib et al., 2015). Amalia and Chitra (2018) reported the presence of *Pseudomonas fluorescense* bacteria among other microorganisms in WRW. It is a potential biocontrol agent that adapts well to plant roots and can help plants fight against pathogens or be resistant to disease (Hoffland et al., 1996). Furthermore, the bacteria mentioned above can produce phytohormones, which stimulate growth and increases cell enlargement. These microbes play a role in controlling pathogens that cause rust and triggering the plant growth to be more effective (Hairudin, 2015). Sairi et al. (2018) reported that *Bacillus spp.* and *Lactobacillus spp.* to be the common genus in WRW upon fermentation. Ahemad and Kibret (2014) reported using both genera to increase plant growth either as biofertilizer or as a biocontrol agent against plant disease. However, WRW not only supports the growth of bacteria but also several fungi species, such as *Trichoderma*, *Penicillium* and *Saccharomyces*, found upon fermentation for seven days, these fungi are beneficial to plant growth (Sairi et al., 2018). WRW has also been used as growth media for lactic acid bacteria (Watanabe et al., 2011; Watanabe et al., 2009).

LIMITATIONS

To our knowledge, this paper is the first review the specific use of WRW as a plant fertilizer. Most of the prior studies on WRW were done at the diploma and undergraduate level, which together with non-peer reviewed journals, made up 90% WRW studies. Only 10% of the 41 WRW studies were published in peer-reviewed journals. For this review, the

use of students' reports and non-indexed journals were inevitable because of the lack of literature on the WRW use as a plant fertilizer. This indicates a knowledge gap in WRW reuse in agriculture.

Most WRW studies did not report the application frequency of the WRW, how WRW was applied, or even the area of the field or plot used. Furthermore, most of the WRW studies did not carry out the chemical analyses on the WRW used; neither did they analyze the initial and final plant and soil nutrient content. Consequently, it is unknown if, or by how much, the WRW had increased the nutrient content of the various test crops and soils due to WRW application alone. The effect of WRW on many basic soil physicochemical properties was also not measured. All their studies were focused only on a limited number of plant growth parameters. WRW studies that did WRW nutrient analyses examined only the macronutrients (N, P, K), none on the micronutrient contents, with few comparisons with NPK mineral fertilizer. WRW studies so far have all been to examine WRW effects over a short-term period (e.g., one planting cycle). But WRW may have a long-term impact on the soil nutrients as well as the soil microbial population. Although many research papers on WRW lack scientific robustness, they remain useful because their findings, at best, suggest that WRW can be beneficial to plant growth and yield as well as increase beneficial soil bacteria for soil health.

CONCLUSIONS AND RECOMMENDATIONS

WRW contains nutrients that could supplement conventional fertilizers (Table 1). It was reported to increase the growth of many crops ranging from the above to below-ground biomass (Table 2). Furthermore, it has also been used in combination with other wastes and was observed to increase plant growth. Various rates of the WRW have been used, with no reported negative effects even at high WRW rates. WRW appears suitable as a supplemental organic fertilizer to other organic and chemical fertilizers. Thus far, the severe limitation on WRW research is the lack of scientific rigor, lack of research methodology description, and, most importantly, the bulk of the study was published in non-indexed reports. Therefore, the results from these researches are at best tentative.

The following is recommended for a detailed evaluation of WRW as organic fertilizer, soil amendment, and source of soil microbial population increase:

1. Soils should be subjected to initial and final physicochemical and nutrient analyses to ascertain how the use of the WRW would alter the soils.
2. Soil microbial study should be incorporated in the study of WRW, particularly the soil microbial population, as WRW contains minerals and compounds essential for their growth and multiplication.
3. Long-term studies over several planting cycles on WRW should be conducted.

4. Periodic soil nutrient content and microbial population should be carried out to ascertain the temporal effect of WRW, particularly over prolonged periods.
5. The use of WRW should be compared with the use of conventional mineral fertilizer and other organic soil amendments (such as composts and palm oil mill effluent).

ACKNOWLEDGEMENT

The helpful assistance from the laboratory staff of Faculty of Agriculture, Uni. Putra Malaysia is acknowledged.

REFERENCES

- Abbas, A., Murtaza, S., Aslam, F., Khawar, A., Rafique, S., & Naheed, S. (2011). Effect of processing on nutritional value of rice (*Oryza sativa*). *World Journal of Medical Sciences*, 6(2), 68-73.
- Aghtape, A. A., Ghanbari, A., Sirousmehr, A., Siahshar, B., Asgharipour, M., & Tavssoli, A. (2011). Effect of irrigation with wastewater and foliar fertilizer application on some forage characteristics of foxtail millet (*Setaria italica*). *International Journal of Plant Physiology and Biochemistry*, 3(3), 34-42.
- Ahemad, M., & Kibret, M. (2014). Mechanisms and applications of plant growth promoting rhizobacteria: Current perspective. *Journal of King saud University-science*, 26(1), 1-20. <http://dx.doi.org/10.1016/j.jksus.2013.05.001>
- Akib, M. A., Setiawaty, H., Haniarti, H., & Sulfiyah, S. (2015). Improving the quality of “Leri” rice washing waste by different period of fermentation and yeast concentration as an alternative liquid organic fertilizer. *International Journal of Agriculture System*, 2(2), 153-162. <http://dx.doi.org/10.20956/ijas.v2i2.31>
- Amalia, N., & Chitra, A. (2018). The effect of application of rice dishwater and manure as organic fertilizer to the growth of mustard (*Brassica juncea* L.). *Agroland: Agricultural Science Journal*, 5(2), 74-82.
- Amoro, I., Laura, M., Yolanda, M., & Jose, L. A. (2019). Wastewater and leafy greens. *Encyclopaedia for Food Security and Sustainability*, 3, 385-389. <https://doi.org/10.1016/B978-0-08-100596-5.22431-1>
- Andrianto, H. (2007). *Pengaruh air cucian beras pada Adenium* [Effect of washed rice water on Adenium] (Unpublished undergraduate thesis). Universitas Muhamadiyah Surakarta, Indonesia.
- Ariwibowo, F. (2012). *Pemanfaatan kulit telur ayam dan air cucian beras pada pertumbuhan tanaman tomat (Solanum lycopersicum) dengan media tanam hidroponik* [Utilization of chicken eggshells and rice washed water on the growth of tomato plants (*Solanum lycopersicum* L.) with hydroponic growing media] (Unpublished undergraduate thesis). Universitas Muhammadiyah Surakarta, Indonesia.
- Babu, P., Subhasree, R., Bhakayaraj, R., & Vidhyalakshmi, R. (2009). Brown rice-beyond the color reviving a lost health food - A review. *American-Eurasian Journal of Agronomy*, 2(2), 67-72.
- Bahar, A. (2016). Pengaruh pemberian limbah air cucian beras terhadap pertumbuhan tanaman kangkung darat (*Ipomoea reptans* Poir) [Effect of applying washed rice wastewater on the growth of land spinach (*Ipomoea reptans* Poir)]. *Jurnal Ilmiah Mahasiswa Fakultas Pertanian*, 3(2), 1-9.

- Balkhair, K. S., El-Nakhlawi, F. S., Ismail, S. M., & Al-Solimani, S. G. (2013). Treated wastewater use and its effect on water conservation, vegetative yeild,yield components and water use efficiency of some vegetable crops grown under two different irrigation systems in western region, Saudi Arabia. *European Scientific Journal*, 9(21), 395-402. <https://doi.org/10.19044/esj.2013.v9n21p%0p>
- Baning, C., Hafnati, R., & Supriatno, S. (2016). Effect of red rice washed water application on vegetative growth of pepper plants (*Piper nigrum* L.). *Jurnal Ilmiah Mahasiswa Pendidikan Biologi*, 1(1), 1-9.
- Bee, Y. G. (2019). *Food supply chain in Malaysia: Review of agricultural policies, public institutional setup and food regulations*. Khazanah Research Institute. Retrieved February 18, 2021, from http://www.krinstitute.org/Discussion_Papers-@-Food_Supply_Chain_in_Malaysia-;_Review_of_Agricultural_Policies,_Public_Institutional_Set-up_and_Food_Regulations.aspx
- Blondine, C., & Yuniarti, R. (2008). Peran serta masyarakat secara mandiri dalam melestarikan *Bacillus thuringiensis* H-14 galur lokal dalam buah kelapa untuk mengendalikan jentik *Anopheles* sp di Kampung Laut Kabupaten Cilacap [The role of the community to independently conserve local strains of *Bacillus thuringiensis* H-14 in coconut fruit to control *Anopheles* sp larvae in Kampung Laut, Cilacap Regency]. *YARSI Medical Journal*, 16(1), 033-038.
- Brown, S., Kurtz, K., Bary, A., & Cogger, C. (2011). Quantifying benefits associated with land application of organic residuals in Washington State. *Environmental Science and Technology*, 45(17), 7451-7458. <https://doi.org/10.1021/es2010418>
- Bukhari (2013). The effect of organic fertilizer and rice washing water on growth and yield of eggplant (*Solanum melongena* L.). *Jurnal Sains Riset*, 3(1), 1-8.
- Chandini, K. R., Kumar, R., & Prakash, O. (2019). *The impact of chemical fertilizers on our environment and ecosystem* (2nd Ed.). Research Trends in Environmental Sciences.
- Cirelli, G. L., Consoli, S., Licciardello, F., Aiello, R., Giuffrida, F., & Leonardi, C. (2012). Treated municipal wastewater reuse in vegetable production. *Agricultural Water Management*, 104, 163-170. <https://doi.org/10.1016/j.agwat.2011.12.011>
- Cogger, C. G. (2005). Potential compost benefits for restoration of soils disturbed by urban development. *Compost Science and Utilization*, 13(4), 243-251. <https://doi.org/10.1080/1065657X.2005.10702248>
- Corcoran, E., Nellesmann, C., Baker, E., Bos, R., Osborn, D., & Savelli, H. (2010). *Sick water? The central role of wastewater management in sustainable development. A rapid response assessment*. UNEP/Earthprint.
- Deepa, G., Singh, V., & Naidu, K. A. (2008). Nutrient composition and physicochemical properties of Indian medicinal rice–Njavara. *Food chemistry*, 106(1), 165-171. <https://doi.org/10.1016/j.foodchem.2007.05.062>
- Diana, R. Y. (2016). *Gardening tips: Benefits of rice washing water for fertilizing plants*. Retrieved May 3, 2020, from <https://mitalom.com/manfaat-air-cucian-beras-untuk-menyuburkan-tanaman/>
- Dini, I. R., & Salbiah, D. (2019). Growth and pepper yields (*Capsicum annum* L.) by giving a formulation of biological fertilizer of cellulolytic bacteria based on organic liquid waste. In *Journal of Physics: Conference Series* (Vol. 1351, No. 1, p. 012097). IOP Publishing.
- Duaja, M. D., Arzita, & Redo, Y. (2012). Growth analysis of Lettuce (*Lactuca sativa* L.) at different type of liquid organic fertilizer. *Jurnal Program Studi Agroekoteknologi*, 1(1), 33-41.

- Duncomb, D. R., Larson, W. E., Clapp, C. E., Dowdy, R. H., Linden, D. R., & Johnson, W. K. (1982). Effect of liquid wastewater sludge application on crop yield and water quality. *Journal of Water Pollution Control Federation*, 54(8), 1185-1193.
- FAO. (2015). *World fertilizer trends and outlook to 2018*. Food and Agriculture Organization of the United Nations Report. Retrieved February 17, 2021, from <http://www.fao.org/3/i4324e/i4324e.pdf>
- Fitriani, C. L. (2019). *Effect of spraying concentration of washed water of various types of rice on plant growth and yield of pak coy (Brassica rapa L.)* (Diploma thesis). Universitas Andalas Padang, Indonesia. Retrieved May 3, 2020, from <http://scholar.unand.ac.id/id/eprint/52640>
- Fitzpatrick, T. B., & Chapman, L. M. (2020). The importance of thiamine (vitamin B1) in plant health: From crop yield to biofortification. *Journal of Biological Chemistry*, 295(34), 12002-12013. <https://doi.org/10.1074/jbc.REV120.010918>
- Gatta, G., Libutti, A., Gagliardi, A., Beneduce, L., Brusetti, L., Borruso, L., Disciglio, G., & Tarantino, E. (2015a). Treated agro-industrial wastewater irrigation of tomato crop: Effects on qualitative/quantitative characteristics of production and microbiological properties of the soil. *Agricultural Water Management*, 149, 33-43. <https://doi.org/10.1016/j.agwat.2014.10.016>
- Gatta, G., Libutti, A., Gagliardi, A., Disciglio, G., Beneduce, L., d'Antuono, M., Rendina, M., & Tarantino, E. (2015b). Effects of treated agro-industrial wastewater irrigation on tomato processing quality. *Italian Journal of Agronomy*, 10(632), 97-100. <https://doi.org/10.4081/ija.2015.632>
- Ghafari, S., Hasan, M., & Aroua, M. K. (2008). Bio-electrochemical removal of nitrate from water and wastewater - A review. *Bioresource Technology*, 99(10), 3965-3974. <https://doi.org/10.1016/j.biortech.2007.05.026>
- Ginting, K. A., Dianita, R., & Rahman A. (2017). *Pengaruh pemberian nitrogen dan fosfor terhadap pertumbuhan legum Calopogonium mucunoides, Centrosema pubescens dan Arachis pintoii* [The effect of nitrogen and phosphorous on the growth of *Calopogonium mucunoides*, *Centrosema pubescens* and *Arachis pintoii*] (Unpublished undergraduate thesis). Fakultas Peternakan Universitas Jambi. Retrieved April 28, 2020, from <https://repository.unja.ac.id/id/eprint/849>
- GRiSP. (2013). *Global Rice Science Partnership Rice almanac* (4th Ed.). International Rice Research Institute.
- Hairudin, R. (2015). Effectiveness of organic fertilizer rice washing water on the growth of mustard plants (*Brassica juncea* L.). *Journal Perbal*, 3(3), 79-84.
- Handiyanto, S., Hastuti, U., & Prabaningtyas, S. (2013, July 6). The effect of rice water washing medium on the speed of mycelium growth of white oyster mushrooms (*Pleurotusostreatus* var. Florida). In *Seminar Nasional X Pendidikan Biologi FKIP UNS* (pp. 1-6). Surakarta, Indonesia.
- Hariyadi, S. P. (2020). The effect of watering on rice washing water, MSG water, and AC (Air Conditioner) wastewater on yields components and tomato yields (*Lycopersicon esculentum* L.) in the deep Peatland. *Universal Journal*, 7, 1-12.
- Harrison, R. (2008). Composting and formation of humic substances. In *Encyclopaedia of Ecology* (pp. 713-719). Academic Press. <https://doi.org/10.1016/B978-008045405-4.00262-7>

- He, Q., Feng, C., Chen, N., Zhang, D., Hou, T., Dai, J., Hao, C., & Mao, B. (2019). Characterizations of dissolved organic matter and bacterial community structures in rice washing drainage (RWD)-based synthetic groundwater denitrification. *Chemosphere*, *215*, 142-152. <https://doi.org/10.1016/j.chemosphere.2018.10.026>
- He, Q., Feng, C., Hu, Q., Li, R., & Chen, N. (2016a). Biological denitrification using rice washing drainage (RWD) as carbon source for removing nitrate from groundwater. *Desalination and Water Treatment*, *57*(46), 21990-21999. <https://doi.org/10.1080/19443994.2015.1127780>
- He, Q., Feng, C., Peng, T., Chen, N., Hu, Q., & Hao, C. (2016b). Denitrification of synthetic nitrate-contaminated groundwater combined with rice washing drainage treatment. *Ecological Engineering*, *95*, 152-159. <https://doi.org/10.1016/j.ecoleng.2016.06.043>
- Helmyati, S., Kiasaty, S., Amalia, A. W., Sholihah, H., Kurnia, M., Wigati, M., Rohana, A., Ishak, W. R. W., Hamid, N. A., Malik, V., & Hu, F. (2020). Substituting white rice with brown and black rice as an alternative to prevent diabetes mellitus type 2: A case-study among young adults in Yogyakarta, Indonesia. *Journal of Diabetes & Metabolic Disorders*, *19*, 749-757. <https://doi.org/10.1007/s40200-020-00555-8>
- Hernawan, E., & Meylani, V. (2016). Physicochemical characteristics analysis of white rice, brown rice, and black rice (*Oryza sativa* L., *Oryza nivara* and *Oryza sativa* L. indica). *Journal Kesehatan Bakti Tunas Husada*, *15*(1), 79-91.
- Hikmah, N. (2015). *Pemanfaatan ekstrak kulit singkong dan air cucian beras pada pertumbuhan tanaman sirsak (Annona muricata L.)* [Utilization of cassava peels extract and washed rice water on the growth of soursop (*Annona muricata* L.)] (Unpublished undergraduate thesis). Universitas Muhammadiyah Surakarta, Indonesia. Retrieved August 7, 2020, from <http://eprints.ums.ac.id/33510/15/Naskah%20Publikasi.pdf>
- Hoffland, E., Hakulinen, J., & Van Pelt, J. A. (1996). Comparison of systemic resistance induced by a virulent and non-pathogenic pseudomonas species. *Phytopathology*, *86*(7), 757-762.
- Ibekwe, A., Gonzalez-Rubio, A., & Suarez, D. (2018). Impact of treated wastewater for irrigation on soil microbial communities. *Science of the Total Environment*, *622*, 1603-1610. <https://doi.org/10.1016/j.scitotenv.2017.10.039>
- Iskaria, G. R. (2017). The growth of hydroponic mustard plant (*Brassica rapa* L.) using the nutrition of washed rice water and chicken egg shells. *Agric Sains Journal of Budidaya Tanaman Perkebunan Politeknik Hasnur*, *3*(2), 42-51.
- Istiqomah, N. (2010). Influence of brown rice washing water application on growth and yield of celery (*Apium graveolens* L.) on Lebak's mashland. *Agroscentiae*, *3*(17), 152-155.
- Istiqomah, N. (2012). Efektivitas pemberian air cucian beras coklat terhadap produktivitas tanaman kacang hijau (*Phaseolus radiatus* L.) pada lahan rawa lebak [Effectiveness of applying washed brown rice water on the productivity of green bean (*Phaseolus radiatus* L.) on lowland swamps]. *Ziraa'ah*, *33*(1), 99-108.
- Itani, T., & Ogawa, M. (2004). History and recent trends of red rice in Japan. *Japan Journal of Crop Science*, *73*, 137-147.
- Jaramillo, M. F., & Restrepo, I. (2017). Wastewater reuse in agriculture: A review about its limitations and benefits. *Sustainability*, *9*(10), 1734-1753. <https://doi.org/10.3390/su9101734>

- Jones, D. L., & Kielland, K. (2012). Amino acid, peptide and protein mineralization dynamics in a taiga forest soil. *Soil Biology and Biochemistry*, 55, 60-69. <https://doi.org/10.1016/j.soilbio.2012.06.005>
- Juliano, B. O. (1985). *Rice: Chemistry and technology* (2nd Ed.). American Association of Cereal Chemists.
- Juliano, B. O. (1993). *Rice in human nutrition*. FAO Food and Nutrition Series (26).
- Juwarkar, A., Dutta, S., & Pandey, R. (1988). Impact of domestic wastewaters on soil microbial populations. *Water, Air, and Soil Pollution*, 39(1-2), 169-177. <https://doi.org/10.1007/BF00250956>
- Kalavrouziotis, I. (2015). The reuse of municipal wastewater in soils. *Global Nest Journal*, 17(3), 474-486. <https://doi.org/10.30955/gnj.001625>
- Kalsum, U. S., Fatimah, & Wasonowati, C. (2011). Effectiveness of washed rice water provision on growth and yield of white oyster mushroom (*Pleurotus ostreatus*). *Journal of Agrovigor*, 4(2), 86-92.
- Kanchanawongkul, V. (2004). Performance comparison on materials surface of paddies hulling for rice- hulling machine. *Engineering for Increasing Productivity*, 13, 3-15.
- Karlina, A., Yursida, & Ruli, J. P. (2013). Growth response of water spinach (*Ipomea reptans*) to the application of liquid organic fertilizer from cow urine and organic fertilizer in tidal land overflow type C. *Journal of Ilmiah Agriculture*, 1, 1-16.
- Khalid, S., Shahid, M., Bibi, I., Sarwar, T., Shah, A. H., & Niazi, N. K. (2018). A review of environmental contamination and health risk assessment of wastewater use for crop irrigation with a focus on low and high-income countries. *International Journal of Environmental Research and Public Health*, 15(5), 895-930. <https://doi.org/10.3390/ijerph15050895>
- Khalid, S., Shahid, M., Dumat, C., Niazi, N. K., Bibi, I., Bakhat, H. F. S. G., Abbas, G., Murtaza, B., & Javeed, H. M. R. (2017). Influence of groundwater and wastewater irrigation on lead accumulation in soil and vegetables: Implications for health risk assessment and phytoremediation. *International Journal of Phytoremediation*, 19(11), 1037-1046. <https://doi.org/10.1080/15226514.2017.1319330>
- Kretschmer, N., Ribbe, L., & Hartmut, G. (2002). Wastewater reuse for agriculture. *Technology Resource Management & Development-Scientific Contributions for Sustainable Development*, 2, 37-64.
- Leandro, M. (2009). *Pengaruh konsentrasi air cucian beras terhadap pertumbuhan tanaman tomat dan terong* [Effect of washed rice water concentrations on the growth of tomato and eggplant]. Retrieved May 26, 2021, from <http://web.archive.org/web/20090731111508/http://cikaciko.blogspot.com/2009/01/pengaruh-konsentrasi-air-cucian-beras.html>
- Lehmann, S. (2011). Resource recovery and materials flow in the city: Zero waste and sustainable consumption as paradigm in urban development. *Journal of Green Building*, 6(3), 88-105.
- Lestari, B. K. (2010). *Efektivitas penyiraman air leri dan ekstrak sari kedelai (Glycine max) terhadap pertumbuhan tanaman cabai hibrida (Capsicum annum L)* [Effectiveness of watering with washed rice water and soybean extract on the growth of hybrid chili (*Capsicum annum L.*)] (Unpublished undergraduate thesis). Universitas Muhammadiyah Surakarta, Indonesia. Retrieved September 11, 2020, from <http://eprints.ums.ac.id/9784/>

- Li, W., & Li, Z. (2009). *In situ* nutrient removal from aquaculture wastewater by aquatic vegetable *Ipomoea aquatica* on floating beds. *Water Science and Technology*, 59(10), 1937-1943. <https://doi.org/10.2166/wst.2009.191>
- Ling, W. H., Cheng, Q. X., Ma, J., & Wang, T. (2001). Red and black rice decrease atherosclerotic plaque formation and increase antioxidant status in rabbits. *The Journal of Nutrition*, 131(5), 1421-1426. <https://doi.org/10.1093/jn/131.5.1421>
- Madaki, Y. S., & Seng, L. (2013). Palm oil mill effluent (POME) from Malaysia palm oil mills: Waste or resource. *International Journal of Science, Environment and Technology*, 2(6), 1138-1155.
- Malakar, M., & Banerjee, S. (1959). Effect of cooking rice with different volumes of water on the loss of nutrients and on digestibility of rice in vitro. *Food Research*, 24, 751-756. <https://doi.org/10.1111/j.1365-2621.1959.tb17330.x>
- Mechri, B., Mariem, F. B., Baham, M., Elhadj, S. B., & Hammami, M. (2008). Change in soil properties and the soil microbial community following land spreading of olive mill wastewater affects olive trees key physiological parameters and the abundance of arbuscular mycorrhizal fungi. *Soil Biology and Biochemistry*, 40(1), 152-161. <https://doi.org/10.1016/j.soilbio.2007.07.020>
- Moradi, A., Teh, C. B. S., Goh, K., Husni, M. A., & Ishak, C. F. (2014). Decomposition and nutrient release temporal pattern of oil palm residues. *Annals of Applied Biology*, 164(2), 208-219. <https://doi.org/10.1111/aab.12094>
- Naidu, R., Megharaj, M., & Owens, G. (2004). Recyclable urban and industrial waste-benefits and problems in agricultural use. In *Managing soil quality: Challenges in modern agriculture* (pp. 219-237). CAB International Oxfordshire.
- Nooten, T. V., Diels, L., & Bastiaens, L. (2008). Design of a multifunctional permeable reactive barrier for the treatment of landfill leachate contamination: Laboratory column evaluation. *Environmental Science and Technology*, 42(23), 8890-8895. <https://doi.org/10.1021/es801704t>
- Nurhasanah, Y. S., Nelly, N., Reka, P., Anik, N., & Muhammad, L. F. (2010). *Potential waste water washing rice as a propagation media for plant probiotic bacteria*. Institute Pertanian Bogor.
- Nurhasanah. (2011). *Rice washing water nutrient content*. Pustaka Belaja.
- Oliveira, A., & Pampulha, M. E. (2006). Effects of long-term heavy metal contamination on soil microbial characteristics. *Journal of Bioscience and Bioengineering*, 102(3), 157-161. <https://doi.org/10.1263/jbb.102.157>
- Park, J. (2013). Environment and health: An overview of current trends at WHO and OECD. *Journal of Environmental Health Sciences*, 39(4), 299-311.
- Pascual, C. D. S., Massaretto, I. L., Kawassaki, F., Barros, R. M. C., Noldin, J. A., & Marquez, U. M. L. (2013). Effects of parboiling, storage and cooking on the levels of tocopherols, tocotrienols and γ -oryzanol in brown rice (*Oryza sativa* L.). *Food Research International*, 50(2), 676-681. <https://doi.org/10.1016/j.foodres.2011.07.013>
- Patindol, J., Flowers, A., Kuo, M. I., Wang, Y. J., & Gealy, D. (2006). Comparison of physicochemical properties and starch structure of red rice and cultivated rice. *Journal of Agricultural and Food Chemistry*, 54(7), 2712-2718. <https://doi.org/10.1021/jf0523418>

- Pescod, M. (1992). *Wastewater treatment and use in agriculture*. FAO Irrigation and Drainage.
- Pimentel, D., & Pimentel, M. H. (2007). *Food, energy, and society*. CRC press.
- Purba, M. A., Fauzi, F., & Sari, K. (2015). Pengaruh pemberian fosfat alam dan bahan organik pada tanah sulfat masam potensial terhadap P-tersedia tanah dan produksi padi (*Oryza sativa* L.) [Effect of applying natural phosphate and organic matter on potential acid sulfate soils on the available soil-P and rice production (*Oryza sativa* L.)]. *Jurnal Agroekoteknologi Universitas Sumatera Utara*, 3(3), 938-948.
- Purnami, W. G., Yuswanti, N. H., & Astiningsih, M. A. (2014). Effect of type and frequency of washed rice water on growth of orchid seeds (*Phalaenopsis sp*) after acclimatization. *Jurnal of Agroekoteknologi Tropica*, 3(1), 22-31.
- Ratnadi, N. W. Y., Sumardika, N. Y., & Setiawan, N. A. G. (2014). Effect of watering rice washing water and urea fertilizer with different concentrations on the growth of henna plants (*Impatiens balsamina* L.). *Journal of Science Biological Education*, 1(1), 1-9.
- Razali, W. A. W., Baharuddin, A. S., Talib, A. T., Sulaiman, A., Naim, M. N., Hassan, M. A., & Shirai, Y. (2012). Degradation of oil palm empty fruit bunches (OPEFB) fibre during composting process using in-vessel composter. *BioResources*, 7(4), 4786-4805.
- Roy, P., Orikasa, T., Okadome, H., Nakamura, N., & Shiina, T. (2011). Processing conditions, rice properties, health and environment. *International Journal of Environmental Research and Public Health*, 8(6), 1957-1976. <https://doi.org/10.3390/ijerph8061957>
- Sadaf, J., Shah, G. A., Shahzad, K., Ali, N., Shahid, M., Ali, S., Hussain, R. A., Ahmed, Z. I., Traore, B., Ismail, I. M., & Rashid, M. I. (2017). Improvements in wheat productivity and soil quality can accomplish by co-application of biochars and chemical fertilizers. *Science of the Total Environment*, 607, 715-724. <https://doi.org/10.1016/j.scitotenv.2017.06.178>
- Sairi, F., Ismail, N., & Ibrahim, N. (2018). The effect of FRAW towards the growth of chilli seedlings and its associated microorganisms. *Malaysian Journal of Microbiology*, 14(6), 606-610. <https://doi.org/10.21161/mjm.1461822>
- Sakiah, & Wahyuni, M. (2018). Analysis of c-organic, nitrogen, phosphorus and potassium in application areas and without application of palm oil mill effluent. *Journal of Agriculture and Veterinary Science*, 11(4), 23-27. <https://doi.org/10.9790/2380-1104012327>
- Santos, C., Fonseca, J., Aires, A., Coutinho, J., & Trindade, H. (2017). Effect of different rates of spent coffee grounds (SCG) on composting process, gaseous emissions and quality of end-product. *Waste Management*, 59, 37-47. <https://doi.org/10.1016/j.wasman.2016.10.020>
- Schulz, R., & Römheld, V. (1997). Recycling of municipal and industrial organic wastes in agriculture: benefits, limitations, and means of improvement. In *Plant Nutrition for Sustainable Food Production and Environment* (pp. 581-586). Springer. https://doi.org/10.1007/978-94-009-0047-9_184
- Shamshuddin, J. (1989). Lime requirements of highly weathered Malaysian soils. *Pertanika Journal of Tropical Agricultural Science*, 12, 109-111.
- Shaviv, A. (2001). Advances in controlled-release fertilizers. *Advances in Agronomy*, 71, 1-49.

- Siagian, A. S. (2018). *Respon pemberian pupuk organik cair air cucian beras terhadap pertumbuhan dan produksi tanaman selada hijau (Lactuca sativa L.)* [Response of organic fertilizer and washed rice water on the growth and production of lettuce (*Lactuca sativa* L.)] (Unpublished undergraduate thesis). Medan Area University, Indonesia. Retrieved May 26, 2021, from <http://repository.uma.ac.id/handle/123456789/10578>
- Sianipar, O. P. (2004). *Pengaruh frekuensi pemberian vitamin B1 dan konsentrasi pupuk KNO₃ terhadap pertumbuhan vegetative bibit anggrek Dendrobium (Sakura white)* [Effect of application frequency of vitamin B1 and KNO₃ fertilizer concentration on the vegetative growth of Dendrobium orchid seeds (Sakura white)] (Unpublished undergraduate thesis). Fakultas Pertanian Universitas Udayana, Indonesia.
- Sommers, L. (1977). Chemical composition of sewage sludges and analysis of their potential use as fertilizers. *Journal of Environmental Quality*, 6(2), 225-232. <https://doi.org/10.2134/jeq1977.00472425000600020026x>
- Sreenivasan, J., Govindan, M., Chinnasami, M., & Kadiresu, I. (2012). Solid waste management in Malaysia - A move towards sustainability. *Waste Management and Integrated Visions*, 2005, 55-70.
- Sullivan, D. M., Bary, A. I., Miller, R. O., & Brewer, L. J. (2018). *Interpreting compost analyses*. Oregon State University Extension Service.
- Sun, H., Terhonen, E., Koskinen, K., Paulin, L., Kasanen, R., & Asiegbu, F. O. (2014). Bacterial diversity and community structure along different peat soils in boreal forest. *Applied Soil Ecology*, 74, 37-45. <https://doi.org/10.1016/j.apsoil.2013.09.010>
- Supraptiningsih, L. K., Nuriyanti, R., & Sutrisno, A. (2019). Processing household waste (washed rice water) into liquid organic fertilizer in probolinggo regency empowering. *Journal Pengabdian Masyarakat Fakultas Psikologi*, 3, 12-20.
- Suryana, H., Titiaryanti, M., & Yuniasih, B. (2017). Effect of types and doses of waste on the growth of oil palm seedlings (pre nursery). *Journal of Agromast*, 2(1), 1-11.
- Syuhaiyah, S. A. (2017). *Use of washed rice water as a fertilizer* (Unpublished Undergraduate report). Universiti Putra Malaysia, Malaysia.
- Teh, C. B. S. (2016). *Availability, use, and removal of oil palm biomass in Indonesia*. Report prepared for the International Council on Clean Transportation. Retrieved April 20, 2020, from <https://theicct.org/publications/availability-use-and-removal-oil-palm-biomass-indonesia>
- The Jakarta Post. (2017). Village in Bogor uses leftover rice water to grow plants. *The Jakarta Post News Desk*. Retrieved May 26, 2021, from <https://www.thejakartapost.com/news/2017/10/07/village-in-bogor-uses-leftover-rice-water-to-grow-plants.html>
- Upadhyay, A., & Karn, S. K. (2018). Brown rice: Nutritional composition and health benefits. *Journal of Food Science and Technology Nepal*, 10, 47-52. <https://doi.org/10.3126/jfstn.v10i0.19711>
- Vermaat, J. E., & Hanif, M. K. (1998). Performance of common duckweed species (*Lemnoideae*) and the waterfern *Azolla filiculoides* on different types of waste water. *Water Research*, 32(9), 2569-2576. [https://doi.org/10.1016/S0043-1354\(98\)00037-2](https://doi.org/10.1016/S0043-1354(98)00037-2)

- Wardiah, L., & Hafnati, L. R. (2014). Potensi limbah air cucian beras sebagai pupuk organik cair pada pertumbuhan pakchoy (*Brassica rapa* L.) [Potential of washed rice water as a liquid organic fertilizer on the growth of pakchoy (*Brassica rapa* L.)]. *Jurnal Biologi Edukasi*, 6(1), 34-38.
- Watanabe, M., Ichinose, K., Sasano, K., Ozaki, Y., Tsuiki, T., Hidaka, H., & Kanemoto, S. (2011). Effect of enzymatic treatment on sedimentation and flocculation abilities of solid particles in rice washing drainage and its relationship with protein profiles. *Journal of Bioscience and Bioengineering*, 112(1), 67-70. <https://doi.org/10.1016/j.jbiosc.2011.03.005>
- Watanabe, M., Makino, M., Kaku, N., Koyama, M., Nakamura, K., & Sasano, K. (2013). Fermentative L-(+)-lactic acid production from non-sterilized rice washing drainage containing rice bran by a newly isolated lactic acid bacteria without any additions of nutrients. *Journal of Bioscience and Bioengineering*, 115(4), 449-452. <https://doi.org/10.1016/j.jbiosc.2012.11.001>
- Watanabe, M., Takahashi, M., Sasano, K., Kashiwamura, T., Ozaki, Y., Tsuiki, T., Hidaka, H., & Kanemoto, S. (2009). Bioethanol production from rice washing drainage and rice bran. *Journal of Bioscience and Bioengineering*, 108(6), 524-526. <https://doi.org/10.1016/j.jbiosc.2009.06.014>
- Wijiyanti, P., Hastuti, E. D., & Haryanti, S. (2019). Effect of fertilizer fermentation period of rice wash water on green mustard plant growth (*Brassica juncea* L.). *Buletin Anatomi dan Fisiologi*, 4(1), 21-28.
- Winance, G. M., Ermaningsih, D., & Eting, D. E. (2018). Effect of utilization of rice washing water and eggshells on the growth of tomato plants (*Lycopersium esculentum* Mill). *BIOS Jurnal Pendidikan Biology dan Pengajaran*, 1(1), 1-9.
- Winpenny, J., Heinz, I., Koo-Oshima, S., Salgot, M., Collado, J., Hernández, F., & Torricelli, R. (2013). *Reutilización del Agua en Agricultura: ¿ Beneficios para Todos? [Water reuse in agriculture: Beneficial to all?]*. Food and Agriculture Organization.
- World Count. (2020). *Tons of waste from households*. Retrieved February 18, 2020, from <https://www.theworldcounts.com/challenges/planet-earth/waste/waste-from-households/story>
- Wulandari, C. G., Muhartini, S., & Trisnowati, S. (2012). Pengaruh air cucian beras merah dan beras putih terhadap pertumbuhan dan hasil selada (*Lactuca sativa* L.) [Effect of washed brown and white rice water on the growth and yield of lettuce (*Lactuca sativa* L.)]. *Vegetalika*, 1(2), 24-35. <https://doi.org/10.22146/veg.1516>
- WWDR. (2016). *The United Nations world water development report*. United Nations Educational, Scientific and Cultural Organization.
- Yulianingsih, R. (2017). Pengaruh air cucian beras terhadap pertumbuhan dan hasil terung ungu (*Solanum melongena* L.). [Effect of rice washing water on growth and yield of superior eggplant (*Solanum Melongea* L.)]. *Publikasi Informasi Pertanian*, 13(24), 61-68.
- Zou, J., Guo, X., Han, Y., Liu, J., & Liang, H. (2012). Study of a novel vertical flow constructed wetland system with drop aeration for rural wastewater treatment. *Water, Air, and Soil Pollution*, 223(2), 889-900. <https://doi.org/10.1007/s11270-011-0910-x>



Measurement of Thermal Comfort in Urban Public Spaces Semarang, Indonesia

Rina Kurniati*, Wakhidah Kurniawati, Diah Intan Kusumo Dewi and Mega Febrina Kusumo Astuti

Department of Urban and Regional Planning, Faculty of Engineering, Diponegoro University, 50275 Semarang, Indonesia

ABSTRACT

Indonesia reported a maximum annual temperature rise of 0.3°C in urban regions. Semarang, the largest metropolitan city in the province of Central Java, is also experiencing an increase in temperature due to climate change therefore activities in urban public spaces are disrupted due to the absence of a comfortable temperature. Urban design elements, including land cover materials, road geometry, vegetation and traffic frequency expressed significant effects on micro-climate. Measurement of Thermal Comfort in Urban Public Spaces Semarang was carried out at the micro level as an old historical district The Old Town and Chinatown. This increment indeed influences thermal comfort level in its outdoor environments which are important for comfortability of outdoor activity. This study aims to analyse surface temperature through Thermal Comfort Measurement. Data was obtained by measuring air temperature, wind speed and humidity in the morning, afternoon, and evening. Inverse distance weighted (IDW), thermal comfort calculations and micro-climate model were employed to evaluate existing physical conditions of these settlements. The results showed both Old Town and Chinatown observed thermal comfort value above 27°C and are categorized as uncomfortable for outdoor activities. This research is contributing to the need to further develop public spaces to potentially adapt to environmental changes.

ARTICLE INFO

Article history:

Received: 18 September 2020

Accepted: 07 December 2020

Published: 31 July 2021

DOI: <https://doi.org/10.47836/pjst.29.3.01>

E-mail addresses:

rina.kurniati@pwk.undip.ac.id (Rina Kurniati)

wakhidahkurniawati@lecturer.undip.ac.id (Wakhidah Kurniawati)

diah.intan@pwk.undip.ac.id (Diah Intan Kusumo Dewi)

mega.febrina18@pwk.undip.ac.id (Mega Febrina Kusumo Astuti)

* Corresponding author

Keywords: Public space, thermal comfort, urban design element

INTRODUCTION

Climate change is more common on a global scale with significant impact in several local population (Handayani et al., 2017; Donaghy, 2007). This phenomenon is

characterized by a rise in sea level, increased surface temperature, abrasion in coastal areas, and damage to marine ecosystems (Zikra et al., 2015). Population growth and its impact on land use triggers temperature increase. Most severe conditions occur in certain urban areas dominated by built-up land with high population density. Increasing urban population poses a critical challenges as a result of the impact to rising surface temperature (Mathew et al., 2018). This phenomenon instigates an extremely intensified city temperatures or is often referred to as the surface urban heat island (SUHI) phenomenon (Mirzaei & Haghghat, 2010).

Indonesia, the fourth most populated country in the world, shows a yearly increase in average surface temperature up to 0.3°C due to the effects of climate change (Emmanuel, 2005). Land use change and illegal logging trigger approximately 85% loss of green open spaces assumed to also contribute to the rising temperatures. Major cities, including Semarang continue to expand and in turn consequently convert agricultural land for building purposes (Pamungkas et al., 2019). Over the last decade, land use diversion had significantly expanded by 13%. This condition triggered a warm surface temperature in the entire Semarang area from 22-40°C in 2018, while the average range was estimated at 18-33°C in 2008. However, the need for land, infrastructure, and buildings are very important to support community activities and are known to greatly influence urban life sustainability. In the debate on the importance of a city in creating a comfortable and safe living conditions, surface temperature is a major indicator with an essential role. Therefore, a city design with the potential to adapt to increasing surface temperature is also very crucial (Djukic et al., 2016).

Semarang City is in the North-Coast of Central Java (Figure 1). As the biggest city in Central Java Province, Semarang grows as busies city which has so many important activities such as trade and services, logistic and port activities as well as the central of government in its province. Transport mass, such as airport, harbour, train station and bus station are developed to support these activities as well as people's travel. Besides, Semarang has potential historical tourism attractions. Historical buildings, old settlements and Dutch colonial heritage areas with European-style architecture still exist in Semarang. Two of a big heritage area is The Old Town and Chinatown.

The Old Town and Chinatown has a strategic location which near to centres of transportation mass such as Tawang Station, Bus Station and Tanjung Mas Port. The proximity of public transports can attract and ease travellers to visit these heritage areas. Besides, The Old Town and Chinatown has been recently positioned as the centre of tourist activities and attractions in Semarang. Since 2014, the local government have continued to carefully revitalize the Old Town into a tourist region. In January 2015, the Old Town and China Town were accepted to be a part of a world heritage temporary list by UNESCO. After revitalizing the Old City and Chinatown area tends to experience an increase in

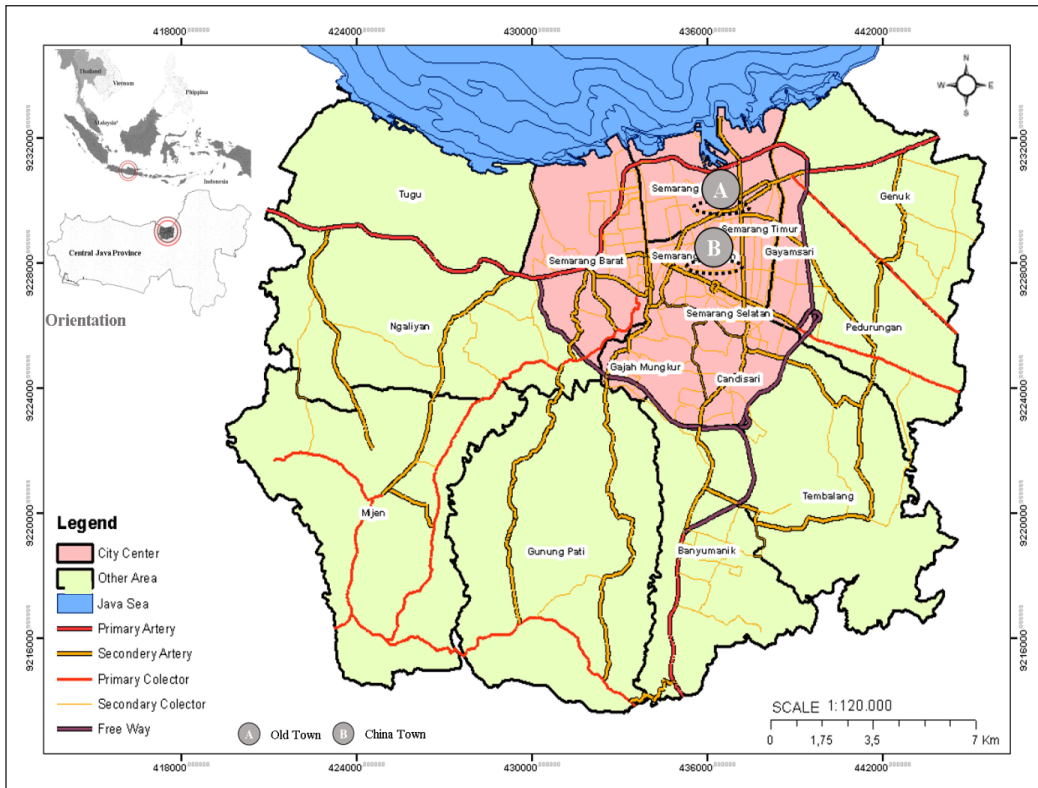


Figure 1. Semarang City, Indonesia

tourist visits compared before revitalization. Tourists visiting the area between the ages of 19-28, which is dominated by the age of 22 (Putri, 2020). Apart from being a hub for tourism development, these two locations are also included in the Bagian Wilayah Kota I (City Area Section) believed to be a centre for trade and services. Most of the tourism activities are carried out in an outdoor setting, including history tours, bicycle rides, and photo hunting. The condition of the hotter open-air environment certainly causes discomfort to the tourists. Therefore, a thermal approach was used to structure the environment to adapt to the urban heat island phenomenon is needed to support tourism activities.

This research was carried out in three primary stages to assess urban design elements. First, the Inverse Distance Weighted (IDW) method is employed to determine the value of an unidentified position using a combination of linear weights from a set of sample points. In this paper, surface temperature sample points were used as an assessment indicator. Second, thermal comfort is calculated by comparing the average temperature of the two locations with standard Temperature Humidity Index (THI), while the third process involved conducting microclimate modeling for urban design elements through correlational and simulation methods.

LITERATURE REVIEW

Urban Public Space

Urban public space is an open space with infrastructures used to support community activities in obtaining protection, satisfaction, and comfort in social life. According to Huat (1992) (as in Purwanto, 2014), it is divided into outdoor public space including roads, pedestrian ways, parks and indoor public spaces include trade and service centers. Whyte (1980) (as in Purwanto, 2014) stated that it is necessary to pay attention to the factors that influence the activities of urban public space, such as the physical factors that connect it with circulation. Therefore, urban public space is not only a landscape design, rather it is also influenced by human activities and tends to impact on the micro climate to provide better air quality (Meziani, 2016).

Climate Sensitive Urban Design (CSUD)

Climate sensitive urban design (CSUD) is a concept in planning and design at the regional level, and is responsive to climate elements as a sustainable development approach (Emmanuel, 2005). The criteria applied in CSUD are micro-climate characteristics including solar lighting, wind speed, and temperature on an urban scale (Kaya & Mengi, 2011; Tapias & Schmitt, 2014). This concept is a potential solution to problems in the context of urban design and a basis to achieve a level of thermal comfort for space users. Kusumastuty et al. (2018) stated the assessment of climate sensitivity to urban design involves two main principles, termed urban environment and the available buildings.

Outdoors Thermal Comfort

Thermal comfort major component in planning and urban designs with a benchmark based on micro-climate element factors influencing regional conditions (Koch-Nielsen, 2002). In addition, the thermal comfort level affecting activities occurs both outside and inside of space. Evaluation of thermal comfort is necessary to become an urban design guide in order to improve the quality of life of urban communities (Koerniawan, 2015), where people get to appreciate on a certain scale. According to Laurie (1990), the condition is comfortable for a standard value of temperature humidity index (THI) estimated between 21-27, and with an ideal temperature acceptable by humans, ranged between 27-28°C with a 40% humidity. However, several factors unarguably influence thermal comfort of outdoor activities, including air temperature, wind speed, humidity, sun exposure (radiation), and other individual active human factors within the environment.

Urban Design Element and Climate

Urban development, believed to increase every year, is possibly responsible for the decline in green open spaces instigating the urban heat island (UHI) phenomenon. Urban design

elements and building functions are among the major factors contributing to thermal comfort in cities (Ragheb et al., 2016). Based on the results of research conducted by Oke (2006), urban design elements, in this case, is categorized as urban landscapes with four basic features assumed to affect open-air temperature (thermal), including urban structure (building dimensions and the spaces formed e.g., road width and distance), land cover (buildings, paving, vegetation, empty land, and water), urban fabric (construction and natural materials), and urban metabolism (heat, water, and pollution due to human activities).

Vegetation as a Natural Component

The availability and arrangement of vegetation shows a positive effect on the formation of the micro-climate (Hakim, 2013). Sufficient vegetation layout tends to influence the direction of movement and wind strength, groundwater quality, micro-climate decline, and passive cooling with shadows. However, the temperature during the day above the open ground surface is higher compared to the temperature under the shade as a result of solar radiation (Lakitan, 2004). Furthermore, vegetation centered on a green open space potentially reduces air temperatures by 2-3°C in the city (Yu & Hien, 2009)

Pavement / Soil Coating

Pavement or soil coating is a significant factor affecting thermal comfort of surrounding buildings against sun exposure (Nikolopoulou & Lykoudis, 2006). According to Johansson (2006), the thermal properties of land cover components greatly contribute to the climatic conditions. These are also affected by the reflectance and absorption values of various materials and the land cover surface. Based on research conducted by Nichol et al. (2009), close relationship between surface temperature and air temperature on changes and types of land cover was established.

Shading

Shading of objects or buildings is among the primary factors to consider in minimizing thermal discomfort due to direct solar radiation in outdoor space. The amount of this energy is influenced by the geometric shape of the surface believed to determine the cover arising from an object or building. In addition, building geometry creates shadow comparable to the sky view factor (SVF). Therefore, there is a large correlation between road geometry, SVF, and surface temperature that is capable of reducing the local air temperature (Shashua-bar & Hoffman, 2003). According to Yeang (2006), in tropical areas, urban heat load from the land cover surface is reduced by optimizing shading. Previous studies have observed a cooling effect caused by the shading element from the geometry and characteristics of trees, e.g., in Tel-Aviv, Israel (Shashua-bar & Hoffman, 2003). Based on the lighting

direction, shading is categorized into two types, including vertical shading angel (VSA) and horizontal shading angel (HSA).

Inverse Distance Weighted (IDW)

Inverse distance weighted (IDW) is a multi-variable interpolation method in processing irregularly spaced data (Gholipour et al., 2013). The interpolation value appears more accurate for close distances between the sample data. However, the weight is not influenced by the location, but linearly changes based on the distance (Pramono, 2008), with evenly or randomly distributed sample data points. The IDW approach is performed using ArcGis10.3 software designed to produce a digital map containing graphic data and attributes.

Thermal Comfort Calculations

The perception of thermal comfort by individuals is basically different even in areas with similar climatic conditions. This awareness is significantly influenced by the wind reaching the skin and the use of clothes and activities. In addition, the thermal comfort is affected by air temperature and humidity. Therefore, the temperature (T) calculation and humidity at each station is measured using Equation 1 (Handoko, 1995):

$$T = (T_{maximum} + T_{minimum})/2 \quad [1]$$

Average air temperatures (T_r) based on measurements at 6 stations randomly distributed in Old Town and Chinatown at 09.30, 12.30 and 16.00, are evaluated by Equation 2:

$$T_r = (T_{09.30} + T_{12.30} + T_{16.00})/3 \quad [2]$$

Average humidity / Relative humidity (RH) based on measurements at 6 stations randomly distributed at 09.30, 12.30 and 16.00, are calculated using Equation 3:

$$RH = (RH_{09.30} + RH_{12.30} + RH_{16.00})/3 \quad [3]$$

Calculation of the temperature humidity index (THI) through the values of air temperature and relative humidity uses the following Equation 4 (McGregor & Nieuwolt, 1998):

$$THI = 0,8 \times T_r + \left(\frac{RH \times T_r}{500} \right) \quad [4]$$

The results of the THI calculation were compared with the standard THI of a comfortable category ranging between 21-27°C, and 40-70% humidity (Laurie, 1990).

Micro-Climate Modelling and Perception of Urban Design

Correlational and simulation methods were applied to model the micro-climate conditions of urban design elements. The correlational method detects the interconnection of variables in a factor with other specified variables (Groat & Wang, 2002). In addition, previous researches have already applied this approach, e.g., Oke (1976) studied to determine the leverage of wind speed on temperature differences. Another research conducted by Shashua-bar and Hoffman (2003) used similar method to describe the effects of tree shadows on surrounding air surface temperatures. For both instances, the effects of urban design elements, including material, shadow, orientation, geometry (H/W), traffic frequency, and the presence of vegetation to micro-climate conditions, with multiple linear regression methods were ascertained. Therefore, in this research, correlational methods were applied in multiple linear regression through statistical data processing application (SPSS).

Subsequently, simulation method was employed to model the system characteristics by using another system, e.g., computer programme. These techniques covered thermal comfort simulation and shadow using ArcGIS, Ecotect Analysis and Sketchup. In addition, 2D data was introduced into the Sketch-up to be converted to a 3-D model and then shadow-modeling was achieved with ArcGIS 10.3. Ecotect analysis is used to model the sunlight direction and the percentage of shading in the area.

METHODS

The research method used is quantitative research methods. Data was collected in a few days by measuring the microclimate, such as solar lighting, wind speed, and air temperature as well as the external thermal comfort, i.e., air temperature, wind speed and humidity in the morning (09.00 am), afternoon (12.30 pm) and evening (04.00 pm). The location points of measurement have been carried out at Old Town which shown in Figure 2 and at Chinatown which shown in Figure 4. This research has been conducted in three stages to evaluate the physical conditions of Old Town and Chinatown. First, inverse distance weighted (IDW) was applied to interpolate the surface by weighting the distance. Second, thermal comfort calculation was employed to identify the level of existing thermal comfort, while the third involved micro-climate modelling to detect the correlation of variables (urban design elements) to air temperatures.

This research was carried out in two major urban public areas used as tourism centers in Semarang, namely Old Town and Chinatown.

Old Town, Semarang

Old Town is a cultural heritage area with colonial architecture and historical tour covering an area of approximately 33 hectares. This area is known as “The Little Nederland” because historically the area was where the Dutch built with European-style architecture (Pratiwo, 2004).

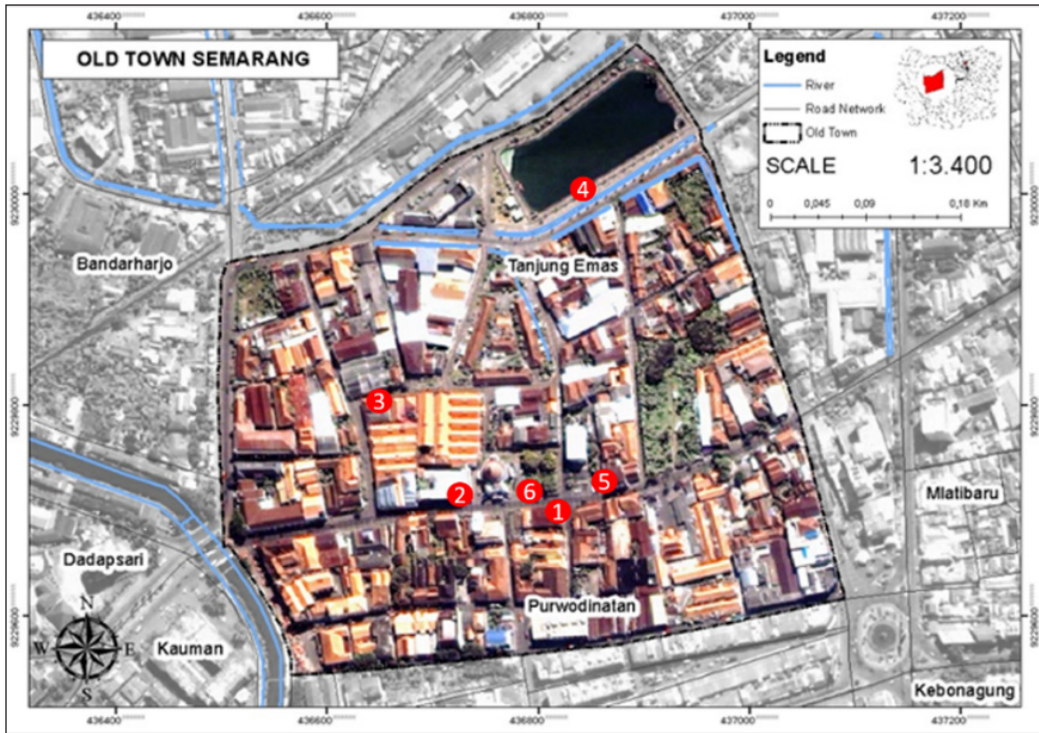


Figure 2. Old Town, Semarang, Indonesia



Figure 3. Six Stations in Old Town, Semarang, Indonesia

Old Town also commonly called *De Hollander* or *Little Netherland*, was initially used as special Dutch residence, and currently documented as a building and environmental planning document as stipulated in the Regional Regulation of Semarang (Number 8 /2003) Lembaran Daerah Kota Semarang, 2003). Old Town is currently used as a designated tourist attraction used to describe the historical architectural, aesthetic, scientific and culture growth of Semarang.

Figure 2 uses points to shows the temperature measurement that are randomly distributed in six stations. Figure 3 shows the current situation in those stations at several locations in Old Town, namely (1) Station 1 pedestrian in front of the Marba building, (2) Station 2 pedestrian in front of PT Indonesian Trading Company, (3) Station 3 in Dream Museum Zone (DMZ) parking area, (4) Tawang polder, (5) Spiegel Restaurant, (6) Srigunting Park.

Chinatown, Semarang

Chinatown is a Chinese settlement where trade and service covering an area of approximately 25.25 hectares. The development of this location is inseparable from Semarang’s history, which is a city often visited by foreigners, including the Chinese.

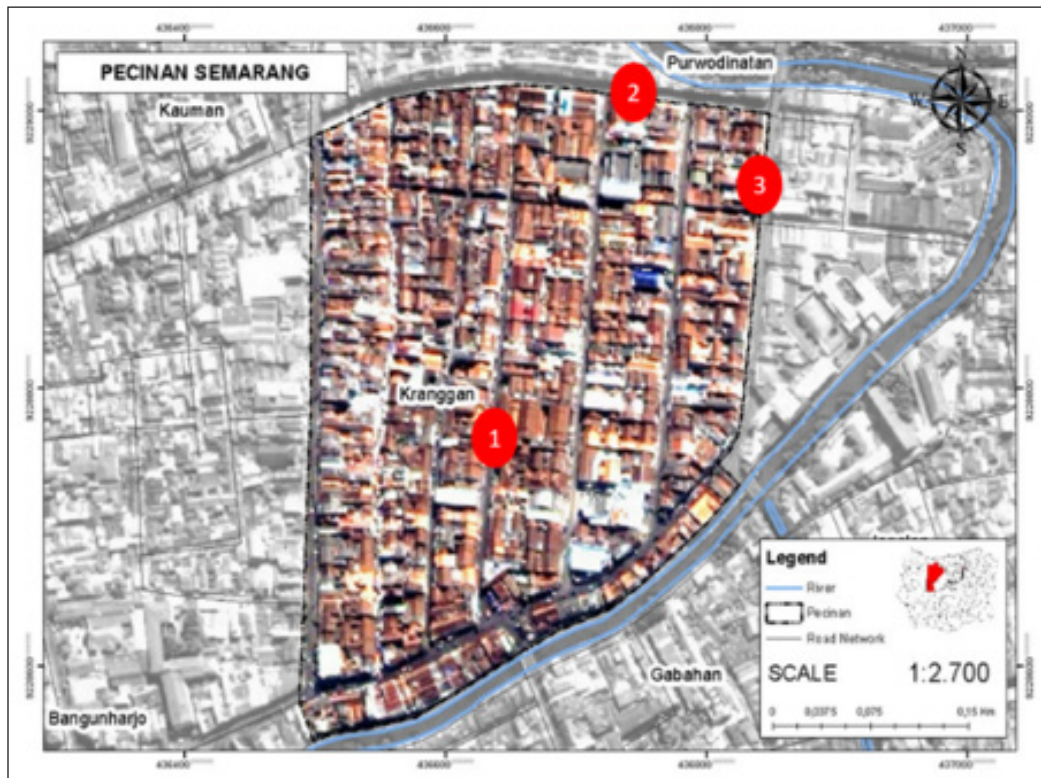


Figure 4. Chinatown, Semarang, Indonesia



Figure 5. Three Stations in Chinatown, Semarang, Indonesia

The buildings in this settlement are grouped in based on functions, namely place to live, trade, provide services, and warehouse for storage. Chinatown is dominated by structures with floors of 8-10 meters large, and floor area ratio (FAR) of 1.0. Figure 4 shows the random distribution of 3 stations in several locations, namely (1) Station 1 in Gg Gambiran Street, (2) Station 2 in Gg Warung Street, (3) Station 3 in Gg Pinggir Street. Figure 5 illustrates the situation at the measurement point in the Chinatown area.

RESULTS

Microclimate Measurement: Air Temperature in Public Space Old Town Semarang

Figure 6 presented three measurements of air temperature in different times. Based on the IDW interpolation results of six stations, the highest average temperature attained was within a range of 35.5 - 36.9°C, while the lowest was 30.0-31.4°C. The results obtained as at 09:30 a.m. in station 1, 2, 5, and 6 were between 30.0-32.7°C. This was lower in 3 and 4 with an average of 34.1-35.5°C and 35.5-36.9°C respectively. Meanwhile, the region outside the evaluation area had a value of 32.7-34.1°C.

The IDW interpolation results at 12:30 p.m., obtained a temperature between 33.7-34.3°C for station 3 and 4, while the highest was at location 1 with an average of 35.4-35.9°C. Also, 5 and 6 had a value of 34.8-35.4°C, while the lowest was at 2 with about 33.2-33.7°C. The region outside the measurement station had a range of 34.3-34.8°C. Furthermore, the highest value measured at 16.00 p.m. was 32.5-32.8°C for 5, and subsequently 6 with an average of 32.1- 32.5°C. Meanwhile station 1 and 3 had a temperature of 31.7- 32.1°C with the lowest range of 31.0-31.3°C detected at station 2 and 4. The area outside was between 31.3-31.7°C.

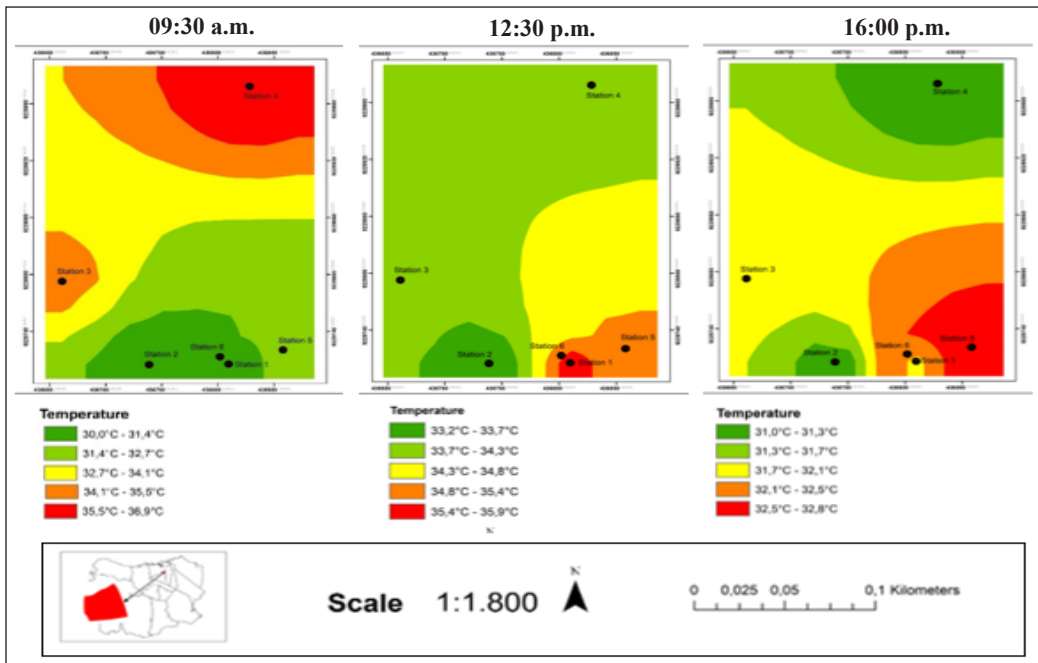


Figure 6. Temperature Measurements in Public Space Old Town Semarang, Indonesia

Microclimate Measurement: Humidity in Public Space Old Town Semarang

The percentage of humidity at station 1 and 2 decreased and attained a value of 62% at 09:30 a.m., while at 12.30 p.m. there was a decline to 52%. This parameter was stable at 09.30 a.m. and 12.30 p.m., then decreased to 52% at 16.00 p.m. for 3. Meanwhile there was a regular decline in 4 from 62% to 55% at 12.30 p.m. reaching 52% at 16.00 p.m. while 5 and 6 tend to fluctuate. The result at each station indicates the humidity level was categorized as normal because the percentage was above the standard intervals of 20-90%. Table 1 demonstrated the influence of temperature range at each location in Public Space Old Town Semarang

Microclimate Measurement: Thermal Comfort in Public Space Old Town Semarang

Table 1 contains the results of the thermal comfort measurement - obtained where each station fall into the uncomfortable category. The highest average temperature was at 36.2°C while the lowest at 30.7°C in the Old Town area. Meanwhile, the peak Temperature Humidity Index (THI) was only 31°C while the base was 29°C. According to Stathopoulos et al. (2004). the ideal air climate for human comfort as an outdoor user is between 27-28°C, while the comfort value ranges from 21-27°C.

Effect of Wind, Vegetation and Air on Thermal Comfort in Public Space Old Town Semarang

The wind speed at each station also affects the thermal comfort level of the outdoor activity. Table 1 demonstrated the average values were between 2-4 m/s, which was categorized as high compared to the standard range of 0.15-0.25 m/s. The beaufort scale classified the wind speed into categories, including light Airs at 09.30 a.m. and 16.00 p.m. for all locations, gentle for 1, 2, 3, and 4, and light breeze for 5 and 6 at 12.30 p.m. In addition, the parameter has no effect on activities based on the outdoor users' perception, because direction and speed basically assist in temperature reduction.

The lack of vegetation is one of the reasons for discomfort in outdoor activity. This is because the presence of plants assist in temperature reduction to 2-3°C. Furthermore, look at Figure 7 is station 1, 2, 5 and 6 that have a higher comfort value than 3 and 4 because of some shady plants' presence. This is able to provide a cooling effect on air through the absorption of solar radiation. The station 3 does not have any vegetation, therefore the climate is hotter in comparison. Meanwhile at 4, there is a little growth, although considered less optimal for lowering the heat in the Tawang pedestrian.

The presence of water in large amounts basically provide a cooler temperature effect to the surrounding region. Also, solar radiations on the surface of water converts the liquid into vapor, therefore humidity is increased with a cooling effect on the area. The expanse of water present in station 4 of polder Tawang assist in surface heat reduction around the region. Furthermore, at 09.30 a.m the temperature in the riverine area termed polder had a range between 35.5-36.9°C, while at 12.30 p.m the value decreased to 33.7- 34.3°C, and continued declining to 31.0-31.3°C at 16.00 p.m. However, this reduction is considered less than optimal because only places with water bodies are reached with a higher value at a radius of 10 meters away.



Figure 7. Existing Vegetation in Public Space Old Town Semarang, Indonesia

Table 1
Micro Climate and Urban Design Elements in Public Space Old Town Semarang, Indonesia

Characteristics	Sun Directions	Shad-owing		Temperature		Wind Velocity (m/s)	Humid-ity	Air Quality		T H I	Building Orientation	Vegetation	Material	Geometric Path (H/W)	Traffic Frequen-tation
		IS	BS	IS	BS			Aqi	Expla-nation						
Station 1															
09.30 a.m.	50°	19%	0	30°	2	62%	21	B			North-South	Decoration, Linier	Paving and concrete	3	High
12.30 p.m.	80°	0%	0	36,6°	4	59%	19	B							
16.00 p.m.	60°	58%	0	34°	2	52%	14	B							
Station 2															
09.30 a.m.	50°	19%	30°	32°	3	62%	18	B			North-South	Decoration, Shading, Linier	Paving and ceramics	2	High
12.30 p.m.	80°	0%	32,9°	34°	4	59%	16	B							
16.00 p.m.	60°	58%	31,4°	34°	2	52%	13	B							
Station 3															
09.30 a.m.	50°	19%	0	35°	3	62%	17	B			East-West	Lack of Vegetation	Paving	-	Low
12.30 p.m.	80°	0%	0	34,2°	4	59%	16	B							
16.00 p.m.	60°	58%	0	31,6°	2	52%	14	B							
Station 4															
09.30 a.m.	50°	19%	0	37,2°	3	62%	17	B			North-South	Shading, Linier	Paving	-	Low
12.30 p.m.	80°	0%	0	33,7°	5	59%	15	B							
16.00 p.m.	60°	58%	0	31°	2	52%	12	B							
Station 5															
09.30 a.m.	50°	19%	32°	33°	2	62%	20	B			North-South	Decoration, Linier	Paving and concrete	2	High
12.30 p.m.	80°	0%	0	34°	3	59%	11	B							
16.00 p.m.	60°	58%	30°	33°	2	52%	14	B							
Station 6															
09.30 a.m.	50°	19%	29°	32°	3	62%	17	B			North-South	Shading, Grid	Paving dan Grass	-	High
12.30 p.m.	80°	0%	33°	34°	3	59%	12	B							
16.00 p.m.	60°	58%	32,7°	33°	3	52%	13	B							

NOT COMFORTABLE (>27°C)

IS= In the Shadow, BS = Beyond the Shadow, Highest Lowest

Microclimate Measurement: Air Temperature in Public Space Chinatown Semarang

This parameter in public space Chinatown is identified through mapping with IDW interpolation in three stations. Figure 8 displays the result with the highest average temperature between 38-39°C while the lowest had a range of 32-33.4°C. The area outside the measurement station was between 33.4-34.7°C and 36.2-37.6°C.

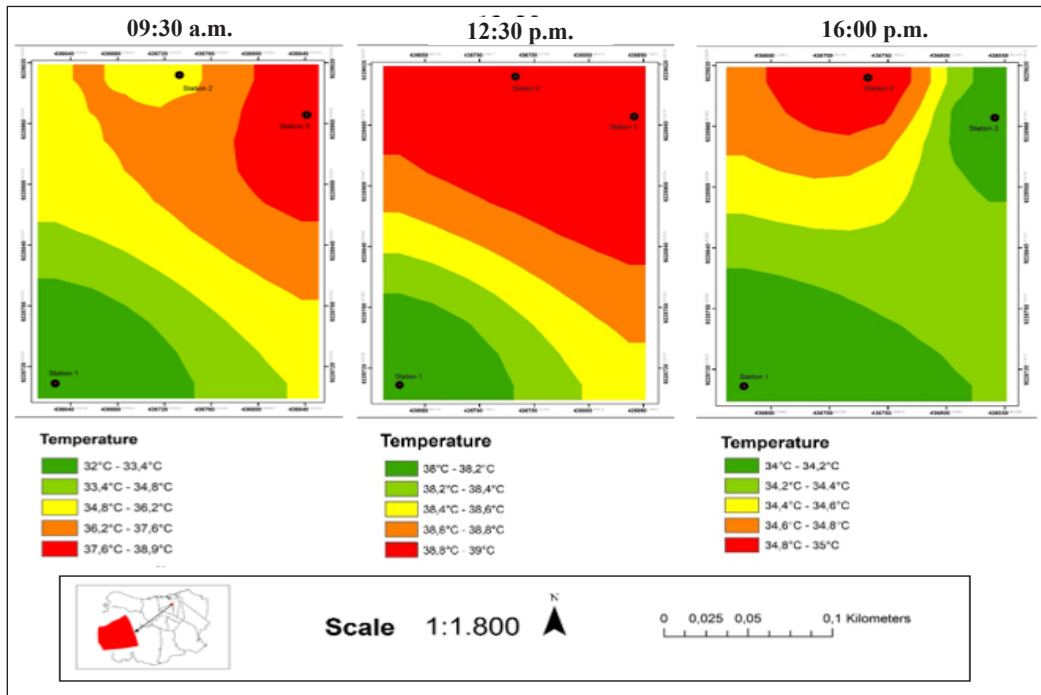


Figure 8. Temperature Measurements in Public Space Chinatown Semarang

Microclimate Measurement: Humidity in Public Space Chinatown Semarang

Table 2 demonstrates the decline in humidity percentage at the three stations. Furthermore, at 09:30 a.m. the level attained a value of 66% and then further decreased to 62% at 12:30 p.m. Meanwhile, at 16.00 p.m., there was a decline to 43% in 1, while at 2 and 3 reached 41%. The humidity per station was categorized as normal because the score between the standard intervals was 20-90%. In addition, this parameter is affected by the change in temperature range.

Microclimate Measurement: Thermal Comfort in Public Space Chinatown Semarang

The result of thermal comfort at each station indicated an uncomfortable category, where the highest and lowest average temperature was determined as 38.9°C and 32.7°C, respectively.

Table 2
Micro Climate and Urban Design Elements in Public Space Chinatown Semarang, Indonesia

Characteristics	Sun Directions	Shad-owing	Temperature		Wind Velocity (m/s)	Humidity	Air Quality		T H I	Building Orientation	Vegetation	Material	Geometric Path (H/W)	Traffic Frequentation
			IS	BS			Aqi	Explanation						
Station 1														
09.30 a.m.	30°	18%	29,2°	31,7°	1	66%	4	B	East-West	Decoration, Shadowing, Linier	Asphalt and Concentrate	3	Low	
12.30 p.m.	80°	0%	0	37,5°	1	62%	10	B						
16.00 p.m.	20°	55%	34°	0	3	43%	16	B						
Station 2														
09.30 a.m.	30°	18%	34,6°	35,8°	2	66%	4	B	North-South	Lack of Vegetation	Paving and Concentrate	2	Medium	
12.30 p.m.	80°	0%	36,5°	38,6°	2	62%	9	B						
16.00 p.m.	20°	55%	30,8°	35°	4	41%	21	B						
Station 3														
09.30 a.m.	30°	18%	37,3°	38,9°	4	66%	5	B	East-West	Decoration, Shadowing, Linier	Paving and Concentrate	3	High	
12.30 p.m.	80°	0%	0	39,4°	2	62%	16	B						
16.00 p.m.	20°	55%	34,1°	0	2	41%	16	B						

NOT COMFORTABLE (>27°C)

IS= In the Shadow, BS = Beyond the Shadow, Highest Lowest

Meanwhile, the peak Temperature Humidity Index (THI) was 34.1 and the base value attained was 33.0. According to Stathopoulos et al. (2004), the ideal air temperature for human comfort as an outdoor user was between 27-28°C, while the comfort value ranges from 21-28°C.

Effect of Wind, Vegetation and Air on Thermal Comfort in Public Space Chinatown Semarang

The wind speed of each station was between 1-4 m/s. This was categorized to have a higher value than the standard of 0.15 -0.25 m/s. According to the beufort scale classification, the wind speed at 1 and 2 was categorized as Light Airs, while at 3 as Light Breeze. Particularly, based on the outdoor users's perception, this parameter does not disturb the activity, because the direction and velocity of the breeze along with vegetation basically assist in temperature reduction. This creates comfort for the space users.

Figure 9 showed the vegetation map in Chinatown with barely any plant form. However, the location was dominated by built-up areas, characterized by the presence of shops and settlements. This city lacks vegetation assemblage, including park, linier or mini gardens in front of the houses due to limited space. The air temperature tends to be high, therefore facilitating the growth of more plants, especially the hanging and creeping varieties necessary to maintain a cooler microclimate.

Furthermore, station 3 is located near to Semarang River. The water body of the river assist in temperature reduction of the surrounding region due to the evaporation effect.

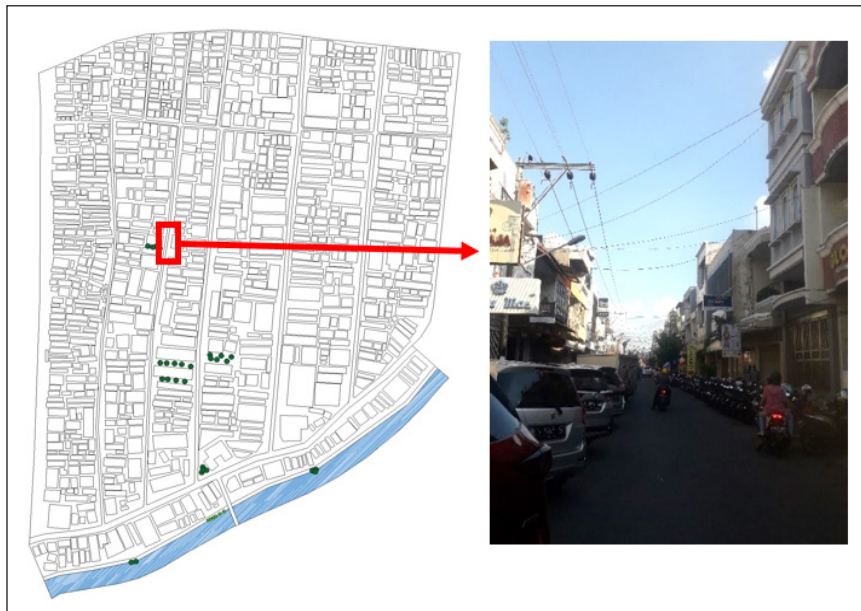


Figure 9. Existing Vegetation in Public Space Chinatown Semarang

The measurement at 09:30 a.m. indicates a range of 37.6-38.8°C. Meanwhile, at 12.30 p.m. there was a rise to 38.8- 39°C with a further decline at 16:00 p.m. to 34 -34.2°C. The waterbody area was lower at 37.4°C at 09.30 a.m., while the value increased to 37.8°C at 12.30 p.m. and 16:00 p.m. respectively.

Climate Analysis on Urban Design Element in Public Space Old Town Semarang

The results of Multiple Linear Regression between microclimate elements, including temperature, wind speed (m/s), and air quality (Aqi) with urban design elements involving land cover materials, geometry (H/W), vegetation, structure orientation, and traffic frequency, contribute to the different relationships between these component. These results demonstrate the effect of material constituents and other factors, including vegetation and traffic frequency on the formation of temperature and air quality. The building geometry element towards the road (H/W) affects the wind speed.

The research conducted by Nichol et al. (2009) demonstrated a significant relationship between land surface and air temperature on changes and types of land cover or thermal material. Also, paving materials in the public space Old Town area produced a thermal value of 1000 J/Kg with a heat absorption and reflectance range of 85-95% and 15-5% respectively. According to Shashua-bar and Hoffman (2003), there is a large correlation between road geometry and land surface heat, especially for creating shadows of objects. In addition, the presence of vegetation with higher LAI reduce thermal radiation by almost 92.55% or air temperature by 2-3°C (Yu & Hien, 2009).

Figure 10 shows the overlay between thermal comfort, wind direction, and building distributions. In general, public space Old Town obtained a thermal comfort value above

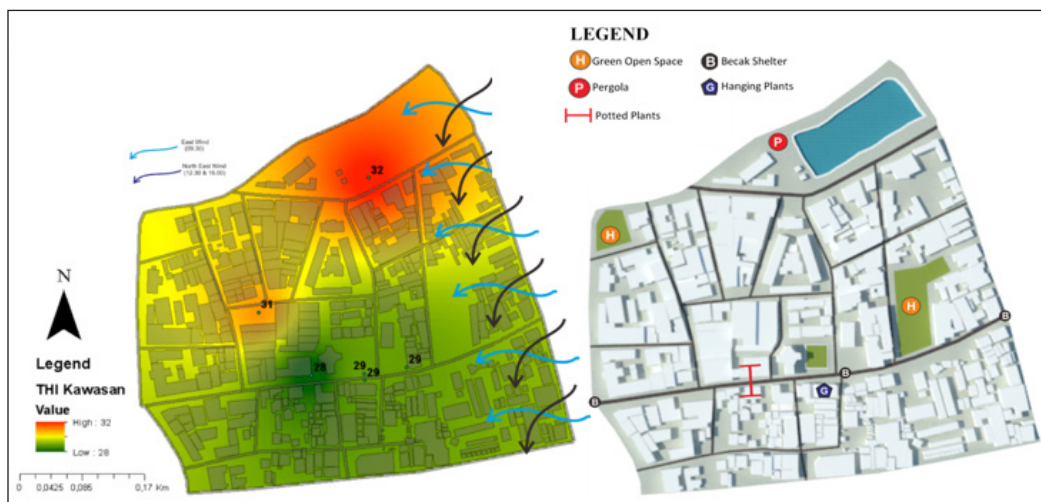


Figure 10. Simulation of THI Value and Wind Direction, and Design Recommendation in Public Space Old Town Semarang

27°C, and was then categorized as uncomfortable for outdoor activities. Irregular structure layout in several partitions contributes to wind flow obstruction and further results to rotating air pockets in the lobby. The northern section of Old Town observed high temperatures due to the movement of dry winds towards the sea. Previous research reported a significant variation in temperature extending to 2.1% between areas closer to the sea level and sections with an altitude away (Purwantara, 2015). These locations prior to the sea level attained relatively warmer surface temperatures characterized by high wind speeds.

Climate Analysis on Urban Design Element in Public Space Chinatown, Semarang

Regression analysis on public space Chinatown showed homogeneous results among the various elements. In general, the micro-climate was influenced by land and building cover materials as well as the traffic rates or environmental activities. Furthermore, public space Chinatown is dominated by two-storey buildings with high density and are mostly built using paving and concrete materials. These materials reflect heat effectively compared to natural products (Nichol et al., 2009). In addition, public space Chinatown is known to perform mixed functions, including historical tourism, residential, and trade area, and therefore activities are always extensive on every occasion.

The simulation results of thermal, wind, and building comfort showed varied wind movement patterns every hour. However, wind movement in this location was more stable compared to public space Old Town due to a more uniform pattern of building layouts with the tendency of a grid shape (Figure 11). The dominance of buildings with square

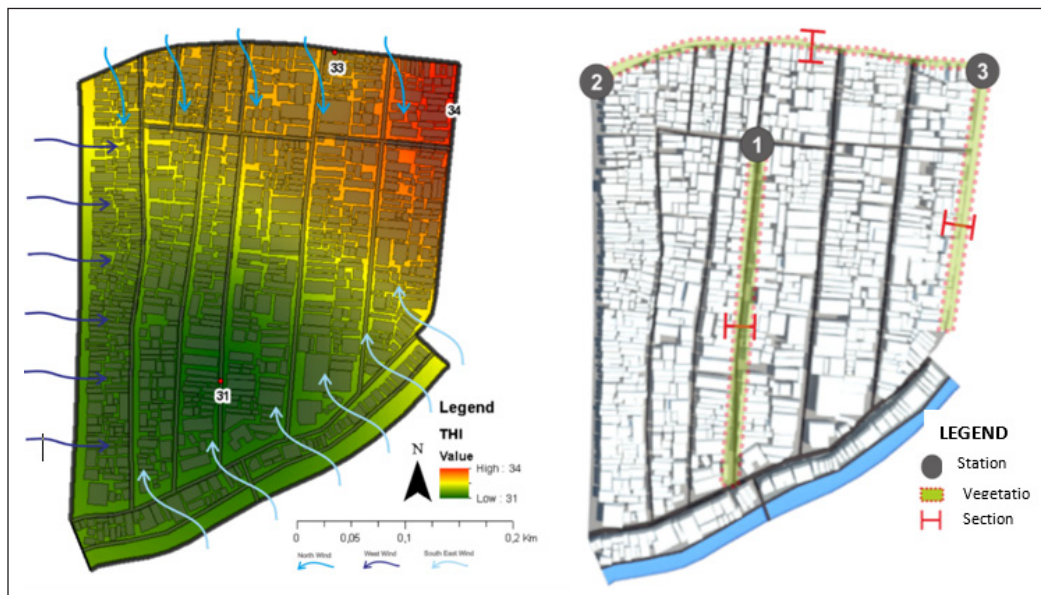


Figure 11. Simulation of THI Value and Wind Direction and Design Recommendation in Public Space Chinatown, Semarang

facades on a straight road led to a more stable airflow in and out the area (Shishegar, 2013). Moreover, the average thermal comfort of public space Chinatown indicated uncomfortable conditions with temperatures above 27°C. Meanwhile, the northern part, including Station 2 and Station 3 appeared the warmest with a thermal comfort level extending to 34°C. The road geometry to the building (H/W) also influenced the formation of air temperature and wind flow (Dursun & Yavas, 2015), where both locations demonstrated a large geometry, and the shading of objects occurred less significant to fill the alley.

DISCUSSION

Table 3 shows the variations in micro-climate characteristics between both locations, where the thermal comfort for public space Old Town was better compared to public space Chinatown. Shading in Old Town is greater than Chinatown, thereby leading to a lower temperature that is far from an ideal condition and nearest 100% in the tropics area. Conversely, lower SVF rate was achieved in the Old Town, which also affected the temperature. Air quality index (Aqi) of Chinatown is better than Old Town, therefore, the score still in the range of ideal condition. Furthermore, the SVF and shading score of Old Town affecting Thermal Comfort in lower than Chinatown. It means the Old Town has a

Table 3
Simulation Results between Old Town and Chinatown Semarang

Category	Ideal Condition	Old Town	Chinatown
Configuration	-	Irregular Pattern	Grid
Building Height	-	8-14 m	8-14 m
Vegetation	-	More Vegetation	Lack
Wind Direction	-	East and Northeast	North, West, and Southeast
Shadowing	The tropics require up to 100% coverage Source: Yeang, 2006	58%	55%
Thermal Comfort	27° - 28 °C Source: Stathopoulos et al. (2004)	31°C	34°C
SVF	The greater the SVF score, the warmer the temperature Source: Lin (2009)	16%	52%
Peak Hours Activity	-	In the Afternoon (Tourism)	Every time (Economic and Business)
Air Quality (Aqi)	<50 Source: U.S. U.S. Embassy and Consulates in Indonesia	15,5	5,6
Factor Affecting	-	Materials, Geometry, Frequency, and Vegetation	Materials and Frequency

cooler temperature than Chinatown, even though both are far from the ideal condition of 27-28°C.

The formation of micro-climate in Old Town area was more influenced by land cover material, geometry, traffic frequency, and the presence of vegetation. Meanwhile, Chinatown was more affected by land cover materials, land cover, and traffic rates. In general, both towns were affected by the conditions of land cover material and traffic due to tourism, economic and business activities.

In Old Town, land cover materials were produced from paving, while historical buildings generally portrayed brightly coloured concrete material structures. The bright colours further increased the surface temperature due to heat reflection and increase in light effects. In addition, the presence of vegetation also influenced the formation of air temperature with higher values during the day above the open ground surface than under the shade as solar radiation on plants are not returned (Lakitan, 2004). Locations with high intensity vegetation tend to effectively reduce air temperature. Meanwhile, areas with high traffic rates and large geometric values generated warmer climate. The building geometry (the ratio of the building's height to the road and its facing orientation) is an important factor known to serve as an indicator for assessing thermal safety in open space (Dursun & Yavas, 2015). Furthermore, building orientation also affects shadow formation, where the best pattern is assumed to face south.

To create a comfortable micro-climate, the arrangement and placement of vegetation is carefully considered (Boutet, 1987). In Old Town, the vegetation was assigned to areas with low thermal comfort levels and high temperatures. Maximization of hanging, potted, vine, and hydroponic vegetation is highly recommended to prevent damaging the natural structure of the existing cover in the cultural heritage area. Conversely, Old Town contained some available land to serve as passive green open space for certain outdoor activities. In addition, the optimization of public transportation, including Bus Trans Semarang and proper parking arrangements is assumed to effectively minimize air pollution and further manage regional traffic activities. Traffic emissions present a significant impact on outdoor thermal comfort as a result of air pollution (Li et al., 2020).

The frequency of traffic directly influences the formation of micro-climate in Chinatown. According to Johansson (2006), materials from land cover components affect the value of reflection and sunlight absorption. The road is made of paving and asphalt materials, while the building is brightly coloured, thereby forming hot climate, where less heat is absorbed. In addition, the land cover generated is very minimal thereby providing limited spaces between buildings. Similarly, as one of the trade and service areas and settlements, traffic in Chinatown is always busy daily. However, this is different from the Old City, where major activities are carried out in the afternoon. Moreover, the position of the sun at certain period, as well as the direction towards the building shows significant

effects on lower surface shadows (Bourbia & Awbi, 2004). The shade from the building greatly reduces the high temperatures occurring in the morning and evening, however, the building orientation does not affect structures with high density. Therefore, vegetation is recommended for these areas in an effort to minimize increasing temperatures.

Chinatown is a protected cultural heritage in Semarang, therefore, there is need to minimize the rate of development causing damage to natural structures through the provision of portable vegetation in pots, vines, and hydroponics to create a serene atmosphere. The selection of hydroponic formation in public space Chinatown varies from Old Town due to a relatively narrow landscape, due to the appearance of more streamlined and easily modified hydroponics in areas with greater residential activities during the day. According to Hendrawati (2016), the provision of water pipes tends to create a peaceful climate, therefore, this plant type is suitable for storage of water and green plants. Apart from vegetation, traffic regulation and activities, such as the *Trans Semarang* public transportation, are also recommended to minimize air pollution and improve connections between areas in Old Town.

CONCLUSION

This study aims to analyse surface temperature in Old Town and Chinatown, Semarang through Thermal Comfort Measurement. Measurement was implemented by collected the microclimate data's such as solar lighting, wind speed, and air temperature as well as the external thermal comfort, i.e., air temperature, wind speed and humidity in the morning, afternoon, and evening. Three stages for evaluate the physical conditions of Old Town and Chinatown are inverse distance weighted (IDW), Thermal Comfort Calculation, and Micro-climate Modelling. The results of thermal comfort measurements in Old Town and Chinatown are categorized as uncomfortable public space for outdoor activities. In general, thermal comfort value is estimated above 27°C, with the highest temperatures occurring at station 4 and station 3. The simulation results and correlations in public space Old Town showed land cover material, road geometry to buildings (H/W), presence of vegetation, and traffic frequency are urban design elements with significant effect on micro-climate formation. Meanwhile, land cover material and traffic rate or environmental activities indicated a considerable consequence in public space Chinatown. In addition, the correlation results revealed building orientation close to the sun also influences shadow formation. The results of data analysis affirmed the presence of shadows with a high tendency to reduce air temperature.

Furthermore, the general concept of applying for increase the thermal comfort involves urban design element factors. The application of environmental adaptation, e.g., optimization of abandoned land as green open spaces, improving the provision of potted gardens, creeping vegetation on building walls, enhancing the use of public transportation

modes, boosting parking pockets, and procuring tourist rickshaws. Optimizing public transportation, procurement of potted plants, hanging plants on building canopy, and vines on building walls are very effective in maintaining a feasible temperature in public space especially Chinatown.

ACKNOWLEDGEMENT

The author is grateful to the “Direktorat Riset dan Pengabdian Masyarakat, Deputi Bidang Penguatan Riset dan Pengembangan, Kementerian Riset dan Teknologi/Badan Riset dan Inovasi Nasional” for funding this research through the Penelitian Dasar Unggulan Perguruan Tinggi (PDUPT) Grant 2020 of Diponegoro University.

REFERENCES

- Bourbia, F., & Awbi, H. B. (2004). Building cluster and shading in urban canyon for hot dry climate part 2: Shading simulations. *Renewable Energy*, 29(2), 291-301. [https://doi.org/10.1016/S0960-1481\(03\)00171-X](https://doi.org/10.1016/S0960-1481(03)00171-X)
- Boutet, T. S. (1987). *Controlling air movement: A manual for architects and builder*. McGraw-Hill.
- Djukic, A., Vukmirovic, M., & Stankovic, S. (2016). Principles of climate sensitive urban design analysis in identification of suitable urban design proposals. Case study: Central zone of Leskovac competition. *Energy and Buildings*, 115, 23-35. <https://doi.org/10.1016/j.enbuild.2015.03.057>
- Donaghy, K. (2007). Climate change and planning: Responding to the challenge. *The Town Planning Review*, 78(4), i-ix. <https://doi.org/10.3828/tpr.78.4.1>
- Dursun, D., & Yavas, M. (2015). Climate-sensitive urban design in cold climate zone: The city of Erzurum, Turkey. *International Review for Spatial Planning and Sustainable Development*, 3(1), 17-38. https://doi.org/10.14246/irspds.3.1_17
- Emmanuel, M. R. (2005). *An urban approach to climate-sensitive design*. Spon Press.
- Gholipour, Y., Shahbazi, M. M., & Behnia, A. (2013). An improved version of inverse distance weighting metamodel assisted harmony search algorithm for truss design optimization. *Latin American Journal of Solids and Structures*, 10(2), 283-300. <https://doi.org/10.1590/S1679-78252013000200004>
- Groat, L., & Wang, D. (2002). *Architectural research methods*. John Wiley & Sons, Inc.
- Hakim, L. (2013). Kajian arsitektur lanskap rumah tradisional Bali sebagai pendekatan desain arsitektur ekologis [Study of traditional balinese house landscape architecture as an ecological architectural design approach]. *NALARs*, 12(1), 85-103. <https://doi.org/10.24853/nalars.12.1.%25p>
- Handayani, W., Rudiarto, I., Setyono, J. S., Chigbu, U. E., & Sukmawati, A. M. (2017). Vulnerability assessment : A comparison of three different city sizes in the coastal area of Central Java, Indonesia. *Advances in Climate Change Research*, 8(4), 286-296. <https://doi.org/10.1016/j.accre.2017.11.002>
- Handoko. (1995). *Klimatologi dasar: Landasan pemahaman fisik atmosfer dan unsur-unsur iklim* (Ed. 2) [Basic climatology: The foundation for physical understanding of the atmosphere and the elements of climate (2nd Ed.)]. Pustaka Jaya.

- Hendrawati, D. (2016). Air sebagai alat pengendali iklim mikro dalam bangunan studi kasus: Taman Sari Royal Heritage Spa, Hotel Sheraton Mustika Yogyakarta [Water as microclimate control tool in buildings case study: Taman Sari Royal Heritage Spa, Hotel Sheraton Mustika Yogyakarta]. *Jurnal Teknik Sipil dan Perencanaan*, 18(2), 97-106. <https://doi.org/10.15294/jtsp.v18i2.7477>
- Johansson, E. (2006). Influence of urban geometry on outdoor thermal comfort in a hot dry climate: A study in Fez, Morocco. *Building and Environment*, 41, 1326-1338. <https://doi.org/10.1016/j.buildenv.2005.05.022>
- Kaya, N., & Mengi, O. (2011, October 24-28). *How sensitive we build to climate? Design for comfortable urban environment*. 47th ISOCARP Congress, Wuhan, China.
- Koch-Nielsen, H. (2002). *Stay cool: A design guide for the built environment in hot climates* (1st Ed.). Routledge. <https://doi.org/10.4324/9781315074429>
- Koerniawan, M. D. (2015). *The simulation study of thermal comfort in urban open spaces of commercial area using EnviMet software*. AIJ Japan.
- Kusumastuty, K. D., Poerbo, H. W., & Koerniawan, M. D. (2018). Climate-sensitive urban design through Envi-Met simulation: Case study in Kemayoran, Jakarta. In *IOP Conference Series: Earth and Environmental Science* (Vol. 129, No. 1, p. 012036). IOP Publishing. <https://doi.org/10.1088/1755-1315/129/1/012036>
- Lakitan, B. (2004). *Fundamental of plant physiology*. PT Raja Grafindo Persada.
- Laurie, M. (1990). *Pengantar kepada arsitektur pertamanan* [Introduction to landscape architecture]. Bandung Intermatra.
- Lembaran Daerah Kota Semarang. (2003). *Rencana tata bangunan dan lingkungan (RTBL) kawasan Kota Lama* (No. 4, Seri E) [Building and environmental planning in old town]. Kota Semarang, Indonesia.
- Li, Z., Zhang, H., Wen, C., Yang, A., & Juan, Y. (2020). Effects of frontal area density on outdoor thermal comfort and air quality. *Building and Environment*, 180(June), Article 107028. <https://doi.org/10.1016/j.buildenv.2020.107028>
- Lin, T. P. (2009). Thermal perception, adaptation and attendance in a public square in hot and humid regions. *Building and Environment*, 44(10), 2017–2026. <https://doi.org/10.1016/j.buildenv.2009.02.004>
- Mathew, A., Khandelwal, S., & Kaul, N. (2018). Investigating spatio-temporal surface urban heat island growth over Jaipur City using geospatial techniques. *Sustainable Cities and Society*, 40, 484-500. <https://doi.org/10.1016/j.scs.2018.04.018>
- McGregor, G. R., & Nieuwolt, S. (1998). *Tropical climatology, an introduction to the climate low latitude* (2nd Ed.). Wiley.
- Meziani, R. (2016). Study of the relationship between building arrangement and visibility of open spaces based on a simplified area evaluation. *Journal of Civil Engineering and Architecture*, 10(12), 1364-1372. <https://doi.org/10.17265/1934-7359/2016.12.007>
- Mirzaei, P. A., & Haghighat, F. (2010). A novel approach to enhance outdoor air quality: Pedestrian ventilation system. *Building and Environment*, 45(7), 1582-1593. <https://doi.org/10.1016/j.buildenv.2010.01.001>
- Nichol, J. E., Fung, W. Y., Lam, K., & Wong, M. S. (2009). Urban heat island diagnosis using ASTER satellite images and ‘ in situ ’ air temperature. *Atmospheric Research*, 94, 276-284. <https://doi.org/10.1016/j.atmosres.2009.06.011>

- Nikolopoulou, M., & Lykoudis, S. (2006). Thermal comfort in outdoor urban spaces: Analysis across different european countries. *Building and Environment*, 41(11), 1455-1470. <https://doi.org/https://doi.org/10.1016/j.buildenv.2005.05.031>
- Oke, T. R. (1976). The distinction between canopy and boundary - layer urban heat islands. *Atmosphere*, 14(4), 268-277. <https://doi.org/10.1080/00046973.1976.9648422>
- Oke, T. R. (2006). Towards better scientific communication in urban climate. *Theoretical and Applied Climatology*, 84(December), 179-190. <https://doi.org/10.1007/s00704-005-0153-0>
- Pamungkas, B. A., Munibah, K., & Soma, S. (2019). Land use changes and relation to urban heat island. Case study: Semarang City, Central Java. In *IOP Conference Series: Earth and Environmental Science* (Vol. 399, No. 1, p. 012069). IOP Publishing. <https://doi.org/10.1088/1755-1315/399/1/012069>
- Pramono, G. H. (2008). Akurasi metode IDW dan kriging untuk interpolasi sebaran sedimen tersuspensi [IDW and kriging method accuracy for interpolation of suspended sediment distribution]. *Forum Geografi*, 22(1), 97-110.
- Pratiwo. (2004, August 23-25). *The city lanning of Semarang 1900-1970*. The 1st International Urban Conference, Surabaya, Indonesia.
- Purwantara, S. (2015). Studi temperatur udara terkini di wilayah di Jawa Tengah dan DIY [Study of air temperature in in Central Java and DI Yogyakarta]. *Geomedia Majalah Ilmiah dan Informasi Kegeografian*, 13(1). <https://doi.org/10.21831/gm.v13i1.4476>
- Purwanto, E. (2014). Privatisasi ruang publik dari civic centre menjadi central business district [A case study of Simpang Lima Area Semarang]. *Jurnal Tataloka*, 16(3), 153. <https://doi.org/10.14710/tataloka.16.3.153-167>
- Putri, S. N. A. K. (2020). *Revitalisasi kawasan Kota Lama Semarang periode tahun 2019: Persepsi wisatawan dan ahli terhadap daya tarik wisata* [Revitalization of the Old City of Semarang in 2019: Perceptions of tourists and experts on tourist attractions]. Diponegoro University.
- Ragheb, A. A., El-Darwish, I. I., & Ahmed, S. (2016). Microclimate and Human comfort considerations in planning a historic urban quarter. *International Journal of Sustainable Built Environment*, 5(1), 156-167. <https://doi.org/https://doi.org/10.1016/j.ijbsbe.2016.03.003>
- Shashua-bar, L., & Hoffman, M. E. (2003). Geometry and orientation aspects in passive cooling of canyon streets with trees. *Energy and Buildings*, 35, 61-68.
- Shishegar, N. (2013). Street design and urban microclimate: Analyzing the effects of street geometry and orientation on airflow and solar access in urban canyons. *Journal of Clean Energy Technologies*, 1(1), 52-56. <https://doi.org/10.7763/jocet.2013.v1.13>
- Stathopoulos, T., Wu, H., & Zacharias, J. (2004). Outdoor human comfort in an urban climate. *Building and Environment*, 39, 297-305. <https://doi.org/10.1016/j.buildenv.2003.09.001>
- Tapias, E., & Schmitt, G. (2014). Climate-sensitive urban growth: Outdoor thermal comfort as an indicator for the design of urban spaces. *WIT Transactions on Ecology and the Environment*, 191, 623-634. <https://doi.org/10.2495/SC140521>

- Yeang, K. (2006). *Ecodesign: A manual for ecological design*. John Wiley & Sons Ltd.
- Yu, C., & Hien, W. N. (2009). Thermal impact of strategic landscaping in cities: A Review. *Advances in Building Energy Research*, 3(1), 237-260. <https://doi.org/10.3763/aber.2009.0309>
- Zikra, M., Suntoyo, & Lukijanto. (2015). Climate change impacts on Indonesian coastal areas. *Procedia Earth and Planetary Science*, 14, 57-63. <https://doi.org/10.1016/j.proeps.2015.07.085>



Efficient Solid Waste Management in Prai Industrial Area through GIS using Dijkstra and Travelling Salesman Problem Algorithms

Gaeithry Manoharam¹, Mohd. Tahir Ismail¹, Ismail Ahmad Abir² and Majid Khan Majahar Ali^{1*}

¹*School of Mathematical Sciences, Universiti Sains Malaysia, 11800 USM, Penang, Malaysia*

²*School of Physics, Universiti Sains Malaysia, 11800 USM, Penang, Malaysia*

ABSTRACT

The fourth industrial revolution (IR 4.0) supports new solid waste management and effective routing system for collection and transport of solid wastes, especially in achieving Penang 2030 vision to become a pollution free smart city. This study will enhance Seberang Perai Municipal Council (MBSP) solid waste routing system in Prai industrial area by implementing Dijkstra and Travelling Salesman Problem (TSP) algorithms using Geographic Information System version 10.1. The route optimization study involved 24 companies in Phase I, Phase II, and Phase IV of Prai industrial area. The authority is currently using only one route to transfer the waste-to-waste transfer station. The Dijkstra algorithm can optimize alternative route 1 distance by 19.74% whereby alternative route 2 ended up with extra distance by 3.73% compared to existing single route used by MBSP. The forward Dijkstra algorithm involves single direction route with cleaning depot (source) as starting point and waste transfer station (destination) as ending point. TSP algorithm is having advantage with return direction route. The alternative route 1 evaluated through TSP algorithm gave shorter distance by 6.61% compared to existing route. Alternative route 1 evaluated through Dijkstra algorithm is potential to save fuel cost by 19.75%. Existing route carries 9.2% per year of transportation carbon emission level. The alternative

route 1 assessed through Dijkstra and TSP algorithms reported lower carbon emission level at 7.4% per year and 8.6% per year, respectively. Findings of this study can help in improving MBSP's routing system and realize Penang 2030 vision.

Keywords: Carbon emission, Dijkstra's algorithm, geographic information system, solid waste management, transportation

ARTICLE INFO

Article history:

Received: 08 September 2020

Accepted: 07 December 2020

Published: 31 July 2021

DOI: <https://doi.org/10.47836/pjst.29.3.02>

E-mail addresses:

gaeithry@gmail.com (Gaeithry Manoharam)

m.tahir@usm.my (Mohd. Tahir Ismail)

iahmadabir@usm.my (Ismail Ahmad Abir)

majidkhanmajaharali@usm.my (Majid Khan Majahar Ali)

* Corresponding author

INTRODUCTION

Modernization and industrialization keep increase managing cost of municipal facilities with waste management operating cost at the top (Omran et al., 2009). Malaysia, a fast-growing country in Asia with no exception to the dilemma of increase in waste generation (Williams, 2012) due to the rapid development and industrialization. In most municipalities in Malaysia, the local government is the one supervising solid waste collection (Penang State Government, 2016). In year 2014, Malaysia spent RM 3.018 billion to cover for the operating expenses of waste management in the country (National Solid Waste Management Department, 2013). Seberang Perai Municipal Council (MBSP) allocated RM 1.241 billion between 2006 and 2010 to cover the cost of solid waste management (SWM). The state and local governments are still responsible for the operating cost on top of financial support by Federal Government for the fundamental expenses. Rise in fuel cost is indirectly impacting operational costs further (Penang State Government, 2016). Increase in industrial zones and living estates, surging waste generation hence becoming a crucial issue all over the world in SWM including Penang, Malaysia (Kumpulan Utusan, 2017).

Transportation is a primary component of any SWM system. It is important in transferring waste from the point of generation to the transfer station or final landfill site (Zam et al., 2007). MBSP faced challenges to identify distance between waste collection points especially in Prai industrial area. It is important to optimize the travelling distance from one waste collection point to another. This study was initiated to identify an optimal route for waste collections and transportation using Geographic Information System (GIS) to optimize the travelling distance, time, and fuel consumption.

The application of Geographic Information System (GIS) in SWM by different countries shown in Table 1. Table 1 is also revealing limited studies done in Malaysia covering the scope of SWM at industrial areas. Additionally, there is no evidence on any study conducted at Prai industrial area using Dijkstra and Traveling Salesman Problem (TSP) algorithms.

This research focused on route optimization of SWM by MBSP at Prai industrial area. The intention of this study is to discover alternative route using GIS Software, compare the route established by MBSP and assess shortest route identified by GIS. Both Dijkstra and TSP algorithms used to identify the minimum distance path. This leads to possible savings in operating cost and waste transferring time. The comparison summary of fuel cost and carbon emissions is a useful input for management of MBSP to march towards green city by 2030.

Following aspects taken into consideration for this research:

1. Transportation of municipal waste generated in Prai industrial area to Ampang Jajar Waste Transfer Station.
2. Directed graph mechanism used for Dijkstra algorithm and Hamilton cycle mechanism used for TSP algorithm.

Table 1
The practice of solid waste management in different countries

No	Author	Location	Method	Criteria
1	(Anghinolfi et al., 2013)	Italy	GIS & MILP Model	Minimize collection and transportation costs.
2	(Chipumuro et al., 2014)	Zimbabwe	Dijkstra Algorithm	Reduction of 10.45% in the total distance travelled.
3	(Bovwe, et al., 2016)	Nigeria	GIS& Ant Colony	
4	(Bhambulkar, 2011)	India	ArcGIS Network Analyst	Route length
5	(Ahmad, 2016)	Qatar	GIS	Time duration
6	(Ghose et al., 2006)	India	GIS	Route Optimization
7	(Patel et al., 2016)	India	Network Analyst	
8	(Beijoco et al., 2011)	Portugal	GIS	
9	(Zam et al., 2007)	Phuentsholing	GIS	
10	(Shamshiry et al., 2011)	Malaysia	Response surface methods (RSM)	Less operation cost and fuel consumption.
11	(Singh et al., 2014)	Kanpur	Dijkstra Algorithm	Get the shortest path and shortest route for one- way, two-way
12	(Kinobe et al., 2015)	Kampal	GIS	Diminish the costs of managing wastes and environmental.
13	(Nguyen-Trong et al., 2017)	Vietnam	GIS	Reduce operation cost of SWM
14	(Tavares et al., 2008)	Portugal	3D route modelling	Savings in fuel & shortest distance

3. Carbon emission rate calculated based on weight (kg) of collected waste and diesel used by trucks in a month to travel between Prai industrial area and Ampang Jajar Waste Transfer Station.
4. Only solid waste consist leftover food, plastic and paper is considered as waste for the purpose of this study. Chemical, metal, and landscaping waste are excluded from this study.
5. The waste collection schedule limited to period between 8 am and 4 pm. The travelling time between points is also excluded in this study.

Network analysis finds the most effective path to solve a network problem by calculating the shortest route with lowest cost on the network from one stop to another or from one stop to several stops (Stewart, 2005). The layout of the waste collection route needs to be well-planned, and the collection should adhere to the planned schedule, as it will help to reduce the unnecessary amount in the budget. Penang control their SWM autonomously. City Council of Penang Island (MBPP) is the administrative body for the island while Municipal Council of Seberang Perai (MBSP) manages the mainland area (Omran et al., 2009). Penang Island is divided into eight zones, consist of Tanjung Tokong,

Batu Maung, Gelugor, Air Itam, Pulau Tikus, Jelutong, Padang Kota Lama, and Balik Pulau. On the other hand, Seberang Perai divided into northern, central, and southern zones which governed by MBSP.

Malaysia's industrial areas are expanding annually. Free industrial zones located in Seberang Perai are second largest industrial area for the State of Penang. The Prai industrial area is divided into four phases, i.e., Prai Industrial Zone Phase I, II, III, and IV, and about 440 industries are operating in these industrial zones (Penang State Government, 2016). According to a MBSP Operation Manager, even though there are 440 companies in Prai Industrial Zone, MBSP only collects solid wastes from 24 companies who pay fees for garbage collection. MBSP collects about 710 kg of wastes in a day, and these companies produce about 252.72 tonnes of waste in a year.

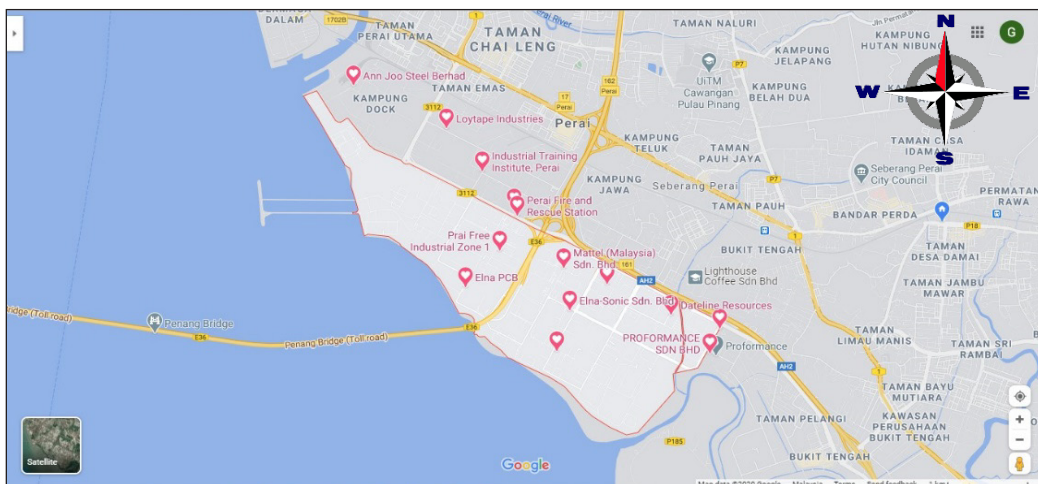


Figure 1. The map of Prai Industrial Zone Phase I research area

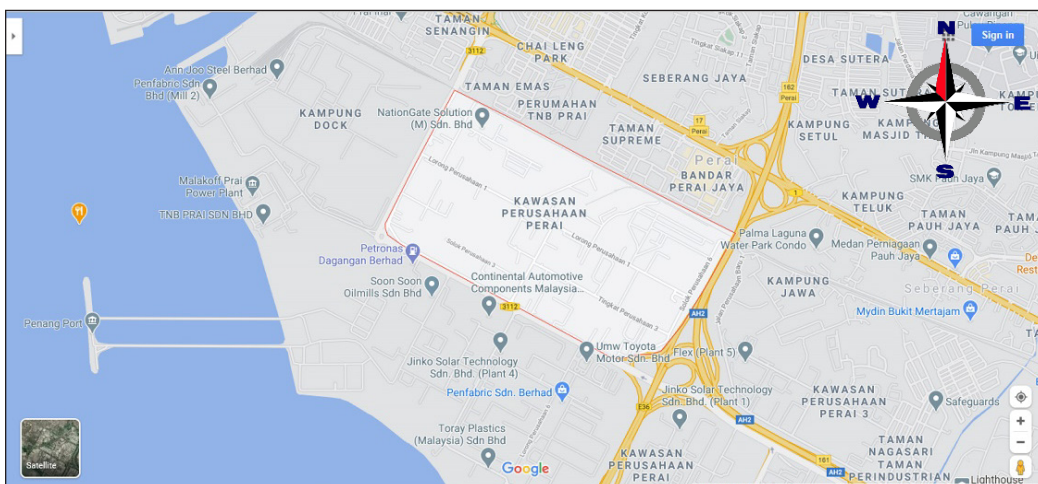


Figure 2. The map of Prai Industrial Zone Phase II research area

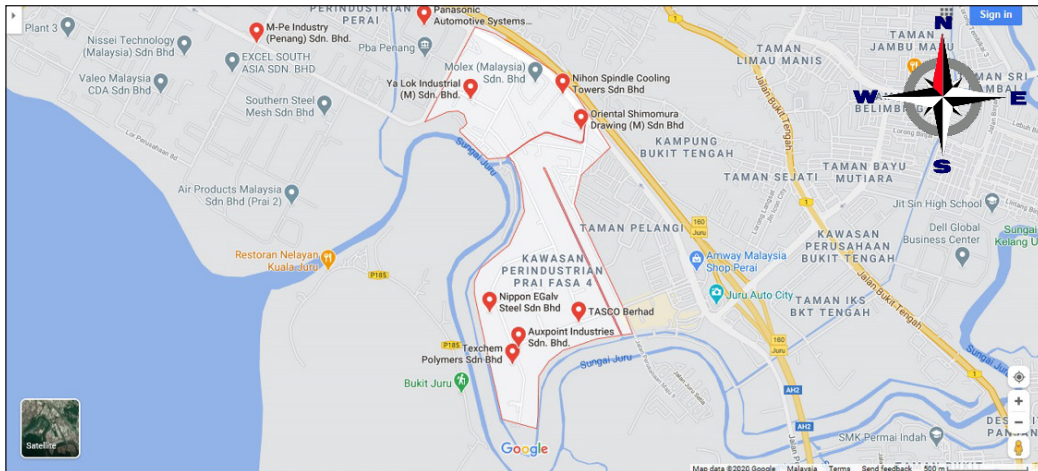


Figure 3. The map of Prai Industrial Zone Phase IV research area

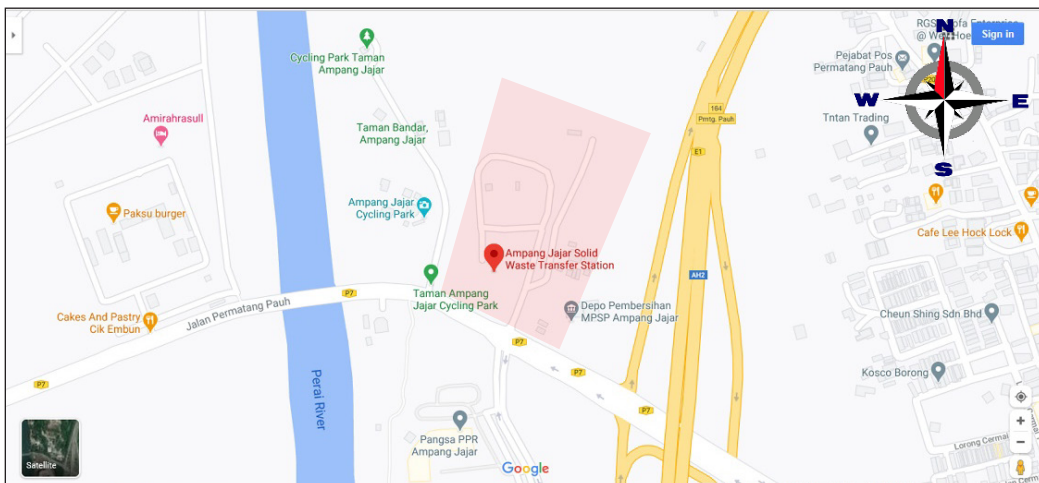


Figure 4. The map of Ampang Jajar waste transfer station research area

In this study paper, firstly the existing route used by MBSP and alternative routes for Prai Industrial Zone Phase I, II and IV were assessed using GIS. Secondly, the shortest path was determined using Dijkstra and TSP algorithms. Fuel cost and carbon emissions rate were determined for existing and alternative routes as a final part of this study. The same method has been used in Vietnam, to reduce the operation cost of SWM (Nguyen-Trong et al., 2017).

Figures 1-3 illustrate the map of Prai Industrial Zones of Penang mainland. The location indicated in Figure 4 represent the Ampang Jajar waste transfer station. MBSP collects and segregates all industrial waste from selected factories at the waste transfer station (Google Map view).

MATERIALS AND METHODS

Data

Data collection is done after reviewing previous studies. This study used both quantitative and qualitative methods. Quantitative data from MBSP was obtained including collection point, collection time, distance travelled, and quantity of labour involved. Meanwhile, a qualitative survey was conducted in Prai Industrial Zone using Global Positioning System (GPS) coordinate for the 24 companies located in Phase I, II and IV.

After data collection, the Dijkstra and TSP algorithms were used in ArcGIS version 10.1 to construct the shortest route. Then the shortest route will be compared with the existing and other alternative routes. The classic Dijkstra algorithm clarifies the single-source, shortest-path problem of the weighted graph in the ArcGIS. The route solver has the option to generate the optimal strings of visited stop locations while TSP is a combination problem solver, meaning there is no straightforward way to find the best sequence. Metaheuristics method used by TSP is also handles time windows during collection stops. It finds the optimal stops to visit and produce shortest distance and time. Figure 5 shows the process flow chart followed during the research.

Data collection was done through interviewing Operation Manager, Industrial Zone from MBSP. It was revealed during the interview session that single garbage truck is being occupied to collect industrial waste from Prai Industrial Zones. Solid waste is collected daily from those 24 paying companies between 7

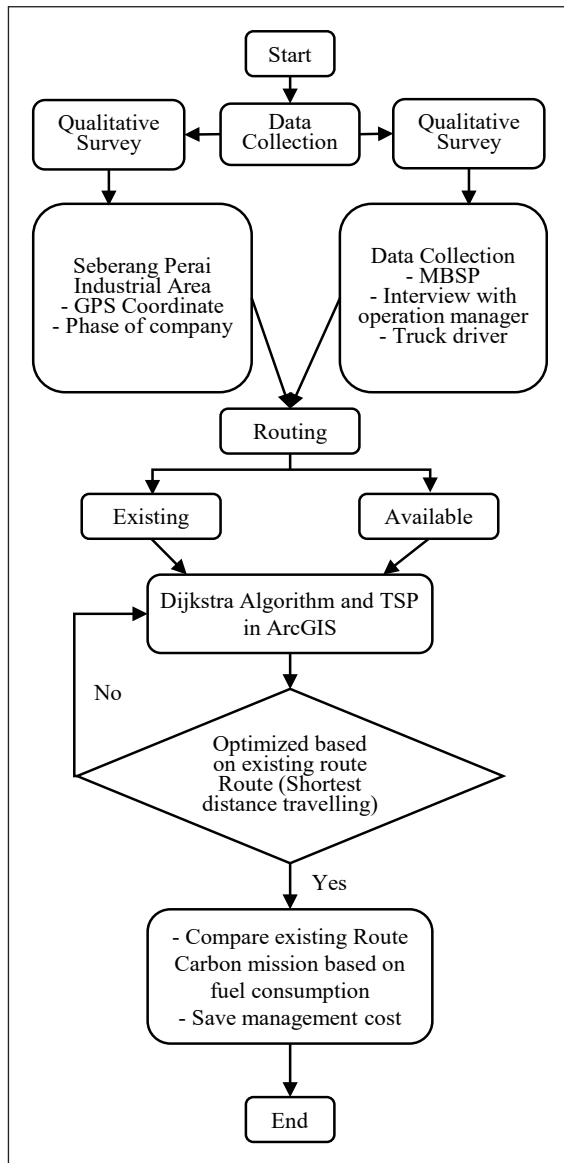


Figure 5. Research process flow chart (Self-design)

a.m. and 7 p.m. Waste collection fees to follow the contract transpired between industries management and MBSP. The number of companies which are paying collection fees to MBSP are listed in Table 2 according to phases of Prai Industrial Zone.

Table 2
Number of industries that paying collection fees in the Prai Industrial Zones

Prai Industrial Zone	Total Factories	Fee Paying Factories
Phase I	239	13
Phase II	100	7
Phase III	42	0
Phase IV	59	4
Total	440	24

Collection Route

The study was conducted in three phases in Prai industrial area. GPS coordinate of collection points (locations of 24 companies) and Ampang jajar Waste Transfer Station identified through high-resolution GPS technology which can be classified as qualitative method. Secondly, the latitude and longitude coordinates for each station entered and mapped in GIS using "Add XY Data" method. Based on entered GPS coordinates, GIS is capable to identify the exact location of the collection points and waste transfer station. Table 3 represents the latitude and longitude of 24 companies in the Prai industrial area.

Table 3
Companies in Prai Industrial Zone Phase I, II and IV

No	Phases	Company names	Latitude	Longitude
1	I	Ann Joo	5.381795	100.375432
2		TNB Perai	5.351284	100.410467
3		POS MPSP	5.361493	100.385988
4		Irichi	5.364293	100.391606
5		ACM Perai	5.358480	100.403987
6		Parker	5.354693	100.410798
7		Food Court MPSP 5	5.353382	100.410995
8		Food Court MPSP Per 6	5.352732	100.405341
9		Food Court MPSP Per 8	5.354020	100.399807
10		LBSB	5.355230	100.410995
11		Loytape Industry	5.37598	100.387418
12		Ann Joo	5.381795	100.375432
13		Mattel	5.360842	100.398997
14		Kastam (MPSP)	5.356349	100.400581
15	II	Loytape Industry	5.37598	100.387418
16		Nation Gate	5.379458	100.387001

Table 3 (continue)

No	Phases	Company names	Latitude	Longitude
17	II	Food Court 3M	5.369801	100.38913
18		ILP Perai	5.372186	100.389312
19		Kastam	5.367332	100.393474
20		Bomba	5.366582	100.3938781
21	IV	Ais Top	5.353314	100.411877
22		Food Court Maju 1 (Shell)	5.351909	100.419253
23		LRG Maju 1 (Bawal)	5.347009	100.417776
24		Kampung Dock	5.345383	100.423161

(Source: MBSP Depot & Google Map)

Geographical Information System (GIS)

The Global Positioning System (GPS) technology was used to optimize the route by using collected data. GPS was used to collect data that later transferred and integrated in the GIS software. The Network Analysis extension in the GIS application was used to calculate the shortest distance. Location of the collection point, waste transfer station, and road network are also considered in the GIS software.

The standard measurement to determine the optimal route or path to specified destination is called metric. Optimal routes are determined by evaluating the metrics and these metrics differ depending on the nature of the routing algorithm. GIS is a widely used application in daily routine involving logistics and transportation industries. The GIS software transforms data from attribute table to topology maps.

Dijkstra Algorithm

Dijkstra algorithm is a one of the mathematical models used to find the shortest path. As noted by Ahuja et al. (1993), Dijkstra algorithm finds the shortest paths from point node S (starting point) to all other nodes in a network with nonnegative arc lengths. Dijkstra algorithm provides a distance labelled $d(i)$ with each node i , which is an upper bound on the shortest path length to node i . At any intermediate step, the algorithm divides the nodes into two groups, which are permanent labelled and temporary labelled. The distance label to any permanent node is defined as the shortest distance from the source to that node. For any temporary node, the distance label is an upper bound on the shortest path distance to that node.

In Dijkstra algorithm, the operation of selecting the minimum distance is labelled as a node selection operation. The operation of checking whether the current labels for nodes i and j satisfy the condition $d(j) > d(i) + C_{ij}$ and, if so, then setting $d(j) = d(i) + C_{ij}$ as a distance update operation. Each shortest path algorithm can determine the tree to

calculate the shortest route distances. The existence of the shortest path tree relies on the following property.

Property 1.1. Ahuja et al., (1993). If the path $S = i_1 - i_2 - \dots - i_h = k$ is the shortest path from node s to node k , then for every $q = 2, 3, \dots, h - 1$, the subpath $s = i_1 - i_2 - \dots - i_q$ is the shortest path from the source node to node i_q .

Let $d(-)$ denotes the shortest path. Property 1.1 mentioned that if P is the shortest path from the source node to some node k , then $d_{(j)} = d_{(i)} + c_{ij}$ for every arc $(i, j) \in P$, the converse of this result is also true; that is, if $d_{(j)} = d_{(i)} + c_{(ij)}$ for every arc in a directed path P from the source to node k , then P must be the shortest path. To establish this result, let $S = i_1 - i_2 - \dots - i_h = k$ be the node sequence in P . Then where $d(i_1) = 0$. By assumption, $d_{(j)} - d_{(i)} = C_{ij}$ for every arc $(i, j) \in P$. using Equation 1.

$$d(k) = c_{i_{h-1}i_h} + C_{i_{h-2}i_{h-1}} + \dots + C_{i_1i_2} = \sum_{i,j \in P} C_{ij} \quad (1)$$

Travelling Salesman Problem (TSP)

As per the Dijkstra algorithm, TSP is also employed in ArcGIS to solve the shortest path. TSP employed any type of constraint that enforces the provision of the problem (Gutin & Punnen, 2002). The below code is used:

n = count of tour stops or count of nodes in the network

i, j, k = indices of stops that can take integer values from 1 to n

t = steps in the route between the stops

$x_{ijt} = 1$ if the edge of the network from i to j is used in step t of the route, 0 otherwise

d_{ij} = distance from stop i to stop j

A simple version of the problem involves visiting subsequent stops from given locations (24 companies) and heading back to the starting point (cleaning depot). The perfect solution is one that minimizes a waste truck's overall travelled distance. The objective function (Z) is the sum of all costs (distances) selected tour elements as shown in Equation 2:

Minimize

$$Z = \sum_{i=1}^n \sum_{j=1}^n \sum_{t=1}^n d_{ij} x_{ijt} \quad (2)$$

The tour is subject to the following constraints. Since the traveler cannot travel between more than one pair of stops at one time, for all values of t , exactly one arc must be traversed, hence (Equation 3):

$$\sum_{i=1}^n \sum_{t=1}^n x_{ijt} = 1 \text{ for all } i \quad (3)$$

For each stop, i , there is just one other stop which is being reached from it, at some time, hence (Equation 4):

$$\sum_{i=1}^n \sum_{t=1}^n x_{ijt} = 1 \text{ for all } t \quad (4)$$

For all stops, there is some other stop from which it is being reached, at some time, hence (Equation 5):

$$\sum_{i=1}^n \sum_{t=1}^n x_{ijt} = 1 \text{ for all } j \quad (5)$$

When a stop is reached at time t , it must be left at time $t + I$, to exclude disconnected sub-tours that would otherwise meet all the above constraints. These sub-tour elimination constraints are formulated as (Equation 6):

$$\sum_{i=1}^n x_{ijt} = \sum_{k=1}^n x_{jkt+1} \text{ for all } j \text{ and } t \quad (6)$$

In addition to the above constraints, the decision variables must be integers taking only the value 0 or 1 (Equation 7):

$$x_{ijt} = 0, 1 \text{ for all } i, j, \text{ and } t \quad (7)$$

If n is the number of stops to be visited, there are $(n-1)!$ possible routes. As the number of stops increases computational time, it will be important to analyse all possible tours between stops to simply provide a problem that is difficult to solve. TSP is proven to be an NP-complete combination optimization problem (Bodin et al., 1983; Hoffman et al., 2013). Although specific large instances of the TSP have been solved with a combination of robust solution procedures and a great deal of computing power, the general difficulty in determining optimal solutions to even modest-sized instances of the TSP is the reason why heuristic solution procedures are employed in GIS applications. The serious consequence of employing those heuristics is the primary motivation for this article.

Like Dijkstra algorithm, TSP algorithm is also used to optimize the route. TSP is a classic algorithm to determine the minimum distance by selecting Closest Facility solution in GIS extension. Few methods and algorithms have been applied for optimizing routing system in SWM.

TSP uses Hamiltonian cycle to optimize the route. Hamiltonian cycle is involving greedy method to resolve optimization problem. Then, the TSP method must find a route for all points visited by waste collection truck. The truck starts at cleaning depot (initial node) and visit all the collection points (intermediate node) exactly once and ends its journey at the same initial point (ending node).

Carbon Emission

UNFCCC (2017) sets 40% as the recommended limit for carbon emission which increases global warming, aims to strengthen the global response to climate change. Carbon emissions calculator used in this study is based on weight of waste and fuel consumption of waste truck attributes (Menikpura & Sang-Arun, 2013).

Daily waste and fuel consumption data were obtained from MBSP Operations Manager. Table 4 shows the data of waste per month in the Prai industrial area for the existing route compared to alternative routes. Equation 8 is used to measure the carbon emissions.

Table 4
Weekly waste collection in Prai industrial area

NO	Company	(kg) per Day	Collection
1	Mattel	1200	3 days /week
2	Food Court 3M	300	Daily
3	Kampung Dok	300	Daily
4	Nation Gate	800	2 days/week
5	Ann Joo	700	2 days/week
6	Elna Sonic	200	3 days/week
7	Food Court MPSP 5	70	Daily
8	Food Court MPSP Per 6	70	Daily
9	Food Court MPSP Per 8	70	Daily
10	Kastam (MPSP)	150	2 days/week
11	Parker	100	2 days/week
12	LBSB	100	2 days/week
13	LRG Maju 1 (Bawal)	100	2 days/week
14	Food Court Maju 1 (Shell)	90	2 days/week
15	Loytape Industry	50	3 days/week
16	Kastam	60	2 days/week
17	ACM Perai	100	1 day/week
18	Bomba	50	2 days/week
19	Ais Top	50	2 days/week
20	ILP Perai	60	1 day/week
21	TNB Perai	50	1 day/week
22	POS MPSP	50	1 day/week
23	Irichi	50	1 day/week
24	Dateline Resources	10	2 days/week
Total		4780	

(Source: MBSP Depot)

$$Emission_T (kg) = \frac{Fuel (unit)}{Waste (kg)} \times energy (MJ/kg) \times EF(kg\backslash co_2) \quad (8)$$

Emission_T = Emission carbon from transportation (kg CO₂/tonnes of waste)

Fuel (unit) = Total amount of fuel consumption per month, (diesel in liter 36.42 MJ/L and natural gas 37.92 MJ/kg)

MJ = amount of energy

EF_{CO₂} = Emission Factors of CO₂ of the fuel (e.g., diesel: 0.074 kg CO₂/MJ, Natural gas: 0.056 kg CO₂/MJ)

RESULTS AND DISCUSSION

Existing Route

The GPS coordinates of companies located in Prai industrial area that getting MBSP waste collection services, processed through Network Analysis extension GIS tool to identify distance between one company to other companies. Name of the routes identified individually on the map. Figure 6 shows the input locations for GIS Network Analysis.

Figure 7 shows the attribute table for existing routes with a total length of 57.1 km based on outcome of GIS Network Analysis. MBSP truck driver using existing routes on daily basis to collect industrial waste and bring it over to Ampang Jajar waste transfer station. Movements between Prai industrial area and Ampang Jajar waste transfer station, passes through the North-South Highway.

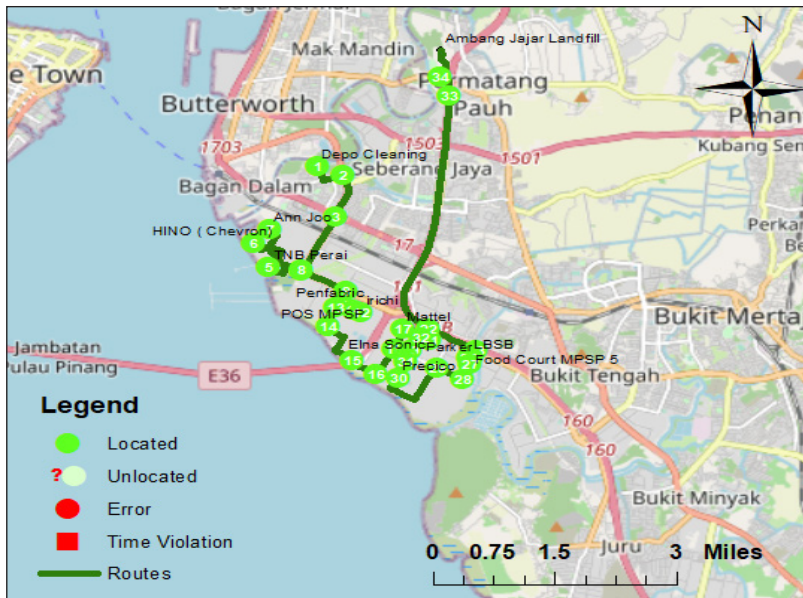


Figure 6. Existing route from Prai industrial area to Ampang Jajar waste transfer station

Routes						
ObjectID	Shape	Name	FirstStopID	LastStopID	StopCount	Total_Length
2	Polyline M	Graphic Pick 1 - Graphic Pick 60	1	60	60	57050.087186

Figure 7. Attribute table for existing route based on GIS Network Analyses

The GIS Network Analysis determined the weight and minimal distance between nodes (from one company to another), for each edge. The scanned image of the road viewed in geographic coordinates enables distances to be measured using GeoMedia’s measuring tool to measure distances in GIS. Route distance was measured in kilometers, and the minimal distance between two companies was narrow.

Alternative Route by Dijkstra Algorithm

For the current study, the speed limit for all trucks was expected to be the same. The shortest route from each collection point to the waste transfer station was created in the Network Analysis extension. The route network consists of nodes (company locations), links connecting depot (initial node) and Ampang Jajar waste transfer station (end node).

Figure 8 shows the alternative route 1 by GIS Network Analysis, node by node. In this route, each company is visited only once, and the truck did not return to the depot. The alternative route 1 (45.8 km) is shorter compared to the existing route (57.1 km). The alternative route 1 uses a route that connects to North-South Highway before reaching waste transfer station as provided in spatial map in Figure 9.

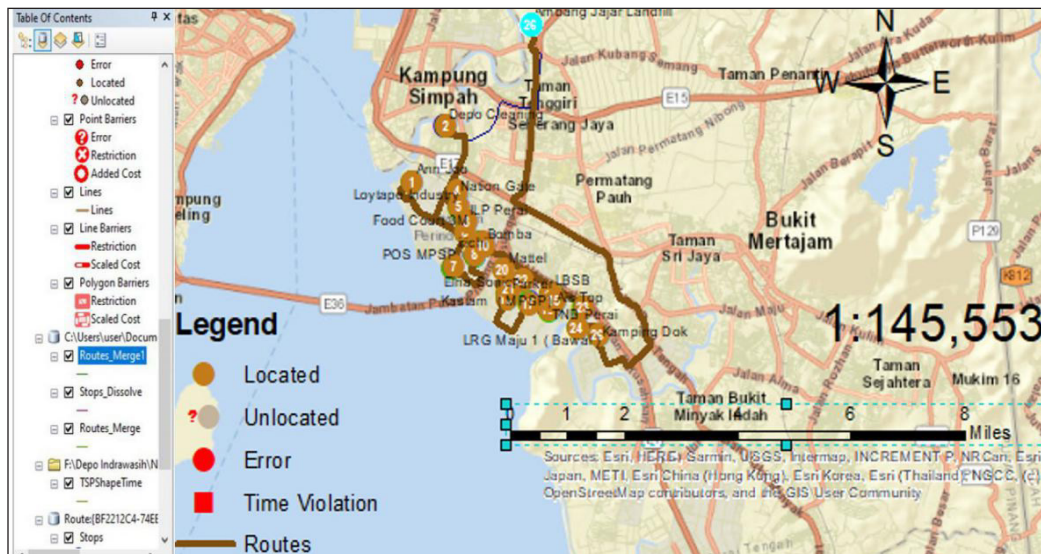


Figure 8. The alternative route 1 by GIS Network Analysis

ObjectID	Shape	Name	FirstStopID	LastStopID	StopCount	Total_Length
7	Polyline M	Location 1 - Location 26	1	26	26	45852.598884

Figure 9. The attribute table of alternative route 1 by GIS Network Analysis

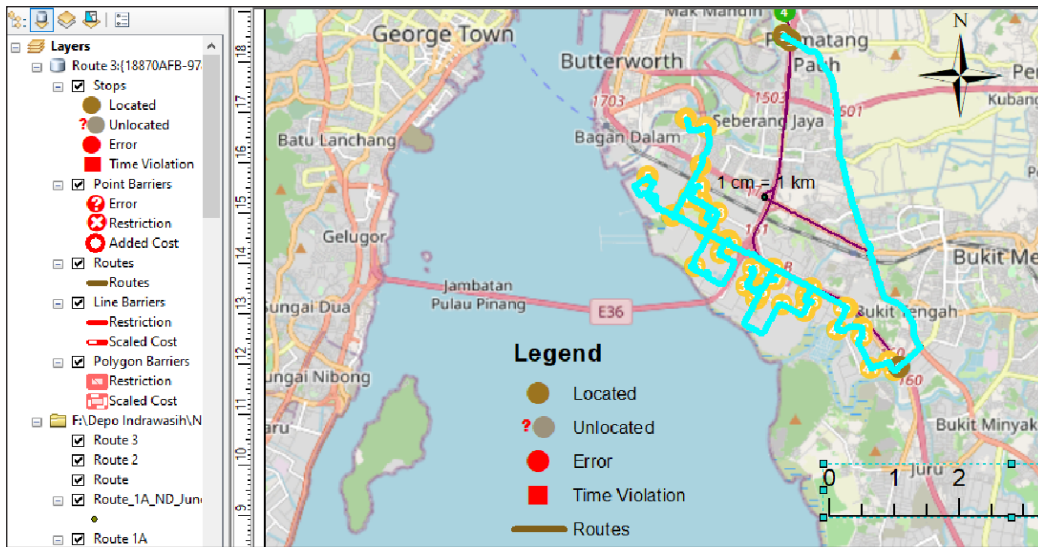


Figure 10. The alternative route 2 by GIS Network Analysis

ObjectID	Shape	Name	FirstStopID	LastStopID	StopCount	Total_Length
3	Polyline M	Graphic Pick 1 - Graphic Pick 35	1	35	26	59606.3245

Figure 11. The attribute table of alternative route 2 by GIS Network Analysis

Figure 9 is an attribute table, belonging to the spatial map shown in Figure 8, which shows the total length of each location. The total distance of traveling is also provided in this attribute table.

GIS Network Analysis also identified alternative route 2 which is 59.6 km in distance that connects to the Ampang Jajar waste transfer station through Bukit Tengah and Permatang Pauh. The alternative route 2 is longer than the existing route (57.1 km) by 2.5 km. Figure 10 shows the alternative route 2 spatial map and Figure 11 shows the alternative route 2 attribute table.

Traveling Salesman Problem (TSP) Algorithm

In this study, the adopted TSP algorithm identifies the minimal closed path that begins at cleaning depot, goes to Ann Joo company, visits the rest of 23 companies exactly once

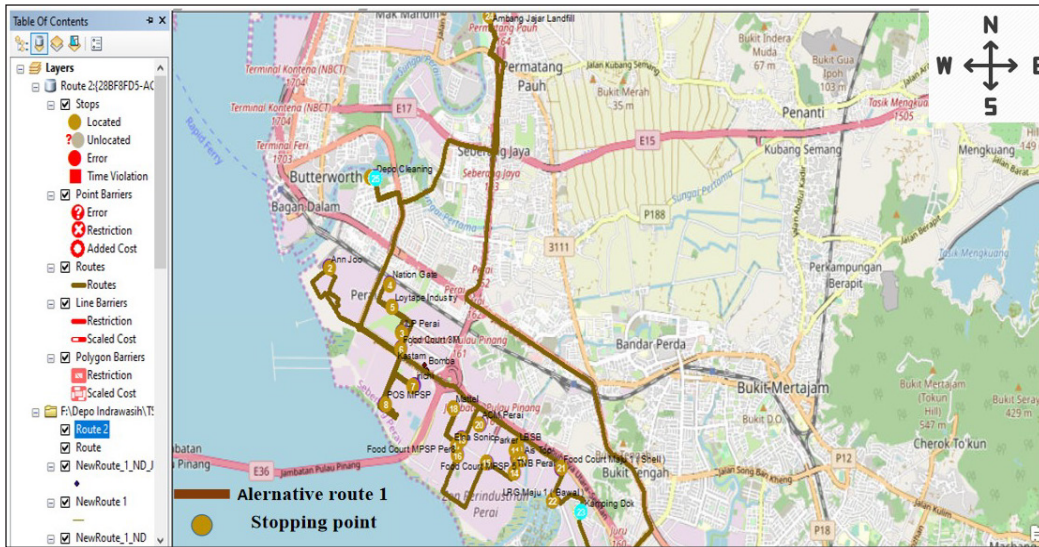


Figure 12. Propose Spatial Map of TSP table from GIS Network Analysis

Routes						
ObjectID	Shape	Name	FirstStopID	LastStopID	StopCount	Total_Length
4	Polyline M	Location 1 - Location 25	1	25	25	53250.801928

Figure 13. The attribute table of location 1 to 25 creates from TSP Network Analysis

before returning to the same cleaning depot. This study found that the TSP method can minimize travelling distance and cost. Figure 12 is a TSP spatial map of the GIS Network Analysis that is connected to each node (company). The attribute table of location 1 to 25 created from TSP Network Analysis is as shown in Figure 13.

Bonomo et al. (2012) used the same method in the waste collection problem and found that Classic TSP method can optimize distance travelled using GIS system. The solution approach, employing graph theory, mathematical programming tools and data correction process were fully discussed in that study. The proposed method reduced the distance traveled by each collection vehicle between 10% to 40% compared to the existing routes.

Comparison between Existing Routes and Proposed Routes

GIS Network Analysis delivers route direction by counting route parameter to achieve objective. The study was intended to plan the cost-efficient waste collection route for transporting waste from Prai industrial area to Ampang Jajar Waste Transfer Station. Table 5 shows the shortest distance calculation by GIS software using Dijkstra and TSP algorithms compared to existing route. Distance between individual node (company) and

total distance of identified routes summarized in the Table 5 in kilometer and percentage. The comparison is done using existing route as base.

The original collection route length is 57.7 km, whereas the alternative route 1 and alternative route 2 proposed by GIS using Dijkstra algorithm are 45.8 km and 59.2 km, respectively, while TSP proposed route is 53.3 km. Figure 14 shows the comparison chart of existing and optimized routes in the studied area.

In Table 5, the nodes are represented by the company's name and distance between nodes is provided in kilometer (km). Length of existing and alternative routes shown at the bottom of Table 5. The comparison represented in kilometer variance and percentage.

Table 5
Comparison of Shortest Path by Using GIS

From Node	To Node	Existing	(DJ)		TSP
		(km)	Alt 1 (km)	Alt 2 (km)	(km)
Depot	Ann Joo	5.1	5.1	5.1	5.1
Ann Joo	ILP Perai	8.1	8.2	8.1	8.1
ILP Perai	Nation Gate	9.6	9.6	9.6	9.6
Nation Gate	LoyTape Industry	10.3	10.3	10.3	10.3
Loytape Industry	Food Court 3M	11.3	11.4	11.3	11.3
Food Court 3M	Irichi	12.2	13.7	12.2	12.2
Irichi	Pos MBSP	13.5	17.2	13.5	13.5
Pos MBSP	Kastam	20.3	17.3	20.3	20.3
Kastam	Bomba	20.4	19.8	20.4	20.4
Bomba	LBSB	20.6	19.9	20.6	20.6
LBSB	Dateline Resources	20.8	20	20.8	20.8
Dateline Resources	Parker	20.9	20.2	20.9	20.9
Parker	FC5	21.2	20.3	21.2	21.2
FC5	Ais Top	21.9	20.6	21.7	21.9
Ais Top	TNB Perai	24.1	21.3	22.0	24.1
TNB Perai	FC6	24.4	23.5	24.6	24.4
FC6	FC8	25.4	23.8	24.9	25.4
FC8	Elna Sonic	26.4	24.8	25.9	26.4
Elna Sonic	Mattel	27.3	25.8	26.9	27.3
Mattel	ACM Perai	30	26.7	27.8	30
ACM Perai	FC 1(Shell)	30.7	29.3	30.5	30.7
FC 1(Shell)	Bawal Shop	31.8	30.1	30.8	31.8
Bawal Shop	Kampung Dock	45.1	31.2	32.2	32.9
Kampung Doc	Landfill	<u>57.07</u>	<u>45.8</u>	<u>59.2</u>	46.6
Landfill	Depot	64.10			<u>53.3</u>
Compare with the existing route (KM)			-11.9	2.13	<u>-3.77</u>
%			-19.74%	3.73%	-6.61%

The negative value indicating shorter travelling distance (optimal results) while positive value reveals increase in travelling distance. Based on results show in Table 5, alternative route 2 is longer by 2.13 kilometer compared to existing route.

In Table 5, the total distance between nodes was calculated. The distance between starting node Depot to node Ann Joo is about 5.1 km and accumulated distance from Ann Joo to ILP Perai is 8.1 km. The variance of 3 kilometer is the net distance between Ann Joo to ILP Perai. Similarly, accumulated distance between node ILP Perai to node Nation Gate is 9.6 kilometer in existing route. The variance of 1.5 kilometer is the net distance between these 2 places. This accumulation of distance happens between nodes until the final node (destination). The sum represents total length of entire route.

Comparing the existing route with alternative route 1 results in a 19.74% reduction of distance. While the alternative route 2 involves 3.73% more distance compared with existing route. Although alternative route 2 is longer than existing route, the MBSP management still can use this route when the existing route is under construction or there is traffic congestion on the normal route.

The TSP method can minimize the distance approximately by 6.61% compared to existing route. This method is more effective in identifying the shortest distance compared to Dijkstra algorithm. The Dijkstra algorithm uses directed path which does not include returning to the initial node while the TSP method returns to the initial node (depot). As per information from MBSP Operations Manager, all the collection trucks will be parked at the cleaning depot at the end of every collection trip. So, the TSP method can identify the shortest route more effectively when the day trucks return to the depot by end of daily waste collection operations.

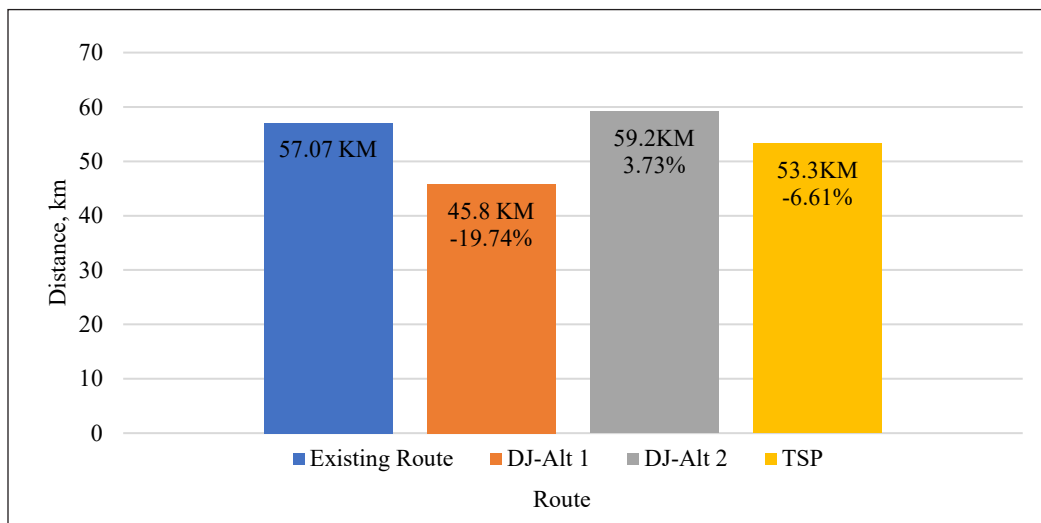


Figure 14. Comparison chart of existing and alternative routes from Prai industrial area to Ampang Jajar Waste Transfer Station.

Kalle et al. (2016) proved that use of GIS can reduce collection time, distance travelled and fuel consumption. Also, they found that GIS also reduces working hours, vehicles wear and maintenance cost. In addition, Zam et al. (2007) also proved that GIS minimizes operational costs by optimizing routes in residential areas.

Cost of Operation

After determining minimum distance, this study also compared the cost of diesel utilized by existing route and alternative routes. The diesel cost is important in determining travelling cost. The diesel price during the study was approximately RM 3 per liter. MBSP Operations Manager mentioned that 700 liters of diesel is consumed by the truck per month.

Table 6 clearly sets out the calculation of diesel cost of waste collection truck for existing route and alternative routes. Figure 15 demonstrates, monthly diesel usage cost reduced from RM 2100.00 to RM 1685.40 (-19.75%) for alternative route 1. Use of

Table 6
Comparison of fuel cost for existing and alternative routes

	Existing Route	DJ-Alt 2	DJ-Alt 2	TSP
Total waste per month (24 Companies), kg	4780	4780	4780	4780
Diesel cost, RM/ l	3	3	3	3
Diesel consumption/ month, l	700			
Diesel consumption/ day, l	23.33			
Total travelled distance/ month, km	1712.1	1374.0	1776.0	1599.0
Diesel consumption/ km, l	0.4089	0.4089	0.4089	0.4089
Diesel consumption/ month, l	700.0	561.8	726.2	653.8
Diesel cost/ month, RM	2100.00	1685.40	2178.60	1961.40
Cost variance, %	-	-19.75%	+3.71%	-6.62%

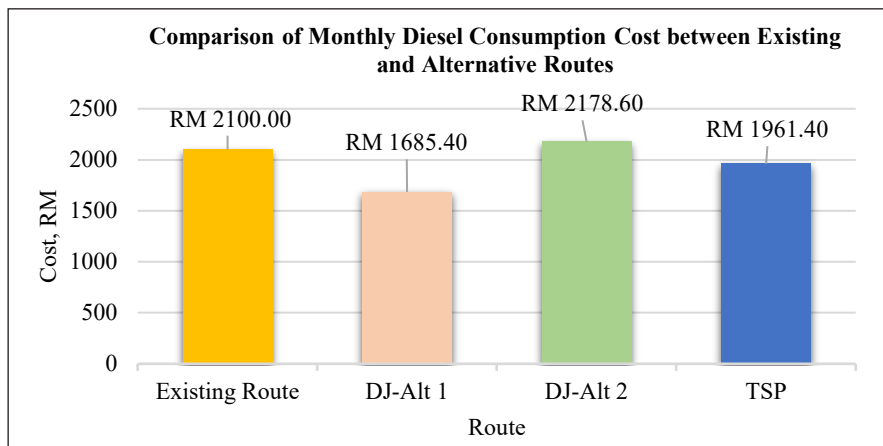


Figure 15. Comparison of monthly diesel consumption cost between existing and alternative routes.

alternative route 2 will increase the cost by RM 178.60 (+3.71%) monthly due to increase in use of diesel consumption. The TSP method resulted in lower diesel cost as well, reduced by RM 138.60 (-6.62%). The diesel cost calculation for TSP method is higher due to return of waste collection truck to cleaning depot or initial starting point. State of Penang spends approximately RM 1 billion for waste management cost alone. This amount can be reduced by optimizing travel routes of waste collecting trucks which leads to overall fuel cost savings. Many researchers used GIS techniques to minimize overall cost of management that involves road travel. Other research (Kinobe et al., 2015; Ahmad, 2016; Kalle et al., 2016; Beijoco et al., 2011) also successfully reduced the cost of SWM transportation by implementing Dijkstra and TSP algorithm methods.

By finding effective routes, not only the cost of diesel is reduced but the savings can be extended to labor cost, traveling cost, daily output or coverage, and truck maintenance cost. The result of this study suggests that MBSP can invest additional fund for truck maintenance to increase efficiency of waste collection process.

Carbon Emission

After determining the diesel cost, this research compares the carbon emission levels for the existing route and alternative routes from Prai industrial area to Ampang Jajar waste transfer station using Equation 8. The total monthly waste of 24 companies and amount of diesel used by waste truck were recorded. From Equation 8, the energy released per liter of diesel is approximately 36.42 and emission factor per liter is 0.74. Table 7 represents the standard of energy content and emission factor in each liter of fuel.

After determining the travelling cost, this research compares the carbon emission levels for the existing route and alternative routes from Seberang Perai industrial area to Ampang Jajar waste transfer station. The Equation 8 was built to calculate carbon emission from transportation in Seberang Perai industrial area to waste transfer station Ampang Jajar. Therefore, the total waste of 24 companies every month and the amount of diesel used by waste truck every month was recorded. In Equation 8, the energy that released per liter

Table 7
Calculation of Carbon Emission in for existing and alternative routes

	Existing route	Alt 1	Alt 2	TSP
Energy Content Per liter	36.42	36.42	36.42	36.42
Emission Factor Per liter	0.074	0.074	0.074	0.074
Monthly waste disposal, kg	143,400	143,400	143,400	143,400
Monthly fuel consumption, liter	700.0	561.8	726.2	653.8
CO₂ Emission_T per month (kg)	0.013	0.011	0.014	0.012
CO₂ Emission_T per year (kg)	0.158	0.127	0.164	0.147
Changes in CO₂ Emission_T, %	-	-19.6	+3.8%	-7.0

of diesel is approximately 36.42 and emission factor per liter approximately 0.74. Table 7 represent the standard of energy content and emission factor that is in each liter of fuel.

Carbon emission for the existing route is 0.013 kg per month, or 0.158 kg per year. Alternative route 1 reported carbon emission level at 0.011 kg per month, or 0.127 kg per year. Alternative route 2 reported slightly higher level of carbon emission; is 0.014 kg per month, or 0.164 kg per year. The carbon emission for TSP method is 0.012 kg per month, or 0.147 kg per year. Alternative route 1 is having lower emission by 19.6% compared to existing route. Similarly, TSP method is also reported lower emission rate by 7.0%. Alternative route 2 reported higher carbon emission level by 3.8% due to longer travelling distance. This reveals route optimization can reduce carbon emission and contributes to greener, cleaner, and healthier state. This finding is aligned with Ghadimzadehi et al. (2015) which found that decreased fuel consumption reduces CO₂ emission from vehicles.

CONCLUSION

The study found that Dijkstra and TSP algorithms are useful to optimize the distance and transportation cost for solid waste management in Prai industrial area via the use of GIS approach by MBSP. The optimum route saves the travelling distance and fuel cost compared to existing route evaluated through Arc Map Network Analysis. The analysis revealed alternative route 1 as the shortest route. This study helps MBSP to control the cost of waste management in terms of travelled distance, fuel, time, and labour. These shortest paths also help MBSP to understand alternative routes in the case of construction or route crowding. The positive outcome of this study is important to achieve the Penang 2030 vision.

ACKNOWLEDGMENTS

We would like to thank the MBSP Waste Management Team that assisted by providing necessary information and School of Mathematical Sciences, University Science Malaysia for the funding.

REFERENCES

- Ahmad, F. I. (2016). *Sustainable solutions for domestic solid waste management in Qatar* (MSc Thesis). Qatar University, Doha, Qatar.
- Ahuja, R. K., Magnanti, T. L., & Orlin, J. B. (1993). *Network flows: Theory, algorithms, and applications*. Pearson Prentice Hall.
- Anghinolfi, D., Paolucci, M., Robba, M., & Taramasso, A. C. (2013). A dynamic optimization model for solid waste recycling. *Waste Management*, 33(2), 287-296. <https://doi.org/10.1016/j.wasman.2012.10.006>
- Beijoco, F., Semiao, V., & Zsigraiova, Z. (2011). Optimization of a municipal solid waste collection and transportation system. *Journal of Waste Management*, 4(33) 793-806.

- Bhambulkar, A. V. (2011). Municipal solid waste collection routes optimized with arc GIS network analyst. *International Journal of Advanced Engineering Sciences and Technologies*, 11(1), 202-207.
- Bodin, L. (1983). Solving large vehicle routing and scheduling problems in small core. In *Proceedings of the 1983 annual conference on Computers: Extending the human resource* (pp. 27-37). Association for Computing Machinery. <https://doi.org/10.1145/800173.809693>
- Bonomo, F., Durán, G., Larumbe, F., & Marengo, J. (2012). A method for optimizing waste collection using mathematical programming: A Buenos Aires case study. *Waste Management & Research*, 30(3), 311-324. <https://doi.org/10.1177/0734242X11402870>
- Bovwe, O., Nwaogazie, I. L., & Agunwamba, J. C. (2016). Development of ant colony optimization software as a solid waste management system. *Current Journal of Applied Science and Technology*, 15(5), 1-19. <https://doi.org/10.9734/BJAST/2016/25080>
- Chipumuro, M., Mawonike, R., & Makoni, T. (2014). Optimizing routing of residential solid waste collection: Case study of Chikova residential area in Zimbabwe. *International Research Journal of Mathematics, Engineering & IT*, 1(3), 23-40.
- Ghadimzadeh, A., Makmom, A. A., Hosea, M. K., Asgari, N., Shamsipour, R., Askari, A., & Narany, T. S. (2015). Review on CO2 Emission from Transportation Sector in Malaysia. *IOSR Journal of Environmental Science, Toxicology and Food Technology*, 9(5), 61-70. <https://doi.org/10.9790/2402-09516170>
- Ghose, M., Dikshit, A., & Sharma, S. (2006). A GIS based transportation model for solid waste disposal - A case study on Asansol municipality. *Journal of Waste Management*, 26(11), 1287-1293. <https://doi.org/10.1016/j.wasman.2005.09.022>
- Gutin, G., & Punnen, A. P. (2002). *Traveling salesman problem and its variations*. Kluwer Academic Publishers.
- Hoffman, K. L., Padberg, M., & Rinaldi, G. (2013). Traveling salesman problem. *Encyclopedia of operations research and management science*, 1, 1573-1578. https://doi.org/10.1007/1-4020-0611-X_1068
- Kalle, A., Mohamed, M. S., & Moncef, Z., (2016). Using GIS-based tools for the optimization of solid waste collection and transport: Case study of Sfax City, Tunisia. *Journal of Engineering*, 2016, Article 4596849. <https://doi.org/10.1155/2016/4596849>
- Kinobe, J., Bosona, T., Gebresenbet, G., & Niwag, C. (2015). Optimization of waste collection and disposal in Kampala city. *Journal of Habitat International*, 49, 126-137. <http://dx.doi.org/10.1016/j.habitatint.2015.05.025>
- Kumpulan Utusan. (2017). *Utusan Melayu (M) Berhad*. Retrieved January 24, 2018, from <http://www.utusan.com.my>
- Menikpura, N., & Sang-Arun, J. (2013). *User manual estimation tool for greenhouse gas (GHG) emissions from municipal solid waste (MSW) management in a life cycle perspective*. Institute for Global Environmental Strategies.
- National Solid Waste Management Department. (2013). *Survey on solid waste composition, characteristics & existing practice of solid waste recycling in Malaysia*. Retrieved December 13, 2018, from <https://jpspn.kpkt.gov.my>

- Nguyen-Trong, K., Nguyen-Thi-Ngoc, A., Nguyen-Ngoc, D., & Dinh-Thi-Hai, V., (2017). Optimization of municipal solid waste transportation by integrating GIS analysis, equation-based, and agent-based model. *Journal of Waste Management*, 59, 14-22. <https://doi.org/10.1016/j.wasman.2016.10.048>
- Penang State Government. (2016). *Official portal Penang state government*. Retrieved August 23, 2018, from <https://www.penang.gov.my/en/awams>
- Omran, A., El-Amrouni, A. O., Suliman, L. K., Pakir, A. H., Ramli, M., & Aziz, H. A. (2009). Solid waste management practices in Penang State: A review of current practices and the way forward. *Environmental Engineering & Management Journal (EEMJ)*, 8(1), 97-106. <https://doi.org/10.30638/eemj.2009.014>
- Patel, M. H., Padhya, P. H., & Zaveri, P. P. (2016). GIS based route optimization for solid waste management: A case study of Surat City. *International Journal for Scientific Research & Development*, 4(04), 32-34.
- Shamshiry, E., Nadi, B., & Mahmud, A. R. (2011). Optimization of municipal waste management. *International Proceedings of Chemical, Biological and Environmental Engineering*, 1(1), 119-121.
- Singh, G., Singh, B., Rathi, S., & Haris, S. (2014). Solid waste management using shortest path algorithm. *International Journal of Engineering Science Invention Research & Development*, 1(2), 60-64.
- Stewart, L. A. (2005, July 25-29). The application of route network analysis to commercial forestry transportation. In *Proceedings of 2005 ESRI International User Conference*. San Diego, USA.
- Tavares, G., Zsigraiova, Z., Semiao, V., & Carvalho, M. D. G. (2008). A case study of fuel savings through optimization of MSW transportation routes. *Management of Environmental Quality: An International Journal*, 19(4), 444-454. <https://doi.org/10.1108/14777830810878632>
- Williams, R. (2012). *Globalization and waste management*. International Solid Waste Management, Singapore.
- Zam, D., Jamtsho, S., Dema, T., & Wangmo, J. C. C., (2007). Optimization of solid waste collection and transportation route in Phuentsholing city using GIS. *Journal of Academia*, 1-8.

Traffic Noise Level Assessment in the Residential Area around Different Road Functions in Malang City, East Java, Indonesia

Ngudi Tjahjono¹, Imam Hanafi², Latipun Latipun³ and Suyadi Suyadi^{4*}

¹Department of Industrial Engineering, Faculty of Engineering, University of Widyagama Malang, Malang, East Java, Indonesia

²Faculty of Administrative Sciences, University of Brawijaya, Malang, East Java, Indonesia

³Faculty of Psychology, University of Muhammadiyah Malang, Malang, East Java, Indonesia

⁴Faculty of Animal Sciences, University of Brawijaya, Malang, East Java, Indonesia

ABSTRACT

Noise due to motorized vehicles is a major problem in urban areas which can interfere with physiological and psychological health. This study aims to determine the extent of noise levels outside and inside the house around the function of different roads in Malang City, East Java, Indonesia. The study was conducted by measuring the traffic noise level using a sound level meter. Measurements were taken in the afternoon between 16.00-21.00 during the peak of heavy traffic and outside working hours when residents were already at home. Statistical Student's t-test analysis was used to test differences in the average noise level outside and inside the house on each road function. Variance analysis was used to compare noise levels around primary arterial roads, secondary arteries, primary collectors, secondary collectors, primary local, and secondary local. From the measurement results, it is known that the noise due to motorized vehicles is 84.28 dB on average. This exceeds the threshold based on the Decree of the State Minister for the Environment Number 48

of 1996. There was a significant difference in noise level between outside and inside the house on each road function. There was no significant difference in noise level between the functions of the road segments both outside and inside the house. The results of the study concluded that the traffic noise level at 16:00 to 21:00 hours on all roads that were targeted for research exceeds the national threshold. It is recommended that the level of traffic noise around roads in

ARTICLE INFO

Article history:

Received: 03 November 2020

Accepted: 10 February 2021

Published: 31 July 2021

DOI: <https://doi.org/10.47836/pjst.29.3.05>

E-mail addresses:

ngudi.widyagama@gmail.com (Ngudi Tjahjono)

imamhanafi@ub.ac.id (Imam Hanafi)

latipun@umm.ac.id (Latipun Latipun)

suyadi@ub.ac.id (Suyadi Suyadi)

* Corresponding author

the city of Malang can be reduced to minimize the negative impact on physiological and psychological health.

Keywords: National threshold, noise level, road function, traffic noise

INTRODUCTION

The increase in the number of motorized vehicles causes many problems in urban areas. This is faced by many big cities in the world. This increase is in line with the increasingly complex human needs that require the support of transportation facilities in the form of motorized vehicles. However, in several big cities in Indonesia the rapid increase in the number of motorized vehicles has not been matched by an increase in the capacity of adequate road infrastructure (Ningsih, 2010). This has become one of the causes of environmental degradation.

Facts obtained from several studies show that the big cities in the world cannot be separated from traffic noise. In cities in India, traffic noise caused by heavy traffic flow conditions in the main corridor Bus Rapid Transport System (BRTS) has exceeded the national standards of the Central Pollution Control Board (CPCB) (Mishra et al., 2010). Likewise in Tehran, most of the business centers and settlements around the main roads are exposed to noise pollution (Alesheikh & Omidvari, 2010).

Research in Bandung shows that the average noise level on all major roads have exceeded the specified quality standards (Pryandana, 2000). On several local roads in Bandung also showed the same condition (Setiawan et al., 2016; Wahyuni et al., 2019). The same results were shown in a study in Manado (Balirante et al., 2020), Meulaboh (Kurnia et al., 2018) and Padang (Putra & Lisha, 2017).

The level of traffic noise that exceeds the threshold of the Decree of the Minister of Environment No. 48 of 1996 can disturb people who are exposed both physiologically and psychologically. There are two stages in the decline in mental health level as a result of poor environmental quality including due to noise factors, namely (a) will directly affect behavior, attitudes and utilization of health services, and (b) long-term related with the accumulation of stress and limited environmental resources (Halim, 2008). Meanwhile, research in primary schools shows that students exposed to traffic noise >61.8 dBA_{Leq} in a school environment have a 10.9 times risk of experiencing psychological health problems (Djaja & Wulandari, 2007), the same thing was also studied at SMPN 3 Kendari (Ibnu, 2019). The accuracy of hearing also decreased (Yadnya et al., 2009). Also found the fact that there is a relationship between noise and hypertension suffered by women who live around the railroad tracks (Rosidah, 2004).

From the revealed facts, it is necessary to do further research on the noise level from motorized vehicle sources in Malang City. The purpose of this study was to determine the

extent of noise levels outside and inside the house around the function of different roads in Malang, East Java, Indonesia.

MATERIALS AND METHOD

Research Location

The research location is in the city of Malang, East Java province, Indonesia (Figure 1). Malang City is the second largest city in East Java after Surabaya. Geographically, the city of Malang is located at position 112° 38' 01.7" East Longitude and 7° 58' 42.2" South Latitude covers an area of 11,006 Km².

Malang City is located in the middle of Malang Regency administration area. North side, bordering Singosari District and Karangploso District Malang Regency. In the south, it is bordered by Tajinan subdistrict and Pakisaji subdistrict, Malang regency. West side, bordering Wagir District Malang Regency and Dau District Malang Regency. East side, bordering Pakis District and Tumpang District, Malang Regency.

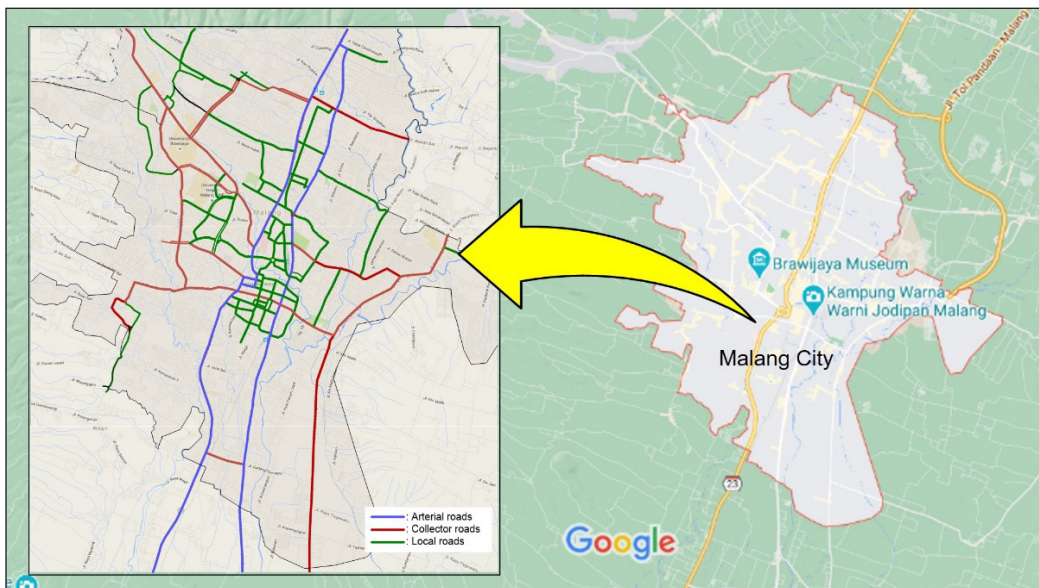


Figure 1. The research location on the arterial, collector, and local roads in the city of Malang

Types of Roads

Judging from the function of the roads contained in the city of Malang can be divided into: Primary Arterial roads, Secondary Arteries, Primary Collectors, Secondary Collectors, Primary Local, Secondary Local. In terms of existing road patterns, the Malang City road transportation pattern is a radial concentric pattern with an inner ring system of the local road network that forms a grid pattern. The total length of the road based on the function

is 663.34 km. The details of the length of the road network in Malang based on the road function are described in Table 1.

Research Methods

The population of the road is the entire road network in the city of Malang. Determination of the sample of road segments is done by selecting the road segments that represent the functions of primary arterial roads, secondary arteries, primary collectors, secondary collectors, primary local and secondary local. The selection of road segments is based on the consideration that in addition to representing the function of the road, there are also many houses that are not used as business premises around the road segments. This consideration was taken because the focus was to find out the condition of motorized traffic noise that exposed the population living in the vicinity. Based on the above criteria, a sample of 41 road sections are spread across 6 road functions.

Noise measurement points are set at least in three places, namely the base, middle and end of each road section. The determination of the three points is expected to be able to represent the character of the flow of motorized vehicles passing along the road.

Data Types and Collection

The data was measured in the form of the distance from the house to the road axis and noise data generated from the road outside and inside the house. Noise level was measured using a Sound Level Meter. The measuring instrument used is the 4 IN 1 Multi-functional Environmental Meter. This tool is capable of measuring noise in the range of $Lo = 30-100$ dB; $Hi = 65-130$ dB.

Data collection points were determined at least at the end, middle and end of the road section. Data was measured based on the ear height of a person sitting in a chair with consideration at rest, many people do it while sitting. Data collection was carried out in the afternoon until evening with the consideration that the residents were already at home. Noise measurements were carried out on terraces and inside residents' houses with a duration of about five minutes. The data recorded was the average noise data over the measurement duration.

Data Analysis

The data collected is carried out reduction and compilation to make an assessment according to the category. Data were analyzed with descriptive statistical tools and analysis of

Table 1
Function and length of roads in Malang City

No	Function of Road	Length (km)
1	Primary Artery	11.82
2	Secondary Artery	15.94
3	Primary Collector	8.16
4	Secondary Collector	27.09
5	Primary Local	9.66
6	Secondary Local	590.67
Total		663.34

Source: "Studi Greater Malang Urban Road Network Study" and "RTRW Kota Malang"

variance. Descriptive analysis is needed to describe the distribution of the distance of the house to the street. While analysis of variance is needed to determine differences in noise levels on each road function.

The description of the data is presented in statistical Table 2 and Figure 2 as a representation of the collected data. Table 2 contains frequency and percentage information on the distance of the house to the ace of the road. While the graph is presented in the form of three-dimensional blocks.

The difference in noise levels between outside and inside the house on each road function is calculated by the Student's t unpaired test. One-way analysis of variance (ANOVA) was calculated using Excel, to see differences in noise levels between each group of road functions.

After that proceed with making a map of Malang city traffic noise in the form of a two-dimensional map for the road sections included in the study.

RESULT

Measurement of motor vehicle noise is carried out on samples of road segments that represent the functions of primary arterial roads, secondary arteries, primary collectors, secondary collectors, primary local and secondary local. The selection of road sections is based on the consideration that in addition to representing the function of the road as well as around these roads there are residents' houses that are not used as places of business.

Distance From House to the Ace of the Street

From the data collected, it was found that most of the houses have a distance from the axle of the road between 5.1 and 10 meters. Of course, such distance is too close to the source of the noise on the road. Furthermore, it can be seen in Table 2 and Figure 2.

From the measurement, information was obtained that the existence of a house on the side of the road is too close to the road. Examples of cases like this can be seen in Figure 3 which was taken from Google Maps and Figure 4 which was taken directly at

Tabel 2

Amount and percentage of distribution of distances from houses to the axle of the road

No	Distance from Road	Frequency	Percentage (%)
1	≤ 5 meters	7	4.52
2	5,1 – 10 meters	128	82.58
3	10,1 – 15 meters	18	11.61
4	15,1 – 20 meters	1	0.65
5	≥ 20,1 meters	1	0.65
Total		155	100.00

Source: Primary Data Processed

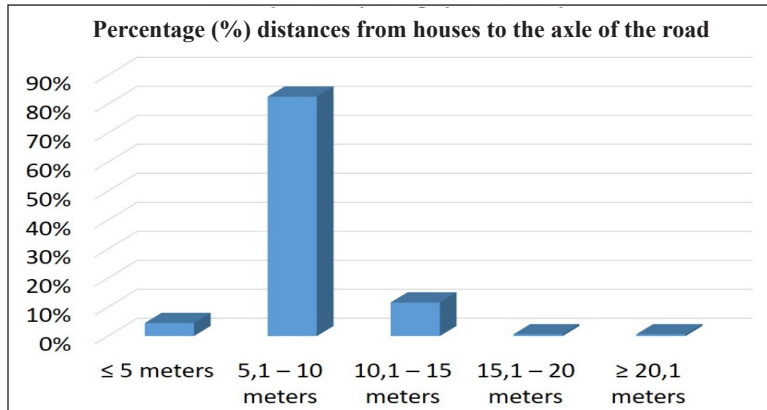


Figure 2. Percentage (%) distances from houses to the axle of the road



Figure 3. An example of the location of a house that is too close to the road. The houses marked with an oval line are located on Candi Panggung and Akordion streets, Malang city.



Figure 4. An example of the images of the houses that were too close to the road, which was taken directly on Akordion streets, Malang city.

the location. A distance that is too close like this has the potential for high levels of noise to which it is exposed.

Analysis of the Mean Noise Level outside and inside the House

Based on research data obtained from measurement, data showed on the mean noise level outside and inside the house for each of the functions can be seen in Table 3. The standard deviation is calculated from the data collected can also be seen in Table 3.

To find out the difference in the mean noise level outside and inside the house for each road function, it was carried out using the unpaired Student's t test. The results can be seen in Table 4.

From the analysis of Student's t-test there was a significant difference at $t_{0.05}$. A significant difference in mean of noise level between outside and inside the house occurs in each function of the road section. These differences show that the noise level outside the house can be significantly reduced inside the house. This is caused by the various kinds of efforts made by residents to reduce noise from motor vehicles on the road.

Some efforts to reduce the noise that is commonly found in houses scattered around roads in the city of Malang, among others, close their homes tightly. Doors and windows

Table 3
Noise level ($\bar{x} \pm s$) outside and inside the house for each road function

No	Road Function		Outside the House	Inside the House
1	Primary Artery	Number of roads, n	4	4
		Mean of noise level, \bar{x}	84.55	70.10*
		Standard deviation, s	1.85	6.09
2	Secondary Artery	Number of roads, n	4	4
		Mean of noise level, \bar{x}	85.13	69.40*
		Standard deviation, s	1.79	3.89
3	Primary Collector	Number of roads, n	2	2
		Mean of noise level, \bar{x}	83.20	67.15*
		Standard deviation, s	0.57	2.62
4	Secondary Collector	Number of roads, n	13	13
		Mean of noise level, \bar{x}	84.50	69.30*
		Standard deviation, s	2.68	4,00
5	Primary Local	Number of roads, n	2	2
		Mean of noise level, \bar{x}	83.15	68.90*
		Standard deviation, s	0.92	1.13
6	Secondary Local	Number of roads, n	16	16
		Mean of noise level, \bar{x}	84.09	66.71*
		Standard deviation, s	3.40	9.15

Source: Primary data processed

Note: * there is a significant difference in $t_{0,05}$

Table 4
Result of T test calculation

No	Road Fungtion	t_{count}	$t_{0.05}$	Conclusion
1	Primary Artery	4.541	1.943	Significant
2	Secondary Artery	7.347	1.943	Significant
3	Primary Collector	8.465	2.920	Significant
4	Secondary Collector	11.382	1.711	Significant
5	Primary Local	13.830	2.920	Significant
6	Secondary Local	7.122	1.645	Significant

Source: Primary data processed

are made tight and even air vents are also closed to reduce noise and prevent dust from entering the room. The curtains that are used to protect the room from the eyes of people outside the house also function as a silencer. Ornamental plants planted on the fence of the house or the terrace of the house can also reduce the intensity of noise from the road. Research has been conducted on various types of plants that can reduce noise in Malang (Tjahjono & Nugroho, 2018) and Sidoarjo (Pudjowati et al., 2013). From both studies, it is known that plant species can effectively reduce noise.

Analysis of Variance of Noise Level on Each Function of Roads

Data collected includes road segments grouped into road functions, the mean noise level in each section presented in Tables 5 and 6.

By using analysis of variance, it can be concluded that there is no significant difference between the functions of road segments (primary arteries, secondary arteries, primary collectors, secondary collectors, primarily local and secondary local) for average noise levels outside the house or inside the house. This shows that the noise level originating from motorized vehicles in the streets of Malang has exceeded the required noise level. Even though the noise inside the house can be muted, it is still above the threshold or greater than 55 dB.

Table 5
Variance analysis for average noise level outside the house

Source	df	SS	MS	F_{count}	F_{table}	
					5%	1%
Treatment	5	9.26	1.85	0.23	2.49	3.60
Error	35	280.56	8.02			
Total	40	289.82				

Source: Primary data processed

Because $F_{count} = 0.23$ is smaller than F_{table} at the level of $1\% = 3.60$, so it can be concluded that there is no difference in noise levels in each treatment group (road function)

Table 6
Variance analysis for average noise level inside the house

Source	df	SS	MS	F _{count}	F _{table}	
					5%	1%
Treatment	5	74.58	14.92	0.32	2.49	3.60
Error	35	1611.93	46.06			
Total	40	1686.52				

Source: Primary data processed

Because $F_{count} = 0.32$ is smaller than F_{table} at the level of $1\% = 3.60$, so it can be concluded that there is no difference in noise levels in each treatment group (road function).

Motor Vehicle Noise Level Mapping in the City of Malang

From the noise measurement data collected then plotted to the Malang City road map which is downloaded from the Google Map. Roads with a noise level exceeding 55 dB are colored red. There is no road noise level below 55 dB.

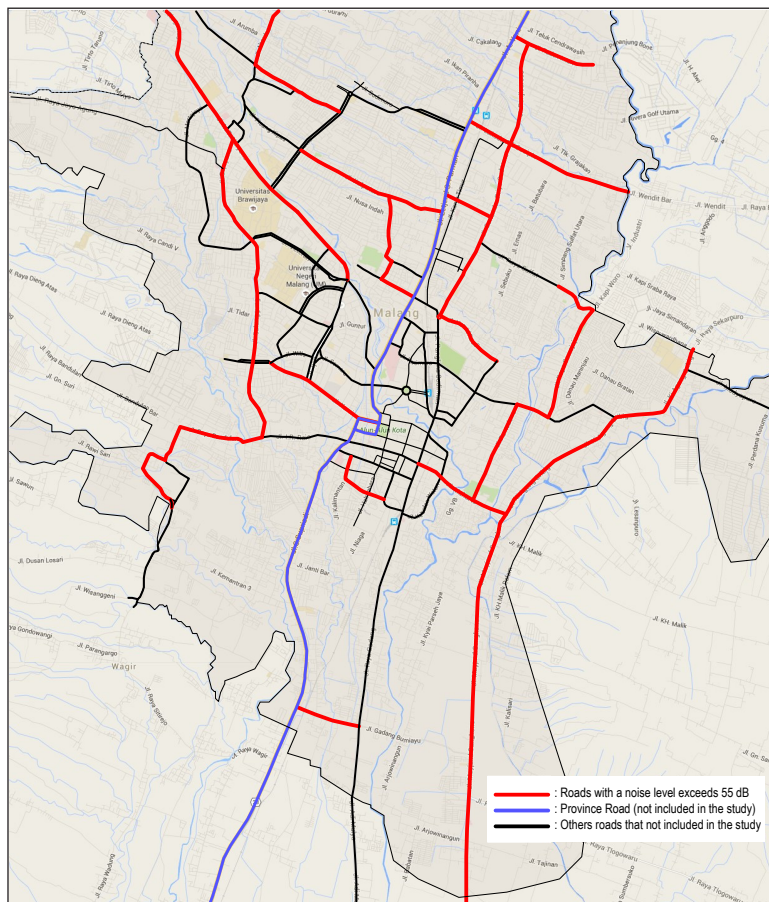


Figure 5. Traffic Noise Map in the Study Area in Malang City

On the map image, the roads marked in blue are provincial roads. Roads that have been measured for noise levels are those that are colored red. As for the blue and black roads, no measurements were taken considering that there are almost no residential areas around them, only business premises. The map can be seen in Figure 5.

DISCUSSION

In the road sections that were the focus of the study, it was found that most of the distance from the house to the main road was 5.1-10 meters (82.58%), while those greater than 10 meters was 12.26%. The very close distance to the road, of course, the greater the noise level.

The average noise level between outside and inside the house, there is a significant difference in each function of the road section. This difference is associated with a significant decrease in noise levels in the house. However, the decrease in noise level is still in the range above the required threshold.

From the analysis of variance, it was concluded that in each group of road functions there was no difference in the average noise level both outside and inside the house. Thus it can be said that all roads in the scope of research in the city of Malang have a noise level that exceeds the required noise level standard.

The results of research in several cities such as Bandung show that the average noise level is above the national standard on the main and local roads (Pryandana, 2000). Likewise, the results of research in Manado (Balirante et al., 2020), Meulaboh (Kurnia et al., 2018), and Padang (Putra & Lisha, 2017) show that the average noise level exceeds the specified quality standards on all major roads. and local. This is the same as what happened in the city of Malang.

If we look at the development of the number of motorized vehicles in Indonesia from 2010 to 2018, it shows an increasing trend. From the total 76,907,127 vehicles in 2010, it increased to 146,858,760 vehicles in 2018. Within eight years, the number of motorized vehicles increased by 91% or 11% per year. With such an increasing trend there is also the potential for an increase in the resulting traffic noise. This happens in big cities throughout Indonesia, including in Malang.

The number of motorized vehicles which increase significantly each year has certainly led to an increase in noise levels on the road. Meanwhile, the speed of increasing road capacity in Malang City has not been able to keep up with the increase in the number of motorized vehicles. Therefore the increase in noise still exceeds the quality standard for the noise level required by the Minister of Environment Decree No. 48 of 1996.

CONCLUSIONS

From the measurement results, that all roads targeted by the study indicate the level of noise caused by motorized traffic exceeds the noise level standard for housing and settlements (55 dB) based on the Decree of the Minister of Environment No. 48 of 1996. The measured average noise level was 84.28 dB, greater than 55 dB. From the analysis of Student's t-test it was found that there was a significant difference between the noise level outside and inside the house on each road function. While from the analysis of variance, it is known that there is no difference in noise level in each road function (primary arteries, secondary arteries, primary collectors, secondary collectors, primarily local and secondary local), both outside and inside the house. This means that the existing noise level has exceeded the specified standard that is 55 dB. It is recommended that noise levels originating from motorized vehicles on Malang city roads can be reduced to meet national requirements.

ACKNOWLEDGEMENT

This article is part of dissertation research in the Environmental Science Doctoral Program, University of Brawijaya Postgraduate Program. This research was funded by the Ministry of Research and Technology and Higher Education (Ristek Dikti) Republic of Indonesia.

REFERENCES

- Alesheikh, A. A., & Omidvari, M. (2010). Application of GIS in urban traffic noise pollution. *International Journal of Occupational Hygiene*, 2(2), 79-84.
- Balirante, M., Lefrandt, L. I. R., & Kumaat, M. (2020). Analisa tingkat kebisingan lalu lintas di jalan raya ditinjau dari tingkat baku mutu kebisingan yang diizinkan [Analysis of traffic noise levels on the highway in terms of permitted noise quality standards]. *Jurnal Sipil Statik*, 8(2), Article 2.
- Djaja, I. M., & Wulandari, R. A. (2007). Pengaruh kebisingan lalu lintas jalan terhadap gangguan kesehatan psikologis anak SDN Cipinang Muara Kecamatan Jatinegara, Kota Jakarta Timur, Propinsi DKI Jakarta, 2005 [The effect of road traffic noise on psychological health problems for children at Cipinang Muara Elementary School, Jatinegara District, East Jakarta City, DKI Jakarta Province, 2005]. *Makara, Kesehatan*, 11(1), 32-37.
- Halim, D. K. (2008). *Psikologi lingkungan perkotaan* [Psychology of the urban environment]. Bumi Aksara.
- Ibnu, S. N. (2019). Pengaruh kebisingan lalu lintas terhadap tingkat ketergangguhan individu siswa (Studi kasus: SMPN 3 kendari) [Influence of traffic noise on disturbance levels of individual students (Case study: SMPN 3 kendari)]. *Jurnal Manajemen Rekayasa (Journal of Engineering Management)*, 1(2), Article 2.
- Kurnia, M., Isya, M., & Zaki, M. (2018). Tingkat kebisingan yang dihasilkan dari aktivitas transportasi (Studi kasus pada sebagian ruas jalan: Manek Roo, Sisingamangaraja dan Gajah Mada Meulaboh) [Noise levels resulting from transportation activities (Case studies on part of the road: Manek Roo, Sisingamangaraja and Gajah Mada Meulaboh)]. *Jurnal Arsip Rekayasa Sipil dan Perencanaan*, 1(2), 1-9. <https://doi.org/10.24815/jarsp.v1i2.10936>

- Mishra, R. K., Parida, M., & Rangnekar, S. (2010). Evaluation and analysis of traffic noise along bus rapid transit system corridor. *International Journal of Environmental Science & Technology*, 7(4), 737-750. <https://doi.org/10.1007/BF03326183>
- Ningsih, D. H. U. (2010). Analisa optimasi jaringan jalan berdasar kepadatan lalu lintas di Wilayah Semarang dengan berbantuan sistem informasi Geografi (Studi kasus Wilayah Dati II Semarang) [Analysis of road network optimization based on traffic density in the Semarang Region with the assistance of geographical information systems (Case study of Dati II Semarang Area)]. *Jurnal Teknologi Informasi DINAMIK*, XV(2), 121-135.
- Pryandana, D. (2000). *Penanganan kebisingan lalu lintas di jalan perkotaan: Studi kasus kota Bandung* [Traffic noise handling on urban roads: A case study of the city of Bandung]. Retrieved October 24, 2020, from <http://elib.unikom.ac.id/gdl.php?mod=browse&op=read&id=itb-s2-pl-2000-Dendi-jalan>
- Pudjowati, U. R., Yanuwadi, B., Sulistiono, R., & Suyadi, S. (2013). Effect of vegetation composition on noise and temperature in Waru—Sidoarjo Highway, East Java, Indonesia. *International Journal of Conservation Science*, 4(4), 459-466.
- Putra, F., & Lisha, S. Y. (2017). Tingkat kebisingan lalu lintas kendaraan di Gedung I Sekolah Tinggi Teknologi Industri (STTIND) Padang [Vehicle traffic noise level in building I of the industrial technology college (STTIND), Padang.]. *Jurnal Sains dan Teknologi: Jurnal Keilmuan dan Aplikasi Teknologi Industri*, 17(1), 1-7. <https://doi.org/10.36275/stsp.v17i1.34>
- Rosidah, R. (2004). *Studi kejadian hipertensi akibat bising pada wanita yang tinggal di sekitar lintasan kereta api di Kota Semarang Tahun 2004* [Study of the incidence of hypertension due to noise in women living around railway tracks in Semarang City, 2004] [MSC Thesis]. Universitas Diponegoro, Indonesia. <http://eprints.undip.ac.id/14510/1/2004MKL3810.pdf>
- Setiawan, I. M. D., Mahardika, I. G., & Adhika, I. M. (2016). Tingkat kebisingan lalu lintas di lingkungan perumahan Dalung Permai Kabupaten Badung [Traffic noise level in the housing environment of Dalung Permai, Badung Regency]. *ECOTROPIC: Jurnal Ilmu Lingkungan (Journal of Environmental Science)*, 10(2), 81-86. <https://doi.org/10.24843/EJES.2016.v10.i02.p01>
- Tjahjono, N., & Nugroho, I. (2018). Tanaman hias sebagai peredam kebisingan [Ornamental plants as noise reducer]. *Conference on Innovation and Application of Science and Technology (CIASTECH)*, 1(1), 703-710.
- Wahyuni, S., Yustiani, Y. M., & Juliandahri, A. (2019). Analisis tingkat kebisingan lalu lintas di Jalan Cihampelas dan Jalan Sukajadi Kota Bandung [Analysis of traffic noise levels on Cihampelas Street and Sukajadi Street, Bandung City]. *Journal of Community Based Environmental Engineering and Management*, 2(1), 9-12. <https://doi.org/10.23969/jcbeem.v2i1.1451>
- Yadnya, I. W. P., Putra, N. A., & Aryanta, I. W. R. (2009). Tingkat kebisingan dan tajam dengar petugas ground handling di Bandara Ngurah Rai Bali [Noise level and sharp hearing of ground handling officers at Ngurah Rai Airport, Bali]. *ECOTROPIC: Jurnal Ilmu Lingkungan (Journal of Environmental Science)*, 4(2).

Factors in Adopting Green Information Technology: A Qualitative Study in Malaysia

Siti Aishah Ramli^{1*}, Boon Cheong Chew¹ and Adi Saptari²

¹Faculty Of Technology Management and Technopreneurship, Universiti Teknikal Malaysia Melaka, Hang Tuah Jaya, Durian Tunggal, 76100 Melaka, Malaysia

²Department Of Industrial Engineering, President University, Ji. Ki Hajar Dewantara, Kota Jababeka, Cikarang Baru, Bekasi 17550, Indonesia

ABSTRACT

Green Information Technology (IT) has emerged as a crucial topic for environmentally and sustainability development. At the same time, Green IT impacts the organisation as well. Studies show there is a lack of a proposed framework in the Green IT literature. As the IT industry is one of the significant sectors supporting the Green Technology Policy, this study objective is to identify the factors rendered in the Green IT adoption and examine the factors that drive the adoption of Green IT in Malaysia. The study referred to the case study to show the most important factors rendered in Green IT adoption in the public sector and the private sector in Malaysia. A qualitative method was applied through a semi-structured interview by using open-ended questions as a guideline with five organisations from the public sector and the private sector. This study prioritises the explanation building as a specific approach to analysis. Results show that there are five factors rendered in Green IT adoption in Malaysia: environmental factor, cost factor, organisational factor, technological factor, and business opportunity factor. This study benefits policymaker, organisations, and other researchers to support Malaysia's pledge to reduce its Greenhouse Gas (GHG) emission intensity of Gross Domestic Product (GDP) by up to 45% by 2030.

Keywords: Green and sustainable practices, green IT, Malaysia

ARTICLE INFO

Article history:

Received: 25 December 2020

Accepted: 01 April 2021

Published: 31 July 2021

DOI: <https://doi.org/10.47836/pjst.29.3.12>

E-mail addresses:

sitiahshahramli@hotmail.com (Siti Aishah Ramli)

bcchew@utem.edu.my (Boon Cheong Chew)

adi.saptari@president.ac.id (Adi Saptari)

* Corresponding author

INTRODUCTION

Green IT has been discussed in many aspects nowadays towards reducing the global carbon emission produced by IT consumptions. In Malaysia, Green IT is considered new to implement. The National

Green Technology Policy was established in Malaysia in 2009 and addresses five strategic thrusts. One of the strategies is to strengthen efforts in promotion and improve the awareness of people in ICT technology (Ministry of Energy, Green Technology and Water of Malaysia, 2009). The 6th Malaysian Prime Minister indicates:

“Green Technology is a blue ocean strategy as it transcends across all sectors of the economy. It provides vast opportunities for government and business to innovate and grow as well as developing new parts of competitiveness” (Kasbun et al., 2016).

Thus, the National Green Technology Policy establishment strengthening the new green ideas for the ICT sector (GreenTech, 2011).

Rad et al. (2018) reported that there is a lack of study in technology adoption. *Studies show that there are organisations in the government sector that emphasise environmental aspects in Green IT adoption* (Junior et al., 2018). While several past studies briefly discussing Green IT adoption in the Malaysia organisation. Rahim & Rahman (2013) briefly discussed the Green IT capabilities and resources in the Malaysia public listed organisation; Esfahani et al. (2015) generally revised the importance of motivational in Green IT implementation in the organisation. Therefore, this study focusses on two objectives. First, to examine the most important factors rendered the Green IT adoption by MAMPU, KeTTHA, GreenTech Malaysia, International Business Machine (IBM) Malaysia and Hewlett-Packard (HP) Malaysia and second, is to propose a framework in implementing the Green IT.

Green IT in Malaysia

The key landmark for the ICT industry in Malaysia started in 1997 when the Multimedia Super Corridor (MSC) Malaysia becomes the national agenda for the nation's development. In July 2009, the National Green Technology Policy (NGTP) was established with a policy statement which is “green technology shall be a driver to accelerate the national economy and promote sustainable development” (GreenTech, 2013). The NGTP outlined five strategic thrusts: i) Strengthen the Institutional Frameworks, ii) Provide a Conducive Environment for Green Technology Development, iii) Intensify Human Capital Development in Green Technology, iv) Intensify Green Technology Research and Innovations and v) Promotion and public awareness. Follows by four pillars in energy, environment, economy and social and focus on six sectors including energy, water, waste, building, manufacturing, and transport (Ministry of Energy Green Technology and Water, 2017). Thus, to achieve the NGTP objective, this study focus on Green ICT Malaysia covers the term of adoption, and factors, as the preparation which directly leads to in-depth understanding and finally able to propose a framework that can be used to ensure the widespread adoption of Green IT in Malaysia.

Technology Adoption Models

This study applies two models - Technology-Organisation-Environment (TOE) and Diffusion of Innovation (DOI). TOE model explains the organisational adoption and execution of technological innovation. This model is recognised as determining factors of organisation level innovation adoption (Cobos et al., 2016; Zhang et al., 2020). Whilst DOI examines innovation adoption from a process perspective (Cobos et al., 2016). TOE is consistent with DOI as both theories recognised as determining factors of organisational level in innovation adoption. For instance, DOI's innovative characteristics and internal and external characteristics of the adopting organisation are accordances with the TOE framework's innovation and organisational contexts (Cobos et al., 2016; Asadi et al., 2017). Besides, TOE and DOI models are aligned to apply in the qualitative method which the researcher conducts this study through a semi-structured interview. From there, the researcher able to find which factors are important in the adoption of Green IT in Malaysia. Besides, through the TOE and DOI framework, the researcher able to apply the models as a guideline in determining the factors that rendered Green IT adoption and place the TOE models factor as the main factor. Therefore, TOE and DOI models are relevant to this study. These models are applied to investigate the factors rendered in Green IT adoption and how the Green IT technology diffused in the organisations.

Green Information Technology (IT)

According to Asadi et al. (2019), the concept of Green IT is affected by and related to sustainability, ecological sustainability, information systems, and information technology concepts. In the meantime, many scholars express Green IT terminologies with green computing, environmentally, sustainable computing, and energy efficiency based on their perspective of business concern and organisation operation. Dalvi-Esfahani et al. (2020) defined Green IT as the process of manufacturing, using, and disposing of all related IT (hardware and software) concerning eco-friendly issues. The definition focuses on both enhancing energy efficiency and intensifying the sustainability of the environment by reducing the pollution released from IT hardware and software. Besides, it is also an example of a green growth initiative pointed at enhancing performance and productivity through sustainable utilization and production of organisational and societal resources (Gazzola et al. 2018). Therefore, this study focuses on Green Information Communication Technology to examine the factors that rendered the Green IT adoption in Malaysia.

The Factors Rendered Green IT Adoption

There are seven factors discusses in Green IT adoption. The factors identify the Green IT adoption based on literature in Malaysia organisation.-Below explain the details.

Technological Factor. Unhelkar (2016) points out that there are two primary technologies in Green IT which are hardware within the organisation and application. De Zoysa and Wijayanayake (2013) illustrate more on the technology areas of Green IT includes the data centre, virtualization, utilization, storage area network and the other application. However, as Green IT adoption possess various scope in the technology aspect, the wide ranges of technical aspects related to design, manufacture, use, and disposal of Green IT technologies are focused. However, most of the studies records technological factor are not tend to organisation studies. For instance, consumers' intention toward adoption of vehicle (Asadi et al., 2020); green fertiliser technology through farmers behaviour (Adnan et al., 2019); green building sector (Azis, 2021) and the awareness of solar energy technology among households (Malik & Ayop, 2020).

Competitive Pressure Factor. Referring to De Zoysa and Wijayanayake (2013), the organisation may feel the pressure from competitors in the same industry, which comes from strong company's background to keep their image. This means when a competitor's products or services are better than our company, we will feel the pressure that our profits will decrease. Simon (2013) expresses that one of the key drivers of successful technology development and adoption is a market formation which is developing marketplace by developing new products and services, identify customer and users' needs, develop viable business models, consider possibilities for exports, and needs for imports. Therefore, companies should adopt technological tools to meet certain demands in the market (Khan & Faizal, 2015).

Organisational Factor. Dash et al. (2016) demonstrate that every organisation pursues to improve their business operation which includes the necessity of strategic planning to adopt new technology in establishing several process stages to improve the organisation performance. In Malaysia organisation, study shows that there is a relationship between Green IT attitude and engagement in support green computing practices (Ojo et al., 2019). Letlonkane and Mavetera (2014) emphasize that top management, such as Chief Information Officer and IT managers have an optimistic attitude on the advantage of adopting Green IT to the organisation. Besides, Molla and Abareshi (2014) examine that actions undertaken by senior management can introduce complementary structures to assist learning and innovation.

Environment Factor. According to Fernando and Wah (2017), environment performance in organisation processes to achieve firms goals for environmental improvement and gas emission reduction in Malaysia. Shameer et al. (2015) highlight that Green IT is the solution concerned with reducing the environmental impact of IT before IT devices are purchased, during their lifetimes and after consumers have finished with them. Given the example of

environmental performance in an organisation, Saha (2014) mentions that electricity is a crucial cause of climate change as the thermal power plants that aid generates electricity also releases a high amount of carbon dioxide and many other harmful particles into the atmosphere. As we know that the consumption of IT generated by electricity, Lee et al. (2013) examine that IT products consume considerable amounts of energy, contributing to the emission throughout their entire life cycle, from production to use and disposal. Shibly (2015) supports that most of the components discovered in prevalent computers are not only harmful to the environment but potentially harmful to human health. However, Asadi et al. (2020) reports that there is still a lack of green initiatives study relates to the environment in Malaysia organisation.

Regulatory Support Factor. According to Zailani et al. (2015) illustrate that the involvement in environmental protection obliged through legal regulations. Taruna et al. (2014) examine that one of the strategies regarding the adoption of Green IT is being as such the countries, especially emphasizing toward the developing countries must have to go through the policies strictly or to adopt Green IT policy seriously. This stated in Unhelkar (2016) indicates that some governments are forcing companies to make a report on their carbon emission every year. Therefore, Murugesan and Gangadharan (2012) highlight that this will bring towards the success of Green IT adoption and implementation and it will confirm the reduction of the carbon footprint from the organisations. This is supported by Mergel and Bretschneider (2013) emphasize where the organisation may follow the regulation to avoid the penalties and other taxes.

Business Opportunity Factor. Singh and Vatta (2016) mention that opportunities in green technology ordain like never in history and organisations are looking at it as a technique to generate new profit centres while trying to support the environment. Unhelkar (2016) claims that the adoption of Green IT provides the opportunity for the organisation to offer product or services to the other organisation at the same time achieve green initiatives and goals. Moreover, Gupta and Kumar (2012) emphasize that major IT companies are already applying green standards to their operations to gain new revenue opportunities and promote social and environmental responsibility influencing customers and market competition. Besides the development of policies and the provision of supervisory support, Lee et al. (2013) state that overseas governments have proactively taken the lead concerning Green IT and technology initiatives by funding R&D collaboration between the government, academia, and industry, and offering incentives for deployment.

Cost Factor. Referring to Chen and Ma (2014) and Dibra (2015), claim that cost is one of the factors in the adoption of new technology. In implementing the new technologies, especially in green technology, the start-up cost was high, but the government believed that

the maintenance costs would be low in the long run, making the technologies cost-effective (Managi et al., 2014). De Zoysa and Wijayanayake (2013) pointed out that even though the time taken to reach breakeven is high, however, government incentives may contribute to the value proposition, and new challenges will come up as new technology, skills, and process changes. Plus, Mohammed et al. (2015) illustrate that the adoption of Green IT is a significant saving in the product costs by utilizing resources efficiently.

Theoretical Framework

The theoretical framework is constructed as a guide for the entire process in this case study. Figure 1 shows the theoretical framework of Green IT adoption based on the collected secondary data from the academic scholar about technology adoption and Green IT. It is formulated to explain, predict, and understand phenomena and to challenge and extend existing knowledge within the limits of critical bounding assumption. The theoretical framework in this case study consists of seven factors which is Technological Factor, Organisational Factor, Environmental Factor, Regulatory Support Factor, Competitive Pressure Factor, Business Opportunity Factor, and Cost Factor. In each of the listed factors has further explanation enables to go in-depth about the research topic. Based on the theoretical framework, the elements guided the whole process for the adoption of Green IT in Malaysia in term of management. As shown in Figure 1, this study concluded that the theoretical framework was constructed based on the research objectives as the research objective is to examine the factors rendered in Green IT adoption and the proposed framework in Green IT adoption. Thus, based on this theoretical framework, the researcher is able to conduct semi-structured interviews to test this theory in order to gain the outcome and finally will be able to propose new framework.

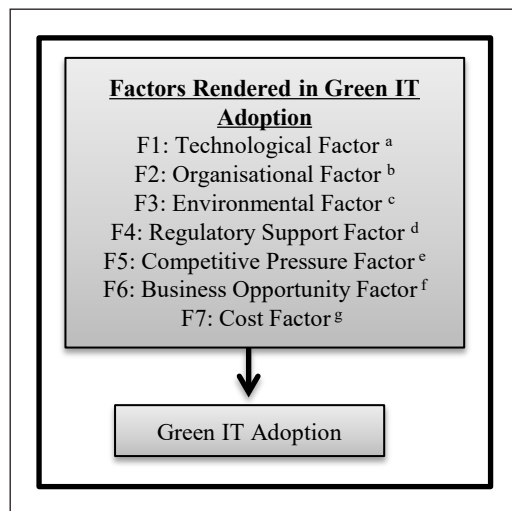


Figure 1. Theoretical framework

MATERIALS AND METHODS

This study is conducted qualitatively in semi-structured interviews and a purposive sampling approach. The 23 respondents participate in these interviews with open-ended questions (six respondents from KeTTHA, six respondents from MAMPU, one respondent from GreenTech Malaysia, six respondents from IBM Malaysia and four respondents from HP Malaysia). The respondents are a policymaker, ICT coordinator, execution of Green

Technology Policy and IT producers. Purposive sampling or judgmental sampling was applied in collecting the data following the opinion of an expert in a particular field is the topic of interest (Martínez-Mesa et al., 2016). This study, specifically selected respondents from public and private company mentioned to contribute to the Green IT adoption topic and sharing their expert knowledge and experiences on the factors and the process of adopting Green IT in organizations. The 23 respondents are sufficient to represent this study as data reached a point of saturation which when the new themes stop emerges, the researcher can conclude that there is no need for more interviews (Saunders et al., 2016). Saunders et al. (2016) claimed that the minimum sample size for in-depth interview is 5 – 25 respondents. Besides, at least 15 interviews were needed for the sample size requirement for all types of qualitative research (Guest et al., 2006). As a rule of thumb, it can be said that interview studies tend to have around 15 participants, which is a number that makes possible practical handling of the data (Brinkmann, 2013).

RESULTS AND DISCUSSIONS

Technological Factor

According to Shibly (2015) stated that technology is not a passive observer, but it is an active contributor in achieving the goals of Green IT. There are three criteria elaborate on the technological factor. First, the company following the trend and direction of technology; second is adopting IT software (green data centre, cloud computing, adopted virtualization of technology); and third is IT hardware (thin client which shared personal computer (PC) that has a small Central Processing Unit (CPU) and optimizing the use of CD, driver, and other hardware which at the end contribute to the electronic waste). Results show that 14 out of 16 respondents agreed technological factor is one of the factors in adopting Green IT. One of the respondents from KeTTHA quotes that

“...Technology is always coming and we need to pursue the technology”.

One of the Respondents from MAMPU agrees that:

“For Green IT technology, the company is constantly looking at new technologies and alerts about the latest technology to support the reduction of carbon emission.

One of the respondents from Green Tech said that:

“The technology that’s appropriate, fulfilling the desired green requirements, will be adopted into the organisation”.

Thus, the similarities public and private sector is the adoption the latest technology such as cloud, green data centre, and virtualization, shared the same views regarding the

technologies are growing over time and they took as an advantage to their organisation to improve the technologies in the organisation. Plus, four respondents from IBM Malaysia and HP Malaysia agree that must grab the new technologies as an opportunity to develop the new products and services to meet the customer expectation based on the circulation of time. One of the respondents from the Company stated that:

“...HP Malaysia is always looking for growth technologies which able to meet the customer expectation at the same time contribute to the eco-friendly by manufacturing a new product which minimizes the use of hazardous materials and fulfils the global requirements”.

Table 1 simplify the result.

Table 1
Technological factor in Green IT adoption

Technological factor criteria	Result from Public Company	Result from Private Company
Follow the trend and direction of technology	<i>“Technology is always coming and we need to pursue the technology” (Respondent from KeTTHA)</i>	<i>“HP Malaysia is always looking for growth technologies which able to meet the customer expectation at the same time contribute to the eco-friendly by manufacturing a new product which minimizes the use of hazardous materials and fulfils the global requirements” (Respondent from HP Malaysia)</i>
Adopting IT software	<i>“For Green IT technology, the company is constantly looking at new technologies and alerts about the latest technology to support the reduction of carbon emission (Respondent from MAMPU)</i>	
IT hardware	<i>“The technology that's appropriate, fulfilling the desired green requirements, will be adopted into the organisation” (Respondent from GreenTech)</i>	

Organisational Factor

There are six criteria in the organisational factor. First, responsible in developing country and plays its role with the nation as stated by Ministry of Energy, Green Technology and Water of Malaysia (2009) that Malaysia has taken serious steps in addressing global emissions problems by launching a program of National Green Technology Policy in 2009. Second criteria are based on three stages of adoption in government which is procurement side (match with a green aspect such as Energy Star, EPEAT), uses side (electric consumption on hardware such as PC, Monitor, server, printer, notebook, and the application) and disposal side (follow government disposal procedure asset 2007). Third, forced by Green Technology Policy and IT as an initiative to develop Green IT. Fourth is top management support to make the organisation a role model or benchmark. The fifth is improving the environmental performance and sixth is the opportunity to gain profit at the same time responsible to provide the best product and services through the adoption.

12 out of 13 respondents were agreed towards this factor. One of the respondents from MAMPU responded:

“...Either organisation wants to adopt it or leave it, the decision is fixed where we need to adopt the Green IT due to Malaysia wants to be seen as the responsible developing country that plays its role with the nation”.

Respondents from IBM Malaysia responded that:

“...We adopt green to the organisation first in each operation of IT, and then we will deliver to the customers”.

Thus, the results show that the similarities between public and private sector through top management think are Green IT able to improve the overall performance at the same time being a benchmark in supporting Green Technology Policy, the adoption also one of the values for the organisation to be leading in the development of ICT technologies and provide the best solutions to the nation. Table 2 quotes the result.

Table 2
Summarize of organisational factor in Green IT adoption

Organisational factor criteria	Result from Public Company	Result from Private Company
Responsible in developing country	<i>“...Either organisation wants to adopt it or leave it, the decision is fixed where we need to adopt the Green IT due to Malaysia wants to be seen as the responsible developing country that plays its role with the nation” (Respondent from MAMPU)</i>	<i>“...We adopt green to the organisation first in each operation of IT, and then we will deliver to the customers” (Respondent from IBM Malaysia)</i>
Three stages of adoption in government:		
<ul style="list-style-type: none"> • procurement side • uses side • disposal side 		
Forced by green technology policy		
Top management support		
Improve the environmental performance		
Opportunity to gain profit		

Environment Factor

For the environment factor, there are six criteria listed. First, reduce energy usage on the hardware of IT; second is implementing of cloud which could reduce electronic waste; third is preserving resources; fourth is responsibility leading to climate changes and commits to reducing the carbon footprint; fifth able to manage its environmental impact by adopting environmentally responsible emphasized in every department including operation, manufacturing, supply chain and sixth is specified all products meet the global green standard such as Restriction of Hazardous Substances (RoHS), Energy Star and Waste

Electrical and Electronic Equipment Directive (WEEE). In this factor, 13 out of 13 stated this is the reason they are adopted Green IT. One of the KeTTHA respondent stated that:

“After Green IT was adopted in KeTTHA, it can be seen that reduction around 60% to 70% of energy”.

This is supported by KeTTHA and Green Computing Initiative (2012) claimed that through the measurement via Power Usage Efficiency (PUE) tools, it can be seen that previous conventional technology, the new generation facility has enabled energy savings of 61.79%. The similarities among five organisations: the reducing of energy consumption and carbon emission from the operation. One of the IBM Malaysia respondents claim that:

“...As we can see, companies need IT equipment for business matters connected with the other individual or organisation. Besides, IT hardware such as a PC, printer, storage and other equipment contained hazardous materials which produced lots of carbon emissions. From there, the company starts to produce all the equipment and technology that suits the environment and people concern”.

Differences can be seen where the public sector is more on the using and disposing side where monitoring is easier than the private sector. The private sector needs to focus on every side of adoption, which is manufacturing, design, using and dispose of. It includes monitoring to achieve the mission in reducing the consumption of energy and decreasing the carbon emission. Table 3 simplifies the result.

Business Opportunity Factor

The criteria of business opportunity recorded sixth factor. First is producing products and services which can be commercialized to the internal and external of Malaysia. Second is high demand in a business opportunity. The third is the government more towards strategic collaborative engagement sharing the adoption knowledge among the agencies. Fourth is offers other private companies rebate and incentive to implement green technology project as highlighted by MyHijau (2017) that the government also pledged to deliver investment tax such as green investment tax allowance for companies that undertake green technology projects for business purpose, purchase green technology products, equipment and system that qualify as capital assets, and green income tax exemption for the company undertaking new green technology activities approved by GreenTech Malaysia. Fifth is depends on customer requirement and sixth is challenges and listening to the customer as a priority and start producing products. The result shows eight out of ten respondents were agreed towards this factor. One of the GreenTech respondent stated that:

“...Green IT generates an opportunity to an organisation especially for an organisation that produces products and services. GreenTech has produced and

Table 3
Summarize of environmental factor in Green IT adoption

Environment factor criteria	Result from Public Company	Result from Private Company
Reduce energy usage on hardware of IT	<p>“After Green IT was adopted in KeTTHA, it can be seen that reduction around 60% to 70% of energy” (Respondent from KeTTHA)</p>	<p>“...As we can see, companies need IT equipment for business matters connected with the other individual or organisation. Besides, IT hardware such as a PC, printer, storage and other equipment contained hazardous materials which produced lots of carbon emissions. From there, the company starts to produce all the equipment and technology that suits the environment and people concern” (Respondent from IBM Malaysia)</p>
Implementation of Cloud	<p>The measurement via Power Usage Efficiency (PUE) tools, it can be seen that previous conventional technology, the new generation facility has enabled energy savings of 61.79% (KeTTHA and Green Computing Initiative,2012)</p>	
Preserve resource Responsibility leading to climate changes and commits to reduce carbon footprint. Adopting environmentally responsible Meet the global green standard	<p>developed Green IT solution that calls as a thermodynamic solution by ourselves and we already commercialized to the external market. Therefore, today and the future, we have been moving forward by issuing standards, practices and provide advice to the European (EU) market”.</p> <p>A respondent from IBM Malaysia stated:</p> <p>“... IBM Malaysia has adopted Green IT as a company is a leading company which the core business is to provide IT products, design of worldwide data centre, relocation and other services since the establishment of the company. Thus, the adoption of Green IT is a big opportunity to meet the customer requirement at the same time support the global mission to reduce the carbon footprint”.</p>	

Therefore, it is understood that when the organisation looking at the business opportunity side, organisations will see that the adoption of Green IT provides the best profit in end-to-end IT life. Moreover, through the offers by government sector such as financing loan, rebates, tax allowance, and other incentives, the organisation will be able to adopt Green IT as their initiative to face the challenges to meet the customer requirement and lastly fulfil the satisfaction from the products and services. Table 4 quotes the result.

Cost factor

First, initial costs of converting from conventional to Green IT technology is high, but reduction costs can be seen in the operational and provide a solid return to the business in the return of investment (ROI). This is supported by KeTTHA and Green Computing Initiative (2012) that Green IT adoption has reduced the overall expenditure of operating the public sector’s backend IT facilities which currently stands at RM 120 million annually, compared to previously where cost electricity is expected to rise sharply over the next few years, amidst the planned end of gas subsidies coupled with the ever-growing IT facilities

Table 4
Summarize of business opportunity factor in Green IT adoption

Business opportunity factor criteria	Result from Public Company	Result from Private Company
Producing products and services which can be commercialize to the internal and external of Malaysia	“...Green IT generates an opportunity to an organisation especially for an organisation that produces products and services. GreenTech has produced and developed Green IT solution that calls as a thermodynamic solution by ourselves and we already commercialized to the external market. Therefore, today and the future, we have been moving forward by issuing standards, practices and provide advice to the European (EU) market” (Respondent from GreenTech)	IBM Malaysia has adopted Green IT as a company is a leading company which the core business is to provide IT products, design of worldwide data centre, relocation and other services since the establishment of the company. Thus, the adoption of Green IT is a big opportunity to meet the customer requirement at the same time support the global mission to reduce the carbon footprint”. (Respondent from IBM Malaysia)
High demand		
Government-strategic collaborative among the agencies		
Offers other private companies rebate and incentive		
Customer requirement. Customer as priority		

requirement, the amount that government should pay is RM619 million for 2020. Second is reducing cost in term of energy consumption, human resources, and maintenance which decrease the cost up 30% on maintenance cost. Third, the adoption of Green IT will cut the workforce from 50 to only a few workers compared to conventional. Reduce the costs in terms of employment, equipment, expertise, salaries, and many others. Fourth, the public sector is more geared towards performance and service, but private is more concerned with performance and profit. 14 out of 14 agreed cost is one of the factors in adopting Green IT. One respondent from MAMPU claimed that:

“...The development of Green IT is consuming high cost. But it will reduce costs over a long period due to the cost of startup Green IT is quite high. However, saving energy consumption has been greatly reduced where KeTTHA has savings of RM7000 to RM8000 per month when compared with conventional”.

One of the respondents from HP Malaysia believes that:

“...In the development of new technology especially green technology, it utilizes a lot of initial costs and I believed that cost factor is one of the reason company adopt Green IT due to the profit that will gain from the production of a green product that generates from an expensive price on the market”.

Based on the five organisations, it demonstrates that organisations believed converting to the Green IT requires high cost due to the certain high technologies with the green specification. Even though the cost of development is expensive, it proved that the development would help organisations toward efficiency, cost-saving, and increase the performance. However, as the private sector is looking for the profit, they believed that the adoption would show the impact based on the supporting of customers to their products. Thus, it shows that cost is a small issue to be compared with the return they obtain from the products and services. Table 5 quote the result.

As a conclusion, the result discussed above, shown that regulatory support factor and competitive pressure factor is not influence by the adoption of Green IT for the public and private sector. The reason is the respondents are not looking for regulatory and competitive in the adoption of Green IT. Plus, 11 out of 12 stated the regulatory support factor and 7 out of 11 clarified competitive are not relevant to adopt Green IT. The results rendered to the environmental factor, cost factor, organisational factor, technological factor, and business opportunity factor. It is not denying that the government sector is more toward performances of service to the society without thinking of competition among each other, whereas this study found that competitive pressure among private sector is not valid due to small market in Malaysia.

Table 5
Summarize of cost factor in Green IT adoption

Cost factor criteria	Result from Public Company	Result from Private Company
Initial costs is high but reduction costs can be seen in the operational	<i>"...The development of Green IT is consuming high cost. But it will reduce costs over a long period due to the cost of startup Green IT is quite high. However, saving energy consumption has been greatly reduced where KeTTHA has savings of RM7000 to RM8000 per month when compared with conventional"</i> (Respondent from MAMPU)	<i>"...In the development of new technology especially green technology, it utilizes a lot of initial costs and I believed that cost factor is one of the reason company adopt Green IT due to the profit that will gain from the production of a green product that generates from an expensive price on the market".</i> (Respondent from HP Malaysia)
Reduce cost of: energy consumption, employment, equipment, expertise, salaries. in public sector (performance and service) in private sector (performance and profit)		

The Proposed Framework in Implementing Green IT

Results from the first objective to identify rendered factors are environmental factor, cost factor, organisational factor, technological factor, and business opportunity factor. The results lead to the second objective in proposing a framework on the factors rendered in Green IT adoption. As this study is based on a deductive approach which using the theoretical framework to help organize and direct the data analysis, the researcher analysed the data based on the research questions and research objectives at the same time using the theoretical framework as a guideline. Figure 2 shows the Proposed Framework in implementing Green IT.

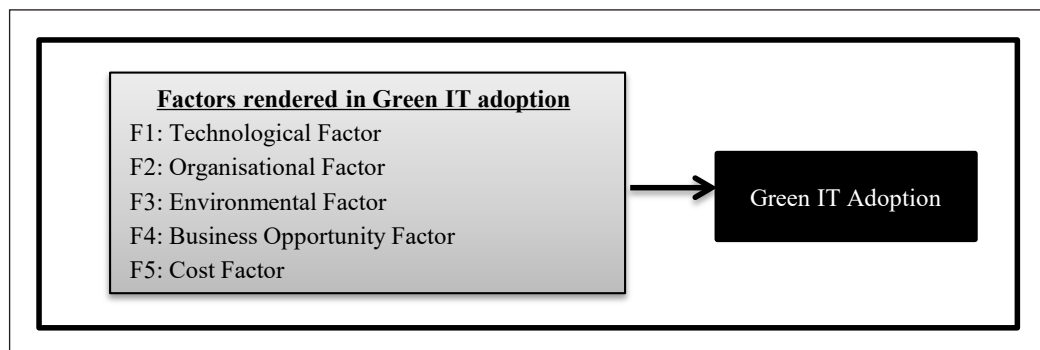


Figure 2. The proposed framework in implementing the Green IT

Figure 2 shows significant in this study. This is related to the strategy to develop the proposed framework of Green IT adoption in Malaysia, starting from the literature review on the research objective. After the researcher gone through the literature reviews, the researcher constructed the theoretical framework which consists of seven factors of Green IT adoption as shown in Figure 1. Secondly, after the theoretical framework was constructed, the researcher collected the data through a semi-structured interview. The interviewer conducted to gain an in-depth understanding regarding the Green IT adoption at the same time to test the theoretical framework with five organisations that have their roles in the adoption of Green IT. Next, this study explained based on a deductive approach which using the theoretical framework to help organise and direct the data analysis, the researcher analysed the data using explanation building based on the research questions and research objectives at the same time using the theoretical framework as a guideline. Therefore, Figure 2 is an outcome of a theoretical framework that called a proposed framework which can be assisting policymaker, organisations such as public and private sector and other researchers to support Malaysia's pledge to reduce its Greenhouse Gas (GHG) emission intensity of Gross Domestic Product (GDP) by up to 45% by 2030.

CONCLUSION AND RECOMMENDATION

This study aims to identify the factors rendered in the Green IT adoption in Malaysia and examine the factors that drive the adoption of Green IT in Malaysia. First, there are seven factors rendered in Green IT adoption in Malaysia (Figure 1). Two models are applied (TOE and DOI) to investigate the factors rendered in Green IT adoption and how the Green IT technology diffused in the organisations. Second, through the semi-structured interview, the result shows that the regulatory support factor and competitive pressure factor is not influential in the adoption of Green IT in the public and private sector. The reason is the respondents are not looking for regulatory and competitive in the adoption of Green IT. The results are more focus on the environmental factor, cost factor, organisational factor, technological factor, and business opportunity factor (Figure 2). It is not denying that the government sector is more toward performances of service to the society without thinking of competition among each other, whereas this study found that competitive pressure among the private sector is not valid due to the small market in Malaysia.

This study concluded that competitive pressure happens when it comes to market positioning and competitive pressure would not happen if the company is looking forward and focuses on the environmental responsibility to achieve the goal and improve the quality of business. In terms of the regulatory support factor, the researcher agreed that the respondents are not looking for the regulatory due Green IT in Malaysia is still new and the development of policy, regulation, enforcement is quite difficult. Thus, there are two parameters have been considered by the government body to encourage more organisation

to adopt Green IT which is surveying numbers of the organisation have been adopted Green IT and start to prepare the development of Green IT policy and its enforcement with concern on several elements that would win both sectors.

Nonetheless, there are several benefits to the proposed framework. The proposed framework will go to the policymaker as a policymaker is acting as a funnel to gather information through consultation, research and to reduce and extract from the information, policy or set of policies that serve to promote what is the preferred course of action. From the new framework that been proposed, the policymaker able to see that regulatory support factor is petty looking by the organisations as Green IT policy does not exist yet in Malaysia. From the Green IT policy development, policymaker will be able to stringent the enforcement to the organisations to adopt the Green IT. Besides, from the proposed framework, MAMPU, KeTTHA and GreenTech will be able to develop the Green IT strategies and Green IT agendas to ensure that the Green IT could improve the adoption and well-spread implementation among the public and private sector. They also need to strengthen the activities which will lead the organisation to attract to adopt Green IT. Moreover, the proposed framework also provides the benefit to all private company including IT producers or service providers as a guideline for them to produce, designing, manufacturing Green IT products. The proposed framework also significance to the other researchers who willing to conduct further research. The proposed framework can be a guideline and reference for the researchers to conduct the other renewable energy sources such as solar computing as an innovative suggestion to the organisation where this initiative has been developed and produced by the other countries such as solar photovoltaic keyboard as Malaysia market about the solar photovoltaic in still low development.

ACKNOWLEDGEMENT

The author(s) extend their gratitude to Associate Professor Dr Chew Boon Cheong and Professor Ir Adi Saptari for guidance during this study research. This study is part of a dissertation which was submitted as partial fulfilment to meet requirements for the degree of Master at Universiti Teknikal Malaysia Melaka.

REFERENCES

- Adnan, N., Nordin, S. M., Bahruddin, M. A., & Tareq, A. H. (2019). A state-of-the-art review on facilitating sustainable agriculture through green fertilizer technology adoption: Assessing farmers behavior. *Trends in Food Science & Technology*, 86, 439-452. <https://doi.org/10.1016/j.tifs.2019.02.040>
- Asadi, S., Pourhashemi, S. O., Nilashi, M., Abdullah, R., Samad, S., Yadegaridehkordi, E., Aljojo, N., & Razali, N. S. (2020). Investigating influence of green innovation on sustainability performance: A case on Malaysian hotel industry. *Journal of cleaner production*, 258, Article 120860. <https://doi.org/10.1016/j.jclepro.2020.120860>

- Asadi, S., Razak, A., Hussin, C., & Mohamed, H. (2017). Telematics and informatics organizational research in the field of green IT: A systematic literature review from 2007 to 2016. *Telematics and Informatics*, 34(7), 1191-1249. <https://doi.org/10.1016/j.tele.2017.05.009>
- Asadi, S., Yadegaridehkordi, E., Nilashi, M., & Samad, S. (2019). Green information technology adoption: A systematic literature review. *Journal of Soft Computing and Decision Support Systems*, 6(3), 8-17.
- Azis, S. S. A. (2021). Improving present-day energy savings among green building sector in Malaysia using benefit transfer approach: Cooling and lighting loads. *Renewable and Sustainable Energy Reviews*, 137, Article 110570. <https://doi.org/10.1016/j.rser.2020.110570>
- Brinkmann, S. (2013). *Qualitative interviewing*. Oxford university press.
- Chen, H., & Ma, T. (2014) Technology adoption with limited foresight and uncertain technological learning. *European Journal of Operational Research*, 239(1), 266-275. <https://doi.org/10.1016/j.ejor.2014.03.031>
- Cobos, L. M., Mejia, C., Ozturk, A. B., & Wang, Y. (2016). A technology adoption and implementation process in an independent hotel chain. *International Journal of Hospitality Management*, 57, 93-105. <https://doi.org/10.1016/j.ijhm.2016.06.005>
- Dalvi-Esfahani, M., Alaadini, Z., Nilashi, M., Samad, S., Asadi, S., & Mohammadi, M. (2020). Students' green information technology behavior: Beliefs and personality traits. *Journal of Cleaner Production*, 257, Article 120406. <https://doi.org/10.1016/j.jclepro.2020.120406>
- Dash, P., Pattnaik, S., & Rath, B. (2016). Technology adoption process under internal uncertain environment in financial institutions: A case study with reference to public sector banks in India. *International Journal of Applied Engineering Research*, 11(1), 162-172.
- De Zoysa, M., & Wijayanayake, J. (2013). The influential factors of green IT adoption in data centres of Sri Lankan banks. *Journal of Emerging Trends in Computing and Information Sciences*, 4(12), 908-915.
- Dibra, M. (2015). Rogers theory on diffusion of innovation-the most appropriate theoretical model in the study of factors influencing the integration of sustainability in tourism businesses. *Procedia-Social and Behavioral Science*, 195, 1453-1462. <https://doi.org/10.1016/j.sbspro.2015.06.443>
- Esfahani, M. D., Rahman, A. A., & Zakaria, N. H. (2015). Green IT/IS adoption as corporate ecological responsiveness: An academic literature review. *Journal of Soft Computing and Decision Support Systems*, 2(1), 35-43.
- Fernando, Y., & Wah, W. X. (2017). The impact of eco-innovation drivers on environmental performance: Empirical results from the green technology sector in Malaysia. *Sustainable Production and Consumption*, 12, 27-43. <https://doi.org/10.1016/j.spc.2017.05.002>
- Gazzola, P., Del Campo, A. G., & Onyango, V. (2019). Going green vs going smart for sustainable development: Quo vadis? *Journal of Cleaner Production*, 214, 881-892. <https://doi.org/10.1016/j.jclepro.2018.12.234>
- GreenTech Malaysia. (2011). *Green ICT – The Malaysia's perspectives green technology corporation Malaysia*. Retrieved June 10, 2019, from https://home.jeita.or.jp/greenit-pc/activity/asia/file/Green ICT ___ The Malaysias_Perspectives.pdf

- GreenTech Malaysia. (2013). *National green technology policy: Cleantech made in Germany industry symposium Malaysian green technology corporation green technology corporation Malaysia*. Retrieved June 10, 2019, from <http://www.gtai.de/GTAI/Content/EN/Meta/Events/Invest/2013/Reviews/Powerhouse/Downloads/presentation-130409-malaysia-ismail-malaysian-green-tech-corp.pdf?v=2>
- Guest, G., Bunce, A., & Johnson, L. (2006). How many interviews are enough? An experiment with data saturation and variability. *Field Methods, 18*(1), 59-82. <https://doi.org/10.1016/j.jclepro.2018.12.234>
- Gupta, S., & Kumar, V. (2012). Sustainability as corporate culture of a brand for superior performance. *Journal of World Business, 48*(3), 311-320. <https://doi.org/10.1016/j.jwb.2012.07.015>
- Junior, B. A., Majid, M. A., & Romli, A. (2018). Green information technology for sustainability elicitation in government-based organisations: An exploratory case study. *International Journal of Sustainable Society, 10*(1), 20-41. <https://doi.org/10.1504/IJSSOC.2018.092648>
- Kasbun, R., Adnan, A. S., Khalid, N., & Jaafar, H. (2016). Green ICT practices and challenges: Electronic waste disposals steps awareness in overcoming environmental erosion. *International Conference on Information Technology and Multimedia 2016, 1*, 34-40.
- KeTTHA & Green Computing Initiative. (2012). *The green data centre: Achieving the true potential of sustainable computing*. A Joint Research Report by the Ministry of Energy, Green Technology and Water Malaysia and The Green Computing Initiative. Putrajaya, Malaysia: Author.
- Khan, H., & Faisal, M. N. (2015). A grey-based approach for ERP vendor selection in small and medium enterprises in Qatar. *International Journal of Business Information System, 19*(4), 465-487. <https://doi.org/10.1504/IJBIS.2015.070205>
- Lee, S. G., Trimi, S., & Kim, C. (2013). The impact of cultural differences on technology adoption. *Journal of World Business, 48*(1), 20-29. <https://doi.org/10.1016/j.jwb.2012.06.003>
- Letlonkane, L., & Mavetera, N. (2014). An investigation of factors that inform green IT practices in the North West Provincial Government of South Africa. *Mediterranean Journal of Social Sciences, 5*(20), Article 163. <https://doi.org/10.5901/mjss.2014.v5n20p163>
- Malik, S. A., & Ayop, A. R. (2020). Solar energy technology: Knowledge, awareness, and acceptance of B40 households in one district of Malaysia towards government initiatives. *Technology in Society, 63*, Article 101416. <https://doi.org/10.1016/j.techsoc.2020.101416>
- Managi, S., Hibiki, A., & Shimane, T. (2014). Efficiency of technology adoption: A case study in waste-treatment technology. *Resource and Energy Economics, 36*(2), 586-600. <https://doi.org/10.1016/j.reseneeco.2013.09.002>
- Martínez-Mesa, J., González-Chica, D. A., Duquia, R. P., Bonamigo, R. R., & Bastos, J. L. (2016). Sampling: How to select participants in my research study? *Anais brasileiros de dermatologia, 91*(3), 326-330. <https://doi.org/10.1590/abd1806-4841.20165254>.
- Mergel, I., & Bretschneider, S. I. (2013). A three stage adoption process for social media use in government. *Public Administration Review, 73*(3), 390-400. <https://doi.org/10.1111/puar.12021>
- Ministry of Energy Green Technology and Water. (2017). *Green Technology Master Plan Malaysia 2017 - 2030*. Putrajaya, Malaysia: Author.

- Ministry of Energy Green Technology and Water Malaysia. (2009). *National Green Technology Policy* (1st Ed.). Putrajaya, Malaysia: Author.
- Mohammed, M. A., Muhammed, D. A., & Abdullah, J. M. (2015). Green computing beyond the traditional ways. *International Journal of Multidisciplinary and Current Research*, 3, 787-792.
- Molla, A., & Abareshi, V. C. A. (2014). Green IT beliefs and pro-environmental IT practices among IT professionals. *Information Technology & People*, 27(2), 129-154. <https://doi.org/10.1108/ITP-10-2012-0109>
- Murugesan, S., & Gangadharan, G. R. (2012). *Harnessing green IT: Principles and practices*. Wiley Publishing.
- MyHijau. (2017). *Green incentive*. Retrieved July 10, 2019, from <https://www.myhijau.my/green-incentives/>
- Ojo, A. O., Raman, M., & Downe, A. G. (2019). Toward green computing practices: A Malaysian study of green belief and attitude among information technology professionals. *Journal of Cleaner Production*, 224, 246-255. <https://doi.org/10.1016/j.jclepro.2019.03.237>
- Rad, M. S., Nilashi, M., & Dahlan, H. M. (2018). Information technology adoption: A review of the literature and classification. *Universal Access in the Information Society*, 17(2), 361-390. <https://doi.org/10.1007/s10209-017-0534-z>
- Rahim, R. E. A., & Rahman, A. (2013). Resource-based framework of green IT capability toward firms' competitive advantage. In *Proceedings of the 17th Pacific Asia Conference on Information System* (pp. 18-22). Association for Information Systems.
- Saha, B. (2014). Green computing. *International Journal of Computer Trends and Technology (IJCTT)*, 14(2), 46-50.
- Saunders, M., Lewis, P., & Thornhill, R. (2016). *Research methods for business student* (7th Ed.). Pearson Education Ltd.
- Shameer, A. P., Haseeb, V. V., & Mol, V. K. M. (2015). Green approach for reducing energy consumption-A case study report. *International Journal*, 5(1), 1-10.
- Shibly, A. (2015). Green computing – Emerging issues in IT. *ResearchGate*, 1-15. <https://doi.org/10.13140/RG.2.1.1729.4248>
- Simon, C. (2013). *Driving new technology adoption in South Africa's energy sector*. Retrieved July 10, 2019, from <http://pubs.iied.org/pdfs/17178IIED.pdf>
- Singh, J. V., & Vatta, S. (2016). Green computing: Eco friendly technology. *International Journal of Engineering Research and General Science*, 4(1), 280-283.
- Taruna, S., Singh, P., & Joshi, S. (2014). Green computing in developed and developing countries. *International Journal in Foundations of Computer Science & Technology (IJFCST)*, 4(3).
- Unhelkar, B. (2016). *Green IT strategies and applications: Using environmental intelligence*. CRC Press.
- Zailani, S., Govindan, K., Iranmanesh, M., Shaharudin, M. R., & Chong, Y. S. (2015). Green innovation adoption in automotive supply chain: The Malaysian case. *Journal of Cleaner Production*, 108, 1115-1122. <https://doi.org/10.1016/j.jclepro.2015.06.039>

Zhang, Y., Sun, J., Yang, Z., & Wang, Y. (2020). Critical success factors of green innovation: Technology, organization and environment readiness. *Journal of Cleaner Production*, 264, Article 121701. <https://doi.org/10.1016/j.jclepro.2020.121701>

Magnesium-Palm Kernel Shell Biochar Composite for Effective Methylene Blue Removal: Optimization via Response Surface Methodology

Nur Hanani Hasana¹, Rafeah Wahi^{1*}, Yusralina Yusof¹ and Nabisab Mujawar Mubarak²

¹Faculty of Resource Science and Technology, Universiti Malaysia Sarawak, 94300 UniMAS, Kota Samarahan, Sarawak, Malaysia

²Department of Chemical and Energy Engineering, Faculty of Engineering and Science, Curtin University, 98009 Miri, Sarawak, Malaysia

ABSTRACT

This study investigates the properties and potential application of Mg-PKS biochar composite for methylene blue solution (MB) adsorption. The Mg-PKS biochar composite was developed from palm kernel shell biochar via steam activation followed by MgSO₄ treatment and carbonization. The effect of process parameters such as solution pH (4-10), contact time (30-90 min) and adsorbent dosage (0.1-0.5 g) were investigated via central composite design, response surface methodology. Results revealed that the Mg-PKS biochar composite has irregular shapes pore structure from SEM analysis, a surface area of 674 m²g⁻¹ and average pore diameters of 7.2195 μm based on BET analysis. RSM results showed that the optimum adsorption of MB onto Mg-biochar composite was at pH 10, 30 min contact time and 0.5 g/100 mL dosage with a removal efficiency of 98.50%. In conclusion, Mg treatment is a potential alternative to other expensive chemical treatment methods for biochar upgrading to the adsorbent.

Keywords: Adsorption, magnesium treatment, methylene blue, palm kernel shell biochar, response surface methodology

ARTICLE INFO

Article history:

Received: 02 February 2021

Accepted: 16 April 2021

Published: 31 July 2021

DOI: <https://doi.org/10.47836/pjst.29.3.28>

E-mail addresses:

nurhananihasana@gmail.com (Nur Hanani Hasana)

wrafeah@unimas.my (Rafeah Wahi)

yyusralina@unimas.my (Yusralina Yusof)

mubarak.mujawar@curtin.edu.my (Nabisab Mujawar Mubarak)

* Corresponding author

INTRODUCTION

Methylene blue (MB) is a common basic dye applied in paper colouring, hair dye, cotton dyeing and others (Ba et al., 2020). Methylene blue was also studied for medical uses, including antimicrobial chemotherapy,

biomedical colouring for cell staining, phototherapy and cancer research (Sahu et al., 2020). However, exposure to MB at high concentration can affect human health, for example, difficulty in breathing, retching, nausea, gastritis, and diarrhoea (Sahu et al., 2020). At doses greater than 7.0 mg/kg, MB could cause high blood pressure, mental disorder, and abdominal pain (Albadarin et al., 2016).

Adsorption, ion exchange, and precipitation are some of the approaches that always have been improved to extract dyes, including MB, from wastewaters (Karaer & Kaya, 2016). Adsorption is the most preferred technique to remove organic contaminants from an aqueous solution as it has produced results with high removal capacity (Alene et al., 2020). The effectiveness of the adsorption process is attributed to several factors related to the adsorbent used, for instance, large specific surface area, porous structure, enhanced functional groups and mineral components (Tan et al., 2015).

Adsorption of MB using adsorbents derived from agricultural waste-based biochar has received considerable attention in previous studies due to its low raw material cost and good adsorption capacity (Niran et al., 2018; Kuang et al., 2020). Its utilization as an adsorbent also helps to solve the problems of agricultural waste management. Several researches have been carried out on the use of chemically modified biochar as an adsorbent for the removal of MB. For example, sulfuric acid-treated coconut leaves biochar (Jawad et al. 2016), and phosphoric acid-treated PKS biochar (Niran et al., 2018) has been studied for MB adsorption from aqueous solution. Most previous studies focused on MB removal by acid/base treated biochar and rarely by minerals.

At the same time, previous studies indicated that Mg treatment could effectively improve the biochar properties and adsorption capacities. Mg salts and their oxides have several advantages for biochar's chemical treatment due to its low treatment cost, easy availability, and environmental soundness (Zhao et al., 2018). Mg salt which has a good dehydration ability could react with the carbohydrate polymers in biomass to maximize the release of volatile matter during pyrolysis. The process results in Mg-biochar composite with excellent porosity, which in turn, improves the adsorption properties (Shen et al., 2018). Mg-biochar composite has been studied for the removal of phosphate (Jung & Ahn, 2015; Zhang et al., 2012), nitrate (Zhang et al., 2012), lead (Jellali et al., 2016), and levofloxacin (Zhao et al., 2018) from aqueous solution. However, there is currently no published information available on the applicability of Mg-PKS biochar composite to remove MB from an aqueous solution, especially concerning the removal efficiency and adsorption capacity. Considering the applicability of Mg biochars in treating several common pollutants in water, it is crucial to evaluate the potential application of Mg-PKS biochar composites for removing common dyes, such as MB, from wastewater.

This paper reports the properties and application of Mg-PKS biochar composite derived from palm kernel shell (PKS) biochar for MB removal. In this work, Mg-PKS biochar

composite was developed via steam activation of PKS biochar, which was followed by Mg treatment and carbonization. The efficiency of Mg-PKS biochar composite for the removal of MB from aqueous solution was investigated. The effect of process factors such as pH, contact time and dosage via RSM were also determined.

MATERIALS AND METHOD

Preparation of Mg-PKS Biochar Composite

The PKS biochar used as a precursor for Mg-PKS biochar composite was prepared through fast carbonization via rotary kiln (800°C, 10 min), followed by steam activation for 8 h. The biochar was washed with distilled water to eliminate impurities and dried before mineral treatment. PKS biochar (0.5 mm, 20 g) were soaked in 500 mL MgSO₄·7H₂O (30°C, 60 h) (Zhao et al., 2018), vacuum filtered, and oven-dried (90°C for 12 h). The Mg-PKS biochar composite was then carbonized (500°C, 30 min) (Zhao et al., 2018). The resulting Mg-PKS biochar composite was cooled to room temperature, rinsed with distilled water to remove debris, and dried prior to use.

Adsorbent Characterization

The proximate analyses of biochar samples were conducted based on ASTM D3173, ASTM D3174, and ASTM D3175. The carbon, hydrogen, nitrogen, sulfur, and oxygen content of the adsorbent were determined using CHNS Elemental Analyzer (ThermoFisher Scientific Flashmart, United States). The Brunauer–Emmett–Teller (BET) analysis of surface area and pore volume of adsorbents were determined using Surface Area Analyzer (Quantachrome® ASiQwin™, United States) with nitrogen (N₂) adsorption technique (Sartape et al., 2012). The functional groups of adsorbents were determined via Fourier Transform Infrared Spectroscopy (FTIR) (Thermo Nicolet Is10, United States) analysis.

Stock Solution Preparation

MB stock solution (Bendosen, Malaysia) was prepared by dissolving 1 g of MB in 1000 ml distilled water to obtain 1000 ppm concentration (Fatiha & Belkacem, 2015). UV/Vis spectrophotometer (JASCO V-730, Japan) at a wavelength of 665 nm, was used to evaluate the concentration of MB. Calibration was conducted using various standard concentrations of MB solution (1, 2, 3, 4, 5, 6, and 7 ppm) (Hasbullah et al., 2014). The amount of MB absorbed at equilibrium, q_e (mg/g), was calculated using Equation 1 (Gnanasundaram et al., 2017).

$$q_e = \left(\frac{(C_0 - C_e)V}{W} \right) \quad \text{Equation 1}$$

Whereas the adsorption efficiency (%) of MB was calculated by using Equation 2 (Gnanasundaram et al., 2017).

$$\text{Percentage removal (\%)} = \left(\frac{C_0 - C_e}{C_0} \times 100 \right) \quad \text{Equation 2}$$

Where,

C_0 = initial concentration of MB (mg/l)

C_e = equilibrium concentration in liquid phase (mg/l)

V = volume of solution

W = mass of adsorbent

Adsorption Study via Response Surface Methodology (RSM) approach

Response surface methodology (RSM) with central composite design (CCD) was employed to optimize the MB removal parameters by Mg-PKS biochar composite. RSM was chosen as the statistical technique to verify the relationships between the independent parameters and their effect on the adsorption (Mousavi et al., 2017). CCD was applied to study the effects of pH (4-10), contact time (30-90 min) and adsorbent dosage (0.1-0.5 g) on the removal efficiency of MB by Mg-PKS biochar composite (Table 1). Each factor was ranged in terms of +1 and -1, signifying high and low levels, respectively.

Table 1
Experimental factors design using CCD

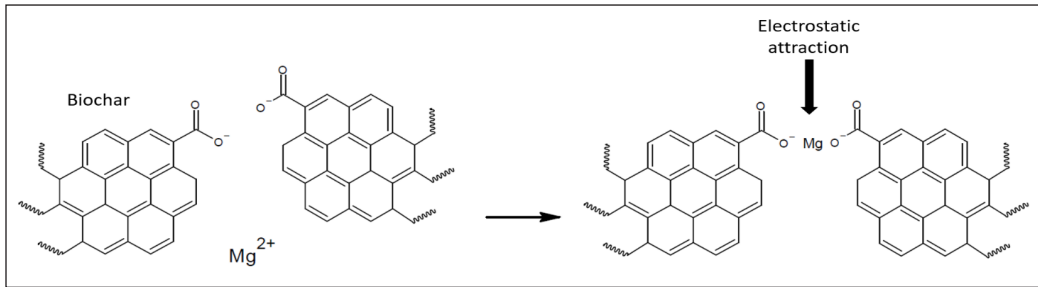
Parameters	Units	Low	High
pH	pH	4	10
Contact time	min	30	90
Adsorbent dosage	g	0.1	0.5

RESULTS AND DISCUSSION

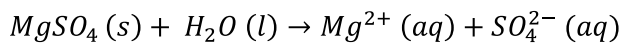
Preparation of Mg-PKS Biochar Composite

The modification of PKS biochar was carried out to improve the adsorption capability of the biochar as an adsorbent. In this study, PKS biochar was chemically modified with magnesium sulfate. Scheme 1 displayed the proposed mechanism for the impregnation of Mg on biochar.

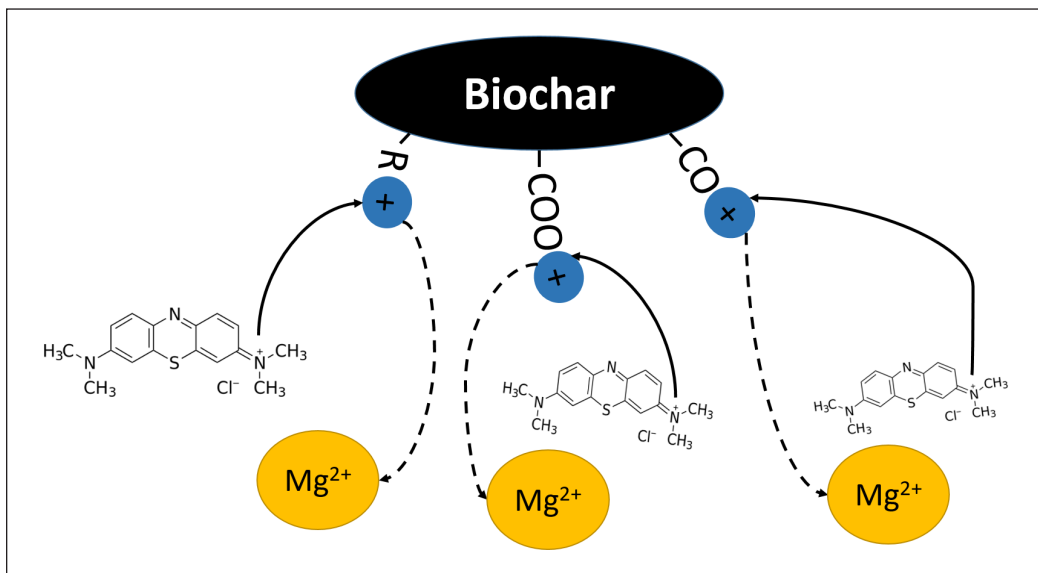
The compound was formed during the modification process of biochars, where the biochars were soaked in magnesium sulphate. The Mg^{2+} from $MgSO_4$ would bind or attract the negatively charged biochar, as shown in the equation as follows.



Scheme 1. Proposed mechanism for modification of Mg-PKS biochar composite



Mg is a positively charged compound as well as MB, thus, the repulsion between Mg and MB might happen. However, based on the SEM image of Mg-PKS biochar composite (Figure 1b), it can be observed that the Mg-treatment did not cover the whole biochar surface, thus leaving the negatively charged surface as it is, indicating that electrostatic interaction might occur between Mg-PKS biochar composite and MB. Cation exchange might also involve the adsorption of MB onto PKS biochar (Fan et al., 2016; Zhu et al., 2015). MB is widely used as a standard reagent for cation exchange determination in soil (Zhu et al., 2015). Scheme 2 is the proposed mechanism of MB adsorption onto the surface of Mg PKS biochar.



Scheme 2. Proposed mechanism of the adsorption of MB onto the surface of Mg PKS biochar

The occurrence of cation exchange during the adsorption of MB might occur when Mg compounds on the biochar surface are released and replaced with MB. The possibility of intraparticle diffusion and pore diffusion to occur is also higher during the adsorption of MB onto all chemically modified biochar (Fan et al., 2016; Mahmoudi et al., 2015). Surface complexation comprising a few functional groups such as $-CH$, $-OH$, $-CO$, and $-COOH$ are inclined to be involved in MB binding onto the surface of biochar as well (Fan et al., 2016). The aromatic structures of both biochar and MB could instigate $\pi-\pi$ (π) stacking interactions, causing MB to be readily adsorbed by biochar, facilitating the adsorption process (Wu et al., 2014).

Adsorbent Characterization

Ultimate and Proximate Analysis. Table 2 displays the element content of the Mg-PKS biochar composite for both ultimate and proximate analysis. The highest element content in the samples is carbon, followed by other elements like oxygen, hydrogen, nitrogen and sulfur. Carbon and oxygen can be regarded as significant elements in the samples, while hydrogen, nitrogen and sulfur are the minor elements since they are in low concentration (Liew et al., 2017).

Table 2
Ultimate and proximate analysis for steam activated biochar and Mg-PKS biochar composite

Elements	Ultimate analysis		Elements	Proximate analysis	
	Steam activated biochar (%)	Mg-PKS biochar composite (%)		Steam activated biochar (%)	Mg-PKS biochar composite (%)
Carbon	70.37	62.81	Moisture content	10.81	19.28
Hydrogen	2.02	1.70	Ash content	26.62	28.48
Nitrogen	0.25	0.34	Volatile matter	45.90	14.26
Oxygen	26.78	32.72	Fixed carbon	11.84	37.97
Sulfur	0.57	2.43			

High carbonization temperature enhances the carbon content of biochar, related to the aromatic part of the biochar (Wahi et al., 2015). Carbon content is an essential aspect of identifying valuable and excellent biochar (Mahmood et al., 2015). From Table 2, it can be observed that Mg-PKS biochar composite has a high fraction of carbon content of 62.81%. This biochar can be regarded as a promising biochar owing to the fact that its carbon content is higher than 60% (Mahmood et al., 2015). There is no significant change in nitrogen content since nitrogen functional groups cannot generate vaporized molecules, but they can produce complex substances (Fang et al., 2014). In terms of sulfur content, there is a high

possibility that sulfur was not detectable in raw PKS because the concentration discovered was below the lowest detection limit of the CHN analyzer (Liew et al., 2017). Mg-PKS biochar composite exhibits a negligibly low concentration of sulfur of 2.43%. The sulfur content might be derived from the sulfate of $\text{MgSO}_4 \cdot 7\text{H}_2\text{O}$ during the loading process.

Mg-PKS biochar composite shows high moisture content (19.28%), which might be due to biochar being soaked in $\text{MgSO}_4 \cdot 7\text{H}_2\text{O}$ solution for 60 h. The reason might be caused by the washing process during the modification of the PKS biochar. Biomass with a moisture content of more than or equal to 40% is not deemed suitable for carbonization since the process will require more energy and time, which are not economically feasible (Tripathi et al., 2016). Ash content is incombustible minerals such as calcium, magnesium, phosphorus, sodium, potassium, and iron found in the biomass (Pinto et al., 2019; Patel & Gami, 2012). Mg-PKS biochar composite has an ash content of 28.48%, which is likely due to the addition of Mg minerals in the biochar (Zhao et al., 2018).

Volatile matter contains flammable gases, namely methane, hydrogen, oxygen and carbon monoxide, and non-flammable gases (Sarkar, 2015). The volatile matter for the Mg-PKS biochar composite is 14.26%. High-volatile biochar combusts more readily than biochar with low volatile matter due to a high amount of combustible gases (Sarkar, 2015). The high temperature used during the carbonization process was responsible for the volatile matter to discharge from weaker bonds hence being released to the atmosphere (Antunes et al., 2017). Biochar with low residual volatile matter is a valuable characteristic of the biochar to act as an adsorbent. The chemical compounds that might be released by the remaining volatile matter in the biochar may react with reactants or products that are parts of any suitable chemical reaction and then produce side products or solely contaminate the products straight away (Lam et al., 2018). High release of volatile matter leads to the production of biochar with additional new pores, hence improving the surface area of the biochar (Liu et al., 2015; Wahi et al., 2015).

Fixed carbon is the residue left in the biochar after devolatilization occurs, and subtracts moisture and ash content (Sarkar, 2015). It is fundamentally carbon comprises of oxygen, hydrogen, nitrogen and sulfur, which are in small quantity (Sarkar, 2015). The fixed carbon in the biochar has the possibility to develop the structure of carbons into pores, which further denotes the potential improvement of the adsorption sites of the biochar (Liew et al., 2017).

SEM Analysis. SEM analysis was piloted to observe the external morphology and pores formation of steam activated PKS biochar and Mg-PKS biochar composite, as revealed in Figure 1a and b, respectively. The presence of pores can be seen clearly in the sample consisting of both small and large pores. The large pores could efficiently enhance many liquid-solid adsorption processes (Rout et al., 2016). Highly porous biochar has the benefit

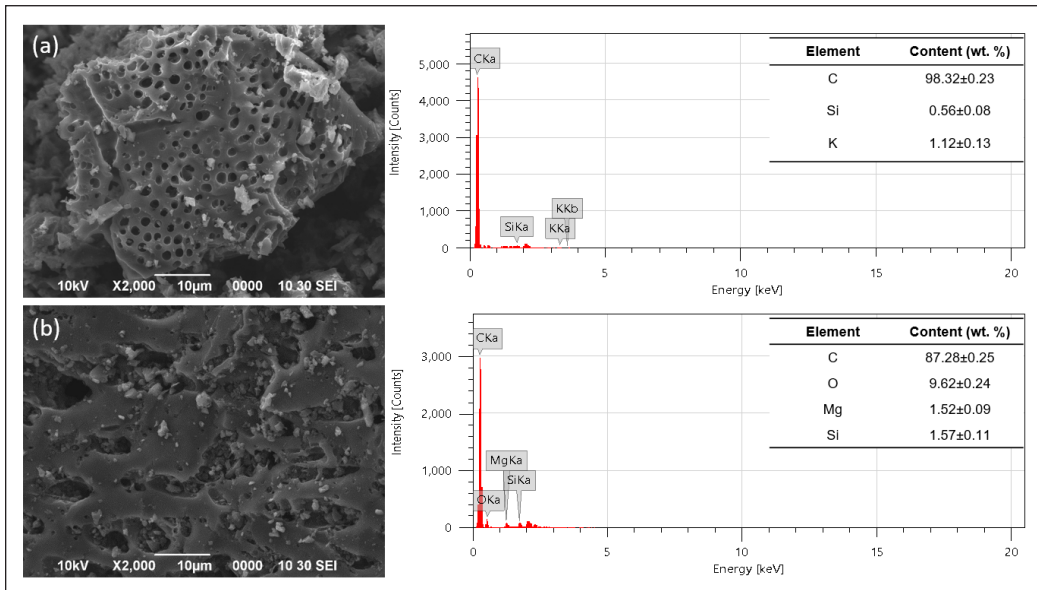


Figure 1. SEM and EDX spectra images of (a) steam activated PKS biochar 2000x, (b) Mg-PKS biochar composite 2000x

of more adsorption of organic pollutants (Rout et al., 2016). Mg-PKS biochar composite displayed irregular-shaped pore structures, including a few notable particles that might be the chemicals. Mg component has been adequately coated on the biochar since the presence of Mg particles can be spotted on the surface of the biochar. The negatively charged surface of biochar attracted the positively charged Mg, thus facilitating the coating process onto the biochar's surface (Rajapaksha et al., 2016). Figure 1 also provides energy dispersive spectroscopic (EDX) results that verify the presence of elements such as carbon (C), silicon (Si), magnesium (Mg), oxygen (O) and potassium (K) in both biochars. Figure 1a indicated that steam activated PKS biochar comprised of C, Si and K with a weight percentage of 98.32±0.23%, 0.56±0.08% and 1.12±0.13%, respectively. Whereas in Figure 1b, the EDX spectra proved the presence of Mg in the Mg-PKS biochar composite with a weight percentage of 1.52±0.09%. The presence of C, O and Si in biochar was also validated with weight percentages of 87.28±0.25%, 9.62±0.24% and 1.57±0.11%, respectively. Steam activated PKS biochar has average pore diameters of 1.80±0.32 µm while Mg-PKS biochar composite with average pore diameters of 7.2195±3.5404 µm.

BET Analysis. The surface area and total pore volume of the Mg-PKS biochar composite were computed using the BET instrument. Surface area and pore volume are a few of the essential characteristics for carbon adsorbent, namely charcoal, activated carbon and biochar, to identify its adsorption capacity (He et al., 2018). The bigger the surface area, the better its adsorptive capacity (Liao et al., 2013). In the current study, the sample was

ground to the size of 0.50 mm. The results discovered that the surface area and total pore volume of steam activated PKS biochar are $592 \text{ m}^2\text{g}^{-1}$ and $0.353 \text{ cm}^3\text{g}^{-1}$. Table 3 displayed the comparison of surface area and total pore volume for raw PKS, PKS biochar and Mg-PKS biochar composite.

Table 3
Surface area and total pore volume for raw PKS, PKS biochar and Mg-PKS biochar composite

Sample	Raw PKS	PKS biochar	Mg-PKS biochar composite
Surface area (m^2g^{-1})	0.848	592	674
Total pore volume (cm^3g^{-1})	0.003	0.353	0.424

Chemical activation and high carbonization temperature affect the size of the surface area of biochar, which leads to the development of additional pores on the biochar (Antunes et al., 2017). Volatile matters discharged during carbonization assist the pore formation in the biochar structure (Antunes et al., 2017). In addition, steam explosion can also affect the size of the surface area of biochar, which can be observed in previous study where biochar derived from wheat, rice, and cotton straws displayed a large specific surface area ($>180 \text{ m}^2\text{g}^{-1}$) (Xue-jiao et al., 2019). The Mg-PKS biochar composite was able to show the highest surface area, which is $674 \text{ m}^2\text{g}^{-1}$. The plausible reason for the high surface area is the reaction between MgCl_2 , which has a good dehydration ability, and the carbohydrate polymers in biomass. The reaction increases the release of volatile matter and enables the creation of more pores during pyrolysis at high temperature (Shen et al., 2018). Shen et al. (2018) showed a similar result where MgO-treated corncob biochar ($26.56 \text{ m}^2\text{g}^{-1}$) has a greater surface area than the surface area of corncob biochar which is $0.07 \text{ m}^2\text{g}^{-1}$.

However, a few studies displayed different results where the surface area of Mg-PKS biochar composite is smaller than the PKS biochar due to the accumulation of Mg elements on the surface of biochar (Fang et al., 2014; Riddle et al., 2019). Mg-PKS biochar composite made from PKS displayed a relatively large surface area compared to other feedstocks such as corncob and wood chips, where at least numerous of them are below $< 500 \text{ m}^2\text{g}^{-1}$ (Shen et al., 2018; Zhao et al., 2018). The outcome shows that the chemical modification of PKS biochar has increased its surface area and adsorption capacity. Table 4 presented the comparison of surface properties between Mg-PKS biochar composite and other chemically modified biochars. Mg-PKS biochar composite has the highest surface area ($674 \text{ m}^2\text{g}^{-1}$) compared to other Mg biochars and other chemically modified biochars.

FTIR Analysis. The information on the existence of various surface functional groups of the samples is obtained by FTIR spectroscopy. The FTIR spectra of the Mg-PKS biochar composite are presented in Figure 2. The main characteristics that indicate cellulose, hemicellulose, and lignin in the PKS biochar are when the functional groups such as

Table 4
Comparison of Mg-PKS biochar composite surface properties with other Mg treated biochars

Biochar	Characteristics			Reference
	Surface area (m ² g ⁻¹)	Pore volume (cm ³ g ⁻¹)	Total pore diameters (μm)	
Mg-PKS biochar composite	674	0.424	7.22±3.54	Present study
MgO-treated corncob biochar	26.56	–	–	Shen at al. (2018)
Mg modified biochar	490.294	–	–	Fang et al. (2014)
MgO-impregnated wood chips biochar	225	–	–	Zhao et al. (2018)
Mg-treated carrot biochar	12.65	0.0133	0.0042	Carvalho et al. (2019)
Mg-impregnated biochar	66.1	–	–	Riddle et al., (2019)

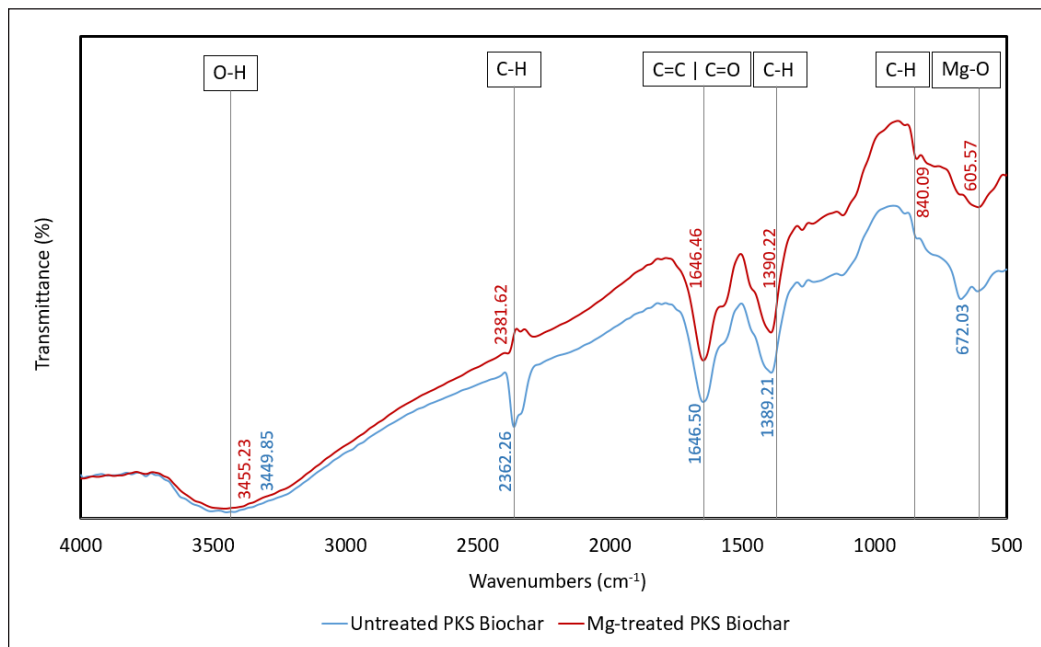


Figure 2. FTIR spectra for steam activated PKS biochar and Mg-PKS biochar composite

C–O, C=O, C–H and O–H present in the spectra (Johari et al., 2016). The bands that are slightly shifted to a new one in biochar demonstrate that chemical exchanges transpired on the modified biochar surface (Komnitsas & Zaharaki, 2016). The presence of strong and broad bands between 3200 and 3500 cm⁻¹ could be deduced to the O–H stretching vibrations indicative of hydroxyl group and water adsorption by the samples (García et al., 2018). This peak range is also ascribed to the presence of crystalline cellulose (Liu & Han, 2015). From the Figure 2, the peaks at 3455.23 cm⁻¹ and 3449.85 cm⁻¹ ascribe to O–H stretching vibrations demonstrating the presence of chemical compounds like alcohol, phenol, or carboxylic acid (Liew et al., 2017).

A series of peaks at 800–400 cm^{-1} in the case of Mg-PKS biochar composite can be credited to Mg–O and O–Mg–O, which suggests the presence of Mg oxyhydroxides (Zhao et al., 2018). The peaks of the Mg-PKS biochar composite imply that magnesium particles do not influence the structure of functional groups in Mg-PKS biochar composite (Fang et al., 2014). Additional OH groups were produced on Mg-PKS biochar composite, which may be responsible for the adsorption ability of biochar (Zhao et al., 2018). The bands at around 600 cm^{-1} in all samples can also be assigned to C–H bending vibrations in aromatic compounds (Komnitsas & Zaharaki, 2016).

The peaks at 1646.50 and 1646.46 cm^{-1} can be consigned to carbon species in the form of C=C stretching vibration, suggesting the presence of aromatic and alkene compounds in the samples (Liew et al., 2017; Rugayah et al., 2014). Similarly, according to Jindo et al. (2014), the peaks between 1650 cm^{-1} and 1620 cm^{-1} may also denote the presence of C=C stretching vibration indicative of the aromatics group, which appears for all samples. On the contrary, Johari et al. (2016) proposed that the peaks around $\sim 1600 \text{ cm}^{-1}$ can be attributed to C–O or C=O stretching vibration corresponding to functional groups like alcohols, esters, ether, and carboxylic acid. Correspondingly, García et al. (2018) also agreed that the band around 1625 cm^{-1} signifies the presence of C=O deformation of aldehydes, ketones, and carboxyl groups. Notably, the C–H ($-\text{CH}_2$ and $-\text{CH}_3$) bending vibrations at the peaks ranged from 1407.81 to 1388.26 cm^{-1} in all samples, possibly indicate the presence of alkanes components. The peaks around $\sim 2350 \text{ cm}^{-1}$ represent strong O=C=O stretching vibrations in all biochar samples, showing carbon dioxide (Komnitsas & Zaharaki, 2016). Table 5 summarized the peaks obtained in this study.

Table 5
Summary of the peaks obtained from FTIR spectra

Wavenumber (cm^{-1})	Assignments	Wavenumber of samples (cm^{-1})	
		Steam activated PKS biochar	Mg-PKS biochar composite
3500–3200	O–H stretching indicative of alcohol, phenol or carboxylic acid	3449.85	3455.23
~ 2350	CO_2 stretching	2362.26	2381.62
1700–1600	C=O or C=C stretching in aromatic ring or alkenes	1646.50	1646.46
1500–1300	C–H (CH_2 and CH_3) bending in alkanes	1389.21	1390.22
900–600	C–H bending vibrations in aromatic compounds	672.03	605.57
800–400	Mg–O and O–Mg–O	–	605.57

Adsorption Study via the RSM approach

MB removal via adsorption by Mg-PKS biochar composite to determine the independent parameters, namely pH (factor A), contact time (factor B), and adsorbent dosage (factor

C), with their effect on removal of MB. Mg-PKS biochar composite is chosen for the optimization study because it showed the highest MB removal percentage compared to other biochar. Optimization of MB adsorption study was finalized using central composite design (CCD), a sub-program of RSM, through Design-Expert (version 12.0) software. The response can be associated with the operating parameters by linear or quadratic models (Ozturk & Sahan, 2015). Seventeen experimental runs were carried out to develop the correlation between the functional variables of Mg-PKS biochar composite to the removal of MB from an aqueous solution. The parameters used in this study are pH (4–10), contact time (30–90 min) and adsorbent dosage (0.1–0.5 g), as well as their response (percentage MB removal efficiency).

Based on Table 6, MB removal efficiency by Mg-PKS biochar composite ranged between 59.44% and 98.50%. Run 6 has the highest MB removal efficiency, 98.50%, operated at pH 10, contact time of 30 min and adsorbent dosage of 0.5 g. Simultaneously, Run 1 displayed the lowest removal efficiency of MB of 59.44% with an adsorbent dosage of 0.1 g, a contact time of 30 min and pH 4. MB reached equilibrium after 30 min based on the experimental data for the lowest and highest removal efficiency of MB. This result is supported by a few types of research that also recommended the sufficient time taken for removal of MB to attain equilibrium is 30 min (Bendaho et al., 2015; Ocholi et al., 2016;

Table 6
Experimental factors and response for MB removal by Mg-PKS biochar composite

Run	Parameters			Mg-PKS biochar composite	
	pH	Time (min)	Dosage (g)	Actual MB removal efficiency (%)	Predicted MB removal efficiency (%)
1	4	30	0.1	59.44	58.96
2	10	30	0.1	91.03	92.00
3	4	90	0.1	86.10	83.95
4	10	90	0.1	85.31	85.27
5	4	30	0.5	79.83	79.70
6	10	30	0.5	98.50	100.48
7	4	90	0.5	88.57	87.44
8	10	90	0.5	76.17	76.49
9	4	60	0.3	75.72	79.61
10	10	60	0.3	93.88	90.65
11	7	30	0.3	75.06	72.72
12	7	90	0.3	70.23	73.23
13	7	60	0.1	87.54	89.24
14	7	60	0.5	96.27	95.23
15	7	60	0.3	87.16	83.65
16	7	60	0.3	88.20	83.65
17	7	60	0.3	76.93	83.65

Tang et al., 2017). The highest (Run 6) and the second highest (Run 14) percentage MB removal have the adsorbent dosage of 0.5 g, whereas the lowest (Run 1) and the second lowest (Run 12) percentage MB removal with an adsorbent dosage of 0.1 g and 0.3 g, respectively. The removal of MB amplified as the adsorbent dosage increased. It might be due to the improved availability of the adsorption sites and surfaces of the adsorbents (Pathania et al., 2017).

Run 6 has a pH of 10, indicative of alkaline solution, while Run 1 has a pH of 4, signifying that the solution system is acidic. Alteration of pH value can enhance the adsorption process (Guarín et al., 2018). When pH condition is low (acidic), there is an electrostatic repulsion between hydrogen ions, magnesium ions and the positively charged MB ions on the biochar surface, thus restricting the adsorption process of MB on the negatively charged adsorbent (Marrakchi et al., 2017; Pandimurugan & Thambidurai, 2016; Pang et al., 2017). At high pH conditions (alkali), deprotonation took place on the biochar surface, causing the surface to become negatively charged, assisting the adsorption of MB (Guarín et al., 2018). Hence, it is recommended to conduct adsorption of MB at a pH value of 10.

Design-Expert software provided a few statistical tables such as linear, two-factor interaction (2F1), quadratic and cubic polynomials to classify the suitable model to describe the relationships between the parameters and the responses for the adsorption study (Stat Ease, 2019). The present study found that the quadratic model fits the data as the software suggested it since the model has the highest R^2 , adjusted R^2 and predicted R^2 , which are 0.9186, 0.8139 and 0.6531, respectively, as compared to other models. The multiple correlation coefficient, R^2 , nearer to 1, indicates a better correlation between experimental and predicted values (Thakkar & Saraf, 2014). The equations of the quadratic model are as follows (Equation 3):

$$\text{MB removal efficiency (\%)} = 83.65 + 5.52A + 0.2520B + 2.99C - 7.93AB - 3.07AC - 4.32BC + 1.4.8A^2 - 10.68B^2 + 8.58C^2 \quad \text{Equation 3}$$

A, B and C represent pH of a solution, contact time and adsorbent dosage, respectively. The coefficient with one factor illustrates the effects of the variable itself, whereas the coefficient with two factors demonstrates the effect of the interaction between two factors (Wahi et al., 2014). Furthermore, the coefficient with the power of two represents the effect of quadratic factors. The negative signs denote the antagonistic effect, and the positive signs display synergistic effects (Wahi et al., 2014).

Figure 3 revealed the predicted versus actual plot of MB removal efficiency for Mg-PKS biochar composite. Based on the Figure 3, the scheme presented an excellent capability of the developed quadratic model, which fit all the experimental results due to the apparent

small distances between the cluster of points and the diagonal line. Ideally, all the points are reasonably near the diagonal line, which can be observed from the Figure 3. When the actual removal efficiency is 59.44%, the predicted value should be considered close to the real value, 58.96%.

Design-Expert software can also be applied to evaluate the statistical analyses to visualize the effects of the selected parameters on the Mg-PKS biochar composite adsorption capacity. Analysis of variance (ANOVA) is utilized to assess the numerical significance of the quadratic

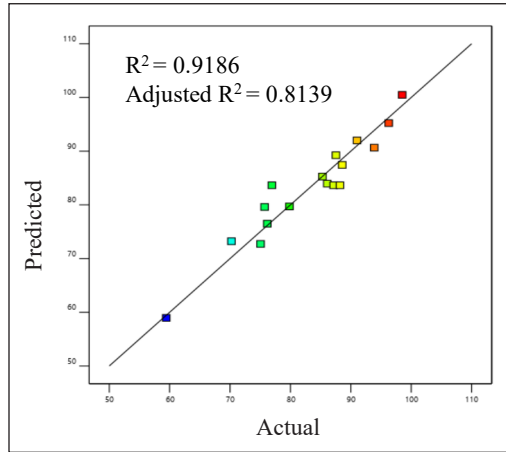


Figure 3. Predicted vs actual removal efficiency of MB using Mg-PKS biochar composite

model equation between pH value, contact time and adsorbent dosage, as displayed in Table 7. ANOVA is summarized by presenting the sum and mean of squares for each factor, degree of freedoms, F-values, and p-values. The significance of the quadratic model is analyzed by using F-test ANOVA. The model with the F-value of 8.78 showed that the model is significant. There is only a 0.46% possibility that this large F-value could ensue because of noise. When the F-value of the factor is getting larger, its effect on the response will also become greater (Kim, 2014). Prob > F or p-values less than 0.05 signify that

Table 7
ANOVA results of the regression model for the optimization of MB adsorption by Mg-PKS biochar composite

Source	Sum of Squares	Degree of Freedom	Mean Square	F-value	p-value Prob>F	
Model	1503.20	9	167.02	8.78	0.0046	significant
A-pH	305.04	1	305.04	16.03	0.0052	
B-Time	0.64	1	0.64	0.03	0.8602	
C-Dosage	89.52	1	89.52	4.70	0.0667	
AB	503.24	1	503.24	26.44	0.0013	
AC	75.22	1	75.22	3.95	0.0871	
BC	149.04	1	149.04	7.83	0.0266	
A ²	5.85	1	5.85	0.31	0.5967	
B ²	305.48	1	305.48	16.05	0.0051	
C ²	197.33	1	197.33	10.37	0.0147	
Residual	133.22	7	19.03			
Lack of Fit	55.64	5	11.13	0.29	0.8873	not significant
Pure Error	77.582	2	38.79			
Correlation Total	1636.42	16				

the model terms used are significant (Thakkar & Saraf, 2014; Wahi et al., 2014). In this study, factors A, AB, BC, B² and C² are regarded as significant model terms. The 'lack of fit F-value' of 0.29 denotes the lack of fit value is insignificant relative to the pure error. There is an 88.73% probability that this massive 'lack of fit F-value' could happen because of noise. Non-significant lack of fit is compulsory for the model to fit.

In the present work, the pH value of the solution attained the highest F-value (16.03) amongst contact time (0.03) and adsorbent dosage (4.70), with a p-value of 0.0052 (less than 0.05), indicating that pH factor has substantial influence in the removal of MB by Mg-PKS biochar composite. The interaction between the effects of pH and time (AB) obtained a high F-value of 26.44 and p-value of 0.0013 as well as the effects of time and dosage (BC) (F-value of 7.83; p-value of 0.0266), proving that the respective interactions give a significant result on the responses whereas AC (F-value of 3.95; p-value of 0.0871) has fewer notable effects. The quadratic function of the effect of contact time (B²) and adsorbent dosage (C²) with high F-values of 16.05 and 10.37, respectively, have a better remarkable effect as compared to the effect of pH (A²) with a lower F-value of 0.31.

Three-dimensional response surface graphs that are disclosed in Figure 4a-c describe the behaviour of the combined effects of various parameters on MB removal efficiency. Figure 4 shows, 3D response surface graph and contour plot, are showing the effect of (a) pH and time, (b) time and adsorbent dosage, and (c) pH and adsorbent dosage on MB removal efficiency by Mg-PKS biochar composite.

Figure 4a showed that shorter contact time is needed as the pH value increased to achieve the highest MB removal efficiency onto Mg-PKS biochar composite. It is observed that the combination of pH 10 and contact time of 30 min with a fixed adsorbent dosage of 0.5 g gave the highest removal of 98.50%. Figure 4b described that adsorption took about 30 min to reach equilibrium with 0.5 g as adsorbent dosage. In contrast, Figure 4c revealed that when the combination of adsorbent dosage and pH conditions increased, high removal efficiency could be attained. The red regions on the graph plots indicate the highest removal of MB based on different parameters. The blue areas on the plots visualize the lowest removal efficiency of MB by Mg-PKS biochar composite. The optimization analysis recommends using a pH value of 10, contact time of 30 min, and adsorbent dosage of 0.5 g to achieve 100% MB removal. The result is comparable with previous study whereby the optimized pH value was obtained at pH 9.5 and dosage of 0.6 g by using maple biochar (Allouss et al., 2019). Another study using cellulose-based beads mentioned that maximum adsorption capacity for MB was obtained at higher pH (9–10) (Choi et al., 2020). However, Mousavi et al. (2017) showed that the best maximum adsorption was found to be at pH 3, a dosage of 0.2 g/L with a contact time of 10 min. This result is the opposite of the current study, probably due to the type of adsorbent used, which is *N. microphyllum* activated carbon.

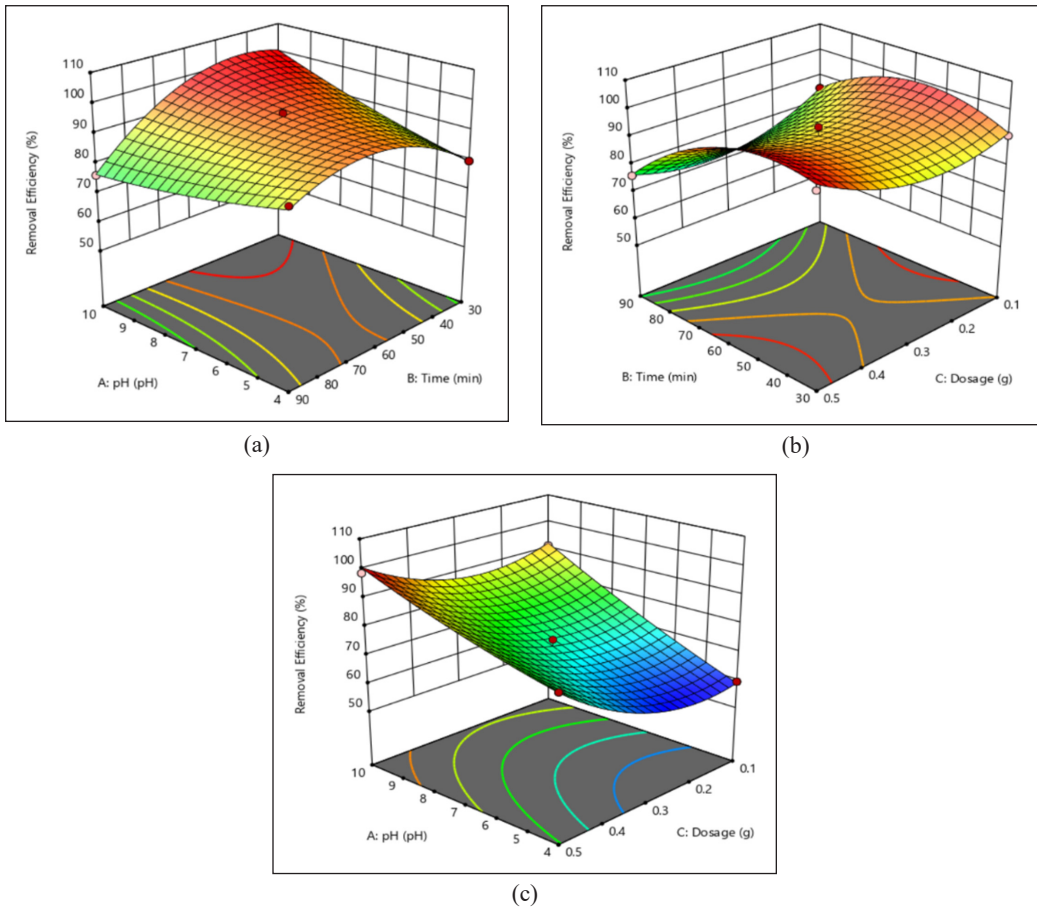


Figure 4. 3D response surface graph and contour plot showing the effect of (a) pH and time, (b) time and adsorbent dosage, and (c) pH and adsorbent dosage on MB removal efficiency by Mg-PKS biochar composite

Validation Experiment

The factors affecting the removal performance of MB by Mg PKS biochar were attained via Design-Expert software: The optimum combination of pH, contact time and adsorbent dosage suggested by the software were 8.72, 54.07 min and 0.2828 g, respectively. Based on the RSM analysis, the predicted removal efficiency was 87.62%. Validation experiments were conducted under the optimum parameters of pH 8.5, contact time of 55 min and dosage of 0.3 g. Table 8 is the results of validation experiments.

From the Table 8, the actual experimental MB removal efficiency was found to be 84.97%. The percentage deviation from the predicted value was 3.02%, which means the error is small (Zhou et al., 2019). Thus, it can be concluded that the RSM model could predict the removal efficiency of MB by Mg-PKS biochar.

Table 8
Validation experiment results under optimum parameters

Run	Parameters			Mg-PKS biochar composite	
	pH	Time (min)	Dosage (g)	Experimental MB removal efficiency (%)	Predicted MB removal efficiency (%)
1	8.5	55	0.3	84.97	87.62

Biochar Properties Comparison

Table 9 shows the comparison of the properties between steam activated PKS biochar and Mg-PKS biochar. Based on the characterization of both biochars, Mg-PKS biochar has a larger surface area of $674 \text{ m}^2\text{g}^{-1}$ compared to steam activated PKS biochar ($592 \text{ m}^2\text{g}^{-1}$). Mg-PKS biochar also has a larger total pore volume of $0.424 \text{ cm}^3\text{g}^{-1}$ than the total pore volume of steam activated PKS biochar, which is $0.353 \text{ cm}^3\text{g}^{-1}$. Both biochars contained high carbon content. The carbon in the biochar can develop the carbons' structures into pores, indicating the potential enhancement of the sorption sites on the surface of the biochar (Liew et al., 2017). Mg-PKS biochar is porous as the adsorbent displayed high adsorption capacity. O-H groups are present in both biochars (Figure 2). However, Mg-PKS biochar composite managed to generate extra O-H groups, which facilitate the adsorption ability of Mg-PKS biochar (Zhao et al., 2018). The band spectra that representing the O-H group shifted to higher wavenumbers because of the increase in the interactions between the hydroxyl group of the biochar and MB (Komnitsas & Zaharaki, 2016). Adsorption of contaminants from aqueous solution by adsorbents is caused by chemical interactions such as electrostatic interaction, cation exchange and surface precipitation (Sizmur et al., 2017).

Table 9
Comparison of the properties between steam activated PKS biochar and Mg-PKS biochar

Properties	Steam activated PKS biochar	Mg-PKS biochar
Specific surface area	$592 \text{ m}^2\text{g}^{-1}$	$674 \text{ m}^2\text{g}^{-1}$
Pore volume	$0.353 \text{ cm}^3\text{g}^{-1}$	$0.424 \text{ cm}^3\text{g}^{-1}$
Organic matter	70.37%	62.81%
Porosity	-	Porous
Functional groups	O-H present	Extra O-H generated
Adsorption	-	Higher adsorption capacity

CONCLUSION

Mg-biochar composite developed from PKS biochar exhibits excellent adsorbent properties and high removal efficiency for MB in an aqueous solution. The Mg-PKS biochar composite has irregular shape pore structure, a surface area of $674 \text{ m}^2\text{g}^{-1}$ and average pore diameters

of 7.2195 μm . The optimum removal of MB onto Mg-PKS biochar composite was at pH 10, 30 min contact time and 0.5 g/100 mL dosage with a removal efficiency of 98.50%. This study suggests the potential application of Mg treatment as an alternative to other chemical treatment for biochar upgrading to adsorbent for removing MB from water bodies.

ACKNOWLEDGEMENT

The authors thank the Ministry of Higher Education Malaysia and Universiti Malaysia Sarawak for funding this work (Fundamental Research Grant Scheme; Grant No.: F07/FRGS/1494/2016).

REFERENCES

- Albadarin, A. B., Collins, M. N., Naushad, M., Shirazian, S., & Mangwandi, C. (2016). Activated lignin chitosan extruded blends for efficient adsorption of methylene blue. *Chemical Engineering Journal*, 307, 264-272. <https://doi.org/10.1016/j.cej.2016.08.089>
- Alene, A. N., Abate, G. Y., & Habte, A. T. (2020). Bioadsorption of basic blue dye from aqueous solution onto raw and modified waste ash as economical alternative bioadsorbent. *Journal of Chemistry*, 2020, Article 8746035. <https://doi.org/10.1155/2020/8746035>
- Allouss, D., Essamlali, Y., Amadine, O., Chakir, A., & Zahouily, M. (2019). Response surface methodology for optimization of methylene blue adsorption onto carboxymethyl. *RSC Advances*, 9, 37858-37869. <https://doi.org/10.1039/c9ra06450h>
- Antunes, E., Jacob, M. V., Brodie, G., & Schneider, P. A. (2017). Silver removal from aqueous solution by biochar produced from biosolids via microwave pyrolysis. *Journal of Environmental Management*, 203, 264-272. <https://doi.org/10.1016/j.jenvman.2017.07.071>
- Ba, O. S., Ka, H., Shoe, T., Ya, H., & Yo, N. (2020). Novel approach for effective removal of methylene blue dye from water using fava bean peel waste. *Scientific Reports*, 10, 1-10. <https://doi.org/10.1038/s41598-020-64727-5>
- Bendaho, D., Driss, T. A., & Bassou, D. (2015). Removal of cationic dye methylene blue from aqueous solution by adsorption on Algerian clay. *International Journal of Waste Resources*, 5(1), 1-6. <https://doi.org/10.4303/2252-5211.1000175>
- Carvalho Eufrásio Pinto, M., David Da Silva, D., Amorim Gomes, A. L., Menezes Dos Santos, R. M., Alves De Couto, R. A., Ferreira De Novais, R., Leopoldo Constantino, V. R., Tronto, J., & Pinto, F. G. (2019). Biochar from carrot residues chemically modified with magnesium for removing phosphorus from aqueous solution. *Journal of Cleaner Production*, 222, 36-46. <https://doi.org/10.1016/j.jclepro.2019.03.012>
- Choi, Y., Gurav, R., Kim, H. J., Yang, Y., & Bhatia, S. K. (2020). Evaluation for simultaneous removal of anionic and cationic dyes onto maple leaf-derived biochar using response surface methodology. *Applied Sciences*, 10(9), Article 2982. <https://doi.org/10.3390/app10092982>
- Fan, S., Tang, J., Wang, Y., Li, H., Zhang, H., Tang, J., Wang, Z., & Li, X. (2016). Biochar prepared from co-pyrolysis of municipal sewage sludge and tea waste for the adsorption of methylene blue from aqueous

- solutions: Kinetics, isotherm, thermodynamic and mechanism. *Journal of Molecular Liquids*, 220, 432-441. <https://doi.org/10.1016/j.molliq.2016.04.107>
- Fang, C., Zhang, T., Li, P., Jiang, R. F., & Wang, Y. C. (2014). Application of magnesium modified corn biochar for phosphorus removal and recovery from swine wastewater. *International Journal of Environmental Research and Public Health*, 11(9), 9217-9237. <https://doi.org/10.3390/ijerph110909217>
- Fatiha, M., & Belkacem, B. (2015). Adsorption of methylene blue from aqueous solutions using natural clay. *Journal of Materials and Environmental Science*, 3(5), 1-7. <https://doi.org/10.4172/2157-7587.1000143>
- García, J. R., Sedran, U., Zaini, M. A. A., & Zakaria, Z. A. (2018). Preparation, characterization, and dye removal study of activated carbon prepared from palm kernel shell. *Environmental Science and Pollution Research*, 25(6), 5076-5085. <https://doi.org/10.1007/s11356-017-8975-8>
- Gnanasundaram, N., Loganathan, M., & Singh, A. (2017). Optimization and performance parameters for adsorption of Cr⁶⁺ by microwave assisted carbon from *Sterculia foetida* shells. *IOP Conference Series: Materials Science and Engineering*, 206(1), 1-10. <https://doi.org/10.1088/1757-899X/206/1/012065>
- Guarín, J. R., Moreno-Pirajan, J. C., & Giraldo, L. (2018). Kinetic study of the bioadsorption of methylene blue on the surface of the biomass obtained from the Algae *D. antarctica*. *Journal of Chemistry*, 2018, Article 2124845. <https://doi.org/10.1155/2018/2124845>
- Hasbullah, T. N. A. T., Selaman, O. S., & Rosli, N. A. (2014). Removal of dye from aqueous solutions using chemical activated carbon prepared from jackfruit (*Artocarpus heterophyllus*) peel waste. *UNIMAS E-Journal of Civil Engineering*, 5(1), 34-38.
- He, R., Peng, Z., Lyu, H., Huang, H., Nan, Q., & Tang, J. (2018). Synthesis and characterization of an iron-impregnated biochar for aqueous arsenic removal. *Science of the Total Environment*, 612, 1177-1186. <https://doi.org/10.1016/j.scitotenv.2017.09.016>
- Jawad, A. H., Rashid, R. A., Ishak, M. A. M., & Wilson, L. D. (2016). Adsorption of methylene blue onto activated carbon developed from biomass waste by H₂SO₄ activation: Kinetic, equilibrium and thermodynamic studies. *Desalination and Water Treatment*, 57(52), 25194-25206. <https://doi.org/10.1080/19443994.2016.1144534>
- Jellali, S., Diamantopoulos, E., Haddad, K., Anane, M., Durner, W., & Mlayah, A. (2016). Lead removal from aqueous solutions by raw sawdust and magnesium pretreated biochar : Experimental investigations and numerical modelling. *Journal of Environmental Management*, 180, 439-449. <https://doi.org/10.1016/j.jenvman.2016.05.055>
- Jindo, K., Mizumoto, H., Sawada, Y., Sanchez-Monedero, M. A., & Sonoki, T. (2014). Physical and chemical characterization of biochars derived from different agricultural residues. *Biogeosciences*, 11(23), 6613-6621. <https://doi.org/10.5194/bg-11-6613-2014>
- Johari, K., Saman, N., Tien, S. S., Siew Chin, C., Kong, H., & Mat, H. (2016). Removal of elemental mercury by coconut pith char adsorbents. *Procedia Engineering*, 148, 1357-1362. <https://doi.org/10.1016/j.proeng.2016.06.588>
- Jung, K., & Ahn, K. (2015). Fabrication of porosity-enhanced MgO/biochar for removal of phosphate from aqueous solution : Application of a novel combined electrochemical modification method. *Bioresource Technology*, 200, 1029-1032. <https://doi.org/10.1016/j.biortech.2015.10.008>

- Karaer, H., & Kaya, I. (2016). Synthesis, characterization of magnetic chitosan/active charcoal composite and using at the adsorption of methylene blue and reactive blue. *Microporous and Mesoporous Materials*, 232, 26-38. <https://doi.org/10.1016/j.micromeso.2016.06.006>
- Kim, H. (2014). Analysis of variance (ANOVA) comparing means of more than two groups. *Restorative Dentistry and Endodontics*, 7658, 74-77. <https://doi.org/10.5395/rde.2014.39.1.74>
- Komnitsas, K. A., & Zaharaki, D. (2016). Morphology of modified biochar and its potential for phenol removal from aqueous solutions. *Frontiers in Environmental Science*, 4(April), 1-11. <https://doi.org/10.3389/fenvs.2016.00026>
- Kuang, Y., Zhang, X., & Zhou, S. (2020). Adsorption of methylene blue in water onto activated carbon by surfactant modification. *Water*, 12, 1-19. <https://doi.org/10.3390/w12020587>
- Lam, S. S., Liew, R. K., Cheng, C. K., Rasit, N., Ooi, C. K., Ma, N. L., Ng, J. H., Lam, W. H., Chong, C. T., & Chase, H. A. (2018). Pyrolysis production of fruit peel biochar for potential use in treatment of palm oil mill effluent. *Journal of Environmental Management*, 213, 400-408. <https://doi.org/10.1016/j.jenvman.2018.02.092>
- Liao, P., Zhan, Z., Dai, J., Wu, X., Zhang, W., Wang, K., & Yuan, S. (2013). Adsorption of tetracycline and chloramphenicol in aqueous solutions by bamboo charcoal: A batch and fixed-bed column study. *Chemical Engineering Journal*, 228, 496-505. <https://doi.org/10.1016/j.cej.2013.04.118>
- Liew, R. K., Nam, W. L., Chong, M. Y., Phang, X. Y., Su, M. H., Yek, P. N. Y., Ma, N. L., Cheng, C. K., Chong, C. T., & Lam, S. S. (2017). Oil palm waste: An abundant and promising feedstock for microwave pyrolysis conversion into good quality biochar with potential multi-applications. *Process Safety and Environmental Protection*, 115, 57-69. <https://doi.org/10.1016/j.psep.2017.10.005>
- Liu, W. J., Jiang, H., & Yu, H. Q. (2015). Development of biochar-Based functional materials: toward a sustainable platform carbon material. *Chemical Reviews*, 115(22), 12251-12285. <https://doi.org/10.1021/acs.chemrev.5b00195>
- Liu, Z., & Han, G. (2015). Production of solid fuel biochar from waste biomass by low temperature pyrolysis. *Fuel*, 158, 159-165. <https://doi.org/10.1016/j.fuel.2015.05.032>
- Mahmood, W. M. F. W., Ariffin, M. A., Harun, Z., Ghani, J. A., Ishak, N. A. I. M., & Rahman, M. N. A. (2015). Characterisation and potential use of biochar from gasified oil palm wastes. *Journal of Engineering Science and Technology*, 10(2014), 45-54. https://www.researchgate.net/publication/287534129_Characterisation_and_potential_use_of_biochar_from_gasified_oil_palm_wastes
- Mahmoudi, K., Hamdi, N., & Srasra, E. (2015). Study of adsorption of methylene blue onto activated carbon from lignite. *Surface Engineering and Applied Electrochemistry*, 51(5), 427-433. <https://doi.org/10.3103/S1068375515050105>
- Marrakchi, F., Ahmed, M. J., Khanday, W. A., Asif, M., & Hameed, B. H. (2017). Mesoporous-activated carbon prepared from chitosan flakes via single-step sodium hydroxide activation for the adsorption of methylene blue. *International Journal of Biological Macromolecules*, 98, 233-239. <https://doi.org/10.1016/j.ijbiomac.2017.01.119>

- Mousavi, S. A., Mehralian, M., Khashij, M., & Parvaneh, S. (2017). Methylene blue removal from aqueous solutions by activated carbon prepared from *N. Microphyllum* (AC-NM): RSM analysis, isotherms and kinetic studies. *Global Nest Journal*, 19(4), 697-705.
- Niran, O. B., Olawale, S. A., & Ushie, U. J. (2018). Isotherm studies of adsorption of methylene blue by palm kernel shell. *Asian Journal of Applied Chemistry Research*, 1(1), 1-9. <https://doi.org/10.9734/AJACR/2018/41300>
- Ocholi, O. J., Gimba, C. E., Ndukwe, G. I., Turoti, M., Abechi, S. E., & Edogbanya, P. R. O. (2016). Effect of time on the adsorption of methylene blue, methyl orange and indigo carmine onto activated carbon. *IOSR Journal of Applied Chemistry*, 9(9), 55-62. <https://doi.org/10.9790/5736-0909015562>
- Ozturk, D., & Sahan, T. (2015). Design and optimization of Cu (II) adsorption conditions from aqueous solutions by low-cost adsorbent pumice with response surface methodology. *Polish Journal of Environmental Studies*, 24(4), 1749-1756. <https://doi.org/10.15244/pjoes/40270>
- Pandimurugan, R., & Thambidurai, S. (2016). Synthesis of seaweed-ZnO-PANI hybrid composite for adsorption of methylene blue dye. *Biochemical Pharmacology*, 4(1), 1332-1347. <https://doi.org/10.1016/j.jece.2016.01.030>
- Pang, J., Fu, F., Ding, Z., Lu, J., Li, N., & Tang, B. (2017). Adsorption behaviors of methylene blue from aqueous solution on mesoporous birnessite. *Journal of the Taiwan Institute of Chemical Engineers*, 77, 168-176. <https://doi.org/10.1016/j.jtice.2017.04.041>
- Patel, B., & Gami, B. (2012). Biomass characterization and its use as solid fuel for combustion. *Iranica Journal of Energy & Environment*, 3(2), 123-128. <https://doi.org/10.5829/idosi.ijee.2012.03.02.0071>
- Pathania, D., Sharma, S., & Singh, P. (2017). Removal of methylene blue by adsorption onto activated carbon developed from *Ficus carica* bast. *Arabian Journal of Chemistry*, 10, 1445-1451. <https://doi.org/10.1016/j.arabjc.2013.04.021>
- Pinto, M. D. C. E., da Silva, D. D., Gomes, A. L. A., dos Santos, R. M. M., de Couto, R. A. A., de Novais, R. F., Constantino, V. R. L., Tronto, J., & Pinto, F. G. (2019). Biochar from carrot residues chemically modified with magnesium for removing phosphorus from aqueous solution. *Journal of Cleaner Production*, 222, 36-46. <https://doi.org/10.1016/j.jclepro.2019.03.012>
- Rajapaksha, A. U., Chen, S. S., Tsang, D. C. W., Zhang, M., Vithanage, M., Mandal, S., Gao, B., Bolan, N. S., & Ok, Y. S. (2016). Engineered/designer biochar for contaminant removal/immobilization from soil and water: Potential and implication of biochar modification. *Chemosphere*, 148(October), 276-291. <https://doi.org/10.1016/j.chemosphere.2016.01.043>
- Riddle, M., Bergström, L., Schmieder, F., Lundberg, D., Condon, L., & Cederlund, H. (2019). Impact of biochar coated with magnesium (hydr)oxide on phosphorus leaching from organic and mineral soils. *Journal of Soils and Sediments*, 19(4), 1875-1889. <https://doi.org/10.1007/s11368-018-2197-7>
- Rout, T., Pradhan, D., Singh, R. K., & Kumari, N. (2016). Exhaustive study of products obtained from coconut shell pyrolysis. *Journal of Environmental Chemical Engineering*, 4(3), 3696-3705. <https://doi.org/10.1016/j.jece.2016.02.024>

- Rugayah, A. F., Astimar, A. A., & Norzita, N. (2014). Preparation and characterisation of activated carbon from palm kernel shell by physical activation with steam. *Journal of Oil Palm Research*, 26(3), 251-264.
- Sahu, S., Pahi, S., Tripathy, S., Singh, S. K., Behera, A., Sahu, U. K., & Patel, R. K. (2020). Adsorption of methylene blue on chemically modified lychee seed biochar: dynamic, equilibrium, and thermodynamic study. *Journal of Molecular Liquids*, 315, Article 113743. <https://doi.org/10.1016/j.molliq.2020.113743>
- Sarkar, D. (2015). Fuels and combustion. In *Thermal power plant* (pp. 91-137). Elsevier. <https://doi.org/10.1016/B978-0-12-801575-9.00003-2>
- Sartape, A., Mandhare, A., Salvi, P., Pawar, D., Raut, P., Anuse, M., & Kolekar, S. (2012). Removal of Bi (III) with adsorption technique using coconut shell activated carbon. *Chinese Journal of Chemical Engineering*, 20(4), 768-775. [https://doi.org/10.1016/S1004-9541\(11\)60247-4](https://doi.org/10.1016/S1004-9541(11)60247-4)
- Shen, Z., Zhang, J., Hou, D., Tsang, D. C. W., Ok, Y. S., & Alessi, D. S. (2018). Synthesis of MgO-coated corncob biochar and its application in lead stabilization in a soil washing residue. *Environment International*, 122, 357-362. <https://doi.org/10.1016/j.envint.2018.11.045>
- Sizmur, T., Fresno, T., Akgül, G., Frost, H., & Moreno, E. (2017). Biochar modification to enhance sorption of inorganics from water. *Bioresource Technology*, 246, 34-47. <https://doi.org/10.1016/j.biortech.2017.07.082>
- Stat-Ease. (2021). *Response surface*. Retrieved December 03, 2019, from <https://www.statease.com/docs/v11/tutorials/multifactor-rsm/>
- Tan, X., Liu, Y., Zeng, G., Wang, X., Hu, X., Gu, Y., & Yang, Z. (2015). Application of biochar for the removal of pollutants from aqueous solutions. *Chemosphere*, 125, 70-85. <https://doi.org/10.1016/j.chemosphere.2014.12.058>
- Tang, R., Dai, C., Li, C., Liu, W., Gao, S., & Wang, C. (2017). Removal of methylene blue from aqueous solution using agricultural residue walnut shell: Equilibrium, kinetic, and thermodynamic studies. *Journal of Chemistry*, 2017, 1-10. <https://doi.org/10.1155/2017/8404965>
- Thakkar, A., & Saraf, M. (2014). Application of statistically based experimental designs to optimize cellulase production and identification of gene. *Natural Products and Bioprospecting*, 4, 341-351. <https://doi.org/10.1007/s13659-014-0046-y>
- Tripathi, M., Sahu, J. N., & Ganesan, P. (2016). Effect of process parameters on production of biochar from biomass waste through pyrolysis: A review. *Renewable and Sustainable Energy Reviews*, 55, 467-481. <https://doi.org/10.1016/j.rser.2015.10.122>
- Wahi, R., Aziz, S. M. A., Hamdan, S., & Ngaini, Z. (2015). Biochar production from agricultural wastes via low-temperature microwave carbonization. In *2015 IEEE international RF and microwave conference (RFM)* (pp. 244-247). IEEE Conference Publication. <https://doi.org/10.1109/RFM.2015.7587754>
- Wahi, R., Chuah, L. A., Ngaini, Z., Nourouzi, M. M., & Choong, T. S. Y. (2014). Esterification of M. sagu bark as an adsorbent for removal of emulsified oil. *Journal of Environmental Chemical Engineering*, 2(1), 324-331. <https://doi.org/10.1016/j.jece.2013.12.010>
- Wu, Z., Zhong, H., Yuan, X., Wang, H., Wang, L., Chen, X., Zeng, G., & Wu, Y. (2014). Adsorptive removal of methylene blue by rhamnolipid-functionalized graphene oxide from wastewater. *Water Research*, 67, 330-344. <https://doi.org/10.1016/j.watres.2014.09.026>

- Xue-jiao, C., Qi-mei, L. I. N., Rizwan, M., Xiao-rong, Z., & Gui-tong, L. I. (2019). Steam explosion of crop straws improves the characteristics of biochar as a soil amendment. *Journal of Integrative Agriculture*, *18*(7), 1486-1495. [https://doi.org/10.1016/S2095-3119\(19\)62573-6](https://doi.org/10.1016/S2095-3119(19)62573-6)
- Zhang, M., Gao, B., Yao, Y., Xue, Y., & Inyang, M. (2012). Synthesis of porous MgO-biochar nanocomposites for removal of phosphate and nitrate from aqueous solutions. *Chemical Engineering Journal*, *210*, 26-32. <https://doi.org/10.1016/j.cej.2012.08.052>
- Zhao, X., Yi, S., Dong, S., Xu, H., Sun, Y., & Hu, X. (2018). Removal of Levofloxacin from aqueous solution by Magnesium-impregnated Biochar: Batch and column experiments. *Chemical Speciation and Bioavailability*, *30*(1), 68-75. <https://doi.org/10.1080/09542299.2018.1487775>
- Zhou, R., Zhang, M., Zhou, J., & Wang, J. (2019). Optimization of biochar preparation from the stem of *Eichhornia crassipes* using response surface methodology on adsorption of Cd²⁺. *Scientific Reports*, *9*, 1-17. <https://doi.org/10.1038/s41598-019-54105-1>
- Zhu, S., Fang, S., Huo, M., Yu, Y., Chen, Y., Yang, X., & Geng, Z. (2015). A novel conversion of the groundwater treatment sludge to magnetic particles for the adsorption of methylene blue. *Journal of Hazardous Materials*, *292*, 173-179. <https://doi.org/10.1016/j.jhazmat.2015.03.028>



Evaluation and Application of New-Semarang Coastal Resources Management

Alin Fithor*, Slamet Budi Prayitno, Frida Purwanti and Agus Indarjo

Faculty of Fisheries and Marine Science, Diponegoro University, Semarang 50275, Indonesia

ABSTRACT

The beach in Semarang's city has a variety of uniqueness with a variety of types and potential. The beach located on the north coast of Semarang city has various characteristics and strengths, and weaknesses. In overcoming differences in management and avoiding misunderstandings between governments, it prioritizes managing the coastal location. At least four integrated coastal management sub-systems consist of Human Resources Management, Accessibility, Beach Location Infrastructure, and Management Policies. This research was conducted from April 2020 until August 2020, to determine the most appropriate alternative strategy to be chosen and implemented in coastal location management. Study analysis with an Analytical Hierarchy Process-AHP analytical technique use with Application R - Open sources. The integrated coastal area management can as the most appropriate coastal location management strategy to implement the current situation and future planning. Alternative methods planned for use are the Availability of a Security Guard, Ease of Access with Signage, Parking Lots, and Rule or regulations to an Integrated Location. The study results stated that the best strategy is management collaboration in the form of interrelated rules.

Keywords: Analytical hierarchy process, coastal, management strategy, policy

ARTICLE INFO

Article history:

Received: 03 February 2021

Accepted: 24 May 2021

Published: 31 July 2021

DOI: <https://doi.org/10.47836/pjst.29.3.29>

E-mail addresses:

afithor@gmail.com (Alin Fithor)

sbudiprayitno@gmail.com (Slamet Budi Prayitno)

frpurwanti@gmail.com (Frida Purwanti)

indarjoa@yahoo.com (Agus Indarjo)

* Corresponding author

INTRODUCTION

As a strategic port city, Semarang has natural resources offered to the city government for the central government to continue as an attractive new magnet. History begins in the 8th century AD, namely a coastal area called Pragota (now Bergota) and was part of the ancient Mataram kingdom. At that time, the area was a port and in front of it

was a cluster of small islands. As a result of the deposition, which is still ongoing, these clusters are now coalesced to form the land.

According to regional governance, the definition of regional autonomy is the rights, authorities, and obligations of the autonomous region to regulate and manage government affairs and the interests of regional communities in the system of the Unitary State of the Republic of Indonesia. The beach tourism sector plays an important role in realizing the welfare needs of the community through recreation and travel and increasing state income to realize people's welfare. The beach tourism sector is a sector that can develop as a source of regional income.

The role of the city government in developing the existing and untapped beach tourism potential. Semarang City must be able to compete with other cities as a tourist destination, not only as a transit city but also as a national and international tourist destination. Other benefits obtained at once are the opening of job opportunities for the community, an increase in the beach tourism industry sector, and an increase in local revenue. The city government has made no effort to produce positive results, but the management of the coastal beach tourism sector is still considered inadequate compared to other regions. The community still lacks information about tourist objects and the lack of public facilities to support beach tourism activities. There are still many conditions for damaged and unkempt tourist objects and beach tourism preservation activities or events that are still less varied.

Broadly speaking, the role of government in beach tourism development is to provide infrastructure (not only in physical form), expand various forms of facilities, coordinate activities between government and private officials, regulation, and general promotion abroad. However, it also needs input from academia as part of development. The criticism and suggestions from this journal are to build a coastal beach tourism area with several recommendations to do at this time.

LITERATURE REVIEW

Coastal resources provide various environmental products and services that support various living needs and various economic activities. The potential of coastal recreation can give hope for the adequacy of the financial needs of people's lives, especially those living around the coast. The most formidable challenge is that the Semarang coastline's length occurs by jutting into the sea with significant changes every year (Bott & Braun, 2019; Fithor et al., 2013).

Under the spatial planning and governance in the Semarang city government environment, Semarang's northern coastal area is worth making new beach tourism a magnet to increase tourists' number. The choices of resources become an essential matter that influences the direction of utilization. It means that utilizing the type of resources might require shifting to be raised into a new attraction (Brand & Spencer, 2019; Liu et al., 2019).

The requirements for developing a beach tourism location are human resources, access roads, infrastructure for coastal zones, and management policy (Wever et al., 2012). The management policy continues to develop the beach tourism area to support management wisely. The beach location can benefit Semarang as a provider of alternative beach tourism at affordable prices and bring a new attraction for beach tourism (Lithgow et al., 2019).

Various studies have multiple systems in life; decision-making considers providing a better perception and a more systematic approach in this study area. Decision-making can do in the field of human resources and management. Decision-making and selection processes become increasingly technical and automatically calculate the qualifications and rankings of alternative individuals by eliminating or minimizing the subjectivity of the decisions indicated (Artiningsih et al., 2016; Buchori et al., 2018).

Sholeh and Farid (2021) presented shared beach tourism that can be solved using an analytic hierarchy process analysis discussed in a more depth manner that has been proven very efficient in selecting and ranking processes. Thus, it uses as a calculation means in this study.

The maritime beach tourism sector is inseparable from the community and local government's participation as a regulator. This role can implement in various forms of the beach tourism service business. The existence of the potential of these natural attractions cannot develop optimally. This condition has become a valuable component, including ecosystems, communities, and socioeconomic risks under pressure from marine dynamics (Liu et al., 2019).

Various studies conducted but reviving the atmosphere of beach tourism locations' novelty seems not to have been studied yet. New attractions in management can be a management challenge. Marina Beach has now managed in a mature and integrated manner is the only coastal area managed directly by the Semarang City Government. However, the government has not managed other beaches, such as Maron, Tirang, Baruna, and Cipta. Therefore, the private sector's role can take over one or several coastal locations as an offer from the city government to the private sector, for there are many locations that might be new attractions in Semarang (Nurhidayah & McIlgorm, 2019).

This study recommends wise management to build strategic locations to be new attractions to create a unique atmosphere and the latest offers to several beach tourism sectors in Semarang. Smart management requirements include 1) the principle of expediency to the leading industry and 2) Urban development policies equally developed indiscriminately.

MATERIALS AND METHODS

This study was conducted in the coastal area of Semarang City precisely as in the following map; namely several legendary beaches in the city of Semarang (Figure 1) (Sunaryo et al.,

2018). Good management can produce some visitors who can increase the beach tourism area, besides non-natural beach tourism in Semarang (Solihin et al., 2020).

This study is an evaluation made as a prospect of better utilization and management, especially in the area's control to better policies and provision of other coastal regions considered necessary for educational beach tourism.

This method uses a boxplot reading in the image to see the distribution of data where the maximum value, minimum value, quartile 1, 2, and 3, and extreme data will be visible. The advantage is that this application is open source and free of charge, complete output with visualization, and much of its use comes from the internet network. The weakness is that it is difficult for the ordinary person to do.

Data Collection Method

Data collected includes the average and characteristics of the tourist destination, including the number of samples divided into informants, the city government, the private sector, and visitors or tourists.

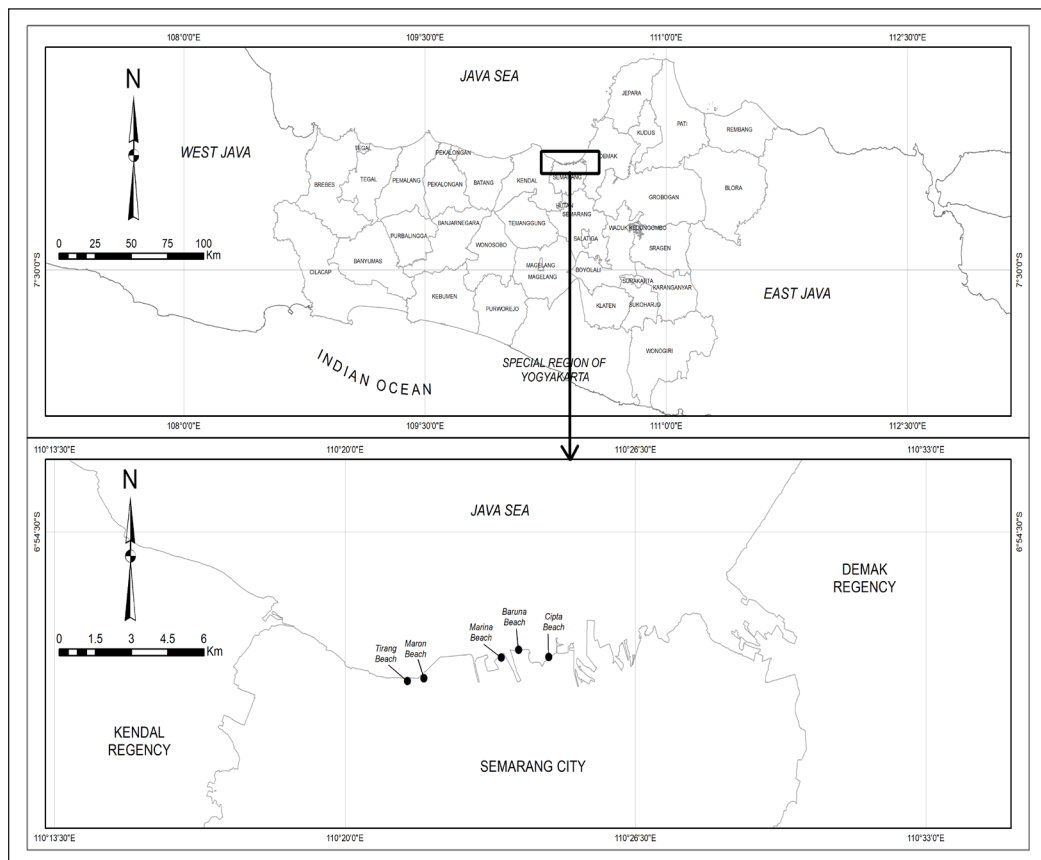


Figure 1. Research location

Types and Data Sources

Primary data is data taken directly from the source that is a research object. The research item in materials and terms determines the best choice for having recreation (Dube et al., 2021). Secondary data is data taken indirectly from the source. In this final report, secondary data obtained from library books, scientific journals, papers, theses, and searching for information from the internet, which serves as the theoretical basis and complementary primary data, besides Table 1 below.

Table 1
Pairwise comparison scale

Intensity of Importance	Definition
1	The equal importance of both elements
3	Weak importance of one element over another
5	The essential or vital essence of one aspect over another
7	Demonstrated importance of one factor over another
9	The absolute volume of a component over another
2,4,6,8	Intermediate values between two adjacent judgments

Method of Collecting Data

Rstudio is an IDE (integrated development environment) of the R programming language (Zheng et al., 2020). Steps to enter data into Rstudio:

1. Create a New Project in Rstudio, select a directory (e.g., E), then type the project name.
2. Insert the excel file into the same folder as the Rstudio project.
3. Import data directly using the 'import data' feature. Or you can type the code `-library(readxl) - beach <- read_excel("Pantai.xlsx", sheet = "according to which sheet will be analyzed")`
4. Make sure you have installed the readxl packages; if not, you can type the code. `install.packages("readxl")`.
5. Make sure you are connected to the Internet when installing packages.

Criteria and Alternative Assessment

A scale of 1 to 9 is the best in expressing opinions on various issues. In this AHP, alternative assessment can do by the direct method (direct), the method used to enter quantitative data (Sholeh & Farid, 2021). Considerations for pairwise comparisons to gain overall importance through the following stages, besides in Table 2 below.

Table 2
The framework of the value evaluation and follow-up of the indicators

Indicator	Criteria
A1. Security officer availability	Human Resources (A)
A2. Customer service availability	
A3. Cleaning service availability	
A4. Entrance ticket availability	
B1. Easy access for private vehicles	Accessibility (B)
B2. Easy access to public transportation	
B3. Ease of access with signage	
B4. Ease of access with expressway and railroad	
C1. Parking lot	Infrastructure (C)
C2. Swimming pool	
C3. Kids garden	
C4. Jogging track	
D1. Rules or regulations related to studying tour groups	Policy (D)
D2. Rules or regulation related to tourist-specific locations	
D3. Rules or regulation related to an integrated location	
D4. Rules or regulation related to management authority	

RESULTS

This study found both government and private sector made similar evaluations. There was the role of visitors but only a little in terms of enjoying beach tourism objects. It should underline that Indonesia’s policy manager always experiences a deadlock in management that often overlaps.

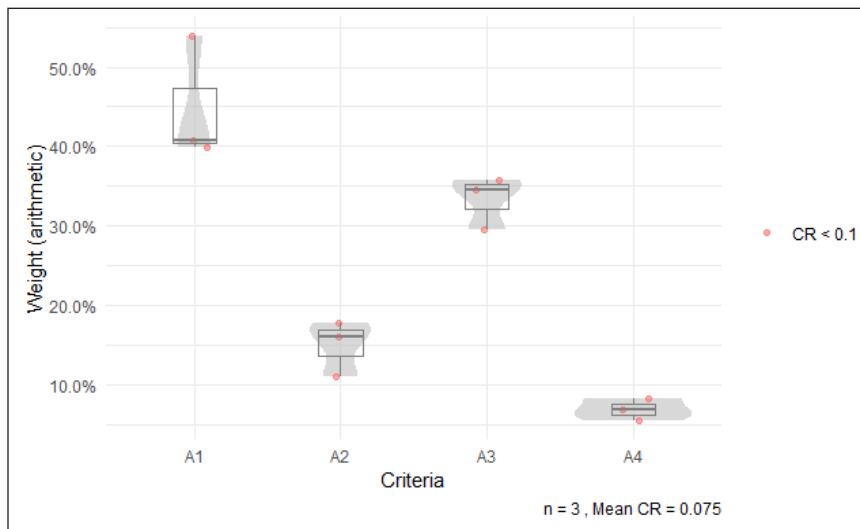


Figure 2. Boxplot RStudio for human resources - A

In Figure 2, the boxplot shows that A1 criterion has the highest proportion of weight compared to other criteria. The boxplot position of each criterion follows the calculation of the weight proportion that has previously to obtain. The average CR is 0.075.

Based on the priority value, in the A1 boxplot, the image shows a priority weight of 44.87%, and below, the square image already represents, it can determine that the A1 criterion can select as a priority in making decisions—security guard – A1 needs for beach tourism object in Semarang. The moral responsibility of residents is still very lacking in terms of maintaining cleanliness. It has become the residents’ bad habit. Convenience and some attractions affect several beaches, with moderate category values in management (Abbasi-Moud et al., 2021).

In Figure 3, the boxplot shows that the B3 criterion has the highest proportion of weight compared to other criteria. The boxplot position of each criterion follows the calculation of the weight proportion that has previously to obtain. The average CR is 0.107.

Nurhidayah and McIlgorm (2019) ease access to signage is essential in collaboration with residents around the beach by placing object choices in Semarang’s society. In the B3 boxplot, the image shows a priority weight of 52.88%, and below, the square image already represents. Existing policies from the past few years need to be evaluated and improved according to the existing access. Analysis of tourist visits is required to manage without building new locations (Abbasi-Moud et al., 2021).

In Figure 4, the boxplot shows that the C1 criterion has the highest proportion of weight compared to other criteria. The boxplot position of each criterion follows the calculation of the weight proportion that has previously to obtain. The average CR is 0.144.

In the C1 boxplot, the image shows a priority weight of 43.75%, and below, the square image already represents. Furthermore, economic value is uncertain, but the government’s

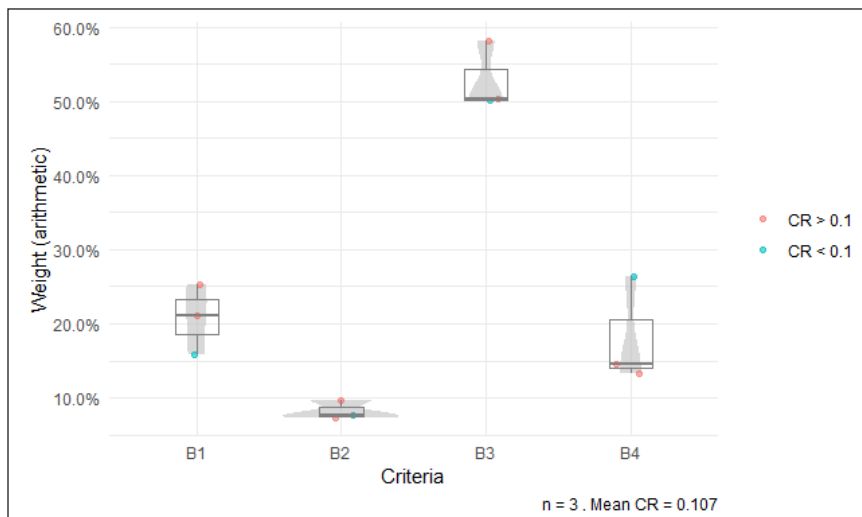


Figure 3. Boxplot RStudio for accessibility – B

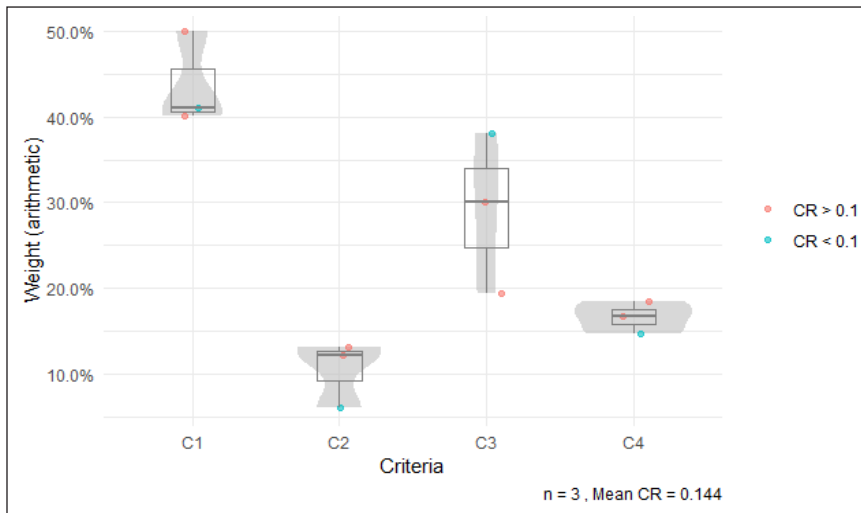


Figure 4. Boxplot RStudio for infrastructure – C

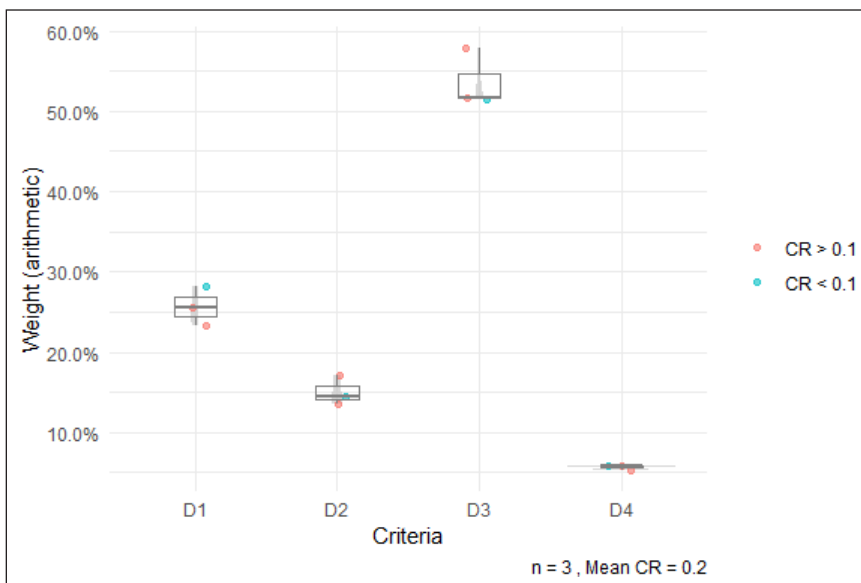


Figure 5. Boxplot RStudio For policy - D

relationship should raise economic value rather than regional expenditure income (Sunaryo et al., 2018). Just a Parking lot is undoubtedly an absolute beach tourism undertaking with third parties. It makes managers focus on beach tourism vehicles' security, provide entry tickets for treatment (not anyone who can manage it), and convenience in the tourist sites.

In Figure 5, the boxplot shows that the D3 criterion has the highest proportion of weight compared to other criteria. The boxplot position of each criterion follows the calculation of the weight proportion that has previously to obtain. The average CR is 0.2.

In the D3 boxplot, the image shows a priority weight of 53.66%, and below, the square image already represents (Antunes do Carmo, 2019). The construction of the sea highway on the city's north coast has become a chance for the residents to make it easy to bring in tourists from outside Semarang (Artiningsih et al., 2016). The interview with the respondents, especially with the city leaders, might evaluate several beaches' current management concept, whether they are still following their land. New policies on the priority scale become a vital object to avoid misunderstandings (Azhar, 2021).

DISCUSSION

This study resulted in a new strategy in terms of beach recreation management. Instead of strengthening cooperation between individuals, prioritizing a new system might be better instead. The designs provide security personnel, free access to the coast supported by highways and railroads, plan parking lots and prioritize integrated management policies.

Those strategies expect to be a new strategy for refreshing the Semarang city government. Therefore, cross-sectoral cooperation is needed with one of the manifestations to divert the management of beach tourism areas in some of these beach locations belonging to the Semarang city government. Hopefully, this strategy also can be adapted to other beaches. The city government takes the following steps in implementing the following strategies.

Planning

Strategic planning that schedules development activities, all programs that support and create good community services, including efforts to improve the performance and capacity of the bureaucracy, management systems and utilization of information technology with policies directed at increasing tourist visits, improving the management of objects and beach tourism partnerships in the form of 1). Improve the performance of the apparatus; 2). Increasing the quality and quantity of beach tourism destinations; 3). Increase the number of foreign and domestic tourist visits; 4). Improve the facilities and infrastructure and event; 5). Increase the professionalism of human beach tourism resources (Sholeh & Farid, 2021; Solihin et al., 2020).

Organizing

The findings show that city governments have limited human resources in carrying out their duties and functions. The ability to exist human resources is not optimal because not all of them know about beach tourism (Bott & Braun, 2019).

Program Implementation and Implementation

The field's findings reveal that having human resources who do not have an educational background in the beach tourism sector makes it difficult to optimize performance, while the beach tourism sector is a complex field (Dube et al., 2021; Sholeh & Farid, 2021).

Findings in the field the implementation of strategies to improve the quality and quantity of beach tourism destinations is carried out by developing existing tourist destinations and searching for and exploring undiscovered potential beach tourism objects to become new tourist attractions. However, the implementation has not been optimal, as evidenced by the disappointment felt by tourists and business actors with the condition of facilities and access to several beach beach tourism attractions—the process of determining/developing a long attraction and the attitude of indigenous people.

The implementation of the strategy to increase the number of foreign and local tourist visits by adding several tourist attractions in various tourist objects and significant recurring events held every year. Implementation of beach tourism promotion and marketing activities essential in beach tourism development, making promotional materials, procuring promotional media at home and abroad. Collaboration with private parties, namely hotels and travel tours, in the form of an appeal to provide space for beach tourism promotion and offers of tour packages to tourist objects. However, behind the increase, in its implementation, a problem was found that was sufficient to increase tourist visits. The problem is branding, which tourists still know as a transit city, not a destination city.

Implementing strategies to improve the infrastructure to be less than optimal where there were complaints from tourists regarding traveling comfort, limited budgets, and lack of synergy between stakeholders and related service offices. However, efforts to recommend permits for tourist attractions, and fostering the implementation of beach tourism following the legislation, have continued to be carried out to results in satisfactory results where the number of hotels has increased on average and reached the targeted number.

This partnership-building activity program is scheduled and carried out regularly. In this activity, education on beach tourism gives to beach tourism business actors from the government by presenting speakers who are competent in their fields—carrying out the development of beach tourism activities, discussing the urgency of the problems found and solving problems, and finding the best solutions to overcome the problems experienced by beach tourism business actors. Training and coaching focus and order human resources engaged in the existing beach tourism sector by implementing such training, education, and coaching can help beach tourism human resources optimally and create HR professionalism.

Monitoring and Evaluation

To determine the extent to which the strategic plan requires evaluation activities annually, the government does not evaluate the strategy annually. The beach tourism management strategy is only a plan and does not work as it should (Bott & Braun, 2019).

CONCLUSION

Management consistency needs a more dignified beach recreation management framework- this the private sector's desire to manage new beach tourism to increase its income and employees. City governments must improve planning for area preservation, management, maintenance, and quality development of beach beach tourism areas. Improvements in the bureaucratic system to facilitate the planning process to increase the quality and quantity of beach tourism destinations must be more intense in coordination between related agencies to carry out activities to improve facilities and infrastructure in several coastal beach tourism. Making technological developments and globalization, providing more opportunities for the community to take an active role in beach tourism marketing activities by organizing creative activities so that people are more enthusiastic about beach tourism activities. Increase cooperation with the private sector by planning and implementing beach tourism activities involving the private sector to feel given a forum and support to participate in joint activities. Improve coordination with beach tourism activists and entrepreneurs. It enabled Semarang City's branding as a beach beach tourism destination by holding various promotional activities and beach tourism activists and entrepreneurs, conducting cooperation in coastal beach tourism management with the private sector.

ACKNOWLEDGEMENTS

This research received no specific grant from any funding agency in the public, commercial, or not-for-profit sectors.

REFERENCES

- Abbasi-Moud, Z., Vahdat-Nejad, H., & Sadri, J. (2021). Beach tourism recommendation system based on semantic clustering and sentiment analysis. *Expert Systems with Applications*, 167, Article 114324. <https://doi.org/10.1016/j.eswa.2020.114324>
- Antunes do Carmo, J. S. (2019). The changing paradigm of coastal management: The Portuguese case. *Science of the Total Environment*, 695, Article 133807. <https://doi.org/10.1016/j.scitotenv.2019.133807>
- Artiningsih, Setyono, J. S., & Yuniartanti, R. K. (2016). The challenges of disaster governance in an Indonesian multi-hazards city: A case of Semarang, Central Java. *Procedia - Social and Behavioral Sciences*, 227(November 2015), 347-353. <https://doi.org/10.1016/j.sbspro.2016.06.081>
- Aznar, J. P. (2021). Differentiation and pricing strategies for hotels in sun and beach destinations. *Managerial and Decision Economics*, 42(2), 289-293. <https://doi.org/10.1002/mde.3234>
- Bott, L. M., & Braun, B. (2019). How do households respond to coastal hazards? A framework for accommodating strategies using the example of Semarang Bay, Indonesia. *International Journal of Disaster Risk Reduction*, 37(April), Article 101177. <https://doi.org/10.1016/j.ijdrr.2019.101177>
- Brand, J. H., & Spencer, K. L. (2019). Potential contamination of the coastal zone by eroding historic landfills. *Marine Pollution Bulletin*, 146(April), 282-291. <https://doi.org/10.1016/j.marpolbul.2019.06.017>

- Buchori, I., Pramitasari, A., Sugiri, A., Maryono, M., Basuki, Y., & Sejati, A. W. (2018). Adaptation to coastal flooding and inundation: Mitigations and migration pattern in Semarang City, Indonesia. *Ocean and Coastal Management*, 163(July), 445-455. <https://doi.org/10.1016/j.ocecoaman.2018.07.017>
- Dube, K., Nhamo, G., & Chikodzi, D. (2021). Rising sea level and its implications on coastal beach tourism development in Cape Town, South Africa. *Journal of Outdoor Recreation and beach tourism*, 33(27209), Article 100346. <https://doi.org/10.1016/j.jort.2020.100346>
- Fithor, A., Indarjo, A., & Ario, R. (2013). Studi kesesuaian wisata dan mutu air laut untuk ekowisata rekreasi pantai di Pantai Maron Kota Semarang [Study of tourism suitability and sea water quality for coastal recreation ecotourism at Maron Beach, Semarang City]. *Diponegoro Journal of Marine Research*, 2(4), 31-35.
- Lithgow, D., Martínez, M. L., Gallego-Fernández, J. B., Silva, R., & Ramírez-Vargas, D. L. (2019). Exploring the co-occurrence between coastal squeeze and coastal beach tourism in a changing climate and its consequences. *Beach Tourism Management*, 74(January 2018), 43-54. <https://doi.org/10.1016/j.tourman.2019.02.005>
- Liu, G., Cai, F., Qi, H., Zhu, J., Lei, G., Cao, H., & Zheng, J. (2019). A method to nourished beach stability assessment: The case of China. *Ocean and Coastal Management*, 177(178), 166-178. <https://doi.org/10.1016/j.ocecoaman.2019.05.015>
- Nurhidayah, L., & McIlgorm, A. (2019). Coastal adaptation laws and the social justice of policies to address sea level rise: An Indonesian insight. *Ocean and Coastal Management*, 171(February 2018), 11-18. <https://doi.org/10.1016/j.ocecoaman.2019.01.011>
- Sholeh, M., & Farid, A. (2021). Policy analysis of marine beach tourism of Gili Iyang Island, Madura, Indonesia. *IOP Conference Series: Earth and Environmental Science*, 674(1), Article 27209. <https://doi.org/10.1088/1755-1315/674/1/012018>
- Solihin, L., Kusumastanto, T., Fauzi, A., & Yulianda, F. (2020). Institutional arrangement of conservation areas for sustainable marine beach tourism in Gili Matra water beach tourism park, Indonesia. *AACL Bioflux*, 13(6), 3542-3555.
- Sunaryo, S., Ambariyanto, A., Sugianto, D. N., Helmi, M., Kaimuddin, A. H., & Indarjo, A. (2018). Risk analysis of coastal disaster of Semarang City, Indonesia. *E3S Web of Conferences*, 31, 1-5. <https://doi.org/10.1051/e3sconf/20183112009>
- Wever, L., Glaser, M., Gorris, P., & Ferrol-Schulte, D. (2012). Decentralization and participation in integrated coastal management: Policy lessons from Brazil and Indonesia. *Ocean and Coastal Management*, 66, 63-72. <https://doi.org/10.1016/j.ocecoaman.2012.05.001>
- Zheng, W., Cai, F., Chen, S., Zhu, J., Qi, H., Cao, H., & Zhao, S. (2020). Beach management strategy for small islands: Case studies of China. *Ocean and Coastal Management*, 184(July), Article 104908. <https://doi.org/10.1016/j.ocecoaman.2019.104908>

Immobilized Microalgae using Alginate for Wastewater Treatment

Amanatuzzakiah Abdul Halim* and Wan Nor Atikah Wan Haron

Department of Biotechnology Engineering, Kulliyah of Engineering, International Islamic University Malaysia (IIUM), Jalan Gombak, 53100 Kuala Lumpur, Malaysia

ABSTRACT

Organic and inorganic substances are released into the environment because of domestic, agricultural, and industrial activities which contribute to the pollution of water bodies. Removal of these substances from wastewater using conventional treatment involves high energy cost for mechanical aeration to provide oxygen for aerobic digestion system. During this process, the aerobic bacteria rapidly consume the organic matter and convert it into single cell proteins, water, and carbon dioxide. Alternatively, this biological treatment step can be accomplished by growing microalgae in the wastewater. *Chlorella vulgaris* immobilized in calcium alginate was used to study the removal efficiency of main nutrients in wastewater such as ammonium and phosphate that act as an important factor in microalgae growth. The immobilized cells demonstrated higher percentage of ammonium and phosphate removal of 83% and 79% respectively, compared to free-suspended cells (76% and 56%). COD removal recorded was 89% and 83% for immobilized cells and free-suspended cells, respectively. The kinetics parameters of nutrients removal for immobilized *C. vulgaris* in synthetic wastewater were also determined. The specific ammonium removal rates (R_A) and phosphate removal rates (R_P) for *Chlorella vulgaris* in synthetic wastewater were 8.3 mg.L⁻¹day⁻¹ and 7.9 mg.L⁻¹day⁻¹, respectively. On the other hand, the kinetic coefficient for each nutrient removal determined were $k_A = 0.0462 \text{ L.mg}^{-1} \text{ day}^{-1} \text{ NH}_4$ and $k_P = 0.0352 \text{ L.mg}^{-1} \text{ day}^{-1} \text{ PO}_4^{3-}$. This study proves the application of immobilized microalgae cells is advantageous to the wastewater treatment efficiency. Furthermore, optimization on the

immobilization process can be conducted to further improve the nutrients removal rates which potentially can be applied in the large-scale wastewater treatment process.

Keywords: Alginate, ammonium removal, cell immobilization, COD, microalgae, nutrients removal, phosphate removal

ARTICLE INFO

Article history:

Received: 02 February 2021

Accepted: 30 April 2021

Published: 31 July 2021

DOI: <https://doi.org/10.47836/pjst.29.3.34>

E-mail addresses:

amana@iiu.edu.my (Amanatuzzakiah Abdul Halim)

atikahwanharon@gmail.com (Wan Atikah Wan Haron)

* Corresponding author

INTRODUCTION

Microalgae are unicellular photosynthetic organisms consist of both prokaryotic and eukaryotic and commonly grow in various aquatic environments. Photosynthetic algae are important to the global nutrients cycle such as carbon and oxygen and about 40% of photosynthesis is performed by microalgae (Benedetti et al., 2018). They can easily grow with adequate amounts of carbon (C), nitrogen (N), and phosphorus (P) with other essential trace elements (Stockenreiter et al., 2016). In recent years, microalgae have been widely applied in various biotechnology areas such as aquaculture, cosmetic, food and pharmaceutical industries (Rizwan et al., 2018). In addition to that, microalgae have shown a great potential to treat the industrial wastes such as petroleum, heavy metals, dyes, and toxic gases (Kaur et al., 2019; Qiu et al., 2019). These versatile microalgae can also be used in the treatment of agro-industrial (Halim et al., 2019) and aquaculture effluent (Tejido-Nunez et al., 2019).

Water pollution that mainly consists of nitrogen and phosphorus has become a serious issue to environment which contributes to eutrophication. Eutrophication is known as the nutrient enrichment that may change the structure and function of aquatic ecosystems (Pacheco et al., 2015). It can cause damage to biodiversity, ecosystem sustainability and affects human health. Alternatively, these pollutants can be utilized for microalgae growth. Both water medium and necessary nutrients are freely available from the wastewater that are ideal for microalgae cultivation. With various mode of metabolism, microalgae can remove a common pollutant from the water course. Therefore, integrating wastewater treatment with algae cultivation may have the economic potential and simultaneously promoting green technology to treat wastewater as well as contributing to the algae-based chemicals production.

Utilization of free suspended microalgae cells in wastewater treatment has a great potential in removing the nutrients in the wastewater. Despite of the low cost and shorter hydraulic retention time (HRT) compared to the conventional wastewater treatment, this system has low cell loadings and biomass removal issue. The nature of the cells that are negatively charged and small in size (5-50 μm) prevent cells aggregation (Wu et al., 2012). Therefore, the removal of the algal biomass from the treated water requires high energy intensive and costly operation. Various methods have been used to address the biomass removals such as centrifugation, filtration, flotation, and flocculation. On the other hand, immobilization technique can be used to solve the biomass harvesting issue and simultaneously retaining the high-value biomass for further processing.

Various methods of microalgae immobilization have been reported (Kaparaku, 2017). Among them are adsorption on a surface, encapsulation, entrapment within a matrix and containment within a polymer. Majority of the works used entrapment method by employing natural and synthetic polymers. The utilization of alginate bead has been considered as one of the most suitable methods for cell immobilization. This is due to their characteristics

of mild gelation properties, inert aqueous matrix with high porosity that help preserve the physiological properties and functionality of the encapsulated cells (Gao et al., 2016). Moreover, the entrapped microalgae are protected from mechanical stress while nutrients and metabolites can diffuse through the semi-permeable bead (Acarregui et al., 2012). Studies have shown that immobilized cells are more efficient in removing N and P with higher cell loading as compared to free suspended cells (De-Bashan & Bashan, 2010). In this study, microalgae were immobilized in alginate beads and the removal efficiency of the main nutrients and COD was compared with free suspended microalgae cells. The kinetics parameters of nutrients removal for immobilized *C. vulgaris* in synthetic wastewater were also determined.

METHOD

Microalgae Strains

Chlorella vulgaris (Algae Research Laboratory, Institute of Ocean and Earth Sciences, University Malaya) was grown in Tris–acetate–phosphorus (TAP) media and 150 rpm in a rotary shaker. The microalgae cells were grown at room temperature (25°C) in 12 hours light and 12 hours dark cycles.

Immobilization of Microalgae

150 mL of microalgae containing 5×10^6 cells/mL was centrifuged at 3500 rpm for 10 minutes. The cells were suspended and mixed with 80 mL of 2% alginate solution, and slowly mixed with a stirrer for 15 minutes. The alginate beads were obtained by dropping the alginate–algae mixture from a syringe into 2% CaCl₂ solution. The beads formed were left for 1 hour in the solution for hardening process. These beads were washed off several times with sterile distilled water until their pH reached pH 7.

Synthetic Wastewater Preparation

Synthetic wastewater for the experiment was prepared using the following components (mg/L): Glucose (256.41), NH₄Cl (35.33) and KH₂PO₄ (43.8) to obtain 300 mg/L of Chemical Oxygen Demand (COD), 10 mg/L of ammonium and 10 mg/L of phosphorus. The pH was adjusted to 7 with KOH (Hernandez et al., 2006; Mujtaba et al., 2015).

Determination of Microalgae Growth

Cell number was determined once in every two days, using a hemacytometer under a microscope. 10 µl of cell suspension (or 1 drop from a transfer pipette) was added to the hemacytometer and cells were observed under the microscope. For immobilized cells in alginate beads, ten beads were taken from flask and solubilised by immersion in 1 mL of

4% NaHCO₃ solution for 30 minutes before the cells were observed under microscope. In determining the optical density, 1 mL of the sample was taken every two days and measured by spectrophotometer at 680 nm of wavelength.

Analytical Tests

The performance of wastewater treatment by microalgae system was indicated by the percentage of COD and nutrients (i.e., ammonium and phosphorus) removals. The percentage of removal was calculated as shown in Equation 1.

$$\% \text{ of removal} = \frac{\text{Initial concentration (mg/L)} - \text{Final concentration (mg/L)}}{\text{Initial concentration (mg/L)}} \times 100$$

[1]

Standard methods for the examination of wastewater were used to analyse the COD, ammonium, and phosphorus removals (APHA, 1999). COD, ammonium, and phosphorus were respectively analysed by closed reflux of colorimetric method, phenate method and ascorbic acid method.

RESULTS AND DISCUSSION

Growth of *C. Vulgaris* in TAP Media

The growth profile of free suspended and immobilized *Chlorella vulgaris* in TAP media is shown in Figure 1. Two main growth phases were observed during 10 days of experiment (log phase and stationary phase). No lag phase was observed for both microalgae cultures. The cells number increased exponentially and reached the maximum cells concentration of 53×10^6 cells/mL and entered the stationary phase on day eight of the experiment for free suspended cells. Similar trend was observed for immobilized *C. vulgaris* which showed rapid growth with maximum cells concentration of 64×10^6 cells/mL. Immobilized cells showed better growth than free suspended cells as reported by other studies (Aguilar-May & Sanchez-Saavedra, 2009; Singh, 2003). Ruiz-Marin et al. (2010) reported similar observation on the cell growth where the cells number increased rapidly once the beads were added into the medium. However, immobilized cells may also undergo lag phase because of cell adaptation to the new environment (Shen et al., 2017). The specific growth rate of the immobilized cells is comparable to the free suspended cells during the exponential phase which are 0.13 day^{-1} and 0.10 day^{-1} , respectively. This result shows that the growth of the encapsulated algal cells was not reduced compared to the free cells. The medium nutrients can diffuse through the semi-permeable beads allowing the cell to undergo the cell division process. On the contrary, some entrapment matrices made from synthetic material may produce small pore bead size that restricts nutrients diffusion which affect the

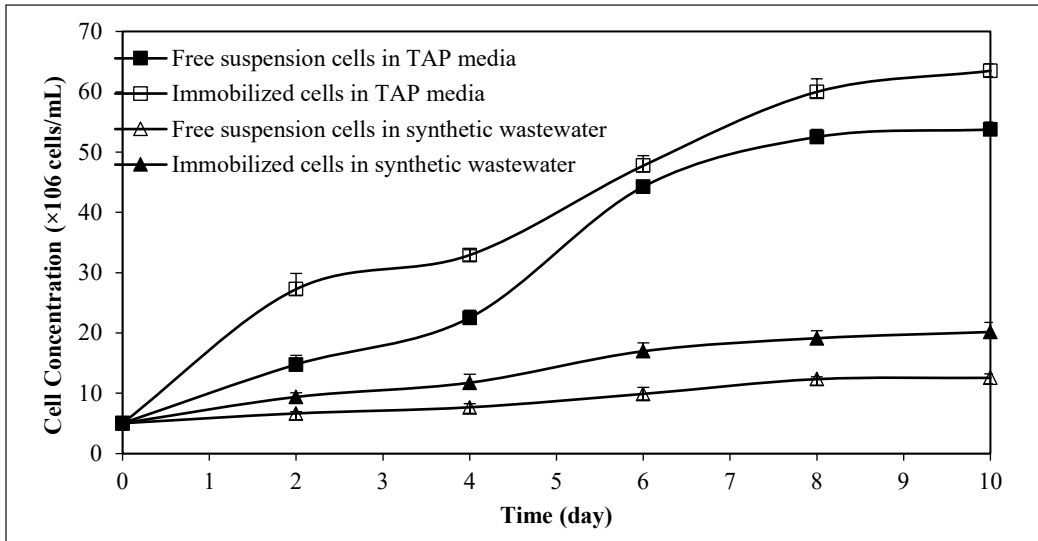


Figure 1. Growth profile of *Chlorella vulgaris* in TAP media and synthetic wastewater. Error bar shows one standard deviation of mean (n=3)

cell morphology and viability (Shen et al., 2017). Moreover, high cell loading may impede the cell growth as there is limited space for the cell to grow or possibly due to restriction on nutrient movement (Leenen et al., 1996). Nevertheless, the results prove that alginate can be used efficiently for cell immobilization.

Growth of *Chlorella vulgaris* in Synthetic Wastewater

The growth profile of both free suspended cells and immobilized cells cultivated in synthetic wastewater is illustrated in Figure 1. Similar trend of growth was observed for both cultures as compared to the growth in TAP media. Maximum concentration for free suspended cells and immobilized cells were 13×10^6 cells/mL and 20×10^6 cells/mL respectively. The increase in cell numbers indicated that the algal cells were able to undergo cell division when cultivated in a limited nutrient medium. While the specific growth rate of free suspension cells and immobilized cells were 0.119 day^{-1} and 0.122 day^{-1} respectively. The maximum number of cells grown in synthetic wastewater were slightly lower than the one cultivated in TAP media which was expected as TAP media contains optimum nutrients needed for microalgae growth while the synthetic medium only consist a few nutrients. However, these data show that synthetic wastewater were able to support the growth of the cells with the minimum nutrients of ammonium, phosphate, and carbon source (glucose).

Nutrients Removal

The removal of ammonium by the free suspended and immobilized cells is shown in Figure 2. Nitrogen in the form of ammonium is essential to many functional components

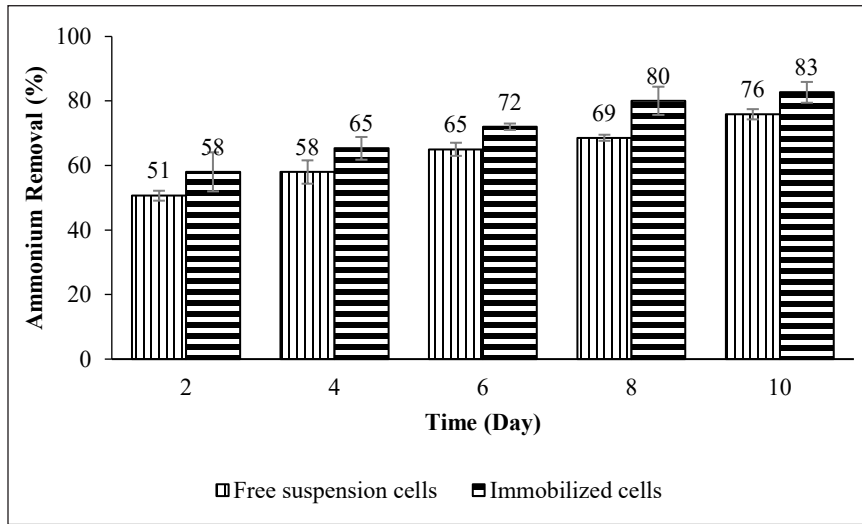


Figure 2. The percentage removal of ammonium by free suspension cells and immobilized cells. Error bar shows one standard deviation (n=3)

of algae and reported to be the main source of nitrogen for algae. The nutrient uptake occurs through direct assimilation between the cells and ammonium based on the form and concentration available (Sanz-Luque et al., 2015). Both cells type achieved rapid removal of 51-58% on day 2 and gradually increased until day 10. The rate of ammonium removal is at the highest during the first two days when the nutrient availability was high. The high ammonia concentration triggered the rapid uptake where the cells passed from a least concentrated to a more concentrated medium. As the day progressed, the nutrient uptake slows down and achieved a total of 76% and 83% ammonium removal on day 10 for free and immobilized cells, respectively. The results show the immobilized *C. vulgaris* has slightly higher percentage removal than the free suspended cells. These values were well correlated with the cell concentration profile in Figure 1. Similar trend was reported by several studies on higher ammonium removal for alginate-immobilized microalgae as compared to the free suspended cells (Banerjee et al., 2019; Soo et al., 2017).

The phosphate uptake by the cells started slowing around 21% and 26 % on day 2 and achieved final removal of 56% and 79% on day 10 for free cells and immobilized cells respectively (Figure 3). The percentage nutrient removal by microalgae cells is lower for phosphate compared to the ammonium especially for free suspended cells. In general, ammonium is the most preferable nitrogen source as it requires less energy for its uptake compared to the other form of nutrients (Delgadillo-Mirquez et al., 2016). Similar trend was observed by other studies which reported higher removal of ammonium compared to phosphate (Samsudin et al., 2018; Shen et al., 2017). Rapid removal of COD was observed on day 2 by freely suspended (61%) and immobilized (71%) *C. vulgaris* (Figure 4). The percentage removal gradually increased until day 10 with maximum removal of 89% by

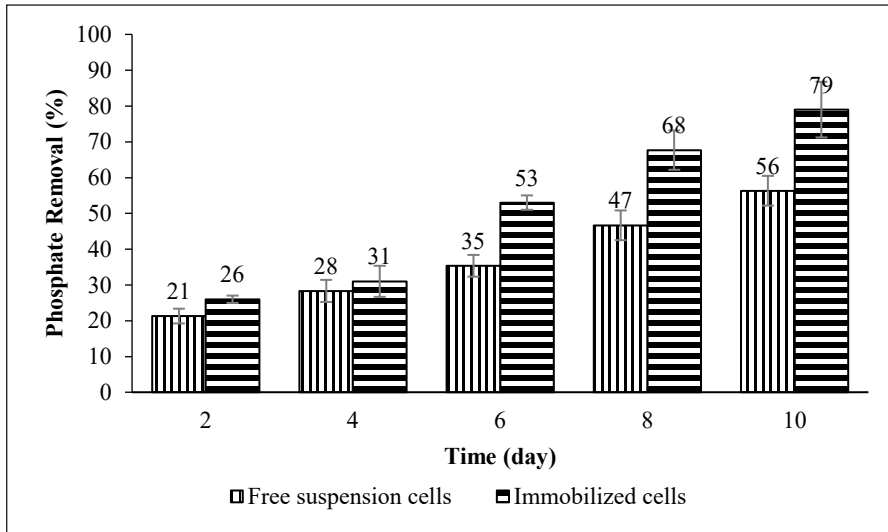


Figure 3. The percentage removal of phosphate by free suspension cells and immobilized cells. Error bar shows one standard deviation (n=3)

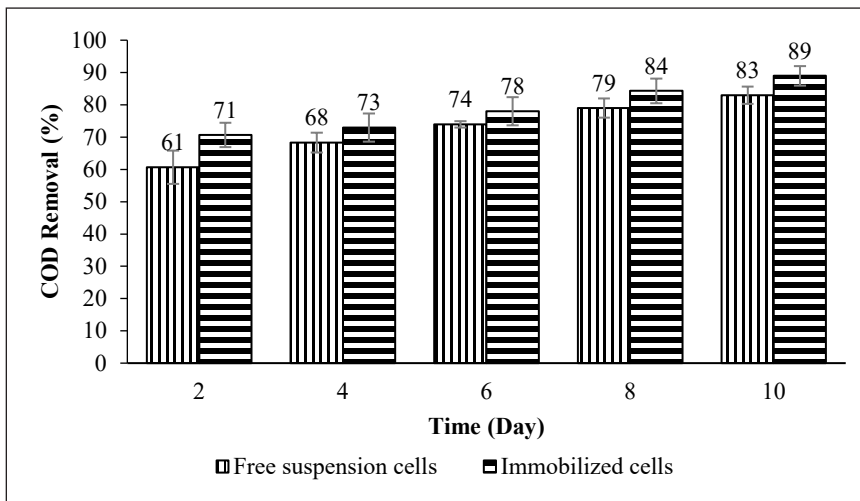


Figure 4. The percentage removal of COD by free suspension cells and immobilized cells. Error bar shows one standard deviation (n=3)

the immobilized cells and 83% for free cells. On the first 2 days of the cell cultivation, the cells were actively doubling their number in which reflected the higher uptake of glucose that provide high amount of energy needed for the cell's activities, hence the consumption of glucose as the carbon source was very high within the short period. This indicates high efficiency removal of COD by microalgae cells.

Based on the results discussed above, the performance of nutrient removal of immobilized microalgae is relatively higher compared to the free cells. Immobilized

Chlorella vulgaris exhibits uptake rates of 23%, 7% and 6% higher than suspended free algae for phosphate, ammonium, and COD, respectively. This result is consistent with the previous findings in other study (Covarrubias et al., 2012). The enhanced removal performance can be described based on the chemical interactions between alginate matrix and the nutrients. The presence of carboxyl group (COO⁻) attracts cations and the free binding site on the surface of the alginate matrix provides the medium for physical adsorption for both NH₄⁺ and PO₄³⁻ ions before assimilation process occur by the encapsulated algae (Banerjee et al., 2019). Higher adsorption rate is expected with increment in alginate concentration. The optimum adsorption rate was achieved at 3% alginate concentration with high removal of nutrients conducted using *Chlorella vulgaris* (Banerjee et al., 2019). The removal of nutrients by the alginate bead alone was reported to be minimal compared to the alginate-immobilized microalgae cells (Banerjee et al., 2019). Even though the contribution of alginate in removing nutrients are evident, the primary mechanism of nutrient removal through microalgae uptake is more significant compared to the chemical and physical processes. Moreover, the utilization of immobilized cells using alginate matrix provides protective environment against the mechanical shear stress and external microorganisms contamination which enhanced the overall nutrients removal performance.

Kinetics of Nutrient Removal by Immobilized *Chlorella vulgaris*

In this study, the ammonium and phosphate removal rates were determined using Equation 2.

$$R = \frac{S_o - S_i}{t_i - t_o} \quad [2]$$

Where R represents the removal rate of nutrients (ammonium and phosphate), S_o represents the initial concentration of nutrients, S_i is the nutrient concentration at time t_i and t_i is the time when there was no significant change taking place for nutrient concentration. The specific ammonium removal rates (R_A) and phosphate removal rates (R_P) for *Chlorella vulgaris* in synthetic wastewater were 8.3 mg.L⁻¹.day⁻¹ and 7.9 mg.L⁻¹.day⁻¹, respectively.

In this study, ammonium and phosphate removal fitted well with the second order reaction of equal initial concentration of nutrients (ammonium and phosphate). The defining second-order differential Equation 3 and 4 as below:

$$-r_A = -\frac{dC_A}{dt} = kC_A^2 = kC_{A0}^2(1 - X_A)^2 \quad [3]$$

Which on integration yields

$$\frac{1}{C_A} - \frac{1}{C_{A0}} = \frac{1}{C_{A0}} - \frac{X_A}{1 - X_A} = kt \quad [4]$$

Therefore, the reaction of ammonium and phosphate can be expressed by Equation 5.

$$C_A = C_{A0} e^{-kt} \tag{5}$$

where C_A represents nutrient concentration at time t , C_{A0} represents the initial concentration of nutrient, and k is the second order reaction constant.

Experimental data given in Figure 2 were plotted in the form of $1/C_A$ versus time as shown in Figure 5. From the slope and intercept of best fit line of this plot, kinetic coefficient of ammonium removal by *C. vulgaris* were determined with $k_A = 0.0462 \text{ L.mg}^{-1} \text{ day}^{-1} \text{ NH}_4$ ($R^2 = 0.9806$).

Similarly, from the experimental data in Figure 3, the coefficient for phosphate removal was found with $k_p = 0.0352 \text{ L.mg}^{-1} \text{ day}^{-1} \text{ PO}_4^{3-}$ from the intercept and slope of best fit line of $1/C_A$ versus time, ($R^2 = 0.8711$) as illustrated in Figure 6.

The yield coefficient for ammonium and phosphate removal was calculated using Equation 6.

$$Y = \frac{C - C_0}{S_0 - S} \tag{6}$$

where Y is the yield of biomass linked with the consumption of nutrients, S_0 is initial nutrient concentrations and S is final nutrient concentration. C represents the concentration of cells with respect to the nutrient S and C_0 is the initial concentration of the cells. Therefore, the kinetics parameters of nutrients removal for *C. vulgaris* in synthetic wastewater are summarized in Table 1.

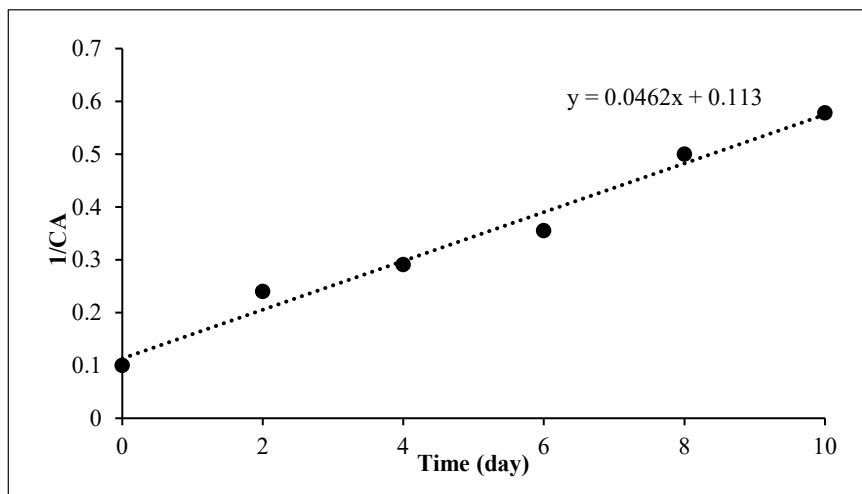


Figure 5. Determination of kinetic coefficient for ammonium removal by *C. vulgaris*

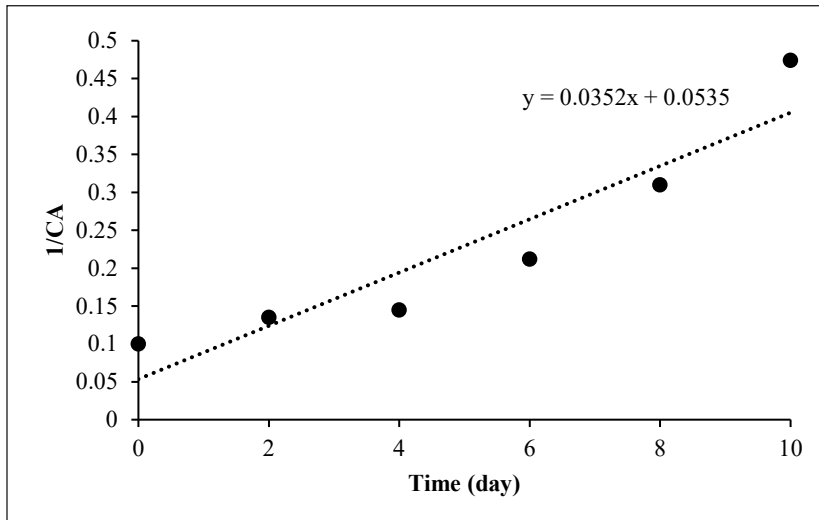


Figure 6. Determination of kinetic coefficient for phosphate removal by *C. vulgaris*

The specific ammonium removal rates (R_A) and phosphate removal rates (R_P) for *C. vulgaris* obtained were $8.3 \text{ mg.L}^{-1}\text{day}^{-1}$ and $7.9 \text{ mg.L}^{-1}\text{day}^{-1}$, respectively. Other studies reported various results depending on the condition of the experiments such as the initial nutrient concentration, reaction time, and bead's condition. Aslan and Kapdan (2006) reported $10.5 \text{ mg NH}_4 \text{ L}^{-1}\text{day}^{-1}$ and $2.0 \text{ mg PO}_4^{3-} \text{ L}^{-1}\text{day}^{-1}$ while Lau et al. (1998) obtained $5.44 \text{ mg NH}_4 \text{ L}^{-1}\text{day}^{-1}$ and $1.3 \text{ mg PO}_4^{3-} \text{ L}^{-1}\text{day}^{-1}$, both were using *C. vulgaris* cells. On the other hand, the biomass yield

based on ammonium and phosphate consumption obtained were $0.0407 \text{ mg.mg}^{-1}\text{NH}_4$ and $0.0318 \text{ mg.mg}^{-1} \text{ PO}_4^{3-}$ respectively. The ratio of $\frac{Y_A}{Y_P}$ (0.781) indicates the amount of the ratio of P/A required (mg P consumed/mg A consumed) to produce the same unit amount of biomass. The kinetic coefficient for ammonium and phosphate removal were determined based on second order reaction model with $k_A = 0.0462 \text{ L.mg}^{-1} \text{ day}^{-1} \text{ NH}_4$ and $k_P = 0.0352 \text{ L.mg}^{-1} \text{ day}^{-1} \text{ PO}_4^{3-}$. In other study the kinetic coefficients reported were $k_A = 0.00249 \text{ L.mg}^{-1} \text{ day}^{-1} \text{ NH}_4$ and $k_P = 0.192 \text{ L.mg}^{-1} \text{ day}^{-1} \text{ PO}_4^{3-}$ for ammonium and phosphate removal by *C. vulgaris* respectively (Banerjee et al., 2019). The difference value between these kinetic coefficients is due to the different conditions of the experiments as well as the model used.

Table 1
Kinetics parameters of nutrients removal for immobilized *C. vulgaris* in synthetic wastewater

Kinetics Parameters	Data
Initial N/P (mass ratio)	1
R_A (mg.L ⁻¹ day ⁻¹)	8.3
R_P (mg.L ⁻¹ day ⁻¹)	7.9
Y_A (mg mg ⁻¹ A)	0.0407
Y_P (mg mg ⁻¹ P)	0.0318
Y_P / Y_A	0.781
k_A (L.mg ⁻¹ day ⁻¹ NH ₄)	0.0462
k_P (L.mg ⁻¹ day ⁻¹ PO ₄ ³⁻)	0.0352

CONCLUSION

This present study demonstrated that alginate immobilized *C. vulgaris* showed higher nutrients (ammonium and phosphate) and COD removal efficiency from the synthetic wastewater than the free cells. The percentage removal of ammonium and phosphate for immobilized cells were about 83% and 79%, respectively compared to free suspension cells which were 75% for ammonium removal and 56% for phosphate removal. Similarly, with the COD, over 80% of glucose were removed from the synthetic wastewater by both the alginate immobilized microalgae cells and free cells within 10 days. The main reasons for high removal performance could be correlated to the high metabolic activities of the immobilized cells and the interaction between the supporting materials and the nutrients ions in wastewater. The kinetics data determined in this study include, the specific ammonium removal rates (R_A) and phosphate removal rates (R_P) which were 8.3 mg.L⁻¹.day⁻¹ and 7.9 mg.L⁻¹.day⁻¹, respectively. Moreover, the kinetic coefficient for each nutrient removal obtained were $k_A = 0.0462$ L.mg⁻¹ day⁻¹ NH₄ and $k_P = 0.0352$ L.mg⁻¹ day⁻¹ PO₄³⁻. The findings from this study provide some insights on the utilization of immobilized cells in wastewater treatment. Nevertheless, this method can be further integrated with several components such as CO₂ biofixation and biofuel production to efficiently manage the environmental issues.

ACKNOWLEDGEMENT

The research was conducted using the facilities provided by the Department of Biotechnology Engineering, International Islamic University Malaysia.

REFERENCES

- Acarregui, A., Murua, A., Pedraz, J. L., Orive, G., & Hernandez, R. M. (2012). A perspective on bioactive cell microencapsulation. *BioDrugs*, 26, 283-301. <https://doi.org/10.1007/bf03261887>
- Aguilar-May, B., & Sánchez-Saavedra, M. P. (2009). Growth and removal of nitrogen and phosphorus by free living and chitosan-immobilized cells of the marine cyanobacterium *Synechococcus elongates*. *Journal of Applied Phycology*, 21, 353-360. <https://doi.org/10.1007/s10811-008-9376-7>
- APHA. (1999). *Standard methods for the examination of water and wastewater part 4000 inorganic nonmetallic constituents*. American Public Health Association. <https://doi.org/10.2105/SMWW.2882.067>
- Aslan, S., & Kapdan, I. K. (2006). Batch kinetics of nitrogen and phosphorus removal from synthetic wastewater by algae. *Ecological Engineering*, 28, 64-70. <https://doi.org/10.1016/j.ecoleng.2006.04.003>.
- Banerjee, S., Tiwade, P. B., Sambhav, K., Banerjee, C., & Bhaumik, S. K. (2019). Effect of alginate concentration in wastewater nutrient removal using alginate-immobilized microalgae beads: Uptake kinetics and adsorption studies. *Biochemical Engineering Journal*, 149, Article 107241. <https://doi.org/10.1016/j.bej.2019.107241>

- Benedetti, M., Vecchi, V., Barera, S., & Dall'Osto, L. (2018). Biomass from microalgae: The potential of domestication towards sustainable biofactories. *Microbial Cell Factories*, 17(1), 1-18. <https://doi.org/10.1186/s12934-018-1019-3>
- Covarrubias, S. A., de-Bashan, L. E., Moreno, M., & Bashan, Y. (2012). Alginate beads provide a beneficial physical barrier against native microorganisms in wastewater treated with immobilized bacteria and microalgae. *Applied Microbiology and Biotechnology*, 93, 2669-2680. <https://doi.org/10.1007/s00253-011-3585-8>
- De-Bashan, L. E., & Bashan, Y. (2010). Immobilized microalgae for removing pollutants: Review of practical aspects. *Bioresource Technology*, 101(6), 1611-1627. <https://doi.org/10.1016/j.biortech.2009.09.043>
- Delgadillo-Mirquez, L., Lopes, F., Taidi, B., & Pareau, D. (2016). Nitrogen and phosphate removal from wastewater with a mixed microalgae and bacteria culture. *Biotechnology Reports*, 11, 18-26. <https://doi.org/10.1016/j.btre.2016.04.003>
- Gao, H., Khera, E., Lee, J. K., & Wen, F. (2016). Immobilization of multi-biocatalysts in alginate beads for cofactor regeneration and improved reusability. *Journal of Visualized Experiments*, (110), Article 53944. <https://doi.org/10.3791/53944>
- Halim, A. A., Samsudin, A., Azmi, A. S., & Nawati, M. M. N. (2019). Nutrient and chemical oxygen demand (COD) removals by microalgae-bacteria co-culture system in palm mill oil effluent (POME). *IJUM Engineering Journal*, 20(2), 22-31. <https://doi.org/10.31436/ijumej.v20i2.1109>
- Hernandez, J., Luz, E., & Bashan, Y. (2006). Starvation enhances phosphorus removal from wastewater by the with *Azospirillum brasilense*. *Enzyme and Microbial Technology*, 38, 190-198. <https://doi.org/10.1016/j.enzmictec.2005.06.005>
- Kaparapu, J. (2017). Micro algal immobilization techniques. *Journal of Algal Biomass Utilization*, 8(1), 64-70.
- Kaur, H., Rajor, A., & Kaleka, A. S. (2019). Role of phycoremediation to remove heavy metals from sewage water: Review article. *Journal of Environmental Science and Technology*, 12, 1-9. <https://doi.org/10.3923/jest.2019.1.9>
- Lau, P. S., Tam, N. F. Y., & Wong, Y. S. (1998). Effect of carrageenan immobilization on the physiological activities of *Chlorella vulgaris*. *Bioresource Technology*, 63(2), 115-121. [https://doi.org/10.1016/S0960-8524\(97\)00111-9](https://doi.org/10.1016/S0960-8524(97)00111-9)
- Leenen, E. J. T. M., Dos Santos, V. A. P., Grolle, K. C. F., Tramper, J., & Wijffels, R. H. (1996). Characteristics of and selection criteria for support materials for cell immobilization in wastewater treatment. *Water Research*, 30(12), 2985-2996. [https://doi.org/10.1016/s0043-1354\(96\)00209-6](https://doi.org/10.1016/s0043-1354(96)00209-6)
- Mujtaba, G., Rizwan, M., & Lee, K. (2015). Simultaneous removal of inorganic nutrients and organic carbon by symbiotic co-culture of *Chlorella vulgaris* and *Pseudomonas putida*. *Biotechnology and Bioprocess Engineering*, 20(6), 1114-1122. <https://doi.org/10.1007/s12257-015-0421-5>
- Pacheco, M. M., Hoeltz, M., Moraes, M. S. A., & Schneider, R. C. S. (2015). Microalgae: Cultivation techniques and wastewater phycoremediation. *Journal of Environmental Science and Health. Part A, Toxic/hazardous Substances & Environmental Engineering*, 50(6), 585-601. <https://doi.org/10.1080/10934529.2015.994951>

- Qiu, S., Wang, L., Champagne, P., Cao, G., Chen, Z., Wang, S., & Ge, S. (2019). Effects of crystalline nanocellulose on wastewater-cultivated microalgal separation and biomass composition. *Applied Energy*, 239, 207-217. <https://doi.org/10.1016/j.apenergy.2019.01.212>
- Rizwan, M., Mujtaba, G., Memon, S. A., Lee, K., & Rashid, N. (2018). Exploring the potential of microalgae for new biotechnology applications and beyond: A review. *Renewable and Sustainable Energy Reviews*, 92, 394-404. <https://doi.org/10.1016/j.rser.2018.04.034>
- Ruiz-Marin, A., Mendoza-Espinosa, L. G., & Stephenson, T. (2010). Growth and nutrient removal in free and immobilized green algae in batch and semi-continuous cultures treating real wastewater. *Bioresource Technology*, 101(1), 58-64. <https://doi.org/10.1016/j.biortech.2009.02.076>
- Samsudin, A., Azmi, A. S., Nawi, M. N., & Halim, A. A. (2018). Wastewater treatment by microalgae-bacteria co-culture system. *Malaysian Journal of Microbiology*, 14(2), 131-136. <https://doi.org/10.21161/mjm.97818>
- Sanz-Luque, E., Chamizo-Ampudia, A., Llamas, A., Galvan, A., & Fernandez, E. (2015). Understanding nitrate assimilation and its regulation in microalgae. *Frontiers in Plant Science*, 6(10), 1-17. <https://doi.org/10.3389/fpls.2015.00899>
- Shen, Y., Gao, J., & Li, L. (2017). Municipal wastewater treatment via co-immobilized microalgal-bacterial symbiosis: Microorganism growth and nutrients removal. *Bioresource Technology*, 243, 905-913. <https://doi.org/10.1016/j.biortech.2017.07.041>
- Singh, Y. (2003). Photosynthetic activity, and lipid and hydrocarbon production by alginate-immobilized cells of *Botryococcus* in relation to growth phase. *Journal of Microbiology and Biotechnology*, 13(5), 687-691.
- Soo, C. L., Chen, C. A., Bojo, O., & Hii, Y. S. (2017). Feasibility of marine microalgae immobilization in alginate bead for marine water treatment: Bead stability, cell growth, and ammonia removal. *International Journal of Polymer Science*, 2017, Article 6951212. <https://doi.org/10.1155/2017/6951212>
- Stockenreiter, M., Haupt, F., Seppälä, J., Tamminen, T., & Spilling, K. (2016). Nutrient uptake and lipid yield in diverse microalgal communities grown in wastewater. *Algal Research*, 15, 77-82. <https://doi.org/10.1016/j.algal.2016.02.013>
- Tejido-Núñez, Y., Aymerich, E., Sancho, L., & Refardt, D. (2019). Treatment of aquaculture effluent with *Chlorella vulgaris* and *Tetradismus obliquus*: The effect of pretreatment on microalgae growth and nutrient removal efficiency. *Ecological Engineering*, 136, 1-9. <https://doi.org/10.1016/j.ecoleng.2019.05.021>
- Wu, Z., Zhu, Y., Huang, W., Zhang, C., Li, T., Zhang, Y., & Li, A. (2012). Evaluation of flocculation induced by pH increase for harvesting microalgae and reuse of flocculated medium. *Bioresource Technology*, 110, 496-502. <https://doi.org/10.1016/j.biortech.2012.01.101>



Treat-ability of *Manihot esculenta* Peel Extract as Coagulant Aid for Stabilised Leachate

Siti Nor Aishah Mohd-Salleh¹, Nur Shaylinda Mohd-Zin^{1*}, Norzila Othman¹, Yashni Gopalakrishnan¹ and Norshila Abu-Bakar^{1,2}

¹Faculty of Civil Engineering and Built Environment, Universiti Tun Hussien Onn Malaysia, 86400 Parit Raja Batu Pahat, Johor, Malaysia

²Department of Civil Engineering, Politeknik Sultan Abdul Halim Mu'adzam Shah, Bandar Darulaman, 06000 Jitra, Kedah, Malaysia

ABSTRACT

Agro-waste can be commercialised into another useful product such as natural coagulant for wastewater treatment. The purpose of this study was to quantify the ability of agro-waste (*Manihot esculenta* peel extract (MEP)) as an aid alongside the utilisation of chemical coagulant (polyaluminium chloride (PAC)) based on the removal percentages of selected parameters at the optimum coagulant dosage and pH of stabilised leachate. Series of jar tests were used to compare the leachate treatments using single and the dual coagulant of PAC and MEP with respective standard methods to analyse the removal parameters, i.e., Colorimetric (APHA Method:5220 C, HACH Method:8000) for chemical oxygen demand (COD), Conductimetric (APHA Method: 4500-N, HACH Method: 8038) for ammonia nitrogen (AN), Nephelometric (APHA Method:2130) for turbidity, Spectrophotometric (APHA Method: 2120 B, HACH Method: 8025) for colour, and Gravimetric (APHA Method:2540 D, HACH Method:630) for suspended solids (SS). Leachate treatment using the application of single PAC coagulant at the optimum conditions of 3,750 mg/L

dosage and pH 6.0 of leachate managed to remove about 54.1%, 28%, 91.1%, 98%, and 98% for COD, AN, turbidity, colour, and SS, respectively. Meanwhile, by using dual coagulant at the optimum dosages of 3,500 mg/L (PAC) and 250 mg/L (MEP), and pH 7.0 of leachate, the treatment achieved higher removal except for the colour parameter. The final removal outcomes of this study were 58.3% of COD,

ARTICLE INFO

Article history:

Received: 10 February 2021

Accepted: 03 May 2021

Published: 31 July 2021

DOI: <https://doi.org/10.47836/pjst.29.3.36>

E-mail addresses:

sitinoraishah.salleh@gmail.com (Siti Nor Aishah Mohd-Salleh)

nursha@uthm.edu.my (Nur Shaylinda Mohd-Zin)

norzila@uthm.edu.my (Norzila Othman)

yashni_g@yahoo.com (Yashni Gopalakrishnan)

norshilaabubakar@yahoo.com (Norshila Abu-Bakar)

* Corresponding author

34% of AN, 96.9% of turbidity, 92.1% of colour, and 99% of SS. The application of MEP as coagulant aid also managed to reduce the aluminium (Al) content in PAC dosage from 577.5 mg/L to 539.0 mg/L without affecting much of its efficiency.

Keywords: Coagulation-flocculation; jar test; natural coagulant; polyaluminium chloride; removal efficiency

INTRODUCTION

The percolation of rainwater through the degraded solid waste in the open landfill has resulted in the generation of leachate (Aziz et al., 2015). According to its classification, the composition of leachate may contain loads of toxic elements, which are harmful to the environment. The ignorance to treat leachate through proper disposal also could cause unpleasant pollution to receiving waters such as ground aquifers (Kamaruddin et al., 2015). The contents of chemical oxygen demand (COD), ammonia nitrogen (AN), and heavy metals are among a few of most environmental threats that become the significant considerations for leachate to be treated (Yusoff & Zuki et al., 2015). COD is a chemical indicator that indicates the required oxygen to oxidise soluble and suspended organic matter. The high concentration of COD signs the degradation of the dissolved oxygen levels in water bodies. Meanwhile, the high level of AN can cause toxicity to aquatic life and human beings when the leachate leaks to the water resources (Mehmood et al., 2009). For instance, the villagers around Simpang Renggam's landfill site (SRLS) are jeopardised due to the exposure of contaminated water sources with high levels of AN. The untreated AN also becomes the main factor of reduced performances for biological treatments, dissolved oxygen reduction, and speeded up eutrophication in surface water (Aziz et al., 2015). Meanwhile, the high concentrations of suspended solids (SS), turbidity, and colour would eventually result in the poor aesthetic quality of the water (Wang et al., 2017).

Physical and chemical treatments such as the coagulation-flocculation (CF) process using jar test with the help of coagulating agents are favoured for the treatment of stabilised leachate due to its characteristics (Syafalni et al., 2012). In the CF treatment, the usage of effective coagulants is important. In this study, to tackle the drawbacks of chemical coagulant, the raw *Manihot esculenta* peel extract (MEP) peel is used and recycled as a natural coagulant aid to treat stabilised leachate. The peels were obtained from a chip's factory at Parit Raja, Johor, Malaysia. MEP may have been used as a coagulant aid in water and wastewater treatment, but MEP is never used for leachate treatment to the best of our knowledge. The chemical analysis of MEP has verified its competence as a natural coagulant through the existence of polysaccharides form of sugars (holocellulose and starch). Besides, the existence of functional groups (carboxyl, hydroxyl, and amino groups) from pectin, cellulose, and amino acids may also have cogency as flocculating agent (Mohd-Salleh et al., 2020a; Asharuddin et al., 2017). Asharuddin et al. (2018) used the same source of coagulant and alum as a dual coagulant to remove turbidity from dam

water and achieved 91.47% removal. The MEP as the natural coagulant used in this study is made and developed from scratch without any chemical modification. Therefore, the purpose of this study was to quantify the ability of agro-waste (MEP) as an aid alongside the utilisation of chemical coagulant (PAC) based on the removal percentages of COD, AN, turbidity, colour and SS at the optimum coagulant dosage and pH of stabilised leachate. Basically, this study attempts to develop a green coagulant aid for the treatment of high-strength polluted wastewater. The effort of the study is also relevant as the developed natural coagulant could emphasise more usage of agro-waste as a natural material and give benefits to low social communities. This approach aims to increase the recycling and recovery rate of waste while improving the management of landfills to reduce the amount of waste and pollution. Furthermore, the findings would be useful for conserving human health and the environment as the consequence of the treatment of landfill leachate. In the dimension of economic development, this study would assist in sustainable energy for drivers and enablers and increasing innovation and productivity to the next level in the imperatives by focusing on natural coagulants and landfill leachate. Specifically, this study may also be a jumping-off point towards researchers, through the optimisation of leachate pH and dosages of PAC and MEP as a guideline to select a suitable condition range for leachate treatment with better removal percentages of respective contaminants in the future.

MATERIALS AND METHODS

Leachate Sampling

The leachate sample was taken from the Simpang Renggam landfill site (SRLS) (1°53'41 "N 103°22'35" E). SRLS is built in 1996 and still operating up to 2019 with 6 hectares in total size. As for now, the landfill is closed to focus on the treatment of left leachate. Approximately 250 tons of solid wastes were disposed into SRLS daily during its operation, which was over the limit practice. Based on the latest leachate characterisation study done by Mohd-Salleh et al. (2020b) and Zailani et al. (2018) that used the leachate samples taken from the same study area, the landfill was validated to generate stabilised leachate.

Preparation of *Manihot Esculenta* Extract Peel Coagulant and Stock Solution

Manihot esculenta peels (MEP) were collected from the chip's factory at Parit Raja, Johor, Malaysia. There is no cost to produce this natural coagulant because it is an agro-waste taken from the chip's factory for free. On the same day, upon arrival in the laboratory, the peels were separated from the big tubers and washed with tap water to remove the attached soils and impurities. The preparation of starch powder from the peels was according to the study done by Asharuddin et al. (2017) and Mohd-Salleh et al. (2020a). The brown peels were expelled, and only the white flesh from the cortex was scratched using a scratcher. The

white flesh was blended using a domestic blender with distilled water. Next, the white flesh solution was filtered using a muslin cloth to filter the flesh waste. The blended white flesh was settled down for 24 hours, and the excess distilled water was rinsed out. The sticky blended white flesh was spread onto a tray and sundried until completely dry. Finally, the dried white flesh was smashed into a fine powder and stored in a tight container at room temperature. Figures 1 and 2 show the peels and their powder form. The stock solution of MEP was made in a concentration of 1% by diluting 1 gram of MEP into 100 mL of distilled water. A preliminary study was done to select the optimum concentration of MEP between 0.5%, 1%, 3%, 5%, and 7% in treating leachate, of which 1% of MEP had shown satisfactory removal (Mohd-Salleh et al., 2020a). Thus, it was used in this study.



Figure 1. *Manihot esculenta* peels

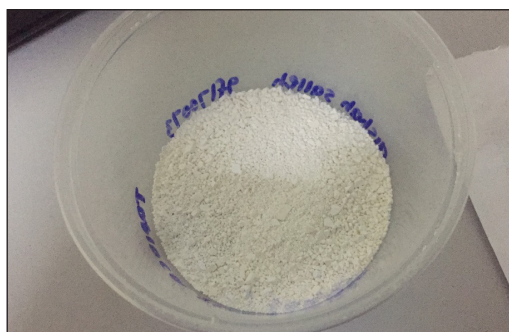


Figure 2. Powder form of MEP extract

Preparation of Polyaluminium Chloride Stock Solution

Polyaluminium chloride (R&M brand) was purchased from the local laboratory supplier that cost \$15 per bottle. The preparation of PAC's stock solution was done by following the methodology of Mohd-Salleh et al. (2018) and Ni et al. (2015) that used 10% of PAC. The coagulant needed to be prepared freshly; thus, it was prepared on the same day as the jar test for the CF process. To make a 10% concentration of the stock solution, 10 grams of PAC were weighed and diluted into 100 mL of distilled water. The compound formula for PAC is $Al_2Cl(OH)$ with total 174.75 g/m of molar mass ($Al=26.982$, $O=16$, $H=1$, $Cl=35.45$).

Experimental Procedure

The CF experiments were performed in a conventional jar-test apparatus (VELP-Scientifica, Model: J LT6, Italy) comprising six paddle rotors ($2.5\text{ cm} \times 7.5\text{ cm}$), equipped with 6 beakers of 1 L each. The operating conditions of the jar test in this study were according to the study of Shaylinda et al. (2014). Two mixing stages were applied, i.e., rapid mixing at 200 revolutions per minute (rpm) for 4 minutes and slow mixing at 30 rpm for 15 minutes. The time and speed for rapid and slow mixings were set with an automatic controller. The settling process was set for 30 minutes. The volume of the leachate sample used in the

study was 500 mL (Zainol et al., 2011). In the jar test of the CF process, two factors were considered in determining the optimum treatment process, i.e., the coagulant dosage and leachate pH by dual and single coagulants of PAC and MEP.

In the CF treatment process, by using a single coagulant, a range of coagulant dosages of single MEP and PAC would be added into the respective altered pH of the leachate sample, right before the rapid mixing started. While for the treatment process using a dual coagulant, a range of coagulant dosage of MEP was added in the second stage of flocculation. The idea of dual coagulant was similar to the double dosage of different coagulants in one treatment. The dosage of PAC was added before the rapid mixing started, while the addition of MEP was done before the slow mixing of the jar test. The pH of the leachate sample was altered by using 1N hydrochloric acid (HCl) and 1N sodium hydroxide (NaOH) to obtain the desired pH 3.0-10.0 range. The experiments were carried out based on the conventional optimisation method of the one-factor-at-a-time (OFAT) method, which involved the try and error practices (Shaylinda et al., 2014).

Optimisation of Coagulant Dosage and Leachate pH

The selected range of dosages in leachate treatment by using a single PAC coagulant was from 2,250 mg/L to 4,500 mg/L (Mohd-Salleh et al., 2018). This dosage range was decided based on the preliminary study of dosage optimisation by using macro and micro ranges of coagulant dosages. While for PAC application in dual coagulant, the optimum dosage obtained from the CF was used as a constant factor while varying the dosage of MEP. For the dosage of 1% MEP as a coagulant aid, the dosages used were 50 mg/L-500 mg/L (Mohd-Salleh et al., 2020a). Again, this range was chosen from a preliminary study to decide the appropriate MEP range dosage to aid in the CF process using dual coagulant.

The optimisation of dosage was carried out first by altering the pH of the leachate sample into pH 7.0. It was selected due to its neutral properties that are desired in most treatments. After the best dosage was obtained, the pH optimisation was taken place by adjusting the pH from 3.0 to 10.0. In the first dosage optimisation of PAC and MEP in this study, the amount of single optimum PAC at 3,750 mg/L was used as a constant dosage following the study of Mohd-Salleh et al. (2018). Consequently, the different MEP dosages started from 50 mg/L to 500 mg/L was used as the coagulant aid. To achieve this, the pH of the leachate sample and the PAC dosage were remained constant at pH 7.0 and 3,750 mg/L dosage, respectively. The optimum conditions of these factors and the treatments' efficiency would be determined by the highest removal percentages on COD, AN, turbidity, colour, and SS. After accomplishing the jar tests, supernatant samples were withdrawn from the beaker by using a plastic syringe from the point located about 3 cm from the surface for the analysis and kept into another bottle. The analysis was done within the next 5 minutes after the settling process to prevent any changes in the characteristics of

the treated leachate samples with respective standard methods to analyse the removal parameters, i.e., Colorimetric (APHA Method:5220 C, HACH Method:8000) for COD, Conductimetric (APHA Method: 4500-N, HACH Method: 8038) for AN, Nephelometric (APHA Method:2130) for turbidity, Spectrophotometric (APHA Method: 2120 B, HACH Method: 8025) for colour, and Gravimetric (APHA Method:2540 D, HACH Method:630) for SS. The measurement of all parameters was also done in the triplicate analysis by following the standard method of water and wastewater (APHA, 2017) to come out with the mean readings. The formula to calculate the removal percentage was based on Equation 1.

$$\text{Percentage removal (\%)} = \frac{\text{Initial concentration} - \text{Final concentration}}{\text{Initial concentration}} \times 100 \quad [1]$$

Meanwhile, Equation 2 below is the calculation for the Al content in the PAC dosage.

$$\begin{aligned} 10\% &= (10 \text{ g}/100 \text{ mL}) \times (1,000 \text{ mg}/1 \text{ g}) \times (1,000 \text{ mL}/1 \text{ L}) & [2] \\ &= 100,000 \text{ mg/L} \\ &= (100,000 \text{ mg/L}) (X) = (3,750 \text{ mg/L}) \times (500 \text{ mL}) \\ &X, V1 = 18.75 \text{ mL} \end{aligned}$$

Dosage of Al in 3,750 mg/L of PAC

$$\begin{aligned} &= (1.54 \text{ g}/100 \text{ mL}) \times (1,000 \text{ mg}/1 \text{ g}) \times (1,000 \text{ mL}/1 \text{ L}) \\ &= 15,400 \text{ mg/L} \\ &= (15,400 \text{ mg/L}) (18.75 \text{ mL}) = (X) \times (500 \text{ mL}) \\ &X = 577.5 \text{ mg/L of Al} \end{aligned}$$

RESULTS AND DISCUSSION

Coagulation-flocculation Treatment Process of Leachate Using Dual Coagulant of PAC and MEP

Effect of PAC and MEP Dosages. The ability of MEP as a coagulant aid in the treatment of stabilised leachate is carried out first by pairing it with PAC in the first optimisation process. Figure 3 shows the outcome of dosages optimisation of PAC and MEP in term of removal percentages of respective parameters. Using this combination of a primary coagulant of PAC and a coagulant aid, pleasing results were given even though at the minimal dosage of MEP. The major removal was done by the PAC coagulant itself since the high dosage was added. Based on the observations of Figure 3, the removal outcomes were high, especially for turbidity, colour, and SS parameters. Increasing the MEP dosage

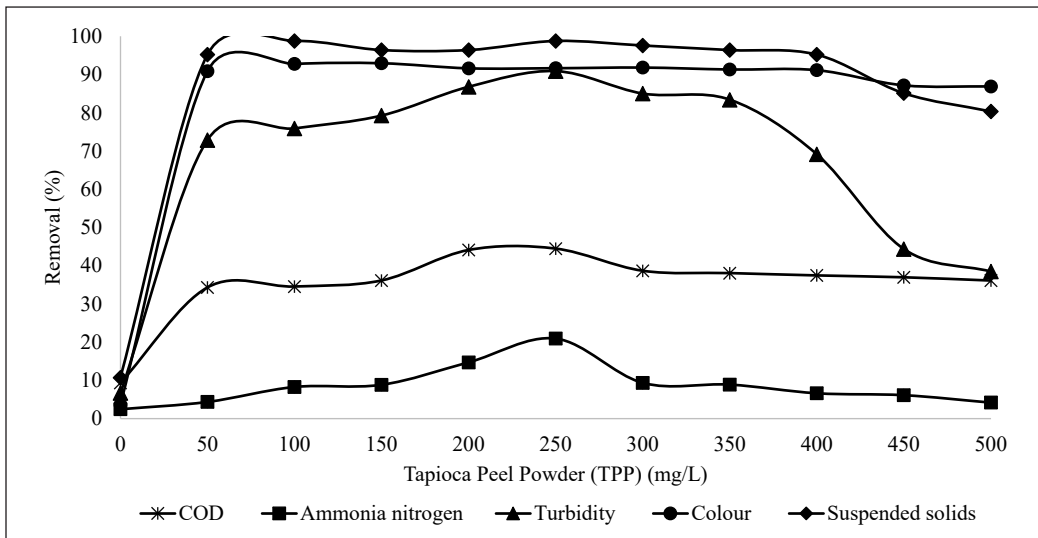


Figure 3. Dual coagulant at pH 7.0 with PAC (3,750 mg/L) and MEP (50-500 mg/L)

did not significantly affect the turbidity, colour, and SS removal, but rather it resulted in a linearly constant removal pattern.

The removal for colour and SS at all MEP dosages was quite satisfying by achieving more than 80% removal. However, there was a bit of fluctuating removal for the turbidity parameter, especially at the final dosages range. This might be due to the high dosage of MEP that caused the addition of turbidity in the leachate sample. The highest elimination obtained by COD, AN, and turbidity was obvious to happen at 250 mg/L of MEP by removing 44.5%, 20.9%, and 90.9% removal, respectively. Thus, according to this, 250 mg/L was decided as the optimum MEP dosage, with the removal of 44.5% COD, 20.9% AN, and 90.9% turbidity, 91.7% colour, and 98.8% SS. For the next optimisation, by using the reduced optimum amount of MEP dosage at 250 mg/L, the PAC dosage was varied again to verify the optimum dosage that happened at 3,750 mg/L. Figure 4 shows the removal results using PAC dosage varied from 500 mg/L to 5,000 mg/L, respectively.

Based on the evaluations of Figure 4, the removal of COD, turbidity, colour, and SS continued to increase as the dosage increased. However, the removals started to remain constant at the PAC dosage of 2,000 mg/L and decreased gradually at the dosage of 4,000 mg/L. While for AN, the removal was lower compared to another four parameters. It was noticeable that the elimination of AN was the highest at the dosage of 3,000 mg/L and 3,500 mg/L with 33.4% and 33.8%, respectively, just by having a 0.4% difference. For other parameters, the high removal could be observed at the dosage of 3,000 mg/L and 3,500 mg/L as well, with a very close gap. At the dosage of 3,000 mg/L, the removal for all parameters was 55.9% of COD, 33.4% of AN, 93.1% of turbidity, 96.3% of colour, and 99% of SS. While for 3,500 mg/L, the achieved removals were 57.4%, 33.8%, 95.8%,

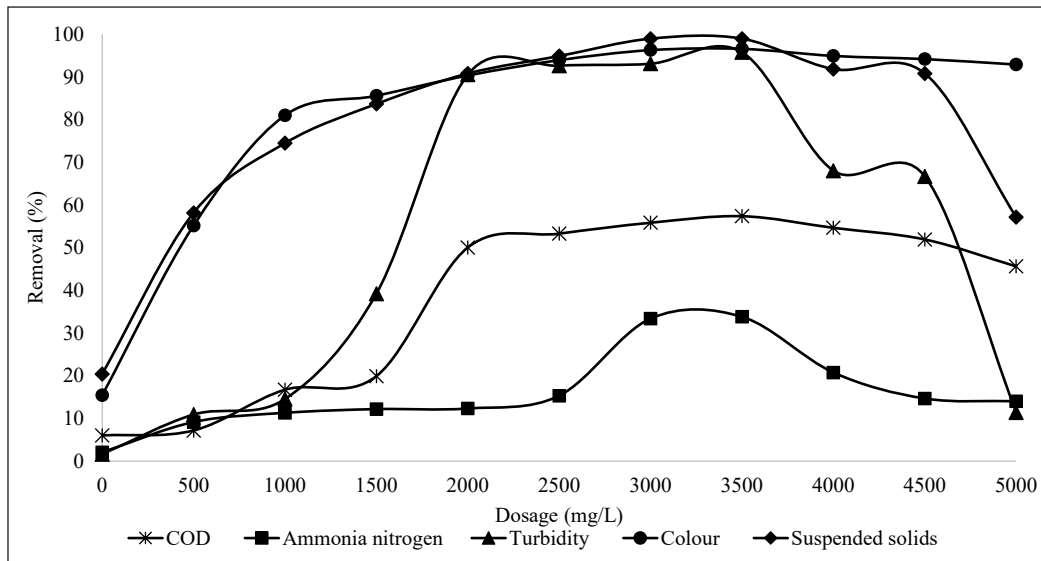


Figure 4. Dual coagulant at pH 7.0 with MEP (250 mg/L) and PAC (500-5,000 mg/L)

96.6%, and 99% for COD, AN, turbidity, colour, and SS, respectively. Thus, based on the removals, the PAC dosage of 3,500 mg/L was determined as the optimum PAC for dual coagulant, with the aid of optimum MEP dosage at 250 mg/L. Hence, the optimum dosages of both PAC and MEP were obtained at 3,500 mg/L and 250 mg/L, respectively, by applying the dosages at pH 7.0 of leachate samples.

Effect of Leachate pH Using PAC and MEP Coagulants. The next optimisation was carried out to discover the optimum pH condition that worked best for the combination of PAC as primary coagulant and MEP as the coagulant aid in this study. The samples' pH was varied from pH 3.0 to pH 10.0 by using 3,500 mg/L PAC dosage and 250 mg/L MEP dosage, as shown in Figure 5. Based on the CF process of dual coagulant in Figure 5, the removals of colour and SS were started quite high at pH 3.0, but it decreased as the pH increased to pH 6.0. However, at pH 7.0, it rose again and became the highest reduction with 92.1% and 99% removals, respectively. The turbidity parameter was also observed to be effectively removed at pH 7.0 with a 96.9% reduction. The removal for turbidity started low at pH 3.0 with 18.8% elimination. Even though the removal for colour and SS at pH 3.0 was quite satisfying, the turbidity of the treated sample was not well eliminated. The high elimination was observed to be at pH 7.0 and pH 8.0 with 58.3% and 57.8%, respectively, with less than 5% difference for the removal of COD. Meanwhile, for AN, the elimination was high at both pH 6.0 and pH 7.0 with 35.5% and 34% removal, respectively, with less than 5% difference. However, most of the highest elimination of parameters happened at the neutral pH 7.0 of leachate samples. Therefore, it was decided that the dual coagulant

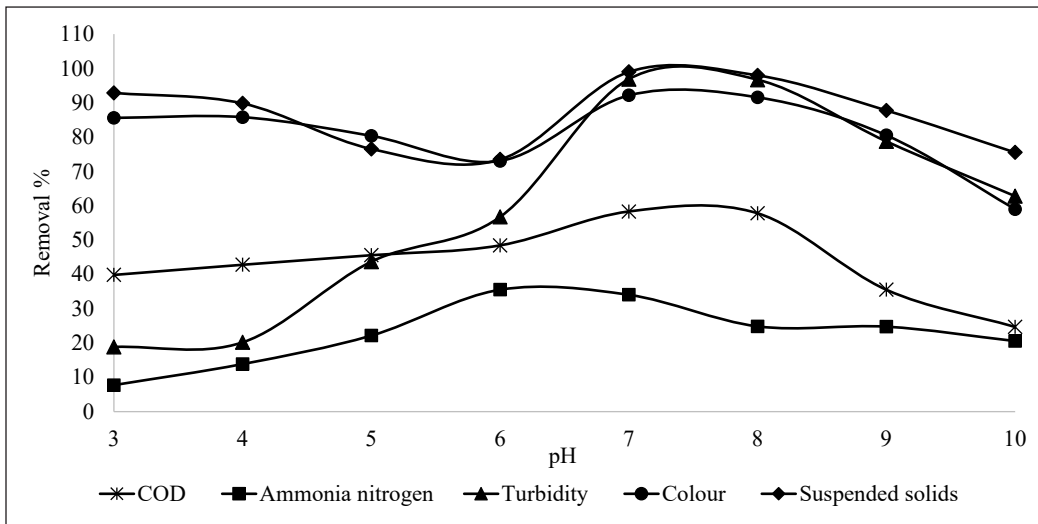


Figure 5. Dual coagulant of PAC (3,500 mg/L) and MEP (250 mg/L) at varied pH 3.0-10.0

worked effectively at pH 7.0 by eradicating 58.3% of COD, 34% of AN, 96.9% of turbidity, 92.1% of colour, and 99% of SS as the final results.

Performance Comparison of Dual Coagulant (PAC and MEP) With Previous Studies.

The performance of dual coagulant in the present study was compared with the capability of other studies that utilised primary coagulant with a coagulant aid in treating the leachate sample. In dual coagulant practice, the inorganic coagulant such as PAC promotes the colloid destabilisation with the key mechanism of charge neutralisation. The addition of a polymer would act as the bridging agent in encouraging the small colloids to agglomerate together and become bigger and heavy flocs (Mohd-Salleh et al., 2020c; Awang & Aziz, 2012). The matching pair of PAC and other natural coagulants as dual coagulants were investigated based on their performance to remove the respective contaminants in the comparison studies. The appropriate teaming would generate good achievements in the CF process, which was the highlight point in the significance studies of dual coagulant. It was such a good undertaking that many kinds of research had been made on the locally grown plants to diverge their function, such as being a sustainable coagulant for water and wastewater treatment.

Al-Hamadani et al. (2011) had studied the capability of PAC and psyllium husk as the dual coagulating agent of leachate treatment. They obtained the neutral pH of 7.2 as the ideal leachate pH with 400 mg/L of psyllium husk and 7,200 mg/L of PAC dosages with satisfying removals, i.e., 64% of COD, 90% of colour, and 96% of SS. The tobacco leaf (1000 mg/L dosage) was also used as the coagulant aid by obtaining the apparent COD removal at 91% indeed with 1,500 mg/L dosage of PAC at pH 6.0 (Rusdizal et al., 2015).

The result for the AN parameter (54% removal) was also good enough to initiate the leaf as a competitive natural coagulant.

However, a bit lower removal was observed for physical parameters of turbidity and SS at 21% and 48%, respectively (Rusdizal et al., 2015). Tobacco leaf could be classified as an anionic coagulant with -3.57 mV zeta potential, which had a higher negative charge than tapioca starch at -0.56 mV (Azizan et al., 2020; Rusdizal et al., 2015). The attraction of the opposite charges in the treated sample using tobacco leaves is possibly stronger than others; thus, it succeeded in removing the high percentages of organic contaminants (Rusdizal et al., 2015). The same starch source was also reported in the study of Asharuddin et al. (2018) to remove turbidity from dam water. The term used for the natural coagulant was cassava peel starch (CPS). It was used as an aid with alum and achieved a high turbidity removal with 91.47%, at the optimum conditions of pH 9.0, 7.5 mg/L of alum dosage, and 100 mg/L of CPS dosage. The addition of CPS in the treatment system also reduced about 50% of the alum dosage (Asharuddin et al., 2018). Hence, based on the comparison performance, it is proven that natural coagulant extracted from agro-waste like MEP has a positive effect on improving coagulation treatment.

Comparison of Treated Leachate Sample with EQA 2009. The final concentrations value of evaluated parameters in treated leachate using PAC and PAC+MEP coagulants and the Environmental Quality (Control of pollution from solid waste transfer station & landfill) Regulation 2009 under the laws of Malaysia Environmental Quality Act 1974 are shown in Table 1. The CF treatment on 500 mL leachate sample using a single coagulant of PAC managed to remove about 54.1% of COD, 28.0% of AN, 91.1% of turbidity, 98.0% of colour, and 98.0% of SS, by employing pH 6.0 of leachate and 3,750 mg/L of PAC dosage. Meanwhile, for the application of dual coagulant, the combination of 3,500 mg/L (PAC), 250 mg/L (MEP) and pH 7.0 of leachate achieved better removal except for colour parameter, with 57.4% of COD, 33.8% of AN, 95.8% of turbidity, 96.6% of colour, and 99.0% of SS. The comparison of removal percentages using PAC and PAC+MEP is tabulated in Table 2.

Table 1
Comparison of the final concentration of treated leachate with EQA 2009

Parameter	Treated leachate with PAC	Treated leachate with PAC + MEP	Malaysia's EQA 2009
COD (mg/L)	1,157.6	465.0	400.0
AN (mg/L)	816.3	417.5	5.0
Turbidity (NTU)	12.2	2.3	n.a.
Colour (ADMI)	144.2	191.18	100.0
SS (mg/L)	5.9	1.0	50.0

Table 2
Comparison of the removal percentages between PAC and PAC+MEP

Parameter	Removal (%) using PAC	Removal (%) using PAC + MEP
COD (mg/L)	54.1	57.4
AN (mg/L)	28.0	33.8
Turbidity (NTU)	91.1	95.8
Colour (ADMI)	98.0	96.6
SS (mg/L)	98.0	99.0
Optimised conditions	pH 6.0 of leachate 3,750 mg/L (PAC)	pH 7.0 of leachate 3,500 mg/L (PAC) + 250 mg/L (MEP)

From this finding, it was observed that the superiority of the treatment possibly happened due to the high molecular weight of MEP that helped to stimulate the flocculation development. Simultaneously, the adsorption bridging mechanism influences the aggregation process due to the interaction of high-molecular-weight coagulant and natural polysaccharide composition with impurities in the leachate sample (Mohd-Salleh et al., 2020c; Li et al., 2015; Oladoja, 2016). Besides, the removal mechanism of charge neutralisation for the treatment using PAC was also expected to be superior to PAC+MEP, considering the higher dosage. This was because PAC would encounter hydrolysis activity that resulted in amorphous aluminium hydroxide $Al(OH)_3$ (Aljuboori et al., 2015). Based on the comparison with local's regulations, only the SS parameter from both treatments complied with the discharge standard. Even though the other parameters did not meet the limit set by the local regulations, the outcome was reasonable by considering the sample used was the raw leachate, without any prior treatments at the landfill site.

CONCLUSIONS

In conclusion, based on the observations on the effectiveness of single coagulant PAC and dual coagulant (PAC + MEP), it could be denoted that the combination of PAC and MEP as the primary coagulant and the coagulant aid could enhance the removal of respective parameters, which was better than the performance of single coagulant of PAC alone. The treatability studies on stabilised leachate using 10% PAC with the optimum conditions happened at pH 6.0 and dosage 3,750 mg/L. Meanwhile, the highlight findings were in the utilisation of both PAC and MEP, in the optimised conditions of pH 7.0, 3,500 mg/L dosage of PAC, and 250 mg/L dosage of MEP, respectively, with a 6.7% reduction of Al content dosage from 577.5 mg/L of single PAC coagulant to 539 mg/L in dual coagulant. Thus, the new MEP coagulant was verified to offer the full role-play as a coagulant aid by producing a good synergistic effect together with the coagulating benefits from PAC. This was especially in obtaining the neutral pH and lower chemical dosage content as the ideal conditions for the treatment system. Overall, this study concluded a distinctive conclusion

that natural coagulants isolated from agro-waste could also enhance the treatment of highly polluted wastewater like leachate, which most other scholars did not prefer for a treatment. It is desirable to have further research on green natural coagulants to improve leachate and wastewater treatments in the future.

ACKNOWLEDGEMENTS

This research was supported by Universiti Tun Hussien Onn Malaysia (UTHM) through TIER 1 Grant Vot H860.

REFERENCES

- Al-Hamadani, Y. A. J., Yusoff, M. S., Umar, M., Bashir, M. J. K., & Adlan, M. N. (2011). Application of psyllium husk as coagulant and coagulant aid in semi-aerobic landfill leachate treatment. *Journal of Hazardous Materials*, 190(1-3), 582-587. <http://doi.org/10.1016/j.jhazmat.2011.03.087>
- Aljuboori, A. H. R., Idris, A., Al-joubory, H. H. R., Uemura, Y., & Abubakar, B. I. (2015). Flocculation behavior and mechanism of bioflocculant produced by *Aspergillus flavus*. *Journal Environment Management*, 150, 466-471.
- APHA. (2017). *Standard methods for the examination of water and wastewater* (23rd Ed.). American Public Health Association.
- Asharuddin, S. M., Othman, N., Shaylinda, M. Z. N., & Tajarudin, H. A. (2017). A chemical and morphological study of cassava peel: A potential waste as coagulant aid. In *MATEC Web of Conferences*, 103(4), Article 06012. <http://doi.org/10.1051/mateconf/201710306012>
- Asharuddin, S. M., Othman, N., Shaylinda, N., Zin, M., Tajarudin, H. A., Din, M. F., & Kumar, V. (2018). Performance assessment of cassava peel starch and alum as dual coagulant for turbidity removal in dam water. *International Journal of Integrated Engineering*, 10(4), <http://doi.org/10.30880/ijie.2018.10.04.029>
- Awang, N. A., & Aziz, H. A. (2012). Hibiscus rosa-sinensis leaf extract as coagulant aid in leachate treatment. *Journal of Applied Water Science*, 2(4), 293-298. <http://doi.org/10.1007/s13201-012-0049-y>
- Aziz, S. Q., Aziz, H. A., Bashir, M. J. K., & Mojiri, A. (2015). Assessment of various tropical municipal landfill leachate characteristics and treatment opportunities. *Global NEST Journal*, 17(3), 439-450.
- Azizan, M. O., Shaylinda, M. Z. N., Mohd-Salleh, S. N. A., Mohd-Amdan, N. S., Yashni, G., Fitryaliah, M. S., & Afnizan, W. M. W. (2020). Treatment of leachate by coagulation-flocculation process using polyaluminum chloride (PAC) and tapioca starch (TS). In *IOP Conference Series: Materials Science and Engineering*, 736, Article 022029. <http://doi:10.1088/1757-899X/736/2/022029>
- Kamaruddin, M. A., Yusoff, M. S., Aziz, H. A., & Hung, Y. T. (2015). Sustainable treatment of landfill leachate. *Journal of Applied Water Science*, 5(2), 113-126. <http://doi.org/10.1007/s13201-014-0177-7>
- Li, S., Lv, Y., & Liu, Z. (2015). Preparation of composite coagulant of PFM-PDMDAAC and its coagulation performance in treatment of landfill leachate. *Journal of Water Reuse and Desalination*, 5(2), 177-188. <http://doi.org/10.2166/wrd.2015.093>

- Mehmood, M. K., Adetutu, E., Nedwell, D. B., & Ball, A. S. (2009). *In situ* microbial treatment of landfill leachate using aerated lagoons. *Journal of Bio resource Technology*, 100(10), 2741-2744. <http://doi.org/10.1016/j.biortech.2008.11.031>
- Mohd-Salleh, S. N. A., Mohd-Zin, N. S., Othman, N., Mohd-Amdan, N. S., & Mohd-Shahli, F. (2018). Dosage and pH optimization on stabilized landfill leachate via coagulation-flocculation process. In *MATEC Web of Conferences* (Vol. 250, p. 06007). EDP Sciences. <https://doi.org/10.1051/mateconf/201825006007>
- Mohd-Salleh, S. N. A., Shaylinda, M. Z. N., Othman, N., Yasni, G., & Norshila, A. B. (2020a). Optimisation of tapioca peel powder as natural coagulant in removing chemical oxygen demand, ammonia nitrogen, turbidity, colour, and suspended solids from leachate sample. In *Water and Environmental Engineering* (pp. 69-86). UTHM Publishing.
- Mohd-Salleh, S. N. A., Shaylinda, M. Z. N., Othman, N., Azizan, M. O., Yashni, G., & Afnizan, W. M. W. (2020b). Sustainability analysis on landfilling and evaluation of characteristics in landfill leachate: A case study. In *IOP Conference Series: Materials Science and Engineering*, 736, Article 072002. <https://doi.org/10.1088/1757-899X/736/7/072002>
- Mohd-Salleh, S. N. A., Shaylinda, M. Z. N., Othman, N., Yasni, G., & Norshila, A. B. (2020c). Coagulation performance and mechanism of a new coagulant (Polyaluminium chloride-tapioca peel powder) for landfill leachate treatment. *Journal of Engineering Science and Technology*, 15(6), 3709-3722.
- Ni, F., He, J., Wang, Y., & Luan, Z. (2015). Preparation and characterisation of a cost-effective red mud/polyaluminum chloride composite coagulant for enhanced phosphate removal from aqueous solutions. *Journal of Water Process Engineering*, 6, 158-165.
- Oladoja, N. A. (2016). Advances in the quest for substitute for synthetic organic polyelectrolytes as coagulant aid in water and wastewater treatment operations. *Journal of Sustainable Chemistry and Pharmacy*, 3, 47-58. <http://doi.org/10.1016/j.scp.2016.04.001>
- Rusdizal, N., Aziz, H. A., & Mohd-Omar, F. (2015). Potential use of polyaluminium chloride and tobacco leaf as coagulant and coagulant aid in post-treatment of landfill leachate. *Avicenna Journal Environmental Health Engineering*, 2(2), 1-5. <http://doi.org/10.1007/978-3-7091-0693-8>
- Shaylinda, M. Z. N., Aziz, H. A., Adlan, M. N., Ariffin, A., Yusoff, M. S., & Dahlan, I. (2014). Treatability study of partially stabilized leachate by composite coagulant (Pre-hydrolyzed iron and tapioca flour). *International Journal of Scientific Research in Knowledge*, 2(7), 313-319. <http://doi.org/10.12983/ijsrk-2014-p0313-0319>
- Syafalni, Lim, H. K., Ismail, N., Abustan, I., Murshed, M. F., & Ahmad, A. (2012). Treatment of landfill leachate by using lateritic soil as a natural coagulant. *Journal of Environmental Management*, 112, 353-359. <http://doi.org/10.1016/j.jenvman.2012.08.001>
- Wang, B., Shui, Y., He, M., & Liu, P. (2017). Comparison of flocs characteristics using before and after composite coagulants under different coagulation mechanisms. *Journal of Biochemical Engineering*, 121, 107-117. <http://doi.org/10.1016/j.bej.2017.01.020>
- Yusoff, M. S., & Zuki, N. A. M. (2015). Optimum of treatment condition for *Artocarpus heterophyllus* seeds starch as natural coagulant aid in landfill leachate treatment by RSM. *Journal of Applied Mechanics and Materials*, 802, 484-489. <http://doi.org/10.4028/www.scientific.net/AMM.802.484>

- Zailani, L. W. M., Mohd-Amdan, N. S., & Shaylinda, M. Z. N. (2018). Characterisation of leachate at Simpang Renggam landfill site, Johor, Malaysia. In *IOP Conference Series: Earth and Environmental Science*, 140(1), Article 012053. <http://doi.org/10.1088/17551315/140/1/012053>
- Zainol, N. A., Aziz, H. A., Yusoff, M. S., & Umar, M. (2011). The use of poly aluminum chloride for the treatment of landfill leachate via coagulation and flocculation processes. *Research Journal of Chemical Sciences*, 1(3), 34-39.

Sequestration of Pb(II) from Aqueous Environment by Palm Kernel Shell Activated Carbon: Isotherm and Kinetic Analyses

Ekemini Monday Isokise¹, Abdul Halim Abdullah^{1,2*} and Tan Yen Ping²

¹Material Synthesis and Characterization Laboratory, Institute of Advanced Technology, Universiti Putra Malaysia, 43400 UPM, Serdang, Selangor Darul Ehsan, Malaysia

²Department of Chemistry, Faculty of Science, Universiti Putra Malaysia, 43400 UPM, Serdang, Selangor Darul Ehsan, Malaysia

ABSTRACT

In this work, activated carbons were produced by the thermochemical treatment of palm kernel shells with different activation time. The developed products (activated carbon samples) were described by their surface area, porosity, and applied for lead(II) ions separation from liquid phase. By prolonging the activation time beyond 2h, some of the micropores collapsed to form mesopores without causing a significant transformation in the surface area. The influences of solution pH, mass of biosorbents, concentration of Pb(II) ions, and temperature on the entrapment of lead(II) ions explored. Based on experimental outcome,

the best-suited condition for the Pb(II) uptake was 0.13 g AC-4, 250 mg L⁻¹ concentration, and pH 4. The Pb(II) entrapment process is thermodynamically exothermic and spontaneous. The adsorption data fit the Langmuir monolayer adsorption model, with 222 mg g⁻¹ as maximum sorption capacity, and the Ho-second-order kinetics model suitably described the process rate.

ARTICLE INFO

Article history:

Received: 4 January 2021

Accepted: 19 April 2021

Published: 19 July 2021

DOI: <https://doi.org/10.47836/pjst.29.3.17>

E-mail addresses:

kemsguy@gmail.com (Ekemini Monday Isokise)

halim@upm.edu.my (Abdul Halim Abdullah)

typ@upm.edu.my (Tan Yen Ping)

*Corresponding author

Keywords: Activated carbon, adsorption, heavy metals, isotherm, palm kernel shell

INTRODUCTION

Presence of heavy metal ions, especially lead in water bodies constitute environmental pollution because they are not biodegradable and highly poisonous to human and aquatic organisms. The discharge of industrial effluent without apposite treatment, jeopardize the environment and consequently public health (Krika et al., 2016). Lead extrudes into the environment through mining and smelting, paint and rubber industries, and battery manufacturing, recycling, and disposal. Content of lead in industrial effluent varied from one industrial activity to another, while the regulated contamination level is 0 ppm, according to the United States Environmental Protection Agency (EPA, 2017). Several separation techniques, including electrocoagulation, chemical oxidation and precipitation, ion-exchange, and membrane filtration, are available for separating heavy metal ions from liquid phase.

The methods highlighted above are not without shortcomings. For instance, chemical precipitation and coagulation methods are straightforward to operate and inexpensive, but excessive sludge is generated, leading to disposal problem. The ion-exchange treatment progression is non-selective and highly depend on pH (Malik et al., 2016). Adsorption is the favourable and commonly adopted technique for the sequestration of heavy metals ions because of its eco-friendliness and simple procedure, produce limited secondary environmental pollution, and capable of removing low concentration heavy metal ions (Zuo, 2014; Tang et al., 2017). Among various solid adsorbents employed, activated carbon is a widely used due to its larger surface area and porosity. The use of agricultural and industrial wastes as starting ingredients in the manufacture of activated carbon has gained interest because of the high expenses associated with commercial activated carbon, coal, and lignite.

One of the major exporters of products from palm oil is Malaysia. The associated waste products generated from the industrial milling operation of the palm oil produce such as trunks, mesocarp fiber, empty fruit bunches, fronds, and its shells (Poudel et al., 2017; Sani et al., 2015). Approximately 60 % of the resulted fibers and shells are employed as fuel for electricity and steam generation, out of the industrial wastes (Shafie et al., 2012). This scenario highlights the necessity to convert the overwhelming waste biomaterials by searching for new economic applications. Because of the abundance of palm kernel shells (PKS), the translation of PKS to activated carbon is desirable and has received substantial attention (Table 1) as it proven to be a viable and sustainable ingredient for the activated carbon (AC) preparation (Xu et al., 2017). AC can be synthesized via the physical, chemical activation process or combination of both physical and chemical method of activation. During chemical activation operation, the use of activating agents, such as $ZnCl_2$, KOH , and H_3PO_4 , is vital in altering the textural features in PKS made ACs. H_3PO_4 is selected for this study due to lower environmental and toxicological challenge (Khadiran et al.,

2014). These chemical agents are desiccating naturally and affect the thermal denaturing and thwart tar formation or development during the manufacturing of the activated carbon (Saygılı & Güzel 2018).

Numerous studies, as shown in Table 1, focused on the influence of carbonization temperature and the activating agent on the physicochemical features of the activated carbon. However, studies on the effect of activation time are limited. This study aimed to examine the impact of activation time on the physical and chemical features of the produced AC, and its adsorptive performance towards Pb(II) from liquid environment. To delineate the PKS sourced activated carbon capability in the management of lead-bearing wastewater, adsorption isotherm and kinetic data were also modeled and analyzed.

Table 1

Preparation and application of palm kernel shell based activated carbon

Preparation method	Application	Reference
Physical steam activation (800°C)	Palm Oil Mill Effluent	Rugayah et al. (2014)
Chemical activation (ZnCl ₂ , 550°C)	CO ₂ capture	Hidayu and Muda (2016)
Chemical activation (KOH, 500-900°C)	-	Andas et al. (2017)
Chemical activation (ZnCl ₂ , 500-550°C, 1h)	Dye removal	Garcia et al. (2018)
Chemical activation (H ₃ PO ₄ , 550°C, 2h)	Water treatment (Grey water)	Razi et al. (2018)
One stage CO ₂ activation	CO ₂ capture	Rashidi and Yusuf (2019)

MATERIALS AND METHOD

Preparation and Characterization of ACs (Biosorbents)

The PKS was impregnated first by concentrated orthophosphoric acid at the feed ratio of PKS to acid (1:2) based on weight. Measured 100 g of PKS powder was introduced to phosphoric acid (85 % by weight) solution (120 mL) and thoroughly agitated manually. The impregnated samples were oven-dried for 24 hours at 110°C. Then, the impregnated PKS sample (10 g) was thermally activated at 600°C in a vertical tubular furnace under

N₂ gas flow of 20 mL min⁻¹ for predetermined duration (1 to 4 hours). The resulting AC cooled to room temperature, then rinsed severally with deionized H₂O, until the pH of the filtrate is constant, filtered, and oven-dried at 110°C for 24 hours. The powder activated carbon (AC) produced was denoted as AC-#, where # is the activation time of 1 to 4 hour.

The ACs pore diameter, volume and surface area was determined from N₂ adsorption-desorption isotherm (Quantachrome Autosorb-1) using the Brunauer–Emmet–Teller (BET) and Barrett-Joyner-Halenda (BJH) method, respectively. The iodine number and Methylene blue number was determined using standard procedures (Nunes & Guerreiro, 2011). The pH drift approach was employed to determine the zero-point charge (pH_{pzc}) of the ACs (Wang et al., 2009; Wang & Jian, 2013).

Batch Adsorption Experiments

The lead(II) ions stock solution was prepared by adding predetermined mass of Pb(NO₃)₂ salt (Fisher Scientific, Malaysia) in 1.0 L deionized water in a volumetric flask. Prior to each experimental adsorption study, solution of various Pb(II) ion concentrations were made via dilution of the standard solution with deionized water. The adsorptive uptake of Pb(II) onto the activated carbon as a function of time, amount of adsorbent (0.1-0.6 g), Pb(II) concentration (100-250 mg L⁻¹), initial solution pH (1-5) and temperature (25-50 °C) were investigated using batch experiment. The solution pH was varied to the predefined value by the dropwise addition of 1.0 M NaOH or HCl solution. In a typical adsorption experiment, a measured quantity of AC add into 250 mL flasks containing 200 mL of identified concentration of Pb(II) ions. The mixture was agitated at 110 rpm speed using a temperature-controlled water bath shaker (Memmert, Germany) for 120 min. At certain time intervals, an aliquot of the sample was collected and analyzed using an AAS spectrophotometer (Thermo Scientific-S series). All experiments were executed in triplicates at 25°C. The extent (%) of metal uptake and the adsorption capacity was determined respectively by Equations 1 and 2.

$$\text{Removal}(\%) = \frac{(C_0 - C_t)}{C_0} \times 100 \quad [1]$$

$$q_t = \frac{(C_0 - C_t)}{m} \times V \quad [2]$$

C₀ (mg L⁻¹) denote initial concentration of Pb(II) ions, q_t (mg g⁻¹) and C_t (mg L⁻¹) is the amount of Pb(II) adsorbed by the AC adsorbent and the Pb(II) concentration in solution at time t, respectively. V (L) and m (g) represent respectively the volume of metal solution, and weight of AC used.

RESULTS AND DISCUSSION

Surface Characterization of Prepared AC

The percentage yield of the produced ACs at different activation time is presented in Table 2. The decrease in the yield of AC-1 to AC-4 is due to the increased loss of volatile constituents in the PKS with longer activation time.

Table 2

N₂-BET surface area and porosity of PKS activated carbons prepared at different activation times

Sample	Yield (%)	Surface Area (m ² /g)	Average Pore D(Å)	Micropore Volume (cm ³ /g)
AC-1	47.4	1059	21.631	0.6442
AC-2	44.3	1083	25.290	0.6956
AC-3	42.6	1004	22.557	0.0625
AC-4	39.8	1040	21.092	0.5551

The adsorption and desorption isotherm of N₂ at -196°C of the prepared activated carbons is shown in Figure 1. Both AC-1 and AC-2 exhibited the typical type I isotherm as IUPAC classification, which suggests a predominantly microporous structure activated carbon. However, at prolonged activation time, the adsorption isotherm showed type IV isotherm and a small hysteresis loop, indicating the development of mesopores in the sample. Figure 2 displays the distribution of pore size of the prepared ACs, confirmed the change in the porosity of the ACs from microporous to micro-mesoporous with longer activation period. Table 2 also reveals that the surface area and the porosity of the ACs increase with increasing activation time up to 2h before it decreases at prolonged activation time. This result shows that the number of micropores increases initially, which corresponds to the increased surface area but then collapsed to form mesopores, bring about a shrinkage in the surface area of the AC.

The amounts of micropores and mesopores of the prepared ACs can be deduced from iodine value and methylene blue (MB) value, respectively. Figure 3 depicts the iodine and MB sorption onto the PKS based activated carbon samples. The iodine and MB adsorption capacity increased by 15% and 10% when the activation time is prolonged from 1 to 4 h. This result indicates a small change in porosity with lengthier activation time, this agreed with the previous report of Mopoung et al. (2015). A slight reduction in iodine value at 4 h activation time could be probably associated to the collapse of the micropores to form mesopores.

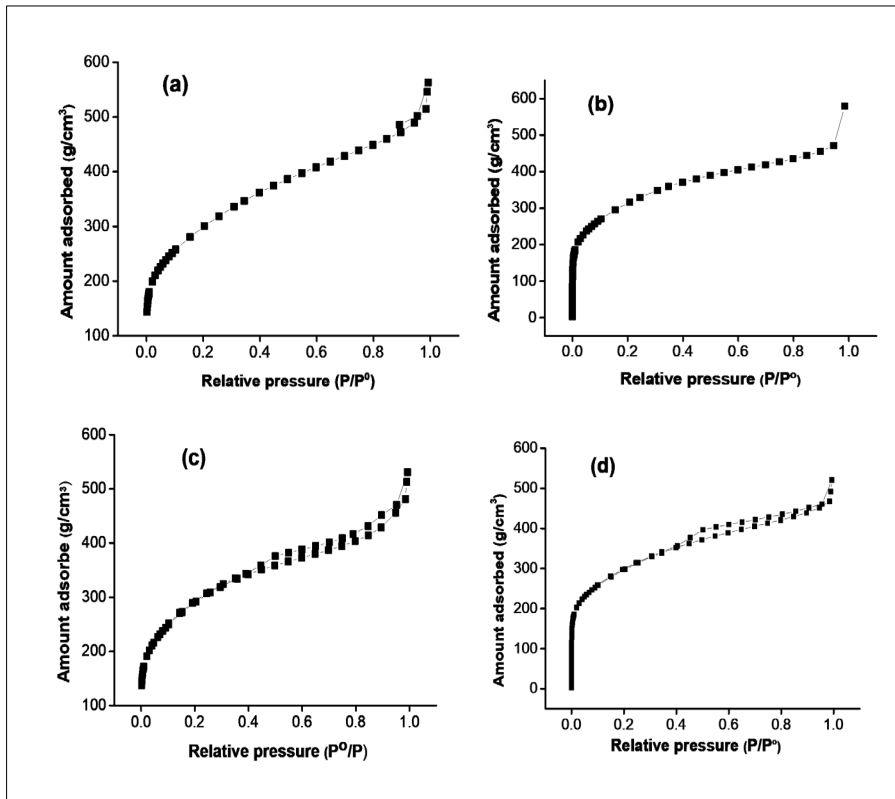


Figure 1. N₂ adsorption-desorption isotherm for (a) AC-1, (b) AC-2, (c) AC-3 and (d) AC-4

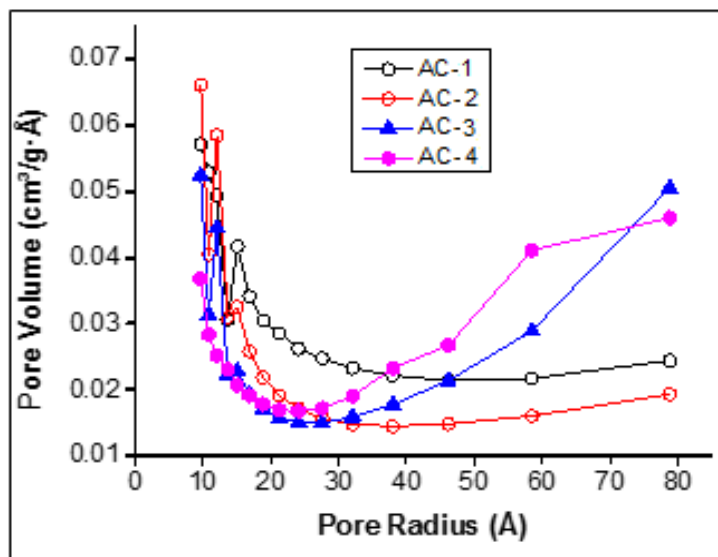


Figure 2. Pore size distribution of the prepared ACs

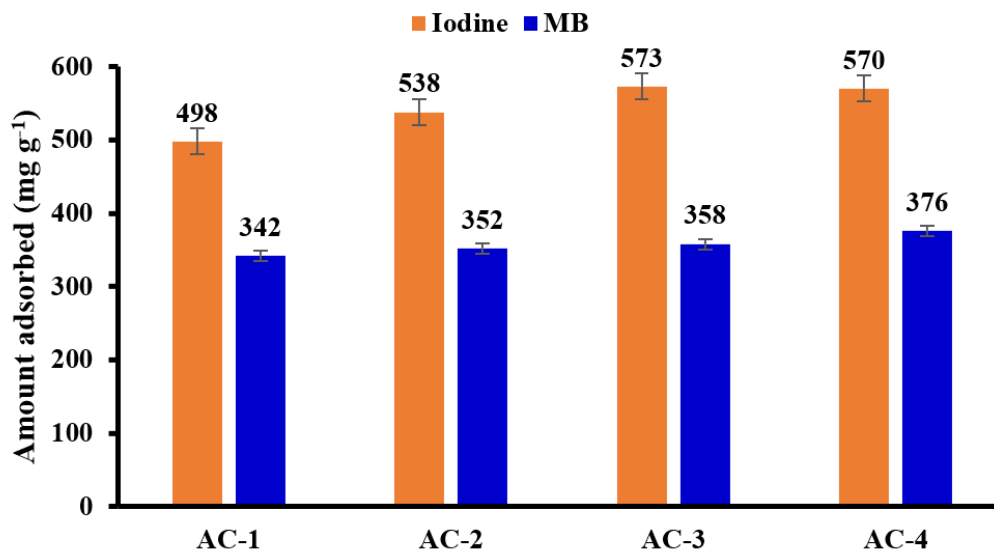


Figure 3. Iodine and MB uptake by various AC samples

Adsorption Performance of Activated Carbon

To select the best adsorbent, the produced ACs were screened by adsorbing Pb(II) ion in batch adsorption studies. Figure 4 depicts that there is insignificant variance in the Pb(II) ion uptake by AC-3 and AC-4. In this work, AC-4 was selected as an adsorbent for other experiments due to highest adsorption capacity.

Figure 5 shows the extent (in %) of Pb(II) removal and the AC-4 sorption capacity, as a function of adsorbent quantity. The percentage Pb(II) sequestration increased as the AC dose increases to 0.2 g but remained quite constant with further mass increment. This observation could be due to the agglomeration of adsorbent, inhibiting Pb(II) from attaching to the AC surface. However, the adsorption capacity (q_e) presented the opposite trend. The decline is attributable to the growing number of vacant sites as the ratio of lead (II) ions to the sorption sites reduces with increasing AC doses (Amarasinghe & Williams, 2007). Judging by both the extent of lead uptake and the amount adsorbed, the optimum AC weight for the separation experiment is selected as 0.13 g.

Figure 6 illustrates the time and initial lead (II) concentration as parameters that influence the uptake Pb(II) by AC. The removal extent decreases as the initial concentration of Pb(II) ion increases, while the quantity adsorbed increases. With a fixed amount of AC, the number of available vacant sites is constant. At low concentration of metal ion, the ratio of adsorption sites to lead ion is large, leading to a high percentage of removal (Figure 6A). However, this ratio becomes smaller at high metal concentration, ensuing into a lower

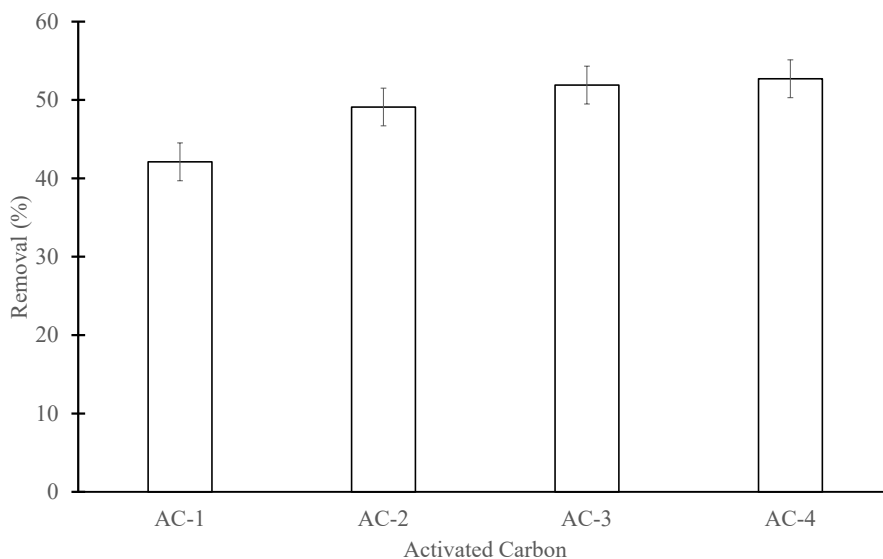


Figure 4. Removal of Pb by activated carbon prepared at different activation time
(Condition: 50 mg L⁻¹ of Pb(II); 0.1 g of AC, pH of solution = 4)

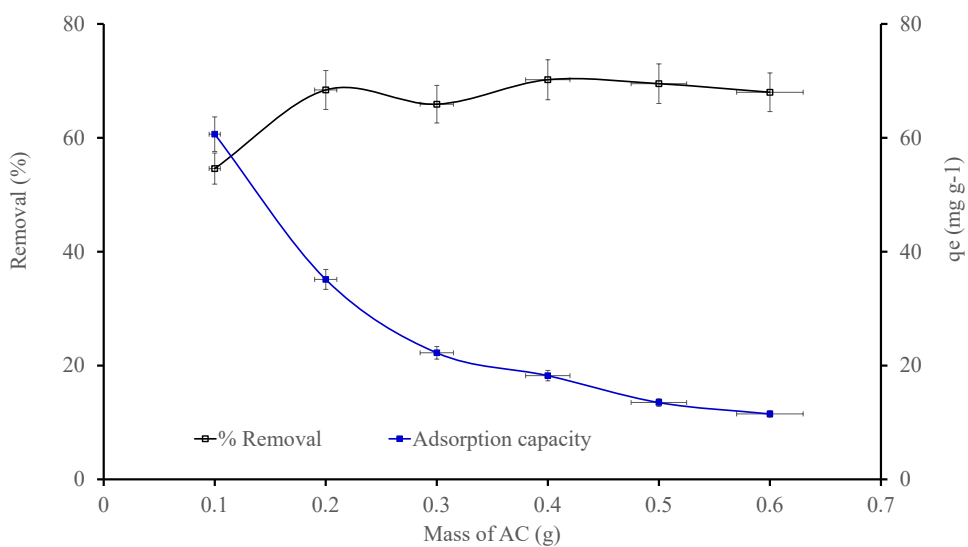


Figure 5. Extent of Pb(II) ion uptake and adsorption capacity of AC-4 at different adsorbent dosage. (Pb(II) = 50 mg L⁻¹; Solution pH = 4)

percentage lead removal. In the same vein, as the lead concentration increases, the driving power to subdue the resistance between metal ion in aqueous phase and solid sorbent phases becomes stronger, culminate to rise in adsorption capability. The adsorption ability increased rapidly up during the first 40 min contact time of the experiment as revealed in Figure 6B. This is associated to the handiness of a greater number of unoccupied sorption sites. It then gradually decreased because of repulsion forces between the attached metal ions and the ions present in the mixture, eventually equilibrium is attained as the solid surface become saturated.

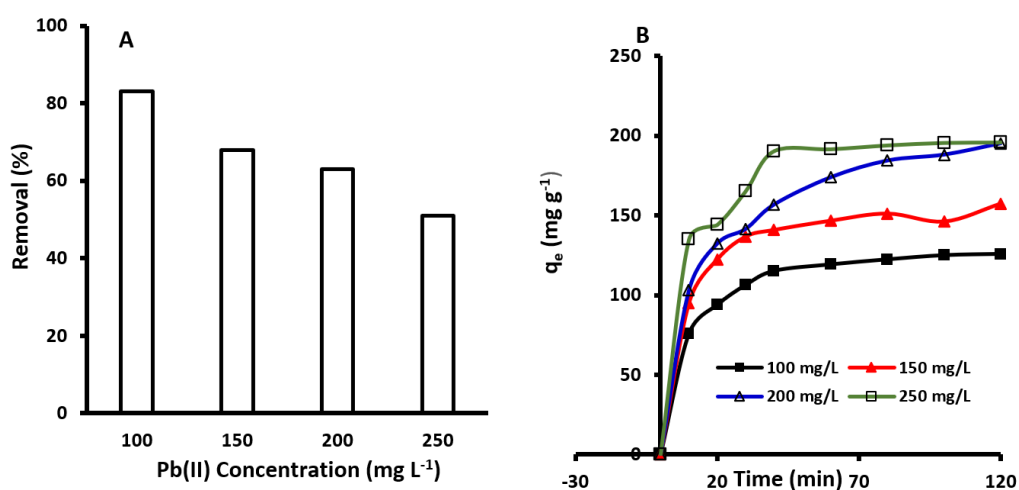


Figure 6. The adsorption of various concentration of Pb(II) ions on AC-4 (Condition: 0.13 g AC-4, pH of solution = 4)

The pH has an essential influence on the separation of metals because it defines the charge on adsorbent surface, the ionization extent, and speciation of adsorbate (Mouni et al., 2011). The pH of point zero charge, pH_{pzc} , of the AC-4, as estimated using the pH drift method, was 2.8, which implies that the biosorbent surface was charged positively at $pH < 2.8$ and negatively charged at pH higher than 2.8. Since lead ions are well-known for precipitation $[Pb(OH)_2]$ at pH greater than 7, the impact of solution pH on Pb(II) ions entrapment onto AC-4 was examined in 1-5 pH range (Figure 7).

The quantity of lead ion adsorbed was found low in highly acidic environments (pH 1-2) owing to existence of electrostatic revulsion between metal ions and positively charged AC-4 surface. Moreover, struggle for the vacant sites between the abundantly available H^+ ions and Pb(II) ion, also propelled reduction in Pb(II) uptake. The uptake of lead ion is more significant at a pH range of 3 to 5, with the highest sorption capacity of 93 mg g^{-1}

observed at pH 4. The enhancement of the quantity of adsorbed Pb(II) was induced by the electrostatic attraction between the metal ion and the AC-4 negatively charged surface. This phenomenon was also described by Zaini et al. (2009) in batch entrapment of lead unto cattle-manure-compost based AC. A decline in Pb(II) removal was witnessed at pH above 4, this is due to soluble hydroxide complexes formation.

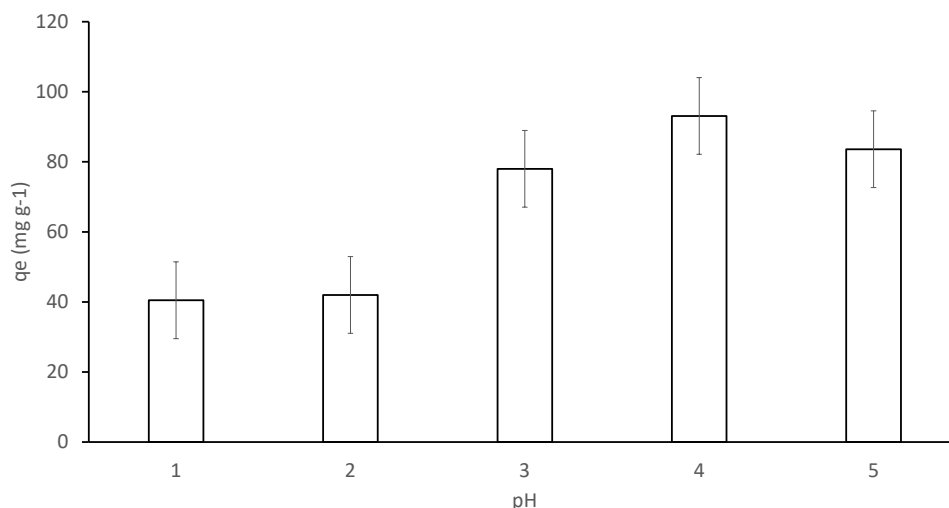


Figure 7. Sequestration of Pb(II) on AC-4 at different pH of the Pb(II) solution (Condition: 0.13 g AC-4; 80 mg L⁻¹ Pb(II))

Adsorption Isotherm, Kinetics, and Thermodynamics

To delineate the lead ions sequestration pattern, the adsorption behavior of lead on AC-4 was explored by fitting the experimental data to the Langmuir and Freundlich adsorption isotherm model. The linear form of the two models is respectively, represented by Equation 3 and 4.

$$\frac{C_e}{q_e} = \frac{1}{K_L q_m} + \frac{1}{q_m} C_e \quad [3]$$

$$\log q_e = \log K_F + \frac{1}{n} \log C_e \quad [4]$$

C_e and q_e represents the concentration (mg L⁻¹) of lead ions, and the quantity (mg g⁻¹) of Pb(II) ion entrapped at equilibrium. q_m is the Langmuir maximum adsorption capacity (mg g⁻¹). K_L represents the Langmuir parameter (L mg⁻¹) associated with the binding site affinity. n and K_F are Freundlich constants associated with the intensity and sorption capacity,

respectively. The results presented in Figure 8 and Table 3 show that the Langmuir model provides a well fit with a R²-value of 0.992, signifying a monolayer adsorption process. However, the possibility of multi-layer adsorption is not ruled out based on the R² value greater than 0.8 as indicated by Table 3.

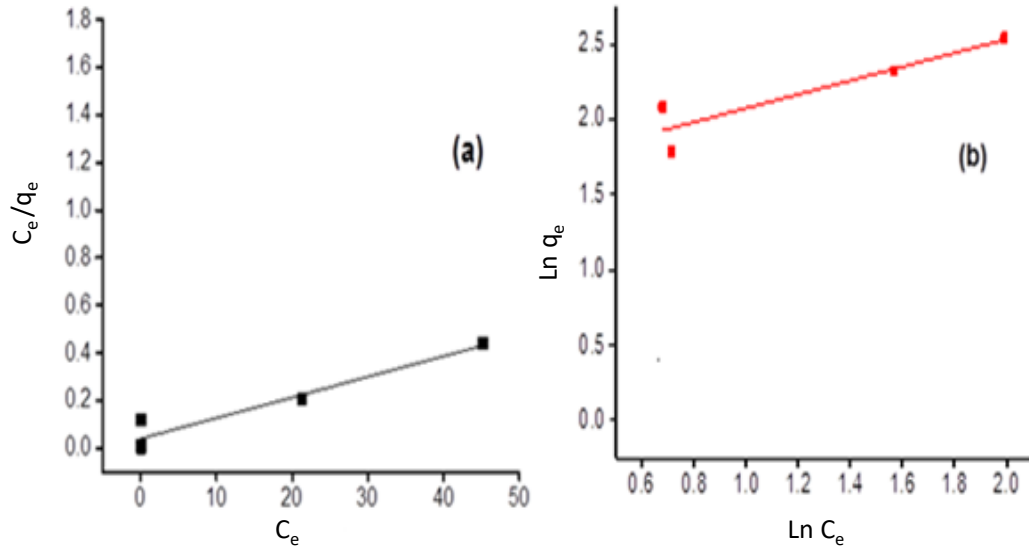


Figure 8. Adsorption isotherm of Pb(II) linearized according to (a) Langmuir (b) Freundlich

Table 3

Isotherm parameters for Pb(II) sequestration onto AC-4

AC-4	Langmuir isotherm			Freundlich isotherm		
	q_m (mg g ⁻¹)	K_L (L mg ⁻¹)	R ²	K_F	n	R ²
	222.22	0.067	0.992	59.43	3.85	0.843

The adsorption experimental data were also fitted to proven kinetics models; pseudo-first order (PFO), pseudo-second order (PSO), and intraparticle diffusion (IPD), to analyse the adsorption mechanism and estimate the reaction rate constant. The linearized form of the PFO and PSO kinetic models are presented, accordingly in Equations 5 and 6.

$$\ln(q_e - q_t) = \ln q_e - k_1 t \tag{5}$$

$$\frac{t}{q_t} = \frac{1}{k_2 q_e^2} + \frac{1}{q_e} t \tag{6}$$

where k_1 and k_2 represent the rate constant for the PFO and PSO, while q_e and q_t denote respectively the quantity of lead ions adsorbed at equilibrium and at any specified time t . The model constants, sorption capacities, and the correlation coefficient (R^2) for the Pb(II) ion uptake at different concentrations, on AC-4 are presented in Table 4. According to R^2 values and the excellent closeness of the calculated q_e to the experimental q_e , the adsorption data fitted the PSO kinetics well, indicating that the sorption process is ruled by the handiness of the vacant adsorption sites than the lead ion concentrations (Arshadi et al., 2014). The entrapment process strongly involved complexation of metal ions with the binding sites on AC-4. Hence, chemical adsorption is assumed the rate controlling step.

The impact of diffusion in the mechanism of lead ion uptake was analyzed employing the intra-particle diffusion (IPD) model, in which its linear form is defined by Equation 7.

$$q_t = k_{id}t^{1/2} + C \tag{7}$$

k_{id} is the intra-particle diffusion rate constant ($\text{mg g}^{-1} \cdot \text{min}^{-1/2}$), and C is attributed to the boundary layer depth. The IPD model plot, Figure 9 illustrated multilinearities throughout the whole-time range, an indication of a multi-step sorption process. The initial first step is due to the entrapment of lead onto the adsorbent’s surface through boundary layer diffusion (Abdelwahab et al., 2013), while the subsequent adsorption step is attributed to the pore diffusion of metal ions into the solid adsorbent where the rate controlling step is IPD (Gao et al., 2013).

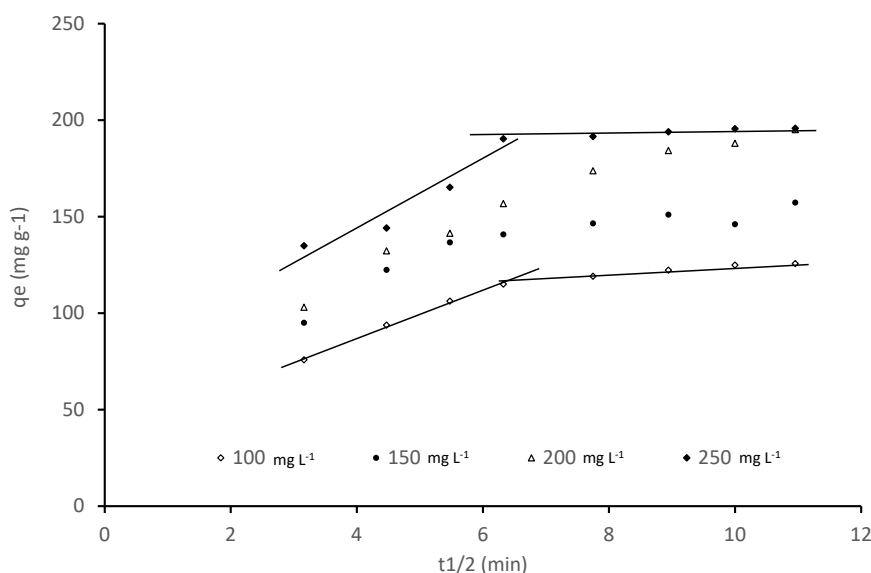


Figure 9. The IPD modeling of Pb uptake by AC-4 at varied concentrations (Initial pH = 4; ads. dosage = 0.13 g)

Table 4

Kinetics parameters for sequestration of lead (II) on AC-4

C₀ (mg L⁻¹)	100	150	200	250
q _e , expt. (mg g ⁻¹)	125.7	157.4	195.1	195.9
PFO				
q _e , calc. (mg g ⁻¹)	86.5	90.6	119.8	91.2
k ₁ (min ⁻¹)	0.0514	0.0450	0.0286	0.0344
R ²	0.9949	0.9672	0.9925	0.9164
PSO				
q _e , calc. (mg g ⁻¹)	135.1	161.3	212.8	208.3
k ₂ (g mg ⁻¹ min ⁻¹)	9.54 × 10 ⁻⁴	9.61 × 10 ⁻⁴	3.57 × 10 ⁻⁴	7.68 × 10 ⁻⁴
R ²	0.9998	0.9972	0.9985	0.9983
IPD				
k ₁	12.49	18.13	15.10	17.35
R ²	0.9966	0.9892	0.9804	0.9174
k ₂	2.37	3.11	6.34	1.30
R ²	0.9781	0.8114	0.9758	0.9612

Adsorption thermodynamics of Pb(II) on AC-4 was study by carrying out the adsorption experiment at different temperatures. The thermodynamic parameters, namely Gibb's free energy (ΔG°), enthalpy (ΔH°) and entropy (ΔS°) associated with the Pb(II) uptake, were calculated with the aid of Equations 8-10:

$$\Delta G^\circ = -RT \ln K_C \quad [8]$$

$$\ln K_C = \left(\frac{\Delta S}{R}\right) - \left(\frac{\Delta H}{R}\right)\frac{1}{T} \quad [9]$$

$$K_C = C_{\text{ads}}/C_{\text{sol}} \quad [10]$$

R represent the universal gas constant, K_C denote the equilibrium constant, and C_{ads} and C_{sol} is the concentration of Pb(II) adsorbed on the AC-4 and present in the solution at equilibrium, respectively. By using van't Hoff plot (Figure 10), the ΔH° and ΔS° can be estimated from the gradient and intercept of the linear graph. ΔG° , ΔH° , and ΔS° deduced are presented in the inset of Figure 9. With increasing temperature, the ΔG° value became more negative, indicating the increase in the degree of spontaneity, attributed to the increased

mobility and diffusion of the ions into the adsorbent's pore sites. As for enthalpy, the value is negative and fall between 2.1 and 20 kJ mol⁻¹, designating that uptake of lead(II) ion by AC-4 is a physical sorption process and exothermic (in nature). Furthermore, there is decline in the randomness at the AC sorbent-Pb(II) adsorbate solution interface during Pb(II) uptake as revealed by the negative entropy value. This is consistent with the report by Hannachi et al. (2019) on the separation of cadmium ions from aqueous environment with novel xerogel adsorbents.

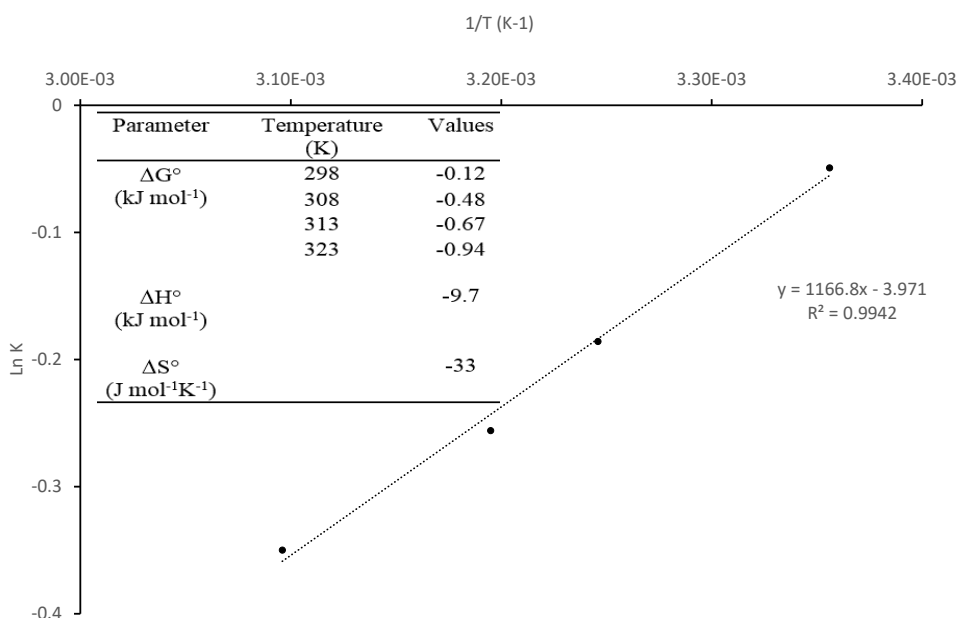


Figure 10. Vant Hoff plot for Pb(II) uptake and the thermodynamic parameters

The sorption capacity of AC-4 is compared with previous work reported in the literature (Table 5) in evaluating the potential use of the AC derived from the palm kernel shell to remove Pb(II) in water. The AC-4 shows higher capacities for lead removal compared to activated carbons derived from other agro-wastes. The significant variation in the adsorbent capacity could be due to the precursor properties, the methods in the synthesis of the AC, and the experimental adsorption conditions used.

Table 5

Adsorption capacities (q_m) of lead(II) ion with various agro-waste sourced ACs.

AC	Experimental Conditions	Q_m (mg g ⁻¹)	References
palm shell activated carbon	Dosage : 0.65 g L ⁻¹ ; pH:4; T:25°C	222.22	This study
Hazelnut husks activated carbon	Dosage : 12 g L ⁻¹ ; pH:6.7; T:28°C	13.05	Imamoglu and Oktay (2008)
grapeseed activated carbon	Dosage : 10 g L ⁻¹ ; pH:5; T:25°C	71.430	Baylan and Meriçboyu (2016)
Coffee waste residue activated carbon	Dosage : 1 g L ⁻¹ ; pH: 5; T:27°C	95.2	Yeung et al. (2014)
Bamboo activated carbon	Dosage:10 g/L; pH:7; T:27°C	124.2	Ademiluyi and Nze (2016)

CONCLUSION

Conversion of PKS to microporous AC biosorbents was successful via the chemical and thermal activation method. Although, extension of the activation period beyond 2 hours ensued in the collapse of micropores to mesopore, the surface area of the activated carbons was not significantly affected. The activated carbon produced after 4 hours of activation time (AC-4) exhibited the highest adsorption capacity towards lead metal uptake from aqueous solution. The suited optimum condition for the sequestration of Pb(II) was 0.13 g AC-4, 250 mg/L Pb(II) solution, and pH 4. The entrapment of Pb(II) on AC-4, was spontaneous and exothermic. The adsorption fitted the Langmuir adsorption model, with a maximum adsorption capacity of 222 mg/g, and the pseudo-second-order kinetics model signifying chemisorption between biosorbents and lead molecules. The produced activated carbon is efficient in removing heavy metal ions in the aqueous environment and could be used as promising adsorbent for the removal of lead ion during wastewater and water treatment.

ACKNOWLEDGEMENT

The authors appreciate the Institute of Advanced Technology and Chemistry Department, Faculty of Science, Universiti Putra Malaysia (UPM) for the research facilities.

REFERENCES

- Abdelwahab, O., Amin, N. K., & El-Ashtouky, E. S. Z. (2013). Removal of zinc ions from aqueous solution using a cation exchange resin. *Chemical Engineering Research and Design*, 91(1), 165-173. <https://doi.org/10.1016/j.cherd.2012.07.005>

- Ademiluyi, F. T., & Nze, J. C. (2016). Multiple adsorption of heavy metal ions in aqueous solution using activated carbon from nigerian bamboo. *International Journal of Research in Engineering and Technology*, 5(1), 164-169. <https://doi.org/10.15623/ijret.2016.0501033>
- Amarasinghe, B. M. W. P. K., & Williams, R. A. (2007). Tea waste as a low cost adsorbent for the removal of Cu and Pb from wastewater. *Chemical Engineering Journal*, 132(1-3), 299-309. <https://doi.org/10.1016/j.cej.2007.01.016>.
- Andas, J., Rahman, M. L. A., & Yahya, M. S. M. (2017). Preparation and characterization of activated carbon from palm kernel shell. In *IOP Conference Series: Materials Science and Engineering* (Vol. 226, No. 1, p. 012156). IOP Publishing. <https://doi.org/10.1088/1757-899X/226/1/012156>
- Arshadi, M., Amiri, M. J., & Mousavi, S. (2014). Kinetic, equilibrium and thermodynamics investigation of Ni(II), Cd(II), Cu(II) and Co(II) adsorption on barley straw ash. *Water Resource and Industry*, 6, 1-17. <https://doi.org/10.1016/j.wri.2014.06.001>.
- Baylan, N., & Meriçboyu, A. E. (2016). Adsorption of lead and copper on bentonite and grapeseed activated carbon in single- and binary-ion systems. *Separation Science and Technology*, 51(14), 2360-2368. [10.1080/01496395.2016.1212888](https://doi.org/10.1080/01496395.2016.1212888).
- EPA. (2017). *National primary drinking water regulations*. United States Environmental Protection Agency.
- Gao, J. J., Qin, Y. B., Zhou, T., Cao, D. D., Xu, P., Hochstetter, D., & Wang, Y. F. (2013). Adsorption of methylene blue onto activated carbon produced from tea (*Camellia sinensis* L.) seed shells: Kinetics, equilibrium, and thermodynamics studies. *Journal of Zhejiang University Science B*, 14(7), 650-658. <https://doi.org/10.1631/jzus.B12a0225>.
- Garcia, J. R., Sedron, U., Zaini, M. A. A., & Zakaria, Z. A. (2018). Preparation, characterization and dye removal study of carbon prepared from palm kernel shell. *Environmental Science and Pollution Research*, 25(6), 5076-5085. <https://doi.org/10.1007/s11356-017-8975-8>
- Hannachi, Y., Hafidh, A., & Ayed, S. (2019). Effectiveness of novel xerogels adsorbents for cadmium uptake from aqueous solution in batch and column modes: Synthesis, characterization, equilibrium, and mechanism analysis. *Chemical Engineering and Design*, 143, 11-23. <https://doi.org/10.1016/j.chemd.2019.01.006>
- Hidayu, A. R., & Muda, N. (2016). Preparation and characterization of impregnated activated carbon from palm kernel shell and coconut shell for CO₂ capture. *Procedia Engineering*, 148, 106-113. <https://doi.org/10.1016/j.proeng.2016.06.463>
- Imamoglu, M., & Oktay, T. (2008). Removal of copper (II) and lead (II) ions from aqueous solutions by adsorption on activated carbon from a new precursor hazelnut husks. *Desalination* 228(1-3), 108-113. <https://doi.org/10.1016/j.desal.2007.08.011>.
- Khadiran, T., Hussein, M. Z., Zainal, Z., & Rusli, R. (2014). Textural and chemical properties of activated carbon prepared from tropical peat soil by chemical activation method. *BioResources*, 10(1), 986-1007. <https://doi.org/10.15376/biores.10.1.986-1007>
- Krika, F., Azzouz, N., & Ncibi, M. C. (2016). Adsorptive removal of cadmium from aqueous solution by cork biomass: Equilibrium, dynamics and thermodynamic studies. *Arabian Journal of Chemistry*, 9, S1077-S1083. <https://doi.org/10.1016/j.arabjc.2011.12.013>

- Malik, D. S., Jain, C. K., & Yadav, A. K. (2016). Removal of heavy metals from emerging cellulosic low-cost adsorbents : A review. *Applied Water Science* 7, 2113-2136. <https://doi.org/10.1007/s13201-016-0401-8>.
- Mopoung, S., Inkum, S., & Anuwetch, L. (2015). Effect of temperature on micropore of activated carbon from sticky rice straw by H₃PO₄ activation. *Carbon-Science and Technology*, 7(3), 24-29.
- Mouni, L., Merabet, D., Bouzaza, A., & Belkhiri, L. (2011). Adsorption of Pb(II) from aqueous solutions using activated carbon developed from apricot stone. *Desalination*, 276(1-3), 148-53. <https://doi.org/10.1016/j.desal.2011.03.038>
- Nunes, C. A., & Guerreiro, M. C. (2011). Estimation of surface area and pore volume of activated carbon by methylene blue and iodine numbers. *Quimica Nova*, 34(3), 472-476. <https://doi.org/10.1590/S0100-40422011000300020>
- Poudel, J., Ohm, T. I., Gu, J. H., Shin, M. C., & Oh, S. C. (2017). Comparative study of torrefaction of empty fruit bunches and palm kernel shell. *Journal of Material Cycles and Waste Management*, 19(2), 917-927. <https://doi.org/10.1007/s10163-016-0492-1>
- Rashidi, N. A., & Yusuf, S. (2019). Production of palm kernel shell-based activated carbon by direct physical activation for carbon dioxide adsorption. *Environmental Science and Pollution Research*, 26(33), 33732-33746. <https://doi.org/10.1007/s11356-018-1903-8>
- Razi, M. A. M., Al-Gheethi, A., Al-Qaini, M., & Yousef, A. (2018). Efficiency of activated carbon from kernel shell for treatment of grey water. *Arab Journal of Basic and Applied Sciences*, 25(3), 2018, 103-110. <https://doi.org/10.1080/25765299.2018.1514142>
- Rugayah, A. F., Astimar, A. A., & Norzita, N. (2014). Preparation and characterization of activated carbon from palm kernel shell by physical activation with steam. *Journal of Oil Palm Research*, 26(3), 251-264.
- Sani, Y. M., Raji, A. O., Alaba, P. A., Aziz, A. R. A., & Daud, W. M. A. W. (2015). Palm frond and spikelet as environmentally benign alternative solid acid catalysts for biodiesel production. *BioResources*, 10(2), 3393-3408. <https://doi.org/10.15376/biores.10.2.3393-3408>
- Shafie, S. M., Mahlia, T. M. I., Masjuki, H. H., & Ahmad-Yazid, A. (2012). A review on electricity generation based on biomass residue in Malaysia. *Renewable and Sustainable Energy Reviews*, 16(8), 5879-5889. <https://doi.org/10.1016/j.rser.2012.06.031>
- Saygılı, H., & Güzel, F. (2018). Novel and sustainable precursor for high-quality activated carbon preparation by conventional pyrolysis: Optimization of produce conditions and feasibility in adsorption studies. *Advanced Powder Technology* 29(3), 726-736. <https://doi.org/10.1016/j.apt.2017.12.014>.
- Tang, C., Shu, Y., Zhang, R., Li, X., Song, J., Li, B., Zhang, Y., & Ou, D. (2017). Comparison of the removal and adsorption mechanisms of cadmium and lead from aqueous solution by activated carbons prepared from *Typha Angustifolia* and *Salix Matsudana*. *RSC Advances*, 7(26), 16092-16103. <https://doi.org/10.1039/C6RA28035H>
- Wang, L., & Jian, L. (2013). Removal of methylene blue from aqueous solution by adsorption onto crofton weed stalk. *BioResources* 8(2), 2521-2536.
- Wang, Z., Shirley, M. D., Meikle, S. T., Whitby, R. L. D., & Mikhalovsky, S. V. (2009). The surface acidity of acid oxidised multi-walled carbon nanotubes and the influence of in-situ generated fulvic acids on their stability in aqueous dispersions. *Carbon* 47(1), 73-79. <https://doi.org/10.1016/j.carbon.2008.09.038>

- Xu, M., Li, D., Yan, Y., Guo, T., Pang, H., & Xue, H. (2017). Porous high specific surface area-activated carbon with co-doping N, S and P for high-performance supercapacitors. *RSC Advances* 7(69), 43780-43788. <https://doi.org/10.1039/C7RA07945A>
- Yeung, P. T., Chung, P. Y., Tsang, H. C., Tang, J. C. O., Cheng, G. Y. M., Gambari, R., Chui, C. H., & Lam, K. H. (2014). Preparation and characterization of bio-safe activated charcoal derived from coffee waste residue and its application for removal of lead and copper ions. *RSC Advances*, 4(73), 38839-38847. <https://doi.org/10.1039/C4RA05082G>
- Zaini, M. A. A., Okayama, R., & Machida, M. (2009). Adsorption of aqueous metal ions on cattle-manure-compost based activated carbons. *Journal of Hazardous Materials*, 170(2-3), 1119-1124. <https://doi.org/10.1016/j.jhazmat.2009.05.090>
- Zuo, X. (2014). Preparation and evaluation of novel thiourea / chitosan composite beads for copper(II) removal in aqueous solutions. *Industrial and Engineering Chemistry Research*, 53(3), 1249-1255. <https://doi.org/10.1021/ie4036059>

Rhodamine 6g Removal from Aqueous Solution with Coconut Shell-Derived Nanomagnetic Adsorbent Composite (Cs-Nmac): Isotherm and Kinetic Studies

Palsan Sannasi Abdullah*, Lim Kai Wen, Huda Awang and Siti Nuurul Huda Mohammad Azmin

Faculty of Agro-Based Industry, Universiti Malaysia Kelantan, Jeli Campus 17600 Jeli, Kelantan, Malaysia

ABSTRACT

Untreated effluents from the textile industry containing colorant dyes are harmful to the environment, aquatic organisms, and human health. Among these effluents, Rhodamine 6G is known as a corrosive and irritant dye. A coconut shell-derived nanomagnetic adsorbent composite (CS-NMAC) was developed to remove Rhodamine 6G from aqueous solution. Physical and adsorption properties of CS-NMAC were characterized via Brunauer–Emmett–Teller (BET) surface area analysis (S_{BET} : 1092.17 m²/g; total pore volume: 0.6715 cm³/g), X-ray diffraction (Fe₃O₄ [θ =35.522], Fe₂O₃ [θ =35.720] and FeO [θ =41.724]) and Fourier transform infrared spectroscopy (Fe–O, C–H, asymmetric C=C=C, CN and O–H). CS-NMAC was found to be electropositive within a broad pH range of 3–10) owing to the presence of nanoscale iron oxides on the surface of the coconut shell-derived adsorbent that enhanced the chemical and electrochemical outputs. Isotherm study revealed that the adsorption process of Rhodamine 6G followed a multilayer type of adsorption onto a heterogeneous surface. Freundlich model fitted better ($R^2 = 0.981$) than

the other models (Langmuir, Temkin and BET). The maximum adsorption capacity was 32.02 mg/g. Rhodamine 6G removal by CS-NMAC obeyed the pseudo-second-order reaction ($R^2 = 0.9995$) as opposed to other kinetic models. CS-NMAC has the potential to become an effective treatment for dye pollution.

ARTICLE INFO

Article history:

Received: 10 February 2021

Accepted: 21 May 2021

Published: 31 July 2021

DOI: <https://doi.org/10.47836/pjst.29.3.40>

E-mail addresses:

palsan.abdullah@umk.edu.my (Palsan Sannasi Abdullah)

kaiwenlim1@gmail.com (Lim Kai Wen)

hudaawang@gmail.com (Huda Awang)

huda.ma@umk.edu.my (Siti Nuurul Huda Mohammad Azmin)

*Corresponding author

Keywords: Adsorption, dye, isotherm, nanomagnetic, Rhodamine 6G

INTRODUCTION

Textile operators are the 3rd largest exporter of Malaysian products and a notable contributor to the country's economic growth (Azlan & Haseeb, 2019). However, the industry consumes enormous amounts of water and dyes during manufacturing processes. The effluents containing dyes derived from the textile industry continuously contaminate the water resources (Sundarajoo & Maniyam, 2019).

Rhodamine 6G is an azo dye with one or more $-N=N-$ groups attached to an aromatic structure. The dye is chemically stable and recalcitrant because of its chromophoric characteristics (Miranda et al., 2019).

Exposure to Rhodamine 6G dye is detrimental to health as it can cause allergic dermatitis and severe damage to the nervous system (Rasheed & Bilal, 2017). Over the past decades, many approaches for cleaning up dye pollutants have been developed and applied (Sahu & Singh, 2019). According to Wimalawansa (2013), the commonly used water treatment methods are chemical coagulation, sludge sedimentation, filtration, reverse osmosis, and carbon adsorption. Among these methods, activated carbon is widely used in the industry to remove dye pollutants. Although activated carbon is effective for cleaning up dye pollutants, its cost can become high (Sahu & Singh, 2019). Several approaches that involve the use of adsorbents have been proposed to overcome this problem. For example, *Clitoria fairchildiana* pods can adsorb up to 73.84 mg g^{-1} of Rhodamine 6G dye through chemisorption, but its application is time consuming (Miranda et al., 2019). Ni–Al-layered double oxides can remove dyes with 16% removal efficiency (Intachai et al., 2019). Therefore, high-quality adsorbents must not only be cost effective but also have competitive performance and are environmentally friendly (Suwunwong et al., 2020).

Various biocarbon materials have attracted increased attention owing to their innovativeness, modifiability, low cost, ease of preparation and ecofriendliness. Biocarbon is a carbon-rich, porous, and finely ground materials derived from carbonaceous biomass through limited air thermal decomposition process (Godwin et al., 2019). The biocarbon surface is generally negatively charged because of the dissociation of functional groups containing oxygen. As biocarbon uses carbonaceous biomass for processing, agricultural wastes can be possibly exploited to produce biocarbon (Vyavahare et al., 2019). Coconut wastes have been identified as a potential carbonaceous biomass for biocarbon because of its abundance, high biodegradability, and low cost (Nadzri et al., 2020). Moreover, the ash of coconut shells contains silicon oxide (SiO_2) at the same level as the components of metal matrix composites (Bahrami et al., 2016). The International Union of Pure and Applied Chemistry classifies the pore diameter of coconut shell biocarbon (micropores) with mesoporosity having the average pore diameter of adsorbent pores (Muzarpar et al., 2020). Therefore, the biocarbon derived from coconut shells is a potent adsorbent (Nadzri et al., 2020).

Although the performance of biocarbon in removing pollutants is effective, the separation of powdered biocarbon from an aqueous solution is difficult (Godwin et al., 2019). Physical modifications have been made to overcome this problem. Magnetic precursors, such as hematite, magnetite, siderite, and pyrite, are transformed into magnetic particles and attached onto the biocarbon surface. The application of magnetic particles to the separation process has been getting attention since the 1990s (Booker et al., 1991). Magnetic properties facilitate the separation of biocarbon from aqueous solution, thereby avoiding secondary pollution (Feng et al., 2020). However, magnetic powdered carbon adsorbent aggregates with weak dispersion in the presence of a magnetic field; thus, the application of iron oxide nanoparticles to powdered activated carbon not only rapidly adsorbs contaminants but also has a stronger ferromagnetic property that can be homogeneously dispersed in solution (Guo et al., 2020).

Moreover, the synthesis of coconut shell-derived nanomagnetic adsorbent composites (CS-NMAC) involves chemical coprecipitation. In this study, chemical coprecipitation was adopted because this process is easy to control. The common magnetic precursors used in the chemical coprecipitation were Fe^{3+} and Fe^{2+} . A magnetic precipitate was generated on the surface of the adsorbent composite by adding an alkaline solution into the magnetic precursor solution with the dispersed adsorbent composites (Feng et al., 2021). Furthermore, a surfactant crosslinker was applied in the synthesis process to obtain relatively stable nanomagnetic adsorbent composites (Li et al., 2019).

Many studies have investigated the adsorption of Rhodamine 6G. However, the mechanism of adsorption by CS-NMAC has not been elucidated yet. CS-NMAC contains magnetite (FeO^-) that has an interesting property: it is an amphoteric compound. Therefore, the efficiency of dye removal using CS-NMAC was investigated in terms of isotherm, kinetics, and mechanisms during adsorption reaction.

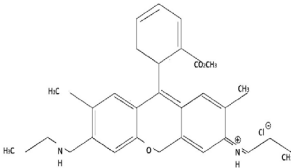
MATERIALS AND METHODS

Chemicals and Reagents

All chemicals and reagents used in this study, namely, ammonium hydroxide ($\text{NH}_3 \cdot \text{H}_2\text{O}$), ammonium hydroxide (NH_4OH), hydrochloric acid (HCl), nitric acid (HNO_3), sulfuric acid (H_2SO_4), sodium hydroxide (NaOH), potassium hydroxide (KOH), iron (III) chloride hexahydrate ($\text{FeCl}_3 \cdot 6\text{H}_2\text{O}$), iron (II) sulphate heptahydrate ($\text{FeSO}_4 \cdot 7\text{H}_2\text{O}$), potassium hydroxide (KOH), 70% of ethanol and distilled water, were of analytical grade. Commercial activated carbon (CAC) obtained from Friendemann Schmidt. Rhodamine 6G dye was purchased from Sigma Life Science. Rhodamine 6G, also known as basic red 1 ($\text{C}_{28}\text{H}_{31}\text{N}_2\text{O}_3\text{Cl}$), with 95% dye content was used without further purification. The properties of Rhodamine 6G are given in Table 1.

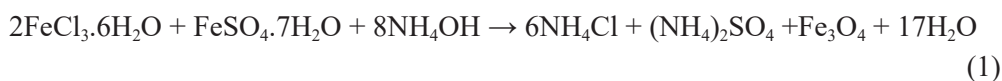
Table 1

Properties of Rhodamine 6G

Molecular name	Molecular formula	Molecular structure	Molecular weight (g mol ⁻¹)	Solubility (mg mL ⁻¹)	Colour
Rhodamine 6G	C ₂₈ H ₃₁ ClN ₂ O ₃		479.01	20	Red brown

Preparation of CS-NMAC

The preparation process commenced with carbonization of raw CS via the modified top lit up draft carbonization drum method. Afterward, the carbonized CS was ground into powder. CS-NMAC was prepared following a previously described method with slight modifications (Sannasi et al., 2021; Wannahari et al., 2018). The specific surface area and pore volume of the carbonized CS powder were increased by subjecting it to KOH activation at a ratio of 1:3 (carbonized CS powder:KOH) with slow agitation. The mixture was left for approximately 5–6 h to ensure complete intercalation of K into carbon compound. The intercalation reaction resulted in permanent expansion of carbon lattice in the carbon matrix (Wang & Kaskel, 2012). Subsequently, KOH was washed away from the expanded carbon lattice in the carbon matrix by repeatedly using deionized water (ddH₂O). The clean powder was dried at 90°C–100°C prior to heating at 800°C–900°C at a rate of 10°C/min for 15–30 min in a muffle furnace. The obtained sample allowed to cool down and then neutralized with 5% HCl before subsequent modification steps. CS-NMAC synthesis involved treatment with nitric acid (HNO₃) solution for 1 h at 80 °C to remove impurities from the adsorbent surface. A solution was then prepared with continuous stirring. First, FeCl₃.6H₂O and FeSO₄.7H₂O were dissolved in 450 mL of ddH₂O for 30 min at 30°C. Afterward, 30–60 mL of NH₄OH was added at 70°C for 1 h, followed by 5 g ammonium hydroxide (NH₃.H₂O) solution and the CS-modified biocarbon powder. Finally, 6 mL of epichlorohydrin was added into the solution and mixed at 85°C for 1 h. Epichlorohydrin served as a crosslinker to form chemical bonds between Fe₃O₄ and the CS-modified biocarbon powder. The solution was sonicated (Q Sonica) at 80 λ for 1 h, followed by more continuous stirring at 85°C for 1 h. The mixture that formed with precipitate allowed to cool down at 28°C, and the precipitate was washed with ddH₂O and ethanol. The sample (CS-NMAC) was dried at 50°C and collected using an external magnetic bar. The chemical reaction for generating CS-NMAC is as defined in Equations 1 and 2.



Sample Purification

The newly synthesized CS-NMAC was sorted according to particle size range by using a sieve filter (45–300 μm). The samples were repeatedly washed and filtered to remove impurities until the filter appeared clear with a pH approaching 7. The samples were dried in an oven at 80°C for 3–5 d and later kept in a container prior to use.

Characterization of CS-NMAC

Images of CAC and CS-NMAC were obtained using a scanning electron microscope (Jeol JSM-IT100) with a voltage of 10 KV at 2000 \times magnification. CS-NMAC morphology was examined via X-ray diffraction (XRD; Bruker, D8 Advance XRD) under following conditions: room temperature; CuK α radiation $\lambda=1.5406 \text{ \AA}$; and scan range $2\theta: 5^\circ\text{--}90^\circ$. The diffraction peaks were analysed using the Diffract Plus Eva software. CS-NMAC surface characteristics, including Brunauer–Emmett–Teller (BET) surface area, pore volume and pore size, were obtained via BET analysis of N₂ adsorption–desorption isotherm measurement at 77 K. Infrared spectrum of absorption was measured via Fourier transform infrared (FTIR) spectroscopy to identify chemical bonds. Functional groups and molecular components were detected and identified from the infrared absorption spectrum (Jasmin et al., 2013).

Effect of Contact Time and pH

The experiment was performed in batch mode under following parameters: room temperature (27 °C); 25.5 mg L⁻¹ initial dye concentration; 0.05 g CS-NMAC; and agitation at 150 rpm (Orbital shaker 14A-OBS602). The effects of contact time were evaluated by analysing the samples for 15–60 min and again for 5–30 min to determine the existence of quasiequilibrium situation according to patterns of adsorption at shorter times. The effects of pH were assessed by analysing the samples at pH 3–10.

Batch Adsorption Experiment

First, 0.05 g of CS-NMAC was added into Rhodamine 6G solution at different concentrations (1–15 mg/mL) and agitated at 150 rpm. Afterward, CS-NMAC was separated from the sample solution using an external magnetic bar. The remaining solution was analysed using a Thermo Scientific Genesys 20 UV–Visible spectrophotometer at 440–570 nm.

The adsorption capacity of Rhodamine 6G dye by CS-NMAC at equilibrium, q_e (mg/g), was determined by Equation 3.

$$q_e = \left[\frac{C_o - C_e}{W} \right] V, \quad (3)$$

where q_e is the amount of Rhodamine 6G dye adsorbed to the adsorbent (mg/g or mg g⁻¹), C_o is the initial concentration of Rhodamine 6G dye (mg L⁻¹), C_e is the equilibrium concentration of Rhodamine 6G dye (mg L⁻¹), V is the volume of solution (L) and W is the weight of adsorbents (CS-NMAC) used (g).

The percentage of Rhodamine 6G dye removal was calculated from Equation 4.

$$\% \text{ Adsorption or } \% \text{ Dye Removal} = \left[\frac{C_o - C_e}{C_o} \right] \times 100\% \quad (4)$$

Where C_o (mg L⁻¹) and C_e (mg L⁻¹) are the initial concentration and the equilibrium concentration of Rhodamine 6G dye, respectively.

Adsorption Isotherm and Kinetic Studies

Adsorption equilibrium experiments were conducted using different concentrations of Rhodamine 6G dye solution (5, 10, 15, 20, and 25 mg L⁻¹) under optimized parameters: contact time of 14.33 min, adsorbent dose of 0.05 g, particle size of 190.26 μm and pH 6.54. The equilibrium data calculated from the formula were used to fit the corresponding isotherm models. Freundlich, Langmuir and Temkin isotherms are widely adopted in dye removal studies (Santhi & Kumar, 2015; Wannahari et al., 2018). Variations in different isotherm models with their corresponding linear form of isotherm models are presented in Table 2. In the present study, Langmuir, Freundlich and Temkin isotherms were calculated using Equations 5, 6, and 7, respectively, to determine the adsorption capacity of the adsorbents at different concentrations of dye solution.

$$q_e = q_m - \left(\frac{1}{K_L} \right) \left(\frac{q_e}{C_e} \right) \quad (5)$$

Where q_e is the uptake of Rhodamine 6G at equilibrium (mg/g), q_m is Langmuir maximum uptake of adsorbate per unit mass of adsorbent (mg/g), K_L is Langmuir constant related to rate of adsorption (L/mg) and C_e is concentration of Rhodamine 6G at equilibrium (mg/L) (Wannahari et al., 2018).

$$\ln q_e = \ln KF + \left(\frac{1}{n} \right) \ln C_e \quad (6)$$

Where q_e is the uptake of Rhodamine 6G at equilibrium (mg/g), K_F is the Freundlich adsorption constant (L/mg) and C_e is the concentration of Rhodamine 6G at equilibrium (Wannahari et al., 2018).

$$q_e = \left(\frac{RT}{b} \right) \ln Kt + \left(\frac{RT}{b} \right) \ln C_e \quad (7)$$

Where q_e is the uptake at equilibrium (mg/gb), b is Temkin constant (heat of sorption) (J/mol) and Kt is Temkin isotherm constant (Lg^{-1}) (Nimibofa et al., 2017).

The kinetics of Rhodamine 6G removal were investigated under optimized parameters of 26.12 mg/L dye concentration, 0.05 g adsorbent dose, 190.26 μm particle size and pH 6.54 and different contact times ranging from 5 min to 25 min with a time interval of 5 min. The kinetics of Rhodamine 6G adsorption from aqueous solution were analysed using pseudo-first-order, pseudo-second order and intra-particle diffusion models. The compatibility of the experimental data with the kinetic model was ensured using the correlation coefficient (R^2) value. A high R^2 value indicates that the model fits the Rhodamine 6G dye adsorption kinetics (Vijayakumar et al., 2012). The equations for pseudo-first-order, pseudo-second order and intra-particle diffusion kinetic models are given in Equation 8, 9, and 10, respectively.

$$\ln(qe - qt) = \ln qe - K_1 t \quad (8)$$

Where q_e is the amount of Rhodamine 6G adsorbed at equilibrium (mg/g), qt is the amount of dye adsorbed at any time (mg/g) and K_1 is a rate constant of the pseudo-first-order kinetic model (min^{-1}) (Vijayakumar et al., 2012).

$$\frac{t}{qt} = \frac{1}{K_2 qe^2} + \frac{t}{qe} \quad (9)$$

Where q_e is the uptake of Rhodamine 6G at equilibrium (mg/g), qt is the uptake of Rhodamine 6G at any time (mg/g) and K_2 is the rate constant for pseudo-second-order kinetic model (min^{-1}) (Vijayakumar et al., 2012).

$$q_t = k_i t^{\frac{1}{2}} + c \quad (10)$$

Where qt is the uptake of Rhodamine 6G at any time (mg/g), k_i is intra-particle diffusion rate constant ($\text{mg/g} \cdot \text{min}^{-1}$) and c is a constant of the thickness of the boundary layer (mg/g) (Wannahari et al., 2018).

Comparison between CS-NMAC and CAC in Rhodamine 6G removal

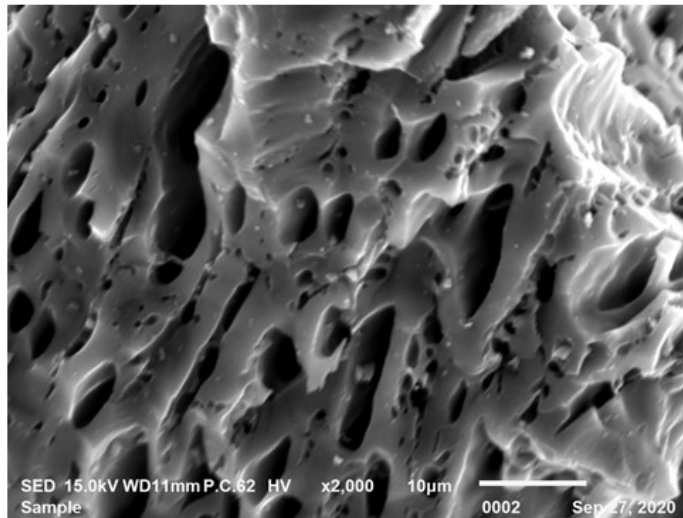
First, 0.05 g each of 74–250 μm CS-NMAC and CAC was added into an Erlenmeyer flask containing 26 mg/L Rhodamine 6G (pH 6.54). Afterward, the samples were agitated at 180 rpm for 14 min. The sample containing CS-NMAC was then separated using a magnet and a filter paper. Meanwhile, the sample containing CAC was filtered using a filter paper. Finally, the absorbance at 530 nm for each sample was recorded using a spectrophotometer.

RESULTS AND DISCUSSION

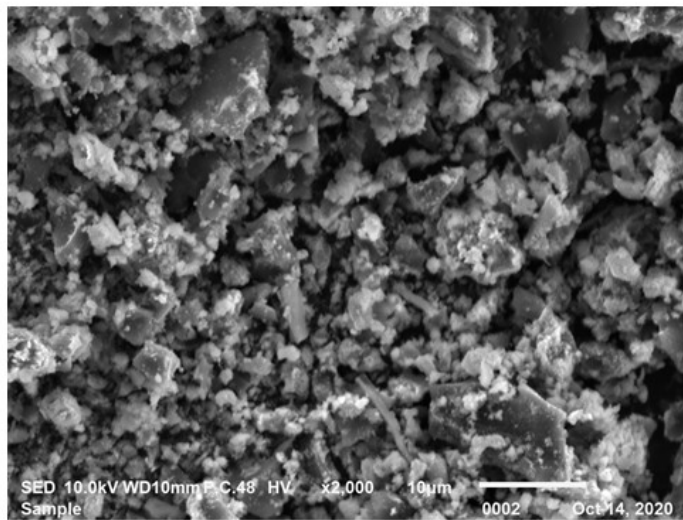
Characterization of CS-NMAC

The morphological structures of both CAC and CS-NMAC are presented in Figure 1.

Compared with CAC, iron oxide nanoparticles are embedded on the CS-NMAC matrix without obvious aggregations. This condition indicated that the CS-NMAC matrix and the iron oxide nanoparticles had a good mechanical binding.



(a)



(b)

Figure 1. SEM images of (a) CAC and (b) CS-NMAC at 2000 \times magnification at 10.0 kV

The surface of the CS-derived adsorbent was modified by adding iron oxide nanoparticles. The existence of these nanosized iron oxide materials on the surface of CS-NMAC was confirmed via XRD analysis (Figure 2). The iron oxide nanoparticles, namely, magnetite (Fe_3O_4), maghemite ($\gamma\text{-Fe}_2\text{O}_3$), hematite ($\alpha\text{-Fe}_2\text{O}_3$) and wuestite (FeO), are superparamagnetic; thus, they display a strong ferromagnetic behaviour (Kandpal et al., 2014).

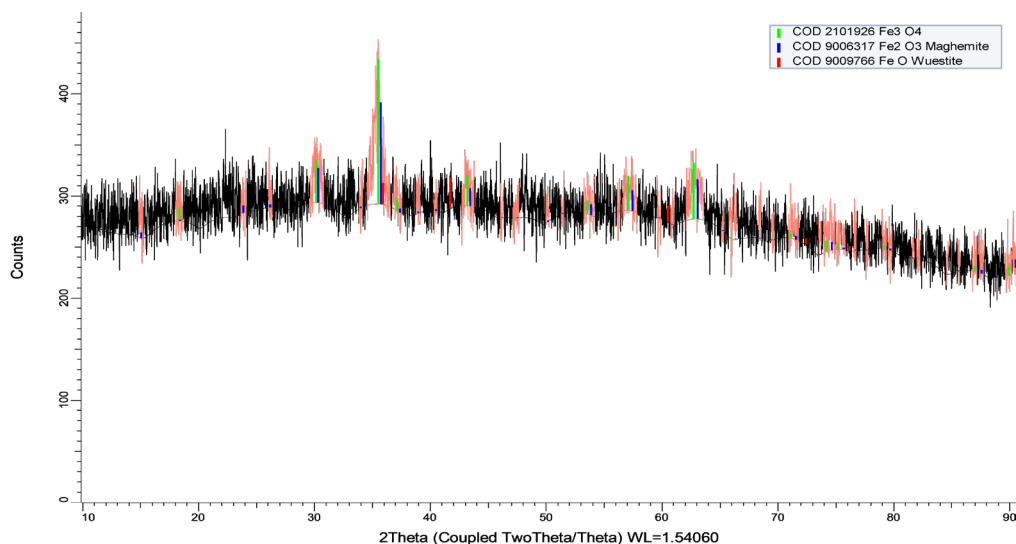


Figure 2. X-ray diffractogram for CS-NMAC with 100% relative intensity spectra for Fe_3O_4 ($\theta=35.522$), Fe_2O_3 ($\theta=35.720$) and FeO ($\theta=41.724$)

The BET surface area (S_{BET}) and total pore volume (TPV) of CS-NMAC were $1092.17 \text{ m}^2/\text{g}$ and $0.6715 \text{ cm}^3/\text{g}$, respectively. These S_{BET} and TPV values of CS-NMAC were higher than those of other magnetic adsorbents reported in the literature: -magnetic iron oxide nanoparticles derived from *Cyanometra ramiflora* fruit extract waste ($107.97 \text{ m}^2/\text{g}$, $0.13 \text{ cm}^3/\text{g}$) (Bishnoi et al., 2017); magnetic biochar derived from *Astragalus membranaceus* residues ($203.7 \text{ m}^2/\text{g}$, $0.187 \text{ cm}^3/\text{g}$) (Kong et al., 2017); activated carbon derived magnetic CS ($951.84 \text{ m}^2/\text{g}$, $0.6715 \text{ cm}^3/\text{g}$) (Hao et al., 2018); and magnetic corn waste straw ($313.9 \text{ m}^2/\text{g}$, $0.22 \text{ cm}^3/\text{g}$) (Khan et al., 2020). Thus, CS-NMAC is expected to have a better performance in adsorption than the magnetic iron oxide nanoparticles derived from other carbonaceous biomass owing to its high porosity.

Effects of Contact Time and pH

The effects of contact time on the percentage of Rhodamine 6G removal are depicted in Figure 3(a). The percentage of Rhodamine 6G removed was paltry after 33 min. Thus, steady state approximation was likely reached, and this result was accepted as a

quasiequilibrium situation (Mane & Babu, 2011). By contrast, at the second phase (after 33 min), the process became slow as repulsive forces occurred between the adsorbate and the adsorbent. The reaction achieved the maximum point when a longer contact time was applied.

The quasiequilibrium situation for a shorter time (below 30 min) was also tested in a separate experiment [Figure 3(b)]. The percentage of dye removed gradually increased from 5 min to 20 min, and the increase in the amount of dye removed was small from 20 min to 30 min. According to Patrick et al. (2014), at the initial phase of the adsorption process, adsorption rapidly occurs there are more vacant and available sites.

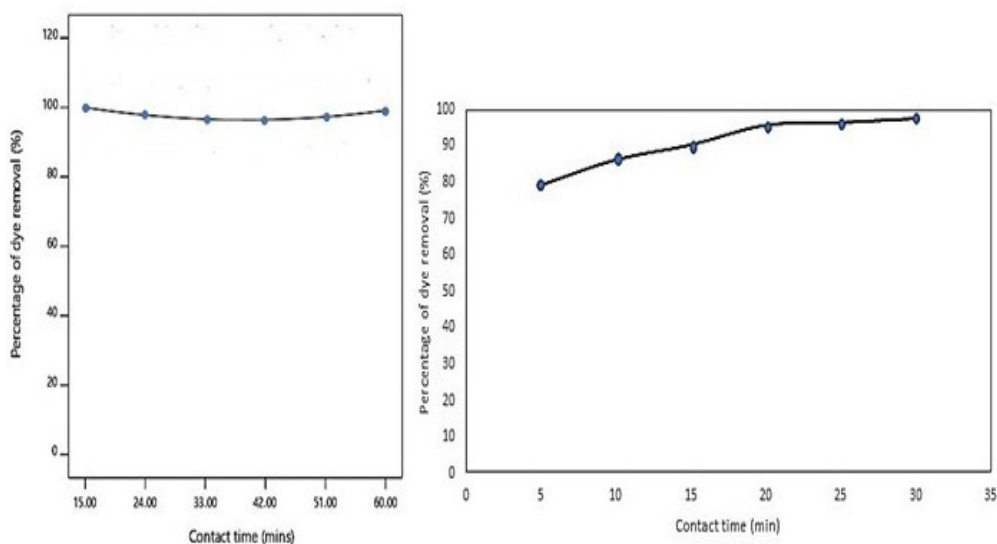


Figure 3. Percentage removal (%) of Rhodamine 6G by CS-NMAC in batch adsorption reaction at 27°C, 150 rpm and 0.05 g CS-NMAC according to (a) 15–60 min and (b) 5–30 min of contact time.

The initial solution pH was tested because pH governs the surface charge of CS-NMAC and speciation of polluting dyes. The percentage of dye removed increased as pH increased (Figure 4), demonstrating that CS-NMAC was electropositive within a wide range of pH from 3 to 10. The initial pH of the dye solution affected the functional groups on the surface of CS-NMAC. Adsorption occurred because of electrostatic interaction (alkene) and hydrogen bonding (hydroxyl) on the surface of CS-NMAC and the dye. According to Ahmadgurabi et al., (2018), the cationic functional group (NH^+) of Rhodamine 6G forms a hydrogen bond with the anionic functional (FeO^-) of CS-NMAC in basic pH media. Such reaction occurred because magnetite (FeO^-) has amphoteric properties. Moreover, the nature of CS-NMAC was electropositive within a wide pH range (3–10) during adsorption

because the alkaline mineral ash on the surface of the adsorbent was released into the solution (Kuang et al., 2020).

Furthermore, pH only had a slight effect on the percentage of dye removed not only because of the presence of amphoteric FeO^- functional group on the CS-NMAC surface but also because of the salting out effect phenomenon, which occurred because high salt concentrations affect pH and solution solubility. Decreases in the amount of Rhodamine 6G dye in solution due to the salting out effect induced the diffusion towards the hydrophobic surface of CS-NMAC. Such interaction later increased adsorption efficiency (Reguyal & Sarmah, 2018).

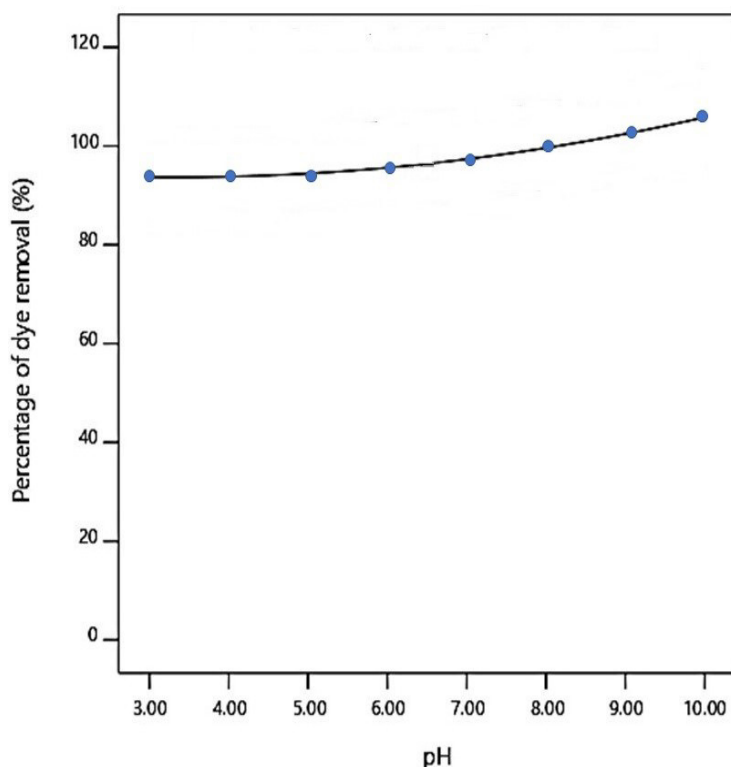


Figure 4. Percentage removal (%) of Rhodamine 6G by CS-NMAC in batch adsorption reaction at 27 °C, 150 rpm and 0.05 g CS-NMAC according to pH.

Equilibrium Adsorption Isotherm Studies

The performance and mechanism of dye removal were predicted and compared by fitting the experimental data into the corresponding linearized isotherm models (Figure 5). The respective parameters of each model are summarized in Table 2.

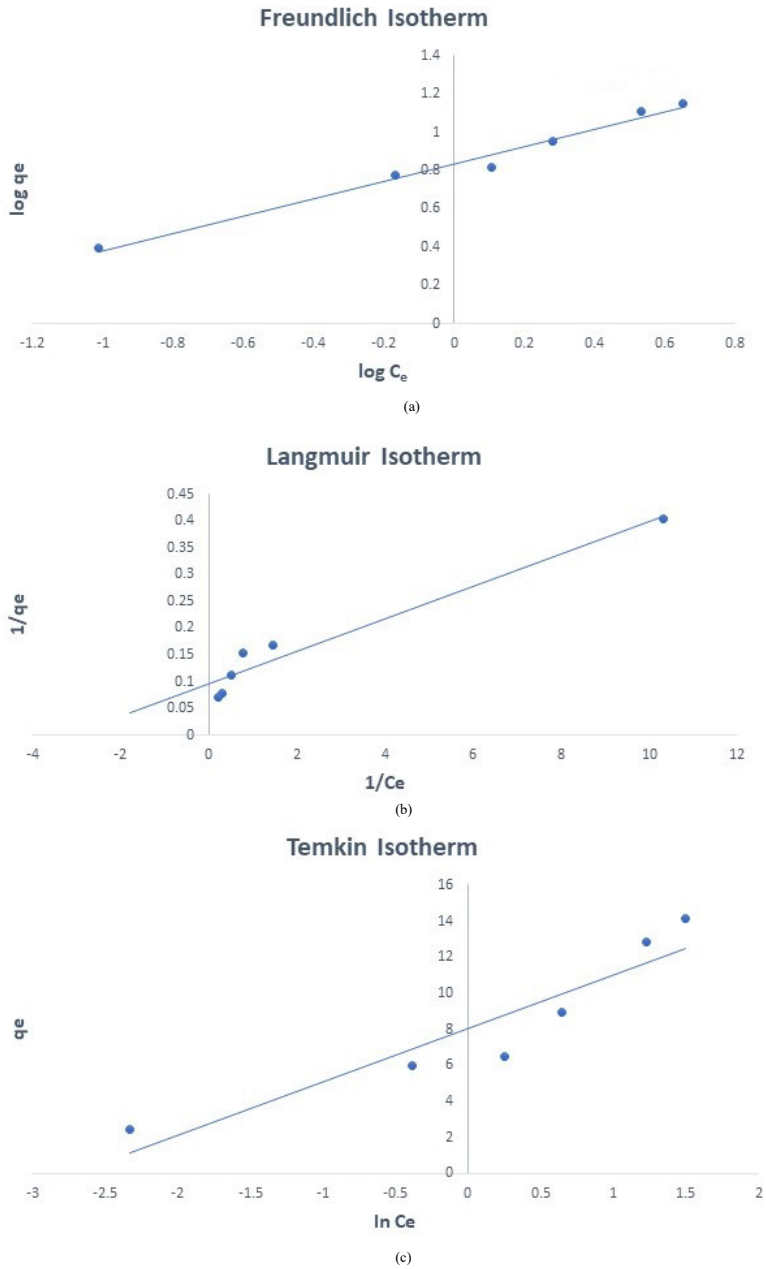


Figure 5. Graphs depicting the removal of Rhodamine 6G in aqueous solution by CS-NMAC at 27°C; 5, 10, 10, 15, 20 and 25 mg/L initial concentration (C_0); 0.05 g adsorbent dose; 150 rpm agitation rate; and 14.33 min contact time: (a) Langmuir isotherm, (b) Freundlich isotherm and (c) Temkin isotherm.

Table 2

Isotherm model parameters for Rhodamine 6G adsorption

Isotherm models	Parameters	Values
Freundlich	K_F	6.864
	n	2.208
	q_m (mg/g)	32.020
	R^2	0.981
Langmuir	K_L	0.3179
	R_L	0.0309–0.1367
	q_m (mg/g)	33.0033
	R^2	0.9514
Temkin	b (J/mol)	24.08
	K_T (L/g)	15.107
	R^2	0.8649

Among the isotherm models, the Freundlich model had the highest R^2 value of 0.981. The n value ($n = 2.208$) was sufficiently high for separation and indicating that Rhodamine 6G removal favoured the Freundlich isotherm model. An n value equals to one ($n = 1$) indicates that the partition between the adsorbent and the adsorbate is independent of concentration. However, when the n value greater unity ($n > 1$), the reaction has high affinity towards the occurrence of chemisorption between the adsorbate and the adsorbent; thus, it is considered chemisorption (Wang et al., 2015). This route reflects a multilayered adsorption process on a heterogeneous surface, which has the advantage of having more adjacent carbon atoms to provide interaction with adsorbing molecules. Similar findings were reported by Wannahari et al. (2018) and Mohammed et al. (2017) for the removal of heavy metals (Cu^{2+}). A comparison of the Rhodamine 6G adsorption performance among the other adsorbents in terms of adsorption capacity is shown in Table 3. The adsorption capacity of CS-NMAC was higher than that of the other adsorbents because of its high S_{BET} value, which indicated that CS-NMAC had a large surface area for adsorption.

Table 3

Comparison of the adsorption capacities of Rhodamine 6G with the adsorbents

Adsorbent	Adsorption capacity (mg/g)	Model	pH	S_{BET} (m^2/g)	References
Moroccan natural phosphate	6.84	Langmuir	5.2	18.8	Bensalah et al. (2017)

Table 3 (Continued)

Adsorbent	Adsorption capacity (mg/g)	Model	pH	SBET (m ² /g)	References
Kappa-carrageenan grafted with N-hydroxyethylacrylamide	8.38	Freundlich	>7	0.0502	Kulal and Badalamoole (2020)
Fe ₃ O ₄ -composited biochar derived from rice husk	9.42	Langmuir	7	Not cited	Suwunwong et al. (2020)
Mesoporous silica nanoparticles	13.70	Langmuir	Not cited	1078	Kachbouri et al. (2018)
Coconut shell-derived nanomagnetic adsorbent composite	32.02	Freundlich	7	1092.17	This study

Kinetic Models for the Adsorption of Rhodamine 6G Dye

The mechanism and potential rate-controlling step of Rhodamine 6G adsorption by CS-NMAC by applying adsorption kinetics models consisting of pseudo-first-order, pseudo-second order and intra-particle diffusion kinetic models. The obtained correlation coefficients (R^2) were used to assess the applicability of the kinetic models (Sharifi & Shoja, 2018). The values of the adsorption kinetic model constants are summarized in Table 4. The pseudo-second-order kinetic model showed an excellent correlation coefficient ($R^2 = 0.9995$) compared with the pseudo-first order and intra-particle diffusion models (Figure 6). Aside from high correlation value, the pseudo-second order showed high proximity between the experimental uptake capacity ($q_{e(\text{exp})}$) (14.445 mg/g) and the calculated uptake capacity ($q_{e(\text{cal})}$) (15.1515 mg/g), indicating that the adsorption of Rhodamine 6G to CS-NMAC was controlled by chemisorption. The presence of iron oxide nanoparticles endowed CS-NMAC with a strong ferromagnetic property. During the adsorption reaction, the Rhodamine 6G dye considerably faded, and the powdered CS-NMAC aggregated and homogeneously dispersed toward the external magnetic field. As a result, the strong ferromagnetic properties allowed for convenient separation and overcame the problem of remaining adsorbent residues. Valence forces were involved in the chemisorption process by sharing or exchanging electrons between the Rhodamine 6G dye molecules and the CS-NMAC surface (Figure 7).

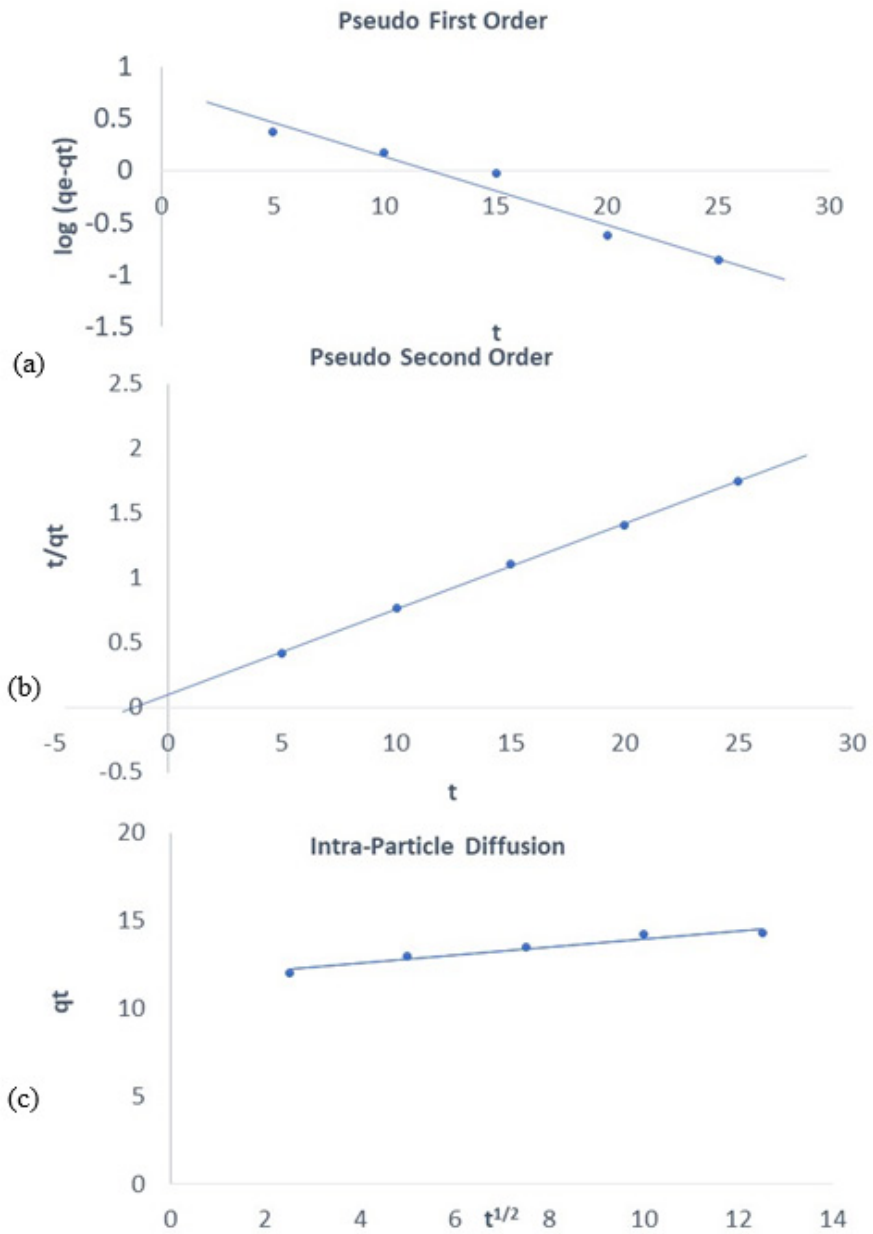


Figure 6. Representation of (a) pseudo-first order, (b) pseudo-second order and (c) intra- particle diffusion plots for Rhodamine 6G adsorption into CS-NMAC at 27 °C, 150 rpm agitation, 26.12 mg/L dye concentration and adsorbent dose of 0.05 g.

Table 4

Values of kinetic model constants for the adsorption of Rhodamine 6G

q_e (exp) (mg/g)	PSEUDO-FIRST ORDER			Pseudo-second order		
	q_e (cal) (mg/g)	k_1 (min ⁻¹)	R ²	q_e (cal) (mg/g)	k_2 (min ⁻¹)	R ²
14.4450	6.11223	0.1500	0.9572	15.1515	0.0437	0.9991

q_e (exp) (mg/g)	INTRAPARTICLE DIFFUSION		
	K_i (g/mg min ⁻¹)	C	R ²
14.4450	0.2296	11.6870	0.9469

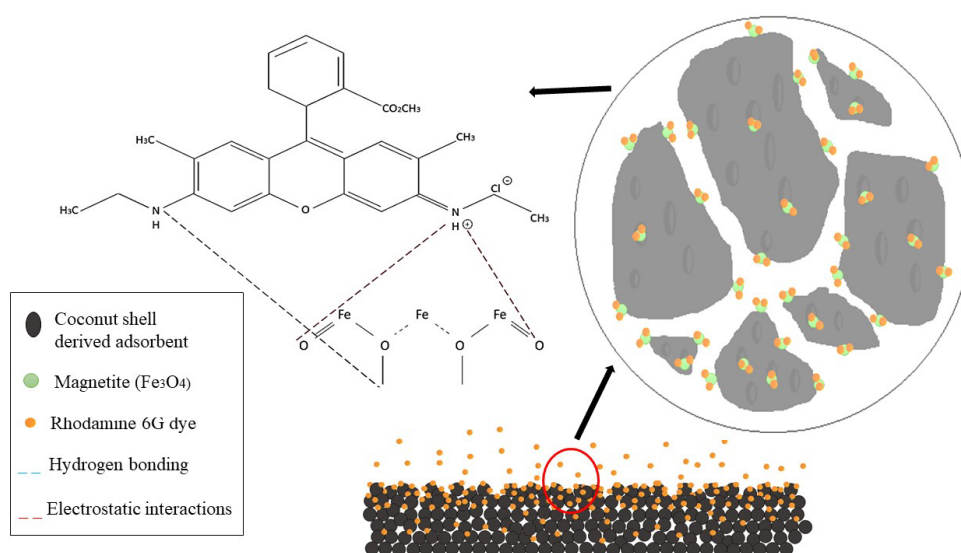


Figure 7. Chemisorption between Rhodamine 6G and surface of CS-NMAC

FTIR Analysis after Rhodamine 6G Adsorption into CS-NMAC

The peaks with respect to chemical functional groups observed before and after Rhodamine 6G dye adsorption are plotted in Figure 8. FTIR analysis was performed within 500–4000 cm⁻¹ to identify the functional groups on the surface of CS-NMAC that formed bonding structures during adsorption.

The peaks of CS-NMAC at 1716.07 cm^{-1} that appeared before adsorption and at 1718.53 cm^{-1} that appeared after adsorption were attributed to CN stretching. The peak at 1988.94 cm^{-1} corresponded to the C–H functional group before adsorption, but it shifted to 1845.52 cm^{-1} after adsorption. Prior to the adsorption reaction, asymmetric C=C stretching was observed at 1999.28 cm^{-1} , which later appeared at 1988.63 cm^{-1} after the reaction. The shift in CS-NMAC peaks during the adsorption reaction indicated interactions between the active sites on the surface of the adsorbent functional group and Rhodamine 6G (Sharifi & Shoja, 2018).

Moreover, the shift in O–H vibration peaks within $3522.17\text{--}3688.95\text{ cm}^{-1}$ before adsorption and the shift in O–H stretching peaks within $3503.76\text{--}3702.70\text{ cm}^{-1}$ after adsorption, as well as the shift in the peak intensity of Fe–O stretching from within $506.16\text{--}575.72\text{ cm}^{-1}$ to within $502.15\text{--}575.78\text{ cm}^{-1}$ after adsorption, affirmed the formation of hydrogen bonds. Popoola (2019) reported that the formation of hydrogen bonds during Cd^{2+} adsorption by nanomagnetic walnut shell rice husk was due to shifts in the peak of O–H.

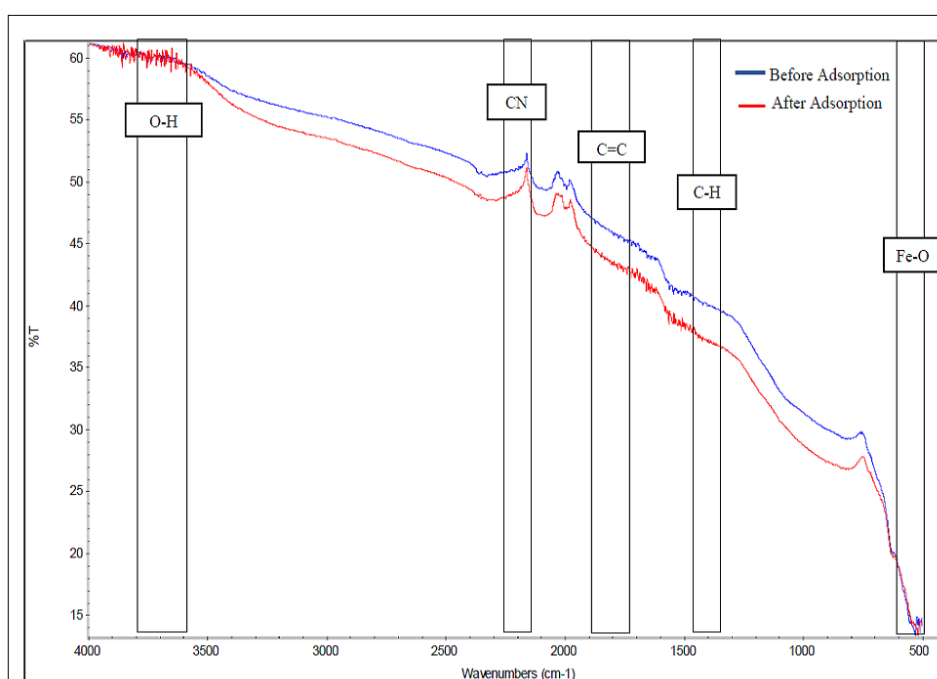


Figure 8. FTIR spectra of CS-NMAC before and after adsorption of Rhodamine 6G dye

Comparison of Removal Efficiency of CS-NMAC with that of CAC

The effectiveness of CS-NMAC in removing Rhodamine 6G from aqueous solution was evaluated via adsorption experiments by using CAC under the optimized conditions. CAC

was produced via steam activation ($\sim 1,000^{\circ}\text{C}$). The different methods for separating and removing Rhodamine 6G dye and the percentage of their removal are presented in Table 5.

Table 5

Percentage of Rhodamine 6G dye removal for each adsorption

Adsorbent	Separation Method	Percentage of Dye Removal (%)	Uptake Capacity q (mg/g)
CS-NMAC	Magnet + Filtration	99.9968	31.219
CAC	Filtration	99.9964	28.029

CAC and the nanomagnetic biocarbon composite both exhibited good adsorption capacity and achieved high removal efficiency (Table 5). Both displayed high percentage ($\sim 99\%$) of Rhodamine 6G dye removal; thus, they were effective adsorbents. The adsorption capacity of CS-NMAC (nonsteam activated) was also high and comparable to that of steam-activated CAC because of the availability and higher affinity of nanomagnetic particles. The presence and characteristics of nanoparticles affected the adsorption capacity of the adsorbents.

Moreover, CS-NMAC held a competitive advantage over CAC in terms of diamagnetic properties. Nanomagnetic biocarbon composites that resulted from the modification and innovation of biocarbon could be easily separated from the solution and thus resolve the separation problem of CAC. Furthermore, CS-NMAC could adsorb various pollutants, such as cationic dye (Rhodamine 6G, this study) and heavy metals (Cr^{2+}) (Wannahari et al., 2018) because of the amphoteric properties of magnetite (Fe_3O_4) on the surface of the adsorbent.

CONCLUSION

CS-NMAC was found to have a high active area for adsorption as indicated by S_{BET} ($1092.17 \text{ m}^2/\text{g}$) and PVT ($0.6715 \text{ cm}^3/\text{g}$). Both characteristics are advantageous for surface-bound adsorption processes. The presence of maghemite, hematite and wuestite as confirmed by XRD analysis indicated that nanosized iron oxide particles were embedded on the matrix of the CS-NMAC surface. FTIR analysis revealed that the FeO functional group on the surface of CS-NMAC was vital to the adsorption and separation in solution. The best fit model for CS-NMAC adsorption was found to be the Freundlich model ($R^2 = 0.981$), which revealed that adsorption occurred on the heterogeneous surface with a maximum adsorption capacity of 32.020 mg/g . However, Rhodamine 6G adsorption obeyed the pseudo-second-order reaction, implying the onset of chemisorption in the process. This

situation likely occurred owing to the valence electron of surface atoms of maghemite, hematite and wuestite crystals. Furthermore, the dye removal performance was comparable to that of CAC but with a more convenient magnetic separation of the used material from the solution. Therefore, iron oxide nanoparticles on the surface of CS-NMAC not only greatly influenced the performance in adsorption but also enhanced the isotherm and kinetics of the adsorbent.

ACKNOWLEDGEMENT

The authors acknowledge the financial support from Universiti Malaysia Kelantan (R/SGJP/A07.00/01397A/005/2018/00570).

REFERENCES

- Ahmadgurabi, N. G., Koochi, A. D., & Pirbazari, A. E. (2018). Fabrication, characterization regeneration and application of nanomagnetic Fe₃O₄ @ fish scale as a bio-adsorbent for removal of methylene blue. *Journal of Water and Environmental Nanotechnology*, 3(3), 219-234. <https://doi.org/10.22090/jwent.2018.03.003>
- Azlan, A., & Haseeb, M. (2019). Radio frequency identification (RFID) technology as a strategic tool towards higher performance of supply chain operations in textile and apparel industry of Malaysia. *Uncertain Supply Chain Management*, 7(2), 215-226. <https://doi.org/10.5267/j.uscm.2018.10.004>
- Bahrami, A., Soltani, N., Pech-Canul, M. I., & Gutierrez, C. A. (2016). Development of metal-matrix composites from industrial/agricultural waste materials and their derivatives. *Critical Reviews in Environmental Science and Technology*, 46(2), 143-208. <http://dx.doi.org/10.1080/10643389.2015.1077067>
- Bensalah, H., Bekheet, M. F., Alami, S., & Ouammou, M. (2017). Removal of cationic and anionic textile dyes with Moroccan natural phosphate. *Journal of Environmental Chemical Engineering*, 5(3), 2189-2199. <https://doi.org/10.1016/j.jece.2017.04.021>
- Bishnoi, S., Kumar, A., & Selvaraj, R. (2017). Facile synthesis of magnetic iron oxide nanoparticles using inedible *Cynometra ramiflora* fruit extract waste and their photocatalytic degradation of methylene blue dye. *Materials Research Bulletin*, 97, 121-127. <https://doi.org/10.1016/j.materresbull.2017.08.040>
- Booker, N. A., Keir, D., Priestley, A. J., Ritchie, C. B., Sudarmana, D. L., & Woods, M. A. (1991). Sewage clarification with magnetite particles. *Water Science & Technology*, 23, 1703-1712.
- Feng, Z., Chen, H., Li, H., Yuan, R., Wang, F., Chen, Z., & Zhou, B. (2020). Preparation, characterization, and application of magnetic activated carbon for treatment of biologically treated papermaking wastewater. *Science of The Total Environment*, 713, Article 136423. <https://doi.org/10.1016/j.scitotenv.2019.136423>
- Feng, Z., Yuan, R., Wang, F., Chen, Z., Zhou, B., & Chen, H. (2021). Preparation of magnetic biochar and its application in catalytic degradation of organic pollutants: A review. *Science of The Total Environment*, 765, Article 142673. <https://doi.org/10.1016/j.scitotenv.2020.142673>
- Godwin, P. M., Pan, Y., Xiao, H., & Afzal, M. T. (2019). Progress in preparation and application of modified biochar for improving heavy metal ion removal from wastewater. *Journal of Bioresources and Bioproducts*, 4(1), 31-42. <https://doi.org/10.21967/jbb.v4i1.180>

- Guo, Z., Chen, R., Yang, R., Yang, F., Chen, J., Li, Y., Zhou, R., & Xu, J. (2020). Science of the total environment synthesis of amino-functionalized biochar / spinel ferrite magnetic composites for low-cost and efficient elimination of Ni (II) from wastewater. *Science of the Total Environment*, 722, Article1 37822. <https://doi.org/10.1016/j.scitotenv.2020.137822>
- Hao, Z., Wang, C., Yan, Z., Jiang, H., & Xu, H. (2018). Magnetic particles modification of coconut shell-derived activated carbon and biochar for effective removal of phanol from water. *Chemosphere*, 211, 962-969. <https://doi.org/10.1016/j.chemosphere.2018.08.038>
- Intachai, S., Pimchan, P., & Sumanatrakul, P. (2019). Synthesis of NiAl - layered double oxide as inorganic adsorbent for eliminating dye from solution. *Naresuan University Journal: Science and Technology*, 4(27), 66-74. <https://doi.org/10.14456/nujst.2019.37>
- Jasmin, S., Jan, M. R., Haq, A., & Khan, Y. (2013). Removal of rhodamine B from aqueous solutions and wastewater by walnut shells: Kinetics, equilibrium and thermodynamics studies. *Frontiers of Chemical Science and Engineering*, 7(4), 428-436. <https://doi.org/10.1007/s11705-013-1358-x>
- Kachbouri, S., Mnasri, N., Elaloui, E., & Moussaoui, Y. (2018). Tuning particle morphology of mesoporous silica nanoparticles for adsorption of dyes from aqueous solution. *Journal of Saudi Chemical Society*, 22(4), 405-415. <https://doi.org/10.1016/j.jscs.2017.08.005>
- Kandpal, N. D., Sah, N., Loshali, R., Joshi, R., & Prasad, J. (2014). Co-precipitation method of synthesis and characterization of iron oxide nanoparticles. *Journal of Scientific & Industrial Research*, 73, 87-90.
- Khan, Z. H., Gao, M., Qiu, W., Islam, S., & Song, Z. (2020). Mechanisms for cadmium adsorption by magnetic biochar composites in an aqueous solution. *Chemosphere*, 246, Article 125701. <https://doi.org/10.1016/j.chemosphere.2019.125701>
- Kong, X., Liu, Y., Pi, J., Li, W., & Liao, Q. (2017). Low-cost magnetic herbal biochar: Characterization and application for antibiotic removal. *Environmental Science and Pollution Research*, 24, 6679-6687. <https://doi.org/10.1007/s11356-017-8376-z>
- Kuang, Y., Zhang, X., & Zhou, S. (2020). Adsorption of methylene blue in water onto activated carbon by surfactant modification. *Water*, 12(587), 1-19. <https://doi.org/doi:10.3390/w12020587>
- Kulal, P., & Badalamoole, V. (2020). Hybrid nanocomposite of kappa-carrageenan and magnetite as adsorbent material for water purification. *International Journal of Biological Macromolecules*, 165, 542-553. <https://doi.org/10.1016/j.ijbiomac.2020.09.202>
- Li, C., Gao, Y., Li, A., Zhang, L., Ji, G., Zhu, K., & Wang, X. (2019). Synergistic effects of anionic surfactants on adsorption of norfloxacin by magnetic biochar derived from furfural residue. *Environmental Pollution*, 254, 1-8. <https://doi.org/10.1016/j.envpol.2019.113005>
- Mane, V. S., & Babu, P. V. V. (2011). Studies on the adsorption of brilliant green dye from aqueous solution onto low-cost NaOH treated saw dust. *Desalination*, 273(2-3), 321-329. <https://doi.org/10.1016/j.desal.2011.01.049>
- Miranda, A., Serrão, N. O., Celestino, G. D. G., Takeno, M. L., Tiago, N., Antunes, B., Stefan, I., Lizandro, M., & Freitas, F. A. D. (2019). Removal of rhodamine 6G from synthetic effluents using *Clitoria fairchildiana* pods as low-cost biosorbent. *Environmental Science and Pollution Research*, 27, 2868-2880. <https://doi.org/10.1007/s11356-019-07114-6>

- Mohammed, M. A., Abubakar, B. I. & Kurna, B. B. (2017). Equilibrium and kinetics studies of adsorption of safranin-O from aqueous solutions using pineapple peels. *Arid Zone Journal of Engineering, Technology and Environment*, 13(6), 671-687.
- Muzarpar, M. S., Leman, A. M., Rahman, K. A., Shayfull, Z., & Irfan, A. R. (2020). Exploration sustainable base material for activated carbon production using agriculture waste as raw materials: A review exploration sustainable base material for activated carbon production using agriculture waste as raw materials: A review. In *IOP Conference Series: Materials Science and Engineering* (Vol. 864, No. 1, p. 012022). IOP Publishing. <https://doi.org/10.1088/1757-899X/864/1/012022>
- Nadzri, S. N. I. H. A., Sultan, M. T. H., Shah, A. U. M., Safri, S. N. A., Talib, A. R. A., Jawaid, M., & Basri, A. A. (2020). A comprehensive review of coconut shell powder composites: Preparation, processing, and characterization. *Journal of Thermoplastic Composite Materials*, 1-24. <https://doi.org/10.1177/0892705720930808>
- Nimibofa, A., Augustus, N. E., & Donbebe, W. (2017). Modelling and interpretation of adsorption isotherms. *Journal of Chemistry*, 2017, 1-11. <https://doi.org/10.1088/1757-899X/864/1/012022>
- Patrick, E., Ebere, M., & Echegi, U. S. (2014). Effect of process factors on the adsorption of MB dye using *Adenia lobata* Fiber. *International Journal of Innovative Research in Science, Engineering and Technology*, 3(10). <https://doi.org/10.15680/IJRSET.2014.0310004>
- Popoola, L. T. (2019). Nano-magnetic walnut shell-rice husk for Cd (II) sorption: Design and optimization using artificial intelligence and design expert. *Heliyon*, 5(8), Article e02381. <https://doi.org/10.1016/j.heliyon.2019.e02381>
- Rasheed, T., & Bilal, M. (2017). Reaction mechanism and degradation pathway of rhodamine 6G by photocatalytic treatment. *Water Air Soil Pollution*, 228(291), 1-10. <https://doi.org/10.1007/s11270-017-3458-6>
- Reguyal, F., & Sarmah, A. K. (2018). Adsorption of sulfamethoxazole by magnetic biochar: Effects of pH, ionic strength, natural organic matter and 17 α -ethinylestradiol. *Science of the Total Environment*, 628, 722-730. <https://doi.org/10.1016/j.scitotenv.2018.01.323>
- Sahu, O., & Singh, N. (2019). Significance of bioadsorption process on textile industry wastewater. In *The impact and prospects of green chemistry for textile technology* (pp. 367-416). Woodhead Publishing. <https://doi.org/10.1016/B978-0-08-102491-1.00013-7>
- Sannasi, P., Awang, H., & Barasarathi, J. (2021). Synthesis of magnetic activated carbon treated with sodium dodecyl sulphate. *Pertanika Journal of Science and Technology*, 29(1), 427-444. <https://doi.org/10.47836/pjst.29.1.24>
- Santhi, M., & Kumar, P. E. (2015). Adsorption of rhodamine B from an aqueous solution: Kinetic, equilibrium and thermodynamic studies. *International Journal of Innovative Research in Science, Engineering and Technology*, 4(2), 497-510. <https://doi.org/10.1016/B978-0-08-102491-1.00013-7>
- Sharifi, S. H., & Shoja, H. (2018). Optimization of process variables by response surface methodology for methylene blue dye removal using spruce sawdust/Mgo nano-biocomposite. *Journal of Water Environment Nanotechnology*, 3(2), 157-172. <https://doi.org/10.22090/JWENT.2018.02.007>

- Sundarajoo, A., & Maniyam, M. N. (2019). Enhanced decolourization of congo red dye by Malaysian rhodococcus UCC 0010 immobilized in calcium alginate. *Journal of Advanced Research Design*, 62(1), 1-9.
- Suwunwong, T., Patho, P., Choto, P., & Phoungthong, K. (2020). Enhancement the rhodamine 6G adsorption property on Fe₃O₄ -composited biochar derived from rice husk. *Materials Research Express*, 7, Article 025511. <https://doi.org/10.1088/2053-1591/ab6b58>
- Vijayakumar, G., Tamilarasan, R., & Dharmendirakumar, M. (2012). Adsorption, kinetics, equilibrium and thermodynamic studies on the removal of basic dye rhodamine-B from aqueous solution by the use of natural adsorbent perlite. *Journal of Materials and Environmental Science*, 3(1), 157-170. <https://doi.org/10.1016/j.arabjc.2016.11.009>
- Vyavahare, G., Jadhav, P., Jadhav, J., Patil, R., Aware, C., Patil, D., Gophane, A., Yang, Y. H., & Gurav, R. (2019). Strategies for crystal violet dye sorption on biochar derived from mango leaves and evaluation of residual dye toxicity. *Journal of Cleaner Production*, 207, 296-305. <https://doi.org/10.1016/j.jclepro.2018.09.193>
- Wang, J., & Kaskel, S. (2012). KOH activation of carbon-based materials for energy storage. *Journal of Material Chemistry*, 22(45), 23710-23725. <https://doi.org/10.1039/C2JM34066F>
- Wang, J., Liu, G., Li, T., & Zhou, C. (2015). Physicochemical studies toward the removal of Zn(ii) and Pb(ii) ions through adsorption on montmorillonite-supported zero-valent iron nanoparticles. *RSC Advances*, 5(38), 29859-29871. <https://doi.org/10.1039/C5RA02108A>
- Wannahari, R., Sannasi, P., Nordin, M. F. M., & Mukhtar, H. (2018). Sugarcane bagasse derived nano magnetic adsorbent composite (SCB-NMAC) for removal of Cu²⁺ from aqueous solution. *ARP Journal of Engineering and Applied Sciences*, 13(1), 1-9.
- Wimalawansa, S. J. (2013). Purification of contaminated water with reverse osmosis: effective solution of providing clean water for human needs in developing countries. *International Journal of Emerging Technology and Advanced Engineering*, 3(12), 75-89.

Length-weight Relationship and Relative Condition Factor of Two Dominant Species (*Cyclocheilichthys apogon* and *Notopterus notopterus*) at Subang Lake, Selangor, Malaysia

Xeai Li Chai¹, Rohasliney Hashim^{1*}, Muhammad Nur Aiman Rahmat¹, Mohamad Hamizan Kamaludin¹, Nur Ain Habullah¹ and Izharuddin Shah Kamaruddin²

¹Department of Environment, Faculty of Forestry and Environment, Universiti Putra Malaysia, 43400 UPM, Serdang, Selangor Darul Ehsan, Malaysia

²Department of Aquaculture, Faculty of Agriculture, Universiti Putra Malaysia, 43400 UPM, Serdang, Selangor Darul Ehsan, Malaysia

ABSTRACT

Length-weight relationships and relative condition factors were conducted to provide information on fish species' growth conditions and general well-being in the freshwater habitat. This study was conducted using fish as a bioindicator for the health of the ecosystem. *Cyclocheilichthys apogon* (Beardless barb) and *Notopterus notopterus* (Bronze featherback) are the most dominant species in Subang Lake. A four-month sampling was conducted to collect the sample of Beardless barb and Bronze featherback. A total of 422 individuals

of Beardless barb and 344 individuals of Bronze featherback were measured and weighed. The mean total length of Breadless barb was 13.11 ± 1.31 cm with the mean weight of 31.88 ± 9.93 g. The mean of the total length and weight of Bronze featherback was 16.05 ± 2.07 cm and 30.38 ± 15.63 g. Both fish species showed negative allometric growth with the exponent b value 2.884 and 2.886, respectively. The condition factor of Beardless barb (1.184 ± 0.134) and Bronze featherback (1.010 ± 0.163) obtained from this study reflects a fair growth condition based on K value by

ARTICLE INFO

Article history:

Received: 1 March 2021

Accepted: 19 April 2021

Published: 31 July 2021

DOI: <https://doi.org/10.47836/pjst.29.3.44>

E-mail addresses:

shailychai94@gmail.com (Xeai Li Chai)

rohasliney@upm.edu.my (Rohasliney Hashim)

muhammadnuraiman399@gmail.com (Muhammad Nur Aiman Rahmat)

mohamadhamizan1012@gmail.com (Mohamad Hamizan Kamaludin)

nurain0496@yahoo.com (Nur Ain Habullah)

izharuddin@upm.edu.my (Izharuddin Shah Kamaruddin)

*Corresponding author

Barnham & Baxter (2003). Further studies need to be conducted to determine the significant impacts that affect fish species' growth conditions.

Keywords: Freshwater fishes, length-weight relationship, relative condition factor, Subang lake

INTRODUCTION

The information such as the fish species' growth pattern, general health of fish, habitat conditions, and the fish's morphological characteristics can be revealed by the Length-weight relationships (LWR) (Jisr et al., 2018; Froese, 2006). LWR is widely applied in fisheries management because it provides information on the stock condition and indicates the degree of stabilization of fish's taxonomic characters (Isa et al., 2010). There are several studies of the length-weight relationship and condition factor in Malaysia. According to Amonodin et al. (2018), there were approximately 102 LWR studies of 64 species that belong to 20 families. The Cyprinidae was the most studied family in the Malaysian freshwater system. Amonodin et al. (2018) documented a higher number of fish species experienced positive allometric growth, whereas a lower number of fish species experienced negative allometric growth in the Malaysian freshwater system. The variation of fish growth was attributed by the environmental condition, seasonal variation, general fish condition, age, maturity, health, and stomach fullness (Kaur & Rawal, 2017). Fish species experienced positive allometric growth in a generally healthy environment with sufficient food supply and good water quality condition, whereas, fish species experienced negative allometric growth in a poor environmental condition. Also, the variation of fish growth was affected by the adaptive response of fish response to the ecological condition (Kaur & Rawal, 2017).

Meanwhile, the condition factor is used to demonstrate the state of fish well-being and useful indicators of fish growth rate (Farooq et al., 2017). A fish's condition indicates the fish's current physical and biological circumstances; thus, the condition factor provides essential information about the present and future population success via its association with growth, reproduction, and survival. Apparently, in a favorable environmental condition, fish species should demonstrate faster growth rates, more significant reproductive potential, and higher survival rates (Pope, 2007). According to Karna et al. (2012), environmental condition is an important factor that induced the phenotypic flexibility. Also, most studies suggested that there is a significant relationship between temperature, population size, and the maturity of fish.

The Subang Lake is an undisturbed endorheic lake surrounded by hilly and forested area, and there is no study concerning the fish LWR and condition, especially on these native species (Beardless barb and Bronze featherback) found in the lake. Hence, this study's objective was to estimate the LWR of two dominant native species, Beardless barb and Bronze featherback, and determine the K_n that evaluates fish growth condition to further

relate to the environment condition. Consequently, this knowledge is essential to local management to prioritize the control and coordination fisheries' management options for native species in Subang Lake. This study demonstrates the understanding of these native species' growth and their condition in a small and undisturbed water body.

MATERIALS AND METHODS

This study was conducted at Subang Lake, located in Petaling District, with a latitude of 3.1672° N and a longitude of 101.4798° E (Figure 1). Subang Lake is an endorheic lake and was built in 1950. The capacity of Subang Lake is about 777.00 mg. The impounding capacity of Subang Lake is 3531.8 mL, and the impounding area is 96 hectares. The catchment area of Subang Lake is 10.16 km², and the maximum depth is 8.5 m. The study area was divided into seven sampling points which are Muka Sauk (SP1), Tanjung Panjang (SP2), Tanjung Batu 4 (SP3), Tanjung Jelutong (SP4), Tanjung Hantu (SP5), Tanjung Ampang (SP6), and Tanjung Terung (SP7) (Figure 2).

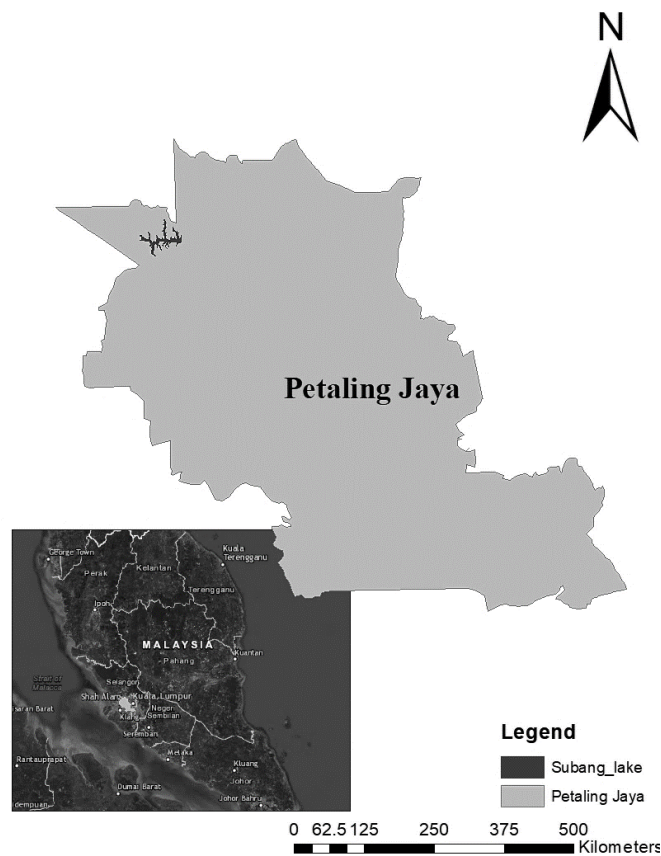


Figure 1. The location of Subang Lake in Selangor, Malaysia

The sampling was carried out four months (July 2018, June 2019, August 2019, and October 2019) using five different mesh sizes of gill net (1 ½ inch, 2 inches, 3 inches, 4 inches, and 5 inches) and two fish traps. The sampling locations were stratified-randomly selected with major coverage of Subang Lake. The gill nets and fish traps were set overnight in four consecutive days at each sampling point from morning 0800h and checked every four hours until 1800h. The total length of individual fish was measured using the measuring board in centimeter, and the weight of individual fish was taken as the nearest gram using an electronic balance (LT2002, Smith).

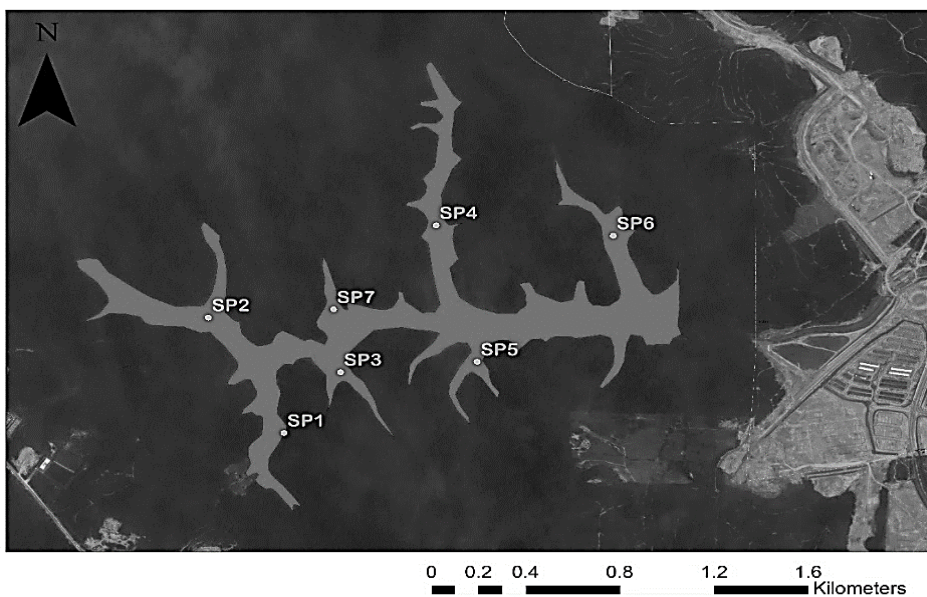


Figure 2. The distribution of seven sampling points in Subang Lake

The growth pattern of the fish can be determined by the score of the growth exponents, b . According to Froese (2006), the allometric growth versus isometric growth and the different body shapes of the individual species can be determined from the 82% of the variance in a plot of $\log a$ over b . In most fishes, the value of $b > 3.0$ indicates a positive allometric growth where the relative body thickness or plumpness is increased with the length, whereas when the value of $b < 3.0$ indicates negative allometric growth. The fish body growth is relatively less rotund as the length increases (Amonodin et al., 2018). The current form of LWR determines the length-weight relationship, and also, the linear regression analysis is used to determine the length-weight (log-transformed) relationship (Froese, 2006). The linear regression of LWR is $\log W = \log a + b \log L$, whereas the modern form of LWR is defined as Equation 1.

$$W = aL^b \quad [1]$$

Where,

W = Body weight (g)

L = Total length (cm)

a = coefficient

b = exponent

The condition factor is also used to determine the fishes' condition in their habitat (Jones et al., 1999). The relative condition factor of fish is determined by using the observed weight and the estimated weight. The relative condition factor is suitable for value $b < / > 3$. The relative condition factor (K) is used to assess a specific environment's fitness for fish growth through the deviation of an organism from the sample's average weight (Jisr et al., 2018). According to Le Cren (1951), $K \geq 1$ indicates the fish's growth condition is a good and contrary condition when $K < 1$. However, Barnham and Baxter (2003) stated that the K value greater than 1.4 is categorized as excellent fish growth, whereas less than 1.0 showed a poor growth pattern. The mean condition factor (K) is defined as Equation 2.

$$K = W/W' \quad [2]$$

Where,

W = Observed weight of fish individual

W' = Estimated weight of fish individual

Descriptive statistical analysis was conducted by calculating the mean values of the length-weight relationship and the relative condition factor of Beardless barb and Bronze featherback throughout the sampling periods because of these factors affecting the length-weight relationship, such as habitat and seasonal effect. Stomach fullness, maturity stage, age, and sex were not considered (Hamid et al., 2015).

RESULTS AND DISCUSSIONS

A total of 422 individuals of Beardless barb and 344 individuals of Bronze featherback were captured in this study (Table 1). Both fish species were the dominant species in Subang Lake. The total length of Breadless barb at Subang Lake ranged from 10.0 cm to 16.9 cm with the mean total length of 13.11 ± 1.31 cm, and the weight ranged from 11.80 g to 70.52 g with the mean weight of 31.88 ± 9.93 g (Table 1). The mean of the total length and weight of Bronze featherback is 16.05 ± 2.07 cm and 30.38 ± 15.63 g (Table 1). The total length of Bronze featherback ranged from 9.80 cm to 26.40 cm, and the weight of Bronze featherback varied from 4.99 g to 153.04 (Table 1). The coefficient of determination (r^2) value of Beardless barb and Bronze featherback was 0.8588 and 0.8828, respectively

(Table 1). A lower value of r^2 indicated a narrow range of fish size with higher correlation and statistical significance (Gaygusuz et al., 2012). The lower value of r^2 also affected by human error during data collection and inconsideration of outliers of length and weight during the LWR calculation. Good quality of prediction of linear regression was obtained from the high coefficient of determination values.

The b value of Beardless barb and Bronze featherback was 2.884 and 2.886, respectively, categorized as negative allometric growth (Table 1). The negative allometric growth was recorded for both fish species ($b < 3$) suggested that the fish species have a relatively slow growth rate. According to Froese (2006), the expected b value was varied from 2.5 – 3.5. The b value that exceeded the range of standard b value was considered a consequence of small sample sizes (Gaygusuz et al., 2012); however, the case did not happen in this study. The K value of Beardless barb (1.184) and Bronze featherback (1.010) indicated that the fish have a fair growth pattern (Barnham & Baxter, 2003). The condition factor was associated with the LWR that was recorded in this study.

Table 1

Summary of length-weight relationship and relative condition factor. K value was based on Barnham and Baxter (2003)

Species	N	Lmin-max (cm)	Wmin-max (g)	a	b	r^2	Growth behavior	K
<i>Cyclocheilichthys apogon</i> (Beardless barb)	422	10.0 - 16.9	11.80 - 70.52	0.01843	2.884	0.8588	Negative allometric	1.184
<i>Notopterus notopterus</i> (Bronze featherback)	344	9.80 - 26.40	4.99 - 153.04	0.0095	2.886	0.8828	Negative allometric	1.010

The negative allometric growth of both fish species, Beardless barb and Bronze featherback, was recorded in the present study. This result is in accord to Nyanti et al. (2018) where a negative allometric growth of Beardless barb ($b = 2.678$) was recorded from downstream of the Batang Ai Dam (Malaysia); however, the condition factor of Beardless barb was in good condition ($K > 1$) (Table 2). Food availability and the environmental condition were the significant factors that affect the length-weight relationship and growth condition of fish in Batang Ai Dam. The findings of Rosli and Zain (2016), Zulkaffi et al. (2016), Hamid et al. (2015), and Isa et al. (2010) indicated a positive allometric growth of Beardless barb in most of the Malaysian freshwater bodies (Table 2).

Several previous studies recorded that Bronze featherback has positive allometric growth ($b > 3$). For instance, the positive allometric growth of Bronze featherback was

recorded at Pedu Lake (Kedah) and Sukhna Lake (India) with 3.25 (Isa et al., 2010) and 3.57, respectively (Kaur & Rawal, 2017) (Table 2). According to Dubey et al. (2012), Bronze featherback has a positive allometric growth in the less disturbance or favorable condition in River Ken (India). Besides, negative allometric growth was reported in the finding of Khan (2003) due to several factors such as the selectivity of gill nets, relatively cold climate, and the lower productivity of Tilaiya Reservoir. Sarkar et al. (2013) documented that difference in parameter b value was attributed to the differences in the specimens' observed length ranges. The positive allometric growth was recorded in the study by Kaur and Rawal (2017) due to the smaller range of length (21.00 – 28.30 cm); however, the length ranges of Bronze featherback ($N = 344$) caught in Subang Lake were more comprehensive (9.80 cm to 26.40 cm).

The finding of Martin-Smith (1996) categorized the b value range from 2.60 – 2.75 as flattened body shape, whereas the b value ranged from 2.88 – 3.15 as a heavy-bodied. The expected range of exponent b value was 2.5 – 3.5. Although negative allometric growth was obtained in the current study, the results were within the expected range and considered heavy-bodied. According to Isa et al. (2010), a higher value of b showed that the environment is more favorable for the fish species. Moreover, Rosli and Zain (2016) and Dalu et al. (2013) suggested the variation of b value was due to the variation of length and weight, seasonal variation, gonad maturity, diet, health, food availability, and other environmental factors.

The relative condition factor (K) in the present study for both fish species was greater than 1. According to Le Cren (1951), $K > 1$ reflects a healthier physiological state. However, Barnham and Baxter (2003) stated that the K value greater than 1.40 is categorized as good to excellent growth condition, whereas the K value lower than 1.0 categorized as poor growth condition. Barnham and Baxter (2003) have a comprehensive identification of fish conditions than Le Cren (1951). Hence, the condition of the Beardless barb and Bronze featherback were found to be relatively fair ($1 < K < 1.40$) at Subang Lake based on the standard of Barnham and Baxter (2003). This study found that both Beardless barb and Bronze featherback dominated Subang Lake. Therefore, both fishes condition indicated that Subang lake provides adequate food supply and favorable environmental conditions for them to survive and grow. According to Sharip et al. (2017), Subang Lake was a mesotrophic-eutrophic lake with the domination of green algae, which provides sufficient food for both fish species. Furthermore, seasonal variation, breeding activities, and biological activities indicated no physiological stress to these populations. With a distinctive slender and elongated body, giving Bronze featherback a knife-like appearance (Kumar & Karin, 2016), it was evident that its body increases more in length than in weight. Thus, the body form and shape strongly affect the relative condition. Logically, the morphological factors also influence body form and weight, and, by extension, condition

factor. It is possible for an individual fish could increase energetic fitness without a change in body weight.

Table 2

Literature reports of allometric growth of fish compared to findings in the current study

Species	Study area	N	b	Location (Literature)	N	b	References
<i>Cyclocheilichthys apogon</i> (Beardless barb)	Subang Lake	422	2.884	Batang Ai dam	208	2.678	Nyanti et al. (2018)
				Muda Reservoir	Males: 166	Males: 3.150	Rosli and Zain (2016)
					Females: 141	Females: 3.185	
				Temengor Reservoir	233	3.157	Hamid et al. (2015)
Kerian River basin	46	3.516	Isa et al. (2010)				
<i>Notopterus notopterus</i> (Bronze featherback)	Subang Lake	344	2.886	Sukhna Lake	45	3.570	Kaur and Rawal (2017)
				River Ken	28	3.32	Dubey et al. (2012)
				Pedu Lake	120	3.250	Isa et al. (2010)
				Tilaiya Reservoir	300	2.902	Khan (2003)

* N = number of individuals, b = exponent b (slope of the equation $W = \log a + b \log L$)

CONCLUSION

In conclusion, both fish species are in a healthy intermediate state (fair condition growth) when the K value is greater than 1.4. Subang lake's ecological factors are observed to support these dominant fishes. The negative allometric growth of both fish species may be attributed to the fish's morphological characteristics. The results of the length-weight relationship (LWR) and relative condition factor (Kn) recorded in this study contribute to the knowledge of the fish condition in Subang Lake and the relevant information in the conservation management of Subang Laker's fish. The results obtained can also provide useful information about the fish communities in an endorheic lake.

ACKNOWLEDGMENT

The authors wish to thank funding from Geran Putra Universiti Putra Malaysia (UPM) (GP/2017/9564500) for completing the study. Also, high appreciation to Mohd Sulkifly Ibrahim, Abdul Rahman Sokran @ Mohamad, and Dalina Jaafar for their help and assistance for this study in 2018. Apart from that, high gratitude for Pengurusan Air Selangor Sdn. Bhd. and Lembaga Urusan Air Selangor for their approval for the authors to carry out their study smoothly in Subang Lake. Finally, thank you for the kindest cooperation given by the supervisor of Subang Lake, Mohd Rezza Haizad Abdullah, and all the staff (Rajuddin Hamid, Yusof Rohman, and Muhammad Fadzil Idris).

REFERENCES

- Amonodin, M. R., Fadzil, N. F. M., Azmai, A. M. N., & Hashim, R. (2018). A review of length-weight relationships of freshwater fishes in Malaysia. *Transylvanian Review of Systematical and Ecological Research*, 20(1), 55-68. <https://doi.org/10.1515/trser-2018-0005>
- Barnham, C. P. S. M., & Baxter, A. (2003). *Condition factor, K, for salmonid sh.* State of Victoria, Department of Primary Industries.
- Dalu, T., Nhwatiwa, T., & Clegg, B. (2013). Length-weight relationships and condition factors of six fish species caught using gill nets in a tropical African reservoir, Zimbabwe. *Transactions of the Royal Society of South Africa*, 68(1), 75-79. <https://doi.org/10.1080/0035919X.2012.733318>
- Dubey, V. K., Sarkar, U. K., Kumar, R. S., Mir, J. I., Pandey, A., & Lakra, W. S. (2012). Length-weight relationships (LWRs) of 12 Indian freshwater fish species from an un-impacted tropical river of Central India (River Ken). *Journal of Applied Ichthyology*, 28(5), 854-856. <https://doi.org/10.1111/j.1439-0426.2012.02005.x>
- Farooq, N., Qamar, N., Rashid, S., & Panhwar, S. K. (2017). Length-weight relationship of eleven species of marine catfishes from the northern Arabian Sea coast of Pakistan. *Chinese Journal of Oceanology and Limnology*, 35(5), 1218-1220.
- Froese, R. (2006). Cube law, condition factor and weight-length relationships: History, meta-analysis and recommendations. *Journal of Applied Ichthyology*, 22(4), 241-253. <https://doi.org/10.1111/j.1439-0426.2006.00805.x>
- Gaygusuz, Ö., Aydin, H., Emiroğlu, Ö., Top, N., Dorak, Z., Gaygusuz, Ç. G., Baskurt, S., & Tarkan, A. S. (2012). Length-weight relationships of freshwater fishes from the western part of Anatolia, Turkey. *Journal of Applied Ichthyology*, 29(1), 285-287. <https://doi.org/10.1111/jai.12015>
- Hamid, M. A., Mansor, M., & Nor, S. A. M. (2015). Length-weight relationship and condition factor of fish populations in Temengor Reservoir: Indication of environmental health. *Sains Malaysiana*, 44(1), 61-66. <https://doi.org/10.17576/jsm-2015-4401-09>
- Isa, M. M., Rawi, C. S., Rosla, R., Shah, S. A. M., & Shah, A. S. R. M. (2010). Length – weight relationships of freshwater fish species in Kerian River Basin and Pedu Lake. *Research Journal of Fisheries and Hydrobiology*, 5(1), 1-8.

- Jisr, N., Younes, G., Sukhn, C., & El-Dakdouki, M. H. (2018). Length-weight relationships and relative condition factor of fish inhabiting the marine area of the Eastern Mediterranean city, Tripoli-Lebanon. *The Egyptian Journal of Aquatic Research*, 44(4), 299-305
- Jones, R. E., Petrell, R. J., & Pauly, D. (1999). Using modified length-weight relationships to assess the condition of fish. *Aquacultural engineering*, 20(4), 261-276.
- Karna, S. K., Sahoo, D., Panda, S., Vihar, V., Bhaban, M., & Nagar, S. (2012). Length weight relationship (LWR), growth estimation and length at maturity of *Etroplus suratensis* in Chilika Lagoon, Orissa, India. *International Journal of Environmental Sciences*, 2(3), 1257-1267.
- Kaur, V., & Rawal, Y. K. (2017). Length-weight relationship (LWR) in *Notopterus notopterus* (Pallas) from Sukhna Lake, Chandigarh. *IOSR Journal of Pharmacy and Biological Sciences*, 12(4), 63-65. <https://doi.org/10.9790/3008-1204046365>
- Khan, M. A. (2003). Length-weight relationship and relative condition index of *Notopterus notopterus* (Pallas) of Tilaiya Reservoir, Bihar. *Records of The Zoological Survey of India*, 101, 233-239.
- Kumar, K. H., & Kiran, B. R. (2016). Relative condition factor of feather back, *Notopterus Notopterus* (Pallas) from Jannapura Pond, Bhadravathi Taluk, Karnataka. *International Journal of Scientific Research in Science, Engineering and Technology*, 2(1), 36-39.
- Le Cren, E. D. (1951). The length-weight relationship and seasonal cycle in gonad weight and condition in the perch (*Perca fluviatilis*). *The Journal of Animal Ecology*, 20(2), 201-219. <https://doi.org/10.2307/1540>
- Martin-Smith, K. M. (1996). Length/weight relationships of fishes in a diverse tropical freshwater community, Sabah, Malaysia. *Journal of Fish Biology*, 49(4), 731-734. <https://doi.org/10.1006/jfbi.1996.0201>
- Nyanti, L., Soo, C., Ling, T., Sim, S., Grinang, J., Ganyai, T., & Lee, K. (2018). Physicochemical parameters and fish assemblages in the downstream river of a tropical hydroelectric dam subjected to diurnal changes in flow. *Hindawi International Journal of Ecology*, 2018, 1-9.
- Pope K. L. (2007) Condition. In C. S. Guy & M. L. Brown (Eds.), *Analysis and interpretation of freshwater fisheries data* (pp. 423-471). American Fisheries Society.
- Rosli, N. A. M., & Zain, K. M. (2016). Preliminary assessment on autecological studies of beardless barb, *Cyclocheilichthys apogon* (valenciennes, 1842) from Muda Reservoir of Kedah, Malaysia. *Tropical life sciences research*, 27(supp1), 63-69. <https://doi.org/10.21315/tlsr2016.27.3.9>
- Sarkar, U. K., Khan, G. E., Dabas, A., Pathak, A. K., Mir, J. I., Rebello, S. C., Pal, A., & Singh, S. P. (2013). Length weight relationship and condition factor of selected freshwater fish species found in River Ganga, Gomti and Rapti, India. *Journal of Environmental Biology*, 34, 951-956.
- Sharip, Z., Yusoff, F. M., & Ismail, W. R. (2017). Trophic state characterisation for Malaysian lake. In M. Maghfiroh, A. Dianto, T. Jasalesmana, I. Melati, O. Samir, & R. Kurniawan (Eds.), *The 16th World Lake Conference* (pp. 442-447). Research Center for Limnology, Indonesian Institute of Sciences.
- Zulkafli, A. R., Amal, M. N. A., Shohaimi, S., Mustafa, A., Ghani, A. H., Ayub, S., Hashim, S., Anuar, M. I., & Hasfai, M. P. (2016). Length-weight relationships of 13 fish species from Pahang River, Temerloh District, Pahang, Malaysia. *Journal of Applied Ichthyology*, 32(1), 165-166. <https://doi.org/10.1111/jai.12959>

Review article

Revisiting Solar Photovoltaic Roadmap of Tropical Malaysia: Past, Present and Future

Hedzlin Zainuddin^{1*}, Hazman Raziq Salikin¹, Sulaiman Shaari¹,
Mohamad Zhafran Hussin² and Ardin Manja¹

¹Faculty of Applied Sciences, Universiti Teknologi MARA, 40450 Shah Alam, Selangor, Malaysia

²Faculty of Electrical Engineering, Universiti Teknologi MARA Cawangan Johor, Kampus Pasir Gudang, 81750 Masai, Johor, Malaysia

ABSTRACT

Environmental issues and economic factors such as emission of Greenhouse Gases (GHGs), fossil fuel depletion and fluctuation of oil prices are also the reason behind the utilization of sunlight as a source of energy. Even though with the spread of unprecedented pandemic of COVID 19, the industry of solar photovoltaic (PV) is surviving at a very promising rate compared to the oil industry. Malaysia has a high potential to be successful at harnessing solar energy as this country is located within the equatorial region. The government of Malaysia (GoM) introduced various policies, acts and incentives programs for the purpose of increasing this country's potential to harness solar energy. Along with the efforts, goals and aims have also been set as a benchmark to measure Malaysia's success in utilizing sunlight as an energy source. This study reviews the roadmap programs executed by GoM to elucidate the significant roles played in the development of solar PV starting from a few pilot projects in 1980s until present. The roadmap focuses on incentive

programs namely Feed-in Tariff (FiT), Net Energy Metering (NEM), Self-Consumption Scheme (SELCO), Large Solar Scale (LSS), Supply Agreement with Renewable Energy (SARE) and 'Peer-to-Peer' (P2P), which complement all the projects and solar PV applications in Malaysia. The contributing result of this roadmap is the highlights on the continuous solar PV programs stimulated by GoM, the identification and effort to improve the less performing GoM incentive

ARTICLE INFO

Article history:

Received: 13 January 2021

Accepted: 13 April 2021

Published: 31 July 2021

DOI: <https://doi.org/10.47836/pjst.29.3.25>

E-mail addresses:

hedz1506@uitm.edu.my (Hedzlin Zainuddin)

hazman_raziq@yahoo.com (Hazman Raziq Salikin)

solarman1001@gmail.com (Sulaiman Shaari)

mzhafran@uitm.edu.my (Mohamad Zhafran Hussin)

ardinmanja92@gmail.com (Ardin Manja)

* Corresponding author

programs combined with the positive responses from communities and industries, have laid a strong platform to forecast a promising future of solar PV industry in Malaysia.

Keywords: Feed-in tarif; large solar scale; net energy metering; peer-to-peer; self-consumption scheme

INTRODUCTION

Malaysia's electricity demand is forecasted to rise by 35% in 2030 from 14 007 MW in 2008. The rise in demand for electricity calls for the utilization of renewable energy as an alternative to non-renewable energy sources. Malaysia is blessed with an abundance of renewable energy sources, particularly sunlight. The average annual sum of global horizontal irradiation (GHI) of Malaysia is between 1400 kWh/m² to 1900 kWh/m² (Samaiden, 2020). On top of that, Malaysia receives on average 12 hours of sunlight daily (Aziz et al., 2016; Bakh et al., 2014). Harnessing solar energy for source of sustainable energy can be done by utilising solar photovoltaic (PV) technology (Pacudan, 2018). Through proper policy and encouraging incentives, solar energy potential to become this country's source of sustainable energy can be enhanced (Pacudan, 2016).

Various initiatives have been carried out by the GoM in order to maximize solar energy harnesses (Hussin et al., 2012). In 2000, Fifth Fuel Policy 2000 which included renewable energy as the fifth fuel in the energy mix was introduced during the 8th Malaysia Plan (Bakh et al., 2014; Maulud & Saidi, 2012; Petinrin & Shaaban, 2015). Renewable Energy Act 2011 (Act 725) was introduced by the GoM to implement a special tariff for enhancing the generation and utilization of renewable energy in Malaysia. Feed-in Tariff (FiT) was the tariff highlighted in the act (Sustainable Energy Development Authority, 2011) and was the foundation policy for solar PV in Malaysia (ASEAN Centre for Energy, 2016). The incentive programs were taken very seriously by GoM, hence the incentive programs were introduced under the Ninth and Tenth Malaysia Plan (2011-2015). The programs have stimulated PV systems installations by providing benefits to the applicants.

Four more major programs have been employed consecutively as an effort to harness renewable energy sources in Malaysia namely Net Energy Metering (NEM), Self-Consumption Scheme (SELCO), Large Solar Scale (LSS), Supply Agreement with Renewable Energy (SARE) and 'Peer-to-Peer' (P2P). Besides these five significant and recent programs, there are many more programs successfully executed by GoM in the past; but this study is limited to discuss in-depth of these five programs.

The objective of this paper is to trace the roadmap of solar PV in Malaysia. The roadmap is presented in a timeline, which has been divided into three different categories which are past, present and future. The significance of this study is to forecast the future development of solar PV in Malaysia, acknowledge and encourage the application of best practice mechanisms in promoting solar PV and learn the drawbacks of the less performing incentive programs related to solar PV development.

ROADMAP OF SOLAR PHOTOVOLTAIC (PV)

The roadmap includes the development of solar PV in Malaysia, incentives carried out for facilitating the utilization of solar PV technologies, and any events related to solar PV in Malaysia.

Past

In the 1980s, solar PV applications were first used for rural electrification and to power telecommunications infrastructure. The PV system used was off-grid photovoltaic (OGPV), which required minimum maintenance due to its simple operation (Almaktar et al., 2015). In order to provide electrical energy to rural communities in Malaysia, more rural electrification programs were accepted by the Ministry of Rural Development. Under the initiatives of the Ministry of Energy, Water and Communications (MEWC) and support from the Japanese New Energy and Industrial Technology Development Organization, a pilot project of solar PV was implemented in Marak Parak, Sabah in the year 1995 (Almaktar et al., 2015; Solangi et al., 2011). The project implemented was an OGPV system consisted of 1887 solar panels (Dalimin, 2018).

Chua et al. (2011) mentioned that the Grid-Connected Photovoltaic (GCPV) in Malaysia was first installed in July 1998 in Universiti Tenaga Nasional, having 3.15 kWp capacity. Following the event, British Petroleum (BP) Malaysia installed 8 kWp GCPV at BP petrol station and Universiti Kebangsaan Malaysia (UKM) installed 5.5 kWp GCPV at Solar Energy Research Park. These were three of six pilot projects of GCPV in Malaysia aimed to minimize consumer's electricity bills by reducing the amount of electricity imported from the grid (Almaktar et al., 2015; Ruoss, 2007).

Ruoss (2007) stated that the first house to have Building Integrated Photovoltaic (BIPV) installed was the home of Tenaga Nasional Berhad (TNB) senior officer's house in Port Dickson with 3.15 kWp capacity in August 2000. The second BIPV was installed at a house in Shah Alam in November 2000 with a capacity of 3.24 kWp. In November 2001, another BIPV with a capacity of 2.8 kWp was installed in Subang Jaya (Mekhilef et al., 2012; Ruoss, 2007). These three BIPV home installations were the continuity of the GCPV



Figure 1. Port Dickson, Shah Alam and Subang Jaya first home installed BIPV (Haris et al., 2003)

pilot project in Universiti Tenaga Nasional, BP petrol station and Solar Energy Research Institute (SERI). Figure 1 shows the image of the first three home installed BIPV system.

Under the 8th Malaysia Plan (2001-2005), Fifth Fuel Policy was implemented in 2000 to introduce renewable energy as a part of the energy mix (Chua & Oh, 2012). The implementation of this policy was driven by the increase of oil price and depletion of fossil fuel (Maulud & Saidi, 2012; Petinrin & Shaaban, 2015). Small Renewable Energy Program (SREP) was launched in 2001 with an aim to make renewable energy sources contribute to 5% of electricity generation (Malaysian Building Integrated Photovoltaic Project Team, 2006). Unfortunately, only 0.3% of electricity was contributed from renewable energy sources by 2005 (Spicher et al., n.d).

Along with the 9th Malaysia Plan (2006-2010), a Five-year project called Malaysian Building Integrated Photovoltaic (MBIPV) was launched on 25 July 2005. The MBIPV project aimed to provide an encouraging environment of BIPV application in Malaysia so that solar energy uptake can be intensified (Almaktar et al., 2015; Petinrin & Shaaban, 2015). Consequently, dependency on fossil fuels as a source of energy can be reduced. Under MBIPV, a program Suria1000 was launched on 22nd June 2007 as a financial incentive to aid the MBIPV project (Mekhilef et al., 2012).

Present

National Renewable Energy Policy and Action Plan (NREPAP) was launched in April 2011. This policy was also included in the 10th Malaysia Plan (2011-2015) (Almaktar et al., 2015). Under the 10th Malaysia Plan, FiT was introduced as an incentive to increase renewable energy utilization (Chua et al., 2011). The mechanism of FiT is investors are rewarded upon electricity generation. The FiT was quite desirable because the program was a business opportunity as it encourages the export of electricity generated to the grid. The benefits of FiT are guaranteed payment, consumers have access to the grid and the creation of jobs (Pacudan, 2018). According to Bakh et al. (2014), 8% of yearly degression is very discouraging to investors. Table 1 shows the FiT rates after the yearly 8% degression rate and also the details of bonus FiT rates for Solar PV installations (Sustainable Energy Development Authority, 2012):

11th Malaysia Plan covers the time span of 2016 until 2020. In 2017, FiT was no longer an incentive program for solar PV but limited to biomass, wind and small hydro (Chen et al., 2018). Three new incentive programs were introduced under the 11th Malaysia Plan which are NEM, SELCO and LSS (Ahmad, 2019a).

Net Energy Metering (NEM). NEM was introduced to replace FiT. The concept of NEM is consumer utilise the electricity generated from solar PV and export the excess energy generated to the grid to be sold to utility (Sustainable Energy Development Authority, 2017).

Table 1

FiT rates for solar PV (21 years from FiT commencement date) (Sustainable Energy Development Authority, 2012)

Basic rates according to installed capacity	FiT rate (RM)		
	2012	2013	2014
Installed capacity up to and including 4 kWp	1.23	1.1316	1.0411
Installed capacity above 4 kWp and up to and including 24 kWp	1.20	1.1040	1.0157
Installed capacity above 24 kWp and up to and including 72 kWp	1.18	1.0856	0.9988
Installed capacity above 72 kWp and up to and including 1 MWp	1.14	1.0488	0.9649
Installed capacity above 1 MWp and up to and including 10 MWp	0.95	0.8740	0.8041
Installed capacity above 10 MWp and up to and including 30 MWp	0.85	0.7820	0.7194
Bonus FiT rates according to the following criteria (one or more)	2012	2013	2014
Use as installation in buildings or building structures	+0.2600	+0.2392	+0.2201
Use as building materials	+0.2500	+0.2300	+0.2116
Use of locally manufactured or assembled solar PV modules	+0.0300	+0.0276	+0.0254
Use of locally manufactured or assembled solar PV inverters	+0.0100	+0.0092	+0.0085

Instead of being paid for gross electricity generated as in FiT, consumers are paid based on the net energy generated (Razali et al., 2019). However, due to its poor financial return of RM 0.31/kWh for low voltage PV (below 1 kV), NEM that was initially introduced in 2016 failed miserably (Sustainable Energy Development Authority, 2020). To fix the flaw of NEM, the GoM introduced a new NEM in January 2019 in which excess energy is exported to the grid on a one-on-one offset basis (same gazetted tariff, *GT*). The mechanism of the new NEM is calculated based on Net Charge Amount (NCA). NCA is expressed as Equation 1 (Ahmad, 2019b):

$$NCA = (z \times GT) - (y \times GT) \quad [1]$$

Whereby,

z = energy imported

y = energy exported

Application of solar PV under NEM is open to broader types of consumer, which are domestic, commercial, agricultural and industrial consumer. The cumulative net metered rooftop solar capacity, increased by 7.8 times from the first three years of the new version of NEM implementation (The Malay Mail, 2020). A study was also conducted to compare the previous and present NEM. The study found that the new NEM is more cost saving for most large and medium consumers excluding small scale consumers (Razali et al., 2019). Figure 2 shows the significant increase in cumulative net metered rooftop solar capacity after 11 months of new NEM implementation (Bhambhani, 2020).

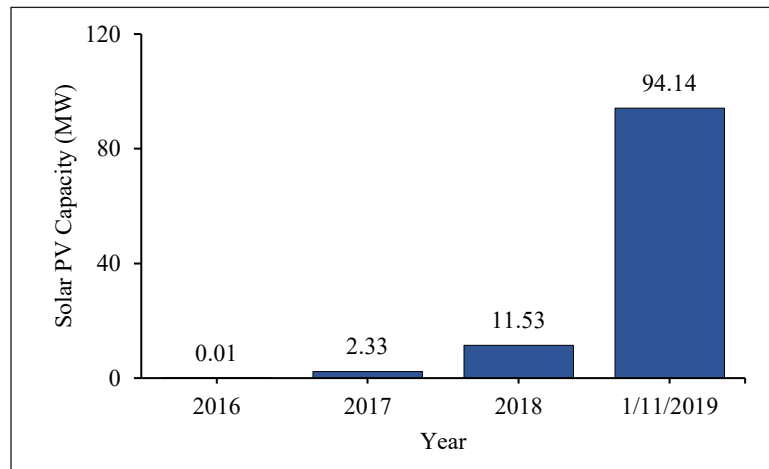


Figure 2. Cumulative net metered rooftop solar PV capacity in Malaysia (Bhambhani, 2020)

Self-Consumption (SELCO). Self-consumption (SELCO) is a scheme in which consumers generate electricity from solar PV for their own consumption that cannot be exported to the grid (Ahmad, 2019b; Chen et al., 2018). Solar PV installed under the SELCO scheme can be on-grid or off-grid. If it is on-grid, the capacity limit is 75% of the maximum demand of the existing installation, meanwhile for off-grid type there is no capacity limit. According to Chiew (2019), excess energy generated under the SELCO scheme goes to waste. The participants for the SELCO scheme are limited to only individual and commercial premise consumers (Ahmad, 2019b). Under the SELCO scheme, a private generating license is compulsory for the system beyond 72kW (Sustainable Energy Development Authority, 2017). By the end of 2018, the total capacity recorded under the SELCO scheme was 60 MW (Chen et al., 2018).

Large Solar Scale (LSS). Large Solar Scale (LSS) is a bidding program to lower the levelized cost of energy (LCOE) for LSS PV plant development (Samaiden, 2020). This incentive program is for a local company with a minimum of 51% equity interest. Chen et al. (2018) stated that besides NEM, LSS is also reported to be the main driver of solar PV markets in Malaysia contributing to gigawatt worth of solar potential in Malaysia. In 2016, the first LSS tender achieved an aggregate capacity of 200 MW and 60 MW in Peninsular Malaysia and Sabah respectively (Energy, 2019). The increased aggregate capacity of 360 MW for Peninsular Malaysia and 100 MW for Sabah was achieved in the second tender in 2017. The third LSS bidding opened in February 2019 targeted 500 MW of aggregate capacity and waiting to be commissioned in 2021. Post COVID-19 has strengthened Malaysia's solar PV industry with the announcement of the fourth LSS with a targeted capacity of one gigawatt. This fourth cycle is expected to be operating by end of 2023 (NST Business, 2020).

Supply Agreement with Renewable Energy (SARE). Supply Agreement with Renewable Energy (SARE) was announced by GoM on 18th October 2018 and the mechanism started on the 1st January 2019. SARE aims to transform Malaysia's energy landscape to be greener. This act involves three parties which are prosumer, asset owner or investor and utility provider. The advantage of SARE is the zero upfront cost when installing a GCPV system. There are three types of solar solution under SARE, which are solar Power Purchase Agreement (PPA), Solar Hybrid and Solar Lease. Both Solar PPA and Solar Lease can enjoy zero upfront cost but not for a solar hybrid which requires approximately 20% contribution. These three types will also differ in terms of the contract term, solar tariff rate, installment and metering requirement (Tenaga Nasional Berhad, 2020). Nevertheless, the uncertainty in the trading is still significant to study and to find ways of mitigation in strengthening the programs and making it more financially attractive.

Peer-to-peer (P2P). Peer-to-peer (P2P) energy trading is introduced by GoM to increase the momentum of the community to produce green energy. The pilot run of P2P took place in November 2019 in two phases; 'Alpha run' and 'Beta run'. Malaysia is the second country in ASEAN to execute P2P after Thailand (Sustainable Energy Development Authority, 2019). P2P mechanism allows a consumer who generates green energy via NEM and has surplus energy to sell the surplus to other consumers. The consumer with the surplus of green energy is called 'prosumers'. The bridge between the prosumers and customers is the utility grid, which is the TNB grid in Peninsular Malaysia. The bridge cost has to be taken into account in calculating the economic return.

This scheme enables the prosumer to sell green energy to other consumers of higher tariff (tariff B) at an estimated profit of 10% higher than the production cost of the green energy. On the other hand, the consumer can enjoy an estimated 11% saving from this trade. Since the program is still in the pilot run stage, a reliable forecast of the economic return of this program is still debated. One of the drawbacks is on the untraded energy; is it a condition when the amount of surplus energy is greater than the traded energy. A pilot run involved up to 5 prosumers and up to 8 consumers employing 'regulatory sand box' was conducted in Malaysia with the involvement of multiple bodies including GoM (Sustainable Energy Development Authority, 2019). In this study, an analysis of the result from the pilot run was conducted and Figure 3 shows the percentage of untraded energy during the pilot run from November 2019 to June 2020. The minimum, median and maximum untraded energy were 4%, 18.5% and 54% respectively. It is significant to notify that maximum untraded energy was in March 2020 during the Movement Control Order (MCO) due to the unprecedented pandemic COVID-19 in Malaysia, where the majority of industries, which represents the consumers were shut down. This is one of the identified drawbacks of this program, which the untraded energy is a bonus to the utility company and not pleasant to the prosumers.

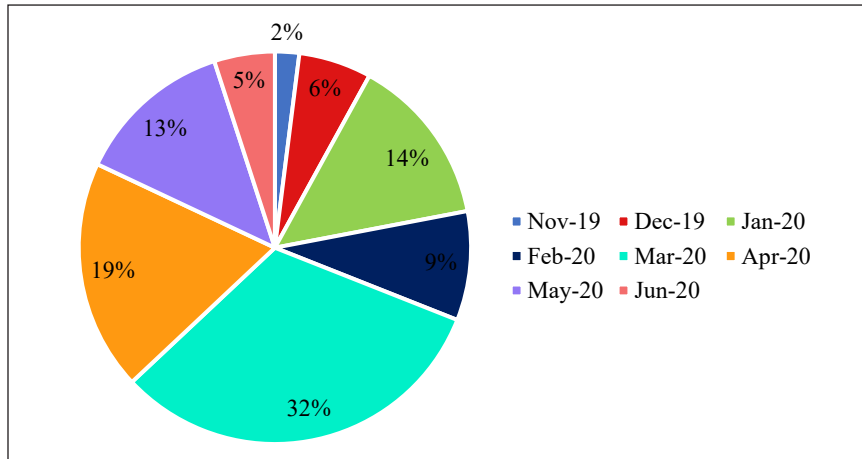


Figure 3. Percentage of untraded energy during P2P pilot run from November 2019 to June 2020

Future

The way forward of the Solar PV roadmap is forecasted to be very promising when the GoM has positioned two solar PV initiatives under the Ministry of Energy, Science, Technology and Environment Malaysia (MESTECC) in the ‘The eleventh Malaysia Plan’ (RMK11). The two initiatives are extending access to basic infrastructure in providing electricity by applying solar PV together with micro and pico hydro in the remote area, and ensuring solar PV contribution in renewable energy electricity generation by executing big scale program (LSS) and net energy metering (Kementerian Hal Ehwal Ekonomi, 2018). Even though RMK 11 has just ended, the GoM announcement of the target to achieve 20% of renewable energy contribution in the energy mix by the year 2025 continues to keep the solar PV industry at high momentum (Choong, 2019). Hence, Malaysia is also said to harness solar power up to 17 075 MW solar capacity by the year 2030. Consequently, this will contribute to 11.4% of the energy mix in Malaysia (Bhambhani, 2016). Figure 4 shows the Malaysia PV target from 2020 until 2030. The effort of GoM in keeping the future of solar PV has also proven with the new initiative of the Renewable Energy Transition Roadmap 2035 (RETR), which will help in strategizing to achieve 20% of renewable energy contribution in the energy mix by the year of 2025 (Kementerian Tenaga dan Sumber Asli, 2021).

The trend that portrays the bright future of solar PV as a promising sector is also observed when one of the GoM programs, which is LSS4 has attracted 138 bidders. This program of LSS4 as described in the previous section will eventually create job opportunities for approximately 12, 000 people (Yee, 2021).

Furthermore, one of the major and dominant players of energy providers in Malaysia, Tenaga Nasional Berhad (TNB) is also seen to be progressing very fast through their

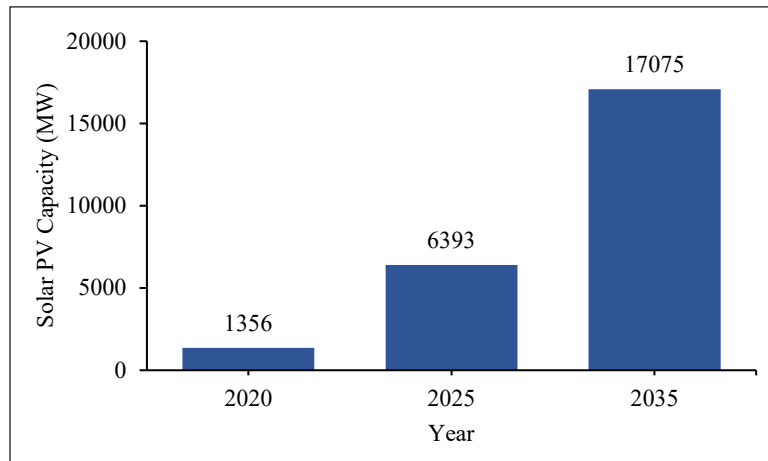


Figure 4. Malaysia Solar PV Capacity Target (Bhambhani, 2016)

investment and involvement in the Solar PV sector. The GoM initiatives together with the positive acceptance of the industry players depict and interpret the bright future of solar PV in Malaysia.

CONCLUSION

Malaysia has a high potential to succeed in harnessing solar energy due to its location that provides almost consistent high solar irradiation all year round with slight monthly variation. Environmental issues and economic factors should be the main driver for harnessing solar energy because harnessing unlimited energy can reduce dependency on non-renewable energy sources such as fossil fuel and yet provide a worthy financial return to investors. The GoM has been doing a great job in continuously upgrading flawed incentive programs to maximize this country's potential to harness solar energy. Finally, the most effective program would be the one that provides the highest financial return to its investor. The solar PV road map in Malaysia has witnessed the success of solar PV development and proven the role of the GoM in keeping the solar PV momentum to become a promising energy sector in Malaysia.

ACKNOWLEDGMENTS

The authors express gratitude to GoM for funding this research under 600-IRMI/FRGS 5/3 (446/2019) and 600-IRMI/FRGS 5/3 (083/2019).

REFERENCES

- Ahmad, A. (2019a). *Briefing by the Sustainable Energy Development Authority*. Sustainable Energy Development Authority (SEDA) Malaysia. Retrieved mJuly 8, 2020, from <http://www.massa.net.my/mimos/>

- Ahmad, A. (2019b). *Briefing on the new NEM, Introduction to self-consumption (SELCO) and RPVI directory application*. Retrieved July 8, 2020, from <http://www.seda.gov.my/download/presentation-materials/>
- Almaktar, M., Rahman, H. A., Hassan, M. Y., & Omar, W. Z. W. (2015). Photovoltaic technology in Malaysia: Past, present, and future plan. *International Journal of Sustainable Energy*, 34(2), 128-140. <https://doi.org/10.1080/14786451.2013.852198>
- Asean Centre for Energy. (2016). Levelized cost of electricity of selected renewable technologies in the ASEAN member states. In *ASEAN Centre for Energy*. Retrieved July 8, 2020, from https://tuewas-asia.org/wp-content/uploads/2017/05/4-ASEAN-RESP_LCOE-final-Nov-2016.pdf
- Aziz, A., Dewi, P., Wahid, S. S. A., Arief, Y., & Aziz, N. (2016). Evaluation of solar energy potential in Malaysia. *Trends in Bioinformatics*, 9, 35-43. <https://doi.org/10.3923/tb.2016.35.43>
- Bakh, B., Saadatian, O., Alghoul, M., Ibrahim, Y., & Sopian, K. (2014). Solar electricity market in Malaysia: A review of feed-in tariff policy. *Environmental Progress & Sustainable Energy*, 34(2), 600-606. <https://doi.org/10.1002/ep.12023>
- Bhambhani, A. (2016). *Net metering in Malaysia*. Retrieved July, 8, 2020, from <http://taiyangnews.info/markets/net-metering-in-malaysia/>.
- Bhambhani, A. (2020). *108 MW: Malaysia's net metered PV capacity till Nov 2019*. Retrieved July, 8, 2020, from <http://taiyangnews.info/markets/108-mw-malysias-net-metered-pv-capacity-till-nov-2019/>.
- Chen, W., Han, T. W., Damiri, N. A., & Zaki, N. H. M. . (2018). *National survey report of PV power applications in Malaysia 2018*. Retrieved July, 8, 2020, from https://iea-pvps.org/wp-content/uploads/2020/01/NSR_Malaysia_2018.pdf
- Chiew, S. (2019). *Types of solar power systems in Malaysia*. Retrieved July, 8, 2020, from <https://solarvest.my/2018/08/15/types-solar-power-systems/>
- Choong, J. (2019). Yeo: Malaysia aiming for 20pc renewable energy use by 2025. *The Malay Mail*. Retrieved July, 8, 2020, from <https://www.malaymail.com/news/malaysia/2019/09/03/yeo-malaysia-aiming-for-20pc-renewable-energy-use-by-2025/1786768>
- Chua, S. C., & Oh, T. (2012). Solar energy outlook in Malaysia. *Renewable and Sustainable Energy Reviews*, 16, 564-574. <https://doi.org/10.1016/j.rser.2011.08.022>
- Chua, S. C., Oh, T. H., & Goh, W. W. (2011). Feed-in tariff outlook in Malaysia. *Renewable and Sustainable Energy Reviews*, 15(1), 705-712. <https://doi.org/10.1016/j.rser.2010.09.009>
- Dalimin, M. (2018). *Creating electricity from sunlight: Progress in science, technology and development of photovoltaics*. Retrieved July, 8, 2020, from <http://www.uthm.edu.my/en/downloads/e-books/86-2018siri3-nohdalimin/file>
- Energy, G. (2019). *Malaysia renewable energy 2025: Private financing key to reaching target*. Retrieved July 8, 2020, from <https://www.power-technology.com/comment/malaysia-needs-us8-billion-investment-to-achieve-20-renewable-energy-target-by-2025/>
- Haris, A. H., Ismail, I. S. S., & Penyelidikan, K. I. (2003). *Building integrated photovoltaic (BIPV) applications in malaysia: Current status & achievements*. TNB Research Sdn Bhd.

- Hussin, M. Z., Hasliza, N., Yaacob, A., Zain, Z. M., Omar, A. M., & Shaari, S. (2012). A development and challenges of grid-connected photovoltaic system in Malaysia. In *2012 IEEE Control and System Graduate Research Colloquium* (pp. 191-196). IEEE Conference Publication. <https://doi.org/10.1109/ICSGRC.2012.6287160>
- Kementerian Hal Ehwal Ekonomi. (2018). *Pelan pelaksanaan dasar: Kajian separuh penggal Rancangan Malaysia Kesebelas 2016-2020* [Implementation policy plan: The mid-term review of the eleventh Malaysia plan 2016-2020.]. Retrieved March 9, 2021, from <https://www.kkmm.gov.my/pdf/KPI/PPD%20KSP.pdf>
- Kementerian Tenaga dan Sumber Asli. (2021). *Bahagian tenaga boleh baharu* [Renewable energy section]. Retrieved March 9, 2021, from <https://www.ketsa.gov.my/ms my/MengenaiKetsa/MaklumatBahagian/Pages/BahagianTenagaBolehBaharu.aspx>
- Maulud, A. L., & Saidi, H. (2012). The Malaysian fifth fuel policy: Re-strategising the Malaysian renewable energy initiatives. *Energy Policy*, *48*, 88-92. <https://doi.org/10.1016/j.enpol.2012.06.023>
- Mekhilef, S., Safari, A., Mustafa, W. E. S., Saidur, R., Omar, R., & Younis, M. A. A. (2012). Solar energy in Malaysia: Current state and prospects. *Renewable and Sustainable Energy Reviews*, *16*(1), 386-396. <https://doi.org/10.1016/j.rser.2011.08.003>
- Malaysian Building Integrated Photovoltaic Project Team. (2006). *Inception report: Malaysia building integrated photovoltaic technology application (MBIPV) project*. Retrieved July 8, 2020, from <https://www.yumpu.com/en/document/read/43136959/inception-report-malaysia-building-integrated-mbipv-project>
- NST Business. (2020). Malaysia opens RM4 bil bid for 1GW of solar plants. *New Straits Times*. Retrieved July 8, 2020, from <https://www.nst.com.my/business/2020/06/598704/malaysia-opens-rm4-bil-bid-1gw-solar-plants>
- Pacudan, R. (2016). Road map for power market integration in the Brunei-Indonesia-Malaysia-Philippines (BIMP) Region. In Y. Li & S. Kimura (Eds.), *Achieving an integrated electricity market in Southeast Asia: Addressing the economic, technical, institutional, and geo-political barriers*. ERIA Research.
- Pacudan, R. (2018). Feed-in tariff vs incentivized self-consumption: Options for residential solar PV policy in Brunei Darussalam. *Renewable Energy*, *122*, 362-374. <https://doi.org/10.1016/j.renene.2018.01.102>
- Petinrin, J. O., & Shaaban, M. (2015). Renewable energy for continuous energy sustainability in Malaysia. *Renewable and Sustainable Energy Reviews*, *50*, 967-981. <https://doi.org/10.1016/j.rser.2015.04.146>
- Razali, A., Abdullah, M. P., Hassan, M. Y., & Hussin, F. (2019). Comparison of new and previous net energy metering (NEM) scheme in Malaysia. *ELEKTRIKA- Journal of Electrical Engineering*, *18*, 36-42. <https://doi.org/10.11113/elektrika.v18n1.141>
- Ruoss, D. (2007). *Equatorial sunshine: The Malaysia BIPV programme - Renewable energy world*. Retrieved July 1, 2020, from <http://www.renewableenergyworld.com/articles/print/volume-10/issue-1/solar-energy/equatorial-sunshine-the-malaysia-bipv-programme-51560.html>
- Samaiden. (2020). *Large scale solar (LSS)*. Retrieved July 1, 2020, from <https://samaiden.com.my/solar-photovoltaic/#lss>

Environmental Assessment of Groundwater Quality for Irrigation Purposes: A Case Study Of Hillah City In Iraq

Zaid Abed Al-Ridah¹, Ahmed Samir Naje^{1*}, Diah Fliah Hassan ¹ and Hussein Ali Mahdi Al-Zubaid ²

¹College of Water Resources Engineering, Al-Qasim Green University, Babylon, Iraq

²Department of Environmental Engineering, College of Engineering, University of Babylon, Babylon, Iraq

ABSTRACT

This study was conducted to evaluate the groundwater quality of wells located around the Hillah city of Iraq, for the purposes of determining its suitability as water for agricultural irrigation, according to the Irrigation Water Quality Index (IWQI). The number of wells that are being investigated was 24. The spatial distribution of water quality parameters was investigated using ArcGIS software. Ten parameters were established for the dry and wet seasons of 2018 and 2019, which include pH, electric conductivity (EC), total dissolved solids (TDS), calcium, potassium, magnesium, bicarbonate, sodium, chloride and sulfuric. The results showed that all pH and sodium absorption ratio values were within the allowable limits. About 69%, and 75% electric conductivity, total dissolved solids, values respectively were higher than the allowable limits. Most values of positive and negative ions were higher than the allowable limits. In 2018, the water quality of (4%) of wells number was classified as moderate restriction and approximately 96% was poor quality in dry season, while the IWQI was enhanced in the wet season. In 2019, the quality of water was dropped as most of the water quality was classified as severe restriction and few in the high restriction for the dry season. These values were increased in the wet season

due to the freshwater dilution effect. Water quality index show that a large percentage of the wells have poor water quality leads to severe restriction for irrigation requirements and need relatively high permeability soils and salt-resistant plants.

ARTICLE INFO

Article history:

Received: 08 December 2020

Accepted: 01 April 2021

Published: 31 July 2021

DOI: <https://doi.org/10.47836/pjst.29.3.10>

E-mail addresses:

zaidalmnsory@yahoo.com (Zaid Abed Al-Ridah)

ahmednamesamir@yahoo.com (Ahmed Samir Naje)

diaafliah@wrec.uoqasim.edu.iq (Diah Fliah Hassan)

alzubaidih10@gmail.com (Hussein Ali Mahdi Al-Zubaid)

* Corresponding author

Keywords: Groundwater, irrigation, spatial distribution, water quality index, wells

INTRODUCTION

Water is an important source of life for human societies and other living creatures (Al-Ridah et al., 2020). Geographically, Iraq is one of the Middle Eastern countries that suffer from a semi-arid climate. The main source of water in Iraq is the Tigris and Euphrates rivers, whose water sources are from Turkey. Recently, and specifically since 1990, Turkey started construction of the GAP “Southeastern Anatolia Project “project, which consists of 24 dams and led to a significant decrease in the water supply to Iraq (Al-Mohammed & Mutasher, 2013). Therefore, it is necessary to search for an additional source that reduces the lack of water revenues for the country. Groundwater is one of the most important other alternative water sources that are used for various purposes, including irrigation, drinking, and industry (Abdullah et al., 2015). When groundwater gets polluted, it becomes difficult to get rid of pollution even when it is stopped from its source. Therefore, assessing groundwater quality for different purposes is necessary. The Water Quality Index (WQI) is used in terms of numbers to assess the quality of water to be used for any purpose (Mahmood et al., 2013). The Water Quality Index (WQI) is an effective way to classify, manage, and define groundwater quality as a single parameter. It measures water quality for multiple purposes (drinking, irrigation, and industries) by converting a set of water quality variables into a single value to determine the water quality in general (Boateng et al., 2016). WQI is a mathematical model used to convert water quality variables into a single value that represents the water quality level for a specific place and time (Gidey, 2018). The city of Hilla is characterized as an agricultural city with a high density, which requires large quantities of irrigation water. These quantities are mostly prepared from the Euphrates river and its branches in the city. Also, due to the low water imports, as mentioned above, groundwater is used in different places of the region to supply water to plants for agricultural lands around the city or for public and private gardens within the city. Therefore, the objective of current study is to investigate the suitability of groundwater in the region for the purpose of irrigation requirements using the irrigation water quality index (IWQI) and to make a spatial distribution of water quality elements to obtain a map of the quality of groundwater in the Hilla city.

MATERIALS AND METHOD

Area of the Study

The city of Hillah is in the center of Iraq. The main source of irrigation and drinking water is the Euphrates River and its multiple branches. About 24 shallow wells in the area were dug in unconfined aquifer as shown in detail in Table 1 and as shown by its spatial distribution according to Figure 1. The studied area covers about 80 by 40 Km and its climate is characterized by being hot, dry in summer, cool and less rainy in winter (Al-Dabbas & Al-Ali, 2016). Its soil is alluvial clay, sandy soils and containing on organic matter with

Table 1
Depth and location of wells

No.	1	2	3	4	5	6	7	8	9	10	11	12
Depth (m)	12	9	10	12	9	7	14	10	12	10	12	9
X	44.432	44.420	44.400	44.396	44.393	44.541	44.571	44.469	44.464	44.577	44.395	44.377
Y	32.483	32.462	32.406	32.398	32.449	32.546	32.657	32.627	32.621	32.577	32.645	32.640
No.	13	14	15	16	17	18	19	20	21	22	23	24
Depth (m)	12	10.5	12	12	10	9	11	9	9	9	9	7.5
X	44.430	44.465	44.372	44.428	44.381	44.364	44.343	44.668	44.873	44.950	44.990	44.905
Y	32.673	32.302	32.209	32.251	32.349	32.380	32.467	32.399	32.448	32.488	32.533	32.321

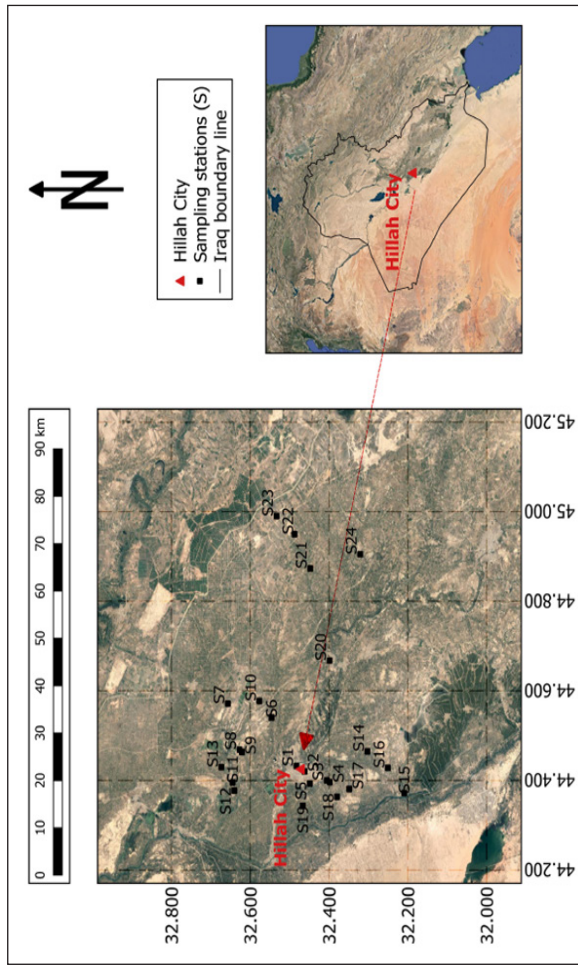


Figure 1. The area of the study

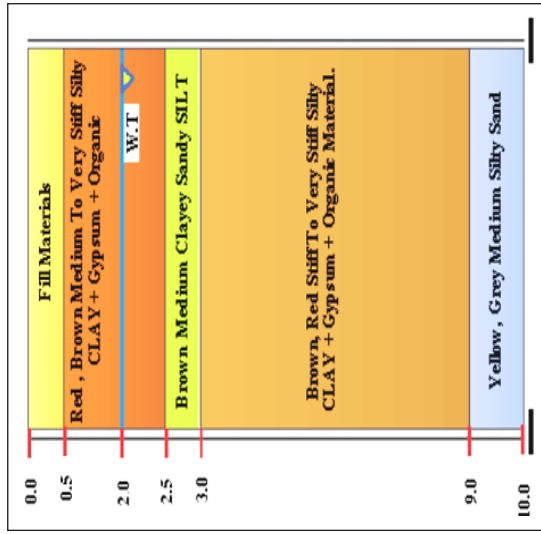


Figure 2. Soil profile of the study area adopted from Chabuk et al. (2017)

soft and weak cohesion properties due to relatively high levels of groundwater in most of its regions as shown in Figure 2 (Al-Khaqani, 2006; Al-Zubaydi et al., 2016; Chabuk et al., 2017). Tests were conducted for the water produced from it for the dry seasons (July) and wet seasons (January) and for two consecutive years (2018-2019). The study includes ten water quality parameters which are pH, Total Dissolved Solids (TDS), Electric Conductivity (EC), Calcium (Ca^{2+}), Potassium (K^+), Magnesium (Mg^{2+}), Bicarbonate (HCO_3^-), Sodium (Na^+), Chloride (Cl^-), Sulfuric (SO_4^-). The standard methods are used in the laboratory to test water quality parameters and to calculate the water quality index for the region.

Irrigation Water Quality Index (IWQI)

To assess the quality of groundwater in Hillah city to determine their suitability for irrigation purposes, IWQI was used (Meireles et al., 2010). In this method and for the purpose of calculating the relative weight, the estimated values for each parameter (which should be used) must be from the irrigation water quality data according to the University of California Consultation Committee (UCCC), Ayers and Westcot (1999), and Abbasnia et al. (2018).

The first step to build a model is to determine the influencing and controlling elements of the water quality used for irrigation. The elements (EC, Na^+ , Cl^- , and HCO_3^-), as well as the sodium absorption ratio SAR, were considered because they had the greatest influence on IWQI, as stated in Meireles et al. (2010). The second step is to determine the measurement values for the water quality (q_i) based on Table 2 according to Ayers and Westcot (1985), the values of (q_i) are calculated from Equation 1:

$$q_i = q_{\max} - \left[\frac{(x_{ij} - x_{\text{inf}})}{x_{\text{amp}}} \times q_{\text{imap}} \right] \quad (1)$$

Where:

q_i : limiting values parameter for quality measurement.

q_{imax} : maximum value of q_i for the class.

x_{ij} : observed parameter value.

x_{inf} : equivalent value to the lower limit of the class to which the parameter belongs.

q_{iamp} : class amplitude.

x_{amp} : class amplitude to which the parameter belongs.

For calculating the value (x_{amp}) of the last class in Table 2 for each element, the upper limit was considered equal to the highest value calculated in the analysis of water quality data. The cumulative weight (w_i) is calculated according to Majeed et al. (2016) from Table 3 where the values of (w_i) are normalized and therefore when combined they are equal to 1.

The water quality index is calculated from the following Equation 2:

$$\text{IWQI} = \sum_{i=1}^n q_i w_i \quad (2)$$

Where (IWQI) is the irrigation water quality index and it is a non-dimensional value between 0 and 100. For any sample, the higher value of (IWQI) gives the best quality of water according to Table 4 (Bernardo, 1995; Holanda & Amorim, 1997).

Table 2
Water quality measurement (q_i) parameter limiting value adopted from Ayers & Westcot (1985)

q_i	EC ($\mu\text{s/cm}$)	SAR (meq/L) ^{0.5}	Na ⁺ (meq/L)	Cl ⁻ (meq/l)	HCO ₃ ⁻ (meq/l)
85-100	200≤EC<750	SAR<3	2≤Na<3	Cl<4	1≤HCO ₃ <1.5
60-85	750≤EC<1500	3≤SAR<6	3≤Na<6	4≤Cl<7	1.5≤HCO ₃ <4.5
35-60	1500≤EC<3000	6≤SAR<12	6≤Na<9	7≤Cl<10	4.5≤HCO ₃ <8.5
0-35	EC<200 or EC≥3000	SAR≥12	Na<2 or Na≥9	Cl≥10	HCO ₃ <1 or HCO ₃ ≥8.5

Table 3
IWQI parameters weights (w_i) adopted from Majeed et al. (2010)

Parameters	w_i
EC	0.211
Na ⁺	0.204
HCO ₃ ⁻	0.202
Cl ⁻	0.194
SAR	0.189
Total	1

Table 4
Irrigation water quality index features adopted from Bernardo (1995) and Holanda and Amorim (1997).

WQI	Water use restrictions	Recommendation	
		Soil	Plant
85-100	No restriction (NR)	It can be used for most soils with a low potential to cause salinity and sodium problems, and filtration is recommended within irrigation practices, except for soils with very low permeability.	There are no toxic risks for most plants
70-85	Low restriction (LR)	It is recommended for use on irrigated soils with light texture or moderate permeability, and salt filtering is recommended. Soil sodium may occur in soils with heavy texture, and it is recommended to avoid their use on soils with high clay levels of 2: 1.	Avoid plants that are sensitive to salt
55-70	Moderate restriction (MR)	It can be used on soils with medium to high permeability values, while suggesting moderate salt leaching.	Plants with moderate salt tolerance can be grown.

Table 4 (continue)

WQI	Water use restrictions	Recommendation	
		Soil	Plant
40-55	High restriction (HR)	It can be used on soils with high permeability without compact layers. A high frequency irrigation schedule should be adopted for water with an EC higher than 2.000 dS m-1 and SAR above 7.0.	It should be used to irrigate plants with medium to high salt tolerance with special salinity control practices, with the exception of water with low values of sodium, chloride, and HCO ₃ .
0-40	Severe restriction (SR)	Its use for irrigation should be avoided under normal conditions. In special cases, they may be used occasionally. Water with low levels of salt and a high specific absorption rate requires the application of gypsum. In soils with high salt content, the soil should be of high permeability, and excess water should be used to avoid salt accumulation.	Only plants with high salt tolerance, except for water with very low values of Na, Cl and HCO ₃

Note: SR – severe restriction; HR – high restriction; MR – moderate restriction; LR – no restriction.

RESULTS AND DISCUSSION

Water Quality Parameters and Spatial Distribution

The statistical parameters represented by the mean and standard deviation (SD) of the ten water quality parameters are presented in Table 5. It is noted that the mean rate in the dry season of the concentration of most water quality data exceeds the mean in the wet season for the same year due to the dilution process during high levels of water in the wet season (Hassan et al., 2017). Using the program (ArcGIS) and by taking advantage of interpolation and drawing the spatial distribution on the map of the region under study for the average concentration of the ten water quality parameters, which includes the locations of wells numbered from 1 to 24 as shown in Figures 3 and 4.

pH Effect. pH is affected by dissolved salts in groundwater such as carbonates, bicarbonate, silicates, fluorides, and other salts in the dissociated form. High values (pH) indicate the presence of sodium and low values reflect the presence of free acids in water (Kushwah et al., 2012). The spatial distribution shows that the values of the (pH) are closely related and rise in the southern part (well 14 and 20) and the northwestern (well 11, 12, and 19). It decreases in the eastern part (well 20, 22 and 24) and the northern (well 10 and 7) on the map. The amount of the value of (pH) ranges from 7.01 to 7.93 with an average value of 7.32. These values are all within the parameters of the Food and Agriculture Organization (FAO) (6.5-8.5) (Ayers & Westcot, 1999).

Electrical Conductivity (EC) Effect. EC is a good indicator for measuring the amount of dissolved solids in groundwater; therefore, it is used to detect pollutants in water. Through

Table 5
Statistical parameters of water quality data.

Year & season	Parameter	pH	EC (µs/cm)	TDS (mg/L)	K (mg/L)	Na (mg/L)	Mg (mg/L)	Ca (mg/L)	Cl (mg/L)	SO4 (mg/L)	HCO3 (mg/L)	SAR
2018 Dry	Min.	7.11	1518	1220	0.975	208.84	20.16	43.4	157.85	113	106.3	2.32
	Max.	7.77	10190	8021	124.8	736	133	250	1200	866	955	8.82
	Mean	7.28	5158.17	3746.33	42.60	421.94	63.51	128.74	662.65	545.88	527.90	5.57
	SD	0.17	2796.21	1995.23	43.84	145.15	35.33	57.68	239.48	235.23	226.49	1.67
2018 Wet	No. of samples	24	24	24	24	24	24	24	24	24	24	24
	Min.	7.01	900	621	1	68	20	39	159	96	90	1.15
	Max.	7.71	8310	6956	91	502	125	195	856	655	704	7.04
	Mean	7.34	3323.58	2702.04	26.51	294.92	57.00	103.55	422.88	353.94	329.54	4.10
2019 Dry	SD	0.21	2193.36	1670.43	30.33	137.73	31.24	40.47	196.77	164.38	167.90	1.67
	No. of samples	24	24	24	24	24	24	24	24	24	24	24
	Min.	7.07	1688	1430	2.2	208.84	50	111	302	520	208	1.76
	Max.	7.93	6570	5300	80	575	188	366	800	1412	676	5.32
2019 Wet	Mean	7.32	4025.58	3062.88	44.51	416.63	130.88	245.67	571.06	987.08	458.72	3.81
	SD	0.21	1421.23	1068.83	25.73	103.93	41.14	74.21	121.19	257.64	124.15	0.81
	No. of samples	24	24	24	24	24	24	24	24	24	24	24
	Min.	7.09	1628	1723	2	128	5.16	17.6	181	295.68	181	1.49
2019 Wet	Max.	7.91	6120	4116	66	580	159	360	781	1290	551	18.15
	Mean	7.34	3839.88	2656.67	22.93	357.71	65.81	138.72	452.08	719.07	342.96	5.23
	SD	0.24	1219.53	681.90	19.59	135.49	44.72	87.82	189.73	285.10	114.41	3.17
	No. of samples	24	24	24	24	24	24	24	24	24	24	24

measuring electrical conductivity, one can gain the concentration of salts and mineral substances in groundwater (Deshmukh, 2013). Noting the spatial distribution of (EC), their values are high in the eastern parts (wells 20, 21, 22, and 24), the far west (wells 12, 16 and 19) and low in the central western part (wells 1, 6, 7, 8, 9, and 10) of the map. It is noted that the values of electrical conductivity were confined between 1518 $\mu\text{s} / \text{cm}$ and 10190 $\mu\text{s} / \text{cm}$ for the dry season of the year 2018. According to the specifications of FAO, (31%) of all groundwater samples are moderate salinity (700– 3000 $\mu\text{s}/\text{cm}$) and the rest are very salty (above 3000 $\mu\text{s}/\text{cm}$).

Total Dissolved Solids (TDS) Effect. Dissolved solids consist of water leaching through the soil, dissolved limestone, gypsum, rocks exposed to erosion and other salts. The flow of water through the subsurface and geological formations carries with it many salts and dissolved ions, thus changing the quality of the groundwater (Jain et al., 1997). Increasing concentrations of dissolved salts such as sodium, magnesium, chlorides, sulfates, and calcium carbonate in addition to human activities will contribute to increase the amount of salinity in the groundwater and thus increasing the amount of TDS (Salama et al., 1999). Through the spatial distribution of (TDS), it is noted that its values are high in the eastern parts (wells 20, 21, 22, and 24), the far west (wells 12, 16, and 19). Yet, it is low in the central western part (wells 1, 6, 7, 8, 9, and 10). The lowest value for (TDS) is (1220 mg /L) at the highest value (8021 mg /L) in the dry season of 2018. The food and agriculture organization has determined the values of (TDS) as causing a slight to moderate restriction in the use of irrigation water (Slight to Moderate of Restriction on use if its value is between (450-2000 mg/L) and severe restriction if it increases above this limit. It was noted that 25% of the measured samples with TDS values were described as slight to moderate restriction and the rest were highly restricted water in use.

Cation (K^{2+} , Na^+ , Mg^{2+} and Ca^{2+}) Effect. The most important sources of cation in groundwater are weathering processes of soil and rocks, whether sedimentary or igneous, and human activities. They reach groundwater by filtering water through the soil (Sravanthi & Sudarshan, 1998; Basha et al., 2010; Lateef, 2011). Mostly, the spatial distribution shows that the values of cations on the map are high in the southeast and northwestern part and decrease in the eastern and northern part on the map. Through Table 5, the lowest values were ($\text{K} = 0.975 \text{ mg/L}$ in the dry season of 2018, $\text{Na}^+ = 68 \text{ mg/L}$ for the wet season of the same year, $\text{Mg}^{2+} = 5.16 \text{ mg/L}$ for the wet season of 2019 and $\text{Ca}^{2+} = 17.6 \text{ mg/L}$ for the wet season of 2019). The highest values were ($\text{K}^{2+} = 124.8 \text{ mg/L}$ is in the dry season of 2018, $\text{Na}^+ = 736 \text{ mg/L}$, for the wet season for the same year, $\text{Mg}^{2+} = 159 \text{ mg/L}$ for the wet season for 2019 and $\text{Ca}^{2+} = 366 \text{ mg/L}$ for the dry season of the same year). The acceptable limitations for positive elements are ($\text{K}^{2+} < 10 \text{ mg/L}$, $\text{Na}^+ < 50 \text{ mg/L}$, $\text{Mg}^{2+} < 24 \text{ mg/L}$, $\text{Ca}^{2+} < 75 \text{ mg/L}$).

<120 mg/L). For four seasons, the results of the groundwater analysis showed that 65%, 100%, 90% and 60% of the observed values for K^{2+} , Na^+ , Mg^{2+} and Ca^{2+} respectively, are higher than the desired limits.

Anion (Cl^- , SO_4^{2-} , HCO_3^-) Effect. The important source of chloride salts (Cl^-) in groundwater is weathering processes for rocks and soil and are transported to groundwater by filtration. While sulfates (SO_4^{2-}), groundwater reaches it through weathering processes of (sulphide-bearing) or soil can be another source for sulfates. Further, evaporation deposits can also be a source for sulfates. Another important source is airborne pollutants containing sulfur oxides and converts them to sulfuric acid during rain fall to filter into the soil (Singh et al., 2012; Mallick, 2017). Having bicarbonate ions (HCO_3^-) in groundwater is associated with the presence of magnesium and calcium ions or is released from rocks, soil and the disintegration of the gypsum or the presence of carbon dioxide and calcium carbonate water that interact in the presence of water to produce (HCO_3^-) (Ravikumar & Somashekar, 2015; Al-Qawati et al., 2018). In general, the spatial distribution of anions values on the map shows that they are high in the southern part and somewhat western part and low in the northern part excepting the wells 12 and 13 on the map. The lowest value was ($Cl^- = 157.85$ mg/L in the dry season, $SO_4^{2-} = 96$ mg/L, for the wet season, and $HCO_3^- = 90$ mg/L for the wet season) for the year 2018. As for the highest value of $Cl^- = 1200$ mg/L in the dry season of 2018, $SO_4^{2-} = 1412$ mg/L, for the dry season of 2019, and $HCO_3^- = 955$ mg/L for the season dry for the year 2018. Allowed values for negative elements are ($Cl^- < 140$ mg/L, $SO_4^{2-} < 400$ mg/L, $HCO_3^- < 120$ mg/L). For four seasons, the results of the groundwater analysis showed that 100%, 75% and 97% of the values of Cl^- , SO_4^{2-} and HCO_3^- , respectively, were higher than the permissible values.

Sodium Absorption Ratio (SAR). SAR is an important component for assessing the validity of irrigation water. The higher the sodium concentration in irrigation water is the more sodium absorption will increase. This reduces the validity of irrigation water. The effect of irrigation water on soil permeability to water depends on the interference between the flocculating effects of specific conductance and the diffusion effect of sodium. If the specific conductance is high, this increases the soil's tolerance to water with a high SAR (Bhat et al., 2018). The distribution of the value of (SAR) spatially distributed scattered over the directions of the map may seem high for wells (4, 10, 12, 16, and 22), and low for other wells (7, 14, 17, 18, and 21). The FAO organization has defined different ranges of the value of (SAR). The higher the electrical conductivity is the greater the negative impact of the (SAR) on the water viability for irrigation purposes. The maximum value was in the dry season of the year 2018 and was (SAR = 5.27). The lowest value (SAR = 1.49) was in the wet season of 2019 and is somewhat close to the corresponding value in

the year 2018 (SAR = 1.51). For SAR values between (0-3 and 3-6), the values of (EC) were ($<700, 700-2000$ and $> 2000 \mu\text{s} / \text{cm}$) leading to problems ranging from zero-effect, medium to high-impact, respectively.

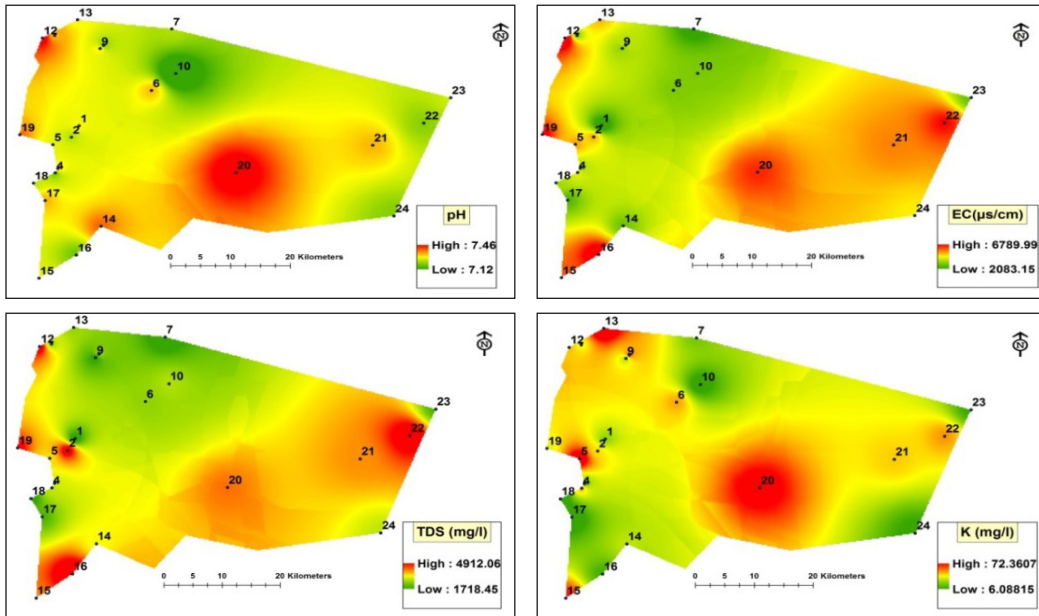


Figure 3. Spatial distribution of average of pH, EC, TDS and K^+ in the studied area

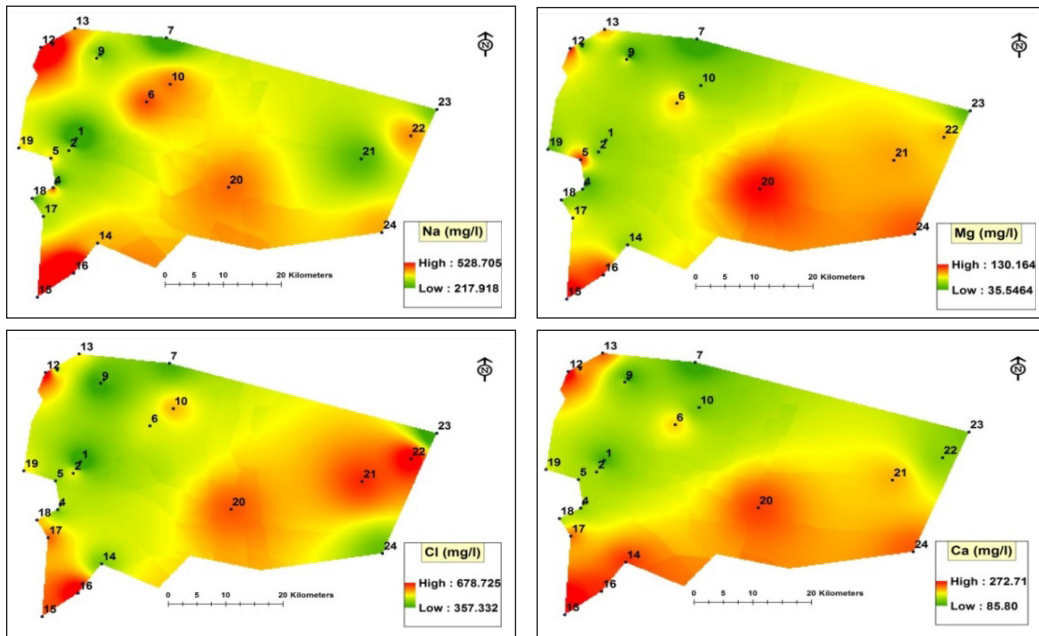


Figure 4. Spatial distribution of average Na^+ , Mg^{2+} , Ca^{2+} , Cl^- , SO_4^- , HCO_3^- and SAR in the studied area

Irrigation Water Quality Index (IWQI)

Based on Equations 1 and 2 as well as Table 2 and 3, the Water Quality Index (IWQI) for the dry and wet seasons of 2018 and 2019 for all wells was calculated. The values of (IWQI) are shown in Figure 5. Figure 5 shows the changes in the values of (IWQI) over the four seasons of most wells where the highest values of (IWQI) were in the wet season of 2018 and the lowest values in the dry season for the same year. The annual rate of (IWQI) values were calculated for each season separately and as in Table 6. Table 6 shows that the water quality in the wet season is of higher value (IWQI) than most of the dry season for most wells. In general, the high-water levels in the wet season in the Hilla River and the branching irrigation canals raise the water level (Al-Amar, 2015). Consequently, this reduces the concentrations of water quality elements due to dilution which leads to high values of (IWQI) and improvement of groundwater quality accordingly. By comparing the values of (IWQI) with the determinants in Table 4, the quality of the well water can be classified into several classes, as shown in Table 7. For example, (67%) of the wells in the dry season of 2018 can be classified under the category (SR) and (29%) and (4%) of the

Table 6
Wells IWQI of each season and year

Well No.	Mean of IWQI		Overall mean of IWQI	Well No.	Mean of IWQI		Overall mean of IWQI
	Dry	Wet			Dry	Wet	
1	43.08	58.81	50.95	13	31.25	53.20	42.22
2	32.58	51.89	42.24	14	45.93	44.66	45.29
3	39.55	56.23	47.89	15	29.60	42.31	35.95
4	30.58	46.52	38.55	16	26.77	34.86	30.81
5	35.46	39.79	37.62	17	46.68	43.45	45.07
6	40.16	41.05	40.60	18	51.87	48.93	50.40
7	41.96	66.72	54.34	19	34.28	44.15	39.21
8	36.32	49.27	42.80	20	26.94	48.63	37.78
9	47.66	56.97	52.31	21	32.17	47.82	40.00
10	35.49	45.69	40.59	22	26.18	43.21	34.70
11	40.45	40.53	40.49	23	37.38	63.16	50.27
12	25.50	36.53	31.01	24	35.29	39.08	37.19

Table 7
IWQI classification of groundwater quality

IWQI	Water Use Restrictions	2018		2019	
		Dry	Wet	Dry	Wet
0-40	SR	67%	37.5%	62.5%	41.7%
40-55	HR	29%	33.3%	37.5%	45.8%
55-70	MR	4%	8.3%	12.5%
70-85	LR	20.8%

wells under the category (HR) and (MR), respectively, and so on. Through the schedule, we can say that these wells in the best conditions suffer from restrictions in use for irrigation purposes and the problem is more than that in the dry season.

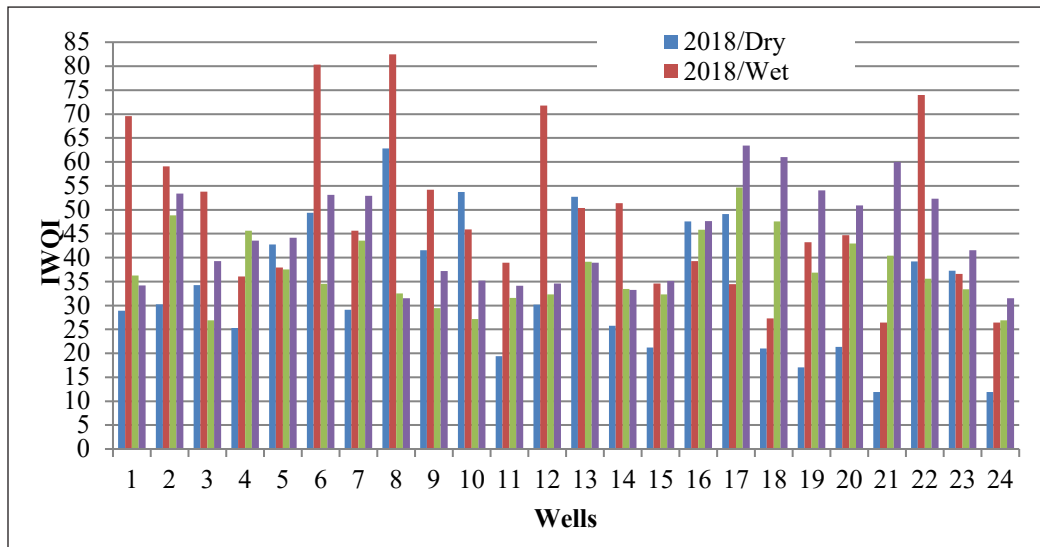


Figure 5. The four seasonal variation at each well is shown starting with 2018 (dry), 2018 (wet) followed by 2019 (dry) and lastly 2019 (wet).

CONCLUSION

The main conclusions of this study can be summarised as:

1. The values of (IWQI) were higher in the wet season than in the dry season, since the dry season results in a decline in the discharge of the Hilla River and its branches, which provides fresh water to the region's wells.
2. The spatial distribution shows that there is a slight variation of pH values with an irregular change in the values of (SAR) for all wells and for the years of study in its dry and wet seasons.
3. High (EC) and (TDS) levels in groundwater suggest high salinity, which is caused by soil leaching. It is hard to use for direct irrigation. The spatial distribution of EC and TDS is high in the eastern and western parts of the area map, but low in the central western parts.
4. For the positive ions, 65%, 100%, 90%, and 60% of observed values K^{2+} , Na^{+} , Mg^{2+} and Ca^{2+} , respectively, were higher than the permissible limits. The spatial distribution on the map is high in the southeastern and northwestern part and low in the eastern and northern part. As for the negative ions, 100%, 75%, and 97% of the values for Cl^{-} , SO_4^{2-} , and HCO_3^{-} , respectively, were also higher than the

permissible limits. The spatial distribution on the map is high in the southern part as well as the part Western and low in the northern part.

5. The SAR values do not cause significant problems in filtering the main components into the soil. (85%) of (SAR) values between (3-6) and (EC) values greater than (1200 $\mu\text{s} / \text{cm}$). 15% of the SAR values between (0-3) where EC are greater than (700 $\mu\text{s}/\text{cm}$). The spatial distribution of SAR values is random on the map, depending on the change in sodium concentrations.
6. For dry and wet seasons, a large percentage of wells have poor water quality and need relatively high permeability soils and salt-resistant plants.

ACKNOWLEDGEMENTS

The authors thank for Al-Qasim Green University (collage of water resources engineering) and Ministry of Higher Education, Iraq for support this research.

REFERENCES

- Abbasnia, A., Radfard, M., Mahvi, A. H., Nabizadeh, R., Yousefi, M., Soleimani, H., & Alimohammadi, M. (2018). Groundwater quality assessment for irrigation purposes based on irrigation water quality index and its zoning with GIS in the villages of Chabahr, Sistan and Baluchistan, Iran. *Data in Brief*, 19, 623-631. <https://doi.org/10.1016/j.dib.2018.05.061>
- Abdullah, T., Salahuddin, A., & Al-Ansari, N. (2015). Effect of agricultural activities on groundwater vulnerability: Case study of Halabja Salsadiq Basin, Iraq. *Journal of Environmental Hydrology*, 23(10)
- Al-Amar, H. A. (2015) The quality of ground water for selected area in south of Babylon Governorate/Iraq. *IOSR Journal of Applied Geology and Geophysics*, 3(4), 29-36. <https://doi.org/10.9790/0990-03412936>
- Al-Dabbas, M. A., & Al-Ali, E. A. (2016). Computation of climatic water balance for greater Musaiyab project site in Babylon Governorate-Central of Iraq. *Iraqi Journal of Science*, 57(2C), 1445-1451
- Al-Khaqani, M. (2006). *Study the phenomenon of swelling clay soils in the city of Hillah* (Unpublished Master's thesis). College of Science, University of Baghdad, Iraq.
- Al-Mohammed, F. M., & Mutasher, A. A. (2013). Application of water quality index for evaluation of groundwater quality for drinking purpose in dibdiba aquifer, Kerbala city, Iraq. *Journal of University of Babylon*, 21(5), 1647-1660
- Al-Qawati, M., El-Qaysy, M., Darwesh, N., Sibbari, M., Hamdaoui, F., Kherrati, I., El Kharrim, K., & Belghyti, D. (2018). Hydrogeochemical study of groundwater quality in the west of Sidi Allal Tazi, Gharb area, Morocco. *Journal of Materials and Environmental Sciences*, 9(1), 293-304. <https://doi.org/10.26872/jmes.2018.9.1.33>
- Al-Ridah, Z. A., Al-Zubaidi, H. A. M., Naje, A. S., & Ali, I. M. (2020). Drinking water quality assessment by using water quality index (WQI) for Hillah River, Iraq. *Ecology, Environment and Conservation Paper*, 26(1), 390-399.

- Al-Zubaydi, J. H., Al-Kaily, A. A., & Al-Rubaey, M. Q. (2016). Engineering properties of soft clay stabilized with lime materials, emulsified asphalt and bentonite sodium for sub grade of road under construction in Hilla city-Babylon governorate. *International Journal of Civil Engineering and Technology*, 7(5), 347-367.
- Ayers, R. S., & Westcot, D. W. (1985). *Water quality for agriculture* (Vol. 29). Food and Agriculture Organization of the United Nations.
- Ayers, R. S., & Westcot, D. W. (1999). *The water quality in agriculture*. UFPB.
- Basha, A. A., Durrani, M. I., & Paracha, P. I. (2010). Chemical characteristics of drinking water of Peshawar. *Pakistan Journal of Nutrition*, 9(10), 1017-1027. <https://doi.org/10.3923/pjn.2010.1017.1027>
- Bernardo, S. (1995). *Manual of irrigation* (4th Ed.). UFV.
- Bhat, M. A., Wani, S. A., Singh, V. K., Sahoo, J., Tomar, D., & Sanswal, R. (2018). An overview of the assessment of groundwater quality for irrigation. *Journal of Agricultural Science and Food Research*, 9(1), Article 1000209.
- Boateng, T. K., Opoku, F., Acquah, S. O., & Akoto, O. (2016). Groundwater quality assessment using statistical approach and water quality index in Ejisu-Juaben Municipality, Ghana. *Environmental Earth Sciences*, 75(6), Article 489. <https://doi.org/10.1007/s12665-015-5105-0>
- Chabuk, A., Al-Ansari, N., Hussein, M. H., Kamaledin, S., Knutsson, S., Pusch, R., & Laue, J. (2017). Soil characteristics in selected landfill sites in the Babylon Governorate, Iraq. *Journal of Civil Engineering and Architecture* 11, 348-363. <https://doi.org/10.17265/1934-7359/2017.04.005>
- Deshmukh, K. K. (2013). Impact of human activities on the quality of groundwater from Sangamner Area, Ahmednagar District, Maharashtra, India. *International Research Journal of Environment Sciences*, 2(8), 66-74.
- Gidey, A. (2018). Geospatial distribution modeling and determining suitability of groundwater quality for irrigation purpose using geospatial methods and water quality index (WQI) in Northern Ethiopia. *Applied Water Science*, 8, Article 82. <https://doi.org/10.1007/s13201-018-0722-x>
- Hassan, T., Parveen, S., Bhat, B. N., & Ahmad, U. (2017). Seasonal variations in water quality parameters of River Yamuna, India. *International Journal of Current Microbiology and Applied Sciences*, 6(5), 694-712. <https://doi.org/10.20546/ijemas.2017.605.079>
- Holanda, J. S., & Amorim, J. A. (1997). Management and control salinity and irrigated agriculture water. *Congresso Brasileiro de Engenharia setting*, 26, 137-169. <http://dx.doi.org/10.18535/ijetst/v3i09.10>
- Jain, C. K., Sharma, M. K., & Omkar, K. (1997). Ground water quality variation in district Jammu. *Indian Journal Of Environmental Protection*, 17(6), 401-405.
- Kushwah, R. K., Malik, S., Majumdar, K., & Bajpai, A. (2012). Wastewater quality studies of inlet and outlet at municipal wastewater treatment plant at Bhopal, India. *International Journal of Chemical Sciences*, 10(2), 993-1000.
- Lateef, K. H. (2011). Evaluation of ground water quality for drinking purpose for Tikrit and Samarra cities using water quality index. *European Journal of Scientific Research*, 58(4), 472-481.

- Mahmood, A. A., Eassa, A. M., Muayad, H. M., & Israa, Y. S. (2013). Assessment of ground water quality at Basrah, Iraq by water quality index (WQI). *Journal of University of Babylon*, 21(7), 2531-2543.
- Majeed, S. A. A. D., Mohammed, O. I., & Hassan, W. H. (2016, December 27-29). Determining irrigation water quality index for evaluation groundwater quality of Green-Belt Zone, Karbala, Iraq. In *4th International Congress on Civil Engineering, Architecture and Urban Development* (pp. 1-12). Shahid Beheshti University, Tehran, Iran.
- Mallick, J. (2017). Hydrogeochemical characteristics and assessment of water quality in the Al-Saad Lake, Abha Saudi Arabia. *Applied Water Science*, 7(6), 2869-2882. <https://doi.org/10.1007/s13201-017-0553-1>
- Meireles, A., Andrade, E. M., Chaves, L., Frischkorn, H., & Crisostomo, L. A., (2010). A new proposal of the classification of irrigation water. *Revista Ciencia Agronomica*, 413, 349-357. <http://dx.doi.org/10.1590/S1806-66902010000300005>
- Ravikumar, P., & Somashekar, R. K. (2015). Principal component analysis and hydrochemical facies characterization to evaluate groundwater quality in Varahi river basin, Karnataka state, India. *Applied Water Science*, 7(2), 745-755. <https://doi.org/10.1007/s13201-015-0287-x>
- Salama, R. B., Otto, C. J., & Fitzpatrick, R. W. (1999). Contributions of groundwater conditions to soil and water salinization. *Hydrogeology Journal*, 7, 46-64. <https://doi.org/10.1007/s100400050179>
- Singh, C. K., Kumari, R., Singh, N., Mallick, J., & Mukherjee, S. (2012). Fluoride enrichment in aquifers of the Thar desert: Controlling factors and its geochemical modelling. *Hydrological Processes*, 27(17), 2462-2474. <https://doi.org/10.1002/hyp.9247>
- Sravanthi, K., & Sudarshan, V. (1998). Geochemistry of groundwater, Nacharam Industrial area, Ranga Reddy district, A.P. India. *Journal of Environmental Geochemistry*, 1(2), 81-88. <https://doi.org/10.1007/s13201-016-0441-0>



Designing the Ergonomic Press and Molding Machine of Cassava Chips for Sustainable Development in SMEs

Silviana^{1*}, Andy Hardianto¹, Naif Fuhaid² and Dadang Hermawan²

¹Department of Industrial Engineering, Universitas Widyagama Malang,
Jl. Borobudur 35 Malang, 65125, Indonesia

²Department of Mechanical Engineering, Universitas Widyagama Malang,
Jl. Borobudur 35 Malang, 65125, Indonesia

ABSTRACT

The sustainability of the SMEs depends on how the SMEs could compete with their competitor. Utilizing technology is a way that can be used to survive in those competitions. Unfortunately, some of the SMEs in Indonesia could not afford to utilize the technology due to financial problems. Therefore, the aim of this research is to create an ergonomic working environment by utilizing the technology through the design of the press and molding machine. In its application, the concepts of Rapid Entire Body Assessment (REBA) and Rapid Upper Limb Assessment (RULA) were used to assess the working posture. The results of this assessment show that the working environment of this SME, especially in the pressing and molding process was not ergonomic and need to be improved. The given improvement is in the form of press and molding machine design and its prototype. The designing process was done using the concept of Quality Function Deployment (QFD). On the other side, to assess the level of success for the given design and machine, the REBA and RULA assessment was carried out. The results of the REBA and RULA assessment for the new machine showed that it could decrease the previous score of both REBA and RULA.

The results of this research are expecting to increase the production capacity, minimizing the occurrence of MSDs, and improving the quality of the chips. In the long-term, it will be able to increase the competitiveness of this SME.

ARTICLE INFO

Article history:

Received: 17 January 2021

Accepted: 30 April 2021

Published: 31 July 2021

DOI: <https://doi.org/10.47836/pjst.29.3.24>

E-mail addresses:

silviana.hakim@gmail.com (Silviana)

andyhardian@gmail.com (Andy Hardianto)

naif.uwg@gmail.com (Naif Fuhaid)

dadang@widyagama.ac.id (Dadang Hermawan)

* Corresponding author

Keywords: Ergonomic, posture, quality function deployment, rapid entire body assessment, rapid upper limb assessment

INTRODUCTION

The use of technology has an important role both in big company and SMEs. With the existence technology, it can provide convenience in all aspects and even the users seem to be spoiled by the various conveniences that can be done. Besides, the use of technology could help the company to increase their competitiveness (Ahmedova, 2015). In contrary, many SMEs in Indonesia has a lot of difficulties such as lack of skills, funding, and technology which could decrease the ability to increase the competitiveness (Maksum et al., 2020). Whereas according to Ramayah et al. (2005) maintain the business competitiveness is the most important factor to keep the SMEs sustain in the long-term business survival.

The use of technology considered as an innovation in the business and machinery is categorized as a technology tools in the business operation (Rahman et al., 2016). The use of machinery in SMEs could shorten the production time, produce a product with a precise size, so that in the future it will be able to meet the market demand. Moreover, the use of machinery could minimize the occurrence of musculoskeletal disorders (MSDs) since most of the machine was made based on the certain health standard and pay attention to the user safety. MSDs are the injuries or pain in the joints of the body, ligaments, nerves, muscles, and structures that support the body or it can be called as a disorders that affect the movement of the body or the human skeletal muscle system (Revadi et al., 2019). Punchihewa (2010) stated that force (load), repetition, and posture such as prolonged static loads and forceful exertion, the extreme postures, and repetitive motion are the main factors that could causes MSDs.

This research was conducted in one of SMEs which produce cassava chips and located in Tulungagung, East Java, Indonesia. This SMEs produce chips using traditional tools, to be exact, they mold the chips by the fork and press it. Those action has been done in repetitive. In the long-term, this matter could lead to the musculoskeletal disorders (MSDs). Besides, since this process was done manually, it can affect the size of the chips. The results of observations in the field showed that the chips have a different diameter and thickness. Therefore, an effort is needed to deal with these various problems. The objective of this research is to design the ergonomic press and molding machine using the concept of ergonomic and Quality Function Deployment (QFD). In the future, this machine design is expected to be able to increase the production capacity, produce chips with more precise size, and be able to reduce the possibility of MSDs due to repetitive motion. Furthermore, in the long-term this machine is expected to be able to increase the competitiveness of this SMEs.

LITERATURE REVIEW

Biomechanics studies the strength, endurance, speed, accuracy, and limitations of humans in carrying out the activities. This factor is closely related to material handling activities,

such as manual lifting and moving, and other jobs that involve a lot of body muscles. Besides, work posture is a determining point in analyzing the effectiveness of a job. If the work posture that has been carried out by the operator is good and ergonomic, then it can be ascertained that the results obtained by the operator will be good, but if the operator's work posture is wrong or not ergonomic then the operator will be easily tired, and it may cause the MSDs. If the operator is easily tired, the results of the work will also decrease and are not as expected (Akshintina & Susanty, 2017).

Rapid Upper Limb Assessment (RULA) is the survey method in ergonomic which is used as an investigation tools in determine the MSDs. It is the simplest, easiest to understand, and quick to complete. This method used to assess the biomechanical and the work postures based on the body position while doing the activity. The assessment of RULA can be done with the help of RULA worksheet that has been proposed. RULA assessment is mainly focus on the upper body, which consist of neck, trunk, upper arm, and lower arm. Besides, this method also assess the function of muscle and the loads (Ijaz et al., 2020). RULA is a method to analyzing the ergonomics of a work posture with the use of the upper body. RULA analysis is carried out if there is a report about the complaints in the upper body caused by unergonomic postures. The RULA method is easy to use because it does not require any special equipment in its implementation. Some of the factors analyzed by the RULA method are work position in a static state, workload, work period, and also muscle energy used (Tiogana & Hartono, 2020).

Meanwhile, Rapid Entire Body Assessment (REBA) is the most detailed assessment since it assesses all the movement of the entire body while doing the activity. This method was developed to evaluate the potential work related to the MSDs. Besides, REBA was designed to make it easy to understand and there is no need for the high skill or expensive equipment. The REBA worksheet and a stationary was the things that needed when conducting this assessment (Tiogana & Hartono, 2020). The aim of this method is to divide the body to a different portion then separately assess it based on its angles. As well as the RULA, the REBA assessment was conducted using the help of REBA worksheet. In this assessment, the scores were obtained from the body postures alignment, the weight on muscles and the coupling scores. The final scores of REBA assessment is the summation of values from both groups. According to Ijaz et al. (2020) the loading of biomechanical and postural has always been successfully assessed using this simple worksheet. The scores were obtained from a different body part such as trunk, neck, and legs in the section A, whereas the section B consist of the assessment of the upper and lower arm, wrist, and wrist twist. In the section C, the summation of both score in section A and B was conducted. The REBA assessment could highlight and determine the level of urgency.

The use of RULA and REBA assessment made the analysis of work posture are easy and reliable. Moreover, Kee et al. (2020) stated in their research that RULA is the best

technique that could be used for assessing the working posture. On the other hand, some of the research also highlighted the use of this method if it will be used alone or combined it with other method. Punchihewa (2010) stated that conducting the REBA technique without being combined with other method will be failed to give the best solution to minimize the MSDs. It will be better if the designing process was included in those assessment. Therefore, in this research the designing process using QFD will be included.

Quality Function Deployment (QFD) is the deployment tools which is widely used in the total quality management (TQM). QFD is a process to translating the requirements of customer into the technical requirements of a product. This process started with capturing the voice of customer into the product and fed into the product through the technical definitions of each customer demand in the effective way (Shil et al., 2010). In the product planning, a trade-off will be reached if the customer requirements and the technical adaptability are be depicted through the house of quality (HOQ). QFD approach is based on the deploying consumer expectations (What) in term of design and production-parameters (How). The correlations between what and how will be explained in the HOQ matrix. This matrix allows the integrations between the related elements to analyzing the product competition and to identifying the synergies and the contra-dictions between different characteristic of the product. Thus, this matrix offers the advantages for the user, the designer, and also for the decision maker of the product development (Marsot, 2005).

RESEARCH METHODOLOGY

This study was conducted at the Cassava Chips-SMEs in Tulungagung, East Java, Indonesia. This research was divided into three main stages, first is the observation in the field, followed by an assessment of work posture using the REBA RULA method, and ended by the designing process. The results of the observation in the field showed that this SME was facing problems such as the use of traditional equipment that causes the chips has a different size, and the work environment which is not ergonomic. Therefore, the objectives of this research are to designing the press and molding machine that can be used to minimize those problems. Figure 1 shows the stages of this research.

This research began with the observation stages, this stage has been done to find out the problems that are currently faced by this SME. The next step is to conduct the literature review. This step is done to find out the appropriate method that can be used to solve those problems. After finding out the appropriate method, the next stage is the assessment. This

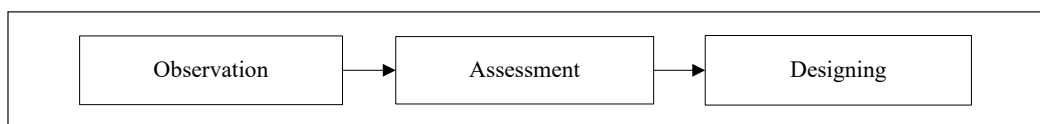


Figure 1. The stages of the research

assessment is conducted to assess the current condition and to double-check the working posture during the production process. The concepts of REBA and RULA were used to conducting that assessment. The results of the assessment will be used as a reference in designing the machine. The last stages, the designing stages was conducted using the concept of QFD. The designing process was done according to the voice of the customer and prioritizing scale in the HOQ matrix. The designing process also includes the prototyping of the machine.

RESULTS AND DISCUSSION

The results of field observations indicate that this SME is still using traditional equipment in its production process. Even though it has a large market demand, in practice the carried-out production capacity is still insufficient. This is due to inadequate production equipment. This SME produces cassava chips as its main product. The process of making these chips begins with peeling the cassava skin, which is the main ingredient, then the cassava will be milled and stored in the refrigerator for two days. The cassava dough that has been stored in the refrigerator for 2 days will be mixed with various spices, stirred, and molded. The molding process was done in the standing position and was traditionally undertaken using the help of a tray and fork. A tablespoon of the dough will be pressed into the tray and will be molded using a fork. The molding process is carried out repetitively so that in the long-term it may cause MSDs. In addition, due to the manual use of tools, the results of the molding also have different thicknesses and diameters. So, it can be said that this traditional pressing and molding process is able to have a negative impact on the sustainability of this SME. Therefore, it is necessary to design the ergonomic press machine so that the negatives impact can be reduced.

The next step of producing the cassava chips is steaming. The cassava dough that has been molded will be steamed for approximately 4-5 minutes. After being steamed, the dough will be dry in the sun for about 2-3 days. The last step is the packaging process, this SME produced 2 kinds of chips package that is the raw and the cooked one. All those variants will be packed in 2 ounces or 1 kg packaging. In this research, the focus will be on the pressing and molding process since it has a problem that needs to be improved. The improvement begins with conducting the assessment using REBA & RULA concepts. The objective of this assessment is to check or assess the current work posture in the pressing and molding process. Figure 2 shows the results of the REBA assessment.

Figure 2 explain the step of conducting REBA assessment. The results of the assessment showed that the REBA score is 5 which means that the work posture in pressing and molding process are in the medium risk and further investigation and change are needed. This matter will be used as a reference to design the machine. Furthermore, the RULA assessment was also carried out. Figure 3 shows the step of RULA assessment.

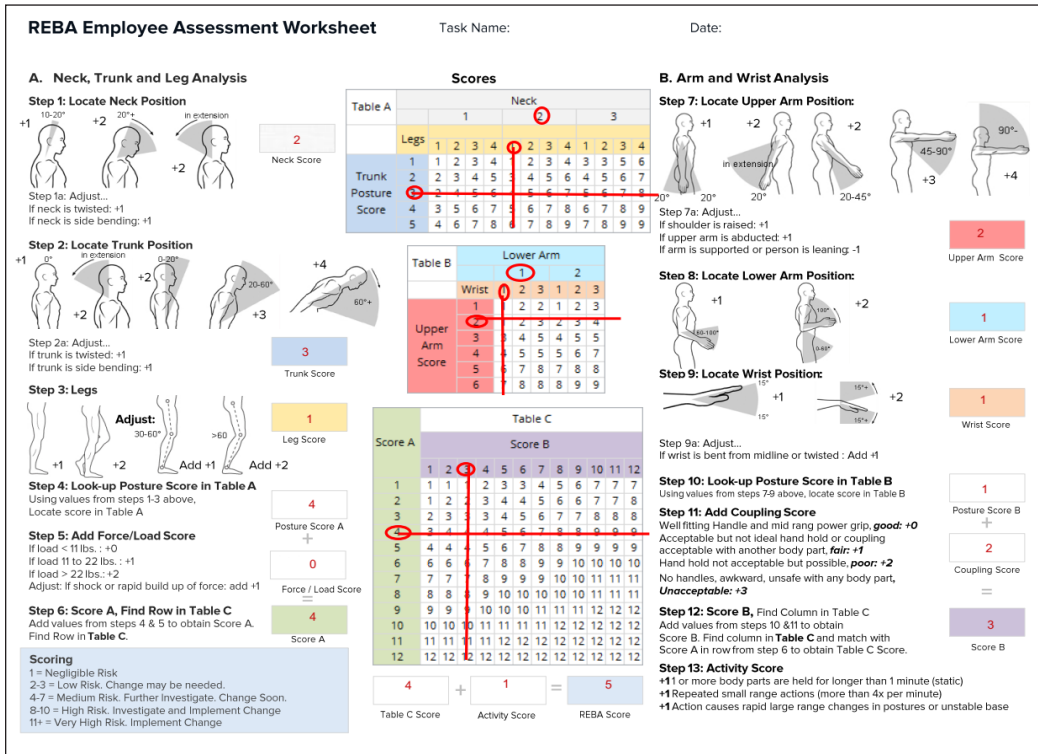


Figure 2. The results of REBA assessment

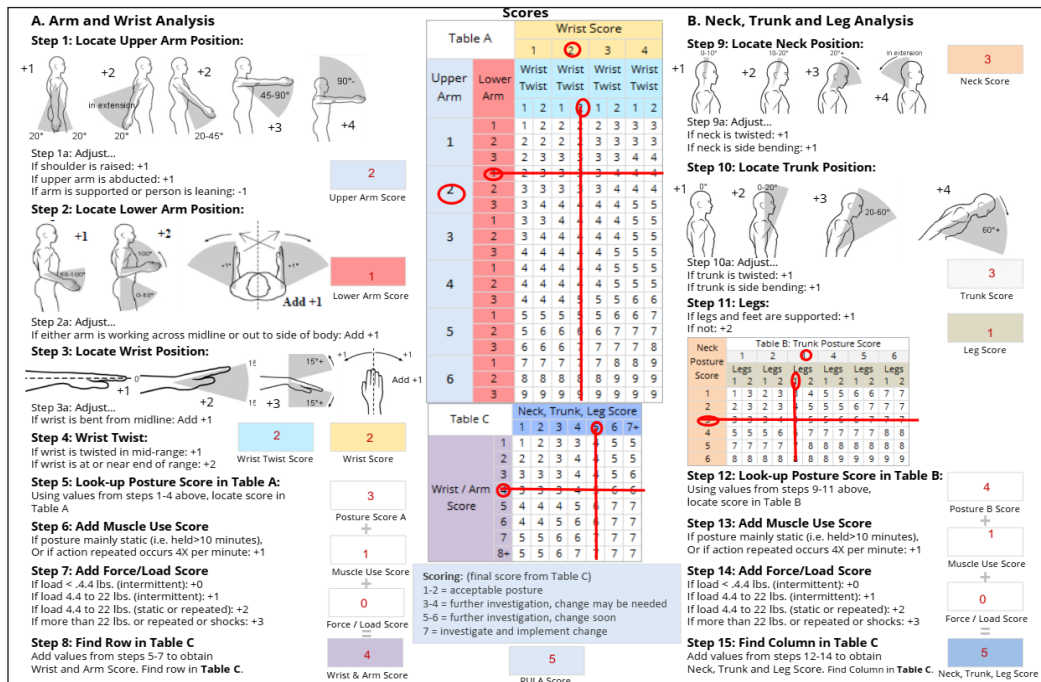


Figure 3. The results of RULA assessment

The results of the assessment showed that the RULA score is 5 which means further investigation and change are needed soon. The risk assessment that has been done using REBA and RULA concepts needs to be combined with other methods to providing the appropriate solutions. According to Punchihewa (2010), some researchers used the REBA technique to assess the risk of MSDs but it is not combined with other methods. As a result, those tools failed to provide the best solution to minimize the MSDs. This method might be useful if the designed process is integrated to help the designers to communicate about the requirements. QFD is the potential method that could improving this drawback. QFD is a helpful method that could communicating the requirements for the design with other information of the product design. Besides, QFD also known as the powerful tool in fulfills the customer satisfaction by translating the voice of customer in the designing or product development (Shil et al., 2010). On the other sides, Hashim and Dawal (2012) stated that QFD can be used as a tools to help the prioritizing process of the design requirement based on their important values so that the customer expectations can be fulfilled. Considering the advantages of QFD, therefore the designing process of press and molding machine will be conducted using QFD.

The first step before designing the HOQ matrix is to propose the list of the voice of customers. This step was conducted through the interview with the employee of this SME. The results of the interview will be used as the statement in the questionnaire. A Likert scale from 1 to 5 was used to give the answer. The questionnaires will be distributed to all the employees and the owner, which is a total 30 number of people. The results of the questionnaire will be evaluated using reliability tests and validity tests. The aim of this test is to determine the validity or suitability of the questionnaire which is used by researchers to obtain data from respondents. The reliability and validity tests were conducted using the help of SPSS software. Figure 4 shows the results of the reliability test.

Figure 4 shows that the data obtained from the respondents are reliable since the Cronbach's Alpha is 0.426 which is greater than the score of the R table, 0.361. Therefore, it can be concluded that the data was reliable and consistent. Meanwhile, to figure out the validity of the data, a validity test was conducted. Figure 5 shows the results of the validity test using SPSS.

The results of validity tests using SPSS shows that the value of Pearson Correlation to all the variable has a greater value than the R table which is 0.361. Therefore, it concluded that the used data was valid. Furthermore, all the gathered voice of customers will be used and placed in the left-hand column of HOQ matrix. Meanwhile, the technical requirements will be identified by the QFD team or in this research is known as the

Reliability Statistics	
Cronbach's Alpha	N of Items
.426	7

Figure 4. Results of Reliability Test

		V1	V2	V3	V4	V5	V6	V7	Total
V1	Pearson Correlation	1	-0.027	0.074	0.137	0.091	-0.087	0.201	0.428*
	Sig. (2-tailed)		0.889	0.697	0.472	0.631	0.647	0.286	0.018
	N	30	30	30	30	30	30	30	30
V2	Pearson Correlation	-0.027	1	-0.039	0.398*	0.014	0.216	0.000	0.475**
	Sig. (2-tailed)	0.889		0.838	0.029	0.943	0.251	1.000	0.008
	N	30	30	30	30	30	30	30	30
V3	Pearson Correlation	0.074	-0.039	1	0.339	0.000	-0.183	0.473**	0.465**
	Sig. (2-tailed)	0.697	0.838		0.067	1.000	0.334	0.008	0.010
	N	30	30	30	30	30	30	30	30
V4	Pearson Correlation	0.137	0.398*	0.339	1	0.040	0.120	0.136	0.652**
	Sig. (2-tailed)	0.472	0.029	0.067		0.835	0.527	0.472	0.000
	N	30	30	30	30	30	30	30	30
V5	Pearson Correlation	0.091	0.014	0.000	0.040	1	0.013	0.069	0.373*
	Sig. (2-tailed)	0.631	0.943	1.000	0.835		0.946	0.715	0.042
	N	30	30	30	30	30	30	30	30
V6	Pearson Correlation	-0.087	0.216	-0.183	0.120	0.013	1	0.066	0.367*
	Sig. (2-tailed)	0.647	0.251	0.334	0.527	0.946		0.728	0.046
	N	30	30	30	30	30	30	30	30
V7	Pearson Correlation	0.201	0.000	0.473**	0.136	0.069	0.066	1	0.569**
	Sig. (2-tailed)	0.286	1.000	0.008	0.472	0.715	0.728		0.001
	N	30	30	30	30	30	30	30	30
Total	Pearson Correlation	0.428*	0.475**	0.465**	0.652**	0.373*	0.367*	0.569**	1
	Sig. (2-tailed)	0.018	0.008	0.010	0.000	0.042	0.046	0.001	
	N	30	30	30	30	30	30	30	30

Figure 5. The Results of Validity Test using SPSS

*. Correlation is significant at the 0.05 level (2-tailed).

**. Correlation is significant at the 0.01 level (2-tailed).

researchers. Besides, the relationship between the customer requirements and technical requirements were also generated by the QFD team. In the right-hand column, competitive analysis was performed with five competitors. The relations between the technical requirements and the degree of difficulty were established based on the knowledge of the experts, and also the recommendations of the consultants (Erdil & Arani, 2019). Figure 6 shows the proposed HOQ that has been done in this research.

The results of the HOQ matrix show that the voice of customer which has the highest importance level, respectively are the conveniences while using the machine, user friendly, has an ergonomic design, and can increasing the production capacity. Therefore, the

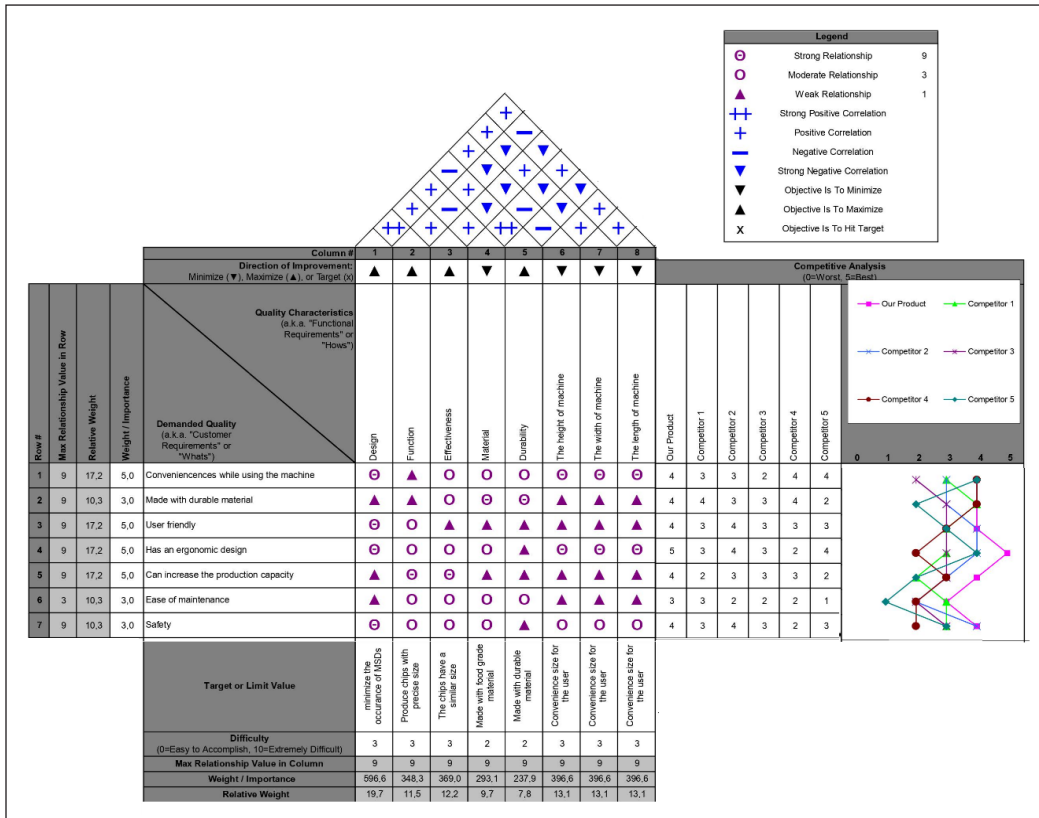


Figure 6. The HQQ Matrix



Figure 7. The design of pressing and molding machine

given design of press and molding machine will be referring to those attributes so that the customer satisfaction can be fulfilled. Figure 7 shows the proposed design of pressing and molding machine.

According to the voice of a customers, the provided machine design is ergonomically designed in such a way as to provide conveniences to its users. Hence, the size of the

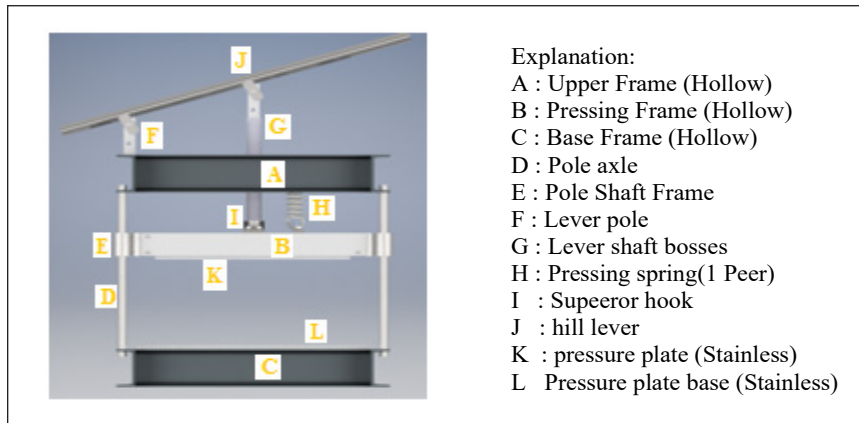


Figure 8. The part of the machine



Figure 9. The prototype of pressing machine

machine is being concerned so that the fatigue could be reduced. Besides, to avoid fatigue when doing the pressing and molding process, the machine design will be placed on the table so that the body position while doing the pressing and molding is in a sitting position. Figure 8 shows that it has a user-friendly design so that it will be easier to use, even the maintenance process is easy to do. This design is expected to increase the number of production capacity of this SME. Figure 9 shows the prototype of this design.

Figure 9 shows that the machine was executed by hand but in an ergonomic manner. Besides, this machine was made for the sitting position. The used material consists of iron and stainless steel. As stated in the previous section, this SME still utilizes the traditional equipment to do the pressing and molding process, and which done manually so that it will take a long time to press and molding the chips and resulting in the differences in both

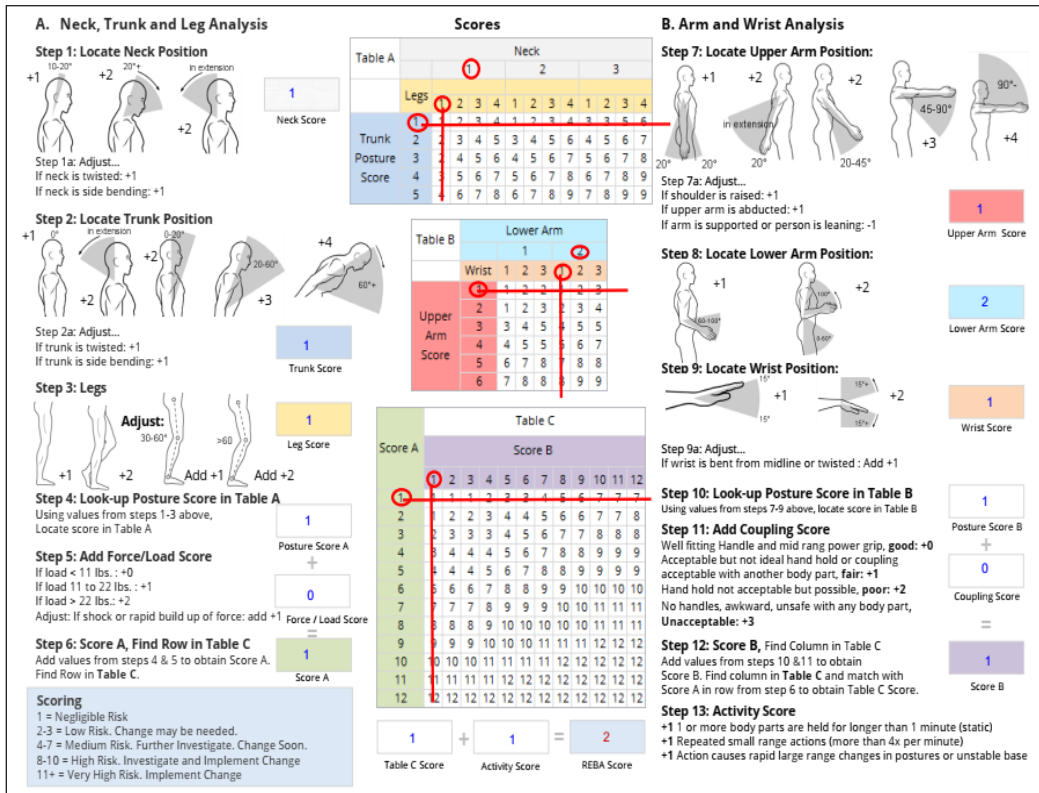


Figure 10. The Results of REBA assessment

the thickness and the diameter. Some of the advantages offered by this machine are the molding time is 0.5 minutes per tray which is 16 chips in a tray, the used of this machine could minimize the occurrence of fatigue, has a strong and stable construction, and utilizes the food grade material. On the other side, to prove that the given design has been able to reduce the problems faced by this SME, the assessment using REBA and RULA was conducted once more. Figure 10 shows the results of the REBA assessment meanwhile Figure 11 shows the results of the RULA assessment.

The results of the REBA assessment show that the score of REBA was 2 which means that the new machine has a low risk, and the change may be needed. When compared with the previous assessment, the score has been decreased from 5 to 2. Besides, the results of the RULA assessment also showed the significant results. Figure 11 shows the calculation of RULA assessment.

The results of the RULA assessment for the given machine also gave positive feedback. Figure 11 shows that the score of the RULA assessment is 2 which means acceptable posture. Compared with the previous assessment, the new machine is succeeding to decrease the score from 5 to 2.

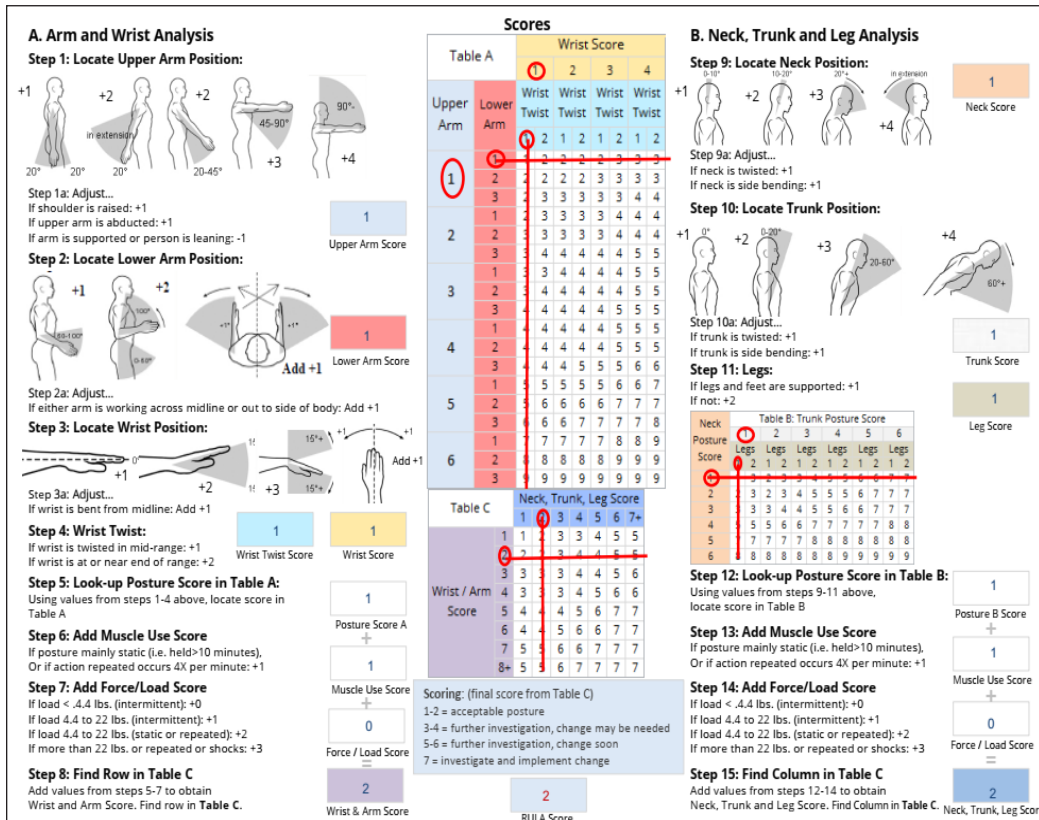


Figure 11. The Results of RULA assessment

CONCLUSION

The results of the posture assessment using REBA RULA show that the pressing and molding processes need to be improved. The improvement process is carried out by designing a pressing and molding machine. The results on the HOQ matrix show that the conveniences of the user, has an ergonomic design, user friendly, and could increase the production capacity are the voice of customers with the largest priority score. Therefore, the given design will refer to these requirements. This research is not only designing the machine but also create the machine prototype which also refers to the customer requirements. The designed machine is capable to produce 16 chips in 0.5 minutes and the production results have a high degree of precision. Besides, to prove that the given recommendations gave the positives impacts, the REBA and RULA assessment of the new machine was conducted. The results of the REBA and RULA assessment show that the use of a new machine could decrease the score from the previous assessment. Therefore, it can be concluded that the use of the new machine is able to solve the problems faced by this SME. For future research, a cost analysis might be needed.

ACKNOWLEDGEMENT

This project is funded by The Ministry of Research, Technology and Higher Education-Directorate General of Higher Education, Indonesia. We are so thankful for the financial support from Ministry of Research, Technology and Higher Education- Directorate General of Higher Education.

REFERENCES

- Ahmedova, S. (2015). Factors for Increasing the Competitiveness of Small and Medium- Sized Enterprises (SMEs) in Bulgaria. *Procedia - Social and Behavioral Sciences*, 195(February), 1104-1112. <https://doi.org/10.1016/j.sbspro.2015.06.155>
- Akshinta, P. Y., & Susanty, A. (2017). Analisis RULA (rapid upper limb assessment) dalam menentukan perbaikan postur pekerja las listrik resiko musculoskeletal disorders [Analysis RULA (rapid upper limb assessment) in determining improvement posture workers electrical welding in a welding shop electricity to reduce the risk musculoskeletal disorders]. *Industrial Engineering Online Journal*, 6(1), 1-10.
- Erdil, N. O., & Arani, O. M. (2019). Quality function deployment: More than a design tool. *International Journal of Quality and Service Sciences*, 11(2), 142-166. <https://doi.org/10.1108/IJQSS-02-2018-0008>
- Hashim, A. M., & Dawal, S. Z. M. (2012). Kano model and QFD integration approach for ergonomic design improvement. *Procedia - Social and Behavioral Sciences*, 57(October), 22-32. <https://doi.org/10.1016/j.sbspro.2012.09.1153>
- Ijaz, M., Ahmad, S. R., Akram, M., Khan, W. U., Yasin, N. A., & Nadeem, F. A. (2020). Quantitative and qualitative assessment of musculoskeletal disorders and socioeconomic issues of workers of brick industry in Pakistan. *International Journal of Industrial Ergonomics*, 76(August 2019), Article 102933. <https://doi.org/10.1016/j.ergon.2020.102933>
- Kee, D., Na, S., & Chung, M. K. (2020). Comparison of the ovako working posture analysis system, rapid upper limb assessment, and rapid entire body assessment based on the maximum holding times. *International Journal of Industrial Ergonomics*, 77(December 2019), Article 102943. <https://doi.org/10.1016/j.ergon.2020.102943>
- Maksum, I. R., Rahayu, A. Y. S., & Kusumawardhani, D. (2020). A social enterprise approach to empowering micro, small and medium enterprises (SMEs) in Indonesia. *Journal of Open Innovation: Technology, Market, and Complexity*, 6(3), Article 50. <https://doi.org/10.3390/joitmc6030050>
- Marsot, J. (2005). QFD: A methodological tool for integration of ergonomics at the design stage. *Applied Ergonomics*, 36(2), 185-192. <https://doi.org/10.1016/j.apergo.2004.10.005>
- Punchihewa, H. K. G. (2010). *The potential of quality function deployment (QFD) in reducing work-related musculoskeletal disorders* (Doctoral dissertation). Loughborough University, England. Retrieved February 23, 2021, from https://repository.lboro.ac.uk/articles/thesis/The_potential_of_Quality_Function_Deployment_QFD_in_reducing_work-related_musculoskeletal_disorders/9356639
- Rahman, N. A., Yaacob, Z., & Radzi, R. M. (2016). An overview of technological innovation on SME survival: A conceptual paper. *Procedia - Social and Behavioral Sciences*, 224(August 2015), 508-515. <https://doi.org/10.1016/j.sbspro.2016.05.427>

- Ramayah, T., Lim, Y. C., & Mohamed, S. (2005). SME e-readiness in Malaysia: Implications for planning and implementation. *Sasin Journal of Management*, 11(1), 103-120.
- Revadi, C. E., Gunawan, C. S., & Rakasiwi, G. J. (2019). Prevalensi dan faktor-faktor penyebab musculoskeletal disorders pada operator gudang industri ban PT X Tangerang Indonesia [Prevalence and factors causing musculoskeletal disorders at the operator of tire industry warehouse PT X Tangerang, Indonesia]. *Jurnal Ergonomi Indonesia (The Indonesian Journal of Ergonomic)*, 5(1), 10-15. <https://doi.org/10.24843/jei.2019.v05.i01.p02>
- Shil, N. C., Ali, M. A., & Paiker, N. R. (2010). Robust customer satisfaction model using QFD. *International Journal of Productivity and Quality Management*, 6(1), 112-136. <https://doi.org/10.1504/IJPM.2010.033887>
- Tiogana, V., & Hartono, N. (2020). Analisis Postur Kerja dengan Menggunakan REBA dan RULA di PT X [Worker posture analysis using REBA and RULA at PT X.]. *Journal of Integrated System*, 3(1), 9-25. <https://doi.org/10.28932/jis.v3i1.2463>

Numerical Simulations and Experimental Validation on LBW Bead Profiles of Ti-6Al-4V Alloy

Harish Mooli, Srinivasa Rao Seeram, Satyanarayana Goteti and Nageswara Rao Boggarapu*

Department of Mechanical Engineering, Koneru Lakshmaiah Education Foundation, Deemed to be University, Green Fields, Vaddeswaram, Guntur-522 502, India

ABSTRACT

The lightweight titanium alloys possess good resistance to corrosion and temperature. They are used in turbine engines and aircraft structures. The strength of weld joint is dependent on thermal history in the weld zone and the weld bead geometry. The quality of weld can be improved by specifying the optimal welding parameters. Trial-and-error experimental methods are time-consuming and expensive. This paper deals with Computational Fluid Dynamics (CFD) models to carry out three-dimensional thermo-fluid analysis. Buoyancy and Marangoni stress are incorporated. Temperature dependent properties of Ti-6Al-4V alloy and the process conditions are specified for generating the weld bead profile. The CFD model is validated initially through comparison of existing test data. Further studies are made by conducting tests on the pulsating laser welding of Ti-6Al-4V alloy. The effects of welding speed, pulse width and pulse frequency on the weld bead geometry are examined. This study confirms the adequacy of modeling and simulations of weld bead geometry with test results.

Keywords: Beam diameter, frequency, power, pulse width, weld bead

ARTICLE INFO

Article history:

Received: 06 February 2021

Accepted: 02 April 2021

Published: 31 July 2021

DOI: <https://doi.org/10.47836/pjst.29.3.32>

E-mail addresses:

harish.m313@gmail.com (Harish Mooli)

ssrao@kluniversity.in (Srinivasa Rao Seeram)

gotetisatya@yahoo.co.in (Satyanarayana Goteti)

bnrao52@rediffmail.com (Nageswara Rao Boggarapu)

* Corresponding author

INTRODUCTION

Welding is one of the critical technologies in most of the relevant engineering applications. Gas Tungsten Arc Welding (GTAW) and Electron Beam Welding (EBW) are widely being used in aerospace, automotive, chemical, food, medical and nuclear industries. Laser Beam Welding (LBW), a fusion joining technique, is

characterized by small Heat Affected Zone (HAZ) and Fusion Zone (FZ), and minimal distortion. Advanced research is directed towards development of modeling and simulation tools, in addition to the process control in welding metallurgy (Wu et al., 2018; Ruan et al., 2018; Dal & Peyre, 2017; D'Ostuni et al., 2017; Popescu et al., 2017). Extensive studies are made on laser weld joint properties of metallic materials such as Al-based alloys (Zhang et al., 2017), AZ31 alloy (Lu et al., 2018), Al-steel (Cui et al., 2017; Casalino et al., 2017), steels (Górka & Stano, 2018; Mohammed et al., 2017; Xue et al., 2017; Evin & Tomáš, 2017), and Ti-based alloys (Zeng et al., 2017; Sánchez-Amaya et al., 2017; Caiazzo et al., 2017b). Mashinini & Hattingh (2018) have utilized LBW for joining 3 mm thick Ti-6Al-4V alloy sheets. Chmelíčková et al. (2020) have characterized butt welds of Ti-6Al-4V alloy sheets. Welding has been performed using a pulsed Neodymium-doped Yttrium Aluminum Garnet (Nd:YAG) laser under argon shielding gas atmosphere. The effects of LBW processes for titanium alloys are examined on weld pool shape, bead width, HAZ and other weld bead characteristics.

Kumar et al. (2017) have performed LBW of Ti-6Al-4V alloys in butt configurations. Rajulu et al. (2018) have conducted experiments to examine the weld bead characteristics considering the process variables (such as pulse frequency, pulse width, welding speed, and pulse energy). Empirical relations are developed using response surface methodology (RSM) for the bead geometry in terms of the process variables. Caiazzo et al. (2017a) have conducted number of weld trials on Ti-6Al-4V plates in corner joint followed by microstructure and microhardness tests. Optimal LBW process variables are identified with minimal undercut and porosity. Liu et al. (2014) have made the fatigue damage evolution on pulsating laser welding of Ti-6Al-4V alloy. Amaya et al. (2013) have observed fine grain microstructure by low heat input causing enhancement in the critical nominal strain delaying crack-initiation. Cai et al. (2017) have used pure Ti-filler with laser to improve the welding properties of γ -Ti-Al alloy. Boccarusso et al. (2015) have examined the influence of LBW parameters on defects in Ti-6Al-4V hot rolled sheets. Junaid et al. (2017) have performed pulsating laser welding of Ti-5Al-2.5Sn alloy to examine the effect of LBW parameters on weld pool shape, pulse overlap, oxide formation and microstructure (using Scanning Electron Microscope (SEM) and Optical Microscope (OM)). Laser peak power indicates significant effects on the FZ oxygen contents and grain size. Weld pool shape is controlled by the peak power and heat input per unit length. Kashaev et al. (2016) have analyzed the morphology of butt and T-joints in LBW of Ti-6Al-4V alloy and achieved low porosity in the desired seam geometry. Hong and Shin (2016) have adopted a multi-physics prediction model to analyze the bead profile and properties in laser welding of Ti-6Al-4V alloy.

The strength of weld joint is dependent on thermal history in the weld bead geometry. To improve the quality of weld, there is a need for specifying the optimal welding parameters.

Time consuming trial-and-error approaches are expensive. Computational welding mechanics (CWM) has become an active field in the Welding Science and Technology. However, use of CWM in industries is in the initial stage. A CFD model for 3D thermo-fluid analysis is developed incorporating the buoyancy and Marangoni stress. Temperature dependent properties including the process conditions are specified for estimating the weld bead profile. The CFD model is validated initially through comparison of existing test data. Later on, tests are conducted for further validation of the developed model on the pulsating laser welding of Ti-6Al-4V alloy. The influence of welding speed, pulse width and pulse frequency on weld bead geometry are investigated. The test results are compared with three dimensional unsteady numerical simulations.

MATERIALS AND METHODS

Titanium alloys are light in weight and possess good resistance to corrosion and temperature. Welding tests are conducted with pulsed laser beam on Ti-6Al-4V alloy to study the weld pool geometry. A three-dimensional fluid flow and heat transfer model is developed for generation of weld bead geometry using a volumetric laser heat source. Details on the model development and welding process simulations using Ansys 16 fluent are presented below. This section also highlights the validity of numerical simulations with test results.

Thermo-fluid Analysis

In laser welding, thermo-fluid phenomena were examined by integrating the user defined functions with the code of finite volume method in ANSYS and solving the Navier–Stokes and the k - ε equations in mushy zone and regions of weld pool as in Equation 1 (Satyanarayana et al., 2018; Satyanarayana et al., 2019a; Satyanarayana et al., 2019b).

The continuity equation is:

$$\frac{\partial \rho}{\partial t} + \nabla \cdot (\rho \vec{V}) = 0 \quad [1]$$

Here ρ , t and \vec{V} are the density, time and the weld pool velocity respectively.

The density (ρ) and the liquid mass fraction (f_L) are defined in Equation 2 and 3:

$$\rho = f_L \rho_L + f_S \rho_S = f_L \rho_L + (1 - f_L) \rho_S \quad [2]$$

$$\begin{aligned} f_L &= 0 \quad \text{for } T \leq T_S \\ &= (T - T_S)(T_L - T_S)^{-1} \quad \text{for } T \in [T_S, T_L] \\ &= 1 \quad \text{for } T \geq T_L \end{aligned} \quad [3]$$

The momentum Equation 4 is as below (ANSYS, 2013; ANSYS, 2016):

$$\frac{\partial(\rho\vec{V})}{\partial t} + \nabla \cdot (\rho\vec{V}\vec{V}) = -\nabla p + \mu \nabla^2 \vec{V} + \rho\vec{g} + \vec{S}_w \quad [4]$$

Here p , μ and $\rho\vec{g}$ are the static pressure, viscosity, and the gravitational body force.

Denoting A_{mush} as the mushy zone constant and \vec{w} as the pull velocity, the source term (or momentum frictional dissipation) in the mushy zone is expressed as Equation 5 (Voller & Prakash, 1987; Brent et al., 1988)

$$\vec{S}_w = (f_L^3 + 10^{-3})^{-1} (1 - f_L)^2 (\vec{w}) A_{mush} \quad [5]$$

The enthalpy-porosity technique of Jalali and Najafi (2010) is adopted to identify the interface from the phase change.

The energy Equation 6 is:

$$\frac{\partial(\rho H)}{\partial t} + \nabla \cdot (\rho\vec{V}H) = \nabla \cdot (\kappa \nabla T) + S \quad [6]$$

Here $H (\equiv h + \Delta H)$, $h \left(= h_{ref} + \int_{T_{ref}}^T C_p dT \right)$ and S are the enthalpy, sensible heat, and volumetric heat source, respectively. C_p , h_{ref} and κ are respectively, the specific heat, reference enthalpy and thermal conductivity.

The latent heat (ΔH) for a solid is zero, whereas in case of a liquid (Equation 7),

$$\Delta H = m_L L \quad [7]$$

Here L is the latent heat of the liquid metal. Top surface of the flat weld pool normal velocity is zero.

The shearing stress (Equation 8),

$$\tau = \frac{\partial \sigma}{\partial T} \nabla T \quad [8]$$

The lumped convection coefficient (Akbari et al., 2014): $h_c = 2.4 \times 10^{-3} \varepsilon T^{1.61}$ is used for imposing conditions of convection and radiation on all surfaces. Due to laser, a transient heat flux is considered on the top surface.

Introducing the Stefan–Boltzmann constant (σ_{SB}), emissivity (ε), and the ambient temperature (T_a), the energy balance is of the form (Equation 9) (Satyanarayana, 2020):

$$\kappa \frac{\partial T}{\partial z} = q - h_c (T - T_a) - \sigma_{SB} \varepsilon (T^4 - T_a^4) \quad [9]$$

For laser, the volumetric heat flux (q_v) is a Gaussian distribution of the form (Equation 10).

$$q_v = \frac{2P}{\pi r_0^2 \delta} i(t) \exp\left(1 - \frac{r^2}{r_0^2}\right) \left(1 - \frac{y}{\delta}\right) \quad [10]$$

Here P is the absorbed laser power. The current radius (r) is from cone axis. r_0 is the radius of laser beam. y is the depth and δ is the thickness. In pulsed laser welding, the time-based function, $i(t) = 1$, when the pulse is active, whereas $i(t) = 0$, when the pulse is inactive.

Model is developed for fluid flow and heat transfer using Ansys16 Fluent as in (Satyanarayana et al., 2018; Satyanarayana et al., 2019a; Satyanarayana et al., 2019b). User defined functions (UDF) are embedded. Residual stresses can be evaluated by exporting the thermal history from CFD analysis to Ansys16 FEA solver. Procedure for welding process simulations is highlighted briefly below:

- Step-1:** Creation of the computational domain and component geometry.
- Step-2:** Creation of fine and coarse meshes near and away from heat source.
- Step-3:** Selection of phases and turbulence models.
- Step-4:** Introduction of user defined codes (UDFs).
- Step-5:** Specification of thermal and physical material properties.
- Step-6:** Application of boundary conditions.
- Step-7:** Specification of number of time steps and iterations (solution convergence including welding and cooling phase).
- Step-8:** Laser beam activation with starting and end positions.
- Step-9:** Acquiring information on temperature and fluid flows.
- Step-10:** Increase the time step to improve the solution. Otherwise, move to Step-12
- Step-11:** Change of laser beam position proceed to Step-9
- Step-12:** Record the weld bead profile and temperature distribution;
- Step-13:** Export the geometry and solution files from Fluent to Finite Element Analysis (FEA) solver.
- Step-14:** Specification of reference temperature, mechanical properties to FEA solver.
- Step-15:** Check the mesh configuration
- Step-16:** Import thermal loads from CFD to FEA
- Step-17:** Application of structural boundary conditions
- Step-18:** Solving for stress and strain in the weld coupon.
- Step-19:** Increase in time-step for the incompleteness of job. Otherwise go to Step-21.

Step-20: To simulate transient state, the previous time step results are applied as initial conditions and go to Step-18.

Step-21: Record the results. Stop numerical simulations.

The above procedure is followed to examine the impact of thermo-physical properties on various performance indicators. This paper presents CFD analysis results for checking the adequacy of the weld bead profiles.

Validity of Numerical Simulations

Numerical simulations are performed on pulsed laser welding to examine the adequacy of the developed 3D flow model through comparison with existing test data. Jiang et al. (2019) have conducted pulsed laser welding on $50 \times 20 \times 3$ mm Ti-6Al-4V alloy plates. Table 1 gives specifications of machine configurations.

Table 1
Details on the pulsed laser welding of 3mm thick Ti-6Al-4V alloy (Jiang et al., 2019)

S. No.	Machine Specifications	
1	Laser source	Nd:YAG pulsed IQL-20
2	Maximum power	750W
3	Pulse wavelength	1.06
4	Laser variable range	0.2 to 25ms
5	Pulse frequency	1-250 Hz
6	Pulse energy	0 to 40J
7	Spot diameter	0.7mm
8	Focal distance	6mm

The following temperature dependent properties as in (Rai, 2008) are considered in the present numerical simulations. Specific heat of solid is 670 J/kg K, whereas it is 730 J/kg K in liquids. Viscosity of liquid is 0.005 kg/m.s. Melting heat is 370000 J/kg. Solidus temperature is 1878 K. Liquidus temperature is 1928 K.

The density, $\rho(\text{kg/m}^3)$ in terms of temperature, $T(K)$ is defined in Equation 11 and 12.

$$\rho_s = 4420 - 0.154(T - 300) \tag{11}$$

$$\rho_L = 3920 - 0.68(T - 1928) \tag{12}$$

Thermal conductivity, $\kappa(W.m^{-1}.K^{-1})$ in terms of temperature, $T(K)$ is defined as Equation 13.

$$\begin{aligned} \kappa &= -0.32 + 1.46 \times 10^{-2} T \quad \text{for } 1400 < T < 1850K \\ &= -6.66 + 1.83 \times 10^{-2} T \quad \text{for } 1950 < T < 2700K \end{aligned} \tag{13}$$

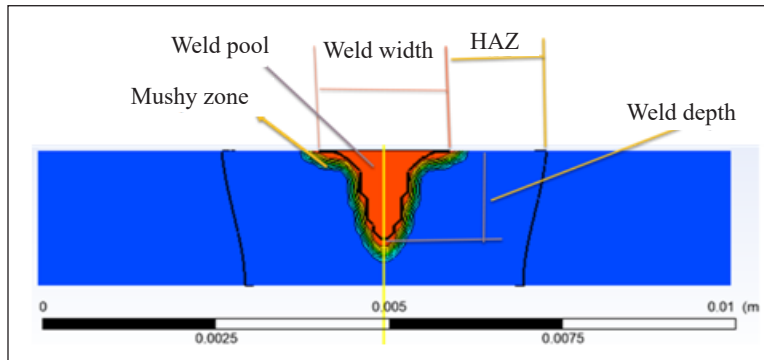


Figure 1. Nomenclature of the weld bead profile

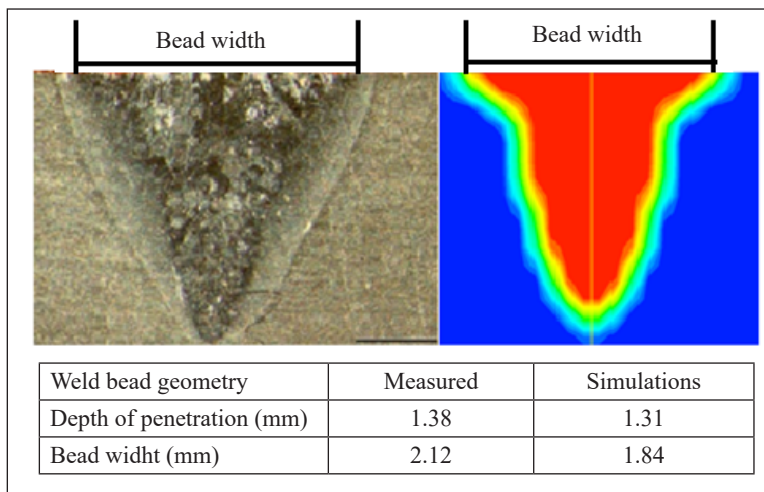


Figure 2. Comparison of simulated weld bead geometry with the test result (Jiang et al., 2019)

Following the procedure in the preceding section for laser welding process simulations on Ti-6Al-4V alloy, weld pool cross-section is generated at the 240W of average power, 25Hz frequency, 4.2 ms pulse width and 0.7mm beam diameter. Figure 1 shows the nomenclature of CFD simulation weld bead profile. Figure 2 shows the comparison of the experimental and numerical CFD simulations of the weld bead profile. Numerical simulation results in Figure 2 indicate the validity with test data (Jiang et al., 2019).



Figure 3. Experimental set-up for pulsed LBW of Ti-6Al-4V alloy

Experiments are performed to examine the adequacy of the temperature dependent properties, modeling, and numerical simulations of pulsated laser beam welding of Ti-6Al-4V alloy. A 16kW Nd:YAG pulsed mode integrated with CNC (Computer Numerical Control) station is used. Figure 3 shows the experimental set-up. Pulsated laser welding has been carried out on 50 × 20 × 2 mm Ti-6Al-4V alloy plates. Butt joint is the configuration. The laser heat source moves along the direction of work-piece length. The workpiece is supported by clamping device to minimize distortion and displacement. Ti-6Al-4V alloy contains highly oxidized elements.

RESULTS AND DISCUSSION

During welding, there is a possibility of oxidation under atmospheric condition. Shielding gas argon is used to overcome such problems. Pulse frequency (Hz), pulse width (ms), pulse energy (J) and beam diameter (mm) are strongly related with each other (Equation 14 & 15). Table 2 gives the input variables for three test runs.

$$Pulse\ energy\ (J) = \frac{Average\ Power(W)}{Frequency\ (Hz)} \tag{14}$$

$$Peak\ power\ (W) = \frac{Pulse\ energy}{pulse\ width} \tag{15}$$

Table 2
Input variables considered in the pulsated LBW Process

Test Run	Frequency (Hz)	Pulse Width (ms)	Pulse Energy (J)	Average Power (W)	Peak Power (W)	Speed (mm/s)
1	16	9	14	224	1556	2.0
2	14	8	20	280	2550	1.5
3	16	7	14	224	2000	1.0

The weld pool shape for test run-1 is shown in Figure 4. The simulated weld bead geometry is compared with the test run-1 in Figure 5. Temperature distribution is shown in Figure 6. The velocity contour plot in the weld pool is shown in Figure 7.

Peclet number $P_e = \frac{L_R C_p \rho u}{\kappa}$ indicates the relative rate of heat transfer (by convection and conduction). Here, u is the weld pool velocity. ρ , C_p , κ and L_R are respectively, the liquid density, specific heat, liquid metal thermal conductivity and the pool radius. In the present study, $P_e > 5$. This indicates convective heat transfer domination over conduction mode. The heat transfer is due to convection in weld pool. The molten weld pool moves

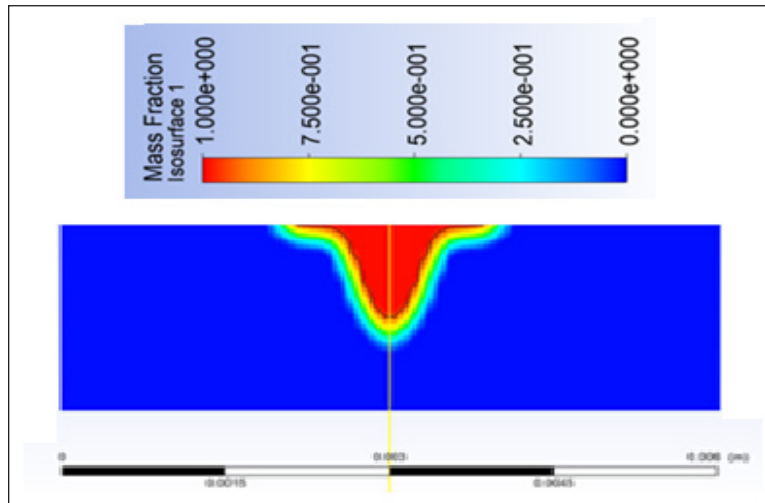


Figure 4. Weld pool shape for test run-1

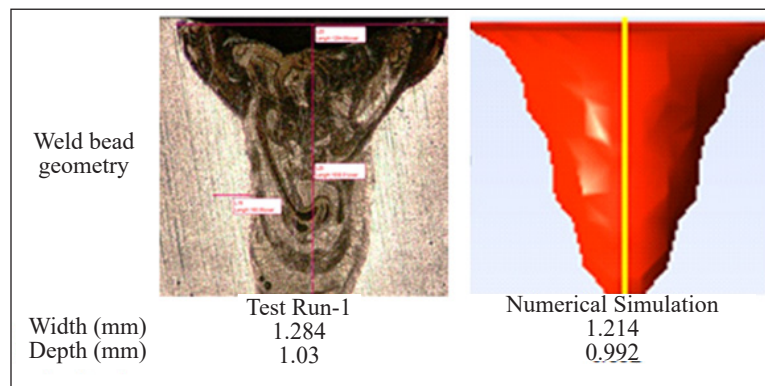


Figure 5. Comparison of simulated weld bead geometry with test run-1

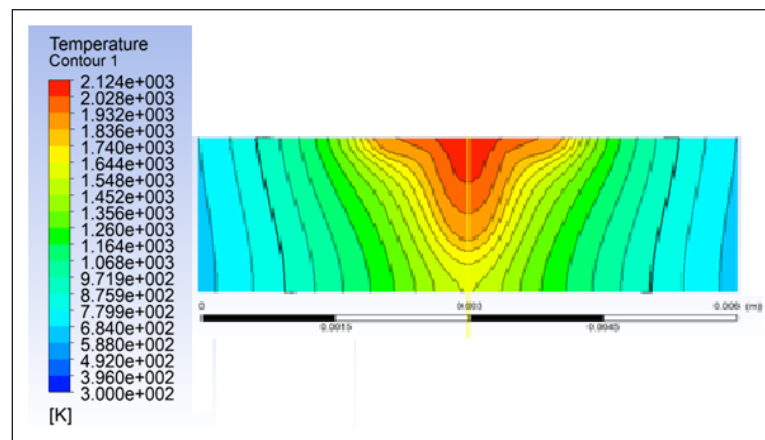


Figure 6. Temperature distribution (test run-1: pulse width= 9 ms; welding speed=2 mm/s)

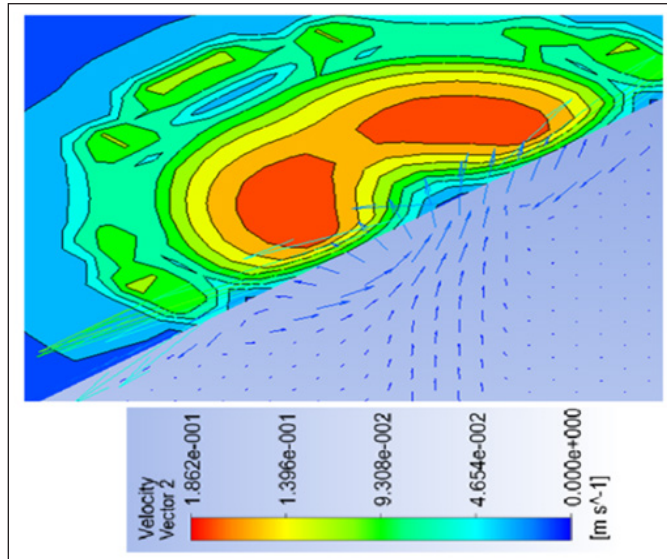


Figure7. Velocity contour plot in the weld pool (test run-1)

from inward to top (or reverse in direction), which depends on the surface tension gradient on pool top surface. The convective movement influences the weld geometry.

Marangoni and buoyancy are driving forces in the weld pool flow. Marangoni (Ma) and Grashof (Gr) numbers show the importance of these forces (Equation 16 & 17).

$$Ma = \frac{\rho L_R}{\mu^2} \frac{\partial \sigma}{\partial T} \Delta T \quad [16]$$

$$Gr = g \rho^2 \beta L_B^3 \frac{\Delta T}{\mu^2} \quad [17]$$

Here g is the gravitational acceleration. ΔT is the difference in weld pool and solidus peak temperatures. L_B is the characteristic length for the buoyancy force in the liquid pool. It is approximately $\frac{1}{8}$ of the weld pool width (Debroy & David, 1995). In this present case study, Ma/Gr is in the order of 10^5 . Hence, the weld pool flow is driven by surface tension gradient.

Figure 8 shows simulated weld bead geometry for test run-2. The temperature distribution is shown in Figure 9. For test run-3, weld bead geometry and temperature distribution are shown in Figures 10 and 11, respectively. Numerical simulations of the weld bead profiles are close to the ones observed from tests. This demonstrates the validity of modeling and specification of temperature dependent properties. Temperature distribution will be useful to estimate residual stress in weld-joints from FEA. Experiments

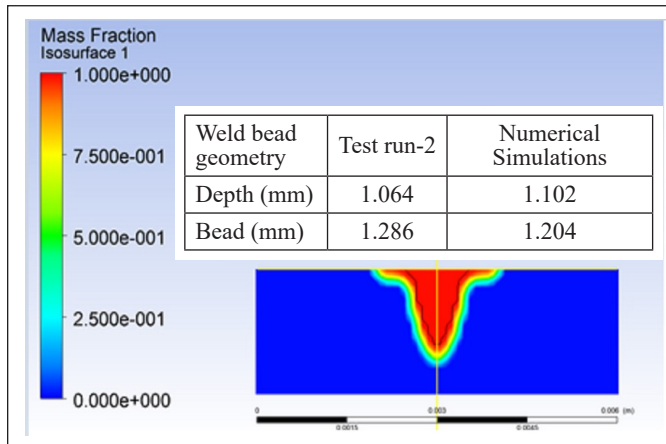


Figure 8. Weld pool shape for pulse width 8 ms and welding speed 1.5 mm/s

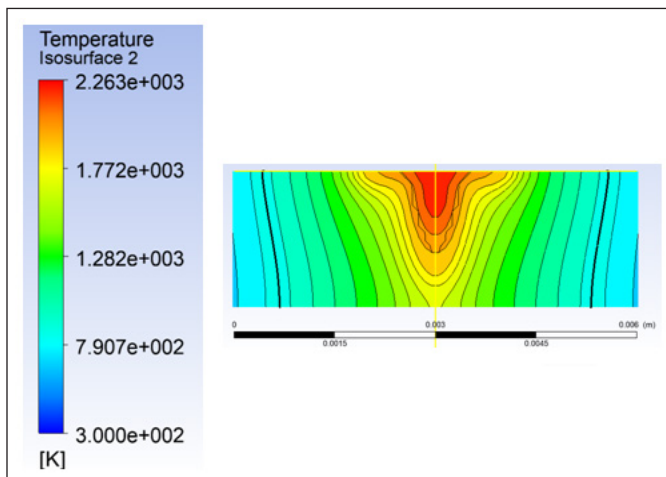


Figure 9. Temperature distribution for test run-2 (pulse width= 8 ms; welding speed= 1.5 mm/s)

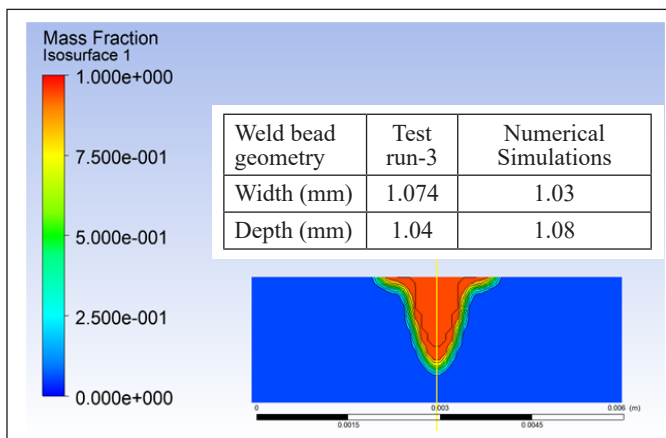


Figure 10. Weld pool shape for pulse width 7 ms and welding speed 1.0 mm/s

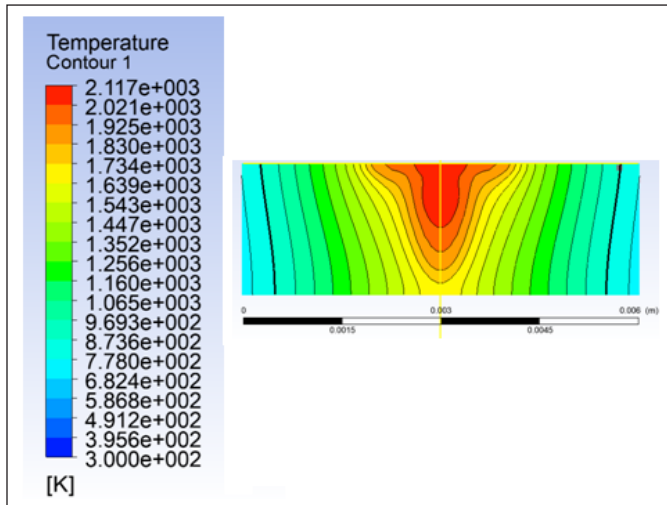


Figure 11. Temperature distribution for test run-3 (pulse width= 7 ms; welding speed= 1.0 mm/s)

are conducted to study the impact of frequency on weld pool dimensions at constant speed, pulse width and pulse energy varying frequency from 12 to 16 Hz. Both weld width and depth are increased (Table 3). The quality of weld depends on heat transfer process, power density and interaction time (Equation 18 & 19).

$$Power\ density = \frac{Laser\ power}{Area\ of\ laser\ beam} \quad [18]$$

$$Interaction\ time = \frac{Beam\ Diameter}{Welding\ speed\ of\ the\ laser\ beam\ source\ and\ heat\ transfer} \quad [19]$$

The Laser power is increased with increasing the frequency; the plate receives high energy for the interaction time causing increase in the absorbed energy by melting pool and its temperature. This results in high weld width and depth. The test results of Table 4 confirm the effect of pulse energy. Tests are conducted by doubling the welding speed keeping other parameters constant. This reduces the interaction time of the laser beam to half. When the welding speed is increased test results in Table 5 indicate increase in

Table 3
Weld bead geometry with varying frequency

Test Run	Frequency (Hz)	Pulse width (ms)	Pulse Energy(J)	Average Power(W)	Peak Power(W)	Speed (mm/s)	Weld Width (mm)	Weld Depth (mm)
4	12	9	14	168	1556	1	1.05	0.68
5	16	9	14	224	1556	1	1.314	0.98

Table 4
Weld bead geometry with varying pulse energy

Test Run	Frequency (Hz)	Pulse width (ms)	Pulse Energy(J)	Average Power(W)	Peak Power(W)	Speed (mm/s)	Weld Width (mm)	Weld Depth (mm)
6	14	8	16	224	2000	1.5	0.916	0.476
7	14	8	20	280	2550	1.5	1.064	1.286

Table 5
Weld bead geometry with varying weld speed

Test Run	Frequency (Hz)	Pulse width (ms)	Pulse Energy(J)	Average Power(W)	Peak Power(W)	Speed (mm/s)	Weld Width (mm)	Weld Depth (mm)
8	12	9	18	216	2000	1	1.056	1.292
9	12	9	18	216	2000	2	1.264	0.774

weld width and decrease in depth. The width of melting is increased due to reducing heat interaction time and aggregation of melted material in the upper layer. It should be noted that frequency, pulse energy and welding speed are the welding parameters controlling bead width. These three parameters are commonly known to affect the weld bead. Though the frequency and pulse energy are same for the bead widths of test run-1 and test run-3 (Figures 5 and 10), the high welding speed reduces the heat input to the bead resulting reduction in the width and depth of penetration. But only penetration was narrow for test run-1 as compared to test run-3. This may be due to high welding speed and pulse width with low peak power in test run-1. In general, the width of melting is increased because less penetration laser beam to the lower layers due to reducing heat interaction time and aggregation of melted material in the upper layer.

CONCLUSIONS

Welding tests are conducted with pulsed laser beam on Ti-6Al-4V alloy to study the weld pool geometry. A three-dimensional fluid flow and heat transfer model is developed for generation of the weld bead geometry, temperature and velocity contours in the weld pool using a volumetric laser heat source. The major findings are:

- Numerical simulations are comparable with the results of existing and conducted experiments.
- Convection heat transfer is the major process in weld pool shape formation.
- The temperature gradient on the weld pool top surface plays a major role.
- The weld pool size depends on the power density and interaction time. High power density and low interaction time result in high weld depth and low weld width.
- High frequency increases the weld pool volume.

Modeling and simulations will be useful in generating the weld geometry and temperature profiles in FZ and HAZ. It is possible to control the laser welding parameters for achieving optimal weld pool geometry and to minimize the developmental cost for new applications. It is planned to adopt the Taguchi design of experiments, which will minimize the number of numerical simulations and provide information for full factorial design of experiments. Multi-objective optimization concepts can be utilized to select the optimal LBW parameters for achieving narrow weld bead width with full depth of penetration.

ACKNOWLEDGEMENTS

The authors wish to acknowledge greatly to Optilase, India's first Laser Process Development center, SIDCO Women's Industrial Estate, Thirumullaivoyal, Chennai – 600 062 Tamilnadu, India, for providing facilities to carry out the experimental studies. Finally, the authors are grateful to the reviewers for their constructive criticism to improve the clarity of presentation.

REFERENCES

- Akbari, M., Saedodin, S., Toghraie, D., Shoja-Razavi, R., & Kowsari, F. (2014). Experimental and numerical investigation of temperature distribution and melt pool geometry during pulsed laser welding of Ti6Al4V alloy. *Optics & Laser Technology*, 59, 52-59. <https://doi.org/10.1016/j.optlastec.2013.12.009>
- Amaya, J. S., Amaya-Vázquez, M. R., & Botana, F. J. (2013). Laser welding of light metal alloys: Aluminium and titanium alloys. In *Handbook of Laser Welding Technologies* (pp. 215-254). Woodhead Publishing. <https://doi.org/10.1533/9780857098771.2.215>
- ANSYS. (2013). *ANSYS fluent theory guide*. ANSYS Inc.
- ANSYS. (2016). *ANSYS® academic research, release 16.0, ANSYS Fluent in ANSYS Workbench User's Guide*. ANSYS Inc.
- Boccarusso, L., Arleo, G., Astarita, A., Bernardo, F., de Fazio, P., Durante, M., Giudice, G., Minutolo, F. M. C., Sepe, R., & Squillace, A. (2015). Effect of the process parameters on the geometrical defects of Ti-6Al-4V hot rolled sheets laser beam welded. In *Key Engineering Materials* (Vol. 651, pp. 901-906). Trans Tech Publications Ltd. <https://doi.org/10.4028/www.scientific.net/KEM.651-653.901>
- Brent, A. D., Voller, V. R., & Reid, K. T. J. (1988). Enthalpy-porosity technique for modeling convection-diffusion phase change: application to the melting of a pure metal. *Numerical Heat Transfer, Part A Applications*, 13(3), 297-318. <https://doi.org/10.1080/10407788808913615>.
- Cai, X., Sun, D., Li, H., Guo, H., Gu, X., & Zhao, Z. (2017). Microstructure characteristics and mechanical properties of laser-welded joint of γ -TiAl alloy with pure Ti filler metal. *Optics & Laser Technology*, 97, 242-247. <https://doi.org/10.1016/j.optlastec.2017.07.011>.
- Caiazza, F., Alfieri, V., Corrado, G., Argenio, P., Barbieri, G., Acerra, F., & Innaro, V. (2017a). Laser beam welding of a Ti-6Al-4V support flange for buy-to-fly reduction. *Metals*, 7(5), Article 183. <https://doi.org/10.3390/met7050183>

- Caiazza, F., Alfieri, V., Astarita, A., Squillace, A., & Barbieri, G. (2016b). Investigation on laser welding of Ti-6Al-4V plates in corner joint. *Advances in Mechanical Engineering*, 9(1). <https://doi.org/10.1177/1687814016685546>
- Casalino, G., Leo, P., Mortello, M., Perulli, P., & Varone, A. (2017). Effects of laser offset and hybrid welding on microstructure and IMC in Fe–Al dissimilar welding. *Metals*, 7(8), Article 282. <https://doi.org/10.3390/met7080282>.
- Chmelíčková, H., Hiklová, H., Václavek, L., Tomáščík, J., & Čtvrtlík, R. (2020). Characterization of titanium laser welds. *Acta Polytechnica CTU Proceedings*, 27, 145-148. <https://doi.org/10.14311/APP.2020.27.0145>.
- Cui, L., Chen, B., Qian, W., He, D., & Chen, L. (2017). Microstructures and mechanical properties of dissimilar Al/Steel butt joints produced by autogenous laser keyhole welding. *Metals*, 7(11), Article 492. <https://doi.org/10.3390/met7110492>.
- D'Ostuni, S., Leo, P., & Casalino, G. (2017). FEM simulation of dissimilar aluminum titanium fiber laser welding using 2D and 3D Gaussian heatsources. *Metals*, 7(8), Article 307. <https://doi.org/10.3390/met7080307>.
- Dal, M., & Peyre, P. (2017). Multiphysics simulation and experimental investigation of aluminum wettability on a titanium substrate for laser welding-brazing process. *Metals*, 7(6), Article 218. <https://doi.org/10.3390/met7060218>.
- DebRoy, T., & David, S. A. (1995). Physical processes in fusion welding. *Reviews of Modern Physics*, 67(1), Article 85. <https://doi.org/10.3390/met7110504>.
- Evin, E., & Tomáš, M. (2017). The influence of laser welding on the mechanical properties of dual phase and TRIP steels. *Metals*, 7(7), Article 239. <https://doi.org/10.3390/met7070239>
- Górka, J., & Stano, S. (2018). Microstructure and properties of hybrid laser arc welded joints (laser beam-mag) in thermo-mechanical control processed S700MC steel. *Metals*, 8(2), Article 132. <https://doi.org/10.3390/met8020132>.
- Hong, K. M., & Shin, Y. C. (2016). Analysis of microstructure and mechanical properties change in laser welding of Ti6Al4V with a multiphysics prediction model. *Journal of Materials Processing Technology*, 237, 420-429. <https://doi.org/10.1016/j.jmatprotec.2016.06.034>.
- Jalali, A., & Najafi, A. F. (2010). Numerical modeling of the solidification phase change in a pipe and evaluation of the effect of boundary conditions. *Journal of Thermal Science*, 19(5), 419-424. <https://doi.org/10.1007/s11630-010-0403-z>.
- Jiang, D., Alsagri, A. S., Akbari, M., Afrand, M., & Alrobaian, A. A. (2019). Numerical and experimental studies on the effect of varied beam diameter, average power and pulse energy in Nd: YAG laser welding of Ti6Al4V. *Infrared Physics & Technology*, 101, 180-188. <https://doi.org/10.1016/j.infrared.2019.06.006>.
- Junaid, M., Khan, F. N., Rahman, K., & Baig, M. N. (2017). Effect of laser welding process on the microstructure, mechanical properties and residual stresses in Ti-5Al-2.5 Sn alloy. *Optics & Laser Technology*, 97, 405-419. <https://doi.org/10.1016/j.optlastec.2017.07.010>.

- Kashaev, N., Ventzke, V., Fomichev, V., Fomin, F., & Riekehr, S. (2016). Effect of Nd: YAG laser beam welding on weld morphology and mechanical properties of Ti–6Al–4V butt joints and T-joints. *Optics and Lasers in Engineering*, 86, 172-180. <https://doi.org/10.1016/j.optlaseng.2016.06.004>.
- Kumar, C., Das, M., Paul, C. P., & Singh, B. (2017). Experimental investigation and metallographic characterization of fiber laser beam welding of Ti-6Al-4V alloy using response surface method. *Optics and Lasers in Engineering*, 95, 52-68. <https://doi.org/10.1016/j.optlaseng.2017.03.013>.
- Liu, J., Gao, X. L., Zhang, L. J., & Zhang, J. X. (2014). A study of fatigue damage evolution on pulsed Nd: YAG Ti6Al4V laser welded joints. *Engineering Fracture Mechanics*, 117, 84-93. <https://doi.org/10.1016/j.engfracmech.2014.01.005>.
- Lu, G. F., Zhang, L. J., Pei, Y., Ning, J., & Zhang, J. X. (2018). Study on the size effects of H-Shaped fusion zone of fiber laser welded AZ31 joint. *Metals*, 8(4), Article 198. <https://doi.org/10.3390/met8040198>.
- Mashinini, P. M., & Hattingh, D. G. (2018). Influence of Laser Power and Traverse Speed on Weld Characteristics of Laser Beam Welded Ti-6Al-4V Sheet. *Mechanical Stress Evaluation by Neutron and Synchrotron Radiation: MECA SENS 2017*, 4(2018), 59-64. <http://dx.doi.org/10.21741/9781945291678-9>
- Mohammed, G. R., Ishak, M., Ahmad, S. N. A. S., & Abdulhadi, H. A. (2017). Fiber laser welding of dissimilar 2205/304 stainless steel plates. *Metals*, 7(12), Article 546. <https://doi.org/10.3390/met7120546>.
- Popescu, A. C., Delval, C., & Leparoux, M. (2017). Control of porosity and spatter in laser welding of thick AlMg5 parts using high-speed imaging and optical microscopy. *Metals*, 7(11), Article 452. <https://doi.org/10.3390/met7110452>.
- Rai, R. (2008). *Modeling of heat transfer and fluid flow in keyhole mode welding* (Doctoral dissertation). The Pennsylvania State University, USA.
- Rajulu, C. G., Krishna, A. G., & Rao, T. B. (2018). An integrated evolutionary approach for simultaneous optimization of laser weld bead characteristics. *Proceedings of the Institution of Mechanical Engineers, Part B: Journal of Engineering Manufacture*, 232(8), 1407-1422. <https://journals.sagepub.com/doi/10.1177/0954405416667431>.
- Ruan, X., Zhou, Q., Shu, L., Hu, J., & Cao, L. (2018). Accurate prediction of the weld bead characteristic in laser keyhole welding based on the stochastic kriging model. *Metals*, 8(7), Article 486. <https://doi.org/10.3390/met8070486>.
- Sánchez-Amaya, J. M., Pasang, T., Amaya-Vazquez, M. R., Lopez-Castro, J. D. D., Churiaque, C., Tao, Y., & Pedemonte, F. J. B. (2017). Microstructure and mechanical properties of Ti5553 butt welds performed by LBW under conduction regime. *Metals*, 7(7), Article 269. <https://doi.org/10.3390/met7070269>.
- Satyanarayana, G. (2020). *Thermal and fluid flow simulations in conduction mode laser beam welding of zirconium alloys* (Doctoral dissertation). Koneru Lakshmaiah Education Foundation, India.
- Satyanarayana, G., Narayana, K. L., & Rao, B. N. (2018). Numerical simulations on the laser spot welding of zirconium alloy endplate for nuclear fuel bundle assembly. *Lasers in Manufacturing and Materials Processing*, 5(1), 53-70. <https://doi.org/10.1007/s40516-018-0061-7>

- Satyanarayana, G., Narayana, K. L., Rao, B. N., Slobodyan, M. S., Elkin, M. A., & Kiselev, A. S. (2019a). Numerical simulation of the processes of formation of a welded joint with a pulsed ND: YAG laser welding of ZR-1% NB alloy. *Thermal Engineering*, 66(3), 210-218. <https://doi.org/10.1134/S0040601519030066>
- Satyanarayana, G., Narayana, K. L., & Rao, B. N. (2019b). Numerical investigation of temperature distribution and melt pool geometry in laser beam welding of a Zr-1% Nb alloy nuclear fuel rod end cap. *Bulletin of Materials Science*, 42(4), Article 170. <https://doi.org/10.1007/s12034-019-1873-6>
- Voller, V. R., & Prakash, C. (1987). A fixed grid numerical modelling methodology for convection-diffusion mushy region phase-change problems. *International Journal of Heat and Mass Transfer*, 30(8), 1709-1719. [https://doi.org/10.1016/0017-9310\(87\)90317-6](https://doi.org/10.1016/0017-9310(87)90317-6).
- Wu, J., Zhang, H., Feng, Y., & Luo, B. (2018). 3D multiphysical modelling of fluid dynamics and mass transfer in laser welding of dissimilar materials. *Metals*, 8(6), Article 443. <https://doi.org/10.3390/met8060443>.
- Xue, X., Pereira, A. B., Amorim, J., & Liao, J. (2017). Effects of pulsed Nd: YAG laser welding parameters on penetration and microstructure characterization of a DP1000 steel butt joint. *Metals*, 7(8), Article 292. <https://doi.org/10.3390/met7080292>.
- Zeng, Z., Oliveira, J. P., Bu, X., Yang, M., Li, R., & Wang, Z. (2017). Laser welding of BTi-6431S high temperature titanium alloy. *Metals*, 7(11), Article 504. <https://doi.org/10.3390/met7110504>
- Zhang, X., Li, L., Chen, Y., Yang, Z., & Zhu, X. (2017). Experimental investigation on electric current-aided laser stake welding of aluminum alloy T-joints. *Metals*, 7(11), Article 467. <https://doi.org/10.3390/met7110467>.



Thermal Comfort Performance of Naturally Ventilated Royal Malaysian Police (RMP) Lockup in Hot and Humid Climate of Malaysia

Bismiazan Abd. Razak^{1,2*}, Mohd. Farid Mohamed¹, Wardah Fatimah Mohammad Yusoff¹ and Mohd. Khairul Azhar Mat Sulaiman¹

¹Faculty of Engineering and Built Environment, Universiti Kebangsaan Malaysia, 43600 UKM, Bangi, Selangor, Malaysia

²Architecture Branch of the Public Works Department, IPJKR Malaysia, Tingkat 11, Menara Tun Ismail Mohamed Ali (TIMA), Jalan Raja Laut, 50350 Kuala Lumpur, Malaysia

ABSTRACT

Thermal comfort performance of three vacant naturally ventilated Royal Malaysia Police (RMP) case study lockups (LK1 in Penang, LK2 in Melaka & LK3 in Kuala Lumpur) was measured during monsoon change period from Northeast Monsoon to Southeast Monsoon. According to NGO's report and previous studies, the lockups condition is very poor and hot which contribute to discomfort among detainees. The objectives of the study are to investigate thermal comfort performance of the lockups based on four environmental parameters (T_a , T_r , V_a , & RH) through physical measurement, to predict thermal comfort performance based on operative temperature (T_o) and neutral operative temperature (T_{neutop}), and to compare the results with thermal comfort criteria recommended by ASHRAE 55 standard and previous thermal comfort studies in hot and humid climate. The results show that T_o and T_{neutop} reading of LK1 is exceeding the maximum range recommended by ASHRAE 55 and previous studies by 2% to 8% (T_o) and 1% (T_{neutop}) which categorizing LK1 condition as hot. This is mostly due to high hot airflow brought through an ineffective window opening. The results will be used as reference for improvement towards some aspects such as window opening, building finishes materials, space volume and building orientation in future lockup design.

ARTICLE INFO

Article history:

Received: 03 February 2021

Accepted: 15 April 2021

Published: 31 July 2021

DOI: <https://doi.org/10.47836/pjst.29.3.35>

E-mail addresses:

p101088@siswa.ukm.edu.my; bismiazan@gmail.com

(Bismiazan Abd. Razak)

faridmohamed@ukm.edu.my (Mohd. Farid Mohamed)

wardahyusoff@ukm.edu.my (Wardah Fatimah Mohammad Yusoff)

m.khairulazhar@ukm.edu.my (Mohd. Khairul Azhar Mat Sulaiman)

* Corresponding author

Keywords: Hot-humid climate, naturally ventilated buildings, Royal Malaysian Police lockup, Thermal comfort performance

INTRODUCTION

This paper is about study on thermal comfort performance of Royal Malaysia Police (RMP) lockup to understand the lockups internal level of comfort. The study was conducted on three lockups in three different locations which are Penang, Melaka and Kuala Lumpur during monsoon change period from Northeast Monsoon to Southeast Monsoon which is hot and humid. The results obtained from this study will be used to be compared with international standard such as ASHRAE 55 and the result obtained by other previous researcher on the building not limited to the lockup study since there is no study have been conducted on lockup in Malaysia.

Several criteria have been set during selection of the lockup cells for the field study purposes such as the lockup cells must have complete natural ventilation. All fans and exhaust fans were switched off throughout the study period if any. The selected cells for all case study lockups must have close similarities in terms of cell size and finishing to minimize the difference. In addition to this, field study was conducted on vacant lockup cells to understand maximum thermal comfort at zero attendee (default actual maximum thermal comfort measurement).

Although the study was conducted on three case study lockups at three different locations at different day, it will not affect the objective of the study. Results obtained from the three case study lockups will not be compared but will be used to understand each lockup thermal comfort performance based on window openings and space volume factor.

Royal Malaysian Police (RMP) Lockup

RMP lockup is often associated with guilty individuals or better known as detainees or 'Orang Kena Tangkap' (OKT). It is also known as a place that is bound by various rules, punishments, laws and is categorized as a Prohibited Area and Prohibited Place or 'Kawasan Larangan dan Tempat Larangan' (KLTL) for ordinary people who do not know its actual function and role (PDRM, 1953; SUHAKAM, 2016).

There are two types of RMP lockup namely regular lockup which are available at police stations, and centralized lockup. Both types of lockup have their own function. The regular lockup is only for remand detainees while waiting for the detainees to be taken to court which subsequently serve a sentence in prison. Detainees are usually detained for about a day or not more than 24 hours (PDRM, 1953; Perlembagaan Persekutuan Malaysia, 2010). While the centralized lockup serve to detain detainees for a longer period of time which up to 90 days after being brought to court or during remanded period and this lockup is often used to house detainees involved in serious offenses such as crime, murder, gambling and drugs (SUHAKAM, 2016).

Previous studies on RMP lockup are more qualitative and thematic by using interview, questionnaires and observations as data gathering method. Table 1 shows the previous

Table 1
Studies related to correctional facilities

Research title	Author	Findings
Deaths in Police Custody a Thematic Study on Lock-Up Conditions and Factors Contributing to the Death	(SUHAKAM, 2016)	Studies related to the conditions and factors that contribute to the death of detainees through qualitative and thematic methods in interviews and observations on respondents and study areas.
Field study of the indoor environment in a Danish prison	(Dogbeh et al., 2014)	Qualitative and quantitative study of the indoor air quality of the prison which includes air temperature, relative humidity, and carbon dioxide factors. Quantitative - Use of measuring instruments HOBO U12-012 Temperature/Relative Humidity/ Light/External Data Logger dan Vaisala GMW22 Carbon Dioxide. Qualitative - Use of interview scheme and questionnaire based on ASHRAE-7 standard scale on respondents.
Added Value to Security Building Design Case Study: Police Station in Malaysia	(Zaharin et al., 2019)	Qualitative study related to design planning and layout of RMP police station facilities that meet standard operating procedures (SOP) through observation methods of case studies, scientific studies, interviews, and semi-structured questionnaires on respondents.
Research on the Design Typology of the Royal Malaysian Police (RMP) Lockups	(Razak et al., 2020)	Qualitative study related to the typology of the Royal Malaysian Police (RMP) Lockups through case studies and literature review studies on the design of existing security agency lockups.

studies conducted on rehabilitation facilities building such as lockup and prison locally and globally.

Referring to Table 1, study by SUHAKAM (2016) was qualitative or thematic based on observations and interviews conducted. No measurement instruments at the studied site were scientifically recorded. While the study conducted by Dogbeh et al. (2014) was focusing on qualitative and quantitative study on Indoor Air Quality (IAQ) which include air temperature, relative humidity and carbon dioxide factor. The study by Zaharin et al. (2019) was related to the RMP police station's design and facilities layout planning which coincide with RMP Standard Operating Procedure (SOP) through observation methods of the case studies, scientific studies, interviews and semi-structured questionnaires on respondents. Slightly different in terms of focused subject on study Razak et al. (2020) which it is more to the presentation of information related to the typology of lockup design based on scientific studies, case studies and preliminary analysis. Additionally, no scientific physical measurement instruments related to natural ventilation and RMP lockup thermal comfort were used in the abovementioned studies.

Common issues highlighted by Non-Government Organization (NGO) such as Malaysian Human Rights Commission (SUHAKAM) are natural ventilation which might cause by inefficient window design. Referring to Figure 1, majority of the opinion is on poor

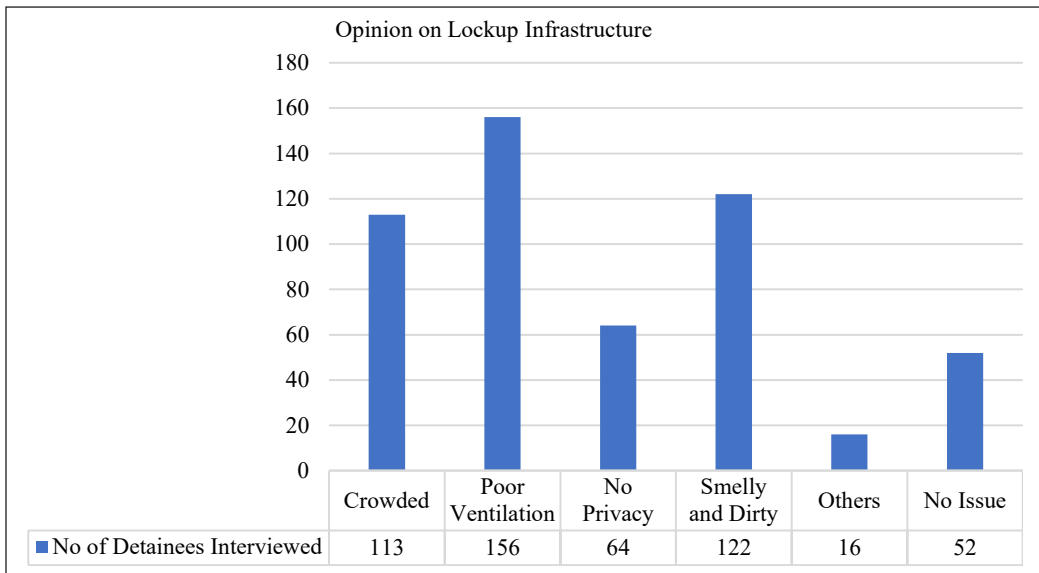


Figure 1. Opinion on lockup cell infrastructure
 Source: (SUHAKAM, 2016)

ventilation with 156 opinions from the detainees. The condition of the lockup is described as hot which contribute to the discomfort among detainees (SUHAKAM, 2016). Based on the statement of the Nelson Mandela Rules, every detainee should be provided with a facility that meets physical and mental needs considering environmental factors such as ventilation (SUHAKAM, 2016). According to Dogbeh et al. (2014), most detainees feel dissatisfied with the thermal comfort and air quality of the indoor environment caused by the lack of ventilation and excessive direct sunlight into the detention space.

However, most studies conducted previously are too brief without proper measurement and analysis to understand further on the contributing factor to the lockups condition. Hence it shows a need to have a field study through physical measurement by using appropriate instrument on the problematic lockup highlighted by the NGO.

The objectives of the study are to investigate lockup thermal comfort performance based on four environmental parameters (T_a , T_r , V_a , & RH) through physical measurement of field study, to predict thermal comfort performance based on the adaptive model indices Operative Temperature (T_o) and Neutral Operative Temperature (T_{neutop}), and to compare the results with thermal comfort criteria recommended by ASHRAE 55 and previous thermal comfort studies in hot and humid climate.

Malaysia Climate

Climate conditions are major influence factor to the design of a building which is close related to the user comfort as well as complying with the efficient construction criteria

(Tharim et al., 2018). Malaysia is well known with the hot and humid climate with minimum annual average temperature between 23.7°C to 26.4°C and maximum annual average temperature between 26.4°C to 31.3°C with an average minimum daily temperature between 23.0°C to 29.0°C and maximum daily temperature between 34.0 °C to 36.9 °C. Malaysia experience high relative humidity rate throughout the year between 40% to 90%. The average annual rainfall distribution rate is between 2000 mm to 2500 mm which makes Malaysia as a country with a relatively high rainfall distribution rate. Malaysia average annual rate of sunlight reception is between 6 to 7 hours a day which is categorized as high compared to other countries given that Malaysia position surrounded by oceans (Jabatan Meteorologi Malaysia, 2020). As a result, it is quite difficult to achieve an efficient level of thermal comfort through natural ventilation in hot and humid climate region.

Thermal Comfort

Thermal comfort is defined as a condition in which the mind describes satisfaction with the thermal environment and it is assessed by subjective assessment (ASHRAE 55, 2017; Yang & Clements-Croome, 2018). Zhang et al. (2007) stated that thermal comfort is a condition associated with the thermal environment satisfaction. The interaction of human terms with the environment involves physical and psychological responses. Thermal interaction between human and surrounding area involves physical and psychological response. This shows that thermal comfort is closely related to the human mind, physical and psychological factor through response towards surrounding environment.

According to building science, thermal comfort is defined as the balance of heat transfer between human and their environmental condition (Tang & Chin, 2017). Thermal comfort can also be influenced by the interaction between the building and the surrounding environment (Tharim et al., 2018). While general perception of thermal comfort is a condition where human mind, physical and psychological respond to the balance of heat transfer influenced by factors such as internal and external environment of the building and human body condition which are very subjective to be measured.

Ventilation through an efficient window's opening either by cross ventilation or stack effect approach as well as a combination of other passive ventilation systems are able to ensure thermal comfort factors such as air temperature, air speed, air humidity and temperature radiation are achieved (Gharakhani et al., 2014). This thermal comfort can also be achieved and experienced regardless of types of clothing worn and individual metabolism rate during any of activities carried out by individual.

However, it is not as easy as expected because natural ventilation with hot and humid climates throughout the year is highly dependent on the surrounding condition (Jiang et al., 2003) such as air speed and wind pressure to bring fresh air into the building to replace existing air, reduce humidity and provide sufficient ventilation in the building. This has

been a great challenge to Architects and Engineers in Malaysia to design a building that can meet all criteria especially on efficient ventilation and high thermal comfort as well as providing a healthy and well perform environment to the user apart from efficient energy consumption (Azizpour et al., 2013; Chan et al., 2013).

Factors Affecting Thermal Comfort. According to ASHRAE 55 (2017), thermal comfort can be influenced by two factors which are physical (environmental) and individual (personal) factor. Physical factor consists of air temperature, air speed, relative humidity and mean radiant temperature. While individual factor consists of metabolic rates and clothing. Meanwhile Al-Absi & Abas (2018) stated that other contributing factors such as perception, acclimatize (Azizpour et al., 2011), experience, age and gender, health conditions, food and drink as well as body shape are also categorized as the third influencing factors to the thermal comfort. All these factors can change according to the time and conditions of the environment as well as individual. In other words, it is difficult to achieve full satisfaction of thermal comfort due to various factors.

A building is designed and built to suit the user's needs, comfortability and criteria (Nordin et al., 2017). As a shelter, a place to carry out activities such as work, leisure, and rest, a building must meet the criteria needed by the users including comfortable, conducive and safe while living in it (Davies & Jokiniemi, 2008; Tharim et al., 2018). A good design concept should emphasize selection of appropriate site (Chan et al., 2013), best orientation and space (Xue et al., 2016), appropriate materials and finishes (Yusoff & Mohamed, 2017), adequate ventilation and lighting as well as appropriate facilities (Xue et al., 2016). All the above criteria are considered best practice for design and built for all types of building including facilities for national security agencies such as the Royal Malaysian Police (RMP) lockup which houses a huge number of detainees.

Table 2 shows summary of previous thermal comfort studies of naturally ventilated building in hot and humid region for various types of building.

Apart from the studies stated in Table 2, other studies related to thermal comfort for naturally ventilated building that have been conducted by previous researchers are more towards residential (Attia & Carlucci, 2015; Han et al., 2007; Kubota et al., 2009; Nur'aini, 2017; Taweekun & Tantiwichien, 2013; Wong et al., 2020), office building (Aminuddin et al., 2012; Damiati et al., 2016), educational facilities such as classroom, kindergarten and hostel (Dahlan et al., 2008; Fabbri, 2013; Kamaruzzaman & Tazilan, 2013). So far there is no thermal comfort study and field investigation have been conducted on correctional facilities especially police lockup in hot and humid climate region. Since there is no reference related to the naturally ventilated correctional facilities in hot and humid climate region, the findings and results obtained from the studies in Table 2 and others are still relevant to be used as reference and guideline for the present study.

Table 2
 Summary of previous thermal comfort studies of naturally ventilated building in hot and humid region

Author	Country	Koppen Climate	Type of building	Type of study	Temperature of comfort / range (°C)
(Webb, 1959)	Singapore	Tropical Rainforest	Buildings	Field study	26.0°C Optimum value (thermally comfort)
(de Dear et al., 1991)	Singapore	Tropical Rainforest	High rise residential (NV) and office building (AC)	Field experiments	29.6°C Neutral temperature (NT) Operative temperature (To) (NV)
(de Dear & Brager, 2002)	Thailand, Indonesia, Singapore	Tropical Monsoon Tropical Rainforest Tropical Rainforest	Office	Field study	26.0 – 27.0°C (26.7°C) Neutral temperature (NT)(NV)
(Wong & Khoo, 2003)	Singapore	Tropical Rainforest	Classroom	Field Study	28.8°C Neutral temperature (NT)
(Feriadi & Wong, 2004)	Indonesia	Tropical Rainforest	Residential	Field study	29.2°C Operative temperature (To) 29.9°C Effective temperature (ET*)
(Zain et al., 2007)	Malaysia	Tropical Rainforest	Residential	Field study	30.9°C Operative temperature (To)
(Djamila et al., 2013)	Malaysia	Tropical Rainforest	Residential	Field study	30.2 °C Neutral Temperature (NT)
(Toe & Kubota, 2013)	Malaysia	Tropical Rainforest	Buildings	Field study	Neutral operative temperatures 24.9 – 31.2°C (hot-humid) 24.8 – 33.7°C (hot-dry) 19.0 – 24.7°C (moderate climates)

Thermal Comfort Evaluation Model. There are two thermal comfort models that are often used by previous researchers to measure the thermal comfort performance of a building which are static model and adaptive model. Static model depends on the controlled environmental conditions (steady-stated condition). Adaptive model is more focused on field studies with a combination of surveys of respondents and also studies on thermal comfort variable (Maarof, 2014). For the present study purpose, adaptive model by using operative temperature and neutral operative temperature indices is implemented.

Adaptive Model - Operative Temperature (To) and Neutral Operative Temperature (Tneutop). Adaptive model relates with indoor temperature or acceptable temperature ranges to climatological parameters or outdoor thermal environmental variable especially for naturally ventilated building (de Dear & Brager, 2002; Toe & Kubota, 2013) and also

fundamental of physics and physiology factors (ASHRAE 55, 2017; de Dear & Brager, 2002). These factors are important for adaptive models in determining expectations and perceptions of thermal perception by the occupants (de Dear & Brager, 2002). Various adaptive indices have been used by previous researchers in determining comfort condition in their study such as Operative Temperature (T_o), Effective Temperature (EF^*), Standard Effective Temperature (SET), Equatorial Thermal Index (ETI), Adaptive Comfort Standard (ACS) and more.

In the present study, operative temperature (T_o) indices is used to calculate and analyze the mean radiant temperature reading (T_r) results obtained through physical measurement from the globe temperature (T_g) (50 mm diameter black globe thermometer probe) in case study lockup according to ASHRAE 55 (López-Pérez et al., 2019). Various equations have been introduced by the previous researcher in the calculations of operative temperature. According to ASHRAE 55 method, Equation 1 was used to calculate operative temperature.

$$T_o = AT_a + (1-A) T_r \quad (1)$$

Where

T_o = operative temperature

T_a = average air temperature

T_r = mean radiant temperature

A can be selected from the following values as a function of the average air speed V_a ($V_a < 0.2$ m/s

($A = 0.5$), V_a 0.2 m/s to 0.6 m/s ($A = 0.6$), V_a 0.6 m/s to 1.0 m/s ($A = 0.7$)

Operative temperature was then analyzed by using a new adaptive equation produced by Toe & Kubota (2013) which is Neutral Operative Temperature (T_{neutop}). Neutral operative temperature equation was chosen based on a comprehensive study and analysis through meta-analysis of the ASHRAE RP-884 database with reference to two major adaptive standard which are ASHRAE and BSI EN 15251. Both are developed specifically for naturally ventilated building in countries with hot and humid climate such as Malaysia. This equation is also formulated by considering prevailing outdoor air temperature, indoor air speed and relative humidity. Therefore, the T_{neutop} determined by Equation 2 is more suitable for the present study.

$$T_{neutop} = 0.57T_{outdm} + 13.8 \quad (2)$$

Where

T_{neutop} = indoor neutral operative temperature

T_{outdm} = daily mean outdoor air temperature

METHODS

Case Study Lockups

The case study lockups details are shown in Table 3 and Figure 2. The lockups were recommended by RMP based on previous findings by SUHAKAM.

Table 3
Case study lockup background

Case study lockup	State Police District	Background
LK1 Jalan Patani	North East District Police Headquarters, Penang. (Figure 2a)	Single storey building consists of 14 cells with two different capacity: 3 or 6 detainees per cell. LK1 main purpose is to temporarily house male detainees as well as foreign detainees before being remanded in court.
LK2 Alor Gajah	Alor Gajah District Police Headquarters, Melaka. (Figure 2b)	Located on the ground floor of two-storey building. It consists of 11 adult male detention cells, 3 female detention cells and 2 juvenile detention cells. All cells are capable to accommodate between 1 to 3 prisoners at a time. Gazetted in 2001, LK2 serves as a centralized lockup and temporary place for detainees before being remanded in court.
LK3 Jinjang Kuala Lumpur Central	Sentul District Police Headquarters, Federal Territory of Kuala Lumpur (Figure 2c)	A three-story building that almost exclusively serves as lockup with various size and type of cells for male, female, and even juvenile detainees. LK3 consists of a cell designed for 3, 6 or 9 detainees. LK3 main purpose is to house detainees before being remanded in court as well as housing serious offenders facing serious criminal cases such as drug, gambling, human trafficking and gangsterism.

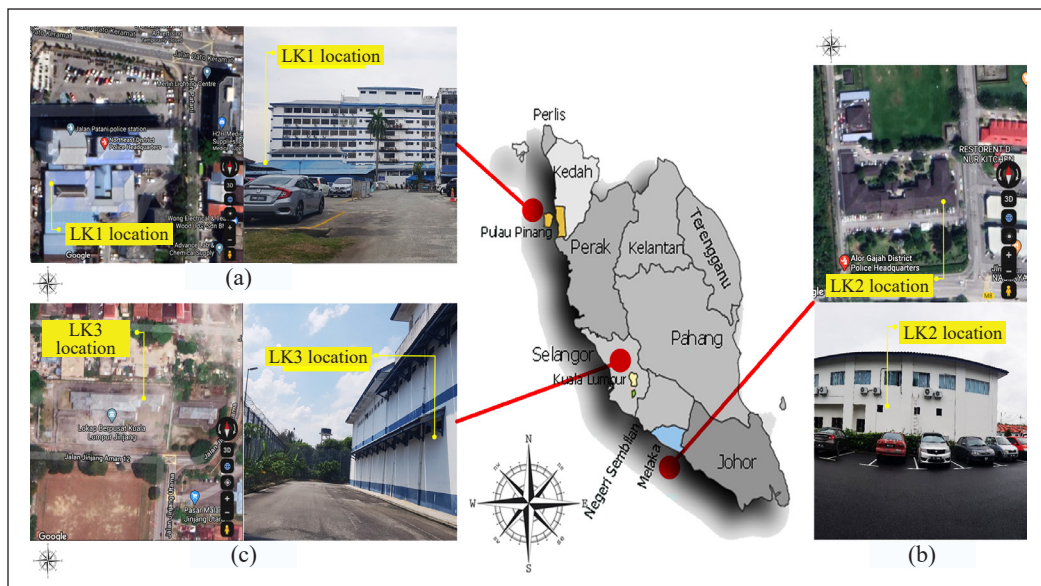


Figure 2. Site and building of the case study lockups: (a) LK1; (b) LK2; (c) LK3

Table 4 shows a summary of the case study lockups location, conceptual floor plan, conceptual section and measuring instrument location (LK1, LK2 and LK3). Table 5 shows a summary of information related to case study lockup (LK1, LK2 and LK3).

Physical Measurement Duration

Physical measurements were carried out between March and August 2020, during monsoon change where Malaysia experience a relatively dry season with wind speeds of less than 15 knots (7.7 m/s) (Jabatan Meteorologi Malaysia, 2020). The average daily temperature during this period of time is considered high which is between 31.2°C to 33.2°C (World Meteorological Organisation, 2020). Physical measurement at this point of time is strongly recommended to understand better on thermal comfort of the lockups in hot and humid climate region (Gharakhani et al., 2014; Xue et al., 2016).

The physical measurements were carried out from 15 to 20 March 2020 for LK1, 20 to 25 July 2020 for LK3 and on 27 July to 1 August 2020 for LK2. This physical measurement was conducted 24 hours of 5 consecutive days. One hour a day was allocated for data collection, battery change and device reset. The total rainfall distribution recorded for the three case study lockups is minimal during the physical measurement period.

Physical Measurement Instrument

Two types of appropriate instruments which comply to the ISO 7726 requirement (ASHRAE 55, 2017) were used to measure four environmental parameters which are air temperature (T_a), mean radiant temperature (T_r), air speed (V_a) and relative humidity (RH). Delta Ohm Thermocouple Infrared Thermometer HD32.23 WBGT-PMV was used to measure indoor parameters and Seven Elements Integrated Weather Sensor WTS700 was used to measure outdoor parameters. Summary of instruments, parameters measuring ranges and recording method are demonstrated in Table 6 and Figure 3.

All physical measurement instrument used are calibrated to ensure that data collected are accurate and to avoid any data discrepancy.

Physical Measurement Procedure and Evaluation of Thermal Comfort Performance

Following Class I field research protocol (Maarof, 2014), three sets of Delta Ohm Thermocouple Infrared Thermometer HD32.23 WBGT-PMV instrument with three different height of leveling from the floor were placed inside the lockup to measure indoor thermal comfort performance. All physical measuring instruments used in this study follow ASHRAE Standard 70 or 113 or ISO 7726. As stated in Table 7, the physical measuring instruments have been placed at the center of the bed (center of the lockup) as it is the main area which usually occupied by the detainees especially for sleeping, sitting, and standing

Table 4
 Summary of case study lockups location, conceptual floor plan, conceptual section and measuring instrument location (LK1, LK2 & LK3)

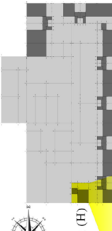
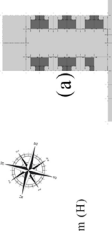
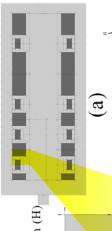
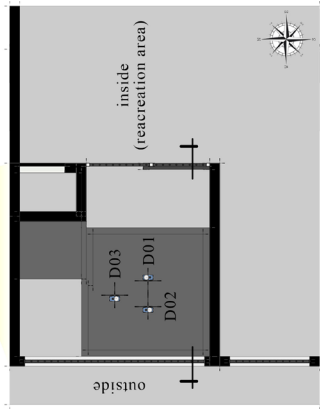
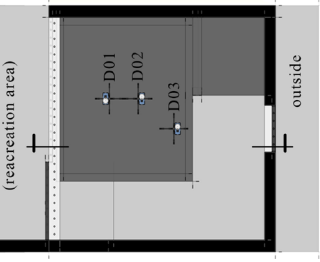
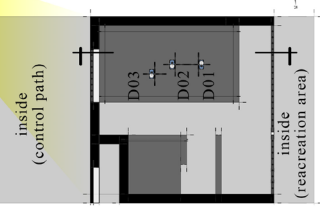
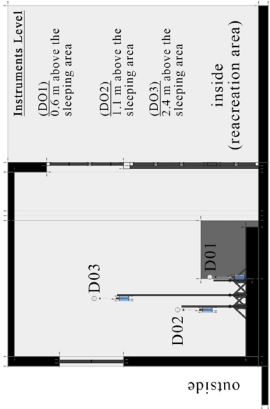
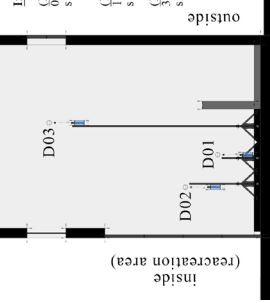
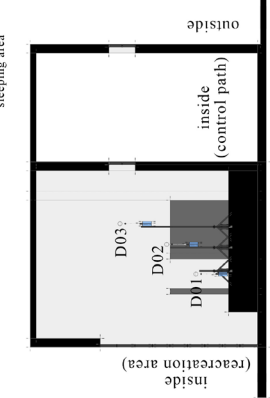
Information	LK1	LK2	LK3
(a) Case study lockups location	<p>LK1 Dimension (3.0 m (W) x 3.0 m (L) x 3.9 m (H))</p> 	<p>LK2 Dimension (3.0 m (W) x 3.0 m (L) x 4.2 m (H))</p> 	<p>LK3 Dimension (3.0 m (W) x 3.0 m (L) x 3.9 m (H))</p> 
(b) Conceptual floor plan and measuring instrument location			
(c) Conceptual section and measuring instrument location	<p>Instruments Level (D01) 0.6 m above the sleeping area (D02) 1.1 m above the sleeping area (D03) 2.4 m above the sleeping area</p> 	<p>Instruments Level (D01) 0.6 m above the sleeping area (D02) 1.1 m above the sleeping area (D03) 3.2 m above the sleeping area</p> 	<p>Instruments Level (D01) 0.6 m above the sleeping area (D02) 1.1 m above the sleeping area (D03) 1.8 m above the sleeping area</p> 

Table 5
Summary of information related to case study lockup (LK1, LK2 & LK3)

Case study lockup and Capacity of detainees (person)	Dimension (W)x(L) x(H)	Window dimension (W)x(L)x(H) (m) and opening direction / prevailing wind direction (north orientation)	Ventilation required according to Malaysia Uniform Building By Law (UBBL) (10%)	Ventilation				Materials and Finishes					
				provided (existing window)	(area (m ²) and percentage (%))	i)	ii)	iii)	iv)	Floor	Wall	Ceiling	Bed
LK1 (1-3)	3.0 m (W) x 3.0 m (L) x 3.9 m (H)	2.7 m (W) x 1.0 m (H)	0.9 m ² 10% of floor area (minimum)	2.7 m ² (30%)		i)	ii)	iii)	iv)	R.C. slab with floor hardener finishes (ceramic tiles for toilet)	IBS concrete panel with emulsion paint (epoxy paint for toilet)	R.C. slab with emulsion paint	R.C. with tongue and groove plank finishes
	3.0 m (L) x 3.9 m (H)	West / West		More than required according to Malaysia UBBL requirements									
	3.0 m (W) x 3.0 m (L) x 4.2 m (H)	0.6 m (W) x 0.6 m (H)	0.9 m ² 10% of floor area (minimum)	0.4 m ² (4%)		i)	ii)			R.C. slab with floor hardener finishes (epoxy paint for toilet)	IBS concrete panel with emulsion paint (epoxy paint for toilet)		
	9.0 m ²	South / South		Less than required according to Malaysia UBBL requirements									
LK2 (1-3)	3.0 m (W) x 3.0 m (L) x 4.2 m (H)	0.9 m (W) x 0.45 m (H)	0.9 m ² 10% of floor area (minimum)	0.4 m ² (4.6%)		i)	ii)	iii)	iv)	R.C. slab with floor hardener finishes (epoxy paint for toilet)	IBS concrete panel with emulsion paint (epoxy paint for toilet)	R.C. slab with emulsion paint	R.C. with tongue and groove plank finishes
	3.0 m (L) x 3.9 m (H)	North / South		Less than required according to Malaysia UBBL requirements									
	3.0 m (W) x 3.0 m (L) x 3.9 m (H)	0.9 m (W) x 0.45 m (H)	0.9 m ² 10% of floor area (minimum)	0.4 m ² (4.6%)		i)	ii)			R.C. slab with floor hardener finishes (epoxy paint for toilet)	IBS concrete panel with emulsion paint (epoxy paint for toilet)		
	9.0 m ²	North / South		Less than required according to Malaysia UBBL requirements									
LK3 (1-3)	3.0 m (W) x 3.0 m (L) x 3.9 m (H)	0.9 m (W) x 0.45 m (H)	0.9 m ² 10% of floor area (minimum)	0.4 m ² (4.6%)		i)	ii)	iii)	iv)	R.C. slab with floor hardener finishes (epoxy paint for toilet)	IBS concrete panel with emulsion paint (epoxy paint for toilet)	R.C. slab with emulsion paint	R.C. with tongue and groove plank finishes
	3.0 m (L) x 3.9 m (H)	North / South		Less than required according to Malaysia UBBL requirements									
	3.0 m (W) x 3.0 m (L) x 3.9 m (H)	0.9 m (W) x 0.45 m (H)	0.9 m ² 10% of floor area (minimum)	0.4 m ² (4.6%)		i)	ii)			R.C. slab with floor hardener finishes (epoxy paint for toilet)	IBS concrete panel with emulsion paint (epoxy paint for toilet)		
	9.0 m ²	North / South		Less than required according to Malaysia UBBL requirements									

Table 6
Summary of instrument, parameters measuring ranges and accuracy

Instrument	Unit / Set	Parameters	Measuring ranges	Accuracy
Indoor Parameters				
Delta Ohm Thermocouple Infrared Thermometer	3	Air temperature	0°C to 100°C	Class 1/3 Din
HD 32.3 WBGT-PMV	(DO1, DO2, DO3)	Air speed	0 to 5 m/s	±0.05 m/s
Probe: AP 3203.2		Relative humidity	5% to 98%	±2.5%
Probe: AP 3217.2		Globe temperature	-10 °C to 100 °C	Class 1/3 Din
Probe: AP 3217.2				
Outdoor Parameters				
Seven Elements Integrated Weather Sensor WTS700	1 (WTS700)	Air temperature	-40°C to 60°C	±0.3°C
		Air speed	0 to 60 m/s	±0.3 m/s
		Relative humidity	0% to 100%	±2%

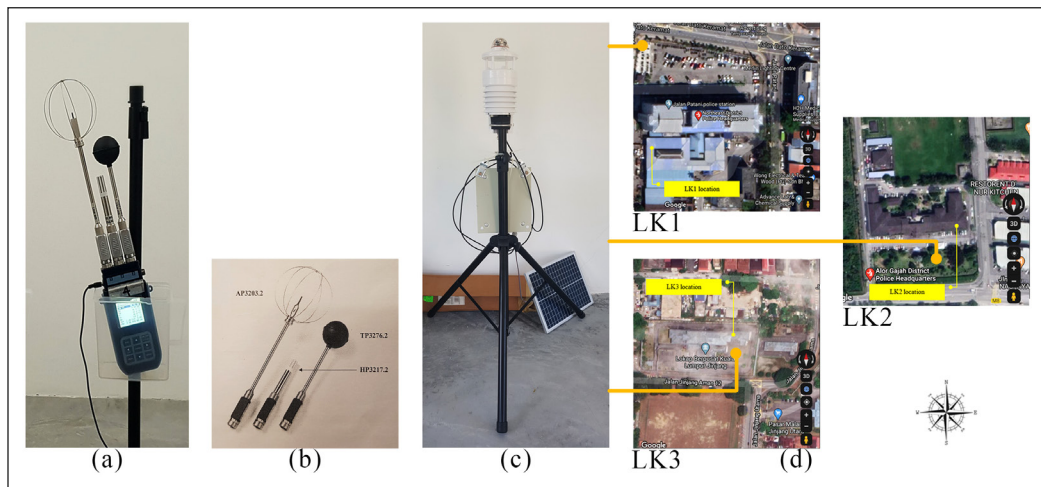


Figure 3. The instruments used in the present study: (a) Delta Ohm Thermocouple Infrared Thermometer; (b) The instruments probe; (c) Seven Elements Integrated Weather Sensor WTS700; (d) Seven Elements Integrated Weather Sensor WTS700 location for all three case study lockups

activities (steady-state conditions). Seven Elements Integrated Weather Sensor WTS700 was located at an open space outside the building with no airflow obstruction.

The evaluation of indoor thermal comfort performance was conducted based on ASHRAE Standard 55 - ‘Thermal Environmental Conditions for Human Occupancy’ recommendation as shown in Table 7 as it is more relevant for this study and recognized globally (Gharakhani et al., 2014; Xue et al., 2016).

RESULTS AND DISCUSSION

This section shows the results obtained based on the field study conducted for all three case study lockups. Statistical summaries of the indoor and outdoor measurements, prediction of

Table 7
Evaluation of thermal comfort performance and physical measurement procedure in accordance with ASHRAE Standard 55 – ‘Thermal Environmental Conditions for Human Occupancy’

Instrument	Parameters	Location	Level	ASHRAE 55 recommendations
Indoor parameters				
Delta Ohm Thermocouple Infrared Thermometer	Air temperature (Ta) Air speed (Va)	Center of case study lockup	0.6 m above the sleeping area (for all three case study lockups)	Meet the requirements in ASHRAE Standard 70 or Standard 113 or ISO 7726
HD 32.3 WBGT-PMV (DO1)	Mean radiant temperature (Tr) Relative humidity (RH)	(sleeping area / bed)		
Delta Ohm Thermocouple Infrared Thermometer	Air temperature (Ta) Air speed (Va)	Center of case study lockup	1.1 m above the sleeping area (for all three case study lockups)	<i>Physical measurement</i>
HD 32.3 WBGT-PMV (DO2)	Mean radiant temperature (Tr) Relative humidity (RH)	(sleeping area / bed)		
Delta Ohm Thermocouple Infrared Thermometer	Air temperature (Ta) Air speed (Va)	1.0 m inward from the center of each of the room’s walls and 1.0 m (3.3 ft) inward from the center of the largest window.	According to existing window of case study lockup height (above sleeping area)	
HD 32.3 WBGT-PMV (DO3)	Mean radiant temperature (Tr) Relative humidity (RH)		(LK1 – 2.4 m) (LK2 – 3.2 m) (LK3 – 1.8 m)	
Outdoor Parameters				
Seven Elements Integrated Weather Sensor WTS700 (WTS700)	Air temperature (Ta) Air speed (Va) Relative humidity (RH)	Open space outside the building with no airflow obstruction	1.8 m above the ground (for all three case study lockups)	Meet the requirements in ASHRAE Standard 70 or Standard 113 or ISO 7726

Source: (ASHRAE 55, 2017)

the indoor operative temperature (T_o) and indoor neutral operative temperature (T_{neutop}) for LK1, LK2 and LK3 were discussed and compared to ASHRAE 55 using parameters range and recommended comfort criteria.

Statistical Summaries of the Indoor and Outdoor Measurements, Analysis of Prediction of the Indoor Operative Temperature (T_o) and Indoor Neutral Operative Temperature (T_{neutop}) for LK1

Figure 4 shows the statistical summaries of the indoor and outdoor measurements recorded from all three measuring instruments in LK1 for five days measurement.

The average indoor air temperature recorded is higher than ASHRAE 55 which is 31.7°C for DO1 and DO3 and 31.4°C for DO2. The readings recorded shows small difference from the average outdoor air temperature with average reading 31.0°C as shown in Figure 4a.

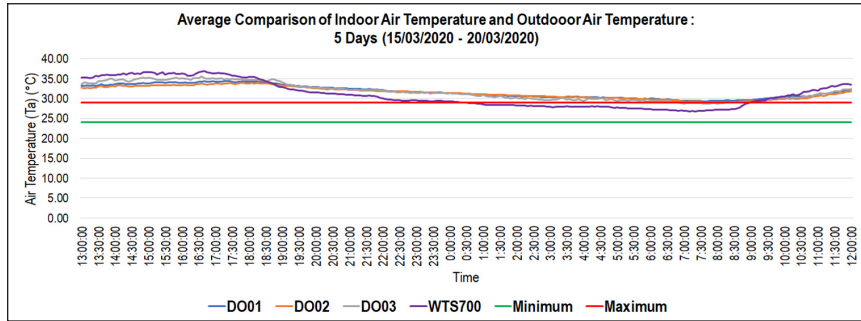
The average indoor air speed recorded by DO1 and DO2 is equal with reading 0.07 m/s for both instruments. However, DO3 shows slightly high average indoor air speed reading which is 0.25 m/s as shown in Figure 4b. The difference in DO3 readings may be influenced by the levelling difference, positioning to the window and window opening. DO3 was levelled slightly higher compared to DO1 and DO2 which at the same time give it a position nearer to the window. The reading collected by the DO3 may highly influenced by high average outdoor air speed 0.77 m/s and large window opening ($2.7\text{ m (W)} \times 1.0\text{ m (H)}$) with 30% of floor area.

The average indoor relative humidity recorded are 60.1% for DO1, 58.2% for DO2, and 59.7% for DO3 as shown in Figure 4c. The average indoor relative humidity recorded are not much different compared to the average outdoor humidity with reading 58.3%. The average indoor relative humidity recorded are good and within the acceptable range by ASHRAE 55. This might be due to the ample mean air speed to facilitate indoor air circulation, which in turn helps in reducing LK1 humidity.

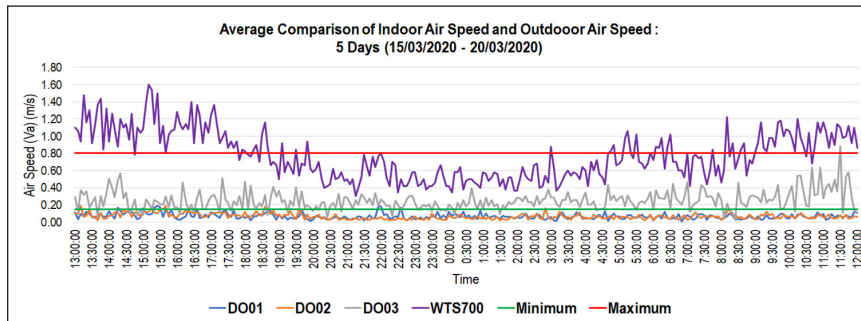
The mean radiant temperature recorded during field measurements are 31.6°C for DO1, 31.3°C for DO2 and 31.5°C for DO3 as shown in Figure 4d. It shows not much difference between the three readings recorded. The mean radiant temperature readings are slightly lower than the result of mean air temperature readings. This indicates that there are other influencing factors.

Indoor and outdoor measurement data obtained were then used to predict operative temperature and neutral operative temperature. In the present study, linear regression by using Equation 1 was selected in calculating operative temperature because it is widely used method for neutral temperature prediction according to ASHRAE 55.

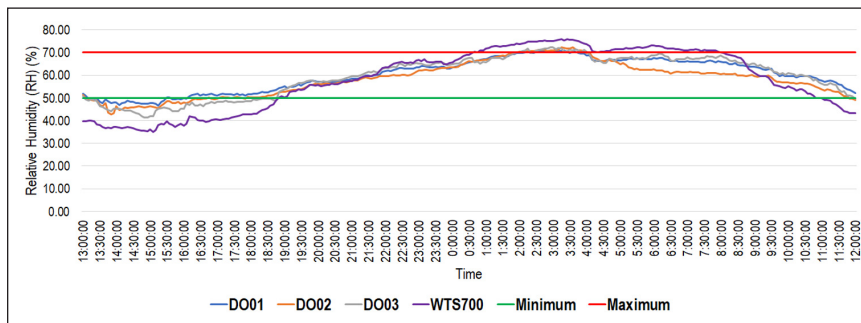
According to Equation 1, the value of A used in the calculation of operative temperature for DO1 and DO2 is 0.5 because the average air speed $<0.2\text{ m/s}$ while for DO3, the value



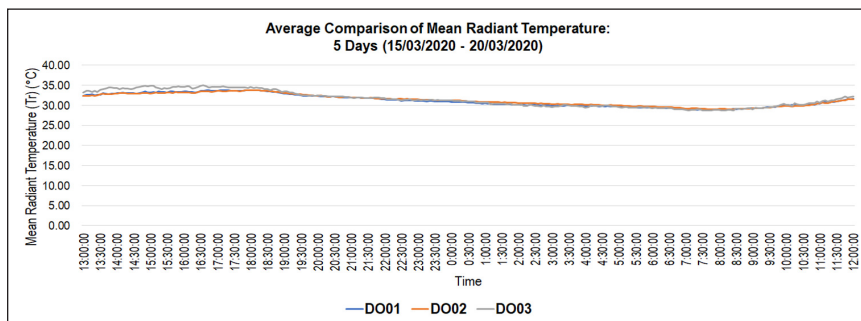
(a)



(b)



(c)



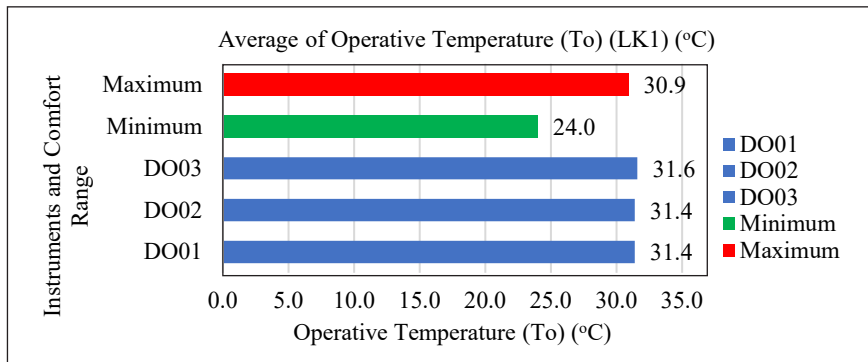
(d)

Figure 4. Statistical summaries of the average comparison indoor and outdoor measurements for LK1: (a) Air temperature; (b) Air speed; (c) Relative humidity; (d) Mean radiant temperature

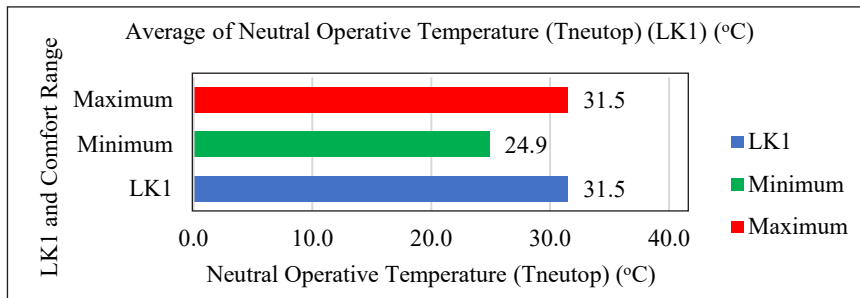
of A used is 0.6 because the average air speed recorded is 0.25 m/s which is in 0.2 m / s to 0.6 m/s range.

The Tneutop determined by Equation 2 was used in calculating neutral operative temperature. To use this equation, daily average outdoor air temperature (T_{outdm}) must be in the range between 19.4°C to 30.5°C and indoor air speed <0.65 m/s at and below neutral operative temperature; ≥ 0.65 above neutral operative temperature. There is no limit for indoor humidity set in this equation. Average indoor air speed for LK1 is within the set limit which is <0.65 m/s while daily average outdoor air temperature for LK1 slightly exceed the set limit by the equation about +0.05°C during calculation.

As a result, the indoor operative temperature is between 31.4°C to 31.6°C while the neutral operative temperature is 31.5°C for LK1 as shown in Figure 5.



(a)

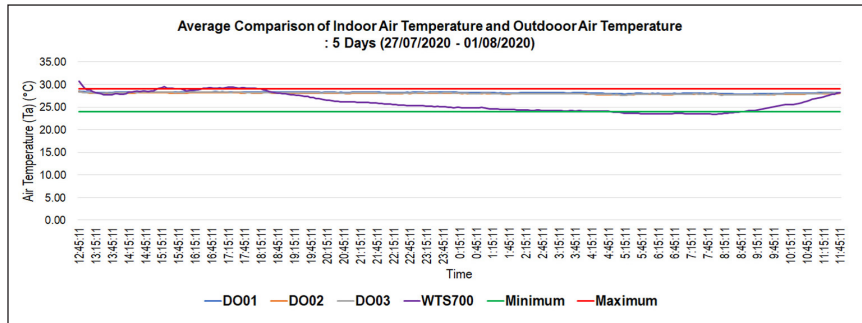


(b)

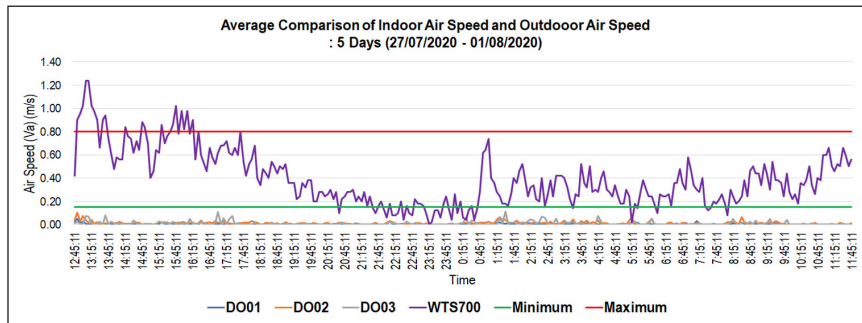
Figure 5. Summaries of the (a) operative temperature and (b) neutral operative temperature prediction for LK1

Statistical Summaries of the Indoor and Outdoor Measurements, Analysis of Prediction of the Indoor Operative Temperature (T_o) and Indoor Neutral Operative Temperature (T_{neutop}) for LK2

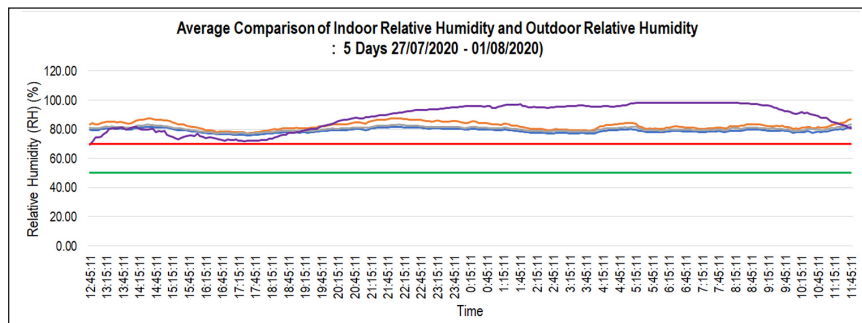
Figure 6 shows the statistical summaries of the indoor and outdoor measurements recorded from all three measuring instruments in LK2 for five days measurement.



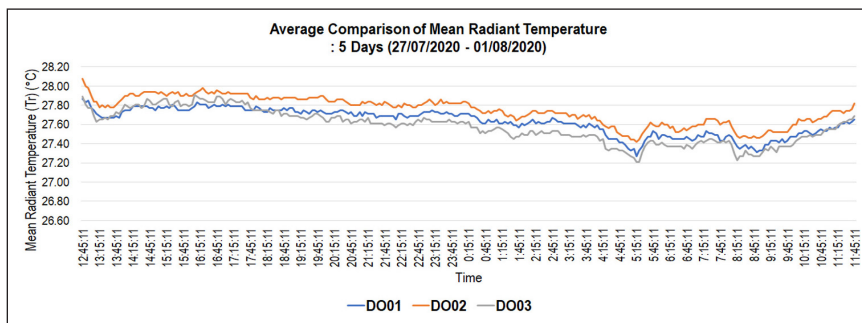
(a)



(b)



(c)



(d)

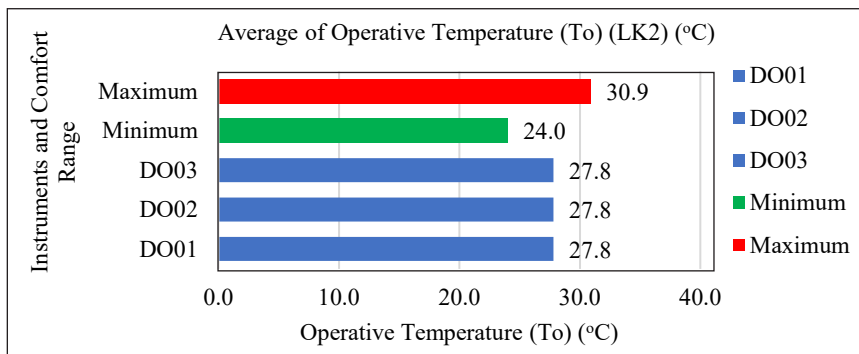
Figure 6. Statistical summaries of the average comparison indoor and outdoor measurements for LK2: (a) Air temperature; (b) Air speed; (c) Relative humidity; (d) Mean radiant temperature

The average indoor air temperature recorded are 28.2°C for DO1, 28.0°C for DO2, and 28.1°C for DO3. The readings recorded are slightly higher than the average outdoor air temperature with readings 26.0°C as shown in Figure 6a.

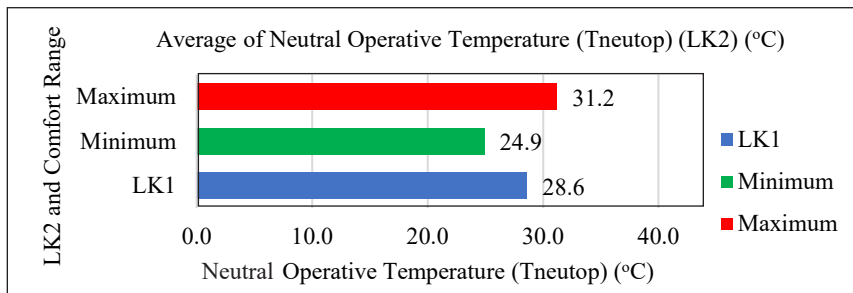
The average indoor air speed recorded by DO1, DO2 and DO3 is too low and not much different compared to each other with readings between 0.00 m/s to 0.01 m/s although the DO3 was positioned near to the window as shown in Figure 6b. This may cause by small window opening (0.6 m (W) x 0.6 m (H)) with 4% of floor area which is below 10% plus 5% unobstructed opening as required by Malaysian UBBL even though average outdoor air speed recorded is 0.39 m/s.

The average indoor relative humidity recorded are 79.0% for DO1, 82.6% for DO2, and 80.3% for DO3 as shown in Figure 6c. Average indoor relative humidity recorded are very high and exceed the acceptable range by ASHRAE 55. This may be due to the insufficient mean air speed to facilitate indoor air circulation, which does not help in reducing LK2 humidity and influenced by high outdoor humidity with average 88.5%.

The average mean radiant temperature recorded during field measurements are 27.6°C for DO1, 27.8°C for DO2, and 27.6°C for DO3 and there is not much difference between the three readings recorded as shown in Figure 6d. The average mean radiant temperature readings are slightly lower than the result of average indoor air temperature readings and



(a)



(b)

Figure 7. Summaries of the (a) operative temperature and (b) neutral operative temperature prediction for LK2

this indicates that there are other influencing factors such as space height where LK2 is slightly higher with 3.2 m height.

According to Equation 1, the value of A used in the calculation of operative temperature for all measurement instruments (DO1, DO2 and DO3) is 0.5 because the average air speed <0.2 m/s which is between 0.00 m/s to 0.01 m/s only.

The average indoor air speed which is between 0.00 m/s to 0.01 m/s and average outdoor air temperature which is between 26.0°C for LK2 is within the set limit and comply with the requirements as prescribed by Equation 2.

The indoor operative temperature has been determined between 27.8°C to 27.9°C while the neutral operative temperature is 28.6°C for LK2 as shown in Figure 7.

Statistical Summaries of the Indoor and Outdoor Measurements, Analysis of Prediction of the Indoor Operative Temperature (T_o) and Indoor Neutral Operative Temperature (T_{neutop}) for LK3

Figure 8 shows the statistical summaries of the indoor and outdoor measurements recorded from all three measuring instruments in LK3 for five days measurement.

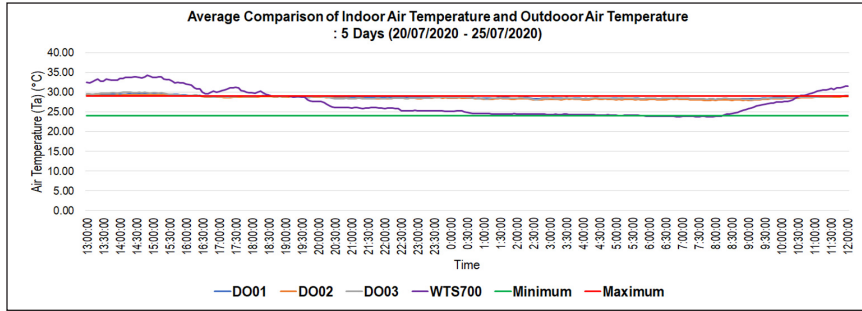
The average indoor air temperature recorded are 28.7 °C for DO1 and DO3 and 28.5 °C for DO2. The readings recorded are slightly higher than the average outdoor air temperature with reading 27.3°C as shown in Figure 8a.

The average indoor air speed recorded by DO1, DO2 and DO3 is also low and not much different with readings between 0.01 m/s to 0.04 m/s although DO3 was positioned near to the window opening as shown in Figure 8b. The low LK3 reading might be influenced by small window opening (0.6 m (W) x 0.6 m (H)) with 4.6% of floor area which is below 10% plus 5% unobstructed opening as required by Malaysian UBBL even though average outdoor air speed recorded is quite high which is between 0.32 m/s to 0.53 m/s. In addition, the average air speed recorded is higher about +0.01 to +0.03 m/s than recorded by LK2.

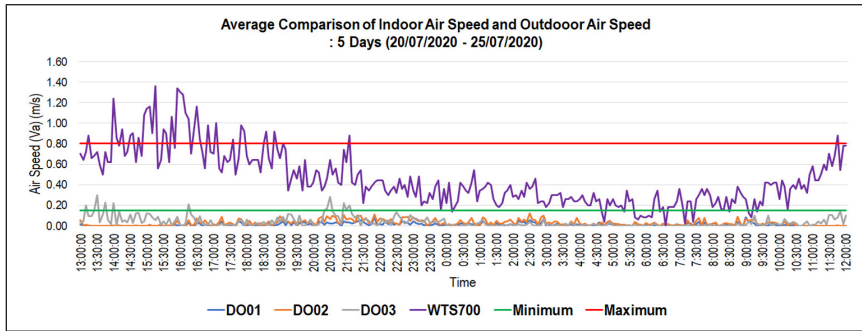
The average indoor relative humidity recorded are 77.5% for DO1, 80.6% for DO2 and 78.8% for DO3 as shown in Figure 8c. Average indoor relative humidity recorded are very high and exceed the acceptable range by ASHRAE 55. This may be due to the low average air speed in facilitating indoor air circulation, which does not help in reducing LK3 humidity. It may also influence by high average outdoor humidity with reading of 81.9%.

The average mean radiant temperature recorded during field measurements are 28.2°C for DO1, 28.3°C for DO2 and 28.4°C for DO3. There is not much difference between the three readings recorded as shown in Figure 8d. The mean radiant temperature is slightly lower than mean air temperature. This indicates other influencing factors such as the effect of epoxy paint finish on the LK3 walls which is still in a good condition during the measurement period.

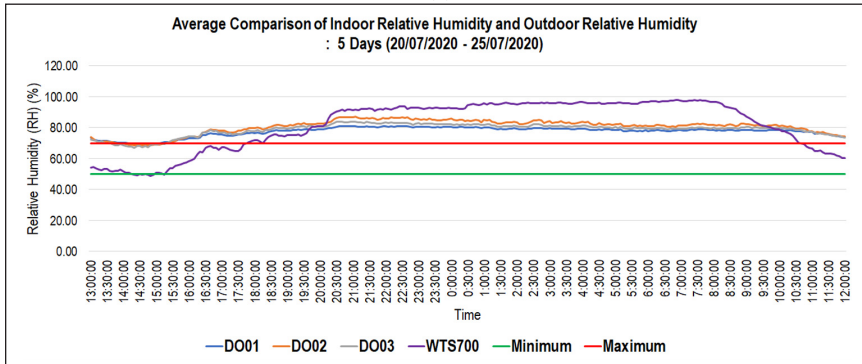
Thermal Comfort Performance of Royal Malaysian Police (RMP) Lockup



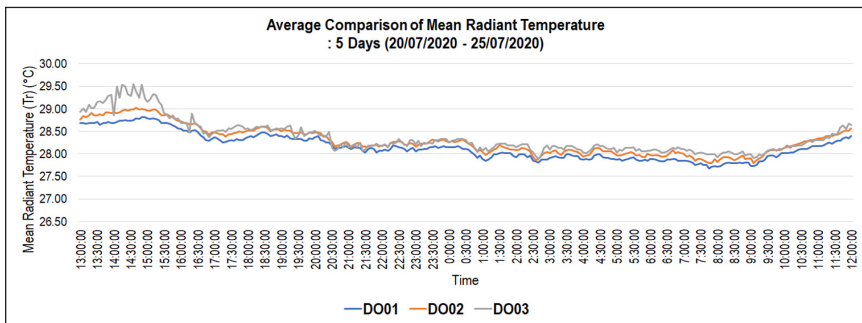
(a)



(b)



(c)



(d)

Figure 8. Statistical summaries of the average comparison indoor and outdoor measurements for LK3: (a) Air temperature; (b) Air speed; (c) Relative humidity; (d) Mean radiant temperature

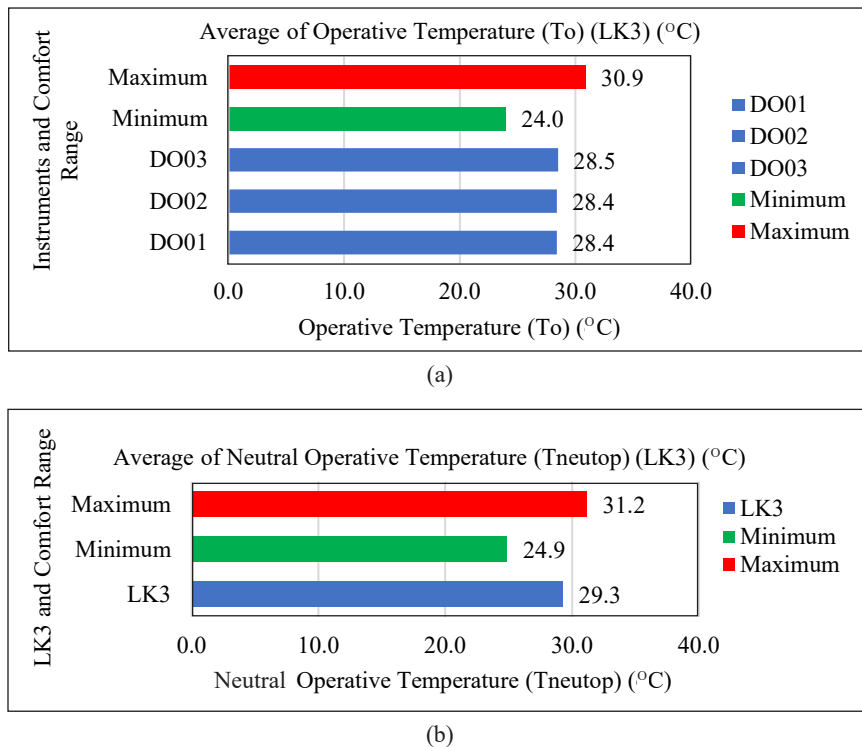


Figure 9. Summaries of the operative temperature and neutral operative temperature prediction for LK3

According to Equation 1, the value of A used in the calculation of operative temperature for all LK3 measurement instruments (DO1, DO2 and DO3) is 0.5 because the average air speed <math>< 0.2 \text{ m/s}</math> which is between 0.01 m/s to 0.04 m/s only.

The average indoor air speed which is between 0.01 m/s to 0.04 m/s and average outdoor air temperature 27.3°C for LK3 is also within the set limit which is between 19.4°C to 30.5°C and comply with the requirements as prescribed by Equation 2.

The indoor operative temperature has been determined between 28.4°C to 28.5°C while the neutral operative temperature is 29.3°C for LK3 as shown in Figure 9.

Discussions and Comparison to ASHRAE 55 and Previous Studies

To evaluate thermal comfort performance, comfort range for thermal comfort recommended by ASHRAE 55 (2017) (minimum range), Zain et al. (2007) (maximum range) and Toe & Kubota (2013) for naturally ventilated building in hot and humid climate were used as shown in Table 8.

The average indoor operative temperature obtained in the present study for LK1 (31.4°C to 31.6°C) is slightly exceeding the maximum limit recommended by ASHRAE 55 (2017) by about +2.4°C to +2.6°C and Zain et al. (2007) by about +0.5°C to +0.7 °C. The average neutral operative temperature obtained in the present study for LK1 (31.5 °C) is also found

Table 8

Comparison of comfort range and recommended comfort criteria among previous studies, ASHRAE 55 and present study

Parameters	(ASHRAE 55, 2017) (minimum range)	(Zain et al., 2007) (maximum range)	(Toe & Kubota, 2013) (minimum to maximum range)	Present study (average)
Operative temperature	24.0°C – 29.0°C	30.9°C	NA	LK1: 31.4°C to 31.6°C LK2: 27.8°C to 27.9°C LK3: 28.4°C to 28.5°C
Neutral operative temperature	NA	NA	24.9 – 31.2 °C	LK1: 31.5°C LK2: 28.6°C LK3: 29.3°C

slightly exceeding the maximum limit by about +0.3 °C compared to the indoor comfort temperature recommended by Toe & Kubota (2013).

The average indoor operative temperature obtained in the present study for LK2 (27.8°C to 27.9°C) and LK3 (28.4°C to 28.5°C) recorded within the minimum and maximum limit as recommended by ASHRAE 55 (2017) and Zain et al. (2007). The average neutral operative temperature obtained in the present study for LK2 (28.6°C) and LK3 (29.3 °C) recorded within the indoor comfort temperature recommended by Toe & Kubota (2013).

CONCLUSION

Field study with physical measurement of the thermal environment and comfort in three different lockups were in hot and humid climate conducted to investigate and analysis the thermal comfort performance and to predict comfort range for all three case study lockups. Although 3 sets of measurement instruments were used in the present study, the reading data obtained between the three instruments were not much different from each other. The conclusions are as follows:

1. LK1 – Average indoor air temperature reading is high which may be due to large window opening. Based on the field measurement, the window opening is 30% of the floor area which 15% exceeding Malaysian UBBL requirement. Other influencing factors are high average outdoor air speed and wind direction which is perpendicular to window opening. Since the field study were conducted during hot season, the air brought into the lockup was hot and dry which cause low relative humidity. The operative temperature obtained is slightly exceeding the maximum range recommended by ASHRAE 55 (2017) by about +2.4°C to +2.6°C and Zain et al. (2007) by about +0.4°C to +0.7°C. The neutral operative temperature obtained in the present study for LK1 (31.5 °C) also found slightly exceeding by about +0.3°C within the recommended by Toe & Kubota (2013).

2. LK2 – Average indoor air temperature reading is within the range recommended by ASHRAE 55 (2017). While indoor relative humidity reading is high which may be due to insufficient indoor air speed which caused by small window opening, 4% of the floor area which 11% below Malaysian UBBL requirement although wind direction is perpendicular with the window opening. The indoor operative temperature obtained is within the minimum and maximum range recommended by ASHRAE 55 (2017) and Zain et al. (2007) while indoor neutral operative temperature for LK2 (28.6 °C) recorded within the recommended by Toe & Kubota (2013).
3. LK3 – Average indoor air temperature reading is within the range recommended by ASHRAE 55 (2017). While indoor relative humidity reading is high which may be due to insufficient indoor air speed which caused by small window opening, 4.6% of the floor area which is 10.4% below Malaysian UBBL requirement and parallel wind direction to the window opening. The indoor operative temperature obtained is within the minimum and maximum range recommended by ASHRAE 55 (2017) and Zain et al. (2007) while indoor neutral operative temperature for LK2 (29.3 °C) recorded within the recommended by Toe & Kubota (2013).
4. In general, this three case study lockups have different window openings and space volume which influence indoor thermal comfort performance. Thus, subsequent study shall look on this aspect to determinant its level of influence.
5. The results of the three case study lockups support most of the statements made by the detainees as stated in NGO's report and previous studies which is the lockup is hot and contribute to discomfort among detainees as mentioned earlier.

This is an early study for future rigorous investigation that will lead to better understanding on the effect of opening design on the thermal comfort performance of lockup. In addition, further study using static models of thermal comfort through the Predicted Mean Vote (PMV) and Percentage of People Dissatisfied (PPD) indexes on existing detainees are recommended to be conducted to compliment the results obtained in this study in producing comprehensive results on the thermal comfort performance of RMP lockups.

ACKNOWLEDGEMENT

The authors would like to take this opportunity to express their gratitude to the National University of Malaysia (UKM) for the support and assistance that was channeled through the Fundamental Research Grant Scheme (FRGS/1/2020/TK0/UKM/02/26) and Dana Cabaran Perdana (DCP-2017-008/5). A sincere appreciation also goes to the Architecture Branch of the Public Works Department (PWD/JKR) Malaysia and the Royal Malaysia Police (RPM).

REFERENCES

- Al-Absi, Z. A., & Abas, N. F. (2018). Subjective assessment of thermal comfort for residents in naturally ventilated residential building in Malaysia. In *IOP Conference Series: Materials Science and Engineering* (Vol. 401, p. 012009). IOP Publishing. <https://doi.org/10.1088/1757-899X/401/1/012009>
- Aminuddin, A. M. R., Rao, S. P., & Hong, W. T. (2012). Thermal comfort field studies in two certified energy efficient office buildings in a tropical climate. *International Journal of Sustainable Building Technology and Urban Development*, 3(2), 129-136. <https://doi.org/10.1080/2093761X.2012.696324>
- ASHRAE 55. (2017). *ASHRAE 55-2017 - Thermal Environmental Conditions for Human Occupancy*. Retrieved June 6, 2020, from www.ashrae.org
- Attia, S., & Carlucci, S. (2015). Impact of different thermal comfort models on zero energy residential buildings in hot climate. *Energy and Buildings*, 102, 117-128. <https://doi.org/10.1016/j.enbuild.2015.05.017>
- Azizpour, F., Moghimi, S., Lim, C. H., Mat, S., Salleh, E., & Sopian, K. (2013). A thermal comfort investigation of a facility department of a hospital in hot-humid climate: Correlation between objective and subjective measurements. *Indoor and Built Environment*, 22(5), 836-845. <https://doi.org/10.1177/1420326X12460067>
- Azizpour, F., Moghimi, S., Mat, S., Lim, C., & Sopian, K. (2011). Objective and subjective assessment of thermal comfort in hot-humid region. In *Proceedings of 5th WSEAS international conferences on Recent Researches in Chemistry, Biology, Environment and Culture* (pp. 207-210). WSEAS Press.
- Chan, S. C., Che-Ani, A. I., & Ibrahim, N. L. N. (2013). Passive designs in sustaining natural ventilation in school office buildings in Seremban, Malaysia. *International Journal of Sustainable Built Environment*, 2(2), 172-182. <https://doi.org/10.1016/j.ijse.2014.01.002>
- Dahlan, N. D., Jones, P. J., Alexander, D. K., Salleh, E., & Dixon, D. (2008). Field measurement and subjects' votes assessment on thermal comfort in high-rise hostels in Malaysia. *Indoor and Built Environment*, 17(4), 334-345. <https://doi.org/10.1177/1420326X08094585>
- Damiati, S. A., Zaki, S. A., Rijal, H. B., & Wonorahardjo, S. (2016). Field study on adaptive thermal comfort in office buildings in Malaysia, Indonesia, Singapore, and Japan during hot and humid season. *Building and Environment*, 109, 208-223. <https://doi.org/10.1016/j.buildenv.2016.09.024>
- Davies, N., & Jokiniemi, E. (2008). *Dictionary of architecture and building construction*. Routledge. <https://doi.org/10.4324/9780080878744>
- de Dear, R. J., & Brager, G. S. (2002). Thermal comfort in naturally ventilated buildings: Revisions to ASHRAE standard 55. *Energy and Buildings*, 34, 549-561. [https://doi.org/10.1016/S0378-7788\(02\)00005-1](https://doi.org/10.1016/S0378-7788(02)00005-1)
- Djamila, H., Chu, C. M., & Kumaresan, S. (2013). Field study of thermal comfort in residential buildings in the equatorial hot-humid climate of Malaysia. *Building and Environment*, 62, 133-142. <https://doi.org/10.1016/j.buildenv.2013.01.017>
- Dogbeh, A., Jomaas, G., Bjarløv, S. P., & Toftum, J. (2014). Field study of the indoor environment in a Danish Prison. *Building and Environment*, 88, 20-26. <https://doi.org/10.1016/j.buildenv.2014.10.025>
- Fabbri, K. (2013). Thermal comfort evaluation in kindergarten: PMV and PPD measurement through datalogger and questionnaire. *Building and Environment*, 68, 202-214. <https://doi.org/10.1016/j.buildenv.2013.07.002>

- Feriadi, H., & Wong, N. H. (2004). Thermal comfort for naturally ventilated houses in Indonesia. *Energy and Buildings*, 36, 614-626. <https://doi.org/10.1016/j.enbuild.2004.01.011>
- Gharakhani, A., Sediadi, E., Khan, T. H., & Sabzevar, H. B. (2014). Use of natural ventilation in Malaysia's future green housing. *Advanced Materials Research*, 935, 316-319. <https://doi.org/10.4028/www.scientific.net/AMR.935.316>
- Han, J., Zhang, G., Zhang, Q., Zhang, J., Liu, J., Tian, L., Zheng, C., Hao, J., Lin, J., Liu, Y., & Moschandreas, D. J. (2007). Field study on occupants' thermal comfort and residential thermal environment in a hot-humid climate of China. *Building and Environment*, 42, 4043-4050. <https://doi.org/10.1016/j.buildenv.2006.06.028>
- Jabatan Meteorologi Malaysia. (2020). *Iklim Malaysia* [Malaysia Climate]. Retrieved May 16, 2020, from <http://www.met.gov.my/pendidikan/iklim/iklimmalaysia>
- Jiang, Y., Alexander, D., Jenkins, H., Arthur, R., & Chen, Q. (2003). Natural ventilation in buildings: Measurement in a wind tunnel and numerical simulation with large-eddy simulation. *Journal of Wind Engineering and Industrial Aerodynamics*, 91(3), 331-353. [https://doi.org/10.1016/S0167-6105\(02\)00380-X](https://doi.org/10.1016/S0167-6105(02)00380-X)
- Kamaruzzaman, K., & Tazilan, A. S. M. (2013). Thermal comfort assessment of a classroom in tropical climate conditions. *Recent Advances in Energy, Environment and Development*, 87-91.
- Kubota, T., Chyee, D. T. H., & Ahmad, S. (2009). The effects of night ventilation technique on indoor thermal environment for residential buildings in hot-humid climate of Malaysia. *Energy and Buildings*, 41, 829-839. <https://doi.org/10.1016/j.enbuild.2009.03.008>
- López-Pérez, L. A., Flores-Prieto, J. J., & Ríos-Rojas, C. (2019). Adaptive thermal comfort model for educational buildings in a hot-humid climate. *Building and Environment*, 150, 181-194. <https://doi.org/10.1016/j.buildenv.2018.12.011>
- Maarof, S. (2014). *Roof designs and affecting thermal comfort factors in a typical naturally ventilated Malaysian mosque* (Doctoral dissertation). Cardiff University.
- Nordin, R. M., Halim, A. H. A., & Yunus, J. (2017). Challenges in the implementation of green home development in Malaysia: Perspective of developers. *IOP Conference Series: Materials Science and Engineering*, 291, 012-020. <https://doi.org/10.1088/1757-899X/291/1/012020>
- Nur'aini, R. D. (2017). Thermal performance simulation of residential building in tropical climate case study: Housing in Bandar Universiti, Malaysia. *International Journal of Built Environment and Scientific Research*, 1(1), 47-52. <https://doi.org/10.24853/ijbesr.1.01.47-52>
- PDRM. (1953). *Peraturan-peraturan lokap 1953* [Lockup rules 1953]. Retrieved November 2, 2020, from https://www.malaysianbar.org.my/document/com_docman/gid/itemid&rid=9641
- Perlembagaan Persekutuan Malaysia. (2010). *Perlembagaan Persekutuan Malaysia* (Jabatan Peguam Negara (ed.); 160A ed., Vol. 6, Issue 1) [Federal Constitution of Malaysia (Attorney General Chambers of Malaysia (ed.); 160A ed., Vol. 6, Issue 1)]. Pesuruhjaya Penyemak Undang-Undang Malaysia. Retrieved October 21, 2019, from <http://www.kptg.gov.my/images/pdf/perundangan-tanah/perlembagaanpersekutuan.pdf>

- Razak, B. A., Mohamed, M. F., Yusoff, W. F. M., & Sulaiman, M. K. A. M. (2020). Research on the design typology of the Royal Malaysian Police (RMP) lockups. *International Journal of Advanced Science and Technology*, 29(9s), 1866-1884.
- SUHAKAM. (2016). *Kematian dalam tahanan polis: Satu kaji selidik mengenai keadaan lokap dan faktor-faktor penyumbang kepada kematian* [Deaths in police custody a thematic study on lock-up conditions and factors contributing to the death.]. Suruhanjaya Hak Asasi Manusia Malaysia. Retrieved October 16, 2019, from www.suhakam.org.my
- Tang, C., & Chin, N. (2017). *Building energy efficiency technical guideline for passive design*. Building Sector Energy Efficiency Project (BSEEP), Malaysia. Retrieved June 7, 2020, from <http://www.mgbc.org.my/bseep-building-energy-efficiency-technical-guideline-for-passive-design/>
- Taweekun, J., & Tantiwichien, A. U. W. (2013). Thermal comfort zone for Thai people. *Engineering*, 5, 525-529. <https://doi.org/10.4236/eng.2013.55062>
- Tharim, A. H. A., Munir, F. F. A., Samad, M. H. A., & Mohd, T. (2018). A field investigation of thermal comfort parameters in green building index (GBI)-rated office buildings in Malaysia. *International Journal of Technology*, 8, 1588-1596. <https://doi.org/10.14716/ijtech.v9i8.2763>
- Toe, D. H. C., & Kubota, T. (2013). Development of an adaptive thermal comfort equation for naturally ventilated buildings in hot-humid climates using ASHRAE RP-884 database. *Frontiers of Architectural Research*, 2, 278-291. <https://doi.org/10.1016/j.foar.2013.06.003>
- Webb, C. G. (1959). An analysis of some observations of thermal comfort in an equatorial climate. *British Journal of Industrial Medicine*, 16, 297-310. <https://doi.org/10.1136/oem.16.4.297>
- Wong, N. H., & Khoo, S. S. (2003). Thermal comfort in classrooms in the tropics. *Energy and Buildings*, 35, 337-351. [https://doi.org/10.1016/S0378-7788\(02\)00109-3](https://doi.org/10.1016/S0378-7788(02)00109-3)
- Wong, N. H., Tan, E., & Adelia, A. S. (2020). Utilization of natural ventilation for hot and humid Singapore. In *Building in Hot and Humid Regions* (pp. 165-184). Springer. https://doi.org/10.1007/978-981-13-7519-4_8
- World Meteorological Organisation. (2020). *World weather*. World Meteorological Organisation. Retrieved July 27, 2020, from <https://worldweather.wmo.int/en/home.html>
- Xue, F., Gou, Z., & Lau, S. (2016). Human factors in green office building design: The impact of workplace green features on health perceptions in high-rise high-density asian cities. *Sustainability*, 8(11), Article 1095. <https://doi.org/10.3390/su8111095>
- Yang, T., & Clements-Croome, D. J. (2018). Natural ventilation in built environment. In *Encyclopedia of Sustainability Science and Technology* (pp. 1-35). Springer Science + Business Media. https://doi.org/10.1007/978-1-4939-2493-6_488-3
- Yusoff, W. F. M., & Mohamed, M. F. (2017). Building energy efficiency in hot and humid climate. In *Encyclopedia of Sustainable Technologies* (pp. 159-168). Elsevier. <https://doi.org/10.1016/B978-0-12-409548-9.10191-5>
- Zaharin, Z., Nordin, J., & Shukri, S. M. (2019, November 6-7). Added value to security building design case study: Police Station in Malaysia. In *ICRP 2019 4th International Conference on Rebuilding Place* (pp. 362-373). Penang, Malaysia. <https://doi.org/10.15405/epms.2019.12.35>

- Zain, Z. M., Taib, M. N., & Baki, S. M. S. (2007). Hot and humid climate: Prospect for thermal comfort in residential building. *Desalination*, 209, 261-268. <https://doi.org/10.1016/j.desal.2007.04.036>
- Zhang, G., Zheng, C., Yang, W., Zhang, Q., & Moschandreas, D. J. (2007). Thermal comfort investigation of naturally ventilated classrooms in a subtropical region. *Indoor and Built Environment*, 16(2), 148-158. <https://doi.org/10.1177/1420326X06076792>

Analytical and Numerical Investigation of Free Vibration Behavior for Sandwich Plate with Functionally Graded Porous Metal Core

Emad Kadum Njim¹, Sadeq H. Bakhy¹ and Muhannad Al-Waily^{2*}

¹University of Technology, Mechanical Engineering Department, Baghdad, Iraq

²University of Kufa, Faculty of Engineering, Mechanical Engineering Department, Najaf, Iraq

ABSTRACT

The current work presents a free vibration analysis of a simply supported rectangular functionally graded sandwich plate using a new analytical model. The core of the sandwich plate is made up of porous metal, and the top and bottom faces are made up of homogenous materials. The core metal properties are assumed to be porosity dependent and graded in the thickness direction according to a simple power-law distribution in terms of the volume fractions of the constituents. The contribution of this paper is to evaluate the performance of functionally graded porous materials (FGPMs) as it is used for many biomedical applications, particularly in tissue engineering. Theoretical formulations are based on the classical plate theory to find the free vibration characteristics of the imperfect

FGM sandwich plate and include different parameters. Parameters included are graded distributions of porosity, power-law index, core metal type, and aspect ratios. A numerical investigation using finite element analysis (FEA) and the modal analysis was conducted with the assistance of the commercial ANSYS-2020-R2 software to validate the analytical solution. To detect the various parameters influencing the fundamental frequencies of sandwich plate comprehensive numerical results are presented in dimensionless tabular and graphical forms. The results reveal that the

ARTICLE INFO

Article history:

Received: 19 February 2021

Accepted: 30 April 2021

Published: 31 July 2021

DOI: <https://doi.org/10.47836/pjst.29.3.39>

E-mail addresses:

emad.njim@gmail.com (Emad Kadum Njim)

20093@uotechnology.edu.iq (Sadeq H. Bakhy)

muhanedl.alwaeli@uokufa.edu.iq (Muhannad Al-Waily)

*Corresponding author

frequency parameter of the sandwich plate increases with the increase of the porosity parameter and number of the constraints in the boundary conditions. Furthermore, the increase in the number of layers leads to an increase in the accuracy of the results for the same FGM core thickness. An accepted agreement can be observed between the proposed analytical solution and numerical results with a maximum error discrepancy of 8%.

Keywords: Free vibration, frequency, functionally graded, porous, sandwich plate

INTRODUCTION

Functionally graded materials (FGMs) are composites with a continuous variation of material properties from one surface to another, thus eliminating the stress concentration found in laminated composites (Thai et al., 2013). Due to its excellent stiffness and toughness and high strength-to-weight ratio, the sandwich structure can be used in many applications, such as automobiles, ship development, transportation, and airlines. This feature has attracted many considerations, and many researchers have conducted continuous static and dynamic inspections of structural engineering under various environmental conditions. Consequently, due to the excellent performance, the use of sandwich structures in the field of micro auxiliary frames is continuously developing (Hadji et al., 2011). Therefore, in a wide range of FGM material types and benefits, it is vital to explore the static and dynamic behavior of auxiliary personnel with FGM, such as beams and plates (Kiani et al., 2011; Anderson, 2003). Due to technical problems in the manufacturing process, pores and micropores may be formed inside the FGM plate, which may cause material quality degradation. The assembly strategy of FGM's is a creative area. The sintering strategy is most widely used because of its cost-saving advantage ratio. In any case, the sintering cycle empowers the development of microvoids or porosities (Kumar et al., 2021). Although crucial improvements have been observed here recently, porosity is still an ongoing defect in FGM. As mentioned above, porosity results from the assembly cycle and can reduce the material's quality. Therefore, this defect's effect is to consider the influence of pores on the unique properties of the transfer pores of the FGM structure (Muc & Flis, 2021). Wang and Zu (2017) considered a rectangular plate's vibration behavior mainly evaluated, pores, and moves in a warm area. The vibration analysis of a porous functionally graded plate made of a mixture of Aluminum (Al) and alumina (Al_2O_3) installed in an elastic medium was introduced by Hayat and Meriem (2019). Zhang et al. (2019) changed the topological design, porosity, and mechanical behavior of functionally graded porous metal biomaterials with added design. Singh and Harsha (2020) studied the effect of porosity and temperature on sandwich S-FGM plates.

Dang et al. (2018) also discussed the free vibration characteristics, which can be inferred from the pores in the FGM test of the rotating graphene-enhanced permeable

nanocomposite barrel shell. Regarding the porosity distribution, Nguyen et al. (2018) studied the mechanical conduction of porous FGP. Therefore, they considered two different porosities, both of which move in the thickness direction (specifically, evenly distributed and unevenly distributed). Zhang and Wang (2017) created eight other porous material structures with varying pore distributions, including gradient distributions. They exposed them to some mechanical tests to evaluate essential material properties, such as Young's modulus. Functionally graded porous materials combine the qualities of FGM and porous materials. In addition to the extremely high stiffness-to-weight ratio, they also have excellent mechanical properties to clarify why these materials are widely used in various fields (Kiani & Eslami, 2012). Usually, the variation of porosity through the thickness of porous plates causes a smooth change in mechanical properties. Therefore, this type of material has received wide applications in aerospace, marine, and biomedical application (Rezaei & Said 2015). Although there are exceptional circumstances, the material's strength will decrease due to these holes' presence, which should be kept in mind for mechanical behavior (Merdaci, 2019).

Kim et al. (2019) proposed three porosity distributions in the thickness direction, together with the research developed by Coskun et al. (2019) and Zhao et al. (2019). The inspiration for the closure came from the uniform distribution of Merdaci (2019). His research recognized that typical functionally graded ceramic/metal square plates have different porosity distributions throughout the thickness. Numerous studies on free vibration for isotropic and functionally graded plates have been reported. Chakraverty and Pradhan (2014) studied the free vibration of thin FG rectangular plates in complex environments. Wattanasakulponga and Ungbhakorn (2014) used a combination of linear and nonlinear analysis to study the influence of porosity parameters on the frequency parameters of FGM constrained end beams. Although some studies have been conducted on sandwich structures with FGM cores to evaluate their bending behavior (Tossapanon & Wattanasakulpong, 2017; Meiche et al., 2011; Neves et al., 2013) and flexural strength (Kapuria et al., 2008; Lashkari & Rahmani, 2016), sandwich structures' free vibration and stability issues fabricated by functionally gradient have been studied. However, investigations on the free vibration of FGM structures with porous metal topology are still limited. The objective of the present research is to investigate the free vibration analysis of an imperfect simply-supported sandwich plate. In this paper, we assume that the functionally graded part is made from one constituent material, whose material properties are changed due to various porosity distribution and graded in the thickness direction according to a power-law distribution. A new representation of the classical plate theory (CPT) is developed to find the free vibration features according to various FGM parameters. The proposed mathematical model used for approximating FGM core properties, such as Young's modulus (E) and material density (ρ) equations, is verified by comparisons between material property results obtained from

volume fraction analysis and the proposed models. The paper also explores the influence of some parameters on the free vibration of the functionally graded sandwich plates such as power-law index, porous metal type, porosity ratio, and length to thickness ratios. By using the FEA method represented by ANSYS software, results of natural frequency and mode shapes of the imperfect FGM sandwich plate with different boundary conditions are presented. Furthermore, the core part is divided into (2-16) layers, and the frequency analysis is performed for both square and rectangular plates to identify the effect of the increasing number of layers on FG structure performance. The numerical results presented herein for functionally graded porous materials are not available in the literature, and hence, should be of interest to the industrial applications.

MATERIALS AND METHOD

Consider a thin rectangular FGM plate composed of ceramic and metal, in which the upper surface is metal-rich, and the underlying surface is ceramic-rich, respectively. The FGM plate is supposed to carry porosities that disperse evenly or unevenly along the plate-thickness direction (Figure 1). The plate’s length, width, and thickness are denoted by a , b and h , respectively. A Cartesian coordinate system (O, x, y, z) on the plate’s middle surface is adopted to describe the plate motion, where x and y define the in-plane coordinates and z denotes the out-of-plane coordinate of the plate. The origin O is at one of the plate corners; however, the volume fraction of FG plate layers can be represented either in exponential law, sigmoid law, or power-law. The ceramic volume fraction V_c is assumed to follow a simple power distribution as Equation 1 (Natarajan & Manickam, 2012).

$$V_c(z) = \left(\frac{z + \frac{h}{2}}{h} \right)^k \tag{1}$$

The volume fraction sum of metal and ceramic is stated as: $V_m(z) + V_c(z) = 1$, where V_m and V_c are volume fractions of metal and ceramic, respectively k is power-law variation index and is a non-negative variable parameter, in which $k \in [0, \infty)$. The value of k equal to zero represents a fully ceramic plate, whereas infinite k indicates a fully metallic plate.

Assuming porosities disperse equally in the metal and ceramic phases, the general material property of the imperfect FGM plate, with a porosity volume fraction β ($\beta \ll 1$), takes the modified form as Equation 2.

$$P(z) = (P_c - P_m) \left(\frac{z + \frac{h}{2}}{h} \right)^k + P_m - \frac{\beta}{2} (P_c + P_m) \tag{2}$$

In Equation 2, P_c and P_m ; are the values of material properties of ceramic and metal, constituents of the FG plate, respectively. For our present formulations, the material properties, viz. Young’s modulus (E) and mass density (ρ) are taken to vary along thickness direction except for Poisson’s ratio (ν), which will assume to be constant for simplicity, based on previous studies, reported by Delale and Erdogan (Meziane et al., 2014).

In general, the two-dimensional plate theories can be categorized into two types: (1) classical plate theory, in which the transverse shear deformation consequences are neglected, and (2) shear deformation plate theories. In the two-dimensional theory, the free vibration, thermal, and stability problems of the FGM structures, the displacement is represented in thickness. In contrast, the lateral displacement is independent of the lateral (or thickness) coordinates. The results of the mathematical model in the coupled governing equation are independent of lateral displacement. Therefore, this type of equation’s analytical solution may be simpler than the three-dimensional elasticity theory (Ambartsumyan et al., 1970).

By using the classical plate theory (CPT), the displacement fields of FG plates across the plate thickness at a distance z away from the middle surface are defined as Equation 3 (Chi & Chung, 2006; Latifi et al., 2013).

$$\begin{aligned} u_x(x, y, z) &= -z \frac{\partial w}{\partial x} \\ u_y(x, y, z) &= -z \frac{\partial w}{\partial y} \\ u_z(x, y, z) &= w(x, y) \end{aligned} \tag{3}$$

Where u_x , u_y , and u_z are the displacement of a point on the reference plane in the x , y , and z directions, respectively, and w represents the mid-plane lateral deflection (x - y plane). The Kirchoff model is not considered the effect of shear deformation due to bending and plane elongation. The non-zero linear strains associated with the displacement field can be expressed as Equation 4.

$$\begin{pmatrix} \epsilon_{xx} \\ \epsilon_{yy} \\ \gamma_{xy} \end{pmatrix} = \begin{pmatrix} \frac{\partial u_x}{\partial x} \\ \frac{\partial u_y}{\partial y} \\ \frac{\partial u_x}{\partial y} + \frac{\partial u_y}{\partial x} \end{pmatrix} = \begin{pmatrix} -z \frac{\partial^2 w}{\partial x^2} \\ -z \frac{\partial^2 w}{\partial y^2} \\ -2z \frac{\partial^2 w}{\partial x \partial y} \end{pmatrix} \tag{4}$$

Where, ϵ_{xx} and ϵ_{yy} ; are the components of the strain in x and y directions, respectively, and γ_{xy} ; is the shear strain. Based on CPT, the stress-strain relations are given by Equation 5 (Wadee, 2001).

$$\begin{aligned}
 \sigma_{xx} &= \frac{E}{1 - \nu^2} (\epsilon_{xx} + \nu\epsilon_{yy}) \\
 \sigma_{yy} &= \frac{E}{1 - \nu^2} (\epsilon_{yy} + \nu\epsilon_{xx}) \\
 \sigma_{xy} &= G\gamma_{xy} = \frac{E}{2(1 + \nu)} \gamma_{xy}
 \end{aligned}
 \tag{5}$$

The linear constitutive relations of a plate, such as the bending and twisting moments M_{xx} , M_{yy} , and M_{xy} respectively on a plate element in the pure bending case can be written as Equation 6 (Baferani et al., 2011).

$$\begin{aligned}
 M_{xx} &= \int_{-\frac{h}{2}}^{\frac{h}{2}} \sigma_{xx} z dz = -D \left(\frac{\partial^2 w}{\partial x^2} + \nu \frac{\partial^2 w}{\partial y^2} \right) \\
 M_{yy} &= \int_{-\frac{h}{2}}^{\frac{h}{2}} \sigma_{yy} z dz = -D \left(\nu \frac{\partial^2 w}{\partial x^2} + \frac{\partial^2 w}{\partial y^2} \right) \\
 M_{xy} &= \int_{-\frac{h}{2}}^{\frac{h}{2}} \sigma_{xy} z dz = -(1 - \nu) D \frac{\partial^2 w}{\partial x \partial y}
 \end{aligned}
 \tag{6}$$

Where (Equation 7),

$$D = \frac{Eh^3}{12(1 - \nu^2)}
 \tag{7}$$

the flexural rigidity of the plate. Alternatively, the second-order equilibrium equation of the Kirchhoff plate theory may be written as Equation 8.

$$\frac{\partial^2 M_{xx}}{\partial x^2} - 2 \frac{\partial^2 M_{xy}}{\partial x \cdot \partial y} + \frac{\partial^2 M_{yy}}{\partial y^2} = I_0 \frac{\partial^2 w}{\partial t^2}
 \tag{8}$$

Substituting the expressions of bending and twisting moments in Equation 6, we can obtain the equation of equilibrium in terms of deflections (w) of the plate as Equation 9.

$$D \left(\frac{\partial^4 w}{\partial x^4} + 2 \frac{\partial^4 w}{\partial x^2 \cdot \partial y^2} + \frac{\partial^4 w}{\partial y^4} \right) + I_0 \frac{\partial^2 w}{\partial t^2} = 0
 \tag{9}$$

Where (I_0) is the inertial coefficient of the plate.

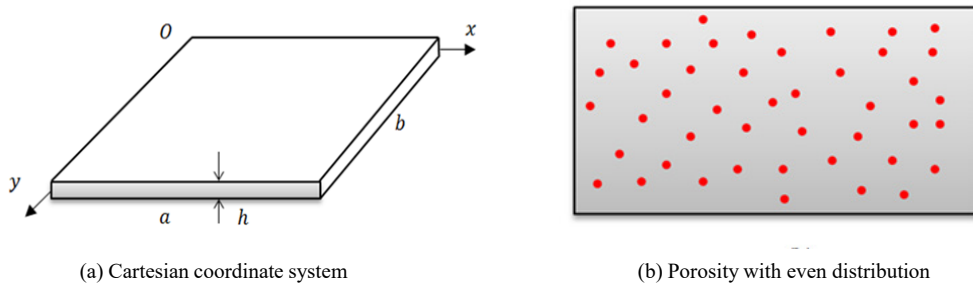


Figure 1. A rectangular FGM plate

Modeling Analysis for FGM Porous Core

This section describes a new mathematical model used to evaluate the free vibration of the rectangular FG plate. By considering the imperfect FGM plate made mainly from one porous metal with a porosity volume fraction, ($\beta \ll 1$) distributed equally in the core metal phase and graded through the plate thickness direction according to a power-law distribution. Accordingly, the suggested rule of the mixture is proposed as Equation 10.

$$P(z) = P_m - P_m \beta \left(\frac{z}{h} + \frac{1}{2} \right)^k \tag{10}$$

In the case of a homogenous plate ($\beta=0$), for the imperfect FGM plate, Young’s modulus (E) and material density (ρ) equations can be expressed as Equations 11 and 12.

$$E(z) = E_m - E_m \beta \left(\frac{z}{h} + \frac{1}{2} \right)^k \tag{11}$$

$$\rho(z) = \rho_m - \rho_m \beta \left(\frac{z}{h} + \frac{1}{2} \right)^k \tag{12}$$

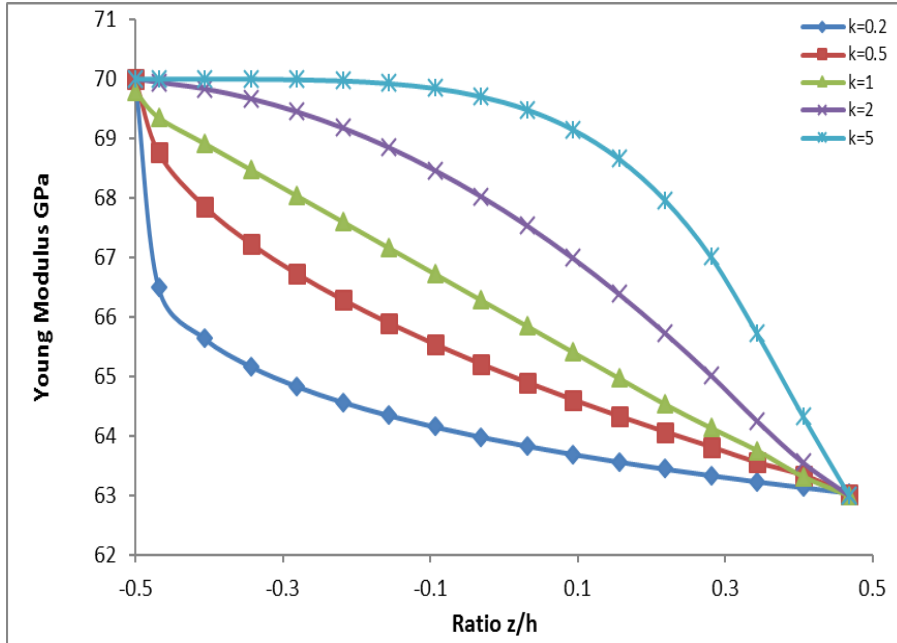
To verify the proposed mathematical models (Equations 11 & 12) used for approximating material properties of imperfect FGM plates, this can be accomplished by comparisons between material property results secured directly from volume fraction analysis and the proposed models. Consider that the FGM plate made from Aluminum (Al) as porous metal whose material properties are: $E_m = 70$ GPa, $\rho = 2702$ Kg/m³; $\nu = 0.3$ (Wattanasakulpong and Chaikittiratana, 2015). Table 1 shows the values of mass per unit length of the FGM plate.

From the comparisons in Table 1, it can be seen that the results predicted by the proposed models match well with those obtained from the volume fraction analysis. Additionally, to predict Young’s modulus (E) across the plate thickness, Figure 2 shows the material properties profile of the imperfect FGM plates using Equations 11 and 12.

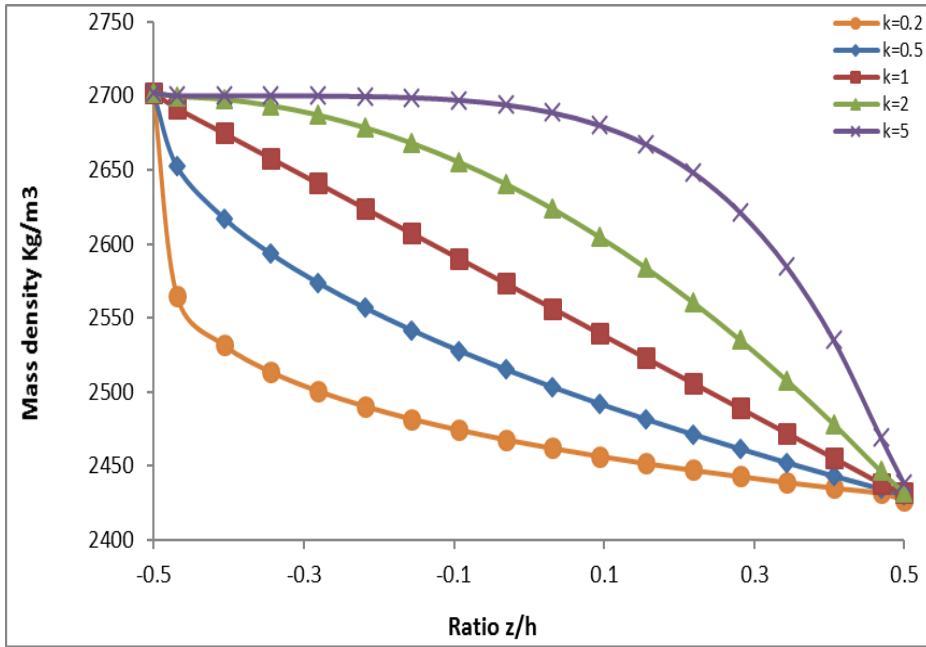
Table 1

Two different techniques used to calculate the mass density of perfect and imperfect cores

k	Material	Volume fraction analysis Mass= $\rho \cdot V_p$	The proposed models (Equation 12)
1,2,.....n	Perfect FGM ($\beta=0$), $V_p=1$	$2700 \cdot 1=2700$	2700
	Imperfect FGM, ($\beta=0.1$), $V_p=1-0.1=0.9$	$2700 \cdot 0.9=2430$	$2700-700 \cdot 0.1=2430$
	Imperfect FGM, ($\beta=0.2$), $V_p=1-0.2=0.8$	$2700 \cdot 0.8=2160$	$2700-0.2 \cdot 2700=2160$
	Imperfect FGM, ($\beta=0.3$), $V_p=1-0.3=0.7$	$2700 \cdot 0.7=1890$	$2700-0.3 \cdot 2700=1890$
	Imperfect FGM, ($\beta=0.4$), $V_p=1-0.4=0.6$	$2700 \cdot 0.6=1620$	$2700-0.4 \cdot 2700=1620$
	Imperfect FGM, ($\beta=0.5$), $V_p=1-0.5=0.5$	$2700 \cdot 0.5=1350$	$2700-0.5 \cdot 2700=1350$



a) The modulus of elasticity (E) variation



(b) The mass densities (ρ) variation

Figure 2. Power-law variation at porosity 10% of (a) Young’s modulus and (b) mass densities of the FG plate.

By using the CPT principle, the equations of motion that are convenient for the displacement components mentioned in Equation 5, including stiffness and inertia for vibration analysis of FGM plate, can be written as Equations 13-15:

$$D = \frac{1}{1 - \nu^2} \int_{-h/2}^{h/2} E(z) \cdot z^2 dz \tag{13}$$

$$D_f = \frac{E_p h^3}{12(1 - \nu^2)} - \frac{\beta E_p h^3}{(1 - \nu^2)} \left(\frac{1}{(k + 3)} - \frac{1}{(k + 2)} + \frac{1}{4(k + 1)} \right) \tag{14}$$

$$I_0 = \int_{-h/2}^{h/2} \rho(z) dz = \rho_p h \left\{ 1 - \frac{\beta}{(k + 1)} \right\} \tag{15}$$

Where, ρ_p and E_p are the mass density and young modulus of the porous metal, respectively (Equation 16 & 17).

$$D_f \left(\frac{\partial^4 w}{\partial x^4} + 2 \frac{\partial^4 w}{\partial x^2 \cdot \partial y^2} + \frac{\partial^4 w}{\partial y^4} \right) + I_0 \frac{\partial^2 w}{\partial t^2} = 0 \tag{16}$$

$$\left(\frac{E_p h^3}{12(1-\nu^2)} - \frac{\beta E_p h^3}{(1-\nu^2)} \left(\frac{1}{(k+3)} - \frac{1}{(k+2)} + \frac{1}{4(k+1)} \right) \right) \left(\frac{\partial^4 w}{\partial x^4} + 2 \frac{\partial^4 w}{\partial x^2 \cdot \partial y^2} + \frac{\partial^4 w}{\partial y^4} \right) + \left(\rho_p h \left\{ 1 - \frac{\beta}{(k+1)} \right\} \right) \frac{\partial^2 w}{\partial t^2} = 0 \tag{17}$$

Equation 17 can be solved by using the separation of the variables method by assuming the function of deflection as defined in Equation 18 (Al-Waily et al., 2020).

$$w(x, y, t) = w(x, y) \cdot w(t) \tag{18}$$

Where, $w(t)$ is the deflection function of the plate to time, and $w(x, y)$ is the deflection function of the sandwich in terms of x and y directions for a simply supported plate. Consider a rectangular plate of length a and width b with its four edges simply supported, as shown in Figure 2. To evaluate the behavior of deflection plate as a function of x and y directions that satisfies the boundary conditions $w=0$ and $M=0$; for all four edges, then, for the deflection equation of plate as a function of x and y direction, as Equation 19 (Leissa, 1969).

$$w(x, y) = \sin \frac{m\pi x}{a} \cdot \sin \frac{n\pi y}{b} \quad (m, n=1, 2, 3, \dots) \tag{19}$$

Then, by substituting Equation 17 into Equation 19, the suggested general equation of motion for FGM rectangular plate is obtained as Equation 20.

$$\frac{E_p h^3}{12(1-\nu^2)} - \frac{\beta E_p h^3}{(1-\nu^2)} \left(\frac{1}{(k+3)} - \frac{1}{(k+2)} + \frac{1}{4(k+1)} \right) \left(\left(\frac{\pi}{a} \right)^4 + \left(\frac{\pi}{b} \right)^4 + 2 \times \left(\frac{\pi}{a} \right)^2 \left(\frac{\pi}{b} \right)^2 \right) \omega(t) + \rho_p h \left(1 - \frac{\beta}{(k+1)} \right) \frac{\partial^2 \omega}{\partial t^2} = 0 \tag{20}$$

Equation 20 is a second-order ordinary differential equation. By comparison, Equation 20 with the general equation of motion of a single degree of freedom for free undamped vibration structure, as Equation 21 (Natarajan & Manickam, 2012).

$$\omega_{mn}^2 w(t) + \frac{\partial^2 w(t)}{\partial t^2} = 0 \tag{21}$$

The suggested equation of natural frequency for FGM rectangular plate can find the natural frequency as Equations 22 and 23.

$$\omega = h \left(\frac{A_0 \left(\frac{\pi}{a} \right)^4 + 2A_0 \left(\frac{\pi}{a} \right)^2 \left(\frac{\pi}{b} \right)^2 + A_0 \left(\frac{\pi}{b} \right)^4}{\rho_p \left(1 - \frac{\beta}{(k+1)} \right)} \right)^{1/2} \tag{22}$$

$$A_0 = \frac{E_p}{12(1 - \nu^2)} - \frac{\beta E_p}{(1 - \nu^2)} \left(\frac{1}{k + 3} - \frac{1}{k + 2} + \frac{1}{4(k + 1)} \right) \quad [23]$$

The dimensionless fundamental frequencies ψ for simply supported FGM square plate can be found as Equation 24.

$$\psi = \frac{\omega L^2}{h} \sqrt{\frac{\int_{-h/2}^{h/2} \rho(z) dz}{\int_{-h/2}^{h/2} E(z) dz}} = \frac{\omega L^2}{h} \sqrt{\frac{\rho_p}{E_p}} \quad [24]$$

Modeling Analysis for FGM Sandwich Plate with FGM Porous Metal Core

FGM sandwich plates are usually represented either in face sheet FGM and uniform core or uniform face sheet with FGM core. In this paper, the second type (sandwich plates with uniform skin and core FGM) is considered and analyzed to study the frequency response of FGM sandwich plates with different boundary conditions. The volume fraction of the FGM sandwich plate is assumed as Equation 25 (Cui et al., 2019).

$$\begin{aligned} V_1(z) &= 0, z \in [h_1, h_2] \\ V_2(z) &= \left(\frac{z - h_2}{h_3 - h_2} \right)^k, z \in [h_2, h_3] \\ V_3(z) &= 1, z \in [h_3, h_4] \end{aligned} \quad [25]$$

For the material characteristics of FGM plate with porosity, they considered to vary continuously within the thickness of the plate according to the power-law distribution (k), (β): is the factor of the distribution of the porosity according to the plate thickness, hence for the even distribution of porosities inside the material, the young's modulus $E(z)$ and mass density $\rho(z)$ of the imperfect FGM plate represented as given in Equations 13 and 14, respectively.

Consider a sandwich plate of length a and width b with its four edges simply supported, comprise mainly from Porous metal core is considered as a functionally graded material owing to the variation of porous ratio inside the core metal while the upper and lower plate, both of them made of same homogenous material as shown in Figure 3, so the elastic constants $E_{UP} = E_{LP}, \nu_{UP} = \nu_{LP} = \nu$ and the mass density $\rho_{UP} = \rho_{LP}$.

To derive the governing differential equation of motion of sandwich panels with an FGM core, Equations 5 and 6 are applied for each layer of the sandwich plate (upper face, core, and lower face), and reassemble them to Equation 11 as it will be discussed in the previous section. Assuming $h_{UP} = h_{LP}$, the general representation for the flexural rigidity and inertia for the sandwich plate (D_{SP} and I_{SP}) can be written as Equations 26-28.

$$D_{SP} = \left(\int_{-\left(\frac{h_{FG}}{2} + h_{LP}\right)}^{-\frac{h_{FG}}{2}} \left\{ \frac{z^2}{(1 - \nu_{LP}^2)} E(z) \right\} dz + \int_{\left(\frac{h_{FG}}{2}\right)}^{\left(\frac{h_{FG}}{2} + h_{UP}\right)} \left\{ \frac{z^2}{(1 - \nu_{UP}^2)} E(z) \right\} dz \right) + \frac{1}{(1 - \nu_{FG}^2)} \left(\int_{-\left(\frac{h_{FG}}{2}\right)}^{\left(\frac{h_{FG}}{2}\right)} \left\{ E_p - \beta E_p \left(\frac{z}{h} + \frac{1}{2} \right)^k \right\} z^2 dz \right) \quad [26]$$

$$D_{SP} = \frac{E_p h^3}{12(1 - \nu^2)} - \frac{\beta E_p h^3}{(1 - \nu^2)} \left(\frac{1}{(k + 3)} - \frac{1}{(k + 2)} + \frac{1}{4(k + 1)} \right) + \frac{E_{UP}}{(1 - \nu_{UP}^2)} \left(\frac{2 \left(\frac{h_{FG}}{2} + h_{UP} \right)^3}{3} - \frac{h_{FG}^3}{12} \right) \quad [27]$$

$$I_{SP} = \rho_p h_{FG} \left\{ 1 - \frac{\beta}{(k + 1)} \right\} + 2\rho h_{UP} \quad [28]$$

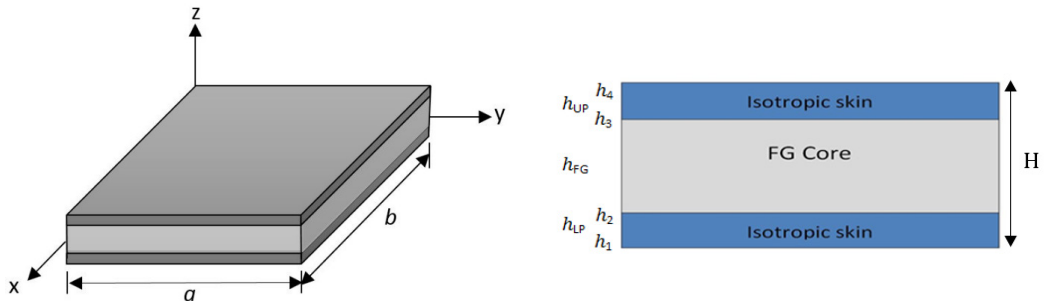


Figure 3. Geometry configurations of FGM porous sandwich plate

To evaluate the natural frequency of the sandwich plate follows the same procedure mentioned in the rectangular plate in Equation 21 to obtain Equation 29.

$$\omega = 2 \left(\frac{\pi}{a} \right)^2 \left(\frac{C(k + 1)}{\rho_p h_{FG} \{k + 1 - \beta\} + 2\rho h_{UP} (k + 1)} \right)^{1/2} \quad [29]$$

To simplify (Equation 30),

$$C = \frac{E_p h_{FG}^3}{12(1 - \nu^2)} - \frac{\beta E_p h_{FG}^3}{(1 - \nu^2)} \left(\frac{1}{(k + 3)} - \frac{1}{(k + 2)} + \frac{1}{4(k + 1)} \right) + \frac{E_{UP}}{(1 - \nu_{UP}^2)} \left(\frac{2 \left(\frac{h_{FG}}{2} + h_{UP} \right)^3}{3} - \frac{h_{FG}^3}{12} \right) \quad [30]$$

Numerical Investigation

The accuracy of the suggested analytical solution can be verified by employ numerical methods. Many numerical techniques are used to solve problems (Sadiq et al. 2020), but the most accurate is the FEA method (Reddy, 1993; Rao, 2004). In this work, the finite element method represented by the ANSYS program (Ver. 2020 R2) was used. A 3D model of the FG sandwich plate is built and the corresponding boundary conditions of the sides of the plate under modal analysis are applied as shown in Figure 4. The precision mesh size is selected and the model has meshed with an 8-node SOLID186 element type with a total number of elements 40000 as shown in Figure 5. The mechanical properties of the FG core are calculated using Equations 11 and 12, while the skin parts are assumed isotropic materials, then inserted into the examined model. In the connection area between the layers and between the layers and the sandwich plat's skin, glue regulations should be made to prevent the development of the pedigree between the layers from respecting each other (Burlayenko & Sadowski, 2020). The modal analysis for the selected models is carried out to identify the free vibration characteristics (natural frequencies and the mode shapes) based on various parameters previously mentioned as shown in Figure 6.

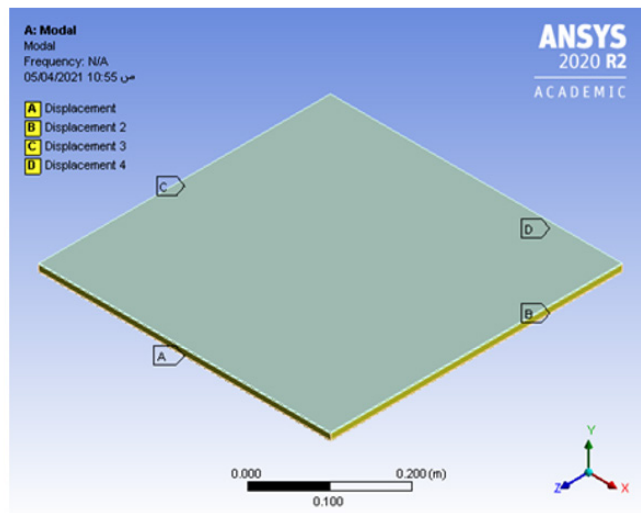


Figure 4. FGM Sandwich plate

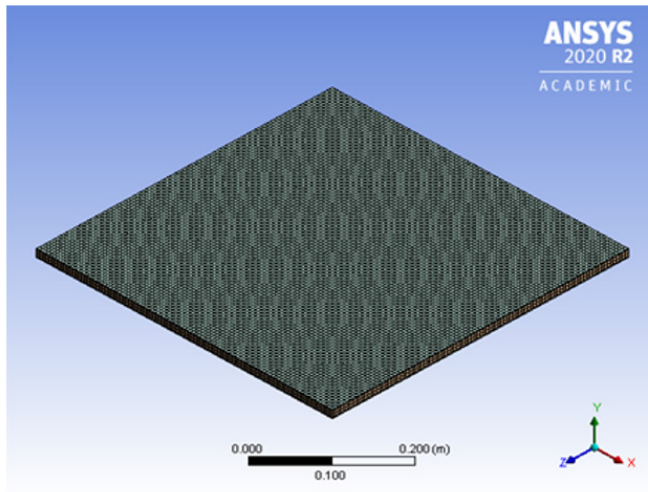


Figure 5. Meshed Model

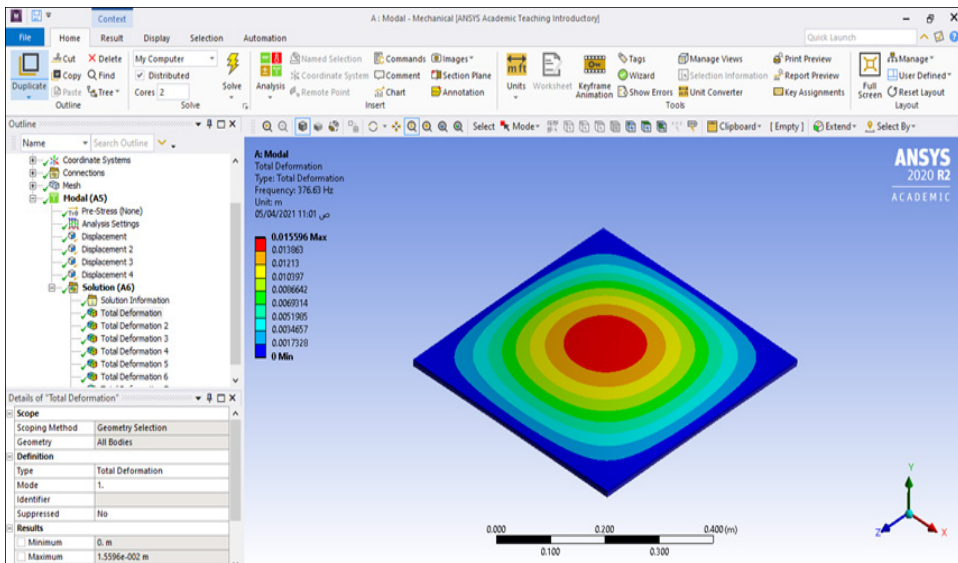


Figure 6. View of Modal Analysis of FGM sandwich plate

RESULTS AND DISCUSSION

In this work, a new mathematical model was derived to evaluate the free vibration characteristics of power-law simply supported FGM rectangular sandwich plates with even porosity distribution. Effects of various properties on frequency parameters are

investigated. The FGM part is composed of a porous metal core with volume fractions that change smoothly through the thickness direction. The natural frequencies are presented for the various metal cores types with a power-law variation. The commercially available software of ANSYS 2020 R2 was also used for verification of the analytical solution, and the obtained results were tabulated and plotted with multiple curves. The material characteristics of the FG core are presented in Table 2, simultaneously, the face sheet is considered made of Aluminum with a mass density of 2702 Kg/m³ and a modulus of elasticity of 70 GPa. The dimensions of plates are taken as $a=b=0.5$ m, the power-law distribution ($k=0,0.5,1,2,5,10,50,100$) and porosity factor ($\beta = 0$ to 0.4), the face sheet thickness is (1, 1.5, 2 and 2.5) mm and FG core heights (5, 6, 8, 10, 12, 20, and 25) mm.

Table 2

Material properties of the FG core

FG core type	Modula's of Elasticity (MPa)	Mass Density Kg/m ³	Poison's Ratio	Ref.
Polyethylene	1100	950	0.42	(Liu et al., 2015)
Peek - 30 % CF	7700	1410	0.44	(Bonnheim et al., 2019)
Peek - 30 % GF	6300	1510	0.34	(Najim & Adwaa, 2014)
Peek -1000 natural	4400	1310	0.40	(Najim & Adwaa, 2014)
Polyurethane foam	7.5	60	0	(Goel et al., 2013)
Foam Dytherm	3.0	100	0	(Goel et al., 2013)

To verify the accuracy of the suggested mathematical model in predicting the natural frequency of FG sandwich plates. Natural frequencies for the sandwich plate with various parameters such as aspect ratio, slenderness ratio, porous factor, FG core thickness, and face sheet thickness are presented in Tables 3-5. Once the natural frequency from Equation 30 has been worked out, the fundamental frequency parameter of a simply supported square FGM sandwich plates with porous FG core with different thickness ratio can be calculated from the following Equation 31.

$$\psi = \frac{\omega L^2}{h} \sqrt{\frac{\rho_0}{E_0}} \quad [31]$$

Where, ω is the natural frequency, L is the length of the plate and h is the total height of the sandwich plate. Suppose that $\rho_0=1$ Kg/m³ and $E_0=1$ MPa. Table 3 present analytical and

numerical results for the first nondimensional frequencies of the sandwich plate for various porosity parameters ($\beta = 0.1, 0.2, 0.3$, and 0.4), power-law indices ($k = 0, 0.5, 1, 2$, and 5), and face sheet thickness ($1, 1.5, 2$ and 2.5 mm) for the FG core metal made of Polyethylene FGM core thickness 10 mm. Data shows that the core topology has a significant role in the frequency parameters as represented in Table 3-5. Fair agreements are found between analytical tests and numerical analyses with a difference of less than 8% . Table 4 gives results obtained by the analytical solution and FEA of the nondimensional frequency of rectangular sandwich plate with FG Polyethylene core, (FG core thickness 12 mm) with various porosity factors ($\beta = 0.1, 0.2, 0.3$, and 0.4), volume fraction index ($k = 0, 0.5, 1, 2$, and 5) and by using five values of aspect ratio ($a/b = 0.25, 0.5, 0.75, 1$ and 2).

It can also be seen that the natural frequencies decrease with increasing gradient index and increase the porous parameter due to the decrease in the material rigidity. An excellent agreement can be observed with a difference of up to 8% , and this percentage is affected by the power-law index and porous factor for the same FG plate thickness. Convergence of the non-dimensional frequencies of square FGM sandwich plate with Polyethylene porous core and aluminum face sheet (2 mm), subject to seven combinations of boundary conditions is presented in Table 5 with respect to thickness ratio ($a/H = 50$) and various porosity factors. It is found that the value of frequency parameter increases with an increase in the number of constraints of the selected model; for example, at porous factor ($\beta = 0.3$) and with a gradient index ($k = 2$), the frequency parameter in the CCCC model is (6.523) while for CCCS it was (6.027), and CSCS equal (5.825), as for SSSS, the value was (5.436), for CCCF edge condition the frequency parameter became (3.894), while for FCFC and FSFS, the frequency parameter was (3.626) and (2.827) respectively.

Table 3

The frequency parameter (ψ) of the sandwich plate with Polyethylene FGM core thickness 10 mm

porosity %	power-law index (k)	face sheet thickness (mm)							
		1		1.5		2		2.5	
		Ana.	Num.	Ana.	Num.	Ana.	Num.	Ana.	Num.
10	0	4.645	4.638	5.158	5.139	5.415	5.531	5.531	5.531
	0.5	4.595	4.601	5.111	5.109	5.372	5.371	5.493	5.502
	1	4.571	4.569	5.088	5.067	5.351	5.361	5.474	5.484
	2	4.546	4.550	5.065	5.060	5.330	5.355	5.455	5.466
	5	4.523	4.534	5.042	5.039	5.309	5.313	5.436	5.442

Table 3 (Continued)

porosity %	power-law index (k)	face sheet thickness (mm)							
		1		1.5		2		2.5	
		Ana.	Num.	Ana.	Num.	Ana.	Num.	Ana.	Num.
20	0	4.806	4.810	5.308	5.340	5.550	5.489	5.652	5.691
	0.5	4.697	4.690	5.207	5.225	5.459	5.431	5.571	5.588
	1	4.645	4.651	5.158	5.188	5.415	5.386	5.531	5.506
	2	4.594	4.589	5.110	5.092	5.371	5.297	5.492	5.477
	5	4.546	4.553	5.064	5.078	5.329	5.245	5.454	5.382
30	0	4.986	4.978	5.472	5.511	5.696	5.680	5.782	5.219
	0.5	4.807	4.911	5.308	5.479	5.550	5.622	5.652	5.145
	1	4.724	4.696	5.231	5.099	5.481	5.579	5.5917	4.988
	2	4.644	4.674	5.157	4.888	5.414	5.515	5.531	4.866
	5	4.569	4.552	5.086	4.857	5.350	5.464	5.473	4.770
40	0	5.189	5.226	5.653	5.714	5.855	5.776	5.921	5.887
	0.5	4.925	5.0996	5.416	5.686	5.646	5.681	5.738	5.686
	1	4.806	4.947	5.308	5.562	5.550	5.590	5.652	5.450
	2	4.696	4.775	5.205	5.441	5.458	5.422	5.570	5.499
	5	4.593	4.694	5.109	5.215	5.370	5.299	5.492	5.456

Table 4

Analytical and Numerical results of the frequency parameter of the rectangular FG sandwich plate with Polyethylene core thickness 12 mm

a/b	power-law index (k)	porosity factor (β)							
		0.1		0.2		0.3		0.4	
		Ana.	Num.	Ana.	Num.	Ana.	Num.	Ana.	Num.
0.25	0	3.2	3.3	3.3	3.3	3.4	3.4	3.5	3.5
	0.5	3.2	3.2	3.2	3.3	3.3	3.4	3.4	3.5
	1	3.2	3.2	3.2	3.3	3.3	3.3	3.3	3.4
	2	3.2	3.2	3.2	3.2	3.2	3.3	3.2	3.3
	5	3.1	3.1	3.2	3.2	3.2	3.2	3.2	3.3

Table 4 (Continued)

<i>a/b</i>	power-law index (<i>k</i>)	porosity factor (β)							
		0.1		0.2		0.3		0.4	
		Ana.	Num.	Ana.	Num.	Ana.	Num.	Ana.	Num.
0.5	0	3.8	3.8	3.9	3.8	4.0	4.1	4.1	4.1
	0.5	3.8	3.7	3.8	3.8	3.9	4.0	4.0	4.1
	1	3.7	3.7	3.8	3.8	3.8	3.9	3.9	3.9
	2	3.7	3.7	3.8	3.8	3.8	3.8	3.8	3.9
	5	3.7	3.7	3.7	3.7	3.7	3.7	3.8	3.9
0.75	0	4.7	4.8	4.9	4.9	5.0	5.3	5.2	5.1
	0.5	4.7	4.7	4.8	4.8	4.9	5.1	5.0	4.8
	1	4.7	4.7	4.7	4.8	4.8	4.9	4.9	4.8
	2	4.6	4.7	4.7	4.8	4.7	4.8	4.8	4.7
	5	4.6	4.6	4.6	4.7	4.7	4.7	4.7	4.7
1	0	6.1	6.1	6.2	6.3	6.4	6.6	6.6	6.6
	0.5	6.0	6.1	6.1	6.3	6.2	6.5	6.3	6.4
	1	6.0	5.9	6.1	6.2	6.1	6.4	6.2	6.3
	2	6.0	5.9	6.0	6.1	6.1	6.1	6.1	6.2
	5	5.9	5.8	5.9	5.9	6.0	6.1	6.0	6.0
1.5	0	9.8	9.9	10.1	10.0	10.4	10.5	10.7	10.7
	0.5	9.8	9.8	9.9	10.0	10.1	10.2	10.3	10.5
	1	9.7	9.8	9.8	9.9	10.0	10.0	10.1	10.1
	2	9.7	9.5	9.8	9.8	9.8	9.9	9.9	10.0
	5	9.6	9.5	9.7	9.7	9.7	9.8	9.8	9.8
2	0	15.1	15.1	15.6	15.4	16.0	15.9	16.5	16.6
	0.5	15.0	15.1	15.3	15.2	15.6	15.6	15.9	16.2
	1	14.9	15.1	15.1	15.1	15.3	15.5	15.6	15.9
	2	14.9	15.0	15.0	15.0	15.1	15.1	15.3	15.7
	5	14.8	15.0	14.9	14.9	14.9	15.0	15.0	15.3

Table 5

Convergence of frequency parameters of square FG sandwich plate with Polyethylene core thickness 10mm, face sheet thickness 2.5mm, for different Boundary conditions

BC's	power-law index (k)	porosity factor (β)			
		0.1	0.2	0.3	0.4
CCCC	0	6.959	7.017	7.141	7.511
	0.5	7.229	7.124	7.185	7.420
	1	7.094	6.796	7.262	7.129
	2	6.799	7.390	6.523	7.287
	5	6.826	6.584	6.878	7.227
	10	7.081	6.882	7.163	6.909
CSCS	0	6.247	6.322	6.404	6.760
	0.5	6.483	6.395	6.592	6.667
	1	6.373	6.092	6.261	6.422
	2	6.125	6.646	5.825	6.536
	5	6.133	6.040	6.007	6.488
	10	6.359	6.189	6.367	5.906
CCCS	0	6.013	6.204	6.358	6.487
	0.5	5.988	6.066	6.172	6.270
	1	5.960	6.030	6.083	6.168
	2	6.049	5.998	6.027	6.049
	5	5.813	5.969	5.971	5.992
	10	6.016	5.942	5.931	5.927
SSSS	0	5.437	5.569	5.713	5.868
	0.5	5.395	5.480	5.570	5.664
	1	5.374	5.437	5.502	5.569
	2	5.353	5.394	5.436	5.479
	5	5.333	5.353	5.373	5.393
	10	5.324	5.3351	5.345	5.356
	2	4.020	4.357	3.894	4.043
	5	3.841	3.945	3.818	4.151
	10	4.015	3.804	3.990	4.211

Table 5 (Continued)

BC's	power-law index (k)	porosity factor (β)			
		0.1	0.2	0.3	0.4
FCFC	0	3.697	3.899	3.970	4.166
	0.5	3.749	3.644	3.954	3.965
	1	3.601	3.860	4.126	3.731
	2	3.688	4.046	3.626	3.726
	5	3.600	3.629	3.654	3.829
	10	3.700	3.468	3.704	3.910
FSFS	0	2.610	2.840	2.628	2.875
	0.5	2.428	3.014	2.618	2.747
	1	2.526	2.664	2.696	2.729
	2	2.248	2.320	2.827	2.520
	5	2.640	2.730	2.740	2.535
	10	3.993	2.507	2.496	2.517
CCCF	0	3.974	4.195	4.240	4.441
	0.5	4.124	3.972	4.310	4.270
	1	3.835	4.115	4.448	3.952
	2	4.020	4.357	3.894	4.043
	5	3.841	3.945	3.818	4.151
	10	4.015	3.804	3.990	4.211

Graphical representations of the natural frequency relationships for simply supported FG sandwich plates given by Eqs. (29 and 30) are shown in Figures 7-16. Figure 7 shows the analytical results of the fundamental natural frequency of the sandwich plate of Polyethylene core porous meal at the porosity percentage ($\beta=10\%$), for various face sheet thicknesses (1, 1.5, 2, and 2.5mm) and the gradient index ($k=0$ to 100). It can be easily noticed that the natural frequency gradually decreases as the power-law exponent increases and increases as the slenderness ratio increases. Figure 8 shows the fundamental natural frequency at five slenderness ratios ($a/H = 5, 10, 20, 25, 50$ and 100) for porous metal comprise from Polyathelen at porosity factor ($\beta=0.1$). From the results drawn in, it is concluded that when the frequencies are low (lower modes of frequency or thin plates) the suggested analytical solution by CPT is close to the numerical solutions, and when the plate thickness increases and for higher mode frequencies, the error percentage in CPT will be higher. Considering the influence of porous metal type, Figure 9 gives details of the analytical results of the natural frequency at porosity ratio ($\beta = 10\%$), for various

porous metals (PEEK 30% CF, PEEK 30% GF, Foam dythem, and Polyurethane foam) at core height 10 mm and face thickness 2.5 mm. It is concluded that the Polyurethane foam has higher stiffness than foam Dythem and all Peek types, respectively, due to the high mechanical properties values. Figure 10 shows the analytical results of the natural frequency at porosity ratio ($\beta = 10\%$), for various face sheet thicknesses (1,1.5,2, and 2.5 mm) with FGM core height 5 mm. Figure 11 plots variation of dimensionless frequencies of FGM rectangular plate at power-law index ($k = 0.5$), and porosity ratio ($\beta = 10\%$) with different aspect ratios ($a/b = 0.25, 0.5, 0.75, 1$ and 2). Figure 12 shows the analytical results of the natural frequency at porosity ratio ($\beta = 10\%$), for various face sheet thicknesses and by using various core metals. Figure 13 shows the impact of number of the layers on the natural frequency of FGM rectangular plate at power-law index ($k = 0.5$) and porosity ratio ($\beta = 10\%$) for different aspect ratio ($a/b = 0.25, 0.5, 0.75, 1$ and 2). It may also be viewed that frequency parameters are increasing with an increase in aspect ratios. The reason may be the rectangular sandwich plate is becoming stiffer gradually with an increase in aspect ratios. Figure 14 presents influences of the number of the layers on the natural frequency at different thickness ratios ($a/H = 20, 25, 50$ and 100) of the square FGM sandwich plate at gradient index ($k = 2$) and porosity ratio ($\beta = 10\%$). From Figure 14, it is found that the natural frequency of plates increases with increasing the aspect ratios, and the effect of the number of layers must lower on frequency curve behavior. Figures 15 and 16 represent a 3D surface plot for variation of dimensionless natural frequencies of simply supported FG sandwich plate at different porous parameters, and various values of face sheet thickness, respectively. Accordingly, in Figure 17, the first six deflections of 3-D mode shapes are generated for simply supported FGM square sandwich plate at porosity ratio ($\beta = 0.0\%$), gradient index ($k = 0.5$), and slenderness ratio ($a/h = 50$). In a similar fashion, it is also possible to display further 3D mode shapes supported by different edge conditions.

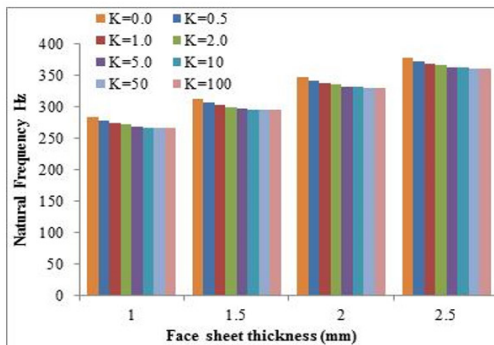


Figure 7. Results of the fundamental natural frequency at Beta =0.2, core height 12mm for various gradient index values.

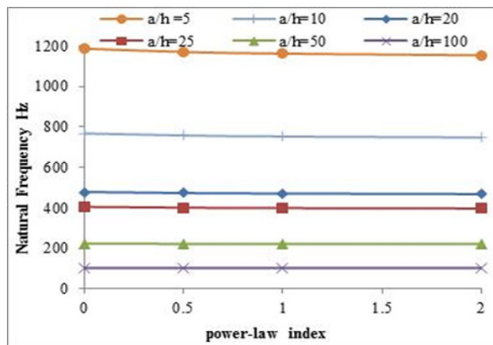


Figure 8. Results of the frequency at Beta =0.1, for various slenderness ratios (a/h)

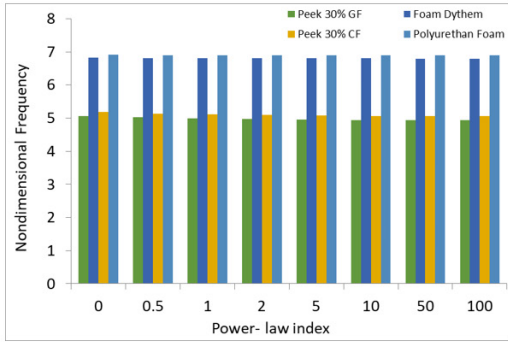


Figure 9. Results of the natural frequency at Beta =0.1, for various porous metals at FG core height 10 mm, and face thickness 2.5 mm

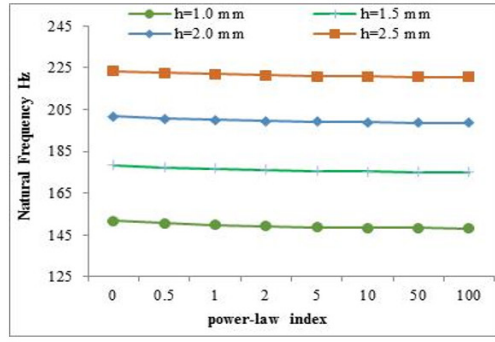


Figure 10. Results of the natural frequency at Beta =0.1, for various face sheet thicknesses with FGM core height 5 mm

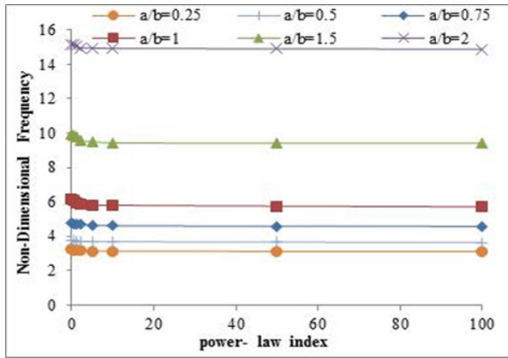


Figure 11. Frequency parameter of a rectangular plate with a different aspect ratio (a/b) at Beta = 0.1, FG core 12 mm, and skin thickness 2 mm

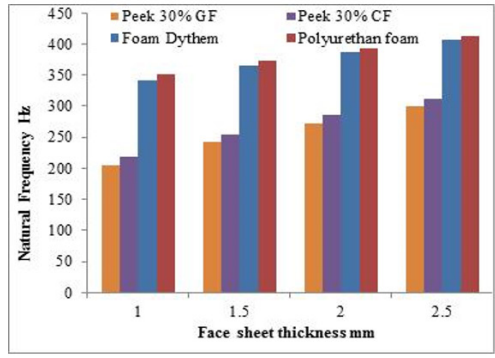


Figure 12. Results of the natural frequency at Beta=0.1, for various face sheet thicknesses

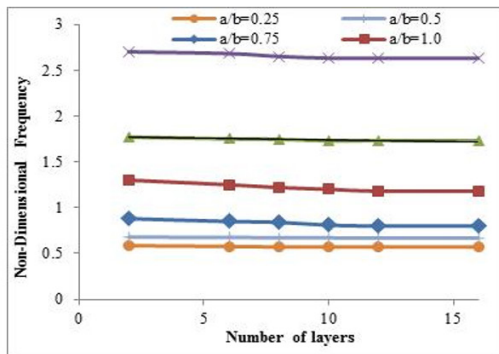


Figure 13. The natural frequency for different number of layers of FGM rectangular plate gradient index k = 2 and Beta=0.1

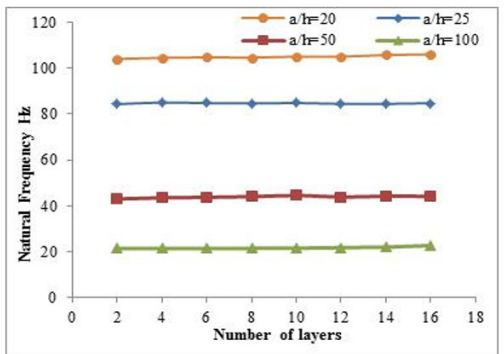


Figure 14. The natural frequency for different number of layers of FGM square plate with gradient index k = 2 and Beta=0.1

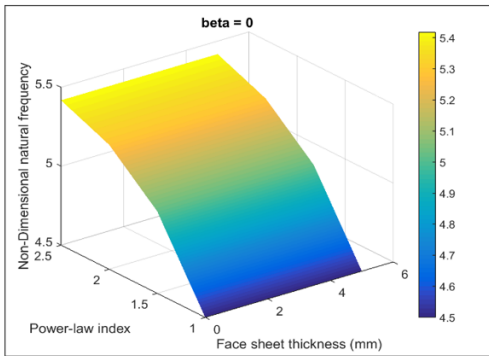


Figure 15. 3D Surface of the frequency parameter of the square sandwich plate at Beta= 0

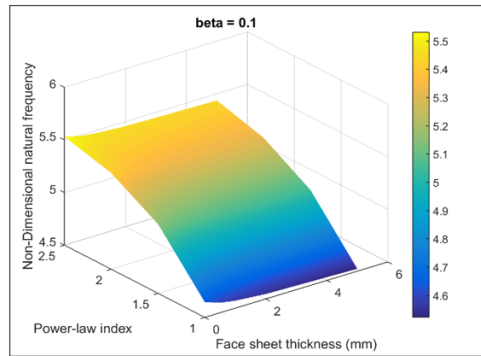


Figure 16. 3D Surface of the frequency parameter of the square sandwich plate at Beta= 0.1

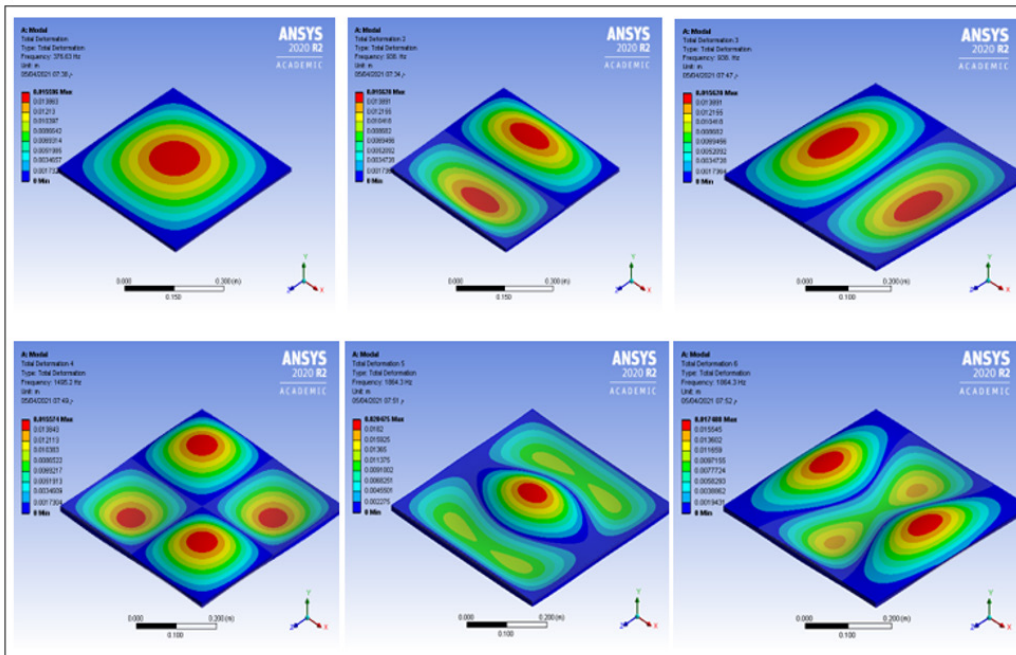


Figure 17. The first six mode shapes of simply supported FGM square sandwich plate at Beta=0.0, k=0.5

CONCLUSION

In this paper, free vibration of functionally graded porous sandwich plate if the material properties vary depending on the thickness with a power distribution are examined. A simple and new accurate mathematical model using CPT principles was presented. The sandwich plate comprises one phase porous metal (Polyethylene, Peek, & Foam) core gluing with

homogeneous skins onto two sides using suitable adhesion. The analytical formulation for free vibration analysis of simply supported plates is provided to predict the free vibration characteristics. A numerical investigation is carried out using ANSYS 2020 R2 to confirm the results of analytical modeling. Results for specific aspect ratio values, FG core material and thickness, face sheet thickness, porous factor, and type of boundary conditions are presented. The paper also explores the impact of various parameters on the free vibration characteristics of the functionally graded sandwich plates such as porous factor, gradient index, as well as aspect ratio. From the above, it can be noticed that:

- It can be observed that the natural frequencies increase with the increased porous factor and decrease with an increase in the volume fraction index k because of a reduction in the volumetric percentage of the core material.
- Lower porosity parameter (Beta) indicates higher structural stiffness, consequently, higher dimensionless natural frequency.
- It can be distinctly shown from the figures and tables, that both of the aspect ratios (a/b) and slenderness ratios (a/h), as well as different material distributions, play vital roles to check the free vibration characteristics of FG sandwich structure.
- The assessment of the impact of porous metal type and porosity distribution characteristics on the performance of the FGM structure confirmed that the Polyathelen foam is the correct choice than other types used in this study.
- Though simplifications are considered in the analytical model, the obtained results show good agreement with FE simulations; the error percentage did not exceed 6%. This percentage increase as the thickness ratio increases in both thickness ratio and gradient index; for example, the error will be diminished with increasing of the thickness ratio ($a/H=100$) at $k=100$.
- The plate frequency parameter increases with the constraint to the boundary conditions; for example, the frequency parameter for CCCC is higher than CCCS. This condition is more than CSCS, and so on, as shown in Table 5. Also from Table 5, it can be concluded that frequencies are increasing with an increase in porosity ratio regardless of the edge conditions and FG parameters considered.
- For the FG core consists of multilayers, it is found that the distribution of natural frequency across the thickness indicates a smooth variation of the same compared to those obtained in the case of the conventional laminated plates.

ACKNOWLEDGEMENT

The authors would like to thank the University of Technology and the University of Kufa, Iraq, to support and fund this study.

REFERENCES

- Al-Waily, M., Al-Shammari, M. A., & Jweeg, M. J. (2020). An analytical investigation of thermal buckling behavior of composite plates reinforced by carbon nano-particles. *Engineering Journal*, 24(3), 11-21. <https://doi.org/10.4186/ej.2020.24.3.11>
- Ambartsumyan, S. A., Ashton, J. E. (Ed), & Cheron, T. (Trans). (1970). *Theory of Anisotropic Plates: Strength, Stability, and Vibration* (Progress in Materials Science Series, Vol. 2). Technomic Publishing Company
- Anderson, T. (2003). A 3-D elasticity solution for a sandwich composite with functionally graded core subjected to transverse loading by a rigid sphere. *Composite Structures*, 60(3), 265-274. [https://doi.org/10.1016/S0263-8223\(03\)00013-8](https://doi.org/10.1016/S0263-8223(03)00013-8)
- Baferani, A. H., Saidi, A. R., & Ehteshami, H. (2011). Accurate solution for free vibration analysis of functionally graded thick rectangular plates resting on elastic foundation. *Composite Structures*, 93(7), 1842-1853. <https://doi.org/10.1016/j.compstruct.2011.01.020>
- Bonnheim, N., Ansari, F., Regis, M., Bracco, P., & Pruitt, L. (2019). Effect of carbon fiber type on monotonic and fatigue properties of orthopedic grade PEEK. *Journal of the mechanical behavior of biomedical materials*, 90, 484-492. <https://doi.org/10.1016/j.jmbbm.2018.10.033>
- Burlayenko, V. N., & Sadowski, T. (2020). Free vibrations and static analysis of functionally graded sandwich plates with three-dimensional finite elements. *Meccanica*, 55(4), 815-832. <https://doi.org/10.1007/s11012-019-01001-7>
- Chakraverty, S., & Pradhan, K. K. (2014). Free vibration of exponential functionally graded rectangular plates in thermal environment with general boundary conditions. *Aerospace Science and Technology*, 36, 132-156. <https://doi.org/10.1016/j.ast.2014.04.005>
- Chi, S., & Chung, Y. (2006). Mechanical behavior of functionally graded material plates under transverse load-Part I: Analysis. *International Journal of Solids and Structures*, 43(13), 3657-3674. <https://doi.org/10.1016/j.ijsolstr.2005.04.011>
- Coskun, S., Kim, J., & Toutanji, H. (2019). Bending, free vibration, and buckling analysis of functionally graded porous micro-plates using a general third-order plate theory. *Journal of Composites Science*, 3(1), Article 15. <https://doi.org/10.3390/jcs3010015>
- Cui, J., Zhou, T., Ye, R., Gaidai, O., Li, Z., & Tao, S. (2019). Three-dimensional vibration analysis of a functionally graded sandwich rectangular plate resting on an elastic foundation using a semi-analytical method. *Materials*, 12(20), Article 3401. <https://doi.org/10.3390/ma12203401>
- Dang, Y. H., Li, Y. H., Chen, D., & Yang, J. (2018). Vibration characteristics of functionally graded graphene reinforced porous nanocomposite cylindrical shells with spinning motion. *Composites Part B: Engineering*, 145, 1-13. <https://doi.org/10.1016/j.compositesb.2018.03.009>
- Goel, M. D., Matsagar, V. A., Marburg, S., & Gupta, A. K. (2013). Comparative performance of stiffened sandwich foam panels under impulsive loading. *Journal of performance of constructed facilities*, 27(5), 540-549. [https://doi.org/10.1061/\(ASCE\)CF.1943-5509.0000340](https://doi.org/10.1061/(ASCE)CF.1943-5509.0000340)
- Hadji, L., Atmane, H. A., Tounsi, A., Mechab, I., & Bedia, E. A. (2011). Free vibration of functionally graded sandwich plates using four-variable refined plate theory. *Applied Mathematics and Mechanics*, 32, 925-942. <https://doi.org/10.1007/s10483-011-1470-9>

- Hayat, S., & Meriem, S. (2019). Vibration analysis of functionally graded plates with porosity composed of a mixture of Aluminium (Al) and Alumina (Al_2O_3) embedded in an elastic medium. *Frattura ed Integrità Strutturale*, 13(50), 286-299. <https://doi.org/10.3221/IGF-ESIS.50.24>
- Kapuria, S., Bhattacharyya, M., & Kumar, A. N. (2008). Bending and free vibration response of layered functionally graded beams: A theoretical model and its experimental validation. *Composite Structures*, 82(3), 390-402. <https://doi.org/10.1016/j.compstruct.2007.01.019>
- Kiani, Y., & Eslami, M. R. (2012). Thermal buckling and post-buckling response of imperfect temperature-dependent sandwich FGM plates resting on elastic foundation. *Archive of Applied Mechanics*, 82, 891-905. <https://doi.org/10.1007/s00419-011-0599-8>
- Kiani, Y., Bagherizadeh, E., & Eslami, M. R. (2011). Thermal and mechanical buckling of sandwich plates with FGM face sheets resting on the Pasternak elastic foundation. *Proceedings of the Institution of Mechanical Engineers, Part C: Journal of Mechanical Engineering Science*, 226(1), 32-41. <https://doi.org/10.1177/0954406211413657>
- Kim, J., Žur, K. K., & Reddy, J. N. (2019). Bending, free vibration and buckling of modified couples stress-based functionally graded porous micro-plates. *Composite Structures*, 209, 879-888. <https://doi.org/10.1016/j.compstruct.2018.11.023>
- Kumar, V., Singh, S. J., Saran, V. H., & Harsha, S. P. (2021). Vibration characteristics of porous FGM plate with variable thickness resting on Pasternak's foundation. *European Journal of Mechanics-A/Solids*, 85, Article 104124. <https://doi.org/10.1016/j.euromechsol.2020.104124>
- Lashkari, M. J., & Rahmani, O. (2016). Bending behavior of sandwich structures with flexible functionally graded core based on high-order sandwich panel theory. *Meccanica*, 51(5), 1093-1112. <https://doi.org/10.1007/s11012-015-0263-4>
- Latifi, M., Farhatnia, F., & Kadkhodaei, M. (2013). Buckling analysis of rectangular functionally graded plates under various edge conditions using Fourier series expansion. *European Journal of Mechanics - A/Solids*, 41, 16-27. <https://doi.org/10.1016/j.euromechsol.2013.01.008>
- Leissa, A. W. (1969). *Vibration of plates* (Vol. 160). Scientific and Technical Information Division, National Aeronautics and Space Administration.
- Liu, Y., Hu, Y., Liu, T., Ding, J. L., & Zhong, W. H. (2015). Mechanical behavior of high density polyethylene and its carbon nanocomposites under quasi-static and dynamic compressive and tensile loadings. *Polymer Testing*, 41, 106-116. <https://doi.org/10.1016/j.polymertesting.2014.11.003>
- Meiche, N. E., Tounsi, A., Ziane, N., Mechab, I., & Bedia, E. A. (2011). A new hyperbolic shear deformation theory for buckling and vibration of functionally graded sandwich plate. *International Journal of Mechanical Sciences*, 53(10), 237-247. <https://doi.org/10.1016/j.ijmecsci.2011.01.004>
- Merdaci, S. (2019). Free vibration analysis of composite material plates case of a typical functionally graded FG plates ceramic/metal with porosities. *Nano Hybrids and Composites*, 25, 69-83. <https://doi.org/10.4028/www.scientific.net/NHC.25.69>
- Meziane, M. A. A., Abdelaziz, H. H., & Tounsi, A. (2014). An efficient and simple refined theory for buckling and free vibration of exponentially graded sandwich plates under various boundary conditions. *Journal of Sandwich Structures and Materials*, 16(3), 293-318. <https://doi.org/10.1177/1099636214526852>

- Muc, A., & Flis, J. (2021). Flutter characteristics and free vibrations of rectangular functionally graded porous plates. *Composite Structures*, 261, 113301. <https://doi.org/10.1016/j.compstruct.2020.113301>
- Najim, A. S., & Adwaa, M. (2014). Studying mechanical properties specially fatigue behavior of (polyether ether ketone)/glass fiber composites in aerospace applications. In *Applied Mechanics and Materials* (Vol. 666, pp. 8-16). Trans Tech Publications Ltd. <https://doi.org/10.4028/www.scientific.net/AMM.666.8>
- Natarajan, S., & Manickam, G. (2012). Bending and vibration of functionally graded material sandwich plates using an accurate theory. *Finite Elements in Analysis and Design*, 57, 32-42. <https://doi.org/10.1016/j.finel.2012.03.006>
- Neves, A. M. A., Ferreira, A. J. M., Carrera, E., Cinefra, M., Roque, C.M.C., Jorge, R. M. N., & Soares, C. M. M. (2013). Static, free vibration and buckling analysis of isotropic and sandwich functionally graded plates using a quasi-3D higher-order shear deformation theory and a meshless technique. *Composites Part B: Engineering*, 44(1), 657-674. <https://doi.org/10.1016/j.compositesb.2012.01.089>
- Nguyen, N. V., Nguyen, H. X., Lee, S., & Xuan, H. N. (2018). Geometrically nonlinear polygonal finite element analysis of functionally graded porous plates. *Advances in Engineering Software*, 126, 110-126. <https://doi.org/10.1016/j.advengsoft.2018.11.005>
- Rao, S. S. (2004). *The finite element method in engineering*. Elsevier.
- Reddy, J. N. (1993). *An introduction to the finite element method*. McGraw-Hill, Inc.
- Rezaei, A. S., & Said, A. R. (2015). Exact solution for free vibration of thick rectangular plates made of porous materials. *Composite Structures*, 134, 1051-1060. <https://doi.org/10.1016/j.compstruct.2015.08.125>
- Sadiq, S. E., Jweeg, M. J., & Bakhy, S. H. (2020). The effects of honeycomb parameters on transient response of an aircraft sandwich panel structure. In *IOP Conference Series: Materials Science and Engineering* (Vol. 928, No. 2, p. 022126). IOP Publishing.
- Singh, S. A., & Harsha, S. P. (2020). Thermo-mechanical analysis of porous sandwich S-FGM plate for different boundary conditions using Galerkin Vlasov's method: A semi-analytical approach. *Thin-Walled Structures*, 150, Article 106668. <https://doi.org/10.1016/j.tws.2020.106668>
- Thai, H. T., Nguyen, T. K., Vo, T. P., & Lee, J. (2013). Analysis of functionally graded sandwich plates using a new first-order shear deformation theory. *European Journal of Mechanics-A/Solids*, 45, 211-225. <https://doi.org/10.1016/j.euromechsol.2013.12.008>
- Tossapanon, P., & Wattanasakulpong, N. (2020). Flexural vibration analysis of functionally graded sandwich plates resting on elastic foundation with arbitrary boundary conditions: Chebyshev collocation technique. *Journal of Sandwich Structures and Materials*, 22(2), 156-189. <https://doi.org/10.1177/1099636217736003>
- Wadec, M. A. (2001). Shear Deformable Beams and Plates: Relationships with Classical Solutions—CM Wang, JN Reddy and KH Lee, Elsevier, 2000, pp. 312,@ \$69.30, ISBN 0080437842. *Engineering Structures*, 7(23), 873-874.
- Wang, Y. Q., & Zu, J. W. (2017). Vibration behaviors of functionally graded rectangular plates with porosities and moving in thermal environment. *Aerospace Science and Technology*, (69), 550-562. <https://doi.org/10.1016/j.ast.2017.07.023>

- Wattanasakulpong, N., & Chaikittiratana, A. (2015). Flexural vibration of imperfect functionally graded beams based on Timoshenko beam theory: Chebyshev collocation method. *Meccanica*, 50(5), 1331-1342. <https://doi.org/10.1007/s11012-014-0094-8>
- Wattanasakulponga, N., & Ungbhakorn, V. (2014). Linear and nonlinear vibration analysis of elastically restrained ends FGM beams with porosities. *Aerospace Science and Technology*, 32(1), 111-120. <https://doi.org/10.1016/j.ast.2013.12.002>
- Zhang, X. Y., Fang, G., Leeflang, S., Zadpoor, A. A., & Zhou, J. (2019). Topological design, permeability and mechanical behavior of additively manufactured functionally graded porous metallic biomaterials. *Acta Biomaterialia*, 84, 437-452. <https://doi.org/10.1016/j.actbio.2018.12.013>
- Zhang, Y., & Wang, J. (2017). Fabrication of functionally graded porous polymer structures using thermal bonding lamination techniques. *Procedia Manufacturing*, 10, 866-875. <https://doi.org/10.1016/j.promfg.2017.07.073>
- Zhao, J., Wang, Q., Deng, X., Choe, K., Zhong, R., & Shuai, C. (2019). Free vibrations of functionally graded porous rectangular plate with uniform elastic boundary conditions. *Composites Part B: Engineering*, 168, 106-120. <https://doi.org/10.1016/j.compositesb.2018.12.044>

Design of Soymilk Product Development from Grobogan Soybean Variety in Indonesia

Andita Sayekti^{1*}, Atris Suyantohadi², Mirwan Ushada² and David Yudianto³

¹Department of Management, Faculty of Economics and Management, Bogor Agricultural University (IPB University), Bogor 16680, Indonesia

²Department of Agroindustrial Technology, Faculty of Agricultural Technology, Universitas Gadjah Mada, Yogyakarta 55281, Indonesia

³Quality Assurance of Food Industry, Politeknik AKA Bogor, Bogor 16154, Indonesia

ABSTRACT

Soybean (*Glycine max* (L.) Merrill) is protein which is cholesterol free. The objective of this study is to develop the downstream product of soybean as soymilk by attribute values. Factors of consumer needs in determining the priority level of the important attributes often have characteristics of uncertainty element and cannot be explicitly determined. The number of samples that used and representing the consumer needs is 100 respondents Special Region of Yogyakarta. This product development uses Value Engineering, while Fuzzy Logic methods uses at the information and determination stage. The results show soymilk

powder attributes that are prioritized by consumers include colour, aroma, taste, price, packaging, nutrient content, and thickness. Based on the creativity stage, there are product concept with flavors original, ginger, chocolate, strawberry, and pandanus for soymilk powder development. The best concept is original flavor with the highest score of 4.68 with a performance value of 9,366.60.

ARTICLE INFO

Article history:

Received: 24 February 2021

Accepted: 23 April 2021

Published: 31 July 2021

DOI: <https://doi.org/10.47836/pjst.29.3.46>

E-mail addresses:

anditasayekti@apps.ipb.ac.id (Andita Sayekti)

atris@ugm.ac.id (Atris Suyantohadi)

mirwan_ushada@ugm.ac.id (Mirwan Ushada)

davidyudianto.se@gmail.com (David Yudianto)

*Corresponding author

Keywords: Grobogan soybean, product development, soymilk, value engineering

INTRODUCTION

As a source of vegetable protein, soybean plays an important role to improve human nutrition (Sui et al., 2018). Soybean demand increase together with food industry development for consumer needs all over the world (Yao et al., 2020). Soybean based products such as tofu, tempeh, and soy sauce require large amounts of soybeans (Yasin et al., 2019). In 2014 and 2015, the average production of local soybean in Indonesia was 819,442 tons per year with the consumption of 2.2 million tons soybean per year (Ningrum et al., 2018). However, it still needs the soybean import by approximately 65% from the total consumption due to the availability of local soybean which only provides approximately 35% from the total consumption. Total national soybean demand tend to increase in average 3.30% annually together with the approximately 1-2% population growth (Zikri et al., 2020). It means that the growth of population will be followed by the enhancement of soybean demand. The soybean production tend to enhance started from 2016 to 2020 by 11.18% per year (Ningrum et al., 2018). The projection of soybean production in Indonesia during 2021 and 2022 are 502,934 and 425,246 tons, respectively (Zikri et al., 2020). As the downstream product of soybean, soymilk has been consumed widely in Asian countries, even accepted in Western countries due to its nutrients and health benefits (Li et al., 2021). Although soymilk has high-quality proteins (Chen et al., 2017) and many essential amino acids (Toro-Funes et al., 2014), the quality of soymilk is quite different than dairy milk. Nevertheless, it still contains essential fatty acids, and has no cholesterol, gluten and lactose that is very appropriate for lactose intolerance consumer because does not cause allergies (Toro-Funes et al., 2015). The other benefits of soymilk are anti-oxidation, prevention of anemia, osteoporosis and cancer because it contains lecithin, isoflavone, vitamin and other nutrients (da Silva Fernandes et al., 2017).

However, the unpleasant tastes of soymilk i.e., bitter, beany and rancid tastes are less preferred by some consumers (Ma et al., 2015). The unpleasant taste can be eliminated by appropriate processing technology and selection of superior soybean variety, such as Grobogan variety (Mustikawati et al., 2018). Grobogan variety was introduced in 2008 by purifying the population of local Malabar Grobogan (Ministry of Agriculture, 2008). Grobogan variety is a national superior soybean with a productivity of 3.4 tons/hectares and the average production yield reaches 2.77 tons/hectares (Mustikawati et al., 2018). Kuntastyuti and Lestari (2017) added that the productivity of that Grobogan variety could be enhanced from 1.65 t/ha to 1.84 t/ha by using 2.5 t manure/ha. The age of plants is approximately 76 days with the seed weight is approximately 18 g/100 seeds (Mustikawati et al., 2018). This weight is followed by Argomulyo and Anjasmoro which are 15.49 g/100 seeds and 14.65 g/100 seeds, respectively. Thus, the other variety with medium and small size level of soybean are 10-14 g/100 seeds and <10 g/100 seeds, respectively (Krisnawati & Adie, 2015). This gives an advantage for Grobogan variety compared to other common

soybeans variety because it has a higher net weight than ordinary soybean seeds. This means that the size of Grobogan soybean variety seeds is larger than other ordinary soybeans seeds. The adaptability of soybean plant capable to grow by quite large in a number of different environmental conditions (Viana et al., 2013). In term of fisiological growth characteristic, Grobogan variety also has capability to adapt even under 50% and 70% of shading (Bestari et al., 2018). This makes it easier to grow soybean crops in the field, especially at the beginning of the rainy season with the limited facilities. Soymilk from local soybean variety, Grobogan, is the most potential downstream product by taste improvement. However, the liquid soymilk product only has approximately 24 hours of shelf life if it is not stored in the refrigerator. This could be a problem during distribution. People also tend to choose the simple product, long time storage and easily obtained. Therefore, product development of soybean focused on powder form and flavor improvement is conducted to gain the market.

Recently, consumers have realized that in order to obtain good value for the money spent. They want to have equal value between money that they spent and the quality of the product that is bought. Producers should market the products that provide good value for consumers and companies. The profits depend on the ability of producers to make high quality products with low cost. Value Engineering is an appropriate method to develop this soybean downstream product. This method is used to get the functionally balanced product concept including minimum costs, maximum performance, and maintaining the expected quality (Heralova, 2016). Fuzzy Logic method is integrated in Value Engineering to maximize the performance of product development method because at the stage of determining the priority ranking of the score ratio of attributes, each attribute has fuzziness characteristics that cannot be expressly categorized with a value of 1 (if the weight exceeds the attribute being compared) and a value of 0 (if less than compared) (Sarkar et al., 2020). Integration of Fuzzy Logic method on Value Engineering in this study is used to organize the fuzzy membership function from the scores that are compared to the ranking determination of priorities used in product design and development. Therefore, fuzziness characteristics in the comparison of the attribute score priority are still considered according to the value of the membership function owned by each of the priority attributes.

MATERIALS AND METHODS

Soymilk Powder Ingredients

The main raw material is local soybeans by Grobogan variety, which was purchased from traditional market in Grobogan District, Central Java, Indonesia. Refined sugar was used for sweeteners. Pandanus, ginger, chocolate, and strawberry flavoring agents which were added for 1.5% respectively was purchased from Bratachem, Yogyakarta.

Soymilk Powder Production

The soybean was soaked in the fresh water for overnight at the room temperature. The soaked soybean which separated from the liquid was prepared to be produced into soymilk. Soymilk was produced by “Maspion” Soya-Bean Milk Maker. This soybean was placed in that machine chamber together with mineral water by soybean and mineral water ratio approximately 200g : 1,5L. After that, the machine was turned on for heating at boiling temperature. When the boiling temperature achieved, the mixer was turned on automatically for 5 minutes. The soymilk processing is complete; thus, it was filtered manually by filter cloth. Furthermore, this liquid form was heated by open pan with gas stove and stirred until the liquid changed into powder form. This product does not use any gum or other hydrocoloid to produce powder particulate. The soybean milk can produce powder without any gum or hydrocoloid to produce the body to the powder. However, this method is especially addressed for small enterprises, so they can produce the soybean powder without addition of cost of production due to buying gum or hydrocoloid as a filler. Proximate analysis and sensory evaluation were conducted by this powder products at Quality Analysis and Standardization Laboratory, Department of Agroindustrial Technology, Universitas Gadjah Mada. The protein, fat, water, ash, and crude fiber contents were determined for all products except product from market which only takes the number of protein and fat contents from its nutrition label. Factors observed on the powder include consumer preferences, quality attributes assessed by consumer preferences, product performance (the value of overall product's appearance), cost production, and value which explains the comparison between performance and cost production. The evaluation of consumer preferences was conducted by questionnaire method to gain the primary data from respondent directly. The result of questionnaire was determined by Likert scale modified by fuzzy logic. Quality attributes assessed by consumer preferences was conducted by determining the priority level of quality attribute development. This determination was gained from the average result of the rank towards quality attribute by respondents from the previous questionnaire combined using fuzzy logic calculations and affirmation (defuzzification) by the centroid method. Product performance (the value of overall product's appearance) was calculated by multiplying the number of respondent assessments towards quality attributes of each concept with the attribute scores. Cost production was calculated by the expense of each raw material and processing cost for a single unit product. The value of the product was calculated by the ratio between performance of each product concept and its cost production.

Data Collection

Data was collected by field observation, questionnaire, sensory evaluation, and literatures observation. Field observations were conducted by two ways including interview and discussion and direct observation. The interview and discussion were carried out by

question and answer directly to the producer of soymilk powder from local soybean variety, Grobogan, to obtain in-depth information about various matters related to the product. Direct observation was done towards the object, namely the production of soymilk powder by roasting method. The roasting method is the method that was explained previously by heating the liquid form on the open pan with gas stove together by stirring until the liquid is changed into powder form. Questionnaire was conducted by giving a list of questions to the respondent to answer. Questionnaire was consisted by 3 steps i.e., preliminary questionnaire, consumer needs questionnaire, and sensory evaluation questionnaire. The first step was done by 30 respondents to assess the priority level for soymilk quality attribute development. The second step was conducted by 100 respondents to gain the quality attributes that were desired by the consumer from the first questionnaire result. The last step of the questionnaire was carried by sensory evaluation to determine the level of performance of the product development design based on the quality attributes of the developed product. This questionnaire used 30 respondents to evaluate the products. The provision of total respondent is appropriate with Wang et al., (2019) who used 10 respondents as trained panelist from School of Life Science in Shanxi University for sensory evaluation of sour porridges product. Furthermore, each answer to the question was determined by a Likert scale modified with fuzzy logic started from 1=very dislike; 2=dislike; 3=like; 4=very like. The respondents of this questionnaire are consumers who know and/or have ever consumed the soymilk. Sensory evaluation was conducted by trained panelists. Literature observation was done by collecting data from scientific books and articles or other sources obtained from ongoing research.

Validity and Reliability Tests

Data from the questionnaire were evaluated for validity and reliability. Validity was measured by SPSS. Validity coefficients that are more than 0.3 are satisfy and give good contribution to the efficiency of a research object. Reliability was measured by Alpha Cronbach method using SPSS. More than 0.50 of Alpha Cronbach value indicates that the variable is reliable. The evaluation is reliable if the alpha coefficient value exceeds the critical value. The criteria for decision making are that if the r results are positive and more than the value of the table, the item will be reliable and vice versa.

Determination of Priority for Quality Attribute Development

The priority order for quality attributes development was determined by the average rating of quality attributes by respondents in the first stage questionnaire. The priority development is the quality attribute which has the lowest average value. The calculations were also combined by fuzzy logic calculations, which begin using the fuzzy set formation

stage (determining the degree of membership for each attribute) and the affirmation stage (defuzzification) using the centroid method.

Determination of Characteristics for Consumer Needs

Quality attributes that have been known and have been determined for priority order in the previous stage were used to identify consumer needs through the second questionnaire. Product specifications obtained from that questionnaire will be used as a basis for developing the product concepts.

Function Analysis System Technique

This analysis begins with brainstorming to determine product concepts that will be developed based on the results of identifying product quality attributes and consumer needs. Furthermore, Function Analysis System Technique (FAST) method was conducted to identify product functions. The FAST was arranged according to function hierarchy which high-level functions are placed on the left and low-level functions are on the right.

Creativity and the Best Product Determination

The creativity stage can be carried out by determining product development specifications by making alternatives of product concept based on the observation and FAST stages that has been conducted on the assessment of consumer needs. Product determination as the last step was divided into five parts i.e., sensory evaluation, performance value, cost of production, product concept value, and the best product concept determination. Sensory evaluation was conducted on various characteristics and concepts of soymilk powder that will be developed. Performance values can be obtained by multiplying the total of respondents' ratings towards quality attributes of each concept with the score of their attributes. At the zero-one calculation stage, the comparison of attributes is done by Fuzzy Logic integration method. This is because the zero-one method in value engineering uses crisp limits (1 and 0) regardless of the value of its membership function. Fuzzy logic serves to fix the exact boundaries of the zero-one method into constraints in fuzzy sets having different membership values. Grouping several values into fuzzy sets with different membership values can solve the discrepancies in the crisp approach of the zero-one method. In addition, 0 and 1 seem unfair because in fact each attribute has a different value or degree. Therefore, the zero one method was integrated with fuzzy logic to find the degree of membership from each attribute. Cost of production was calculated for each of product concept based on the raw material because the other things are assumed to be similar. The value of a product was obtained by comparing the performance of each product concept

with the cost of production. The best product concept is the concept that the highest value based on the questionnaire.

RESULTS AND DISCUSSION

Information Stage

The identity stage of product quality attribute was conducted by brainstorming with researchers who firstly produce soymilk by local soybean from Grobogan. This step was also conducted by interview with consumers to give information about the desired soymilk quality attributes. The results obtain nine important quality attributes namely colour, aroma, taste, price, nutritional content, packaging, viscosity, raw materials, and shelf life. Identification of quality attributes of soymilk powder was done by distributing preliminary questionnaires to 30 respondents aged 20-40 years. Respondents were chosen from who consume soymilk both regularly and non-routinely. They assess the level of importance and give priority order for the development of soymilk quality attributes.

Table 1

Validity and reliability test results of product quality attribute

Quality Attribute	Validity		Reliability	
	Correlation Coefficient	Note	Alpha Coefficient	Note
Colour	0.496	Valid	0.802	Reliable
Aroma	0.698	Valid	0.778	Reliable
Taste	0.410	Valid	0.742	Reliable
Price	0.374	Valid	0.754	Reliable
Nutrition content	0.645	Valid	0.795	Reliable
Packaging	0.433	Valid	0.739	Reliable
Thickness	0.552	Valid	0.706	Reliable
Raw material	0.271	Not Valid	-	-
Shelf life	0.279	Not Valid	-	-

Validity and reliability tests are conducted on the identification results of product quality attributes. The data used are ordinal scale data. Instruments that were used in validity measurement of questionnaire are the results of correlation between the statement score and the overall score of the respondents' statements towards the information in questionnaire. The validity test results in Table 1 show that all correlation coefficients are positive. Nevertheless, there are two quality attributes that have values below 0.364, namely raw

materials and shelf life. Based on the table for Spearman's Rank Correlation by total of sample 30 and significance level 5%, it achieves the value of r table by the α value (0,025) 0.364. Table 1 shows that the r count value is higher than r table value. Thus, it can be stated that the 7 attributes for colour, aroma, taste, price, nutrition content, packaging, and thickness are valid, while 2 attributes for raw material and shelf life are invalid. They can be invalid for data regarding raw material and shelf-life attributes. It can be caused by the differences of consumers interpretations to assess the type of raw materials and their own desire perceptions about the shelf life of the products. These invalid items do not need to be included in the next questionnaire. After validity test, it continues by reliability test to find out the consistency of the measurement of an instrument. The reliability test method is Alpha Cronbach by 95% confidence level or a 5% significance level. The items which is evaluated by reliability test are only items that have been valid. Kim et al. (2020) also used Alpha Cronbach to evaluate the quality of nursing doctoral education by validity and reliability tests.

The reliability test results in Table 1 show that all quality attributes have values above 0.7. It means that all quality attributes are included in the high reliability classification because the reliability coefficient approaches 1.00. Reliable items are considered consistent. It reflects that the measurement results obtained are correct measurement and reliable. From the alpha coefficient values obtained indicate that the attributes have a high level of confidence. The colour value has the highest coefficient value because this item is the most understood and trusted by the respondent. Quality attributes that have been evaluated by validity and reliability tests can be used for the next stage.

Furthermore, the respondents determine the order of priority for quality attributes development in the follow-up questionnaire. After validity evaluation, two attributes are invalid, so seven attributes will be developed. Questionnaires are distributed to 100 respondents. The result of development priority ranking of each quality attributes is used as reference in the development of soymilk powder. The results of priority ranking for development of quality attributes of soymilk powder based on defuzzification process can be seen in Table 2.

Based on the results in Table 2, the priority order of attributes based on score calculation is taste, nutrient content, price, aroma, packaging, colour, and thickness. Whereas based on fuzzy calculations using centroid method, the order of development is taste, nutrient content, packaging, price, aroma, viscosity, and colour. Centroid method determines the center of area of membership function (Rouhparvar & Panahi, 2015). Calculations using the attribute score directly divide the total rating score with the number of respondents. In this calculation, there are several things that need to be improved regarding the selection of information from consumers when filling out the questionnaire. At the initial questionnaire, consumers have been restricted to use explicit Likert values, 1-4. Initial input from the fixed

Table 2

The result of priority development for soymilk powder quality attributes using Attribute Score and Fuzzy Calculations

Quality Attribute	Attribute Score		Fuzzy	
	Attribute Score	Development Priority	Result of <i>Fuzzy</i>	Development Priority
Colour	2.66	6	6.14	7
Aroma	3.81	4	6.98	5
Taste	5.66	1	8.09	1
Price	3.98	3	7.2	4
Nutrition content	5.51	2	7.88	2
Packaging	3.74	5	7.33	3
Thickness	2.64	7	6.51	6

value questionnaire which is calculated by attribute score calculation obtains a fractional value resulting fewer representative data. Fuzzy calculations try to bridge the desires of consumers by providing flexibility to fill scores by fraction values obtaining fractional value computation by fuzzy calculation. Furthermore, defuzzification is conducted to produce crisp value which is more representative for the desires of consumers. When questionnaires distribution, there is scale modification of 1-8 and respondents can fill by fractional numbers. The higher the results exceeding scale 8 shows that the attribute is important to be prioritized because the degree of attribute membership is 1.

Quality attributes that have been determined in priority order in the previous stage are used to identify the consumer needs by distributing the second stage questionnaire. The respondents who are chosen should ever consume soymilk either men or women aged 20-40 years. In this study, the degree of deviation (d) 10% are used with a 95% confidence level (significance level of 5%) and a proportion value (p) 0.5. Based on the calculation, seventy-nine peoples should be used as respondents and 100 respondents will be used in real to get more easily calculation in future. The proportion of respondents in each region can be seen in Table 3. Interview and questionnaires are used for sampling. The quality attributes in question are quality attributes that have previously been declared valid and reliable namely colour, aroma, taste, price, nutrient content, packaging, and viscosity. The output from this stage is evaluation to design the needs of consumers which will be transformed in the product manufacture. The identity and profile of respondents in each regency/district can be seen in Table 4.

Table 3

Total proportion of samples in each regency

Regency	Σ Population Aged 20-40 Years	Proportion (X)	Σ Theoretical Sample	Σ Actual Sample
Yogyakarta	142464	0.173	17.3	18
Bantul	291391	0.3539	35.39	35
Sleman	389550	0.4731	47.31	47
Total	823405	1.00	100	100

Table 4

Identity and profile of respondents

Profile	Assessment Result (%)	
Gender	Male	44
	Female	56
Occupation	Student	75
	Civil Servant	5
	Private Employee	15
	Housewife	2
	Others	3

This second stage questionnaire was conducted randomly towards 100 respondents. The result from this step, 96% of respondents ever consume soymilk and 4% is never. Based on the questionnaire data, the relation of total respondent in percent and their frequency of soymilk consumption follow; 48% consume soymilk <7 times per week; 20% consume soymilk more than twice per week; 16% consume soymilk once per week; 3% consume soymilk every day; 2% consume soymilk >5 times per week; and 11% consume soymilk in uncertain frequency. Based on the exposure of soymilk powder product in market by respondent, 67% of respondents know soymilk powder in market, but 33% do not know because they never find and buy soymilk powder product in the market. In other hand, from the consumer's like and dislike towards soymilk powder product from market, 61% of respondents do not like soymilk powder currently on the market because of unpleasant taste especially beany flavour. Total 39% of respondents like the soymilk powder in the market because of simple, lightweight, easy to carry, and easy to brew. Total 95% of respondents state that the nutrient in soymilk is important for the human body. The results of consumer needs identification can be seen in Table 5.

Table 5

Results of consumer needs identification

No	Question	Answer	Percentage (%)
1	Do you like the soymilk from market?	Yes	31
		No	69
2	Soymilk taste variation	Original	40
		Pandanun	5
		Strawberry	4
		Ginger	6
		Chocolate	41
		Coffee	2
		Vanilla	1
		Honey	1
3	Sugar addition	Yes	61
		No	39
4	Degree of sweetness of soymilk	Very sweet	1
		Sweet	13
		Moderate Sweet	71
5	Soymilk aroma	Pandanun	36
		Vanilla	33
		Chocolate	7
6	Soymilk thickness	Viscous	20
		Moderate Thickness	76
		Aqueous	3
7	Soymilk colour	Original colour	78
		Natural colourant addition	11
8	Soymilk packaging	Alumunium foil	43
		Plastic	33
		Pouch by zipper lock	23
9	Packaging size	Sachet	60
		100 g	22
		200 g	14
10	Price for once drink	IDR 1000-1500	10
		IDR 2000-3000	49
		>IDR 3000	41

Based on the results of the second stage questionnaires distribution, it can be concluded that the soymilk powder desired by consumers has the following specifications (this specifications are then used as a basis for product concept development that will be applied): variation of flavors with original flavors, chocolate, ginger, pandanus, and strawberries; need to add sweeteners (sugar); moderate sweetness level of taste; medium level of thickness; colour like the original colour of soy (brown cream); forms of soymilk powder in sachet packaging using aluminum foil; soybean powder need to be smoother (not much pulp/sediment); the price of soymilk sachets is around IDR 2000-3000.

Analysis Stage

The characteristic development of soymilk powder products based on questionnaires I and II was conducted by identification of product functions. Identification of product functions and their interrelationships was conducted by a function diagram called Function Analysis System Technique (FAST). This diagram represent a function showing the inter-relationship of function to each other in a how and why logic (El-Nashar & Elyamany, 2018). Identification of product functions begins by observation of soymilk powder on the market and direct observation of soymilk powder production (prototype) from Faculty of Agricultural Technology, Universitas Gadjah Mada. This product was developed because of consumer dissatisfaction towards soymilk taste. The comparison product is local soymilk from supermarket which has equal quality to the developed product. Furthermore, it can be identified the functions of soymilk powder products and then these functions can be mapped and can be known for their association by FAST diagram in Figure 1.

From the FAST diagram, it can be identified that soymilk has two primary functions i.e., function of quality and price. The primary function of product quality is followed by secondary functions of colour, aroma, taste, nutrient content, packaging, and thickness. In other hand, price has a secondary function which is cost of production. The secondary function of colour is influenced by the raw material and colouring agent addition in soymilk. The secondary function of aroma is influenced by raw material and kinds of soybean. The secondary function of taste is influenced by the degree of sweetness and addition of other ingredients. The secondary function of nutrient content is determined by the quality of raw materials and raw materials composition. The secondary function of packaging is determined by the kinds of packaging material and information on the packaging. The secondary function of thickness is influenced by kinds and combination of raw materials. The secondary function of production cost is affected by how soymilk products are produced in accordance with the secondary functions of quality i.e., colour, aroma, taste, nutrient content, packaging, and thickness. Attributes that will be developed to determine the design alternative of soymilk product development include:

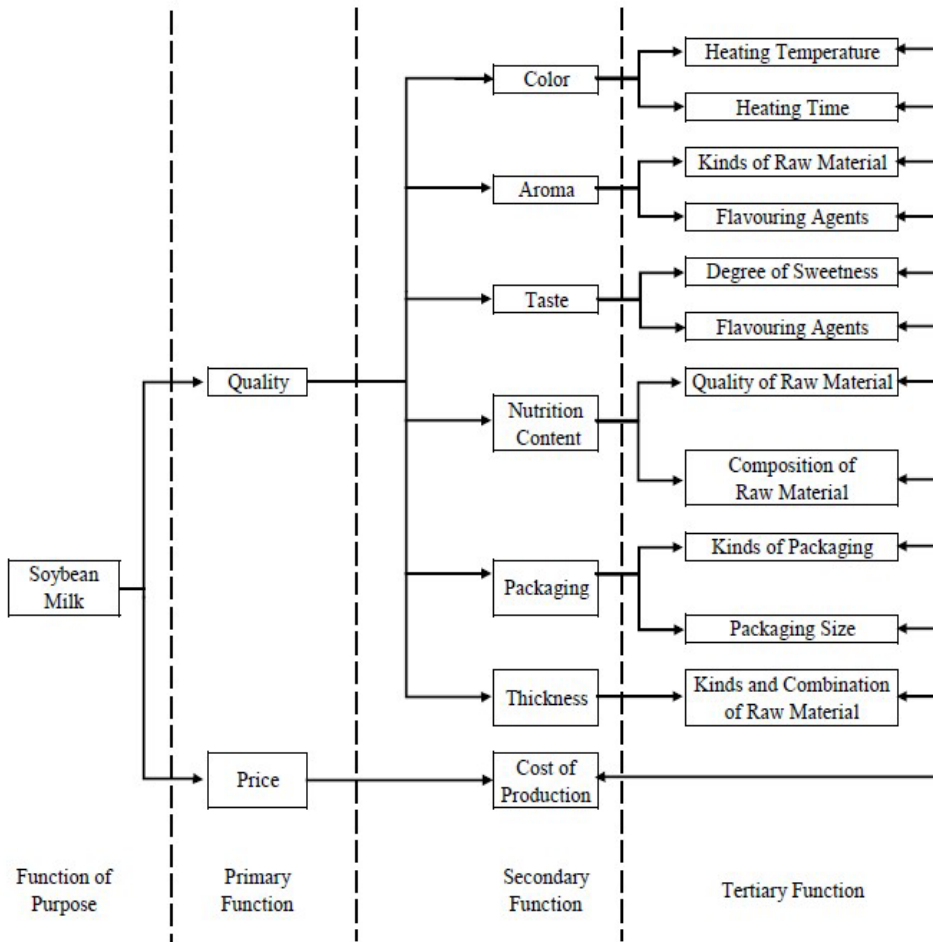


Figure 1. FAST diagram of soymilk product development

a. Taste: the most priority quality attribute to be developed according to respondents. From the results of the second questionnaire distribution, it is found that 40% of respondents want the original taste, 41% chocolate, 6% ginger, 5% pandanus, and 4% strawberry. Total 61% of respondents want a sugar addition into soymilk powder with a moderate level of sweetness.

b. Colour: 78% of respondents want a soymilk powder with a creamy brown colour. Soybeans generally have a creamy brown colour. It makes no additional colourant agent.

c. Aroma: 36% of respondents want a soymilk with soy aroma combined with pandanus aroma. Grobogan soybean has a strong soybean aroma. It is also in accordance with the desired aroma by respondents.

d. Packaging: 60% of respondents want soymilk that is packaged in sachets form. It will make that product ready to be brewed and consumed by adding hot water. Product development will be carried out by production the soymilk products in aluminum foil sachets packaging.

e. Thickness: 76% of respondents want the soymilk with medium thickness.

Creativity Stage

Based on consumer need identification by questionnaire, it will be developed for concept alternatives of soymilk powder products. The alternative product concepts can be seen in Table 6. The alternative products are supported by flavor enhancement ingredients including chocolate, pandanus, strawberry, and ginger.

Table 6

Alternative concepts of soymilk powder products

Product Concept	Ingredient and Proportion
A	Soymilk Liquid : Sugar = 1000 mL : 100 g
B	Soymilk Liquid : Sugar : Ginger = 1000 mL : 100 g : 10 g
C	Soymilk Liquid : Sugar : Chocolate = 1000 mL : 100 g : 2 mL
D	Soymilk Liquid : Sugar : Strawberry = 1000 mL : 100 g : 2 mL
E	Soymilk Liquid : Sugar : Pandanus = 1000 mL : 100 g : 2 mL

Determination Stage

This stage is consisted of sensory evaluation, determination of product performance value, determination of production costs and product concept value, and determination of the best product concept. Comparison between developed products and products from market is conducted to determine the acceptable of developed products to the public. As the beginning of determination stage, sensory evaluation, the soymilk products are tested to 30 trained panelists. They are requested to rate the product quality attributes by Likert scale which 4 is “very good”; 3 is “good”; 2 is “bad”; and 1 is “very bad”. This Likert scale is widely used for sensory evaluation including the microgreens from commercial and local farms in Tuscaloosa, Alabama (Tan et al., 2020). Sugared soymilk instant from market is also included in this sensory evaluation as a comparison product, at the same time. The sensory evaluation result can be seen in Table 7.

Table 7

Sensory evaluation results

Attributes	Product	Attribute Score (Value)				Total Score	Average Score
		1	2	3	4		
Taste	A	2	5	14	9	90	3.00
	B	3	9	10	8	83	2.77
	C	4	13	8	5	74	2.47
	D	4	9	4	13	86	2.87
	E	2	5	11	12	93	3.10
	Market	17	11	1	1	46	1.53
Colour	A	0	1	20	9	98	3.27
	B	0	3	21	6	93	3.10
	C	2	6	21	1	81	2.70
	D	2	0	23	5	91	3.03
	E	0	5	16	9	94	3.13
	Market	4	15	9	2	69	2.30
Aroma	A	1	3	15	11	96	3.20
	B	3	5	14	8	87	2.90
	C	3	9	12	6	81	2.70
	D	2	8	13	7	85	2.83
	E	0	5	12	13	98	3.27
	Market	9	15	4	2	59	1.97
Thickness	A	0	2	23	5	93	3.10
	B	1	1	26	2	89	2.97
	C	0	5	22	3	88	2.93
	D	2	6	15	7	87	2.90
	E	1	0	21	8	96	3.20
	Market	10	9	8	3	64	2.13

Based on the sensory evaluation results, Concept E (pandanus flavor) has the highest score of taste attribute. Major respondents in second questionnaire desire the taste and aroma of pandanus as an alternative to the development of flavor in soymilk powder. The second ranking is Concept A (original) followed by Concept D (strawberry flavor), Concept B (ginger flavor), Concept C (chocolate), and product from market. Product from market has the lowest score in all the evaluated attributes including taste, colour, aroma,

and thickness. This confirms that soymilk products from the market have preferred by the public, especially in terms of bitter, beany and rancid tastes (Ma et al., 2015). Based on the results of colour attribute, Concept A (original) has the highest score of colour attribute. Second questionnaire result shows that more respondents prefer the original colour of soy (brown cream) as an alternative to the development of colour attribute in soymilk powder. The lower score of colour attribute is followed by Concept E, Concept B, Concept D, Concept C, and product from market. Aroma attribute score from Table 7 shows that Concept E (pandanus flavor) has the highest score followed by Concept A (original), Concept B, Concept D, Concept C, and product from market. It has similar reason with the previous result which explain that more respondents from second questionnaire want the pandanus aroma to be an alternative towards the development of aroma in soymilk. For the thickness attribute, Concept E (pandanus flavor) has the highest score followed by Concept A (original), Concept B, Concept C, Concept D, and product from market. The respondents from second questionnaire desire the moderate thickness in soymilk.

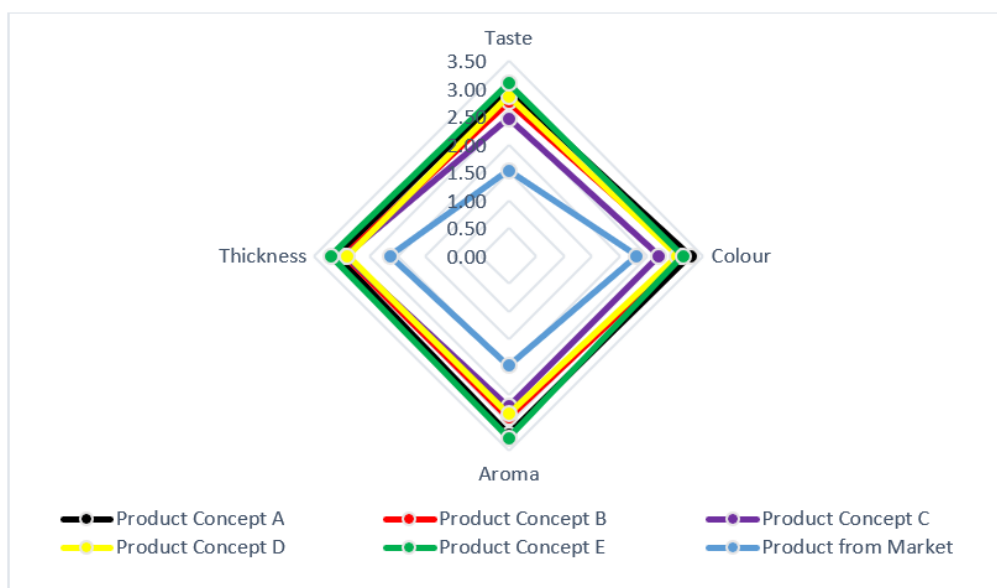


Figure 2. Attribute Value Comparison of Sensory Evaluation Result

Figure 2 informs that Concept E has the highest performance value followed by Concept A, Concept B, Concept D, Concept C, and product from market. It indicates that panelists would rather accept the developed product concepts than product from market. However, product from market tends to have unpleasant taste and odor with high precipitate. Regarding value engineering, sensory evaluation could be used to determine the level of performance of the product development design based on the quality attributes of the product being developed.

In this step, the determination of product performance value is conducted. From the calculation of the attribute score in Table 8, comparison among quality attribute could be made by the zero-one method. The comparative analysis of factor attributes determining product design and development uses zero-one method. This method defines a crisp limit of 1 if the score exceeds the compared attribute and 0 if less than the compared attribute without considering its value of membership function for any score (Sarkar et al., 2020). This condition has an inappropriate impact because each compared score has unconsidered membership value. Fuzzy Logic method could improve the definite limits on zero-one method in Value Engineering into limits in fuzzy sets that have different membership values. Grouping several values into fuzzy sets with different membership values could resolve the discrepancies on the crisp approach in zero-one method in Value Engineering. The comparison results of quality attributes by fuzzy logic can be seen in Table 9.

Based on Table 9, comparison among quality attributes could be made by zero-one method. The higher attribute score will get 1 and the lower one is 0. The similar attribute comparison will be given (-). However, 0 and 1 are considered unfair because each attribute has different value or degree. Therefore, the zero-one method will be integrated by fuzzy logic method which will begin by finding the degree of membership of each attribute. From the comparison results of quality attributes by fuzzy logic, taste has the highest value to be developed, then followed by aroma, colour, and thickness. Comparison on each compared

Table 8

Calculation of attribute score

Attribute	Importance Level				Total	Total Score	Attribute Score (%)	Ranking
	1	2	3	4				
Taste	0	3	9	18	30	105	35	1
Colour	12	12	3	3	30	57	19	3
Aroma	1	5	16	8	30	91	30.33	2
Thickness	17	10	2	1	30	47	15.67	4
Total	30	30	30	30	120	300	100	-

Table 9

Comparison results of quality attributes by zero-one and fuzzy logic

Method	Attribute	Taste	Colour	Aroma	Thickness	Total	Ranking
Zero-One	Taste	-	1	1	1	3	1
	Colour	0	-	0	1	1	3
	Aroma	0	1	-	1	2	2
	Thickness	0	0	0	-	0	4
Fuzzy Logic	Taste	-	1.88	1.15	2.23	5.26	1
	Colour	0.53	-	0.62	1.19	2.34	3
	Aroma	0.87	1.63	-	1.94	4.43	2
	Thickness	0.45	0.84	0.52	-	1.80	4

attribute is stated in fuzzy membership function leading to still have a value according to its membership function limit. This is more appropriate to represent the comparison criteria. The next step is calculation of performance value for each product concept. This value could help to optimize a product concept by maximizing the functional performance of each product concept (Heralova, 2016). The results of performance value calculation for each product concept can be seen in Table 10.

Table 10

The result of performance value calculation for each product concept

Quality Attribute	Taste	Colour	Aroma	Thickness	Performance Value
Attribute Score	38.03	16.92	32.03	13.02	
Product Concept A	90	98	96	93	9366.60
Product Concept B	83	93	87	89	8675.44
Product Concept C	74	81	81	88	7924.93
Product Concept D	86	91	85	87	8665.59
Product Concept E	93	94	98	96	9516.13
Product from Market	46	69	59	64	5639.91

Product performance is stated as good if the value exceeds the comparative product performance value (product from market). Based on Table 10, product E (pandanus) has the highest performance value followed by product A, product B, product D, product C, and product from market.

However, a higher product performance value does not necessarily indicate that the product has a better value. The value of a product is also influenced by the production

costs. In this case, value is a comparison between performance and production costs. It should be considered because products with high performance will get low values if it has high production costs.

In this step, the determination of production costs and product concept value is conducted. The calculation of production costs in this study is limited only to the cost of raw materials because the product development focuses on flavor diversification and the other things are done with the similar process. From the calculation, Product A has the lowest cost of IDR 2,000 followed by product from market IDR 2,072.5, product E IDR 2,244, product B IDR 2,300, and product C and D having similar result IDR 2,303. Furthermore, the value of each product concept could be determined by performance comparison of each product concept with its production cost. The results of value calculation for each product concept can be seen in Table 11.

Table 11
Value of each product concept

Product	Performance	Production Cost (IDR)	Value	Ranking
Product Concept A	9366.6	2000	4.68	1
Product Concept B	8675.44	2300	3.77	3
Product Concept C	7924.93	2303	3.44	5
Product Concept D	8665.59	2303	3.76	4
Product Concept E	9516.13	2244	4.24	2
Product from Market	5639.91	2072.5	2.72	-

Table 12
Proximate analysis profiles of some soymilk powder products

Proximate Analysis	Soymilk Powder Product		
	Developed Product	Commercial Product	
	Product Concept A	Prototype Product	Product from Market
Protein (%)	10.31	6.11	11
Fat (%)	3.76	3.38	2
Water (%)	5.31	1.31	-
Ash (%)	1.07	0.93	-
Crude Fiber (%)	1.12	0.12	-

As the last step, the determination of the best product concept is conducted here. Based on Table 11, product concept A (original flavor) has the highest value due to its lowest production cost. It could be stated that the best concept of this product development is concept A (original flavor) because it has the highest value with a high performance and low cost of production. This product also indicates the preference of the consumer. Proximate analysis profiles of product concept A and other commercial products can be seen in Table 12. Based on Table 12, product concept A has 5.31% of water content, 1.07% of ash content, and 1.12% of crude fiber. This results are closer to study that was conducted by Mazumder & Hongsprabhas (2016). They stated that water content, ash, and crude fiber of spray dried soymilk powder are 1.93%, 3.05%, and 3.59% respectively. In other hand, protein and fat contents are different i.e. 57.26% and 27.6%, respectively (Mazumder & Hongsprabhas, 2016). That contents are higher than the protein and fat contents in this study, 10.31% and 3.76%, respectively. Since the process of soymilk production conducting the soaking method towards the soybean for overnight, it is predicted that a lot of protein dissolve into the liquid soaking medium. This has been confirmed by Martinson et al. (2012) who stated that the soaking of soybean could decrease the protein content. Nilufer-Erdil et al., (2012) also explained that soymilk powder needs to have no less than 38% of soy protein and 13% of soy fat. Product from market only show the number of protein and fat contents which take from its nutrition label, as described in the method part above.

CONCLUSION

The priority of attributes development for soymilk powder are taste, nutrient content perception from respondents, packaging, price, aroma, thickness, and colour. Meanwhile, the consumer needs include variations in taste, sugar addition (medium sweetness), medium thickness, aluminum foil packaging in sachet sizes, and prices ranging from IDR 2000-3000. Five concepts of soymilk powder product development obtained from the creativity stage include product concept A (original), product concept B (ginger), product concept C (chocolate flavor), product concept D (strawberry flavor), and product concept E (pandanus flavor). The best concept is product concept A (original) that has the highest value (4.68), high performance (9,366.60) and low production cost (IDR 2000).

ACKNOWLEDGEMENT

The authors would like to acknowledge the Agroindustrial Technology Department of Universitas Gadjah Mada and Management Department of IPB University - Indonesia for support and encouragement. We also dedicated this to wonderful people in our life (all families). Thanks for the amazing love, unbroken supports, and the prayers that never ends. Praise the Lord.

REFERENCES

- Bestari, A. V., Darmanti, S., & Parman, S. (2018). Physiological responses of soybean [*Glycine max* (L.) Merr.] varieties Grobogan to different shade levels. *Biospecies*, *11*(2), 53-62.
- Chen, J., Wu, Y., Yang, C., Xu, X., & Meng, Y. (2017). Antioxidant and hypolipidemic effects of soymilk fermented via *Lactococcus acidophilus* MF204. *Food & Function*, *8*(12), 4414-4420. <https://doi.org/10.1039/C7FO00701A>
- da Silva Fernandes, M., Lima, F. S., Rodrigues, D., Handa, C., Guelfi, M., Garcia, S., & Ida, E. I. (2017). Evaluation of the isoflavone and total phenolic contents of kefir-fermented soymilk storage and after the in vitro digestive system simulation. *Food Chemistry*, *229*, 373-380. <https://doi.org/10.1016/j.foodchem.2017.02.095>
- El-Nashar, W. Y., & Elyamany, A. H. (2018). Value engineering for canal tail irrigation water problem. *Ain Shams Engineering Journal*, *9*(4), 1989-1997. <https://doi.org/10.1016/j.asej.2017.02.004>
- Heralova, R. S. (2016). Possibility of using value engineering in highway projects. *Selected Papers from Creative Construction Conference 2016*, *164*, 362-367. <https://doi.org/10.1016/j.proeng.2016.11.631>
- Kim, M. J., McKenna, H., Park, C. G., Ketefian, S., Park, S. H., Galvin, K., & Burke, L. (2020). Global assessment instrument for quality of nursing doctoral education with a research focus: Validity and reliability study. *Nurse Education Today*, *91*, Article 104475. <https://doi.org/10.1016/j.nedt.2020.104475>
- Krisnawati, A., & Adie, M. M. (2015). Selection of soybean Genotypes by seed size and its prospects for industrial raw material in Indonesia. *The First International Symposium on Food and Agro-Biodiversity Conducted by Indonesian Food Technologists Community*, *3*, 355-363. <https://doi.org/10.1016/j.profoo.2015.01.039>
- Kuntyastuti, H., & Lestari, S. A. D. (2017). Application of manure and NPK fertilizer on Grobogan variety and Aochi/W-C-6-62 soybean as promise line in lowland Vertisol Ngawi, Indonesia. *Nusantara Bioscience*, *9*(2), 120-125. <https://doi.org/10.13057/nusbiosci/n090205>
- Li, Y., Chen, M., Deng, L., Liang, Y., Liu, Y., Liu, W., Chen, J., & Liu, C. (2021). Whole soybean milk produced by a novel industry-scale microfluidizer system without soaking and filtering. *Journal of Food Engineering*, *291*, Article 110228. <https://doi.org/10.1016/j.jfoodeng.2020.110228>
- Ma, L., Li, B., Han, F., Yan, S., Wang, L., & Sun, J. (2015). Evaluation of the chemical quality traits of soybean seeds, as related to sensory attributes of soymilk. *Food Chemistry*, *173*, 694-701. <https://doi.org/10.1016/j.foodchem.2014.10.096>
- Martinson, K. L., Hathaway, M., Jung, H., & Sheaffer, C. (2012). The effect of soaking on protein and mineral loss in orchardgrass and alfalfa hay. *Journal of Equine Veterinary Science*, *32*(12), 776-782. <https://doi.org/10.1016/j.jevs.2012.03.007>
- Mazumder, M. A. R., & Hongsprabhas, P. (2016). A review on nutrient quality of soymilk powder for malnourished population. *Pakistan Journal of Nutrition*, *15*(6), 600-606. <https://doi.org/10.3923/pjn.2016.600.606>
- Ministry of Agriculture. (2008). *Agriculture Minister Decree No: 238/Kpts/SR.120/3/2008 about Grobogan soybean*. Ministry of Agriculture. Retrieved February 24, 2021, from <http://en.litbang.pertanian.go.id/reshighlight/pangan/grobogan>

- Mustikawati, D. R., Mulyanti, N., & Arief, R. W. (2018). Productivity of soybean on different agroecosystems. *International Journal of Environment Agriculture and Biotechnology*, 3(4), 1154-1159. <http://dx.doi.org/10.22161/ijeab/3.4.1>
- Nilufer-Erdil, D., Serventi, L., Boyacioglu, D., & Vodovotz, Y. (2012). Effect of soy milk powder addition on staling of soy bread. *Food Chemistry*, 131(4), 1132-1139. <https://doi.org/10.1016/j.foodchem.2011.09.078>
- Ningrum, I. H., Irianto, H., & Riptanti, E. W. (2018). Analysis of soybean production and import trends and its import factors in Indonesia. *IOP Conference Series: Earth and Environmental Science*, 142, Article 012059. <https://doi.org/10.1088/1755-1315/142/1/012059>
- Rouhparvar, H., & Panahi, A. (2015). A new definition for defuzzification of generalized fuzzy numbers and its application. *Applied Soft Computing*, 30, 577-584. <http://dx.doi.org/10.1016/j.asoc.2015.01.053>
- Sarkar, T., Bhattacharjee, R., Salauddin, M., Giri, A., & Chakraborty, R. (2020). Application of fuzzy logic analysis on pineapple rasgulla. *International Conference on Computational Intelligence and Data Science*, 167, 779-787. <https://doi.org/10.1016/j.procs.2020.03.410>
- Sui, X., Sun, H., Qi, B., Zhang, M., Li, Y., & Jiang, L. (2018). Functional and conformational changes to soy proteins accompanying anthocyanins: Focus on covalent and non-covalent interactions. *Food Chemistry*, 245, 871-878. <https://doi.org/10.1016/j.foodchem.2017.11.090>
- Tan, L., Nuffer, H., Feng, J., Kwan, S. H., Chen, H., Tong, X., & Kong, L. (2020). Antioxidant properties and sensory evaluation of microgreens from commercial and local farms. *Food Science and Human Wellness*, 9(1), 45-51. <https://doi.org/10.1016/j.fshw.2019.12.002>
- Toro-Funes, N., Bosch-Fusté, J., Latorre-Moratalla, M. L., Veciana-Nogués, M. T., & Vidal-Carou, M. C. (2015). Isoflavone profile and protein quality during storage of sterilised soymilk treated by ultra high pressure homogenisation. *Food Chemistry*, 167, 78-83. <https://doi.org/10.1016/j.foodchem.2014.06.023>
- Toro-Funes, N., Bosch-Fusté, J., Veciana-Nogués, M. T., & Vidal-Carou, M. C. (2014). Changes of isoflavones and protein quality in soymilk pasteurised by ultra-high-pressure homogenisation throughout storage. *Food Chemistry*, 162, 47-53. <https://doi.org/10.1016/j.foodchem.2014.04.019>
- Viana, J. S., Gonçalves, E. P., Silva, A. C., & Matos, V. P. (2013). Climatic conditions and production of soybean in Northeastern Brazil. In *A Comprehensive Survey of International Soybean Research* (p. Ch. 18). IntechOpen. <https://doi.org/10.5772/52184>
- Wang, Q., Liu, C., Jing, Y., Fan, S., & Cai, J. (2019). Evaluation of fermentation conditions to improve the sensory quality of broomcorn millet sour porridge. *LWT*, 104, 165-172. <https://doi.org/10.1016/j.lwt.2019.01.037>
- Yao, H., Zuo, X., Zuo, D., Lin, H., Huang, X., & Zang, C. (2020). Study on soybean potential productivity and food security in China under the influence of COVID-19 outbreak. *Geography and Sustainability*, 1(2), 163-171. <https://doi.org/10.1016/j.geosus.2020.06.002>
- Yasin, U. A., Horo, J. T., & Gebre, B. A. (2019). Physicochemical and sensory properties of tofu prepared from eight popular soybean [*Glycine max* (L.) Merrill] varieties in Ethiopia. *Scientific African*, 6, Article e00179. <https://doi.org/10.1016/j.sciaf.2019.e00179>

Zikri, I., Safrida, S., Susanti, E., & Putri, R. A. (2020). Analysis of trend and determinant factors of imported soybean in the period of 2003-2022. *Advances in Food Science, Sustainable Agriculture and Agroindustrial Engineering*, 3(1), 17-24. <https://doi.org/10.21776/ub.afssae.2020.003.03>



Review article

Contact and Non-contact Heart Beat Rate Measurement Techniques: Challenges and Issues

Wei Leong Khong^{1*}, Muralindran Mariappan² and Chee Siang Chong²

¹*School of Engineering, Monash University Malaysia, 47500 Subang Jaya, Selangor, Malaysia*

²*Faculty of Engineering, Universiti Malaysia Sabah, 88400 UMS, Kota Kinabalu, Sabah, Malaysia*

ABSTRACT

The heart is the most important organ in the human body as it circulates the blood throughout the body through blood vessels. In the human circulatory system, the heart beats according to the body's physical needs. Therefore, the physical condition of a person can be determined by observing the heartbeat rate (HBR). There are plenty of methods that can be used to measure the HBR. Among the methods, photoplethysmography (PPG), electrocardiogram (ECG) and the oscillometric method are the standard methods utilised in medical institutes for continuous measurement of the HBR of a patient. Out of these three methods, PPG is the only method which has evolved to a non-contact imaging-based method from the conventional contact sensory based method. The incentive for developing the non-contact-based imaging PPG method in measuring the HBR provides the advantage of excluding the direct contact of sensors on specific body parts. This brings huge improvements to remote monitoring of healthcare especially for the purpose of social distancing. Moreover, the rapid progression of technology (particularly the interactive electronic gadgets advancement) also motivates researchers and engineers to create a mobile application using the PPG imaging

method, which is feasible in measuring the HBR. Hence, this study seeks to review and present the fundamental concept, the present research and the evolution of the aforementioned methods in measuring the HBR.

Keywords: Electrocardiogram, heart beat rate, oscillometric method, photoplethysmography imaging, photoplethysmography

ARTICLE INFO

Article history:

Received: 22 September 2020

Accepted: 29 January 2021

Published: 31 July 2021

DOI: <https://doi.org/10.47836/pjst.29.3.03>

E-mail addresses:

weileongkhong@gmail.com (Khong Wei Leong)

murali@ums.edu.my (Muralindran Mariappan)

drchonges@gmail.com (Chong Chee Siang)

* Corresponding author

INTRODUCTION

The heart is the key organ in keeping a person alive. When it stops functioning, the oxygen-rich blood is unable to reach the brain and other organs. A person can die in minutes if the heart stops and does not receive immediate treatment. The HBR is the most direct indicator that can reflect the general health of a person. For instance, the HBR is an indicator for diagnosing any cardiac arrhythmia diseases (abnormal heart rhythms or arrhythmia). This disease is one of the chronic cardiovascular diseases (CVDs). To date, CVDs are termed as the most common diseases causing death worldwide. According to Srinivasan & Schilling (2018), it is estimated that 15 to 20% of all death is caused by CVDs and sudden cardiac death.

Cardiac arrhythmia can be classified into three groups - abnormally fast HBR (or also known as tachycardia, if the HBR is over 100 bpm (beats per minute)), abnormally slow HBR (or also known as bradycardia, when HBR is lesser than 60 bpm) and irregular HBR (Kastor, 2002). A crucial preliminary action in discovering the presence of these diseases is to measure the HBR consistently and frequently. In order to extend the lifespan of a patient who has cardiac arrhythmia diseases, the most effective solution is to attentively monitor the HBR and consume medications. Thus, the measurement of the HBR plays an important role in maintaining the health of the heart.

At present, several techniques and devices can be used in measuring the HBR. The most direct method for calculating the HBR is through manual calculation which is done by putting a bare hand on the arterial site in order to sense the pulsation strength or using a stethoscope to listen the sounds of the heartbeats during a specific time period. As technology nowadays is more advanced, the standard methods such as electrocardiography (ECG), photoplethysmography (PPG) and the oscillometric method are implemented in clinical settings to obtain the HBR automatically. These methods have reduced any errors that may have occurred when the HBR is manually taken. In the paper by Khong & Mariappan (2019), the evolution of the PPG methods had been briefly described. This paper represents an extension of that version by Khong & Mariappan (2019); it reviews the pulse rate or the HBR measurement techniques and focuses on its evolution from contact based to non-contact-based methods.

HEART BEAT RATE (HBR)

The HBR is a measurement referring to the speed of heartbeats in one minute with the measurement unit of bpm. It is essential in analysing the normal resting HBR data. The HBR at rest is a snapshot of the heart muscle in pumping the lowest amount of blood that the body needs. During the resting condition, the HBR is normally between 60 bpm to 100 bpm. For active individuals, the HBR can be as low as 40 bpm as their heart muscle is in better condition and does not need to pump frequently to sustain a steady beat. There

are numbers of factors such as emotions, medications, hormones, air temperature, fitness level, activity level, body position, body size, age, and gender. that can affect the normal resting HBR. As these factors can greatly influence the HBR, it is always recommended to check the HBR frequently and at different times of the day under full resting conditions. Table 1 shows the normal resting HBR values.

Table 1
The normal resting heart beat rate values

Group	Heart Beat Rate (bpm)
Birth	130-160
Infants	110-130
Children (1-7 years old)	80-120
Children (over 18 years old)	80-90
Adults	60-80

The HBR can be measured by taking the pulse rate (PR) at places where the arteries run near to the skin i.e., wrists, side of the neck, inside the elbow, top or inner side of the foot, back of the knee or groin. In fact, the PR and the HBR refer to the same physiological parameters but they are measured at different body positions and using different techniques. In the following section, the evolution of the methods used for measuring the HBR or PR are presented.

THE EVOLUTION OF HBR MEASUREMENT TECHNIQUES

As mentioned in the previous section, the HBR can be directly measured from the heart or through analysing the PR at the arterial sites in the human body. According to Ghasemzadeh & Zafari (2011), the ancient Indian and Chinese health professionals identified certain diseases based on the strength and speed of the beating pulse by placing a hand on the patient's wrist. When it came to 1816, Rene Theophile Hyacinthe Laennec designed the first stethoscope to listen to sounds produced by the heart and lung (Roguin, 2006). This process is known as auscultation and it is an accurate method in determining the HBR (Hashem et al., 2010). At first, Laennec's stethoscope was made from rolled paper cone. Laennec subsequently changed the material and designed to a simple wooden tube. The most significant change in the development of the stethoscope occurred in 1961 when Dr. David Littmann developed a single tube binaural stethoscope made from stainless steel or light weight alloy (3M Health Care, 2002). Recently, the Littmann stethoscope has evolved to an electronic stethoscope (Leng et al., 2015). However, the classical Littmann stethoscope is still widely used. Since the manual way in measuring HBR needs high attentiveness and might lead to a human error, the methods that can automatically measure the HBR are highly encouraged. These methods will be reviewed in the following sub-sections.

Electrocardiogram (ECG)

Back in 1780, studies of the cardiac electricity started when Luigi Galvani observed the contraction of a muscle caused by the electrical stimulation of a nerve (Fleming, 1997). About 50 years later, Carlo Matteucci discovered that the muscle that connected to the heart by nerves tissues contracted synchronous with the beating heart and all muscles have an electrical current of contraction (Katz & Hellerstein, 1982). Later in the year 1856, Rudolph von Koelliker and Heinrich Muller verified Matteucci's findings by placing the nerve of a nerve-muscle preparation on a beating heart and measured it with a mechanical galvanometer (Bowbrick & Borg, 2006). They noticed that the heart muscle contracted with every systole of the heart and it twitched after the end of every systole (Fleming, 1997). They also proved that the heart muscle is able to produce electric activity and these phenomena later become the QRS complex and the T wave in the ECG as shown in Figure 1.

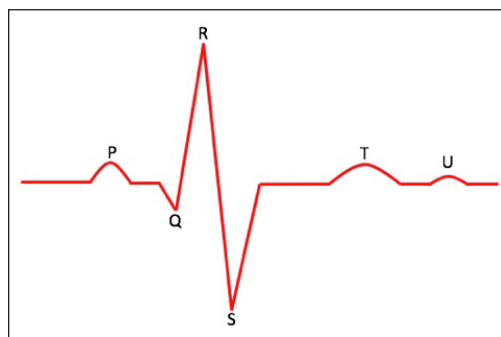


Figure 1. The basic pattern of heart activity obtained from ECG

The next important development of the ECG occurred in 1872 when Gabriel Lippmann introduced the capillary electrometer (Fisch, 2000). This capillary electrometer consists of a glass capillary tube filled with mercury which has contact with sulphuric acid. The surface tension of the mercury altered when there was a potential difference between the acid and mercury. The movements of the mercury are recorded on a photographic paper. Although this method has been used for more than two decades to record any heart electrical activity, it was only applied for the first time on a human heart by Augustus Desire Waller in 1887 (Fleming, 1997). This was also the first time that electrodes were attached on the chest and the back without direct contact to the heart muscle. The subsequent evolutions of these techniques are summarised in first six rows of Table 2.

In 1906, Einthoven developed a standard limb lead system (Lead I, II and III) as the reference positions for the placements of the electrodes. This standard limb lead system forms an equilateral triangle where the heart is located at the centre. The three corners of the equilateral triangle are located at the right arm (RA), left arm (LA) and left leg (LL). Based on the invention of Einthoven, this equilateral triangle is named as Einthoven's triangle. The standard limb lead system is also known as bipolar leads because Lead I measure the bio-potential between RA and LA, Lead II measures the bio-potential between RA and LL, and Lead III measures the bio-potential between LA and LL. In 1924, Einthoven was awarded the Nobel Prize in medicine due to his contribution in inventing the ECG (Yang et al., 2015).

Table 2
The Evolution of ECG Technic

Year	Research(s)	Technics	Remarks
1891	William Bayliss and Edward Starling	Capillary electrometer	Used improved capillary electrometer with a more powerful projecting microscope optics and an additional electrical light to extract 3 different deflections, which later known as P wave, QRS complex and T wave in ECG (Fye, 1994)
1903	Willem Einthoven	String galvanometer	Since frequency response of capillary electrometer is poor, string galvanometer is developed (Madihally, 2010).
1905-1907	Cambridge Instrument Company	Einthoven string galvanometer	Three units Einthoven string galvanometer were successfully manufactured and sold (Fye, 1994)
1909	Edelmann	Small version of the string galvanometer	Set up in Thomas Lewis's laboratory at University College Hospital in London (Fye, 1994)
1909	Alfred Cohn	First Edelmann string galvanometer ECG machine	Introduced to United States and installed at Mt. Sinai Hospital (Geddes & Wald, 2000)
1914	Charles Hindle	First ECG machine	Charles Hindle built the first ECG machine in United States , which was designed by Horatio Williams (Geddes & Wald, 2000)
1934	Frank Norman Wilson	Wilson's central terminal	Wilson's central terminal forms by connecting the electrodes at RA, LA and LL respectively to central terminal. The bio-potentials measured based on Wilson's central terminal are voltage at right arm (VR), voltage at left arm (VL) and voltage at left foot (VF) (Alghatif & Lindsay, 2012).
1938	American Heart Association	Six standard precordial leads	The Cardiac Society of Great Britain and the American Heart Association standardized the name for the six standard precordial leads as V1-V6 (Alghatif & Lindsay, 2012)
1942	Emanuel Goldberger	Augmented leads system	Augmented leads system i.e. augmented vector right (aVR), augmented vector left (aVL) and augmented vector foot can amplify the bio-potentials of VR, VL and VF (Gargiulo, 2015) and replace them in the ECG measurements.
1954	American Heart Association	Twelve leads system	Twelve leads system consists of bipolar leads (Lead I, II, III), augmented leads (aVR, aVL, aVF) and standard precordial leads (V1-V6) has been recommended for standardizing the ECG measurements (Alghatif & Lindsay, 2012).
1957	Normal Holter	Holter ECG	New breakthrough in ECG development. Holter ECG is a portable device and can continuously record the heart activities (HBR and rhythm) for more than 24 hours (Yang et al., 2015).

In 1934, Frank Norman Wilson developed Wilson's central terminal by connecting the electrodes at RA, LA and LL respectively to the central terminal. In Wilson's technique, this central terminal acts as a reference terminal and hence, it is also known as unipolar leads (Alghatirif & Lindsay, 2012). Wilson also based on Wilson's central terminal technique to measure the bio-potential across the chest with six standard precordial leads.

The evolutions about the lead systems are summarised from the seventh to tenth rows of Table 2. Figure 2 shows the Mason-Likar leads position for the ten electrodes to form a twelve-lead ECG system. To date, this twelve-lead ECG system is still applicable to ECG measurements and is also known as the golden standard in measuring the activity of heart in clinical settings including the HBR.

Although the twelve-lead system is able to describe heart activities, the ECG machine is bulky and expensive. Throughout the years, the ECG machine greatly advanced in terms of weight by reducing the Einthoven string galvanometers from 600 pounds to less than 8 pounds (Fisch, 2000). In addition, the number of operators needed was reduced from five to one person. The electrodes used in the ECG machine were also improved from Einthoven's original cylinders, which consist of electrolyte solutions to strap-on electrodes designed by Alfred Cohn in 1920 (Krikler, 1983). In 1932, Rudolph Burger introduced a suction electrode which was later improved by Welsh in the ECG machine (Burch & DePasquale, 1990). In order to avoid the pain caused by the suction electrode, an electrode with adhesive gel was introduced. Silver (Ag) or silver chloride (AgCl) electrodes are the most typical and preferred electrodes used in clinical ECG measurements nowadays for the recording of bio signals (Albulbul, 2016).

Holter's ECG is normally used to monitor patients with heart attacks or after surgery, in evaluating the pacemaker functionality or assessing the efficiency of the medicine. During the period of monitoring, the research subjects were prohibited to get wet, have X-rays or use an electric blanket when wearing the device (UW Health, 2016). In addition, the research subjects were also required to keep a distance from high-voltage areas, electromagnetic fields or metal detectors.

As medical technology advanced, Applied Biomedical Systems BV and AliveCor Inc. invented a handheld ECG device called MyDiagnostick and Kardia Mobile respectively (Desteghe et al., 2017). MyDiagnostick is a rod-like device with electrodes at both ends as illustrated in Figure 3 used for ECG recordings and atrial fibrillation detection. The subject is required to hold the electrodes with both hands for one minute. MyDiagnostick has a USB connector at one end for ECG records to enable the transfer of the readings from the device to a computer. Kardia Mobile is required to connect with a mobile phone that has

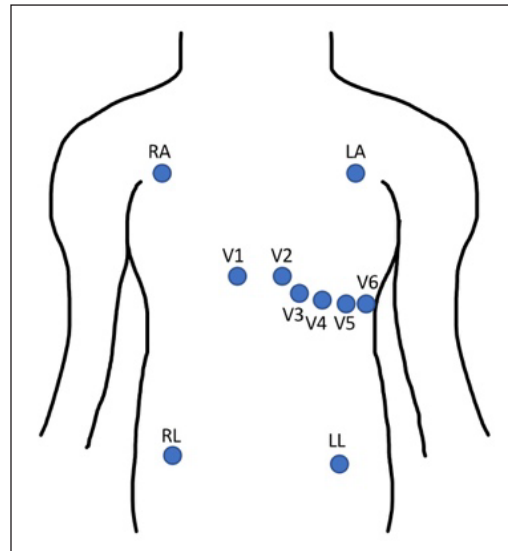


Figure 2. Mason-Likar leads position for the ten electrodes to form a twelve-leads ECG system

the Kardia app installed. Kardia Mobile was invented for single channel ECG recordings, atrial fibrillation detection, heart rhythm diagnosis and the HBR measurement (AliveCor Inc., 2017). The subject is required to place two or more fingers of both hands on the electrodes at both sides of the Kardia Mobile for at least thirty seconds. The other product which can be used for measuring the ECG is Apple Watch Series 4, 5 and 6. However, this feature is not yet available for all the countries.

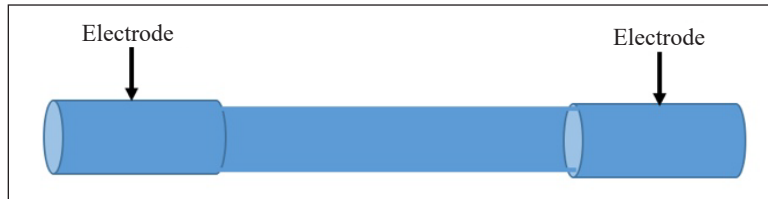


Figure 3. MyDiagnostick designed by Applied Biomedical System BV has electrodes at both end of sides

The ECG is a powerful method for the monitoring of heart activities. Hence, many researchers have built their own circuit for ECG signals extraction. From the peak-to-peak interval of the ECG signals, the HBR can be measured. The main drawback of the ECG is the subject requires contact with the electrodes to obtain the measurements. Therefore, it is very inconvenient.

Oscillometric Method

Oscillometric method is normally used in an automated electronic blood pressure measurement device that consists of inflatable cuff, pressure transducer, circuitry for signals conditioning, analog to digital converter, microcontroller and liquid crystal display (LCD) (Drzewiecki, 2003). Table 3 shows the evolution of the blood pressure measurement

Table 3
The Evolution of Oscillometric Method

Year	Research(s)	Technics	Remarks
1855	Karl von Vierordt	First sphygmograph	Can record the arterial pulsation for blood pressure measurement (Kapse & Patil, 2013).
1860	Etienne Jules Marey	Marey's sphygmograph	Improved the multi-levered and bulky version of Vierordt's sphygmograph and can record the velocity and waveform of the arterial pulsation on a graphical paper by immersing the whole arm inside a glass chamber that filled with water (Kapse & Patil, 2013).
1876	Etienne Jules Marey	Oscillometric method	He observed that the pressure in the cavity was fluctuated when he placed the whole arm inside a pressure cavity and noticed that the pressure fluctuation actually was varied with the amplitude of his pulsation (Geddes, 1991). This amplitude can be used to measure the blood pressure.

techniques. To date, the oscillometric method is still widely used to record the pulsation oscillation but the instrument has been improved by changing the mechanical components to electronic components that can automatically interpret and analyse the pulsation signals.

Although the oscillometric method was mainly developed for the measurement of blood pressure, it can also be used to measure the PR due to the transducer in the inflatable cuff which can sense the oscillation of the pulsation. The oscillometric device normally records the oscillation of the pulsations either by the inflating or deflating of the cuff. The recorded raw pulsation signals are amplified and filtered with a signal conditioning circuitry to separate the pulsation signals. Subsequently, pulsation signals are converted from the analog to digital form. Since the oscillometric device directly measures the arterial pulsation oscillation, the peak-to-peak intervals of the digitized pulsation signals are used for the calculation of the pulse rate (Yamakoshi et al., 2014). The calculated PR is displayed on the LCD.

Typically, three types of automatic oscillometric devices are available in the market i.e., upper arm, wrist, or finger oscillometric device. According to the guideline of the European Society of Hypertension, the upper arm oscillometric device is the most reliable device for the measurement of blood pressure and the PR (Parati et al., 2008) as the brachial artery of upper arm is the main supplier of blood from the arm to the finger. Besides that, the heart is the same level with the upper arm and hence, is able to provide more accurate reading. However, any movement during the pulsation recording causes the results to be rendered inaccurate. Since the automatic oscillometric device is easy to operate, it is widely used for self-health monitoring at home.

Photoplethysmography

Photoplethysmography (PPG) is derived from the word's "photo" and "plethysmography", where photo implies the optical ability and plethysmography represents the measurement of the volumetric changes (Lemay et al., 2014). The PPG measures the HBR by detecting the changes of blood volume within the human cardiovascular system through the application of an optical technique (Allen, 2007). The heart is the core organ and aims to circulate blood throughout the body. Blood contains haemoglobin which is capable of absorbing the radiation of optics. Thus, the variation of blood volume influences the intensity of the remittance spectra as the vascular circuit is illuminated by a light source. By measuring these variations, the timing of cardiovascular events can be examined and it is a valuable information for computing the PR. In view of this relation, the PPG method was developed. The subsequent establishment of contact conventional PPG technique and the recent development of non-contact-based PPG technique are discussed below.

Contact Based Photoplethysmography (PPG)

Pulse oximeter is a typical medical device that applies the PPG method in continuously acquiring the patient's PR in the hospital. Initially, it was innovated to observe the oxygen levels of the human blood. It also has the ability to detect the cardiovascular pulse waves, which propagates via the human microvascular. The PPG signals also conveys PR data that is computed by analysing the PPG either using time domain analysis (time interval between two consequent peaks in the PPG waveform) or frequency domain analysis (PPG spectral analysis by detecting the highest frequency peak) (Zhang, 2015).

With reference to the Beer-Lambert law shown as Equation 1 (Gastel et al., 2016), the principle of pulse oximeter is formed.

$$I = I_0 e^{-\varepsilon(\lambda)cd} \quad [1]$$

where I_0 implies the utilised light source intensity, ε considers the examined substance's specific molar extinction coefficient, λ represents the particular wavelength, c indicates the examined substance's concentration and d depicts the optical path length. I indicates the intensity of the transmitted light.

In compliance with the Beer-Lambert law, the absorbance of the examined substance is directly proportionate to the specific molar extinction coefficient of the examined substance, the concentration of the examined substance and the optical path length. Thus, the equation for calculating the test substance absorbance can be formed as Equation 2 with rearranging Equation 1. A is the absorbance of test substance.

$$A = \ln \frac{I}{I_0} = -\varepsilon(\lambda)cd \quad [2]$$

According to the definition of the Beer-Lambert law, when the light sources illuminate the clamped finger in the pulse oximeter, the light transmits through the skin of the finger and is absorbed by the entire substance of the finger. The substances of the human finger can be broadly grouped into two categories, which are termed as the pulsatile (AC) component (i.e., arterial blood) and the non-pulsatile (DC) components (i.e., muscle, bone, tissues, and venous blood). The AC component is the only substance that performs and varies with time, as it is influenced by the pulsation. Hence, the AC component is intensely affected by the cardiac cycle and undergoes rhythmic small variations based on the amount of absorbed light. Whilst the light being absorbed by the DC components is almost consistent with time, the change maybe very minute as the concentration of haemoglobin amount varies. Typically, the amount of light absorbed by the DC components is assumed to be same to ease the calculation of the pulse oximeter during the cardiac cycle. For the HBR calculation, the time interval from the peak to peak of the PPG signal is adopted. Figure 4

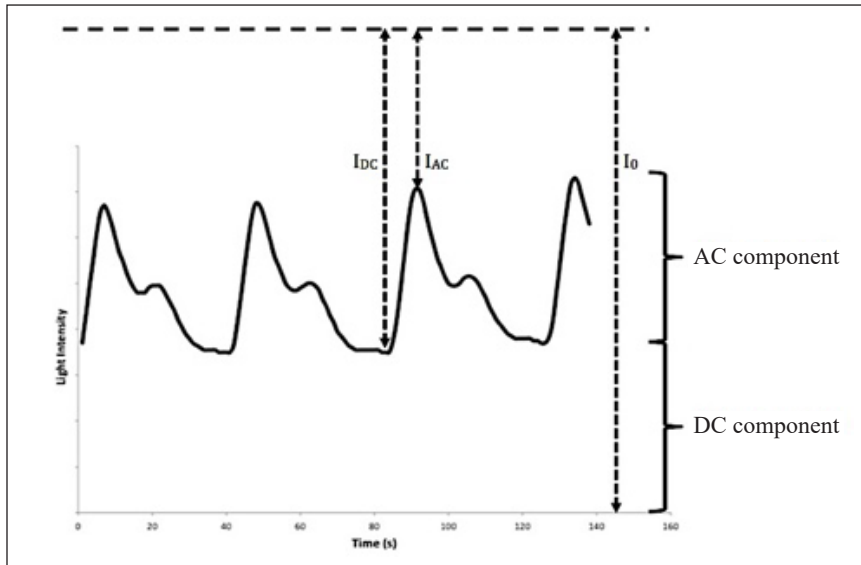


Figure 4. The obtained PPG signal from pulse oximeter with specific wavelength

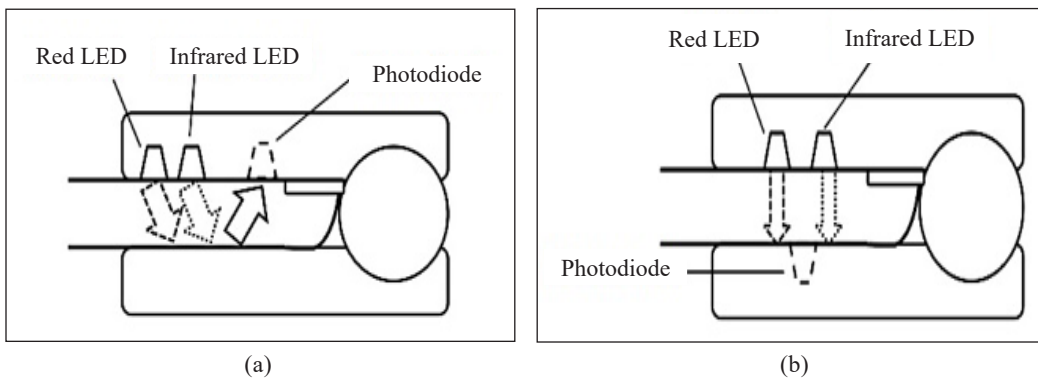


Figure 5. (a) Reflectance; and (b) Transmission type of pulse oximeter

describes the PPG signal, which is obtained from pulse oximeter with specific wavelength. It shows that the upper part of the PPG signal represents the AC component, whereas the lower part of the signal implies the DC components.

In most cases, the pulse oximeter comprises of two light sources (infrared light at 840 nm and red light at 660 nm) to illuminate the human body tissue and a photo-detector to detect the light intensities that re-emit from the human tissue. After the light intensities are collected, they are filtered by a band pass filter circuitry. Subsequently, these filtered signals are digitalized and a microprocessor is implemented to process the signals for the cardiac output measurements. Nowadays, there are generally two types of pulse oximeter available in the market; a reflectance type and a transmission type, as shown in Figure 5 (Laurent et al., 2005). For a reflectance type pulse oximeter, the light sources are attached on the

body tissue surface and placed adjacent with the photo-detector. Within the transmission type pulse oximeter, the photo-detector and light sources are positioned opposite with the body tissue in between.

The development of PPG started in the early 1936 and its early progress is summarised in first four rows of Table 4. For the next two decades, the bulky, heavy, motion sensitive

Table 4
The Development of PPG Technic

Year	Research (s)	Technics	Remarks
1936	Researchers of Stanford and New Jersey	Non-invasive optical method	Initiated the development of non-invasive optical method to examine the blood volumetric variations in rabbit ears (Lemay et al., 2014)
1937	Alrick Hertzman	PPG technique	Published his first finding on measuring human blood volumetric changes from tissues with PPG technique (Alian & Shelley, 2014)
1939	Karl Matthes and Franz Gross	Red and infrared wavelength in PPG technic	Used red and infrared wavelengths to PPG signals and compared their performances (Laurent et al., 2005). The ear prove was introduced to record PPG signals.
1942	Glen Millikan	Ear oximeter	The word 'oximeter' was officially employed and he introduced the ear oximeter, which is a reduced weight of Matthes and Gross's ear probe (Severinghaus, 2007)
1971	Takuo Aoyagi	Dye dilution method in Ear Oximeter	Takuo Aoyagi from Nikon Kohden Company attempt to use dye dilution method for increasing the accuracy of the ear oximeter in measuring cardiovascular events (Aoyagi, 1992)
1975	Nihon Kohden Company	Ear pulse oximeter OLV-5100	Commercialized the first ear pulse oximeter OLV-5100 with incandescent light, photocells and filters to acquire PPG waveform generated by arterial pulse for determining SpO ₂ based on Aoyagi's concept (Severinghaus, 2014)
1981, 1983	Biox and Nellcor Inc.	Pulse oximeter Ohmeda Biox 3700 (Ear probe) and Nellcor N-100 (Finger probe)	Developed and commercialized the pulse oximeter Ohmeda Biox 3700 (with flexible ear probe) (Ohmeda, 1986) and Nellcor N-100 (with flexible finger probe) (Mahgoub et al., 2015). They are the initial pulse oximeter adopted red and infrared LEDs (Ohmeda Biox 3700-wavelength 660nm and 940nm; Nellcor N-100-wavelength 670nm and 940nm), a photodiode and a microcomputer for cardiac output measurements.
1990	Nonin Medical Inc.	Hand-held pulse oximeter	Attributed the next evolution of pulse oximeter by manufactured a portable hand-held pulse oximeter model 8500 (Nonin Medical Inc.,2014).
1991	Nonin Medical Inc.	Fiber Optic sensor	Innovated the pulse oximeter with the fiber optic sensor (Nonin Medical Inc.,2014).
1992	Takuo Aoyagi	Dye of Indocyanine Green (ICG)	Used for cardiac output measurement because ICG has been approved by Food and Drug Administration (FDA) in 1959 for medical diagnostics due to its low toxicity to human health (Sinagra & Dip, 2015).
1995, 2004	Nonin Medical Inc.	Fingertip pulse oximeter	Invented the fingertip pulse oximeter Onyx Model 9500 and Onyx II Model 9550 with Bluetooth and wireless technology correspondingly (Nonin Medical Inc., 2014)

galvanometer and light source used in the ear oximeter still had a limited usage in the medical field. Until 1962, the advancements in semiconductor technology i.e., photodiode, phototransistor and light emitting diode (LED) contributed greatly in reducing the size, increasing the sensitivity and reliability of the oximeter for the PPG measurements (Lemay et al., 2014). According to Aoyagi (1992), the optical density for blood with ICG is determined at wavelength of 805 nm while the blood optical density for blood can only be measured at wavelength of 900 nm. Based on the calculation of the ratio of these two wavelengths, the cardiac output, which is the amount of blood pumped by the heart in a minute is measured. The subsequent evolutions of PPG are summarised in Table 4.

Compared to the finger, the forehead is nearer to the heart and thus, the cardiac output responses are closer relative to the heart rhythms. In addition, the vascular bed in the forehead has blood which is supplied by the supraorbital artery, whereas the finger only involves a capillary bed (Man-Son-Hing, 1968). Therefore, it is validated that the forehead is one of the most apt locations for measuring human physiological parameters.

Due to the rapid growth of the photonic technology, the advancement of the PPG technique is established. Currently, several manufacturers have invented wrist-worn devices to measure the HBR. Shcherbina et al. (2017) had studied and evaluated the accuracies of seven commercial wrist-worn devices, which include the Apple Watch, Samsung Gear S2, Microsoft Band, Fitbit Surge, PulseOn, Basis Peak and Mio Alpha 2. According to the findings, the Apple Watch accomplished the highest accuracy for the measurement of the PR. The Apple Watch is the first product launched by Apple Inc. in year 2014 which is competent in measuring the PR using the PPG signals. To date, Apple has launched up to series 6 of the Apple Watch which is now not only capable in measuring both the PR and the ECG but also the blood oxygen level. However, the measurement of ECG and blood oxygen levels is only available in certain countries. The first Apple Watch series 4 which is able to measure the PR and ECG is shown in Figure 6. In general, the Apple Watch

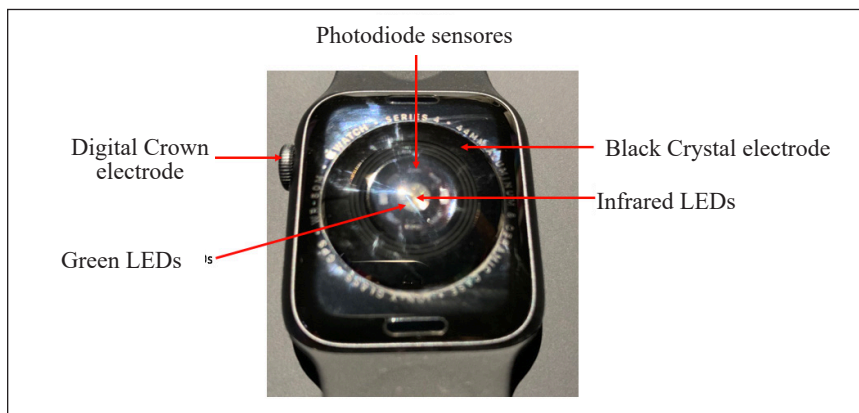


Figure 6. Apple Watch adopts green LEDs or Infrared LEDs and photodiode for PR measurement and Back crystal electrode and digital crown electrode for ECG measurement

utilizes green and infrared lights paired with photodiodes to collect the light intensities for measuring the volume changes of blood around the wrist (Apple Inc., 2020). The infrared light is only applicable for measuring the PR in the background. As the infrared light is insufficient, green light is used for enhancing the light source. Moreover, the brightness of the lights is auto-adjustable based on the detected signal levels.

As a concluding summary from the reviews, the PPG is certified as one of the most outstanding methods to measure the PR and numerous devices have been invented using this technology. Even though the PPG technique is widely implemented for a clinical setting to measure and monitor the physiological parameters, the sensors of the devices i.e., photo sensors and light sources are required to be directly attached on the human skin. This contact basis of the PPG device has created inconvenience for the patients, particularly those with skin problems. In comparison, the recently developed non-contact PPG technology is highly potent for resolving these inconveniences.

Photoplethysmography (PPG) Imaging

With references to the fundamental theory of PPG, engineers and researchers found that the pigmentation of the human skin is feasible in interacting with light. The high advancements of video and video imaging techniques have facilitated the exploration of the video imaging usages by researchers within the health care industries. Video sensors was adopted to replace the photodiode in acting as a photo-detector in collecting the remittance spectra of the skin with both contact and non-contact theory in early 2000s. Its performance in measuring the PR was very promising.

The technology of non-contact PPG imaging had crucially progressed in 2010 when Poh et al. (2010) initiated the utilisation of the built-in webcam in the MacBook Pro for measuring the PR of 12 participants by recording their video images. Investigations were conducted indoor with varying amount of sunlight as the light source. In order to remotely capture the subjects' face for analysis, the webcam was located 0.5 m away from the subjects. The duration of the video recording process was 60 seconds at the rate of 15 fps. In processing, the video signals were processed using 30 seconds moving window with 1 second interval increment. This was the first study which pioneered the blind source separation (BSS) method to reduce the motion artefact from the video signals before it is ready to measure the PR. The BSS method from the Independent Component Analysis (ICA) was implemented by Poh et al. (2010). The ICA aims to separate the signal source mixture into independent components. Once the signals are separated, the power spectrum of the independent component that has the highest Signal to Noise Ratio (SNR) was utilised for computing the HBR while the frequency of the highest peak within 0.75 – 4 Hz was adopted for the PR measurement. The results indicated that the algorithm with the BSS method had higher accuracy than the algorithm without BSS method.

According to Poh et al. (2010), despite used the ICA to reduce the motion artefacts, the pulse frequency computation may occasionally be affected by noise. In order to solve this issue, researchers utilize the past estimations of the pulse frequency by setting a threshold of 12 bpm. If the difference between the current PR estimation and the previous computed PR exceeds the threshold, the algorithm rejects the frequency corresponding to the highest power by searching for the next frequency with the highest power until the threshold is met. If there are no frequencies that meet the threshold, the algorithm remains at the current pulse frequency estimation. Since this method is based on the previous history of PR estimation, once the estimated PR has a false value, it might possibly lead to inaccurate results.

Based on the literature review, the motion artefacts are found as the critical issue for acquiring the HBR out of the non-contact-based PPG imaging signals. Hence, the ICA is still extensively implemented presently for selecting the most noticeable PPG signal in measuring the HBR. According to van der Kooji & Naber (2019), researchers still utilised the ICA for extracting the best signal component of the filtered RGB colour channels to extract the HBR. While the ICA is the well-known approach for the HBR extraction of remote PPG signals, Macwan et al. (2018) enhanced the conventional ICA formulation by augmenting the ICA algorithm using chrominance-based constraints and autocorrelation to a flexible and systematic manner. Macwan et al. (2018) noticed that the enhanced ICA algorithm is feasible in obtaining the most periodic component, which represents the blood volume pulse. Therefore, the obtained signal is consistently nearer to those of the PPG signal which is significant for evaluating the HBR.

Khong et al. (2016) is another study used the built-in 720p FaceTime HD Camera on a MacBook Pro to record video images for PR analysis. Khong et al. (2016) recorded the video in RGB colour mode at the frame rate of 30 fps with pixel resolution of 845 x 480 pixels. The duration of the video images was 1 minute with participants who were seated approximately 0.5 metres in front of the camera. For the light sources, the natural light and fluorescent light were selected to illuminate the participants for the PR measurement. In the study of Khong et al. (2016), only green coloured channels of the video signals were used for the PR extraction and the region of interest was the forehead of the participants. For the video pre-processing step, the researchers normalized the video signals and filtered the video signals with the cut-off frequencies of 0.7 to 4 Hz. This range of frequency was selected because it is the range of PR for a normal person. Subsequently, Khong et al. (2016) used a 6-seconds sliding window to segment the 1 minute of video signals. The time interval between the sliding window was 0.5 seconds. Each of the segmented 6 seconds video signals was transformed to PSD using FFT for estimating the PR. In other words, the researchers estimated the PR measurement every 6 seconds of the video signals.

As a concluding remark, the majority of the available research implemented the frequency domain analysis for measuring the PR except Khong et al. (2017) who utilised

the time domain analysis of the video images for estimating the HBR. Khong et al. (2017) had presented a research for measuring human blood pressure with the non-contact video image processing techniques. In addition, the researchers also showed that analysing the 10 seconds video signals with the time domain analysis is feasible to extract the PR data. From the findings of Khong et al. (2017), it shows that the time domain analysis enables not only the measurement of PR but blood pressure as well.

Other than the consumer level webcam and digital camera, the feasibility of using the smartphone camera in measuring physiological parameters had also been researched. Kwon et al. (2012) utilised the front camera of an iPhone 4 for the remote recording of facials of 10 subjects separately from 0.3m distance to measure their PR. These videos were recorded at the rate of 30 fps for a minute. During the video recording process, the subjects were requested to sit still and stare at the middle of the screen. As an illumination condition, the investigation was conducted indoors with sufficient sunlight. Kwon et al. (2012) had utilised the algorithm of Poh et al. (2010) with MATLAB software for processing the recorded video. Since the researchers acquired a clearer frequency using the highest peak signal of the raw green colour channel, the researchers also concluded that obtaining raw signals of the green colour channel has better performance over those of the ICA approach in selecting the apt component for the PR measurement. Even though the algorithm developed by Kwon et al. (2012) had not yet been implemented in the smartphone, it is validated that the quality of the embedded smartphone camera is competent for capturing the essential signal for the PR measurement.

The camera of smartphone can be used to possibly capture the video images remotely for the PR measurement; it is also able to collect the video images in contact basis for the PR measurement. The researchers of Sukaphat et al. (2016) successfully developed an android application to measure the PR from the subject's fingertip that was gently placed on the embedded camera. As the illumination source, the flashlight of the smartphone was used during the video recording process. From these studies, the researchers proved that the processor and camera on the smartphone nowadays are already sufficient to process video signals for the PR measurement. Since the mobile device is more portable, user friendly and popular, its usage for estimating more physiological parameters should be explored in the future. If the developed application can extract multiple physiological parameters at a non-contact basis, it will be very constructive because contact-based concept device limits the mobility and working ability of the subject. Furthermore, if the finger pressure applied on the camera lens is inappropriate, it could also lead to inaccurate results. From the reviews, the studies that used PPG imaging techniques for the PR measurement are summarised in Table 5.

As a concluding summary of these reviews, a majority existing of studies have utilized the spectral analysis to extract the PR from the captured videos. Generally, the

Table 5
Summary of the studies using PPG imaging technique for HBR measurement

Study & Year	Camera	Light Source	ROI	Contact	Remarks
Zheng & Hu (2007); Hu et al. (2008)	Consumer level digital camera	LED (660 nm, 840/870 nm and 905/940 nm)	Finger	No	- Only obtain PPG signals
Takano & Ohta (2007)	Consumer level digital camera	Ambient Light	Cheek	No	- Frequency domain spectral analysis
Verkruysse et al. (2008)	Consumer level digital camera	Ambient Light	Facial	No	- Frequency domain spectral analysis
Poh et al. (2010); Lewandowska et al. (2011)	Webcam	Ambient Light	Facial	No	- Implemented BSS method - Frequency domain spectral analysis
Kwon et al. (2012)	Smartphone front camera	Ambient Light	Facial	No	- Implemented BSS method - Frequency domain spectral analysis
Sukaphat et al. (2016)	Smartphone Camera	Flashlight	Finger	Yes	- Android based
Zhao et al. (2013)	Near-infrared enhanced Camera	Ambient & LED 830 nm	Facial	No	- Implemented BSS method - Frequency domain spectral analysis
Macwan et al. (2018)	Webcam	Fluorescent & Ambient light	Facial	No	- Implemented BSS method - Frequency domain spectral analysis
Tarassenko et al. (2014)	Digital video camera	Fluorescent & Ambient light	Facial	No	- Implemented Auto-regressive model and pole cancellation - Frequency domain spectral analysis
Khong et al. (2016)	Webcam	Fluorescent & Ambient light	Facial	No	- Frequency domain spectral analysis
Khong et al. (2017)	Webcam	Fluorescent & Ambient light	- Facial - Chest	No	- Time domain spectral analysis
van der Kooji & Naber (2019)	Webcam	Fluorescent light	- Facial - Wrist - Calf	No	- Implemented Improved Semi BSS method - Frequency domain spectral analysis
Gudi et al. (2020); Perepelkina et al. (2020); Zhan et al. (2020)	Webcam / Video Datasets	Video Datasets	- Facial	No	- Implemented learning-based method CNN for better signal acquisition - Time domain spectral analysis

main downside of using the spectral analysis is the necessary choosing of the correct peak frequency for representing the HBR. Hence, researchers have suggested the time domain analysis to be used for processing the signals of video in measuring the PR and it is also suitable in measuring the blood pressure. For choosing the right signal of the video, both the raw green colour channel or applied BSS method are also capable in providing the accurate PR estimations. Yet, Zhao (2016) also stated that BSS method is highly complex and heavy computation is required particularly when the captured signals have been mixed with many independent sources. Therefore, many studies had abandoned the BSS method and only implemented the raw green colour channel for estimating the PR. Based on the reviews, it can be concluded that the videos which are captured under the light sources with specific wavelength (i.e., natural ambient light or fluorescent light) are also adequate in providing the PR measurement.

ISSUES AND CHALLENGES

Although the ECG, the oscillometric method and the PPG, either in contact or non-contact methods, have been used to obtain the HBR, these methods have its own advantages and challenges. When there is a challenge, there will be an opportunity to come up with a solution to counter it. Hence, Table 6 illustrates the advantages and challenges of the respective methods for measuring the HBR. Furthermore, the possible solutions to counter the challenges are shown in Table 6 for future development so that a more convenient, simple, comfortable and accurate method can be applied to obtain the HBR measurement.

Table 6
Advantages, challenges and the solutions of HBR measurement methods

Methods	Advantages	Challenges	Solution
ECG	Non-invasive, reliable and standard method for diagnosing heart activities (Serhani et al., 2020)	Users have to learn the method to operate the monitoring device and placement of electrodes (Aljuaid et al., 2020)	Embedded the electrodes in T-shirts or bed sheets (Bianchi et al., 2010)
		Discomfort or skin irritation in measuring HBR due to the adhesive gel electrodes attachment (Karaoguz et al., 2019)	Developed washable textile electrodes (Ankhill et al., 2018). However, further research is required for the design of wearable devices
		ECG signal quality because it is measured in millivolts and contaminates with noises such as powerline interference, baseline wander, motion artifacts, and electromyographic noise (Kher & Vidyanagar, 2019)	Require efficient filtering and amplifying techniques (Mohaddes et al., 2020)

Table 6 (continue)

Methods	Advantages	Challenges	Solution
		Only one person's reading can be taken at the same time	This challenge is still unsolved.
Oscillometric method	Non-invasive and can measure blood pressure as well	Intermittent measurement not suitable for continuous HBR measurement (Kebe et al., 2020)	This challenge is still unsolved. PPG method is more comfortable way for continuous HBR measurement (Tjahjadi et al., 2020)
		Readings are very sensitive to the posture of the body and arm, motion artifacts (Forouzanfar et al., 2015)	This challenge is still unsolved. However, advance the filtering techniques can help in reducing the effect of motion artifacts and identifying the true pulsation (Forouzanfar et al., 2015).
		Only one person's reading can be taken at the same time	This challenge is still unsolved.
PPG (contact)	Non-invasive and simple to use (Castaneda et al., 2018)	Contact based with wired sensors might cause the discomforts	Non-contact based of using 2 dimensional image matrix for PR measurement (Tamura, 2019).
		Susceptible to motion artifacts caused by movements (Castaneda et al., 2018)	The time and frequency domain signals are filtered mathematically and statistically to eliminate the low frequency of motion artifacts for the signals (Tamura, 2019).
		Insufficient or excessive contact force will influence the quality of the PPG signals (Tamura, 2019).	Correction factors have been proposed to compensate the contact force for a PPG signal but this factor has wide variations among individuals. Hence, a miniaturized thermo-pneumatic type force regulator was designed to regulate the contact force (Sim et al., 2018).
		Infrared light penetrates deeper into the skin but its low intensity has little pulsatile action (Tamura, 2019).	Developed high-power LED and enabled use of green light has better results in a pulsatile action (Tamura, 2019).
		Typically worn on the fingers because of its high signal amplitude can be obtained. However, it is not perfect suited for continuous sensing because the involvement of the fingers in most daily activities (Tamura, 2019).	Wearable PPG devices on different measurement site have been developed. Wristwatch-type PPG device has been developed recently (Tamura, 2019).
		Only one person's reading can be taken at the same time	This challenge is still unsolved.

Table 6 (continue)

Methods	Advantages	Challenges	Solution
PPG (non-contact)	Non-invasive, non-contact mode for long distance measurements and possible to obtain multiple person's HBR at the same time (Tamura, 2019).	Motion artifacts (Sinhal et al., 2020)	Applied BSS method to remove the temporal noise source caused by motion artifacts (Deng & Kumar, 2020).
		Ambient light illumination (Sinhal et al., 2020)	Recent studies also explore the functions of the individual R, G and B color channels for normalizing the color of the illumination (Deng & Kumar, 2020).
		Compressed video for faster processing might lose the information resulting in an inaccurate PR estimation (Sinhal et al., 2020)	Optimized the images before measuring the PR (Sinhal et al., 2020)
		Video images are being captured with multiband spectrum, so it is challenging to identify the suitable spectrum for signal estimation (Sinhal et al., 2020)	Many contemporary studies focus on analysing the visible light spectrum (Sinhal et al., 2020)
		To obtain multiple persons' readings at the same time	Apply face tracking algorithm for multiple person's readings
		Signal quality in leading inaccurate PR measurements (Perepelkina et al., 2020)	Apply learning-based method can enhance the signal quality (Gudi et al., 2020, Zhan et al., 2020 and Perepelkina et al., 2020)

Recently, other problems such as a decreased in the SNR of the PPG signals for the dark skin and aging skin has arisen. This is due to the fact that the number of melanocytes in thinner skin and wrinkles can change the optical properties of skin. Learning-based methods have been designed to learn which sections in the image correspond to the PR. This method does not require any prior knowledge and it will learn the PPG mechanism from scratch. Gudi et al. (2020), Zhan et al. (2020) and Perepelkina et al. (2020) are the recent researchers who used the learning-method of convolution neural network (CNN) to detect the PPG signal from video. The proposed learning-based method can not only accurately estimate the PR from the PPG signals but its performance can be improved by increasing the size of the training set for adapting to various skin conditions such as dark skin and ageing skin. By implementing the learning-based method, the PPG signal quality can be improved by avoiding making the false decision when an invalid PR is extracted from

the untrustworthy PPG signals. However, the disadvantage of the learning-based method is that it requires a large training set and significant computation time when dealing with complex models. Since the PPG analysis is based on a signal processing task, the use of a trainable system with no prior knowledge gives opportunity for efficiency improvement because previous studies already revealed that the PR signal is embedded in average skin colour changes.

CONCLUSION

The HBR refers to the speed of the heartbeats. It is one of the most essential vital signs in indicating the general state of health of a person. For instance, cardiac arrhythmia is detected by examining the HBR. To date, there are three typical methods used for determining the HBR, i.e., ECG, the oscillometric method and PPG. The ECG has been termed as the gold standard for the HBR measurement because it directly measures the HBR from the heart. Although the ECG method is non-invasive and reliable, the users have to learn to operate the monitoring device and the placement of electrodes. Furthermore, the adhesive gel electrodes can cause discomfort and irritation to the skin. Hence, the oscillometric method has been introduced to measure the PR when the measurement of blood pressure is taken. Yet, the oscillometric method is not suitable for long term continuous HBR measurements. Among these three methods, the contact-based PPG technique is extensively applied in medical institutes for continuous monitoring of the PR of a patient due to its aptness. With references to the existing research and techniques, it has been noticed that the PPG method is the only technique that is excellent not only for contact based, but also the non-contact-based method for the purpose of monitoring the PR. Even though the non-contact PPG method has not yet grown maturely, it has high potential to be applied in the remote healthcare industry. In addition, the non-contact PPG imaging method is also highly potent for measuring other vital physiological parameters. From this review, it clearly clarifies that the current trend of the measuring of the HBR has evolved from a contact-based method towards a non-contact-based method especially during this emerging area in video technology. Furthermore, the learning-based method also helps in improving the signal quality for a better extraction of HBR measurements. Lastly, the issues, challenges and solutions have also been summarised in this paper.

ACKNOWLEDGEMENT

The authors would like to acknowledge those who contributed to make this publication successful. The authors also would like to acknowledge the support of Faculty of Engineering and Research & Innovation Management Centre, Universiti Malaysia Sabah under the SLB research grant, grant no. SLB0188-2019 and School of Engineering, Monash University Malaysia.

REFERENCES

- 3M Health Care. (2002). *History of Stethoscopes*. 3M Health Care.
- Albulbul, A. (2016). Evaluating major electrode types for idle biological signal measurements for modern medical technology. *Bioengineering*, 3(20), 1-10. <https://doi.org/10.3390/bioengineering3030020>
- Alghatrif, M., & Lindsay, J. (2012). A brief review: History to understand fundamentals of electrocardiography. *Journal of Community Hospital Internal Medicine Perspectives*, 2, 1-5. <https://doi.org/10.3402/jchimp.v2i1.14383>.
- Alian, A. A., & Shelley, K. H. (2014). Photoplethysmography. *Best Practice & Research Clinical Anaesthesiology*, 28(4), 395-406. <https://doi.org/10.1016/j.bpa.2014.08.006>.
- AliveCor Inc. (2017). *Meet kardia mobile: Your personal EKG*. Retrieved March 2, 2017, from <https://www.alivecor.com/>.
- Aljuaid, M., Marashly, Q., AlDanaf, J., Tawhari, I., Barakat, M., Barakat, R., Zobell, B., Cho, W., Chelu, M. G., & Marrouche, N. F. (2020). Smartphone ECG monitoring system helps lower emergency room and clinic visits in post-atrial fibrillation ablation patients. *Clinical Medicine Insights: Cardiology*, 14, 1-7. <https://doi.org/10.1177/1179546820901508>.
- Allen, J. (2007). Photoplethysmography and its application in clinical physiological measurement. *Physiological Measurement*, 28(3), 1-39. <https://doi.org/10.1088/0967-3334/28/3/R01>.
- Ankhill, A., Tao, X., Cochrane, C., Coulon, D., & Koncar, V. (2018). Washable and reliable textile electrodes embedded into underwear fabric for electrocardiography (ECG) monitoring. *Materials*, 11(2), 1-11. <https://doi.org/10.3390/ma11020256>.
- Aoyagi, T. (1992). Pulse oximetry: Its origin and development. In *Proceedings of the 14th Annual International Conference of the IEEE Engineering in Medicine and Biology Society* (pp. 2858-2859). IEEE Conference Publication. <https://doi.org/10.1109/IEMBS.1992.5761726>
- Apple Inc. (2020). *Monitor your heart rate with apple watch*. Retrieved December 24, 2020, from <https://support.apple.com/en-my/HT204666>.
- Bianchi, A. M., Mendez, M. O., & Cerutti, S. (2010). Processing of signals recorded through smart devices: Sleep-quality assessment. *IEEE Transactions on Information Technology in Biomedicine*, 14(3), 741-747. <https://doi.org/10.1109/TITB.2010.2049025>.
- Bowbrick, S., & Borg, A. N. (2006). *ECG complete*. Elsevier.
- Burch, V. G., & DePasquale, J. M. (1990). *Development of the contact electrode, a history of electrocardiography*. Norman Publishing.
- Castaneda, D., Esparza, A., Ghamari, M., Soltanpur, C., & Nazeran, H. (2018). A review on wearable photoplethysmography sensors and their potential future applications in health care. *International Journal of Biosensors & Bioelectronics* 4(4), 195-202. <https://doi.org/10.15406/ijbsbe.2018.04.00125>.
- Deng, Y., Kumar, A. (2020). Standoff heart rate estimation from video: A review. In *Mobile Multimedia/Image Processing, Security, and Applications 2020* (Vol. 11399, p. 1139906). International Society for Optics and Photonics. <https://doi.org/10.1117/12.2560683>.

- Desteghe, L., Raymaekers, Z., Lutin, M., Vijgen, J., Dilling-Boer, D., Koopman, P., Schurmans, J., Vanduyndhoven, P., Dendale, P., & Heidbuchel, H. (2017). Performance of handheld electrocardiogram devices to detect atrial fibrillation in a cardiology and geriatric ward setting. *Europace*, *19*, 29-39. <https://doi.org/10.1093/europace/euw025>.
- Drzewiecki, G. (2003). Noninvasive arterial blood pressure and mechanics. In J. D. Bronzino (Ed.), *Clinical engineering: Principles and applications in engineering series* (pp. 15-16). CRC Press.
- Fisch, C. (2000). Centennial of the string galvanometer and the electrocardiogram. *Journal of the American College of Cardiology*, *36*(6), 1737-1745. [https://doi.org/10.1016/S0735-1097\(00\)00976-1](https://doi.org/10.1016/S0735-1097(00)00976-1).
- Fleming, P. R. (1997). The beginnings of clinical science: 1860-1900. In *A short history of cardiology* (pp. 106-127). Brill Rodopi.
- Forouzanfar, M., Dajani, H. R., Groza, V. Z., Bolic, M., Rajan, S., & Batkin, I. (2015). Oscillometric blood pressure estimation: Past, present, and future. *IEEE Reviews in Biomedical Engineering*, *8*, 44-63. <https://doi.org/10.1109/RBME.2015.2434215>.
- Fye, W. B. (1994). A history of the origin, evolution, and impact of electrocardiography. *The American Journal of Cardiology*, *73*(13), 937-949. [https://doi.org/10.1016/0002-9149\(94\)90135-x](https://doi.org/10.1016/0002-9149(94)90135-x).
- Gargiulo, G. D. (2015). True unipolar ECG machine for Wilson central terminal measurements. *BioMed Research International*, *2015*, 1-7. <https://doi.org/10.1155/2015/586397>.
- Gastel, M. V., Stuijk, S., & de Haan, G. (2016). New principle for measuring arterial blood oxygenation, enabling motion-robust remote monitoring. *Scientific Reports*, *6*(38609), 1-16. <https://doi.org/10.1038/srep38609>.
- Geddes, L. A. (1991). *Handbook of blood pressure measurement*. Springer Science.
- Geddes, L. A., & Wald, A. (2000). Retrospectroscope: Horatio B Williams and the first electrocardiographs made in the United States. *IEEE Engineering in Medicine and Biology*, *19*(5), 117-121. <https://doi.org/10.1109/51.870240>.
- Ghasemzadeh, N., & Zafari, A. M. (2011). A brief journey into the history of the arterial pulse. *Cardiology Research and Practice*, *2011*, 1-15. <https://doi.org/10.4061/2011/164832>.
- Gudi, A., Bittner, M., & Gemert, J. (2020). Real-time webcam heart-rate and variability estimation with clean ground truth for evaluation. *Applied Sciences*, *10*, 1-24. <https://doi.org/10.3390/app10238630>.
- Hashem, M. M. A., Shams, R., Kader, M. A., & Sayed, M. A. (2010). Design and development of a heart rate measuring device using fingertip. In *Proceedings of the International Conference on Computer and Communication Engineering* (pp. 1-5). IEEE Conference Publication. <https://doi.org/10.1109/ICCCE.2010.5556841>
- Hu, S., Zheng, J., Chouliaras, V., & Summers, R. (2008). Feasibility of imaging photoplethysmography. In *Proceedings of the International Conference on BioMedial Engineering and Informatics* (pp. 72-75). IEEE Conference Publication. <https://doi.org/10.1109/BMEI.2008.365>
- Kapse, C. D., & Patil, B. R. (2013). Auscultatory and oscillometric methods of blood pressure measurement: A Survey. *International Journal of Engineering Research and Applications*, *3*(2), 528-533.

- Karaoguz, M. R., Yurtseven, E., Aslan, G., Deliormanli, B. G., Adiguzel, O., Gonen, M., Li, K. M., & Yilmza, E. N. (2019). The quality of ECG data acquisition, and diagnostic performance of a novel adhesive patch for ambulatory cardiac rhythm monitoring in arrhythmia detection. *Electrocardiology*, *54*, 28-35. <https://doi.org/10.1016/j.jelectrocard.2019.02.012>.
- Kastor, J. A. (2002). *Encyclopedia of life sciences*. Macmillan Publishers Ltd, Nature Publishing Group.
- Katz, L. N., & Hellerstein, H. K. (1982). *Circulation of the blood: Men and Ideas*. Springer.
- Kebe, M., Gadhafi, R., Mohammad, B., Sanduleanu, M., Saleh, H., & Al-Qutayri, M. (2020). Human vital signs detection methods and potential using radars: A review. *Sensors*, *20*(5), 1-38. <https://doi.org/10.3390/s20051454>.
- Kher, R., & Vidyanagar, V. (2019). Signal processing techniques for removing noise from ECG signals. *Journal of Biomedical Engineering and Research*, *3*(101), 1-7. <https://doi.org/10.17303/jber.2019.3.101>.
- Khong, W. L., & Mariappan, M. (2019). The evolution of heart beat rate measurement techniques from contact based photoplethysmography to non-contact based photoplethysmography imaging. In *Proceedings of IEEE International Circuits and Systems Symposium* (pp. 1-4). IEEE Conference Publication. <https://doi.org/10.1109/ICSys47076.2019.8982534>
- Khong, W. L., Rao, N. S. V. K., & Mariappan, M. (2017). Blood pressure measurements using non-contact video imaging techniques. In *Proceedings of the 2nd International Conference on Automatic Control and Intelligent Systems* (pp. 35-40). IEEE Conference Publication. <https://doi.org/10.1109/I2CACIS.2017.8239029>
- Khong, W. L., Rao, N. S. V. K., Mariappan, M., & Nadarajan, M. (2016). Analysis of heart beat rate through video imaging techniques. *Journal of Telecommunication, Electronic and Computer Engineering*, *8*(11), 69-74.
- Krikler, D. M. (1983). Wolff-Parkinson-White syndrome: Long follow-up and an anglo-american historical note. *Journal of the American College of Cardiology*, *2*(6), 1216-1218. [https://doi.org/10.1016/S0735-1097\(83\)80353-2](https://doi.org/10.1016/S0735-1097(83)80353-2).
- Kwon, S., Kim, H., & Park, K. S. (2012). Validation of heart rate extraction using video imaging on a built-in camera system of a smartphone. In *Proceedings of 34th Annual International Conference of the IEEE EMBS* (pp. 2174-2177). IEEE Conference Publication. <https://doi.org/10.1109/EMBC.2012.6346392>
- Laurent, C., Jonsson, B., Vegfors, M., & Lindberg, L. G. (2005). Non-invasive measurement of systolic blood pressure on the arm utilising photoplethysmography: Development of the methodology. *Medical & Biological Engineering & Computing*, *43*, 131-135. <https://doi.org/10.1007/BF02345134>.
- Lemay, M., Bertschi, M., Sola, J., Renevey, P., Parak, J., & Korhonen, I. (2014). *Wearable sensors: Fundamentals, implementation and applications*. Elsevier Inc.
- Leng, S., Tan, R. S., Chai, K. T. C., Wang, C., Ghista, D., & Zhong, L. (2015). The electronic stethoscope. *BioMedical Engineering OnLine*, *14*(66), 1-37. <https://doi.org/10.1186/s12938-015-0056-y>.
- Lewandowska, M., Ruminski, J., Kocejko, T., & Nowak, J. (2011). Measuring pulse rate with a webcam – A non-contact method for evaluating cardiac activity. In *Proceedings of the Federated Conference on Computer Science and Information Systems* (pp. 405-410). IEEE Conference Publication.

- Macwan, R., Benezeth, Y., & Mansouri, A. (2018). Remote photoplethysmography with constrained ICA using periodicity and chrominance constraints. *BioMedical Engineering Online*, 17(22), 1-22. <https://doi.org/10.1186/s12938-018-0450-3>.
- Madihally, S. V. (2010). *Principles of biomedical engineering*. Arctect House.
- Mahgoub, M. T. A., Khalifa, O. O., Sidek, K. A., & Khan, S. (2015). Health monitoring system using pulse oximeter with remote alert. In *Proceedings of International Conference on Computing, Control, Networking, Electronics and Embedded Systems Engineering* (pp. 357-361). IEEE Conference Publication. <https://doi.org/10.1109/ICCNEEE.2015.7381391>
- Man-Son-Hing, C. T. (1968). The diagnosis of treatable cerebrovascular disease. *Canadian Family Physician*, 14(9), 23-25.
- Mohaddes, F., da Silva, R. L., Akbulut, F. P., Zhou, Y., Tanneeru, A., Lobaton, E., Lee B., & Misra, V. (2020). A pipeline for adaptive filtering and transformation of noisy left-arm ECG to its surrogate chest signal. *Electronics*, 9(866), 1-17. <https://doi.org/10.3390/electronics9050866>.
- Nonin Medical Inc. (2014). *A global leader in noninvasive medical monitoring innovations*. Nonin Medical Inc.
- Ohmeda. (1986). *Ohmeda biox 3700 pulse oximeter operating / Maintenance manual*. BOC Health Care.
- Parati, G., Stergiou, G. S., Asmar, R., Bilo, G., de Leeuw, P., Imai, Y., Kario, K., Lurbe, E., Manolis, A., Mengden, T., O'Brien, E., Ohkubo, T., Padfield, P., Palatini, P., Pickering, T., Redon, J., Revera, M., Ruilope, L. M., Shennan, A., ... & Mancia, G. (2008). European society of hypertension guidelines for blood pressure monitoring at home: A summary report of the second international consensus conference on home blood pressure monitoring. *Journal of Hypertension*, 26(8), 1505-1526. <https://doi.org/10.1097/HJH.0b013e328308da66>.
- Perepelkina, O., Artemyev, M., Churikova, M. & Grinenko, M. (2020). HeartTrack: Convolution neural network for remote video-based heart rate monitoring. In *IEEE/CVF Conference on Computer Vision and Pattern Recognition Workshops* (pp. 1163-1171). IEEE Conference Publication.
- Poh, M. Z., McDuff, D. J., & Picard, R. W. (2010). Non-contact, automated cardiac pulse measurement using video imaging and blind source separation. *Optics Express*, 18(10), 10762-10774. <https://doi.org/10.1364/OE.18.010762>.
- Roguin, A. (2006). Rene theophile hyacinthe laennec (1781-1826): The man behind the stethoscope. *Clinical Medicine & Research*, 4(3), 230-235. <https://doi.org/10.3121/cmr.4.3.230>.
- Serhani, M. A., Kassabi, H. T. E., Ismail, H., & Navaz, A. N. (2020). ECG monitoring systems: Review, architecture, processes, and key challenges. *Sensors*, 20(1796), 1-40. <https://doi.org/10.3390/s20061796>.
- Severinghaus, J. W. (2007). Takuo aoyagi: Discovery of pulse oximetry. *International Anesthesia & Analgesia*, 105(6), 1-4. <https://doi.org/10.1213/01.ane.0000269514.31660.09>.
- Severinghaus, J. W. (2014). *The wondrous story of anesthesia*. Springer.
- Shcherbina, A., Mattsson, C. M., Waggott, D., Salisbury, H., Christle, J. W., Hastie, T., Wheeler, M. T., & Ashley, E. A. (2017). Accuracy in wrist-worn, sensor-based measurements of heart rate and energy expenditure in a diverse cohort. *Journal of Personalized Medicine*, 7(3), 1-12. <https://doi.org/10.3390/jpm7020003>.

- Sim, J. K., Ahn, B., & Doh, I. (2018). A contact-force regulated photoplethysmography (PPG) platform. *AIP Advances*, 8, 1-7. <https://doi.org/10.1063/1.5020914>.
- Sinagra, D., & Dip, F. (2015). *Technological advances in surgery, trauma, and critical care*. Springer.
- Sinhal, R., Singh, K., Raghuwanshi, M. M. (2020). *Computer vision and machine intelligence in medical image analysis, advances in intelligent systems and computing*. Springer Nature Singapore Pte Ltd.
- Srinivasan, N. T., & Schilling, R. J. (2018). Sudden cardiac death and arrhythmias. *Arrhythmia & Electrophysiology Review*, 7(2), 111-117. <https://doi.org/10.15420/aer.2018:15:2>.
- Sukaphat, S., Nanthachaiyorn, S., Upphaccha, K., & Tantipatrakul, P. (2016). Heart rate measurement on android platform. In *Proceedings of the 13th International Conference on Electrical Engineering/Electronics, Computer, Telecommunications and Information Technology* (pp. 1-5). IEEE Conference Publication.
- Takano, C., & Ohta, Y. (2007). Heart rate measurement based on a time-lapse image. *Medical Engineering & Physics*, 29(8), 853-857. <https://doi.org/10.1016/j.medengphy.2006.09.006>.
- Tamura, T. (2019). Current progress of photoplethysmography and SPO2 for health monitoring. *Biomedical Engineering Letters*, 9, 21-36. <https://doi.org/10.1007/s13534-019-00097-w>.
- Tarassenko, L., Vilarroel, M., Guazzi, A., Jorge, J., Clifton, D. A., & Pugh, C. (2014). Non-contact video-based vital sign monitoring using ambient light and auto-regressive models. *Physiological Measurement*, 35(5), 807-831. <https://doi.org/10.1088/0967-3334/35/5/807>.
- Tjahjadi, H., Ramli, K., & Murfi, H. (2020). Noninvasive classification of blood pressure based on photoplethysmography signals using bidirectional long short-term memory and time-frequency analysis. *IEEE Engineering in Medicine and Biology Society Section*, 8, 20735-20748. <https://doi.org/10.1109/ACCESS.2020.2968967>.
- UW Health. (2016). *Holter monitoring: A guide to help you get ready*. University of Wisconsin-Madison.
- van der Kooji, K. M., & Naber, M. (2019). An open-source remote heart rate imaging method with practical apparatus and algorithms. *Behavior Research Methods*, 51, 2106-2119. <https://doi.org/10.3758/s13428-019-01256-8>.
- Verkruysse, W., Svaasand, L. O., & Nelson, J. S. (2008). Remote plethysmographic imaging using ambient light. *Optics Express*, 16(26), 21434-21445. <https://doi.org/10.1364/oe.16.021434>.
- Yamakoshi, T., Matsumura, K., Rolfe, P., Hanaki, S., Ikarashi, A., Lee, J., & Yamakoshi, K. I. (2014). Potential for health screening using long-term cardiovascular parameters measured by finger volume-oscillometry: Pilot comparative evaluation in regular and sleep-deprived activities. *IEEE Journal of Biomedical and Health Informatics*, 18(1), 28-35. <https://doi.org/10.1109/JBHI.2013.2274460>.
- Yang, X. L., Liu, G. Z., Tong, Y. H., Yan, H., Xu, Z., Chen, Q., Liu, X., Zhang, H. H., Wang, H. B., & Tan, S. H. (2015). The history, hotspot, and trends of electrocardiogram. *Journal of Geriatric Cardiology*, 12(4), 448-456. <https://doi.org/10.11909/j.issn.1671-5411.2015.04.018>.
- Zhan, Q., Wang, W., & de Haan, G. (2020). Analysis of CNN-based remote-PPG to understand limitations and sensitivities. *Biomedical Optics Express*, 11(3), 1268-1283. <https://doi.org/10.1364/BOE.382637>.

- Zhang, Z. (2015). Photoplethysmography-based heart rate monitoring in physical activities via joint sparse spectrum reconstruction. *IEEE Transactions on Biomedical Engineering*, 62(8), 1902-1910. <https://doi.org/10.1109/TBME.2015.2406332>.
- Zhao, F., Li, M., Qian, Y., & Tsein, J. Z. (2013). Remote measurements of heart and respiration rates for telemedicine. *PLoS ONE*, 8(10), 1-14. <https://doi.org/10.1371/journal.pone.0071384>.
- Zhao, Y. (2016). An improved method for blind source separation. In *Proceedings of the International Conference on Applied Mechanics, Electronics and Mechatronic Engineering* (pp. 1-5). DEStech Publications, Inc. <https://doi.org/10.12783/dtetr/ameme2016/5786>
- Zheng, J., & Hu, S. (2007). The preliminary investigation of imaging photoplethysmographic system. *Journal of Physics: Conference Series*, 85, 1-4. <https://doi.org/10.1088/1742-6596/85/1/012031>.

Application of Cubature Information Filter for Underwater Target Path Estimation

Guduru Naga Divya* and Sanagapallea Koteswara Rao

Department of Electronics and Communication Engineering, Koneru Lakshmaiah Education Foundation, Vaddeswaram, Guntur, AP, India

ABSTRACT

Bearings-only tracking plays a pivotal role in passive underwater surveillance. Using noisy sonar bearing measurements, the target motion parameters (TMP) are extensively estimated using the extended Kalman filter (EKF) because of its simplicity and low computational load. The EKF utilizes the first order approximation of the nonlinear system in estimation of the TMP that degrades the accuracy of estimation due to the elimination of the higher order terms. In this paper, the cubature Kalman filter (CKF) that captures the system nonlinearity upto third order is proposed to estimate the TMP. The CKF is further extended using the information filter (IF) to provide decentralized data fusion, hence the filter is termed as cubature information filter (CIF). The results are generated using Matlab with Gaussian assumption of noise in measurements. Monte-Carlo simulation is done and the results demonstrate that the CIF accuracy is same as that of UKF and this indicates the usefulness of the algorithm for state estimation in underwater with the required accuracy.

Keywords: Bearings-only tracking, cubature Kalman filter, information filter, state estimation, stochastic signal processing

INTRODUCTION

Surveillance is the most significant feature of maritime warfare. The observer submarine is in waters doing their surveillance job. The observer moves at low speeds such that it

does not radiate much noise during tracking of the target. Passive target tracking is the calculation of target's trajectory merely from measurements of signals emerging from the target. These signals could be machinery noise from a target and its detection is usually indicated by an increase in energy above the ambient at certain bearing. Passive

ARTICLE INFO

Article history:

Received: 07 December 2020

Accepted: 01 April 2021

Published: 19 July 2021

DOI: <https://doi.org/10.47836/pjst.29.3.07>

E-mail addresses:

nagadivya.guduru@gmail.com (Guduru Naga Divya)

rao.sk9@gmail.com (Sanagapallea Koteswara Rao)

* Corresponding author

mode helps the observer from not being tracked by the target ship. Observer equipped with hull mounted sonar can pick up the radiated noise of target and can generate bearing measurement of the target. This process is called 'bearings-only target tracking' (BOT).

In BOT process, only one type of measurement namely bearing measurements are available and there are two components of range that is in x and y directions, speed and course to be estimated. Hence the process becomes unobservable for most scenarios. So, observer has to carry out maneuver, for observability of the process and to estimate target motion parameters (TMP) (Koteswararao, 2018). Often observer has to carry out number of S-maneuvers to obtain the estimated TMP with the desired accuracy, whenever measurements are corrupted with high noise.

Tracking process in underwater environment contains dynamic perturbations like time to time change in the environment, velocity of the vehicle, self-noise of the observer and so on. These disturbances or noises that are internal or external to the observer affect the performance of hull mounted array of the sonar and other transducers generating the target and observer measurements. In other words, the target bearing generated is inaccurate and corrupted with noise. The observer contains gyro and log generate observer course and speed respectively. These measurements are also contaminated with noise. However, smoothing of these course and speed measurements is trivial and so this is not covered in this research manuscript.

From the available noisy information, obtaining the information of target regarding its velocity and range with respect to the observer is called target motion analysis (TMA) and in passive listening mode is most popularly called 'Bearings-only target tracking (BOT)'. This is an active research since decades and researchers are trying to a) improve the accuracy in estimated solution using various signal processing algorithms b) generate less complex, easy to implement, less convergence time procedures and so on.

The classical estimator with respect to nonlinear processes is extended Kalman filter (EKF). However, EKF is unreliable for BOT, as in-depth knowledge regarding plant noise and Jacobian of measurement dynamic process are not sufficient. Recently proposed unscented Kalman filter (UKF) (Wan & Van Der Merwe, 2000) and cubature Kalman filter (CKF) (Arasaratnam & Haykin, 2009; Ding & Balaji, 2012) are Jacobian-free filters available to nullify the disadvantages of the EKF.

CKF is the recently developed nonlinear filtering algorithm based on spherical radial cubature rule. CKF has strong mathematical basis in the selection of cubature points and numerical stability than UKF. The computational load using CKF is relatively lower as it uses only $2*L_1$ (L_1 is the dimension of the system) cubature points and UKF uses $2*L_1+1$ sigma points to propagate the state and covariance. When the dimension of the nonlinear system is greater than 3, there is a chance that the chosen sigma points may be negative which render the negative covariance matrix definite whereas cubature points in CKF are

positive indicating the positive definiteness of the covariance matrix. Hence CKF algorithm is considered for this BOT application. Its extension, cubature information filter (CIF) (Pakki et al., 2011; Arasaratnam & Chandra, 2015; Jiang & Cai, 2018) is used such that it is suitable for nonlinear process and at the same time for the implementation of data available from multiple sensors. (In future if measurements are available from passive sonar, periscope, and active radar/sonar, CIF is very much useful for multi sensor data fusion configuration.)

Kalman filter processes all the sensors measurements' centrally to obtain the solution thereby incurring high computational load on the digital computer. Therefore, the information filter is proposed, as it can be extended straight to design multi-sensor fusion algorithms and the computations are also simple than the conventional Kalman filter. Also the initialization of information filter (IF) is simple as it is independent of the system priori state. While determining the inverse of a high dimension augmented matrix, the digital computer may fail which is a big drawback of centralized fusion. The data fusion algorithms can be implemented efficiently in a decentralized way using IF. In comparison to the traditional centralized data fusion algorithms, the decentralized structure is more powerful and efficient in terms of computation and communication (Mutambara, 1998).

In information filter (IF), information state vector and information matrix play an important role. The inverse of the covariance matrix is named as information matrix (IM). The information state vector (ISV) is the product of the IM and the target state vector. In EKF, the target state vector and its covariance matrix are propagated in time domain recursive processing. In IF, the concept of EKF's recursive propagation is applied to IM and ISV which is termed as extended information filter (EIF). EIF is combined with CKF algorithm, named as cubature information filter (CIF) is applied to BOT and the same can be applied in future for multi-sensor applications. The details about CIF are given next section.

Mathematical modeling, design and implementation in Matlab of CIF are carried out as per the requirements of BOT. Initialization of state vector and its covariance matrix are chosen such that the algorithm works for all scenarios. Simulator is developed to feed various tactical scenarios. Simulator also generate the true TMP and observer position. Performance of the algorithm is evaluated against several scenarios in Monte-Carlo simulation. Acceptance criterion is chosen based on some particular weapon guidance and accordingly the convergence of the solution is calculated. The results for one typical scenario is presented.

The aim of this research work is to estimate TMP like range, course, speed and smoothed bearing as early as possible in sea environment. Once target path is estimated, the weapon can be released on to the target. The measurements are assumed to be available from observer's hull mounted sonar. The block diagram of TMP is shown in Figure 1. Further, TMP is used to calculate weapon pre-set parameters for releasing weapon on to a target.

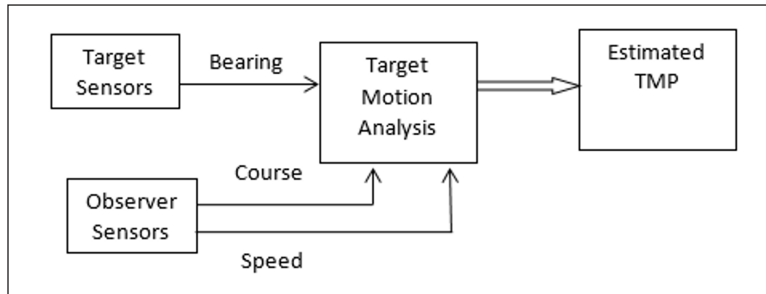


Figure 1. Block diagram of target motion parameters

MATHEMATICAL MODELLING

Target State Equation

In BOT, the target-observer scenario is modelled mathematically based on following assumptions. Initially, the observer is located at (0,0) and the target is located at position P at some range as shown in Figure 2.

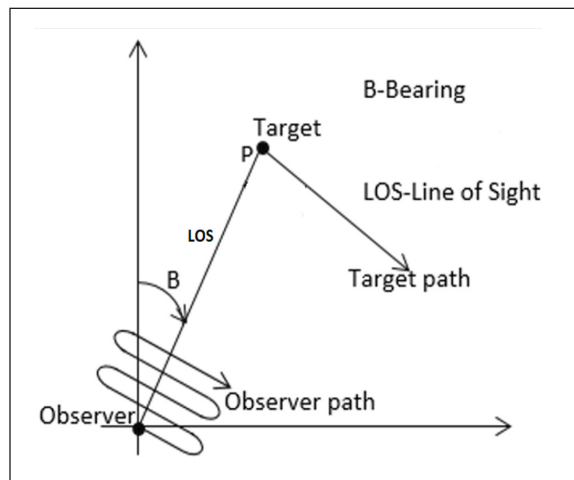


Figure 2. Target and Observer movements

The observer and target are assumed to be heading with constant course and speed. The target's relative state vector (X_s) in Cartesian coordinates w.r.t. observer at input sample (Γ_{st}) is represented as Equation 1.

$$X_s(\Gamma_{st}) = [\dot{r}_x(\Gamma_{st}) \quad \dot{r}_y(\Gamma_{st}) \quad r_x(\Gamma_{st}) \quad r_y(\Gamma_{st})]^T \quad [1]$$

Where $\dot{r}_x(\Gamma_{st})$, $\dot{r}_y(\Gamma_{st})$, $r_x(\Gamma_{st})$, $r_y(\Gamma_{st})$ are the components of speed and range in x and y coordinates respectively at input sample number Γ_{st} . The subsequent instant relative state vector based on the current instant ($X_s(\Gamma_{st} + 1, \Gamma_{st})$) is given by Equation 2.

$$X_s(\Gamma_{st} + 1, \Gamma_{st}) = A(\Gamma_{st} + 1, \Gamma_{st})X_s(\Gamma_{st}) + N_g\varepsilon(\Gamma_{st}) \quad [2]$$

Where $A(\Gamma_{st} + 1, \Gamma_{st})$ is matrix representing the system dynamics given as Equation 3.

$$A(\Gamma_{st} + 1, \Gamma_{st}) = \begin{bmatrix} 1 & 0 & 0 & 0 \\ 0 & 1 & 0 & 0 \\ t & 0 & 1 & 0 \\ 0 & t & 0 & 1 \end{bmatrix} \quad [3]$$

Where ‘t’ represents the interval at which samples are obtained. $\varepsilon(\Gamma_{st})$ is the system noise that is assumed to obey Gaussian distribution having mean=0 and covariance Q . The system noise gain matrix (N_g) is given in matrix form as Equation 4.

$$N_g = \begin{bmatrix} t & 0 \\ 0 & t \\ t^2/2 & 0 \\ 0 & t^2/2 \end{bmatrix} \quad [4]$$

The system noise covariance (Q) is given in matrix form as Equation 5.

$$Q(\Gamma_{st}) = \sigma^2 \begin{bmatrix} t^2 & 0 & t^3/2 & 0 \\ 0 & t^2 & 0 & t^3/2 \\ t^3/2 & 0 & t^4/4 & 0 \\ 0 & t^3/2 & 0 & t^4/4 \end{bmatrix} \quad [5]$$

Where σ^2 is system noise variance.

Measurement Equation

The measured bearing angle b_m is given by Equation 6.

$$b_m(\Gamma_{st} + 1) = \tan^{-1} \left(\frac{r_x(\Gamma_{st}+1)}{r_y(\Gamma_{st}+1)} \right) \quad [6]$$

The measurement model equation (Z) at sample $\Gamma_{st} + 1$ is specified by Equation 7.

$$Z(\Gamma_{st} + 1) = H(\Gamma_{st} + 1)X_s(\Gamma_{st} + 1) + \varkappa_b \quad [7]$$

Where H is the matrix representation of the relationship between X_s and Z . The \varkappa_b is the noise of the measurement. Here the assumption is that the measurement noise follows Gaussian/uniform distribution, with variance σ_b^2 .

The measurement vector $Z(\Gamma_{st})$ is given by Equation 8.

$$Z(\Gamma_{st}) = b_m(\Gamma_{st}) \quad [8]$$

This tracking problem, the aim is to estimate the state vector $X_s(\Gamma_{st})$, from a set of measurements $Z(\Gamma_{st}) = [z(1)z(2) \dots z(\Gamma_{st})]^T$.

Cubature Kalman Filter Algorithm

For many practical applications, the use of EKF is not the best option, as it works well only in a ‘mild’ nonlinear environment and can therefore degrade efficiency. The CKF is the nearest known Bayesian approximation to the nonlinear system with the Gaussian assumption. CKF doesn’t require Jacobian evaluation making it attractive for state estimation. The steps in CKF are organized in two sections i.e. prediction and updation as given below.

Prediction

1. The sigma points are calculated using Equation 9.

$$X_s(i, \Gamma_{st}) = m(\Gamma_{st}) + \sqrt{P(\Gamma_{st})}\chi(i) \quad i = 1, \dots, 2L_1 \tag{9}$$

Where $m(\Gamma_{st})$ and $P(\Gamma_{st})$ is the mean and covariance at input sample number Γ_{st} and L_1 is the dimension of the system. The unit sigma points $\chi(i)$ are defined as Equation 10.

$$\chi(i) = \begin{cases} \sqrt{L_1}e_i, i = 1, \dots, 2L_1 \\ -\sqrt{L_1}e_{i-L_1}, i = n + 1, \dots, 2L_1 \end{cases} \tag{10}$$

where e_i denotes a unit vector in the direction of the coordinate axis i .

2. The sigma points are propagated through the dynamic model as in Equation 11.

$$\hat{X}_s(i, \Gamma_{st} + 1) = A(X_s(i, \Gamma_{st} + 1)), \quad i = 1, \dots, 2L_1 \tag{11}$$

3. The predicted mean $m(\Gamma_{st} + 1, \Gamma_{st})$ and the predicted covariance $P(\Gamma_{st} + 1, \Gamma_{st})$ are calculated using Equations 12 and 13.

$$m(\Gamma_{st} + 1, \Gamma_{st}) = \frac{1}{2L_1} \sum_{i=1}^{2L_1} \hat{X}_s(i, \Gamma_{st} + 1) \tag{12}$$

$$P(\Gamma_{st} + 1, \Gamma_{st}) = \frac{1}{2L_1} \sum_{i=1}^{2L_1} (\hat{X}_s(i, \Gamma_{st} + 1) - m(\Gamma_{st} + 1, \Gamma_{st}))(\hat{X}_s(i, \Gamma_{st} + 1) - m(\Gamma_{st} + 1, \Gamma_{st}))^T + Q(\Gamma_{st}) \tag{13}$$

Updation

1. The sigma points are formed as Equation 14.

$$X_s(i, \Gamma_{st} + 1, \Gamma_{st}) = m(\Gamma_{st} + 1, \Gamma_{st}) + \sqrt{P(\Gamma_{st} + 1, \Gamma_{st})} \chi(i), \quad i = 1, \dots, 2L_1 \quad [14]$$

Where the unit sigma points are defined as in Equation 9.

2. Sigma points are propagated through the measurements model as Equation 15.

$$\hat{Z}(i, \Gamma_{st} + 1) = H(X_s(i, \Gamma_{st} + 1, \Gamma_{st})), \quad i = 1 \dots 2L_1 \quad [15]$$

3. The predicted mean $\mu(\Gamma_{st} + 1)$, the predicted covariance of the measurement $P_{XX}(\Gamma_{st} + 1)$, and the cross-covariance of the state and the measurement $P_{XZ}(\Gamma_{st} + 1)$ are calculated using Equation 16-18.

$$\mu(\Gamma_{st} + 1) = \frac{1}{2L_1} \sum_{i=1}^{2L_1} \hat{Y}(i, \Gamma_{st} + 1) \quad [16]$$

$$P_{XX}(\Gamma_{st} + 1) = \frac{1}{2L_1} \sum_{i=1}^{2L_1} (\hat{Z}(i, \Gamma_{st} + 1) - \mu(\Gamma_{st} + 1)) (\hat{Z}(i, \Gamma_{st} + 1) - \mu(\Gamma_{st} + 1))^T + Q(\Gamma_{st} + 1) \quad [17]$$

$$P_{XZ}(\Gamma_{st} + 1) = \frac{1}{2L_1} \sum_{i=1}^{2L_1} (X(i, \Gamma_{st} + 1, \Gamma_{st}) - m(\Gamma_{st} + 1, \Gamma_{st})) (\hat{Z}(i, \Gamma_{st} + 1) - \mu(\Gamma_{st} + 1))^T \quad [18]$$

4. The filter gain $K(\Gamma_{st} + 1)$ and the filtered state mean $m(\Gamma_{st} + 1)$ and covariance $P(\Gamma_{st} + 1)$ are calculated using Equations 19-21.

$$K(\Gamma_{st} + 1) = P_{XX}(\Gamma_{st} + 1) P_{XZ}^{-1}(\Gamma_{st} + 1) \quad [19]$$

$$m(\Gamma_{st} + 1) = m(\Gamma_{st} + 1, \Gamma_{st}) + K(\Gamma_{st} + 1) [Z(\Gamma_{st} + 1) - \mu(\Gamma_{st} + 1)] \quad [20]$$

$$P(\Gamma_{st} + 1) = P(\Gamma_{st} + 1, \Gamma_{st}) - K(\Gamma_{st} + 1) P_{XZ}(\Gamma_{st} + 1) K^T(\Gamma_{st} + 1) \quad [21]$$

Information Filter

The mathematical modeling of the information filter is given as follows and the detailed explanation for the filter is given in (Pakki et al., 2011).

The information state vector is represented by IX_s , at time index Γ_{st} is given by Equation 22.

$$IX_s(\Gamma_{st}) = IM(\Gamma_{st} + 1, \Gamma_{st}) * X_s(\Gamma_{st} + 1, \Gamma_{st}) \quad [22]$$

Where IM is given as Equation 23.

$$IM(\Gamma_{st} + 1, \Gamma_{st}) = (P(\Gamma_{st} + 1, \Gamma_{st}))^{-1} \quad [23]$$

By substituting the covariance from EIF (Pakki et al., 2011), Equation 22 is given as Equation 24.

$$IM(\Gamma_{st} + 1, \Gamma_{st}) = [A(\Gamma_{st})(IM(\Gamma_{st} + 1, \Gamma_{st} + 1))^{-1}A(\Gamma_{st}) + Q(\Gamma_{st})]^{-1} \quad [24]$$

where $P(\Gamma_{st} + 1, \Gamma_{st})$ is predicted covariance matrix

$Q(\Gamma_{st})$ is covariance of plant noise

$A(\Gamma_{st})$ is transition matrix

The updated information state vector, $IX_s(\Gamma_{st} + 1, \Gamma_{st} + 1)$, and the updated information matrix, $IM(\Gamma_{st} + 1, \Gamma_{st} + 1)$, are given by Equations 25 and 26.

$$IX_s(\Gamma_{st} + 1, \Gamma_{st} + 1) = IX_s(\Gamma_{st} + 1, \Gamma_{st}) + i(\Gamma_{st}) \quad [25]$$

$$IM(\Gamma_{st} + 1, \Gamma_{st} + 1) = IM(\Gamma_{st} + 1, \Gamma_{st}) + I(\Gamma_{st}) \quad [26]$$

Where (Equations 27 and 28)

$$i(\Gamma_{st}) = IM(\Gamma_{st} + 1, \Gamma_{st})P_{xy}(\Gamma_{st} + 1, \Gamma_{st})Q^{-1}(\Gamma_{st})[v(\Gamma_{st}) + P_{xy}^T(\Gamma_{st} + 1, \Gamma_{st})IM^T(\Gamma_{st} + 1, \Gamma_{st})IX_s(\Gamma_{st} + 1, \Gamma_{st})] \quad [27]$$

$$I(\Gamma_{st}) = IM(\Gamma_{st} + 1, \Gamma_{st})P_{xy}(\Gamma_{st} + 1, \Gamma_{st})Q^{-1}(\Gamma_{st})P_{xy}^T(\Gamma_{st} + 1, \Gamma_{st})IM(\Gamma_{st} + 1, \Gamma_{st}) \quad [28]$$

Where the measurement residual, $v(\Gamma_{st})$, is given by Equation 29.

$$v(\Gamma_{st}) = Z(\Gamma_{st}) - \hat{Z}(\Gamma_{st}) \quad [29]$$

Cubature Information Filter

The updated state vector and the updated information matrix obtained from Equations 25 and 26 are used to update the state and covariance obtained from Equations 16-18. Hence the state and covariance using CIF are obtained as follows.

The updated state vector and covariance matrix can are given by Equations 30 and 31.

$$X_s(\Gamma_{st} + 1, \Gamma_{st}) = IM(\Gamma_{st} + 1, \Gamma_{st} + 1)IX_s(\Gamma_{st} + 1, \Gamma_{st} + 1) \quad [30]$$

$$P(\Gamma_{st} + 1, \Gamma_{st} + 1) = IM(\Gamma_{st} + 1, \Gamma_{st} + 1) \quad [31]$$

The performance of the CIF is compared with the standard filter unscented Kalman Filter (UKF). For the detailed mathematical modeling of UKF refer (Wan & Van Der Merwe, 2000).

RESULTS AND DISCUSSION

In target tracking process, there appear two types of perturbations. The first type is self-noise of the observer and the environment. The second type is the difference between the process understood in mathematical modelling of the target's state and the real system dynamics. The source of error for the second type appears due to half knowledge about system nonlinearities and order of the models, plant noise variations due to environment and so on. For example, general assumption is that the target moves at constant velocity, with the disturbances in velocity considered as white noise having very small variance. It may not be true always in all circumstances, due to change in sea environment.

In general, in any modern sonar system, sophisticated hardware with state of art signal processing is used to reduce self-noise. During normal sea state conditions, number of field trials will be carried out to find out self-noise and environmental noise. The same will be used as the input measurement covariance matrix. All raw bearing measurements are corrupted by additive zero-mean Gaussian noise. Here bearing measurements are considered with respect to Y-axis, 0° - 360° and clockwise positive. The measurement interval is 1s i.e., at every second bearing measurement is available and the number of measurement samples taken for simulation is 800 samples. As the measurements are available at every second, the simulation time is taken as 800s. Also Monte- Carlo simulation is carried out to give the confidence of the CIF algorithm. The performance of the CIF algorithm with bearing measurements is evaluated for several geometries. Acceptance criteria gives the acceptable level of errors in estimated values. Only bearing measurement gives the information about the target and this bearing is corrupted with noise due to underwater environment. Hence the errors in the estimated parameters are only reduced using the filtering algorithms but cannot be removed 100%. So there is necessity to know how much error can be accepted in the estimate. This acceptable level of errors in estimates is called acceptance criterion. The acceptable level of errors in the estimated parameters is 3σ for single run and 1σ for 100 Monte-Carlo runs. Based on particular weapon guidance algorithm the acceptable errors are chosen in an estimated range, course and speed as less than or equal to 10% of true range, 5° and 1 m/s respectively for single run (3σ) and 3.33% of true range, 1.67° and 0.33 m/s respectively for 100 Monte-Carlo runs (1σ).

Initialization of State Vector

The following assumptions are made to estimate the target state vector initially as follows. There is no knowledge about the range measurement, the velocity components are initialized

as 5 m/s. Based on the Sonar range of the day the initial range is taken as 5000m. Hence the initial target state vector $X_s(0,0)$ is taken as Equation 32.

$$X_s(0,0) = [5 \quad 5 \quad 5000 \sin B_m(0) \quad 5000 \cos B_m(0)] \quad [32]$$

Initialization of Covariance Matrix

Assuming the initial state vector follows uniform density function, the initial covariance matrix $P(0,0)$ which is a diagonal matrix. These elements are given by Equation 33.

$$P(0,0) = \text{Diag}(4X_s^2(i)/12) \quad \text{where } i = 1,2,3,4 \quad [33]$$

Performance Evaluation of the Algorithm

The measurement is assumed to be available at each second. The turning rate of the observer in underwater is 0.5deg/s. The target is moving at constant velocity. The simulation study is done using Matlab on a personal computer. For making the process observable and thereafter to obtain TMA (i.e., range, course and speed of the target), in general, the observer carries out S-maneuver preferably on the line of sight in azimuth plane. Change in vehicle's course or speed or both is called maneuver. Here course maneuver is implemented as speed maneuver is not recommended due to tactics limitations. In general, one maneuver by observer attains observability of the process and is sufficient to generate solution with required accuracy, in normal sea state conditions. The algorithm is evaluated against numbers of scenarios. The scenarios chosen for the algorithm evaluation are tabulated Table 1. In Table 1, the scenarios are chosen in such a way to suit the real time environment. The initial range is chosen based on the Sonar range of the day. The detectable range of passive sonar vary from few meters to 10km depending on many parameters like ambient (background) noise and self-noise which is termed as Sonar range of the day. Also the homing range of the sophisticated torpedo is 3000m. So, keeping in mind these points the initial range of the target is moderately assumed to be around 4500m. The observer velocity is chosen so that there is less self-noise. Generally, a submarine is used for surveillance in underwater. The submarine can go at a maximum speed of 20knots (18 m/s). However, this will increase the self-noise very much. Tracking the target in passive mode is considered so that the observer is safe from being tracked by the target. There is necessity that the observer should move at lower speeds to reduce the self-noise. So the observer speed is initialized as 5 m/s. This also helps to get the observability of the target. The target course is taken such that the target is heading towards the bow of the observer. Initial bearing is taken such that the target is always heading towards bow of the observer and also for simplicity purpose all the initial bearing angles are taken such that they fall in

first quadrant. The standard deviation (S.D) of noise in the bearing measurement is taken as 0.17° i.e. the maximum error in the measurement is 0.5° .

Table 1
Scenarios chosen for evaluation

S. no.	Target range (m)	Observer speed (m/s)	Target speed (m/s)	Target course (deg)	Target bearing (deg)	S.D of noise in bearing (deg)
1	4500	9	11	165	20	0.17
2	5000	7	10	160	20	0.17
3	5000	7	10	170	20	0.17
4	4000	8	12	135	30	0.17
5	4500	9	11	160	40	0.17
6	5000	7	10	145	20	0.17

Note. S.D- standard deviation

For detailed discussion, let us consider scenario 5 in Table 1. A target ship is moving at 11m/s at a course of 160° , making an initial bearing angle of 40° with the observer. The initial range between the target and observer is 4500m. The observer moves at a speed of 9m/s. The bearing measurements are corrupted with white Gaussian noise whose standard deviations (S.D) are 0.17° . As per the acceptance criteria, the convergence times for single run and Monte-Carlo simulation using CIF and UKF for the scenarios of Table 1 are tabulated in Tables 2 and 3, respectively.

As per the acceptance criteria considered for single run, estimated range is said to be converged when the error in the range estimate is less than or equal to 10% of true range and never diverges thereafter in the period of simulation and the same procedure is followed for course and speed. So in the period of 800s simulation time using CIF, the range estimate error is less than or equal to 10% of true range at 247s first time and converged thereafter without any divergence. Similarly, the course estimate error is less than or equal to 5° at 327s first time and converged thereafter without any divergence and speed estimate error is less than or equal to 1 m/s at 304s first time and converged thereafter without any divergence. It means that the total solution is said to be converged at 327 seconds. Similarly using UKF, the range estimate error is less than or equal to 10% of true range at 196s first time and converged thereafter without any divergence. Similarly, the course estimate error is less than or equal to 5° at 328s first time and converged thereafter without any divergence and speed estimate error is less than or equal to 1 m/s at 307s first time and converged thereafter without any divergence. It means that the total solution is said to be converged at 328 seconds.

As per the acceptance criteria considered for single run, the estimated range is said to be converged when the error in the range estimate is less than or equal to 3.33% of true range and never diverges thereafter in the period of simulation and the same procedure

is followed for course and speed. So in the period of 800s simulation time using CIF, the range estimate error is less than or equal to 3.33% of true range at 267s first time and converged thereafter without any divergence. Similarly, the course estimate error is less than or equal to 1.67° at 351s first time and converged thereafter without any divergence and speed estimate error is less than or equal to 0.33 m/s at 344s first time and converged thereafter without any divergence. It means that the total solution is said to be converged at 351 seconds. Similarly, using UKF, the range estimate error is less than or equal to 3.33% of true range at 261s first time and converged thereafter without any divergence. Similarly, the course estimate error is less than or equal to 1.67° at 369s first time and converged thereafter without any divergence and speed estimate error is less than or equal to 0.33 m/s at 363s first time and converged thereafter without any divergence. It means that the total solution is said to be converged at 369 seconds.

Scenarios 1,4 and 5 converged faster using CIF (consider total convergence times from Monte-Carlo simulation) at 333, 375 and 351 seconds respectively whereas using UKF the same scenarios converged at 354, 439 and 369 seconds respectively. Similarly,

Table 2

Convergence time in seconds of the chosen scenarios for single run

S.no	Convergence time in seconds for single run							
	CIF				UKF			
	R	S	C	CT	R	S	C	CT
1	326	308	262	326	341	266	264	341
2	302	351	352	352	217	227	226	227
3	340	361	355	361	278	235	159	278
4	198	149	216	216	198	149	216	216
5	247	304	327	327	196	307	328	328
6	236	353	370	370	191	176	226	226

Note. R, Range; S, Speed; C, Course; CT, Convergence Time

Table 3

Convergence time in seconds of the chosen scenarios for 100 runs

S.no	Convergence time in seconds for 100 runs							
	CIF				UKF			
	R	S	C	CT	R	S	C	CT
1	333	331	327	333	354	314	334	354
2	324	375	372	375	256	315	278	315
3	358	384	375	384	294	311	200	311
4	306	349	374	374	407	431	439	439
5	267	344	351	351	261	363	369	369
6	352	400	404	404	225	213	284	284

Note. R, Range; S, Speed; C, Course; CT, Convergence Time

scenarios 2,3 and 6 converged faster using UKF (consider total convergence times from Monte-Carlo simulation) at 315, 311 and 284 seconds respectively whereas using CIF the same scenarios converged at 375,384 and 404 seconds respectively. For scenarios 1,4 and 5, CIF is better while UKF is better 2,3 and 6 scenarios. From Tables 2 and 3, it is emphasized that the CIF and UKF are giving total convergence time for all the scenarios comparably. The true and estimated paths of target and observer using CIF and UKF are shown in Figure 3 and 4, respectively. The estimated path of the target in Figure 3 is so

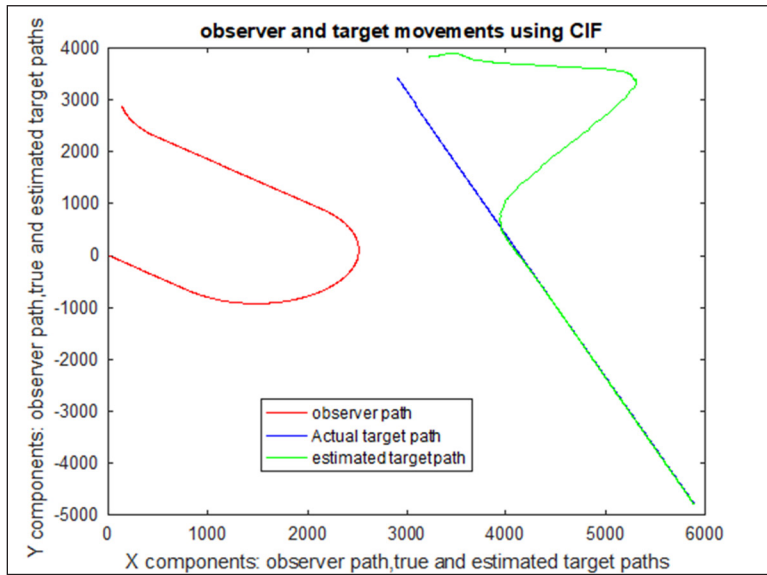


Figure 3. Observer and target movements using CIF

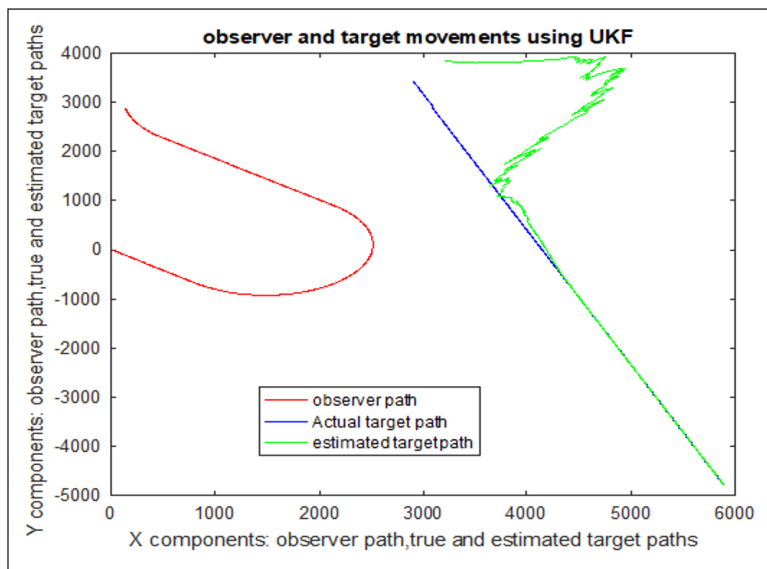
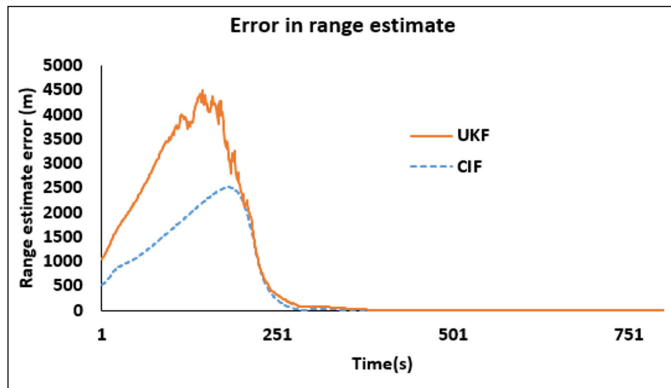


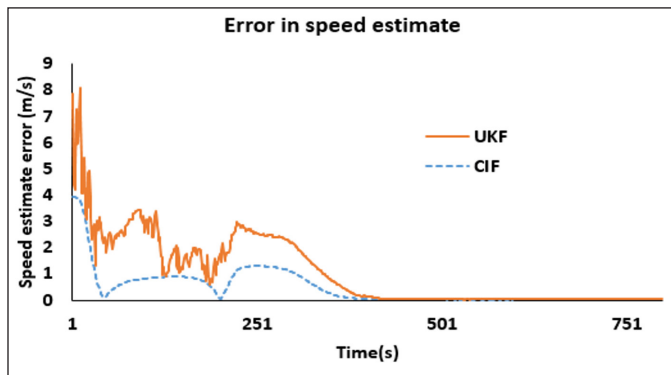
Figure 4. Observer and target movements using UKF

smooth indicating CIF stability. The estimated path using UKF is zigzag indicating the filter instability when compared to CIF.

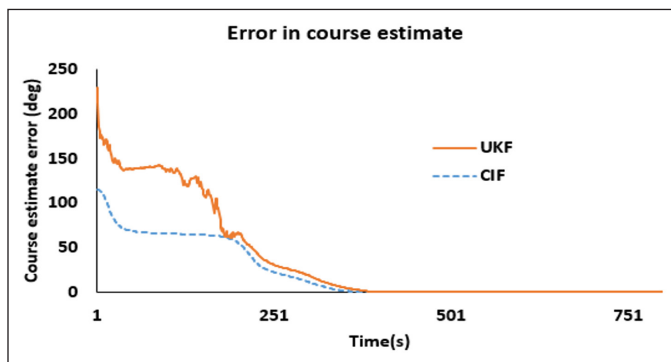
The errors in estimated range, speed and course using CIF and UKF are shown in Figures 5a to 5c, respectively. Similarly, the RMS errors in estimated range, speed and course using CIF and UKF are shown in Figure 6a to 6c, respectively.



(a)



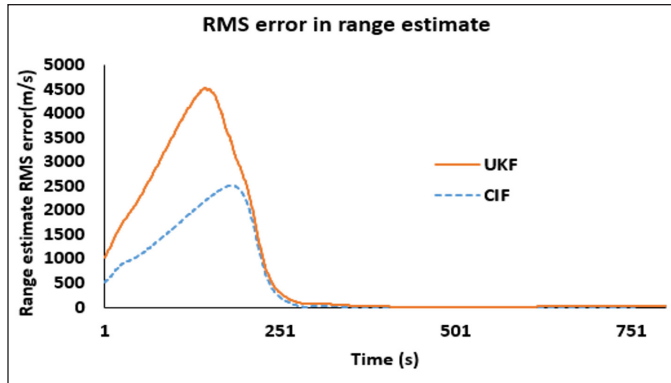
(b)



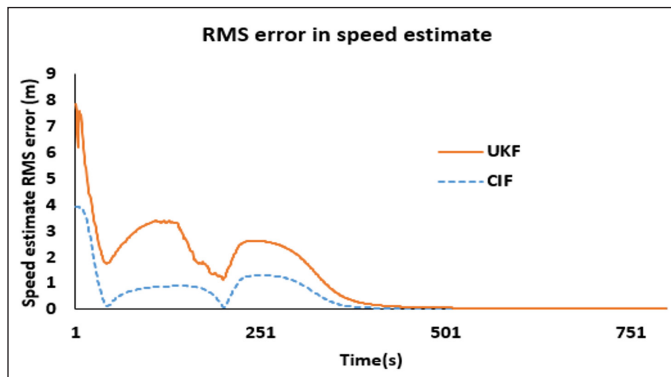
(c)

Figure 5. Error for Scenario 5: (a)Range estimate; (b) Speed estimate; and (c) Course estimate

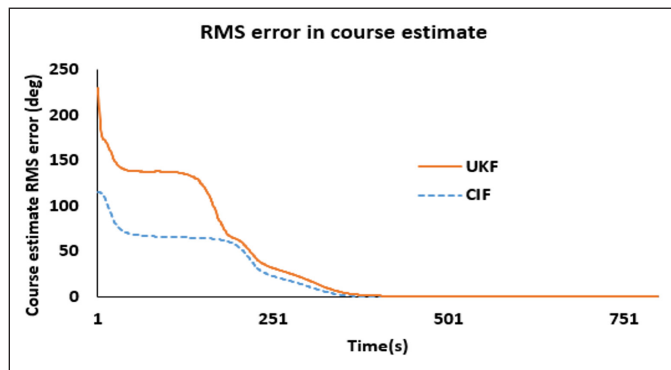
From the Figure 6a, it is understood that the RMS error in range estimate using the CIF (blue dashed line) is very much less which indicates the convergence nature of CIF. Also the curve is very smooth which indicates the CIF filter stability. The RMS error in range estimate of target using the CIF and UKF almost converged at the same time i.e., 267s and 261s (Table 3), respectively. These all indicate the usefulness of the algorithm for



(a)



(b)



(c)

Figure 6. RMS error for Scenario 5: (a) Range estimate; (b) Speed estimate; and (c) Course estimate

state estimation in underwater with the required accuracy. The same can be observed from Figure 6b (Speed estimate RMS error for Scenario 5) and Figure 6c (Course estimate RMS error for Scenario 5) for RMS error in speed and course estimates. As the computations are straightforward in CIF, the RMS error value is found to be less when compared to UKF enabling the CIF to withstand more unstable and higher order system nonlinearity and measurement noises. From the literature till date, UKF is found to be giving solution accurately for systems with Taylor's series of third order. From the analysis done in this research, CIF is found to be giving solution similar to UKF.

CONCLUSION

Target tracking is proposed in underwater using CIF, a less complex and easy to implement algorithm. One of the best advantages of CIF over other filters is the decentralized data fusion ability as the corrected ISV and IM can be obtained by simply adding the associated values to the updated ISV and IMs. Simulator is developed to feed various scenarios and evaluate the algorithm. Performance evaluation of CIF algorithm is carried out in simulation mode and the results are presented for typical scenarios. The convergence times using UKF and CIF are almost near for all the scenarios except for difference of 120s in scenario 6. CIF is found to be appealing simulation results for BOT using single sensor in comparison with UKF with the help of straightforward computations. Keeping in view, the smaller number of computations and decentralized data fusion ability of CIF, CIF is very much useful for state estimation in underwater.

ACKNOWLEDGEMENT

The authors are grateful to the authorities of Koneru Lakshmaiah Education Foundation (Deemed to be university), Vaddeswaram, Guntur, Andhra Pradesh, India for their encouragement towards the research and publication of the paper.

REFERENCES

- Arasaratnam, I., & Chandra, K. B. (2015). Cubature information filters: Theory and applications to multisensor fusion. In *Multisensor Data Fusion* (pp. 216-229). CRC Press.
- Arasaratnam, I., & Haykin, S. (2009). Cubature kalman filters. *IEEE Transactions on Automatic Control*, 54(6), 1254-1269. <https://doi.org/10.1109/TAC.2009.2019800>
- Ding, Z., & Balaji, B. (2012, October 22-25). Comparison of the unscented and cubature Kalman filters for radar tracking applications. In *IET International Conference on Radar Systems (Radar 2012)*. Glasgow, UK. <https://doi.org/10.1049/cp.2012.1695>
- Jiang, H., & Cai, Y. (2018). Adaptive fifth-degree cubature information filter for multi-sensor bearings-only tracking. *Sensors*, 18(10), Article 3241. <https://doi.org/10.3390/s18103241>

- Koteswararao, S. (2018). Bearings-only tracking: Observer maneuver recommendation. *IETE Journal of Research*, 67(2), 193-204. <https://doi.org/10.1080/03772063.2018.1535917>
- Mutambara, A. G. O. (1998). *Decentralized estimation and control for multisensor systems*. CRC Press.
- Pakki, K., Chandra, B., Gu, D. W., & Postlethwaite, I. (2011). Cubature information filter and its applications. In *Proceedings of the 2011 American Control Conference* (pp. 3609-3614). IEEE Conference Publication. <https://doi.org/10.1109/ACC.2011.5990913>
- Wan, E. A., & Van Der Merwe, R. (2000, October). The unscented Kalman filter for nonlinear estimation. In *Proceedings of the IEEE 2000 Adaptive Systems for Signal Processing, Communications, and Control Symposium* (Cat. No. 00EX373) (pp. 153-158). IEEE Conference Publication. <https://doi.org/10.1109/ASSPCC.2000.882463>



Effect of Extraction Time and Temperature on Total Flavanoid Contents of Petai Belalang (*Leucaena leucocephala*) Seed Pretreated by Enzymatic Hydrolysis

Nor Hanimah Hamidi*, Nurul Athirah Mohd Alwi, Haishwari Tarmalingam, Siti Sabirah Ani Kutty and Siti Nur Nadzmiah Mohd Nor

Faculty of Chemical and Process Engineering Technology, Universiti Malaysia Pahang, Lebuhraya Tun Razak, 26300 Gambang, Kuantan, Pahang, Malaysia

ABSTRACT

The abundant availability of *Leucaena leucocephala* (petai belalang) in Malaysia was one of the contributing factors of this research. The phytochemicals obtained from this plant will contribute towards many fields mainly medicine and it becomes more favorable as compared to the modern medicines used these days. Diseases such as cancer, high blood pressure and diabetes are very crucial, and it occurs frequently among all ages of citizens in Malaysia. Therefore, phytochemicals in this plant can be a great substitute of modern medicines. However, lignin is known to interfere with the cell wall polysaccharides digestion, and hence considered as an anti-quality component in forages. To improve phytochemicals extraction, an effective degradation method of lignin is in demand. Thus, the goal of the present study was to investigate the feasibility of using enzymatic hydrolysis by laccase from *Trametes versicolor* (LTV) to breakdown lignin using mild reaction condition. To clarify the effect of enzymatic hydrolysis, a preliminary study on the percentage of lignin removal was conducted that taking the effect of LTV concentration, incubation temperature and time into consideration. The results were then used to analyze total flavonoid contents

(TFC) of *L.leucocephala* seed after the extraction by using microwave-assisted hydrodistillation (MAHD) method. In view of this, extraction temperature and time were varied. TFC was estimated by UV-VIS spectrophotometer for quantification by using quercetin as standard. The result emerge from this study showed that the TFC was high in the extraction temperature of 60°C in 12 min with an average of 1639

ARTICLE INFO

Article history:

Received: 08 December 2020

Accepted: 15 April 2021

Published: 31 July 2021

DOI: <https://doi.org/10.47836/pjst.29.3.08>

E-mail addresses:

nhanimah@ump.edu.my (Nor Hanimah Hamidi)

athirahalwi93@gmail.com (Nurul Athirah Mohd Alwi)

haishwari_tarmalingam@yahoo.com (Haishwari Tarmalingam)

sitinorsabirah96@gmail.com (Siti Sabirah Ani Kutty)

nurnadzmiah@gmail.com (Siti Nur Nadzmiah Mohd Nor)

* Corresponding author

mgQE/g.d.w and the lowest TFC was recorded at 30°C with 677 mgQE/g.d.w. Further analysis showed that enzymatic hydrolysis has assisted the extraction of flavonoids, thus, provided scientific method to extract flavonoid as an alternative therapy for various diseases.

Keywords: Enzymatic hydrolysis, flavonoid, *Leucaena leucocephala*, microwave assisted hydrodistillation, total flavonoid content (TFC)

INTRODUCTION

Flavonoids has been shown to have a profound effect on reducing oxidative stress and preventing and reversing cancer cell developments (Valko et al., 2007). Deposition of flavonoids within the cell wall was originally proposed to account for the poor extractability of flavonoids from some plant material interrupted and surrounded by a lignin matrix (Markam, 1972). Depending on the type of plant, most of plant materials consist of approximately 15 - 35% of lignin. In *L. leucocephala* seed cell wall, antioxidant is embedded with these substances, which make it difficult to obtain pure flavonoids (Rachtanapun et al., 2012). However, most of the studies done on the extraction of flavonoid from *L. leucocephala* did not consider pretreatment process prior to the extraction. Thus, this method was proposed for a better yield of desired product.

Earlier, organosolv method (ethanol/water) was used to isolate lignin from *L. leucocephala*, where they elucidated its structural and thermal behaviour (Tejado et al., 2007). Later, various histological, histochemical and biochemical methods were used to study the structure, histochemistry and chemical composition of tension wood, opposite wood and normal wood of *L. leucocephala* (Pramod et al., 2013). In this study, lignin was isolated from the seed of *L. leucocephala* using fungal laccase (*Trametes versicolor*). In this study, the biological approach is preferable as compared to chemical approach to reduce the possibility of hydrocarbon chain breakage. It is best to be kept in mind that, flavonoids are very sensitive antioxidant. As for the extraction method, microwave-assisted hydrodistillation (MAHD) was used in this study. Previous studies have shown that MAHD has successfully extract the desired product whilst reducing costs, avoiding the use of additives and harmful solvents and improving the effectiveness of the process (Bustamante et al., 2016). As these compounds are very sensitive and specific, the temperature and time of extraction plays an important role on the quality and quantity of the extracts. Thus, the effect of these parameters was considered in this study.

MATERIALS AND METHODS

Materials and Chemicals

L. leucocephala seeds powder was used in this study. Prior to the extraction process, *L. leucocephala* pods were plucked from along Jalan Gambang, Kuantan, Pahang.

Laccase from *Trametes versicolor* (CAS Number: 80498-15-3), quercetin hydrate (CAS Number: 849061-97-8); aluminium chloride (AlCl₃) reagent grade (CAS Number: 7446-70-0); and 2,2'-azino-bis-3-ethylbenzothiazoline-6-sulfonic acid diammonium salt (ABTS) (CAS Number: 30931-67-0) were purchased from Sigma-Aldrich (UK).

Sample Preparation

L. leucocephala seeds were separated from the pods, washed with tap water to remove debris and dried in an oven at 40°C overnight. After drying, the seeds were grinded in blender until fine powder was formed. The powder was kept in chiller (2 °C) until the extraction or enzymatic hydrolysis were conducted.

Enzymatic Hydrolysis

Incubator was switched on at varied temperature 50–90 °C, at 10 °C interval. 5 g of sample was soaked in ammonium acetate buffer (0.1 M, pH 4.5) and ABTS solution (0.1 M). The effect of LTV concentration was analysed by addition of 250 µl of different LTV concentration (0.1, 0.2, 0.3, 0.4 and 0.5 U/ml) and was incubated at 200 rpm for 6 h at 60 °C in a 250 ml Erlenmeyer flask (Hamidi, 2013). After designated reaction time (2–10 h, at 2 h interval), the mixture was left to cool at room temperature and filtered. The solid residue was washed with distilled water and oven-dried at room temperature for 24 h. Black liquor separated from the solid residue was then fractionated by liquid-liquid extraction using methanol at ratio of 1:3, sample to solvent and further concentrated in rotary evaporator for the determination of lignin removal.

Percentage of Lignin Removal

To identify the best condition for enzymatic hydrolysis, One-Factor-at-One-Time (OFAT) procedure was done to determine the best condition for enzymatic hydrolysis of *L. Leucocephala*. Standard analytical procedures (ES ISO 302:2015) were used to identified percentage of lignin removal, based on three parameters (LTV concentration, incubation temperature and time) that may affect the hydrolysis. Therefore, Kappa lignin in raw and treated *L.leucocephala* were determined according to Kappa number TAPPI T 236 om-99 and ES ISO 302:2015. Percentage of lignin removal was calculated using Equation 1 according to the standard analytical procedure:

$$\text{Lignin removal (\%)} = \frac{\text{Kappa lignin } \left(\frac{\text{g}}{\text{ml}}\right) \times 100}{\text{sample mass (g)} \times \text{total volume of solution (mL)}} \quad [1]$$

Microwave assisted Hydrodistillation (MAHD)

MAHD was conducted by using Milestone Ethos E. For the extraction of flavanoid, the chiller temperature and the microwave power were set on 16 °C and 250 W, respectively. The extraction period was varied between 12 – 60 min, at 12 min interval (Jeyaratnam et al., 2016). 5 g of *L. Leucocephala* seed powder and 500 ml deionized water was transferred into 1 L round bottom flask (RBF) (Kusuma & Mahfud., 2017). The extractions were conducted at different extraction temperatures varied between 30–80 °C, at 10 °C interval. After extraction, the extract-solute mixture was filtered, and the extracts were collected for TFC determination.

Determination of Total Flavonoids Content (TFC)

UV-VIS spectrophotometry analysis of flavonoids content in *L. leucocephala* seed extracts requires 5 mg of dried extract (solid) dissolved in 1 ml deionized water was subjected to a general procedure for flavonoids quantification (Oyedemi et al., 2018). Quercetin was used as a standard and the UV detector was set at the wavelength of 415 nm. The adsorbents values were obtained in a spectrophotometer after complexation with AlCl₃ (Kiranmai et al., 2011). Absolute ethanol was used as blank for standard while deionized water was used as blank for samples. Since the extract is in liquid form, extracts volume that equivalent to 5 mg dried extract as represent by Equation 2 for UV-vis analysis and was determined using density by implementing Equation 3.

$$\frac{1}{\rho_{extract}} \left(\frac{ml}{mg} \right) \times 5mg \quad [2]$$

$$\rho_{solution} - \rho_{solvent} = \rho_{extract} \quad [3]$$

Using the linear equation from standard calibration curve, the concentration (mgQE/ml) of flavonoid in analysed sample was determined. The total flavonoids content in extract was calculated by multiplying with volume of solvent used (ml) and divided by mass dry weight seed used (g.d.w) as presented in Equation 4.

$$TFC = \frac{\text{concentration} \left(\frac{mgQE}{ml} \right) \times \text{solvent volume (ml)}}{\text{mass dry weight (g.d.w)}} \quad [4]$$

RESULTS AND DISCUSSION

The Effect of Enzyme Hydrolysis on the Percentage of Lignin Removal

In this investigation, the effect of LTV concentration, reaction temperature and reaction time were considered.

The effect of LTV concentration on the treatment was investigated using different concentration of LTV (0.15, 0.25, 0.35, 0.45, 0.55 and 0.65 mg/ml). The highest percentage of lignin removal was found to be 71.5 % at 0.55 mg/ml of LTV. It is apparent from Figure 1(a) that percentage of lignin removal was increased as the enzyme concentration increases due to the rate of enzymatic reactions that was also increased (Ishmael et al., 2016). However, there was no increase of lignin removal was observed associated with the increment of LTV concentration to 0.65 mg/ml. This result support the idea that the rate of enzymatic reaction increasing proportional to the laccase concentration. This result may be explained by the fact that laccases are known as blue-copper phenoloxidase that catalyse one-electron oxidation by removing one electron, generating phenoxy-free radical products which can lead to polymer cleavage (Pérez et al., 2002). Thus, by increasing LTV concentration, it could facilitate oxidation process and wide range of polymer cleavage. This led to the breakdown of lignin structure, hence increase the percentage of lignin removal.

To assess the optimum incubation temperature that may affect lignin removal, varied temperatures were employed ranged between 30 – 100 °C, at 10 °C interval. The optimum incubation temperature for enzymatic hydrolysis was at 60 °C as shown in Figure 1(b), which remove 72.38 % lignin. The present finding seems to be consistent with other researches which found that 60 °C was the optimum temperature for LTV activity (de Carvalho et al., 1999; Monteiro & de Carvalho., 1998). Further increase in incubation temperature revealing steady decline in the percentage of lignin removal, which indicate the denaturation of the enzyme. However, lignin removal can still be observed even though the incubation temperature was increased up to 100 °C as more than 70 % of lignin was removed. It is appearing favourable that LTV showed an outstanding stability towards higher temperature. The heat tolerance of laccase was suggested to be due to high glycosylation rate that protect laccase from heat denaturation (Slomczynski et al. 1995; Fukushima & Kirk, 1995).

Incubation time is a contributing factor for optimum lignin removal in enzymatic hydrolysis. Therefore, incubation time between 2 – 10 h, at 2 h intervals was deployed to demonstrate the effect. Figure 1(c) shows that there has been a gradual increase in percentage of lignin removal at the first 2 h but steady drop after 6 h of incubation. What can be clearly seen in Figure 1 is the highest percentage of lignin removal, 71 % for seeds were found at 6 h of incubation. Prior studies that have noted the delignification process tends to increase with time of contact between enzyme and substrate until the enzyme activity is slow (Ishmael et al., 2016). In this study, 6 h of incubation was found to be optimum time taken for achieving maximum rate of reaction due to inactivation of enzyme and possibility of repolymerization at reaction time between 8 to 10 h which complies with literature (Gierer, 1985; Monteiro & de Carvalho, 1998). According to these data, we can infer that 6 h of reaction time was optimum for delignification process.

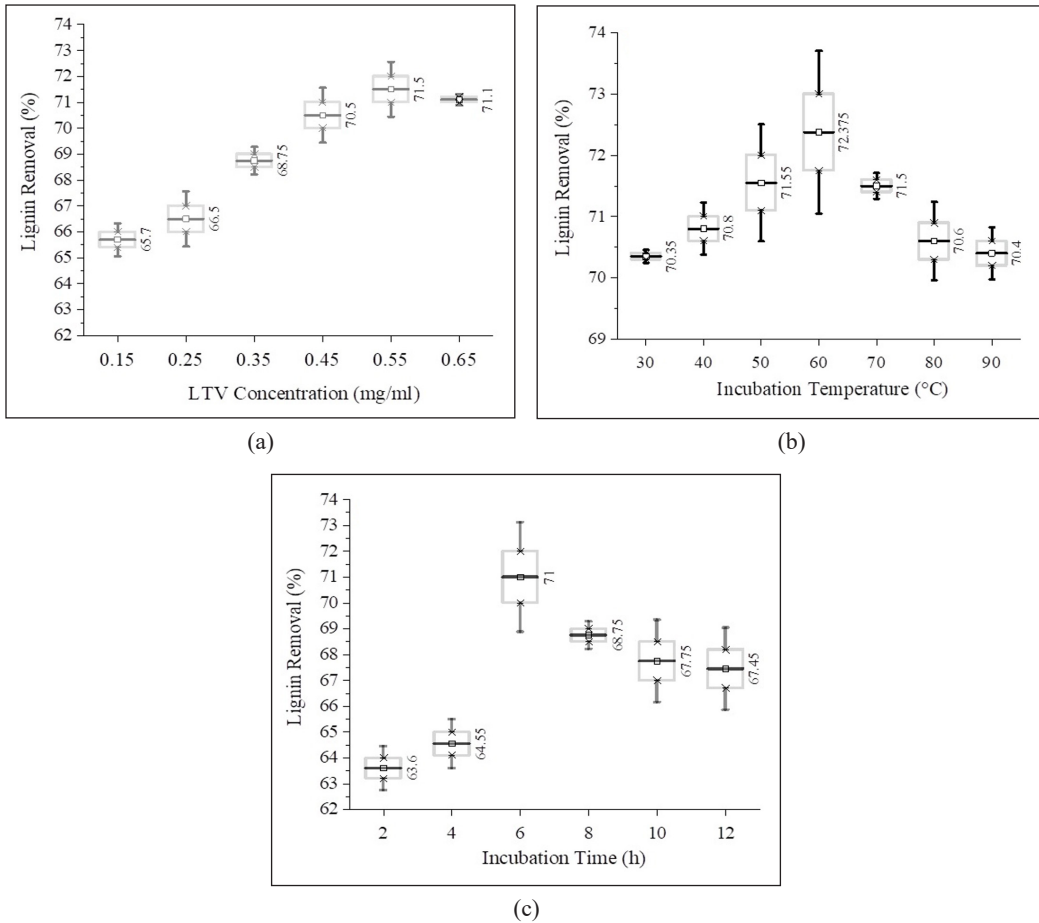


Figure 1. Box plot format graphic showing the effect of (a) LTV concentration, (b) Incubation temperature, (c) Incubation time, with mean, maximum/minimum values of standard deviation. By using One-Way ANOVA analysis by OriginPro 2019b at the 0.05 level, the sample means are significant with p-value of 1.61×10^{-4} , 2.5×10^{-2} and 1.6×10^{-3} , respectively.

The Effect of Extraction Time on Total Flavanoid Content (TFC)

Extraction by MAHD at different times (0, 12, 24, 32, 48, and 60 min) was conducted to encounter the most efficient time to collect the highest amount of flavanoid. It is apparent from Figure 2 that the highest TFC was observed at 12 min of extraction with the content of 1670 mgQE/g.dw compared to the lowest TFC approximately 124 mgQE/g.dw at 60 min. This finding further supported by the extracted sample with the presence of enzymatic hydrolysis revealed the same trend whereby flavanoid yield was highest at 12 min of extraction with TFC of 1943 mgQE/g.dw meanwhile at 60 min the yield excessively decreased to 273 mgQE/g.dw. Both control and hydrolysed sample depicted similarity with highest flavanoid content at 12 min of extraction. These samples revealed about 85 % decrease of flavanoid yield as the extraction were conducted for an hour. The results are in

line with Rezvanpanah et al. (2008) which reported that the optimum extraction time using MAHD was 6 min and 12 min for *Satureja hortensis* and *Satureja Montana*, respectively. This finding further supported by Farhat et al. (2011) who found that less time was required for essential oil extraction thoroughly from orange peels via MAHD extraction that only required 12 min if compared to traditional hydrodistillation (HD) that takes 40 min to be completed. Apart from classical conductive heating methods, microwave extraction methods can heat the entire sample almost simultaneously and at a higher rate (Hashmi & Kim, 2003). When sample is exposed to heat at long period, particles may degrade causing the extract to be not productive due to more inactive compounds extracted (Dent et al., 2013). Therefore, with usage of MAHD, extraction efficiency can be achieved intensively within a short period of time consuming less energy and time proving that this extraction process can be both economic and environmentally friendly. Extraction period of only about 12 min were enough to achieve the highest yield of flavonoids from seeds of this plant.

Previous experiment revealed that enzymatic hydrolysis on seeds of *L. leucocephala* was able to promote delignification at optimum reaction condition (6 h of incubation time, 60 °C incubation temperature and 0.55 mg/ml LTV concentration). In view of this, effect of enzymatic hydrolysis was considered to enhance TFC. The result obtained from the study are presented in Figure 2. Interestingly, there was a significant positive correlation between enzymatic hydrolysis and TFC in which TFC was high in the presence of enzymatic hydrolysis compared with absence of this process.

The obtained result was in line with the study made on effect of hydrolysis in antioxidant extraction whereby laccase-mediator system has appeared to enhance the hydrolysis of lignin (Moilanen et al., 2014). In addition, from research done by Draganescu et al.

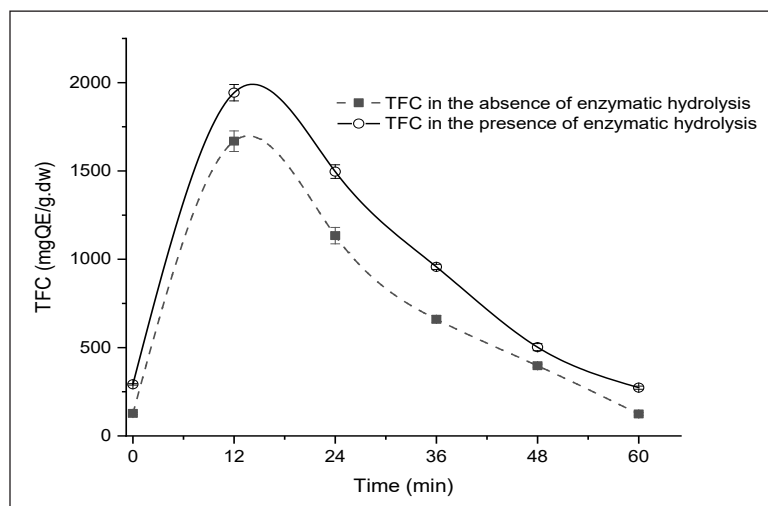


Figure 2. The effect of extraction time on total flavanoid content (TFC) of *L. leucocephala* seed extract with presence and absence of enzymatic hydrolysis. By using One-Way ANOVA analysis by OriginPro 2019b at the 0.05 level, the sample means are significant with p-value of 2.73×10^{-17} and 1.63×10^{-15} , respectively.

(2017), it was found that the contents of oligomers in the flaxseed extract after hydrolysis with lignin peroxidases increased significantly based on the chromatographic peak height when compared with the raw lyophilized flaxseed extract, indicating an advanced, but incomplete process. After enzymatic hydrolysis, the active ingredients may also dissolve more easily in the extraction medium (Pytkowska et al., 2013). These results support the idea that enzymatic hydrolysis approach is particularly suitable to enhance the extraction of natural compounds for optimum yield.

The Effect of Extraction Temperature on Total Flavanoid Content (TFC)

The plot in Figure 3 shows the interaction between extraction temperature and TFC at the fixed 12 min extraction time. It was observed that the value of TFC increased as the temperature increased from 30°C to 60°C. In contrast, increasing the extraction temperature beyond 60°C resulted in the decreased of TFC values. It is encouraging to compare Figure 3 with that found by Azahar et al. (2017) whose found out that the flavonoid content increased as the temperature approached 70°C, and gradually decline as the temperature rise above its optimum temperature. A likely explanation is that higher temperature cause plant tissue rupture, thus solvent was easily to dissolved and degrade active compounds in the plant (Azahar et al., 2017; Yoswathana, 2013). It is apparent from Figure 3 that the best temperature for flavonoid extraction is 60°C regardless of whether the seeds were treated or not prior to extraction. The concentrations of flavonoids were approximately 1639 mgQE/g.dw and 1389 mgQE/g.dw, respectively. The extract comprising the least

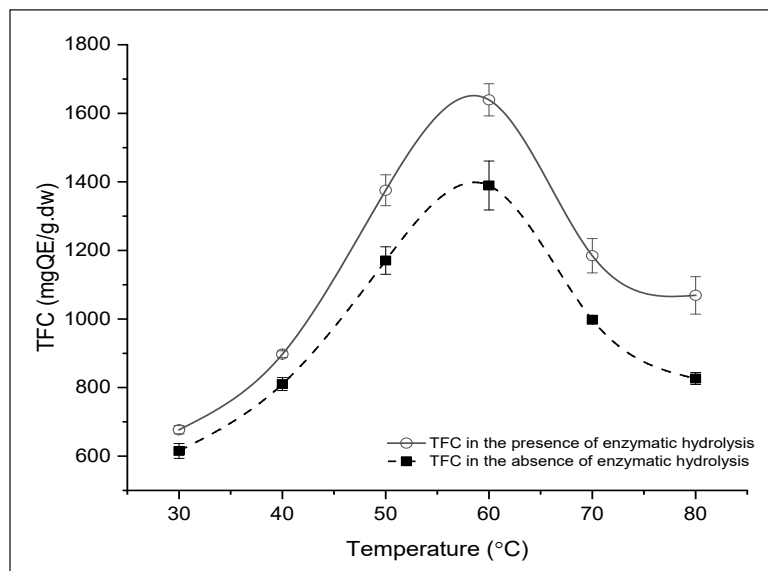


Figure 3. The effect of extraction temperature on total flavanoid content (TFC) of *L. leucocephala* seed extract with presence and absence of enzymatic hydrolysis. By using One-Way ANOVA analysis by OriginPro 2019b at the 0.05 level, the sample means are significant with p-value of 2.9×10^{-11} and 8.5×10^{-11} , respectively.

concentration of flavonoid is in the extraction that was performed at 30°C with 677 mgQE/g.dw for pretreated extracts and 615 mgQE/g.dw for control. Since *L.leucocephala* seeds for the pretreated extracts experienced enzymatic hydrolysis at 60°C for 6 h ahead of extraction, the chances are, more flavonoids were extracted if compared to the extraction process without pretreatment. It is appears that enzymatic hydrolysis of complex lignin in *L.leucocephala* seed enhances the release of flavanoids while preserving their biological potential (Hammed et al., 2013).

CONCLUSION

The efficiency of extraction of flavonoids from *L. leucocephala* depended on the extraction time and temperature by MAHD. The extraction was also enhanced by enzymatic hydrolysis prior to extraction. The relevance of this process is clearly supported by current findings that suggest enzymatic hydrolysis by laccase from *Trametes versicolor* increase percentage of lignin removal, thus TFC value was also increased. The extraction by MAHD is a green method, because it limits the consumptions of toxic solvents and energy by running the process in 12 min at 60°C. It is supported by green pretreatment process which employed the use of laccase to delignifying *L. leucocephala* in 6 h at 60 °C. Moreover, flavonoids are characterized as high in antioxidant contents which indicates a great potential to be applied in dietary supplement industry.

ACKNOWLEDGEMENT

The authors would like to thank the Ministry of Higher Education for providing financial support under Fundamental Research Grant Scheme (FRGS) No. FRGS/1/2018/TK02/UMP/02/19 (University reference RDU190139) and Universiti Malaysia Pahang for laboratory facilities as well as additional financial support under Internal Research grant RDU170345.

REFERENCES

- Azahar, N. F., Gani, S. S. A., & Mokhtar, N. F. M. (2017). Optimization of phenolics and flavonoids extraction conditions of *Curcuma zedoaria* leaves using response surface methodology. *Chemistry Central Journal*, *11*(1), 1-10. <https://doi.org/10.1186/s13065-017-0324-y>
- Bustamante, J., van Stempvoort, S., García-Gallarreta, M., Houghton, J. A., Briers, H. K., Budarin, V. L., Matharu, A. S., & Clark, J. H. (2016). Microwave assisted hydro-distillation of essential oils from wet citrus peel waste. *Journal of Cleaner Production*, *137*, 598-605. <https://doi.org/10.1016/j.jclepro.2016.07.108>
- de Carvalho M. E., Monteiro M. C., & Sant' Anna, G. L. (1999). Laccase from *Trametes versicolor*: Stability at temperature and alkaline conditions and its effect on biobleaching of hardwood kraft pulp. *Applied Biochemistry and Biotechnology*, *77*(79), 723-33. <https://doi.org/10.1385/abab:79:1-3:723>

- Dent, M., Dragović-Uzelac, V., Penić, M., Brnić, M., Bosiljkov, T., & Levaj, B. (2013). The effect of extraction solvents, temperature and time on the composition and mass fraction of polyphenols in dalmatian wild sage (*Salvia officinalis* L.) extracts. *Food Technology and Biotechnology*, *51*(1), 84-91.
- Draganescu, D., Dodi, G., Stoica, I., & Popa, M. I. (2017). Hydrolysis studies of flaxseed extract by high performance liquid chromatography. *Cellulose Chemistry and Technology*, *51*(9-10), 803-811.
- Farhat, A., Fabiano-Tixier, A. S., Maataoui, M. E., Maingonnat, J. F., Romdhane, M., & Chemat, F. (2011). Microwave steam diffusion for extraction of essential oil from orange peel: Kinetic data, extract's global yield and mechanism. *Food Chemistry*, *125*(1), 255-261. <https://doi.org/10.1016/j.foodchem.2010.07.110>
- Fukushima, Y., & Kirk, K. (1995). Laccase component of the *Ceriporiopsis subvermispora* lignin-degrading system. *Applied and Environmental Microbiology*, *61*, 872-876.
- Gierer, J. (1985). Chemistry of delignification - Part 1: General concept and reactions during pulping. *Wood Science and Technology*, *19*(4), 289-312.
- Hamidi, N. H. (2013) *Enzymatic depolymerization of lignin by laccases* (PhD thesis). University of Nottingham, UK.
- Hammed, A. M., Jaswir, I., Amid, A., Alam, Z., Asiyanbi-H, T. T., & Ramli, N. (2013). Enzymatic hydrolysis of plants and algae for extraction of bioactive compounds. *Food Reviews International*, *29*(4), 352-370. <https://doi.org/10.1080/87559129.2013.818012>
- Hashmi, I., & Kim, J. G. (2003). Comparison of degradation studies in a biosimulator by continuous cultivation of *Pseudomonas* and indigenous microorganisms with varied dissolved oxygen concentrations. *International Journal of Environment and Pollution*, *19*(2), 123-138. <https://doi.org/10.1504/IJEP.2003.003744>
- Ishmael, U. C., Rashid, S. S., & Ahmad, N. S. S. N. W. (2016, September 18). Optimization of laccase enzyme pretreatment process parameters of empty fruit bunches (EFB) using one-factor-at-a-time (OFAT). In *Proceedings of the National Conference of Postgraduate Research 2016*. Universiti Malaysia Pahang, Malaysia.
- Jeyaratnam, N., Nour, A. H., & Akindoyo, J. O. (2016). The potential of microwave assisted hydrodistillation in extraction of essential oil from *Cinnamomum Cassia* (cinnamon). *ARP Journal of Engineering and Applied Sciences*, *11*(4), 2179-2183.
- Kiranmai, M., Kumar, C. B. M., & Ibrahim, M. (2011). Comparison of total flavanoid content of *Azadirachta indica* root bark extracts prepared by different methods of extraction. *Research Journal of Pharmaceutical, Biological and Chemical Sciences*, *2*(3), 254-261.
- Kusuma, H. S., & Mahfud, M. (2017). Microwave-assisted hydrodistillation for extraction of essential oil from patchouli (*Pogostemon cablin*) leaves. *Periodica Polytechnica Chemical Engineering*, *61*(2), 82-92. <https://doi.org/10.3311/PPch.8676>
- Markam, K. R. (1972). A novel flavone-polysaccharide compound from *Monoclea forsteri*. *Phytochemistry*, *11*(6), 2047-2053. [https://doi.org/10.1016/S0031-9422\(00\)90171-7](https://doi.org/10.1016/S0031-9422(00)90171-7).
- Moilanen, U., Kellock, M., Várnai, A., Andberg, M., & Viikari, L. (2014). Mechanisms of laccase-mediator treatments improving the enzymatic hydrolysis of pre-treated spruce. *Biotechnology for Biofuels*, *7*(1), 1-13. <https://doi.org/10.1186/s13068-014-0177-8>

- Monteiro, M. C., & de Carvalho, M. E. (1998). Pulp bleaching using laccase from *Trametes versicolor* under high temperature and alkaline conditions. *Applied Biochemistry and Biotechnology - Part A Enzyme Engineering and Biotechnology*, 983, 70-72. https://doi.org/10.1007/978-1-4612-1814-2_91
- Oyedemi, B. O., Oyedemi, S. O., Chibuzor, J. V., Ijeh, I. I., Cooposamy, R. M., & Aiyegoro, A. O. (2018). Pharmacological evaluation of selected medicinal plants used in the management of oral and skin infections in Ebem-Ohafia District, Abia State, Nigeria. *The Scientific World Journal*, 2018, 1-16. <https://doi.org/10.1155/2018/4757458>
- Pérez, J., Muñoz-Dorado, J., De La Rubia, T., & Martínez, J. (2002). Biodegradation and biological treatments of cellulose, hemicellulose and lignin: An overview. *International Microbiology*, 5(2), 53-63. <https://doi.org/10.1007/s10123-002-0062-3>
- Pramod, S., Rao, K. S., & Sundberg, A. (2013). Structural, histochemical and chemical characterization of normal, tension and opposite wood of Subabul (*Leucaena leucocephala* (lam.) de wit.). *Wood Science and Technology*, 47(4), 777-796. <https://doi.org/10.1007/s00226-013-0528-9>
- Pytkowska, K., Bregisz, M., Majewski, S., Ratz-Lyko, A., & Arct, J. (2013). Effect of enzymatic hydrolysis on the antioxidant properties of alcoholic extracts of oilseed cakes. *Food Technology and Biotechnology*, 51(4), 539-546.
- Rachtanapun, P., Luangkamin, S., Tanprasert, K., & Suriyatem, R. (2012). Carboxymethyl cellulose film from durian rind. *LWT – Food Science Technology* 48(1), 52-58. <https://doi.org/10.1016/j.lwt.2012.02.029>
- Rezvanpanah, S., Rezaei, K., Razavi, S. H., & Moini, S. (2008). Use of microwave-assisted hydrodistillation to extract the essential oils from *Satureja hortensis* and *Satureja montana*. *Food Science and Technology Research*, 14(3), 311-314. <https://doi.org/10.3136/fstr.14.311>
- Slomczynski, D., Nakas, J. P., & Tanenbaum, S. W. (1995) Production and characterization of laccase from *Botrytis cinerea*. *Applied and Environmental Microbiology*, 6, 907-912.
- Tejado, A., Peña, C., Labidi, J., Echeverria, J. M., & Mondragon, I. (2007). Physico-chemical characterization of lignins from different sources for use in phenol-formaldehyde resin synthesis. *Bioresource Technology*, 98(8), 1655-1663. <https://doi.org/10.1016/j.biortech.2006.05.042>
- Valko, M., Leibfritz, D., Moncol, J., Cronin, M. T. D., Mazur, M., & Telser, J. (2007). Free radicals and antioxidants in normal physiological functions and human disease. *International Journal of Biochemistry and Cell Biology*, 39(1), 44-84. <https://doi.org/10.1016/j.biocel.2006.07.001>
- Yoswathana, N. (2013). Optimization of ScCO₂ extraction of rambutan seed oil using response surface methodology. *International Journal of Chemical Engineering and Applications*, 4(4), 187-190. <https://doi.org/10.7763/IJCEA.2013.V4.291>



Empirical Model of Ground-Borne Vibration Induced by Freight Railway Traffic

Mohd Khairul Afzan Mohd Lazi*, Muhammad Akram Adnan and Norliana Sulaiman

School of Civil Engineering, College of Engineering, University of Technology MARA, 40450 UiTM, Shah Alam, Selangor, Malaysia

ABSTRACT

Developing an empirical model that can predict ground-borne vibration is required in the modelling process using actual data of ground vibration velocity induced by train traffic collected from sites. In the preliminary and mitigation planning stages of the project, the empirical models developed are expected to predict the ground-borne vibration velocity due to rail traffic. The findings of this research are expected to provide a new perspective for railway planners and designers to improve the national design to improve the quality of life for the residents living close to the rail tracks. This research study firmly fills the information gap towards a fundamental understanding of ground-borne vibration in numerous areas of learning regarding the condition of train operation. This study has developed a prediction model of regression to forecast the peak particle velocity of ground-borne vibration from freight trains based on correlated and fixed parameters. The models developed have considered a few parameters obtained from sites using minimal or without tools altogether. Speed of trains and distance of receivers from the sources were the only significant parameters found in this study and used to simplify the empirical model. Type of soil, which is soft soil, and type of train, which is freight train, were the fixed parameters for this study. The data collected were measured along the ground rail tracks involving human-operated freight trains. Residents from the landed residential areas near the railway tracks were chosen as the receivers. Finally, the peak particle velocity models have been

successfully developed, and validation analysis was conducted. The model can be used by authorities in the upcoming plan for the new rail routes based on similar fixed parameters with correlated parameters from the study.

Keywords: Empirical model, freight train, ground-borne vibration, peak particle velocity

ARTICLE INFO

Article history:

Received: 20 December 2020

Accepted: 03 April 2021

Published: 31 July 2021

DOI: <https://doi.org/10.47836/pjst.29.3.21>

E-mail addresses:

tmm_afzan@yahoo.com (Mohd Khairul Afzan Mohd Lazi)

akram@uitm.edu.my (Muhammad Akram Adnan)

norliana545@uitm.edu.my (Norliana Sulaiman)

* Corresponding author

INTRODUCTION

At present, many regulatory institutions, such as the Union of International Railways (UIC), are demanding the establishment of standard prediction models that can predict vibration impact towards human perception (Hermsworth, 2000). Sulaiman (2018) stresses the importance of developing Malaysia's own vibration limits and local conditions-based control guidelines, as most developed countries already have their own vibration measurement and design requirements. Lazi et al. (2016) also emphasize the importance of establishing Malaysia's own standard based on the local geological conditions especially in the development of public transportation infrastructure.

In various stages of railway design processes and in the evaluation of vibration countermeasures, the establishment of ground-borne prediction models can be used as a predictive tool. Practitioners, particularly local authorities, can use the models at planning stage and provide mitigation suggestions, if necessary, at railway system development stage.

Maintenance of tracks may also be expensive because of the excessive vibration in the rail track structure. The instrument that can be properly used at various stages of the railway design process, including planning for environmental impact assessment, would be a ground vibration prediction model (Bahrekazemi, 2004). In assessing and evaluating the issue of ground-borne vibration, as in Germany and the United Kingdom, most developed countries have their own standards, including the development of guidelines and standards for the assessment and measurement of structural and human ground vibration, such as the Deutsches Institut für Normung (1999), the International Standard Organization (ISO, 1997), and the British Standard (2008). Malaysia has Vibration Limits and Environmental Control Guidelines developed by the Department of Environment Malaysia (2007) from the Ministry of Natural Resources and Environment Malaysia. The guidelines were established to define the appropriate limits for quantitative evaluation of ground vibration. However, the guidelines only define the levels of vibration and no system or equipment is specified to predict or calculate the degree of ground vibration. The only instruments recommended to calculate the vibration level are seismographs and geophones. The affordability of such equipment is the major concern among relevant Malaysian authorities (Sulaiman, 2018). This study attempts to develop a regression model to predict the peak particle velocity of ground-borne vibration induced by freight trains to minimize the dependency on vibration equipment.

To satisfy industrial requirements, such as the operation of public transportation, it is very important to establish guidelines and regulations. This research attempts to generate an empirical model that represents ground-borne vibration based on the condition and parameters of freight rail traffic in Malaysia. In this analysis, the empirical model has the potential to become the basis of the ground-borne vibration prediction tool using simple parameters for future use by related practitioners.

This research study is intended to bridge the knowledge gap about the basic understanding of ground-borne vibration, consisting of a combination of many branches of learning on the state of local rail transportation. Limited findings regarding the level of perceived irritability and annoyance experienced by affected people living near the source of vibrations especially in Malaysia have become the motivation of this study. The study also develops a prediction model of vibration velocity from freight trains. The empirical model produced can predict the ground-borne vibration velocity using local rail traffic parameters. The basic parameters applied in this study have the potential to reduce the dependency on expensive equipment.

LITERATURE REVIEW

Propagation

Typically, after ground-borne vibrations are produced, they propagate to the surrounding area through the soil medium. Propagation characteristics depend on the properties of the soil, parameters, and distance from the source. Compared to stiff or hard ground, soft ground appears to have lower frequency. Soil vibration can travel longer distances from its source at low frequencies. The main factor influencing significant ground vibration is soft soil formation, such as silt or soft clay, which can cause discomfort for individuals living 100 to 200 m away from the rail tracks (Madshus et al., 1996).

The major impact of the soil form on the propagation of ground vibration is shown in Figure 1 (Hajek, 2006), showing how the frequency of soil absorption results in the attenuation of ground vibration. Although this result is from road traffic analysis, the characteristics of different types of soil are clearly demonstrated in terms of vibration velocity and distance to the edge of the pavement. The highest vibration absorption capacity is found in gravel soils and dry sand, while the lowest is peat or soft clay (Watts, 1990). As a result, ground vibration will be rapidly attenuated as the distance along the path of

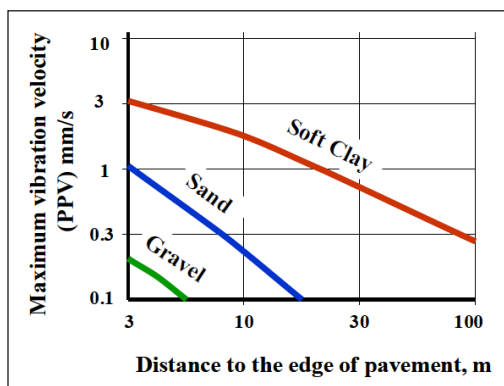


Figure 1. Ground vibration propagation in different types of soil (Hajek, 2006)

ground transmission increases (Hunt & Hussein, 2007). In summary, compared to soft soil, ground vibration in a stiff or hard soil could be attenuated and absorbed much more quickly with distance.

The path of propagation could also be affected by refractions and reflections at the interface between soil and the bedrock and between soil layers. Refraction and reflection could lead to a wave's propagation which deviates from its original path to the receiver. Persson (2016) also reported that

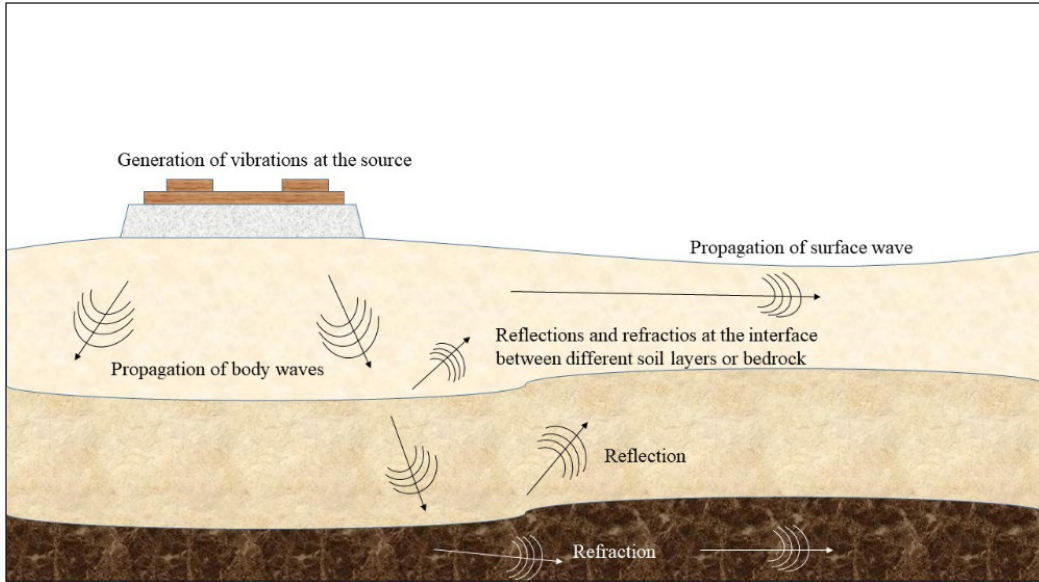


Figure 2. Propagation movement for ground vibration (Persson, 2016)

the propagation velocity for each wave form is controlled by the conditions of the ground soil, as shown in Figure 2.

There are several ways available to determine a vibration’s magnitude. Velocity, displacement, and acceleration are the three most common forms of measuring vibrations (Eitzenberger, 2008). The standard unit for velocity is mm/s, while displacement is mm, and acceleration is mm/s². Velocity is used in this analysis as the values need to be compared to the values used by the standard Malaysian guidelines. The standard guidelines use velocity as the vibration magnitude. The vibration rate is determined by the Peak Particle Velocity (PPV), and it is the most recognized and used vibration measurement. Vibration limits using PPV are recommended by most guidelines and regulations. The maximum particle velocity over the total recorded time is regarded as the peak particle velocity for each recorded waveform as shown in Figure 3 (Alcudia et al., 2007).

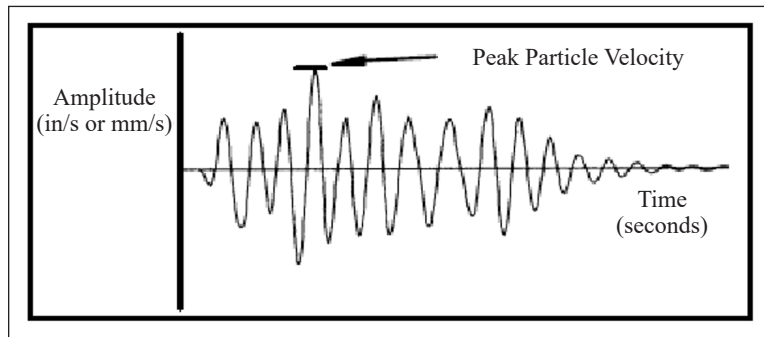


Figure 3. The definition of Peak Particle Velocity (Alcudia et al., 2007)

The PPV is the maximum instantaneous velocity of a particle at a point in a particular time interval. Ground particles vibrate with varying particle velocities when the disturbance from the source of vibrations propagates away from the source with a certain amount of wave velocity. The motion at a given location along the propagation path is represented in three mutually perpendicular components (usually transverse, vertical, and radial or longitudinal). All three components must be calibrated at the same time to ensure the PPV is correctly determined (Avellan et al., 2017). For this study, the PPV was determined as the vibration velocity to be measured.

Vibration Monitoring Technology

Vibration can be detected using a range of sensors. There are sensors designed to measure velocity, acceleration, and displacement based on various types of vibrations, using various measuring technologies, such as microelectromechanical systems or known as MEMS sensors, piezoelectric or PZT sensors, laser Doppler vibrometers, and proximity probes. When deformed, PZT sensors, the most widely used sensors, produce voltages. The vibrations can be interpreted by digitalizing and decoding the voltage signals. The vibration levels and maximum frequency range, as well as other operating environment variables including humidity, temperature, and pH level, should all be considered when choosing vibration sensors (Huang, 2016).

A MEMS sensor is a 3-axis acceleration device with sensitivity in the low-frequency and low-acceleration regions, and its peripheral circuitry is developed. A prototype is built to enable constant measurement of micro-vibrations (Sakaue et al., 2012). For the laser Doppler vibrometer, the angle that the target surface creates with the vibrometer's laser signal is used to determine the transverse displacement, and the change in velocity is read as vector quantity by the laser Doppler vibrometer. When the target surface is perpendicular to the laser, the vibrometer's output reads the same transverse displacement (Garg, 2017).

Review of Prediction Model from Railway Traffic

In the past 30 years, many models have been produced to predict the ground-borne vibrations caused by rail traffic. Table 1 shows a description with independent variables for the predictor variables used in the previously established vibration models for trains.

The prediction models produced by previous researchers were based on the original geological condition and environment study area. The models were developed to predict the velocity of vibration involved with complex parameters. The parameters selected required practitioners to obtain data from service providers or need to have special equipment to get the data. As a summary, the parameters as independent variables include velocity vector, speed factor, distance factor, track quality factor, building amplification factor, and wheel force. The factors or elements used in the previous models are simplified in this research

Table 1
Previous models of ground-borne vibration induced by trains

Author/Year	Study origin	Model	Description
Madshus et al. (1996)	Norway	$V = V_T F_S F_D F_R F_B$	V is the peak particle velocity in mm/s. V_T is the specific vibration level for specific train types. F_S is the speed factor. F_D is the distance factor. F_R is the track quality factor. F_B is the building amplification factor.
Jones and Block (1996)	England	$V_{Dk} = F_D(f) X_{Dk}$, $X_{Dk} = (\sum_{j=-\infty}^{\infty} x_{jk}^2(f))^{1/2}$, $x_{jk}(f) = \sum_{l=0}^N a_{jl} P_l(\cos\theta_j)$	The models are only applicable for freight trains. V_{Dk} is the vertical vibration predicted. X_{Dk} is the total transfer function. $F_D(f)$ is the vertical vibration for sleeper. x_{jk} is the energy sum of the transfer function. k=0 is the vertical response function and k=1 is the lateral. θ is the angle between the normal to the track at the response position and the excitation point on the track.
Suhairy (2000)	Southern Sweden	$V = V_T * \left(\frac{D}{D_0}\right)^B * \left(\frac{S}{S_0}\right)^A * F_R * F_B$	This equation could be used to find the vibration rates for various types of trains at different distances. V is vibration velocity in mm/s. V_T is measure vibration levels for the trains. D is distance from the centre of track. D_0 is reference distance. S is train speed. S_0 is reference speed. B is distance dependent. A is speed dependent exponential. F_R is the track quality factor. F_B is the building amplification factor.
Jiang and Zhang (2004)	Shanghai	$VL = 70 - 13.6 \log(r/10)$	VL is vibration level. r is the distance from the viaduct line's centre in m.
Bahrekazemi (2004)	Sweden	$V = (a \cdot speed + b) \left[\frac{r}{r_0}\right]^{-n}$	V is the particle velocity on the track. a and b are the parameters of the model. n is attenuation power. R is the source distance from the receiver. r_0 is the reference distance.
With et al. (2006)	Sweden	$v_{rms} = (a_1 F_{rms} + a_2)V + (b_1 F_{rms}$	v_{rms} is the r.m.s particle velocity. V is speed of train. F_{rms} is the r.m.s. wheel force applied. a is the gradient. b is the intercept.

Table 1 (continue)

Author/Year	Study origin	Model	Description
Hanson et al. (2006)	United States	$VL \text{ (in dB)} = 20 \log_{10}(v_m/v_{ref})$	v_m is the measured velocity. v_{ref} is the referred velocity. VL is the vibration level.
Paneiro et al. (2015)	Lisbon	$PVS = 0.191 \log(V) - 0.208 \log(D)$	Peak Vector Sum is in mm/s. V is the speed of train in km/h. D is distance in m.

to minimize the dependency on advanced equipment when collecting data to predict the ground-borne vibrations using the developed models.

MATERIALS AND METHODS

Case Study

This research was conducted along the Kereta Api Tanah Melayu Berhad or KTMB railway track from Padang Jawa, Shah Alam, to Klang, Selangor. The railway track is a two-way railway with two (2) train routes, one to Kuala Lumpur and the other to Pelabuhan Klang, Selangor. These site locations were selected to distinguish the variety of vibration magnitudes induced by the trains running on the railway track. The sites were chosen because of the strategic locations, as there were many residential areas along the track that were endangered by the occurrence of ground-borne vibration induced by trains. This research also focused on areas with landed type residential buildings. Figure 4 shows the map of locations of study in Padang Jawa Station, Shah Alam, to Klang Station, Klang.

The route has been chosen due to the existence of landed residential buildings in the areas next to the railway track. There are no vibration barriers located along the sites. The

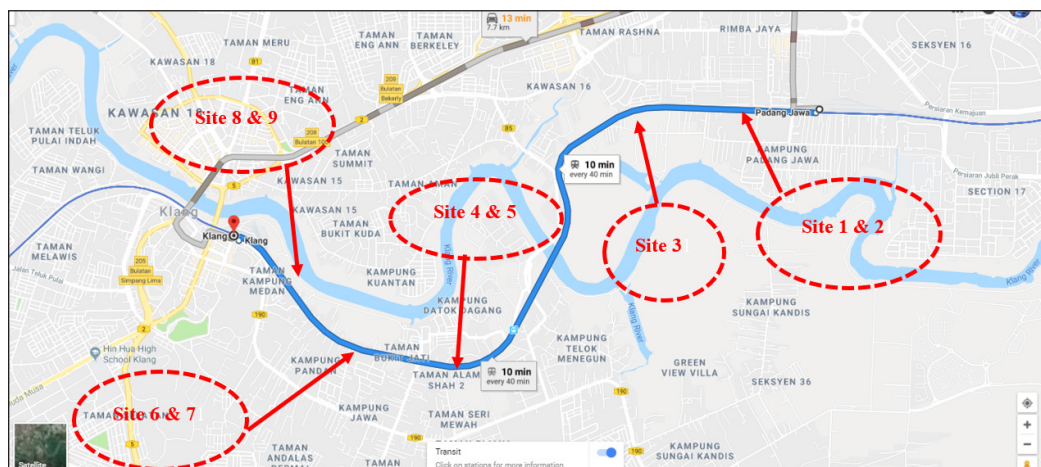


Figure 4. Map of nine sites from Padang Jawa to Klang, Selangor

range of the distance from the residential area to the rail track for this study is less than 30 meters. Field data collected during the site survey are train parameters, the speed of the trains. The ground-borne vibration velocity measurements consist of radial vertical and horizontal wave vibrations. These measurements were obtained using a seismograph installed at the sites. As for site locations, three were chosen from Padang Jawa station to Bukit Badak Station. The other six sites chosen are located between Bukit Badak Station and Klang Station. Hence, there were nine (9) stations chosen altogether. The sites were chosen to be as close as possible to the landed residential areas. Different locations were selected to obtain various speeds of the trains and various distances from the residential areas to the sources. Shah Alam and Klang are the most developed areas and have the highest population in Malaysia.

The proposed sites are located on the Kenny Hill formation and Alluvium formation. Padang Jawa, Shah Alam, is located on the Kenny Hill formation, while Klang is on the contact boundary of Alluvium and Kenny Hill formations (Peng et al., 2004). Figure 5

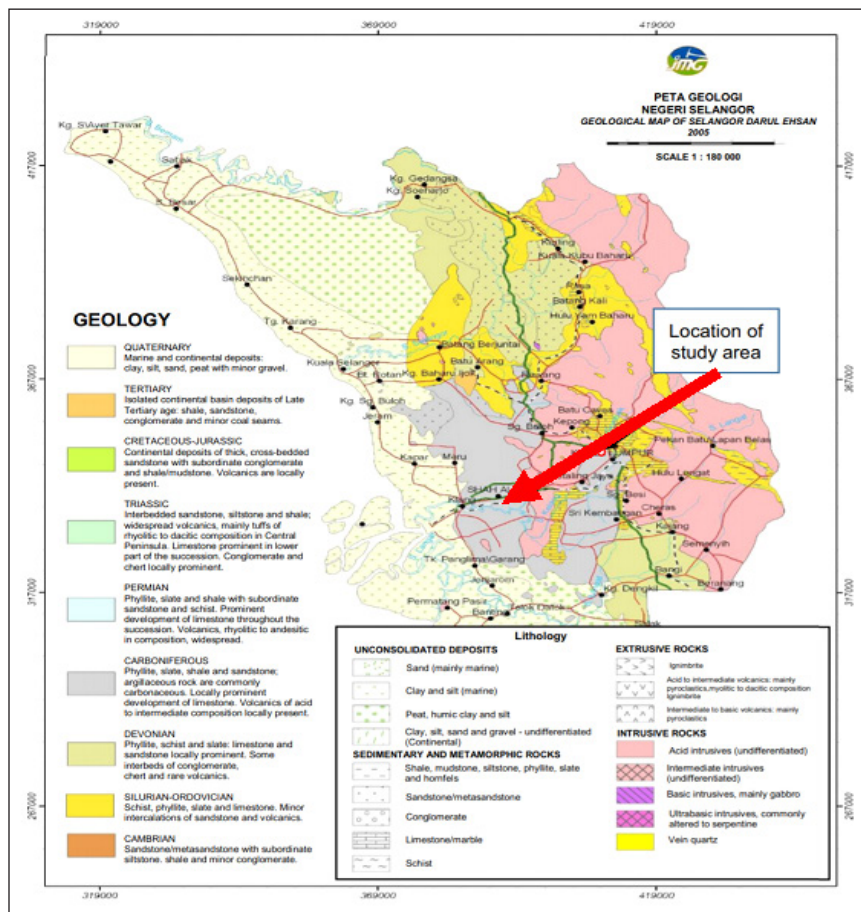


Figure 5. Geology map of studied areas located in the state of Selangor (Roslan, 2017)

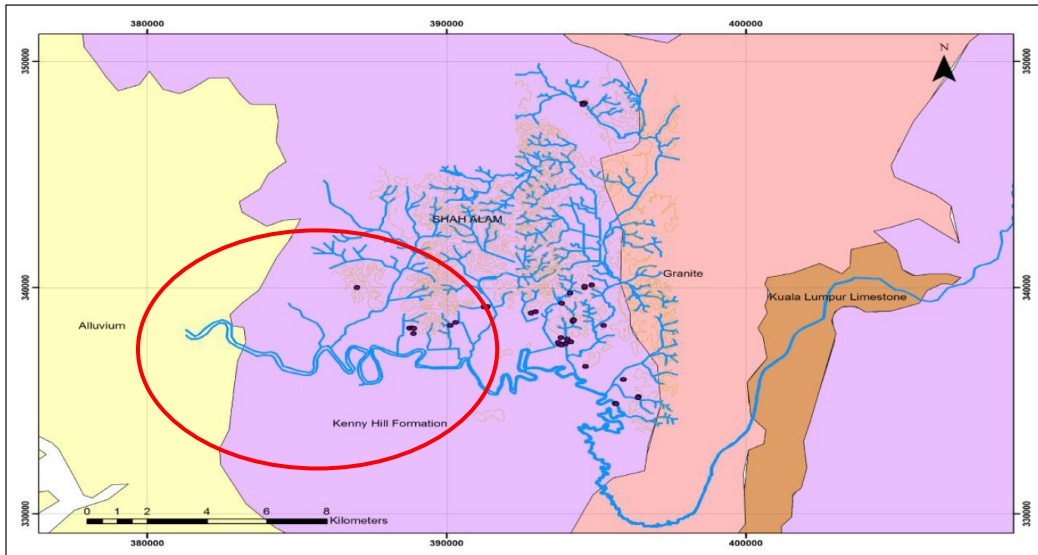


Figure 6. Close-up geological map of studied areas in Shah Alam and Klang (Peng et al., 2004)

shows the geological map of the sites chosen, and Figure 6 shows the close-up version of the geological map of the areas for this research.

Alluvial deposits typically consist of very soft to firm silty clay, with intermediate sandy layers up to 25 m to 30 m in depth. It usually consists of silty sand that lies beneath the silty clay stratum. Residual soils from Grade VI and entirely weathered materials in Grade V resulting from Quartzite weathering are only found at the depths of approximately 40 m. The behaviour of soft alluvial soil is influenced by the source of the parent material, depositional processes, accumulation, redeposition, erosion, and fluctuations in groundwater level. In the Klang region, alluvial soil typically shows a marked stratification, and in these deposits, organic matters, like seashell and decayed wood, are often present (Tan et al., 2004).

The formation of Kenny Hill is a series of sedimentary clastic rocks consisting of interlocking shales, siltstones, mudstones, and Paleozoic upper sandstones. It is usually characterised, as seen in Klang Valley, by undulating terrain of low hills and shallow as well as broad valleys in its outcrop. The subsurface investigation recorded that along the alignment, the Kenny Hill formation is a series of interbedded siltstones, mudstones/shales, and sandstone overlaid by stiff over consolidated soil mainly of silty sand and sandy silty clay. The formation underwent metamorphic events at certain stretches resulting in changes of sandstone or siltstone to quartzite and phyllite/schist, respectively (Khoo et al., 2019). Silty clay soil or clay, defined as soft soil, is geologically young and reaches a balance under its own weight. However, it has not undergone significant secondary or delayed consolidation since its formation. This is distinguished by the fact that it can only bear the soil's overload weight, and any additional load would result in relatively large deformation.

This classification also includes soils that have not completed consolidation under their own weight (Kempfert & Gebreselassie, 2006). Soft soil, as claimed by Sulaiman (2018), and Cenek et al. (2012), is more affected by vibrations, especially vibrations with greater magnitudes compared to other soil types.

Instrumentation and Equipment Strategy Setting Up

Data reading and measurements of ground-borne vibration velocity were conducted for each site using a seismograph meter, also known as the Mini-Seis, produced by White Industrial Seismology Inc. A detailed illustration of the Mini-Seis location is demonstrated in Figure 7. A two-hour midnight time is set to obtain the data from the freight trains since they only operate after passenger commuter operation ends.

Measurement of Train Speed

The train parameter recorded for this research was its speed. The data were chosen as one of the parameters for this modelling since the data can be measured directly at site by recording the time taken for a train to pass a certain distance. The exact time of the train passing through the site was taken to tally with data recorded in the Mini-Seis. To get a precise speed data value from the train, the Stalker XLR Lidar radar speed gun model was used. The train speed was measured in km/h.

The freight train passed the studied sites at midnight after 12.00 a.m. and above after the end of passenger train services. Due to this condition, the data collection for freight train

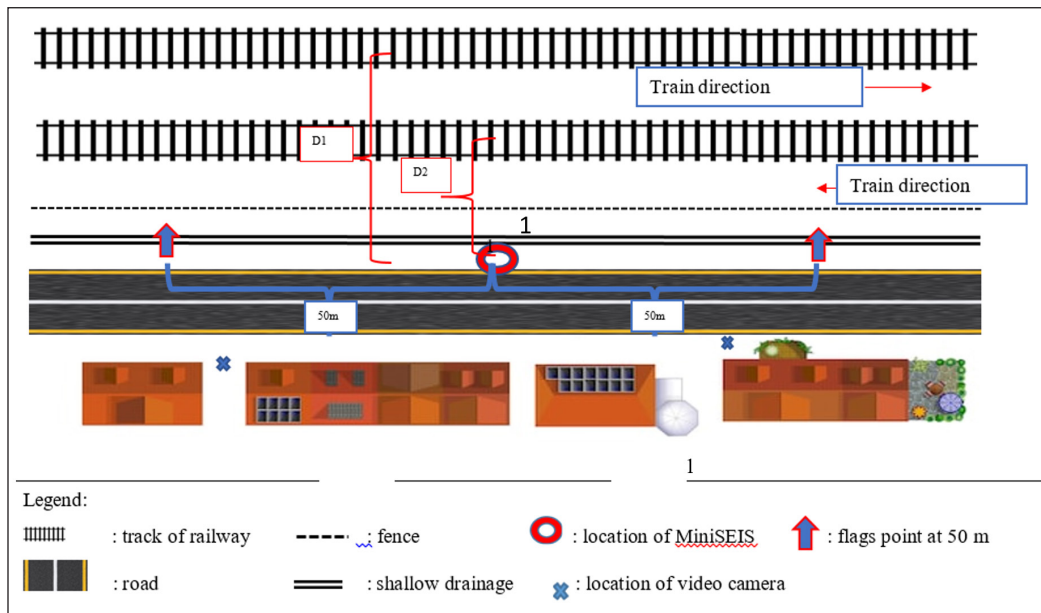


Figure 7. The location of Mini-Seis at site study at midnight session of each site

was done from 2.00 a.m. until 4 a.m.. KTMB cargo services of diesel electric KTM Class 23 from Hitachi, KTM Class 24 by Toshiba, KTM Class 25 from Electro-Motive Diesel, ADtranz DE-AC33C model for Class 26, CKD8C, and CDK8E for Class 29 model were used for the locomotive in freight services. The axle load for the diesel-electric locomotive was 20 tonnes with the loco weight of 120 tonnes (Malay Mail, 2008). In 1996, the United Nations of Economic and Social Commission for Asia and the Pacific or known as ESCAP stated that the load restriction for a single locomotive unit in Malaysia was 1200 tonnes throughout the system (ESCAP, 1996).

Measurement of Embankment Parameter

The height and width of the ballast from the locations of this study were measured. The measurements were recorded using a laser meter and a measuring tape. The distance of the track to the receiver or the location of the Mini-Seis was also recorded. The data were then analysed to find the relationship between the dimension of the ballast with the ground-borne vibration velocity induced by trains. Additionally, the relationship between the distance from the track to the receiver (Mini-Seis) and the ground-borne vibration velocity was also analysed. A laser meter was used as an alternative to measure the distance at inaccessible locations to the researchers. It was also used to validate the distance measurement taken using a measuring tape. From the survey, it was found that the track gauge recorded was 1000 mm, and the type of ballast from granite stone with the composite size of 14mm, 28mm, 50mm, and 63mm. The height and width of ballast varied based on location within the range of 0.12m–0.88m in height and 2.38m–3.19m in width of the ballast. Figure 8 shows the main components of track which are ballast, sleeper and track rail, and the range of dimensions of ballast at site.

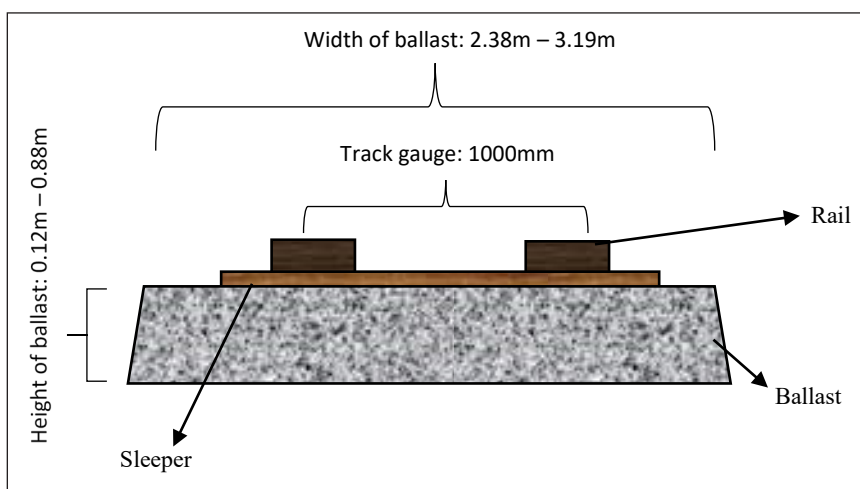


Figure 8. The main component of track with the range of dimension at site

Measurement of Ground Vibration

With a Mini-Seis digital seismograph, ground vibration velocity was measured. A Mini-Seis consists of the monitor as a data logger, a transducer of geophone, and a microphone (White Industrial Seismology Inc., 2009). The geophone and microphone transducer were mounted in residential areas on the ground and were connected to the Mini-Seis monitor as shown in Figure 9. The coordinates of the Mini-Seis were measured using a GPS meter. The time displayed by the Mini-Seis was recorded to tally with the actual time of the trains passing by the designated points to signify the data during data analysis.

As freight trains only operate at midnight after the end of passenger commuter services, the data collection using the Mini-Seis was done at midnight.

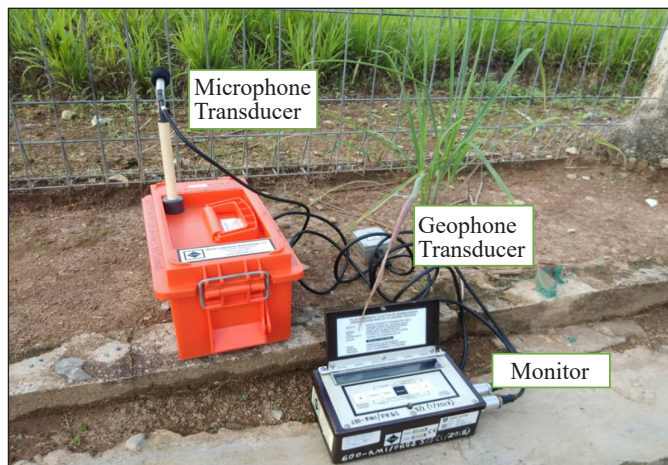


Figure 9. Mini-Seis installed at the studied site

Using the Mini-Seis via the geophone transducer, the lowest vibration velocity level that could be registered was 0.063 mm/s, and the microphone was able to measure up to 148 dB of sound pressure. The seismic channel consists of three longitudinal, transverse, and radial vibration velocity data readings. Using the data analysis programme given, the readings were collected. The distance was measured from the source to the receiver using the Mini-Seis. To define the relationship between the distance of the source to the receiver with the vibration frequency, different distances were calculated at the same site analysis. Those values were then used in the model development process.

RESULTS AND DISCUSSION

Descriptive Statistics of the Empirical Peak Particle Velocity Data

According to Al-Hunaidi (1994) and Roess et al. (2006), the sample size required to estimate a variable in certain confident level is as shown in Equation 1.

$$N = \frac{1.96^2 s^2}{ae^2} \quad [1]$$

Where:

N = number of sample size for 95% confidence interval

s = standard deviation of vibration velocity

ae = limit of acceptable error

The number of 1.96² is for 95% confidence interval, which is the most common approach, to compute the precision and confidence of the sample mean as an estimator of the true mean of the underlying distribution (Roess et al., 2006). The tolerance of acceptable error (ae) is ±0.05mm/s as stated in White Industrial Seismology Inc. (2009) for using Mini-Seis, and the practical use is made based on this overall study for vibration velocities have standard deviation (s) of approximately 0.542mm/s. A sample of 452 vibration velocities are required as shown in Equation 2 with 95% confidence interval.

$$N = \frac{1.96^2(0.542)^2}{(0.05)^2} = 451.41 \approx 452. \quad [2]$$

Mini-Seis produces a peak particle velocity obtained from the ground-borne traverse, radial, and horizontal vibration velocity directions. An overview of the empirical peak particle velocity data has been encapsulated in the descriptive statistics consisting of all variables' information such as the mean value, maximum value, minimum value, median value, skewness, kurtosis value, and standard deviation. From the result produced by the descriptive statistics, extreme values can be recognized during the screening process. The collected data from the study are 772, higher than the sample size. The empirical PPV data after screening are formulated in Table 2.

Table 2
Descriptive statistics for the freight PPV

Variable	Unit	Mean	StDev	Minimum	Median	Maximum	Skewness	Kurtosis
PPV	mm/s	1.395	0.835	0.191	1.191	3.461	1.12	0.58
Speed	km/h	32.30	8.29	15.00	32.00	48.00	0.44	-0.18
Distance	m	9.606	3.227	4.225	10.483	15.075	-4.05	15.26
Height of ballast (1)	m	0.346	0.153	0.120	0.360	0.750	-0.22	-0.99
Height of ballast (2)	m	0.479	0.188	0.210	0.395	0.880	1.31	2.14
Width of Ballast	m	2.684	0.256	2.38	2.65	3.19	0.52	-0.40
Depth of drainage	m	0.100	0.204	0.000	0.000	0.800	1.97	3.23
Width of drainage	m	0.263	0.537	0.000	0.000	1.500	1.80	1.61
Distance of drainage from receivers	m	0.558	1.233	0.000	0.000	5.580	2.56	7.16
Distance of drainage to sources	m	2.545	5.294	0.000	0.000	15.660	1.91	2.15

From Table 2, the PPV recorded from the case study is in the median of 1.191 mm/s, with the maximum data recorded of 3.461 mm/s. This data already exceeds the allowable limit stated in the guidelines for vibration limits and control from the Department of Environment Malaysia (2007). Department of Environment Malaysia states that the allowable limit for residential area is 0.567mm/s, and 1.176mm/s for commercial area. This study clearly shows that the PPV recorded exceeds the limit either for residential or commercial area although the study was conducted at residential areas.

Correlation Analysis for the Freight PPV Parameters

Correlation analysis is used to diagnose the possible relationship between the dependent and independent variables used in the development of the regression models. The correlational hypotheses are described as follows:

H_0 = There is no correlation between two variables.

H_1 = There is a correlation between two variables.

Correlation analysis was used to determine the total possible variable combinations and the results of the overall variables as shown in the correlation matrix in Table 3. Each column consists of r-value and p-value. The p-values are located at the bottom of each row and the r-values are located at the top of each row.

Table 3 shows the correlation values between PPV, speed, distance, height of ballast, depth of drainage, width of drainage, and distance of drainage from receivers to sources. Since this study purposely develops an empirical model for PPV, only significant variables with PPV are considered. Significant variables with PPV are the speed and distance, and the p-values are less than 0.05 for the mentioned variables. The existence of drainage at the locations does not affect PPV since the drainage does not function as barriers as the optimum barrier depth should be in the range of 5 to 20 meters (Orehov et al., 2012). The maximum depth of drainage recorded at site was only 0.8 meter. The height of the ballast, width of ballast, as well as the distance of drainage from receivers to sources also did not have significant impact on the PPV as the p-values were more than 0.05.

Multiple Linear Regressions

The first model for multiple linear regressions was computed with the freight PPV as the response, while the speed of train (s) and distance (d) were the predictors. Table 4 displays the constant values and the three predictors.

The hypotheses for the final estimating mode are declared as follows:

H_0 = The predictor cannot be used for estimating in the PPV model.

H_1 = The predictor can be used for estimating in the PPV model.

Table 4 defines the variables for model of freight trains which are significant with the independent variables in predicting the PPV, where the p-values of the multiple linear

Table 3
The correlation matrix among variables

Variable	PPV	Speed	Distance	Depth of drainage	Width of drainage	Height of ballast (1)	Height of ballast (2)	Width of Ballast (m)	Distance of Drainage from receivers
Speed	0.608 0.000								
Distance	-0.469 0.004	-0.147 0.394							
Depth of drainage	0.056 0.745	-0.070 0.686	0.064 0.711						
Width of drainage	-0.086 0.619	-0.196 0.251	0.437 0.008	0.745 0.000					
Height of ballast (1)	0.325 0.110	0.254 0.135	-0.667 0.000	-0.084 0.627	-0.330 0.049				
Height of ballast (2)	-0.246 0.138	-0.042 0.807	0.399 0.016	-0.164 0.340	-0.114 0.507	-0.374 0.125			
Width of Ballast	0.276 0.103	0.309 0.066	-0.500 0.002	-0.105 0.542	-0.236 0.166	0.407 0.014	-0.110 0.522		
Distance of drainage from receivers	-0.095 0.580	-0.198 0.247	0.215 0.208	0.897 0.000	0.765 0.000	-0.147 0.392	-0.124 0.472	-0.256 0.132	
Distance of drainage to sources	-0.130 0.451	-0.259 0.127	0.435 0.008	0.745 0.000	0.984 0.000	-0.324 0.054	-0.108 0.529	-0.310 0.066	0.812 0.000

Table 4
Multi-linear regression model for freight PPV

Predictor	Coef	SE Coef	T	P	S	R-Sq
Constant	0.5540	0.5461	1.01	0.3128		
Speed	0.05553	0.01232	4.51	0.000	0.597443	51.7%
Distance	-0.10029	0.03163	-3.17	0.003		

Table 5
ANOVA for the model of freight trains

Source	DF	SS	MS	F	P
Regression	2	12.6041	6.3020	17.66	0.000
Residual Error	33	11.7790	0.3569		
Total	35	24.3831			

regression are smaller than 0.05. This indicates that the null hypothesis (H_0) is rejected, and the alternative hypothesis (H_1) is supported. Therefore, in the model to estimate the freight train PPV, these predictors could be used. The standard error of the constant value coefficient is 0.5540, the speed value is 0.05553, and distance is -0.10029. Due to the small values of the standard error for each variable, the values are dependable in predicting the population parameter. The R-squared (R^2) and the square root of the mean square error (S) determine how fit the model is against the collected data (Minitab, 2010). Table 4 shows that the S value is 0.597443, which represents the prediction of the variance of data in the linear relationship between the predictor and the response. R^2 is used to regulate the linear relationship between the predictor and the response. The R^2 value used for the development of the model is 51.7% of the variations.

Table 5 shows the Analysis of Variance (ANOVA) allocation of the output. The hypotheses for this test are described as follows:

H_0 = The PPV model cannot be used for estimating.

H_1 = The PPV model can be used for estimating.

Table 5 proves that the p-value is less than the α -level which is 0.05 leading to the acceptance of the H_1 and the rejection of the H_0 . Therefore, the regression model is deemed significant, and could be used to elaborate or forecast the freight train PPV if the empirical data of the speed and distance are used. In conclusion, the model of estimation is developed as shown in Equation 3 in the form of regression equation for the freight PPV,

$$PPV_{Freight} = 0.554 + 0.0555s - 0.100d \quad [3]$$

Where:

$PPV_{Freight}$ = Peak Particle Velocity (mm/s) for freight type of train

s = Speed of train (km/h)

d = distance of receiver to sources (m)

The Equation 3 shows that the important variable coefficient for this model is the speed which has a positive sign. This implies that the increase of speed leads to an increase in PPV, while the decrease between the receivers and the sources results in the decrease in PPV. This pattern of model is similar to the findings made by Paneiro et al. (2015) when only speed and distance are considered as the parameters for model development.

Justification of the Regression Model Assumptions for Freight Train Model

The next step involved was the residual plot verification process to decide whether the model was appropriate, and the regression projection was identified. The characteristics between the fitted response values and the response values observed were the residual plots. Figure 10 shows the residual versus fit value plot for freight train PPV. From Figure 10, residual plot tends to scatter randomly, and the plot is scattered close to the horizontal line in correspondence to approximately zero residuals. Hence, the proof of missing terms or non-constant variance does not exist (Minitab, 2010).

Normality Test for Residuals of Freight PPV Prediction Model

The goodness-of-fit test and probability plot, such as the Kolmogorov-Smirnov and Anderson-Darling normality tests, determine whether the residuals were normally distributed. Figures 11 and 12 show that the points are scattered closely around the straight line which show that the residuals are normally distributed.

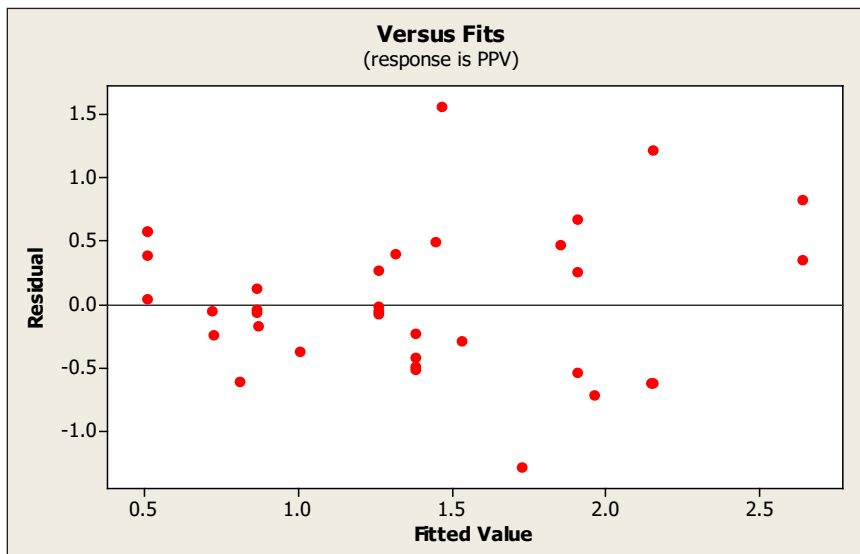


Figure 10. Residual versus fit value plot for freight PPV prediction model

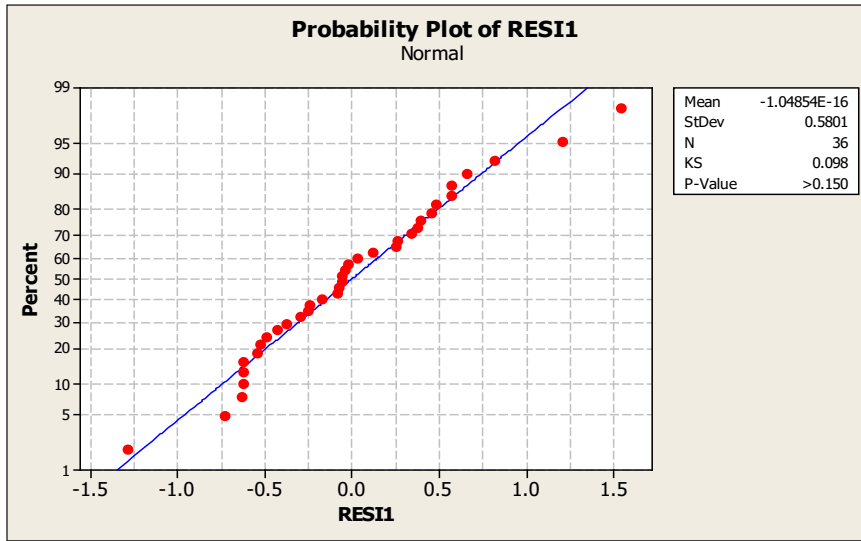


Figure 11. Kolmogorov-Smirnov normality test for freight PPV prediction model

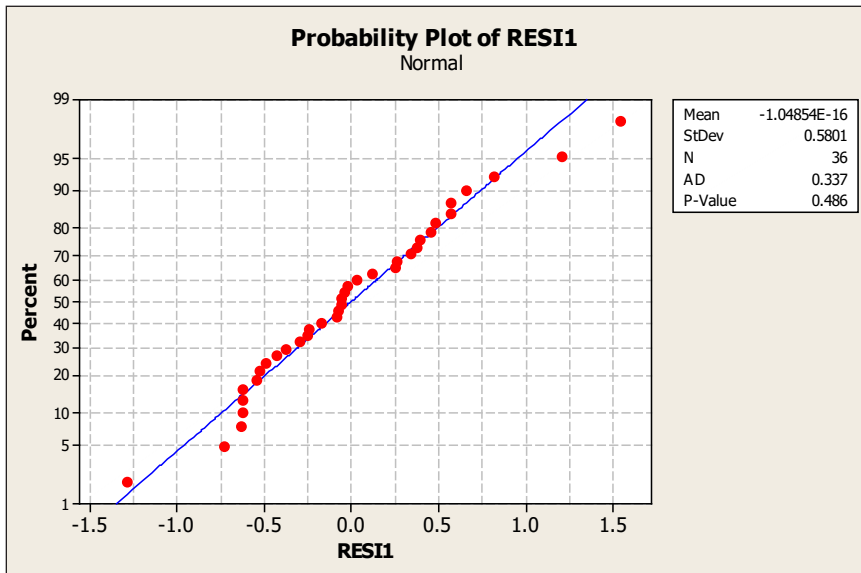


Figure 12. Anderson-Darling normality test for freight PPV prediction model

The tests of hypotheses for Anderson-Darling and Kolmogorov-Smirnov normality tests are described as follows:

H_0 = The residuals for the predicted model are normal.

H_1 = The residuals for the predicted model are not normal.

Since the p-values of the Anderson-Darling and Kolmogorov-Smirnov normality tests are more than 0.05, the H_0 is accepted, and the residuals follow a normal distribution curve.

MODEL VALIDATION

The developed PPV model for freight trains must be evaluated to determine the ability of the model to represent the actual situation and condition to describe the presence of variability in a sample other than the set used for the model development.

Scatterplot of the Freight Model

Figure 13 shows the relationship between the empirical PPV and the predicted PPV for freight trains developed in this research. Figure 13 demonstrates that the points of predicted PPV versus empirically scattered PPV are close around the straight line, indicating that the PPV of the predicted model for freight train can be accepted.

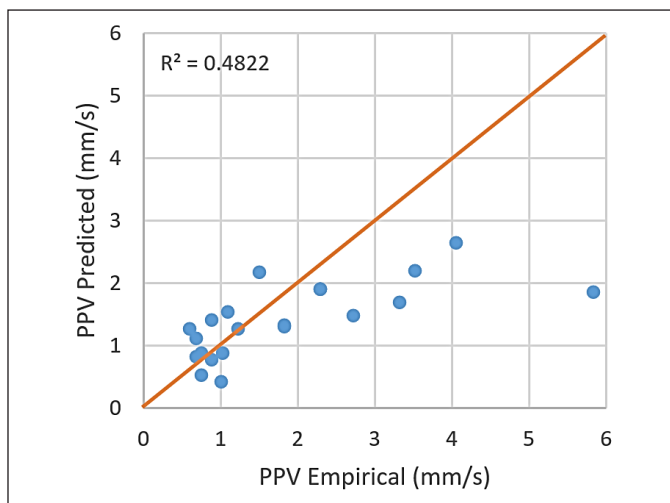


Figure 13. Predicted PPV versus empirical PPV
Where PPV empirical is denoted as empirical PPV (mm/s), and PPV predicted using Equation 1 is denoted as predicted PPV (mm/s).

RSME, MAE, AND MAPE OF PPV MODEL

Table 6 shows the comparison of RMSE, MAE, and MAPE of the PPV for freight train predicted model. As shown in Table 6, the deviation of RMSE from the empirical value of PPV is 0.9712 mm/s, while the deviation of MAE from the empirical value of PPV is 0.7422 mm/s. The MAPE for the empirical value of PPV is 27.2%. Thus, it can be summarised that due to the limited difference values of the RMSE, MAE, and MAPE, the PPV model for freight trains is appropriate to estimate the PPV.

Table 6
RMSE, MAE, and MAPE for PPV freight

MODEL	RMSE (mm/s)	MAE (mm/s)	MAPE (%)
PPV Freight	0.9712	0.7422	27.154

Comparison of Mean for Predicted PPV with Empirical PPV using Paired T-Test

The mean comparison was completed between the PPV from the data observed by taking the validation data set and the predicted PPV as shown in Table 7. The alternative and null hypotheses are as follows:

H_0 = The mean difference for the model is equal to zero.

H_1 = The mean difference for the model is not equal to zero.

The p-value is 0.055, which is greater than 0.05 as shown in Table 7, suggesting that the null hypothesis (H_0) is not rejected at the significance level of 5%. This shows that the PPV of the projected commuter train model does not vary much from the empirical PPV values.

Table 7
Validation analysis result for PPV from freight model

Test	Vab
t-statistic	2.04
p-value	0.055

CONCLUSION

Based on the Equation 3 model developed in the multiple linear regressions, it is established that PPV of the ground-borne vibration velocity could be calculated using the speed of the trains and the distance from the receiver to the sources. It is found that PPV of the ground-borne vibration velocity increases almost linearly when the speed of the train increases. From the regression model, it is discovered that the distance of the receivers (residential areas) to the sources (train tracks) produces a reverse effect on the PPV of the ground-borne induced by freight trains. From Equation 3, when the distance increases, the PPV of ground-borne vibration velocity tends to decrease. The closer the residential houses to the track, stronger ground-borne vibration can be felt by the residents. To summarise, the model developed has been proven to be able to predict the peak value of ground-borne vibration velocity induced by freight trains. The model development and other findings can be used in future research but limited to the characteristics based on the scopes of this study. Practitioners can use the model by using minimal number of tools or even without tools to predict the vibrations induced by freight trains at studied sites. The developed model is user-friendly and easy to use. In addition, it is reliable because the model undergoes the validation and calibration processes. The model developed acts as a bridge between the theoretical knowledge and the actual implementation.

ACKNOWLEDGEMENT

The authors would like to thank the authorities from the Faculty of Civil Engineering, Universiti Teknologi MARA (UiTM) for their constant support and encouragement. Appreciation goes to the Research Management Institute (RMI, UiTM) and Ministry of

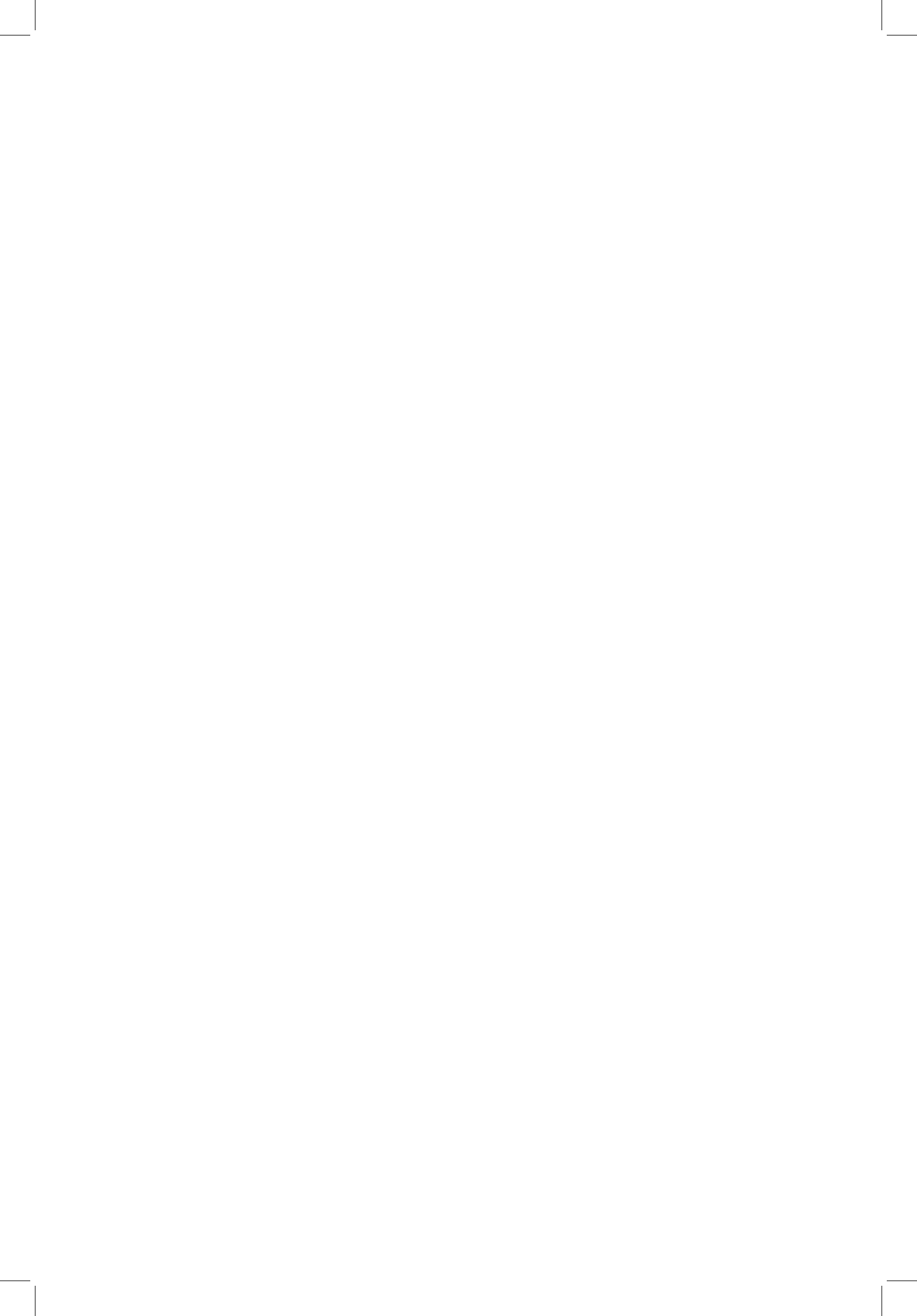
Higher Education Malaysia (MOHE) for the financial support's FRGS Grant scheme: RMI File No: 600-IRMI/FRGS 5/3 (008/2019), Sponsorship File No: FRGS/1/2018/SKK06/UITM/02/5.

REFERENCES

- Alcudia, A. D., Stewart, R. R., Eliuk, N., & Espersen, R. (2007). Vibration and air pressure monitoring of seismic sources. *CREWES Research Report*, 19, 1-14.
- Al-Hunaidi, M. O. (1994). Evaluation of appropriate sample size for measurement of vibration levels induced by rail transit vehicles. *Canadian Acoustics*, 22(3), 181-182.
- Avellan, K., Belopotocanova, E., & Puurunen, M. (2017). Measuring, monitoring and prediction of vibration effects in rock masses in near-structure blasting. *Procedia Engineering*, 191, 504-511. <https://doi.org/10.1016/j.proeng.2017.05.210>
- Bahrekazemi, M. (2004). *Train-induced ground vibration and its prediction* (PhD thesis). Royal Institute of Technology, Stockholm, Sweden. Retrieved September 29, 2019, from http://www.gatewaycog.org/media/userfiles/subsite_9/files/rl/HSRReferenceMaterialsReportsMapsandOtherHSTSections/References-Train-Induced_Ground_Vibration_and_Its_Prediction_2004.pdf
- British Standard. (2008). *BS 6472-1: Measurement and evaluation of human exposure to whole-body mechanical vibration and repeated shock*. Retrieved September 19, 2019, from <https://www.standardsuk.com/products/BS-6472-1-2008>
- Cenek, P. D., Sutherland, A. J., & McIver, I. R. (2012). *Ground vibration from road construction* (No. 485). The National Academies of Sciences, Engineering, and Medicine.
- Deutsches Institut für Normung. (1999). *DIN 4150-3: Structural vibrations – Part 3: Effects of vibration on structures*. Retrieved September 19, 2019, from <https://codehub.building.govt.nz/resources/din-4150-3-1999/>
- Department of Environment Malaysia, (2007). *The planning guidelines for vibration limits and control in the environment*. Ministry of Natural Resources and Environment. . Retrieved October 2, 2018, from <https://environment.com.my/wp-content/uploads/2016/05/Vibration.pdf>
- Eitzenberger, A. (2008). *Train-induced vibrations in tunnels—A review, division of mining and geotechnical engineering, Department of Civil, Mining and Environmental Engineering, Luleå University of Technology* (Technical Report). Retrieved September 30, 2019, from <https://www.diva-portal.org/smash/get/diva2:996052/FULLTEXT01.pdf>
- ESCAP. (1996). *Trans-Asian railway route requirements: development of the Trans-Asian railway in the Indo-China and ASEAN subregion volume 2*. United Nation Economic and Social Commission for Asia and the Pacific. Retrieved January 30, 2020, from <https://www.unescap.org/sites/default/d8files/knowledge-products/Trans-Asian-Railway-Route-Requirements-Volume-2.pdf>
- Garg, P. (2017). *Displacement measurement using a laser Doppler vibrometer mounted on an unmanned aerial vehicle* (Master dissertation). University of the New Mexico, USA. Retrieved September 19, 2019, from https://digitalrepository.unm.edu/cgi/viewcontent.cgi?article=1392&context=ece_etds

- Hajek, J. J., Blaney, C. T., & Hein, D. K. (2006, September 17-20). Mitigation of highway traffic-induced vibration. In *2006 Annual Conference of the Transportation Association of Canada* (pp. 1-13). Charlottetown, Prince Edward Island, Canada.
- Hanson, C. E., Tower, D. A., & Mesiter, L. D. (2006). *Transit noise and vibration impact assessment*. Office of Planning and Environment, Federal Transit Administration (FTA). Retrieved June 02, 2020, from https://docs.vcrma.org/images/pdf/planning/ceqa/FTA_Noise_and_Vibration_Manual.pdf
- Hemsworth, B. (2000). Reducing groundborne vibrations: state-of-the-art study. *Journal of Sound and Vibration*, 231(3), 703-709. <https://doi.org/10.1006/jsvi.1999.2642>
- Huang, Z. (2016). *Intergrated railway remote condition monitoring* (Doctoral dissertation). The University of Birmingham, England. Retrieved June 20, 2019, from <https://etheses.bham.ac.uk/id/eprint/7904/1/Huang17PhD.pdf>
- Hunt, H. E., & Hussein, M. F. (2007). Ground-borne vibration transmission from road and rail systems-prediction and control. In M. J. Crocker (Ed.), *Handbook of Noise and Vibration Control* (pp. 1458-1469). John Wiley & Sons, Inc.
- ISO. (1997). *ISO 2631-1:1997(en) Mechanical vibration and shock — Evaluation of human exposure to whole-body vibration — Part 1: General requirements*. International Organization for Standardization. Retrieved September 19, 2019, from <https://www.iso.org/standard/7612.html>
- Jiang, T., & Zhang, X. (2004, August 1-6). *In situ* experiments and numerical assessment of environmental vibration induced by urban viaduct rail transit in Shanghai. In *13th World Conference on Earthquake Engineering, Canada*. (pp. 1-11). Vancouver, Canada.
- Jones, C. J. C., & Block, J. R. (1996). Prediction of ground vibration from freight trains. *Journal of Sound and Vibration*, 193(1), 205-213. <https://doi.org/10.1006/jsvi.1996.0260>
- Kempfert, H. G., & Gebreselassie, B. (2006). Material properties of soft soils. In *excavations and foundations in soft soils* (pp. 11-55). Springer Science & Business Media.
- Khoo, C. M., Gopalan, T., Rahman, N. A. A., & Mohamad, H. (2019). volume loss caused by tunnelling in Kenny hill formation. *International Journal*, 16(54), 164-169. <https://doi.org/10.21660/2019.54.8316>
- Lazi, M. K. A. M., Mustafa, M., & Abd Rahman, Z. (2016). Assessing pedestrian behavior and walking speed on staircase: A Review. In M. Yusoff, N. Hamid, M. Arshad, A. Arshad, A. Ridzuan & H. Awang (Eds.), *International Civil and Infrastructure Engineering Conference (InCIEC)* (pp. 1019-1029). Springer. https://doi.org/10.1007/978-981-10-0155-0_85
- Madshus, C., Bessason, B., & Hårvik, L. (1996). Prediction model for low frequency vibration from high speed railways on soft ground. *Journal of sound and vibration*, 193(1), 195-203. <https://doi.org/10.1006/jsvi.1996.0259>
- Malay Mail. (2008, October 10). Your voice readymade train wreck. *Malay Mail*. Retrieved August 8, 2019, from https://web.archive.org/web/20081013081610/http://www.mmail.com.my/Readymade_train_wreck.aspx.
- Minitab. (2010). *Minitab statistical software, release 16 for windows, State College, Pennsylvania*. Retrieved February 15, 2019, from <https://www.minitab.com/en-us/products/minitab/>

- Orehov, V. V., Moghanlou, R. N., Negahdar, H., & Varagh, A. M. B. (2012, September 24-28). Investigation effects of trench barrier on the reducing energy of surface waves in soils. In *15th World Conference on Earthquake Engineering* (pp. 24-28). Lisbon, Portugal.
- Paneiro, G., Durão, F. O., e Silva, M. C., & Neves, P. F. (2015). Prediction of ground vibration amplitudes due to urban railway traffic using quantitative and qualitative field data. *Transportation Research Part D: Transport and Environment*, *40*, 1-13. <https://doi.org/10.1016/j.trd.2015.07.006>
- Peng, L. C., Leman, M. S., Hassan, K., Nasib, B. M., & Karim, R. (2004). *Stratigraphic Lexicon of Malaysia*. Geological Society of Malaysia.
- Persson, N. (2016). *Predicting railway-induced ground vibrations*. LUND University. February 02, 2019, from <http://www.byggmek.lth.se/fileadmin/byggnadsmekanik/publications/tvsm5000/web5212.pdf>
- Roess, R. P., Prssas, E. S., & McShane, W. R. (2006). *Traffic engineering* (3rd Ed.). Prentice Hall, Inc.
- Roslan, N. (2017). *The potential susceptibility of urban hardrock aquifers to hydraulic and contaminan stresses: The case of Shah Alam, Malaysia* (Doctoral dissertation). The University of Birmingham, England. Retrieved September 29, 2019, from <https://core.ac.uk/download/pdf/79609683.pdf>
- Sakaue, S., Yao, H., & Suzuki, T. (2012). Applied MEMS Micro-vibration Sensors and Structural Health Monitoring. *Technologies Supporting Society and Industry*, *58*(1), 32-47.
- Suhairy, S. A. (2000). *Prediction of ground vibration from railways*. SP Swedish National Testing and Research Institute. Retrieved January 10, 2019, from <http://doutoramento.schiu.com/referencias/outras/Suhairy,%20Sinan%20al.pdf>
- Sulaiman, N. (2018). *Empirical modelling of ground-borne vibration from road traffic*. (Unpublished Doctoral dissertation). University Putra Malaysia, Malaysia. Retrieved October 10, 2019, from <http://psasir.upm.edu.my/id/eprint/67898/1/FK%202018%2033%20IR.pdf>
- Tan, Y. C., Gue, S. S., Ng, H. B., & Lee, P. T. (2004, March 16-18). Some geotechnical properties of Klang clay. In *Malaysian Geotechnical Conference* (pp. 1-7). Sheraton Subang, Malaysia.
- Watts, G. R. (1990). *Traffic induced vibrations in buildings* (Research report 246). Transport and Road Research Laboratory, Crowthorne, Berkshire. Retrieved June 06, 2019, from <https://www.yumpu.com/en/document/view/25243865/traffic-induced-vibrations-in-buildings-g-r-watts-department-for->
- White Industrial Seismology Inc. (2009). *Mini-seis digital seismograph: Operating manual*. Retrieved October 20, 2019, from <https://whiteseis.com/MemberPages/docspecs/Mini-Seis%20Manual.pdf>
- With, C., Bahrekazemi, M., & Bodare, A. (2006). Validation of an empirical model for prediction of train-induced ground vibrations. *Soil Dynamics and Earthquake Engineering*, *26*(11), 983-990. <https://doi.org/10.1016/j.soildyn.2006.03.005>



Developing a Diamond Framework Model Based on “Integration” of Project Success Measures for Construction Project Management in Yemen

Muaadh Yahya Al-Kuhail^{1*}, Hamoud Ahmed Al-Dafiry², Tarek Abdullah Barakat² and Abdulwahad Al-Ansi¹

¹Civil Engineering Department, Faculty of Engineering, University of Science and Technology, Yemen

²Civil Engineering Department, Faculty of Engineering, Sana'a University, Yemen

ABSTRACT

The most prominent obstacle facing the construction industry in Yemen is mismanagement. Developing appropriate tools, approaches, and standards for managing construction projects will contribute effectively to the development and prosperity of the Yemeni construction industry. This study aims to provide the tools, approaches and standards for project management based on the opinions of the Yemeni advisory bodies. It presents an Integrated Cost, Quality, Time, and Scope (ICQTS) diamond framework model by developing the traditional triangle model in project management providing a practical contribution to researchers and companies working in the construction industry. The study uses a descriptive and analytical approach through a comprehensive literature review followed by a field study using a designed questionnaire distributed to the relevant Yemeni advisory bodies. The study concluded with the development of the traditional triangle model resulting in the introduction of the diamond framework model in the management of construction projects. Integration management was found to have a strong impact on

project success presenting the framework model as an easy and flexible tool that unifies and integrates the processes and roles in the project and directing it towards achieving project stakeholder objectives. The literature largely neglects the impact of integration management in the various models and is mostly overlooked. Inclusion of integration management in the presented model will highlight measures of project success stressing the need to integrate and

ARTICLE INFO

Article history:

Received: 12 January 2021

Accepted: 13 April 2021

Published: 31 July 2021

DOI: <https://doi.org/10.47836/pjst.29.3.23>

E-mail addresses:

emyhk2011@gmail.com (Muaadh Yahya Al-Kuhail)

albonian2000@yahoo.com (Hamoud Ahmed Al-Dafiry)

barakatgroupyemen@gmail.com (Tarek Abdullah Barakat)

w.alansi@ust.edu (Abdulwahad Al-Ansi)

* Corresponding author

manage them together. Future studies may research the differences in the opinions of construction companies.

Keywords: Diamond framework, ICTQS framework, project management, traditional triangle model, Yemen construction industry

INTRODUCTION

Construction projects are unique including the number of parties involved, project complexity and large circulating information. Therefore, construction projects face several challenges that may lead it to stagger (Alwaly & Alawi, 2020). Deficiencies and inefficiencies are frequent issues in the construction industry in all countries of the world, including Yemen, which is considered one of the least developed countries in the construction industry (Alawi et al., 2016; Alawi & Masoud, 2018). A group of studies have examined the factors of failure in the construction industry in Yemen concluding that poor construction project management is the main problematic factor in the construction industry in Yemen (Alaghbari et al., 2018; Al-Sabahi et al., 2014; Gamil & Rahman, 2020). Therefore, developing project management concepts, methods and tools will contribute to improving project management performance (Angarita & Gallardo, 2018).

The traditional triangle is considered one of the most important models in project management, providing a set of project success measures (scope, time, cost, and quality). Recently, however, practitioners and researchers have studied metrics of project success keeping in mind the achievement of project goals from a stakeholder perspective (PMBOK, 2017). Measuring project success is one of the difficult tasks facing researchers and practitioners in project management (PMBOK, 2017) due to the lack of a standard definition of project success as well as unavailability of a specific methodology for measuring it (Kermanshachi, 2016). Mir and Pinnington (2014) and Wateridge (1998) add that few interested in project management seriously think about measures of project success. Wells Jr (1998) laments the lack of interest in defining project success and sufficing to do so only in generic terms. Davis (2014) and Lim and Muhammad (1999) presented a vision for project success through partial and total measures, as the partial measures included time, cost, quality, performance, and safety. The total measures include the partial measures and the actual benefit of the project at the operational stage. The study by Westerveld (2003) supports the traditional triangle method in measuring project success according to the constraints of scope, time, and cost. However, Heravi and Ilbeigi (2012) found that several projects that did not achieve the iron triangle project measures were considered successful as they achieved project stakeholder goals. An example are the North Sea projects performed in the seventies. They suffered cost and time overruns but were considered successful projects since the project stakeholders' objectives were not related to time or cost measures. Ika (2009) and Shenhar et al. (1997) support the view that project success measured by

the extent of adherence to the constraints in the traditional triangle means the project is managed efficiently but neglecting achievement of stakeholder objectives means the project did not meet their expectations. Mir and Pinnington (2014) and Wateridge (1998) indicate that the focus of project managers is generally limited to short-term measures related to project operational constraints to the detriment of long-term metrics related to project stakeholder objectives. Hence the need to develop project management concepts, tools, and measures that will improve construction project management performance in the short and long-terms to achieve both traditional measures as well as project stakeholder objectives.

Adding new measures to develop the traditional triangle model has become a necessity to support the traditional project success metrics. It is also necessary to search for modern methods that keep pace with the recent developments in the concept of project success and to address the shortcomings of the traditional triangle model when managing project implementation. Several studies have indicated the importance of adding other metrics to those of the traditional triangle model (Cao & Hoffman, 2011; Ika, 2009; Nicholas & Steyn, 2017; Shenhar et al., 2001; Silvius et al., 2017; White & Fortune, 2002). These studies confirmed the survival of the main project success metrics of the traditional triangle project. Other researchers indicated the need to add new measures to match the requirements of the current construction industry to improve project management performance since the current traditional triangle model is insufficient to monitor all processes (Atkinson, 1999; Ong et al., 2018).

Therefore, this study seeks to bridge the gap in the literature and aims to:

1. Perform a literature review of the subject matter;
2. Conduct a field study and analyze the responses to develop a new framework model to enhance construction project management performance;
3. Develop a new framework model based on incorporating integration to the traditional triangle model to achieve unification and coordination between all operations and activities in the project and directing them towards achieving project stakeholder objectives.

The new diamond framework model introduces a new idea in construction project management by not relying solely on the traditional project success metrics as constraints but as measures that are traded between them through the addition of “integration” as a new measure. This is to achieve project success from project stakeholder perspective. This study shall present the innovative ICTQS framework model by providing:

1. A comprehensive literature review;
2. The methodology of the study performed and sampling;
3. Questionnaire design and data collection;
4. Data analysis, integration, and triangulation;
5. Results and discussion; and
6. Summary and recommendations.

The result is to achieve the main aims and objectives of the study and to propose a practical framework model in construction project management in Yemen based on the responses of those in the Yemeni construction industry to enhance project management performance.

METHODS

This section shall outline the methodology and methods used. The methodology started with a comprehensive literature review followed by development of the questionnaire and performing the pilot study on the it. The questionnaire was distributed to the respondents and collected, analyzed, and results triangulated with the literature to arrive at the conclusions and development of the Diamond Framework Model. The following subsections provide the steps and details of the methodology and field study.

Literature Review

The literature review incorporated the traditional project metrics and models and the developments thereafter as provided in the following subsections.

The Traditional Triangle Model in Project Management. The traditional triangle model in project management is considered one of the first models to be used on a large scale as it defined the traditional project success measures and the relationship between them. It is still used as a basic reference for many researchers and practitioners in the field of project management. Many studies have used it. It is considered the focus of metrics affecting the success or failure of projects and is used to control project constraints.

Several models providing the main project success factors have evolved from the traditional triangle model shown in Figure 1. In 1969 Martin Barnes explained the factors of “time”, “cost”, “quality” and the relationship between them by drawing a triangle named

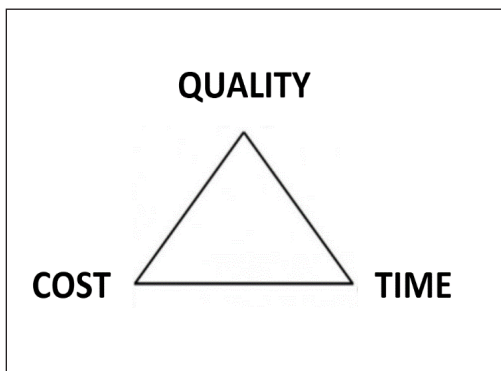


Figure 1. Project triangle model
Source. Barnes (2007)

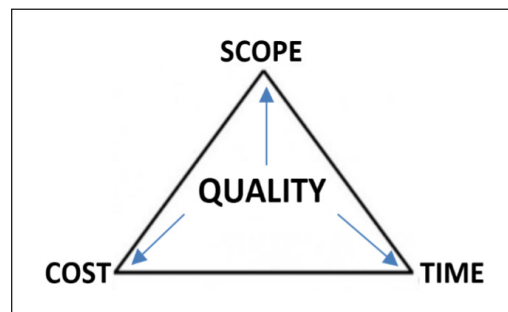


Figure 2. The traditional triangle model in project management
Source. Demirkesen and Ozorhon (2017), Wyngaard et al. (2012)

the “project triangle” (Barnes, 2007). The purpose of this triangle was to illustrate the importance of balancing the three measures to improve project performance and monitoring.

The project triangle model was the building block that researchers built upon to develop measures of project success (Figure 1) (Bennett, 2003; Dobson, 2004; Frame, 2002; Hamilton, 2001; Turner & Simister, 2000). The traditional triangle model in the field of project management emerged representing the main factors of project management success: scope, time, cost, and quality (Figure 2) (PMBOK, 2017).

Developments of the Traditional Triangle Model in Project Management. During the eighties, Barnes (1988) developed the project triangle model and established a new measure, “performance”, replacing it with “quality” and named the new model the “goals triangle”. Other researchers developed the project triangle model into various models, either by adding or changing measures of project success. Among these models is the “tetrahedron” model (Figure 3) that was referred to by Atkinson (1999). Marasco (2004) came out with the “pyramid” model (Figure 4) and Wideman (2004) presented the “quadrupeds” model (Figure 5). Felician (2011) came out with the “iron hexagon” model (Figure 6) and Ebbesen and Hope (2013) presented the “Iron Box” model (Figure 7).

Researchers have named the various models, including the “project triangle” (Devaux, 1999; Major et al., 2003), “triple constraints” (Bennett, 2003; Dobson, 2004; Frame, 2002; Hamilton, 2001; Turner & Simister, 2000), and “the project pyramid” (Marasco, 2004). The basic building blocks of the models (Orr, 2007) remained the “traditional triangle” (Atkinson, 1999), “the golden triangle” (Lock, 2007; Ong et al., 2018), “the triangle of goals and trade-offs” (Barnes, 1988; Williams, 2002), “the square root” (Atkinson, 1999), indicators of success (Williams, 2002), the traditional iron triangle (Figure 8) (Caccamese & Bragantini, 2012), the iron hexagon (Felician, 2011), and the iron box (Ebbesen & Hope, 2013).

When analyzing these models, it is noticed that there is a difference in the types of the measures provided in them except for two measures that were fixed in most models: namely,

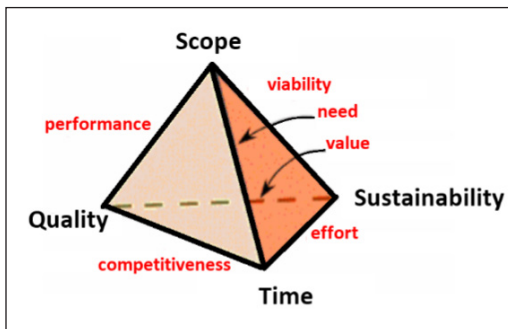


Figure 3. Tetrahedron model
Source: Atkinson (1999)

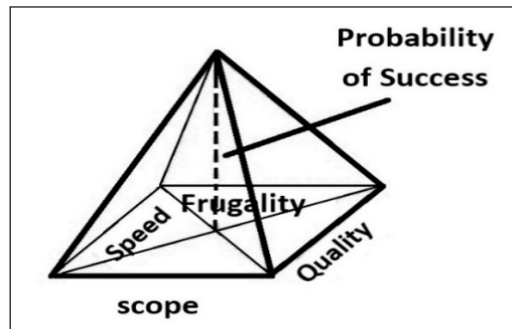


Figure 4. Project pyramid model
Source: Marasco (2004)

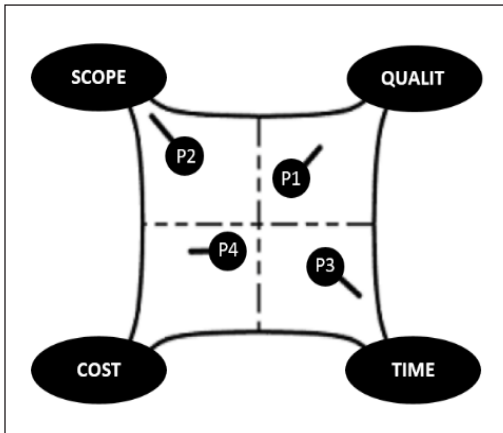


Figure 5. Quadrilaterals model
Source. Wideman (2004)



Figure 6. The Iron Hexagon model
Source. Felician (2011)

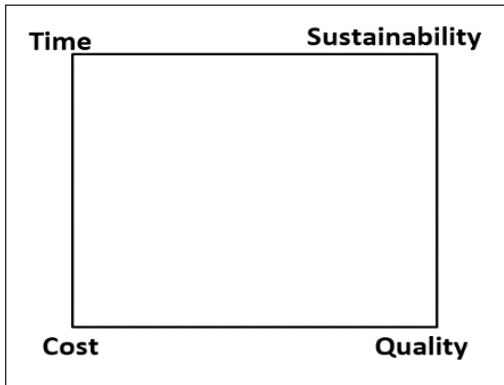


Figure 7. Model of the Iron Box
Source. Ebbesen and Hope (2013)

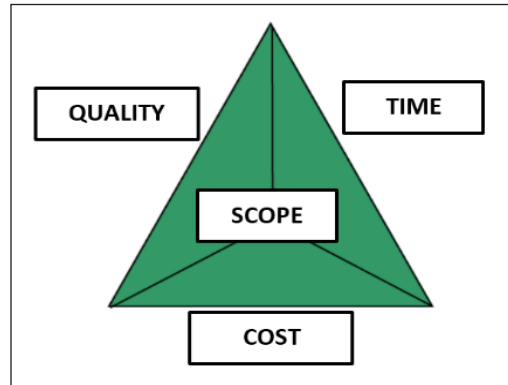


Figure 8. The Traditional Iron model
Source: Caccamese and Bragantini (2012)

“time” and “cost”. Some studies referred to these measures as “schedule” and “budget” (Vahidi & Greenwood, 2009). Over the past fifty years researchers have conducted several studies in the field of project management through which they reached several measures and factors affecting the success of the project (Atkinson, 1999; Caccamese & Bragantini, 2012; Felician, 2011; Nicholas & Steyn, 2017). The development of the model during the last five decades is presented in Table 1.

From Table 1, it is noted that the “traditional triangle model” has been at the forefront of project success measures during the three periods. This model has been the reference and the basis for measures of project success. It can be considered the foundation model on which researchers built on in their studies to achieve traditional success measures. Several alternative measures have been proposed as illustrated in Table 2.

Table 1
Measures and success factors of the project from 1960 until now

Measures & success factors	Periods		
	Period 1 1960s-1980s	Period 2 1980s-2000s	Period 3 2000s - until now
Success measures	"The traditional triangle model" Time, cost, and quality	Traditional Triangle plus: Customer satisfaction, benefits for the organization (ORG), end user satisfaction, benefits for stakeholders, benefits for project staff.	The traditional triangle model: The strategic objective of client organizations and business success, end-user satisfaction, benefits for stakeholders, benefits for project personnel, symbolic and rhetorical assessments of success and failure.
Success factors	Anecdotal lists	Lists of CSFs + set of frameworks.	More comprehensive CSF frameworks, symbolism, and rhetoric of success factors
Confirmation of the study	Project management success	Project / product success	Project / product, portfolio, program success, narration of success and failure

Source. Nicholas and Steyn (2017)

Table 2
Traditional measures and some alternative standards

Traditional measure & standard	Project		
	Project of triangle model	Project of trade-offs	Project of success / failure
Traditional Measures	Time, cost, scope, quality / performance	Time, cost, scope	Time, cost, scope, quality/ performance
Examples of standards recommended presented by Orr (2007)	Specifications, risks, people, resources, exclusion, speed, external environment, information The system, benefits to the organization, benefits to the stakeholder community.	Quality, external environment, management, and project team, Outlook, Resources, Reliability, Control, Service, Response, reputation, market position, profit.	Various stakeholders Success criteria, customer satisfaction The external regulatory environment Project managers, team members.

Source. Orr (2007)

Integration Role in Projects Success. Several studies have indicated the importance and role of “integration” in the success of projects. The study by Demirkesen and Ozorhon (2017) concluded that integration management has a noticeable effect in improving project management performance. This helps achieve the stakeholder project objectives. In their

study, Asif et al. (2010) concluded that “integration” is an approved process to improve the structure of the administrative system and contributes to meeting the requirements of stakeholders. Demirkesen and Ozorhon (2017) and Eisner et al. (1993) also indicated that integration management is one of the most important elements in systems engineering. The study introduced a concept called “integration engineering” that includes environmental operability, requirements and interfaces and testing and validation of the work program as essential elements. The study also indicated the main elements of integration management such as schedule, cost calculation and documents which are the basic components of systems engineering. The researchers imply that project integration management is a prerequisite for the correct coordination between project activities as it impacts on project success.

Studies have shown that there is an important role for effective integration in project management success (Berteaux & Javernick-Will, 2015; Halfawy & Froese, 2007; Ozorhon et al., 2014; Ospina-Alvarado et al., 2016; Tatum, 1990). The Project Management Guide also identified the ten main areas of project management knowledge, and among these areas, project integration management is the first area. This includes planning, assembly, standardization, and coordination processes for integrated project management (PMBOK, 2017).

Comment. The period in which the traditional triangle model appeared until today has been accompanied by significant technological changes and developments. For example, computers and software, structural robots, and artificial intelligence. have affected various aspects of life in general including the construction industry. This has led to the development of measuring project success to include the project’s achievement of project stakeholder objectives. This has also contributed to emergence of modern management approaches to keep pace with these changes through the development of project management processes and tools. Therefore, adding new measures to improve the traditional triangle model has become a necessity to support the traditional project success metrics. It is also necessary to research modern approaches that keep pace with the development of project success metrics addressing aspects of deficiencies in the traditional triangle model.

It is noticeable that each measure of project success in the traditional triangle model deals with a specific aspect of project management. For example, the measure of “time” relates to estimation and management of time for project implementation. Each measure handles one aspect of the project except for the quality measure that affects, and is affected by, other measures (e.g., time and cost). Furthermore, the metrics shown, as well as other metrics not shown in the traditional triangle are interrelated. Therefore, these metrics need a new measure that achieves integration between them to achieve the goals from the stakeholders’ perspective to enhance the probability of achieving project objectives and project success.

The following points are evident from previous studies:

1. The traditional triangle remains the basis for measuring project success;
2. The current measures of project success are insufficient and there is a need to develop the traditional triangle model by adding other measures;
3. Direction of measuring project success includes achieving project stakeholder objectives;
4. Integration has a positive effect on the project success and performance and assist in achieving the project stakeholder objectives;
5. Integration is an important measure for unifying and coordinating the processes and roles in the project and directing them towards project success and the achievement of its objectives.

Research Approach and Design

The researcher conducted a field study in which the main hypothesis was tested through a questionnaire designed by the researcher specifically for this purpose, taking advantage of the PMBOK (2017). The questionnaire was evaluated by a group of academics and practitioners specializing in project management. The advisory bodies that manage construction projects in Yemen were targeted and selected by simple random sampling. The data was collected, analyzed and results obtained. Figure 9 illustrates the methodology and steps used in the study.

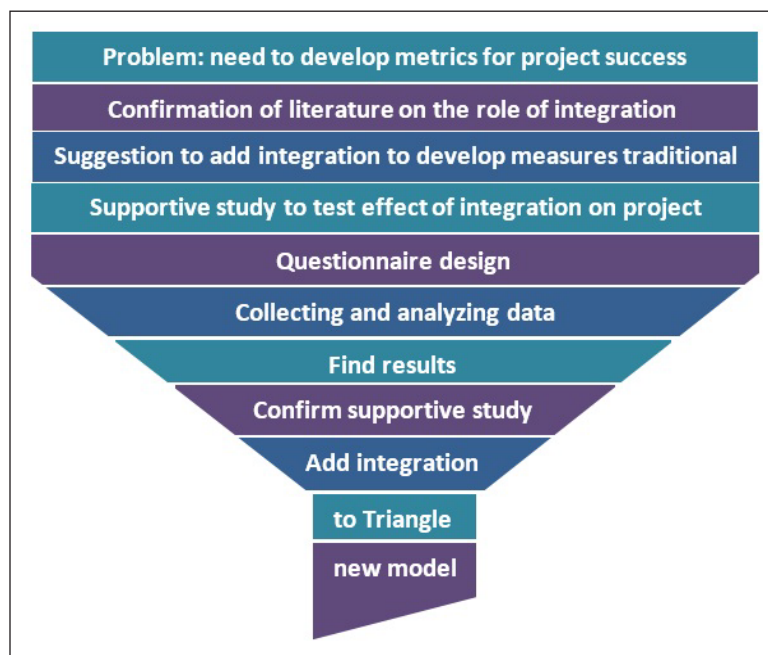


Figure 9. A drawing showing the methodology and steps used in the study

The Study Sample

The target sample included the agencies in charge of managing construction projects in the Republic of Yemen, which numbered 674 according to the database of the Ministry of Industry and Trade (2020). To obtain a statistical representative sample, Equation 1 was used according to Hogg and Tannis (2009) as follows:

$$n = \frac{m}{1 + \left(\frac{m-1}{N}\right)} \quad (1)$$

Whereas:

(m) unlimited sample size,

(N) limited sample size,

To find the value of (m), Equation 2 was used:

$$m = \frac{z^2 \times p \times (1-p)}{\epsilon^2} \quad (2)$$

Whereas:

(z) The value indicates the level of confidence (for example: 2.575, 1.96, and 1.645 represent the confidence levels at 99%, 95%, and 90%, respectively),

(p) The degree of variance between elements of the target sample (0.5),

(ε) Maximum point selection error.

Using a confidence level of 95% and a level of significance at 5% when the sample size is not specified, the estimation of the value of (m) is clarified by applying Equation 2 as follows:

$$m = \frac{(1.96)^2 \times 0.50 \times (1-0.50)}{(0.05)^2} \approx 385$$

When conducting the survey one engineer was targeted for each consulting body with a total of 674 engineers making the total number of the selected sample, (N) equal to 674. Thus, the size of the sample required to make the work successful out of the total target sample can be calculated by applying Equation 1 as follows:

$$n = \frac{385}{1 + \left(\frac{385-1}{674}\right)} = 245$$

Questionnaire Design

The questionnaire was designed to test a main hypothesis H1. Effectiveness of “integration management” has a direct and positive effect on “project success measures”. Figure 10 presents a link between integration management and project success measures, as the questionnaire consisted of three main sections:

1. Information about the consulting bodies, including age, job, years of experience, training courses, methodology used, number of employees, and number of projects;
2. The variables related to achieving the requirements of integration management (the independent variable) included: the development of the project charter, the integration of the project management plan, the integration of directing and managing the project operations, the integration of project knowledge, the integration of follow-up and control of project work, the integration of change, and the closure of the project or the stage;
3. The variables of project success measures in the traditional triangle are: scope, time, cost, and quality, which are usually considered project success metrics (PMBOK, 2017). The second and third sections of the questionnaire were prepared based on the Project Management Manual (PMBOK, 2017) issued by the American Project Management Institute.

As stated previously, the questionnaire was evaluated by a group of specialized academicians and practicing experts to ensure its effectiveness and suitability for the purpose of the study. This pilot study was conducted to ensure the questionnaire is practical for the purpose of the study.

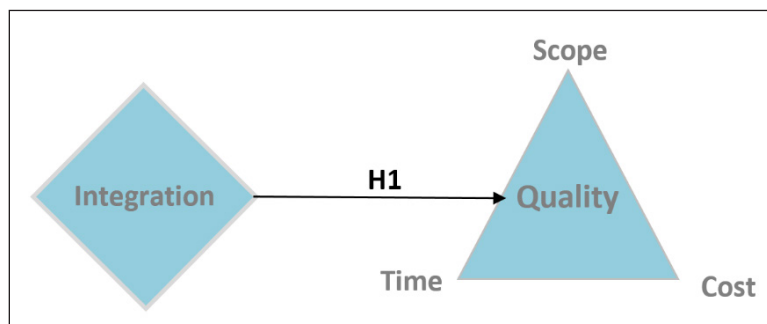


Figure 10. A link between integration management and project success measures

Methods for Data Collection

An online questionnaire was designed and administered to ensure obtaining the required sample size of 245. A simple random sample of 523 questionnaires were delivered and 235 responded on time. 18 questionnaires were excluded because they were not completed

properly. The total number of questionnaires that were used in the analysis was 217 questionnaires, which constitutes 88.57% of the required sample size.

Study Tool Scale. The researcher used a five-point Likert scale for the responses of the study sample as shown in Table 3.

Table 3
Likert scale

Response	Very High	High	Medium	Low	Very Low
Class	5	4	3	2	1

When the engineer (respondent) selects the score (5) for the response it was “very high” and the relative weight in this case is 100% and relative weights for responses are as provided in Table 4 (Likert, 1932).

Table 4
The relative weight

Serial	Verbal Appreciation	Relative weight (from – to)	The rate is 100%
1	Very High	4.20-5.00	100%
2	High	3.40-4.19	85.1%
3	Medium	2.60-3.39	68.5%
4	Low	1.80-2.59	49.8%
5	Very Low	<1.79	< 30%

After performing the validity and reliability test of the questionnaire, the researcher used the calculation of the correlation coefficient, the regression analysis, and the regression variance to test the hypothesis. The results of the analysis of the quantitative data confirmed the effect of integration on project success. This is consistent with the qualitative data obtained from the literature review.

Data Analysis

The data was entered and analyzed through the SPSS Version 23 (Statistical Package for the Social Sciences) program. The researcher tested the validity of the internal consistency, (i.e., the consistency of each axis of the questionnaire) by calculating the correlation coefficients between each axis and the total degree of the axis itself. The results are that the correlation coefficient between each of the paragraphs of the axis and the total score of the axis itself is a function of a significance level value of $\alpha = 0.05$, making the axis true to what was measured.

The stability of the questionnaire is an important characteristic of the study tool and is intended to show that it should give the same results if they are redistributed again under

the same conditions. This means stability in the results obtained from the questionnaire would not change significantly in the event of repeating distribution on the same sample. During certain periods of time, the researcher verified the stability of the study's resolution through the Cronbach's Alpha Coefficient method where the results indicated that all study axes are stable as the internal consistency of all axes reached (0.9590), which is a high value. The higher the value of (Alpha Cronbach), approaching one, the more the internal consistency increases. As for the normal distribution of data test, the researcher did not perform it because the number of questionnaires exceeded thirty questionnaires. Therefore, the data is considered normally distributed (Daher, 2018).

Integration and Triangulation of the New Framework Model

Triangulation mainly aims to strengthen the methodological structure of scientific research. The researcher used multiple methodologies and tools to research the topic to improve the validity of the results. Achieving integration between the different methods and data sources is important to form a complete picture of the topic, as each complement completes the other. Integration assumes that quantitative and qualitative methods do not study the same reality. Each focus on a specific angle. Quantitative data aims to clarify the effect of integration on project success and the development of the framework model in an objective way. The qualitative data obtained from the literature review was about the traditional triangle model, its development, the need to develop it, and the impact of integration on project success. Both the quantitative data obtained from survey responses and the qualitative data obtained from the literature show a good fit. The ICTQS framework model is validated from both sources of data.

RESULTS

The questionnaire collected data on the study sample, which was varied in terms of the employer. It was found that the responses to the questionnaire were: 51.6% are from government agencies, 15.2% are from engineering offices, 13.4% are from contracting companies, and 5.1% are from consulting firms. 74.2% of the respondents were top-level managers, while 25.8% of the respondents were engineers. The results showing the level of success and the level of achieving the requirements of integration management are provided in Table 5.

Table 5
The level of integration management and project success

Serial	Variable	Mean	Standard deviation	Level
1	Integration	3.36	0.74	Medium
2	Project success	3.32	0.64	Medium

It is noticeable that the arithmetic average of the level of achieving the requirements of integration management reached (3.36) with a degree (average) and the standard deviation (0.744). As for the variables of integration management, they were distributed between medium and high degree, where the arithmetic mean of the variable was less than (3) and of relative importance 56.60% and a standard deviation (1) relating to knowledge management. Relating to project closure, the highest mean is (3.62), standard deviation (0.9210) and relative importance of 72% indicating the importance of reviewing all project works and documents before project completion. As for the variables of the project success, the arithmetic mean of all the axes reached (3.32) with a degree (average) for all variables and the standard deviation (0.64). The arithmetic mean of the least variable was (3.2), relative importance of 64%, and a standard deviation (0.717) relating to the schedule variable. Furthermore, the highest arithmetic average is (3.38), standard deviation (0.73) and relative importance of 67.6% relating to the cost management variable showing that project managers are more successful in cost management.

To obtain the relationship between achieving the integration management requirements and the success of the project, the correlation coefficient, the regression analysis, and regression variance were calculated. The value of the correlation coefficient was (0.87) at a significance level (0.00) indicating the existence of a positive, statistically significant relationship, after which an analysis test was used. By simple linear regression, the value of the total correlation coefficient was 0.87, the value of the coefficient of determination was 0.76, and corrected determination coefficient of 0.76 indicating that achieving the integration requirements explains 76% of the changes in the dependent variable. The value of the significance level of 0.00 for the F-test. A value (less than 0.05) means there is an effect attributable to the achievement of integration requirements on the success of the project. This means that there is statistical significance, and accordingly, we accept the hypothesis that states: Effectiveness of “integration management” has a direct and positive effect on “project success measures”.

Through the value of the estimate, it becomes clear that the relationship is positive, and is (0.76). This means that integration management affects 76% of the variance in the success of the project (Figure 11) where the results were obtained from the field study confirming

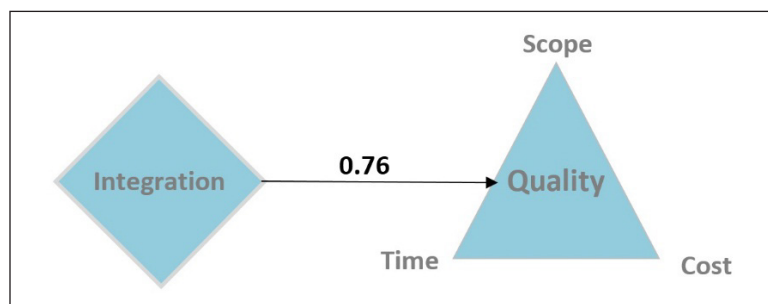


Figure 11. The path parameter between integration management and project success metrics

the important role that integration management plays in the success of the project. We can say that integration management is an important measure of the success of the project. This measure has been developed in the diamond framework template

Proposed Framework

Based on the literature review and the results of the field study that confirmed the effective role of integration management in the success of the project, the researcher developed a modern framework model. This is based on adding integration to the project success metrics in the traditional triangle and developing a new model.

There is no doubt that the measures and factors that the researcher has reached, in addition to the measures of project success in the traditional triangle model, have an impact on the success of a project. The measures of project success in the literature seem to pinpoint certain success measures without due regard to others. The traditional triangle model needs a comprehensive measure that connects and unifies the various project success measures to achieve project stakeholder goals.

Each measure of project success in the traditional triangle model is separate by itself and deals with a certain aspect in project management apart from the quality measure which affects other measures. This effect remains limited in the framework for achieving quality requirements in the project. Therefore, the need for a new measure that incorporates various operations and controls outcomes remains. Activities necessary to integrate, standardize and direct project management processes and activities to achieve project objectives is not clear in the various models. Furthermore, a gap remains between the PMI and the models provided in the literature. It further lacks incorporation of the various stakeholder perspectives.

Project success can be expressed as the level the project has achieved objectives from stakeholder perspective. In the current models' project success depends on the trade-offs between the measures related to project management, which are "scope", "time" and "cost". The trade-offs may be for calculating one measure at the expense of the other two based on the priority given. The project objectives determine the priority which may be for project time when time is the priority. When the cost is a priority, the focus is competition on price. The priority may be for scope when the main objectives are the characteristics and features. There is a tradeoff and balance that needs to be addressed, not only between the three measures, but incorporating other measures and factors. The need for a metric that handles trade-offs between the various project success metrics to achieve project stakeholder goals emerges.

The measure of "integration" can bridge this gap. It includes the integration and standardization of all other measures, processes and activities in project management and ensures a proper trade-off between all measures to achieve project objectives. "Integration"

is defined as “managing operations as well as activities for identification, grouping, standardization and coordination of the various operations of the project in the project management plan” (PMBOK, 2017).

Few previous studies have touched upon adding the “integration” measure to the traditional project success measures “scope”, “time”, “cost”, “quality” to develop the traditional triangle model in project management. This is even though “integration” is one of the most important factors affecting project success and is considered the first area of knowledge in project management (PMBOK, 2017). It is concerned with the performance of the project as a whole and through it the project management plan is developed including all knowledge areas in project management.

Given the main role of integration management in project success and its close link with performance, this study aims to develop measures of project success in the traditional triangle model. It proposes a new and comprehensive framework to improve the performance of project management by relying on development of the traditional triangle model by adding the measure of “integration” to the measures of “scope”, “time”, “cost”, and “quality”. “Integration” includes a set of processes, activities and roles that ensure identification, definition, compilation, standardization, and coordination of the various operations of the project in the project management plan. This will probably lead to achieving the goals in line with the expectations of the stakeholders, as well as continuously monitoring and developing performance.

The above clearly demonstrates that the “integration” measure can be considered the fifth metric that will support the four traditional project success measures through which the traditional triangle model for project management is developed into a new model. The new model is a “Diamond” shape consisting of four peaks. On the four peaks there are the measures “scope”, “time”, “cost”, and “quality” with the fifth measure “integration” at the heart of the Diamond as shown in (Figure 12).

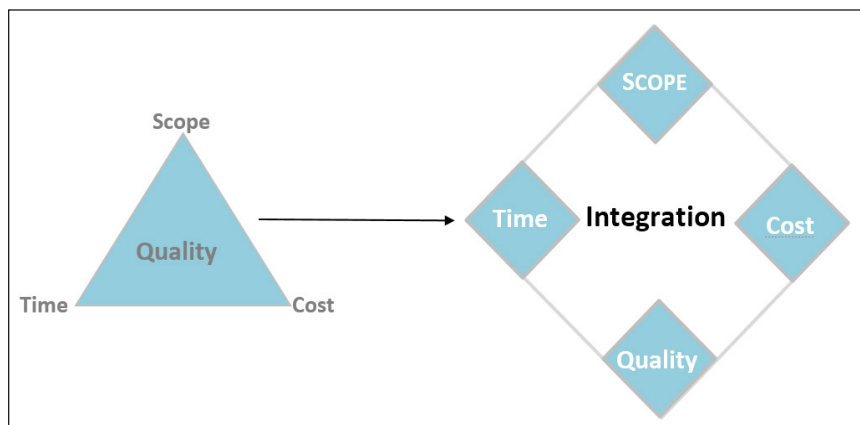


Figure 12. Developing ICTQS Diamond Framework Model for Project Management

Benefits of 'Integration' in the ICTQS Diamond Framework

The benefits of integration are evident through the processes of integration management, as it has a relationship with the elements and stages that have a significant impact on the project's path. Some of the benefits can be summarized in the following points:

1. Integration processes support performance monitoring and contribute to its continuous development through comprehensive planning for all areas of project management. It develops plans based on lessons learned, as well as through the process of continuous business orientation and making corrections at an early stage of project implementation based on periodic performance reports and stakeholders' expectations.
2. Integration supports knowledge in its two parts, "explicit knowledge" and "tacit knowledge". This is done by introducing activities and techniques through which knowledge is integrated between the project team and the continuous development of the areas of knowledge deficiencies within the project team. This ensures that the necessary knowledge is available to the project team at an early stage from the start of the project, especially those relating to the expectations of the stakeholders about the project. This is what continuously enhances the project's performance.
3. Integration is also concerned with controlling the change orders, which is one of the main influences on the progress of the project and the success of its objectives from stakeholder perspective. Its proper management in a way that avoids the project many of the risks affecting the constraints of the project is required.
4. Integration manages the project closing phase and ensures that the initial receipt and final handover, updating and archiving of documents to improve future performance. Furthermore, it verifies stakeholder satisfaction and achieving goals from their perspective to ensure that no risks occur after the closing phase.
5. Integration endeavors to reduce ambiguity and uncertainty, which are problems facing the project team, especially the expectations of the beneficiaries. Success in achieving the project objectives according to the expectations of stakeholders is particularly important. It requires skills to elicit the desires of stakeholders and reach their expectations about the project and is what is achieved through integration management.

DISCUSSION

The research seeks to expand the conceptual boundaries of project management and to provide greater links between research and practice (Winter et al., 2006) until reaching an effective measure of project success, as success is always subjective. The proposed framework was developed by quantitative data obtained through a survey verifying the effect of integration management on project success. This has revealed the great impact

of integration management on the success of the project. This is consistent with other studies which concluded the existence of a critical role for integration management on project success (Asif et al., 2010; Berteaux & Javernick-Will, 2015; Halfawy & Froese, 2007; Ospina-Alvarado et al., 2016; Ozorhon et al., 2014; Silvius et al., 2017; Tatum, 1990). However, we find some differences between the results of the current study and the results of the study by Silvius et al. (2017) which concluded that quality management was the most influential measure on the success of the project. Cost management was the most influential on the success of the project in the current study showing the benefit of developing measures of project success to arrive at metrics that effectively reflect the success of the project.

The benefits of the Diamond Framework can be summarized in the following points:

1. The diamond framework is considered a modern, disciplined, and accurate tool for measuring the success of construction project management.
2. The model works to improve and develop a set of rules and behaviors in managing construction projects in accordance with modern principles of project management.
3. The project team assists in evaluating project management and identifying potential gaps in project management to avoid their negative impacts.
4. The model contributes to enhancing project management performance in all areas by integrating all processes and roles and directing them towards achieving project stakeholder goals.
5. The model provides an improvement for project success metrics in a simple form that can be easily understood.
6. The framework helps make trade-offs between the traditional project constraints geared towards achieving project stakeholder goals.
7. The framework supports knowledge management to continuously develop tools and administrative and technical skills to keep pace with changes and developments.

CONCLUSION

After more than fifty years from the emergence of the traditional triangle model in project management, it has become important to develop it considering the challenges facing the construction industry in the twenty-first century (Barnes, 2007). Among these challenges is the achievement of project stakeholder objectives. From the data collected from the survey and the analysis performed, the need to develop project success measures in the traditional triangle became clear. Adding integration to project success metrics will contribute to achieving project goals and improving performance in general. This study aimed to develop the diamond model grounded in the data. Based on the data the developed model relies on developing the shape and measures of the traditional triangle model in project management by adding “integration”.

The study concluded by the development of the traditional triangle model and the introduction of the Diamond Model (ICTQS) for construction project management, which is a “Diamond” shape consisting of four peaks. On the four peaks, there are the measures of “scope”, “time”, “cost”, and “quality”. The fifth measure of “integration” is at the heart of the diamond where the author concludes that there is a significant impact of integration management on project success based on the fit between the quantitative and qualitative data. Integration enhances the effectiveness of the proposed framework model as a mechanism for project operation and measuring and evaluating project performance. It is also a tool to support the project team in overcoming the problems facing construction project management in Yemen and developing the Yemeni construction industry. The new idea is not based on considering the measures of scope, time, and cost as constraints, but as measures that are traded between them through the new “integration” measure to achieve project success from the project stakeholder perspective.

The study was restricted to studying the opinions of advisory bodies in Yemen. Future studies could address construction companies to study any differences. The researcher recommends continuing the creative development of the traditional triangle model in construction project management. This may be done by reviewing the measures of project success and the relationship between them and the influence on each other to assist the success of construction projects. The study needs further testing to clarify the impact of the implementation of the Diamond Action Framework (ICTQS) on the performance of construction project management and its importance in achieving project stakeholder objectives.

ACKNOWLEDGEMENT

The authors acknowledge the University of Science and Technology, Yemen for funding this study.

REFERENCES

- Alaghbari, W., Saadan, R. S., Alaswadi, W., & Sultan, B. (2018). Delay factors impacting construction projects in Sana'a-Yemen1. *PM World Journal*, 7(12), 1-28.
- Alawi, N. A. M., & Masood, A. (2018). Environmental quality website disclosure in oil and gas sector: The case of MNCs in Yemen. *Journal of Advanced Research in Business and Management Studies*, 11(1), 10-23.
- Alawi, N. A. M., Rahman, A. A., Amran, A., & Nejati, M. (2016). Does family group affiliation matter in CSR reporting? Evidence from Yemen. *Afro-Asian Journal of Finance and Accounting*, 6(1), 12-30. <https://doi.org/10.1504/AAJFA.2016.074541>
- Al-Sabahi, M. H., Al-Hamidi, A. A., Ramly, A., & Rejab, K. M. (2014). Exploring criteria and critical factors for governmental projects implementation in Yemen: A case study. *Journal of Surveying, Construction and Property*, 5(2), 1-17. <https://doi.org/10.22452/jscp.vol5no2.2>

- Alwaly, K. A., & Alawi, N. A. (2020). Factors affecting the application of project management knowledge guide (PMBOK® GUIDE) in construction projects in Yemen. *International Journal of Construction Engineering and Management*, 9(3), 81-91. <https://doi.org/10.5923/j.ijcem.20200903.01>
- Angarita, P., & Gallardo, R. (2018). Study of processes and procedures that affect the success of construction works by construction companies according to the guide to the project management body of knowledge (PMBOK Guide) in the municipality of Ocaña, Norte de Santander. In *Journal of Physics: Conference Series* (Vol. 1126, No. 1, p. 012052). IOP Publishing. <https://doi.org/10.1088/1742-6596/1126/1/012052>
- Asif, M., Fisscher, O. A., de Bruijn, E. J., & Pagell, M. (2010). Integration of management systems: A methodology for operational excellence and strategic flexibility. *Operations Management Research*, 3(3-4), 146-160. <https://doi.org/10.1007/s12063-010-0037-z>
- Atkinson, R. (1999). Project management: Cost, time and quality, two best guesses and a phenomenon, it's time to accept other success criteria. *International Journal of Project Management*, 17(6), 337-342. [https://doi.org/10.1016/S0263-7863\(98\)00069-6](https://doi.org/10.1016/S0263-7863(98)00069-6)
- Barnes, M. (1988). Construction project management. *International Journal of Project Management*, 6(2), 69-79. [https://doi.org/10.1016/0263-7863\(88\)90028-2](https://doi.org/10.1016/0263-7863(88)90028-2)
- Barnes, M. (2007). Some origins of modern project management a personal history. *Project Management World Journal*, 2(11), 1-2.
- Bennett, L. (2003). *The management of construction – A project life cycle approach*. Gower Publishing.
- Berteaux, F., & Javernick-Will, A. (2015). Adaptation and integration for multinational project-based organizations. *Journal of Management in Engineering*, 31(6), Article 04015008. [https://doi.org/10.1061/\(ASCE\)ME.1943-5479.0000366](https://doi.org/10.1061/(ASCE)ME.1943-5479.0000366)
- Caccamese, A., & Bragantini, D. (2012). *Beyond the iron triangle: Year zero*. Project Management Institute.
- Cao, Q., & Hoffman, J. J. (2011). A case study approach for developing a project performance evaluation system. *International Journal of Project Management*, 29(2), 155-164. <https://doi.org/10.1016/j.ijproman.2010.02.010>
- Daher, K. (2018). *Statistical analysis of geographical data using a computer*. Islamic University of Gaza. Retrieved June 27, 2020, from <http://site.iugaza.edu.ps/kabudaher/files/2017/10/%D9%83%D8%AA%D8%A7%D8%A8-%D8%AA%D8%AD%D9%84%D9%8A%D9%84-%D8%A7%D9%84%D8%A7%D8%AD%D8%B5%D8%A7%D8%A6%D9%8A.pdf>
- Davis, K. (2014). Different stakeholder groups and their perceptions of project success. *International Journal of Project Management*, 32(2), 189-201.
- Demirkesen, S., & Ozorhon, B. (2017). Impact of integration management on construction project management performance. *International Journal of Project Management*, 35(8), 1639-1654. <https://doi.org/10.1016/j.ijproman.2017.09.008>
- Devaux, S. A. (1999). *Total project control: A manager's guide to integrated project planning, measuring, and tracking*. Wiley.
- Dobson, M. S. (2004). *The triple constraints in project management*. Management Concepts Inc.

- Ebbesen, J. B., & Hope, A. (2013). Re-imagining the iron triangle: Embedding sustainability into project constraints. *PM World Journal*, 2(3), 1-13.
- Eisner, H., McMillan, R., Marciniak, J., & Pragluski, W. (1993). RCASSE: Rapid computer-aided system of systems (S2) engineering. In *INCOSE International Symposium* (Vol. 3, No. 1, pp. 267-273). Wiley. <https://doi.org/10.1002/j.2334-5837.1993.tb01588.x>
- Felician, A. (2011). *Managing software development projects*. Academy of Economic Studies.
- Frame, J. D. (2002). *The new project management: Tools for an age of rapid change, complexity, and other business realities* (2nd Ed.). Jossey-Bass.
- Gamil, Y., & Rahman, I. A. (2020). Assessment of critical factors contributing to construction failure in Yemen. *International Journal of Construction Management*, 20(5), 429-436. <https://doi.org/10.1080/15623599.2018.1484866>
- Halfawy, M. M., & Froese, T. M. (2007). Component-based framework for implementing integrated architectural/engineering/construction project systems. *Journal of Computing in Civil Engineering*, 21(6), 441-452. [https://doi.org/10.1061/\(ASCE\)0887-3801\(2007\)21:6\(441\)](https://doi.org/10.1061/(ASCE)0887-3801(2007)21:6(441))
- Hamilton, A. (2001). *Managing projects for success: A trilogy*. Thomas Telford Publishing.
- Heravi, G., & Ilbeigi, M. (2012). Development of a comprehensive model for construction project success evaluation by contractors. *Engineering, Construction and Architectural Management*, 19(5), 526-542. <https://doi.org/10.1108/09699981211259603>
- Hogg, R., & Tannis, E. (2009). *Probability and statistical inferences* (8th Ed.). Prentice Hall.
- Ika, L. A. (2009). Project success as a topic in project management journals. *Project Management Journal*, 40(4), 6-19. <https://doi.org/10.1002/pmj.20137>
- Kermanshachi, S. (2016). *Decision making and uncertainty analysis in success of construction projects* (Doctoral dissertation). Texas A & M University, College Station, Texas. Retrieved January 15, 2020, from <https://oaktrust.library.tamu.edu/handle/1969.1/158020>
- Likert, R. (1932). A technique for the measurement of attitudes. *Archives of Psychology*, 22(140), 1-55.
- Lim, C. S., & Mohamed, M. Z. (1999). Criteria of project success: An exploratory re-examination. *International Journal of Project Management*, 17(4), 243-248. [https://doi.org/10.1016/S0263-7863\(98\)00040-4](https://doi.org/10.1016/S0263-7863(98)00040-4)
- Lock, D. (2007). *Project management* (9th Ed.). Gower Publishing.
- Major, I., Greenwood, A., Allen, D., & Goodman, M. (2003). *The definitive guide to project management*. Pearson Education.
- Marasco, J. (2004, May 06). *The project pyramid*. Retrieved March 05, 2020, from <https://www.ibm.com/developerworks/rational/library/4291.html>
- Ministry of Industry and Trade. (2020). *Database of engineering consultancy agencies*. Sana'a, Republic of Yemen.
- Mir, F. A., & Pinnington, A. H. (2014). Exploring the value of project management: Linking project management performance and project success. *International Journal of Project Management*, 32(2), 202-217. <https://doi.org/10.1016/j.ijproman.2013.05.012>

- Nicholas, J. M., & Steyn, H. (2017). *Project management for engineering, business and technology* (5th Ed.). Routledge.
- Ong, H. Y., Wang, C., & Zainon, N. (2018). Developing a quality-embedded EVM tool to facilitate the iron triangle in architectural, construction, and engineering practices. *Journal of Construction Engineering and Management*, 144(9), Article 04018079. [https://doi.org/10.1061/\(ASCE\)CO.1943-7862.0001533](https://doi.org/10.1061/(ASCE)CO.1943-7862.0001533)
- Orr, A. D. (2007). *Advanced project management: A complete guide to key processes, models and techniques* (2nd Ed.). Kogan Page.
- Ospina-Alvarado, A., Castro-Lacouture, D., & Roberts, J. S. (2016). Unified framework for construction project integration. *Journal of Construction Engineering and Management*, 142(7), Article 04016019. [https://doi.org/10.1061/\(ASCE\)CO.1943-7862.0001131](https://doi.org/10.1061/(ASCE)CO.1943-7862.0001131)
- Ozorhon, B., Abbott, C., & Aouad, G. (2014). Integration and leadership as enablers of innovation in construction: Case study. *Journal of Management in Engineering*, 30(2), 256-263. [https://doi.org/10.1061/\(ASCE\)ME.1943-5479.0000204](https://doi.org/10.1061/(ASCE)ME.1943-5479.0000204)
- PMBOK. (2017). *A guide to the project management body of knowledge* (6th Ed.). Project Management Institute.
- Shenhar, A. J., Dvir, D., Levy, O., & Maltz, A. C. (2001). Project success: A multidimensional strategic concept. *Long Range Planning*, 34(6), 699-725. [https://doi.org/10.1016/S0024-6301\(01\)00097-8](https://doi.org/10.1016/S0024-6301(01)00097-8)
- Shenhar, A. J., Levy, O., & Dvir, D. (1997). Mapping the dimensions of project success. *Project Management Journal*, 28(2), 5-13.
- Silvius, A. G., Kampinga, M., Paniagua, S., & Mooi, H. (2017). Considering sustainability in project management decision making: An investigation using Q-methodology. *International Journal of Project Management*, 35(6), 1133-1150. <https://doi.org/10.1016/j.ijproman.2017.01.011>
- Tatum, C. B. (1990). Integration: Emerging management challenge. *Journal of Management in Engineering*, 6(1), 47-58. [https://doi.org/10.1061/\(ASCE\)9742-597X\(1990\)6:1\(47\)](https://doi.org/10.1061/(ASCE)9742-597X(1990)6:1(47))
- Turner, R., & Simister, S. (Eds.) (2000). *Gower handbook of project management* (3rd Ed.). Gower Publishing.
- Vahidi, R., & Greenwood, D. (2009). *Triangles, tradeoffs and success: A critical examination of some traditional project management paradigms*. Retrieved February 28, 2020, from https://www.researchgate.net/profile/Ramesh_Vahidi/publication/264540155_TRIANGLES_TRADEOFFS_AND_SUCCESS_A_CRITICAL_EXAMINATION_OF_SOME_TRADITIONAL_PROJECT_MANAGEMENT_PARADIGMS/links/53e34e9f0cf275a5fddad546.pdf
- Wateridge, J. (1998). How can IS/IT projects be measured for success? *International Journal of Project Management*, 16(1), 59-63. [https://doi.org/10.1016/S0263-7863\(97\)00022-7](https://doi.org/10.1016/S0263-7863(97)00022-7)
- Wells Jr, W. G. (1998). The changing nature of project management. *Project Management Journal*, 29(1), 4-4. <https://doi.org/10.1177/875697289802900101>
- Westerveld, E. (2003). The project excellence model®: Linking success criteria and critical success factors. *International Journal of project management*, 21(6), 411-418. [https://doi.org/10.1016/S0263-7863\(02\)00112-6](https://doi.org/10.1016/S0263-7863(02)00112-6)

- White, D., & Fortune, J. (2002). Current practice in project management—An empirical study. *International Journal of Project Management*, 20(1), 1-11. [https://doi.org/10.1016/S0263-7863\(00\)00029-6](https://doi.org/10.1016/S0263-7863(00)00029-6)
- Wideman, M. (2004). *An exciting new model of project management*. Retrieved February 13, 2020, from <http://www.maxwideman.com/musings/newpmmmodel.htm>.
- Williams, T. (2002). *Modelling complex projects*. John Wiley & Sons.
- Winter, M., Smith, C., Cooke-Davies, T., & Cicmil, S. (2006). The importance of ‘process’ in rethinking project management: The story of a UK government-funded research network. *International Journal of Project Management*, 24(8), 650-662. <https://doi.org/10.1016/j.ijproman.2006.08.008>
- Wyngaard, C. J., Pretorius, J. H. C., & Pretorius, L. (2012). Theory of the triple constraint—A conceptual review. In *2012 IEEE International Conference on Industrial Engineering and Engineering Management* (pp. 1991-1997). IEEE Conference Publication. <https://doi.org/10.1109/IEEM.2012.6838095>



Magnetohydrodynamic Flow and Heat Transfer Over an Exponentially Stretching/Shrinking Sheet in Ferrofluids

Nurfazila Rasli and Norshafira Ramli*

School of Mathematical Sciences, Universiti Sains Malaysia, 11800 USM, Penang, Malaysia

ABSTRACT

In this research, the problem of magnetohydrodynamic flow and heat transfer over an exponentially stretching/shrinking sheet in ferrofluids is presented. The governing partial differential equations are transformed into nonlinear ordinary differential equations by applying suitable similarity transformations. These equations are then solved numerically using the shooting method for some pertinent parameters. For this research, the water-based ferrofluid is considered with three types of ferroparticles: magnetite, cobalt ferrite, and manganese-zinc ferrite. The numerical solutions on the skin friction coefficient, Nusselt number, velocity and temperature profiles influenced by the magnetic parameter, wall mass transfer parameter, stretching/shrinking parameter, and volume fraction of solid ferroparticle are graphically displayed and discussed in more details. The existences of dual solutions are noticeable for the stretching/shrinking case in a specific range of limit.

For the first solution, an increasing number in magnetic and suction will also give an increment of skin friction coefficient and Nusselt number over stretching/shrinking sheet. For the skin friction coefficient only, it is showed a decreasing pattern after the intersection. Besides, the presence of ferroparticles in the fluids causes a high number of the fluid's thermal conductivity and heat transfer rate.

Keywords: Ferrofluids, heat transfer, magnetohydrodynamic, stretching/shrinking

ARTICLE INFO

Article history:

Received: 9 February 2021

Accepted: 22 April 2021

Published: 31 July 2021

DOI: <https://doi.org/10.47836/pjst.29.3.42>

E-mail addresses:

nurfazilarasli17@gmail.com (Nurfazila Rasli)

norshafiraramli@usm.my (Norshafira Ramli)

*Corresponding author

INTRODUCTION

Nanofluid is a fluid that consists of small quantities of nanometer-size (usually less than 100 nm) particles known as nanoparticles. Choi and Eastman (1995) reported nanoparticles are a new way of how heat move the fluids, which show engineered colloids consist of nanoparticles by dispersing in conventional heat transfer fluids. Tiwari and Das (2007) have initiated a model to investigate the characteristics of nanoparticles. Within two-sided lid-driven, there are nanoparticles with a disparately heated square cavity. The effects showed the ability of heat transport might be increased when nanoparticles are mixed with the fluid. These nanoparticles are steadily dispersed and have potential as an efficient heat transport agent because of the more considerable value of thermal conductivity (Muthamilselvan et al., 2010).

Besides, there is a magnetic nanofluid known as ferrofluid which is composed of magnetic nanoparticles. The example of ferrofluids is hematite and magnetite. Besides, ferrofluid is useful since it has a flexible functioning in the existence of a magnetic field. It had drawn the researchers' attention due to a lot of applications in cooling of loudspeakers, mechano-electrical areas and biomedical sections (magnetic resonance tomography, drug delivery, cancer treatment and improvement of magnetic resonance image) (Odenbach, 2003; Blaney, 2007; Shokrollahi, 2013). Ferrofluid also has exhilarating present real-world applications. An extensive advantage is that the liquid can be forced to flow by way of the positioning and vitality of the magnetic field so that the ferrofluid can be arranged very accurately. Ferrofluids have the capability of reducing friction, making them useful in a variety of electronic and transportation applications. The additional different fields in which ferrofluids can be applied are heat transfer, aerospace, and art.

Bhattacharyya (2011) has reported a very systematic method known as the shooting technique to solve the problem of heat transfer. This problem is focused on the two-dimensional flow of Newtonian fluid. This analysis showed that when the parameter of mass suction goes over the limit, the flow is stable because of the exponential shrinking sheet. Then, other achievements have been obtained in both solutions for velocity and temperature profiles. Higher number of mass suction in the first solution caused a rising number in skin friction while decreasing in the second solution. According to Bhattacharyya and Vajravelu (2012), they focused on the shrinking layer which is boundary layer stagnation-point flow and heat transport. Resolving the problem, similarity equations and shooting technique have been applied. They found a small number of similarity solutions obtained in linear shrinking sheet case compared to exponentially shrinking case. When the straining rate is more extensive than the shrinking rate, dual solutions exist with some conditions and the capability of heat absorption may be possible happen. Research of three preferred nanofluids such as copper, alumina, and titania with Prandtl number $Pr = 6.2$ has been considered by Bachok et al. (2012) and heat transfer rate by using the shooting method.

They found that the similarity solution for exponentially stretching/shrinking sheet occurs higher for the linear case. A non-unique solution exists for the shrinking sheet while differ from the stretching part. Then, an increasing value of skin friction and heat movement due to insertion nanoparticles into water-based fluid. Finally, they found the most significant value of skin friction and Nusselt number is copper. Nadeem et al. (2014) researched about nanoparticles specifically in water-based heat transfer at the exponentially stretching sheet. A variety of governing parameters such as temperature, stretching and volume fraction are analyzed to see the effect on the profiles, the physical quantities and heat transfer rate. Runge Kutta 4th order and shooting method are used to determine the ordinary differential equations. They analyzed the temperature profiles increased when the nanofluid volume fraction increases. Then, increasing in stretching parameter also increasing in the skin friction coefficient and rate of heat transmission. Resistance copper absorption in the fluid is higher than titanium dioxide and alumina, which are the same results with the previous study as mentioned above.

Recently, in magnetic fields, many researchers study how the fluid is conducted electrically and the heat transfer of viscous fluid along the surface. A study by Noghrehabadi et al. (2014) found varieties of applications in magnetohydrodynamic (MHD) flow in the engineering and industrial. Bhattacharyya and Pop (2011) have studied the exponentially shrinking sheet along with magnetohydrodynamic movement. By implementing the shooting method, they found how the separation of the boundary layer is delayed. It happened because of the suppression of Lorentz force on the vorticity produced due to the shrinking sheet. An increasing magnetic field also affected the steady outflow of the exponential shrinking layer and produced a lesser amount of wall mass suction. Two different solutions also achieved for the flow field in a particular case. Using the Keller-box method, Ishak (2011) studied a problem of radiation effect on stretching sheet exponentially with magnetohydrodynamic layer flow. He discovered that bigger number of radiation and magnetic existing the regional heat of lower rate. Then, Bhattacharyya and Layek (2014) investigated the porous sheet with the consequence of flow in the magnetohydrodynamic boundary layer of nanofluid. By applying the shooting method, they noted a more significant number in volume fraction of nanofluids and temperature occur because of the magnetic. Besides, due to the exponential stretching sheet, the magnetic field decreased the heat transfer rate. Apart from that, the volume fraction of nanoparticles and temperature inside the boundary layer seemed to increase as a result of this magnetic region. The thickness of the velocity boundary layer becomes thinner due to the mass suction, whereas thicker in the injection case. Alavi et al. (2017) have reported the problem of stretching sheet exponentially over wall temperature, heat flux and magnetohydrodynamic stagnation point flow. The problem is to work out numerically with a method known as Keller-box. An increase in magnetic parameter also increased the velocity. Besides, this happened because

of the existence of wall temperature and heat flux too. Jusoh et al. (2018) have reviewed porous layer stretching/shrinking exponentially and solved by *bvp4c* function known as the finite-difference code of Matlab solver. They found that suction in boundary condition has shown the surface is permeable and dual solutions had occurred in a particular region of the shrinking sheet problem. Higher magnetic parameter increased induced Lorentz force and decreased the momentum within the layer.

Another study, Mansur et al. (2015) have reviewed studies on the influence of suction on magnetohydrodynamic stagnation point flow in nanofluid over a stretching/shrinking sheet. By applying *bvp4c* function from Matlab, they concluded that the first and second solutions existed in shrinking. However, a special solution exists in the stretching case only. An increase of suction and magnetic field will also increase the stability of the skin friction while the heat transfer rate decreases due to the Brownian parameter and thermophoresis parameter. Then, the investigation of the consequence of injection/suction for magnetohydrodynamic flow throughout a porous stretching/shrinking sheet of nanofluids has been found by Naramgari and Sulochana (2016). They noticed for certain parameters; the dual solutions only happen for some range. In the stretching surface, the heat transfer rate is reduced because the magnetic field even the stretching/shrinking and injection/suction parameters can increase the enhancement of heat transfer. Ramli et al. (2018) reported the reaction of uniform heat change and second-order slip on magnetohydrodynamic flow involving the forced convection and a moving plate to study the motion of heat in ferrofluids. They analyzed how the skin friction, Nusselt number, velocity, and temperature affected by the parameter of magnetic, moving, mass transfer, first-order surface slip, second-order surface slip and volume fraction of solid ferroparticles in the form of tabular and graphical presentations by using the shooting method. The final discussion shows that ferrofluids base fluid produced the smallest skin friction and local Nusselt number than kerosene-based ferrofluids in both results. Thus, it delayed the separation of the boundary layer when the volume fraction of ferrofluids combined with the effects of the magnetic, moving, mass transfer, and slip parameters. A problem of linearly stretching/shrinking sheet in nanofluids involving the stagnation-point of magnetohydrodynamic motion has been investigated by Rahman et al. (2019). The titania, alumina and copper are metallic nanoparticles that are used to analyze the volume fraction parameter of the nanoparticles in water with the Prandtl number=6.2. In solving boundary value problems, the function of *bvp4c* from Matlab has been used due to its effectiveness. The final solution shows that the magnetic field and nanoparticles volume fraction will affect the momentum and temperature. Apart from that, non-unique results of dual solutions only obtained for the shrinking sheet case while different results for the stretching sheet case. Then, Mohamed et al. (2019) have reported the impact of Newtonian heating on magnetite. They applied

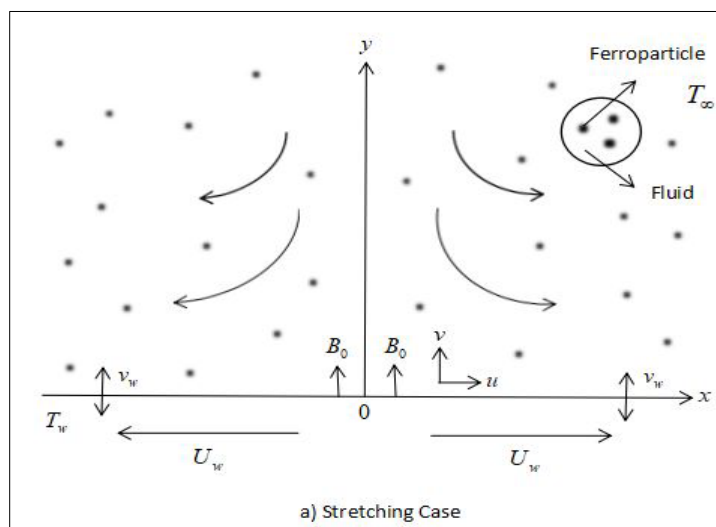
Runge-Kutta-Fehlberg to calculate numerically, and the final solutions shown the magnetite ferrofluid provided greater value for the heat transfer and temperature of the wall than water.

According to the literature, many researchers have attempted the problem of magnetohydrodynamic flow and heat transfer but not specifically in the ferrofluids. In this paper, we want to study the magnetohydrodynamic flow and heat transfer over an exponentially stretching/shrinking sheet in ferrofluids. This research is related to the Tiwari and Das' model. Thus, to interpret the ordinary differential equation, a shooting technique will be applied with the similarity variation. Then, it is resolved numerically and, the numerical results are discussed in detail and plotted graphically.

MATERIALS AND METHOD

Basic Equations

This problem is related with three preferred ferrofluids of magnetohydrodynamic boundary layer flow. The flow is in steady and laminar case. Due to the magnetic field, heat motion over an exponentially stretching/shrinking sheet, have been studied. The supposed temperature of boundary layer of the sheet is $T_w = T_\infty + T_0 e^{x/2L}$ where T_w is the sheet's temperature variable, T_∞ is the free stream temperature predicted to be persistent and T_0 is an ambient temperature to calculate temperature's rate which increase along the surface of the layer. We noted $U_w(x) = ae^{x/L}$ is the stretching/shrinking velocity where, a is the velocity rate of stretching/shrinking with $a > 0$ for stretching, $a < 0$ for shrinking and L is the reference velocity. The physical models and coordinate system are pictured in Figure 1.



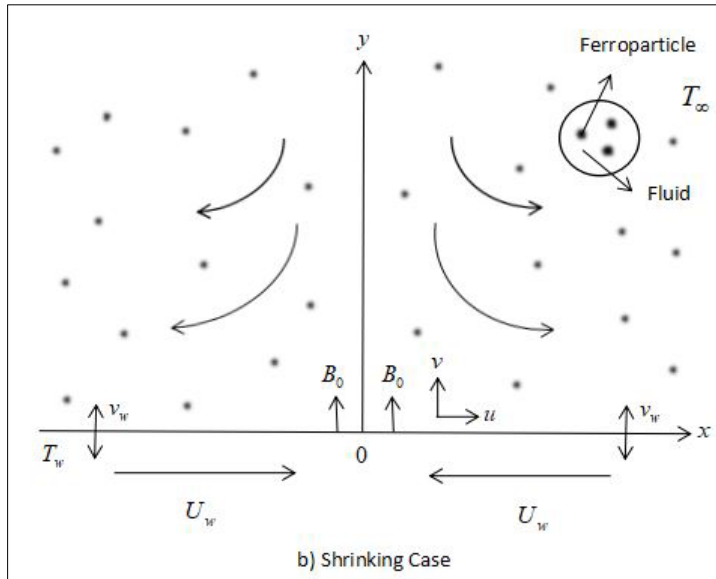


Figure 1. Physical models and coordinate system for stretching and shrinking cases

Basic equations are assumed and under consideration are as follows (Equations 1, 2 & 3) (Bhattacharria & Pop, 2011; Magyari & Keller,1999):

$$\frac{\partial u}{\partial x} + \frac{\partial v}{\partial y} = 0, \tag{1}$$

$$u \frac{\partial u}{\partial x} + v \frac{\partial v}{\partial y} = \nu_{ff} \frac{\partial^2 u}{\partial y^2} - \frac{\sigma B^2}{\rho_{ff}} u, \tag{2}$$

$$u \frac{\partial T}{\partial x} + v \frac{\partial T}{\partial y} = \alpha_{ff} \frac{\partial^2 T}{\partial y^2}, \tag{3}$$

with the following boundary conditions (Equation 4)

$$u = \lambda U_w(x), v = v_w, T = T_w, \text{ at } y = 0, \tag{4}$$

$$u \rightarrow 0, T \rightarrow T_\infty, \text{ as } y \rightarrow \infty,$$

where u and v are the elements of velocity along the x - and y - axes, σ is an electrical conductivity, B is the total magnetic field, λ is the stretching/shrinking parameter, σ is an electrical conductivity, T is the temperature, and v_w is the variable wall mass transfer velocity. Here, ν_{ff} denotes the kinematic viscosity of the ferrofluid, α_{ff} is the thermal diffusivity of the ferrofluid and ρ_{ff} is the density of the ferrofluid, which are defined as Equation 5:

$$\begin{aligned}
 v_{ff} &= \frac{\mu_{ff}}{\rho_{ff}}, \mu_{ff} = \frac{\mu_f}{(1-\phi)^{2.5}}, \alpha_{ff} = \frac{k_{ff}}{(\rho C_p)_{ff}}, \rho_{ff} = (1-\phi)\rho_f + \phi\rho_s, \\
 (\rho C_p)_{ff} &= (1-\phi)(\rho C_p)_f + \phi(\rho C_p)_s, \frac{k_{ff}}{k_f} = \frac{(k_s + 2k_f) - 2\phi(k_f - k_s)}{(k_s + 2k_f) + \phi(k_f - k_s)},
 \end{aligned}
 \tag{5}$$

where μ_{ff} is ferrofluid’s viscosity, μ_f is fluid’s viscosity, ϕ is defined as volume fraction of ferroparticle, $(\rho C_p)_{ff}$ is ferrofluid’s heat capacity, k_{ff} is ferrofluid’s thermal conductivity, k_f is fluid’s thermal conductivity and k_s is solid fraction’s thermal conductivity while ρ_f and ρ_s are the densities of the fluid and of the solid fractions, respectively. The magnetic field $B(x)$ is defined as $B(x) = B_0 e^{x/2L}$, where B_0 denotes a constant magnetic field. Then, V_w is considered to be the velocity of wall mass transfer and is presented by $v_w = v_0 e^{x/2L}$, where $v_0 < 0$ for mass suction and $v_0 > 0$ for mass injection.

By introducing the following similarity transformation, the easier step can be shown by using Equation 1-3 with the subjected boundary conditions as in Equation 4 is defined as Equation 6:

$$\eta = y \left(\frac{a}{2\nu_f L} \right)^{1/2} e^{x/2L}, \psi = (2\nu_f La)^{1/2} f(\eta) e^{x/2L}, \theta(\eta) = \frac{T - T_\infty}{T_w - T_\infty},
 \tag{6}$$

where η is the similarity variables, ν_f is the fluid’s kinematic viscosity and ψ is the stream function which can be specified as $u = \partial\psi / \partial y$ and $v = \partial\psi / \partial x$. By employing Equation 6, Equation 2 and 3 will take the consecutive form of Equations 7 and 8, respectively.

$$\frac{1}{(1-\phi)^{2.5}[(1-\phi) + \phi\rho_s / \rho_f]} f''' + ff'' - 2f'^2 - Mf' = 0,
 \tag{7}$$

$$\frac{1}{Pr [1-\phi + \phi(\rho C_p)_s / (\rho C_p)_f]} \theta'' + f\theta' - f'\theta = 0,
 \tag{8}$$

which primes represent the differentiation of η , $M = 2\sigma B_0^2 L / \rho_f a$ is the magnetic parameter, $Pr = (\mu C_p)_f / k_f$ is the Prandtl number.

The transformation of boundary conditions is defined in Equation 9.

$$\begin{aligned}
 f(0) &= S, f'(0) = \lambda, \theta(0) = 1, \\
 f'(\eta) &\rightarrow 0, \theta(\eta) \rightarrow 0, \text{ as } \eta \rightarrow \infty,
 \end{aligned}
 \tag{9}$$

where the wall mass transfer parameter is defined as S in which mass suction is $S < 0$. and mass injection is $\lambda < 0$ Then stretching/shrinking parameter can be divided into two cases which are $\lambda < 0$ for a shrinking sheet and $\lambda > 0$ for a stretching sheet.

Next, the skin friction coefficient C_f and local Nusselt number Nu_x are known as the physical quantities and are defined as Equation 10.

$$C_f = \frac{\tau_w}{\rho_f U_w^2}, Nu_x = \frac{xq_w}{k(T_w - T_\infty)}, \tag{10}$$

while τ_w is the shear stress and q_w is the surface heat flux shown as in Equation 11.

$$\tau_w = \mu_{ff} \left(\frac{\partial u}{\partial y} \right)_{y=0}, q_w = -k_{ff} \left(\frac{\partial T}{\partial y} \right)_{y=0}, \tag{11}$$

Where, μ_{ff} is the dynamic viscosity and k_{ff} is thermal conductivity of the ferrofluids, respectively. Similarity variables in Equation 6 are applied to obtain Equations 12 and 13.

$$Re_x^{1/2} C_f = \frac{1}{(1-\phi)^{2.5}} f''(0), \tag{12}$$

$$Re_x^{-1/2} Nu_x = -\frac{k_{ff}}{k_f} \theta'(0), \tag{13}$$

In which $Re_x = U_w L / \nu_f$ is the Reynolds number.

RESULT AND DISCUSSION

There is a function of shootlib in Maple software which applicable to run the shooting technique to solve Equations 7 and 8 under Equation 9. For this study, the governing ordinary differential equations must be converted into an initial value problem with the aid of Runge Kutta 4th order method. Besides, we need to guess some of the initial value for physical parameters to determine the missing value of $f''(0)$ and $\theta'(0)$. The finite number of boundary layer thickness $\eta \rightarrow \infty$, namely η_∞ must be chosen and for this study, $\eta_\infty = 10$ is used. Newton-Raphson method is required to iterate the correct guessed of initial number until convergence is satisfied. In this problem, Newton’s method is used to estimate the skin friction and local Nusselt until the results approach zero with the desired efficiency of 10^{-9} . For this study, the dual solutions and all profiles are obtained to satisfy boundary conditions in Equation 9, yet various pattern displays.

The influence of the magnetic parameter, M , stretching/shrinking parameter, λ , mass transfer parameter, S , and volume fraction of solid ferroparticles, ϕ on the skin friction coefficient, $Re_x^{1/2} C_f$, Nusselt numbers, $Re_x^{-1/2} Nu_x$, velocity, $f(\eta)$ and temperature $\theta(\eta)$ were examined. This research involves three preferred ferroparticles which are magnetite, cobalt ferrite, and manganese-zinc ferrite in water-based fluid with $Pr = 6.2$. In addition, the volume fraction of solid ferroparticles ϕ is considered between scale of the $0 \leq \phi \leq 0.2$, where the pure water is presented by $\phi = 0$.

Table 1 shown the data of the base fluids and the following ferroparticles about thermophysical properties which are found from Khan et al. (2015). Besides, to prove

the validity of the current method, the numerical solutions of the local heat $-f''(0)$ are differentiated with those studied by Magyari and Keller (1999) and Bhattacharyya and Layek (2014), as shown in Table 2. Compared to the previous study by Magyari and Keller (1999), their study was performed without the presence of a magnetic field and over exponentially stretching sheet only. Thus, we extend the problem with the presence of magnetic field to observe how the magnetic field will affect the flow/motion of the fluid in the boundary layer over exponentially stretching and shrinking sheets. Then, this present study is also compared to another previous study by Bhattacharyya and Layek (2014). We choose the Prandtl number to be fixed and without the presence of the Lewis number, Brownian motion parameter and thermophoresis parameter effect. The present results are found to be in excellent agreement with the published data and thus gives us some confidence in the present numerical results.

Table 1

Thermophysical properties of fluid and magnetic ferroparticles (Khan et al., 2015)

Physical Properties	Base Fluid	Magnetic nanoparticles		
	Water	Fe ₃ O ₄	CoFe ₂ O ₄	Mn-ZnFe ₂ O ₄
ρ (kg/m ³)	997	5180	4907	4900
C_p (j/Kg.k)	4179	670	700	800
k (W/m.k)	0.613	9.7	3.7	5

Table 2

Values of $-f''(0)$ for $M=0$ when $\lambda=1$, $S=0$ and $\varphi=0$.

	Magyari and Keller (1999)	Bhattacharyya and Layek (2014)	Present study
$-f''(0)$	1.281808	1.2810838	1.28182804

Figures 2-7 represent the different values of M , S and φ when Prandtl number is 6.2. Figures 2-7 demonstrate the effects of skin friction coefficient, and Nusselt number with stretching and shrinking parameter, λ wall mass transfer S and ferroparticle volume fraction φ .

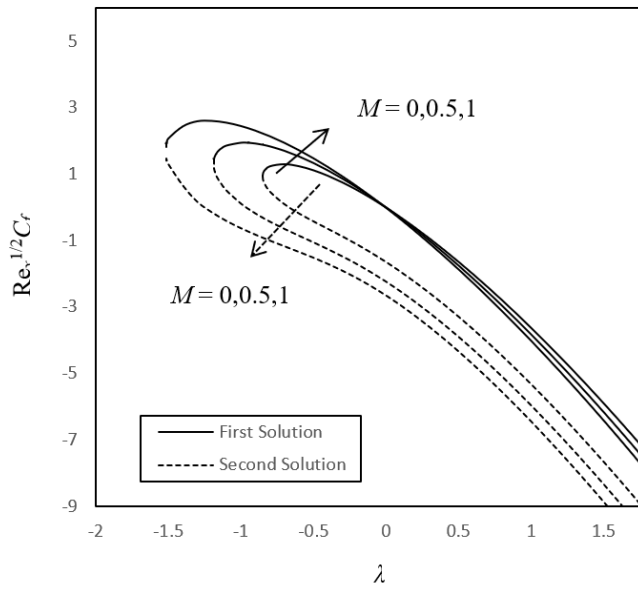


Figure 2. Effects of M on skin friction coefficient with $S=2$ and $\varphi = 0.1$.

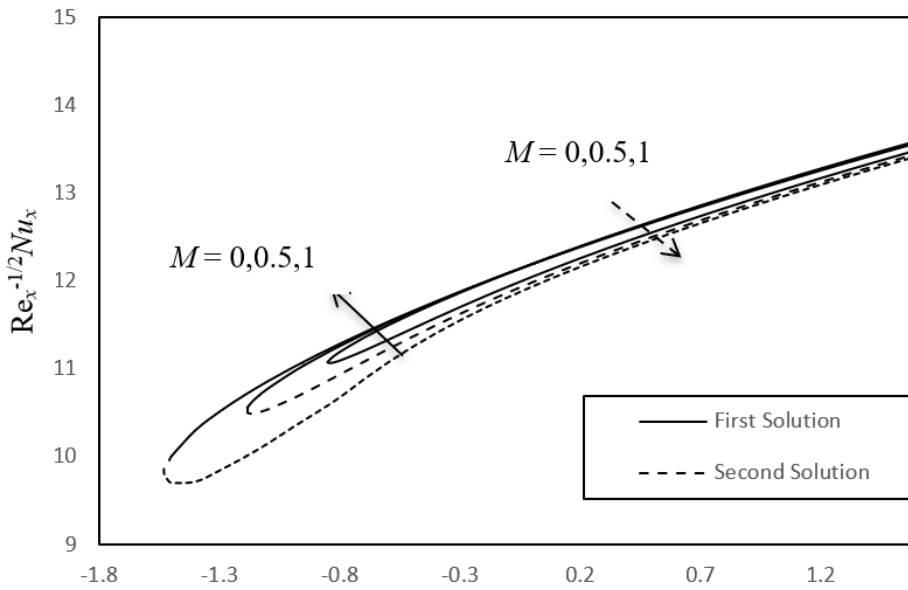


Figure 3. Effects of M on Nusselt number with $S=2$ and $\varphi = 0.1$.

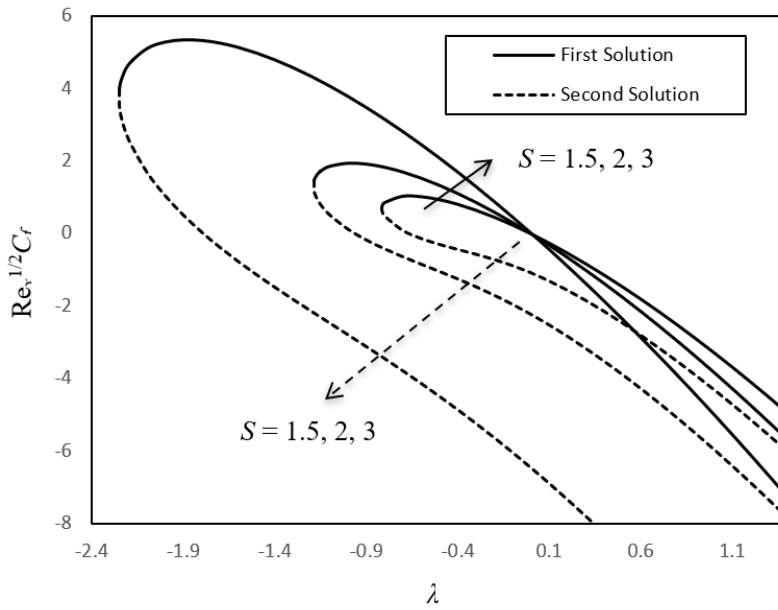


Figure 4. Effects of S on skin friction coefficient with $M=0.5$ and $\varphi = 0.1$.

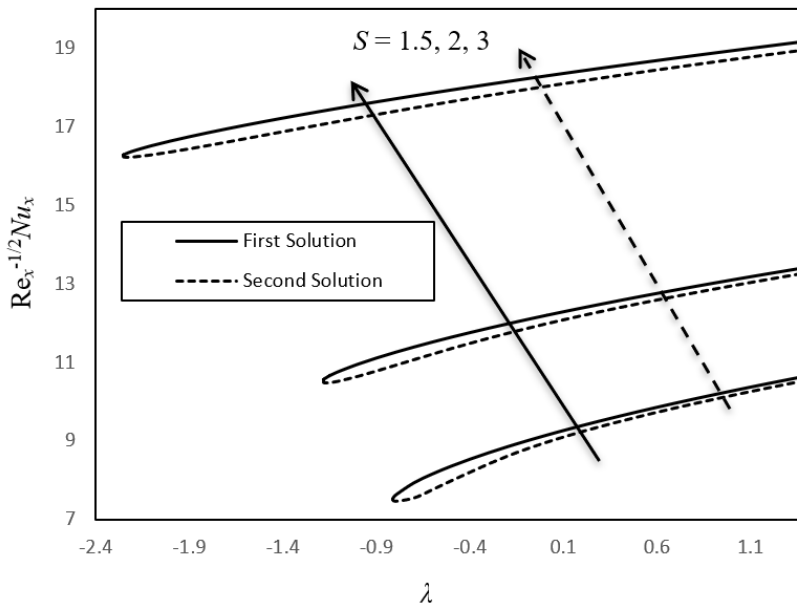


Figure 5. Effects of S on Nusselt number with $M=0.5$ and $\varphi = 0.1$.

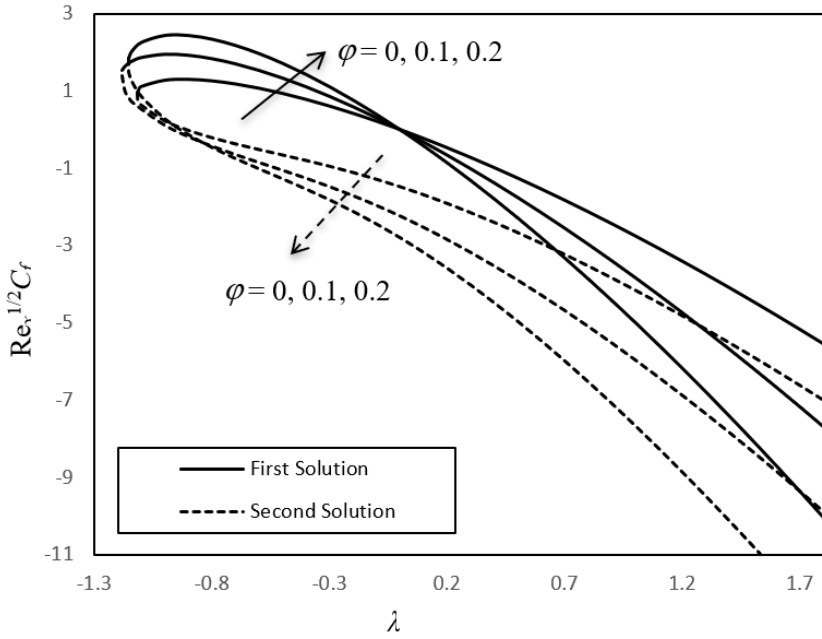


Figure 6. Effects of ϕ on skin friction coefficient with $M=0.5$ and $S = 2$.

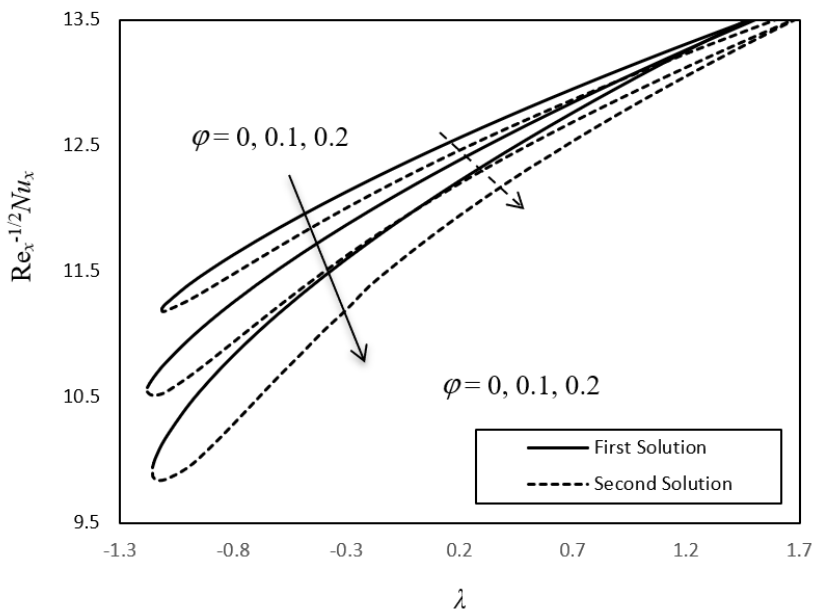


Figure 7. Effects of ϕ on Nusselt number with $M=0.5$ and $S = 2$.

Based on Figures 2-7, we analyzed that there are the first and second solution have occurred in the chosen parameters. Clearly, we can see the solid lines and dash lines which symbolize as the first and second solution, respectively. For this dual solutions, it is seemed that there is no solution when $\lambda < \lambda_c$ or $S < S_c$ or $\varphi < \varphi_c$. This process may affect the boundary layer which help in delaying the boundary layer separation.

On the other hand, we can point out a further discussion for the first solution of Figure 2-7 by considering the first solution is stable and physically realizable. It is found that the magnetic parameter M , mass transfer parameter S , and volume fraction of solid ferroparticles φ , help to enhance the skin friction coefficient and Nusselt number.

Table 3 and 4 display variants of Nusselt number, $Re_x^{-1/2}Nu_x$ and skin friction coefficient, $Re_x^{1/2}C_f$ of magnetic M in water-based ferrofluids when $\lambda = -0.5$, $\varphi = 0.1$, $Pr=6.2$, and $S = 2$. From Table 3, which is in shrinking case $\lambda < 0$, Fe_3O_4 seems to have higher values of skin friction coefficient compared to other ferrofluid mixture. Then, Table 4 presents that $CoFe_2O_4$ have greater value of local Nusselt number. Through Table 1, $CoFe_2O_4$ has a small number of thermal conductivities compared with Fe_3O_4 , reduction of thermal conductivity of $CoFe_2O_4$ may show to a greater value of temperature gradients and may increase the results of the enhancement in heat transfers. We can see that Fe_3O_4 has the highest thermal conductivity among the two ferrofluids. Even though Fe_3O_4 has higher thermal conductivity, temperature gradients decreased and influenced the behaviour of the Fe_3O_4 .

Table 3
Values of $Re_x^{1/2}C_f$ with different values of M

Magnetic nanoparticles	M	Water-based ferrofluids	
		First Solution	Second Solution
Fe_3O_4	0	1.119649602	-0.412911056
	0.5	1.333048294	-1.041749204
	1	1.493337918	-1.514815733
$CoFe_2O_4$	0	1.090512657	-0.375584219
	0.5	1.305552292	-0.993386724
	1	1.465834308	-1.454298252
$Mn-ZnFe_2O_4$	0	1.08976403	-0.374640861
	0.5	1.002688264	-0.99216224
	1	1.465129036	-1.45273698

Table 4
 Values of $Re_x^{-1/2}Nu_x$ with different values of M

Magnetic nanoparticles	M	Water-based ferrofluids	
		First Solution	Second Solution
Fe_3O_4	0	11.62577480	11.45702035
	0.5	11.64393334	11.36790796
	1	11.65675332	11.24915198
$CoFe_2O_4$	0	12.33495424	12.18251108
	0.5	12.35264091	12.10275686
	1	12.36506264	12.01066765
$Mn-ZnFe_2O_4$	0	12.20291839	12.04894697
	0.5	12.22075634	11.96794742
	1	12.23327434	11.87244693

Figures 8-13 show the profiles of velocity and temperature of magnetite ferroparticles related with the magnetic M at λ 0.5, 1, 1.5 when $\phi=0.1$, $S=2$ and $Pr=6.2$. Figures 8-13 indicate increasing of M , decreasing the velocity profiles and rising in the temperature profiles. Because of the magnetic parameter M , the boundary layer's thickness becomes thinner in the first result and then thicker in the next result for all the velocity profiles and temperature profiles displayed. The temperature also increases along with the reduction of heat movement. Physically, an increase in ϕ enhances the thermal conductivity of the fluid and this will help to enhance the momentum and thermal boundary layer thickness.

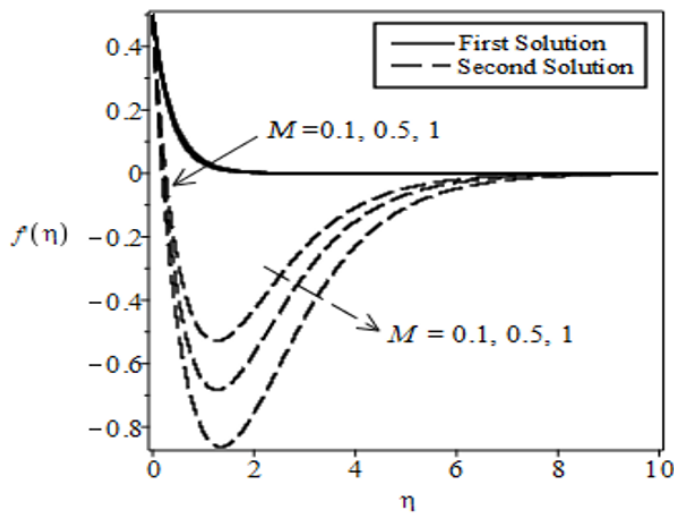


Figure 8. Velocity profiles for various values of M for magnetite at $\lambda=0.5$.

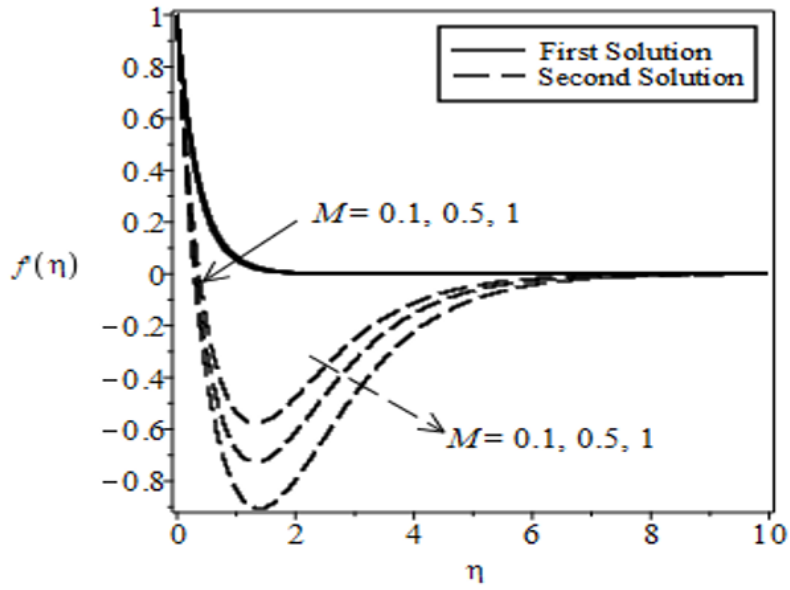


Figure 9. Velocity profiles for various values of M for magnetite at $\lambda=1$.

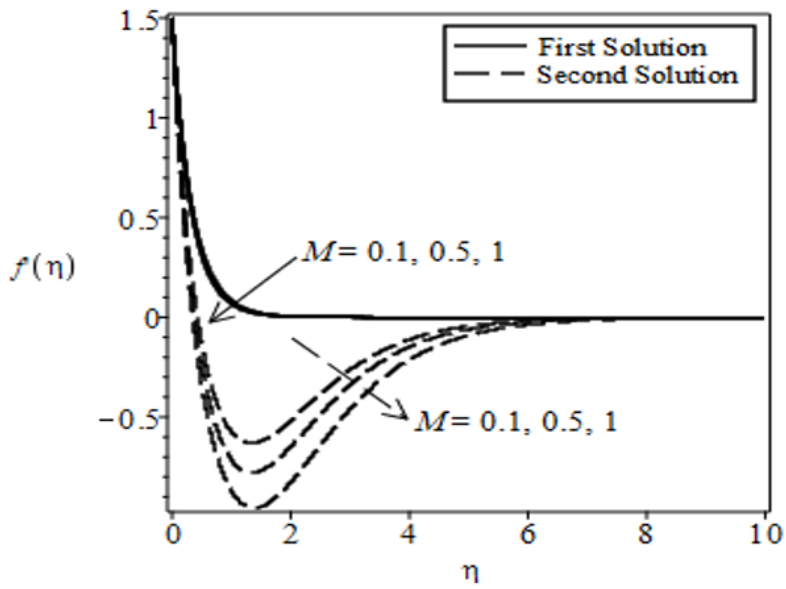


Figure 10. Velocity profiles for various values of M for magnetite at $\lambda=1.5$.

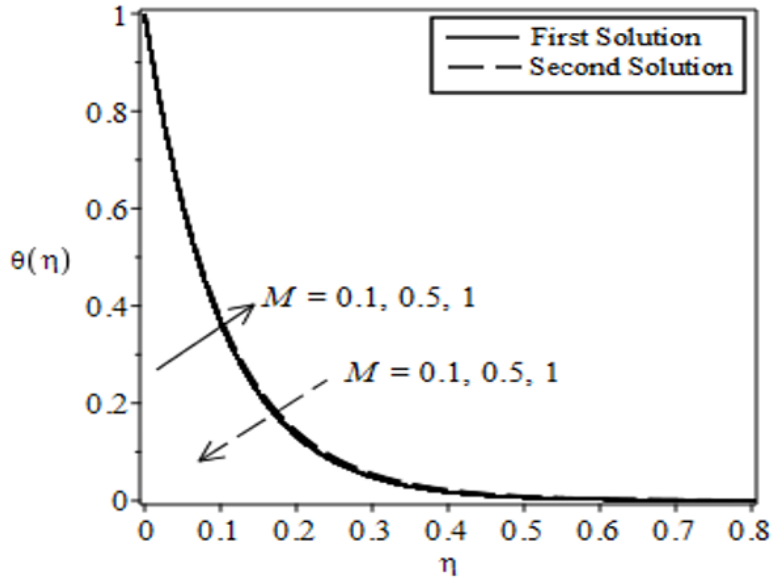


Figure 11. Temperature profiles for various values of M for magnetite at $\lambda=0.5$.

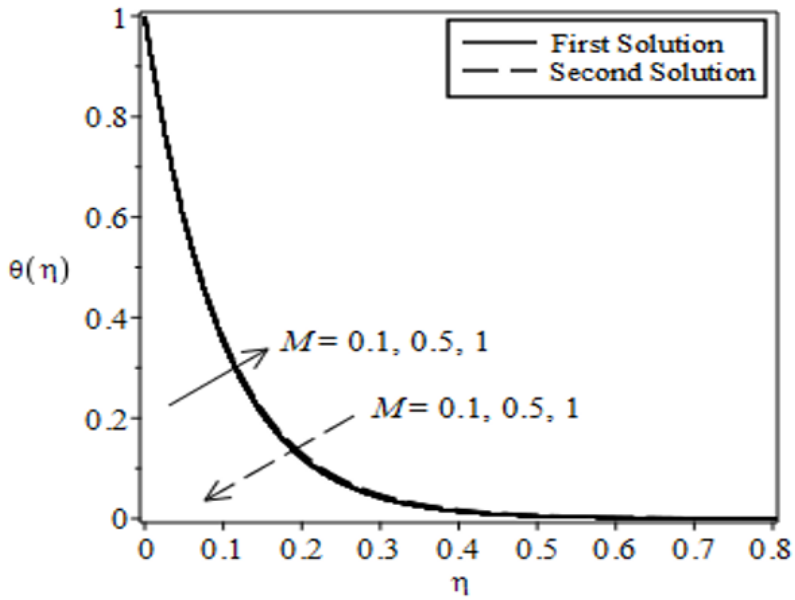


Figure 12. Temperature profiles for various values of M for magnetite at $\lambda=1$.

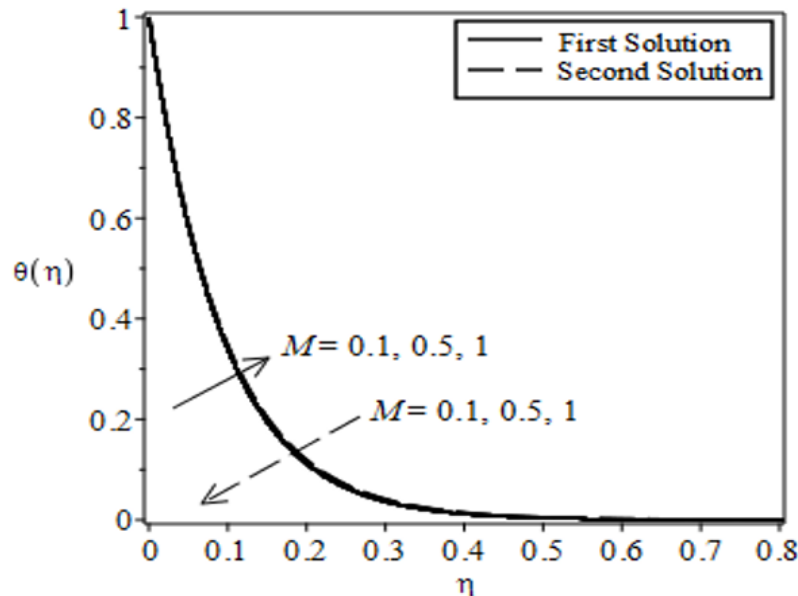


Figure 13. Temperature profiles for various values of M for magnetite at $\lambda = 1.5$.

CONCLUSION

In this study, we focused on a model of Tiwari and Das (2007) under some of assumptions and problem's considerations which are steady, laminar, two-dimensional boundary layer flow of an incompressible ferrofluids and transmission of heat over an exponentially stretching/shrinking sheet. The main purpose of this study to analyze the effect of chosen parameters which are magnetic parameter M , wall mass transfer parameter S , stretching/shrinking parameter λ and volume fraction of solid ferroparticle ϕ on dimensionless physical quantities. A brief of summary conclusions drawn from the analysis are two solutions exist for both stretching/shrinking sheet up to a critical value where the presence of solutions relying upon the values of parameters considered as suction ($S > 1$), stretching/shrinking ($\lambda < 0$)/($\lambda > 0$), magnetic ($M > 0$) and ferroparticle volume fraction ($0 \leq \phi \leq 0.2$). The results displayed increasing in the skin friction caused reduction in the rate of heat motion at layer. We observed magnetite (Fe_3O_4) has the highest number of skin friction compared to cobalt ferrite (CoFe_2O_4) and manganese-zinc ferrite ($\text{Mn-ZnFe}_2\text{O}_4$) in shrinking case, while CoFe_2O_4 has the highest value of local Nusselt number. Besides, the high temperature in the boundary layer because of reduction in velocity profiles and the decrease in velocity profiles due to higher number in the magnetic parameter, which slowed the fluids motion in the boundary layer. Lastly, the rate for heat transfer declined when increasing in temperature profiles with the presence of magnetic field.

ACKNOWLEDGEMENT

Thank you to Universiti Sains Malaysia for funding this interesting research, grant number 304/PMATHS/6315383.

REFERENCES

- Alavi, S. Q., Hussanan, A., Kasim, A. R. M., Rosli, N., & Salleh, M. Z. (2017). MHD stagnation point flow towards an exponentially stretching sheet with prescribed wall temperature and heat flux. *International Journal of Applied and Computational Mathematics*, 3(4), 3511-3523. <https://doi.org/10.1007/s40819-017-0312-x>
- Bachok, N., Ishak, A., & Pop, I. (2012). Boundary layer stagnation-point flow and heat transfer over an exponentially stretching/shrinking sheet in a nanofluid. *International Journal of Heat and Mass Transfer*, 55(25-26), 8122-8128. <https://doi.org/10.1016/j.ijheatmasstransfer.2012.08.051>
- Bhattacharyya, K. (2011). Boundary layer flow and heat transfer over an exponentially shrinking sheet. *Chinese Physics Letters*, 28(7), Article 074701. <https://doi.org/10.1088/0256-307X/28/7/074701>
- Bhattacharyya, K., & Layek, G. C. (2014). Magnetohydrodynamic boundary layer flow of nanofluid over an exponentially stretching permeable sheet. *Physics Research International*, 2014, Article 592536. <https://doi.org/10.1155/2014/592536>
- Bhattacharyya, K., & Pop, I. (2011). MHD boundary layer flow due to an exponentially shrinking sheet. *Magnetohydrodynamics*, 47(4), 337-344. <https://doi.org/10.22364/mhd.47.4.2>
- Bhattacharyya, K., & Vajravelu, K. (2012). Stagnation-point flow and heat transfer over an exponentially shrinking sheet. *Communications in Nonlinear Science and Numerical Simulation*, 17(7), 2728-2734. <https://doi.org/10.1016/j.cnsns.2011.11.011>
- Blaney, L. (2007). Magnetite (Fe₃O₄): Properties, synthesis, and applications. *Leheight Preserve*, 15, 33-81.
- Choi, S. U., & Eastman, J. A. (1995). *Enhancing thermal conductivity of fluids with nanoparticles* (No. ANL/MSD/CP-84938; CONF-951135-29). Argonne National Lab.
- Ishak, A. (2011). MHD boundary layer flow due to an exponentially stretching sheet with radiation effect. *Sains Malaysiana*, 40(4), 391-395.
- Jusoh, R., Nazar, R., & Pop, I. (2018). Magnetohydrodynamic rotating flow and heat transfer of ferrofluid due to an exponentially permeable stretching/shrinking sheet. *Journal of Magnetism and Magnetic Materials*, 465, 365-374. <https://doi.org/10.1016/j.jmmm.2018.06.020>
- Khan, W. A., Khan, Z. H., & Haq, R. U. (2015). Flow and heat transfer of ferrofluids over a flat plate with uniform heat flux. *The European Physical Journal Plus*, 130(4), 1-10. <https://doi.org/10.1140/epjp/i2015-15086-4>
- Magyari, E., & Keller, B. (1999). Heat and mass transfer in the boundary layers on an exponentially stretching continuous surface. *Journal of Physics D: Applied Physics*, 32(5), Article 577. <https://doi.org/10.1088/0022-3727/32/5/012>

- Mansur, S., Ishak, A., & Pop, I. (2015). The magnetohydrodynamic stagnation point flow of a nanofluid over a stretching/shrinking sheet with suction. *PLoS One*, *10*(3), Article e0117733. <https://doi.org/10.1371/journal.pone.0117733>
- Mohamed, M. K. A., Ismail, N. A., Hashim, N., Shah, N. M., & Salleh, M. Z. (2019). MHD slip flow and heat transfer on stagnation point of a magnetite (Fe₃O₄) ferrofluid towards a stretching sheet with Newtonian heating. *CFD Letters*, *11*(1), 17-27.
- Muthtamilselvan, M., Kandaswamy, P., & Lee, J. (2010). Heat transfer enhancement of copper-water nanofluids in a lid-driven enclosure. *Communications in Nonlinear Science and Numerical Simulation*, *15*(6), 1501-1510. <https://doi.org/10.1016/j.cnsns.2009.06.015>
- Nadeem, S., Haq, R. U., & Khan, Z. H. (2014). Heat transfer analysis of water-based nanofluid over an exponentially stretching sheet. *Alexandria Engineering Journal*, *53*(1), 219-224. <https://doi.org/10.1016/j.aej.2013.11.003>
- Naramgari, S., & Sulochana, C. (2016). MHD flow over a permeable stretching/shrinking sheet of a nanofluid with suction/injection. *Alexandria Engineering Journal*, *55*(2), 819-827. <https://doi.org/10.1016/j.aej.2016.02.001>
- Noghrehabadi, A., Ghalambaz, M., Izadpanahi, E., & Pourrajab, R. (2014). Effect of magnetic field on the boundary layer flow, heat, and mass transfer of nanofluids over a stretching cylinder. *Journal of Heat and Mass Transfer Research*, *1*(1), 9-16. <https://doi.org/10.22075/JHMTR.2014.149>
- Odenbach, S. (2003). Ferrofluids-magnetically controlled suspensions. *Colloids and Surfaces A: Physicochemical and Engineering Aspects*, *217*(1-3), 171-178. [https://doi.org/10.1016/S0927-7757\(02\)00573-3](https://doi.org/10.1016/S0927-7757(02)00573-3)
- Rahman, N. H. A., Bachok, N., & Rosali, H. (2019). MHD stagnation point flow over a stretching/ shrinking sheet in nanofluids. *Universal Journal of Mechanical Engineering*, *7*(4), 183-191. <https://doi.org/10.13189/ujme.2019.070406>
- Ramli, N., Ahmad, S., & Pop, I. (2018). MHD forced convection flow and heat transfer of ferrofluids over a moving at plate with uniform heat flux and second-order slip effects. *Scientia Iranica*, *25*(4), 2186-2197. <https://doi.org/10.24200/SCI.2017.4343>
- Shokrollahi, H. (2013). Structure, synthetic methods, magnetic properties and biomedical applications of ferrofluids. *Materials Science and Engineering C*, *33*(5), 2476-2487. <https://doi.org/10.1016/j.msec.2013.03.028>
- Tiwari, R. K., & Das, M. K. (2007). Heat transfer augmentation in a two-sided lid-driven differentially heated square cavity utilizing nanofluids. *International Journal of heat and Mass transfer*, *50*(9-10), 2002-2018. <https://doi.org/10.1016/j.ijheatmasstransfer.2006.09.034>



Development of a Fluidized Bed Dryer for Drying of a Sago Bagasse

Nur Tantiyani Ali Othman* and Ivan Adler Harry

Department of Chemical and Process Engineering, Faculty of Engineering and Built Environment, Universiti Kebangsaan Malaysia, 43600, Bangi UKM, Selangor, Malaysia

ABSTRACT

Sago is an essential source of starch for some regions in the third and developing world. However, the sago processing industry has been producing a large amount of sago waste, and the untreated waste is usually disposed to the nearest river. It not only leads to the environmental problem, but it is illegal under the Environmental Quality Act 1974. Since the sago waste still has high starch content, which is 58%, it can be converted to high value-added products such as poultry feed. However, before being converted to other products, the sago must be dried to remove the moisture content to prevent any bacteria growth and ensure safety health issues have been observed. Recently, drying of sago bagasse using a fluidized bed dryer (FBD) has gained attention since the dry rate of the material is considerably faster compared to other methods. Due to that reason, the drying of the sago bagasse in the FBD is studied using computational fluid dynamic as it can be executed in a short period of time compared to the experimental approach. The FBD model was developed using

ANSYS[®] Fluent academic version 19.2. The effect of the hot air feed temperature; $T=50, 60, 70, \text{ and } 80^{\circ}\text{C}$ and velocity of hot air feed; $v=1-4 \text{ m/s}$ on the sago's behavior and performance of fluidization profile were studied. The simulation results showed that the high temperature and air feed velocity would result in a rapid drying rate. Besides, the optimum drying rate was at $T=60^{\circ}\text{C}$ with the $v=4 \text{ m/s}$ as these conditions give a shorter drying time to achieve of final 10% moisture content. It also has the added advantages of reducing the power energy

ARTICLE INFO

Article history:

Received: 17 December 2020

Accepted: 1 April 2021

Published: 19 July 2021

DOI: <https://doi.org/10.47836/pjst.29.3.13>

E-mail addresses:

tantiyani@ukm.edu.my (Nur Tantiyani Ali Othman)

adlerivan17@gmail.com (Ivan Adler Harry)

*Corresponding author

and cost supply. These optimal conditions are very crucial and should be consider as the dried sago bagasse tend to be retrograded when a higher temperature is applied.

Keywords: ANSYS® fluent, computational fluid dynamic, drying, fluidized bed dryer, sago bagasse

INTRODUCTION

Metroxylon sago Rottb, known as sago palm, is a tropical plant capable of adapting to swamps condition and often found in Southeast Asia, especially in a country like Malaysia, Indonesia and Papua New Guinea. It is one of the oldest tropical plant that is exploited by humans for various uses, for instance, as a form of starch providing the primary source of carbohydrate, the leaves and stem are used as pillars or wall, while the sago pith, which is made of fibre can be used as feedstuff, the starch can be used as fuel, and the raw material can be used for cooking (Putra & Ajiwiguna, 2017). Nowadays, the sago industry is an emergent industry with the potential of sago being the alternative source of starch. In addition, the increase in starch demand further drives this thriving industry, particularly in Malaysia and Indonesia. In Malaysia, Sarawak is the largest producer and exporter with a total of nine active operating processing plants and the export of about 25,000 to 40,000 tonnes of sago products each year (Naim et al., 2016). It has been exported to various countries such as Thailand, Singapore, Japan, and other as well (Bujang, 2008).

Aside from producing the product, this industry also produces a large amount of sago waste or residues which are often mixed with the wastewater and washed off into nearby stream (Vijay et al., 2016). A considerable quantity of the waste effluent has been dumped into the rivers that led to serious environmental problem. Besides, it is a total violation of the environmental Quality Act, 1974. Environmental problem is a worldwide threat to public health; therefore, an alternative method needs to be considered to reduce the discharge of these wastes. Various methods of treatment and conversion of sago has been previously suggested.

The sago effluent has some potential to be converted into alternative high value-added product. As it comprises 58% starch, 23% cellulose, 9.2% hemicellulose, and 4% lignin, it has potential to be turned into a new product, such as bio-conversion into sugar, as well as converted into animal feedstock (Awg-Adeni et al., 2013). However, before it can be converted to the other products, the sago must be dried to a certain amount of moisture content using a drying process to prevent bacterial growth and maintain product quality. There are currently several drying methods, such as sun direct drying and solar drying. Nevertheless, these methods are less effective due to the unstable rate of drying, and the crops are exposed to an unhealthy environment (Awg-Adeni et al., 2013).

A fluidized bed dryer (FBD) is the most established and regularly used drying method for a solid particle. It is gaining attention as it can produce high heat and mass transfer

that can ensure a considerably faster and homogeneous drying process. Furthermore, the temperature feed and velocity of hot air can be monitored closely, and the fluidizing action ensures thorough mixing of the substance. In the drying process, the most important is the optimum rate of drying should be achieved in a short time while remaining cost effective. Due to these situations, the computational fluid dynamic (CFD) was conducted to analyze the drying rate and observe the behaviour of the fluidizing rate inside the FBD. In the CFD process, the numerical methods and algorithm were applied in order to solve the problem of fluid flow.

For instance, Arumuganathan et al. (2017) analyzed the drying of mushrooms using an FBD, and they found that the temperature of a hot air feed affects the rate of drying. They also established that the optimum temperature for the drying of mushrooms is 60°C (Arumuganathan et al., 2017). Other than that, Mortier et al. (2011) applied the CFD simulation approach to analyze the drying profile of wheat grains in an FBD to predict the moisture content of solids at various drying times by applying Eulerian-Eulerian two-fluid models and the kinetic theory.

Anthony and Shyamkumar (2016) applied the ANSYS® Fluent software to observe the drying of sand particles in an FBD (Anthony & Shyamkumar, 2016). They built a 3D model of FBD and studied innumerable parameters, as well as the velocity and temperature distribution of the inlet hot air. Based on previous studies in the oil palm fronds industry, it was found the higher temperature and velocity of hot air feed cause the drying rate to increase (Puspasari et al., 2014). The higher temperature and velocity also cause the drying rate to increase in the Millet Pearl industry (Maheswari, 2015), and a higher temperature can also result in the increase in the rate of coconut drying (Jongyingcharoen et al., 2019).

Others researcher found that mushrooms' optimum drying rate is at the temperature of 60°C (Charles et al., 2012). Besides, the rate of drying decreases as the velocity of hot air feed increases over 5 m/s for drying wheat (Li-Zhen et al., 2019). In the case of the coal industry, the drying rate increases as the temperature of hot air feed increases (Dejahang, 2015). When drying grain, and the temperature of hot air at 200°C will damage the grain. The optimum drying rate of grains is at a temperature less than 100°C (Jannatul et al., 2018). Apart from that, the ideal temperature for sand drying is at 157°C (Anthony & Shyamkumar, 2016).

To gain a deeper understanding of the fluid flow properties in the FBD, aside from the experimental work, the CFD method was proposed. Based on previous numerical studies, the simulation method using CFD has proven in improving design and optimize FBD parameters also able to obtain hydrodynamic data is needed to improve the efficiency of the FBD operation (Hamzehei, 2011; Honarvar & Mowla, 2012; Jalil & Nikbakht, 2017; Othman et al., 2020; Rakesh, et al. 2020). Thus, the goal of this study is to determine the relationship between the drying rate of the sago at various hot air velocities and inlet

temperatures. The profile of the temperature and velocity distribution in the FBD was observed in order to determine the optimum condition for drying of the sago bagasse.

METHODS

In this study, a CFD simulation was conducted to analyze the drying rate of sago in the FBD. The CFD simulation enabled a fluid flow to be observed, determining the heat and mass transfer and other related phenomena inside the FBD. Using numerical methods and algorithms, CFD was capable of solving and analyzing problems involving fluid mechanics. The standard CFD process consisted of several steps, which included the pre-processing, solver as well the post processing stages.

Pre-Processing - Development of FBD Geometry and Meshing Process

In this study, the front view, side view and 3D model of the FBD are developed and designed using ANSYS® Fluent academic version 19.2 (Ansys, 2019). This FBD model is designed based on previous studied previous studies (Yahya & Fudholi, 2016; Othman et al., 2020). The dimensions and the design model for FBD are shown as in Figure 1. The model is a cylinder with a diameter of 600 mm and an overall length of 3000 mm. Two inlets are located at the bottom of the cylinder to supply the hot air inside FBD. Both of the inlets have an inside diameter and length of 60 mm, and the distance between these two inlets is 1000 mm. There is one outlet at the right side with a length of 100 mm, and a diameter of 100 mm for transportation of the dried sago bagasse.

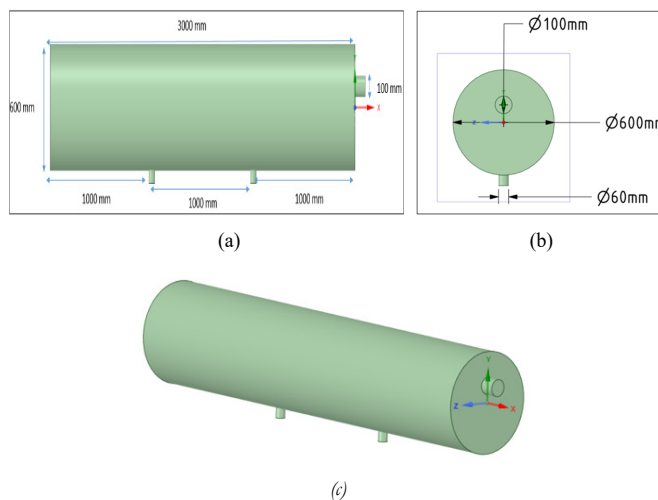


Figure 1. Front view, side view, and 3D model of the FBD

The development of meshing was done after the complete model of FBD has been designed. In the meshing process, the size details should be specified where the elements were fine mesh, and a minimum size of 0.0397 mm was used in this study. Besides, some assumptions were made in this simulation, such as no chemical reaction is taking place during the drying process, well-mixed achieved between the solid and gas phases, no slip condition, the desired final moisture content of the sago is set to be at 10% (wt./wt.), and the size of the particle is not reduced during the drying process. The 3D meshing of the FBD model is shown as in Figure 2.

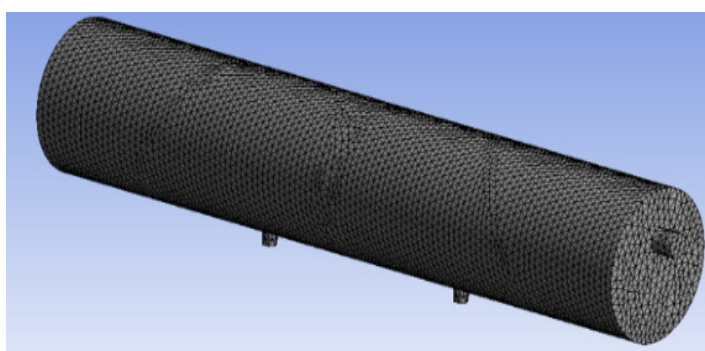


Figure 2. 3D Meshing of the FBD model

Define of A Boundary Condition, Materials and Parameters

Once the problem physics had been identified, the flow physics model and boundary conditions were defined in the ANSYS® Fluent 19.2. In this study, the Eulerian-Eulerian multiphase model was applied, and a turbulent model was selected due to the turbulence flow in the FBD. It is because in the turbulent model, the bubble size of sago bagasse particle is not anymore discrete, but continuous and the bubble phase is less distinguishable than in the bubbling regime. From the previous researchers, it shows the bubbling regime simulation is suitable in the pilot plant while, the turbulent model better simulated for industrial scale experiment. As the flow of air increases, the bed known as FBD bag expands, and particles of sago start a turbulent motion. Due to regular contact with air, the sago bagasse gets dry. Besides, to analyze the transfer of heat between the two-phase gas and solid, the heat transfer model was selected as well. The model of the two-term exponential was also chosen in the function to obtain the moisture ratio.

The wet sago bagasse with the high moisture content (MC) was in the feed, and the hot air was supplied through two inlets below the FBD to dry the wet sago. The dried sago bagasse flowed out the FBD through the outlet. The effect of the inlet hot gas velocity on the rate of drying were analyzed at various velocities ranges; $v=1-4$ m/s. In this case, the

temperature of the hot gas, T and the initial moisture content of sago, MC was kept constant at 50°C and $\text{MC}=80\%$, respectively. The optimum velocity of the hot air feed and that gives the highest rate of drying was chosen as a parameter condition in the next simulation in order to determine the effect of temperature on the rate of drying. Then, the effect of the temperature of hot gas; $T=50\text{-}80^{\circ}\text{C}$ was studied to observe the optimum and the highest rate of drying of the sago bagasse where the air feed velocity and initial moisture content was kept constant at $v=4\text{ m/s}$ and $\text{MC}=80\%$, respectively.

Define of A Boundary Condition, Materials and Parameters

The governing equation used in this study is a conservation of mass and momentum. The conservation of energy and turbulence model is also important to indicate heat transfer and turbulence flow (Argyropoulos & Markatos, 2015). Equation 1 to 7 were applied to the physics model of the simulation to solve the problem involving fluid flow and fluid mechanics in the FBD where \vec{v}_q is a velocity for q phase, p is pressure, \dot{m}_{pq} is a mass transfer from p phase to q phase, \dot{m}_{qp} is a mass transfer from q phase to p phase, h is a heat transfer coefficient, ρ is a density, q is a heat flux, ε is a volume fraction, Q is a heat transfer rate, v is a vector velocity, H is a latent heat and τ is a shear stress tensor. In the ANSYS[®] Fluent simulation, the modules used are electrical current, creeping flow, particle tracing in a fluid flow and transport of species. The electric current module was used to supply the non-uniform electric current fields. The creeping flow was used to simulate fluid flow at very low Reynolds numbers where the inertia term in the Navier-Stokes equation can be ignored.

Conservation of mass (Equation 1),

$$\frac{\delta}{\delta t}(\alpha_q \rho_q) + \nabla \cdot (\alpha_q \rho_q \vec{v}_q) = \sum_{p=0}^n (\dot{m}_{pq} - \dot{m}_{qp}) + S_q \quad [1]$$

Conservation of momentum (Equation 2),

$$\frac{\delta}{\delta t}(\varepsilon_s \rho_s) + \nabla \cdot (\varepsilon_s \rho_s \vec{v}_s) = 0 \quad [2]$$

i) For gas phase (Equation 3),

$$\begin{aligned} \frac{\delta}{\delta t}(\varepsilon_g \rho_g \vec{v}_g) + \nabla \cdot (\varepsilon_g \rho_g \vec{v}_g \vec{v}_g) \\ = -\varepsilon_g \nabla p + \nabla \tau_g + \varepsilon_g \rho_g \vec{g} + K_{gs}(\vec{v}_g - \vec{v}_s) \end{aligned} \quad [3]$$

ii) For solid phase (Equation 4),

$$\begin{aligned} \frac{\delta}{\delta t} (\varepsilon_s \rho_s v_s) + \nabla \cdot (\varepsilon_s \rho_s v_s v_s) \\ = -\varepsilon_s \nabla p + \nabla p_s + \nabla \tau_s^- + \varepsilon_s \rho_s g + K_{sg} (\vec{v}_g - \vec{v}_s) \end{aligned} \quad [4]$$

Continuity equation for solid phase (Equation 5),

$$\frac{\delta}{\delta t} (\varepsilon_s \rho_s) + \nabla \cdot (\varepsilon_s \rho_s v_s) = 0 \quad [5]$$

Conservation of Energy

i) For gas phase (Equation 6),

$$\begin{aligned} \frac{\delta}{\delta t} (\varepsilon_g \rho_g h_g) + \nabla \cdot (\varepsilon_g \rho_g v_g h_g) \\ = -\varepsilon_g \frac{\delta p_g}{\delta t} + \tau_g^-: \nabla \vec{v}_g - \nabla \vec{q}_g + Q_{sg} + \dot{m} \Delta H_{vap} \end{aligned} \quad [6]$$

ii) For solid phase (Equation 7),

$$\begin{aligned} \frac{\delta}{\delta t} (\varepsilon_s \rho_s h_s) + \nabla \cdot (\varepsilon_s \rho_s u_s h_s) \\ = -\varepsilon_s \frac{\delta p_s}{\delta t} + \tau_s^-: \nabla \vec{u}_s - \nabla \vec{q}_s + Q_{gs} - \dot{m} \Delta H_{vap} \end{aligned} \quad [7]$$

RESULTS AND DISCUSSIONS

To inhibit any microbial development and quality decay in the dried sago bagasse as well for storage handling, achieving an ideal drying parameter condition during the early stages is crucial in the drying process. In this simulation study, a final sago volume fraction and a mass fraction of water in the sago bagasse in the FBD were observed and determined at different ranges of inlet hot air velocities and temperatures. The effect of various hot air velocity; 1.0-4.0 m/s on the rate of sago's drying is observed, as shown in Figure 3 where the volume fraction of the sago in the FBD is determined after 5 minutes of the drying process with the feed of the hot gas is supplied at the constant temperature of $T=70^\circ\text{C}$ and the initial moisture content of $\text{MC}=80\%$. The contour of the color bar indicates the range value of the volume fraction of the sago bagasse in the FBD, with the red color showing a higher sago volume fraction. The value of 1.0 indicates almost all the areas in the FBD are covered by sago bagasse. In contrast, the blue color shows a low sago volume fraction in the FBD as a value of zero indicates no sago bagasse can be found in the area.

The right side of Figure 3 shows the cross-sectional view of the inside FBD near the outlet area, while the left side of Figure 3 shows the front view along the FBD. It is shown that the velocity inside the FBD is uneven in all areas where at the higher inlet hot air velocity of $v=3$ and 4 m/s, the sago bagasse is fluidized more vigorously on the upper

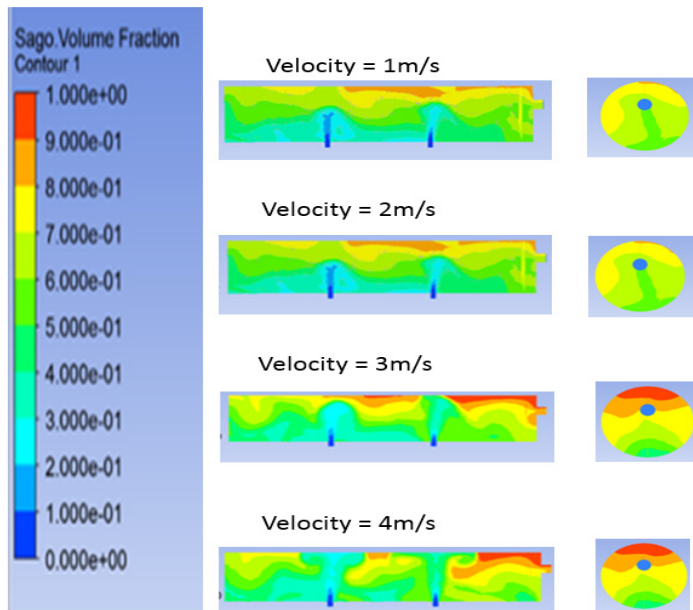


Figure 3. Sago volume fraction distribution in the FBD at various hot air velocities

side of the FBD area. It shows the higher sago fraction with the red color due to higher velocity supplied by hot air from below the FBD, as compared to the lower velocity at $v=1$ and 2 m/s. The cross-sectional view shows that at $v=1$ and 2 m/s, the sago is almost evenly spread inside the FBD. The yellowish-green color is observed, which indicates that most area of the FBD are covered with around 50-70% of the sago content. It shows the moisture content of the sago bagasse is reduced from 80% (v/v) up to 50% (v/v) after going through the drying process when the velocity at $v=1$ and 2 m/s was used.

Meanwhile, with the increment of the hot air velocity at $v=3$ and 4 m/s, the higher fraction of the sago bagasse causes around 90-100% of the sago content to be at the top area of the FBD near the outlet area. This happens due to the fluidization process which occurs inside the FBD because the hot air supply increases the particle's movement and reduce the moisture content of the sago bagasse. It can be concluded that the higher velocity will increase the drying rate due to the rapid movement of air.

Based on these simulation results, the percentage of a water loss of the dried sago bagasse can be calculated using Equation 8, where W_{final} is the final moisture content of the sago and $W_{initial}$ is the initial moisture content of water. Figure 4 shows the result of the percentage of the final moisture content against drying time at various air velocities. It shows the drying time needs to achieve the desired and the standard requirement of the final moisture of the sago bagasse is at MC=10 % which is the fastest condition, which only

takes about 11 minutes when the velocity of hot air is at $v=4$ m/s. While, at $v=1$ m/s, the time needed is considerably longer, which is around 16 minutes. This shows that the higher velocity does not have significant effect; the velocity at $v=3-4$ m/s indicates the optimum condition has been achieved where all the sago bagasse has already had been fluidized.

$$\% \text{ Water loss} = \frac{W_{Final} - W_{initial}}{W_{initial}} \times 100 \quad [8]$$

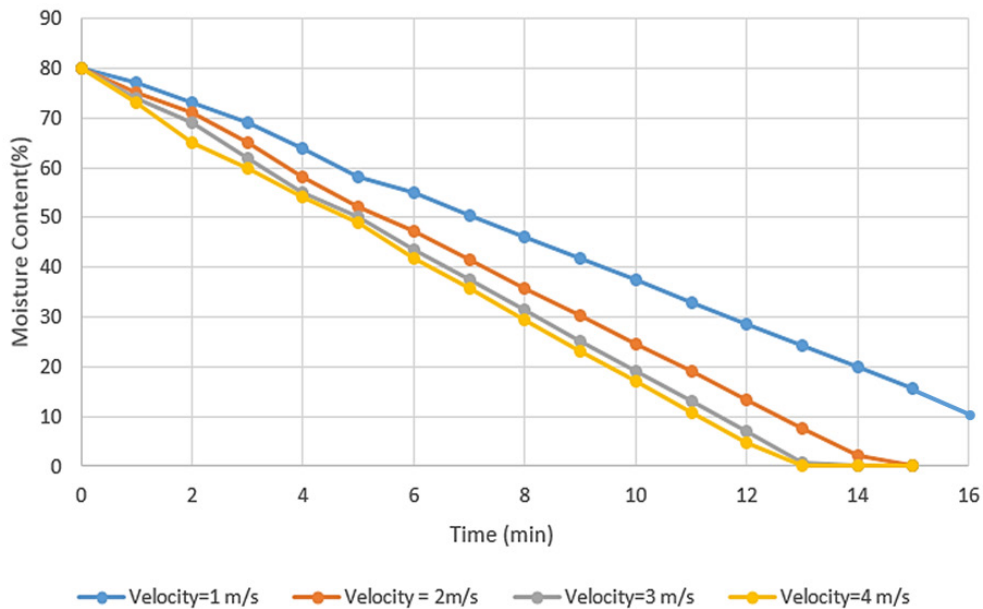


Figure 4. Moisture content of sago bagasse at different inlet velocities of hot gas

Figure 5 shows the flow profile of the sago volume fraction inside the FBD in 35s-time simulation. The colour bar represents the sago volume fraction, where the red color shows the area that has been occupied with the sago bagasse, while the blue color represents the area that has been occupied with the hot air. At $t=0$ s, it shows the almost of the lower part areas in the FBD are covered by sago bagasse, as shown by the red colour. As the drying times take placed, the volume fractions of the sago bagasse have slightly decreased, which is represented by the decrease in the level of red color distribution inside the FBD. It occurs because the sago bagasse was fluidized inside the FBD with the existence of hot air supplies that increase the particle movement and reduce the moisture content of the sago bagasse. It shows the cooling effect that occurs in the FBD as a result of the endothermic reaction from the evaporation process of the water from the sago particle's surface.

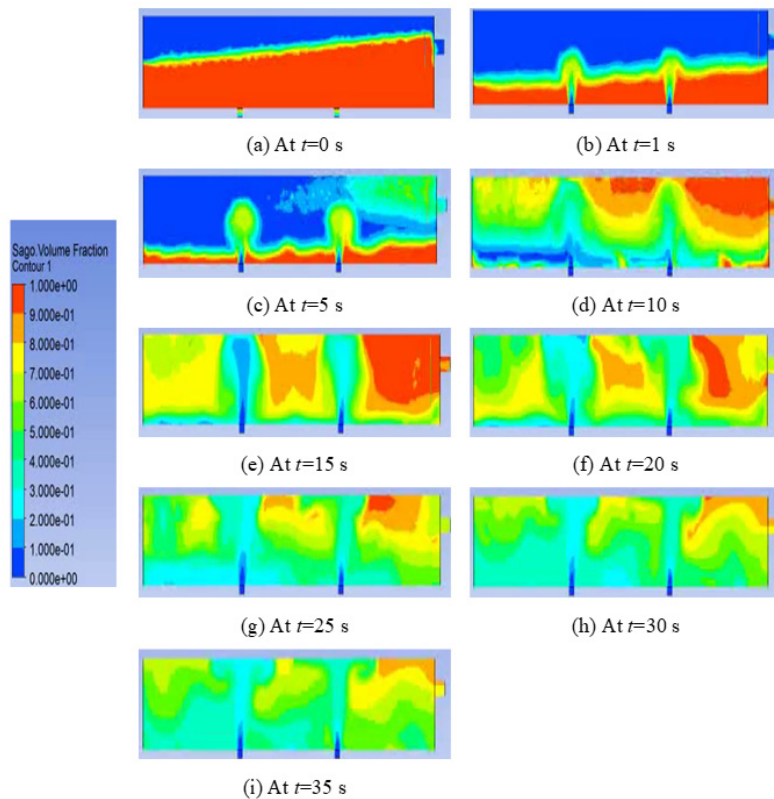


Figure 5. Flow profile of the sago volume fraction inside the FBD at various times

Apart from that, the effect of the temperature on the rate of drying was also studied. Figure 6 shows the temperature profile inside the FBD after the sago bagasse has dried in the 35s time simulation as the hot air is supplied at the bottom side of the FBD. The color bar represents the temperature distribution where the red color shows the highest temperature in the FBD with the value of $T=70^{\circ}\text{C}$. Meanwhile the blue color represents the lowest temperature profile with the value $T=25^{\circ}\text{C}$. At $t=0$ s, it shows the temperature in the FBD is read as room temperature, which is shown by the blue color. As time elapsed, the temperature in the FBD increases from the point of the hot air feed, which helps the drying process of the sago bagasse. It occurs as the heat transfer takes a place inside the FBD due to evaporation process that occurs on the sago particle's surface. This evaporation process is an endothermic reaction where it cools down the surrounding air inside the FBD. This observation of the temperature flow pattern is in agreement with the experimental work done by Okoronkwo et al. (2013) and simulation work done by Othman et al. (2020). As the time elapsed, the temperature distribution inside the FBD was constant, implying that the drying process has occurred by reducing the water content in the sago bagasse. It also

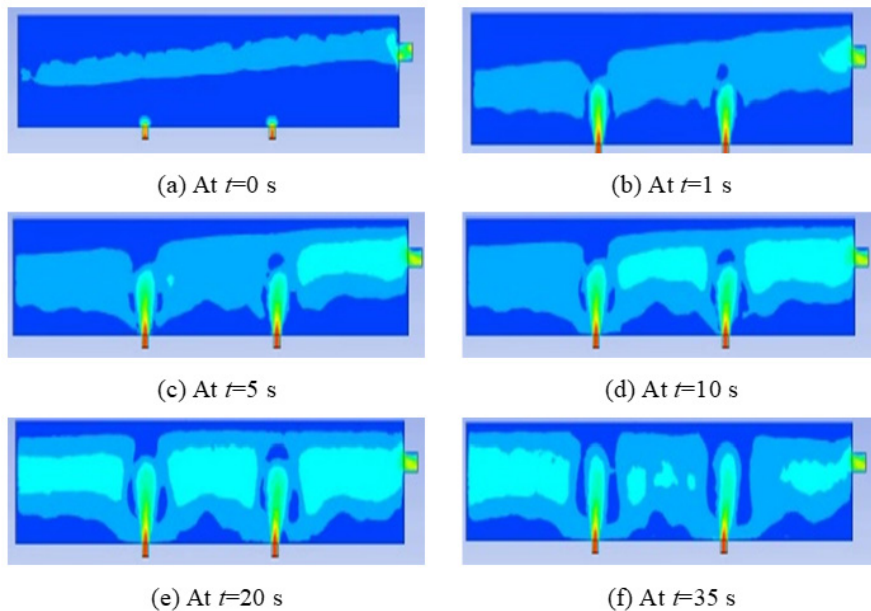


Figure 6. Profile of temperature distribution inside the FBD at various drying times

shows the inlet air feed with those velocities' ranges is sufficient to initiate the fluidization of the sago bagasse process in the designed FBD.

Figure 7 shows the effect of the inlet temperature on the sago volume fraction in the FBD after 5 minutes of a drying process with the hot air was feed at a constant velocity of $v=4$ m/s and the initial moisture content of $MC=80\%$. The right side of Figure 7 shows the cross-sectional view of FBD near the outlet area where the dried sago bagasse distribution does not show any significant difference due to the similar velocity used. However, as the temperature of $T=50^{\circ}\text{C}$ is applied, it can be seen that a higher fraction of sago is observed at the top area of the FBD, indicated by the red color compared to the other tested temperatures.

Based on these simulation results, the drying time needed to achieve the desired of the final moisture content at various inlet hot air temperatures are demonstrated in Figure 8. Figure 8 shows the time taken for the initial moisture content of the sago bagasse to reduce to $MC=10\%$ is the shortest time which is less than 9 minutes with $T=80^{\circ}\text{C}$. Meanwhile, the time needed to achieve the $MC=10\%$ when the hot air feed is at $T=50^{\circ}\text{C}$ is around 11 minutes. Thus, it can be concluded that the higher hot air temperature will increase the rate of drying. In this study, the optimum condition of hot air supplied at $v=4\text{m/s}$ is selected because, under this condition, a shorter drying time can be achieved to obtain the final 10% moisture content compared to others, and a further increase of the inlet velocity will affect

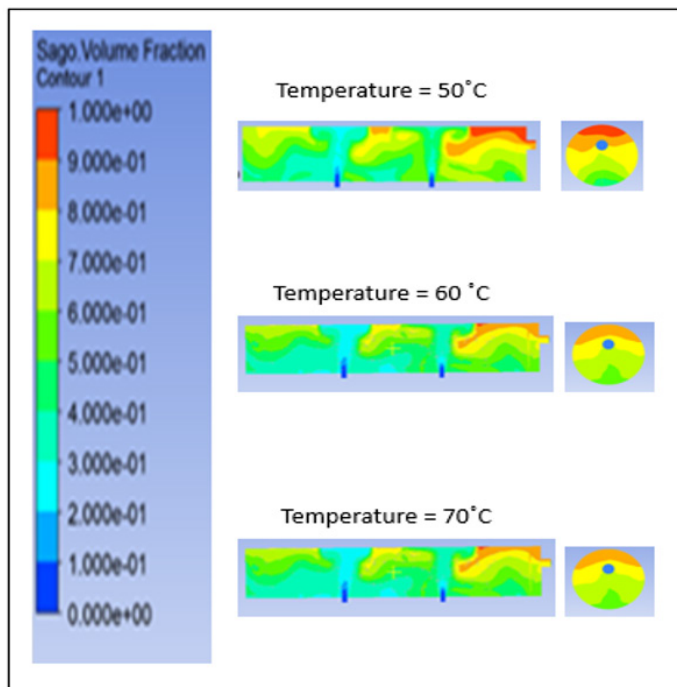


Figure 7. Sago volume fraction inside the FBD at various temperature with similar hot air velocity and moisture content

the power energy and increase the cost. For the hot air feed temperature, $T=60^{\circ}\text{C}$ is selected as the optimum condition shows that $T=50-70^{\circ}\text{C}$, as listed in Figure 8, is ideal for drying sago bagasse compared to others. It has a similar pattern to $T=80^{\circ}\text{C}$ used in previous studies, but the sago bagasse tends to be gelatinous at a higher temperature. Thus, the optimum temperature of $T=60^{\circ}\text{C}$ and velocity of $v=4\text{ m/s}$ is selected based on the highest drying rate of sago bagasse. At this velocity, it will support the sago particle to fluidize as well to reduce the moisture content in the final sago bagasse. Thus, higher inlet temperatures of drying air should be met, which leads to shorter drying times. However, the product quality considerations limit the applicable rise to the air temperature (Mujumdar, 1995; Daud, 2008). Excessive hot air can almost completely dehydrate the sago bagasse surface, making its pores shrink and almost close, leading to crust formation or “case hardening”, which is usually undesirable.

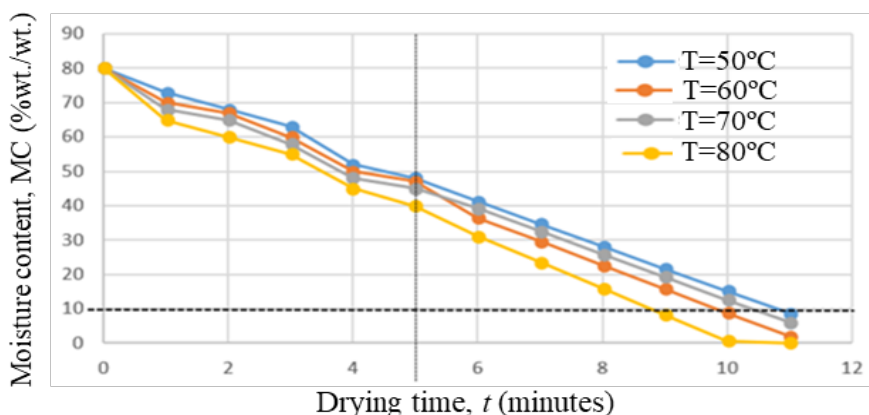


Figure 8. Moisture content against time with different temperature of hot air feed

CONCLUSION

The 3D FBD model was successfully designed by using ANSYS® Fluent academic version 19.2. The simulations were done to study the effect of various ranges of the temperature and velocity of the inlet hot air on the rate of drying of sago bagasse. The simulation results show that the higher inlet velocity, as well as the higher temperature feed, will result in a faster rate of drying. The temperature of $T=60\text{ }^{\circ}\text{C}$ and velocity of $v=4\text{ m/s}$ are selected as the value optimum condition for the drying of sago. This result indicates sago bagasse's feasibility to be converted for animal feed and other high-value products. For future improvements, the study will be expanding to a wide range of operational parameter for more reliable data.

ACKNOWLEDGEMENT

The authors would like to thank Universiti Kebangsaan Malaysia for their financial support under the grants GUP-2017-063 and FRGS/1/2020/TKO/UKM03/2.

REFERENCES

- Ansys, Inc. (2019). *Ansys fluent in Ansys workbench user's guide*. Ansys, Inc.
- Anthony, J., & Shyamkumar, B. (2016). Study on sand particles drying in a fluidized bed dryer using CFD. *International Journal of Engineering Studies*, 8(2), 129-145.
- Argyropoulos, C. D., & Markatos, N. C. (2015). Recent advances on the numerical modelling of turbulent flows. *Applied Mathematical Modelling*, 39(2), 693-732. <https://doi.org/10.106/j.apm.2014.07.001>
- Arumuganathan, T., Manikantan, M. R., Ramanathan, M., Rai, R. D., Indurani, C., & Karthiayani, A. (2017). Effect of diffusion channel storage on some physical properties of button mushroom (*Agaricus bisporus*) and shelf-life extension. *Proceedings of the National Academy of Sciences, India Section B: Biological Sciences*, 87(3), 705-718. <https://doi.org/10.1007/s40011-015-0628-4>

- Awg-Adeni, S., Abd-Aziz, S., Bujang, K., & Hassan, A. (2013). Recovery of glucose from residual starch of sago hampas for bioethanol production. *BioMed Research Corporation*, 9(14), 1-8. <https://doi.org/10.1155/2013/935852>
- Bujang, B. (2008). Potentials of bioenergy from the sago industries in Malaysia. In H. W. Doelle, S. Rokem & M. Berovic (Eds.), *Encyclopedia of Life Support System* (pp. 124-136). Eolss Publishers Co. Ltd.
- Charles, M., David, K., & Brenda, N. (2012). Effect of pretreatments and drying methods on chemical composition and sensory evaluation of oyster mushroom (*Pluerotus oestreatus*) powder and soup. *Journal of Food Processing and Preservation*, 38(1), 457-465. <https://doi.org/10.1111/j.1745-4549.2012.00794.x>
- Daud, R. W. (2008). Fluidized bed dryers-recent advances. *Advanced Powder Technology*, 19, 403-418. <https://doi.org/10.1163/156855208x336675>
- Dejahang, T. (2015). *Low temperature fluidized bed coal drying experiment, analysis and simulation* (Master Thesis). University of Alberta, Canada.
- Hamzehei, M. (2011). CFD modeling and simulation of hydrodynamics in fluidizedbed dryer with experimental validation. *ISRN Mechanical Engineering*, 2011, 1-9. <https://doi.org/10.5402/2011/131087>
- Honarvar, B., & Mowla, D. (2012). Theoretical and experimental drying of a cylindrical sample by applying hot air and infrared radiation in an inert medium fluidized bed. *Brazilian Journal of Chemical Engineering*, 29(2), 231-242. <https://doi.org/10.1590/s0104-66322012000200004>
- Jalil, N., & Nikbakht, A. M. (2017). Numerical simulation of corn drying in a hybrid fluidized bed-infrared dryer. *Journal of Food Process Engineering*, 40(2), Article e12373. <https://doi.org/10.1111/jfpe.12373>
- Jannatul, A., Qinfu, H., & Aibing, Y. (2018). Discrete particle simulation of food grain drying in a fluidised bed. *Powder Technology*, 323, 238-249. <https://doi.org/10.1016/j.powtec.2017.10.019>
- Jongyingcharoen, J. S., Wuttigarn, P., & Assawarachan, R. (2019). Hot air drying of coconut residue: Shelf life, drying characteristics, and product quality. *IOP Conference Series: Earth and Environmental Science*, 301, Article 012033. <https://doi.org/10.1088/1755-1315/301/1/012033>
- Li-Zhen, D., Arun, S. M., Qian, Z., Xu-Hai, Y., Jun, W., Zhi-An, Z., Zhen-Jiang, G., & Hong-Wei, X. (2019). Chemical and physical pretreatments of fruits and vegetables: Effects on drying characteristics and quality attributes – A comprehensive review. *Critical Reviews in Food Science and Nutrition*, 59(9), 1408-1432. <https://doi.org/10.1080/10408398.2017.1409192>
- Maheswari, S. (2015). Drying of pearl millet using fluidised bed dryer: Experiments and modelling. *International Journal of ChemTech Research*, 8(1), 377-387.
- Mortier, C., De Beer, T., Remon, J. P., VerVaet, C., & Nopens, I. (2011). Mechanistic modelling of fluidized bed drying processes of wet porous granules: a review. *European Journal of Pharmaceutics and Biopharmaceutics*, 79(2), 205-225. <https://doi.org/10.1016/j.ejpb.2011.05.013>
- Mujumdar, A. (1995). *Handbook of industrial drying* (2nd Ed.). Dekker Publishing.
- Naim, M., Yaakub, A. N. H., & Awang, H. D. A. (2016). Commercialization of sago through estate plantation scheme in Sarawak: The way forward. *International Journal of Agronomy*, 2016, Article 8319542. <https://doi.org/10.1155/2016/8319542>.

- Orokonkwo, C. A., Nwifo, O. C., Nwaigwe, K. N., Oguuke, N. V., & Anyanmwu, E. (2013). Experimental evaluation of a fluidized bed dryer performance. *The International Journal of Engineering and Science*, 2(6), 45-53.
- Othman, N. T. A. , Din, Z. A. M., & Taakrif, S. M. (2020). Simulation on drying of sago bagasse in a fluidized bed dryer. *Journal of Engineering Science and Technology*, 15(4), 2507-2521.
- Puspasari, I., Meor, Z., Daud, D. W., & Tasirin, S. (2014). Characteristic drying curve of oil palm fibers. *International Journal on Advanced Science, Engineering and Information Technology*, 4(1), 20-24. <https://doi.org/10.18517/ijaseit.4.1.361>
- Putra, N., & Ajiwiguna, A. (2017). Influence of air temperature and velocity for drying process. *Procedia Engineering*, 170, 516-519. <https://doi.org/10.1016/j.proeng.2017.03.082>
- Rakesh, V., & Paliwal, H. K. (2020). Simulation and analysis of plug flow fluidized bed dryer. *International Journal of Innovative Technology and Exploring Engineering*, 9(7), 805-811. <https://doi.org/10.35940/ijitee.g5338.059720>
- Vijay, K. G., Uttara, S., & Amrita, B. (2016). Bioconversion technologies of crude glycerol to value added industrial products. *Biotechnology Reports*, 9, 9-14. <https://doi.org/10.1016/j.btre.2015.11.002>
- Yahya, M., & Fudholi, A. (2016). Performances of fluidized bed drying integrated with biomass furnace for drying of paddy. *Research Journal of Applied Sciences, Engineering and Technology*, 13(6), 473-480. <https://doi.org/10.19026/rjaset.13.3007>



Review Article

Text Messaging Platforms in Mental Health Computerised-based Therapy: A Review

Teh Faradilla Abdul Rahman^{1*} and Norshita Mat Nayan²

¹*Centre of Foundation Studies, Universiti Teknologi MARA, Cawangan Selangor, Kampus Dengkil, 43800 Dengkil, Selangor, Malaysia*

²*Institute of IR4.0, Universiti Kebangsaan Malaysia, 43600 UKM Bangi, Selangor, Malaysia*

ABSTRACT

Mental health comprises emotional, psychological and social well-being. Global mental health problems have shown an increase in its statistics. Some psychotherapy approaches such as Internet-based therapy and mobile therapy have been carried out in clinical settings to improve one's mental health conditions. The objective of this paper is to identify the different kinds of text messaging platforms that have been tested in mental health computerised-based therapy settings. This paper also aimed to identify the effectiveness of the text messaging platforms on different mental health problems specifically. The review considered five databases (Scopus, PubMed, ACM Digital Library, IEEE Xplore and Web of Science) for the article searching process. The retrieved articles

were screened to fulfil the selection criteria including English and Malay language but exclude research protocols, proposals for a prototype application and literature reviews. The search resulted in 3656 articles but only 18 were selected for further review. It was found that web applications were the least used type of text messaging in mental health therapy, followed by mobile applications, whereas SMS was the most popular platform. Overall, the three text messaging platforms showed improvements in depression, anxiety, suicide risk, self-harm risk, mood, eating behaviour and

ARTICLE INFO

Article history:

Received: 9 February 2021

Accepted: 24 May 2021

Published: 31 July 2021

DOI: <https://doi.org/10.47836/pjst.29.3.41>

E-mail addresses:

tehfardilla@uitm.edu.my (Teh Faradilla Abdul Rahman)

norshitaivi@ukm.edu.my (Norshita Mat Nayan)

*Corresponding author

alcohol intake. Mental health treatment through mobile therapy has the potential to help individuals with mental health problems. Suggested future directions for research community includes comparison between two or three types of text messaging platforms used in interventions to identify which platform is the most suitable to improve a particular mental health problem.

Keywords: Delivery of health care, mental health, mobile therapy, psychotherapy, text messaging platform

INTRODUCTION

Mental health is an important aspect that needs to be effectively taken care of in every human's life. There are many types of mental disorders as classified in the International Classification of Diseases-11 (ICD-11) by World Health Organization (WHO, 2019a; WHO, 2019b). Various mental health problems have been identified with the number of cases statistically increasing worldwide and has long been a global crisis. It can lead to other problems such as the inability to carry out daily routine and suicide, which considered as a major disruption in one's daily life.

In 2015, 4.2 million Malaysians were diagnosed with mental health problems (Ministry of Health Malaysia, 2016). This number increased in 2018 with a total of 5.5 million individuals. National Health Morbidity Survey (NHMS) in 2011 showed the percentage of Malaysians suffering from depression was 1.8% (Ministry of Health Malaysia, 2017). The NHMS survey conducted in 2015 on adults (aged 16 and over) and children (ages 5 - 15) found 29.2% of adults and 12.1% of children with depression.

According to the National Anti-Drug Agency (2019), statistics showed there was a significant increase in drug abuse in Malaysia from 2014 to 2016 but decreased in 2017 and 2018 while repeat offenders' cases were reported to have reduced significantly since 2014 to 2018. Nevertheless, these issues need to be curbed in order to avoid the side effects that will have an impact on the mental health of the abuser. Alcohol and substance abuse have been found contributed to the increase of risk in mental health problems such as depression, schizophrenia, bipolar, suicide, paranoia, depression, delusion, and other mental health problems (Mental Health Foundation, 2006; Darvishi et al., 2015; Diraditsile & Rasesigo, 2018; National Institute on Drug Abuse, 2020).

In India, the local community had a constraint to access mental health medical facilities due to the location they lived in was a huge distance away from town where the mental health clinic was located (Alghamdi, 2019). To overcome this, various ways of text messaging therapy have been implemented using computerised approaches. Text messaging therapy for mental health treatments is a method that uses text-based communication in consulting someone with mental health problems via online chat, SMS, mobile apps and other web-based applications. Delivering mental health treatment through these platforms

allow information to be transmitted to patients simultaneously and automatically. It comes with the aim to reduce the symptoms and increase the quality level of one's mental health. This type of health therapy has no time limit, it is available as long as it is needed by anyone with mental health problem. It is worth to note that the text messaging therapy method has been proven to benefit patients in depression management (Senanayake et al., 2019). It is also an acceptable and useful alternative to face-to-face therapy when depressed patients are comfortable with the approach, feel safe to express their feelings in text and trust the existence of an anonymity relationship between patient and therapists (Dwyer et al., 2021). Other than that, text messaging was found as an effective means of communicating the content of treatment to young patients while allowing them to control as well as to protect their privacy and confidentiality (Anstiss & Davies, 2015). In addition, it can save cost by reducing staff turnover (Jiménez-Molina et al., 2019), convenient treatment time and better delivery than traditional methods (Stevens et al., 2019).

Statistics show 92% of adolescents have mobile phones, 79% of them have smartphones, 90% of them use text messaging systems and 98% were active on social media (Aschbrenner et al., 2019). This is an important finding which shows that text messaging systems have a great potential to be used in mental health therapy. Since text messages can be stored in the phone, recipients can read their text over and over again, use video and audio activities for mind therapy as well as monitor their own performance during therapy besides interacting with other patients (Boettcher et al., 2018). It was found in a study, 36 of the 44 participants still kept therapy text messages in their phones for daily reference (García et al., 2019). In addition, there are text messages that attach website addresses or phone numbers to help patients who seek help.

The potential of text messaging as psychological treatments has been proven to be effective to reduce symptoms of mental health problems, easy to reach patients and cost effective. However, the types of platforms frequently used by researchers to treat targeted mental health problems still need to be considered. A previous review did not include types of text messaging platform, instead it focused on the effectiveness of text messaging intervention and concluded text messaging can be used for three different purposes; therapeutic, motivation and supportive (Senanayake et al., 2019). Similar to this, another two reviews added either content of the messages and frequency of the messages as the subgroup analysis variables (Cox & Allida, 2020), or design features, conditions addressed and characteristics of messaging procedure (Berrouiguet et al., 2016) but did not include the type of text messaging platforms as the variable in the reviews. A systematic review (Rathbone & Prescott, 2017) showed evidence of usability, efficacy and effectiveness of SMS and mobile apps as the physical and mental health interventions. However, because only these two types of text messaging platforms were analysed on digital interventions, this review could not draw broader conclusions about the implementation of other types of

text messaging platforms. Different types of text messaging platforms come with different functionalities, purposes and cost. While patients in developed countries and low-income countries might have personal concerns on the technology's usage such as cost, privacy, and accessibility, it is important to identify which type of text messaging platform is suitable for the target user. Thus, there is a need to examine from the text messaging platforms used in the interventions to the effectiveness of each platform in different kinds of mental health problems. The main objective of this article is to examine studies in using text messaging platforms in any forms of intervention, it also highlighted the types of mental health problems involved and the impact of text messaging on mental health. Therefore, this article provides a scoping review of scientific research on text messaging interventions regardless of which platform it used. This study is part of the research on the suitable text messaging types to treat different kinds of mental health problems in the community. The computing readings focusses on text messaging technologies used to deliver the treatment, whereas the mental health readings emphasize on the types of mental health problems mostly treated using technologies and the intervention effectiveness in the psychological field. To the best authors' knowledge, there is less evidence of reviews to represent an overall picture of text messaging platforms used in treating different mental health problems. Hence, this paper is to fill this gap by conducting a scoping review. The research question is that what are the text messaging platforms used in mental health computerised-based therapy? This review has two specific contributions; first, it identifies from past research the different types of text messaging platform used in mental health digital interventions. Second, it focuses and provides clear understanding on which text messaging platform has a positive effect on a particular mental health problem. It is hoped that the findings will give guidelines to other researchers in the psychological field and technologists in the computing field to work together from identification of the suitable text messaging platform for a specific mental health problem to implementation.

METHODS

Data Sources and Search Strategies

Articles' search was done using several databases namely Scopus, ACM Digital Library, IEEE Xplore and Web of Science. The search strategies covered a combination of mental health terms and text messages, which was implemented from October 2019 to February 2020. More advanced keywords were used such as mhealth, WhatsApp, SMS, chat and mobile text messaging. Then, keywords were replaced with other types of mental health problems including depression and anxiety. Each keyword was combined using the logical operators "AND" and "OR". The combination of the terms "text messaging" and "mobile applications" was among the most commonly combined terms with various types of mental health problems in the search. Article search did not consider specific findings of

study as its objective was to obtain as much research information as possible that affect various aspects such as emotion, counselling and frequency of therapy sessions. The list of keywords used in the search is shown in Table 1. The final stage of the search strategy involved doing an abstract reading to filter out irrelevant articles. In addition, the title and abstract filtration process for each article was repeated several times to ensure no similar articles was included in the list. After the potential articles were identified, further reading was made by focusing on the methodology and findings of the study within the scopes of (i) text messaging platforms, (ii) types of mental health problem involved and (iii) the impact of text messaging on mental health. Articles that did not meet the selection criteria were removed from the reading list.

Assessment Risk of Bias

All studies included in this review were assessed for risk of biasness using Cochraen Risk of Bias Tool (Higgins et al, 2020). This review includes assessments on random sequence generation, allocation concealment, blinding, incomplete outcome data, selective reporting, and any other potential sources of bias. The assessment was conducted by one of the authors using the judgement of low, high, or unclear risk.

Table 1

List of selected articles and search terms used

ID	Author	Year	Keywords	Database
S1	Agyapong et al.	2017	text messaging for depression text messaging improves depression	Scopus
S2	Xu et al.	2019	text messaging improves depression	Scopus Web of Science PubMed
S3	Arean et al.	2016	mobile apps and depression	Scopus
S4	Kodama et al.	2016	text messaging impact on mental health	Scopus
S5	Almeida et al.	2018	mhealth SMS and depression	Scopus
S6	Aguilera et al.	2017	text messaging improves mental health	Scopus
S7	Christensen et al.	2013	Web based intervention on depression Mobile therapy intervention depression anxiety mental health	Scopus

Table 1 (Continued)

ID	Author	Year	Keywords	Database
S8	Islam et al.	2019	text messaging for depression text messaging improves depression	Scopus Web of Science PubMed
S9	Kraft et al.	2017	text messages improves depression	Scopus
S10	Menezes et al.	2019	mobile apps and depression	PubMed
S11	García et al.	2019	Text messaging intervention and mental health	Scopus
S12	Shingleton et al.	2016	Motivational text messages on mental health	Web of Science
S13	Anstiss and Davies	2015	text messaging on anxiety OR depression	Web of Science
S14	Bock et al.	2016	text messaging intervention on substance abuse	Web of Science
S15	Zhang et al.	2019	Mobile apps and mental health	PubMed
S16	Agyapong et al.	2018	Text messaging intervention and mental health	Scopus Web of Science
S17	Wolf et al.	2016	Mobile messaging intervention and depression	Web of Science
S18	Renfrew et al.	2020	SMS messaging intervention and mental health	PubMed

Selection Criteria

The selection was done on articles published from 2013 to 2020. The seven-year interval was chosen to obtain better and more mature research findings. Articles to be included in the reading list should meet the criteria of the main search keywords, including various types of mental health problems and types of text messaging platforms. The effects of using text messages on any types of mental health problems were considered. Table 2 explains on the article selection criteria.

Exclusion Criteria

Articles will be excluded from the reading list if they (i) used other than English or Malay languages, (ii) communication through telephone calls, video calls or face-to-face interactions, (iii) did not state the effects of text message treatment, or type of protocol or

treatment prototype, (iv) did not specify the types of text messaging platform used or (v) missed the types of mental health problems treated.

RESULTS AND DISCUSSIONS

A total of 3656 articles were recorded based on keywords included in the database search. All of these papers were displayed based on any categories that met the related keywords: Scopus (n = 1765), PubMed (n = 471), ACM Digital Library (n = 461), IEEE Xplore (n = 556) and Web of Science (n = 403). Only 213 articles were downloaded due to other articles were found came from the same source. Articles published in language other than English or Malay were removed, while all abstracts were read and evaluated for subsequent selection (n = 211). Again, similar articles were removed, leaving a balance of n = 202. Articles in the form of study protocols, suggestions for prototype applications and literature readings were excluded from the reading (n = 8). The remaining articles received for full reading (n = 194) were filtered again to ensure that they met the selection characteristics. Meanwhile, a total of 176 articles did not specify the types of intervention, platform, text message and its effects on any mental health problem. The final number of remaining articles (n = 18) was included in the discussion of this study. Figure 1 shows the flow chart of the study selection process.

Table 2

Article selection criteria and description

Selection	Description
Type of Study	Study on the types of text messaging platforms and their impact on mental illness.
Type of Participant	Study on mental illness patients, degree of seriousness of their illness and participant selection method.
Type of Intervention	Interventions that compare mental health before and after treatment using a text messaging platform.
These involve either one or several groups.	The study needs to clarify the method of treatment delivery.
Comparison	pre and post study within a group or compare one or more intervention groups with one control group.
Findings	Contains an explanation on the effectiveness of the text messaging platform used on any types of mental illness.
Others	Message treatment is text-based, delivered through any platforms such as SMS, mobile applications or websites. The text is in various forms such as reminders, motivations, support and others that may arise from previous studies.

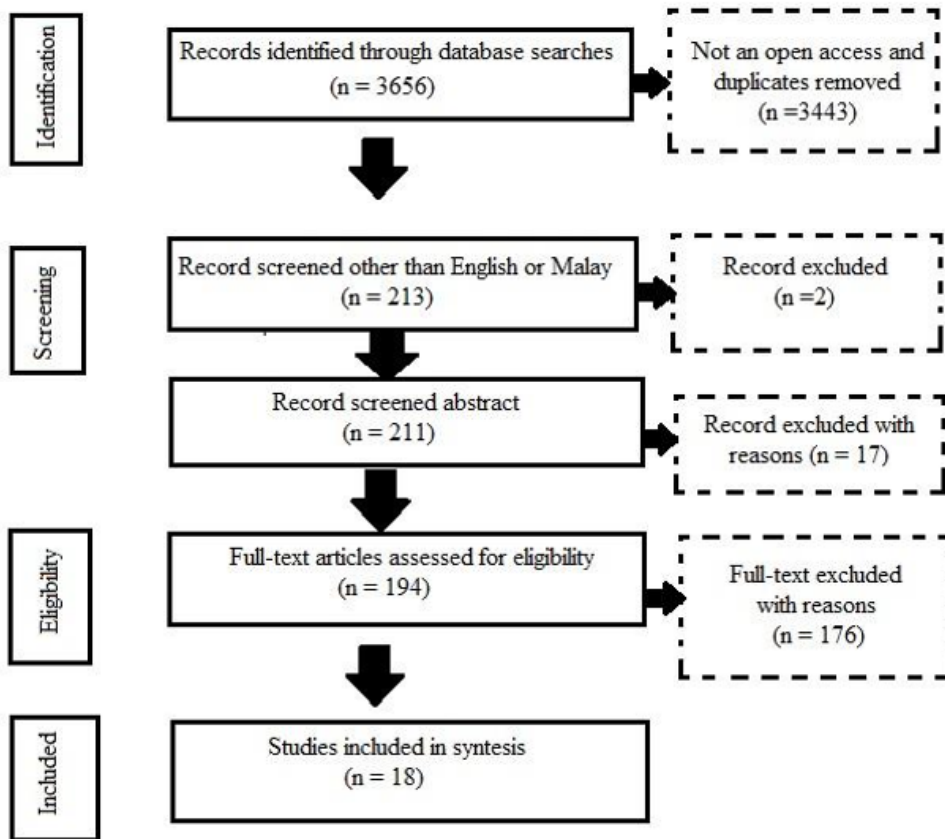


Figure 1. Flow of paper selection through phases of review

Interventions and Comparators

The selected articles came from various research information background including location, population, sample, participants age, intervention group size and intervention length. In summary, five studies were conducted in United States (Arean et al., 2016; Shingleton et al., 2016; Aguilera et al., 2017; Bock et al., 2016; Zhang et al., 2019), three in Australia (Christensen et al., 2013; Islam et al., 2019; Renfrew et al., 2020), two studies in Canada (Agyapong et al., 2017; Agyapong et al., 2018), Germany (Kraft et al., 2017; Wolf et al., 2016) and New Zealand (Anstiss & Davies, 2015; Renfrew et al., 2020) with the remaining of one study in China (Xu et al., 2019), Japan (Kodama et al., 2016), Portugal (Almeida et al., 2018), Brazil and Peru (Menezes et al., 2019) as well as Spain (Garcia et al., 2019). The intervention group target varies in some research where Spanish-speaking Latinos was focused in a study by Aguilera et al. (2017) and a specific gender group (women) by Garcia et al. (2019).

The intervention group size used in all 18 articles are ranged from 12 to 33 people. There was one study did not mention the participants' age (Almeida et al., 2018). The participants' age 18 to 35 years old categorized as young adults were found used in six studies (Agyapong et al., 2017; Areal et al., 2016; Shingleton et al., 2016; Anstiss & Davies, 2015; Bock et al., 2016), ten studies focused on middle-aged adult 36 to 55 years old (Xu et al., 2019; Kodama et al., 2016; Aguilera et al., 2017; Christensen et al., 2013; Kraft et al., 2017; Garcia et al., 2019; Zhang et al., 2019; Agyapong et al., 2018; Wolf et al., 2016; Renfrew et al., 2020), one study stated mean age of participants was 58 years old (Islam et al., 2019) whereas Menezes et al. (2019) used a sample participants with age ranged from 41 to 60 and above. The intervention period also varied between studies where most of the articles ($n = 6$) mentioned a period of 3 months to complete the intervention (Areal et al., 2016; Aguilera et al., 2017; Agyapong et al., 2017; Shingleton et al., 2016; Bock et al., 2016; Agyapong et al., 2018), other studies conducted within 6 weeks (Almeida et al., 2018; Menezes et al., 2019), 10 weeks (Anstiss & Davies, 2015; Renfrew et al., 2020) and 4 months (Kraft et al., 2017; Wolf et al., 2016), whereas some studies lasted for 8 week (Zhang et al., 2019) and 6 months (Xu et al., 2019; Kodama et al., 2016; Christensen et al., 2013; Islam et al., 2019). The shortest period of intervention was conducted within 30 days (Garcia et al., 2019).

Assessment Risk of Bias

Among 18 retrieved studies, there was differences in terms of random sequence generation, allocation concealment, blinding, incomplete outcome data, selective reporting, and other potential sources of biasness (Appendix A).

From all the articles selected, the differences and similarities between the results of the study were analysed based on the types of text messaging platform, types of mental health problems treated and the effects of using text messaging on mental health. The summary for the selection of articles from each database is shown in Table 3.

Types of Text Messaging Platform and Mental Health

Based on the results of selected articles shown in Table 4, there were four major platforms used in the process of providing therapeutic treatment to patients with mental health problems. Twelve studies were found using basic phones to send short text messages such as SMS to treat depression and mood disorders (Islam et al., 2019; Almeida et al., 2018; Aguilera et al., 2017; García et al., 2019; Anstiss & Davies, 2015; Wolf et al., 2016; Zhang et al., 2019), train mind awareness (Kraft et al., 2017; Wolf et al., 2016), anorexia and bulimia (Shingleton et al., 2016), schizophrenia (Xu et al., 2019) and alcohol abuse (Bock et al., 2016; Agyapong et al., 2018). Of all the studies, six of them (Areal et al., 2016; Agyapong et al., 2017; Kodama et al., 2016; Menezes et al., 2019; Zhang et al.,

2019; Renfrew et al., 2020) utilised mobile text application platform as a text therapy medium for patients with depression, anxiety, mood disorders, suicidal intention, self-injury, schizophrenia, schizotypal, mental disorders and delusions. Meanwhile, findings revealed that three studies used websites to treat depression or suicide symptoms (Christensen et al., 2013; Renfrew et al., 2020; Zhang et al., 2019) and one study (Almeida et al., 2018) used online conversation method (chat) to treat depression and mood disorders.

Table 3
Article screening of four databases

Database	Scopus	PubMed	ACM Digital Library	IEEE Xplore	Web of Science
Identified	1765	471	461	556	403
Downloaded	114	15	22	28	34
English or Malay	112	15	22	28	34
Redundant articles removed	111	12	21	27	31
After excluded articles in the form of study protocols, suggestions for prototype applications and literature readings.	106	11	21	27	29
Did not specify the types of intervention, platform, text message and its effects on any mental illness	96	8	21	27	24
Total selected articles	10	3	0	0	5

Table 4
Results summary of selected articles

Article ID	Author	Text messaging platform	Mental health problem	Intervention effects
S1	Agyapong et al.	Mobile Applications	Depression, anxiety, mood	Positive change
S2	Xu et al.	SMS	Mood, schizophrenia	Positive change

Table 4 (Continued)

Article ID	Author	Text messaging platform	Mental health problem	Intervention effects
S3	Arean et al.	Mobile Applications	Depression, mood	Positive effects on emotions, no positive effects on depression
S4	Kodama et al.	Mobile Applications	Mood, suicide, schizophrenia, self-harm	Positive change
S5	Almeida et al.	SMS, Chat	Depression	Positive change
S6	Aguilera et al.	SMS	Depression, mood	Positive change
S7	Christensen et al.	Websites	Anxiety, suicide	Positive change
S8	Islam et al.	SMS	Depression	Positive change
S9	Kraft et al.	SMS	Depression	Positive change
S10	Menezes et al.	Mobile Applications	Depression, suicide	Positive change
S11	Garcia et al.	SMS	Depression, anxiety	Positive change
S12	Shingleton et al.	SMS	Eating disorder	Positive change
S13	Anstiss and Davie	SMS	Depression, anxiety	Positive change
S14	Bock et al.	SMS	Alcohol abuse	Positive change
S15	Zhang et al.	SMS, Mobile Applications, Websites	Depression, anxiety	Positive change
S16	Agyapong et al.	SMS	Alcohol abuse	Positive change
S17	Wolf et al.	SMS	Depression	Positive change
S18	Renfrew et al.	Mobile Applications, Websites	Depression, anxiety	Positive change

As shown in Table 5, depression was the highest ($n = 12$) to be the variable measured (Aguilera et al., 2017; Agyapong et al., 2017; Almeida et al., 2018; Anstiss & Davies, 2015; Arean et al., 2016; Islam et al., 2019; García et al., 2019; Kraft et al., 2017; Menezes et al., 2019; Renfrew et al., 2020; Wolf et al., 2016; Zhang et al., 2019). Six studies conducted their studies on the treatment for anxiety (Agyapong et al., 2017; Anstiss & Davies, 2015; Christensen et al., 2013; García et al., 2019; Renfrew et al., 2020; Zhang et al., 2019). Whereas the number of studies that dealt with mood change was half of the total depression

studies (n = 5) (Aguilera et al., 2017; Agyapong et al., 2017; Arean et al., 2016; Kodama et al., 2016; Xu et al., 2019). Three studies focused on the effects of treatment on suicide aspect (Christensen et al., 2013; Kodama et al., 2016; Menezes et al., 2019). Two studies were conducted on Schizophrenia (Kodama et al., 2016; Xu et al., 2019), while Bock et al. (2016) and Agyapong et al. (2018) focused on patients with alcohol abuse (n = 2). One study examined the effects of treatment on the potential to self-harm (Kodama et al., 2016) and one on mindfulness (Kodama et al., 2016). Only Shingleton et al. (2016) recorded the effects of treatment on anorexia and bulimia.

Table 5

Types of mental disorders identified in each article

Mental Disorder	Frequency	Article ID
Depression	12	S1, S3, S5, S6, S8, S9, S10, S11, S13, S15, S17, S18
Anxiety	6	S1, S7, S11, S13, S15, S18
Mood	5	S1, S2, S3, S4, S6
Suicide	3	S4, S7, S10
Alcohol abuse	2	S14, S16
Schizophrenia	2	S2, S4
Self-harm	1	S4
Eating disorder	1	S12

The Effectiveness of Text Messaging Therapy

Overall, most mental health therapies have been delivered via SMS followed by mobile applications and websites. Although different types of text messaging platforms were used to deliver treatment to different types of mental health problems within each research intervention's unique time range, it is difficult to tell which text messaging platform is the most effective. For example, Xu et al. (2019) used SMS text based to delivery motivational messages and medication reminders to the patients had shown improvements in the aspect of medication adherence. Aguilera et al. (2017) showed a great improvement at 13 weeks of the study where the intervention group stayed at the treatment session longer than the control group. Other studies also have shown a significant improvement in the intervention group that used SMS text messaging to treat depression (Islam et al., 2019; García et al., 2019; Kraft et al., 2017; Anstiss & Davies, 2015; Wolf et al., 2016; Zhang et al., 2019). In addition, two studies also reported improvements in alcohol intervention groups (Agyapong et al., 2018; Bock et al., 2016). However, results from a study show negative correlation between psychiatrists and patients communication, this might be due to low number sample

size ($n = 15$) in the study (Almeida et al., 2018). These shows that each intervention has its own unique elements to consider before delivering the treatment. The elements could be the participants' mental health background, accessibility to text messaging, participants' commitment and treatment goal.

Nonetheless, it is undeniable that SMS and mobile applications delivery method are more efficient in reaching the patients because SMS and mobile application platforms use a push method where the therapy text is delivered to patients on a regular basis and without the effort and motivation of the participants. This is in contrast to the characteristics of the website where patients had to have high discipline and initiative to browse the web for therapy. As such, the mobile app was seen as a great and convenient choice to be used as it can be downloaded by smartphone users worldwide, without having to subscribe to phone line services such as SMS. Patients who are unable to access to urban health services, lack of time or not confidence in accessing treatment can contact mental health professionals from several countries through this smart application (Teles et al., 2019).

Depression was the most commonly found case throughout the reading process which was carried out. Patients have used various platforms, forms of text and presentations for their treatment. Anxiety falls in the second most studied, followed by mood disorders including depression. This finding is in line with the statistics provided by WHO (2019a; 2019b), which revealed 264 million people from the global population who suffered from depression while in 2017, 3.67% of the world's population suffered from anxiety, which exceeded the percentage of depression (3.44%). Statistics from a report Mental Health Foundation (2016) showed that anxiety (5.9%) was at the first place while depression (3.3%) was ranked at the second place in mental health status in the United Kingdom. Whereas in America, anxiety problem was ranked first (19.1%), personality problems in second (9.1%) and depression in third (6.7%) (National Institute of Mental Health, 2017). In Malaysia, referring to the records of patients being discharged from hospitals, depression was ranked second (12.7%) while anxiety was in the fifth place (Ministry of Health Malaysia, 2017). This raised a question of whether or not the patients in this category still need treatment since their number was not as high as schizophrenia patients, which was ranked first (37.5%). Abusive use of substances such as medicines, drugs and alcohol were also serious in Malaysia (8.3%; third place), America (drugs 8% - 12%, alcohol 19%, drugs 65.7%) (American Heart Association, 2019). Besides, the rate of substance abuse had also increased in the United Kingdom.

STUDY LIMITATIONS

According to Cronin et al. (2008), the literature search is generally done within the last five to ten years depending on the amount of information found. In the scoping review of this study, the article search process was limited to within the years of 2013 to 2020 as

it is considered the most up-to-date findings from previous studies to ensure satisfactory findings. Originally, the article search started in 2015, but not many studies have met the required breakdown of information. However, articles published prior to 2013 have been used to support the findings of other studies. Additionally, article selection in this study was done excluding open access and paid articles. This causes some articles related to the scope of this review not to be included in the discussions and some useful information could not be included in the findings.

FUTURE DIRECTIONS

Recent studies have shown that communication technology is very helpful in treating mental health problems. However, rural people have limited access to the use of this technology. Suggested future directions for the research community include available Internet of Things technologies and the accessibility of rural areas to digital therapy. Compared to today's communication development, mobile applications are the major focus of consumers as they facilitate much of the day-to-day business. Therefore, the development of therapeutic applications in smartphone for mental health problems is important as it is easy to reach, able to go across the globe and minimize the constrain in relationship between patients and nurses.

Most of the studies were found using the comparison method of achievement of intervention group (with one type of platform) and control group. Examining the effectiveness of a type of platform for a particular type of mental health problem is also important, given the characteristics differences of digital technology, user accessibility and mental health problem. The diversity of the interventions, research contexts, and digital platforms analysed in this study suggest that comparison between groups using two or three types of text messaging platforms is needed to identify which platform is the most suitable to improve a particular mental health problem.

CONCLUSION

In this era of technology, everyone owns at least a basic cell phone with a majority owning a smartphone. Previous studies have shown that all patients know how to use a cell phone. Although some may not be familiar with the therapeutic application, it is not difficult for them to learn the functionalities of the application. Mobile applications have the potential to treat mood disorders including depression and anxiety (Arean et al., 2016). In order to use this method consistently in self-treatment, initiatives for the development of better delivery methods need to be investigated. Various delivery methods in terms of frequency of text delivery, delivery time and textual content need to be continuously studied to achieve the objectives of therapy and not to burden the patients. Future therapeutic applications need to focused more on the mental health problems suffered by most of the world's

population such as depression, anxiety, substance abuse, schizophrenia and bipolar so that the therapeutic applications can be used more widely and help many people regardless of boundaries and distances. Mental health therapy through the mobile application, SMS and web-based therapy have also been found to be beneficial not only to the individual with mental health problems as a user, but also to family members or close friends as the monitors in the therapy session.

ACKNOWLEDGEMENT

The authors would like to thank Ministry of Education and Universiti Kebangsaan Malaysia for funding this work. This work was funded under the Research University Grant (GUP 2019 067).

REFERENCES

- Aguilera, A., Bruehlman-Senecal, E., Demasi, O., & Avila, P. (2017). Automated text messaging as an adjunct to cognitive behavioral therapy for depression: A clinical trial. *Journal of Medical Internet Research*, *19*(5), Article e148. <https://doi.org/10.2196/jmir.6914>
- Agyapong, V. I. O., Juhás, M., Mrklas, K., Hrabok, M., Omeje, J., Gladue, I., Kozak, J., Leslie, M., Chue, P., & Greenshaw, A. J. (2018). Randomized controlled pilot trial of supportive text messaging for alcohol use disorder patients. *Journal of Substance Abuse Treatment*, *94*(August), 74-80. <https://doi.org/10.1016/j.jsat.2018.08.014>
- Agyapong, V. I. O., Juhás, M., Ohinmaa, A., Omeje, J., Mrklas, K., Suen, V. Y. M., Dursun, S. M., & Greenshaw, A. J. (2017). Randomized controlled pilot trial of supportive text messages for patients with depression. *BMC Psychiatry*, *17*(1), 1-10. <https://doi.org/10.1186/s12888-017-1448-2>
- Alghamdi, N. S. (2019). Monitoring mental health using smart devices with text analytical tool. In *2019 6th International Conference on Control, Decision and Information Technologies (CoDIT)* (pp. 2046-2051). IEEE Conference Publication. <https://doi.org/10.1109/CoDIT.2019.8820381>
- Almeida, A. M. P., Almeida, H. S., & Figueiredo-Braga, M. (2018). Mobile solutions in depression: Enhancing communication with patients using an SMS-based intervention. *Procedia Computer Science*, *138*(January), 89-96. <https://doi.org/10.1016/j.procs.2018.10.013>
- American Heart Association. (2019). *Mental health a workforce crisis*. Retrieved Mar 9, 2020, from <https://ceoroundtable.heart.org/mentalhealth/>
- Anstiss, D., & Davies, A. (2015). "Reach out, rise up": The efficacy of text messaging in an intervention package for anxiety and depression severity in young people. *Children and Youth Services Review*, *58*, 99-103. <https://doi.org/10.1016/j.childyouth.2015.09.011>
- Arean, P. A., Hallgren, K. A., Jordan, J. T., Gazzaley, A., Atkins, D. C., Heagerty, P. J., & Anguera, J. A. (2016). The use and effectiveness of mobile apps for depression: Results from a fully remote clinical trial. *Journal of Medical Internet Research*, *18*(12), Article e330. <https://doi.org/10.2196/jmir.6482>

- Aschbrenner, K. A., Naslund, J. A., Tomlinson, E. F., Kinney, A., Pratt, S. I., & Brunette, M. F. (2019). Adolescents' use of digital technologies and preferences for mobile health coaching in public mental health settings. *Frontiers in Public Health, 7*, 1-9. <https://doi.org/10.3389/fpubh.2019.00178>
- Berrouiguet, S., Baca-García, E., Brandt, S., Walter, M., & Courtet, P. (2016). Fundamentals for future mobile-health (mHealth): a systematic review of mobile phone and web-based text messaging in mental health. *Journal of medical Internet research, 18*(6), Article e135. <https://doi.org/10.2196/jmir.5066>
- Bock, B. C., Barnett, N. P., Thind, H., Rosen, R., Walaska, K., Traficante, R., Foster, R., Deutsch, C., Fava, J. L., & Scott-Sheldon, L. A. J. (2016). A text message intervention for alcohol risk reduction among community college students: TMAP. *Addictive Behaviors, 63*, 107-113. <https://doi.org/10.1016/j.addbeh.2016.07.012>
- Boettcher, J., Magnusson, K., Marklund, A., Berglund, E., Blomdahl, R., Braun, U., Delin, L., Lundén, C., Sjöblom, K., Sommer, D., von Weber, K., Andersson, G., & Carlbring, P. (2018). Adding a smartphone app to internet-based self-help for social anxiety: A randomized controlled trial. *Computers in Human Behavior, 87*, 98-108. <https://doi.org/10.1016/j.chb.2018.04.052>
- Christensen, H., Farrer, L., Batterham, P. J., Mackinnon, A., Griffiths, K. M., & Donker, T. (2013). The effect of a web-based depression intervention on suicide ideation: Secondary outcome from a randomised controlled trial in a helpline. *BMJ Open, 3*(6), 1-9.
- Cox, K. L., & Allida, S. M. (2020). Text messages to reduce depressive symptoms: Do they work and what makes them effective? A systematic review. *Health Education Journal, 80*(3), 253-271. <https://doi.org/10.1177/0017896920959368>
- Cronin, P., Ryan, F., & Coughlan, M. (2008). Undertaking a literature review: A step-by-step approach. *British Journal of Nursing, 17*(1), 38-43. <https://doi.org/10.12968/bjon.2008.17.1.28059>
- Darvishi, N., Farhadi, M., Haghtalab, T., & Poorolajal, J. (2015). Alcohol-related risk of suicidal ideation, suicide attempt, and completed suicide: A meta-analysis. *PLoS ONE, 10*(5), 1-14. <https://doi.org/10.1371/journal.pone.0126870>
- Diraditsile, K., & Rasesigo, K. (2018). Substance abuse and mental health effects among the youth in Botswana: Implications for social research. *Journal of Education, Society and Behavioural Science, 24*(2), 1-11. <https://doi.org/10.9734/jesbs/2018/38304>
- Dwyer, A., de Almeida Neto, A., Estival, D., Li, W., Lam-Cassettari, C., & Antoniou, M. (2021). Suitability of text-based communications for the delivery of psychological therapeutic services to rural and remote communities: Scoping review. *JMIR mental health, 8*(2), Article e19478. <https://doi.org/10.2196/19478>
- García, Y., Ferrás, C., Rocha, Á., & Aguilera, A. (2019). Exploratory study of psychosocial therapies with text messages to mobile phones in groups of vulnerable immigrant women. *Journal of Medical Systems, 43*(8), 1-9. <https://doi.org/10.1007/s10916-019-1393-3>
- Higgins, J. P. T., Savović, J., Page, M. J., Elbers, R. G., & Sterne, J. A. C. (2020). Chapter 8: Assessing risk of bias in a randomized trial. In J. P. T. Higgins, J. Thomas, J. Chandler, M. Cumpston, T. Li, M. J. Page & V. A. Welch (Eds.), *Cochrane handbook for systematic reviews of interventions version 6.1* (pp. 205-228). John Wiley & Sons Inc.
- Islam, S. M. S., Chow, C. K., Redfern, J., Kok, C., Rådholm, K., Stepien, S., Rodgers, A., & Hackett, M. L. (2019). Effect of text messaging on depression in patients with coronary heart disease: A substudy

- analysis from the TEXT ME randomised controlled trial. *BMJ Open*, 9(2), 1-7. <https://doi.org/10.1136/bmjopen-2018-022637>
- Jiménez-Molina, Á., Franco, P., Martínez, V., Martínez, P., Rojas, G., & Araya, R. (2019). Internet-based interventions for the prevention and treatment of mental disorders in Latin America: A scoping review. *Frontiers in Psychiatry*, 10(September), Article 664. <https://doi.org/10.3389/fpsy.2019.00664>
- Kodama, T., Syouji, H., Takaki, S., Fujimoto, H., Ishikawa, S., Fukutake, M., Taira, M., & Hashimoto, T. (2016). Text messaging for psychiatric outpatients. *Journal of Psychosocial Nursing and Mental Health Services*, 54(4), 31-37.
- Kraft, S., Wolf, M., Klein, T., Becker, T., Bauer, S., & Puschner, B. (2017). Text message feedback to support mindfulness practice in people with depressive symptoms: A pilot randomized controlled trial. *JMIR mHealth and uHealth*, 5(5), Article e59. <https://doi.org/10.2196/mhealth.7095>
- Menezes, P., Quayle, J., Claro, H. G., Da Silva, S., Brandt, L. R., Diez-Canseco, F., Miranda, J. J., Price, L. S. N., Mohr, D. C., & Araya, R. (2019). Use of a mobile phone app to treat depression comorbid with hypertension or diabetes: A pilot study in Brazil and Peru. *Journal of Medical Internet Research*, 21(4), 1-12. <https://doi.org/10.2196/11698>
- Mental Health Foundation. (2006). *Cheers? Understanding the relationship between alcohol and mental health*. Mental Health Foundation. Retrieved August 7, 2020, from https://www.drugsandalcohol.ie/15771/1/cheers_report%5B1%5D.pdf
- Mental Health Foundation. (2016). *Fundamental facts about mental health 2016*. Mental Health Foundation, London. Retrieved February 4, 2021, from <https://www.mentalhealth.org.uk/sites/default/files/fundamental-facts-about-mental-health-2016.pdf>
- Ministry of Health Malaysia. (2016). *Press releases mental health problems in Malaysia*. Retrieved March 21, 2020, from https://www.moh.gov.my/moh/modules_resources/english/database_stores/96/337_451.pdf
- Ministry of Health Malaysia. (2017). *Malaysian mental healthcare performance technical report 2016*. Malaysian Healthcare Performance Unit: National Institute of Health. Retrieved July 14, 2020, from <https://www.moh.gov.my/moh/resources/Penerbitan/Laporan/Uмум/Mental%20Healthcare%20Performance%20Report%202016.pdf>
- National Anti-Drug Agency. (2019). *Drugs statistics and report*. Retrieved October 18, 2020, from <https://www.adk.gov.my/en/public/drugs-statistics/>.
- National Institute on Drug Abuse. (2020). *Mental health effects*. Retrieved July 6, 2020, from <https://www.drugabuse.gov/drug-topics/health-consequences-drugmisuse/mental-health-effects>
- National Institute of Mental Health. (2017). *Mental health information statistics*. Retrieved December 12, 2021, from <https://www.nimh.nih.gov/health/statistics/index.shtml>
- Rathbone, A. L., & Prescott, J. (2017). The use of mobile apps and SMS messaging as physical and mental health interventions: Systematic review. *Journal of Medical Internet Research*, 19(8), 1-13. <https://doi.org/10.2196/jmir.7740>
- Renfrew, M. E., Morton, D. P., Morton, J. K., Hinze, J. S., Beamish, P. J., Przybylko, G., & Craig, B. A. (2020). A web- And mobile app-based mental health promotion intervention comparing email, short message

- service, and videoconferencing support for a healthy cohort: Randomized comparative study. *Journal of Medical Internet Research*, 22(1), Article e15592. <https://doi.org/10.2196/15592>
- Senanayake, B., Wickramasinghe, S. I., Chatfield, M. D., Hansen, J., Edirippulige, S., & Smith, A. C. (2019). Effectiveness of text messaging interventions for the management of depression: A systematic review and meta-analysis. *Journal of Telemedicine and Telecare*, 25(9), 513-523. <https://doi.org/10.1177/1357633X19875852>
- Shingleton, R. M., Pratt, E. M., Gorman, B., Barlow, D. H., Palfai, T. P., & Thompson-Brenner, H. (2016). Motivational text message intervention for eating disorders: A single-case alternating treatment design using ecological momentary assessment. *Behavior Therapy*, 47(3), 325-338. <https://doi.org/10.1016/j.beth.2016.01.005>
- Stevens, G. J., Hammond, T. E., Brownhill, S., Anand, M., De La Riva, A., Hawkins, J., Chapman, T., Baldacchino, R., Micallef, J. A., Andepalli, J., Kotak, A., Gunja, N., Page, A., Gould, G., Ryan, C. J., Whyte, I. M., Carter, G. L., & Jones, A. (2019). SMS SOS: A randomized controlled trial to reduce self-harm and suicide attempts using SMS text messaging. *BMC Psychiatry*, 19(1), 4-10. <https://doi.org/10.1186/s12888-019-2104-9>
- Teles, A., Rodrigues, I., Viana, D., Silva, F., Coutinho, L., Endler, M., & Rabelo, R. (2019). Mobile mental health: A review of applications for depression assistance. In *2019 IEEE 32nd International Symposium on Computer-Based Medical Systems (CBMS)* (pp. 708-713). IEEE Conference Publication. <https://doi.org/10.1109/CBMS.2019.00143>
- Wolf, M., Kraft, S., Tschauener, K., Bauer, S., Becker, T., & Puschner, B. (2016). User activity in a mobile phone intervention to assist mindfulness exercises in people with depressive symptoms. *Mental Health and Prevention*, 4(2), 57-62. <https://doi.org/10.1016/j.mhp.2016.02.003>
- World Health Organization. (2019). *ICD-11 for mortality and morbidity statistics*. Retrieved June 16, 2020, from <https://icd.who.int/browse11/l-m/en>
- World Health Organization. (2019). *Mental disorders*. Retrieved January 10, 2020, from <https://www.who.int/news-room/fact-sheets/detail/mental-disorders>
- Xu, D., Xiao, S., He, H., Caine, E. D., Gloyd, S., Simoni, J., Hughes, J. P., Nie, J., Lin, M., He, W., Yuan, Y., & Gong, W. (2019). Lay health supporters aided by mobile text messaging to improve adherence, symptoms, and functioning among people with schizophrenia in a resource-poor community in rural China (LEAN): A randomized controlled trial. *PLoS Medicine*, 16(4), 1-21. <https://doi.org/10.1371/journal.pmed.1002785>
- Zhang, R., Nicholas, J., Knapp, A. A., Graham, A. K., Gray, E., Kwasny, M. J., Reddy, M., & Mohr, D. C. (2019). Clinically meaningful use of mental health apps and its effects on depression: Mixed methods study. *Journal of Medical Internet Research*, 21(12), Article e15644. <https://doi.org/10.2196/15644>

Appendix A

Table Summary of Assessment Risk of Bias

Article ID	Author	Random sequence generation	Allocation concealment	Blinding	Incomplete Outcome Data	Selective reporting	Other biases
S1	Agyapong et al.	Low risk “single-rater-blinded randomized trial involving 73 patients with Major Depressive Disorder.”	Low risk “the intervention group (n = 35) and the control group (n = 38), recruited from four community mental health clinics.”	High risk Participant in intervention group know they need to give feedback based on the treatment received. Assessors were blinded.	Low risk Two participants from each group withdrew. The size is similar, 31 and 32.	Low risk Mentioned protocol used. “The trial is registered with clinicaltrials.gov (NCT02327858).” All outcomes were reported.	Low risk None
S2	Xu et al.	Low risk “2-arm randomized controlled trial.”	Low risk “278 community-dwelling villagers (patient participants) were randomly selected from people with schizophrenia from 9 townships of Hunan, China, and were randomized 1:1 into 2 groups.”	High risk Participant in intervention group know they need to give feedback based on the treatment received. Assessors were blinded.	Low risk “2 participants in the intervention group and 1 in the control group died.” “120 intervention, 117 control. Only small number of missing data.”	Low risk Mentioned protocol used. “Chinese Clinical Trial Registry (ChiCTR-ICR-15006053).” All outcomes were reported.	Low risk None

S3	Areean et al.	Low risk	Low risk	High risk	High risk	Low risk	High risk
		Participants were randomly assigned to interventions group using a random number generator.	“Participants were recruited through Web-based advertisements and social media.”	Participant in intervention group know they need to give feedback based on the treatment received. “Because all assessment was conducted using assessment software, procedures for blinding research assistants was not necessary.”	More than half of the participants enrolled in intervention groups did not download the apps. The number of participants left is not balance in each intervention group.	All pre-specified and expected outcomes of interest are clear and reported. “Clinicaltrials.gov NCT00540865”	High risk Paid study. “Participants were paid US \$20.00 for completing assessments at the 4-, 8-, and 12-week marks.”
S4	Kodama et al.	High risk	Unclear	High risk	Low risk	Low risk	High risk
		Non-random	“Participants were recruited from a university hospital, a psychiatric hospital in Hyogo Prefecture, three medical center hospitals in Kobe City, a private psychiatric hospital, and three psychiatric clinics in Kobe City, Japan (population approximately 1.5 million)”	Participant in intervention group know they need to give feedback based on the treatment received.	High follow-up rate (>96%). “All participants received all text messages, and no one refused receipt of messages. One participant did not complete the questionnaire at 3 months and another at 6 months into the intervention.”	“The study protocol was approved by the Kobe University Research Ethics Committee, Kobe City Medical Center Hospitals and Hyogo Prefectural Psychiatric Hospital.” All outcomes were reported.	High risk First study of its kind. “This is the first study that promotes psychiatric outpatients’ help-seeking and reduction of self-harm using text messaging.”

S5	Almeida et al.	Unclear Not reported the choice of patients and health professionals	Unclear Allocation method was not reported	High risk patients and health professionals know they need to give feedback based on the treatment received.	Low risk All participants completed the study.	High risk Protocol was clearly stated but insufficient. “The study was approved by the Ethical Committee of the Hospital of Magalhães de Lemos, Porto, Portugal.” All outcomes were reported.	Low risk None
S6	Aguilera et al.	High risk nonrandomized design	Unclear Allocation method was not reported. “48 were allocated to the texting condition and 43 were allocated to control group.”	High risk “Neither the therapists and patients nor research assistants were blinded since they participated in the delivery of treatment and data collection.”	Low risk Number of participants in each group is acceptable, did not influence the outcomes. “39 active texting patients in the texting condition, and 40 in the control.”	Low risk Low risk “All procedures and materials were approved by the University of California, San Francisco Institutional Review Board Committee.” All outcomes were reported.	Low risk None

S7	Christensen et al.	Low risk randomised	Low risk "Participants were 155 callers to Lifeline, Australia's 24 h telephone counselling service" "Allocation of participants to trial conditions was conducted independently by a research assistant not involved in the day-to-day running of the trial."	High risk Participant in intervention group know they need to give feedback based on the treatment received.	Low risk "Although there were small effects at post-test and medium effect sizes at follow-up among the intervention conditions, there were no consistent overall effects for conditions."	Low risk All pre-specified and expected outcomes of interest are clear and reported. "Study protocol was approved by the Australian National University Human Research Ethics Committee (Protocol no. 2007/12)." All outcomes were reported.	High risk First of its kind "This was the first study to examine the effect of online interventions on suicide ideation in a helpline using an RCT design."
S8	Islam et al.	Low risk	Low risk "The random allocation sequence was in a uniform 1:1 allocation ratio with a block size of 8 and was concealed from study personnel."	High risk Participant in intervention group know they need to give feedback based on the treatment received.	High risk Imbalance no. of participants in each group after exclusion of missing data. n = 333 in intervention group, n = 350 in control group	Low risk All pre-specified and expected outcomes of interest are clear and reported. "Ethics approval from Western Sydney Local Health Network Human Research Ethics Committee." All outcomes were reported.	Low risk None

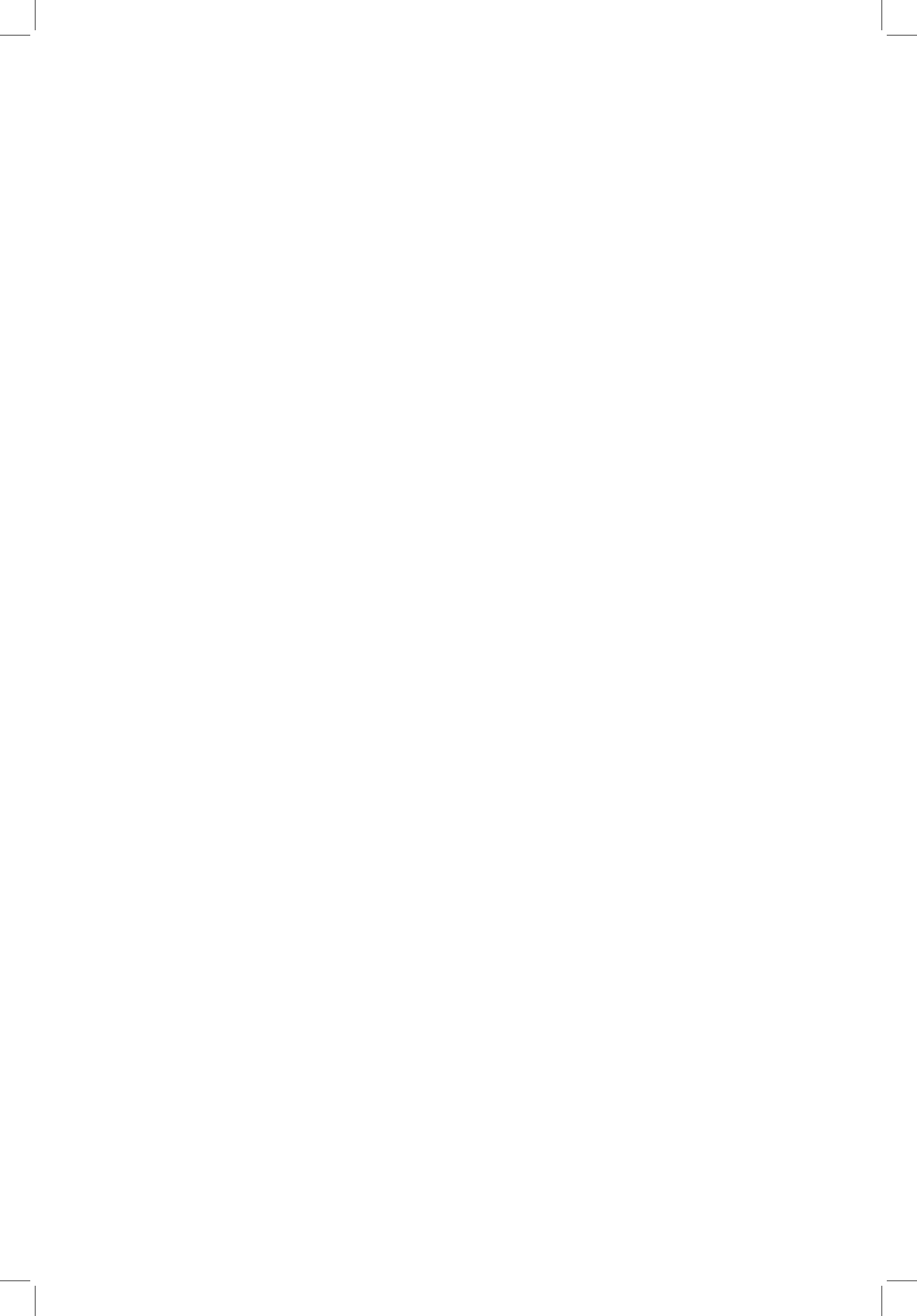
S9	Kraft et al.	Low risk Two-arm randomized clinical trial	Low risk computer-generated random numbers.	High risk Participant in intervention group know they need to give feedback based on the treatment received.	Low risk n = 18 completed intervention while n = 17 completed control	Low risk “The study was approved by Ulm University’s Ethics Committee.” All outcomes were reported.	High risk Paid study “All participants received €25 after returning the follow-up questionnaire. Additionally, participants in the intervention group received €10 at hospital discharge to cover their costs for sending text messages.”
S10	Menezes et al.	Low risk randomized controlled trial	Unclear Allocation method was not reported. All three groups were for intervention.	High risk Participant in intervention group know they need to give feedback based on the treatment received.	High risk Small sample size. n = 17 Sao Paolo, n = 16 Lima 1, n = 16 Lima 2.	Low risk “Approved by local Institutional Review Boards and the US National Institute of Mental Health Data and Safety Monitoring Board.” All outcomes were reported.	High risk Most participants were female. No controlled group to compare with intervention outcomes.

	High risk	High risk	High risk	High risk	Low risk	Low risk
S11	Garcia et al. non-random	High risk Participants were given options to choose which group to join. "All women were contacted and asked to freely choose between the intervention and the control group."	High risk Participant in intervention group know they need to give feedback based on the treatment received.	High risk Imbalance no. of participants between both groups. "the intervention group included a face-to-face therapy session and text messages (n = 46); and the non-equivalent control group included a face-to-face therapy session but no text messages (n = 29)."	Low risk Protocol Number: 2017-12-10597. All outcomes were reported.	None
S12	Shingleton et al. Randomized clinical trial	High risk Allocation method was not mentioned. "Participants were recruited via community and online postings and clinician referrals. Eligible participants were screened through phone and in-person."	High risk Participant in intervention group know they need to give feedback based on the treatment received.	Unclear Small sample size but said to be plausible for this design. "Missing data were not imputed because GEE uses maximum likelihood estimation; therefore, there is little or no need for imputation."	Low risk "All study procedures were conducted at the CARD Eating Disorder Program and were approved by the Boston University Institutional Review Board" All outcomes were reported.	High risk Paid study "They were compensated \$100 for participating in the study and received a \$50 bonus if their compliance rate with the nightly questionnaire and food logs were above 80%."

S13	Anstiss and Davies	<p>Low risk</p> <p>Randomly assigned to intervention and controlled group.</p>	<p>High risk</p> <p>Allocation method was not mentioned.</p>	<p>High risk</p> <p>Participant in intervention group know they need to give feedback based on the treatment received.</p>	<p>High risk</p> <p>Small sample size with high dropout, 7 from intervention group, 11 from controlled group.</p> <p>“Twelve (63%) of the 19 participants who received support from a trained supporter completed the text package and evaluation. Nine (45%) of the 20 participants who did not receive support from a trained supporter, also completed the text package and evaluation.”</p>	<p>Low risk</p> <p>“Ethical Review for the study was sought from the New Zealand Northern X Region Ethics Committee prior to study commencement”</p> <p>All outcomes were reported.</p>	<p>Low risk</p> <p>None</p>
S14	Bock et al.	<p>Low risk</p> <p>two-arm randomized trial</p>	<p>Low risk</p> <p>“Randomization was stratified by gender and by frequent heavy drinking status, which was defined as three or more heavy drinking episodes in the past two weeks.”</p>	<p>High risk</p> <p>Participant in intervention group know they need to give feedback based on the treatment received.</p>	<p>Low risk</p> <p>High engagement and follow up rate.</p> <p>“Overall 93.3% (n = 56) of participants completed the six-week assessment and 88.3% (n=53) completed the final follow-up assessment.”</p>	<p>Low risk</p> <p>All pre-specified and expected outcomes of interest are clear and reported.</p> <p>All outcomes were reported.</p>	<p>High risk</p> <p>Paid study</p> <p>“Participants who completed the surveys received \$30.00 for each time point.”</p>

		Unclear	High risk	Low risk	Low risk	Low risk	High risk
S15	Zhang et al.	Low risk Randomized Allocation method was not mentioned. “participants were recruited between July 2016 and May 2017 via social and print media advertising, research registries, and commercial recruitment firms.”	High risk Participant in intervention group know they need to give feedback based on the treatment received.	Low risk 10 out of 301 participants discontinued the treatment but this number did not influenced the results.	Low risk Protocol under Clinicaltrials.gov NCT02801877 and approved by North western University Institutional Review Board. All outcomes were reported.	Low risk	High risk Most participants were female.
S16	Agyapong et al.	Low risk Randomized “randomized using a series of random numbers generated using Microsoft Excel.”	High risk Participant in intervention group know they need to give feedback based on the treatment received.	Low risk Balance no. of dropouts between both groups. “Participants with missing follow-up data were balanced between the two groups (8 in the text message group and 8 in the control group).”	Low risk “The study protocol was approved by the Research Ethics Board of the University of Alberta and published.” All outcomes were reported.	Low risk	None

S17	Wolf et al.	<p>Low risk</p> <p>Randomized</p>	<p>Low risk</p> <p>computer-generated random numbers.</p> <p>“Recruitment took place at University’s Clinic for Psychiatry Psychotherapy and Psychosomatics in Günzburg, Germany, which is a large psychiatric hospital in rural Bavaria.”</p>	<p>High risk</p> <p>Participant in intervention group know they need to give feedback based on the treatment received.</p>	<p>Unclear</p> <p>Outcomes were reported. However, the actual no. of participants completed the intervention were not stated clearly.</p>	<p>Low risk</p> <p>All outcomes were reported.</p>	<p>Low risk</p> <p>None</p>
S18	Renfrew et al.	<p>Low risk</p> <p>Randomized</p>	<p>Low risk</p> <p>using computer-generating software.</p> <p>“Participants were randomized by a person not on the research team using computer random number generation.”</p>	<p>High risk</p> <p>Participant in intervention group know they need to give feedback based on the treatment received.</p>	<p>Unclear</p> <p>High number of dropouts at 12 weeks of the study. Imbalance no. of participants between one group and the other two intervention groups.</p>	<p>Low risk</p> <p>Low risk</p> <p>All pre-specified and expected outcomes of interest are clear and reported.</p>	<p>Low risk</p> <p>None</p> <p>“Ethics approval was granted from the Avondale Human Research Ethics Committee (Approval No. 2018.09).”</p> <p>All outcomes were reported.</p>



Review article

A Comprehensive Review of Automated Essay Scoring (AES) Research and Development

Chun Then Lim^{1*}, Chih How Bong¹, Wee Sian Wong¹ and Nung Kion Lee²

¹Faculty of Computer Science & Information Technology, Universiti Malaysia Sarawak, 94300 Kota Samarahan, Sarawak, Malaysia

²Faculty of Cognitive Sciences & Human Development, Universiti Malaysia Sarawak, 94300 Kota Samarahan, Sarawak, Malaysia

ABSTRACT

Automated Essay Scoring (AES) is a service or software that can predictively grade essay based on a pre-trained computational model. It has gained a lot of research interest in educational institutions as it expedites the process and reduces the effort of human raters in grading the essays as close to humans' decisions. Despite the strong appeal, its implementation varies widely according to researchers' preferences. This critical review examines various AES development milestones specifically on different methodologies and attributes used in deriving essay scores. To generalize existing AES systems according to their constructs, we attempted to fit all of them into three frameworks which are content similarity, machine learning and hybrid. In addition, we presented and compared various common evaluation metrics in measuring the efficiency of AES and proposed Quadratic Weighted Kappa (QWK) as standard evaluation metric since it corrects the agreement purely by chance when estimate the degree of agreement between two raters. In conclusion, the paper proposes hybrid framework standard as the potential upcoming AES framework as it capable to aggregate both style and content to predict essay grades Thus, the main objective

of this study is to discuss various critical issues pertaining to the current development of AES which yielded our recommendations on the future AES development.

ARTICLE INFO

Article history:

Received: 20 January 2021

Accepted: 24 May 2021

Published: 31 July 2021

DOI: <https://doi.org/10.47836/pjst.29.3.27>

E-mail addresses:

limchunthen95@gmail.com (Chun Then Lim)

chbong@unimas.my (Chih How Bong)

weesian.wong@gmail.com (Wee Sian Wong)

nklee@unimas.my (Nung Kion Lee)

* Corresponding author

Keywords: Attributes, automatic essay scoring, evaluation metrics, framework, human raters, recommendation

INTRODUCTION

The introduction of automated grading essays is an innovative attempt to reduce the effort of examining essays and eliminate assessment biases and its discrepancies. Automated Essay Scoring (AES) appears as a standalone computer software or distributed services that evaluates and scores a written prose (Shermis & Burstein, 2003). The objective of AES is to overcome the time, cost, and reliability issues in manual assessment of essays. It should be made clear that AES is not intended to fully replace the human assessors but to be employed as part of low-stakes classroom assessments to assist teachers' essay marking routine. On the other hand, it can be adopted in large-scale high-stakes assessments for the purpose of increasing reliability, where the AES serves as an additional rater for cross-examination.

AES aims at developing models that can grade essays automatically or with reduced involvement of human raters. It is a Natural Language Processing (NLP) based method and application of assessing educational works especially on writing tasks. AES systems may rely not only on grammars, but also on more complex features such as semantics, discourse, and pragmatics. Thus, a prominent approach to AES is to learn scoring models from previously graded samples, by modelling the scoring process of human raters. When given the same set of essays to evaluate and enough graded samples, AES systems tend to achieve high agreement levels with trained human raters. There are three common AES frameworks: Content Similarity Framework (CSF) which assigns grades or scores to new essays based on closer similarity of the reference essays' scores, Machine Learning Framework (MLF) which treats AES as classification or regression task and classifies the new essays into correspond grade category by using machine learning algorithms, and Hybrid Framework which combines the characteristics of both frameworks.

In a general AES process, the collected essays usually stored as text or Microsoft Word format. Hence, first step is to convert the group of collected essays into Microsoft Excel or json format which contains the content and grade for each essay. The essay content will then undergo pre-processing step such as tokenization, stop word removal, stemming and lemmatization to remove noise. After that, there will be a major difference in different frameworks. In cosine similarity framework, the pre-processed essay content will undergo word representation step which convert the essay into vector form and compared their similarity with gold standard's grade. For machine learning framework, pre-processed essay content will undergo feature selection, useful features will be extracted and act as input data for predict model. Then, suitable machine learning algorithms will be used to train the predict model to classify new essays into corresponding grades. The performance of AES system is then evaluated with measurement metric. The most common evaluation metric is using accuracy of to show the proportion of true results against the total number of predicted grades examined.

Project Essay Grade® (PEG) proposed by Ellis in 1966, is one of the earliest AES systems. The project determines the quality of the essay by focusing on essay writing style (Page, 2003; Rudner & Gagne, 2001). Subsequently, Intelligent Essay Assessor™ (IEA) by Pearson (2010) introduced an AES which could consider the essay's semantic context. In addition, e-rater®, from Educational Testing Service (ETS) is another revolutionary grading tool that uses computational methods to make sense of human natural language by the means of tagging, chunking, and other labels, based on a collection of learner's actual language uses. To date, My Assess, from IntelliMetric® model, is probably the pioneer essay scoring tools solely based on Artificial Intelligence (AI), which with is modelled by 45 computers on human intelligence (Shermis & Burstein, 2003).

Over the course of 40 years, we have started noticing that the trend of AES development and many commercial applications are pretty much emerged in the Western continents, especially in the United States. However, in recent years, there were many literatures on AES reported in Asia: Malaysia, Thailand, Philippine, and Indonesian covering mainly the English language as well as other languages.

To understand how AES has grown to its current state to meet the need in different regions and to anticipate its future development, a detailed survey on AES is essential. Thus, the purpose of this paper is to determine the recent progress of AES and generalize frameworks accordingly. Moreover, this paper lays a spectrum of the development frameworks for the reader by discussing the findings presented in recent research papers.

BACKGROUND

In this section, we provide an overview of AES systems that have achieved great success in commercialization and attracted greater publicity. These systems are mainly proprietary software developed in Western countries. For each product, we will present its vendor/developer, primary focus, essay feature, scoring mechanism, and number of training samples required.

Project Essay Grader® (PEG)

Ellis Page's Project Essay Grader (PEG) is considered as the first AES (Page, 1966). It focuses on evaluating essays based on its writing style by using *trins* and *proxes*. PEG assumes that there exist intrinsic qualities in a person's writing style known as *trins*, which can be measured or correlated with observable components denoted as *proxes* (Rudner & Gagne, 2001). For example, the fluency of an essay (*trin*) can be correlated with the amount of vocabulary (*proxe*). With training set of 100 to 400, PEG facilitates statistical regression analysis to estimate essay scores. To date, PEG has developed more than 500 *trins* to be used to score essays (Measurement Incorporated, 2020).

Intelligent Essay Assessor™ (IEA)

Intelligent Essay Assessor (IEA) is introduced by Pearson Knowledge Technologies (PKT) to assess the quality of essay contents (Foltz et al., 1999; Pearson, 2010)). IEA scores essay by using the Latent Semantic Analysis (LSA), which is a computational distribution model to assess the semantics similarity of texts (Landauer et al., 1998). LSA is operated on domain-specific corpus and the essays are represented through the multidimensional semantic space of the meaning of their contained words and the similarity is derived by comparing with other essay semantic representation (Foltz et al., 1999). IEA differed from other AESs on the aspects that the scores derived from LSA are aligned closely to human graders (Landauer et al., 2020), compared to the scores which are derived by correlation of essay features. In addition, IEA uses NLP techniques to extract essay attributes such as sophistication of lexical uses, grammatical, mechanical, stylistic, and organizational aspects of essays (Zupanc & Bosnic, 2015). Comparing with other ASE, IEA requires only a relatively small number of 100 pre-scored training essays sample for scoring a prompt-specific essay (Dikli, 2006).

IntelliMetric®

Vantage Learning proposed IntelliMetric as a proprietary AES to score essays operationally since 1998 (Vantage Learning, 2020). IntelliMetric is regarded as the very first AES system leveraging on Artificial Intelligence (AI) and Machine Learning (ML) to simulate the scoring process (Dikli, 2006; Hussein et al., 2019). In producing an essay score, IntelliMetric uses more than 400 features (including semantics, syntactics, and discourses), which can be categorized into five groups of IntelliMetric Feature Model: focus and unity (coherence), organization, development and elaboration, sentence structure, mechanics, and conventions in its scoring process. IntelliMetric claims itself of having multiple automated scoring systems at work, each using a different mathematical model (e.g., Linear Analysis, Bayesian and LSA) for essay scoring (Vantage Learning, 2005; Vantage Learning, 2020). Such multiple scoring engine within IntelliMetric emulates the equivalent of a panel of multiple judges for achieving a more accurate final score as compared with a single scoring engine in others. Another distinctive feature of IntelliMetric is its ability in scoring essays in other languages besides English (Elliot, 2003). However, one of the downsides of IntelliMetric is it requires a minimum of at least 300 scored essays to be operated (Zupanc & Bosnic, 2015).

E-rater®

E-rater is developed and used by the Educational Testing Service (ETS) since 1999 (Attali & Burstein, 2006). It relies on patented NLP techniques to extract linguistic features for evaluating the style and content of an essay. E-rater 2.0 makes used of of syntactic,

discourse and topical-analysis module to analyze essay features (Dikli, 2006). The features are grammatical errors, word usage errors, mechanics error, style, organization segments and vocabulary content (Shermis et al, 2010). To date, E-rater version extends the essay scoring features into two areas:

- (i) writing quality: grammar, usage, mechanics, style, organization, development, word choice, average word length, proper prepositions, and collocation usage
- (ii) content or use of prompt-specific vocabulary (Ramineni & Williamson, 2018).

E-rater uses regressing modelling to assign a final score to an essay. In addition, a collection of approximately 250 training essay samples is required for the regression model (Zupanc & Bosnic, 2015).

The comparison of these well-known AES is shown in Table 1.

Table 1
Summary of well-known AES

AES System	Vendor/ Developer	Main Focus	Essay Scoring Mechanism	Essay-Scoring Features	Training Samples Required
PEG	Measurement Incorporated	Style	Statistical	<i>Trins & Proxes</i>	100 - 400
IEA	Pearson Knowledge Technologies	Content	LSA	<ul style="list-style-type: none"> • Content • Style • Mechanics 	100
IntelliMetric	Vantage Learning	Style & Content	AI - cognitive processing, computational linguistics, and classification	<ul style="list-style-type: none"> • Focus & Unity (Coherence) • Organization • Development & Elaboration • Sentence Structure • Mechanics & Conventions 	300
e-rater		Style & Content	Regression Analysis	<ul style="list-style-type: none"> • Grammatical Errors • Word Usage Errors • Mechanics Errors • Style • Organizational Segment • Vocabulary Contents 	250

PAST LITERATURE

In this section, we summarize the development of AES in previous studies and categorized their findings based on the type of attribute, methodology, prediction model and findings (Table 2).

The attribute refers to the aspects evaluated by the proposed models which include style, content, and hybrid. Style attributes focus on linguistic features such as spelling mistakes, essay length and stop word count. Content attributes works to verify the correctness of

Table 2
Summary of AES

Type of Attribute	Methodology	Prediction Model	Measure & Finding	Reference
Style	Natural language processing (Linguistic features)	Nonparametric Weighted Feature Extraction, Stepwise Regression and Discriminant Analysis	Accuracy (51.3%)	(Pai et al., 2017)
		Linear Regression	Close to human rater	(Ramalingam et al., 2018)
		Random Forest	Quadratic Weighted Kappa (0.8014)	(Chen & He, 2013)
Hybrid	Natural language processing (Rhetoric, Organisation, Content)	Bayesian Linear Ridge Regression (BLRR)	Quadratic Weighted Kappa (0.784)	(Phandi et al., 2015)
		Rule-based Expert System	Correlation with rater (0.57)	(Ishioka & Kameda, 2006)
	Vector Space Models (VSM)	Support Vector Regression (SVR)	Average correlation (0.6107)	(Peng et al., 2010)
	Natural language processing (Rhetoric, Organisation, Content and Length)	Rule-based Expert System	Pearson's correlation coefficient (0.562)	(Imaki & Ishihara, 2013)
	Latent Semantic Analysis, number of words, number of spelling mistakes, and word distance.	Linear Regression	Correlation with rater (0.78) Accuracy (96.72%)	(Alghamdi, et al., 2014)
	Latent semantic features	Support Vector Machine for Ranking	Pearson Corelation (0.7248)	(Jin & He, 2015)
	Latent Semantic Analysis, Rhetorical Structure Theory (RST) and hand-crafted features	Rule-based Expert System	Accuracy (78.33%)	(Al-Jouie & Azmi, 2017)
	Latent Semantic Analysis and Feature extraction	Linear Regression	Accuracy (47.16%)	(Contreras et al., 2018)
Content	Latent Semantic Analysis	Artificial Neural Network (ANN)	Mean of error (0.44)	(Loraksa & Peachavanish, 2007)
		Cosine similarity	Accuracy for small class (69.80 % – 94.64 %) Accuracy for medium class (77.18 % - 98.42 %)	(Ratna et al., 2007)

Table 2 (continue)

Type of Attribute	Methodology	Prediction Model	Measure & Finding	Reference
			Accuracy (83.3%)	(Amalia et al., 2019)
		Learning Vector Quantization	Accuracy (96.3%)	(Ratna et al., 2018)
	Topic classified by SVM and assessed by LSA	Frobenius norm	Average accuracy for Japanese (89.175%);	(Ratna et al., 2019a)
			Accuracy for Bahasa Indonesia (72.01%)	(Ratna et al., 2019b)
	GLSA	Cosine similarity	Precision, Recall and F1 scores (0.98)	(Islam & Hoque, 2013)
	Latent Semantic Analysis, Disco2, Damera-levenshtein and N-gram	Similarity degree	Correlation with rater (0.82)	(Shehab et al., 2018)
	Latent Semantic Analysis and Winnowing algorithm	Cosine similarity	Accuracy for LSA (87.78%); Accuracy for Winnowing (86.72%)	(Ratna et al., 2019c)
	Latent Semantic Analysis with multi-level keywords	Compared document vector	Human raters' agreement (86%)	(Ratna et al., 2015)
	Modified LSA and syntactic features	Cosine similarity	RMSE (0.268)	(Omar & Mezher, 2016)
	Enhanced Latent Semantic Analysis	Cosine similarity	Gap with rater (0.242)	(Sendra et al., 2016)
	Latent Semantic Analysis, Probabilistic Latent Semantic Analysis	Cosine similarity	Spearman correlation (0.78)	(Kakkonen et al., 2005)
	Arabic WordNet (AWN)	Cosine similarity	Pearson Corelation (98%)	(Awaida et al., 2019)
	Concept Indexing	Cosine similarity	Exact Agreement Accuracy (0.452)	(Ong et al., 2011)
	Contextualized Latent Semantic Indexing	Support Vector Machine (SVM)	Rating Agreement (89.67)	(Xu et al., 2017)
	Statistic (One-hot encoding)	Convolutional Neural Network (CNN), Long Short-Term Memory (LSTM), Bi-directional Long Short-Term Memory (BiLSTM)	Quadratic Weighted Kappa for LSTM + CNN (0.761)	(Taghipour & Ng, 2016)
	Statistic (Word embedding)	Convolutional Neural Network (CNN)	Average kappa value (0.734)	(Dong & Zhang, 2016)

Table 2 (continue)

Type of Attribute	Methodology	Prediction Model	Measure & Finding	Reference
		CNN and Ordinal Regression (OR)	Accuracy (82.6%)	(Chen & Zhou, 2019)
		Siamese Bidirectional Long Short-Term Memory Architecture (SBLSTMA)	Average Quadratic Weighted Kappa (0.801)	(Liang et al., 2018)
	Statistic (Training word vector)	2-Layer Neural Networks	Quadratic Weighted Kappa (0.9448)	(Nguyen & Dery, 2016)
	Hierarchical Recurrent Neural Network	CNN, LSTM, BiLSTM	Average Quadratic Weighted Kappa (0.773)	(Chen & Li, 2018)
	Natural language processing (Unigram Language Model)	Machine Learning Classifier	Mean accuracy (51.5%)	(Wong & Bong, 2019)
	Natural language processing (Word features, syntactic features, and dependency relation features)	Logistic Regression and k-Nearest Neighbors	Correlation with the rater (0.92)	(Cheon et al., 2015)

content meaning and similarity between an essay with the graded essays. Hybrid attribute facilitating both style and content.

Methodology refers to the methods used to identify the features from the essays. The prediction model records the techniques or algorithms used to predict the score or grade of the essay.

From Table 2, we can see that different researchers have developed their own methodology and used different prediction models. This has proliferated the development of AES because each methodology and prediction model does not seem to be universally accessible to other researchers. Hence, a standard framework of AES needs to be proposed so that all researchers can use, modify, and enhance it in the future. Moreover, the evaluation metric of AES also needs to be standardized so that the performance of AES system can be compared with one and another. Lastly, most of the articles did not described in details of their dataset used in research and therefore other researchers cannot reproduce the same result as they stated in their article.

THE GENERAL FRAMEWORKS OF AES

Despite the increasing number of literature reporting novel approaches for AES implementation, we can summarize them into three major general frameworks: content similarity, machine learning and hybrid.

Content Similarity Framework

The idea of content similarity framework (CSF) is to assign grades or scores to new essays based on closer similarity of the reference essays' scores. The framework requires a gold standard: a collection of human graded reference essays, covering all spectrum of grades or scores on the respective topics. The workflow of content similarity framework is illustrated in Figure 1.

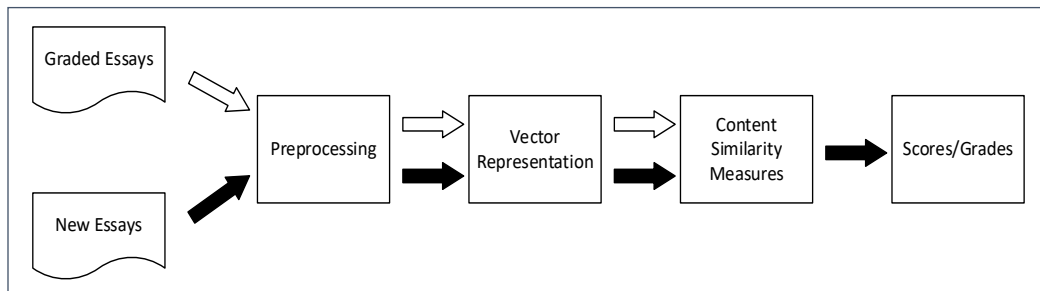


Figure 1. The workflow of a content similarity framework

In this framework, selected essays firstly undergo pre-processing step, which includes tokenization, stop words removal, stemming and lemmatization to reduce the noise in essays. The subject of similarity can be based on (a) syntactic or, (b) semantics indicators, or a combination of both.

(a) Syntactic Indicators. Syntactic indicators refer to the essays' surface features such as part-of-speech, stemmed words, word connectors, and word count. Whereas the semantics indicators refer to the meaning of word, phrase, sentence, and text. It is commonly regarded that the semantics indicators are used to justify the whole or partial essays' semantics similarity (Islam & Hoque, 2013; Omar & Mezher, 2016; Sendra et al., 2016; Landauer et al., 2000; Ghosh & Fatima, 2008). The common syntactic indicators used in AES are spelling checking, stemming, lemmatization, word segmentation (Loraksa & Peachavanish, 2007), n-gram (Islam & Hoque, 2013; Chen & Zhou, 2019; Xu et al., 2017), and normalization (Taghipour & Ng, 2016; Ratna et al., 2019a). These were the essays' surface features, and they are found to be useful in grading essays (Ong et al., 2011). In addition, there were works reported to facilitate external knowledge bases such as WordNet (Omar & Mezher, 2016; Shehab et al., 2018) and ontology (Contreras et al., 2018) to improve grading efficacy.

In addition, the Japanese Scoring System (JESS) demonstrates an example of facilitating syntactic features on essay grades based on three syntactic categories: rhetoric, organization, and contents (Ishioka & Kameda, 2006). These categories are quantified by readability, percentage of long, different words, passive sentences, orderly presentation

idea, and topical vocabularies. The essay score is then derived based on the deduction mechanism of the essay's perfect score. However, the uses of syntax and style alone are not enough to determine the merits of the essay. Thus, JESS used syntactic indicators and semantic indicators in its content analysis.

(b) Semantics Indicators. In recent years, AES solely based on syntactic indicators are getting scarce, as many developments discovered that semantics indicators render more accurate grades or scores. In natural language modelling, a semantic space aims to create representations of the natural language that can represent the context. The most basic semantic space can be tracked back to Vector Space Model (VSM), which was used to derive content similarity based on the co-occurrence word in essays (Al-Jouie & Azmi, 2017).

One of the most popular syntactic-blind semantics indicators is Latent Semantic Analysis (LSA), which excels at deriving content analysis (Landauer et al., 1998). LSA is a distributional model used to derive meaning from a text. LSA was deemed "... a theory and method for extracting and representing the contextual-usage meaning of words by statistical computations applied to a large corpus of text". With LSA, essays are represented as a term-document matrix, which in turn is approximately reduced using singular value decomposition (SVD). The dimension reduction process in LSA is to induce the probable similarity of every word to every other if they are ever occurred in in other essays at a common context. Experiment results showed that the addition of LSA over syntactic features improves the scoring performance of AES (Omar & Mezher, 2016). Many contents similarity-based AES used LSA or any of its variations in deriving grades or scores (Awaida et al., 2019; Amalia et al., 2019; Alghamdi, et al., 2014; Contreras et al., 2018; Ong et al., 2011; Shehab et al., 2018).

On the other hand, Generalized Latent Semantic Analysis (GLSA) is a variant of LSA which considers word sequence and has been reported to be capable of improving the efficacy of AESs (Islam & Hoque, 2013; Sendra et al., 2016). Almost all modern development of AESs reported are composed of both syntactic and semantics features.

The study of essay grading using CSF took two inputs: key answers and student answers (Amalia et al., 2019). Both essay inputs are pre-processed through noise removal, case conversion, tokenization, stopwords removal negation, conversion, stemming, synonym conversion, which are then represented using a term-document matrix where each row corresponded to the term and each column corresponded to the document. Each cell in the matrix represents the occurrence of the term to the documents. A zero value indicate the absence of the term in the documents.

The most common similarity computation is derived through LSA, which is a 2-step process: Singular Vector Decomposition (SVD) and cosine similarity measure. SVD is responsible to decompose the term-document matrix as $D=U\Sigma V^T$. The k largest singular

values (which is dimensionality) is used to approximate D as $D \approx U_k \Sigma_k V_k^T$. Its purpose is to discover “latent” concepts in the matrix. SVD is first applied to the key answers, where each of the student answer is then go through the same pre-processing processes and match it to the most similar key answers using cosine similarity measure to determine the scores. The workflow of essay grading using CSF is illustrated in Figure 2 (Amalia et al., 2019).

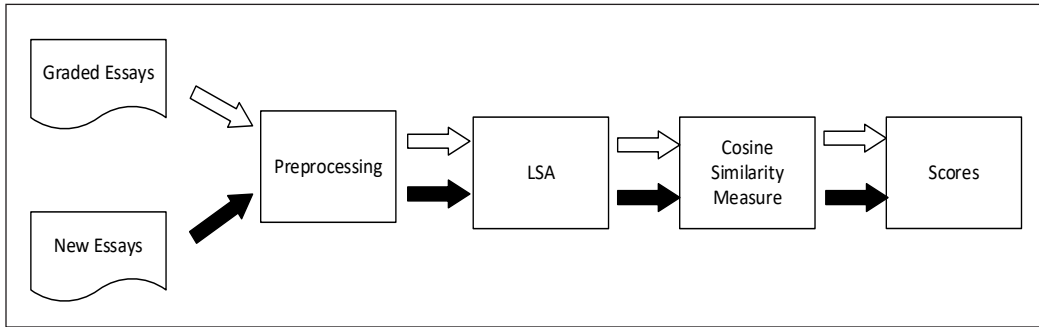


Figure 2. A case of essay grading using CSF (Amalia et al., 2019)

Machine Learning Framework

As shown in Figure 3, in Machine Learning Framework (MLF), essay grading is treated as a multiclass classification problem in which each grade is represented as a class. Modelling requires computational functions to generalize all essays into multi classes. Since AES has been seen as the document classification problem, the machine learning algorithms used are mainly from the categories of regression and classification. The workflow of machine learning framework is illustrated in Figure 3.

Pre-processing is the first process which prepares the data and removes noises. Similar to CSF, all essays will undergo tokenization, stop word removal, stemming and lemmatization processes. Next, the essays are processed to retain significant features in the Feature Selection process. Typical features in MLF were words (Cheon et al., 2015), syntactic and dependency features. Feature selection is an important step in many machine

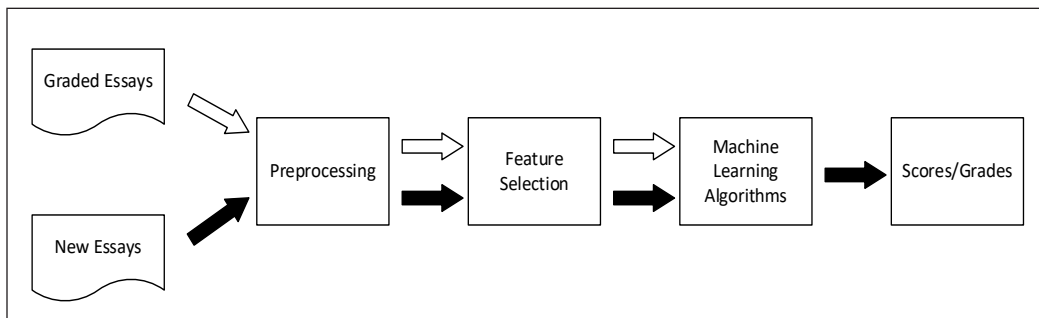


Figure 3. The workflow of a machine learning framework

learning tasks with the purpose to identify a significant feature subspace in reducing redundant features and reducing complex computational space, yielding the optimal essay representation. In this context, feature selection reduced the number of words to prevent the curse of dimensionality that can eventually degrade the accuracy of classification. In general, there are two dimensionality reduction techniques: feature elimination or feature selection. After dimensionality reduction, the selected features will act as inputs to train the machine learning model such as Support Vector Machine (SVM), k-Nearest Neighbors (kNN), Naive Bayes and Artificial Neural Network (ANN).

Like CSF, a machine learning framework requires a gold standard, however, the graded essays are compulsorily to be processed and transformed into a computational model to be used for prediction of grades and scores on new essays. This is one of the significant differences between the CSF and MLF.

The study reported in Taghipour and Ng (2016) adopted MLF to derive essay scores. Both key and student answers are pre-processed with tokenization, case conversion and normalize the essay score in the range of [0,1]. Feature selection is performed through Enhanced AI scoring engine (EASE) is used to derive length-based representation, POS, word overlap with the key answers, and bag of n-gram. The features are then fed into machine learning algorithms such as support vector regression (SVR), Bayesian linear ridge regression (BLRR) and a variant of neural networks to derived student answer scores, resulted marginal increment against the baseline. The workflow of machine learning framework reported in Taghipour and Ng (2016) is illustrated in Figure 4.

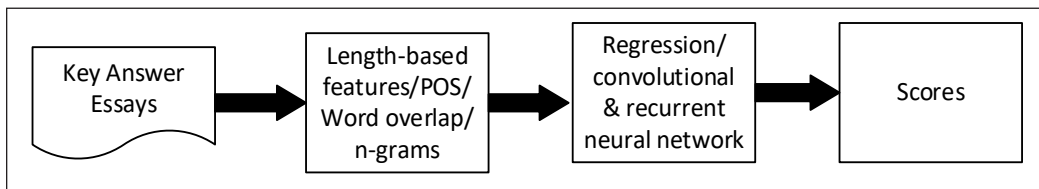


Figure 4. A MLF reported in (Taghipour & Ng, 2016)

Looking at the recent trends in AES, the machine learning framework is gaining popularity in recent years due to the efficacy of SVM (Ratna et al., 2019b; Ratna, et al., 2019a; Xu et al., 2017; Awaida et al., 2019; Chen & Li, 2018) and the ability to represent text context with word embedding (Liang et al., 2018; Taghipour & Ng, 2016) propelled by Artificial Neural Network (ANN) (Loraksa & Peachavanish, 2007; Taghipour & Ng, 2016; Dong & Zhang, 2016; Liang et al., 2018).

Hybrid Framework

The emerging hybrid framework (HF) combines both the goodness of content similarity and machine learning framework in which it capable of aggregating both style and content

to derive essay grades or scores. Different from the general MLF, where machine learning algorithms are directly used to derive the grades or score, the machine learning algorithms in the framework is used to generalize syntactic features (indices, topics, and domain specific keywords) where CSF is used to retrieve the closest key answer score in the semantic space. The process pipeline of hybrid framework is similar with the ML framework except both machine learning algorithms and content similarity measure are used to derive essay scores or grades. Figure 5 illustrates a general workflow of the hybrid framework.

The emerging of recent studies incorporating the hybrid framework have been seen the combining the use of linear regression on selected features, derived from an ontology and using LSA to measure content similarity (Contreras et al., 2018), generalizing essay scores through vectorization with artificial neural network and LSA (Loraksa & Peachavanish, 2007) and twostep process classification with SVM and LSA Framework (Ratna et al., 2019a; Ratna, et al., 2019b)

The studies reported in Ratna et al. (2019c) used two-step grading process as the HF: used Support Vector Machine (SVM) to classify essay’s topic and LSA to compute the similarity between student and key answers. A pre-trained SVM model on key answers’ topics is meant to rule out unrelated topic essays and to route it to the related key answers

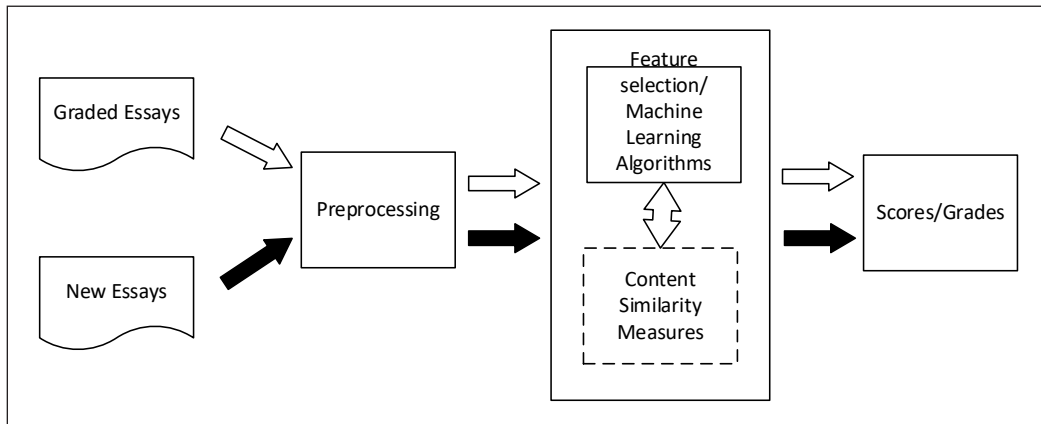


Figure 5. The workflow of a hybrid framework

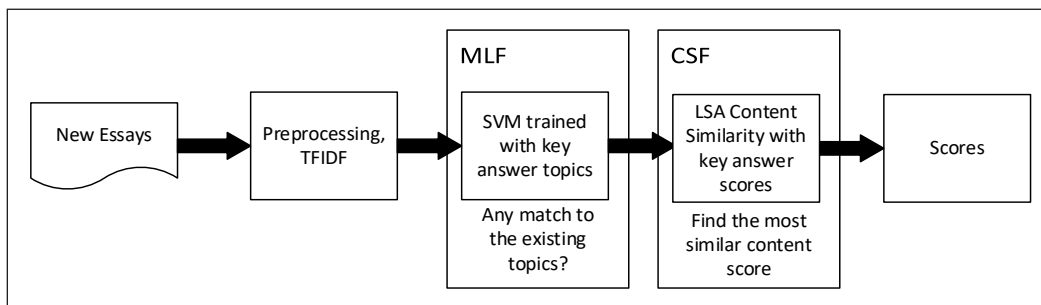


Figure 6. A Hybrid framework reported in (Ratna et al., 2019c)

essay. The LSA is intended to build a semantic space for key answer essays, where each of the student essay's score in the range of [0,100] is obtained by finding the most similar key answer score, using Frobenius norm similarity measure. The studies report substantial accuracy (>95%) as compared to human raters. The workflow of hybrid framework reported in Ratna et al. (2019c) is illustrated in Figure 6.

AES EVALUATION METHOD

In this section, we categorized the automated essay scoring evaluation methods from past literature into five categories. All evaluation methods require the human rater to provide a score or a grade for each essay to act as a reference. Then, the evaluation method will compare the human rater's score with the AES model predicted score to examine the accuracy of the proposed model.

Overall Accuracy

This evaluation method compares the average score manually marked by the human rater and scores automatically generated by the proposed model to examine the accuracy. The predicted result is classified into three classes, which are Exact Agreement Accuracy (EAA), Adjacent Agreement Accuracy (AAA) and Overall Accuracy (OA). Exact Agreement Accuracy is the number of essays with human score equal to AES score over the total numbers of essays, as denoted in Equation 1.

$$EAA = \frac{\text{num_human_equal_aes}}{\text{total number of test essays}} \quad [1]$$

The Adjacent Agreement Accuracy is defined as the ratio of the number of test essays with a human score equal to machine score ± 1 over the total number of test essays and is given by the Equation 2.

$$AAA = \frac{\text{num_human_equal_aes} \pm 1}{\text{Total number of test essays}} \quad [2]$$

Overall Accuracy is the sum of EAA and AAA and is defined as the ratio of the number of test essays with a human score equal to AES score ± 1 over the total number of test essays (Equation 3).

$$OA = EAA + AAA \quad [3]$$

This evaluation method is simple and able to evaluate the accuracy of the scoring model intuitively. However, the result can be inaccurate when the dataset contains an imbalance ratio of data.

Root Mean Square Error

Root Mean Square Error (RMSE) is used to examine the similarity between the human rater's score set and system predicted score set. RMSE is calculated by Euclidean distance hence it can use to evaluate real values such as essay score. Therefore, the accuracy of predict model depends on the similarity between the human rater's score and system predicted score based on Euclidean distance (Omar & Mezher, 2016). RMSE can be calculated as Equation 4.

$$RMSE = \sqrt{\frac{\sum_{i=1}^n (HS_i - SS_i)^2}{n}} \quad [4]$$

where HS_i is human rater's score, SS_i is the system predicted score and n is number of essays. The smaller value of RMSE indicates that the predicted score is more similar to human rater's score and therefore achieve a better scoring.

Mean of Error and Standard Deviation of Errors

The mean error and standard deviation of errors are used to examine the difference between the human rater's score, and the system predicted score. This evaluation method requires a state-of-art system as a baseline to examine the performance of proposed system. The mean of error between human rater's score and baseline system predicted score is calculated and compare with the mean of error between human rater's score and proposed system predicted score. The smaller value of mean of error and standard deviation of error represent the system has better performance in essay scoring. The mean of error and standard deviation of error is calculated by using Equation 5 and 6:

$$\bar{x} = \frac{\sum_{i=1}^n x_i}{n} \quad [5]$$

$$SD = \sqrt{\frac{\sum_{i=1}^n (x_i - \bar{x})^2}{n}} \quad [6]$$

\bar{x} is the arithmetic mean from all errors,

x_i is an absolute value of an error between human score and machine score computed by $x_i = |HumanScore_i - MachineScore_i|, i = 1 \dots n$

n is the number of data set

SD is a standard deviation of error

Pearson's correlation coefficient, Cohen's Kappa Coefficient and Quadratic Weighted Kappa (QWK)

Pearson's correlation coefficient, Cohen's Kappa coefficient and QWK scores are used to examine the degree of agreement between the human rater's score, and the system predicted score. The output of these evaluate methods will between 0 and 1 when 1 means that the system predicted score is complete agreement towards human rater's score and 0 means that is random agreement between system predict score and human rater's score. In interpreting any kappa value, K can be considered as poor when lower than 0.4, fair to good when K between 0.4 and 0.75, and excellent when K is greater than 0.75. To interpret Pearson's correlation, r can be considered as very small when r lower than 0.2, small when r between 0.2 and 0.4, medium when r between 0.4 and 0.6, large when r between 0.6 and 0.8, and very large when r greater than 0.8 (Cheon et al., 2015). Theses evaluation methods are suitable for evaluating the multiclass classification model since it calculates a confusion matrix between the predicted and actual values. Usually, these methods require a state-of-art scoring model as a baseline to examine the performance of the proposed model.

Mean of Accuracy

The scoring model is evaluated by obtaining the mean of accuracy of each test date. In achieving this, the difference between human rater's score and system predicted score will be derived. The accuracy for each test data will be calculated by using Equation 7.

$$Accuracy = 100\% - \frac{|Human\ score - System\ score|}{100} * 100 \quad [7]$$

It should be noted that $|Human\ score - System\ score|$ is an absolute value. By using this formula, the smaller the difference between human rater's score and system predicted score, the higher the accuracy of the scoring model. This evaluation method is suitable for evaluate the actual score of essays but not essay grade due to the gap between essay grade is usually small and result in overrated scoring model accuracy.

ISSUES

There Is No One-Size-Fits-All Solution

Most of the existing essay scoring systems reported thus far performed well in grading pure English essays or essays written in pure European language. However, the system graded a 10-15% lower score on essays containing Asian local content (Ghosh & Fatima, 2008). This is due to the influence of local languages and English written by non-native English speakers. For example, Asian students tend to obtain lower scores in TOEFL exams. Besides, Wong and Bong (2019) claim that the direct adoption of contemporary automated

essay scoring system in the Asian context may not be practical as it may lead to the issue of assessment reliability and validity. Reliability means how well an assessment tool can produce stable and consistent results even in different time and place, whereas validity means how good an assessment tool measures what it is supposed to measure.

Existing Automated Essay Scoring Systems Predict Essay Grade Ineffectively under a Prompt-Independent Setting

Essay prompt refers to an essay title or topic which the writer requires to treat as the main content of the essay. From the literature, majority of the essay scoring mechanism rely on rated essays as the gold standard and the performance of the system is highly dependent on these training data (Jin et al., 2018). However, this approach of training is hard to perform especially when the rated essays for a target prompt are difficult to obtain or even inaccessible due to legal, copyright or privacy issues which lead to inefficacy. In addition, essays for different prompts may differ a lot in the uses of vocabulary, structure, and grammatical characteristics. Hence, these models can hardly be generalized and fail to grade them accurately for non-target prompts. This situation is because prompt-dependent models are designed to learn the features from prompt-specific essays.

Effective AES Systems Requires Expert Tuning

A study by Alikaniotis et al. (2016) stated that the predictive features of the automated essay scoring system need to be manually crafted by human experts to achieve satisfactory performance and the process will consume a lot of time and work. The lack of human experts results in a decrease in AES performance and an increase in the AES development time.

The Relationship between Essay's Features and Grade is not Linear

Most of the existing automated essay scoring systems assume linear relationship between the features of the essay and the essay grade. However, the study by Fazal et al. (2011) stated that there exists a non-linear relationship between the feature vector and essay grade. For example, most of the existing automated essay scoring systems treat the length of essay as an important feature and use it to indicate the quality of essay which means the longer the essay, the higher the essay grade. However, in some specific cases, an essay will be assigned with a lower grade even though it is very long because of the irrelevant content in the essay. Moreover, automated essay scoring system will delete unnecessary and non-meaningful words to filter out keywords to evaluate during processing the essay. This makes automated essay scoring system easy to be fooled by students because it is unable to distinguish between good writing and baloney. In order words, the act of using and repeating some key words from the prompt, fill up lots of space may result in a higher

grade from the automated essay scoring system (Greene, 2018). It is also reported in Davis (2014) that essays can obtain high scores even with gibberish which makes no sense to human readers.

AES are Sensitive to Noise

Fazal et al. (2011) also reported that the noise from the essays will have a negative effect on the performance and efficiency of automated essay scoring system. These noises include punctuation errors, syntax-based errors, morphological, context-based spelling errors, and misspellings. Hence, it is important to rule out the noise before the modeling process because it will lower the performance.

Essay Feedback Given by Automated Essay Scoring System is Unable to Increase Student's Grade Significantly

Darus et al. (2003) had conducted a study in Malaysia to investigate the improvement of students after revising their essays based on the feedbacks given by automated essay scoring system. Based on the results, the revisions made did not significantly increase the score of revised essays for most of the students. Furthermore, students who participate in the relevant research found that the feedback given by automated essay scoring system is useful and informative to a certain extent although their score remained the same. This suggests that feedbacks given in AES are not sufficient in pointing out areas that could potentially increase the students' scores.

AES do not Consider Context and Rating Criteria

To develop a context-aware AES, the essay context information should be reinforced to build an AES which can distinguish poor, ordinary, and excellent essays. Besides, semantic features should be added to assist the AES in context grading process. On the other side, some existing AES only focus on the essay content and did not consider rating criteria behind the essay during grading process (Liang et al., 2018). It is because a few rating criteria are difficult to integrate in AES and therefore lower the accuracy of the system.

DISCUSSION

Standardizing AES Framework

The review of previous studies on AES has shown that various frameworks have been used and this has proliferated the development of AES because each framework does not seem to be universally accessible to other researchers. After reviewed all frameworks used in AES system, we suggest hybrid framework as standard framework for AES as shown in Figure 5 because it is a hybrid framework combines both the goodness of content similarity

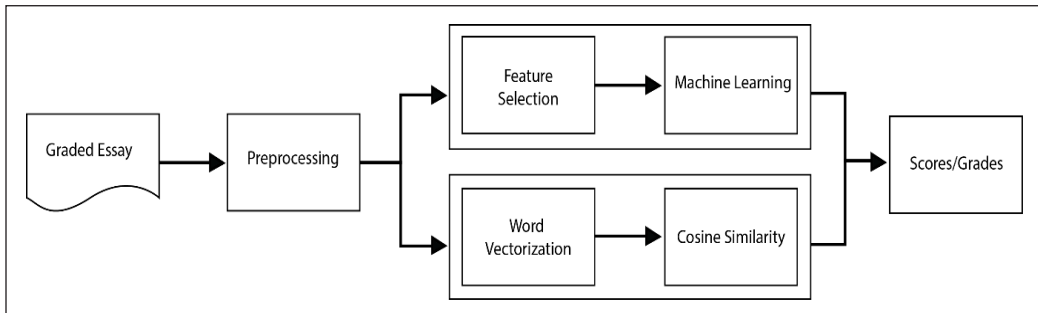


Figure 7. The workflow of proposed standard AES framework

and machine learning framework in which capable to aggregate both style and content to predict essay grades or scores. Besides, this framework enables researchers to apply different predictive models and NLP techniques on it and examine their performance. The workflow of proposed standard AES framework is illustrated in Figure 7.

For Malaysia University English Test (MUET), the marking scheme of an essay is the aggregation of task fulfilment, language, and organisation (Malaysian Examinations Council, 2014). Task fulfilment refers to the ability to understand topic and developing ideas which can be benchmarked with semantic indicators. Whereas the language and organisation refer to the number of grammar error, number of spelling error, use of appropriate vocabulary and coherence of content, are regarded as syntactic indicators. Hence, the machine learning part of our proposed framework is aimed to evaluate language and organisation using where the semantic indicators can be evaluated with content similarity measures.

In this framework, the essays undergo pre-processing such as word tokenization, predicting Parts of Speech, lemmatization and stop words removal to reduce the noises in the essay. Next, the features of the essay such as essay length, word count and misspelled word count may need to be extracted to ensure these features will not result in biased decision after vectorization of essay content. Then, the pre-processed essay undergoes word vectorization step to vectorize the essay content and feature selection to extract syntactic features from essay. Finally, the features and vectors are both treated as the inputs and used to train the predictive model using machine learning and content similarity measures.

Recommended Evaluation Metric

One of the issues with existing literatures is each researcher used different evaluation metrics to examine the performance of AES. This causes discrepancy when comparing the results with another works.

Accuracy has been seen as the most common evaluation metrics used in evaluating the performance of AES by calculating the percentage of matched pairs with human raters.

However, the result may be skew and biased toward the majority class when dealing with imbalanced datasets (Tanha et al., 2020). In real life, dataset normally contains imbalance proportion of grades since the distribution of the essays grade are normal.

Hence, this paper suggests that using Quadratic Weighted Kappa (QWK) score as a standard evaluation metric for AES. QWK is belong to kappa-like family and kappa coefficient has been proven that it can provide valuable information on the reliability of ordinal scale data (Sim & Wright, 2005). Moreover, Wong and Bong (2019) had stated that Kappa value is a better measurement than simple percent agreement calculation in AES because it corrects the percent-agreement for the case of agreement that would be expected purely by chance when estimating the degree of agreement between two raters.

CONCLUSION

Automated Essay Scoring (AES) is a software or service which grade essays with high human rater agreement. The objective of AES is to reduce the cost of time and effort on grading essays. In the current stage, the presence of AES cannot replace human raters in essay grading tasks, but it can assist human raters as a second rater. Most of the AES are developed in Western countries and there is still no commercial AES developed in the Asian region. According to past literature, most studies focused on evaluating essays based on its content by using Latent Semantic Analysis (LSA) technique. Moreover, most of the reported implementations treat AES as a supervised document classification task. Hence, this paper proposed three types of supervised general frameworks (content similarity, machine learning and hybrid) based on the past literature and a new framework which evaluates essays based on content and linguistic features. This review has also shown that different AES research used different evaluation methods to examine the proposed model performance, and this causes difficulty in doing a proper comparative study. Hence, this paper proposes Quadratic weighted kappa (QWK) as a standard method to evaluate AES performance and this can help to standardize the development of AES.

ACKNOWLEDGEMENTS

This study is supported by Kementerian Pendidikan Tinggi Malaysia Prototype Research Grant Scheme PRGS/1/2019/ICT01/UNIMAS/02/1 and Exploratory Research Grant Scheme ERGS/ICT07(01)/1018/2013(15).

REFERENCES

- Alghamdi, M., Alkanhal, M., Al-Badrashiny, M., Al-Qabbany, A., Areshey, A., & Alharbi, A. (2014). A hybrid automatic scoring system for Arabic essays. *AI Communications*, 27(2), 103-111. <https://doi.org/10.3233/aic-130586>

- Alikaniotis, D., Yannakoudakis, H., & Rei, M. (2016). Automatic text scoring using neural networks. In K. Erk & N. A. Smith (Eds.), *Proceedings of the 54th Annual Meeting of the Association for Computational Linguistics* (Volume 1: Long Papers) (pp. 715-725). Association for Computational Linguistics. <https://doi.org/10.18653/v1/p16-1068>
- Al-Jouie, M., & Azmi, A. (2017). Automated evaluation of school children essays in Arabic. *Procedia Computer Science*, 117, 19-22. <https://doi.org/10.1016/j.procs.2017.10.089>
- Amalia, A., Gunawan, D., Fithri, Y., & Aulia, I. (2019). Automated Bahasa Indonesia essay evaluation with latent semantic analysis. *Journal of Physics: Conference Series*, 1235, Article 012100. <https://doi.org/10.1088/1742-6596/1235/1/012100>
- Attali, Y., & Burstein, J. (2006). Automated essay scoring with e-rater® V.2. *Journal of Technology, Learning, and Assessment*, 4(3), 1-29.
- Awaida, S. A., Shargabi, B. A., & Rousan, T. A. (2019). Automated Arabic essays grading system based on F-score and Arabic wordnet. *Jordanian Journal of Computers and Information Technology (JJCIT)*, 5(3), 170-180. <https://doi.org/10.5455/jjcit.71-1559909066>
- Chen, H., & He, B. (2013). Automated essay scoring by maximizing human-machine agreement. In *Proceedings of the 2013 Conference on Empirical Methods in Natural Language Processing* (pp. 1741-1752). Association for Computational Linguistics.
- Chen, M., & Li, X. (2018). Relevance-based automated essay scoring via hierarchical recurrent model. In *2018 International Conference on Asian Language Processing (IALP)* (pp. 378-383). IEEE Conference Publication. <https://doi.org/10.1109/ialp.2018.8629256>
- Chen, Z., & Zhou, Y. (2019). Research on automatic essay scoring of composition based on CNN and OR. In *2019 2nd International Conference on Artificial Intelligence and Big Data (ICAIBD)* (pp. 13-18). IEEE Conference Publication. <https://doi.org/10.1109/icaibd.2019.8837007>
- Cheon, M., Seo, H. W., Kim, J. H., Noh, E. H., Sung, K. H., & Lim, E. (2015). An automated scoring tool for Korean supply-type items based on semi-supervised learning. In *Proceedings of the 2nd Workshop on Natural Language Processing Techniques for Educational Applications* (pp. 59-63). Association for Computational Linguistics and Asian Federation of Natural Language Processing. <https://doi.org/10.18653/v1/w15-4409>
- Contreras, J. O., Hilles, S., & Abubakar, Z. B. (2018). Automated essay scoring with ontology based on text mining and nltk tools. In *2018 International Conference on Smart Computing and Electronic Enterprise (ICSCEE)* (pp. 1-6). IEEE Conference Publication. <https://doi.org/10.1109/icscee.2018.8538399>
- Darus, S., Stapa, S. H., & Hussin, S. (2003). Experimenting a computer-based essay marking system at Universiti Kebangsaan Malaysia. *Jurnal Teknologi*, 39(E), 1-18. <https://doi.org/10.11113/jt.v39.472>
- Davis, B. (2014). *Essay grading computer mistakes gibberish for genius*. Retrieved August 28, 2020, from http://www.realclear.com/tech/2014/04/29/essay_grading_computer_mistakes_gibberish_for_genius_6784.html
- Dikli, S. (2006). An overview of automated scoring of essays. *Journal of Technology, Learning, and Assessment (JTLA)*, 5(1), 1-35.

- Dong, F., & Zhang, Y. (2016). Automatic features for essay scoring—an empirical study. In *Proceedings of the 2016 conference on empirical methods in natural language processing* (pp. 1072-1077). Association for Computational Linguistics. <https://doi.org/10.18653/v1/D16-1115>
- Elliot, S. M. (2003). IntelliMetric: From here to validity. In M. D., Shermis & J. C. Burstein (Eds.), *Automated essay scoring: A cross-disciplinary perspective* (pp. 71-86). Routledge
- Fazal, A., Dillon, T., & Chang, E. (2011). Noise reduction in essay datasets for automated essay grading. In *OTM Confederated International Conferences On the Move to Meaningful Internet Systems* (pp. 484-493). Springer. https://doi.org/10.1007/978-3-642-25126-9_60
- Foltz, P. W., Laham, D., & Landauer, T. K. (1999). The intelligent essay assessor: Applications to educational technology. *Interactive Multimedia Electronic Journal of Computer-Enhanced Learning*, 1(2), 939-944.
- Ghosh, S., & Fatima, S. S. (2008). Design of an automated essay grading (AEG) system in Indian context. In *TENCON 2008-2008 IEEE Region 10 Conference* (pp. 1-6). IEEE Conference Publication. <https://doi.org/10.1109/tencon.2008.4766677>
- Greene, P. (2018). *Automated essay scoring remains an empty dream*. Retrieved September 8, 2020, from Forbes: <https://www.forbes.com/sites/petergreene/2018/07/02/automated-essay-scoring-remains-an-empty-dream/#4474e4f74b91>
- Hussein, M. A., Hassan, H., & Nassef, M. (2019). Automated language essay scoring systems: A literature review. *PeerJ Computer Science*, 5, Article e208 <https://doi.org/10.7287/peerj.preprints.27715v1>
- Imaki, J., & Ishihara, S. (2013). Experimenting with a Japanese automated essay scoring system in the L2 Japanese environment. *Papers in Language Testing and Assessment*, 2(2), 28-47.
- Ishioka, T., & Kameda, M. (2006). Automated Japanese essay scoring system based on articles written by experts. In *Proceedings of the 21st International Conference on Computational Linguistics and 44th Annual Meeting of the Association for Computational Linguistics* (pp. 233-240). Association for Computational Linguistics. <https://doi.org/10.3115/1220175.1220205>
- Islam, M. M., & Hoque, A. L. (2013). Automated Bangla essay scoring system: ABESS. In *2013 International Conference on Informatics, Electronics and Vision (ICIEV)* (pp. 1-5). IEEE Conference Publication. <https://doi.org/10.1109/iciev.2013.6572694>
- Jin, C., & He, B. (2015). Utilizing latent semantic word representations for automated essay scoring. In *2015 IEEE 12th Intl Conf on Ubiquitous Intelligence and Computing and 2015 IEEE 12th Intl Conf on Autonomic and Trusted Computing and 2015 IEEE 15th Intl Conf on Scalable Computing and Communications and Its Associated Workshops (UIC-ATC-ScalCom)* (pp. 1101-1108). IEEE Conference Publication. <https://doi.org/10.1109/UIC-ATC-ScalCom-CBDCCom-IoP.2015.202>
- Jin, C., He, B., Hui, K., & Sun, L. (2018). TDNN: a two-stage deep neural network for prompt-independent automated essay scoring. In *Proceedings of the 56th Annual Meeting of the Association for Computational Linguistics (Volume 1: Long Papers)* (pp. 1088-1097). Association for Computational Linguistics. <https://doi.org/10.18653/v1/p18-1100>
- Kakkonen, T., Myller, N., Timonen, J., & Sutinen, E. (2005). Automatic essay grading with probabilistic latent semantic analysis. In *Proceedings of the second workshop on Building Educational Applications Using NLP* (pp. 29-36). Association for Computational Linguistics.

- Landauer, T. K., Foltz, P. W., & Laham, D. (1998). Introduction to latent semantic analysis. *Discourse Processes, 25*, 259-284.
- Landauer, T. K., Laham, D., & Foltz, P. W. (2000). The intelligent essay assessor. *IEEE Intelligent Systems, 15*, 27-31.
- Liang, G., On, B. W., Jeong, D., Kim, H. C., & Choi, G. S. (2018). Automated essay scoring: A siamese bidirectional LSTM neural network architecture. *Symmetry, 10*(12), Article 682. <https://doi.org/10.3390/sym10120682>
- Loraksa, C., & Peachavanish, R. (2007). Automatic Thai-language essay scoring using neural network and latent semantic analysis. In *First Asia International Conference on Modelling & Simulation (AMS'07)* (pp. 400-402). IEEE Conference Publication. <https://doi.org/10.1109/ams.2007.19>
- Malaysian Examinations Council. (2014). *Malaysian university English test (MUET): Regulations, test specifications, test format and sample questions*. Retrieved March 15, 2021, from https://www.mpm.edu.my/images/dokumen/calon-peperiksaan/muet/regulation/Regulations_Test_Specifications_Test_Format_and_Sample_Questions.pdf
- Measurement Incorporated. (2020). *Automated essay scoring*. Retrieved June 4, 2020, from <https://www.measurementinc.com/products-services/automated-essay-scoring>
- Nguyen, H., & Dery, L. (2016). Neural networks for automated essay grading. *CS224d Stanford Reports*, 1-11.
- Omar, N., & Mezher, R. (2016). A hybrid method of syntactic feature and latent semantic analysis for automatic Arabic essay scoring. *Journal of Applied Sciences, 16*(5), 209-215. <https://doi.org/10.3923/jas.2016.209.215>
- Ong, D. A., Razon, A. R., Guevara, R. C., & Prospero C. Naval, J. (2011, November 24-25). Empirical comparison of concept indexing and latent semantic indexing on the content analysis of Filipino essays. In *Proceedings of the 8th National Natural Language Processing Research Symposium* (pp. 40-45). De La Salle University, Manila.
- Page, E. B. (1966). The imminence of... grading essays by computer. *Phi Delta Kappan, 47*(5), 238-243.
- Page, E. (2003). Project essay grade: PEG. In M. Shermis, & J. Burstein (Eds.), *Automated essay scoring: A cross-disciplinary perspective* (pp. 43-54). Lawrence Erlbaum Associates Publishers.
- Pai, K. C., Lu, Y., & Kuo, B. C. (2017). Developing Chinese automated essay scoring model to assess college students' essay quality. In *Proceedings of the 10th International Conference on Educational Data Mining* (pp. 430-432).
- Pearson. (2010). *Intelligent essay assessor (IEA)™ fact sheet*. Pearson Education. Retrieved June 4, 2020, from <https://images.pearsonassessments.com/images/assets/kt/download/IEA-FactSheet-20100401.pdf>
- Peng, X., Ke, D., Chen, Z., & Xu, B. (2010). Automated Chinese essay scoring using vector space models. In *2010 4th International Universal Communication Symposium* (pp. 149-153). IEEE Conference Publication. <https://doi.org/10.1109/IUCS.2010.5666229>
- Phandi, P., Chai, K. M. A., & Ng, H. T. (2015). Flexible domain adaptation for automated essay scoring using correlated linear regression. In *Proceedings of the 2015 Conference on Empirical Methods in Natural*

- Language Processing* (pp. 431-439). Association for Computational Linguistics. <https://doi.org/10.18653/v1/D15-1049>
- Ramalingam, V. V., Pandian, A., Chetry, P., & Nigam, H. (2018). Automated essay grading using machine learning algorithm. In *Journal of Physics: Conference Series* (Vol. 1000, No. 1, p. 012030). IOP Publishing. <https://doi.org/10.1088/1742-6596/1000/1/012030>
- Ramineni, C., & Williamson, D. (2018). Understanding mean score differences between the e-rater® automated scoring engine and humans for demographically based groups in the GRE® general test. *ETS Research Report Series, 2018*(1), 1-31. <https://doi.org/10.1002/ets2.12192>
- Ratna, A. A. P., Budiardjo, B., & Hartanto, D. (2007). SIMPLE: System automatic essay assessment for Indonesian language subject examination. *Makara Journal of Technology, 11*(1), 5-11.
- Ratna, A. A. P., Purnamasari, P. D., & Adhi, B. A. (2015). SIMPLE-O, the Essay grading system for Indonesian Language using LSA method with multi-level keywords. In *The Asian Conference on Society, Education & Technology 2015* (pp. 155-164). The International Academic Forum.
- Ratna, A. A. P., Arbani, A. A., Ibrahim, I., Ekadiyanto, F. A., Bangun, K. J., & Purnamasari, P. D. (2018). Automatic essay grading system based on latent semantic analysis with learning vector quantization and word similarity enhancement. In *Proceedings of the 2018 International Conference on Artificial Intelligence and Virtual Reality* (pp. 120-126). Association for Computing Machinery. <https://doi.org/10.1145/3293663.3293684>
- Ratna, A. A. P., Kaltsum, A., Santiar, L., Khairunissa, H., Ibrahim, I., & Purnamasari, P. D. (2019a). Term frequency-inverse document frequency answer categorization with support vector machine on automatic short essay grading system with latent semantic analysis for Japanese language. In *2019 International Conference on Electrical Engineering and Computer Science (ICECOS)* (pp. 293-298). IEEE Conference Publication. <https://doi.org/10.1109/ICECOS47637.2019.8984530>
- Ratna, A. A. P., Khairunissa, H., Kaltsum, A., Ibrahim, I., & Purnamasari, P. D. (2019b). Automatic essay grading for Bahasa Indonesia with support vector machine and latent semantic analysis. In *2019 International Conference on Electrical Engineering and Computer Science (ICECOS)* (pp. 363-367). IEEE Conference Publication. <https://doi.org/10.1109/ICECOS47637.2019.8984528>
- Ratna, A. A. P., Santiar, L., Ibrahim, I., Purnamasari, P. D., Luhurkinanti, D. L., & Larasati, A. (2019c). Latent semantic analysis and winnowing algorithm based automatic Japanese short essay answer grading system comparative performance. In *2019 IEEE 10th International Conference on Awareness Science and Technology (iCAST)* (pp. 1-7). IEEE Conference Publication. <https://doi.org/10.1109/ICAWS.2019.8923226>
- Rudner, L., & Gagne, P. (2001). An overview of three approaches to scoring written essays by computer. *Practical Assessment, Research & Evaluation, 7*, Article 26.
- Sendra, M., Sutrisno, R., Hariyanto, J., Suhartono, D., & Asmani, A. B. (2016). Enhanced latent semantic analysis by considering mistyped words in automated essay scoring. In *2016 International Conference on Informatics and Computing (ICIC)* (pp. 304-308). IEEE Conference Publication. <https://doi.org/10.1109/IAC.2016.7905734>

- Shehab, A., Faroun, M., & Rashad, M. (2018). An automatic Arabic essay grading system based on text similarity Algorithms. *International Journal of Advanced Computer Science and Applications*, 9(3), 263-268. <https://doi.org/10.14569/IJACSA.2018.090337>
- Shermis, M. D., & Burstein, J. (2003). *Automated essay scoring: A cross-disciplinary perspective*. Lawrence Erlbaum Associates Publishers.
- Shermis, M. D., Burstein, J., Higgins, D., & Zechner, K. (2010). Automated essay scoring: Writing assessment and instruction. *International Encyclopedia of Education*, 4(1), 20-26. <https://doi.org/10.1016/B978-0-08-044894-7.00233-5>
- Sim, J., & Wright, C. C. (2005). The Kappa statistic in reliability studies: Use, interpretation, and sample size requirements. *Physical Therapy*, 85(3), 257-268.
- Taghipour, K., & Ng, H. T. (2016). A neural approach to automated essay scoring. In *Proceedings of the 2016 Conference on Empirical Methods in Natural Language Processing* (pp. 1882-1891). Association for Computational Linguistics. <https://doi.org/10.18653/v1/d16-1193>
- Tanha, J., Abdi, Y., Samadi, N., Razzaghi, N., & Asadpour, M. (2020). Boosting methods for multi-class imbalanced data classification: an experimental review. *Journal of Big Data*, 7(1), 1-47. <https://doi.org/10.1186/s40537-020-00349-y>
- Vantage Learning. (2005). *How IntelliMetric™ works*. Retrieved June 4, 2020, from http://www.vantagelearning.com/docs/intellimetric/IM_How_IntelliMetric_Works.pdf
- Vantage Learning. (2020). *IntelliMetric®: Frequently asked questions*. Retrieved June 4, 2020, from <http://www.vantagelearning.com/products/intellimetric/faqs/#LongUsed>
- Wong, W. S., & Bong, C. H. (2019). A study for the development of automated essay scoring (AES) in Malaysian English test environment. *International Journal of Innovative Computing*, 9(1), 69-78. <https://doi.org/10.11113/ijic.v9n1.220>
- Xu, Y., Ke, D., & Su, K. (2017). Contextualized latent semantic indexing: A new approach to automated Chinese essay scoring. *Journal of Intelligent Systems*, 26(2), 263-285. <https://doi.org/10.1515/jisys-2015-0048>
- Zupanc, K., & Bosnic, Z. (2015). Advances in the field of automated essay evaluation. *Informatica*, 4(39), 383-396.



PRIB-CDS: An Energy Efficient Low Duty Cycle Broadcasting Scheme for Wireless Sensor Network

Anubhama Ramasamy^{1*} and Rajendran Thangavel²

¹Department of Computer Science, Periyar University, Periyar Palkalai Nagar, Salem, 636011, Tamilnadu, India

²Department of Computer Science, Government Arts and Science College, Kangeyam, Tirupur, 638701, Tamilnadu, India

ABSTRACT

Low duty cycling is a widely adapted technique to conserve energy in the most used Medium Access Control (MAC) protocols in Wireless Sensor Networks (WSN). But such low duty cycle-based MAC protocols perform poorly under broadcast traffic as they suffer from redundant retransmission and maximization of relay nodes problems. Addressing these issues is critical, as the advent of IoT and ubiquitous computing applications has increased the demand for broadcast support. Our previous work, Preamble based Receiver Initiated Broadcasting MAC (PRIB-MAC) performed well in most parameters under broadcast traffic, but it had scope for improvement in reducing the number of transmissions. In this paper, we propose the PRIB-Connected Dominating Set (PRIB-CDS), built on top of PRIB-MAC with the addition of dynamic forwarding technique by forming a forwarding set with the help of Greedy algorithm. The simulation results of our proposed PRIB-CDS algorithm shows that it has reduced the number of transmissions significantly as it reduces forwarding nodes and balances the energy between the nodes to avoid re-broadcasting the data.

Keywords: Broadcasting, CDS, dynamic forwarding, MAC, PRIB-MAC, retransmission, WSN

ARTICLE INFO

Article history:

Received: 05 December 2020

Accepted: 01 April 2021

Published: 31 July 2021

DOI: <https://doi.org/10.47836/pjst.29.3.09>

E-mail addresses:

anubhama.r@gmail.com (Anubhama Ramasamy)

rajendran_tm@yahoo.com (Rajendran Thangavel)

* Corresponding author

INTRODUCTION

In WSN, broadcasting can be used in different scenarios like network topology discovery process, network configuration process, routing process, information dissemination and so on. In the recent developments of IoT and ubiquitous computing techniques, the sensor node can communicate via multiple hops without centralized control. Naturally,

WSN nodes are very small in size and can function in the IoT and Ubiquitous computing applications with limited energy where the nodes can operate many years without human interruptions.

To meet the energy efficiency requirements, WSN employs various asynchronous low duty cycling techniques, where the nodes sleep and wake-up on their own schedules to conserve energy and several sender-initiated and receiver-initiated mechanisms are proposed to achieve coordination among the nodes (Anubhama & Rajendran, 2017). But these techniques perform poorly for broadcast traffic, as the broadcasting techniques like repeated unicast proposed in Asynchronous Duty cycle Broadcasting (ADB) and flooding lead to redundancy, increased latency, and energy consumption (Sun et al., 2009; Guo et al., 2011). Therefore, providing a solution for energy efficient broadcasting in low duty cycled networks is an important issue in WSN, which we have tried to address in our previous work PRIB-MAC (Anubhama & Rajendran, 2020b). As an alternative to repeated unicast for broadcasting, it employed short preambles as part of the receiver-initiated low duty cycle mechanism. The results were promising with improved network coverage and reduced control overhead and energy consumption.

However, re-transmission is a common issue in these low duty cycle-based protocols which can be effectively reduced by using dynamic forwarding techniques (Anubhama & Rajendran, 2020a). In dynamic forwarding, the forwarder node is elected by using any one of the mechanisms such as Cluster based, On-demand or Multiple Criteria based, and Connected Dominating Set (CDS) based.

In Cluster based mechanism, WSN nodes form a cluster and choose the cluster head based on energy, distance, or any other criteria (Fouchal, 2012). On-demand algorithm chooses the forwarder node by calculating a threshold value, based on the residual energy level of the nodes or distance of the node from source to destination or both energy and distance. This works comparatively well in unicast than broadcast (Tan & Chan, 2010; Rehena et al., 2013). In CDS, each node in the network must learn the 1-hop or 2-hop information of its neighbors and it chooses the forwarding node by calculating the degree of node or by using the range of each node.

Cluster based and On-demand algorithms focus more on achieving node coverage in broadcast operations (Vijayasharmila et al., 2015; Afia et al., 2019). However, these algorithms are known to have the limitation of centralized node failure and time delay, respectively. In comparison with the other dynamic forwarding algorithms, the CDS method is well employed in avoiding retransmissions and reducing the number of relay nodes, which will result in reducing energy consumption.

Based on the network topology, the CDS construction algorithms can be further classified into centralized and decentralized. In centralized, the entire control of the network is maintained by a single node and if that central control fails, the entire network collapses. In decentralized, each node manages themselves, therefore a single node failure does not affect

the entire network. The decentralized algorithm can be further classified into distributed and localized algorithms. The decision process of distributed algorithms is decentralized, and it is classified as pruning-based and MIS-based CDS construction algorithms. But the decision process of a localized algorithm is distributed where it involves continuous communication rounds and is further classified into Addition-based and subtraction-based localized algorithms. The Addition-based localized CDS construction algorithm begins with commonly disconnected nodes, and then adds other nodes to create the CDS. According to the type of initial subset, the Addition-based localized CDS construction algorithms are further classified into MIS-based algorithm and tree-based algorithm, which incorporates search techniques such as greedy and heuristic search. Subtraction-based localized CDS construction algorithms systematically remove nodes from the initial CDS, which is a set of all the nodes in the network.

The next section discusses some of the related works in forwarder selection based on distributed CDS construction algorithms. The materials and method section discusses the design and implementation of PRIB-CDS protocol, the result and discussion section describe the simulation results for PRIB-CDS in comparison with other broadcasting protocols and we conclude the paper with scope for future enhancements.

RELATED WORKS

To avoid retransmission and to achieve better broadcasting, dynamic forwarding techniques play an important role in asynchronous broadcasting MAC protocols, where election of forwarders is efficiently done using distributed CDS approach. Here some of the existing distributed CDS approaches are discussed based on their complexity, running time, stability and overhead.

The distributed pruning-based algorithm uses two phases to construct the CDS (Alzoubi et al., 2002). First, MIS (Maximal Independent Set) is identified by forming a spanning tree using the distributed leader election algorithm and next, the dominating tree is identified. All the nodes in the dominating tree form the CDS. This algorithm suffers from time and message complexity.

The Self-Pruning and Dominant-Pruning (DP) algorithms are proposed to deal with low-cost flooding tree problems by using different heuristic search flooding methods (Hyojun & Chongkwon, 2001). In self-pruning, each node knows their 1-hop neighbour information by exchanging adjacent node information and it suffers from message overhead. Whereas in dominant pruning, each node calculates their 2-hop neighbour information by exchanging the adjacent node list with neighbour and the sender chooses the adjacent node to forward the packet to complete the flooding. But this leads to energy depletion of the source node and it also consumes more bandwidth. The improved self pruning algorithm works based on self pruning, in which every node makes its own decision to rebroadcast

the packet depending on its neighbour details (Rab et al., 2017). It completes its broadcast with a smaller packet header, but it uses extended neighbour knowledge that contains 3-hop neighbour information, which is used to find its forwarder. This algorithm takes more computational time to decide its forwarding node. The Counter Based Dominant Pruning (CDP) algorithm is constructed by combining the advantage of counters-based scheme and Dominant Pruning (Hoque et al., 2020). It avoids the problem of the host receiving the same message again while broadcasting using some threshold value. However, this algorithm suffers from functional overheads.

In a distributed MIS-based algorithm first independent nodes are found using a searching algorithm and then MIS (Maximal Independent Set) nodes are interconnected (Das & Bharghavan, 1997). This algorithm is further classified as single initiator and multiple initiator algorithms. Single initiators algorithm uses a MCDS (Minimum Connected Dominating Set) and spine methods to construct the routing techniques in wireless networks (Das et al., 1997). It is very expensive for maintaining. The multi-initiator algorithm proposes a message/time distributed algorithm and is designed to solve the problems in computing forwarding set by calculating MCDS (Cheng et al., 2006). But it suffers from a high message complexity problem.

The Addition based localized MIS algorithm constructs the CDS in two different stages in which Maximum Independent Set is identified by selecting the neighbor nodes with the highest count repeatedly and then applying localized searching techniques to increase additional nodes (Hong et al., 2013; Zhou et al., 2005). The tree based localized CDS algorithm is composed of three phases that are choosing the number of initiators, using the timer for forming the CDS tree, adding additional bridge nodes for connecting the neighbors respectively which results in increased time complexity.

The subtraction based localized algorithm consists of two stages to construct the CDS whereas at first each node collects and exchanges messages about its 2-hop and 1-hop neighbor details and it removes itself from the CDS if a direct connection between any pair of its 1-hop neighbors exists followed by which some heuristic search rules are applied which results in reducing the CDS size (Dai & Wu, 2004).

Among these CDS based algorithms, the localized CDS construction algorithms work well in calculating the forwarder node and the Addition-based CDS construction algorithm produces smaller CDS than the Subtraction-based CDS construction algorithms. In comparison with the other heuristics search algorithms, greedy algorithms generate smaller CDS which in turn reduces the number of transmissions. Hence, to enhance our previous work of PRIB-MAC (Anubhama & Rajendran, 2017) and propose an energy efficient low duty cycle broadcasting scheme for WSN, we focus on forming the CDS using a greedy algorithm. The simulation results are compared with PRIB-MAC and some of the existing state of the art broadcasting schemes like, ADB (Sun et al., 2009) and SALB (Hong et al., 2013).

MATERIALS AND METHODS

Network Model

Let us consider there are n nodes in the network, which are equally distributed in equal transmission range of one unit. The given network is defined as a graph $G(V,E)$ in which V is the set of nodes and E is the edge where an edge is represented as $\{u,v\} \in E$ where u and v are the nodes within the communication range. G represents a non unit disk graph. Let $N(v)$ is a neighbour set of node v (including v) then $N(V) = \text{Union}_{v \in V} N(v)$ is a set of all nodes of V and V covers U if $U \subseteq N(V)$.

A fractional x -hop detail of a node v is a subgraph $G_x(v) = (N_x(v), E_x(v))$ of the network G . Here $N_x(v)$ is the x -hop neighbour set and $E_x(v)$ is the x -hop connection set of v . Now we can specify $N_0(v) = \{v\}$ and $N_x(v) = \text{Union}_{u \in N_{x-1}(v)} N(u)$ for $x \geq 1$ and $E_x(v) = \{(u,w) | u \in N_{x-1}(v) \wedge w \in N_x(v)\}$ includes link among the nodes in $N_x(v)$. But excludes the link between two nodes which will be precisely x hops from v . $G_x(v)$ collected from v by sending x rounds of "Hello" packet. It is shown in Figure 1 and if v has 1-hop neighbour details, then it knows all its neighbours but not the link between these neighbours. The entire x -hop details of a node v is a subgraph $G^1_x(v) = (N_x(v), E^1_x(v))$, Where $E^1_x(v) = \{(u,w) | u, w \in N_x(v)\}$ is the entire x -hop connection set of v and that details is collected by sending $(x+1)$ rounds of "Hello" packet. We assume each node assigns its own sleeping schedule in asynchronous manner and can transmit the data when it wakes up but receives the data only during its active time slots.

Problem Formation

In this work we consider a multisource broadcasting scheme, where every node in the network can broadcast the data to the rest of nodes in the network. Each forwarding node receives the data from source and retransmits among its neighbours to complete the broadcasting operation. Thus the broadcasting problem in WSN with different sleep/wake

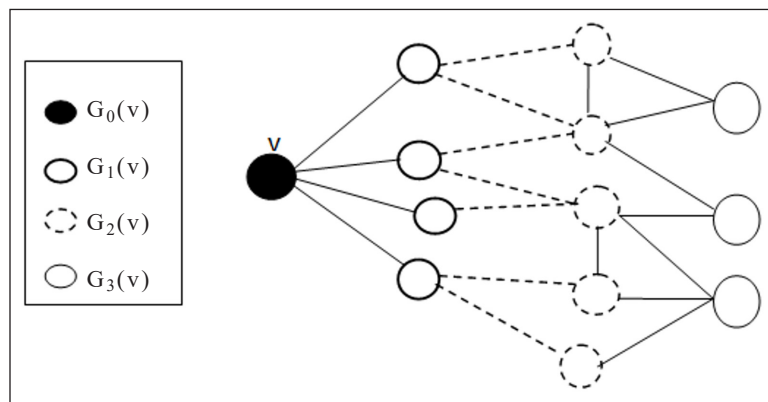


Figure 1. Fractional x -hop information

up schedules has to be redefined by forming a forwarding set $F(G)$ from $G(V,E)$ which will be a subset of V . The data will be forwarded via forwarding set $F(G)$.

Proposed Protocol

PRIB-CDS is based on our existing work PRIB-MAC, in which the source broadcasts the data to the neighbour nodes by employing a short preamble. In Receiver Initiated approach, the source waits for the beacon from its neighbor nodes. Even after receiving the beacon, the source delays sending the data by sending a short preamble to its neighbors, which gives additional time for its neighbor nodes to wake up. This avoids repeated unicast by covering more nodes in a single transmission. PRIB-CDS has two key phases of operation: Construction of forwarding set and broadcast using forwarder defined in $F(G)$.

Construction of Forwarding Set

In a given network $G(V,E)$, each node knows its x -hop subgraph $G_x(v) = ((N_x(v), E_x(v)))$ and it select the forward node set $F(G)$ from its i -hop neighbour set $N(v)$ to cover its next-hop neighbour set $N_j(v)$, that is $F(G) \cup \{v\}$ is a MCDS for $G_x(v)$. $F(G)$ is also known as a coverage set of v . When u selects v as a forward node then v is called selector of u and several selectors may exist for a single node. Statement 1 and Statement 2 define retransmission state and MCDS, respectively.

Statement 1

A forwarder will be able to transmit the message only when it receives the first packet from the selector.

Statement 2

In a given WSN network $G(V,E)$, the nodes other than the Primary Source node (which has the data to be sent) fall under Minimum Connected Dominating Set (MCDS) for broadcasting. The forwarding set $F(G)$ is formed from MCDS for effective broadcasting.

Algorithm 1. Greedy algorithm for calculating forwarding set $F(G)$

- 1: If a node is in $H_2(G)$ and if it is covered only by u then add $u \in H_1(G)$ to $F(G)$.
- 2: Check the uncovered node in $F(G)$. (If a node in $H_2(G)$ is not covered by $F(G)$ then it is called an uncovered node).
- 3: If u envelops highest number of uncovered nodes in $H_2(G)$ then add $u \in H_1(G)$ to $F(G)$.

The above greedy Algorithm 1 is used to calculate the forwarding set $F(G)$. The selection of $F(G)$ is explained in Figure 2. From that $N(v)$ is covered when v transmits.

Therefore $H_2(v)=(N_2(v)-N(v))$ is used instead of $N_2(v)$. The neighbour u is important because a node in $H_2(v)$ is only covered by u . In the above Algorithm 1, first cover the required neighbours and then neighbours with higher degree nodes are selected to cover $H_2(v)$. If two neighbours are in the same degree, any one of the nodes is selected to form a forwarding set $F(G)$. This can be identified by selecting the node with the minimum number of connected nodes.

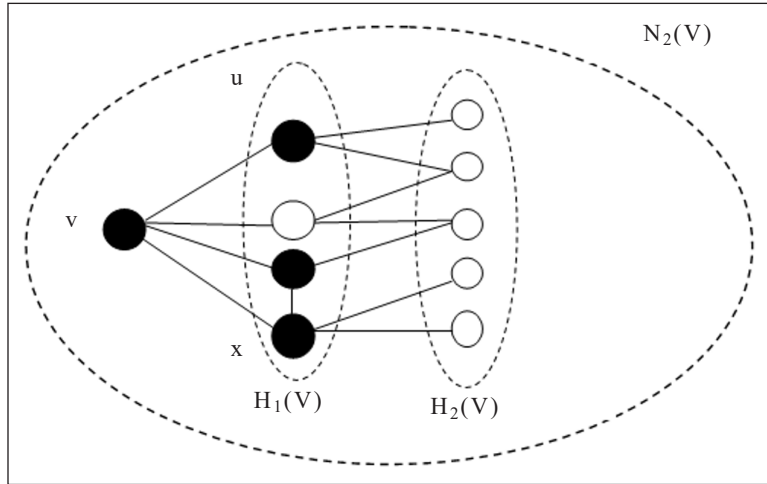


Figure 2. Each node v selects a few 1-hop neighbours to envelop its 2-hop neighbours.

Broadcasting Operation in PRIB-CDS

The Algorithm 2 presents a forwarding mechanism for the nodes in forwarding set $F(G)$ constructed by Algorithm 1.

Algorithm 2. Forwarding Algorithm to Broadcast the Data

Based on the ID and data SEQ

If the data is received for the first time **then**

If channel is free and data to send **then**

Switch to T_x mode and wait for beacon

Let $FRWD_SET$ be the set of nodes and in $F(G)$ except the source node S

If $\exists u \in FRWD_SET$ and receive beacon from the u **then**

send a preamble tie (wait for t_{in}) to u

Until $t_{time\ out}$ and the data broadcasting occurs.

end if

end if

end if

go to sleep mode

In Algorithm 2, the FRWD_SET is the set of all the nodes in $F(G)$ except the source node S . When any of the nodes in FRWD_SET receives the beacon from its neighbour u , it sends a short preamble time t_{in} to its receiver to keep the receiver awake until $t_{time\ out}$. The time t_{in} is refreshed after every preamble. All the receiver nodes that wake up during the inter preamble duration send their beacons and at the end of preamble duration, the data is forwarded to all the receivers that received the preamble. Every source node maintains an ID in the broadcast packets to differentiate the data between the source nodes and adds a sequence number SEQ to identify the sequence. If every node in the forwarding set succeeds in delivering the broadcasted packets to its neighboring nodes, all nodes in the network are assured to receive the broadcast packets, as the broadcast forwarding set of PRIB-CDS is a CDS.

Minimum number of transmissions to complete a broadcast in the network is assumed to be A_{min} . The maximum delay time set for a source is represented as $t_{time\ out}$ and the number of active forwarders/receivers which would be sending the beacon to the source/forwarders is represented as T_{nodes} . Also, we assume that the nodes with two extreme time differences set can be covered within two cycles of maximum delay time i.e., $2 t_{time\ out}$.

Since the transmission to a node is only according to the number of active forwarders/receivers in $t_{time\ out}$, the number of necessary transmissions is at most $\min(\Delta, |T_{nodes}|)$. The numbers of transmissions of PRIB-CDS are bounded by $[\min(\Delta, |T_{nodes}| + c)](A_{min} + 1)$, where c is constant.

To cover its 2-hop neighbor nodes, the 1-hop nodes of node u need at most R_2 transmission totally, where R_2 is the number of node u 's 2-hop neighbor nodes. Also, the 2-hop nodes of node u will need to transmit messages to node u 's 3-hop neighbor nodes through their 1-hop nodes, respectively. Denoting the number of node u 's 3-hop neighbor nodes as R_3 , the numbers of transmissions to cover all 3-hop neighbor nodes of node u are at most $2R_3$ because each 3-hop node connects to only one 1-hop node in the worst case. Therefore, the numbers of transmissions M to finish the broadcast equal.

$$|S|(\min(\Delta, |T_{nodes}| + R_2 + 2R_3))$$

where S is the dominating set. Hence a constant c is used to denote the upper bound of $R_2 + R_3$.

RESULT AND DISCUSSION

The performance of PRIB-CDS is evaluated for some of the key parameters in broadcasting such as number of transmissions, network coverage and energy efficiency. The results are compared against our previous work PRIB-MAC upon which PRIB-CDS is built on and some of the state broadcasting protocols in WSN such as ADB, an RI-MAC based asynchronous duty cycled protocol and SALB, an asynchronous CDS based local broadcasting protocol for WSN.

Simulation Methodology

The simulation is done using OMNET++ simulation engine. We deployed 6 to 21 nodes, randomly distributed over a 300mX300m square region within 125m to 225m transmission range where the size of each broadcast packet remains the same for every node. Preambles are special packets sent back-back to keep the node awake. Instead of sending several preambles back-back, source can send the preamble after a particular interval of time, which is less than the data time out interval of receivers. The parameters used in the simulation environment are given in Table 1.

Table 1
Parameters used in simulation

Parameter	Value
Area	300mX300m
Total No.of nodes	6 to 21
Transmission range	125mX225m
Time Slot	1s
Time interval per hop	0.3s
Preamble Duration	0.002s to 0.05s

Simulation Results

Number of Transmissions. The line chart in Figure 3 shows the number of transmissions in PRIB-CDS and PRIB-MAC with varying preamble durations. For PRIB-MAC, it takes 8 transmissions for 100% coverage in a 7-node network and the preamble duration has no effect on the number of transmissions as it suffers from retransmission issues. Use of dynamic forwarding in PRIB-CDS shows significant improvement in reducing the number of transmissions as the preamble duration increases.

Figure 4 compares the number of transmissions in PRIB-CDS, ADB, PRIB-MAC and SALB for different network sizes. In ADB, the number of transmissions increases exponentially for a 21-node network to 43 as it performs repeated unicast transmission to achieve broadcasting. Similarly, PRIB-MAC shows linear increase of 25 transmissions for 21 node networks as it suffers from retransmission issues. SALB performs better as the

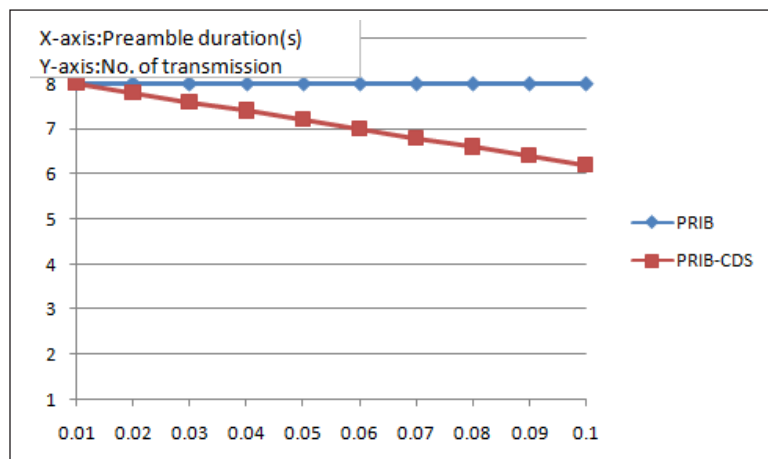


Figure 3. Number of transmissions with different preamble duration

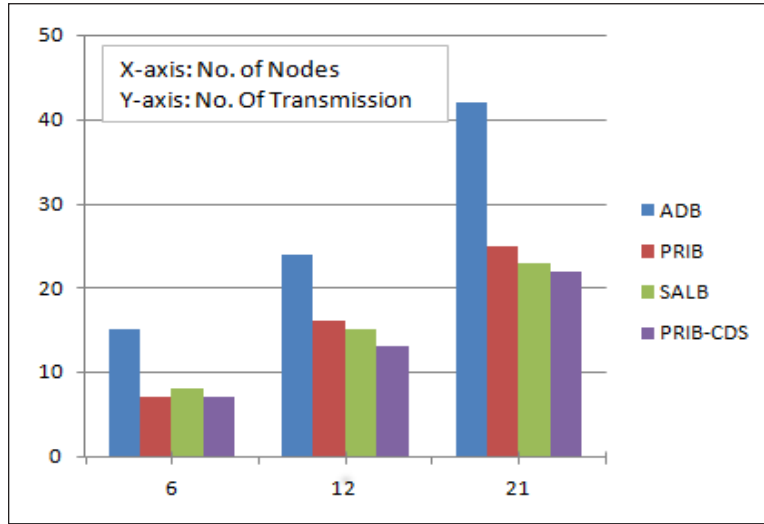


Figure 4. Number of transmissions for different network sizes

network size scales up i.e, 22 transmissions for 21 node networks but when the network size is small it needs 9 transmissions for 6 node networks as each dominator must transmit to its dominant one by one, and there exists redundant paths between the dominators in the forwarding set. PRIB-CDS shows marked improvement across network sizes due to the combination preamble-based approach and the CDS based dynamic forwarding technique.

Network Coverage Time

The line chart in Figure 5 shows the network coverage of PRIB-CDS compared against SALB, PRIB-MAC and ADB. PRIB-CDS achieves full coverage within 3.05s compared with ADB, PRIB-MAC. ADB performs poorly as it requires repeated transmission to

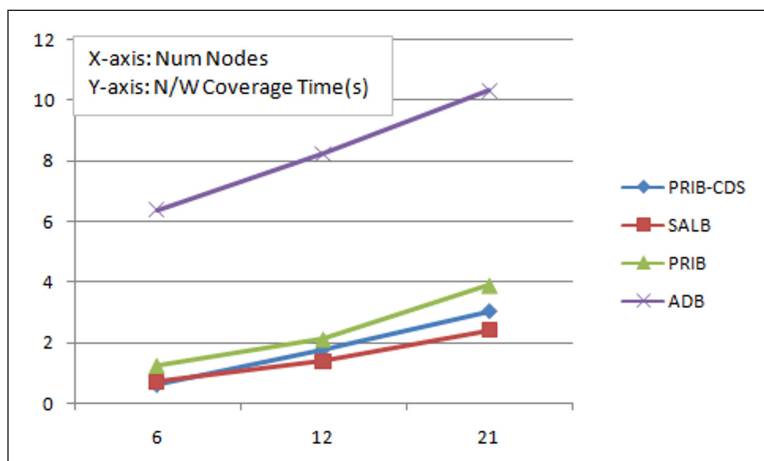


Figure 5. Network coverage time(s) with different numbers of nodes

achieve full coverage. All the other three protocols perform reasonably well with PRIB-MAC taking slightly more time due to preamble delays and retransmissions issues due to the lack of proper forwarding techniques. Both PRIB-CDS and SALB perform well with SALB doing slightly better than PRIB-CDS. It must be noted PRIB-CDS takes a slightly more time than SALB (2.5s) though it performs better in number of transmissions. It could be caused by delay due to contention in PRIB-CDS. In Figure 2 shows that two adjacent nodes could be selected as forwarder nodes even if they lie within the transmission range of one another and when these nodes try to rebroadcast the data, they will access the medium at the same time resulting in contention.

Energy Consumption

Figure 6 shows the average energy consumption in percentage for PRIB-CDS and other protocols. As expected, ADB consumes more energy than the other protocols because of its repeated unicasting approach. To keep the receiver active, senders send lots of beacons which results in high energy consumption (34% to 36%) for both sender and receiver nodes as the repeated unicast approach results in redundant transmissions. PRIB-MAC performs poorly (11%) compared to PRIB-CDS (4%) as it suffers from retransmission issues during broadcasting due to lack of a proper forwarding mechanism. The line chart shows that PRIB-CDS performs the best with 4% consumption for 21 node networks and the average energy consumption decreases as the network size increases. It is slightly better than SALB (5%) as the sender nodes employ short preambles to cover more nodes in the asynchronous duty cycle. Furthermore, in SALB, when the size of the network is small, each dominator transmits to its dominant one by one, which is the same as repeated unicast resulting in higher energy consumption.

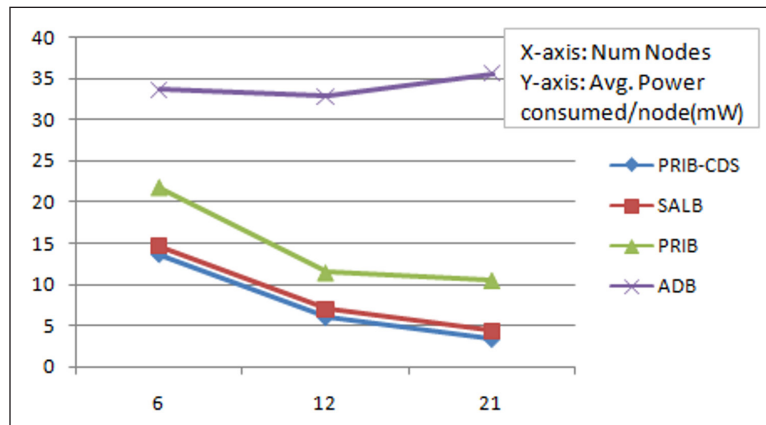


Figure 6. Average energy Consumption (%)

CONCLUSION

We have presented an efficient and robust broadcasting scheme PRIB-CDS, for low duty cycled Wireless Sensor Networks, which builds on to the advantages of the preamble-based approach in PRIB-MAC, by reducing the number of retransmissions by forming a forwarding set. Our proposed PRIB-CDS algorithm uses a CDS based approach to find the forwarder node in addition to the use of short preambles, which improves key performance metrics of broadcasting such the number of transmissions, average energy consumption and network coverage time when compared to the multiple unicast approach proposed in ADB. Comparisons against another CDS based approach in SALB shows significant reduction in the number of transmissions and energy consumption, with scope for improvement in delay to achieve 100% node coverage.

ACKNOWLEDGEMENT

The author would like to thank her brother and sister for providing support to this research work and grateful to peer reviewers who have saved her from many mistakes through comments. The author hopes this research can provide benefits and contribute to further research.

REFERENCES

- Afia A., Tahrira O., Diana S., & Ferdous, C. N. (2019). Construction of connected dominating set to reduce contention in wireless ad-hoc network. In *6th International Conference on Networking Systems and Security* (pp. 59-67). Association for Computing Machinery. <https://doi.org/10.1145/3362966.3362975>
- Alzoubi, K. M., Wan, P. J., & Frieder, O. (2002). New distributed algorithm for connected dominating set in wireless ad hoc networks. In *Proceedings of the 35th Annual Hawaii International Conference on System Sciences* (pp. 3849-3855). IEEE Conference Publication. <https://doi.org/10.1109/HICSS.2002.994519>
- Anubhama, R., & Rajendran, T. (2017). A survey on MAC protocols for wireless sensor networks. *Annals of Computer Science and Information Systems*, 10, 121-126. <http://dx.doi.org/10.15439/2017R26>
- Anubhama, R., & Rajendran, T. (2020a). A study of dynamic forwarding techniques in wireless sensor networks. In M. Sundaresan & W. R. Varuna (Eds.), *Proceeding of International E-Conference of Innovations in Information Technology (IECIIT-2020)* (pp. 28-34). Coimbatore Institute of Information Technology, India.
- Anubhama, R., & Rajendran, T. (2020b). PRIB-MAC: A preamble-based receiver initiated MAC protocol for broadcast in wireless sensor networks. *Sādhanā*, 45(1), Article 79. <https://doi.org/10.1007/s12046-020-1322-7>
- Cheng, X., Ding, M., Du, D. H., & Jia, X. (2006). Virtual backbone construction in multihop ad hoc wireless networks. *Wireless Communications and Mobile Computing*, 6(2), 183-190. <https://doi.org/10.1002/wcm.378>

- Dai, F., & Wu, J. (2004). An extended localized algorithm for connected dominating set formation in ad hoc wireless networks. *IEEE Transaction on Parallel Distributed Systems*, 15(10), 908-920. <https://doi.org/10.1109/TPDS.2004.48>
- Das, B., & Bharghavan, V. (1997). Routing in ad-hoc networks using minimum connected dominating sets. In *Proceedings of ICC'97-International Conference on Communications* (Vol. 1, pp. 376-380). IEEE Conference Publication. <https://doi.org/10.1109/ICC.1997.605303>
- Das, B., Sivakumar, R., & Bharghavan, V. (1997). Routing in ad hoc networks using a spine. In *Proceedings of Sixth International Conference on Computer Communications and Networks* (pp. 34-39). IEEE Conference Publication. <https://doi.org/10.1109/ICCCN.1997.623288>
- Fouchal, S., Monnet, Q., Mansouri, D., Mokdad, L., & Ioualalen, M. (2012). A clustering method for wireless sensors networks. In *2012 IEEE Symposium on Computers and Communications (ISCC)* (pp. 000888-000892). IEEE Conference Publication. <https://doi.org/10.1109/ISCC.2012.6249414>
- Guo, S., Kim, S. M., Zhu, T., Gu, Y., & He, T. (2011). Correlated flooding in low-duty-cycle wireless sensor networks. In *2011 19th IEEE International Conference on Network Protocols* (pp. 383-392). IEEE Conference Publication. <https://doi.org/10.1109/ICNP.2011.6089078>
- Hyojun, L., & Chongkwon, K. (2001). Flooding in wireless ad hoc networks. *Computer Communications*, 24(3-4), 353-363. [https://doi.org/10.1016/S0140-3664\(00\)00233-4](https://doi.org/10.1016/S0140-3664(00)00233-4)
- Hong, J., Li, Z., Lu, D., & Lu, S. (2013). Sleeping schedule-aware local broadcast in wireless sensor networks. *International Journal of Distributed Sensor Networks*, 9(12), 451970. <https://doi.org/10.1155/2013/451970>
- Hoque, S., Majumder, R., Islam, S., & Anannya, T. T. (2020). Reducing redundancy by optimizing dominant pruning algorithm for wireless ad hoc networks. In *Proceedings of the International Conference on Computing Advancements* (pp. 1-9). Association for Computing Machinery. <https://doi.org/10.1145/3377049.3377073>
- Rab, R., Sagar, S. A. D., Sakib, N., Haque, A., Islam, M., & Rahman, A. (2017). Improved self-pruning for broadcasting in ad hoc wireless networks. *Wireless Sensor Network*, 9(02), 73-86. <https://doi.org/10.4236/wsn.2017.92004>
- Rehena, Z., Roy, S., & Mukherjee, N. (2013). Efficient data forwarding techniques in Wireless Sensor Networks. In *2013 3rd IEEE International Advance Computing Conference (IACC)* (pp. 449-457). IEEE Conference Publication. <https://doi.org/10.1109/IAdCC.2013.6514268>
- Sun, Y., Gurewitz, O., Du, S., Tang, L., & Johnson, D. B. (2009). ADB: An efficient multihop broadcast protocol based on asynchronous duty-cycling in wireless sensor networks. In *Proceedings of the 7th ACM conference on embedded networked sensor systems* (pp. 43-56). Association for Computing Machinery. <https://doi.org/10.1145/1644038.1644044>
- Tan, H. X., & Chan, M. C. (2010). A²-MAC: An adaptive anycast mac protocol for wireless sensor networks. In *2010 IEEE Wireless Communication and Networking Conference* (pp. 1-6). IEEE Conference Publication. <https://doi.org/10.1109/WCNC.2010.5506098>
- Vijayasharmila, S., Kumar, P. G., & Kamalesh, S. (2015). A survey on connected dominating sets (CDS) both in the wireless sensor networks and wireless ad hoc networks. *International Journal of Engineering Research & Technology*, 4(2), 898-905.

Zhou, D., Sun, M. T., & Lai, T. H. (2005). A timer-based protocol for connected dominating set construction in IEEE 802.11 wireless networks. In *The 2005 Symposium on Applications and the Internet* (pp. 2-8). IEEE Conference Publication. <https://doi.org/10.1109/SAINT.2005.9>

Speech Emotion Recognition Using Deep Learning LSTM for Tamil Language

Bennilo Fernandes* and Kasiprasad Mannepalli

Department of Electronics & Communication Engineering, Koneru Lakshmaiah Education Foundation, Guntur, Andhra Pradesh, India

ABSTRACT

Deep Neural Networks (DNN) are more than just neural networks with several hidden units that gives better results with classification algorithm in automated voice recognition activities. Then spatial correlation was considered in traditional feedforward neural networks and which do not manage speech signal properly to it extend, so recurrent neural networks (RNNs) were implemented. Long Short-Term Memory (LSTM) systems is a unique case of RNNs for speech processing, thus considering long-term dependencies Deep Hierarchical LSTM and BiLSTM is designed with dropout layers to reduce the gradient and long-term learning error in emotional speech analysis. Thus, four different combinations of deep hierarchical learning architecture Deep Hierarchical LSTM and LSTM (DHLL), Deep Hierarchical LSTM and BiLSTM (DHLB), Deep Hierarchical BiLSTM and LSTM (DHBL) and Deep Hierarchical dual BiLSTM (DHBB) is designed with dropout layers to improve the networks. The performance test of all four model were compared in this paper and better efficiency of classification is attained with minimal dataset of Tamil Language. The experimental results show that DHLB reaches the best precision of about 84% in recognition of emotions for Tamil database, however, the DHBL gives 83% of efficiency. Other design layers also show equal performance but less than the above models DHLL & DHBB shows 81% of efficiency for lesser dataset and minimal execution and training time.

Keywords: BiLSTM, DNN, Emotional Recognition, LSTM, RNN

ARTICLE INFO

Article history:

Received: 30 January 2021

Accepted: 15 April 2021

Published: 31 July 2021

DOI: <https://doi.org/10.47836/pjst.29.3.33>

E-mail addresses:

bennij05@gmail.com (Bennilo Fernandes)

mkasiprasad@gmail.com (Kasiprasad Mannepalli)

* Corresponding author

INTRODUCTION

Advanced pipeline consists of various protocols and hand-engineered creation method depend on top speech processing. They define an end-to-end language method,

named “Artificial Language” whereby machine learning overrules these steps in the process. The above method, combined with such a classification algorithm, produces improved speed on difficult language processing activities than conventional technique, while still being somewhat easier. Deep Speech performs admirably recently written approaches mostly on phone line. As the result, one should always elaborately design the parts of the network for reliability to enhance effectiveness on such a function like recognizing voice in a loud background. Under comparison, exploiting neural networks, the framework utilizes deeper processing end-to end. To strengthen the overall quality, we reap the benefits of its information represented by deep learning models to train through massive data.

In this article, the characteristics of LSTM, and BiLSTM were analyzed for emotional voice recognition implemented to Tamil emotional information set and used a suitable clustering technique. To classify data sets, distinct user defined classifiers are based end-to-end utilizing CTC. The paper is, as continues to follow, organized. First it describes integrated research in the community of emotional voice recognition and machine learning and then gives the brief introduction about RNN and its layers. Then describes the feature extraction variables that are implemented and details about the dataset collection. Then the research performed, and the outcome are reported. Followed by the conclusion and discussions.

MATERIALS AND METHODS

In deep learning more than 20 years ago, feed-forward neural network analysis was carried were examined (Liu, Z. T. et al., 2018; Cummins et al., 2017; Mustaqeem, & Kwon, 2020; Mannepalli et al., 2016a; Hussain et al., 2019). Recurrent neural networks and fully connected layers models were being used at almost the same time in voice recognition (Huang et al., 2019; Khan et al., 2019; Karim et al., 2019; Khalil et al., 2019). Most recent, with an almost all state-of-the-art speech task comprising a few other types of recurrent neural network, DNNs are becoming a feature throughout the ASR pipeline (Zhang et al., 2019; Tzirakis et al., 2018; Mannepalli et al., 2016b; Kumar et al., 2017). It has also been noticed that convolutionary networks are useful for acoustic systems (Badshah et al., 2019; He et al., 2016; Jiang, 2019; Wang et al., 2018). In nation-of-the-art recognizers, deep neural networks, generally LSTMs (Rao et al., 2018; Khamparia et al., 2019; Navyasri et al., 2017) are now just starting to be implemented and perform well coevolutionary layers for the retrieval of functions (Krizhevsky et al., 2012; Rao & Kishore, 2016; Ocquaye et al., 2019). It has also tested systems in both bidirectional and unidirectional recurrence. End-to-end emotional speech recognition is indeed a popular field of research that, when it is used to score the performances of DNN-HMM (Zeng & Xiao, 2019; Xie et al., 2018; Kishore & Prasad, 2016) shows promising performance. The RNN group performed well enough with graphemic results in emotional speech recognition. It is exposed that the

CTC-RNN system performed well during determining of emotional recognition although a vocabulary will still be required in either case (Sainath et al., 2015; Tzirakis et al., 2017; Ma et al., 2016). In addition, the CTC-RNN process were to be pre-trained with a DNN back propagation network provided by frame-wise formations first from HMM system (Zhang et al., 2018; Liu, B. et al., 2018; Ma et al., 2018; Sastry et al., 2016). In addition, without depending on the frame-wise groupings for preprocessing, we practice the CTC-RNN channels. To date, the exploitation of volume in neural networks has also been important to the field's success.

Recurrent Neural Network (RNN)

The Sequential data theory is used by RNNs. The RNN, a neural network with a recent memory that affects forecasting accuracy besides observations, sequences files contained in RNN memory is being used. In the conventional neural network, the concept of using RNN rather than the convolutional neural network is that any inputs are not dependent on one another. Therefore, use of recurrent neural networks in emotional speech processing is a better idea (Mustaqeem & Kwon, 2020).

LSTM

German researchers identified LSTM or Long Short-Term Memory with in mid-90s mostly as difference of its recurring channel to long short-term memory modules. It is indeed one generation closer with RNN. Whereas the issue of dimensionality reduction and explosion slope has been endured by a recurring channel, these were developed to the two issues described previous section. Analyzing the design methodology of LSTM, the layers of input and output are comparable to others in the RNN. In the center node or the replicating module, the difference lies. In LSTM, the repetition part uses 4 layers rather than one, as in RNN. Such layers come into contact with each other in LSTM, but this communication appears to be part of LSTM's decision-making procedure. The Figure 1 below shows the repetitive subsystem architecture.

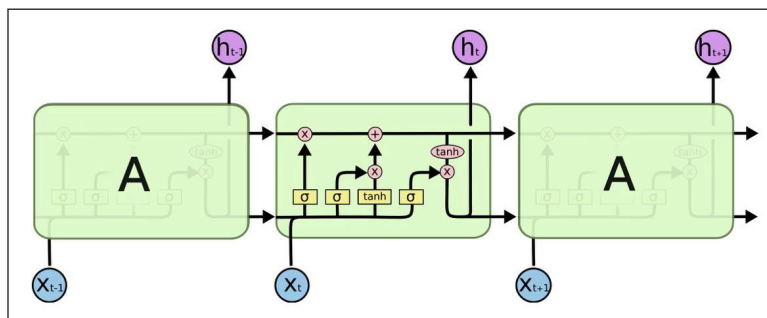


Figure 1. Sequential LSTM layer internal architecture

The line graph which represents plus, and cross symbol show the state of its node and behaves as major factor to LSTM. LSTM can change reflective process throughout the cell. It behaves like a chain which determines the amount of information from all 4 layers to also be handled. The '+' and 'X' represent the gates in each state of the cell. Gates chooses to either allow the data to next phase or not. Individuals are composed of an artificial neural layer including its sigmoid and a point wise procedure of multiplying. The sigmoid part provides the given number between 0 and 1, characterizing how often data to just let through in. Second, it is necessary to determine the latest data is stored throughout the total numbers, that is achieved by referencing the information of the input gate layer and the above-mentioned input training algorithm. Updating the new cell state will be the next input mode. Then it preceded by the objectives have been met computation, completed by the hidden layers of the output.

BiLSTM

Schuster and Paliwal (1997) developed bi-directional recurrent neural networks (BRNN) to incorporate 2 different hidden LSTM layers from reverse direction to almost the similar outcome to overcome the drawbacks of a singular LSTM cell which can only collect prior framework but not have the future context. By this architecture, the activation function can use the comparison to previous framework of specific aspects. The sequence input $x = (x_1, x_2, \dots, x_n)$ is measured by a BiLSTM again from reverse direction with a forward hidden pattern $\vec{h} = (\vec{h}_1, \vec{h}_2, \dots, \vec{h}_n)$ and a primitive hidden sequence $\overleftarrow{h} = (\overleftarrow{h}_1, \overleftarrow{h}_2, \dots, \overleftarrow{h}_n)$. The encrypted variable y_t , e, is established by the convolution including its finalized outputs forward and backward, $y_t = [\vec{h}_t, \overleftarrow{h}_t]$ (Equation 1-4).

$$\vec{h}_t = \sigma (W_{\vec{h}x}x_t + W_{\vec{h}\vec{h}}\vec{h}_{t-1} + b_{\vec{h}}) \tag{1}$$

$$\overleftarrow{h}_t = \sigma (W_{\overleftarrow{h}x}x_t + h_{\overleftarrow{h}t-1} + b_{\overleftarrow{h}}) \tag{2}$$

$$h_t = W_{hh}\vec{h}_t + W_{hh}\overleftarrow{h}_t + b_h \tag{3}$$

$$y_t = W_{\vec{h}y}\vec{h}_t + W_{\overleftarrow{h}y}\overleftarrow{h}_t + b_y \tag{4}$$

Where the throughput pattern of the first hidden units is $y = (y_1, y_2, \dots, y_n)$. In addition, there may be some relevant studies assistance to demonstrate that even a high system structure is much more effective than a simplistic one in portraying a few other functions. Thus, this paper has identified a layered BiLSTM network in which the y_t output again from lower layer will become the higher layer feedback. Figure 2 illustrates the loaded BiLSTM system.

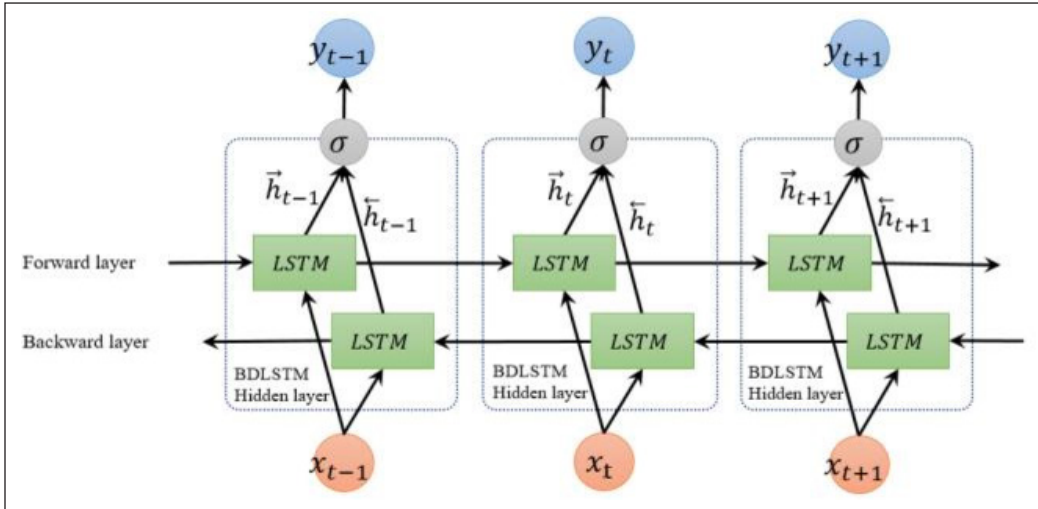


Figure 2. BiLSTM layer internal architecture

Describing $Q = (q_1, q_2, \dots, q_n)$ as well as $A = (a_1, a_2, \dots, a_n)$ to portray discussion patterns and response sequential output during which n and m signify the duration of the answers to questions including both q_t and a_t clearly show the responses to questions throughout the t -th sentences. To acquire their previous hidden structures, HQ and HA, a layered BiLSTM over the responses to questions, and the arithmetic is as continues to follow in which d seems to be the hidden layer factor (Equation 5-8).

$$h_t^q = sBiLSTM(h_{t-1}^q, h_{t+1}^q, q_t), h_0^q = 0, \quad [5]$$

$$h_t^a = sBiLSTM(h_{t-1}^a, h_{t+1}^a, a_t), h_0^a = h_n^q, \quad [6]$$

$$H_Q = [h_1^q, h_2^q, \dots, h_n^q] \in R^{d \times n} \quad [7]$$

$$H_A = [h_1^a, h_2^a, \dots, h_m^a] \in R^{d \times m} \quad [8]$$

Feature Extraction

Mel Frequency Cepstral Coefficients (MFCC). MFCC is determined by the characteristics of listening in the human ear, which simulates the human auditory system using a nonlinear frequency unit. The Fast Fourier Transform (FFT) technique is optimally used to transform, as explained in, each sample frame from the time domain into the frequency domain (Equation 9).

$$S[k] = \sum_{n=0}^{N-1} s[n] \cdot e^{-\frac{j2\pi nk}{N}}, 0 \leq k \leq N - 1 \quad [9]$$

The mel filter bank is composed of overlapping triangular filters with the cutoff frequencies determined by the two adjacent filters' center frequencies. The filtration has centre frequencies linearly distributed, and fixed mel scale bandwidth. The logarithm seems to have the impact, mentioned in, of shifting multiplier into addition (Equation 10).

$$F[m] = \log \sum_{n=0}^{N-1} |x[k]|^2 H_m[k], 0 \leq m \leq M \quad [10]$$

Ultimately, to find the MFCC, the Discrete Cosine Transform (DCT) of the log wavelet packet energy is computed (Equation 11).

$$c[n] = \sum_{m=1}^M s[n] \cdot e^{\frac{-j2\pi nk}{N}}, 0 \leq k \leq N - 1 \quad [11]$$

MFCC Delta

MFCC Delta, also known as variance and maximum speed coefficients. The features of MFCC vector explains only the power spectral functions of single frames, but in speech data the information will be obtained in dynamic values and more variation in features, what the trajectories of the MFCC features extracted are done with over time. It gives an out turns that calculating and appending the MFCC trajectories to the vectors of real and original features increases the performance of ASR by quite a bit (if we have 12 MFCC coefficients, we would also get 12 delta coefficients, which would combine to give a length 24 feature vector). The following formula is employed to calculate the delta coefficients (Equation 12):

$$d_t = \frac{\sum_{n=1}^N n(c_{t+n} - c_{t-n})}{2 \sum_{n=1}^N n^2} \quad [12]$$

where d_t is a delta coefficient, t frames are computed in terms of the static coefficients c_{t+n} to c_{t-n} . A typical value for N is 2.

The Bark Scale

It is based on the key throughput idea, is predictable underneath 500 Hz. e Bark scale outcomes from portraying an entire band of wavelengths with sequences of critical bands and not allowing to merge them. The Bark 1 to 24 numbers are the 24th critical band in the proceedings. Equivalent Rectangular Bandwidth ERB respective logarithmic and sequential; that every dimension is like Bark scale as it also offers an approximation of bandwidths of high noise filters, and therefore utilizes rectangular (unachievable recognition) band-pass filters to efficiently optimize filter modelling. The case hardening conversion would be between ERB and Hertz.

Spectral Kurtosis

The component associated with the execution of extracting features is spectral kurtosis, but it symbolizes the statistical relationship from both voice samples (Xie et al., 2018). Throughout the transmissions, the spectral kurtosis could still be described as the value of kurtosis of the variables of voice, and therefore is described as Equation 13:

$$F_5 = \frac{a_4\{S^*(m), S^*(m), S^*(m), S^*(m)\}}{a_2\{S^*(m), S^*(m)\}^2} \quad (13)$$

During which $S^*(m) \in \{S(m), S^c(m)\}$ the complicated conjugate of the process parameters $S^c(m)$ is demonstrated by $S(m)$ as well as the accumulated fourth and second order are stated by a_4 and a_2 .

Spectral Skewness

The spectral skewness (Wang et al., 2018) demonstrates the irregularities in the spectrum 's distribution of the voice signal on its average rating. The spectral skewness further assumes the energy level of its spectrum via transfer. Unless the energy size is low upon this distribution left side, it will be very strong if the spectral variable of skewness contains its speech signal.

Dataset

The emotional voice signals are recorded through mobile apps for training and research. All inputs are captured in 44KHz frequency mono signal. The samples collected were utilized for the simulation purpose. Speech information is obtained from 10 individual male and female speakers individually. Every speaker has been asked to utter 10 times each sentence in different emotions like anger, happy, sad, fear, disgust, neutral and boredom. The sentence I have taken is "Na nalla iruken ennaku onnum illa". Both male and female speakers report a total of 1400 emotional speech data samples. These samples were taken into consideration for this design flow analysis. A sentence-based samples were recorded by students of arts. For testing purpose, the samples were collected with co-working faculty to identify their emotions during their counselling period. Totally 50 samples were collected with same 44KHz through same mobile apps. Thus these 50 samples were tested to identify the emotions of working faculty. Since the training data base were collected by the professional actors, taking that Tamil emotional data as base the testing emotion database can be identified with more accuracy and perfection.

RESULTS AND DISCUSSION

With sequential data input, the emotional speech database is analyzed in this design layer. The speech signal is converted to LSTM / BiLSTM Layers as sequential vectors and

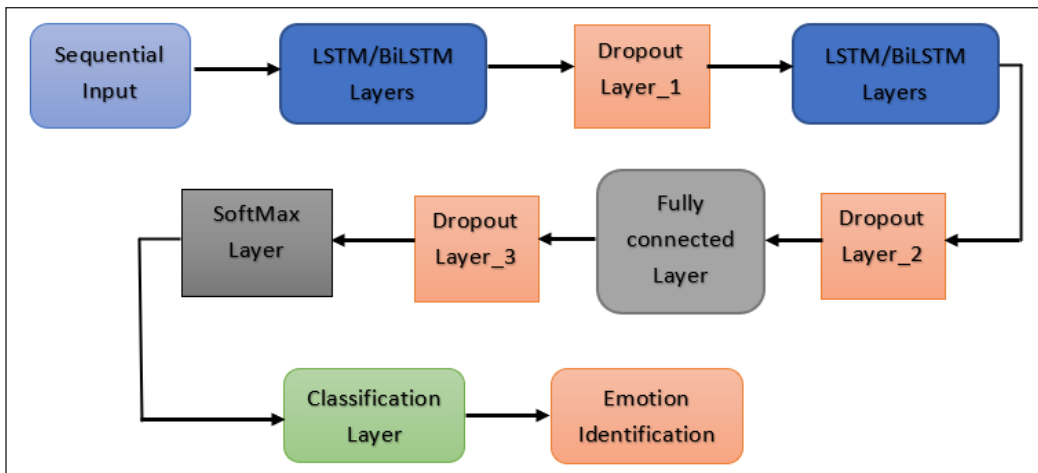


Figure 3. Proposed DNN design layer architecture

then passed to them. MFCC, MFCC delta, Bark spectrum, Spectral kurtosis and Spectral Skewness are the extraction characteristics selected for this design analysis shown in Figure 3. For testing and training, all the characteristics were examined and concatenated for each speech data to identifies its mean and standard deviation. The vector feature per sequence is assigned to 20 and total number of feature overlapping is 10. With these characteristics the evaluation for different design layer structures that have been fixed. Adam is the optimizing algorithm used here. The Adam optimization algorithm is applied to back-propagation, which has been utilized in many areas recently for the analysis of deep learning and other applications like artificial intelligence and computer vision. Integration, some of the common features of Adam, is directly forwarded for experimentation. Effectiveness in computation. Tiny specifications for recollection. Wavelet transform for adjusting patterns diagonal direction. Well suited for problems with information- and/or parameter-size. Good for goals that are non-stationary.

For very noisy/ or scattered gradients, an effective algorithm. Hyper-parameter interpretation is user-friendly and usually includes minor changes. Optionally, during each single era, the data must optimize the training weights numerous times. The volume of material which is included in almost every transformation in sub-epoch weight is known as the size of the batch. For example, with a 50-voice test set, an entire batch size would be 1000, a 500 or 200 or 100 mini batch size, and batch size will define the deep function of training and testing of data, thus mini batch size is set to 250 and for the evaluation, the number of hidden layers is 500 and the initial learning rate is 0.005 and the max epoch is 10. Well after the epoch increases, the iteration can increase the efficiency by continuously training data, but the accuracy and loss during iteration remain the same. The accuracy level of the training dataset after 10 epochs has not been modified. The timeline for the learning rate is piecemeal. Dropout is a method that addresses both problems. This prevents

overfitting and provides a way to effectively combine numerous different neural networks exponentially. The word dropout refers to the dropping out of units in a neural network (hidden and visible). In the simplest case, each unit is maintained with a fixed probability p , independent of other units, where p can be selected using a validation set or simply set to 0.5, which seems to be almost optimal for several networks and operations. The optimal retention probability, however, for the input units is generally closer to 1 than to 0.5. For design layer analysis three dropout layers were accomplished after each LSTM. The probability values are 0.5 each. The LSTM / BiLSTM design layer was analyzed by fixing all these parameters.

Deep Hierarchal LSTM&LSTM (DHLL) Model

As mentioned before the input speech signal is converted into the sequential data and processed to the dropout layer. The performance of the models is analyzed to reach a conclusion that DHLL model generates confusion matrix with 10-fold cross validation. Since cross folding is random each evaluation output shows different accuracy level a mean of 5 evaluation was considered for DHLL accuracy rate. Among the average 10 folds cross valuation fold 3 shows 85.7% of accuracy and fold 4 and 6 shows 83.98% of accuracy shown in Figure 4, where other folds also show better performance of accuracy around 70-80%. In the testing phase 50 samples of emotions were given as input for analysis of emotional recognition. From the 5 evaluation the best and higher accuracy level obtained in DHLL is 80.1%.

In the five evaluation the time taken to training and evaluation of classification timings were considered from Figure 5. While taking the mean value for training of DHLL takes around 7.86 Mins and to evaluate the classification it takes around 1.36 mins.

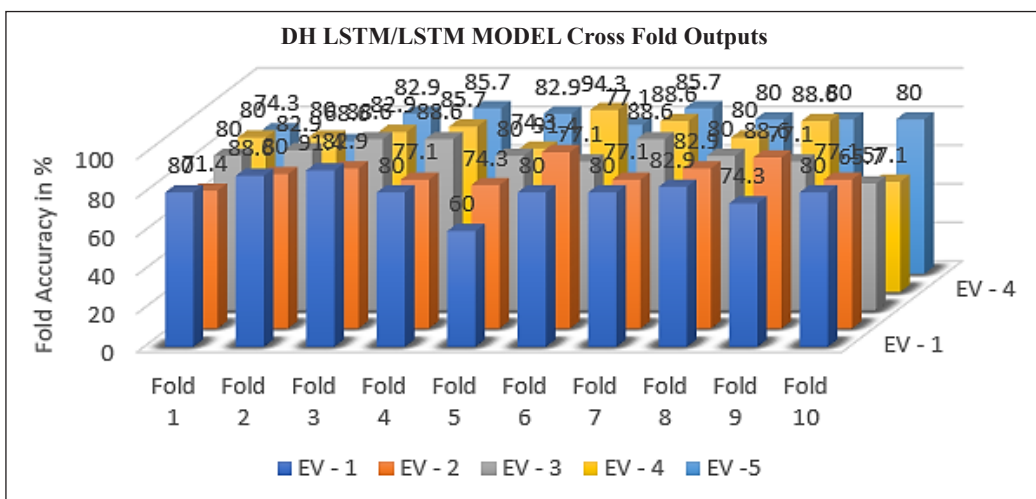


Figure 4. DHLL Cross fold output for multiple evaluation

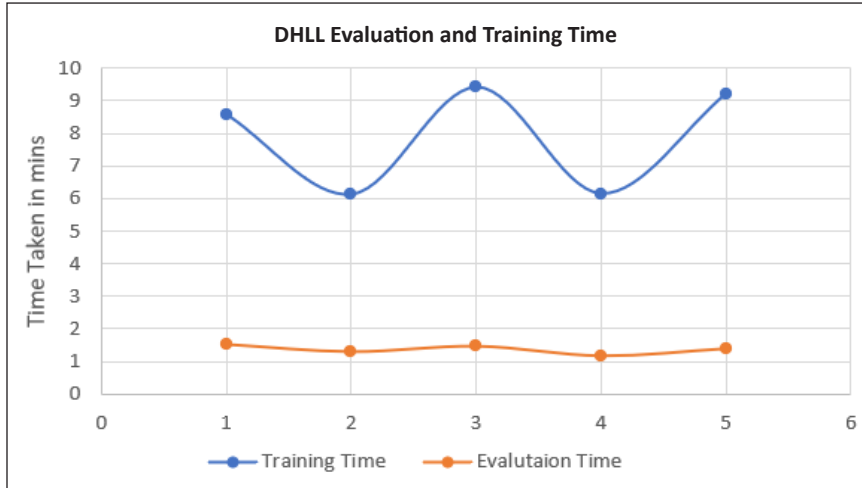


Figure 5. DHLL performance of evaluation time and training time

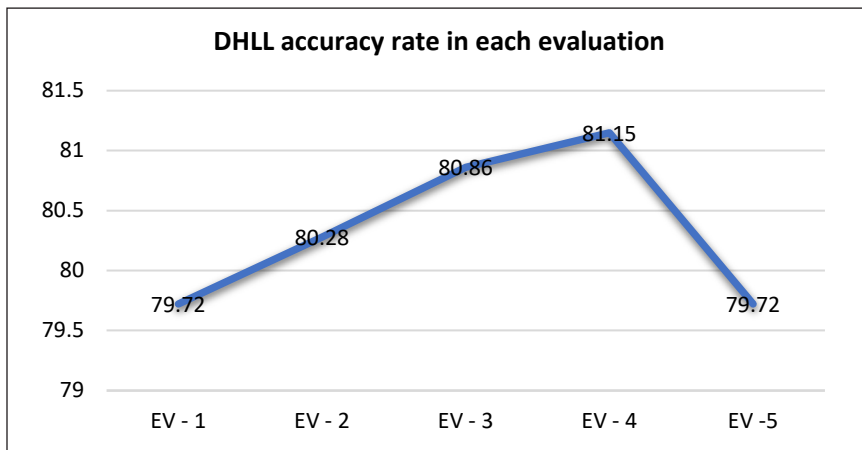


Figure 6. DHLL accuracy rate for 5 evaluations

Finally, by considering the higher accuracy level iteration it shows time taken is 6.14 and 1.18 for training and evaluation (Figure 6). Since the data set is recorded with 44khz of mono signal the evaluation time for training the dataset extend to 9.41mins, but the accuracy level is low than the best accuracy rate.

Thus, from Figure 6 its concluded that best accuracy obtained for Tamil emotional dataset in DH LSTM/LSTM model is 81.1%, but disgust is lagging at higher rate. From Figure 7, it is clear that still emotions like disgust are mapped or overlapped with other emotions like boredom and sadness. The confusion matrix shows emotions like anger and neutral shows better accuracy rate of 96% and 92%. Whereas other emotions have some average performance towards their own parent class. Emotion like sadness, disgust and happiness has only 68% of accuracy and 32% of loss can be seen in row normalization.

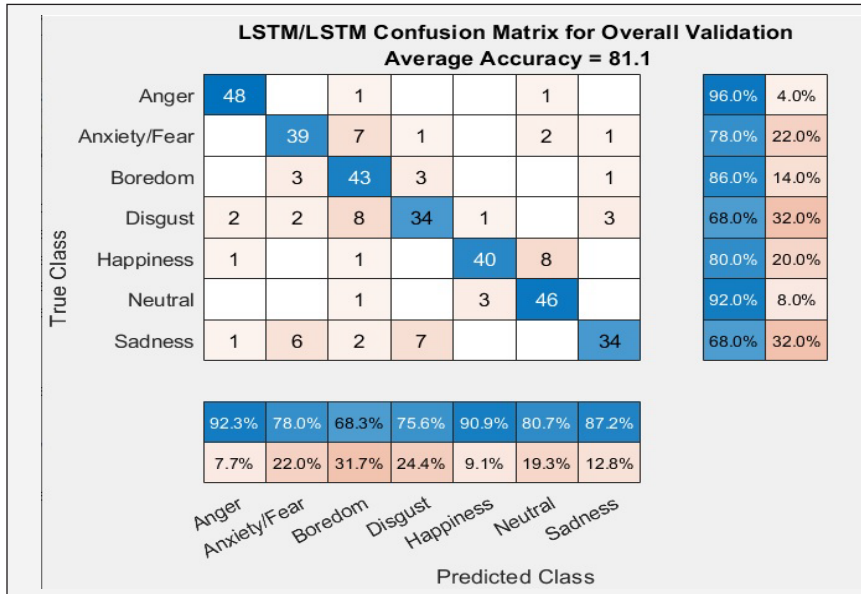


Figure 7. Cross fold confusion matrix for DHLL

Deep Hierarchal LSTM & BiLSTM (DHLB) Model

The performance of DHLB models is analyzed to reach a conclusion that DHLB model generates confusion matrix with 10-fold cross validation as final classification output. AS like DHLL max 5 times the simulation is evaluated to find the consistent in accuracy level. Among 5 simulation the average 10 folds cross valuation fold 3 shows 88.58% of accuracy and fold 2 and 9 shows 84.56% of accuracy shown in Figure 8, where other folds also show better performance of accuracy around 70-80%. In the testing phase same 50 samples of data used in DHLL is utilized for analysis. Each iteration there is a small variation in identification of emotional recognition. The average accuracy level for 5 evaluation is around 81.54%.

Now by analyzing the time factor the five evaluation the time taken to training and evaluation of classification timings were considered from Figure 9. While taking the mean value it is clear that for training of DHLB takes around 5.63 Mins and to evaluate the classification it takes around 1.05 mins.

From Figure 10 the accuracy level in each simulation is established. As the cross-validation folds are random the accuracy level changes randomly. But it lies in the range of 80 to 84. In each simulation the training time and the evaluation time also varies, but only seconds of variation can be identified. Among the 5 simulation results, in second iteration higher range of results is identified i.e., 83.43%.

Finally, by considering the higher accuracy level iteration it shows that for the given input Tamil database DHLB model gives 83.4% of efficiency (Figure 11).

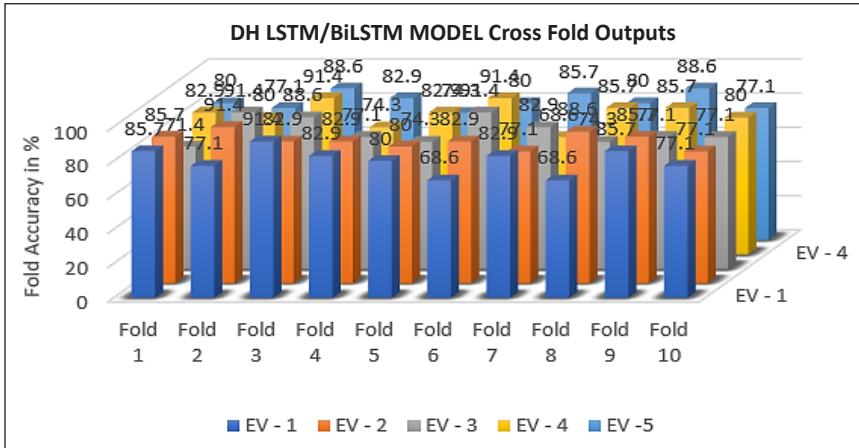


Figure 8. DHLB cross fold output for multiple evaluation

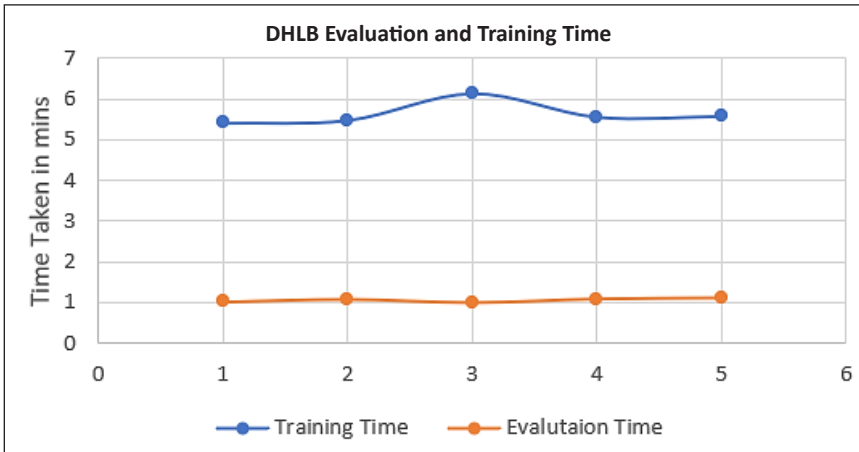


Figure 9. DHLB performance of evaluation time and training time

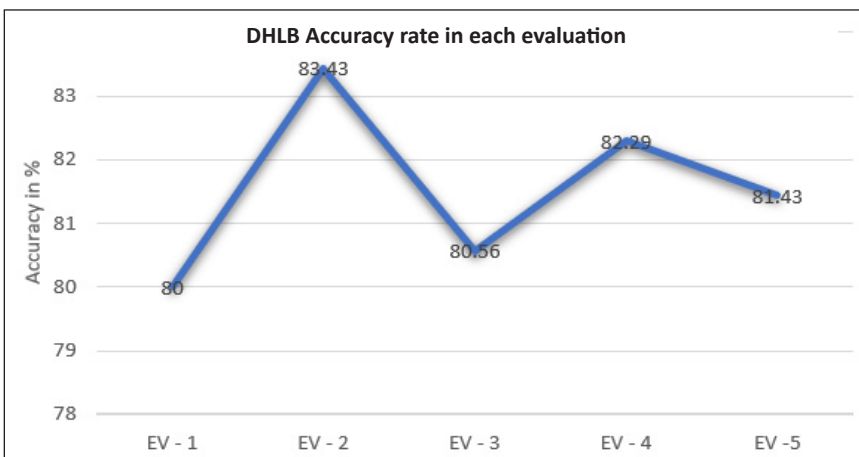


Figure 10. DHLB accuracy rate for 5 evaluations

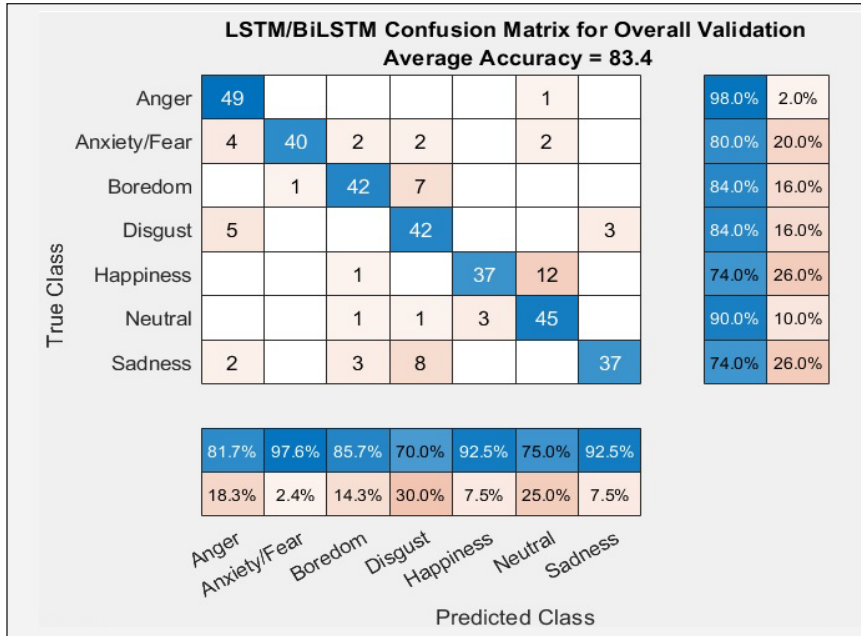


Figure 11. Cross fold confusion matrix for DHLB

In the confusion matrix, emotions like anger and neutral gives higher rate of 98% and 90%. As like DHLL this model also lags in other emotional states. Happy and Neutral emotions lags in DHLB model. Only 74% of accuracy is obtained in both states and shows lowest of all emotion recognition. Fear, Boredom and Disgust shows 80% and 84% of accuracy.

Deep Hierarchical BiLSTM & LSTM (DHBL) Model

The DHBL models is analyzed to reach a conclusion that DHBL technique generates confusion matrix with 10-fold cross validation as final classification output. As like DHLB max 5 times the simulation is evaluated to find the consistent in accuracy level. Among 5 simulation the average 10 folds cross valuation fold 6 shows 88.56% of accuracy and fold 5, 3, and 8 shows 84% and 82% of accuracy shown in Figure 12, where other folds also show better performance of accuracy around 70-80%. In the testing phase same 50 samples of data used in DHLL is utilized for analysis. Each iteration there is a small variation in identification of emotional recognition. The average accuracy level for 5 evaluation is around 81.3%.

Now by analyzing the time factor the five evaluation the time taken to training and evaluation of classification timings were considered from Figure 13. While taking the mean value it is clear that for training of DHBL takes around 10.4 Mins and to evaluate the classification it takes around 0.54 mins.

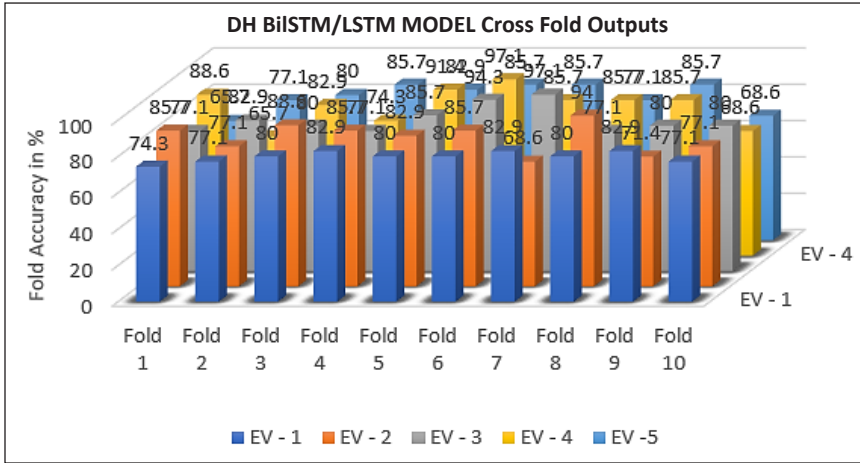


Figure 12. DHBL cross fold output for multiple evaluation

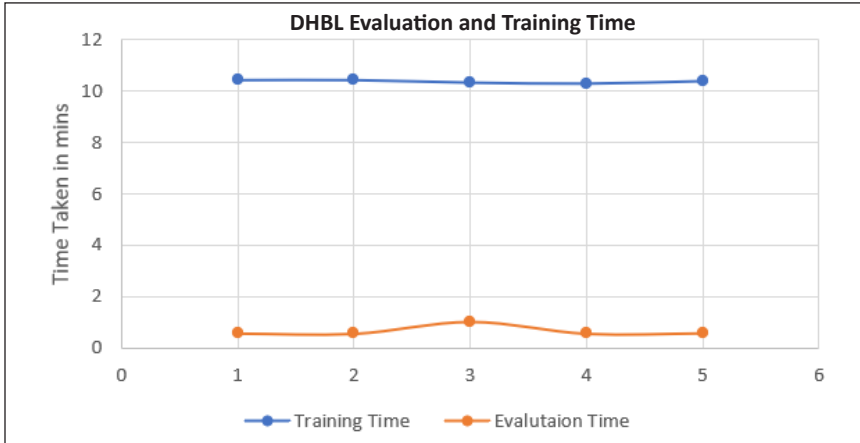


Figure 13. DHBL performance of evaluation time and training time

From Figure 14 the accuracy level in each simulation is established. As the cross-validation folds are random the accuracy level changes randomly. But it lies in the range of 79 to 84. In each simulation the training time and the evaluation time also varies, but only few seconds of variation can be identified. Among the 5 simulation results, in third iteration shows higher range of results is identified i.e., 83.13%.

Finally, by considering the higher accuracy level iteration it shows that for the given input Tamil database DHBL model gives 83.13% of efficiency (Figure 15). In the confusion matrix, emotions like anger and neutral gives higher rate of 98% and 92%. As like DHLL this model also lags in other emotional states. Disgust and Sadness emotions lags in DHBL model. Only 64% of accuracy is obtained in both disgust and sadness states and shows lowest of all emotion recognition. Fear, Boredom and Disgust shows 80% and 86% of accuracy.

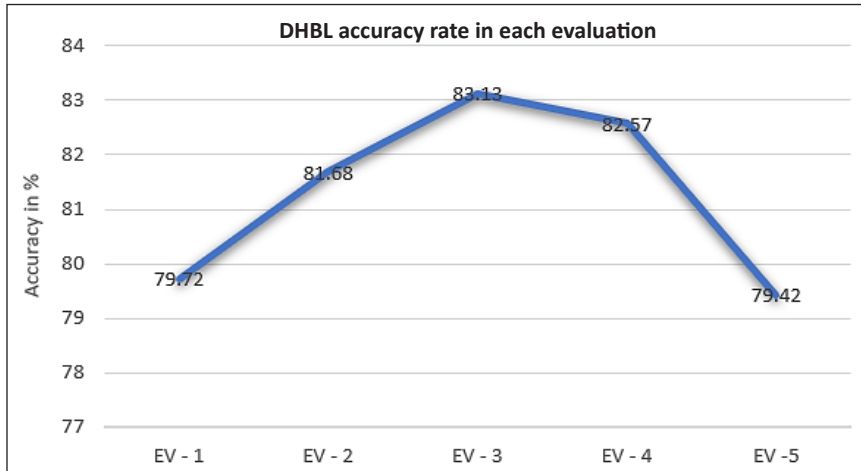


Figure 14. DHBL accuracy rate for 5 evaluations

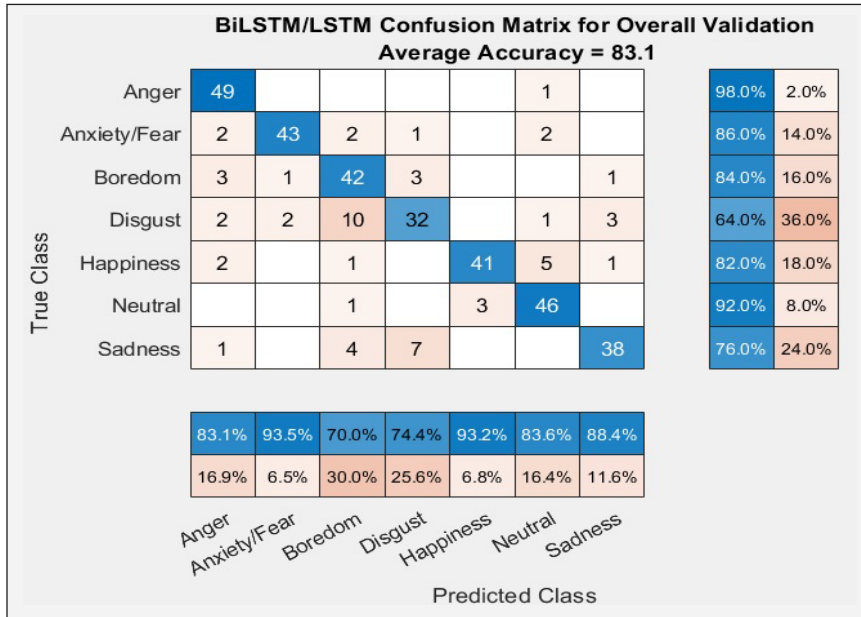


Figure 15. Cross fold confusion matrix for DHBL

Deep Hierarchical BiLSTM & BiLSTM (DHBB) Model

The DHBB models is analyzed to reach a conclusion that DHBB technique generates confusion matrix with 10-fold cross validation as final classification output. As like other models max 5 times the simulation is evaluated to find the consistent in accuracy level. Among 5 simulation the average 10 folds cross valuation fold 3 shows 86.26% of accuracy and fold 4 and 8 shows 80% of accuracy shown in Figure 16, where other folds also show better performance of accuracy around 70-80%.

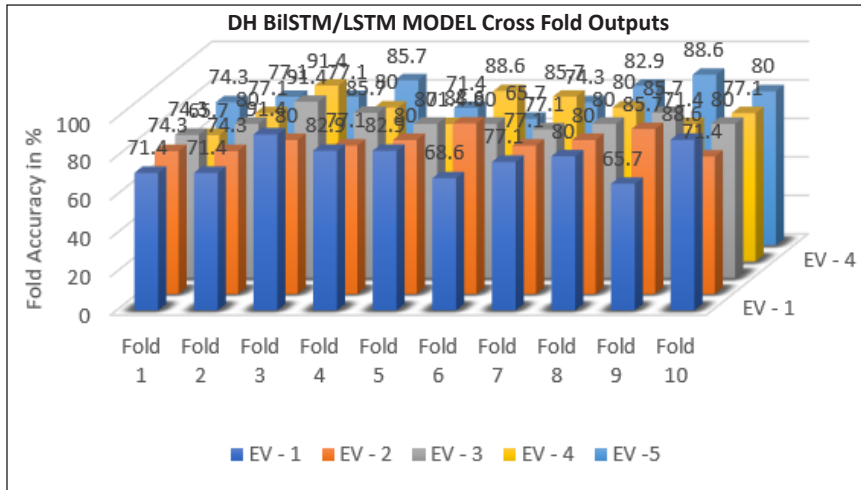


Figure 16. DHBB cross fold output for multiple evaluation

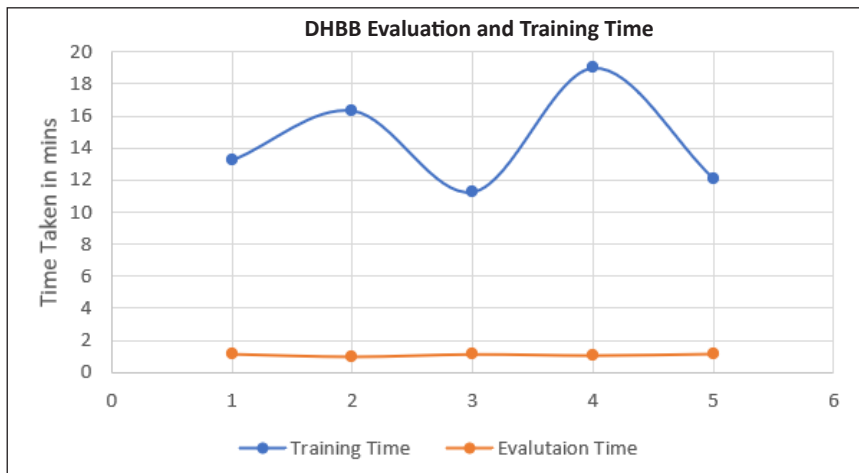


Figure 17. DHBB performance of evaluation time and training time

Each iteration there is a small variation in identification of emotional recognition. The average accuracy level for 5 evaluation is around 79.42%. Now by analyzing the time factor the five evaluation the time taken to training and evaluation of classification timings were considered from Figure 17. While taking the mean value it is clear that for training of DHBB takes around 14.3 Mins and to evaluate the classification it takes around 1.14 mins.

From Figure 18 the accuracy level in each simulation is established. As the cross-validation folds are random the accuracy level changes randomly. But it lies in the range of 78 to 82. In each simulation the training time and the evaluation time also varies, but only few seconds of variation can be identified. Among the 5 simulation results, in third iteration shows higher range of results is identified i.e., 83.13%.

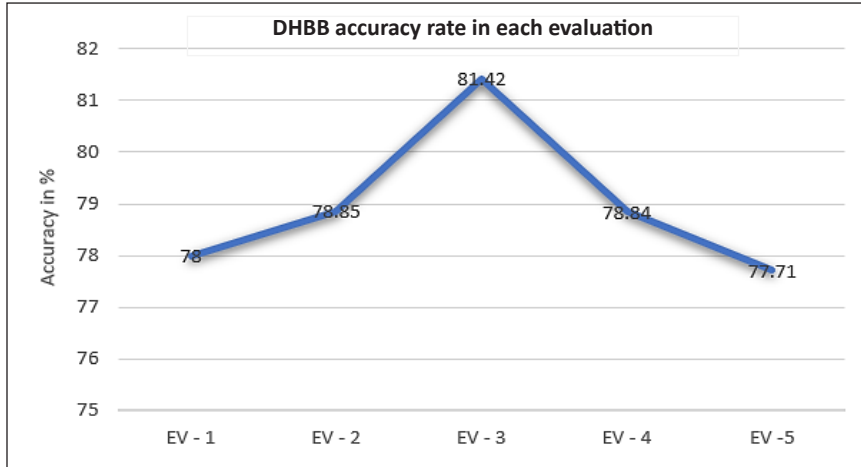


Figure 18. DHBB accuracy rate for 5 evaluations

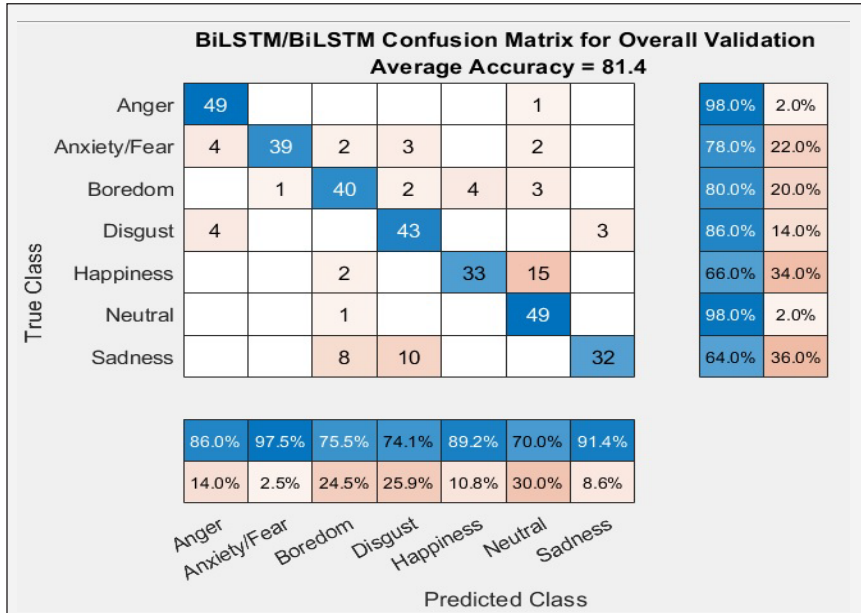


Figure 19. Cross fold confusion matrix for DHBB

Finally, by considering the higher accuracy level iteration it shows that for the given input Tamil database DHBB model gives 81.4% of efficiency (Figure 19).

In the confusion matrix, emotions like anger and neutral gives higher rate of 98%. As like DHLL this model also lags in other emotional states. Happiness and Sadness emotions lags in DHBB model. Only 64% of accuracy is obtained in both happiness and sadness states and shows lowest of all emotion recognition. Fear, Boredom and Disgust shows 80% and 86% of accuracy.

Table 1
Cross fold accuracy of DH LL/LB/BL/BB layers

Fold Accuracy/Methodology	DHLL	DHLB	DHBL	DHBB
Fold 1	80	81.7	77.1	74.3
Fold 2	80	97.4	82.9	80
Fold 3	82.9	82.9	80	91.4
Fold 4	85.7	82.9	77.1	85.7
Fold 5	74.3	80	85.7	80
Fold 6	94.3	82.9	94.3	80
Fold 7	88.6	77.1	97.1	77.1
Fold 8	80	86.6	77.1	80
Fold 9	88.6	85.7	80	85.7
Fold 10	57.1	77.1	80	80

Table 2
Overall performance of DH LL/LB/BL/BB models

Overall Performance (5 Iteration)	DHLL	DHLB	DHBL	DHBB
Best Accuracy	81.15	83.43	83.13	81.42
Average accuracy	80.346	81.542	79.42	78.964
Best Training Time	6.12	5.41	10.27	11.26
Average Training Time	7.89	5.634	10.378	11.388
Best Evaluation Time	1.18	1.01	0.56	1.01
Average Evaluation Time	1.368	1.056	0.656	1.114

Thus, Tables 1 and 2 show the overall performance of the entire designs. Comparing with all the models DHLB shows better performance than the other models. Also, DHBL also achieves equal performance to DHLB. Both the models give accuracy of 84% for the collected Tamil emotional database. Now comparing the training time for all models DHLB acts better than DHBL. Even though DHBL shows equal performance towards DHLB, it takes more time for training the database.

More than half of the time is reduced in DHLB. Also, from Figures 20 and 21, it is clear that in cross fold 2 achieves highest percentage of accuracy of 97.4%. Among all model only 5.41 mins were taken to train the database in DHLB model, whereas DHBL & DHBB takes around 11 mins to complete the training. After training the testing is done to identify the different emotional classification for the input 50 samples. In testing also DHLB shows better evaluation time than other models, it takes only 1.05 mins to complete the evaluation.

In most efficient DHLB gives better performance in RNN followed by DHBL it is most. The LSTM model takes the least time for training and evaluation, where other techniques take slightly more time and DHBB takes the highest time. The results obtained

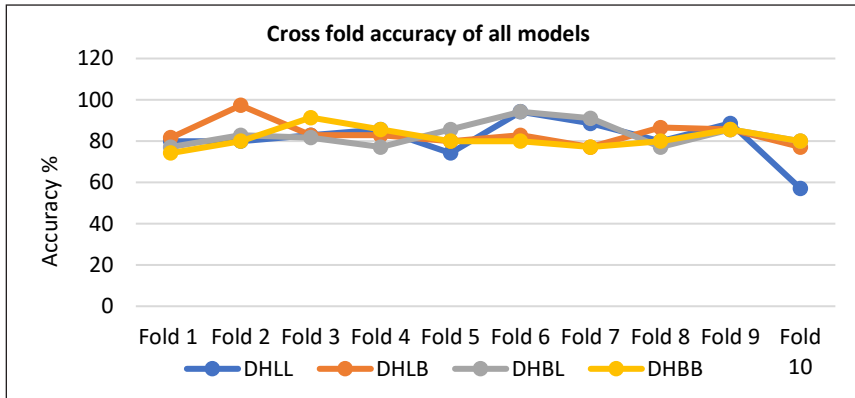


Figure 20. Cross fold accuracy of all different models

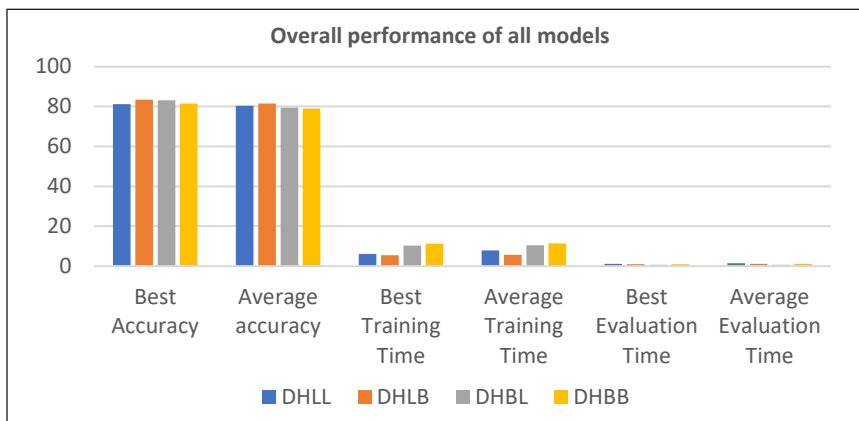


Figure 21. Overall Performance of all models

from different models are generated and presented effectively in this paper. We believe that further research can enhance this model and optimize it with lots of computation and data.

CONCLUSION

Since standard feedforward neural networks cannot handle speech data well (due to lacking a way to feed information from a later layer back to an earlier layer), thus, RNNs have been introduced to take the temporal dependencies of speech data into account. Furthermore, RNNs cannot handle the long-term dependencies due to vanishing/exploding gradient problem very well. Therefore, LSTMs and BiLSTM were introduced to overcome the shortcomings of RNNs. This paper evaluated RNN with hierarchal of LSTM and BiLSTM with dropout layers are compared their performances on interchanging the layers for a reduced Tamil emotional speech data set. Four different architectures were evaluated; DHLL, DHLB, DHBL and DHBB with dropout layers and the evaluation measures used were accuracy, loss, training time and evaluation time. The results show that the DHLB

performs better than other models. Accuracy rate of 84% is achieved with minimum loss in each seven basic emotions and time taken for training and evaluation is also less than the other models. Thus, the recommendation for the reduced Tamil emotional speech data set is to use DHLB since it returned good efficiency of recognition values within an acceptable running time. Future work will include parameter optimization to investigate the influence on different parameter settings. Furthermore, the learning rate, dropout rate as well as higher numbers of neurons in the hidden layers will be experimented with to get more better performance.

ACKNOWLEDGEMENT

Authors would like to acknowledge the management of KL University, AP, India for supporting this work and the faculty members who supported them for making the data available for this research.

REFERENCES

- Badshah, A. M., Rahim, N., Ullah, N., Ahmad, J., Muhammad, K., Lee, M. Y., Kwon, S., & Baik, S.W. (2019). Deep features-based speech emotion recognition for smart affective services. *Multimedia Tools and Applications*, 78(5), 5571-5589. <https://doi.org/10.1007/s11042-017-5292-7>.
- Cummins, N., Amiriparian, S., Hagerer, G., Batliner, A., Steidl, S., & Schuller, B. W. (2017). An image-based deep spectrum feature representation for the recognition of emotional speech. In *Proceedings of the 25th ACM international conference on Multimedia* (pp. 478-484). Association for Computing Machinery. <https://doi.org/10.1145/3123266.3123371>.
- He, K., Zhang, X., Ren, S., & Sun, J. (2016). Deep residual learning for image recognition. In *Proceedings of the IEEE conference on computer vision and pattern recognition* (pp. 770-778). Computer Vision Foundation. <https://doi.org/10.1109/CVPR.2016.90>.
- Huang, J., Chen, B., Yao, B., & He, W. (2019). ECG arrhythmia classification using STFT-based spectrogram and convolutional neural network. *IEEE Access*, 7, 92871-92880. <https://doi.org/10.1109/ACCESS.2019.2928017>.
- Hussain, T., Muhammad, K., Ullah, A., Cao, Z., Baik, S. W., & De Albuquerque, V. H. C. (2019). Cloud-assisted multiview video summarization using CNN and bidirectional LSTM. *IEEE Transactions on Industrial Informatics*, 16(1), 77-86. <https://doi.org/10.1109/TII.2019.2929228>.
- Jiang, S. (2019). Memento: An emotion-driven lifelogging system with wearables. *ACM Transactions on Sensor Networks (TOSN)*, 15(1), 1-23. <https://doi.org/10.1145/3281630>.
- Karim, F., Majumdar, S., & Darabi, H. (2019). Insights into LSTM fully convolutional networks for time series classification. *IEEE Access*, 7, 7718-67725. <https://doi.org/10.1109/ACCESS.2019.2916828>.
- Khalil, R. A., Jones, E., Babar, M. I., Jan, T., Zafar, M. H., & Alhussain, T. (2019). Speech emotion recognition using deep learning techniques: A review. *IEEE Access*, 7, 117327-117345. <https://doi.org/10.1109/ACCESS.2019.2936124>

- Khamparia, A., Gupta, G., Nguyen, N. G., Khanna, A., Pandey, B., & Tiwari, P. (2019). Sound classification using convolutional neural network and tensor deep stacking network. *IEEE Access*, 7, 7717-7727. <https://doi.org/10.1109/ACCESS.2018.2888882>.
- Khan, S. U., Haq, I. U., Rho, S., Baik, S. W., & Lee, M. Y. (2019). Cover the violence: A novel Deep-Learning-Based approach towards violence detection in movies. *Applied Sciences*, 9(22), Article 4963. <https://doi.org/10.3390/app9224963>.
- Kishore, P. V. V., & Prasad, M. V. D. (2016). Optical flow hand tracking and active contour hand shape features for continuous sign language recognition with artificial neural network. *International Journal of Software Engineering and its Applications*, 10(2), 149-170. <https://doi.org/10.1109/IACC.2016.71>
- Krizhevsky, A., Sutskever, I., & Hinton, G. E. (2012). Imagenet classification with deep convolutional neural networks. *Advances in Neural Information Processing Systems*, 25, 1097-1105. <https://doi.org/10.1145/3065386>.
- Kumar, K. V. V., Kishore, P. V. V., & Kumar, D. A. (2017). Indian classical dance classification with adaboost multiclass classifier on multi feature fusion. *Mathematical Problems in Engineering*, 20(5), 126-139. <https://doi.org/10.1155/2017/6204742>.
- Liu, B., Qin, H., Gong, Y., Ge, M., Xia, W., & Shi, L. (2018). EERA-ASR: An energy-efficient reconfigurable architecture for automatic speech recognition with hybrid DNN and approximate computing. *IEEE Access*, 6, 52227-52237. <https://doi.org/10.1109/ACCESS.2018.2870273>.
- Liu, Z. T., Wu, M., Cao, W. H., Mao, J. W., Xu, J. P., & Tan, G. Z. (2018). Speech emotion recognition based on feature selection and extreme learning machine decision tree. *Neurocomputing*, 273, 271-280. <https://doi.org/10.1016/j.neucom.2017.07.050>.
- Ma, X., Wu, Z., Jia, J., Xu, M., Meng, H., & Cai, L. (2018, September 2-6). Emotion Recognition from Variable-Length Speech Segments Using Deep Learning on Spectrograms. In *Interspeech* (pp. 3683-3687). Hyderabad, India. <https://doi.org/10.21437/Interspeech.2018-2228>.
- Ma, X., Yang, H., Chen, Q., Huang, D., & Wang, Y. (2016). Depaudionet: An efficient deep model for audio based depression classification. In *Proceedings of the 6th international workshop on audio/visual emotion challenge* (pp. 35-42). Association for Computing Machinery. <https://doi.org/10.1145/2988257.2988267>.
- Mannepalli, K., Sastry, P. N., & Suman, M. (2016a). FDBN: Design and development of fractional deep belief networks for speaker emotion recognition. *International Journal of Speech Technology*, 19(4), 779-790. <https://doi.org/10.1007/s10772-016-9368-y>
- Mannepalli, K., Sastry, P. N., & Suman, M. (2016b). MFCC-GMM based accent recognition system for Telugu speech signals. *International Journal of Speech Technology*, 19(1), 87-93. <https://doi.org/10.1007/s10772-015-9328-y>
- Mustaqeem, & Kwon, S. (2020). A CNN-assisted enhanced audio signal processing for speech emotion recognition. *Sensors*, 20(1), Article 183. <https://doi.org/10.3390/s20010183>.
- Navyasri, M., RajeswarRao, R., DaveeduRaju, A., & Ramakrishnamurthy, M. (2017). Robust features for emotion recognition from speech by using Gaussian mixture model classification. In *International Conference on Information and Communication Technology for Intelligent Systems* (pp. 437-444). Springer. https://doi.org/10.1007/978-3-319-63645-0_50.

- Ocquaye, E. N. N., Mao, Q., Song, H., Xu, G., & Xue, Y. (2019). Dual exclusive attentive transfer for unsupervised deep convolutional domain adaptation in speech emotion recognition. *IEEE Access*, 7, 93847-93857. <https://doi.org/10.1109/ACCESS.2019.2924597>.
- Rao, G. A., & Kishore, P. V. V. (2016). Sign language recognition system simulated for video captured with smart phone front camera. *International Journal of Electrical and Computer Engineering*, 6(5), 2176-2187. <https://doi.org/10.11591/ijece.v6i5.11384>
- Rao, G. A., Syamala, K., Kishore, P. V. V., & Sastry, A. S. C. S. (2018). Deep convolutional neural networks for sign language recognition. *International Journal of Engineering and Technology (UAE)*, 7(Special Issue 5), 62-70. <https://doi.org/10.1109/SPACES.2018.8316344>
- Sainath, T. N., Vinyals, O., Senior, A., & Sak, H. (2015). Convolutional, long short-term memory, fully connected deep neural networks. In *2015 IEEE international conference on acoustics, speech and signal processing (ICASSP)* (pp. 4580-4584). IEEE Conference Publication. <https://doi.org/10.1109/ICASSP.2015.7178838>.
- Sastry, A. S. C. S., Kishore, P. V. V., Prasad, C. R., & Prasad, M. V. D. (2016). Denoising ultrasound medical images: A block based hard and soft thresholding in wavelet domain. *International Journal of Measurement Technologies and Instrumentation Engineering (IJMTIE)*, 5(1), 1-14. <https://doi.org/10.4018/IJMTIE.2015010101>
- Schuster, M., & Paliwal, K. K. (1997). Bidirectional recurrent neural networks. *IEEE Transactions on Signal Processing*, 45(11), 2673-2681. <https://doi.org/10.1109/78.650093>.
- Tzirakis, P., Trigeorgis, G., Nicolaou, M. A., Schuller, B. W., & Zafeiriou, S. (2017). End-to-end multimodal emotion recognition using deep neural networks. *IEEE Journal of Selected Topics in Signal Processing*, 11(8), 1301-1309. <https://doi.org/10.1109/JSTSP.2017.2764438>.
- Tzirakis, P., Zhang, J., & Schuller, B. W. (2018). End-to-end speech emotion recognition using deep neural networks. In *2018 IEEE international conference on acoustics, speech and signal processing (ICASSP)* (pp. 5089-5093). IEEE Conference Publication. <https://doi.org/10.1109/ICASSP.2018.8462677>.
- Wang, H., Zhang, Q., Wu, J., Pan, S., & Chen, Y. (2018). Time series feature learning with labeled and unlabeled data. *Pattern Recognition*, 89, 55-66. <https://doi.org/10.1016/j.patcog.2018.12.026>
- Xie, Y., Liang, R., Tao, H., Zhu, Y., & Zhao, L. (2018). Convolutional bidirectional long short-term memory for deception detection with acoustic features. *IEEE Access*, 6, 76527-76534. <https://doi.org/10.1109/ACCESS.2018.2882917>.
- Zeng, M., & Xiao, N. (2019). Effective combination of DenseNet and BiLSTM for keyword spotting. *IEEE Access*, 7, 10767-10775. <https://doi.org/10.1109/ACCESS.2019.2891838>.
- Zhang, A., Zhu, W., & Li, J. (2019). Spiking echo state convolutional neural network for robust time series classification. *IEEE Access*, 7, 4927-4935. <https://doi.org/10.1109/ACCESS.2018.2887354>.
- Zhang, S., Zhang, S., Huang, T., & Gao, W. (2018). Speech emotion recognition using deep convolutional neural network and discriminant temporal pyramid matching. *IEEE Transactions on Multimedia*, 20(6), 1576-1590. <https://doi.org/10.1109/TMM.2017.2766843>.

An Analysis of Emotional Speech Recognition for Tamil Language Using Deep Learning Gate Recurrent Unit

Bennilo Fernandes* and Kasiprasad Mannepalli

Department of Electronics & Communication Engineering, Koneru Lakshmaiah Education Foundation, Guntur, Andhra Pradesh, India

ABSTRACT

Designing the interaction among human language and a registered emotional database enables us to explore how the system performs and has multiple approaches for emotion detection in patient services. As of now, clustering techniques were primarily used in many prominent areas and in emotional speech recognition, even though it shows best results a new approach to the design is focused on Long Short-Term Memory (LSTM), Bi-Directional LSTM and Gated Recurrent Unit (GRU) as an estimation method for emotional Tamil datasets is available in this paper. A new approach of Deep Hierarchical LSTM/BiLSTM/GRU layer is designed to obtain the best result for long term learning voice dataset. Different combinations of deep learning hierarchical architecture like LSTM & GRU (DHLG), BiLSTM & GRU (DHBG), GRU & LSTM (DHGL), GRU & BiLSTM (DHGB) and dual GRU (DHGG) layer is designed with introduction of dropout layer to overcome the learning problem and gradient vanishing issues in emotional speech recognition. Moreover, to increase the design outcome within each emotional speech signal, various feature extraction combinations are utilized. From the analysis an average classification validity of the proposed DHGB model gives 82.86%, which is slightly higher than other models like DHGL (82.58), DHBG (82%), DHLG (81.14%) and DHGG (80%). Thus, by comparing all the models DHGB gives prominent outcome of 5% more than other four models with minimum training time and low dataset.

ARTICLE INFO

Article history:

Received: 04 February 2021

Accepted: 01 April 2021

Published: 31 July 2021

DOI: <https://doi.org/10.47836/pjst.29.3.37>

E-mail addresses:

bennij05@gmail.com (Bennilo Fernandes)

mkasiprasad@gmail.com (Kasiprasad Mannepalli)

* Corresponding author

Keywords: Bi-Directional Long Short-Term Memory, emotional recognition, Gated Recurrent Unit, Long Short-Term Memory

INTRODUCTION

Deep learning is applied often for identify a large course of various layers of cells generated by neural networks. For many years neural network is utilized in emotional recognition, in brief. Deep architecture mechanism is practiced in huge area may even though there are some other tech innovations in such development and rapid, the significant rise in processing method using GPUs has done it much easier to analyzes bigger sets of data (Kumar et al., 2017; Mannepalli et al., 2016a; Li et al., 2014). Deep learning models have several applications in various fields, but in the domain of speech processing in specific, numerous accomplishments were seen. For instance, a machine learning design called Convolutional Neural Networks (CNNs) is designed to replicate the actions of the cerebral system (Rao et al., 2018; Schwarz et al., 2015; Ravanelli et al., 2016). The issue of speaker identification contains data from time-series. Feedforward neural networks are unilateral in which the outcomes of one layer are directed to the next layer. Such feedforward networks are unable to preserve past data. Furthermore, so if Deep Neural Network (DNN) is optimized to evaluate speech recognition predefined challenges are caused, such as separate talking rates and spatial dependencies (Srivastava et al., 2014; Mannepalli et al., 2016b; Ioffe & Szegedy, 2015). DNNs can hardly design review the existing acoustic screen windows that they are unable to describe various talking rates (Abdel-Hamid et al., 2014; Sastry et al., 2016; Zhang et al., 2016; Rao & Kishore, 2016). A whole other system course that includes sequences in the input units to anticipate the value of a particular period venture by maintaining the relevant data at the previous iteration is the Recurrent Neural Network (RNN). The whole process facilitates RNNs to control different talking rates.

In this article, the characteristics of LSTM, BiLSTM, and GRU were analyzed for emotional voice recognition implemented to Tamil emotional information set and used a suitable clustering technique. To classify data sets, distinct user defined classifiers are based end-to-end utilizing Connectionist Temporal Classification (CTC) (Liu et al., 2014). The integrated research in the community of emotional voice recognition and machine learning. The methodology gives the brief introduction about RNN and its layers. Followed by the feature extraction variables that are implemented. Then the dataset collection and its details were described in brief perspective. With the collected data research performance and the outcome are reported and followed by the conclusion and discussions are provided by comparing the other models.

MATERIALS AND METHODS

Historically, conceptual models are based for computer vision. Usually, iterative methods consist of Maximum-A-Posteriori (MAP) assessment, Gaussian Mixture Models (GMMs), and Hidden Markov Models (HMM) (Kishore et al., 2016; Ravanelli et al., 2017; Zhou et al., 2016). Such existing methods require significant knowledge (i.e., understanding of a

specific word) and fully Automated Speech Recognition (ASR) document preprocessing. For several problems, dialect simulation is crucial, including such speaker recognition, machine translation or channels offered. To plot patterns to feature vectors, both RNNs and LSTMs have also been used. As outlined, LSTM communication techniques are seen to be greater than regular modeling RNNs for Context Free Language (CFL) and Context Sensitive Language (CSL) (Hochreiter & Schmidhuber, 1997; Graves et al., 2013; Krizhevsky et al., 2012). Additionally, Graves et al. (2013) also introduced deep LSTM RNNs and assessed the voice recognition structure. On a led to a large language processing problem, the quality of LSTM, RNN and DNN configurations has been analyzed and compared (Sak et al., 2014; Chen et al., 2015; Weninger et al., 2015). A few tests are done also on TIMIT voice information source utilizing BiLSTM, deep BiLSTMs, RNNs, and modified configurations. BiLSTM systems were used during the phonology training set. Outcomes have also established that symmetric LSTM connection information unlike nonlinear LSTM and conventional RNNs on clip-wise phonetic categorization.

The classification data demonstrate that bi - directional LSTM is an appropriate design for speaker recognition under which data sets is essential. Recurrent neural networks of Gated Recurrent Units (GRU) have been created (Erdogan et al., 2015; Eyben et al., 2013; Pascanu et al., 2013). GRUs has some similarity to LSTMs, both of which have been modelled to deal with long-term dependence. GRUs do, even then, get a fewer component unlike LSTMs. All other designs were used for harmonic soundtrack simulation and for voice recognition projects. The findings demonstrate which GRUs are highly useful as LSTMs. The method is linked, which uses a symmetric RNN to accelerate up the quality of voice recognition. To assess and analyze the outcomes of normal appearing channels, notably bi - directional RNN, bidirectional LSTM, and bidirectional GRU, shows better outcome for the collected Tamil emotional database.

Recurrent Neural Network (RNN)

The training algorithm composed of cells is RNN or Recurring Neural Network. As everyone and every nerve cell is using its inner memory for storing records of various instruction, it is indeed primarily important when analyzing data sets. In RNN, with exception of preceding neural networks in which past simulations output must be identified in ability to forecast the next results, the sector relies on supplied data. It is possible to think of RNN also as system which conveys all arithmetic or remembers every sequence that was occurred so far What this implies exactly would be that input signals are considered by RNN one would be the recent information, and the prior computational complexity behave as the next input (Jozefowicz et al., 2015; Chung et al., 2014; Laurent et al., 2016). It includes an input data, neurons in the hidden layer, like many other neural networks.

LSTM

The intense active learning for storing significant data using Neural Network have not ever attains the optimum level of the system. This is majorly when the regressive procedure known decaying slope, the relative error disappears. In 1997, Hochreiter and Schmidhuber analyzed the problem of back propagation and made a new algorithm named Long-Short Term Memory (LSTM) for Neural Networks. In LSTM layer, there have been 4 new hidden layers introduced to the neural network and titled gates (Figure 1) (Weninger et al., 2015).

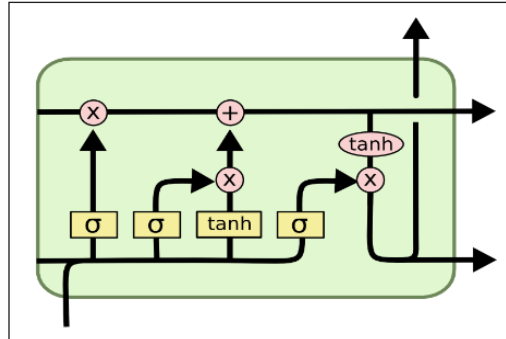


Figure 1. Sequential LSTM layer internal architecture

BiLSTM

Its efficiency at period “t” in BiLSTM itself is not like past because next sections including its pattern in a singular segment. Such as two parallel RNNs, symmetric RNNs, it only means going forward, or it ends up going downward and computes the mutual production between both RNNs based on everyone's previous hidden. In this study, humans then use multilayered idea of the LSTM model, using two-layer system with both primitive and the forward passage in our procedure. The total principle of its recommended layered BiLSTM.

The interior design can be seen in the given Figure 2, which symbolizes the bidirectional RNN preprocessing step and combines this same internal layer including forward and regressive passage in the output units (Graves et al., 2013). The system is verified on 50% information, which again is divided again from learning process and utilize pass-entropy to calculate the failure rate also in test dataset. Adam optimization with 0.001 training data can be used for production efficiency. Either forward or regressive passage throughout the deep BiLSTM system consists of materials that deepen everyone's system to measure the

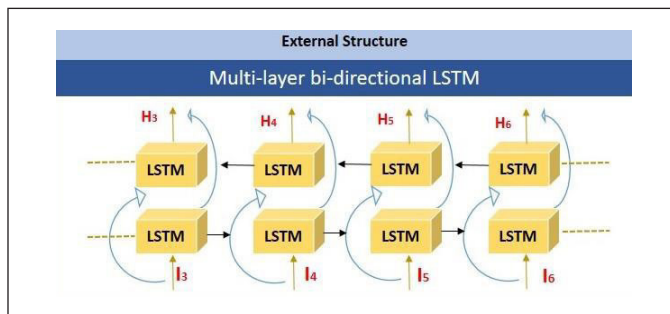


Figure 2. BiLSTM layer internal architecture

outcome in moment again from previous then next pattern as its system was performing in both paths.

GRU

RNNs constitute another very role to fulfil capable of learning short and long-term voice constraints. After all, RNNs could even possibly obtain spatial features in a vibrant way, enabling this same system to openly calculate the type of relevant data to be used for every other sequence of the moment. And these so-called gated RNNs, where its main premise is to incorporate a stacking method to help support this same data exchange thru the varying time stages, are a popular pattern.

Shortest path problems were also remedied inside this design relatives by developing better “alternate routes” where the patterns could even disable appropriate information stages shown in Figure 3. The latest book system called GRU, which is premised only on four multiplier doors, will have spurred to a notable effort to clarify LSTMs. The conventional GRU building is characterized, through specific, by given Equations 1-4:

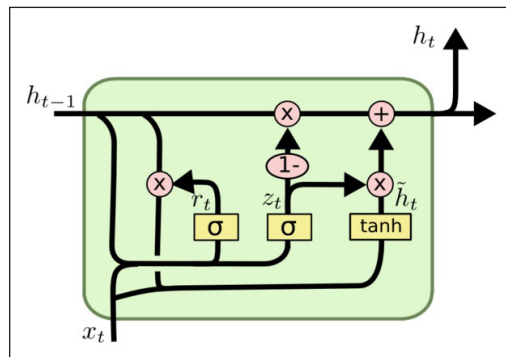


Figure 3. GRU layer internal architecture

$$z_t = \sigma(W_z x_t + U_z h_{t-1} + b_z) \tag{1}$$

$$r_t = \sigma(W_r x_t + U_r h_{t-1} + b_r) \tag{2}$$

$$\tilde{h}_t = \tanh(W_h x_t + U_h (h_{t-1} \Theta r_t) + b_h) \tag{3}$$

$$h_t = z_t \Theta h_{t-1} + (1 - z_t) \Theta \tilde{h}_t \tag{4}$$

In which, in both, z_t and r_t were also formulas relating to the official release and refresh gates, even as h_t is really the scale parameter for both the existing time t . There are element-wise algebraic expressions indicated with Θ . Logistic sigmoid $\sigma(\cdot)$ operates seem to be the detections between both gates, which restrict z_t and r_t to ideals scale between 0 and 1. The existing original input x_t (e.g., a variable of function generators) feeds the system, whereas the method variables are now the matrix W_z, W_r, W_h (the feed-forward connexions) and U_z, U_r, U_h (the repeated strength training). Eventually, the design requires b_z, b_r, b_h adaptable partiality matrices, which are introduced prior to applying the variations.

Just like illustrated in Equation 3, intermolecular interaction between both the gene transcription h_{t-1} and the candidate running level h_t is 1d, the present state node \tilde{h}_t . This same measurement variables are set by the z_t formative assessments, which chooses what else their transactions would be updated by components. The critical feature besides learning these dependencies was that sequential imputation. In reality, unless z_t is near to just one, this same opening area is held constant and therefore can remain constant after an unreasonable sequence of iterations in moment. From other side, if z_t is near to 0, this same system strongly favors h_t , which varies depending extra strongly mostly on existing hidden and output states closer to it. The assert of the applicant \tilde{h}_t .

Feature Extraction

Mel Frequency Cepstral Coefficients (MFCC). MFCC is determined by the characteristics of listening in the human ear, which simulates the human auditory system using a nonlinear frequency unit. The Fast Fourier Transform (FFT) technique is optimally used to transform, as explained in Equation 5, each sample frame from the time domain into the frequency domain.

$$S[k] = \sum_{n=0}^{N-1} s[n] \cdot e^{\frac{-j2\pi nk}{N}}, 0 \leq k \leq N - 1 \quad [5]$$

The mel filter bank is composed of overlapping triangular filters with the cutoff frequencies determined by the two adjacent filters' centre frequencies. The filtration has centre frequencies linearly distributed, and fixed mel scale bandwidth. The logarithm seems to have the impact, mentioned in Equation 6, of shifting multiplier into addition.

$$F[m] = \log \sum_{n=0}^{N-1} |x[k]|^2 H_m[k], 0 \leq m \leq M \quad [6]$$

Ultimately, to find the MFCC, the Discrete Cosine Transform (DCT) of the log wavelet packet energy is computed as Equation 7.

$$c[n] = \sum_{m=1}^M s[n] \cdot e^{\frac{-j2\pi nk}{N}}, 0 \leq k \leq N - 1 \quad [7]$$

MFCC Delta

MFCC Delta, also known as variance and maximum speed coefficients. The features of MFCC vector explains only the power spectral functions of single frames, but in speech data the information will be obtained in dynamic values and more variation in features, what the trajectories of the MFCC features extracted are done with over time. It gives an out turns that calculating and appending the MFCC trajectories to the vectors of real and

original features increases the performance of ASR by quite a bit (if we have 12 MFCC coefficients, we would also get 12 delta coefficients, which would combine to give a length 24 feature vector). The following Equation 8 is employed to calculate the delta coefficients.

$$d_t = \frac{\sum_{n=1}^N n(c_{t+n} - c_{t-n})}{2 \sum_{n=1}^N n^2} \quad [8]$$

Where d_t is a delta coefficient, t frames are computed in terms of the static coefficients c_{t+n} to c_{t-n} . A typical value for N is 2.

The Bark Scale

It is based on the key throughput idea, is predictable underneath 500 Hz. e Bark scale outcomes from portraying an entire band of wavelengths with sequences of critical bands and not allowing to merge them. The Bark 1 to 24 numbers are the 24th critical band in the proceedings. Equivalent Rectangular Bandwidth ERB respective logarithmic and sequential; that every dimension is like Bark scale as it also offers an approximation of bandwidths of high noise filters, and therefore utilizes rectangular (unachievable recognition) band-pass filters to efficiently optimize filter modelling. The case hardening conversion would be between ERB and Hertz.

Spectral Kurtosis

The component associated with the execution of extracting features is spectral kurtosis, but it symbolizes the statistical relationship from both voice samples. Throughout the transmissions, the spectral kurtosis could still be described as the value of kurtosis of the variables of voice, and therefore is described as Equation 9,

$$F_5 = \frac{a_4\{S^*(m), S^*(m), S^*(m), S^*(m)\}}{a_2\{S^*(m), S^*(m)\}^2} \quad [9]$$

During which $S^*(m) \in \{S(m), S^c(m)\}$ the complicated conjugate of the process parameters $S^c(m)$ is demonstrated by $S(m)$ as well as the accumulated fourth and second order are stated by a_4 and a_2 .

Spectral Skewness

The spectral skewness demonstrates the irregularities in the spectrum 's distribution of the voice signal on it is average rating. The spectral skewness further assumes the energy level of it is spectrum via transfer. Unless the energy size is low upon this distribution left side, it will be very strong if the spectral variable of skewness contains its speech signal.

Dataset

The emotional voice signals are recorded through mobile apps for training and research. All inputs are captured in 44KHz frequency mono signal. The samples collected were utilized for the simulation purpose. Speech information is obtained from 10 individual male and female speakers individually. Every speaker has been asked to utter 10 times each sentence in different emotions like anger, happy, sad, fear, disgust, neutral and boredom. Both male and female speakers report a total of 1400 emotional speech data samples. These samples were taken into consideration for this design flow analysis. A sentence-based samples were recorded by students of arts. For testing purpose, the samples were collected with co-working faculty to identify their emotions during their counselling period. Totally 50 samples were collected with same 44KHz through same mobile apps. Thus these 50 samples were tested to identify the emotions of working faculty. Since the training data base were collected by the professional actors, taking that Tamil emotional data as base the testing emotion database can be identified with more accuracy and perfection.

RESULTS AND DISCUSSION

With sequential data input, the emotional speech database was analyzed in this design layer. The speech signal was converted to LSTM / BiLSTM / GRU Layers as sequential vectors and then passed to them. The MFCC, MFCC delta, Bark spectrum, Spectral kurtosis & Spectral Skewness are the extraction characteristics selected for this design analysis (Figure 4). For testing and training, all the characteristics were examined and concatenated for each speech data to identifies its mean and standard deviation. The vector feature per sequence is assigned to 20 and total number of feature overlapping is 10. With these characteristics the evaluation for different design layer structures that have been fixed. Adam is the optimizing algorithm used here. The Adam optimization algorithm is applied to back-propagation, which has recently seen wider adoption for deep learning applications in computer vision and artificial intelligence processing.

Integration, some of the common features of Adam, is directly forwarded for experimentation. Effectiveness in computation. Tiny specifications for recollection. Wavelet transform for adjusting patterns diagonal direction. Well suited for problems with information- and/or parameter-size. Good for goals that are non-stationary. For very noisy/ or scattered gradients, an effective algorithm. Hyper-parameter interpretation is user-friendly and usually includes minor changes. Optionally, during each single era, the data must optimize the training weights numerous times. The volume of material which is included in almost every transformation in sub-epoch weight is known as the size of the batch. For example, with a 50-voice test set, an entire batch size would be 1000, a 500 or 200 or 100 mini batch size, and batch size will define the deep function of training and testing of data, thus mini batch size is set to 250 and for the evaluation, the number

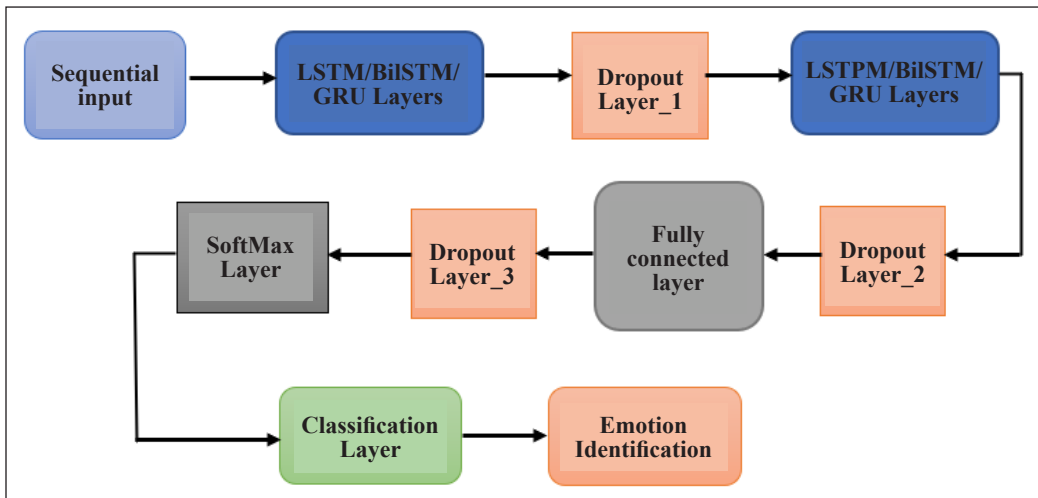


Figure 4. Proposed design flow architecture

of hidden layers is 500 and the initial learning rate is 0.005 and the max epoch is 10. Well after the epoch increases, the iteration can increase the efficiency by continuously training data, but the accuracy and loss during iteration remain the same. The accuracy level of the training dataset after 10 epochs has not been modified. The timeline for the learning rate is piecemeal. Dropout is a method that addresses both problems. This prevents overfitting and provides a way to effectively combine numerous different neural networks exponentially. The word dropout refers to the dropping out of units in a neural network (hidden and visible). In the simplest case, each unit is maintained with a fixed probability p , independent of other units, where p can be selected using a validation set or simply set to 0.5, which seems to be almost optimal for several networks and operations. The optimal retention probability, however, for the input units is generally closer to 1 than to 0.5. For design layer analysis three dropout layers were accomplished after each LSTM /BiLSTM /GRU. The probability values are 0.5 each. The LSTM /BiLSTM /GRU design layer was analyzed by fixing all these parameters.

Deep Hierarchal LSTM & GRU (DHLG) Model

As mentioned before the input speech signal is converted into the sequential data and processed to the dropout layer. The performance of the models is analyzed to reach a conclusion that DHLG model generates confusion matrix with 10-fold cross validation. Since cross folding is random each evaluation output shows different accuracy level a mean of 5 evaluation was considered for DHLG accuracy rate.

Among the average 10 folds cross valuation fold 2 and 4 shows 88.6% of accuracy and fold 3 and 7 shows 85.72% of accuracy, where other folds also show better performance

of accuracy around 65 -80% (Figure 5). In the testing phase 50 samples of emotions were given as input for analysis of emotional recognition. From the 5 evaluation the best and higher accuracy level obtained in DHLG is 81.1%.

Now by analyzing the time factor the five evaluation the time taken to training and evaluation of classification timings were considered and shown in Figure 6. While taking the mean value it is clear that for training of DHLG takes around 7.11 mins and to evaluate the classification it takes around 1.06 mins.

From Figure 7 the accuracy level in each simulation is established. As the cross-validation folds are random the accuracy level changes randomly. But it lies in the range of 76 to 82. In each simulation the training time and the evaluation time also varies, but only seconds of variation can be identified. Among the 5 simulation results, in fifth iteration higher range of results is identified i.e., 81.14%.

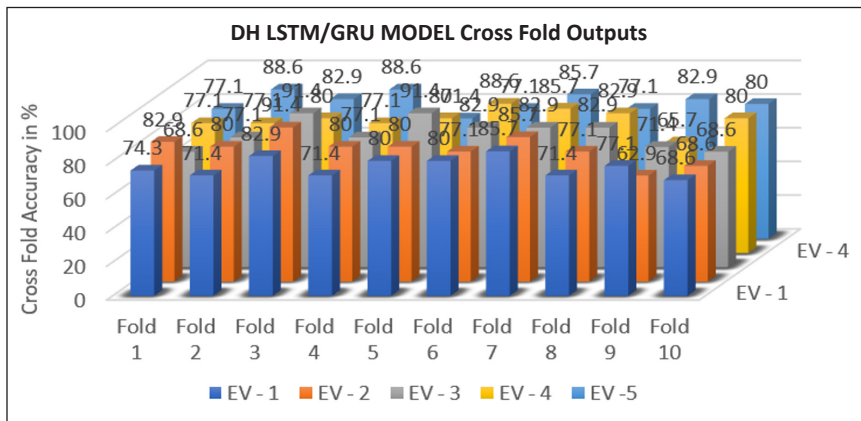


Figure 5. DHLG Cross fold output for multiple evaluation

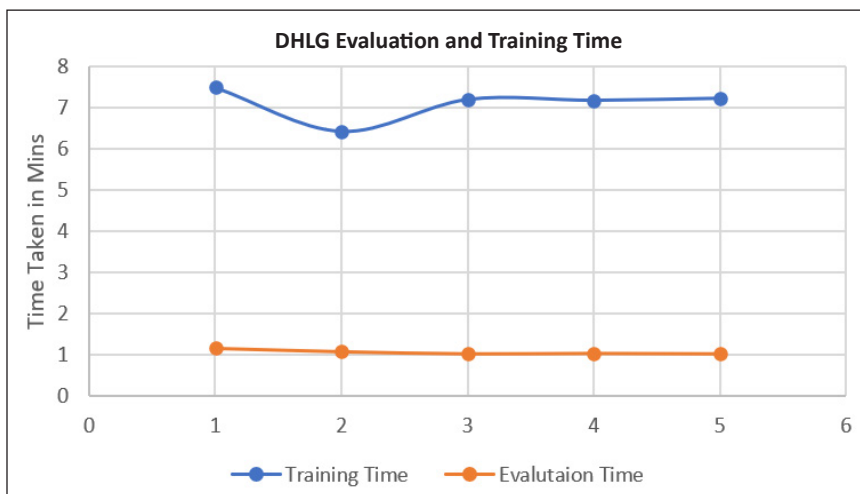


Figure 6. DHLG performance of evaluation time and training time

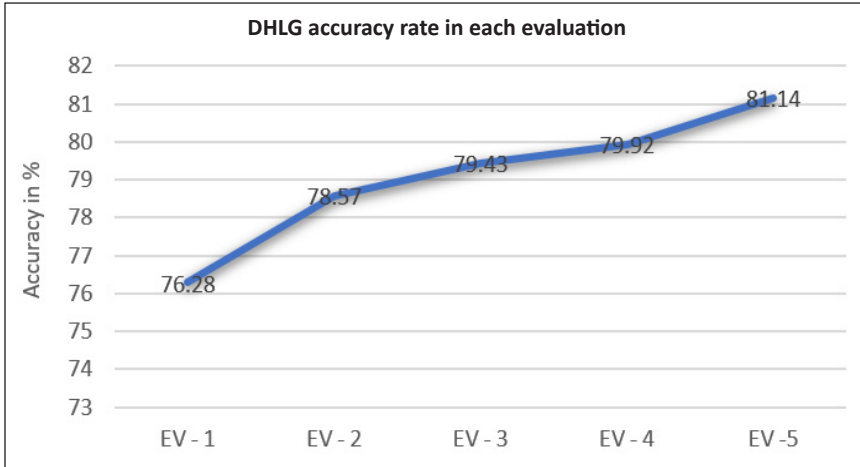


Figure 7. DHLG accuracy rate for 5 evaluations

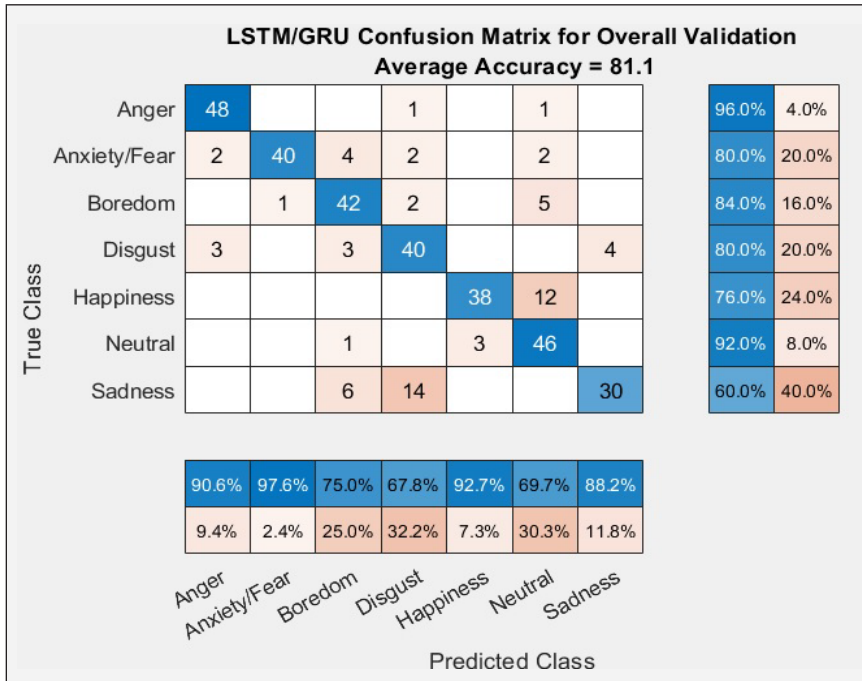


Figure 8. Cross fold confusion Matrix for DHLG

Finally, by considering the higher accuracy level iteration, Figure 8 clearly shows that for the given input Tamil database DHLG model gives 81.1% of efficiency. In the confusion matrix, emotions like anger and neutral gives higher rate of 96% and 92%. As this model also lags in other emotional states. Happy and Neutral emotions lags in DHLG model. Only 76% and 60% of accuracy is obtained in both states and shows lowest of all emotion recognition. Fear, Boredom and Disgust shows 80% and 84% of accuracy.

Deep Hierarchal BiLSTM & GRU (DHBG) Model

The DHBG models is analyzed to reach a conclusion that DHBG technique generates confusion matrix with 10-fold cross validation as final classification output. As like DHLG max 5 times the simulation is evaluated to find the consistent in accuracy level. Among 5 simulation the average 10 folds cross valuation fold 3 shows 90.02% of accuracy and fold 3 and 9 shows 82% of accuracy, where other folds also show better performance of accuracy around 72 -80% (Figure 9). In the testing phase same 50 samples of data used in DHLG is utilized for analysis. Each iteration there is a small variation in identification of emotional recognition. The average accuracy level for 5 evaluation is around 82.0%.

Now by analyzing the time factor the five evaluation the time taken to training and evaluation of classification timings were considered from Figure 10. While taking the mean value it is clear that for training of DHBG takes around 16.33 mins and to evaluate the classification it takes around 1.184 mins.

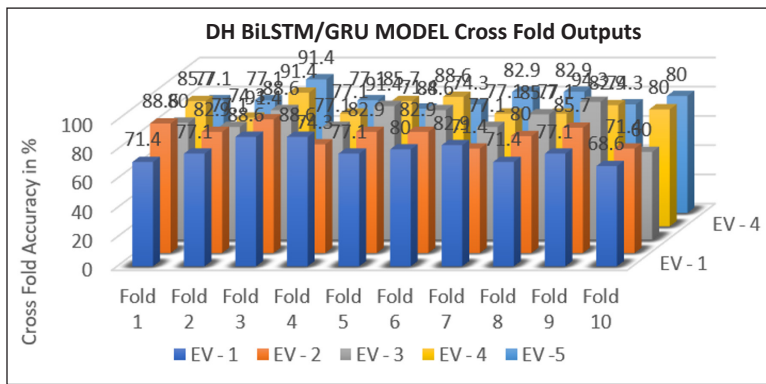


Figure 9. DHBG Cross fold output for multiple evaluation

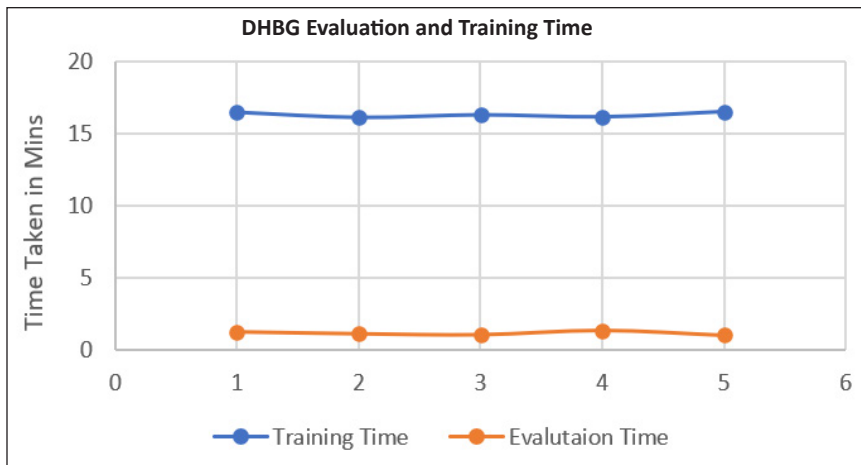


Figure 10. DHBG Performance of Evaluation time and Training Time

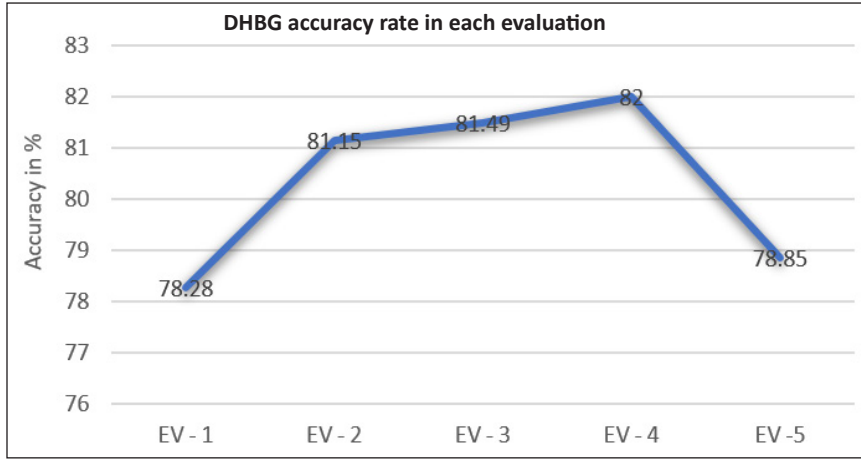


Figure 11. DHBG accuracy rate for 5 evaluations

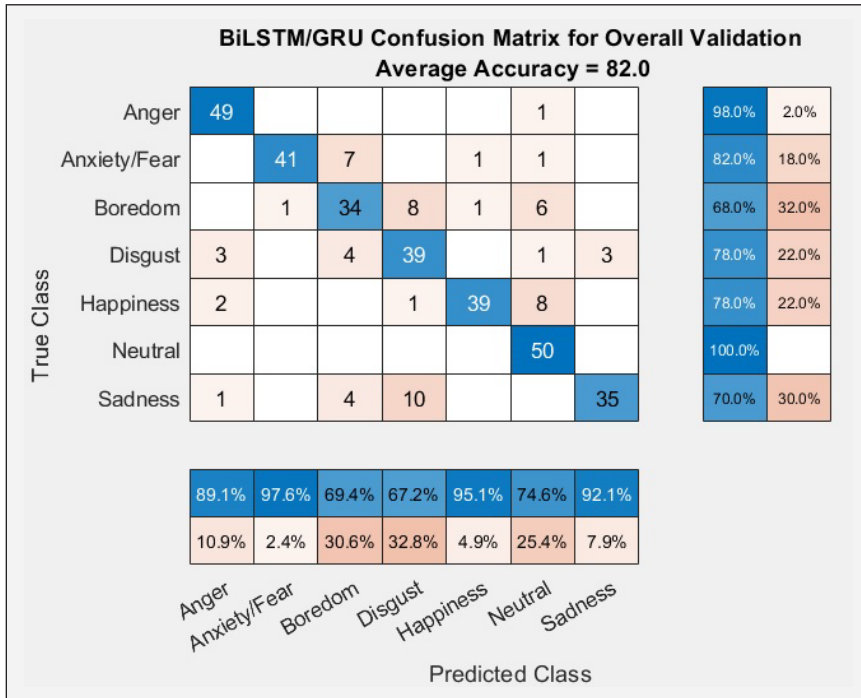


Figure 12. Cross fold confusion Matrix for DHBG

From Figure 11 the accuracy level in each simulation is established. As the cross-validation folds are random the accuracy level changes randomly. But it lies in the range of 78 to 82. In each simulation the training time and the evaluation time also varies, but only few seconds of variation can be identified. Among the 5 simulation results, in fourth iteration shows higher range of results is identified i.e., 82%.

Finally, by considering the higher accuracy level iteration, Figure 12 clearly shows that for the given input Tamil database DHBG model gives 82% of efficiency. In the confusion matrix, emotions like anger and neutral gives higher rate of 98% and 100%. As like DHLG this model also lags in other emotional states. Boredom and Sadness emotions lags in DHBL model. Only 68% and 70% of accuracy is obtained in both boredom and sadness states and shows lowest of all emotion recognition. Fear, Happiness and Disgust shows 78% and 82% of accuracy.

Deep Hierarchal GRU & LSTM (DHGL) Model

The DHGL models is analyzed to reach a conclusion that technique generates confusion matrix with 10-fold cross validation as final classification output. As like DHLG max 5 times the simulation is evaluated to find the consistent in accuracy level. Among 5 simulation the average 10 folds cross valuation fold 6 shows 89.52% of accuracy and fold 2 and 3 shows 82% of accuracy, where other folds also show better performance of accuracy around 68 -78% (Figure 13).

In the testing phase same 50 samples of data used in DHLG is utilized for analysis. Each iteration there is a small variation in identification of emotional recognition. The average accuracy level for 5 evaluation is around 80.74%.

Now by analyzing the time factor the five evaluation the time taken to training and evaluation of classification timings were considered from Figure 14. While taking the mean value it is clear that for training of DHGL takes around 5.48 mins and to evaluate the classification it takes around 1.122 mins.

From Figure 15 the accuracy level in each simulation is established. As the cross-validation folds are random the accuracy level changes randomly. But it lies in the range of 76 to 82. In each simulation the training time and the evaluation time also varies, but

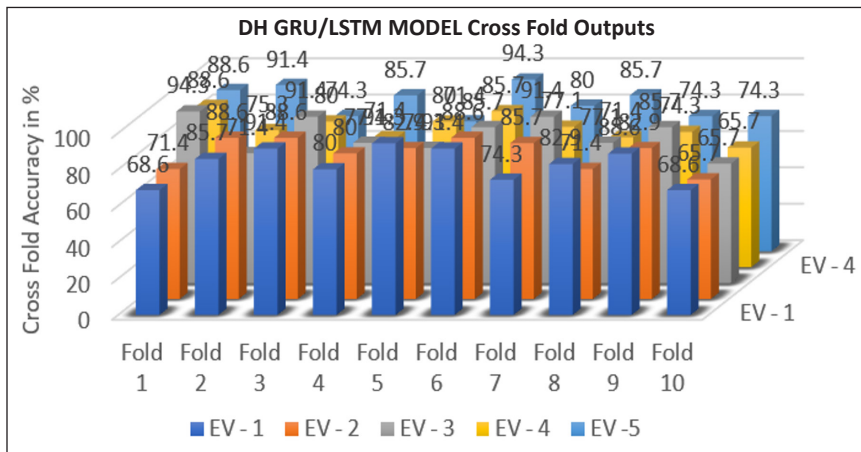


Figure 13. DHGL Cross fold output for multiple evaluation

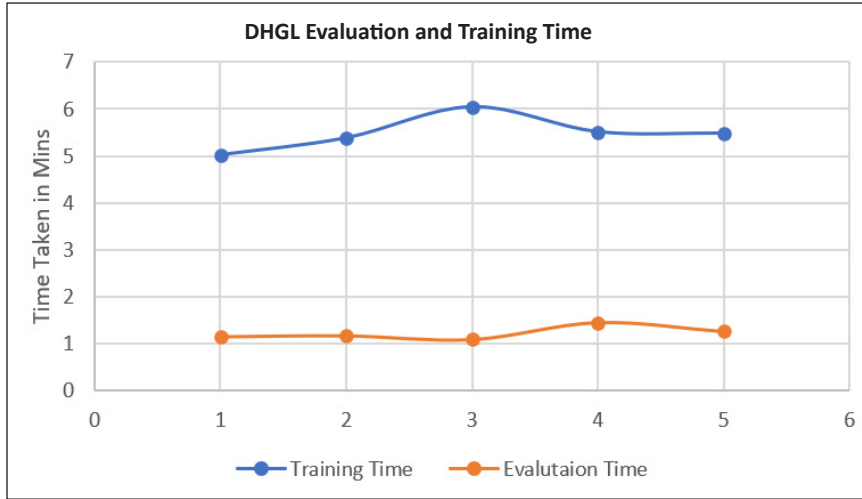


Figure 14. DHGL performance of evaluation time and training time

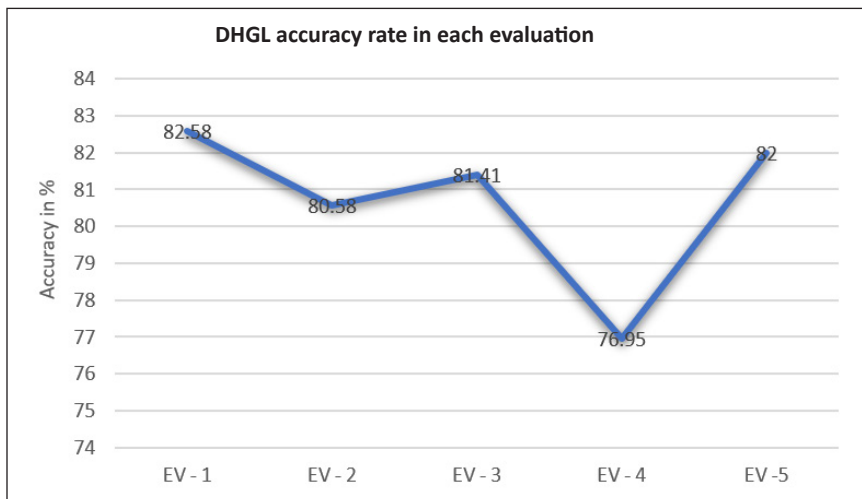


Figure 15. DHGL accuracy rate for 5 evaluations

only few seconds of variation can be identified. Among the 5 simulation results, in first iteration shows higher range of results is identified i.e., 82.58%.

Finally, by considering the higher accuracy level iteration, Figure 16 clearly shows that for the given input Tamil database DHGL model gives 82.58% of efficiency. In the confusion matrix, emotions like anger and neutral gives higher rate of 98% and 96%. As like DHBG this model also lags in other emotional states. Boredom, Didgust and Sadness emotions lags in DHGL model. Only 74% of accuracy is obtained in all boredom. disgust and sadness state and shows lowest of all emotion recognition. Fear and Happiness shows 82% and 74% of accuracy.

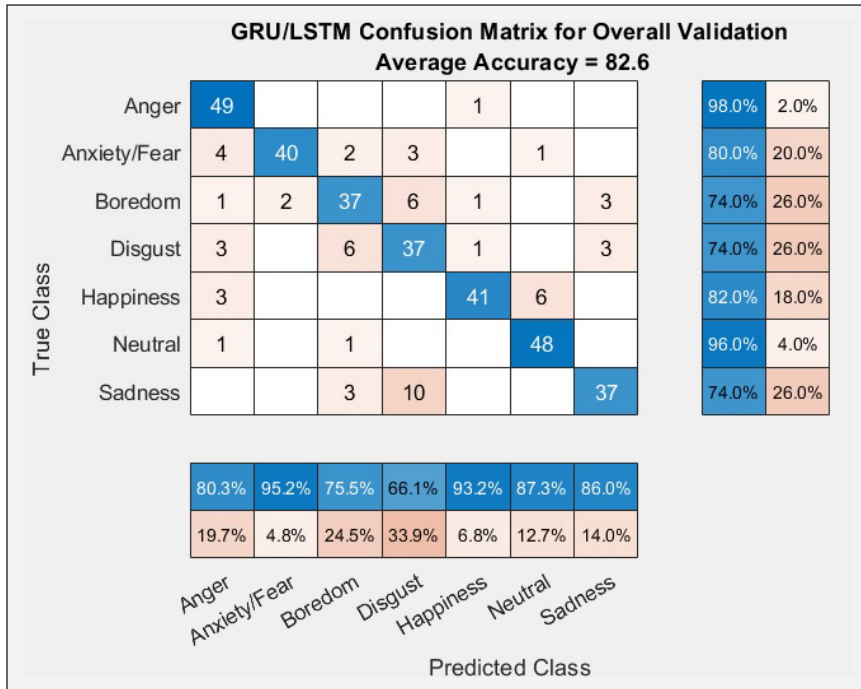


Figure 16. Cross fold confusion Matrix for DHGL

Deep Hierarchal GRU & BiLSTM (DHGB) Model

The DHGB models is analyzed to reach a conclusion that technique generates confusion matrix with 10-fold cross validation as final classification output. As like DHLG max 5 times the simulation is evaluated to find the consistent in accuracy level. Among 5 simulation the average 10 folds cross valuation fold 7,6 and 4 shows 84.02% of accuracy and fold 1, 5 and 9 shows 81% of accuracy, where other folds also show better performance of accuracy around 74 -80% (Figure 17).

In the testing phase same 50 samples of data used in DHLG is utilized for analysis. Each iteration there is a small variation in identification of emotional recognition. The average accuracy level for 5 evaluation is around 81.03%.

Now by analyzing the time factor the five evaluation the time taken to training and evaluation of classification timings were considered from Figure 18. While taking the mean value it is clear that for training of DHBG takes around 6.23 mins and to evaluate the classification it takes around 1.104 mins.

From Figure 19, the accuracy level in each simulation is established. As the cross-validation folds are random the accuracy level changes randomly. But it lies in the range of 78 to 82. In each simulation the training time and the evaluation time also varies, but only few seconds of variation can be identified. Among the 5 simulation results, in first iteration shows higher range of results is identified i.e., 82.86%.

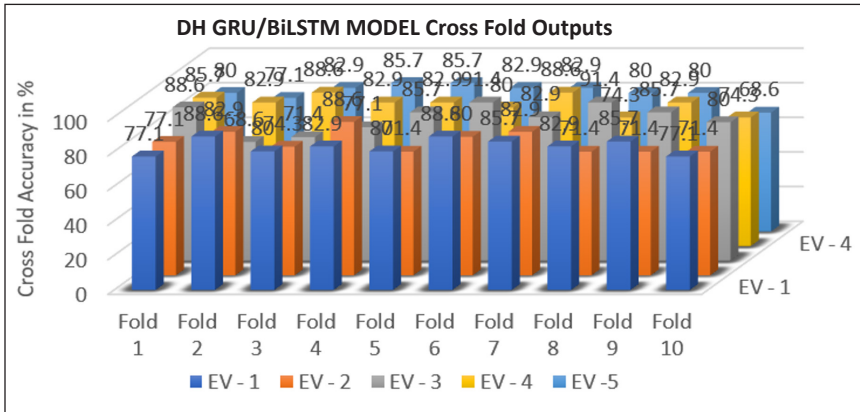


Figure 17. DHGB Cross fold output for multiple evaluation

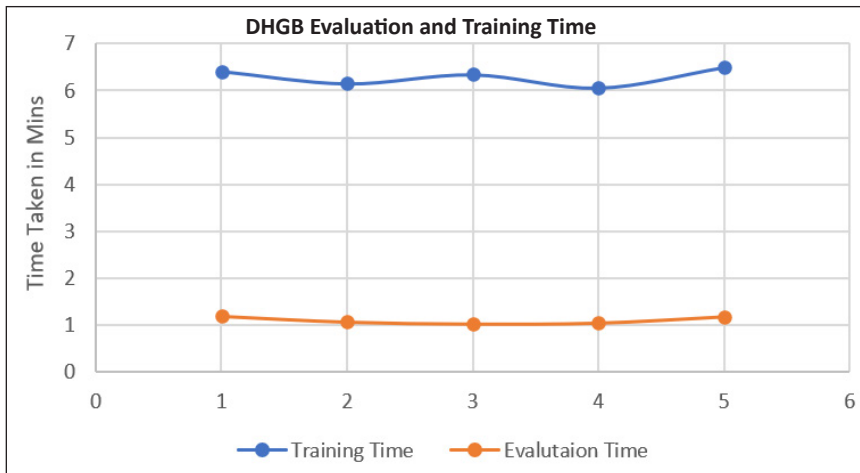


Figure 18. DHGB performance of evaluation time and training time

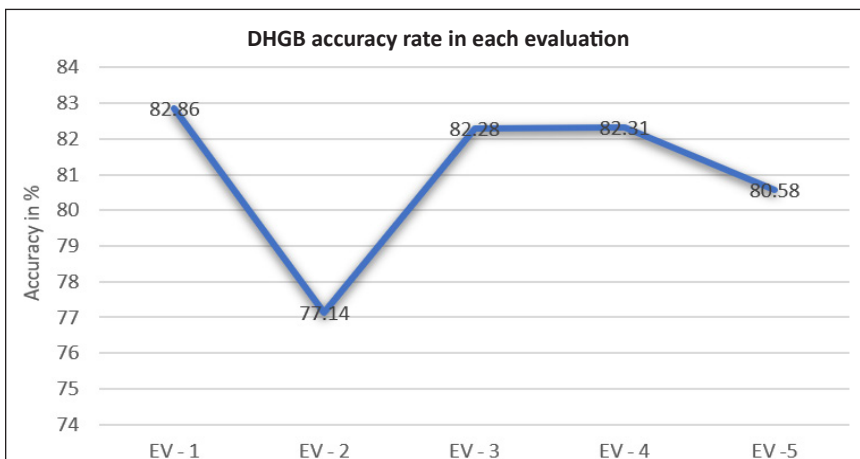


Figure 19. DHGB performance of evaluation time and training time

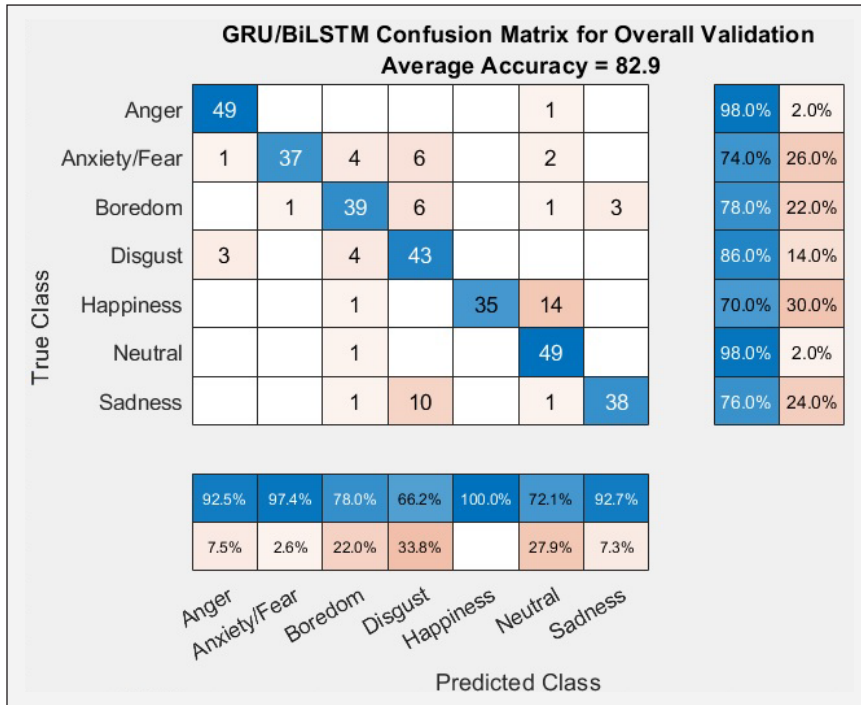


Figure 20. Cross fold confusion Matrix for DHGB

Finally, by considering the higher accuracy level iteration Figure 20, clearly shows that for the given input Tamil database DHGB model gives 82% of efficiency. In the confusion matrix, emotions like anger and neutral gives higher rate of 98%. As like DHLG this model also lags in other emotional states. Happiness and fear emotions lags in DHGB model. Only 70% and 74% of accuracy is obtained in both boredom and sadness states and shows lowest of all emotion recognition. Boredom, and sadness shows 76% and 78% of accuracy.

Deep Hierarchal GRU & GRU (DHGG) Model:

The DHBG models is analyzed to reach a conclusion that DHGG technique generates confusion matrix with 10-fold cross validation as final classification output. As like DHBG max 5 times the simulation is evaluated to find the consistent in accuracy level. Among 5 simulation the average 10 folds cross valuation fold 3 & 9 shows 83.98% of accuracy and fold 4, 5 and 7 shows 80% and 83% of accuracy, where other folds also show better performance of accuracy around 73 -78% (Figure 21). In the testing phase same 50 samples of data used in DHLG is utilized for analysis.

Each iteration there is a small variation in identification of emotional recognition. The average accuracy level for 5 evaluation is around 80%. Now by analyzing the time factor the five evaluation the time taken to training and evaluation of classification timings were

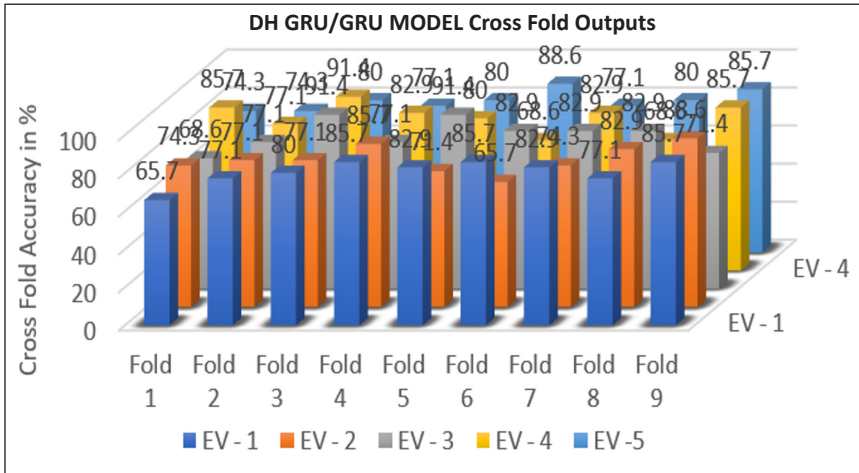


Figure 21. DHGG Cross fold output for multiple evaluation

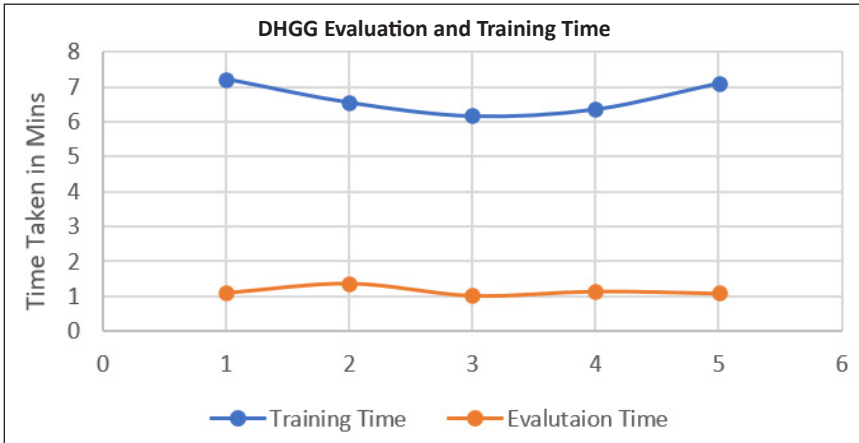


Figure 22. DHGG Performance of Evaluation time and Training Time

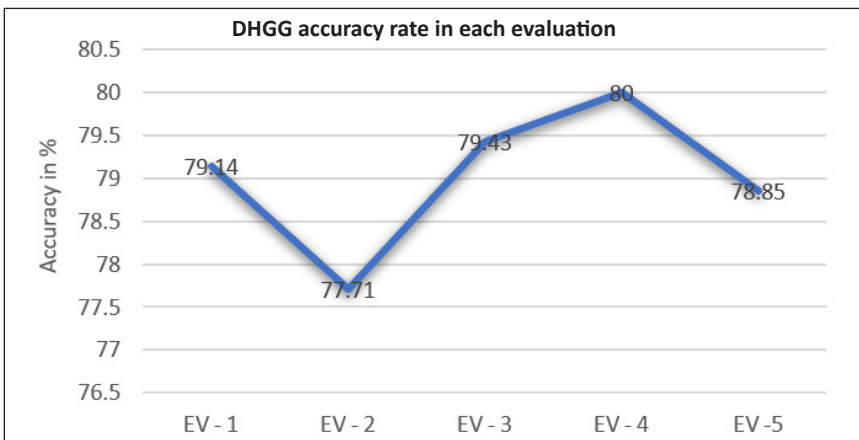


Figure 23. DHGG accuracy rate for 5 evaluations

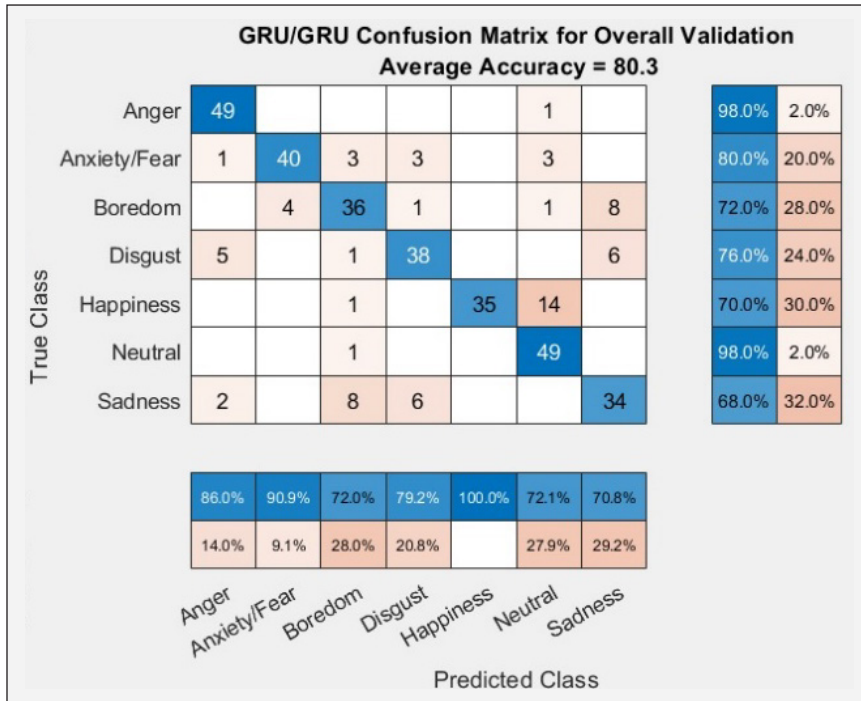


Figure 24. Cross fold confusion Matrix for DHGG

considered from Figure 22. While taking the mean value it is clear that for training of DHBG takes around 6.62 mins and to evaluate the classification it takes around 1.14 mins.

From Figure 23, the accuracy level in each simulation is established. As the cross-validation folds are random the accuracy level changes randomly. But it lies in the range of 77 to 80. In each simulation the training time and the evaluation time also varies, but only few seconds of variation can be identified. Among the 5 simulation results, in fourth iteration shows higher range of results is identified i.e., 80.03%.

Finally, by considering the higher accuracy level iteration Figure 24, clearly shows that for the given input Tamil database DHGG model gives 80.03% of efficiency. In the confusion matrix, emotions like anger and neutral gives higher rate of 98%. As like DHLG this model also lags in other emotional states. Happiness and Sadness emotions lags in DHGG model. Only 70% and 68% of accuracy is obtained in both happiness and sadness states and shows lowest of all emotion recognition. Fear, Boredom and Disgust shows 80% and 72% of accuracy.

Tables 1 and 2 shows the overall performance of the entire designs. Comparing with all the models DHBG shows better performance than the other models. Also, DHGG also achieves equal performance to DHLG. Both the models give average accuracy of 82% for the collected Tamil emotional database shown in Figure 25. Now comparing the training time for all models DHBG lags when compared with other models.

Table 1
Cross fold accuracy of DH LG/BG/GL/GB/GG layers

Methodology	Fold Accuracy/	DHLG	DHBG	DHGL	DHGB	DHGG
Fold 1		77.1	85.7	68.6	77.1	85.7
Fold 2		88.6	74.3	85.7	88.6	77.1
Fold 3		82.9	90.4	91.4	80	91.4
Fold 4		88.6	77.1	80	82.9	82.9
Fold 5		71.4	85.7	92.3	94.4	80
Fold 6		77.1	88.6	91.4	88.6	68.6
Fold 7		85.7	77.1	74.3	85.7	82.9
Fold 8		77.1	77.1	82.9	82.9	68.6
Fold 9		82.9	82.9	88.6	85.7	85.7
Fold 10		80	80	68.6	77.1	77.1

Table 2
Overall performance of DH LG/BG/GL/GB/GG models

Overall Performance (5 Iteration)	DHLG	DHBG	DHGL	DHGB	DHGG
Best Accuracy	81.14	82	82.58	82.86	80
Average accuracy	78.968	80.452	80.704	81.034	79.026
Best Training Time	7.19	16.15	5.02	6.06	6.17
Average Training Time	7.114	16.334	5.486	6.29	6.676
Best Evaluation Time	1.03	1.05	1.09	1.03	1.03
Average Evaluation Time	1.068	1.184	1.224	1.104	1.15

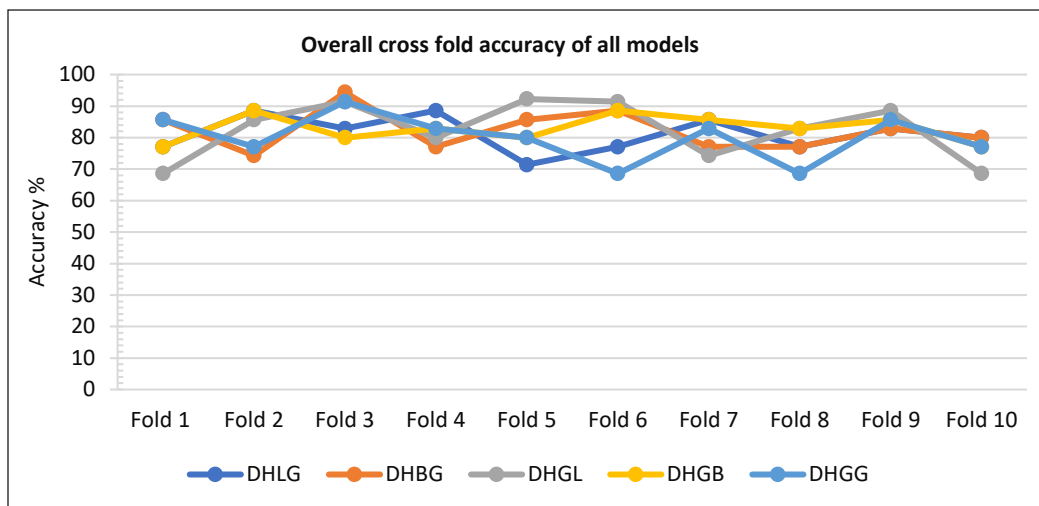


Figure 25. Overall graphical representation of all models cross fold accuracy

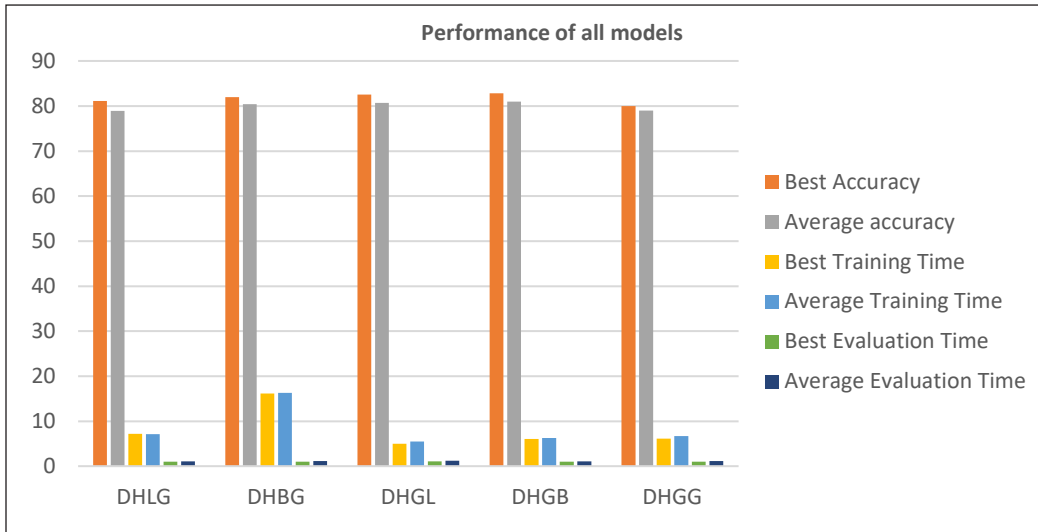


Figure 26. Overall performance of all models

Even though DHBG shows equal performance towards DHLG and DHGG, it takes more time for training the database. More than half of the time is reduced in DHLG. Around 17 mins were taken to train the database in DHBG model, whereas DHLG takes around 7.24 mins to complete the training and DHGG takes 6.36 for training the dataset.

After training the testing is done to identify the different emotional classification for the input 50 samples. In testing also DHBG shows lower evaluation time than other models, it takes only 1.36 mins to complete the evaluation. But other models have better evaluation and training time and its lagging in accuracy level shown in Figure 26.

In most efficient way GRU and followed by BiLSTM gives better performance in RNN followed by GRU and LSTM is slightly less. Comparing the cross fold from above table in DHGB fold 5 gives more accuracy rate of 94.4% and in DHGL also fold 5 yields more accuracy of 92.3%. The DHBG model takes more time for training and evaluation, where other techniques take slightly less time of 5.02 mins and 1.03 mins. The results obtained from different models are generated and presented effectively in this paper. Thus, the further research in design layers can enhance this model and optimize it with lots of computation and data.

CONCLUSION

The purpose of this design work is to introduce a deep learning technique and to design the concepts in different emotional datasets among speech stimuli. Very precisely, the objective was to improve a system (classifier) which might decide whether a particular system recognize the emotions for the collected Tamil language database. Towards this

end, the design implemented in this architecture focused on Deep Hierarchical LSTM / BiLSTM and GRU that to a large extent recognizes various emotional speech envelopes. The purpose of using the RNN in the voice envelope direction is to bring the network to attain more ability, through its precision, error, training, and evaluation time. Thus, it analyzes the emotional speech signal and its efficiency. Thus, comparing the classification analysis of proposed system based on LSTM / BiLSTM / GRU and the findings proved that the DHGB model performs better than the other four models for the given dataset. In the seven basic emotions anger and neutral has higher rate of identification level about 98% and emotions like fear and happiness has average accuracy rate of about 86% and only 74% of accuracy is achieved for other disgust, sadness, and boredom emotions. The classification accuracy of 82.86% is achieved with minimal losses in DHGB and the time required for preparation and assessment is also lesser than other models and further the models can be improved by different optimization methods for training the dataset, hence accuracy level can be increased with higher rate.

ACKNOWLEDGEMENT

Authors would like to acknowledge the KL University, AP, India for supporting this work and the faculty members who supported them for making the data available for this research.

REFERENCES

- Abdel-Hamid, O., Mohamed, A. R., Jiang, H., Deng, L., Penn, G., & Yu, D. (2014). Convolutional neural networks for speech recognition. *IEEE ACM Transactions on Audio, Speech, and Language Processing*, 22(10), 1533-1545. <https://doi.org/10.1109/TASLP.2014.2339736>.
- Chen, Z., Watanabe, S., Erdogan, H., & Hershey, J. R. (2015, September 6-10). Speech enhancement and recognition using multi-task learning of long short-term memory recurrent neural networks. In *Sixteenth Annual Conference of the International Speech Communication Association* (pp. 3274-3278). Dresden, Germany. <https://doi.org/10.1109/SLT.2016.7846281>
- Chung, J., Cho, K., & Bengio, Y. (2014, December 8-13). Empirical evaluation of gated recurrent neural networks on sequence modeling. In *NIPS 2014 Deep Learning and Representation Learning Workshop* (pp. 2342-2350). Montreal, Canada. <https://doi.org/10.5555/3045118.3045367>.
- Erdogan, H., Hershey, J. R., Watanabe, S., & Le Roux, J. (2015). Phase-sensitive and recognition-boosted speech separation using deep recurrent neural networks. In *2015 IEEE International Conference on Acoustics, Speech and Signal Processing (ICASSP)* (pp. 708-712). IEEE Conference Publication. <https://doi.org/10.1109/ICASSP.2015.7178061>.
- Eyben, F., Weninger, F., Squartini, S., & Schuller, B. (2013). Real-life voice activity detection with lstm recurrent neural networks and an application to hollywood movies. In *2013 IEEE International Conference on Acoustics, Speech and Signal Processing* (pp. 483-487). IEEE Conference Publication. <https://doi.org/10.1109/ICASSP.2015.7178061>.

- Graves, A., Jaitly, N., & Mohamed, A. R. (2013). Hybrid speech recognition with deep bidirectional LSTM. In *2013 IEEE workshop on automatic speech recognition and understanding* (pp. 273-278). IEEE Conference Publication. <https://doi.org/10.1109/ASRU.2013.6707742>.
- Hochreiter, S., & Schmidhuber, J. (1997). Long short-term memory. *Neural Computation*, 9(8), 1735-1780. <https://doi.org/10.1162/neco.1997.9.8.1735>.
- Ioffe, S., & Szegedy, C. (2015, July 7-9). Batch normalization: Accelerating deep network training by reducing internal covariate shift. In *International conference on machine learning* (pp. 448-456). Lille, France. <https://doi.org/10.5555/3045118.3045167>.
- Jozefowicz, R., Zaremba, W., & Sutskever, I. (2015, July 7-9). An empirical exploration of recurrent network architectures. In *International conference on machine learning* (pp. 2342-2350). Lille, France. <https://doi.org/10.5555/3045118.3045367>.
- Kishore, P. V. V., & Prasad, M. V. D. (2016). Optical flow hand tracking and active contour hand shape features for continuous sign language recognition with artificial neural network. *International Journal of Software Engineering and its Applications*, 10(2), 149-170. <https://doi.org/10.1109/IACC.2016.71>
- Krizhevsky, A., Sutskever, I., & Hinton, G. E. (2012). Imagenet classification with deep convolutional neural networks. *Advances in Neural Information Processing Systems*, 25, 1097-1105. <https://doi.org/10.1145/3065386>.
- Kumar, K. V. V., Kishore, P. V. V., & Kumar, D. A. (2017). Indian classical dance classification with adaboost multiclass classifier on multi feature fusion. *Mathematical Problems in Engineering*, 20(5), 126-139. <https://doi.org/10.1155/2017/6204742>.
- Laurent, C., Pereyra, G., Brakel, P., Zhang, Y., & Bengio, Y. (2016). Batch normalized recurrent neural networks. In *2016 IEEE International Conference on Acoustics, Speech and Signal Processing (ICASSP)* (pp. 2657-2661). IEEE Conference Publication. <https://doi.org/10.1109/ICASSP.2016.7472159>.
- Li, J., Deng, L., Gong, Y., & Haeb-Umbach, R. (2014). An overview of noise-robust automatic speech recognition. *IEEE/ACM Transactions on Audio, Speech and Language Processing*, 22(4), 745-777. <https://doi.org/10.1109/TASLP.2014.2304637>
- Liu, Y., Zhang, P., & Hain, T. (2014). Using neural network front-ends on far field multiple microphones based speech recognition. In *2014 IEEE International Conference on Acoustics, Speech and Signal Processing (ICASSP)* (pp. 5542-5546). IEEE Conference Publication. <https://doi.org/10.1109/ICASSP.2014.6854663>.
- Mannepalli, K., Sastry, P. N., & Suman, M. (2016a). FDBN: Design and development of fractional deep belief networks for speaker emotion recognition. *International Journal of Speech Technology*, 19(4), 779-790. <https://doi.org/10.1007/s10772-016-9368-y>
- Mannepalli, K., Sastry, P. N., & Suman, M. (2016b). MFCC-GMM based accent recognition system for Telugu speech signals. *International Journal of Speech Technology*, 19(1), 87-93. <https://doi.org/10.1007/s10772-015-9328-y>
- Pascanu, R., Mikolov, T., & Bengio, Y. (2013). On the difficulty of training recurrent neural networks. *Proceedings of Machine Learning Research*, 28(3), 1310-1318. <https://doi.org/10.5555/3042817.3043083>.

- Rao, G. A., & Kishore, P. V. V. (2016). Sign language recognition system simulated for video captured with smart phone front camera. *International Journal of Electrical and Computer Engineering*, 6(5), 2176-2187. <https://doi.org/10.11591/ijece.v6i5.11384>
- Rao, G. A., Syamala, K., Kishore, P. V. V., & Sastry, A. S. C. S. (2018). Deep convolutional neural networks for sign language recognition. *International Journal of Engineering and Technology (UAE)*, 7(Special Issue 5), 62-70. <https://doi.org/10.1109/SPACES.2018.8316344>
- Ravanelli, M., Brakel, P., Omologo, M., & Bengio, Y. (2016). Batch-normalized joint training for DNN-based distant speech recognition. In *2016 IEEE Spoken Language Technology Workshop (SLT)* (pp. 28-34). IEEE Conference Publication. <https://doi.org/10.1109/SLT.2016.7846241>.
- Ravanelli, M., Brakel, P., Omologo, M., & Bengio, Y. (2017). A network of deep neural networks for distant speech recognition. In *2017 IEEE International Conference on Acoustics, Speech and Signal Processing (ICASSP)* (pp. 4880-4884). IEEE Conference Publication. <https://doi.org/10.1109/ICASSP.2017.7953084>.
- Sak, H., Senior, A. W., & Beaufays, F. (2014). Long short-term memory recurrent neural network architectures for large scale acoustic modeling. *Proceeding of Interspeech*, 22(1), 338-342. <https://doi.org/10.1007/s10772-018-09573-7>
- Sastry, A. S. C. S., Kishore, P. V. V., Prasad, C. R., & Prasad, M. V. D. (2016). Denoising ultrasound medical images: A block based hard and soft thresholding in wavelet domain. *International Journal of Measurement Technologies and Instrumentation Engineering (IJMTIE)*, 5(1), 1-14. <https://doi.org/10.4018/IJMTIE.2015010101>
- Schwarz, A., Huemmer, C., Maas, R., & Kellermann, W. (2015). Spatial diffuseness features for DNN-based speech recognition in noisy and reverberant environments. In *2015 IEEE International Conference on Acoustics, Speech and Signal Processing (ICASSP)* (pp. 4380-4384). IEEE Conference Publication. <https://doi.org/10.1109/ICASSP.2015.7178798>.
- Srivastava, N., Hinton, G., Krizhevsky, A., Sutskever, I., & Salakhutdinov, R. (2014). Dropout: A simple way to prevent neural networks from overfitting. *Journal of Machine Learning Research*, 15, 1929-1958. <https://doi.org/10.5555/2627435.2670313>.
- Weninger, F., Erdogan, H., Watanabe, S., Vincent, E., Le Roux, J., Hershey, J. R., & Schuller, B. (2015). Speech enhancement with LSTM recurrent neural networks and its application to noise-robust ASR. In *International conference on latent variable analysis and signal separation* (pp. 91-99). Springer. https://doi.org/10.1007/978-3-319-22482-4_11
- Zhang, Y., Chen, G., Yu, D., Yaco, K., Khudanpur, S., & Glass, J. (2016). Highway long short-term memory rnns for distant speech recognition. In *2016 IEEE International Conference on Acoustics, Speech and Signal Processing (ICASSP)* (pp. 5755-5759). IEEE Conference Publication. <https://doi.org/10.1109/ICASSP.2016.7472780>
- Zhou, G. B., Wu, J., Zhang, C. L., & Zhou, Z. H. (2016). Minimal gated unit for recurrent neural networks. *International Journal of Automation and Computing*, 13(3), 226-234. <https://doi.org/10.1007/s11633-016-1006-2>.



Performance Evaluation of Heuristics and Meta-Heuristics Traffic Control Strategies Using the *UTNSim* Traffic Simulator

Ng Kok Mun^{1*} and Mamun Ibne Reaz²

¹*School of Electrical Engineering, College of Engineering, Universiti Teknologi MARA, 40450 Shah Alam, Selangor, Malaysia*

²*Department of Electrical, Electronic and Systems Engineering, Faculty of Engineering and Built Environment, Universiti Kebangsaan Malaysia, 43600 UKM Bangi, Selangor, Malaysia*

ABSTRACT

In the past few decades, intelligent traffic controllers have been developed to responsively cope with the increasing traffic demands and congestions in urban traffic networks. Various studies to compare and evaluate the performance of traffic controllers have been conducted to investigate its effect on traffic performances such as its ability to reduce delay time, stops, throughputs and queues within a traffic network. In this paper, the authors aim to present another comparative study on heuristics versus meta-heuristics traffic control methods. To our knowledge, such comparison has not been conducted and could provide insights into a purely heuristic controller compared to meta-heuristics. The study aims to answer the research question “Can heuristics traffic control strategies outperformed meta-heuristics in terms of performance and computational costs?” For this purpose, a heuristics model-based control strategy (MCS) which was previously developed by the authors is compared to genetic algorithms (GA) and evolution strategy (ES) respectively on a nine intersections symmetric network. These control strategies were implemented via simulations on a traffic simulator called *UTNSim* for three different types of traffic scenarios. Performance indices such as average delays, vehicle throughputs and the computational time of these controllers were evaluated. The results revealed that the heuristic MCS outperformed GA and ES with superior performance in average delays whereas vehicle throughputs were

in close agreement. The computation time of the MCS is also feasible for real-time application compared to GA and ES that has longer convergent time.

ARTICLE INFO

Article history:

Received: 14 February 2021

Accepted: 10 May 2021

Published: 31 July 2021

DOI: <https://doi.org/10.47836/pjst.29.3.38>

E-mail addresses:

ngkokmun@uitm.edu.my (Ng Kok Mun)

mamun.reaz@gmail.com (Mamun Ibne Reaz)

* Corresponding author

Keywords: Evolution strategy, genetic algorithm, heuristics algorithm, meta-heuristics algorithm

INTRODUCTION

Intelligent traffic control systems have been developed throughout the decades to improve traffic flow and ease congestions in urban traffic networks. These traffic-responsive systems devise the most effective signal timing plans to optimize traffic flow by adjusting the splits, cycle time and offset at individual intersections. Traffic control methods can be categorized into model-based and non-model based traffic responsive control, route guidance and driver information systems, computational intelligence and agent-based methods (Ng et al., 2013).

Computational intelligence includes artificial intelligence and meta-heuristics methods. Meta-heuristics intelligence methods such as ant colony optimization, bee colony optimization, particle swarm optimization, genetic algorithms, evolutionary programming, just to name a few, have been implemented to devise optimal signal timing plans. These methods aim to solve nonlinear programming problems through heuristic search of near optimal solutions. Tan et al. (2017) proposed a decentralized genetic algorithm (GA) with adaptive fitness function for minimizing average network delay. Each signalized intersection in the traffic network that comprised of four signalized intersections has its own controller. The GA assists the controllers to optimize traffic signal at morning peak hours by finding optimum solution through a process of fitness evaluation, selection and reproduction. Similar optimal solution of single objective function such as delay time is also conducted by Cao & Luo (2019). In another work, GA has been implemented to solve a multiobjective signal optimization problem in a nine intersections network to maximize system throughputs, minimize travelling delays, enhance traffic safety, and avoid spillovers (Li & Sun, 2018). The application of GA on multi objective function was performed by Davydov et al. (2019) on a road map fragment described using a microscopic traffic simulator.

In the area of model-based traffic responsive control, traffic models play an important role to predict future traffics parameters in the urban traffic network. Subsequently, control methods such as dynamic programming (Dang & Rudova, 2018), linear programming (Li et al., 2014; Zhang et al., 2015; Grandinetti et al., 2015), quadratic programming (Aboudolas et al., 2010; Le et al., 2015) and multivariable regulators (Diakaki et al., 2002) were implemented to optimize traffic performance. These produced optimal solutions by solving a set of mathematical functions. On the other hand, model-based traffic responsive control can be solved by purely heuristics algorithms. Lammer & Helbing (2008) developed decentralized heuristic control algorithm that anticipates current and future queues at the intersection. Le et al. (2015) proposed similar heuristics method called max-pressure (back-pressure) algorithms to regulate queues optimally in urban network. Other heuristics algorithms such as gating and perimeter control (Hajiahmadi et al., 2015) and demand balance control (Zhou et al., 2016) were implemented on oversaturated network based on

the network fundamental diagram (NFD). Recently, the authors proposed a heuristic model-based control strategy (MCS) for urban networks. The MCS improved performance of average delays up to 24% when compared with existing fixed-time system and successfully regulates queue spillbacks (Ng et al., 2019).

Performance evaluation needs to be conducted to assess the performance of traffic networks with or without any control scheme. Performance evaluation has been conducted on traffic streams without any control schemes such as ramps and highways (Basri et al., 2020; Saha et al., 2015) and networks with control schemes (Al-Kandari et al., 2013; Stevanovic et al., 2017). Based on the literature review in the next section, performance evaluation of heuristics traffic control strategy in relative comparison with meta-heuristics methods had not been investigated. Such comparison is needed and may provide insights on the performance and behavior of heuristics against meta-heuristics control algorithms. Hence, the research question at hand is “Can heuristics traffic control strategies outperformed meta-heuristics in terms of performance and computation costs?” In view of this; a comparative study on the heuristics model-based control strategy (MCS) by Ng et al. (2019) against meta-heuristics methods in Hajbabaie et al. (2011) is presented in this paper.

The MCS heuristics algorithm is compared respectively with genetic algorithm (GA) and evolution strategy (ES) (a type of evolution programming) by Hajbabaie et al. (2011) on a nine-intersection symmetric case study network. The performance of the MCS, GA and ES is evaluated based on average delays, network throughputs and computation time. This study is conducted via simulations using a traffic simulator namely *UTNSim* (Ng et al., 2018; Ng et al., 2019). The next section in this paper provides the literature review and the research gaps. The method section gives an overview of the MCS and meta-heuristics control algorithms respectively, and the experimental setup of the nine-intersection symmetric case study network. Subsequently simulation results of controller effects on traffic performances are presented and discussed.

LITERATURE REVIEW

Whenever a control scheme is introduced to an urban traffic system; proper evaluation needs to be conducted on these proposed control schemes to ascertain their effectiveness in improving traffic performances. For example, Al-Kandari et al. (2013) compared vehicle throughputs by four different control methods on a single four phase signalized intersection. Stevanovic et al. (2017) compared adaptive traffic control with existing time-of-day (TOD) signal timing plans based on average delays, total delay travel time and number of stops. The study shown that adaptive traffic control reduced average delays, travel time and number of stops in recurring and non-recurring traffic conditions.

Many research works have been conducted in optimizing traffic control performances using meta-heuristics methods. Performance evaluation on these methods was done in

relative comparison with other control methods. For example, Gao et al. (2019) compares the performance of an improved artificial bee colony algorithm (IABC) with mixed integer linear programming (MILP) on a simple network that comprised of three traffic intersections. The IABC underperformed in terms of optimal solutions but performed better in computational time compared to MILP. Toivio et al. (2020) implemented GA to derive optimized membership functions for a fuzzy controller. The GA optimized fuzzy controller outperformed the default fuzzy controller and the Tasman-Zanker field controller in terms of average delays. Doostali et al. (2020) derived optimal vehicle flow using GA and directed graph. The proposed method was compared to adaptive control and fixed-time system to evaluate queue length and waiting time at approaches. A review presented by Shaikh et al. (2020) shows that GA had been evaluated in comparison with the classical Webster timing scheme, MAXBAND and fixed-time systems. Many other comparative studies on meta-heuristics controller performances have been conducted such as GA versus conventional fuzzy logic (Tan et al., 2019) and comparison of GA, Hill Climbing and Simulated Annealing in Cantarella et al. (2015).

Heuristics control methods were also compared relatively with other control methods to investigate their effects on the road networks. The MCS heuristics algorithm which was developed by the authors had been compared previously with fixed-time system (Ng et al., 2019). The MCS improved performance of average delays up to 24% when compared with existing fixed-time system and successfully regulates queue spillbacks. The hierarchical demand balance controller in Zhou et al. (2016) was compared to centralized controller and fixed-time system. It was found that the centralized controller has the best performance in terms of total time spent and total delay time of vehicles in the network. Le et al. (2015) compared their proposed backpressure policy algorithm against greedy and proportional policy algorithms in terms of network throughputs and congestion. Lammer and Helbing (2008) compared the proposed self-organized traffic control against optimization strategy, cycle-based strategy and stabilization strategy.

To the best of our knowledge, based on the review, performance evaluation of heuristics traffic control strategy in relative comparison with meta-heuristics methods had not been investigated. Such comparison is needed and may provide insights on the performance and behavior of heuristics control algorithms, which is also used to address non-linear traffic behaviors. Although meta-heuristics methods may provide optimal solutions systematically using an objective function; it can be weighed down by computational costs. Hence, the research question at hand is “Can heuristics traffic control strategies outperformed meta-heuristics in terms of performance and computation costs?” As such comparison has not been conducted previously; this may bring insights into the benefits that may be offered by heuristics in comparison with meta-heuristics algorithms.

MATERIALS AND METHODS

Model-based Control Strategy

Figure 1 provides an overview of the closed loop behaviour of the model-based control strategy (MCS) introduced by Ng et al. (2019). The MCS is an extension to traffic simulator called *UTNSim* developed by Ng et al. (2015; 2016). The *UTNSim* comprised of the traffic network diagram editor (TNDE) and a traffic simulator based on the LWR-IM (Ng et al., 2018). On the other hand, the components of the MCS are NET-PREDICT, NET-CONTROL and INT-CONTROL. These algorithms were developed to perform network wide traffic predictions and coordinates control action at each of the signalized intersection within an urban traffic network (UTN) (Ng et al., 2019).

The NET-PREDICT perform predictions based on the LWR-IM traffic model to produce estimations of platoon size, platoon arrival time and queues at each signalized intersection within the UTN by using measured traffic data or simulated inputs. The NET-CONTROL algorithm consolidates these estimations from the NET-PREDICT and calculates queue spillbacks at each link entering a signalized intersection. Based on these traffic estimates, it coordinates network wide control by calling the INT-CONTROL heuristics algorithm at each signalized intersection. The control action at each signalized intersection is regulated by the INT-CONTROL heuristics algorithm that updates new phase durations to optimize traffic flow. In addition, this algorithm also regulates queue spillbacks at the intersections.

Figure 2 shows the predicted parameters at a signalized intersection by the NET-PREDICT. The incoming vehicle platoons from adjacent intersection is described as $clrd_a$ and $clrd_b$, which depicts the clearing time needed for the platoons to pass through the

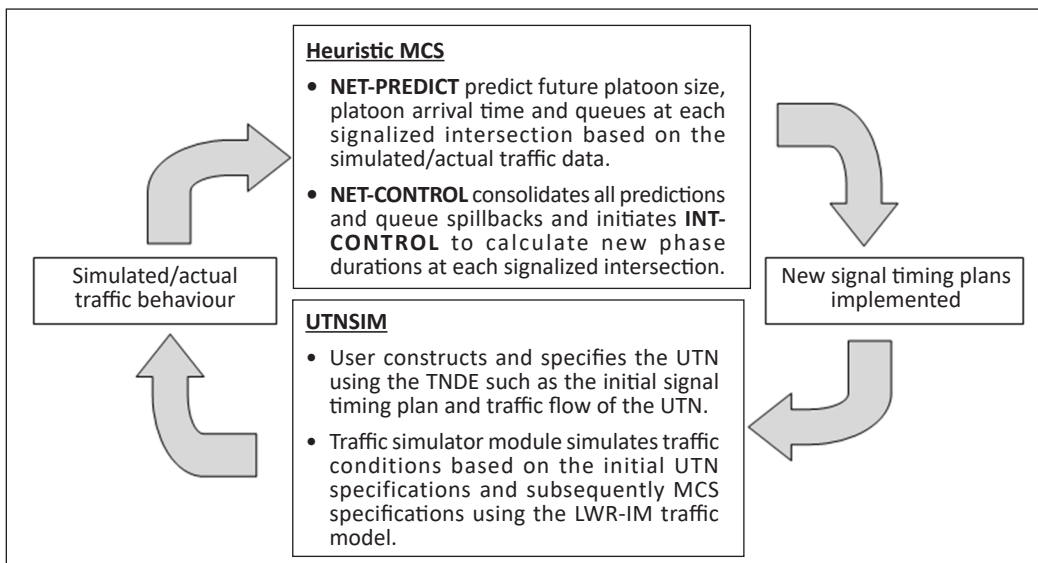


Figure 1. An overview of model-based control strategy in Ng et al. (2019)

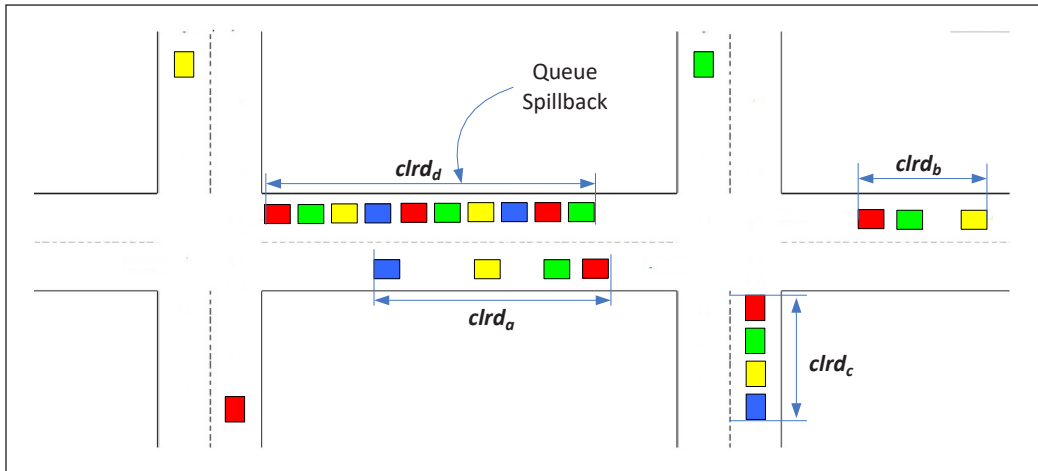


Figure 2. Predicted platoon and queue parameters at signalized intersections

intersection. Each platoon is described with estimated arrival time at the intersection. The length of the queue at the intersection is also described with a clearing time (i.e., $clrd_c$). An intersection may also encounter queue spillbacks (Figure 2) when the queue occupies up to 80% of the link length with a predicted clearing time $clrd_d$. The INT-CONTROL takes into consideration all these predicted parameters and adjust phase durations based on the proportionate method in responding to incoming vehicle platoons and queue clearing time. In addition, a queue regulation strategy is also embedded in the algorithm to regulate queue spillbacks. The detail description and functions of the INT-CONTROL heuristics algorithm can be referred in Ng et al. (2019).

Genetic Algorithm (GA) and Evolution Strategy (ES)

Hajbabaie et al. (2011) applied the GA and ES respectively to signal optimization problems in urban traffic networks. GA is a type of evolutionary computing inspired by evolutionary biology. The evolution process in GA includes inheritance, selection, crossover, and mutation. The GA created an initial population randomly or by mean of heuristics. Everyone in the population carries a fitness value calculated based on the objective function. Based on the fitness values, two parents are chosen from the initial population in the selection step. These parents' is crossed over, leading to two new individuals. The new individuals are mutated to form new individuals for the next generation. The fitness value of the newly created individuals will be evaluated. This whole process of selection, crossover, and mutation is repeated until certain termination criteria are met. On the other hand, the ES involves three steps i.e., recombination, mutation, and selection. In recombination, individuals among parents are selected and then recombined. In general, new individuals are generated from the recombinant via mutation and selection.

Hajbabaie et al. (2011) applied the GA and ES respectively to the following signal optimization problem given by Equation 1:

$$Max \sum_{t=1}^N \sum_{i=1}^N \sum_{\varphi=2}^{\phi_{ti}} n_{i\varphi}^t - \sum_{t=1}^N \sum_{i=1}^N \sum_{\varphi=2}^{\phi_{ti}} \delta_{i\varphi}^t q_{i\varphi}^t \quad [1]$$

subject to:

$$2 \leq \phi_{ti} \leq 6 \quad t = 0, \dots, T; \quad i = 1, \dots, N$$

$$gmin_{i\varphi}^t \leq g_{i\varphi}^t \leq gmax_{i\varphi}^t \quad t = 0, \dots, T; \quad i = 1, \dots, N; \quad \varphi = 1, \dots, \phi$$

$$0 \leq off_{i\varphi}^t \leq C_i^T \quad t = 0, \dots, T; \quad i = 1, \dots, N; \quad \varphi = 1, \dots, \phi$$

where:

T is the number of study periods; N is the total number of intersections; ϕ_{ti} is the number of signal phases at intersection i ; at time period t ; $n_{i\varphi}^t$ is the total number of vehicles processed by intersection i , at time period t , in phase φ ; $q_{i\varphi}^t$ is the queue length at intersection i , at time period t , waiting to be served by phase φ ; and $\delta_{i\varphi}^t$ is the penalty weight for queue length at intersection i , at time period t , waiting to be served by phase φ .

The chromosome or individuals in each respective GA or ES population, forms a vector which is a set of decisions variables. This vector contains signal timing parameters for each intersection i , for all defined time intervals t such as phase plan φ , green time for each phase $g_{i\varphi}^t$, and offset $off_{i\varphi}^t$. Hence, the implementation of the GA and ES respectively will produce decision variables that will optimize queue dissipation in the network based on Equation 1.

The generation of optimal signal timing plans according to Equation 1 from GA is illustrated in Figure 3(a) (Hajbabaie et al., 2011). The selection of parents was implemented using a tournament selection with a pressure of 6.7%. There are various methods to perform crossover such as single-point, multi-point, two-point, and uniform crossover. In the crossover stage, Hajbabaie et al. (2011) implemented uniform crossover to select chromosome of the offspring probabilistically from one of the parents. To generate two individuals, two parents selected by the tournament selection were used. Next, bitwise mutation was applied by flipping each bit of the chromosome to produce new individuals according to the probability of mutation. These are repeated until the termination criterion.

In ES, a parent μ can be mutated to form a single individual notated as, $\mu + 1$; or multiple individuals, $\mu + \lambda$ where $\lambda > 1$. Hajbabaie et al. (2011) performed the $\mu + \lambda$ as illustrated in Figure 3(b). In the recombination stage, $\rho \geq 1$ individuals among parents are selected and then recombined. If $\rho > 1$; recombinants are generated using both discrete and

intermediate methods. However, if $\rho = 1$ individual is selected; no recombination is done, and the new offspring is simply equal to its parent. In the mutation stage, the recombinants are mutated using single component mutation that results in concentric spheres around the parental state. The process of mutation will generate λ descendants out of μ parents. The selection process will choose the μ best individuals out of the $\mu + \lambda$ individuals to form the next population. This process of recombination, mutation and selection is repeated until the termination criteria. The process terminated over a total of ten runs and the average fitness value for everyone is obtained. In each run, the solution must meet all the constraints, else it will be discarded, and a new solution is generated.

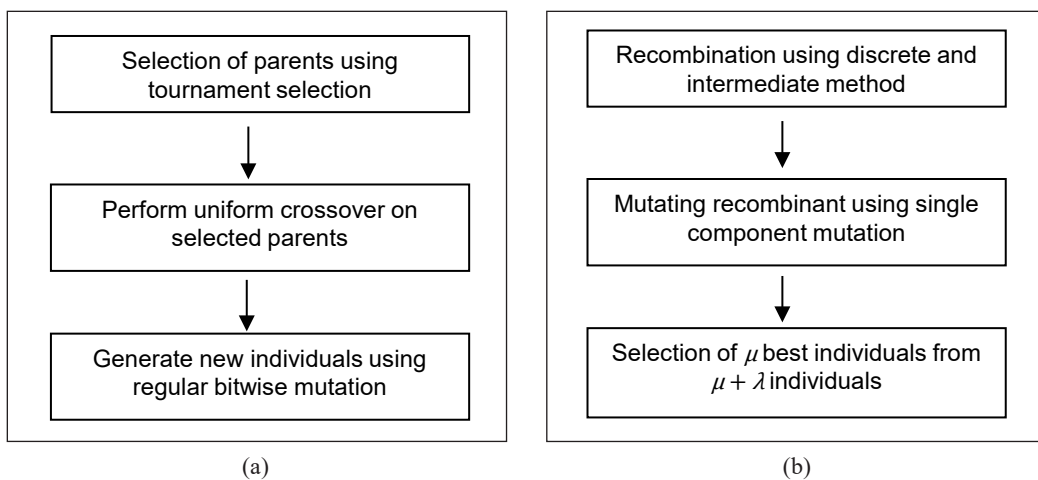


Figure 3. (a) Genetic Algorithm; and (b) Evolutionary System

Experimental Setup

The small hypothetical nine intersections symmetric case-study network in Hajbabaie et al. (2011) is employed in this work to evaluate the MCS and optimization compared to GA and ES algorithms. Figure 4 shows this small network which is symmetric in volume and geometry and composed of nine intersections (a three-by-three square) that is approximately 610 m (2000 ft) apart from each other. All streets are assumed to have two lanes (one per direction) and there are exclusive left-turn pockets, approximately 305 m (1000 ft) in length, at the intersections. The phase sequence in each intersection is shown in Figure 5. The turning rates at the intersections are 10% of vehicles turned right, 20% of the vehicles turned left and the rest went through. These turning percentages are estimated as the percentage of incoming volume from a single lane. A short study period of 15 minutes is conducted with the traffic demand fixed with the rate of 1000 veh/h/ln at each entry point.

Based on the specifications in this traffic case-study, Hajbabaie et al. (2011) applied ES and GA (refer to GA and ES in previous section) to produce optimal signal settings for the network in Figure 4. The network in Figure 4 was described in VISSIM software. The GA

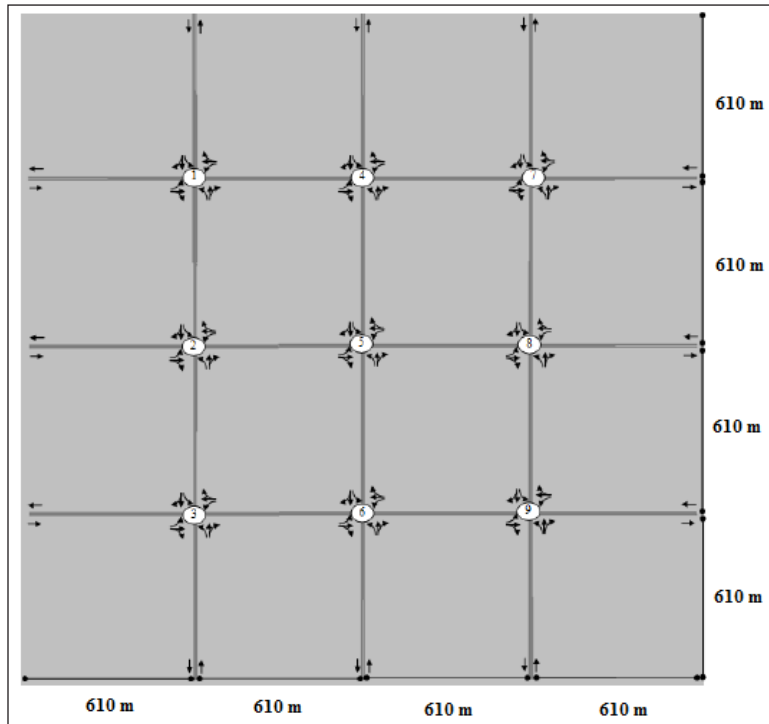


Figure 4. Nine intersections symmetric case study network as illustrated in Hajbabaie et al. (2011)

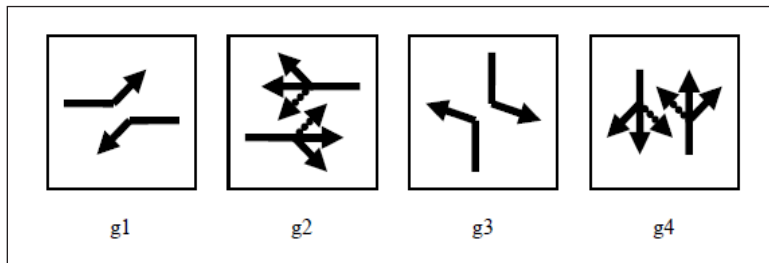


Figure 5. Phase sequence as illustrated in Hajbabaie et al. (2011)

and ES optimal timing plans were implemented in VISSIM. ES and GA were applied to the network in Figure 4 for three scenarios: (i) no overloading; (ii) 10% network overloading and (iii) 20% network overloading. Simulations were performed for a 15-minute analysis period in VISSIM based on the timing plans generated by ES and GA. The performances of the ES and GA approaches were analyzed and evaluated in terms of average delays, network throughputs, average number of stops, average speeds, efficient use of green time and queue overflows.

The comparative evaluation of the heuristic MCS with GA and ES comprise of the following steps:

- The *UTNSim* simulator was used to specify the network in Figure 4 with similar specifications to simulate average delays and network throughputs by adopting similar timing plans produced by GA and ES for the three scenarios of overloading: (i) no overloading; (ii) 10% network overloading and (iii) 20% network overloading. These GA and ES optimal timing plans can be referred in Hajbabaie et al. (2011). The average delays and network throughputs generated by *UTNSim* were compared with results from VISSIM to ascertain compatibility of both platforms. The simulated results in this step which have been conducted previously in Ng and Reaz (2017) had proven that *UTNSim* and VISSIM are compatible platforms.
- Upon ascertaining that *UTNSim* and VISSIM are compatible and comparable platforms for implementing the network; the relative comparison of traffic performances produced by the MCS with GA and ES approaches can be implemented using *UTNSim*.
- The heuristic MCS was implemented for no overload, 10% overload and 20% network overload, respectively. Simulations were conducted for an analysis period of 15 minutes. The optimized simulation was conducted with maximum green not exceeding 50% of the cycle time at each intersection; minimum green of 7 s; the minimum cycle time set at 50 s whereas the maximum cycle time set at 70 s. Average delays and network throughputs simulated for each situation using the MCS algorithm were compared with results produced by the GA and ES. The results were analyzed to observe if there is any improvement contributed by the heuristic MCS compared to these meta-heuristic approaches. Simulation using the *UTNSim* was conducted on a computer operating on an Intel Core i5 processor at 2.4 GHz.
- The third evaluation aims to tabulate and evaluate the average computation time (ACT) of the MCS in implementing each of the scenarios mentioned.

RESULTS AND DISCUSSION

The results simulated by the *UTNSim* using GA and ES timing plans are shown in Tables 1 and 2. Table 1 shows comparison of average delays between MCS and GA whereas Table 2 shows the comparison between MCS and ES.

Referring to Tables 1 and 2, further improvement on average delays produced by meta-heuristics methods is observed in all the scenarios simulated by the heuristic MCS. Figure 6 shows a graphical comparison of average delays produced by MCS, GA and ES respectively for all three scenarios. It is evident that the MCS has the best performance in terms of average delays. The MCS heuristic algorithm improved average delays for overloaded networks by more than 20%, when compared with GA and ES. On the other

Table 1
Comparison of MCS and GA average delays and network throughputs

Scenario	Average delays			Network Throughput			ACT (sec)
	MCS (s/veh)	GA (s/veh)	Improvement (%)	MCS (%)	GA (%)	Diff. (%)	
NOL	177.48	194.74	8.86	71.55	70.47	1.08	4.04
10% OL	200.36	250.87	20.13	75.68	74.80	0.88	4.54
20% OL	208.34	263.33	20.88	79.89	79.11	0.78	4.35

Table 2
Comparison of MCS and ES average delays and network throughputs

Scenario	Average delays			Network Throughput			ACT (sec)
	MCS (s/veh)	ES (s/veh)	Improvement (%)	MCS (%)	ES (%)	Diff. (%)	
NOL	177.48	191.83	7.48	71.55	70.68	0.87	4.04
10% OL	200.36	253.76	21.04	75.68	76.16	-0.48	4.54
20% OL	208.34	266.12	21.71	79.89	78.64	1.25	4.35

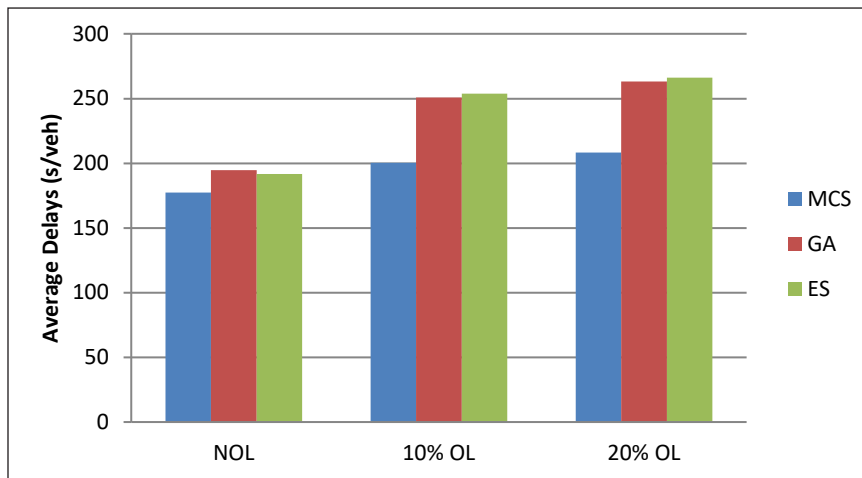


Figure 6. Average delays by MCS, GA and ES

hand, improvement of average delays for non-overloaded situations is 8.86% and 7.48% respectively.

The network throughput is defined as the total number of completed trips. This can be determined in terms of the total number of vehicles that had left the network at the end of the analysis period. For the network in this case study, 3000 vehicles entered the network at the end of the analysis period of 15 minutes. The network throughputs in Tables 1 and 2 show the percentage of vehicles out of the 3000 that completed their trips and left the network. It is observed that MCS, GA and ES network throughputs are similar and

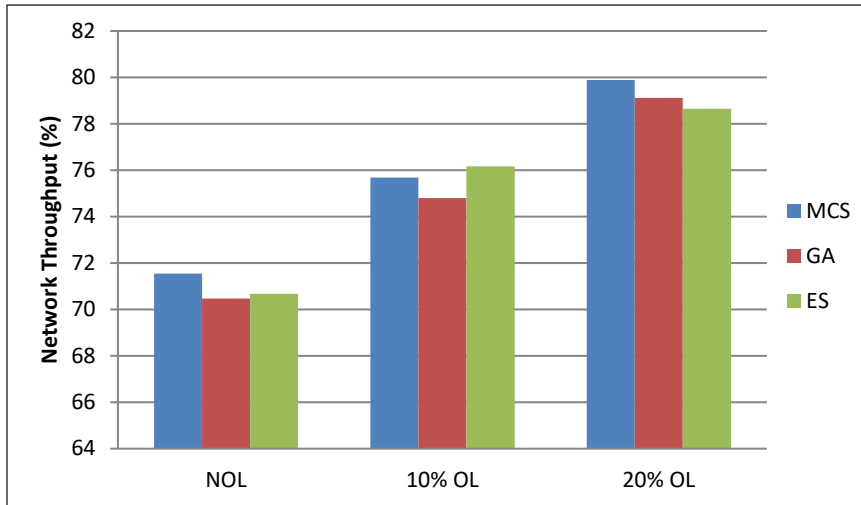


Figure 7. Vehicle throughputs by MCS, GA and ES

closer in agreement for all scenarios. Figure 7 shows a graphical comparison of network throughputs produced by MCS, GA and ES respectively for all three scenarios. Overall, MCS performed slightly better by producing higher throughputs compared to GA and ES in most scenarios except in 10% OL where it is 0.48% lesser compared to ES.

The improvement achieved by the MCS is primarily due to the consideration of both existing queues and incoming traffic at the respective intersection which are pre-processed into clusters by the NET-PREDICT algorithm. The NET-PREDICT utilizes schedule of an upstream intersection to predict the predicted output flows beyond the local prediction horizons of downstream neighbours. Due to the chain of propagation in the entire network, this provides a look-ahead in the optimization process that can avoid myopic mistakes at each local intersection. On the other hand, the GA and ES methods in Hajbabaie et al. (2011) only consider existing queues in its objective function. Myopic mistakes could be apprehended by not taking into consideration the anticipated incoming flows.

Based on the objective function and related constraints, the GA and ES searched for an optimal solution that converges to a single timing plan for the whole analysis period. The heuristic MCS breaks the entire analysis period into multiple cycles or time horizons. Based on predicted traffics from the NET-PREDICT for each time horizon, the algorithm generates an optimal timing plan for each time horizon. Hence, there are multiple sets of timing plans generated within the analysis period to cope with varying traffic demands. Table 3 shows generated timing plans for MCS, GA and ES respectively for 20% OL. For brevity, only signal timing plans for three intersections are shown. Each intersection comprised of four signal phases namely E-W L (East-West Left Turn); E-W R-T (East-West Right-Through); N-S L (North-South Left Turn) and N-S R-T (North-South Right-Through), that indicates the direction of the vehicles going through the signal phase. The

Table 3
MCS, GA and ES timing plans for 20% OL

Inter-section	Signal Phase	MCS Green Phase Duration at Cycle:										GA	ES	
		1	2	3	4	5	6	7	8	9	10	11	All cycles	All cycles
1	E-W L	11	7	8	22	15	29	25	7	25	22	7	6	6
	E-W R-T	24	28	26	7	19	11	11	35	7	21	31	52	52
	N-S L	11	7	8	21	14	23	26	7	13	13	7	6	6
	N-S R-T	24	28	27	20	22	7	7	21	25	14	25	54	54
	Total CL	70	70	69	70	70	70	69	70	70	70	70	118	118
2	E-W L	7	7	22	18	26	21	11	11	7	11	16	6	6
	E-W R-T	13	20	19	13	7	10	21	28	28	29	26	46	46
	N-S L	21	18	8	22	26	26	10	7	7	7	7	6	6
	N-S R-T	29	25	21	7	11	10	27	24	28	23	21	42	44
	Total CL	70	70	70	60	70	67	69	70	70	70	70	100	102
3	E-W L	11	8	7	21	13	23	12	35	35	31	20	6	6
	E-W R-T	24	28	19	9	20	13	28	7	7	7	17	52	52
	N-S L	11	7	15	19	9	21	7	7	9	11	8	6	6
	N-S R-T	24	27	29	21	28	8	23	21	19	21	25	50	50
	Total CL	70	70	70	70	70	65	70	70	70	70	70	114	114

sum of all green phase durations equals the intersection total cycle length (Total CL). It can be observed that MCS green phase durations varies for each signal cycle according to traffic conditions whereas GA and ES green phases converged to a single value throughout the analysis period. Compared to a meta-heuristic search method, there is a stronger guarantee that the heuristics approach in the MCS that is tailored to flow information and adaptive timing plan could achieve better performance.

The ACTs in Tables 1 and 2 ranged between 4.04 to 4.35 s when the nine intersections network was simulated with an Intel Core i5 processor. Wey (2000) stated that the degree of forewarning in real-time networks is unlikely to exceed 15 s. Hence, control actions that respond below 15 s can respond accurately in real-time situations. The ACTs achieved in this work has performed excellently beyond this 'benchmark'. In addition, the control time step for an MPC is normally below 5 minutes for traffic network control (Schutter et al., 2010); thus, the ACTs of the MCS is well suited for real-time application. In contrast, the GA and ES takes 4 minutes for each simulation run in VISSIM (Hajbabaie et al., 2011) which is inferior compared to MCS.

CONCLUSION

This comparative study on the performance of heuristics versus meta-heuristics control methods have shown that heuristics could outperformed meta-heuristics optimization

control methods by producing greater reduction in average delays and improve traffic throughputs. This has shown somewhat that heuristics method could also provide optimal solutions in a nonlinear environment. In addition, due to extensive search in GA and ES for optimal solutions; the heuristics MCS fare better in computational time, which provide immediate benefits for its application in online real-time traffic control and optimization.

ACKNOWLEDGEMENT

This work is funded by the Ministry of Education Malaysia through the Fundamental Research Grant Scheme (FRGS) no: FRGS/1/ 2019/TK04/UITM/02/38.

REFERENCES

- Aboudolas, K., Papageorgiou, M., Kouvelas, A., & Kosmatopoulos, E. (2010). A rolling horizon quadratic-programming approach to the signal control problem in large scale congested urban road networks. *Transportation Research Part C: Emerging Technologies*, 18(5), 680-694. <https://doi.org/10.1016/j.trc.2009.06.003>
- Al-Kandari, A., Al-Shaikhli, I., & Najaa, A. (2013). Comparative study between traffic control methods using simulation software. *International Journal of Machine Learning and Computing*, 3(5), 424-429. <https://doi.org/10.7763/ijmlc.2013.v3.353>
- Basri, N. S. H., Mohamed, N. A., Adnan, M. A., Mohamed, N. F., & Zainuddin, N. H. (2020). Instantaneous speed ratio of traffic flowing through a merging area at kilometer 31.6 on the highway from Shah Alam to Kuala Lumpur. *Pertanika Journal of Science & Technology*, 28(2), 565-578.
- Cantarella, G. E., Luca, S. D., Pace, R. D., & Memoli, S. (2015). Network signal setting design: Meta-heuristic optimisation methods. *Transportation Research Part C*, 55, 24-45. <https://doi.org/10.1016/j.trc.2015.03.032>
- Cao, H., & Luo, J. (2019). Coordinated optimization control of regional traffic signals based on vehicle average delay model. In *2019 2nd International Conference of Intelligent Robotic and Control Engineering (IRCE)* (pp. 72-77). IEEE Conference Publication. <https://doi.org/10.1109/irce.2019.00022>
- Dang, Q. V., & Rudová, H. (2018). Enhanced scheduling for real-time traffic control. In *2018 IEEE Symposium Series on Computational Intelligence (SSCI)* (pp. 578-585). IEEE Conference Publication. <https://doi.org/10.1109/ssci.2018.8628731>
- Davydov, I., Tolstykh, D., Kononova, P., & Legkih, I. (2019). Genetic based approach for novosibirsk traffic light scheduling. In *2019 15th International Asian School-Seminar Optimization Problems of Complex Systems (OPCS)* (pp. 31-36). IEEE Conference Publication. <https://doi.org/10.1109/opcs.2019.8880158>
- Diakaki, C., Papageorgiou, M., & Aboudolas, K. A. (2002). Multivariable regulator approach to traffic-responsive network-wide signal control. *Control Engineering Practice*, 10(2), 183-195. [https://doi.org/10.1016/s0967-0661\(01\)00121-6](https://doi.org/10.1016/s0967-0661(01)00121-6)
- Doostali, S., Babamir, S. M., Dezfoli, M. S., & Neysiani, B. S. (2020). IoT-based model in smart urban traffic control: Graph theory and genetic algorithm. In *2020 11th International Conference on Information*

- and *Knowledge Technology (IKT)* (pp. 119-121). IEEE Conference Publication. <https://doi.org/10.1109/IKT51791.2020.9345623>.
- Gao, K., Wu, N., & Wang, R. (2019). Meta-heuristic and MILP for solving urban traffic signal control. In *2019 International Conference on Industrial Engineering and Systems Management (IESM)* (pp. 1-5). IEEE Conference Publication. <https://doi.org/10.1109/iesm45758.2019.8948068>.
- Grandinetti, P., Garin, F., & Canudas-de-Wit, C. (2015). Towards scalable optimal traffic control. In *2015 54th IEEE Conference on Decision and Control (CDC)* (pp. 2175-2180). IEEE Conference Publication. <https://doi.org/10.1109/cdc.2015.7402529>
- Hajbabaie, A., Medina, J. C., & Benekohal, R. F. (2011). *Traffic signal coordination and queue management in oversaturated intersections* (No. 047IY02). NEXTRANS Center (US).
- Hajiahmadi, M., Haddad, J., De Schutter, B., & Geroliminis, N. (2015) Optimal hybrid perimeter and switching plans control for urban traffic networks. *IEEE Transactions on Control Systems Technology*, 23(2), 464-478. <https://doi.org/10.1109/tcst.2014.2330997>
- Lammer, S., & Helbing, D. (2008). Self-control of traffic lights and vehicle flows in urban road networks. *Journal of Statistical Mechanics: Theory and Experiment*, P04019, 1-34. <https://doi.org/10.1088/1742-5468/2008/04/p04019>
- Le, T., Kovačs, P., & Walton, N. (2015). Decentralized signal control for urban road networks. *Transportation Research Part C: Emerging Technologies*, 58, 431-450. <https://doi.org/10.1016/j.trc.2014.11.009>
- Li, Y., Canepa, E., & Claudel, C. (2014). Optimal traffic control in highway transportation networks using linear programming. In *2014 European Control Conference (ECC)* (pp. 2880-2887). IEEE Conference Publication. <https://doi.org/10.1109/ecc.2014.6862338>
- Li, X., & Sun, J. (2018). Signal multiobjective optimization for urban traffic network. *IEEE Transactions on Intelligent Transportation Systems*, 19(11), 3529-3537. <https://doi.org/10.1109/tits.2017.2787103>
- Ng, K. M. Reaz, M. B. I., & Ali, M. A. M. (2019). Model-based control strategy for oversaturated traffic regimes based on the LWR-IM traffic model. *IET Intelligent Transportation System*, 13(5), 896-904. <https://doi.org/10.1049/iet-its.2018.5381>
- Ng, K. M., Reaz, M. B. I., Ali, M. A. M., & Chang, T. G. (2013). A brief survey on advances of control and intelligent systems methods for traffic-responsive control of urban networks. *Tehnički vjesnik*, 20(3), 555-562.
- Ng, K. M., & Reaz, M. B. I. (2015). An integrated approach for platoon-based simulation and its feasibility assessment. *PLoS ONE*, 10(3), 1-25. <https://doi.org/10.1371/journal.pone.0114406>
- Ng, K. M., & Reaz, M. B. I. (2016). Platoon interactions and real-world traffic simulation and validation based on the LWR-IM. *PLoS ONE*, 11(1), 1-17. <https://doi.org/10.1371/journal.pone.0144798>
- Ng, K. M., & Reaz, M. I. (2017). Development and validation of the LWR-IM traffic simulator. In *2017 7th IEEE International Conference on Control System, Computing and Engineering (ICCSCCE)* (pp. 40-44). IEEE Conference Publication. <https://doi.org/10.1109/iccscce.2017.8284376>
- Ng, K. M., Reaz, M. B. I., & Rahiman, M. H. F. (2018). UTNSim: A new traffic simulator based on the LWR-IM mesoscopic traffic model. *Journal of Engineering Science and Technology*, 13(3), 589-608.

- Saha, P., Sarkar, A. K., & Pal, M. (2015). Evaluation of performance measures of two-lane highways under heterogeneous traffic. *Pertanika Journal of Science & Technology*, 23(2), 223-239.
- Schutter, B. D., Hellendoorn, H., Hegyi, A., Van den Berg, M., & Zegeye, S. K. (2010). Model-based control of intelligent traffic networks. *Intelligent Systems, Control and Automation: Science and Engineering*, 40(1), 277-310.
- Shaikh, P. W., El-Abd, M., Khanafer, M., & Gao, K. (2020). A review on swarm intelligence and evolutionary algorithms for solving the traffic signal control problem. In *IEEE Transactions on Intelligent Transportation Systems* (pp. 1-16). IEEE Conference Publication. <https://doi.org/10.1109/TITS.2020.3014296>.
- Stevanovic, A., Dakic, I., & Zlatkovic, M. (2017). Comparison of adaptive traffic control benefits for recurring and non-recurring traffic conditions. *IET Intelligent Transport Systems*, 11(3), 142-151. <https://doi.org/10.1049/iet-its.2016.0032>
- Tan, M. K., Chuo, H. S. E., Yeo, K. B., Chin, R. K. Y., Huang, S., & Teo, K. T. K. (2019). Decentralized traffic signal control for grid traffic network using genetic algorithm. In *2019 IEEE 6th International Conference on Engineering Technologies and Applied Sciences (ICETAS)* (pp. 1-6). IEEE Conference Publication. <https://doi.org/10.1109/icetas48360.2019.9117490>
- Tan, M. K., Chuo, H. S. E., Chin, R. K. Y., Yeo, K. B., & Teo, K. T. K. (2017). Optimization of traffic network signal timing using decentralized genetic algorithm. In *2017 IEEE 2nd International Conference on Automatic Control and Intelligent Systems (I2CACIS)* (pp. 62-67). IEEE Conference Publication. <https://doi.org/10.1109/i2cacis.2017.8239034>
- Toivio, T., Kosonen, I., & Roncoli, C. (2020). A multilayer optimisation framework for policy-based traffic signal control. In *2020 Forum on Integrated and Sustainable Transportation Systems (FISTS)* (pp. 347-352). IEEE Conference Publication. <https://doi.org/10.1109/FISTS46898.2020.9264870>.
- Wey, W. M. (2000). Model formulation and solution algorithm of traffic signal control in an urban network. *Computers, Environment and Urban Systems*, 24, 355-377.
- Zhang, Y., Su, R., & Gao, K. (2015). Urban road traffic light real-time scheduling. In *2015 54th IEEE conference on decision and control (CDC)* (pp. 2810-2815). IEEE Conference Publication. <https://doi.org/10.1109/cdc.2015.7402642>
- Zhou, Z., Lin, S., & Xi, Y. (2016). A hierarchical urban network control with integration of demand balance and traffic signal coordination. *IFAC-PapersOnLine*, 49(3), 31-36. [https://doi.org/10.1061/41177\(415\)122](https://doi.org/10.1061/41177(415)122)

Effect of Stick - Slip Phenomena between Human Skin and UHMW Polyethylene

Emad Kamil Hussein*, Kussay Ahmed Subhi and Tayser Sumer Gaaz

*Al-Mussaib Technical College TCM, Al-Furat Al-Awsat Technical University ATU,
P.O. Box 51006, Al-Mussaib, Babil, Iraq*

ABSTRACT

The present paper investigates experimentally effect of applied load and different velocity on the coefficient of friction between two interacting surfaces (human skin and Ultra-high-molecular-weight polyethylene (UHMW- polyethylene) at static and dynamic friction. It is possible to conclude specific point based on the above practical part and frictional analysis of this investigation as the most important mechanical phenomenon was creep has been observed a stick time interval where the static friction force is significantly increased during this stroke. The analytical model for stick-slip of skin and UHMWPE is proposed. The difference between static and kinetic friction defines the amplitude of stick-slip phenomena. The contact pressure, the sliding velocity, and rigidity of system determine the stability conditions of the movement between skin and UHMWPE. Experiments were carried out by developing a device (friction measurement). Variations of friction coefficient during the time at different normal load 4.6 and 9.2 N and low sliding velocity 4, 5, 6 and 7 mm/min were experimentally investigated. The results showed that the friction coefficient varied with the normal load and low sliding velocity. At static friction, the coefficient of friction decreased when the time increases, whereas, at dynamic friction, the coefficient of friction decreased when the time increased at normal load 4.6 and 9.2 N.

Keywords: Friction dynamic, friction static, human skin, stick-slip

ARTICLE INFO

Article history:

Received: 02 December 2020

Accepted: 16 February 2021

Published: 31 July 2021

DOI: <https://doi.org/10.47836/pjst.29.3.06>

E-mail addresses:

SHARAF.MOHAREB@gmail.com; emad_kamil72@atu.edu.iq

(Emad Kamil Hussein)

Kussaysubhi@atu.edu.iq (Kussay Ahmed Subhi)

Tayser1Gaaz@gmail.com (Tayser Sumer Gaaz)

* Corresponding author

INTRODUCTION

Human skin is considered as a complex multilayers tissue with a viscoelastic (non-linear) mechanical property, so that means it will exhibit a specific direct contact with other materials, especially in case of

frictional behavior considering contribution of each layer. Researchers are stimulated to investigate such kind of human skin friction.

Crowther et al. (2004) investigated a direct contact effect of applying normal load and probe frictional sliding speed on the biotribological features of skin and analyzing such specific frictional behavior and mechanism. A multi-specimen friction rig has been employed to conduct the experimental part of this investigation, where the normal load varies from starting value of 0.1 up to 0.9 N. So, because of this increment, both of normal displacement and the associated coefficient of friction are increased, formation of two frictional components adhesion and deformation was behind of this increment. On the other side, creation of stick-slip phenomenon was the main factor that contributes to rise the value of the induced coefficient of friction as the sliding speed from initial value of 0.5 millimeter per second up to a final value of 4 millimeters per second. In addition, based on hysteresis friction principle, Tang et al. (2008) presented a detailed logic explanation of the expected mutual influence of normal load and sliding speed on frictional behavior of skin.

Chatelet et al. (2008) reviewed a recent factor that was closely related to human skin frictional tribology including experimental examination for human skin frictional factors based on many zones in human body. First factor under investigation was direct contact skin pressure induced under wide range of boundary conditions and measurements. Derler and Rotaru (2013) concluded that almost all previous researches were explaining about the two frictional components, adhesion and deformation. Furthermore, it is seen that dry skin gives a specific value of coefficient of friction ranging around 0.5 but the situation is completely different in case of moist skin where the same coefficient under the same loading conditions is fluctuating above-leading to decrease contact pressure significantly.

Derler and Rotaru (2013) developed a special device that is used to measure complementary features to the viscoelastic properties of human skin by employing a dynamic indenter, so the two important parameters were human skin stiffness exactly like this one for an elastic element, spring, and the damping coefficient like the vicious element, dashpot, where these two mechanical parameters are completing the other essential tribological properties of human skin. Results showed that complex modulus measured by this modified dynamic indentation technique was about 7.2 KPa for aged volunteer and 10.7 for younger ones, hence, the main reason that causes such variation in the measured values was the nature of human skin as a function of time and the associated semi degeneration of some specific layers with human skin as time goes on.

Dong et al. (2017a) have developed a special tribo-acoustical probe that has been used to measure a friction noise via recording the generated sound of a pressure level in case of direct dynamic contact between two mating surfaces, the first one is representing an artificial finger when rubbing on various surfaces. An attached microphone has been installed to the modified sensing system to soundtrack different levels of the generated

sounds and then comparing these acquired sounds to precisely assess smoothness in all rubbing cases. Final observations showed that friction noise gives an excellent indication of softness and smoothness in such tribological friction cases.

Dong et al. (2017b) studied mechanical and viscoelastic properties of human skin in vivo as a first step to assess the direct and side effects of cosmetical and medical products on human skin. Boyer et al. (2007) developed a non-invasive rig that is used to examine viscoelastic properties of human skin in vivo based on direct dynamic indentation. Obtained findings showed the Kelvin-Voigt model was well expressing the mechanical behaviors of such kind of skin with dynamic indentation effect. In addition, a mean value of stiffness and damping coefficient were also considered into account to compare skin viscoelastic features. Final experimental outcomes showed an accurate value of the measured factors, which surely means it is possible to use this device as a viscoelastic Tribometer in future work.

Mulliah et al. (2004) examined some definite parameters including finger hydro-lipid skin film, overall shape, precise surface roughness, and rigidity for both men and women on friction conditions in case of direct rubbing between these fingers and other selected surfaces. Four surfaces were considered in this research, two of them are real and the remaining is virtual. A developed stimulator named STIMTAC has been employed to achieve goals for both cases of men's and women's fingers skin. A significant dissimilarity between men's and women's finger surface topography has been also observed and this fact is due to men's finger skin are rougher than for women's fingers.

Perfilyev et al. (2013) conducted an experimental investigation about the stick-slip phenomenon in case of friction between the index finger pad in direct sliding on wet surface and smooth surface glass taking into consideration the amount of the applied force and the associated sliding velocity by engaging a tri-axial force plate rig. The attained coefficient of friction during the stick-slip phase was 30% lower than for the case of stationary sliding, plus final finding exhibits that during the stick-slip period coefficient of friction varies by about $\pm 25\%$ around the mean value, hence it is accepted to consider the achieved results as a basis of artificial skin in mechanical manipulators especially in the interaction between precision riggings and soft tissues.

Terrand-Jeanne and Martins (2016) created a comparison between the obtained elastic constant (stiffness) for collagen and elastin within human skin with other same investigations in previous publications. The basis of this paper was about the precise examination of viscoelastic properties of human skin via determining the variation of stress-strain interaction, so as usual the induced stiffness was measured directly from the elastic stress-strain diagram, meanwhile, the collagen fibril length was acquired from the mathematical slope of a viscous stress-strain diagram. Finally, stiffness for collagen was about 4.4 GPa and for elastin 4 MPa, and this is due to alterations in the collagen forms and the associated natures in human skin and tendon which may significantly affect such specific viscoelastic properties.

Tu and Fort (2004) have suggested a parametric finite element contact homogenization simulation procedure to predict the expected effect of the skin topography nature including microstructure on the measured response of human skin friction, so depending on simulation of sliding of different indentation probes on human skin. Results illustrate the significant effect of the real complex geometry of human skin cross-sectional microstructure on the induced deformation component of such kind of specific friction and hence the complicity leads to increase this essential component plus the generated global friction coefficient was differing from the local one where the global was lower than the other coefficient.

Wee et al. (2001) studied the formation of the stick-slip phenomenon in two cases, the first one was in the case of low sliding speed of the probe on the opposite surface, meanwhile, the second case was at a very low sliding speed. It is considered that the induced static coefficient of friction (μ_s) between the two mating surfaces must be greater than the kinetic coefficient of friction (μ_k) conclusion was stated that using bearing will significantly decrease the effect of stick-slip occurrence. In this research, the Effect of Stick-Slip Phenomena between Human Skin and UHMW Polyethylene has been investigated experimentally. Velocity and force were the main indicators of the analysis of the skin characterization.

MATERIALS AND METHODS

The first part device called (stick-slip device) manufactured in Romania related to the mechanical parts whereas the electronic parts were designed and instated on the device by the authors to measures the skin friction at different velocities as shown in Figure 1. The main parts of this device are the electric motor, gearbox, tangential sensor, and load cell sensor modified by the authors (Figures 2 and 3).

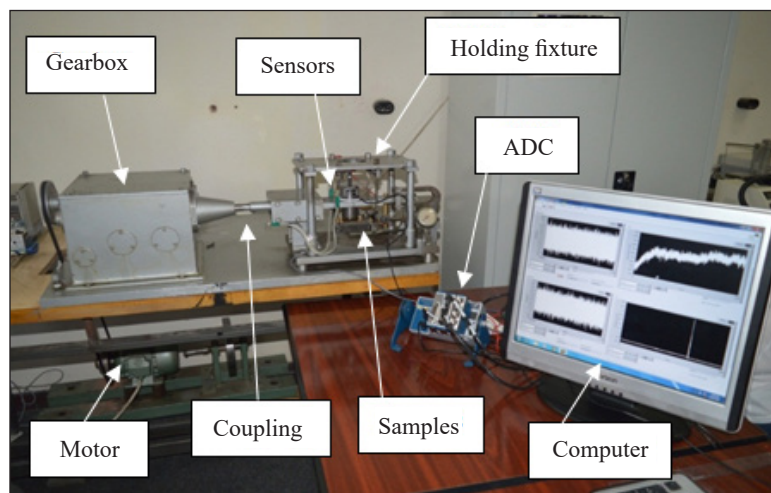


Figure 1. The developed rig

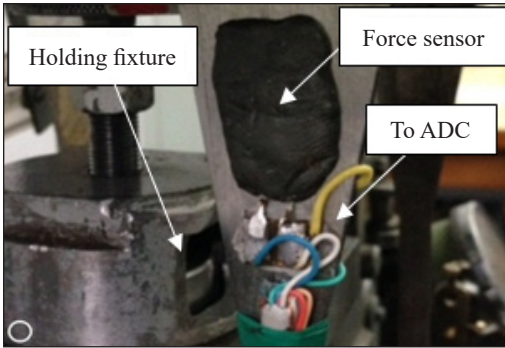


Figure 2. The attached tangential force sensor

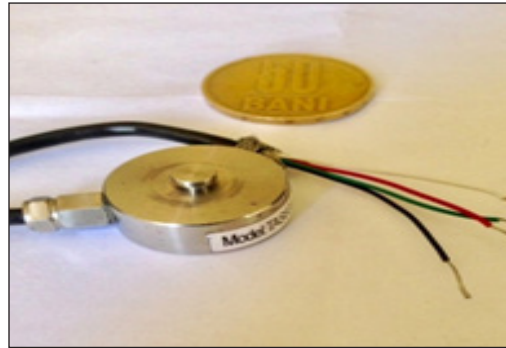


Figure 3. The employed load cell sensor



Figure 4. The employed ADC

In case of requiring a directly applied load, then it is usually depending on the so-called load cell, and this kind of sensors can transform applied load or pressure up to 10 Kg into an electrical pulse, in other words, the load cell measures the variance in electrical resistance based on the amount of the applied load so that means the electrical resistance variation is directly proportional

to the associated applied load, force or pressure. In many specific cases of friction, it is best to use disk load cells, that are having a suitable design and flexible handling with the frictional case under consideration than the bar-style cells. Load cells are manufactured from alloy steel and are having four strain gages, four electric resistances that are forming the Wheatstone electrical bridge, which is used to measure unknown value electric resistance by creating a balance in the other two terminals (legs) of the bridge. There are many types of such electric bridges and the common one is having (220 * 13 * 1000) mm dimensions.

Regarding stick-slip the device, a Converter was used to transfer the signal from analog to digital was connected between the sensors and computer model (NI cDAQ-917) as shown in Figure 4. The all-force measurement data was used for the data analyses for which specific programs were developed using the software LabVIEW. The tip used in this study made from UHMW polyethylene with a dimension (diameter is 7 mm; section area is 38.5 mm²).

Conditions

In this study, the ambient conditions were as follows, room temperature 25°C and approximate humidity of about (38-45) %, The experiment was repeated at less three times and the average was considered. Before the examinations, the prepared skin was

well prepared to fit the local laboratory boundary conditions for at least 10 minutes, the test sites were marked to ensure repeatability of the data. The index finger skin has been very well cleaned by using the Ethanol alcohol and then washed with sterilized water. Before starting the investigation as much as other examinations plan, at the same moment the indenter tip UHMW polyethylene material also cleaned with ethanol and water. All friction measurements were carried out by the same subject (male, 49 years), using the index finger of the dominant.

Device for Friction Study at Low Slipping Velocity

- The employed rig has been modified by attaching a suitable load (force) sensor to be connected to a specific software program named LabVIEW via a desktop computer and then adjusted and normalized by checking various load values starting from zero up to 1800 grams with step increment of 150 grams per each step, where the first experimental step was setting the nominated skin without any tension or compression stresses as shown in Figure 1.
- ASTM D3108 Standard Test Method for Coefficient of Friction, Yarn to Solid Material has been employed to carry out the results. The author observed the new device has a higher accuracy with a lower price compared with the UMT device. However, before the experimental with the second device (stick-slip device) starting there are several parameters were adjusted as follows:
 - Time duration for each frictional test was about 60 seconds, and the total number of repetitions were 48 single frictional tests.
 - Maximum sliding distance of the finger with UHMWPE was between 4-7 mm.
 - Range of normal forces is 4.6 up to 9.2 N.
 - Sliding velocities were 4, 5, 6 and 7 mm/min.

First Step. Applied normal force 9.2N at different velocities (4, 5, 6, 7 mm/min) as shown in Figure 5 the stick-slip phenomena appeared at the time (0 – 60 sec), for velocity 4mm/min the stick-slip is very clear compared to other velocities.

Second Step. Applied normal force 4.6 N at different velocities (4, 5, 6,7 mm/min) as shown in Figure 6 the stick-slip phenomena appeared at the time (0-40 sec), for velocity 5mm/min the stick-slip is clear compared to other velocities.

RESULTS AND DISCUSSION

The final practical and experimental results of this investigation have been acquired from the employed modified devices that are related to clarifying the outcome of frictional behavior of human skin at various boundary conditions, so these gained results are listed below.

Stick-slip Device

The stick-slip behavior of the index finger sliding and UHMW polyethylene was examined as a function of normal applied force and the associated sliding velocity in this specific kind of frictional measurement by using (stick-slip device). The friction coefficients during stick-slip were (min=0.27, max= 0.32), which clearly gained to be typical of about 25.6% lower than those of stationary sliding test (min=0.36, max=0.43) as shown in Figure 5. Stick-slip frictional tests noted took place throughout the entire frictional experiments or alternated with the stationary sliding frictional phases.

It was observed at the applied load of 9.2 N decrease the coefficient of friction with the increase in the velocity of sliding friction significantly compared to when the load of 4.6 Newton due to human skin shows a complicated surface topography and, viscoelastic properties (non-linear behavior), resulting in a very complex mechanical direct contact conditions and specific frictional behavior. Physiological responses including sweating will additionally complicate this mutual contact mechanics by interactively varying the caused interface between the human skin and counter-surface at the region under consideration. Also, detected for a normal applied force of about 9.2 N the full detailed breakdown displays that the periods of formation of sticking were a direct factor of around two greater than the periods of slipping. In contrast, observed for a normal force of 4.6 N the detailed analysis shows that the periods of sticking were a factor of around 3 times longer than that of the periods of slipping. As shown in Figures 5 and 6 when drawing zoom.

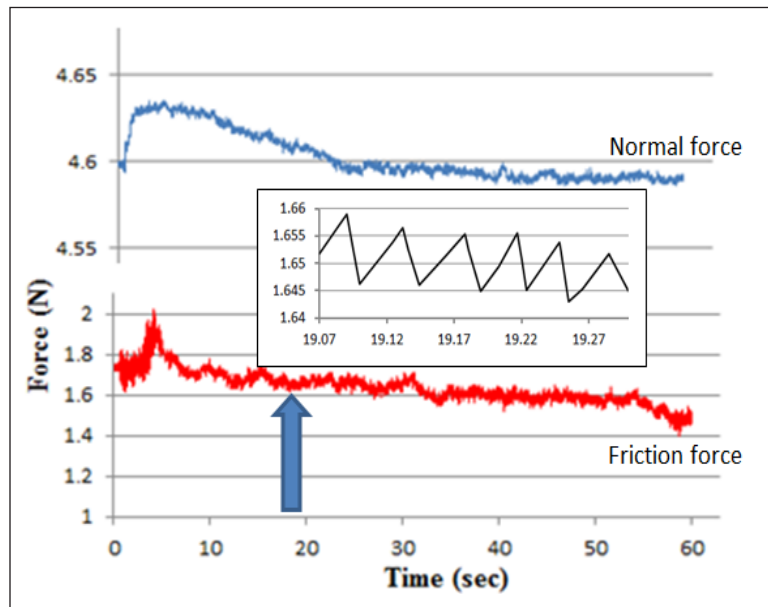


Figure 5. Normal force against test time duration, at load of 4.6 N

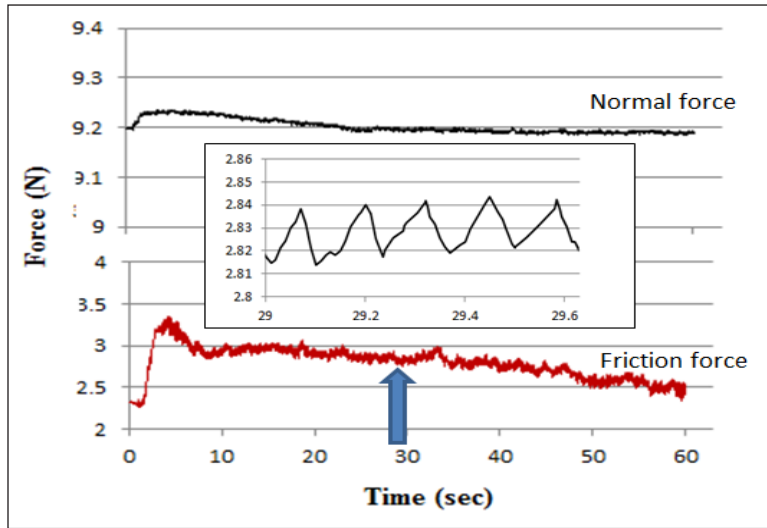


Figure 6. Normal force vs test time, at load 9.2 N

Effect of Sliding Velocity and Friction Mechanism

The sliding velocity and friction mechanism were done by logically increasing sliding velocity from 0.3 mm/min to 7 mm/min. As sliding velocity increases friction coefficient decreases and hence through assessment fitting the correlation coefficient reaches up to 0.96 and 0.91 at normal load 4.6 N and 9.2 N respectively as shown in Figure 7. During the sliding hypothesis, almost all the sliding energy is released when the applied stress is completely removed from the contact region skin. The hysteretic skin friction was relatively small in amount because of lost a small amount of energy, whereas, at higher values of sliding speed, the local deformation rate on the employed skin is also increased and the obtained deformation is so difficult to local recover instantaneously.

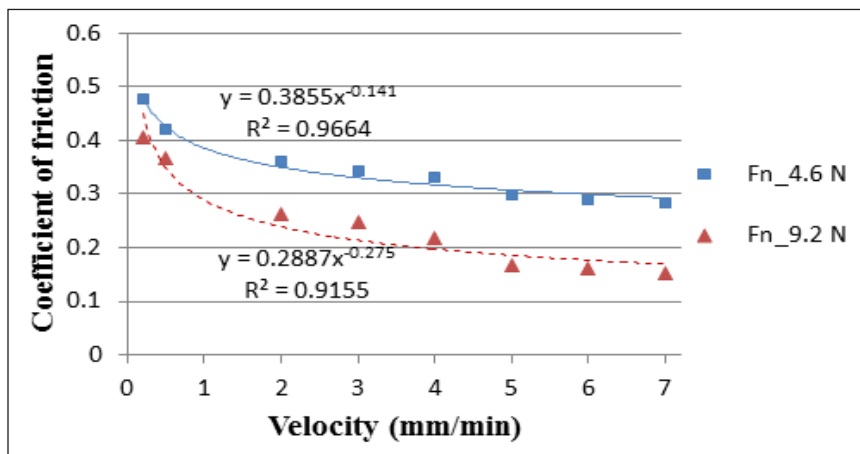


Figure 7. Coefficient of friction vs velocity

Effect of Normal Load and its Mechanism

The examinations of applying normal loads were conducted by the gradual increase of the applied normal loads from an initial value of 2.3 N up to 19.3 N. The obtained results with a fitted curve of the gained coefficient of friction against the applied normal loads are shown in Figure 8. Figure 8 shows the results of the load based on the practically measured coefficients of friction. Here, the mean friction coefficient was mathematically calculated for the principal sliding phases and graphically plotted against the induced mean normal force. The two sole factors that are leading to such relatively small values of the standard deviations between (0.0045-0.0161) were the expected variations in the total friction force during the stick-slip phase as well as variations in the direction normal force applied by the external weight during each individual frictional experiment. A fit to the gained results by using the so-called Power-law function when use different velocity gives Equation 1 and 2:

$$\mu(F_n) = 0.6777 F_n^{-0.29} \tag{1}$$

$$\mu(F_n) = 0.695 F_n^{-0.441} \tag{2}$$

The correlation coefficient reaches 0.973 and 0.948, respectively as the coefficient of friction is proportional to the applied normal load, where μ denotes the friction coefficient and F_n the normal force.

To accurately estimate the rising direct contact pressure at the specified skin region, the contact area of the human index finger was measured as a function of the applied normal force. The specified area of the finger direct contact area with UMHW polyethylene area measured in mm² on the normal force F_n (N) approximately associated to the function as shown in the following Equation 3:

$$A(F_n) = 0.275 F_n^{-0.195} \tag{3}$$

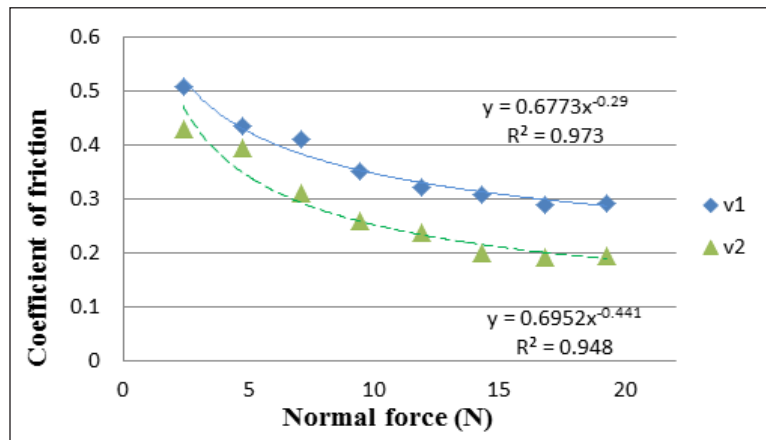


Figure 8. Coefficient of friction against normal load

Figure 9 presents the pressure-dependence of the friction coefficients. It is clear to be distinguished that the real contact area between the index finger and UHMW polyethylene on the infinitesimal level is considerably smaller than that of the apparent contact area, causing to relatively higher real contact pressures in the definite skin contact zones, therefore, it can be supposed that the micro-mechanical behavior of skin is characterized by a higher modulus of elasticity.

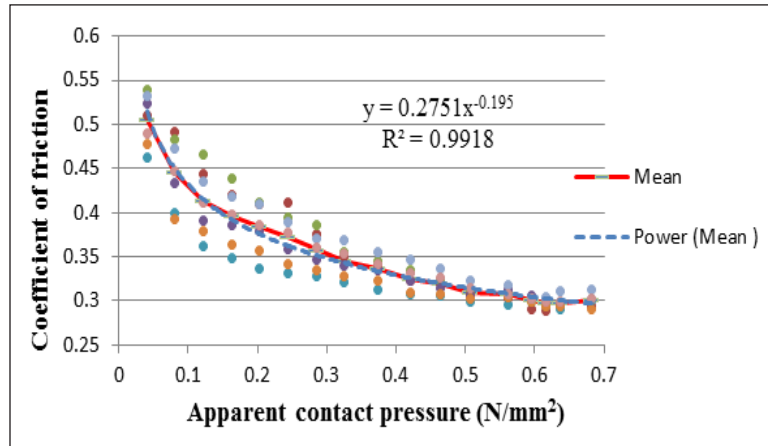


Figure 9. Coefficient of friction as a function of contact pressure

CONCLUSION

- It is possible to conclude specific point based on the above practical part and frictional analysis of this investigation as:
- One of the most important mechanical phenomenon was creep has been observed a stick time interval where the static friction force is significantly increased during this stroke, The analytical model for stick-slip of skin and UHMWPE is proposed.
- The difference between static and kinetic friction defines the amplitude of stick-slip phenomena. The contact pressure, the sliding velocity, and rigidity of system determine the stability conditions of the movement between skin and UHMWPE.
- The normal applied load effects the frictional behavior of human skin friction and the coefficient of friction shows utterly load dependence.
- When the normal load increases from 2.3 N to 19.3 N, the friction coefficient of skin decrease.
- The sliding speed influences the frictional behavior of human index finger skin when the adjusted sliding speed is increasing from initial value of 0.3 mm/min up to 7 mm/min, and the coefficient of friction decreases, plus the “stick-slip” phenomenon appears.

- Obtained results for the stick–slip friction tests with the human finger might be valuable in connection with the improvement of the prosthetic socket and for the accurate control of the formation of stick–slip friction between of the skin and the inner layer of the socket.

ACKNOWLEDGEMENT

The present work was undertaken under the support of the State Company for Fabrics Industries (SCFI), for the preparing and providing of all fabrics, and funded by Al-Furat Al-Awsat Technical University (ATU), Iraq. Also, many thanks for the all amputee persons. The author acknowledges the constant support encouragement of Professor Dr. Eng. Andrei Tudor, Politehnic Univ. of Bucharest, Romania, and Prof. Dr. Eng. Muhsin J. J. Head of P&O Eng. Dept. at College of Engineering, Nahrain University, Baghdad, Iraq.

REFERENCES

- Boyer, G., Zahouani, H., Le Bot, A., & Laquieze, L. (2007). In vivo characterization of viscoelastic properties of human skin using dynamic micro-indentation. In *2007 29th Annual International Conference of the IEEE Engineering in Medicine and Biology Society* (pp. 4584-4587). IEEE Conference Publication. <https://doi.org/10.1109/IEMBS.2007.4353360>
- Chatelet, E., Michon, G., Manin, L., & Jacquet, G. (2008). Stick/slip phenomena in dynamics: Choice of contact model. Numerical predictions & experiments. *Mechanism and Machine Theory*, *43*(10), 1211-1224. <https://doi.org/10.1016/j.mechmachtheory.2007.11.001>
- Crowther, A., Zhang, N., Liu, D. K., & Jeyakumaran, J. K. (2004). Analysis and simulation of clutch engagement judder and stick-slip in automotive powertrain systems. *Proceedings of the Institution of Mechanical Engineers, Part D: Journal of Automobile Engineering*, *218*(12), 1427-1446. <https://doi.org/10.1243/0954407042707731>
- Derler, S., & Rotaru, G. M. (2013). Stick–slip phenomena in the friction of human skin. *Wear*, *301*(1-2), 324-329. <https://doi.org/10.1016/j.wear.2012.11.030>
- Dong, C., Shi, L., Li, L., Bai, X., Yuan, C., & Tian, Y. (2017a). Stick-slip behaviours of water lubrication polymer materials under low speed conditions. *Tribology International*, *106*, 55-61. <https://doi.org/10.1016/j.triboint.2016.10.027>
- Dong, C., Yuan, C., Bai, X., Qin, H., & Yan, X. (2017b). Investigating relationship between deformation behaviours and stick-slip phenomena of polymer material. *Wear*, *376*, 1333-1338. <https://doi.org/10.1016/j.wear.2017.01.061>
- Mulliah, D., Kenny, S. D., & Smith, R. (2004). Modeling of stick-slip phenomena using molecular dynamics. *Physical Review B*, *69*(20), Article 205407. <https://doi.org/10.1103/PhysRevB.69.205407>
- Perfilyev, V., Moshkovich, A., Lapsker, I., Laikhtman, A., & Rapoport, L. (2013). The effect of vanadium content and temperature on stick–slip phenomena under friction of CrV (x) N coatings. *Wear*, *307*(1-2), 44-51. <https://doi.org/10.1016/j.wear.2013.08.012>

- Tang, W., Ge, S. R., Zhu, H., Cao, X. C., & Li, N. (2008). The influence of normal load and sliding speed on frictional properties of skin. *Journal of Bionic Engineering*, 5(1), 33-38. [https://doi.org/10.1016/S1672-6529\(08\)60004-9](https://doi.org/10.1016/S1672-6529(08)60004-9)
- Terrand-Jeanne, A., & Martins, V. D. S. (2016). Modeling's approaches for Stick-Slip phenomena in drilling. *IFAC-PapersOnLine*, 49(8), 118-123; <https://doi.org/10.1016/j.ifacol.2016.07.428>
- Tu, C. F., & Fort, T. (2004). A study of fiber-capstan friction. 2. Stick-slip phenomena. *Tribology International*, 37(9), 711-719; <https://doi.org/10.1016/j.triboint.2004.02.009>
- Wee, H., Kim, Y. Y., Jung, H., & Lee, G. N. (2001). Nonlinear rate-dependent stick-slip phenomena: Modeling and parameter estimation. *International Journal of Solids and Structures*, 38(8), 1415-1431; [https://doi.org/10.1016/S0020-7683\(00\)00058-5](https://doi.org/10.1016/S0020-7683(00)00058-5)

Development of Mini CNC Machine Design and Building for Making Ceramic Cup and Bowl Prototype

Anantakul Intarapadung

Faculty of Industrial Technology, Phranakhon Rajabhat University, 9 Changwattana Road, Bangkhen Bangkok, 10220, Thailand

ABSTRACT

This article aimed to describe the design and building of a 3-axis mini computer numerical control (CNC) machine for making a ceramic cup and bowl prototype that helps achieve a fully-automated production process using a small budget. Step motors were used to control the movement of the 3 axes, X, Y, and Z axis, of the Mini CNC machine. Automated operating system was controlled through unipolar microstepping driver and spindle adjustment PC interface board. The operating system was controlled by Mach 3 software, G-code command. Based on a test using a prototype milling of a lotus leaf ceramic bowl with a diameter of 130 centimeter and height of 65 millimeter, it was found that the depth of cut in milling each round was 6 millimeter, the test of building a dry clay lotus leaf bowl with a hard plaster lotus leaf bowl, fine milling with feeding speed of 1000 - 3,000 (mm / min), and increasing the spindle speed of 10,000 - 15,000 (rpm), circular milling cutter with a depth of 0.1 (mm). In each circular, the increase of the feeding speed and the spindle speed would reduce the time required for building. The smoothness of the lotus leaf bowl surface depended on the hardness of the material used to make the prototype. When comparing the performance with the 5-axis CNC machines on the market, it was found that the performance was similar, but the Mini CNC Machine had size, weight, and price less than others.

Keywords: Ceramic, G-code, mini CNC

ARTICLE INFO

Article history:

Received: 10 January 2021

Accepted: 01 April 2021

Published: 31 July 2021

DOI: <https://doi.org/10.47836/pjst.29.3.22>

E-mail address:

anantakul@pnu.ac.th

ISSN: 0128-7680

e-ISSN: 2231-8526

INTRODUCTION

Manufacturing high quality products with time saving and cost saving in the production process is a basic need of industry operators in a highly competitive situation. Therefore, it is necessary to employ a computer system

to assist in manufacturing (Computer Integrated Manufacturing, CIM) (Delaram & Valilai, 2018). A basic principle of computer integrated manufacturing involves computer numerical control or CNC using a CNC machine is more precise than humans (Li, et al., 2020).

There are different types of CNC machines in the market and the popular ones are 2-axis and 3-axis CNC machines (Yousefian, et al., 2020). Major components of CNC machines are mechanical design, drive modules, and system software (Lin & Koren, 1996). Mechanical design is composed of system structure, drive modules consist of microprocessor, and the last part – system software used for milling a work-piece is controlled by G-code command and NC-code command (Madekar, et al., 2016).

Mini CNC machine uses the same operating system as other CNC machines but the objective of the maker is to save cost in purchasing a large and expensive CNC machine with redundant mechanisms more than necessary for medium-sized and small-sized enterprises including moving and installation that requires a large place and specialists (Sarkar, et al., 2020).

Mini CNC ceramics machine is an automated milling machine for prototyping ceramic cups and bowls. It can facilitate milling prototypes from 50 millimeter circumference and 50 millimeter height to 100 millimeter circumference and 200 millimeter height. The machine structure is conveniently installed and moved. Its operative system is similar to that of other CNC machines. A 3-D model using computer-aided design is saved in the dwg file type. The file is converted into a path of the machine using G-code command or NC-code command. The prototype obtained from the CNC ceramic milling machine is exactly like the design more precise than humans and the price of the machine is cheaper than the ones in the market (Jinan Style Machinery Co., L., 2021).

MATERIALS AND METHOD

Mini CNC Machine

CNC technology has been widely used in the production process. Moreover, a control board is cheap and bought easily these days like each model of Arduino board designed to support mini CNC machine which can be applied to other devices easily because a free software download is offered for control software including software used for the development (Hirani, 2019). Currently, a mini milling machine is developed to serve various kinds of automatic work such as the development of automatic plotter and automatic PCB cutting machine. The purpose of making the mini CNC machine is cost saving and it can be used with PC, Arduino ATMEGA 328 control board that is cheap and easy to find. It can facilitate G-code command for PCB drawing and drilling, CD/DVD writer, stepper motors, Servo motor, motor drivers, and design of 2-D building sketch (Kumar, et al., 2017).

Utilizing CNC technology to make ceramic prototypes for replacing conventional manufacturing process- Producing a prototype mold is a time-consuming process. Solid

Work software used to design ceramic products can reduce design time and a path of milling can be checked before feeding to CNC machine for making a ship prototype and a prototype model. The findings from this study indicated that new technology can help artists produce their pieces of work with Solidwork software and make a product prototype using a CNC machine based on an interdisciplinary approach between ceramic production process and digital production technology (Yousefian, 2020).

3-Axis CNC Machine

The design and development of 3-Axis CNC router machine with microcontroller can achieve a variety of complex workpieces with low cost. The machine supports cutting, reaming, marking, drilling, and milling for wood, acrylic, and PCB box. The microcontroller can facilitate design and image processing software such as ArtCam and InkScape that can convert the movement procedure of end mills in milling and reaming using G-code and GRBL software to control the operating system of the mini CNC machine. Test results and precision test showed that the machine can work efficiently on a work area of 280 width, 170 length, and 65 millimeter height (Patel et al., 2019).

Implementation

The mini CNC ceramic machine consists of 3 subsystems, i.e. mechanical system, electronic system, and computer software. The steps for making the machine are as follow:

- Step 1 – design operating control electrical circuit
- Step 2- design operating mechanism
- Step 3 – install hardware devices
- Step 4 – design workpieces for testing the machine operating system
- Step 5 – compare milling efficiency on each material.

Step to Design Operating Control Electrical Circuit

The microcontroller is used to control the movement of workpieces on the 3 axes, X, Y, and Z axis through step motors using G-code command converted from the designed 3-D model. The designed electrical circuit block is shown in Figure 1.

Based on Figure 1, when a computer receives G-code command, step motors control the movement of the 3 axes, X, Y, and Z axis of the Mini CNC machine in circular motion. Automated operating system is controlled through unipolar microstepping driver and spindle adjustment PC interface board.

Step to Design Operating Mechanism and Install Hardware Devices

The mini CNC ceramic machine consists of aluminum structure for installing ball screw. The machine moves in a straight line on X axis with 41.0 centimeter length, Y axis with

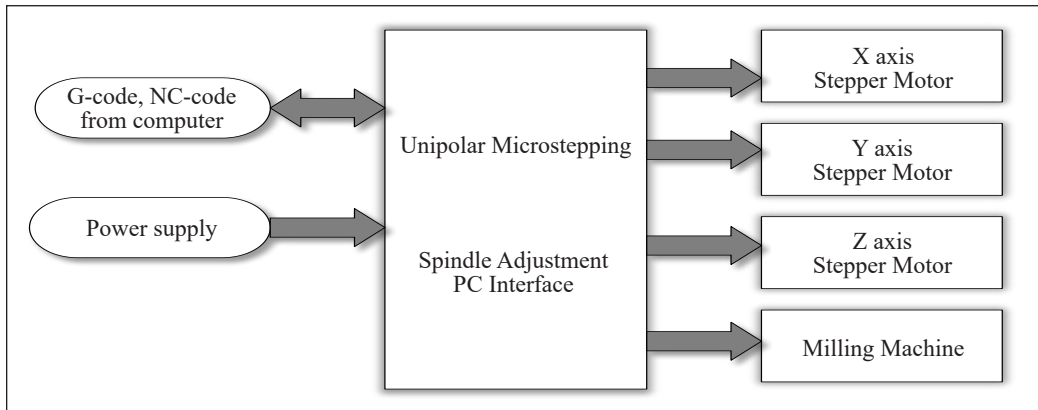


Figure 1. Electrical circuit of the mini CNC ceramic machine

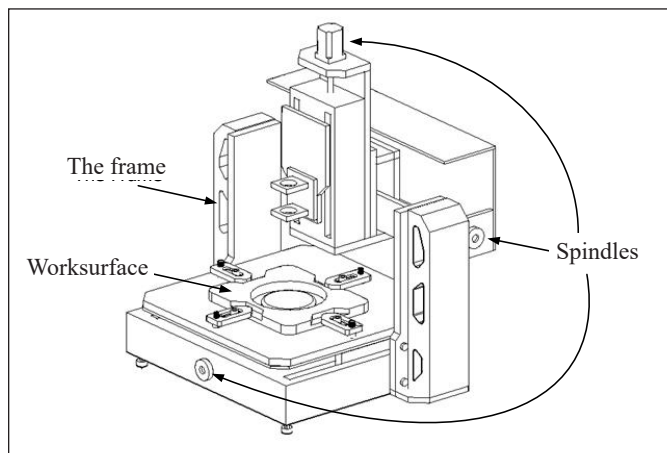


Figure 2. Mini CNC ceramic machine structure

37.5 centimeter length, and Z axis with 240 centimeter length. The movement is controlled by step motors and a holding tray including an end mill bracket with 46.2 centimeter width, 50 centimeter length, and 66.5 centimeter height as seen in Figure 2.

Step motor as shown in Figure 3a, is a device used to control the movement on each axis. Automated operating system is controlled through unipolar microstepping driver in Figure 3b, for driving, signals are given to motor phases arranged in a correct order to ensure smooth spinning as seen in Figure 3.

Spindle adjustment PC interface as shown in Figure 4a is a device used to control the spinning of end mills. A spinning control board is activated by G-code command as seen in Figure 4b.

Table 1 shows details of hardware devices mounted to the structure of the mini CNC ceramic machine as seen in Figure 2. Mini CNC ceramic machine capability is summarized in Table 2.

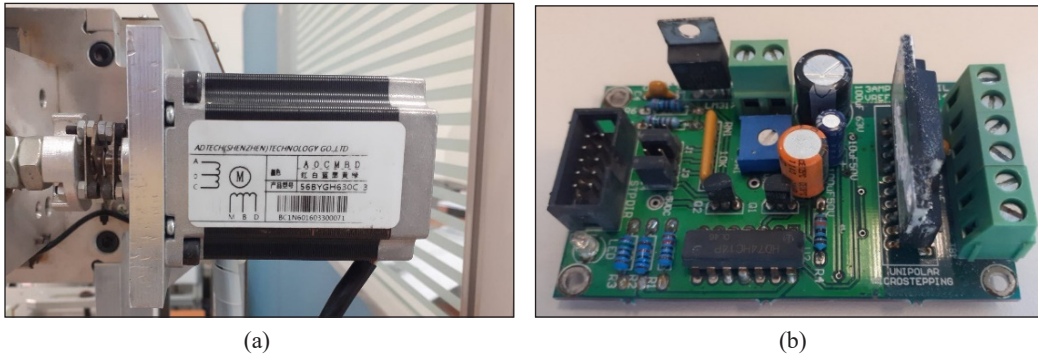


Figure 3. Unipolar Microstepping Board: (a) Stepping motor; and (b) Microstepping board

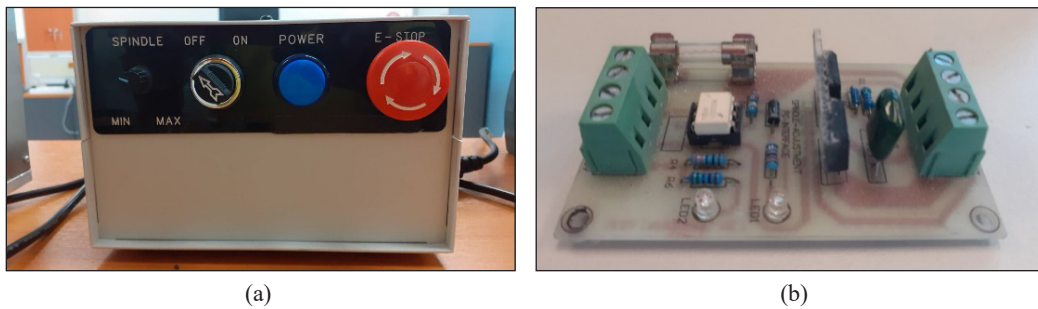


Figure 4. INNER Microchip Driver Interface v.2.0: (a) Control box; and (b) Driver board

Table 1
Details of devices in the mini CNC milling machine

Linear system	
1. Linear	TBI Linear No. 15, X axis 410 mm. length, Y axis 375 mm. length, Z axis 240 mm. length.
2. Block	TBI Block No. 15 for X, Y, Z axis.
Motion system	
1. Ball Screw	TBI 16 mm. diameter.
2. Stepping motor	400 Watt 220 Volt alternating current
Structure	
1. Ball bearing	SKF ball bearing no. 6000
2. Rubber engine mounting	SKF
3. Conduit pipe	LC-LIDA
Controller cabinet system	
1. Power Supply	Delta 24 volts 6.5 amps
Board	
1. Board and spindle driver	INNER Microchip Driver Interface v.2.0
2. Fan	24 volt
3. Switch Button	Emergency button (E-Stop), On / Off button (Switch On / Off)

Table 1 (continue)

Linear system	
4. IC	IC alternating current AC socket 3 leg
Milling device	
End mill	Maktec MT910, 20,000 millimeter/minute 260 watt, end mill size = 6.35 millimeter
Electrical system	
Electricity	220 volt AC

Table 2

Details of the mini CNC ceramic machine capability

Item	Details
Work area	Work area of (X axis) mm. * 300 (Y axis) mm. * 150 (Z axis) mm.
Height	≥ 70 mm.
Machine Size	625 × 510 × 410 mm
Connection	USB port
Linear and driving system	Driving X,Y,Z axis using ball screws and round shaft linear slide.
Driving motor	Step motor with a speed of 1440 rounds/second.
Spindle	With a speed of 20,000 rounds per minute (rpm).
Speed in milling	0-3500 mm/min
Precision	The machine is commanded to move at least 0.0025 mm.
Milling speed	0-3500 mm/min
Precise positioning	± 0.05 mm
Command code	G-code / NC-code
Weight of machine	60 kg.
Structure of machine	Aluminum alloys

Step to Design Work Piece for Testing the Machine Operating System

Software designed to control the operating system of the mini CNC ceramic machine comprises 2 parts as one part used to design shapes of 3-D ceramic products and the part used to control the operating system of the machine for milling workpieces to meet the designed shapes. The software used to design shapes of ceramic products in this study, a lotus leaf ceramic bowl, with a diameter of 130 centimeter and height of 65 millimeter, was Aspire 8.0 as seen in Figure 5.

The Aspire 8.0 was converted to the command for the movement of end mills using Mach 3 software, G-code command as seen in Figure 6.

RESULTS AND DISCUSSIONS

Outcome of Assembly of structure

The designed structure and controller in this study can facilitate the installation of prototype

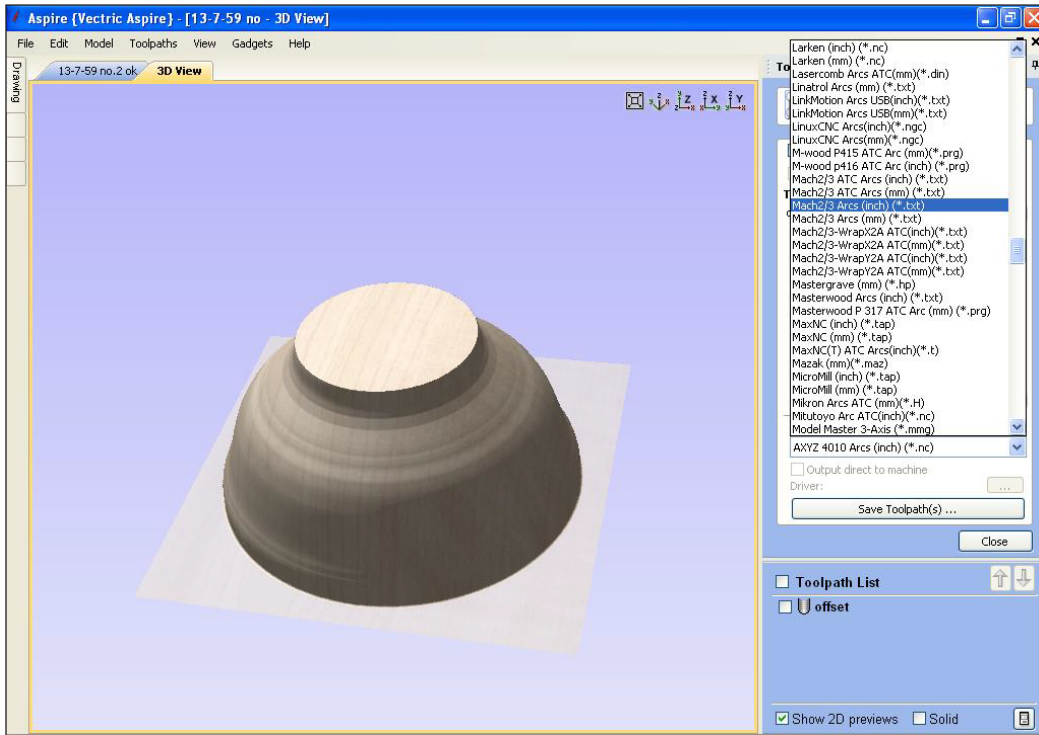


Figure 5. Size of the workpiece, actual motorcycle wheel that passed milling

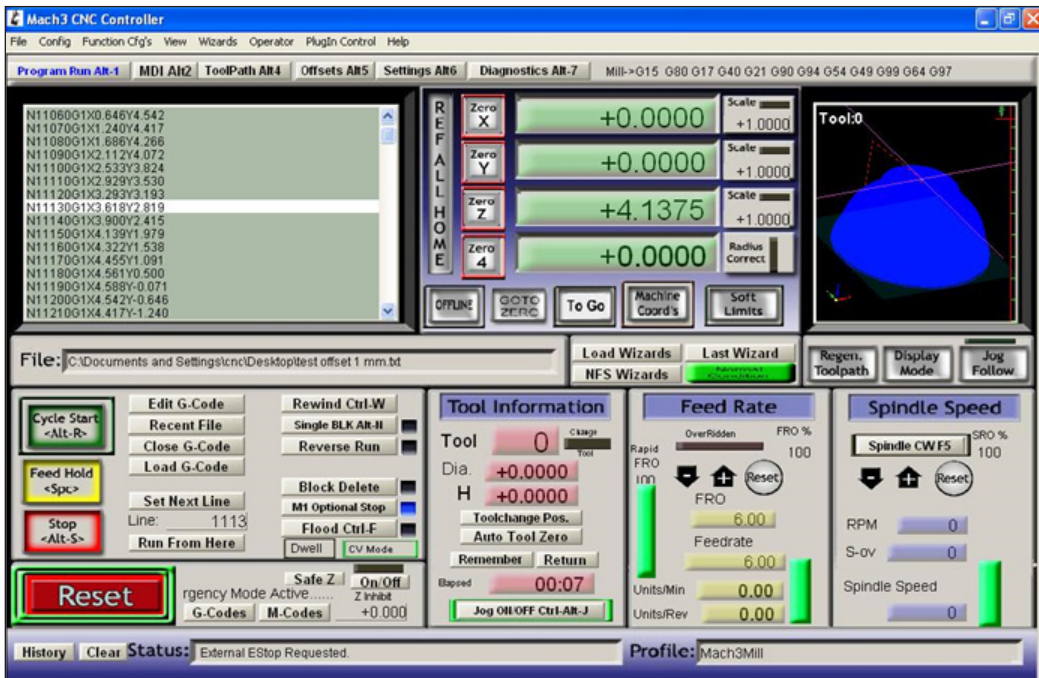


Figure 6. Running G-code file on Mach 3.

materials in making ceramic cups and bowls on a milling machine work area of 300 millimeter width, 300 millimeter length, and 200 millimeter height as seen in Figure 7.

Computer software used to control the activation of the mini CNC ceramic machine was connected to the operating system box comprising on/off button, emergency stop button, and speed adjustment button (Spindle) for controlling the rotational speed of end mills. All components are shown in Figure 8.

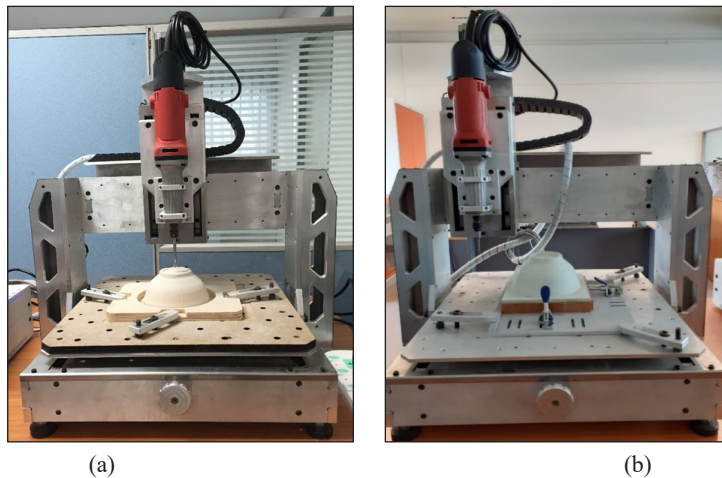


Figure 7. The mini CNC ceramic machine for lightweight and thin products: (a) Clay bowl; and (b) Plaster bowl

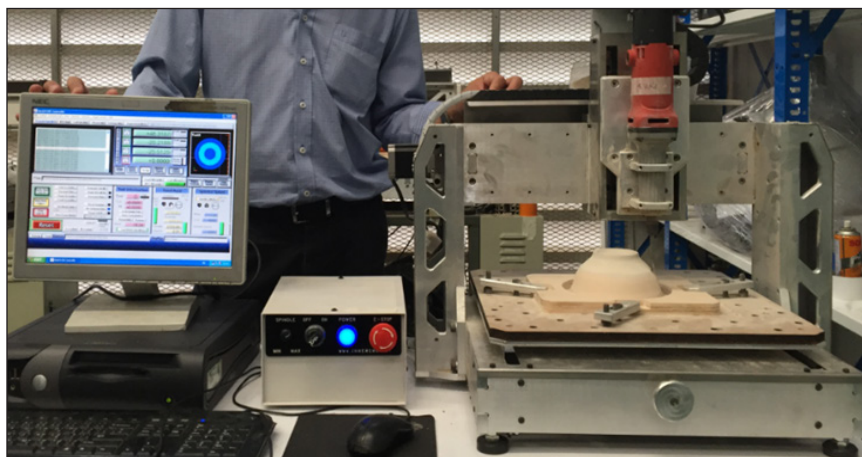


Figure 8. Assembly of hardware and software to operate a small CNC ceramic machine.

Contour Frees Test

The G-code command obtained from the conversion of the designed lotus leaf bowls were given to the software controlling the operating system of the mini CNC ceramic machine

using Mach 3. The feeding speed was set between 1000, 2000, 3000 (mm / min), and the motor speed of 10000, 12000, 15000 (rpm). The cutter was moved in a circular motion with the starting point of the cutter ran in the top position of the bottom of the bowl, and then descended in the cutting stratification at 0.1 mm. The result was able to create a prototype of a ceramic lotus leaf bowl, diameter 130 mm, height 65 mm, both dry clay material and hard plaster as shown in Figure 9.

Testing result of running the milling machine for cup and bowl work pieces were made from clay and hard plaster to figure out an appropriate condition for using the machine, and variables specified for feeding to the control program are shown in Table 3.

According to the table showing the values used to figure out an appropriate condition of the mini CNC milling machine, it was found that the looping pattern according to the shape of work pieces, and continuous moving without moving in reverse direction to the starting point were the test of milling based on a real condition of 3-D work pieces.

Which was slow in the X-Y plane and only changed in the Z axis. For checking the milling conditions in each circular, the milling can be formed a lotus leaf bowl with a smooth surface as required as in Figure 10.

From the milling test of lotus leaf bowl, dry clay and hard plaster in each cycle measured from the depth of each cycle of 0.1 mm by increasing feeding speed and spindle speed

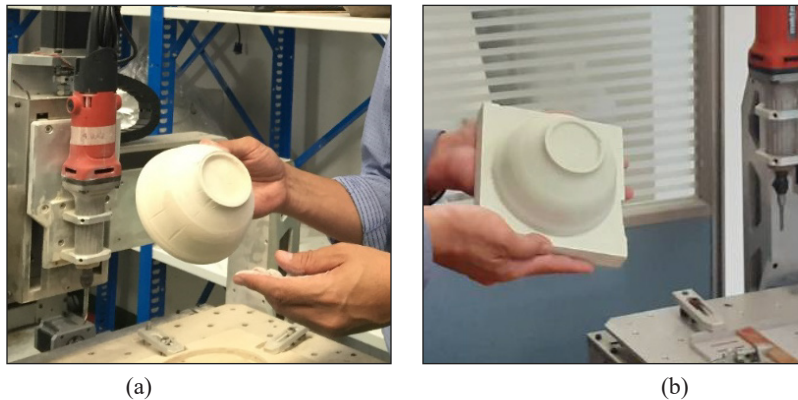


Figure 9. Outcome of ceramic work piece milling bowls: (a) Clay bowl; and (b) Plaster bowl

Table 3

Variables and values used to randomly figure out an appropriate condition for milling work pieces

Variables	Chosen values in the test
Feed Rate	1,000, 2,000, 3,000 (mm / min)
Spindle Motor	10,000, 12,000, 15,000 (rpm)
Patterns of path	Looping pattern according to the shape of work pieces (Follow part).
Moving in reverse direction for milling in each layer.	Continuous moving without moving in reverse direction to the starting point.



Figure 10. Outcome of milling ceramic work pieces of bowls

was found to be a little different. It depended on the speed and hardness of the material used as in Tables 4 and 5.

When comparing the milling efficiency from Table 4 and 5, it was found that the time difference was slight. The dry clay lotus leaf bowls took less time than the small plaster lotus leaf bowls. The smoothness of the skin was similar and met the needs of ceramic operators. The performance comparison results of the 3-axis mini CNC ceramic milling machine with commercially available 5-axis mini CNC machines were as shown in Table 6.

By comparison with the 5-axis CNC machines (Jinan Style Machinery Co., 2021) that were available in the market, the performance was similar, but the mini CNC machines were much cheaper. The size and weight of the machine were also less, so it was suitable for small ceramic enterprises (SMEs) who wanted to reduce their production capital and had less production space.

Table 4
Test result with the lotus leaf bowl made from dry clay

Test of slow movement with looping pattern			
Feeding speed (mm/min)	1,000	2,000	3,000
Spindle Speed (rpm)	10,000	12,000	15,000
Step Down Pass Depth (mm)	0.1	0.1	0.1
Total Machine Time	2.05	1.47	1.12

Table 5
Test result with the lotus bowl made from hard plaster

Test of slow movement with looping pattern			
Feeding speed (mm/min)	1,000	2,000	3,000
Spindle Speed (rpm)	10,000	12,000	15,000
Step Down Pass Depth (mm)	0.1	0.1	0.1
Total Machine Time	2.38	2.15	1.45

Table 6
Compare 3 axis-mini CNC and 5 Axis CNC Router Technical Parameters

Item	3 axis-mini CNC (Ceramic mini-CNC)	5 Axis CNC Router (STYLECNC)
Work area (X,Y,Z)	300* 300 * 150 mm.	1300*2500*950mm
Machine Size	625 × 510 × 410 mm	4260 * 2150 * 3300 mm.
Output power of Spindle	260 w	10kw
Spindle speed	20,000 rpm/min	22,000 rpm/min
Speed in milling	0-3500 mm/min	0 – 2,700 mm/min
Milling speed	0-3500 mm/min	0 – 2,700 mm/min
Precise positioning	±0.05 mm	±0.001mm
Total power	150 w	30 kw
Total weight	60 kg.	12000 kgs
Structure of machine	Aluminum alloys	T-slot & Vacuum combined table
Price Range	\$3,500	\$100,000.00 - \$110,00.00

Note. Data from Jinan Style Machinery Co., (2021)

CONCLUSION

The mini CNC ceramic machine model for making a ceramic cup and bowl prototype obtained from this study can facilitate the milling of workpieces with 50 millimeter circumference, 50 millimeter height to 100 millimeter circumference, and 200 millimeter height. Performance test results showed that running a 6.5 mm cutter with a fine milling method, the feed speed was associated with an increase in spindle speed that would take less time to mill. In addition, hard plaster bowls were found to be smoother and more tender than dry clay bowls. However, the major factor of error was the unsmoothness of the driving system with unstable values. Guidelines for improving the mini CNC ceramic machine are, (1) to lessen error found in all axes of the machine, devices in each axis of the driving support system should be replaced with higher efficient devices and (2) to prevent dust during the milling, a closed system should be used by allowing a dust collection system to suck up dust that occurs while the machine is running.

ACKNOWLEDGEMENT

This research study is supported by the research fund from the Research and Development Institute of Phranakhon Rajabhat University, Bangkok Thailand.

REFERENCES

- Delaram, J., & Valilai, O. F. (2018). An architectural view to computer integrated manufacturing systems based on axiomatic design theory. *Computers in Industry, 100*, 96-114. <https://doi.org/10.1016/j.compind.2018.04.009>

- Hirani, A. (2019). *Design of mini CNC using arduino uno*. Retrieved November 10, 2020, from <https://www.irjet.net/archives/V6/i4/IRJET-V6I4I201.pdf>
- Jinan Style Machinery Co., L. (2021). *5 axis CNC router technical parameters*. Retrieved February 8, 2021, from <https://www.stylecnc.com/5-axis-cnc-machine/5-axis-cnc-router.html>
- Kumar, M. A., Krishnaraj, J., & Reddy, R. B. G. S. (2017). Mini CNC 2D sketcher for accurate building drawing. *International Journal of Civil Engineering and Technology*, 8(6), 543-549.
- Li, B., Zhang, H., Ye, P., & Wang, J. (2020). Trajectory smoothing method using reinforcement learning for computer numerical control machine tools. *Robotics and Computer-Integrated Manufacturing*, 61, Article 101847. <https://doi.org/10.1016/j.rcim.2019.101847>
- Lin, R. S., & Koren, Y. (1996). Real-time interpolators for multi-axis CNC machine tools. *Manufacturing Systems*, 25, 145-149.
- Madekar, K. J., Nanaware, K. R., Phadtare, P. R., & Mane, V. S. (2016). Automatic mini CNC machine for PCB drawing and drilling. *International Research Journal of Engineering and Technology (IRJET)*, 3(02), 1107-1108.
- Patel, M. P. N., Pavagadhi, M. S. D., & Acharya, S. G. (2019). Design and development of portable 3-Axis CNC router machine. *International Research Journal of Engineering and Technology (IRJET)*, 6(3), 1-452.
- Sarkar, B., Khan, A. I., Rana, A. K., & Kundu, S. (2020). Quantification of the phase fraction in multiphase steel and 2D design using mini CNC plotter. In *IOP Conference Series: Materials Science and Engineering* (Vol. 810, No. 1, p. 012066). IOP Publishing. <https://doi.org/10.1088/1757-899X/810/1/012066>
- Yousefian, O., Balabokhin, A., & Tarbutton, J. (2020). Point-by-point prediction of cutting force in 3-axis CNC milling machines through voxel framework in digital manufacturing. *Journal of Intelligent Manufacturing*, 31(1), 215-226. <https://doi.org/10.1007/s10845-018-1442-7>

Synthesis and Characterization of Composite Materials with Enhanced Thermo-Mechanical Properties for Unmanned Aerial Vehicles (Uavs) and Aerospace Technologies

Zahid Iqbal Khan¹, Zurina Mohamad^{1*}, Abdul Razak Rahmat¹ and Unsia Habib^{1,2}

¹Enhanced Polymer Research Group, School of Chemical and Energy Engineering, Universiti Teknologi Malaysia, 81310, Skudai, Johor, Malaysia

²Department of Chemical, University of Engineering and Technology, Peshawar, Pakistan

ABSTRACT

Lightweight and high strength composite materials are vital for unmanned aerial vehicles (UAVs) and aerospace technologies with desired characteristics. Carbon composite materials exhibit extraordinary properties for UAVs and aerospace applications. This study aimed to discover the best-prepared composition of composites material having epoxy LY-5052 and carbon fibres laminate for UAVs. Besides, to develop a low cost with high specific strength composite material for aerospace application to replace metallic alloys. In this work, the vacuum bag technique is used to prepare rectangular strips of three different ratios of carbon fibre/epoxy laminates [(40:60), (50:50) and (60:40)] to obtain the best composite in terms of properties. The thermo-mechanical and viscoelastic behaviour of composite materials were evaluated using differential scanning calorimetry (DSC), universal testing

machine (UTM) and dynamic mechanical analysis (DMA). The tensile strength of epoxy LY5052 composites with 60 wt% has enhanced to 986%, and glass transition temperature (T_g) was improved from 71°C to 110°C. Overall, 60 wt% carbon fibre exhibits better thermo-mechanical properties with lightweight, which may be a future composite material for aerospace, especially UAVs technologies.

Keywords: Aerospace and unmanned aerial vehicle, carbon fibres, composite materials, thermo-mechanical, vacuum bag technique

ARTICLE INFO

Article history:

Received: 21 December 2020

Accepted: 1 April 2021

Published: 19 July 2021

DOI: <https://doi.org/10.47836/pjst.29.3.15>

E-mail addresses:

iqbal.zahid@graduate.utm.my (Zahid Iqbal Khan)

r-zurina@utm.my (Zurina Mohamad)

r-razak@utm.my (Abdul Razak Rahmat)

unsia@uetpeshawar.edu.pk (Unsia Habib)

*Corresponding author

INTRODUCTION

Currently, carbon fibre composites have broad applications in aerospace, for examples, Unmanned Aerial Vehicles (UAVs) used in military and routine applications (i.e., considering the air contamination, research, polar area observing, and animal calculations along with significant military field) (Schlothauer et al., 2020). The interest for more flexibility, successful payload UAVs is enlarging, where composite materials are assuming a basic function in the advancement of these new elite UAVs with exceptional composite material properties (lightweight and high quality) (Ramirez-Atencia et al., 2020). These composite materials are established by twice Young's modulus when contrasted with various types of metals and aluminium alloys with half low weight retention (Giones & Brem, 2017). In any argument, high stiffness, corrosion resistance, thermal and vibration damping characteristics are viewed as the most significant properties mulled over when working with UAV's composite materials (Ramirez-Atencia et al., 2020). The composite materials, the blending components, comprised of a few stages with various physicochemical properties. Composites are separated into reinforced filler and matrix following their capability. The most typically used matrix materials are metals, ceramics, and polymers. While, the reinforcement fillers are carbon, glass, boron, and aramid.

UAVs and aerospace technologies are manufactured mostly from aluminium, titanium, and steel, which reduced UAVs flight time due to heavyweight. The carbon fibre composites are exhibiting low density as compared to metals. However, mechanical damage is susceptible when composites being subjected to tension, flexural and impact loads (Shokrieh et al., 2013). Rahmani et al. (2014) investigated the effect of fibre orientation and fibre content in terms of mechanical properties by utilizing various epoxies. However, the prepared composites were brittle, elongation at break and impact strength was much lower while our research focuses on a different aspect of mechanical and thermal properties. Ridzuan & Jagan (2019) investigated the carbon fibres composite (CFC) for motorbikes' arms by utilizing hand layup process. However, there was no information regarding the epoxy used and curing time of epoxy was much longer to be 48 hours. Afshar et al. (2020) investigated the carbon fibre epoxy composite having different epoxy compared to us with the other motive. The motive of their research was the effect of environmental exposure with a metallic coating. The metallic coating increased the composite material's density and may not be suitable for various aerospace applications. Muralidhara et al. (2020) investigated the carbon fibres with boron carbide particles' insertion by utilizing LY1564 epoxy. The process adopted was much longer. Also, the information on tensile and flexural strength of the composite was not reported. Kaybal et al. (2020) were investigated the carbon fibres composites with a different epoxy. The researchers evaluated the effect of boron nitride reinforcement on the machinability of composite materials. The correlation of fibre orientation and resin, the effect of hardener over epoxy, inter-facial strength with

respect to electrical, thermal, thermo-mechanical, inter-laminar fracture and vibration characteristics of composite with different types of the epoxy matrix were established by various researchers (Batabyal et al., 2018; Ashori et al., 2019; Kaybal et al., 2020; Ekşi & Genel, 2017; Kaleemulla & Siddeswarappa, 2010; Minty et al., 2018; Muralidhara et al., 2020; Ornaghi et al., 2010; Rahmani et al., 2014; Ridzuan & Jagan, 2019; Lee et al., 2018; Vasudevan et al., 2018). However, no one has used LY5052 epoxy for 40, 50 and 60 wt% of carbon fibre composites. Epoxy LY5052 exhibits outstanding mechanical and thermal properties besides lightweight. It can be best suited for replacing aluminium, titanium and steel if reinforced with carbon fabrics. This work is the continuation of work published by Khan et al. (2020) to explore further the mechanical and thermal-mechanical properties of epoxy LY-5052 and carbon fibres composites at various ratios.

This study investigated the effect of laminated carbon fibres on epoxy LY5052 at three different ratios, i.e., A=40, B=50 and C=60 wt% [A=CF/Epoxy (40:60), B=CF/Epoxy (50:50), C= CF/Epoxy (60:40)] of composites properties in terms of tensile strength, tensile modulus, tensile strain, flexural strength, flexural modulus, storage modulus, $\tan\delta$ and density with the simple and easy process. Where; CF stands for carbon fibres. The main objective was to compare the best suitable ratio of carbon fibres reinforced composite using a special epoxy for structural applications. The advantages include the processing method applied, low cost, ease of production and handling, lower safety requirements.

MATERIALS AND METHODS

Materials

Matrix resin Araldite LY-5052 and the release agent QZ-13 were bought from Huntsman Petrochemical Co. Table 1 presents the properties of Araldite LY-5052 provided by the manufacturer. Unidirectional carbon fabrics (6k) were imported from Boto Corp, Korea. Table 2 denotes the physical and chemical properties of carbon fabric as provided by the manufacturer. The remaining materials, such as vacuum bags, brushes and metal scrapers and gloves for the hand layup process, were purchased from the local market. Glass mould and vacuum pump were utilized to manufacture composites.

Preparation of Composites

The composite manufacturing details were obvious elsewhere (Hassan, 2012; Reddy et al., 2019). The composites having 1.5 mm thickness were prepared by hand layup vacuum bagging technique. Glass mould was coated with a releasing agent. Samples of the composites were prepared at ratios of 40, 50 and 60 wt% [A=CF/Epoxy (40:60), B=CF/Epoxy (50:50), C=CF/Epoxy (60:40)]. A brush and metal scraper were used to wet the fabrics properly, and the samples were sealed in a polyethylene sheet through sealant tape.

Table 1

Properties of Epoxy-LY5052

Properties	Values
Flashpoint	$\geq 140^{\circ}\text{C}$
Cure cycles	1 day at room temperature
Glass transition temperature (T _g).	50 °C, at room temperature curing
Tensile strength	49-71 Mega Pascal (MPa)
Elongation	1.5 - 2.5 %
Tensile modulus	3350-3750 MPa
Flexural strength	130-140 MPa
Viscosity at 25°C	1000 – 1500 centipoise [cps]
Poisson's ratio	0.35

A vacuum pump pipe was inserted in polyethylene sheet through a sealed hole to create a vacuum. In the vacuum bagging unit, the vacuum of -27 mm of Hg was employed for 5 hours and left the laminates in the setup for 24 hours. All the samples were then shifted to a heat treatment furnace for post-curing at 80°C for 2 hours. The physical and mechanical properties of carbon fabrics are mentioned in Table 2.

Table 2

Properties of carbon fabrics

Properties	Values
Fibre Diameter (μm)	8
Density (10^3kgm^{-3})	1.75
Young's modulus (GPa)	250
Tensile strength (GPa)	2.7
Elongation %	1
Coefficient of Thermal Expansion ($10^{-6}^{\circ}\text{C}^{-1}$)	-0.4
Thermal conductivity ($\text{Wm}^{-6}\text{C}^{-1}$)	24

Characterization

Mechanical Testing. The mechanical testing (stress-strain) of the composites was carried out using a universal testing machine (Zwick/Roell Z020). The tensile and flexural testing was performed according to ASTM standard D-3039 and D-3518, respectively, at room temperature.

Dynamic Mechanical Analysis (DMA). A dynamic mechanical analyzer (Perkin-Elmer DMA7e) was utilized to evaluate storage modulus, loss modulus and tan delta (δ) of the composite materials. Dynamic mechanical analysis (DMA) tests were carried out according to ASTM D-4065. The size of the DMA samples was 50x12 mm². Each type of test was done five times, and the average was taken.

Differential Scanning Calorimetry (DSC). Differential scanning calorimetry of the composite materials was performed through the DSC analysis instrument Model: TA 2920. DSC of all the samples was done at the rate of 10°C per minute heating. A nitrogen atmosphere was applied during the DSC testing of samples.

Density. The density of the sample was checked according to the GB-1033 test method for density standard so that the density of the composites can be compared with the known density of aluminium, titanium, and steel.

RESULTS AND DISCUSSION

Mechanical Properties

Figure 1 demonstrates tensile strength, tensile modulus and strain% for pure epoxy and carbon fibres composites (CFC). In Figure 1a the tensile strength of pure epoxy was 47.3 MPa. The tensile strength of epoxy LY-5052 was increased in all proportions after the incorporation of fibres. i.e., 412.56, 462.2 & 513.68 MPa for 40,50 and 60 wt% of carbon fibers respectively. The difference in tensile strength in pure epoxy and CFC was mainly because of the tensile strength of carbon fabrics. The increase in tensile strength was attributed to the constraining effect of fibres on the movement of polymer chains of epoxy.

Figure 1b illustrates the tensile modulus of pure epoxy and its composites with carbon fibres. The tensile modulus of pure epoxy was recorded as 1.8 GPa. The upsurge of 9.93, 11.59 and 11.76 GPa in tensile modulus was observed with the incorporation of 40, 50 and 60% carbon fibres. Figure 1c illustrates the strain percentage of epoxy and its composites at ratios of 40,50 and 60 wt%. The strain percentage of pure epoxy was improved amazingly with the incorporation of carbon fabrics. There was an increase of 84.75 % in strain% with the incorporation of 60 wt% of fibres, as presented in Figure 1c. The simultaneous increase

in tensile strength and strain% at 60 wt% of fibres compared to other ratios was the sign of higher impact toughness. The tensile results are in accord with the work of Rahmani et al. (2014) and Cai et al. (2016).

Table 3 demonstrates the flexural strength of pure epoxy and its composites. The flexural strength of epoxy was recorded as 70 MPa. The upsurge of 515, 552 and 609 MPa was noticed for 40, 50 and 60 wt% of carbon composites. The rise in flexural strength with increasing fibres content resulted from the restricted movement of polymer chains of epoxy and the pinning effect of embedded fibres. The flexural modulus of laminates has also been shown in Table 3. It has been observed that with the incorporation of carbon fibres in epoxy LY 5052, the flexural modulus enhanced greatly. The higher properties exhibited by CF/ Epoxy laminates are due to the better integral characteristics of carbon fibres, as reflected in Table 3. The flexural results are in accordance with the work of Barkoula et al. (2005) and Turla et al. (2014).

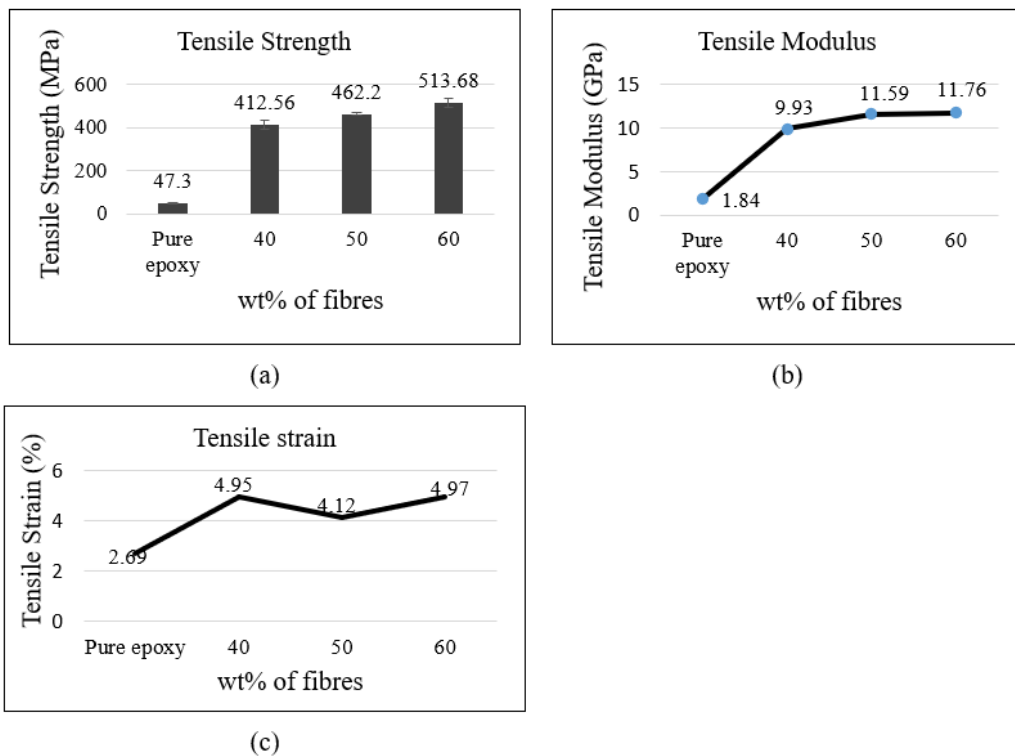


Figure 1. (a) Tensile strength of CFC (b) Tensile modulus of epoxy CFC (c) Tensile strain of CFC

Table 3

Flexural strength and modulus of all the carbon fibres composites

Formulations (Carbon fibres/epoxy)	Flexural Strength (MPa)	Flexural Modulus (GPa)
Pure epoxy LY5052	70 ± (11.94)	0.73 ± (0.02)
40:60	515 ± (8.71)	10.53 ± (0.52)
50:50	552 ± (6.44)	10.62 ± (0.11)
60:50	609 ± (16.73)	10.77 ± (0.17)

Thermal Properties of Laminates

Figure 2 represents the Differential Scanning Calorimetry (DSC) curves for epoxy and its composites. The glass transition (T_g) of epoxy was improved at all proportions. The T_g of epoxy-LY5052 was recorded 71°C. The T_g was increased to 110°C with CFC at 40 wt% of carbon fibres (CF/Epoxy 40:60), as shown in Figure 2. The rise for T_g in 50 wt% and 60 wt% (CF/Epoxy (50:50) and CF/Epoxy (60:40)) was up to 39°C. The increase in T_g was due to the restricted movement of polymer chains. The DSC results were in accordance with the results of Vasudevan et al. (2018) & Ekşi and Genel (2017).

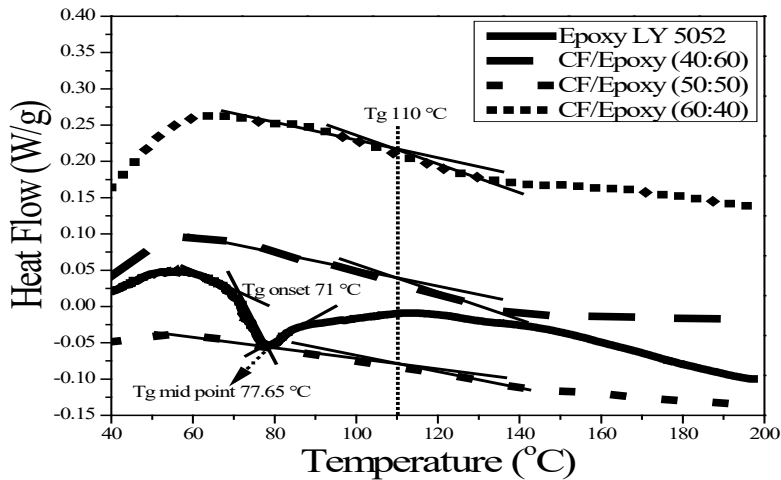


Figure 2. Heat flow vs transition temperature of carbon fibre composites

Dynamic Mechanical Analysis (DMA)

Loss Modulus. Figure 3 shows the loss modulus of epoxy and its composites. The loss modulus of epoxy was improved with the addition of carbon fibres. The peaks were shifted towards higher temperature with the incorporation of fibres, as shown in Figure 3. Broadening and shifting of peaks toward increasing temperatures was the confirmation of increment in the T_g . It may be attributed to the immobilization of the matrix chain with fibres. The results were in agreement with the study of Ornaghi et al. (2010).

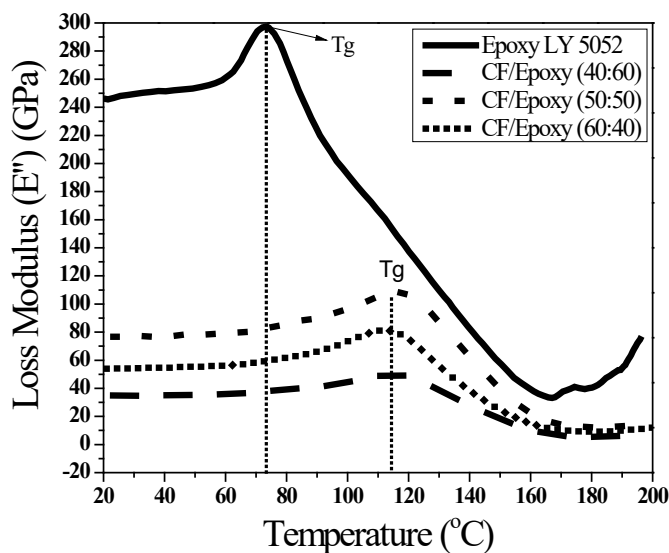


Figure 3. Loss modulus vs temperature ($^{\circ}\text{C}$) of carbon fibres composites

Storage Modulus. Figure 4 shows the storage modulus of epoxy and its composites. The storage modulus of epoxy was increased at all proportions with the incorporation of carbon fibres. The storage modulus of epoxy was recorded to be 4.7 GPa. The storage modulus was increased to 8 GPa with the incorporation of 40 wt% of continuous carbon fibres. An increase up to 21 GPa was noticed with 50 wt% fibres. However, in the case of 60 wt% of fibres, the storage modulus was reduced to 18 GPa. It was slightly lower than the composite with 50 wt% fibres. This is expected due to the reduce interfacial bonding at the higher carbon fibre content.

The reduce interfacial bonding can be supported by the reduce T_g value from storage modulus (Figure 3) and damping (Figure 5) curves for CFC with 60 wt% carbon fibre then 50 wt% carbon fibre. DMA analysis is known to characterize fibre and matrix composites interfacial bonding at the molecular level (Dong & Gauvin, 1993). The T_g of CFC is

related to the matrix chain mobility that increases with increased interfacial bonding and chain entanglement in composites. The higher value of storage modulus was reflecting the higher stiffness of composites. Apart from comparing the storage modulus values, it was established that composites viscoelastic behaviour revealed from the storage modulus decreases with increasing temperature. The drop-in modulus for epoxy was observed in the range of 70-100°C, while it was improved to the range of 100-140°C for composites, as shown in Figure 4. It happened plausibly due to the restriction in molecular mobility of polymer chains of epoxy. These results were confirmed the significant increase in Tg of composites at all proportions and coincide with the work of Backes et al. (2018).

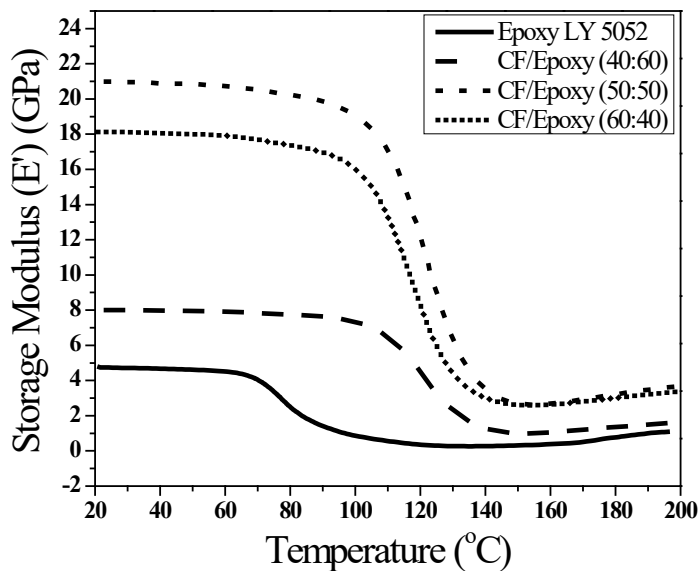


Figure 4. The storage modulus of carbon fibre composites

Tan δ. Figure 5 is showing the tan δ results of epoxy and carbon fibres composites. Tan δ can be obtained from DMA results and can be defined as storage modulus/loss modulus. This property usually represents the damping factor of the materials, which was improved by incorporating carbon fibres. Figure 5 shows that the peaks were shifted in the right direction, which confirms the increase of glass transition temperature (Tg). An increase in Tg is related to the increased in interfacial bonding in the composites material. At higher carbon fibre content (60 wt%), the Tg is slightly reduced revealed that the interfacial bonding is reduced at the higher fibre content. The results were in agreement with the study of Ornaghi et al. (2010).

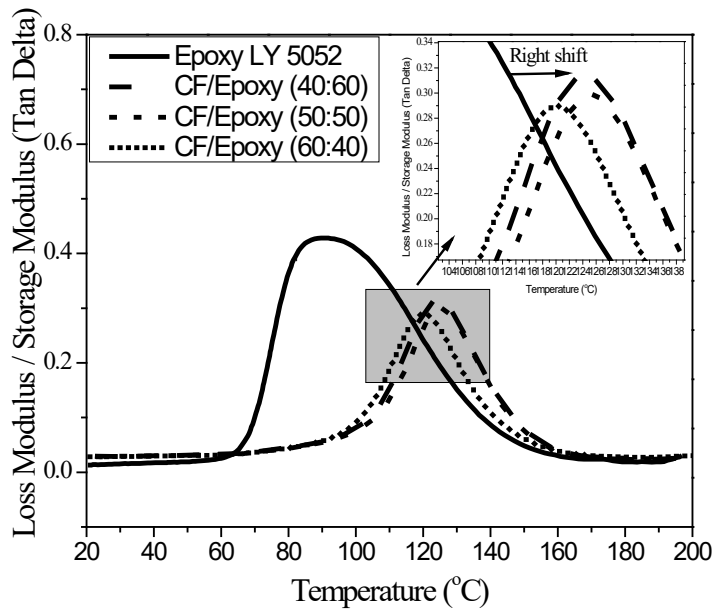


Figure 5. Tan Delta of carbon fibre composites

Density

Table 4 represents the density of epoxy and its composites. Densities of the composites were found much lower than known densities of aluminium (2.7 g/cm^3), titanium (4.5 g/cm^3) and steel (8.05 g/cm^3). The density of the composites shown in Table 4 confirmed the composite's lightweight compared to aluminium.

Table 4

The density of carbon fibres composites

Samples	Density g/cm^3
Resin LY 5052	$1.16 \pm (0.01)$
Carbon Fibre /Epoxy Composite 40:60	$1.33 \pm (0.015)$
Carbon Fibre /Epoxy Composite 50:50	$1.31 \pm (0.005)$
Carbon Fibre /Epoxy Composite 60:40	$1.53 \pm (0.051)$

CONCLUSIONS

The study's objective was to investigate thermo-mechanical properties of epoxy LY-5052 in lightweight carbon fibres composites to replace the heavy metal in UAVs and aerospace applications. The results indicated that mechanical, thermal, and thermo-mechanical properties of special structural epoxy LY5052 upsurged with fibre laminate at all proportions. However, the tensile strength, flexural strength, and CFC thermal properties at 60 wt% were highest and superior. Furthermore, the increase of fibres beyond this ratio would create wettability issues associated with the bonding interaction between CF/Epoxy, resulting in lower properties. The glass transition temperature of composites, irrespective of their mixing ratios, was much higher than epoxy. The increase was 54.92% for CFC. The decrease in loss modulus was noticed with the rise of carbon fibres in composites, which is beneficial and represents the better damping factor. Conversely, the storage modulus amplified significantly with increasing fibre content in composites. Overall, the epoxy LY-5052 and carbon fibre composites exhibit superior properties for structure application of UAVs and aerospace in terms of lightness, stiffness, and strength compared to Al, Ti and steel.

ACKNOWLEDGEMENTS

This study acknowledged the Ministry of Education Malaysia (MOE) and Universiti Teknologi Malaysia (UTM) for providing funding under GUP 05G85, 05G86, 08G50, 05G52 and FRGS Grant 5F185 (FRGS/1/2019/TK05/UTM/02/17).

REFERENCES

- Afshar, A., Mihut, D., & Chen, P. (2020). Effects of environmental exposures on carbon fiber epoxy composites protected by metallic thin films. *Journal of Composite Materials*, 54(2), 167-177. <https://doi.org/10.1177/0021998319859051>
- Ashori, A., Ghiyasi, M., & Fallah, A. (2019). Glass fiber-reinforced epoxy composite with surface-modified graphene oxide: Enhancement of interlaminar fracture toughness and thermo-mechanical performance. *Polymer Bulletin*, 76(1), 259-270. <https://doi.org/10.1007/s00289-018-2387-x>
- Backes, E. H., Passador, F. R., Leopold, C., Fiedler, B., & Pessan, L. A. (2018). Electrical, thermal and thermo-mechanical properties of epoxy/multi-wall carbon nanotubes/mineral fillers nanocomposites. *Journal of Composite Materials*, 52(23), 3209-3217. <https://doi.org/10.1177/0021998318763497>
- Barkoula, N. M., Peijs, T., Schimanski, T., & Loos, J. (2005). Processing of single polymer composites using the concept of constrained fibers. *Polymer Composites*, 26(1), 114-120. <https://doi.org/10.1002/pc.20082>
- Batabyal, A., Nayak, R. K., & Tripathy, S. (2018). Evaluation of mechanical properties of glass fibre and carbon fibre reinforced polymer composite. *Journal of Communication Engineering & Systems*, 8(2), 2321-5151.
- Cai, D., Zhou, G., & Silberschmidt, V. V. (2016). Effect of through-thickness compression on in-plane tensile strength of glass/epoxy composites: Experimental study. *Polymer Testing*, 49, 1-7. <https://doi.org/10.1016/j.polymertesting.2015.10.015>

- Dong, S., & Gauvin, R. (1993). Application of dynamic mechanical analysis for the study of the interfacial region in carbon fiber/epoxy composite materials. *Polymer Composites*, 14(5), 414-420. <https://doi.org/10.1002/pc.750140508>
- Ekşi, S., & Genel, K. (2017). Comparison of mechanical properties of unidirectional and woven carbon, glass and aramid fiber reinforced epoxy composites. *Acta Physica Polonica A*, 132(3), 879-882. <https://doi.org/10.12693/APhysPolA.132.879>
- Giones, F., & Brem, A. (2017). From toys to tools: The co-evolution of technological and entrepreneurial developments in the drone industry. *Business Horizons*, 60(6), 875-884. <https://doi.org/10.1016/j.bushor.2017.08.001>
- Hassan, M. A. (2012). Physical and thermal properties of fiber (S-TYPE) - Reinforced composite araldite resin (GY 260). *Al-Qadisiya Journal For Engineering Sciences*, 5(4), 341-346.
- Kaleemulla, K. M., & Siddeswarappa, B. (2010). Influence of fiber orientation on the in-plane mechanical properties of laminated hybrid polymer composites. *Journal of Reinforced Plastics and Composites*, 29(12), 1900-1914. <https://doi.org/10.1177/0731684409340806>
- Kaybal, H. B., Unuvar, A., Kaynak, Y., & Avcı, A. (2020). Evaluation of boron nitride nanoparticles on delamination in drilling carbon fiber epoxy nanocomposite materials. *Journal of Composite Materials*, 54(2), 215-227. <https://doi.org/10.1177/0021998319860245>
- Khan, Z. I., Arsad, A., Mohamad, Z., Habib, U., & Zaini, M. A. A. (2020). Comparative study on the enhancement of thermo-mechanical properties of carbon fiber and glass fiber reinforced epoxy composites. *Materials Today: Proceedings*, 39, 956-958. <https://doi.org/10.1016/j.matpr.2020.04.223>
- Lee, J., Ni, X., Daso, F., Xiao, X., King, D., Gomez, J. s., Varela, T. B., Kessler, S. S., & Wardle, B. L. (2018). Advanced carbon fiber composite out-of-autoclave laminate manufacture via nanostructured out-of-oven conductive curing. *Composites Science and Technology*, 166, 150-159. <https://doi.org/10.1016/j.compscitech.2018.02.031>
- Minty, R. F., Yang, L., & Thomason, J. L. (2018). The influence of hardener-to-epoxy ratio on the interfacial strength in glass fibre reinforced epoxy composites. *Composites Part A: Applied Science and Manufacturing*, 112, 64-70. <https://doi.org/10.1016/j.compositesa.2018.05.033>
- Muralidhara, B., Babu, S. P. K., & Suresha, B. (2020). Studies on dynamic mechanical and thermal properties of boron carbide filled carbon fiber/epoxy composites. *Materials Today: Proceedings*, 1-5. <https://doi.org/10.1016/j.matpr.2019.12.204>
- Ornaghi, H. L., Bolner, A. S., Fiorio, R., Zattera, A. J., & Amico, S. C. (2010). Mechanical and dynamic mechanical analysis of hybrid composites molded by resin transfer molding. *Journal of Applied Polymer Science*, 118(2), 887-896. <https://doi.org/10.1002/app.32388>
- Rahmani, H., Najafi, S. H. M., Saffarzadeh-Matin, S., & Ashori, A. (2014). Mechanical properties of carbon fiber/epoxy composites: Effects of number of plies, fiber contents, and angle-ply Layers. *Polymer Engineering and Science*, 54(11), 2676-2682. <https://doi.org/10.1002/pen.23820>
- Ramirez-Atencia, C., Rodriguez-Fernandez, V., & Camacho, D. (2020). A revision on multi-criteria decision making methods for multi-UAV mission planning support. *Expert Systems with Applications*, 160, Article 113708. <https://doi.org/10.1016/j.eswa.2020.113708>

- Reddy, C. V., Raju, C. J. S., Babu, P. R., & Ramnarayanan, R. (2019). Effect of benzoxazine on epoxy based carbon fabric reinforced composites for high strength applications. In *Proceedings of International Conference on Intelligent Manufacturing and Automation* (pp. 353-367). Springer. https://doi.org/10.1007/978-981-13-2490-1_32
- Ridzuan, A., & Jagan, T. (2019). Design and analysis of carbon fibre composite monorack arm for motorcycle. *International Journal of Integrated Engineering*, *11*(7), 152-161. <https://doi.org/10.30880/ijie.2019.11.07.020>
- Schlothauer, A., Fasel, U., Keidel, D., & Ermanni, P. (2020). High load carrying structures made from folded composite materials. *Composite Structures*, *250*(June), Article 112612. <https://doi.org/10.1016/j.compstruct.2020.112612>
- Shokrieh, M. M., Daneshvar, A., Akbari, S., & Chitsazzadeh, M. (2013). The use of carbon nanofibers for thermal residual stress reduction in carbon fiber/epoxy laminated composites. *Carbon*, *59*, 255-263. <https://doi.org/10.1016/j.carbon.2013.03.016>
- Turla, P., Kumar, S. S., Reddy, P. H., & Shekar, K. C. (2014). Processing and flexural strength of carbon fiber and glass fiber reinforced epoxy-matrix hybrid composite. *Bulletin of Materials Science*, *37*(3), 597-602.
- Vasudevan, A., Kumaran, S. S., Naresh, K., & Velmurugan, R. (2018). Experimental and analytical investigation of thermo-mechanical responses of pure epoxy and carbon/Kevlar/S-glass/E-glass/epoxy interply hybrid laminated composites for aerospace applications. *International Journal of Polymer Analysis and Characterization*, *23*(7), 591-605. <https://doi.org/10.1080/1023666X.2018.1468599>



Electromechanical Characteristics of Core Free Folded Dielectric Electro-active Polymer Soft Actuator

Abdul Malek Abdul Wahab*, Muhamad Azhan Anuar and Muhamad Sukri Hadi

Faculty of Mechanical Engineering, Universiti Teknologi MARA, 40450 Shah Alam, Selangor, Malaysia

ABSTRACT

This paper investigates the active dynamic and electromechanical characteristics of a new thin folded dielectric electro-active polymer actuator developed by Danfoss PolyPower. The high voltage is supplied to the actuator during dynamic testing to identify the effect of the electrical field on dynamic characteristics. The electromechanical characteristics are investigated by varying the amplitude and frequency of the voltage supplied. The experimental results, such as natural frequency, amplitude response, and loss factor are presented to show the influence of such an electrical field on the characteristic of the actuator. There is a reduction of resonance frequency from 14 Hz to 12 Hz as voltage supply up to 2000 V. The actuating response of the actuator was subjected more to frequency rather than the amplitude of the voltage supplied. Hence, the results may guide the exploration of a new folded thin actuator as an active vibration controller.

Keywords: Active dynamic, core free, dielectric electro-active polymer, electromechanical, thin actuator

ARTICLE INFO

Article history:

Received: 31 March 2021

Accepted: 21 May 2021

Published: 31 July 2021

DOI: <https://doi.org/10.47836/pjst.29.3.47>

E-mail addresses:

abdmalek@uitm.edu.my (Abdul Malek Abdul Wahab)

azhan788@uitm.edu.my (Muhamad Azhan Anuar)

msukrihadi@uitm.edu.my (Muhamad Sukri Hadi)

*Corresponding author

INTRODUCTION

A material that has human muscle characteristics potentially could provide an effective alternative to conventional actuator technology. Energy density, strain, actuation pressure, response time and efficiency are the important elements of an actuator material that need to be considered. In addition, the environmental tolerance,

fabrication complexity, and reliability also need to be considered for good actuator designs (Pelrine et al., 2000). Thus, rapid developments and research of the so-called artificial muscle led to the design of dielectric electro-active polymers (DEAP). These materials can undergo large deformation, respond quickly and have high energy density hence they were also called artificial muscles (Berardi et al., 2010). Other attributes of dielectric elastomer include fast response, no noise, lightweight and low cost (Suo, 2010).

The ability of DEAP to deform by applying voltage is like the deformation shown by any dielectric material subjected to electric field. However, the corresponding deformation was markedly enhanced by the softness of the polymer itself, as well as compliance of the electrodes. These two key-features distinguish actuating devices made of dielectric elastomer from those based on different electric-field-driven electrics, such as piezoelectric and electrostrictive materials (Carpi et al., 2008). Kornbluh et al. (1999) suggested that, the dielectric elastomer showed the promising potential for being used not only as actuator but as well as sensor and generator, or it may be used to replace existing impractical technologies.

Besides that, one of the unique properties of DEAP is that it can be formed in any complex shapes and still provide actuation. Li et al. (2018) fabricated stacked dielectric elastomer actuator to enhance the homogenous and reproducible properties of the actuator. Hau et al. (2016) described how to establish DEAP membrane actuators to become high force actuator that can be pushed to the high double-digit Newton range and beyond. One of the most popular shape of DEAP actuator was tubular or cylindrical shape (Berardi et al., 2010; Carpi, et al., 2003; Carpi & de Rossi, 2004; Sarban, et al., 2011; Tryson et al., 2010; Wissler et al., 2007). For these shapes of DEAP actuator, the principal work was 'push actuator'. To date, very few studies have explored on the DEAP actuator working as 'pull actuator' (Wahab et al., 2020).

Thus, the purpose of the present study is to investigate the new core free folded thin DEAP actuator established by PolyPower®. In this paper, the experimental works are conducted to identify the electromechanical characteristics of the actuator as static and harmonic voltage was supplied.

MATERIAL AND METHOD

Folded Thin DEAP Actuator

The actuator was made-up from sheets of dielectric elastomer that was developed by Danfoss PolyPower A/S (Benslimane et al., 2002; Berardi, 2013; Sarban et al., 2011). The actuator was fabricated by rolling multilayers of PolyPower DEAP sheet which were then pressed to form a flat and thin structure as shown in Figure 1. It was fully made-up from DEAP sheet without any supporting material or core inside the flat rolling structure that resulting soft and flexible actuator. For voltage supply, flexible wires and conductive tape

were attached at whichever side of electrodes. At each end of the actuator, hard plastic clipper was put to ensure the actuator always in the flat structure shape. Table 1 shows the geometry of the flat structure actuator used in this study.



Figure 1. (a) A rolled multilayer DEAP composite pressed to form a flat structure. (b) A photograph of the final assembly of Poly Power flat DEAP actuator (Rahimullah Sarban, 2011)

The new actuating formation described in this work provide a simple means to obtain an electrically contractile thin, soft, flexible (human muscle looks alike) and uniform actuator. For this thin actuator, the corrugated surface is the basic actuating force. This condition ensures the elongation of the actuator is in axial direction and in maximum condition (Berardi, 2013; Sarban et al., 2011). It is also avoiding the complexity of fabrication of any shape actuator either in tubular or flat thin condition.

Table 1
Actuator specifications and properties

Geometry	Value	Material constant	Value
Actuator's length (m), L	0.28	ϵ (F/m)	$8.854e^{-12}$
Actuator's width (m), w	0.07	ϵ_0 (dimensionless)	3.1
Weight (kg), M	0.0645	Elastic Modulus (MPa), Y	1.1
Clipper's weight (kg), Mc	0.105	Laminate's thickness (μ m), h	70
		Young's Modulus (MPa), E	1.1
		Density (kg/m^3), ρ	1100

*Source: (Berardi, 2013)

Active Dynamic Testing

The purpose of this experiment was to identify the effect of electrical field towards the dynamic response of the new actuator. Figure 2 shows the diagram and the setting of equipment for the experiment. One end of flat DEAP pull actuator was clamped at static iron beam and another end was hung freely. This condition is in single degree of freedom (SDOF). The pre-stretch condition of flat DEAP pull actuator due to the mass of caliper (M_c) was assumed as equilibrium condition. Electro-magnetic shaker was used to excite the actuator in only one direction, so that the modal response in just that direction can be obtained. The signal used to drive the shaker in the tests was set as pseudo random. The transfer function of acceleration per unit force (accelerance) has been acquired by spectrum analyser for 30 s, rectangular windows and over an average of 75 times. The tests were conducted by supplying a voltage from 0 to 2 kV, in steps of 500 V.

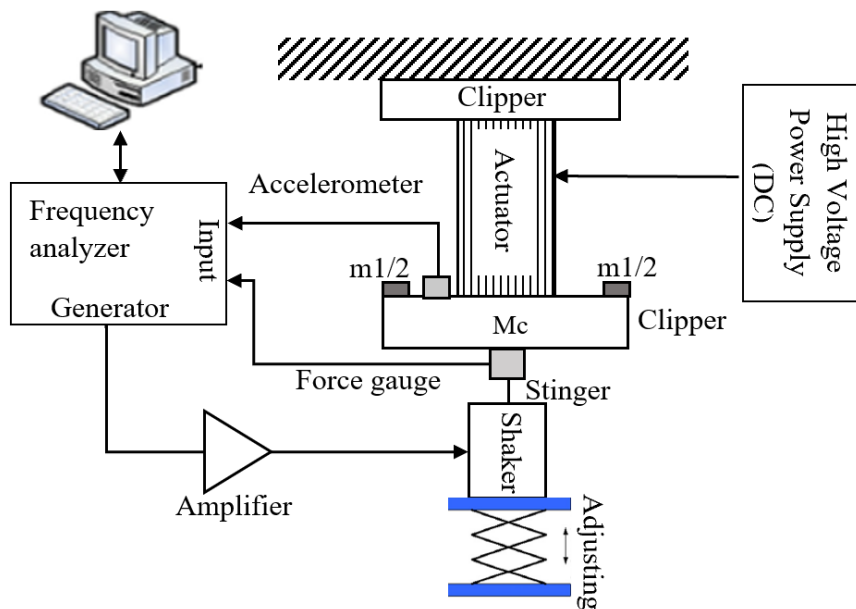


Figure 2. Active dynamic testing

Electromechanical Testing

In order to identify the electromechanical response, harmonic electrical inputs were stimulated with the actuator. Figure 3 shows the experiment set up.

In this experiment the voltage inputs were peak to peak value for 500V, 1000V, 1500V and 2000V. Frequency for each value of voltage has been changing in step of 3Hz up to 21Hz. The Fourier coefficient for each data has been determined by FFT calculation and graph amplitude-frequency for each voltage has been plotted.

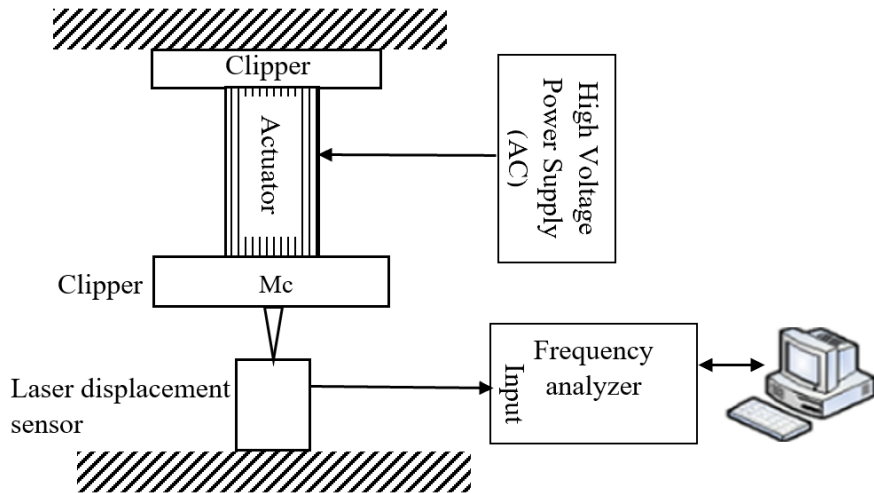


Figure 3. Harmonic electrical input testing

RESULTS AND DISCUSSION

Active Dynamic Characteristic

The finding suggests that, the natural respond of the actuator in this work is at low frequency range. The first order mode of resonance is around 14 Hz at zero voltage supplied. Figure 4 shows that the voltage applied at 500 V, 1000 V and 1500 V do not affect the natural frequency of the actuators. Only at 2000 V, the effect of high voltage can be observed with reduction of natural frequency into 12 Hz.

The loss factor of the actuator was calculated using 3dB method. Referring to Table 2, the voltage supplied does affect the loss factor of the actuator as the highest lost factor of 0.7917 occurs at 2000 V. As voltage was supplied towards dielectric elastomer, the electric field was created due to existence of charges. The electric field established electrostatic pressure which is created pressure on the elastic sheet of DEAP that caused a compression of the elastomer sheet (Pelrine et al., 1998). The electric field dictate the electrostatic pressure (Onyenucheya et al., 2019). Thus, as voltage increased which mean electric field strength increases, the more stretches and reduces of the thickness of the elastomer sheet. As a result, the stiffness of the actuator decreases. Hence, resulting in the decreasing of the natural frequency of the actuator. This condition is in line with Berardi (2013).

Electromechanical Characteristics

Figure 5 shows the first Fourier coefficient of flat DEAP pull actuator for voltage at 500V, 1000V, 1500V and 2000V at varying frequencies 0Hz – 21Hz. It can be seen at zero frequency input, the higher voltage produced higher stroke or actuating response. As

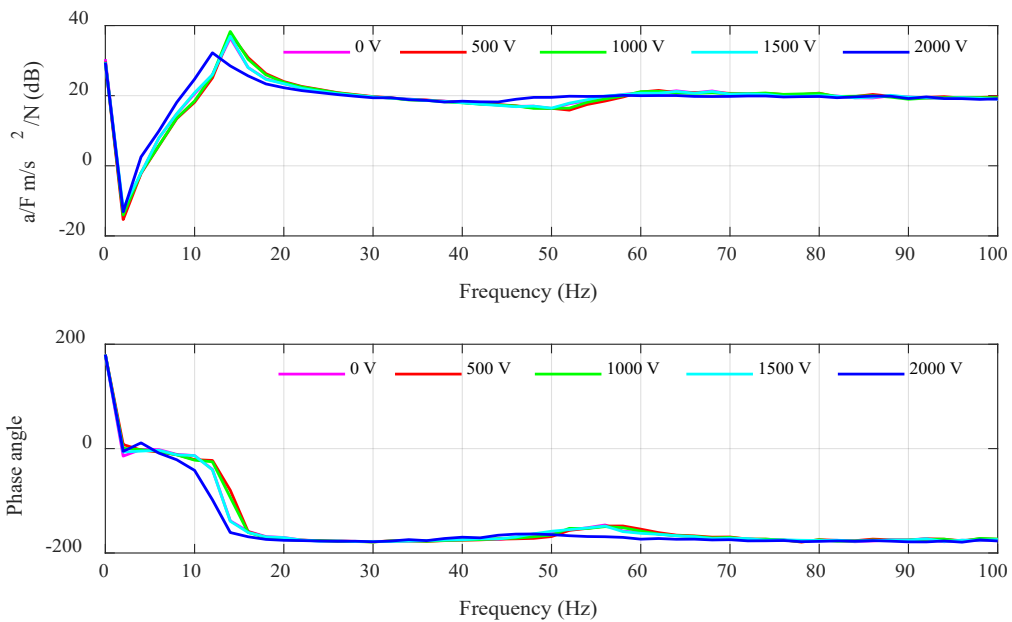


Figure 4. Acceleration per unit force for different DC voltage supply at mass = 0 (pre-stretch due to clipper mass of 105 g)

Table 2

The effect of voltage on loss factor of prototype actuators

Voltage (V)	Loss Factor
0	0.3929
500	0.4107
1000	0.3393
1500	0.3929
2000	0.7917

crosses the frequency range, the highest stroke for each voltage occurs at around 12 Hz. This was the range of natural frequency for the actuator which has been determine during dynamic testing. Beyond the resonance frequency, the amplitudes were decreased to zero for each of different voltage.

In theory, the resonance frequency of an actuator is dependent on its stiffness and mass while the peak values at resonances are dependent on the materials damping coefficients. Results indicate that damping of this actuator growths as voltage increases. The elastomeric

material is highly deforming as high voltage is applied. This deformation causes the internal friction to rise and as a result the occurrence of energy loss is increased.

Actively actuator is the main part of active vibration control technology. The actively actuators reduce the unwanted vibrations in structure by exciting the vibrating structures with harmonic motion resulting in an overall vibration reduction. At the initial of the frequency range, the high voltage of harmonic electrical inputs produce high stroke is due to inhomogeneity of the actuator (Bertoldi & Gei, 2011). As high voltage applied, the thickness of the actuator starts to varies due to deformation occurs at the actuator (Suo, 2010) . This condition contributes to increasing the elongation of the actuator.

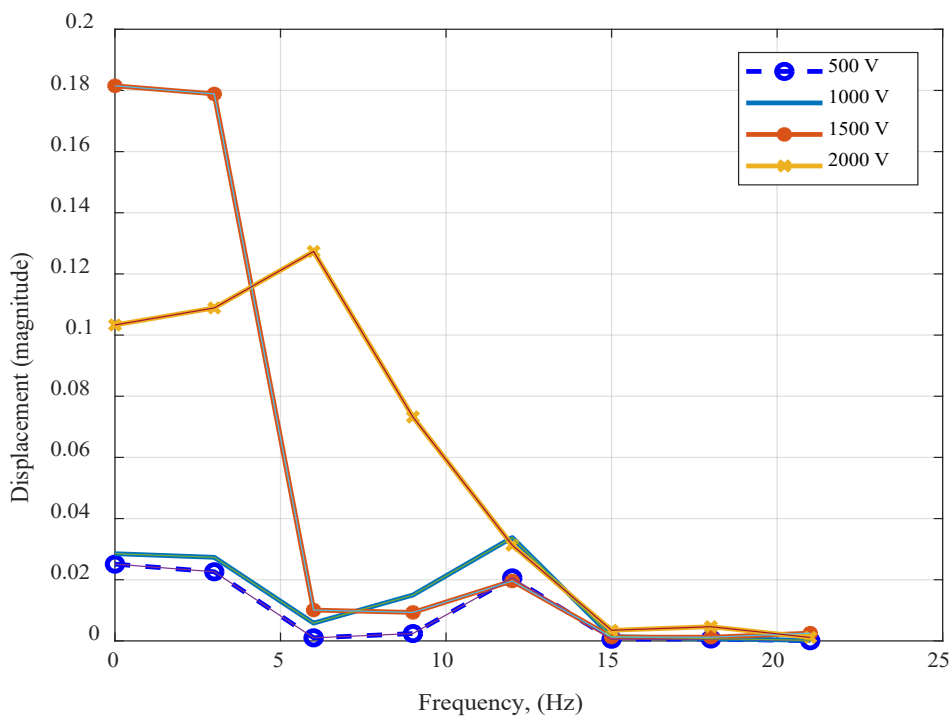


Figure 5. Fourier coefficient versus Frequency for a harmonic response of the actuator

Across the frequency range, the actuating response of the actuator was subjected more on frequency rather than the amplitude of the voltage supplied. This was consistent with Molberg et al. (2009), who suggested that the performance of elastomer actuator was dominated by the frequency dependence of the elastic response and was less influenced by dielectric properties. In fact, over the frequency range the amplitude of the actuator is constant as dielectric remaining roughly constant although different voltage supplied.

The results also show that the actuator has the potential to provide harmonic motion with moderate operating speed.

CONCLUSION

In this work, the effect of electric field toward dynamic and electromechanical characteristic of the new core free folded thin DEAP actuator were investigated. It was found that the natural frequency of the actuator reduces from 14 Hz into 12 Hz as voltage supplied up to 2000 V. For the harmonic electrical stimulation, near to zero frequency, the high actuating response for high voltage input is due to inhomogeneity of the actuator. Across the frequency of harmonic electrical input, the actuating response of the actuator depending more on frequency rather than amplitude. The performance of this actuator for active vibration control is necessary in the future study.

ACKNOWLEDGEMENTS

The authors would like to thank Danfoss PolyPower A/S who supplied the soft actuators. The authors would also like to acknowledge the Institute of Sound and Vibration Research (ISVR) and Tony Davies High Voltage at the University of Southampton where the dynamics and electromechanical experiments were carried out.

REFERENCES

- Benslimane, M., Gravesen, P., & Sommer-Larsen, P. (2002). Mechanical properties of dielectric elastomer actuators with smart metallic compliant electrodes. In *Smart Structures and Materials 2002: Electroactive Polymer Actuators and Devices (EAPAD)* (Vol. 4695, pp. 150-157). International Society for Optics and Photonics. <https://doi.org/10.1117/12.475160>
- Berardi, U. (2013). Modelling and testing of a dielectric electro-active polymer (DEAP) actuator for active vibration control. *Journal of Mechanical Science and Technology*, 27(1), 1-7. <https://doi.org/10.1007/s12206-012-0915-4>
- Berardi, U., Mace, B., Rustighi, E., & Sarban, R. (2010, June 13-15). Dynamic testing and modelling of DEAP push actuators. In *International Conference and Exhibition on New Actuators and Drive Systems - Actuator 2010*. Bremen, Germany
- Bertoldi, K., & Gei, M. (2011). Instabilities in multilayered soft dielectrics. *Journal of the Mechanics and Physics of Solids*, 59(1), 18-42. <https://doi.org/10.1016/j.jmps.2010.10.001>
- Carpi, F., Chiarelli, P., Mazzoldi, A., & de Rossi, D. (2003). Electromechanical characterisation of dielectric elastomer planar actuators: Comparative evaluation of different electrode materials and different counterloads. *Sensors and Actuators A: Physical*, 107(1), 85-95. [https://doi.org/10.1016/S0924-4247\(03\)00257-7](https://doi.org/10.1016/S0924-4247(03)00257-7)

- Carpi, F., & de Rossi, D. (2004). Dielectric elastomer cylindrical actuators: Electromechanical modelling and experimental evaluation. *Materials Science and Engineering: C*, 24(4), 555-562. <https://doi.org/10.1016/j.msec.2004.02.005>
- Carpi, F., Frediani, G., Mannini, A., & De Rossi, D. (2008). Contractile and buckling actuators based on dielectric elastomers: devices and applications. In *Advances in Science and Technology* (Vol. 61, pp. 186-191). Trans Tech Publications Ltd. <https://doi.org/10.4028/www.scientific.net/AST.61.186>
- Hau, S., York, A., & Seelecke, S. (2016). High-force dielectric electroactive polymer (DEAP) membrane actuator. In *Electroactive Polymer Actuators and Devices (EAPAD) 2016* (Vol. 9798, p. 97980I). International Society for Optics and Photonics. <https://doi.org/10.1117/12.2220775>
- Kornbluh, R. D., Pelrine, R., Joseph, J., Heydt, R., Pei, Q., & Chiba, S. (1999, May). High-field electrostriction of elastomeric polymer dielectrics for actuation. In *Smart Structures and Materials 1999: Electroactive Polymer Actuators and Devices* (Vol. 3669, pp. 149-161). International Society for Optics and Photonics. <https://doi.org/10.1117/12.349672>
- Li, Z., Sheng, M., Wang, M., Dong, P., Li, B., & Chen, H. (2018). Stacked dielectric elastomer actuator (SDEA): Casting process, modeling and active vibration isolation. *Smart Materials and Structures*, 27(7), Article 75023. <https://doi.org/10.1088/1361-665X/aabea5>
- Molberg, M., Leterrier, Y., Plummer, C. J. G., Walder, C., Lowe, C., Opris, D. M., Nuesch, F. A., Bauer, S., & Manson, J. E. (2009). Frequency-dependent dielectric and mechanical behavior of elastomers for actuator applications. *Journal of Applied Physics* 106, Article 054112. <https://doi.org/10.1063/1.3211957>
- Onyenucheya, B., Allen, J., Pierre, K., Zirnheld, J., & Burke, K. (2019). Dielectric Elastomers: An Investigation in Strain Dependent Electrostatic Pressure of Soft Compliant Dielectric. In *2019 IEEE Pulsed Power & Plasma Science (PPPS)* (pp. 1-4). IEEE Conference Publication. <https://doi.org/10.1109/PPPS34859.2019.9009996>
- Pelrine, R. E., Kornbluh, R. D., & Joseph, J. P. (1998). Electrostriction of polymer dielectrics with compliant electrodes as a means of actuation. *Sensors and Actuators, A: Physical*, 64(1), 77-85. [https://doi.org/10.1016/S0924-4247\(97\)01657-9](https://doi.org/10.1016/S0924-4247(97)01657-9)
- Pelrine, R., Kornbluh, R., Joseph, J., Heydt, R., Pei, Q., & Chiba, S. (2000). High-field deformation of elastomeric dielectrics for actuators. *Materials Science and Engineering C*, 11(2), 89-100. [https://doi.org/10.1016/S0928-4931\(00\)00128-4](https://doi.org/10.1016/S0928-4931(00)00128-4)
- Sarban, R., Jones, R. W., Mace, B. R., & Rustighi, E. (2011). A tubular dielectric elastomer actuator: Fabrication, characterization and active vibration isolation. *Mechanical Systems and Signal Processing*, 25(8), 2879-2891. <https://doi.org/10.1016/j.ymsp.2011.06.004>
- Suo, Z. (2010). Theory of dielectric elastomers. *Acta Mechanica Solida Sinica*, 23(6), 549-578. [https://doi.org/10.1016/S0894-9166\(11\)60004-9](https://doi.org/10.1016/S0894-9166(11)60004-9)

- Tryson, M. J., Sarban, R., & Lorenzen, K. P. (2010). The dynamic properties of tubular DEAP actuators. In *Electroactive Polymer Actuators and Devices (EAPAD) 2010* (Vol. 7642, p. 764200). International Society for Optics and Photonics. <https://doi.org/10.1117/12.847297>
- Wahab, A. M. A., Rustighi, E., & A., Z. (2020). Actuation and dynamic mechanical characteristics of a core free flat dielectric electro-active polymer soft actuator. *Journal of Mechanical Engineering and Sciences*, 14(4), 7396-7404. <https://doi.org/10.15282/jmes.14.4.2020.08.0582>
- Wissler, M., Mazza, E., & Kovacs, G. M. (2007). Electromechanical coupling in cylindrical dielectric elastomer actuators. In *Electroactive Polymer Actuators and Devices (EAPAD) 2007* (Vol. 6524, p. 652409). International Society for Optics and Photonics. <https://doi.org/10.1117/12.714946>

Methylmercury Detection in Maternal Blood Samples by Liquid Chromatography with Inductively Coupled Plasma Mass Spectrometry

Amirah Abedinlah¹, Saliza Mohd Elias^{1*}, Sarva Mangala Praveena¹, Suhaili Abu Bakar², Zulida Rejali³ and Juliana Jalaludin¹

¹Department of Environmental and Occupational Health, Faculty of Medicine and Health Sciences, Universiti Putra Malaysia, 43400 UPM, Serdang, Selangor, Malaysia

²Department of Biomedical Sciences, Faculty of Medicine and Health Sciences, Universiti Putra Malaysia, 43400 UPM, Serdang, Selangor, Malaysia

³Department of Obstetrics and Gynaecology, Faculty of Medicine and Health Sciences, Universiti Putra Malaysia, 43400 UPM, Serdang, Selangor, Malaysia

ABSTRACT

Methylmercury (MeHg) is one type of mercury (Hg) species known to be very toxic to humans, especially pregnant women and their fetuses. This study aims to obtain and validate the optimum condition of liquid chromatography with inductively coupled plasma mass spectrometry (LC-ICP-MS) to test MeHg concentration. To date, there is limited research that is focused on the maternal blood MeHg samples using LC-ICP-MS in Malaysia. Before analysis, collected blood (500 µL) was placed into a 15 mL polypropylene test tube, followed by the addition of extractant solution [0.10% (v/v) HCl + 0.05% (m/v) L-cysteine + 0.10% (v/v) 2-mercaptoethanol] to the sample and sonicated for 15 minutes. The MeHg level was detected from the sample solution using the LC with Zorbax Eclipse XDB-C18 (4.6 x 12.5 mm, 5 µm) (Agilent Technologies) guard column and analytical column (4.6 x 150 mm, 5 µm) and was quantified by using the ICP-MS. The recovery of MeHg was in the range of 106 to 112% with RSD of less than 10%, followed by the LOD and LOQ

ARTICLE INFO

Article history:

Received: 3 March 2021

Accepted: 30 April 2021

Published: 31 July 2021

DOI: <https://doi.org/10.47836/pjst.29.3.45>

E-mail addresses:

amirah6788@gmail.com (Amirah Abedinlah)

saliza_me@upm.edu.my (Saliza Mohd Elias)

suhaili_ab@upm.edu.my (Suhaili Abu Bakar)

smpraveena@upm.edu.my (Sarva Mangala Praveena)

zulida@upm.edu.my (Zulida Rejali)

juliana@upm.edu.my (Juliana Jalaludin)

*Corresponding author

values of 0.216 and 0.766 $\mu\text{g/L}$, respectively. The MeHg appeared at a retention time of fewer than 5 minutes. The results reported that the median (IQR) of maternal blood MeHg level in Malaysian pregnant women was 1.70 (8.90) $\mu\text{g/L}$, which is 9.7% lower than the LOD value and 11.2% higher than the guideline value of 3.5 $\mu\text{g/L}$ of MeHg in maternal blood.

Keywords: LC-ICPMS, maternal blood, methylmercury determination, validation

INTRODUCTION

Mercury (Hg) is a heavy metal that exists ubiquitously in the environment. It has been listed as one of the heavy metals with evidence and proven to cause detrimental health effects to humans. The Hg toxicity to its target organs in human varies according to species and forms, resulting in a different range of toxicity, including carcinogenicity, mutagenicity, and teratogenicity (Jeevanaraj et al., 2015). Organic Hg compounds are more toxic than inorganic Hg compounds due to the lipophilic characteristics and chemical properties of organic Hg that makes it penetrate the membrane and enter the cells easily (Baharuddin et al., 2012). MeHg is one of the organic forms of Hg species known to be very toxic to both humans and the environment. MeHg is derived from the methylation process of Hg through microbes' reaction, especially in the aquatic ecosystem (Jeevanaraj et al., 2016).

Exposure to Hg and MeHg poses a threat to human health, especially among susceptible individuals such as pregnant women. MeHg is a toxic organic compound that targets the brain and can cross the blood-brain and placental barriers, thus are especially detrimental to the fetuses during the developmental stage (National Research Council, 2000b). Based on the previous studies that conducted the Hg and MeHg exposure in maternal blood and cord blood, the results indicated that the concentration level was higher in cord blood compared to the maternal blood (Soon et al., 2014; Huang et al., 2017; Lee et al., 2010). This observation is due to the high affinity of Hg and MeHg that crosses the placenta. The phenomenon is also expected in the present study; however, we found there was difficulty in sampling the cord blood sample due to the different location of respondent's give birth which is outside of Selangor state.

Several areas in Malaysia, such as West Port, Straits of Malacca, Prai, and Johor, were reported to have a high concentration of Hg in the environment due to the anthropogenic metal loads from industrial activities (Praveena et al., 2013). Hg levels in humans is affected by the dietary fish intake, environmental conditions, and different geographical areas. The West Coast of Peninsular Malaysia showed high concentration of Hg levels contaminated in food (Praveena et al., 2013). In a specific case study, Abdullah et al. (2015) conducted a study of Hg and MeHg accumulation in several fish species in the Manjung coastal area. This area can be influenced by the rapid development from anthropogenic and agricultural

activities, waste and toxic effluent, quarries, and residential developments. The authors found that the levels of Hg and MeHg in fish caught were ranged from 65.13 to 106.10 $\mu\text{g}/\text{kg}$. Although the levels were below the guideline limit set in the Malaysian Food Act (1983) (1000 $\mu\text{g}/\text{kg}$), the higher consumption of fish and marine products could affect the Hg accumulation in the body. Therefore, fish consumption from this area is a major concern to pregnant woman in Malaysia due to great pollution from anthropogenic activities.

The previous studies had attempted to analyze the presence of MeHg in multiple media such as sediment, water, and other biological samples. However, there is limited research focusing on the maternal blood MeHg samples using LC-ICP-MS in Malaysia. The detection of MeHg concentration in biological samples such as blood, hair, nail, and urine were determined to assess the degree of MeHg exposure and determine the detrimental health effects that could have happened. However, the Hg concentrations in both blood and hair are accepted as the valid biological samples of MeHg exposure (Mergler et al., 2007), although both are providing a different reflection of exposure (National Research Council, 2000b). In this study, the detection of MeHg concentration in the blood sample was conducted to assess the degree of exposure in the maternal blood among pregnant women. The concentration in maternal blood will reflect the MeHg exposure in the fetuses. According to Kim et al. (2011), the MeHg concentration in the fetuses was higher than in mothers. Based on maternal exposure, the researchers are able to estimate exposure concentration in the fetus and calculate the health risk assessment of Hg exposure.

The problem statement of this study was there is no data available for methylmercury exposure among pregnant women in Malaysia. Table 1 shows the distribution of MeHg concentration among pregnant women population found in other studies. Besides that, the investigation on Hg exposure level from fish consumption found in the hair that was conducted in Petaling District among women at reproductive age showed that 40.9% of them had exceeded the recommended dose of 0.1 $\mu\text{g}/\text{g}$ (Jeevanaraj et al., 2015). This finding propels the current study to focus on the Petaling District to examine the MeHg concentration level from fish consumption. A recent Malaysian study on the Hg exposure from marine fishes which obtained from the wholesale market of the Fisheries Development Authority of Malaysia (LKIM) and fisherman's market in Selangor, showed that seven marine fish species such as Spanish mackerel, golden snapper, torpedo scad, four-finger threadfin, pale-edged stingray, sin croaker and red snapper had total Hg concentration exceeding the FAO/WHO recommendation value of 0.5 mg/kg , with the maximum concentration of 0.90 mg/kg was reported in golden snapper (Jeevanaraj et al., 2016).

The standard methods used to detect the MeHg or Hg concentrations are by using gas chromatography (GC) or by using the high-performance liquid chromatography (HPLC) together with an elemental specific detector such as inductively coupled plasma mass spectrometry (ICP-MS) (Rodrigues et al., 2010). However, the liquid chromatography

(LC) was the most selected separation technique used for Hg speciation compared to the GC because there is no necessity to derive Hg species into volatile compounds before the separation process (Rodrigues et al., 2010). This paper aimed to validate a simple extraction method using the LC-ICPMS technique to detect MeHg in the maternal blood sample, as modified from Rodrigues et al. (2010). The validation step represents a tool essential to prove the claimed function or a specific analytical method to measure the samples for the desired purpose (Tanase et al., 2006) and ensure reliable analytical data.

Table 1

Distribution of MeHg concentration among worldwide population found in other studies

Location	Population	Median	Mean	Range	References
Selangor, Malaysia	Pregnant women – maternal blood	1.70	1.98	0.11 – 9.90	Present study
Charleston, South Carolina, USA	Pregnant women – early gestation	-	0.58	0.01 – 2.70	Donohue et al. (2018)
	Pregnant women – late gestation	-	0.46	0.01 – 2.10	
Seoul and Busan, Korea	Pregnant women – maternal blood	-	2.60	NA	Kim et al. (2011)
St. Lawrence, Canada	Pregnant women – first trimester	-	0.36	NA	Morrissette et al. (2004)
	Pregnant women – second trimester	-	0.30	NA	
	During give birth	-	0.23	NA	
Sweden	Pregnant women – early gestation		0.94	< LOD – 6.8	Vahter et al. (2000)
	Pregnant women – late gestation		0.73	< LOD – 2.8	
Korea	Pregnant women	4.05		3.81 – 4.32	Wells et al. (2016)
Mexico	Pregnant women – all trimesters		3.40	Min=0.29-0.43 Max=11.89-31.15	Basu et al. (2014)

MATERIALS AND METHODS

Study Location and Subjects

The study location was selected based on the data from the previous study by Jeevanaraj et al. (2016) that showed 40.9% of women at reproductive age in the Petaling District had MeHg concentration exceeding the recommended EPA RfD (1 µg/g of hair THg) in their hair samples. Thus, the present study has selected study subject based on the following criteria: pregnant women aged from 20 - 49 years old, with the stage of pregnancy from 12 - 40 weeks and from the 7 Maternal and Child Health Clinics based in the Petaling District. The sample size estimation for one group was used to calculate the sample size and the formula was adopted from Lemeshow et al. (1990). After substituting the values into the formula, the desired sample size of this study was 211 after considered the 20% non-response rate. The area probability sampling technique was used to recruit the respondents from each clinic. The clinics were divided into three groups: low, medium and high density, classified based on the density of the respondents who visited the clinic. After classified the area, the sample size for each clinic was calculated until it reached the desired sample size of 211. The sample collected from each area was presented in the Table 2.

Table 2

Selection of Respondents with Probability Proportionate to Size Method

Clinic (Sub-District)	Estimated number of pregnant women in the clinic	Cumulative number of pregnant women in the clinic	Cluster number	Total number of respondents from each clinic
Low density				
Batu 13, Puchong	1,123	1541	1	10
Total	1,541			
% Representative	1,541 / 27, 092 = 5%		1/21 = 5%	
Medium density				
Sri Kembangan	3,372	6,979	2 – 5	40
Taman Medan	3,690	10,669	6 – 8	30
Kelana Jaya	3,732	14,401	9 & 10	20
Batu 14, Puchong	3,826	18,227	11 – 13	30
Total	14, 620			
% Representative	14,620 / 27, 092 = 54%		12/21 = 56%	
High density				
Seksyen 19	4,277	2,2504	14 – 17	40
Seksyen 7	4,588	2,7092	18 – 21	40
Total	8,865			
% Representative	8,865 / 27, 092 = 33%		8/21 = 38%	210 ≈211

Chemicals and Reagents

All the plastic and glassware materials used in this study were soaked in 10% (v/v) nitric acid (HNO₃) for 24 hours before rinsing five times with ultra-pure water and then dried using nitrogen gas. The purpose of soaking the plastic and glassware in acid is to remove residues entirely from glassware that may contaminate the sample during analysis. A 1000 mg/L standard solution of Methylmercury Chloride (CH₃ClHg) in H₂O was obtained from Alfa Aesar. The calibration standard was freshly prepared on daily basis over the range of 0.0-20.0 µg/L through serial dilution of the stock solution. The other chemicals for the detection were the trace metal grade hydrochloric acid (HCl) (34-37% v/v) Thermo Fisher Scientific, USA), while L-cysteine mixture (97% m/v), 2-mercaptoethanol (≥ 99.9% v/v), ammonium acetate (99.99% m/v) and HPLC grade methanol (≥ 99.9% v/v) were obtained from Sigma-Aldrich (USA).

Standard Reference Material

NIST SRM 955c Toxic Metals in Caprine Blood was purchased from the National Institute of Standard and Technology (NIST, USA) that includes the mass fraction certification of the total organic and inorganic Hg contents in the blood sample.

Instrumentation

An Agilent LC 1260 was interfaced to the Agilent ICP-MS 7900 series, consisting of the essential compartments for the analysis, the isocratic pump, the automatic sampler, the degasser, and the column compartment. The MeHg species were separated using the LC with Zorbax Eclipse XDB-C18 (4.6 x 12.5 mm, 5 µm) (Agilent Technologies) guard column and analytical column (4.6 x 150 mm, 5 µm) followed by the quantification using the ICP-MS. The signal identification was achieved by comparing the retention time (RT) of the standards and analytes, while the matrix spike (i.e., blood sample with known concentration) was used to confirm the peak standard and analytes in the samples. The MeHg level was quantified using a single ion at m/z 202 for Hg against the calibrated external standards.

The instrument was tuned using 1 µg/L tuning solution from the ICP-MS Stock Tuning Solution diluted with ultra-pure water. The instrument was optimized daily, and the performance checking was conducted for optimum performance of the instrument. For better results, the LC Column (Zorbax Eclipse XDB-C18) was preconditioned by pumping the methanol (HPLC grade) at 0.4 mL/min for at least 2 hours. Next, the column was conditioned with the mobile phase solution using the same flow rate and lasted for at least 30 minutes. The operational conditions of the instrument were shown in Table 3 and 4.

Table 3

Operational Condition (Agilent LC 1260 Isocratic Pump)

Setting Items	Setting Values
Column	Zorbax Eclipse XDB C18, 4.6 x 150 mm, 5µm
Guard column	Eclipse XDB C18 4.6 x 12.5 mm, 5µm
Column temperature	Ambient
Mobile phase	0.05% (v/v) 2-mercaptoethanol, 0.4% (m/v) L-cysteine, 0.06 mol/L ammonium acetate and 5% (v/v) methanol, (pH 6.6-6.7)
Mobile phase Flow rate	1 ml/min
Injection volume	100 µL
Run time	10 min (600 sec)
Measurement	Peak high

Table 4

Operational Condition (Agilent Technologist ICP-MS 7900)

Setting Items	Setting Values
RF power	1200 W
Dilution gas	0.40 – 0.60 L/min
Carrier gas	0.6 - 0.8 L/min
Sampling depth	10.0 – 11.0 mm
Nebuliser	Miramist
Nebuliser gas flow	0.5 rps
Spray chamber	Quartz Scott style spray chamber (2°C)
Interface cones	Platinum sampler and skimmer cones
Isotopes	²⁰² Hg
Gas mode	He mode

Extraction Method

The sample extraction was carried out by referring to the previous methods described by Rodrigues et al. (2010) with slight modification. A total of 500 µL of NIST SRM 955c toxic metals in caprine blood (Level 3) was placed into a 15 mL polypropylene test tube. The extraction solution (0.05% of L-cysteine, 0.10% of 2-mercaptoethanol, 0.10% of HCl) was added to the polypropylene tube until the markup volume of 5 mL and then sonicated for 15 minutes. The sample was then centrifuged for 5 minutes at 3500 rpm and filtered

through a 0.22 µm Nylon filter. Finally, the supernatant was placed in the vial for the LC-ICPMS analysis.

Preparation of Calibration Standard

The working standard of MeHg was freshly prepared by diluting the methylmercury chloride 1000 mg/L (Alfa Aesar) in water solution (i.e., stock solution in the extractor solution). A linear equation was obtained by plotting the peak area against the standard concentration at seven points ranged from 0 to 20 µg/L. A calibration curve was prepared using the Agilent Mass Hunter software by plotting the peak high of the standards versus the concentration. The calibration curve was shown in Figure 1.

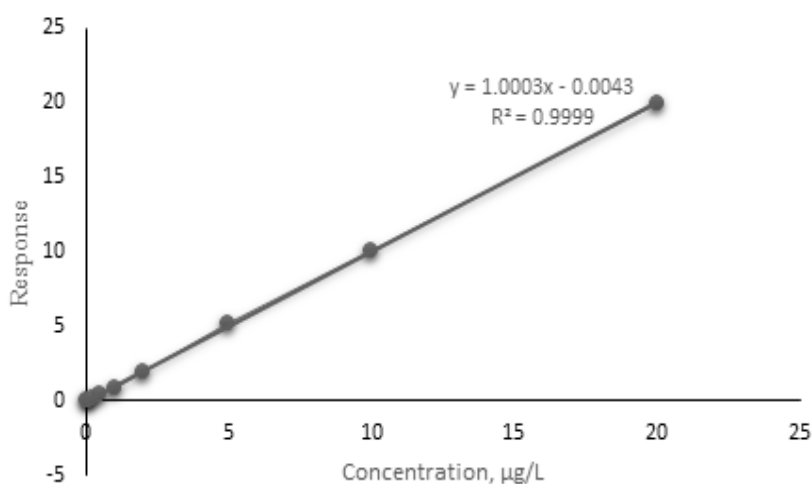


Figure 1. Calibration curve of MeHg Chloride (Standard) (0-20 µg/L)

Method Validation

The method was validated by using the NIST SRM 955c toxic metals in caprine blood, as shown in Table 5. The value observed in the current method was in good agreement with the established target value for the SRM 955c. The LOD was calculated as the mean blank plus with three times the standard deviation of blank, while the LOQ was calculated as the mean blank plus with ten times the standard deviation of the blank (Association of Analytical Committees, 2002). For results below the LOD, the value was replaced by divided by square root of two (Shim et al., 2017; Patel et al., 2019; Taylor et al., 2016; Jo et al., 2015; Gil et al., 2011).

Table 5

MeHg in the NIST SRM 955c. The values obtained are indicated as mean (SD), n=10

Sample	Target Value	LC-ICP-MS method
	MeHg concentration ($\mu\text{g/L}$)	MeHg concentration ($\mu\text{g/L}$)
NIST SRM 955c	4.5 ± 1.0	4.6 ± 0.4

Application of Method

A total of 215 blood samples were collected from pregnant women who visited seven Maternal and Child's Health Clinic from the Petaling District of Selangor under the Ministry of Health Malaysia. Three mL of the blood sample was collected from each respondent by the nurse in the clinic following the best practice of the blood withdrawn procedure. The sample was transferred into the K₂EDTA vacutainer blood tube with a lavender cap containing anticoagulant and then inverted several times to mix with the anticoagulant to avoid the blood clot. The blood samples collected from the respondents were immediately placed in a cool box equipped with coolant to maintain the low temperature and transported to the Environmental Health Laboratory of UPM. The samples were stored at -20°C in a deep freezer until further analysis. The samples were extracted and quantified using the same method as described for NIST SRM 955c.

Quality Control

All 20 samples were analysed under the same analytical condition and assigned as one batch for quality checking. All parts of the equipment in contact with samples and reagents were demonstrated to ensure the interference-free before conducted the analysis.

Statistical Analysis

The SPSS statistical software Version 23 was used in statistical analysis. The median value was used in the analysis due to the non-normality of the data.

Ethical Consideration

The study was ethically approved by the UPM's Ethics Committee for Research Involving Human Subject (JKEUPM) (Ref: UPM/TNCPI/RMC/1.4.18.2) and by the Medical Research and Ethics Committee (MREC) with registered National Medical Research Registration (NMRR) ID of 16-782-30590.

RESULTS

This method validation was performed by using the LC-ICP-MS to detect MeHg in the blood samples. To the best of our knowledge, this was the first study reported in the Selangor state of Malaysia to determine the MeHg compound in blood samples. The validation was performed to ensure and confirm that the criteria used were in an acceptable range for the intended use of the MeHg detection in the blood sample using the LC-ICP-MS. The R^2 value of more than 0.995 indicates a good and stringent linear relationship between the concentration and the corresponding peak area.

The performance of an instrument was evaluated by calculating the LOD and LOQ values. The LOD value is determined at the point where the minimum analyte concentration can be detected and reliably distinguished from zero using the instrument. The LOD value was determined by multiplying the standard deviation by 3. The LOQ value refers to the point with the lowest analyte concentration determined quantitatively with an acceptable precision level and accuracy. The LOQ value was measured as ten times the standard deviation from LOD (Shrivastava & Gupta, 2011). The analytical method validation was shown in Table 6.

The acceptable range of sample recovery is from 70 to 120%, with an RSD value of ≤ 20 (Wadhwa et al., 2015; Olmedo et al., 2010). The recovery range in this study was 106 to 112% with the RSD value of $< 10\%$ and shows that the method can perform maximum extraction repeatedly, and the validated method is applicable for blood sample extraction using the LC-ICP-MS. Figure 2a and 2b show the chromatograms of MeHg species in the standard solution and blood sample.

The method validation was used to detect the maternal MeHg in blood samples collected among pregnant women from one of the districts in Selangor, Malaysia. The results are given in Table 7. The median (IQR) value was 1.70 (8.90) $\mu\text{g/L}$, and the geometric mean (GM) value was 1.98 $\mu\text{g/L}$. A total of 11.2% of pregnant women have exceeded the recommended RfD of 3.5 $\mu\text{g/L}$ MeHg in the maternal blood sample. The range showed that the lowest detected value was one-fold lower than that of the LOD value. The data also showed that nearly 10% of the respondents had a lower detection value than the calculated LOD value.

DISCUSSION

The rapid growth of development and human activities in Malaysia has contributed to contamination and human exposure. The method validation was used to detect the MeHg in maternal blood sample among pregnant women in Selangor, Malaysia. Previously, Jeevanaraj et al. (2016) have found that almost 50% of women in their reproductive age in the Petaling district had exceeded the limit of Hg in their hair which indicated an alarming level of Hg exposure through fish consumption. This current study was conducted among

Table 6
Analytical method validation estimation

	MeHg analysis
LOD ($\mu\text{g/l}$)	0.216
LOQ ($\mu\text{g/l}$)	0.766
Calibration range	0.0 – 20.0 $\mu\text{g/L}$
Linear equation	$y = 1.003x - 0.0043$
$R^2 \pm \text{SD}$	0.999 ± 0.001
Precision (% RSD)	
- Repeatable	0.332
- Reproducible	4.799
Recovery (%)	112 ± 4.23

Table 7
Maternal blood MeHg concentration in respondent (N=215)

	MeHg levels ($\mu\text{g/L}$)
Range ($\mu\text{g/L}$)	0.11 – 9.90
Total below LOD, n (%)	21 (9.7)
Average value ($\mu\text{g/L}$)	1.98
Median (IQR) ($\mu\text{g/L}$)	1.70 (8.90)
Total Exceeded RfD, n (%)	24 (11.2)

Note. IQR = Interquartile range, RfD = Reference dose

pregnant women, the susceptible group vulnerable to sensitive compound/chemicals such as Hg and MeHg. Selangor state was chosen as the location of the study because it is located in the Klang Valley area, which is known to contribute to environmental issues such as pollution and lead to health problems (Suhaimi et al., 2020; Shahrir et al., 2019). The Petaling district was chosen based on the previous study conducted by Jeevanaraj et al. (2016), who reported the findings of Hg exposure via fish consumption among women in the Petaling area. This study was conducted to investigate the MeHg exposure in pregnant women, one of the Hg species which is known to be very toxic to human health.

Our study found that 11.2% of pregnant women in this study had maternal blood MeHg above the guideline limit of 3.5 $\mu\text{g/L}$. The United States of Environmental Protection Agency (USEPA) has revised the RfD for Hg in cord blood from the reference dose of 58 $\mu\text{g/L}$, as recommended by the National Research Council (2000a). After considering the effects of in utero MeHg exposure to child development from the Faroese, New Zealand

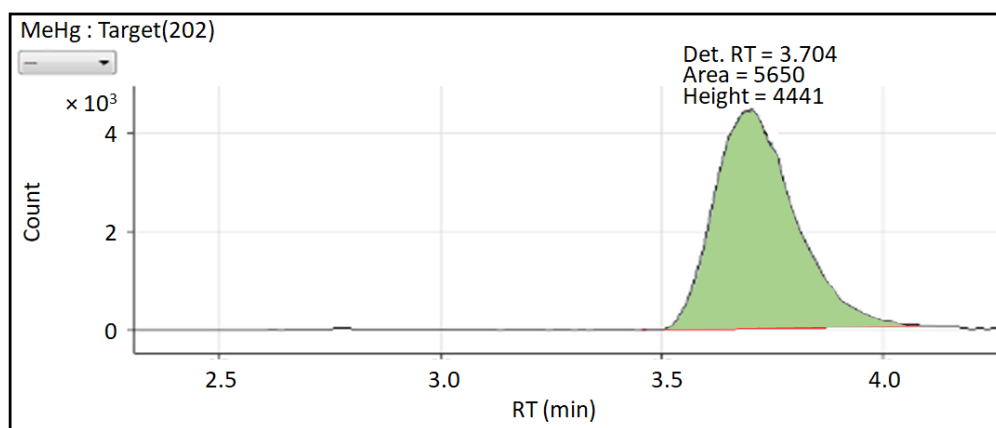


Figure 2a. A standard solution that contains MeHg under an optimised condition with a retention time of MeHg at minute 3.50

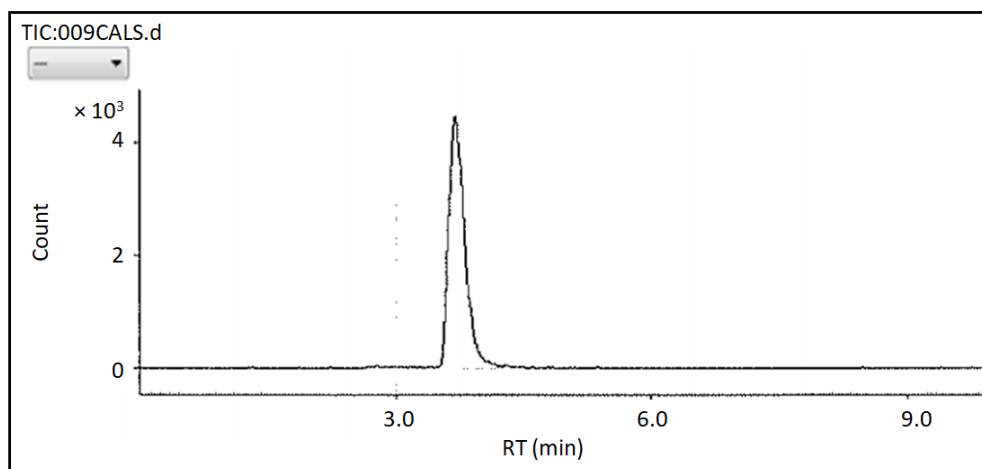


Figure 2b. Chromatogram showing the peak of MeHg species in the blood sample

and Seychelles cohort studies, USEPA has adopted the use of 10 uncertainty factor (UF) value to calculate the $5.8 \mu\text{g/L}$ Hg RfD in cord blood (Rice et al., 2003). The RfD of $5.8 \mu\text{g/L}$ Hg in cord blood indicates the association with increased risk of learning disabilities in fetuses. However, Stern and Smith (2003) suggested that the maternal blood Hg level should be revised to $3.5 \mu\text{g/L}$, as cord blood levels are on average 70% higher than maternal blood levels (Mahaffey et al., 2004). Previous studies by Basu et al. (2014), Razzaghi

et al. (2014), Donohue et al. (2018), Miranda et al. (2011), Mortazavi et al. (2017), and Silbernagell et al. (2011) used this guideline limit to associate their maternal blood Hg and MeHg exposure levels. Meanwhile, Cusack et al. (2017) has suggested that this guideline limit might be the most applicable guideline for comparison until an updated guideline limit for maternal blood MeHg concentration is determined.

The concentration of maternal blood MeHg in this study was compared to other population studies conducted worldwide. The blood MeHg concentration reported in this study was higher when compared to the studies by Donohue et al. (2018), Morrissette et al. (2004), and Vahter et al. (2000). The difference was due to the fewer fish and seafood consumption during the pregnancy, as recommended by the US Food and Drug Administration (FDA) and Environmental Protection Agency (EPA). Both agencies recommend to avoid the consumption of certain fish types that contained high mercury concentration, including shark, swordfish, king mackerel and tilefish (Razzaghi et al., 2014). Another possible reason for the lower MeHg concentration in pregnant women might be due to the hemodilution and other physiological changes that are related to pregnancy (Vahter et al., 2000), and could also be caused by the MeHg movement from the maternal blood to the cord blood (Kim et al., 2011).

On the other hand, the blood MeHg concentration reported in the present study was lower than results reported by Basu et al. (2014) in the Early Life Exposure in Mexico to Environmental Toxicant (ELEMENT) cohort study among trimester pregnant women in Mexico City. The cohort study found that 28.6 to 39.2% exceeded the 3.5 $\mu\text{g/L}$ across all the trimesters. Besides that, the study also found that high mercury exposure among pregnant women was because of high fish and seafood intakes. In Mexico, seafood was consumed nearly 7 times a month in about 700 to 800 grams each time, and canned tuna was the most popular item consumed. These findings showed that the fishes and seafood consumption in Mexico was approximately 2 times higher than the amount of seafood consumed by the other women of child-bearing age in America (442 grams/month; EPA, 2002).

In our study, the type of marine fish intake and maternal blood MeHg level in pregnant women was examined. The finding shows that the top five marine fishes that are mostly consumed by the respondents were Indian mackerel, torpedo scad, yellow-banded scad, Spanish mackerel and pomfret. This finding was in line with the previous study by Ahmad et al. (2015), who have identified the most preferred seafood among the Malaysian in Peninsular Malaysia, and they reported that the majority of respondents preferred Indian mackerel (70.9%), followed by yellowtail scad (26.2%), pomfret (22.6%) and tuna (21.8%), as compared to other types of seafood. Another similar study on Hg exposure via fish consumption was by Jeevanaraj et al. (2016), who conducted a study in Selangor and found that the most preferred marine fish species was the Indian mackerel (55%), followed by torpedo scad (31.6%), Indian scad (15.2%), yellow-banded scad (12%), Eastern little

tuna (11.7%) and Japanese threadfin bream (10.5%). This shows that most of the people in the Klang Valley would prefer the mackerel and scads species over the other fish species.

In this study, the consumption of all seafood types (i.e., prawn, squid, crab and cockles and marine fishes) were not significantly associated with the maternal blood MeHg concentration among the respondents. This may be due to the low consumption amount of seafood and marine fishes among respondents in this study. Most of the respondents in this study were found to consume seafood and fish of small size on a monthly and weekly basis. Besides that, the lower Hg accumulation may be due to the respondents' preference that mostly favoured marine fishes, therefore contributing to the relationship between fish and seafood consumption with the MeHg accumulation. The Hg concentration in muscles of fish species mostly consumed by the respondents in this study showed the values below the Malaysian Food Regulation 1985 and Joint FAO/WHO Expert Committee on Food Additives (JECFA) guideline limit of 0.5 mg/kg (Jeevanaraj et al., 2016; Ahmad et al., 2015; Hajeb et al., 2008).

The minimum concentration of MeHg found in this study was lower while the maximum concentration was higher, compared to the studies conducted in Korea and Portugal. No Malaysian study on the MeHg concentration in the blood sample was found. Apparently, in the context of community health, the prevalence of 11.2% that exceeded the guideline limit of 3.5 µg/L reflects that the harmful exposure of Hg through fish consumption is at an alarming stage among the consumers. Regardless of the susceptible group, the Hg exposure can affect any individuals in the population who had consumed food contaminated with Hg, especially fish and seafood.

The measured maternal blood MeHg showed that 11.2% of the respondents had accumulated MeHg concentration beyond the guideline limit of 3.5 µg/L. The prevalence of exceeding limit reflects the current exposure among pregnant women with non-occupational exposure, typically due to fish consumption. The women in the highly exposed group are a critical concern to the health regulatory authorities and government bodies. These policymakers need to regulate the policy and guideline on advisory consumption of fish-contained Hg and proposing a health surveillance program among pregnant women to protect them from the over-accumulation of Hg and MeHg in their body.

CONCLUSION

The method for detecting MeHg in the blood sample and the extraction and instrument method detection carried out in this study was effective and accurate. The results from the samples showed that this study population was possibly exposed to MeHg via ingestion route through fish consumption. Exposure to the toxic substance during pregnancy may harm the unborn baby and lead to neurotoxicity. Therefore, there is a pressing need for

further investigation and evaluation among the susceptible group, especially on their dietary intake and other possible sources of exposure, in order to plan for a subsequent risk management approach.

ACKNOWLEDGMENTS

We thanked the Ministry of Higher Education Malaysia for the Fundamental Research Grant Scheme (FRGS) Project No: FRGS/1/2016/SKK06/UPM/02/11 fund granted for this project to Dr Chin Teen Teen, Ms Nazirah Ariffin and Ms Annie Johanna Ahmad from ALS Technichem (M) Sdn Bhd, Bukit Jelutong, Selangor for the assistance throughout the laboratory analysis and all the respondents who involved in this research.

REFERENCES

- Abdullah, A., Hamzah, Z., Saat, A., Wood, A. K., & Alias, M. (2015). Accumulation of mercury (Hg) and methyl mercury (MeHg) concentrations in selected marine biota from Manjung Coastal Area. *Malaysian Journal of Analytical Sciences*, *19*(4), 669-678.
- Ahmad, N. I., Noh, M. F. M., Mahiyuddin, W. R. W., Jaafar, H., Ishak, I., Azmi, W. N. F. W., Veloo, Y., & Hairi, M. H. (2015). Mercury levels of marine fish commonly consumed in Peninsular Malaysia. *Environmental Science and Pollution Research*, *22*(5), 3672-3686. <https://doi.org/10.1007/s11356-014-3538-8>.
- Association of Analytical Committees. (2002). Appendix D: Guidelines for collaborative study procedures to validate characteristics of a method of analysis, official methods of analysis manual. *Interlaboratory Collaborative Study*, 1-12
- Baharuddin, N., Saim, N., Osman, R., Zain, S. M., Juahir, H., & Saari, S. R. (2012). Determination of organic and inorganic mercury species in Sungai Kinta, Perak by reversed-phase high performance liquid chromatography (HPLC) on-line coupled with ICP-MS. *Malaysian Journal of Analytical Sciences*, *16*(2), 134-141.
- Basu, N., Tutino, R., Zhang, Z., Cantonwine, D. E., Goodrich, J. M., Somers, E. C., Rodriguez, L., Schnaas, L., Solano, M., Mercado, A., & Peterson, K. (2014). Mercury levels in pregnant women, children, and seafood from Mexico City. *Environmental Research*, *135*, 63-69. <https://doi.org/10.1016/j.envres.2014.08.029>
- Cusack, L. K., Smit, E., Kile, M. L., & Harding, A. K. (2017). Regional and temporal trends in blood mercury concentrations and fish consumption in women of child-bearing Age in the united states using NHANES data from 1999–2010. *Environmental Health*, *16*(1), 1-11. <https://doi.org/10.1186/s12940-017-0218-4>
- Donohue, A., Wagner, C. L., Burch, J. B., & Rothenberg, S. E. (2018). Blood total mercury and methylmercury among pregnant mothers in Charleston, South Carolina, USA. *Journal of Exposure Science & Environmental Epidemiology*, *28*(5), 494-504. <https://doi.org/10.1038/s41370-018-0033-1>
- EPA. (2002). *Estimated per capita fish consumption in the United States* (Report EPA-821-C-02-003). U.S. Environmental Protection Agency.

- Gil, F., Hernández, A. F., Márquez, C., Femia, P., Olmedo, P., López-Guarnido, O., & Pla, A. (2011). Biomonitorization of cadmium, chromium, manganese, nickel and lead in whole blood, urine, axillary hair and saliva in an occupationally exposed population. *Science of The Total Environment*, 409(6), 1172-1180. <https://doi.org/10.1016/j.scitotenv.2010.11.033>
- Hajeb, P., Selamat, J., Ismail, A., Bakar, F. A., Bakar, J., & Lioe, H. N. (2008). Hair mercury level of coastal communities in Malaysia: A linkage with fish consumption. *European Food Research and Technology*, 227(5), 1349-1355. <https://doi.org/10.1007/s00217-008-0851-9>
- Huang, S. H., Weng, K. P., Lin, C. C., Wang, C. C., Lee, C. T. C., Ger, L. P., & Wu, M. T. (2017). Maternal and umbilical cord blood levels of mercury, manganese, iron, and copper in southern Taiwan: A cross-sectional study. *Journal of the Chinese Medical Association*, 80(7), 442-451. <https://doi.org/10.1016/j.jcma.2016.06.007>
- Jeevanaraj, P., Hashim, Z., Elias, S. M., & Aris, A. Z. (2015). Total mercury (THg), lead (Pb), cadmium (Cd) and arsenic (As) in hair samples: Method validation and quantification among women at reproductive age in Selangor. *International Journal of Science: Basic Applied Research*, 24(4), 332-347.
- Jeevanaraj, P., Hashim, Z., Elias, S. M., & Aris, A. Z. (2016). Mercury accumulation in marine fish most favoured by Malaysian women, the predictors and the potential health risk. *Environmental Science and Pollution Research*, 23, 23714-23729. <https://doi.org/10.1007/s11356-016-7402-x>
- Jo, S., Woo, H. D., Kwon, H. J., Oh, S. Y., Park, J. D., Hong, Y. S., Pyo, H., Park, K. S., Ha, M., Kim, H., & Sohn, S. J. (2015). Estimation of the biological half-life of methylmercury using a population toxicokinetic model. *International Journal of Environmental Research and Public Health*, 12(8), 9054-9067. <https://doi.org/10.3390/ijerph120809054>.
- Kim, D. S., Kim, G. B., Kang, T., & Ahn, S. (2011). Total and methyl mercury in maternal and cord blood of pregnant women in Korea. *Toxicology and Environmental Health Sciences*, 3(4), 254-257. <https://doi.org/10.1007/s13530-011-0099-9>
- Lee, B. E., Hong, Y. C., Park, H., Ha, M., Koo, B. S., Chang, N., & Jo, S. J. (2010). Interaction between GSTM1/GSTT1 polymorphism and blood mercury on birth weight. *Environmental health perspectives*, 118(3), 437-443. <https://dx.doi.org/10.1289%2Fehp.0900731>.
- Lemeshow, S., Hosmer, D. W., Klar, J., Lwanga, S. K., & World Health Organization. (1990). *Adequacy of sample size in health studies*. Wiley.
- Mahaffey, K. R., Clickner, R. P., & Bodurow, C. C. (2004). Blood organic mercury and dietary mercury intake: National health and nutrition examination survey, 1999 and 2000. *Environmental health perspectives*, 112(5), 562-570. <https://dx.doi.org/10.1289%2Fehp.6587>.
- Mergler, D., Anderson, H. A., Chan, L. H. M., Mahaffey, K. R., Murray, M., Sakamoto, M., & Stern, A. H. (2007). Methylmercury exposure and health effects in humans: A worldwide concern. *AMBIO: A Journal of the Human Environment*, 36(1), 3-11. [https://doi.org/10.1579/0044-7447\(2007\)36\[3:MEAHEI\]2.0.CO;2](https://doi.org/10.1579/0044-7447(2007)36[3:MEAHEI]2.0.CO;2)
- Miranda, M. L., Edwards, S., & Maxson, P. J. (2011). Mercury levels in an urban pregnant population in Durham County, North Carolina. *International Journal of Environmental Research and Public Health*, 8(3), 698-712. <https://doi.org/10.3390/ijerph8030698>.

- Morrisette, J., Takser, L., St-Amour, G., Smargiassi, A., Lafond, J., & Mergler, D. (2004). Temporal variation of blood and hair mercury levels in pregnancy in relation to fish consumption history in a population living along the St. Lawrence River. *Environmental Research*, 95(3), 363-374. <https://doi.org/10.1016/j.envres.2003.12.007>.
- Mortazavi, S. M. J., Mortazavi, G., & Paknahad, M. (2017). Methylmercury exposure in women of child-bearing age and children. *Workplace Health & Safety*, 65(2), 52-52. <https://doi.org/10.1177/2165079916682746>
- National Research Council. (2000a). *Scientific frontiers in developmental toxicology and risk assessment* (2nd Ed.). National Academy of Sciences.
- National Research Council. (2000b). *Toxicological effects of methylmercury*. National Academies Press (US). <https://doi.org/10.17226/9899>.
- Olmedo, P., Pla, A., Hernandez, A. F., Lopez-Guarnido, O., Rodrigo, L., & Gil, F. (2010). Validation of a method to quantify chromium, cadmium, manganese, nickel and lead in human whole blood, urine, saliva and hair samples by electrothermal atomic absorption spectrometry. *Analytica Chimica Acta*, 659(1-2), 60-67. <https://doi.org/10.1016/j.aca.2009.11.056>
- Patel, N. B., Xu, Y., McCandless, L. C., Chen, A., Yolton, K., Braun, J., Jones, R. L., Dietrich, K. N., & Lanphear, B. P. (2019). Very low-level prenatal mercury exposure and behaviors in children: The HOME Study. *Environmental Health*, 18(1), 2-12. <https://doi.org/10.1186/s12940-018-0443-5>.
- Praveena, S. M., De Burbure, C., Aris, A. Z., & Hashim, Z. (2013). Mini review of mercury contamination in environment and human with an emphasis on Malaysia: status and needs. *Reviews on environmental health*, 28(4), 195-202. <https://doi.org/10.1515/revh-2013-0011>.
- Razzaghi, H., Tinker, S. C., & Crider, K. (2014). Blood mercury concentrations in pregnant and nonpregnant women in the United States: National health and nutrition examination survey 1999-2006. *American Journal of Obstetrics and Gynecology*, 210(4), 357.e1-357.e9 <https://doi.org/10.1016/j.ajog.2013.10.884>.
- Rice, D. C., Schoeny, R., & Mahaffey, K. (2003). Methods and rationale for derivation of a reference dose for methylmercury by the US EPA. *Risk Analysis: An International Journal*, 23(1), 107-115. <https://doi.org/10.1111/1539-6924.00294>
- Rodrigues, J. L., de Souza, S. S., de Oliveira Souza, V. C., & Barbosa Jr, F. (2010). Methylmercury and inorganic mercury determination in blood by using liquid chromatography with inductively coupled plasma mass spectrometry and a fast sample preparation procedure. *Talanta*, 80(3), 1158-1163. <https://doi.org/10.1016/j.talanta.2009.09.001>
- Sahrir, S., Abdullah, A. M., Ponrahono, Z., & Sharaai, A. H. (2019). Environmetric study on air quality pattern for assessment in Klang Valley, Malaysia. *International Journal of Recent Technology and Engineering*, 8(1S), 17-24.
- Shim, Y. K., Lewin, M. D., Ruiz, P., Eichner, J. E., & Mumtaz, M. M. (2017). Prevalence and associated demographic characteristics of exposure to multiple metals and their species in human populations: The United States NHANES, 2007–2012. *Journal of Toxicology and Environmental Health, Part A*, 80(9), 502-512. <https://doi.org/10.1080/15287394.2017.1330581>.

- Shrivastava, A., & Gupta, V. B. (2011). Methods for the determination of limit of detection and limit of quantitation of the analytical methods. *Chronicles of Young Scientists*, 2(1), 15-21. <https://doi.org/10.4103%2F2229-5186.79345>
- Silbernagel, S. M., Carpenter, D. O., Gilbert, S. G., Gochfeld, M., Groth, E., Hightower, J. M., & Schiavone, F. M. (2011). Recognising and preventing overexposure to methylmercury from fish and seafood consumption: Information for physicians. *Journal of Toxicology*, 2011, 1-7. <https://doi.org/10.1155/2011/983072>
- Soon, R., Dye, T. D., Ralston, N. V., Berry, M. J., & Sauvage, L. M. (2014). Seafood consumption and umbilical cord blood mercury concentrations in a multiethnic maternal and child health cohort. *BMC Pregnancy and Childbirth*, 14(1), 2-6. <https://doi.org/10.1186/1471-2393-14-209>.
- Stern, A. H., & Smith, A. E. (2003). An assessment of the cord blood: Maternal blood methylmercury ratio: Implications for risk assessment. *Environmental health perspectives*, 111(12), 1465-1470. <https://dx.doi.org/10.1289%2Fehp.6187>.
- Suhaimi, N. F., Jalaludin, J., & Juhari, M. A. M. (2020). The impact of traffic-related air pollution on lung function status and respiratory symptoms among children in Klang Valley, Malaysia. *International Journal of Environmental Health Research*, 1-12. <https://doi.org/10.1080/09603123.2020.1784397>
- Tanase, I. G., Popescu, I. L., & Pana, A. (2006). An analytical method validation for atomic absorption spectrometry analysis of total zinc from insulin. *Analele Universitatii din Bucuresti-Chimie*, 1, 45-50.
- Taylor, C. M., Golding, J., & Emond, A. M. (2016). Blood mercury levels and fish consumption in pregnancy: Risks and benefits for birth outcomes in a prospective observational birth cohort. *International Journal of Hygiene and Environmental Health*, 219(6), 513-520. <https://doi.org/10.1016/j.ijheh.2016.05.004>
- Vahter, M., Åkesson, A., Lind, B., Björs, U., Schütz, A., & Berglund, M. (2000). Longitudinal study of MeHg and inorganic mercury in blood and urine of pregnant and lactating women, as well as in umbilical cord blood. *Environmental Research*, 84(2), 186-194. <https://doi.org/10.1006/enrs.2000.4098>
- Wadhwa, S. K., Kazi, T. G., Afridi, H. I., & Talpur, F. N. (2015). Interaction between carcinogenic and anti-carcinogenic trace elements in the scalp hair samples of different types of Pakistani female cancer patients. *Clinica Chimica Acta*, 439, 178-184. <https://doi.org/10.1016/j.cca.2014.10.007>.
- Wells, E. M., Herbstman, J. B., Lin, Y. H., Jarrett, J., Verdon, C. P., Ward, C., Caldwell, K. L., Hibbeln, J. R., Witter, F. R., Halden, R. U., & Goldman, L. R. (2016). Cord blood methylmercury and fetal growth outcomes in Baltimore newborns: Potential confounding and effect modification by omega-3 fatty acids, selenium, and sex. *Environmental Health Perspectives*, 124(3), 373-379. <https://doi.org/10.1289/ehp.1408596>

Detection of COVID-19 from Chest X-ray and CT Scan Images using Improved Stacked Sparse Autoencoder

Syahril Ramadhan Saufi^{1*}, Muhd Danial Abu Hasan¹, Zair Asrar Ahmad¹, Mohd Salman Leong² and Lim Meng Hee²

¹*School of Mechanical Engineering, Universiti Teknologi Malaysia (UTM), 81310 Skudai, Johor Bahru, Malaysia*

²*Institute of Noise and Vibration, Universiti Teknologi Malaysia (UTM), 54100 Kuala Lumpur, Malaysia*

ABSTRACT

The novel Coronavirus 2019 (COVID-19) has spread rapidly and has become a pandemic around the world. So far, about 44 million cases have been registered, causing more than one million deaths worldwide. COVID-19 has had a devastating impact on every nation, particularly the economic sector. To identify the infected human being and prevent the virus from spreading further, easy, and precise screening is required. COVID-19 can be potentially detected by using Chest X-ray and computed tomography (CT) images, as these images contain essential information of lung infection. This radiology image is usually examined by the expert to detect the presence of COVID-19 symptom. In this study, the improved stacked sparse autoencoder is used to examine the radiology images. According to the result, the proposed deep learning model was able to achieve a classification accuracy of 96.6% and 83.0% for chest X-ray and chest CT-scan images, respectively.

ARTICLE INFO

Article history:

Received: 4 December 2020

Accepted: 1 April 2021

Published: 19 July 2021

Keywords: COVID-19, CT scan, deep learning, image classification, X-ray

DOI: <https://doi.org/10.47836/pjst.29.3.14>

E-mail addresses:

msramadhan93@gmail.com (Syahril Ramadhan Saufi)

muhd_danial200@yahoo.com (Muhd Danial Abu Hasan)

zair@utm.my (Zair Asrar Ahmad)

salman.leong@gmail.com (Mohd Salman Leong)

limmenghee@gmail.com (Lim Meng Hee)

*Corresponding author

INTRODUCTION

Coronavirus (COVID-19) is a disease caused by a severe acute respiratory syndrome (SARS-CoV-2). This virus was detected in December 2019 in Wuhan, Hubei Province, China. According to Huang et al. the most

common symptoms on the infected patient in Wuhan, China were fever, cough and myalgia or fatigue (Huang et al., 2020). COVID-19 has spread worldwide, and it has caused a dead around three million peoples around the world. However, the vaccination programme has been conducted worldwide to prevent the spread of COVID-19. Four possible methods can be used to detect the COVID-19 virus from human such as enzyme-linked immunosorbent assay (ELISA), loop-mediated isothermal amplification (LAMP), lateral flow and reverse transcription-polymerase chain reaction (RT-PCR). RT-PCR is the common method used in COVID-19 detection on the human body. However, this method requires 45 to 90 minutes to obtain the result (Bustin & Nolan, 2020) and it has a lack of accuracy on the early-stage infected patient (Zu et al., 2020). Due to large volume of samples, the analysis of RT-PCR can take several days.

According to Zu et al. (2020), radiologic examination can be used in detecting infected patient. Besides, Salehi et al. (2020) did review that there is an abnormal occur on infected patient' chest which can be seen using computer tomography (CT) image. The diagnosis using CT scan on infected patient's chest outperformed RT-PCR method in many cases (Salehi et al., 2020). According to X. Yang et al. (2020), the early disease can be detected using CT scan method and the authors have conducted a comprehensive review on chest radiography analysis. Also, several studies have shown the capability of COVID-19 detection using chest X-ray images (Luo et al., 2019; Purohit et al., 2020; Apostolopoulos & Mpesiana, 2020). However, both CT-scan and X-ray images require an expert to examine the image.

Machine learning is a method that has become a popular choice in providing an automated diagnosis for any disease. The machine learning can provide a more accurate and consistent result. The implementation of the machine learning model can assist the radiologist in making a correct decision since there is a lot of patient out there waiting for the result. With a massive number of tests, it may cause a high tendency of making a wrong examination from the image due to limited diagnosis time. The architecture of simple machine learning has recently been explored to create a deeper machine learning model architecture that can produce a complete model without requiring any manual feature preparation (Ozturk et al., 2020; Saufi et al., 2019). By taking advantage of the deep learning model, this study implements the deep learning method in diagnosing the non-infected and infected patient of COVID-19 virus using the radiology image such as CT scan and X-ray images. The deep learning model has a high capability of producing a result with a split second when the model is properly trained. Hence, the effective quantitative analysis of these images can be used as a complementary result before getting the result from RT-PCR. To date, RT-PCR has a best standard on the examination of COVID-19 as it directly analysing the virus at DNA level.

The stacked sparse autoencoder (SSAE) model has been used in this analysis. SSAE model is among the popular model in deep learning. However, the SSAE model comes with several challenges such as hyperparameter tuning and computer processing time. The hyperparameter should be tuned properly to obtain an accurate diagnosis result. This hyperparameter is usually tuned manually which is time-consuming. Hence, this study utilised the differential evolution method to optimise the hyperparameter of SSAE model. The proposed model is developed to deal with several types of data such as a statistical parameter, images, and raw series data. Also, it has the ability in dealing with low sample dataset and it did not require any image enhancement on the dataset for image classification analysis.

MATERIALS AND METHODS

Stacked Sparse Autoencoder Architecture

The stacked sparse autoencoder is built by stacking the sparse autoencoder with many numbers. As shown in Figure 1, the Sparse autoencoder comprises the encoder, hidden layer, and decoder features. The encoder mapped the input data using $h = f(w_1x + b)$ into hidden representation ($h \in R^k$) and the following function $\hat{x} = g(w_2h + b)$ is used to reconstruct the hidden representation. Sparse autoencoder (SAE) imposes a restriction on the hidden autoencoder units that cause inactive hidden unit activation (Wang et al., 2018). The reconstruction error of sparse autoencoder is shown in Equation 1.

$$E(w, b) = \frac{1}{2} \|h_{w,b}(x) - y\|^2 + \beta \sum_{j=1}^n KL(\rho \|\hat{\rho}_j) + \frac{\lambda}{2} \sum_{l=1}^{nl} \sum_i^{sl-1} \sum_j^{sl} (W_{ij}^{(l)})^2 \tag{1}$$

where the Kullberg-Leibler divergence is represented as $KL(\rho \|\hat{\rho}_j) = \rho \log \frac{\rho}{\hat{\rho}_j} + (1 - \rho) \log \frac{1-\rho}{1-\hat{\rho}_j}$, β is a sparsity penalty term weight, ρ is the sparsity parameter and $\hat{\rho}_j$ is the average activation of the hidden unit. The sparse autoencoder cannot identify the useful data as the purpose of the network for obtaining useful information. By restricting the weight, w and bias, b using the sparsity term, the useful data is obtained at the hidden layer. At the end of the multiple sparse autoencoder layer, another layer called Softmax classifier is stacked. This layer is intended to identify the useful features of information processed by the sparse autoencoder. In Equation 2, the equation of Softmax is defined.

$$h_{\theta}(x^i) = \begin{bmatrix} p(y^i = 1|x^i; \theta) \\ p(y^i = 2|x^i; \theta) \\ \vdots \\ p(y^i = k|x^i; \theta) \end{bmatrix} = \frac{1}{\sum_{i=1}^k e^{\theta_j^T x^i}} \begin{bmatrix} e^{\theta_1^T x^i} \\ e^{\theta_2^T x^i} \\ \vdots \\ e^{\theta_k^T x^i} \end{bmatrix}, \tag{2}$$

where $\theta_1, \theta_2, \dots, \theta_k \in \mathfrak{R}^{n+1}$ are the model parameters and $1 / \sum_{i=1}^k e^{\theta_j^T x^i}$ normalizes the distribution to ensure that the sum value is equal to one.

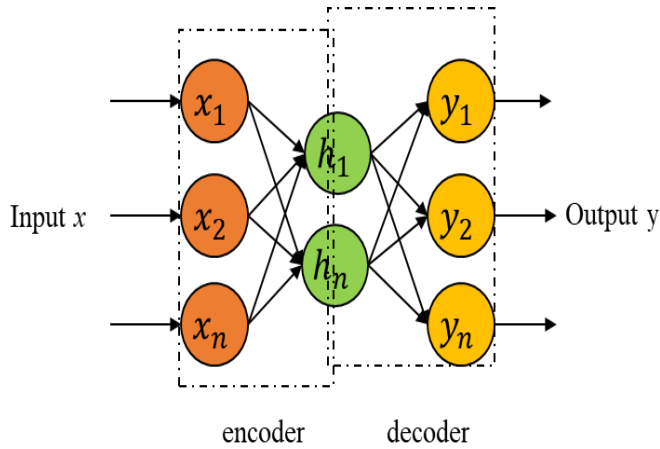


Figure 1. Sparse autoencoder architecture

Proposed Model

Several modifications were involved in the built model. First to decrease the training time of the model, the resilient backpropagation (Rprop) algorithm is implemented. Then using the differential evolution (DE) optimization process, the hyperparameters including weight regulariser, the number of hidden units, sparsity regulariser and sparsity proportion are optimized. DE is among the finest methods of optimization, based on studies examined by Wahab et al. (2015). These techniques have been used to detect rotating machinery failure, and the result has shown that the efficiency of the deep learning model can be enhanced. Throughout the analysis, however some hyperparameters are kept constant, such as the number of epochs, the number of sparse autoencoders, and loss function. The epoch was set to 500, to form the proposed model, two sparse autoencoders were stacked and the msespase was used as the loss function. For each sparse autoencoder, there are four significant hyperparameters and using differential evolution, the hyperparameters value are optimized. Furthermore, using a resilient backpropagation algorithm, the training function of this network was optimized. Figure 2 shows the entire architecture of the proposed model (improved stacked sparse autoencoder). It is important to note that when training and testing using the machinery dataset, the proposed model did not require any image processing. The proposed method is therefore used in this paper to detect the presence of the COVID-19 virus on photographs of chest X-ray and CT scans.

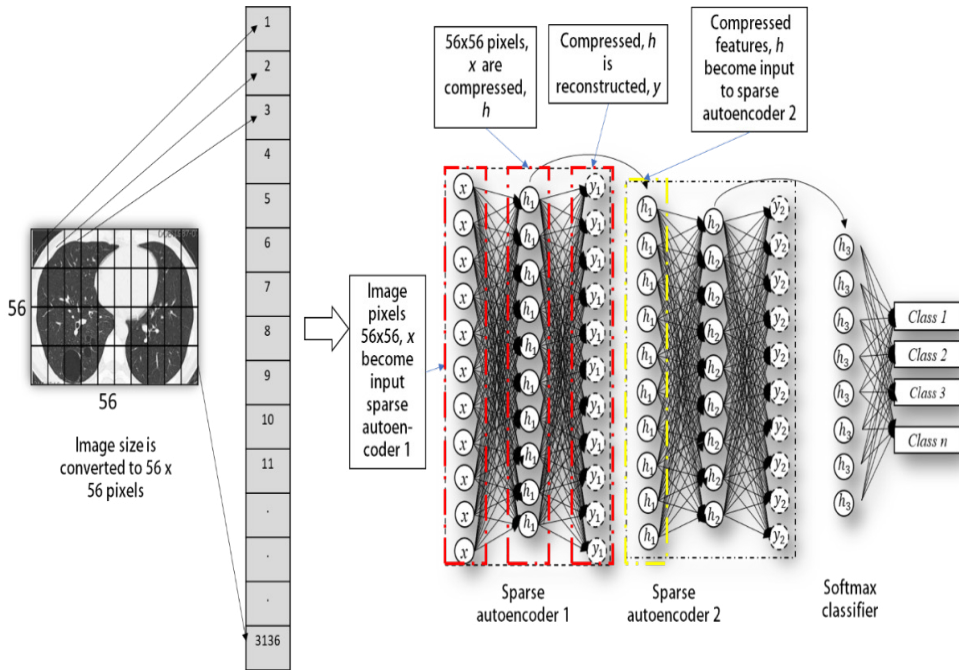


Figure 2. The proposed model architecture

Differential Evolution Optimisation. Differential evolution (DE) is used in to deal with the hyperparameter selection issue discussed in the previous section. DE is a metaheuristic optimization that uses genetic algorithm operations. As the population grows, the algorithm inevitably changes its search behaviour from discovery to exploitation due to its self-referential mutation. The primary aim of DE is to use mutation and crossover to produce new vectors. For the next generation, the selection process decides the vectors that will succeed. For each target vector $X_{i,g}$, a mutant vector is generated via the Equation 3:

$$V_{i,G} = X_{r_1^i,G} + F \cdot (X_{r_2^i,G} - X_{r_3^i,G}), \tag{3}$$

where $i = 1, \dots, NP$, r_1, r_2, r_3 are random numbers, $r_1 \neq r_2 \neq r_3 \neq i$, x is a decision vector, and F is an amplification factor ($[0 \ 1]$) that determines the differential variation of $(X_{r_2^i,G} - X_{r_3^i,G})$.

The parent vector information for the trial vector U is crossover with the mutated vector using Equation 4 and 5.

$$U_{i,G+1} = (U_{1i,G+1}, U_{2i,G+1}, \dots, U_{Di,G+1}), \tag{4}$$

and

$$U_{ji,G} \begin{cases} V_{ji,G+1} & \text{if } (rand_{i,j}[0,1] \leq Cr \text{ or } j = j_{rand}) \\ X_{ji,G} & \text{otherwise} \end{cases}, \quad (5)$$

where $j = \{1,2, \dots, D\}$, $Cr [0,1]$ is the crossover rate, the random number is $rand_{i,j} [0,1]$, and $j_{rand} (1,2, \dots, D)$ is randomly selected to ensure that $U_{ji,G}$ gets at least one component from $V_{i,G}$.

For the next generation, selection is the process of choosing a vector between $(U_{i,G+1})$ and $(X_{i,G})$. A vector with a higher fitness value is chosen via Equation 6.

$$X_{i,G+1} = \begin{cases} U_{i,G} & \text{if } f(U_{i,G}) < f(X_{i,G+1}) \\ X_{i,G} & \text{if } f(U_{i,G}) \geq f(X_{i,G+1}) \end{cases} \quad (6)$$

Resilient Backpropagation. The supervised learning algorithm relies heavily on the backpropagation algorithm, as the algorithm can assist the model to find the appropriate parameter value for the lowest training function, such as weight, w and bias, b . There are a lot of algorithms for backpropagation that can be used to adjust the weight and bias so that a stable model is achieved by the model. However, the deep learning model has a deep architecture that causes the training function to be more complicated compared to the shallow learning model and not all the available backpropagation model can tune the deep learning model. Since the SAE model is a deep learning family, it is crucial to select the best backpropagation algorithm. Therefore, in this study, a backpropagation algorithm called the resilient backpropagation algorithm was selected.

Resilient backpropagation was proposed by Riedmiller and Braun (1993). The concept of this method is to repeatedly analyze the chain rule to calculate the effect of weight and bias with respect to an error function in the machine-learning model architecture. Compared to other methods, this method uses separate weight updates. By considering the sign of the error gradient, the algorithm updates the weight of the network and the weight update is defined as Equation 7.

$$\Delta_{ij}(t) = \begin{cases} \eta^+ \Delta_{ij}(t-1), & \text{if } \frac{\delta E}{\delta w_{ij}}(t-1) \cdot \frac{\partial E}{\partial w_{ij}}(t) > 0 \\ \eta^- \Delta_{ij}(t-1), & \text{if } \frac{\delta E}{\delta w_{ij}}(t-1) \cdot \frac{\partial E}{\partial w_{ij}}(t) < 0 \\ \Delta w_{ij}(t-1), & \text{otherwise} \end{cases} \quad (7)$$

When the element of $\partial E/\partial w_{ij}$ maintains its sign from one iteration to the next consecutive iteration, the factor of η^+ helps increase the component Δ_{ij} . Meanwhile, when the partial derivative when the partial derivative $\partial E/\partial w_{ij}$ changes its sign from one iteration to the next consecutive iteration, the factor of η^- helps to minimize the variable Δ_{ij} . The η^+ value is 1.2 while the η^- value is 0.5 are set in this study. The weight will update based on Equation 8.

$$\Delta w_{ij}(t) = \begin{cases} -\Delta_{ij}, & \text{if } \frac{\delta E}{\delta w_{ij}} > 0 \\ +\Delta_{ij}, & \text{if } \frac{\delta E}{\delta w_{ij}} < 0 \\ 0, & \text{otherwise} \end{cases} \quad (8)$$

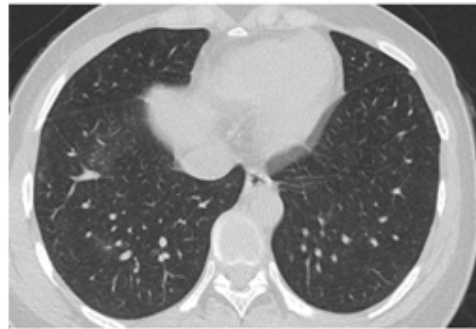
The details of the algorithm can be referred to the owner of this method (Riedmiller & Braun, 1993).

Data Collection and Preparation

The COVID-19 dataset from chest CT-scan and X-ray images were referred from X. Yang et al. (2020) and Ozturk et al. (2020), respectively. The details of the Chest CT and X-ray examination on the data collection, imaging parameters and the imaging system have been thoroughly discussed by W. Yang et al. (2020) and Ozturk et al. (2020). For the analysis of the proposed model, the CT-scan and chest X-ray dataset were obtained from open access sources in which the utility of the dataset was evaluated and confirmed by a senior radiologist. The open-source dataset can be obtained from He et al. (2020) and Cohen et al. (2020). The image example has been shown in Figure 3 and 4. In this study, there is no image enhancement has been done on the image as the original image is directly used to study the performance of the proposed model on the original image. However, there are only a simple image pre-processing has been done by resizing the image into 56x56 pixels. It is important to note that the size of the image affect the deep learning model processing because a large size of an image takes a long training time (Verstraete et al., 2017). Also, the data has been normalised to increase the efficiency of the proposed model and prevent the network from overfitting (Srivastava et al., 2014).



a) Non-COVID-19



b) COVID-19

Figure 3. CT-Scan of chest images

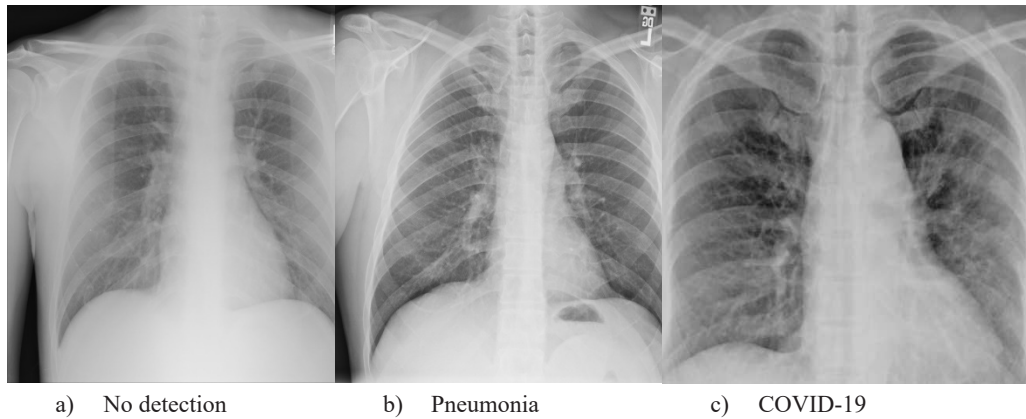


Figure 4. X-ray of chest images

Tables 1 and 2 below show data distribution for CT scan images and X-ray images, respectively. The training data will be used to generalise the sparse autoencoder parameters (weight and bias) that will be optimised using a back-propagation algorithm. The model is validated using the validation data of data to calculate the sparse autoencoder model's accuracy on the selected hyperparameter value. If the model does not achieve acceptable accuracy, the hyperparameter will be changed using the differential evolution algorithm. The process will continue until the model reaches the 0% training accuracy on the validation data. Then, the model will be evaluated using test dataset.

Table 1

Data distribution for CT scan images

Data	No finding	COVID-19
Train	100	100
Valid	50	50
Test	50	50
Total	200	200

Table 2

Data distribution for X-ray images

Data	No finding	Pneumonia	COVID-19
Train	100	100	60
Valid	50	50	25
Test	50	50	40
Total	200	200	125

RESULTS AND DISCUSSION

The performance of the proposed model during the training process has been shown in Figures 5 and 6 on chest CT-Scan and X-ray images, respectively. The proposed model performed well on both datasets as the performance achieved 0% training error means that the model has already generalized the information from the training and validation image. Hence, the model is ready to be evaluated using the test dataset. It can be noticed that the model required different epochs number to reach the lowest training error. Then, the model is tested with test dataset and the result on the CT-scan and X-ray images have been tabulated in Tables 3 and 4, respectively. There are five types of the score are calculated to quantify the performance of the proposed model such as sensitivity, specificity, precision, accuracy, and F1-score. The definition and formula on each score can be referred to in (Tharwat, 2018). From Table 3, it can be noticed that the proposed model achieved around 81% to 86% for all scores. Hence, it shows that there is no bias toward one class on classification performance. The performance of the proposed model is satisfactory as several other research reaches more or less the same as the proposed model performance (Ying et al., 2020; Zheng et al., 2020).

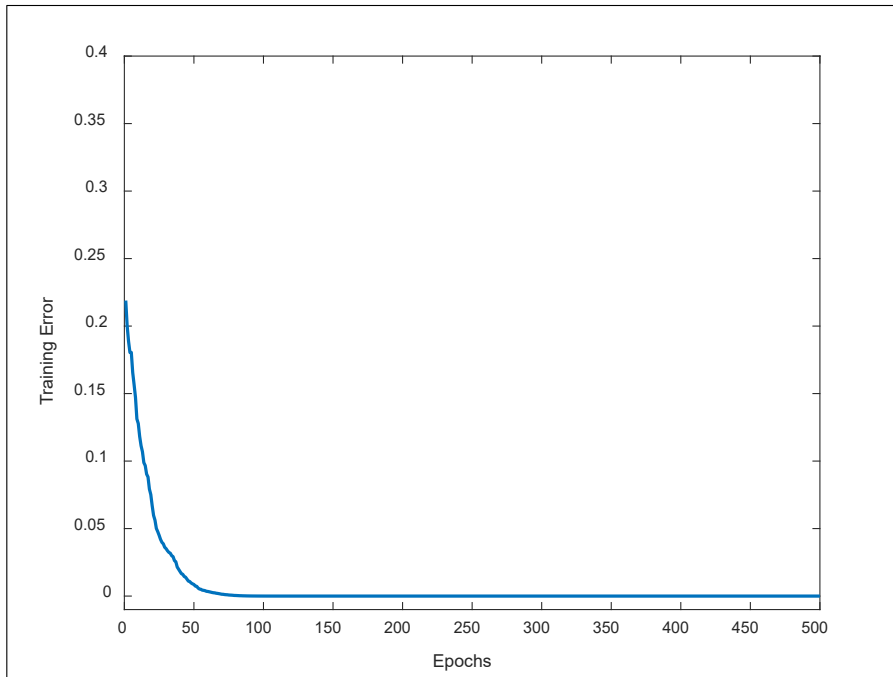


Figure 5. Training performance of the proposed model on CT-Scan images

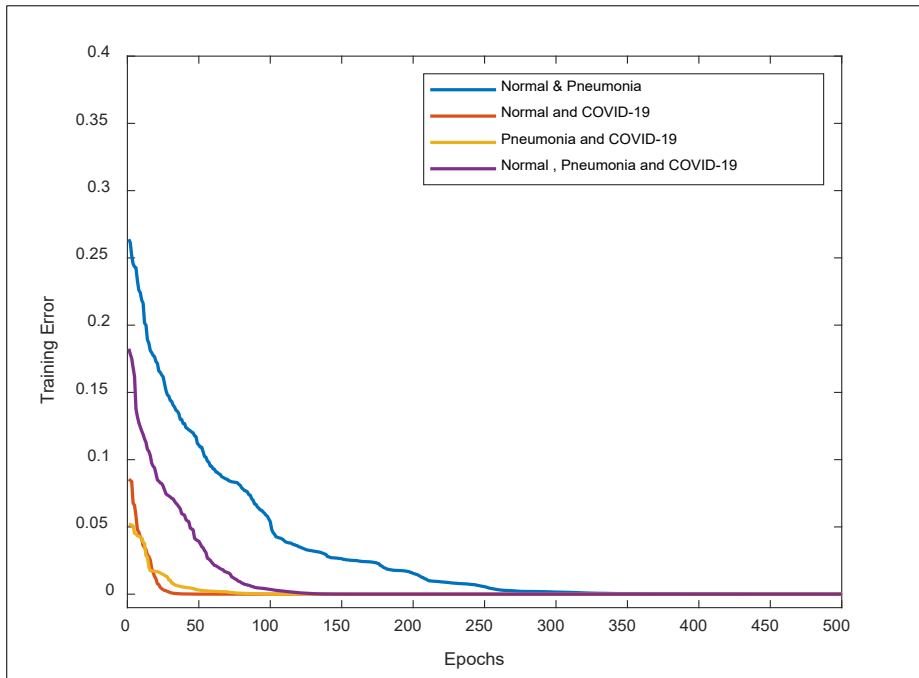


Figure 6. Training performance of the proposed model on X-ray images

Table 3

CT-Scan images result on the test dataset

Sensitivity	Specificity	Precision	F1-Score	Accuracy
81.13%	85.11%	86.00%	83.50%	83.00%

Table 4

X-ray images result on the test dataset

No.	Conditions	Sensitivity	Specificity	Precision	F1-Score	Overall Accuracy
1	Normal & COVID-19	95.6%	92.5%	94.0%	94.95%	94.4%
2	Pneumonia & COVID-19	96.08%	97.37%	98.0%	97.03%	96.6%
3	Normal & Pneumonia	81.13%	85.11%	86.0%	83.5%	83.0%
4	Normal	74.00%	91.01%	82.22%	77.90%	82.0%
	Pneumonia	80.00%	85.39%	75.47%	77.67%	
	COVID-19	94.87%	96.00%	90.24%	92.50%	

Besides, the proposed model has been tested with X-ray image dataset. The dataset has been distributed to four conditions as shown in Table 4. The proposed model achieved 92% to 95.6% for all scores on the first condition. Meanwhile, the model achieved 96 to 98% for all score on the second condition which is the highest performance over other conditions. From the result, it can be noticed that the proposed model can detect accurately the different chest X-ray images between pneumonia and COVID-19 patient. However, the performance of the proposed model dropped when tested with third and fourth conditions of the dataset. This is due to the incapability of the model to detect accurately the different chest X-ray images between normal and pneumonia patient. There is slightly different in the calculation of forth condition datasets as each class has its own scores value except the overall accuracy. From each score on each class, the performance of the proposed model can be observed in each class. From the result of forth condition dataset, the model suffers a difficulty to differentiate the normal and pneumonia patient. Throughout the analysis there is no major overfitting issue occur on the proposed model as there is no big difference in the training and testing performance of the model on both datasets.

The proposed model performance has been compared with the shallow learning model such as an artificial neural network (ANN) and support vector machine (SVM). Both models are the popular shallow models that are always been used in many applications like mechanical engineering, biomedical engineering, and medicine. Hence, both models have been trained and test with chest CT-scan and X-ray images. The diagnosis accuracy is used to compare the performance of shallow leaning model with proposed model method. Bayesian optimisation is used to optimise the hyperparameter of the SVM model. On the CT-scan images as shown in Table 5, the ANN and SVM models, the models achieved 73.3% and 75.5%, respectively. Meanwhile, on the X-ray images as shown in Table 6, the ANN model can achieve more than 80% accuracy on datasets 2 (Pneumonia and COVID-19 dataset). However, the ANN model achieved below 80% for the rest of the datasets. Meanwhile, optimised SVM model achieved more than 80% accuracy on datasets 1 (Normal & COVID-19) and 2 (Pneumonia & COVID-19). However, the optimised SVM model achieved below 80% on datasets 3 (Normal & Pneumonia) and 4 (Normal, Pneumonia & COVID-19). In comparison, the proposed model performance on both images' dataset is more accurate compared to the shallow learning model that shows the capability of deep learning over shallow learning model on image classification analysis.

The proposed model performance is compared with other similar studies as published in public journal that use the convolutional neural network model (Hemdan et al., 2020; Purohit et al., 2020; Wang et al., 2020). Convolutional neural network (CNN) is the common method used in many applications especially for image classification analysis. The comparative study between the proposed model and CNN model is shown in Tables 7 and 8 for CT scan and X-ray images, respectively. On the X-ray images, the comparative study

used normal and COVID-19 conditions. The proposed model performed better compared VGG16 and VGG19 as shown in Table 7 and 8. VGG16 is the CNN model that was used to win the competition of ImageNet in 2014. While VGG19 is the improve version of CNN that has a better performance compared to VGG16 but VGG19. CNN model is known to have more hyperparameter that need to be set compared to the proposed model. This is one of the factors the CNN model is difficult to handle. Meanwhile, another improvement has been conducted by Wang et al. (2020) as the authors tend to use deeper architecture of CNN network on CT scan images. With deeper architecture the number of hyperparameter will increase that cause the network is difficult to handle. However, the result produced by the deeper CNN model is lower compared to the proposed model. According to the result, the proposed model performed significantly better since it uses simple architecture, as mentioned in the preceding section, instead of complicated signal and image processing and deeper learning architecture.

Table 5
CT-Scan images result on the test dataset

Shallow learning	Accuracy
ANN	73.3%
Optimize SVM	75.5%

Table 6
X-ray images result on the test dataset

Datasets	Class distribution	ANN	Optimize SVM
1	Normal & COVID-19	75.0%	81.4%
2	Pneumonia & COVID-19	83.9%	85.1%
3	Normal & Pneumonia	61.4%	75.5%
4	Normal, Pneumonia & COVID-19	62.6%	73.2%

Table 7
Comparative analysis with a similar study on X-ray images

Model	Sensitivity %	Specificity %	Precision %	F1-Score %	Overall Accuracy %
Proposed model	95.6	92.5	94.0	94.95	94.4
Purohit et al. (2020) VGG16	81.52	99.25	99.0	89.0	90.4

Table 7 (Continued)

Model	Sensitivity %	Specificity %	Precision %	F1-Score %	Overall Accuracy %
Hemdan et al. (2020) VGG19	90.0	-	91.5	90.0	90.0

Table 8

Comparative analysis with a similar study on CT scan images

Model	Sensitivity %	Specificity %	Precision %	F1-Score %	Accuracy %
Proposed model	81.13	85.11	86.0	83.5	83.0
Purohit et al. (2020) VGG16	93.62	63.76	72.0	88.0	78.7
Wang et al. (2020) CNN Dens-net	93.0	-	76.0	83.0	82.0

CONCLUSION

This paper has presented an improved SSAE to detect and diagnose COVID-19 on chest CT scan images and chest X-ray images. The proposed model did not require manual feature extraction and it can achieve satisfactory performance on COVID-19 dataset without image enhancement method on the image. This analysis proved that the proposed model can be used on other applications not only on machinery diagnosis. The selection of hyperparameter on deep learning is crucial as it may provide a good diagnosis result. Future research may implement the image enhancement on the dataset with a large size of the dataset to increase the classification accuracy.

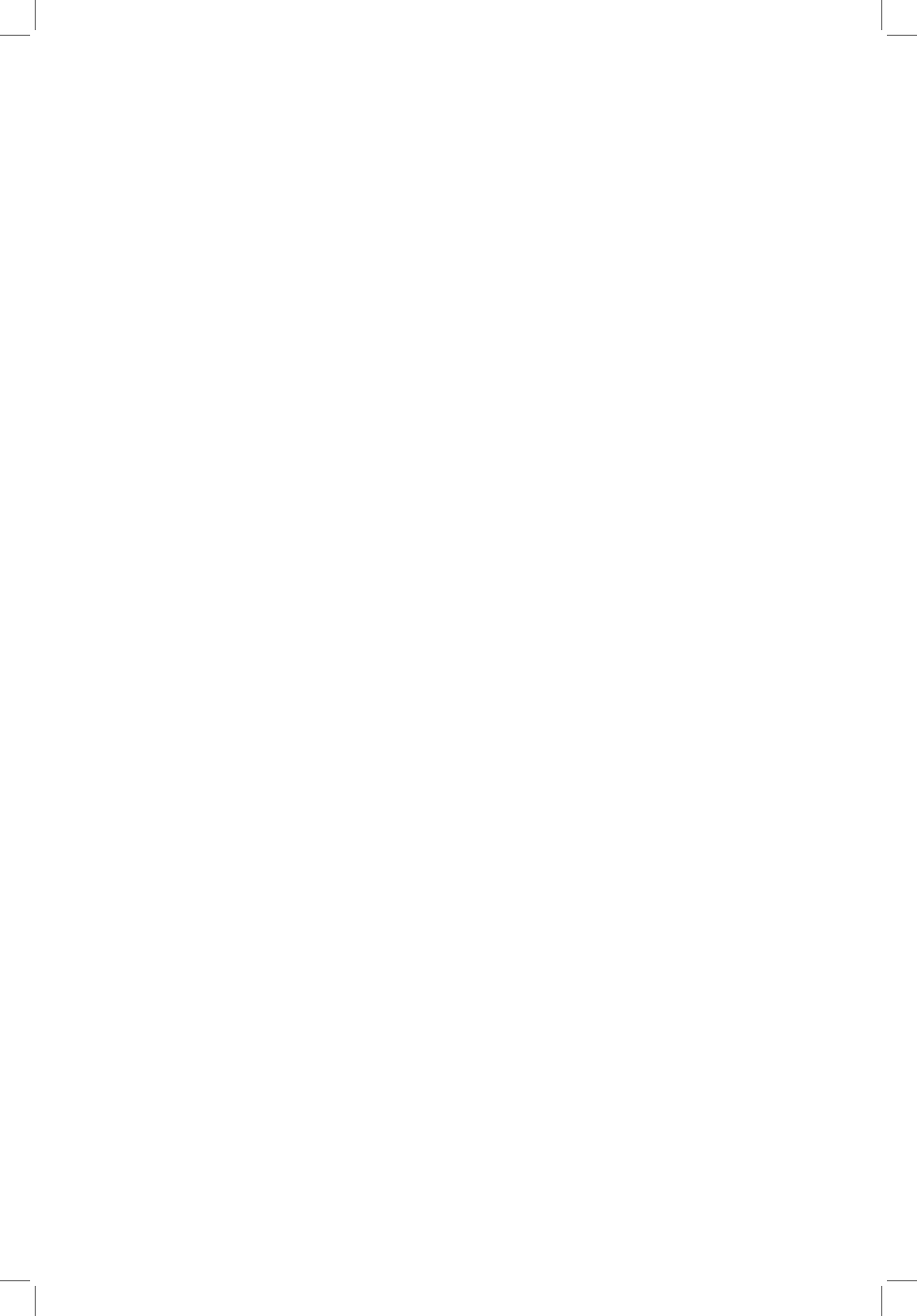
ACKNOWLEDGMENT

The authors would like to extend their greatest gratitude to the Institute of Noise and Vibration UTM for funding the current study under the Higher Institution Centre of Excellence (HICoE) Grant Scheme (R.K130000.7843.4J227 and R.J130000.7824.4J234). Additional funding for this research came from the UTM Research University Grant (Q.K130000.2543.11H36) and the Fundamental Research Grant Scheme (R.K130000.7840.4F653) from The Ministry of Higher Education, Malaysia.

REFERENCES

- Apostolopoulos, I. D., & Mpesiana, T. A. (2020). Covid-19: Automatic detection from X-ray images utilizing transfer learning with convolutional neural networks. *Physical and Engineering Sciences in Medicine*, 43(2), 635-640. <https://doi.org/10.1007/s13246-020-00865-4>
- Bustin, S. A., & Nolan, T. (2020). RT-qPCR testing of SARS-CoV-2: A primer. *International Journal of Molecular Sciences*, 21(8), Article 3004. <https://doi.org/10.3390/ijms21083004>
- Cohen, J. P., Morrison, P., Dao, L., Roth, K., Duong, T. Q., & Ghassemi, M. (2020). *GitHub - iee8023/covid-chestxray-dataset: We are building an open database of COVID-19 cases with chest X-ray or CT images*. Retrieved March 22, 2021, from <https://github.com/iee8023/COVID-chestxray-dataset>
- He, X., Yang, X., Zhang, S., Zhao, J., Zhnag, Y., Xing, E., & Xie, P. (2020). *Sample-efficient deep learning for COVID-19 diagnosis based on CT scans*. Retrieved March 22, 2021, from <https://github.com/UCSD-AI4H/COVID-CT>
- Hemdan, E. E. D., Shouman, M. A., & Karar, M. E. (2020). COVIDX-Net: A framework of deep learning classifiers to diagnose COVID-19 in X-ray images. *ArXiv*, 1-14.
- Huang, C., Wang, Y., Li, X., Ren, L., Zhao, J., Hu, Y., Zhang, L., Fan, G., Xu, J., Gu, X., Cheng, Z., Yu, T., Xia, J., Wei, Y., Wu, W., Xie, X., Yin, W., Li, H., Liu, M., ... & Cao, B. (2020). Clinical features of patients infected with 2019 novel coronavirus in Wuhan, China. *The Lancet*, 395(10223), 497-506. [https://doi.org/10.1016/S0140-6736\(20\)30183-5](https://doi.org/10.1016/S0140-6736(20)30183-5)
- Luo, L., Xiong, Y., Liu, Y., & Sun, X. (2019). Adaptive gradient methods with dynamic bound of learning rate. *ArXiv:1902.09843, 2018*, 1-19.
- Ozturk, T., Talo, M., Yildirim, E. A., Baloglu, U. B., Yildirim, O., & Acharya, U. R. (2020). Automated detection of COVID-19 cases using deep neural networks with X-ray images. *Computers in Biology and Medicine*, 121, Article 103792. <https://doi.org/10.1016/j.compbiomed.2020.103792>
- Purohit, K., Kesarwani, A., Kisku, D. R., & Dalui, M. (2020). COVID-19 detection on chest X-Ray and CT scan images using multi-image augmented deep learning model. *BioRxiv*, 15-22. <https://doi.org/10.1101/2020.07.15.205567>
- Riedmiller, M., & Braun, H. (1993). A direct adaptive method for faster backpropagation learning: The RPROP algorithm. In *IEEE international conference on neural networks* (pp. 586-591). IEEE Conference Publication. <https://doi.org/10.1109/ICNN.1993.298623>
- Salehi, S., Abedi, A., Balakrishnan, S., & Gholamrezanezhad, A. (2020). Coronavirus disease 2019 (COVID-19): A systematic review of imaging findings in 919 patients. *American Journal of Roentgenology*, 215(1), 87-93. <https://doi.org/10.2214/AJR.20.23034>
- Saufi, S. R., Ahmad, Z. A., Leong, M. S., & Lim, M. H. (2019). Challenges and opportunities of deep learning models for machinery fault detection and diagnosis: A review. *IEEE Access*, 7(1), 122644-122662. <https://doi.org/10.1109/ACCESS.2019.2938227>
- Srivastava, N., Hinton, G., Krizhevsky, A., Sutskever, I., & Salakhutdinov, R. (2014). Dropout: A simple way to prevent neural networks from overfitting. *Journal of Machine Learning Research*, 15, 1929-1958. <https://doi.org/10.1214/12-AOS1000>

- Tharwat, A. (2018). Classification assessment methods. *Applied Computing and Informatics*, 17(1), 168-192. <https://doi.org/10.1016/j.aci.2018.08.003>
- Verstraete, D., Ferrada, A., Droguett, E. L., Meruane, V., & Modarres, M. (2017). Deep learning enabled fault diagnosis using time-frequency image analysis of rolling element bearings. *Hindawi Shock and Vibration*, 2017, 1-29. <https://doi.org/10.1155/2017/5067651>
- Wahab, M. N. A., Nefti-Meziani, S., & Atyabi, A. (2015). A comprehensive review of swarm optimization algorithms. *PLoS ONE*, 10(5), 1-36. <https://doi.org/10.1371/journal.pone.0122827>
- Wang, S., Kang, B., Ma, J., Zeng, X., Xiao, M., Guo, J., Cai, M., Yang, J., Li, Y., Meng, X., & Xu, B. (2020). A deep learning algorithm using CT images to screen for Corona Virus Disease (COVID-19). *MedRxiv*, 1-23. <https://doi.org/https://doi.org/10.1101/2020.02.14.20023028>
- Wang, Y., Liu, M., Bao, Z., & Zhang, S. (2018). Stacked sparse autoencoder with PCA and SVM for data-based line trip fault diagnosis in power systems. *Neural Computing and Applications*, 5, 1-13. <https://doi.org/10.1007/s00521-018-3490-5>
- Ying, S., Zheng, S., Li, L., Zhang, X., Zhang, X., Huang, Z., Chen, J., Zhao, H., Wang, R., Chong, Y., Shen, J., Zha, Y., & Yang, Y. (2020). Deep learning enables accurate diagnosis of novel Coronavirus (COVID-19) with CT images. *MedRxiv*, 1-10. <https://doi.org/10.1101/2020.02.23.20026930>
- Yang, W., Sirajuddin, A., Zhang, X., Liu, G., Teng, Z., Zhao, S., & Lu, M. (2020). The role of imaging in 2019 novel coronavirus pneumonia (COVID-19). *European Radiology*, 30, 4874-4882. <https://doi.org/10.1007/s00330-020-06827-4>
- Yang, X., He, X., Zhao, J., Zhang, Y., Zhang, S., & Xie, P. (2020). COVID-CT-dataset: A CT scan dataset about COVID-19. *ArXiv Preprint ArXiv:2003.13865*, 1-14.
- Zheng, C., Deng, X., Fu, Q., Zhou, Q., Feng, J., Ma, H., Liu, W., & Wang, X. (2020). Deep learning-based detection for COVID-19 from chest CT using weak label. *MedRxiv*, 1-13. <https://doi.org/10.1101/2020.03.12.20027185>
- Zu, Z. Y., Jiang, M. D., Xu, P. P., Chen, W., Ni, Q. Q., Lu, G. M., & Zhang, L. J. (2020). Coronavirus disease 2019 (COVID-19): A perspective from China. *Radiology*, 296(2), E15-E25. <https://doi.org/10.1148/radiol.2020200490>



Short communication

Determination of Antioxidant Compounds, Proximate Compositions and Assessment of Free Radical Scavenging Activities of *Nypa Fruticans* Wurmb. Sap

Siti Fatimah Roqiah Yahaya^{1*}, Niza Samsuddin¹, Suhana Mamat¹, Rozita Hod², Nor Zamzila Abdullah^{3,4}, Nor Azlina A. Rahman⁵ and Siti Zaiton Mat So'Ad⁶

¹Department of Biomedical Sciences, Kulliyah of Allied Health Science, International Islamic University Malaysia, Bandar Indera Mahkota, 25200 Kuantan, Pahang, Malaysia

²Department of Community Health, Faculty of Medicine, UKM Medical Centre, Jln Yaakob Latif, Bandar Tun Razak, Cheras, 56000 Kuala Lumpur, Malaysia

³Department of Pathology and Laboratory Medicine, Kulliyah of Medicine, International Islamic University Malaysia, Bandar Indera Mahkota, 25200 Kuantan, Pahang, Malaysia

⁴Consultant Chemical Pathologist, Sultan Ahmad Shah Medical Centre @IIUM, Bandar Indera Mahkota, 25200 Kuantan, Pahang, Malaysia

⁵Department of Physical Rehabilitation Sciences, Kulliyah of Allied Health Science, International Islamic University Malaysia, Bandar Indera Mahkota, 25200 Kuantan, Pahang, Malaysia

⁶Department of Pharmaceutical Chemistry, Kulliyah of Pharmacy, International Islamic University Malaysia, Bandar Indera Mahkota, 25200 Kuantan, Pahang, Malaysia

ABSTRACT

Nipa palm sap (NPS) as source of medicine traditionally used to treat various diseases. This study identified good radical scavenging activity in NPS with the IC₅₀ value of 33.36 µg/mL using 2, 2-diphenyl-1-picrylhydrazyl (DPPH) assay. NPS comprises of moisture (72.44%), ash (1.04%), protein (7.04%), carbohydrate (19.48%), fat (0%), and energy level (106 kcal). Glucose (0.3%) and fructose (1.8%) were detected using high-performance liquid

chromatography. Maleic acid, cinnamic acid, chlorogenic acid, and kaempferol were the predominant compounds revealed by ultra-high-performance liquid chromatography. Overall, NPS has the potential antioxidants sources with significant health benefits and values for commercialisation.

Keywords: Antioxidant, DPPH, nipa palm sap, proximate analysis, UHPLC

ARTICLE INFO

Article history:

Received: 27 January 2021

Accepted: 24 May 2021

Published: 31 July 2021

DOI: <https://doi.org/10.47836/pjst.29.3.30>

E-mail addresses:

sitifatimahroqiah@gmail.com (Siti Fatimah Roqiah Yahaya)

niza_shamsuddin@iium.edu.my (Niza Samsuddin)

suhana@iium.edu.my (Suhana Mamat)

rozita.hod@ppukm.ukm.edu.my (Rozita Hod)

zamzila@iium.edu.my (Nor Zamzila Abdullah)

nazara@iium.edu.my (Nor Azlina A. Rahman)

dszaiton@iium.edu.my (Siti Zaiton Mat So'Ad)

* Corresponding author

INTRODUCTION

From prehistoric time, global population relies primarily on traditional medicine like plants and animals to alleviate various ailments (Ekor, 2014). This approach persisted in Asia and America Latin populations because of their historical facts, cultural evidence, and beliefs (Ekor, 2014). The use of natural antioxidants from natural plants have gained considerable scientific interests because of their natural origin and lower detrimental side effects (Lourenço et al., 2019).

There is also increased consumption of exogenous antioxidants by the public, for example, ascorbic acid (i.e., Vitamin C), tocopherol-net (i.e., Vitamin E), carotenoids and polyphenols that are present in fruits, vegetables, cereals, beverages, and other food products. This is due to the belief that these products could support the antioxidative defence system (Lourenço et al., 2019).

Nipa palm (*Nypa fruticans* Wurm.) is a palm species that can found at the coastlines and estuarine habitats distributed all over Malaysia. In Peninsular Malaysia, Kelantan is one of the states with broad coverage of nipa palm vegetation besides Perak, Selangor, and Terengganu (Hamdan et al., 2012). Hamdan et al. (2012) reported that nipa palm was grown and located in Kota Bharu and Tupat, Kelantan covering 204.575 ha of land area. The nipa palm contains the infructescence that can be tapped to yield abundant of sap called nipa palm sap (NPS) (Hafizi et al., 2018). Alternatively, NPS can be freshly consumed or fermented into wine (Phetrit et al., 2020).

Preliminary studies of NPS showed that it exhibits high phenolic and flavonoid content, as well as antioxidant activity (Hafizi et al., 2018; Phetrit et al., 2020; Sukairi et al., 2019). Based on the local's belief, NPS has the medicinal potential to treat fever, gout, kidney stone and metabolic syndrome such as diabetes and hypertension (Mohd et al., 2011; Sukairi et al., 2019). This drink is well-known among the elderly citizens of some countries such as Malaysia, Philippines, Indonesia, Thailand, Sri Lanka, and India, where they believed NPS could be as an energy booster, remedy for fever, helps in the digestion process and as a medication for certain chronic diseases (Tamunaidu et al., 2013, Yusoff et al., 2015; Hafizi et al., 2018; Phetrit et al., 2020). However, these postulations required further investigations.

Although NPS have shown good antioxidant activities with high concentration of phenolic and flavonoid contents, the study that reports on individual phenolic and flavonoid compounds in NPS remains unnoticed. The information of antioxidants compounds derived from NPS is essential to determine the quality of the sap and to explore the ability of its antioxidants compound to produce the therapeutic effect that leads to health improvements of local consumers in Malaysia. Hence, the present study aims to determine the antioxidant activity, proximate compositions, and individual antioxidant compounds of NPS produced in Kg Pulau Gajah, Kota Bharu, Kelantan.

MATERIALS AND METHODS

Chemicals

All chemicals used in this study were purchased from the Sigma–Aldrich (Chemie, Steinheim, Germany), Merck (Darmstadt, Germany) and Nacalai-Tesque (Kyoto, Japan) manufacturers. All reagents were used as follows: 2,2-diphenyl-1-picrylhydrazyl (DPPH), ascorbic acid (99.93%, analytical grade), kaempferol ($\geq 97\%$, HPLC grade), gallic acid (98%, analytical grade), coumaric acid ($\geq 95\%$, HPLC grade), quercetin ($\geq 95\%$, HPLC grade), caffeic acid (99%, HPLC grade), cinnamic acid (99%, analytical grade), chlorogenic acid ($\geq 95\%$, HPLC grade), maleic acid (97%, analytical grade), protocatechuic acid ($\geq 98\%$, HPLC grade), vanillic acid ($\geq 95\%$, analytical grade), rutin ($\geq 9\%$, HPLC grade), methanol (99%), distilled water, formic acid (85%, analytical grade), and acetonitrile (99%, HPLC grade).

Sample Collection

Fresh samples of NPS were obtained from Kampung Pulau Gajah, Kelantan, Malaysia in April 2019. The nipa palm with matured fruit was randomly selected to yield sap twice per day. The long stalks containing infructescence were cut and tapped carefully to yield the sap, with a sterile plastic bag being attached to the end of the stalk for sap collection.

After the collection process of approximately 5-6 hrs, the collected sap was immediately filtered, stored into 500 mL Schott bottle, and packed in boxes with ice. All samples were immediately transported back to the laboratory and kept at -20°C for a few days before sample preparation. The species identity of the sample was verified by Dr. Shamsul Khamis, a plant biologist from Universiti Kebangsaan Malaysia (UKM). A Voucher Specimen of the sample (PIIUM 0314) was stored at the Herbarium (UKMB) Faculty of Science and Technology.

Sample Preparation

The collected sap was transferred into a labelled 500 mL round conical flask and incubated in -80°C freezer (SANYO ultra-low temperature freezer, model MDF-U53V) for deep freezing and then being transferred to freeze-dryer (CHRIST Christ, Beta 2-8 LDplus). The samples were freeze-dried for one week. The freeze-dried yield was 105.3 g/500mL of sap. The dried samples were then kept at 4°C for further experiments. The sample preparation steps were conducted carefully to preserve the amounts and activity of antioxidant compounds in the samples.

Determination of Antioxidant Capacities

DPPH Radical Scavenging Activity. In this study, the 2,2-diphenyl-1-picrylhydrazyl assay was modified from Prasad et al. (2013) and Yusoff et al. (2015) methods using 96

wells microplates. Briefly, 100 μL of DPPH (i.e., 0.5mM dissolve in methanol) was mixed with different sample concentrations (i.e., 1.95–62.5 $\mu\text{g}/\text{mL}$) in a 96-well plate. For the blank assay, DPPH solution was added with 100 μL of methanol. The prepared plate was immediately inserted into a spectrophotometer (SpectraMax Plus 384). The absorbance value at 517 nm was noted after 30 min incubation in the dark at room temperature. The ascorbic acid dissolved in distilled water was used as the standard. The change of colour of the DPPH solution from violet to pale yellow at $\lambda=517$ nm reveals the DPPH radical-scavenging activity. The measurement was conducted in triplicates, and the percentage of DPPH inhibition (%) was obtained using the following Equation 1.

$$(\% \text{ DPPH inhibition}) = \left[\frac{A_{ctr} - A_s}{A_{ctr}} \right] \times 100 \quad [1]$$

Where A_{ctr} and A_s denote the absorbance of the control (blank) and sample or standard, respectively. IC_{50} values obtained from the graphical plot of percentage inhibition against concentration were used to determine the free radical scavenging activity of the sample.

Proximate Analysis

The proximate composition of NPS includes moisture, ash, energy, protein, carbohydrate, and fat contents were measured using the standard protocols set by the Association of Official Analytical Chemists (2000). The Kjeldahl method was used to determine the protein content of the sample. Briefly, the percentage of nitrogen (% Nitrogen) was multiplied with the factor of 6.25 to obtain the percentage of protein (% Protein) in the samples. Total moisture in the sample was determined using oven drying method at 100°C for 3 hrs until the constant weight was obtained and ash content in the sample was determined by heating in the furnace at 550°C to constant mass. Fat was determined by Soxhlet extraction with petroleum ether as a solvent. The carbohydrate content (%) and energy value (kcal) were determined by calculation as follows, respectively.

$$\text{Total Carbohydrate (\%)} = [100 - \% \text{ Moisture} - \% \text{ Protein} - \% \text{ Fat} - \% \text{ Ash}]$$

$$\text{Total energy} = (\% \text{ Protein} \times 4) + (\% \text{ Fat} \times 9) + (\% \text{ Carbohydrate} \times 4)$$

Determination of Sugar Profiles

The sugar profile was determined according to the method of Association of Official Analytical Chemists (2000). Jasco high-performance liquid chromatography (HPLC) was used with a carbohydrate column (Prevail™ Carbohydrate ES, 250 x 4.6 mm, 5 μm size)

and an evaporative light scattering detector (ELSD). The working temperature was fixed at 35°C. The acetonitrile solution and deionised H₂O (83:17) were used as the mobile phase, with a flow rate of 1.0-1.3 mL/min and injection volume ranging from 10-20 µL. The total run time was 10 min. Before HPLC analysis, the solutions were filtered using a 0.45 µm syringe filter (nylon) to eliminate particulates.

The sugar standard consisting of D-glucose, D-fructose, sucrose, and maltose were diluted in acetonitrile and deionised H₂O (1:1). The identification of sugar compounds was performed by comparing retention times with the standard. All the detection of samples and standards repeated in triplicate. The concentration of the sugar compounds, expressed in gram per 100 mL, was calculated by comparing their peak areas to a calibrated standard curve.

Identification and Quantification of Phenolic Compounds Using Ultra-High-Performance Liquid Chromatography (UHPLC-MS/MS)

The chromatographic separation was performed using Agilent 1100 series HPLC system together with Sciex 3200 hybrid trap triple quad tandem mass spectrometer to identify phenolic compounds of NPS. The method used was conducted according to Kong et al. (2012) with a slight modification. Phenolic compounds were chromatographically separated using a column Phenomenex Synergy RP C18, 100A (100 mm x 3 µm x 2.0 mm) maintained at 40 °C. Twenty microliters of the sample were injected into the system and ran using a specific elution program. Briefly, 0.1 (% v/v) formic acid with water was used for the mobile phase A while 0.1 (% v/v) formic acid with acetonitrile was used for the mobile phase B. The flow rate was maintained at 0.6 mL/min. The mobile phase composition was modified following gradient solvent system: 0 min, 1% B; 0.5 min, 1% B; 16.00 min, 35% B; 18.00 min, 100% B; 20.00 min, 1% B. The total runtime was 54.5 min.

The standards used were kaempferol, gallic acid, coumaric acid, quercetin, caffeic acid, cinnamic acid, chlorogenic acid, and maleic acid. Each of the standard (0.01-10 ppm) and the sample were filtered through a 0.45 µm pore size membrane filter before injecting with the aliquots (20 µL).

The phenolic compounds were identified by comparing the retention times with available standards, which is based on the bases of their peak areas and expressed in part per million (ppm). The analysis was carried out in triplicate determinations.

Statistical Analysis

The data were presented as mean±SD of three replicate and analysed by using Microsoft Excel 2016.

RESULTS

Antioxidant Capacities

DPPH Radical Scavenging Activity. The DPPH radical scavenging activities obtained from the antioxidant activities of the NPS, and ascorbic acid are shown in Table 1, which corresponded to the three analytical replicates. DPPH radical scavenging activity of NPS and ascorbic acid increased with the increase in the concentration (Table 1). The IC₅₀ value of NPS was 33.36±0.96 µg/mL. However, ascorbic acid showed the highest antioxidant activity with an IC₅₀ value of 21.29±0.74 µg/mL.

Table 1
Percentage of DPPH radical scavenging activity at different concentrations of Nipa palm sap

Concentration of sample (µg/mL)	Percentage of inhibition (%)		IC ₅₀ (µg/mL)	
	Nipa palm sap*	Ascorbic acid*	Nipa palm sap*	Ascorbic acid*
1.95	21.99±2.82	43.71±1.45	-	-
3.9	24.5±3.57	45.01±0.54	-	-
7.81	27.76±2.57	47.85±0.11	-	-
15.63	40.41±0.48	51.43±1.62	-	21.29±0.74
31.25	50.87±0.67	52.39±1.41	-	-
62.5	60.01±0.45	62.03±2.30	33.36±0.96	-

Note. All values are expressed as mean ± SD of triplicate measurement.

Proximate Composition and Sugar Type

Proximate compositions of NPS are shown in Table 2. The compositional analysis of NPS indicated the contents of moisture, ash, protein, carbohydrate, and fat as 72.44%, 1.04%, 7.04%, 19.48%, and 0%, respectively, with an energy value of 106 kcal (Table 2). The type and concentration of sugar in NPS are also presented in (Table 2). The sugar components of NPS consisted of glucose (0.3 g/100mL) and fructose (1.8 g/100mL). The total concentration of sugar in nipa palm sap was 2.1 g/100mL.

Table 2
Proximate compositions and sugar profile of nipa palm sap expressed in g/100mL

Composition	Sap
Moisture	72.44±0.005
Ash	1.04±0.001
Energy (kcal)	106±0.094
Protein	7.04±0.001
Carbohydrate	19.48±0.024
Fat	0.00±0.00
Total Sugar	2.1±0.000
Glucose	0.3±0.000
Fructose	1.8±0.000
Sucrose	ND
Maltose	ND

Note. ND = non-detectable. Values are expressed as mean ± SD from three determinations.

Identification and Quantification of Phenolic Compounds

There are several phenolic and flavonoid compounds such as kaempferol, quercetin, gallic acid, cinnamic acid, caffeic acid, coumaric acid, maleic acid and chlorogenic acid that can

Table 3
Phenolic and flavonoids compounds of nipa palm sap

Compounds	Retention time (min)	[M-H-]/ Fragment (m/z)	Nipa palm sap (ppm)
Kaempferol	4.25	285/93	0.0407±0.0011
Quercetin	4.11	301/151	0.0251±0.0041
Gallic Acid	0.58	169/125.1	0.0093±0.0012
Cinnamic acid	1.64	147/103	0.0741±0.0029
Caffeic acid	1.74	179/135	0.0169±0.0008
Coumaric acid	2.8	163/119.1	0.0250±0.0026
Maleic acid	0.56	115/71	0.0745±0.0096
Chlorogenic acid	1.55	353/191	0.0494±0.0001
Protocatechuic acid	-	-	ND
Vanillic acid	-	-	ND
Rutin	-	-	ND

Note. ND = Not detected

be found in NPS. The maleic acid, cinnamic acid, and chlorogenic acid were identified to be the major compounds present in NPS. Among the identified phenolic compounds, the content of maleic acid was the highest in NPS (0.0745±0.0096 ppm) while the lowest content was gallic acid (0.0093±0.0012 ppm) (Table 3). Following the phenolic compounds in NPS, cinnamic acid was identified as the second most abundant with 0.0741±0.0029 ppm, followed by chlorogenic acid (0.0494±0.0001 ppm) and kaempferol (0.0407±0.0011 ppm). The coumaric acid, quercetin and caffeic acid were detected in a minor amount (<0.03 ppm).

DISCUSSION

The moisture content value of NPS was 72.44% indicated that the NPS might has a shorter life span due to the growth of microorganisms that degrade the constituents and compounds (Olalude et al., 2015). Phetrit et al. (2020) reported that the NPS cultivated in southern parts of Thailand contained approximately 77.69% moisture, 95.92% of total sugar (dw), 0.49% protein (dw), and 3.32% ash (dw). In contrast to the present study, the NPS collected from eastern parts of Malaysia had lower moisture (72.44%) and sugar contents (10.1% dw) but had higher protein (33.43% dw) and ash contents (4.95% dw). These discrepancies of the various chemical constituents may be related to harvest date, time, location, and year-to-year growing period (Sharp et al., 2014). Recent study conducted by Cavender et al. (2019) reported that harvested period had a greatly effect to influence the variations of sugar contents.

The amount of protein content in NPS at 7.04% indicated that it could be used as a protein supplement for muscle development and maintaining human health (Wakili et al.,

2015). Likewise, the fat content was 0% and indicated that the NPS is a food source with a low cholesterol level (Olalude et al., 2015). Furthermore, the ash content was 1.04% and indicated that the NPS contains low mineral composition (Wakili et al., 2015). Besides that, the NPS can be classified as carbohydrate-rich juice due to its high carbohydrate content of 19.48%. The high carbohydrate contents of NPS indicated that it can be used as a good energy source for the body (Olalude et al., 2015) and is suitable to be processed as raw materials for the juice production.

Our findings from the standard antioxidant assay using the DPPH molecules showed that the NPS exhibited good antioxidant activity with the value of IC_{50} 33.36 μ g/mL, which is higher than those studies reported by Hafizi et al. (2018) and Sukairi et al. (2019). The antioxidant activity of the sap reported in this study was also higher than nipa palm of different plant structures/products, such as nipa palm fruits and nipa palm vinegar with the IC_{50} values of 7.78 mg/L and 36 μ g/mL, respectively (Prasad et al., 2013; Yusoff et al., 2015). According to Sowndhararajan and Kang (2013), a lower the IC_{50} value indicates the higher antioxidant activity.

Further investigation for this study was focused on the bioactive compounds present in NPS to understand the physiological functions in giving therapeutics effects due to the antioxidant potency. Based on the data presented in Table 3, it can be concluded that our results were corroborated with Prasad et al. (2013) that reported chlorogenic acid and kaempferol as among the major compounds found in the nipa palm fruit cultivated in the north part of Malaysia. In addition, cinnamic acid, quercetin, gallic acid were also detected in nipa palm fruit.

However, Prasad et al. (2013) also reported that the nipa palm fruits comprised protocatechuic acid and rutin. In contrast, the protocatechuic acid and rutin compounds were not detected in the NPS extract in this study. Similarly, another study conducted by Pherit et al. (2020) has detected the presence of vanillic acid but not the rutin compound. In comparison with this study, neither of these two compounds were detected. Based on Ahmed et al. (2015), these contradictory results for phenolics and flavonoids might be due to the use of different extraction solvents as well as the distribution of both compounds varied and not consistent among different plant samples.

Previous studies reported that NPS have antidiabetic effects by inhibiting the α -amylase and α -glucosidase activities, the two key enzymes linked to type-2 diabetes (Hafizi et al., 2018; Phetrit et al., 2020). Consistent with the literature, this research has discovered a high amount of phenolic compounds and flavonoids that may contribute to the biological and medicinal properties of the NPS. Several animal experiments and epidemiological studies have demonstrated that chlorogenic acid and kaempferol exerted antidiabetic activity by delaying carbohydrate digestion and glucose absorption in rats and may have antihypertensive effects in human (Al-Numair et al., 2015; Zhao et al., 2012).

In a biological system, the phenolic and flavonoid compounds act as free radical-trapping agents with antioxidant, antimicrobial and antifungal activities (Lourenço et al., 2019). *In vivo* studies indicated that phytonutrients such as chlorogenic acid and kaempferol might be vital in protecting the biological systems from oxidative stress (Al-Numair et al., 2015; Zhao et al., 2012). Therefore, the beneficial effects of bioactive compounds present in the NPS may possess antioxidant activity gives protective elements from chronic diseases.

The NPS consumption has been attributed to the ability to promote good health and provide some degree of protection towards chronic diseases due to different bioactive compounds. The findings of this study will lead to the following research, which is a community trial study to investigate the potential of NPS as a health supplement in improving health status. Thus, these data play a vital role and will be part of the larger study in future that could be commercialised as a healthy drink.

CONCLUSION

In conclusion, the NPS showed a good antioxidant activity with a recorded IC_{50} value of 33.36 $\mu\text{g/mL}$. The proximate compositions of NPS indicated that moisture, ash, protein, carbohydrate, fat, and energy were presented at 72.44%, 1.04%, 7.04%, 19.48%, 0%, and 106 kcal, respectively. In addition, the NPS comprised of two types of sugars, which is fructose (0.3g/100mL) and sucrose (1.8g/100mL). Besides that, maleic acid, cinnamic acid, chlorogenic acid and kaempferol were significant antioxidant compounds present in the NPS. It can be postulated that the antioxidant compounds found in the NPS can combat the free radicals in our body system and have great potential to be commercialised as a healthy drink with scientific evidence and validation.

ACKNOWLEDGEMENTS

The authors acknowledge the financial assistance from the Ministry of Higher Education, Malaysia in providing Fundamental Research Grant Scheme (FRGS 152130454) to support this research study.

REFERENCES

- Ahmed, I. A., Mikail, M. A., Ibrahim, M., Hazali, N., Rasad, M. S. B. A., Ghani, R. A., Wahab, R. A., Arief, S. J., & Yahya, M. N. A. (2015). Antioxidant activity and phenolic profile of various morphological parts of underutilised *Baccaurea angulata* fruit. *Food Chemistry*, 172, 778-787. <https://doi.org/10.1016/j.foodchem.2014.09.122>
- Al-Numair, K. S., Chandramohan, G., Veeramani, C., & Alsaiif, M. A. (2015). Ameliorative effect of kaempferol, a flavonoid, on oxidative stress in streptozotocin-induced diabetic rats. *Redox Report*, 20(5), 198-209. <https://doi.org/10.1179/1351000214Y.0000000117>

- Association of Official Analytical Chemists (2000). *Official methods of analysis of AOAC international* (17th Ed.). AOAC International.
- Cavender, G., Liu, M., Fernandez-Salvador, J., Hobbs, D., Strik, B., Frei, B., & Zhao, Y. (2019). Effect of different commercial fertilizers, harvest date, and storage time on two organically grown blackberry cultivars: Physicochemical properties, antioxidant properties, and sugar profiles. *Journal of Food Quality*, 2019, 1-17. <https://doi.org/10.1155/2019/1390358>
- Ekor, M. (2014). The growing use of herbal medicines: Issues relating to adverse reactions and challenges in monitoring safety. *Frontiers in Pharmacology*, 4(10), 1-10. <https://doi.org/10.3389/fphar.2013.00177>
- Hafizi, S. A., Razip, A. M., Aliana, W. S., & Tarmizi, W. Y. (2018). Crystallisation and biological studies of *Nypa fruticans* Wurmb Sap. *Indonesian Journal of Pharmaceutical Science and Technology*, 1(1), 37-42. <https://doi.org/10.24198/ijpst.v1i1.16122>
- Hamdan, O., Aziz, H. K., Shamsudin, I., & Barizan, R. S. R. (2012). *Status of mangroves in Peninsular Malaysia*. Forest Research Institute Malaysia.
- Kong, K. W., Mat-Junit, S., Aminudin, N., Ismail, A., & Abdul-Aziz, A. (2012). Antioxidant activities and polyphenolics from the shoots of *Barringtonia racemosa* (L.) Spreng in a polar to a polar medium system. *Food Chemistry*, 134(1), 324-332. <https://doi.org/10.1016/j.foodchem.2012.02.150>
- Lourenço, S. C., Moldão-Martins, M., & Alves, V. D. (2019). Antioxidants of natural plant origins: From sources to food industry applications. *Molecules*, 24(22), Article 4132. <https://doi.org/10.3390/molecules24224132>
- Mohd, Z. M. S., Mohamed, R. O., & Mohd, W. S. (2011). Determination of hydrocyanic acid in Nipah fruit (*Nypa fruticans*). *Malaysian Journal of Analytical Sciences*, 15(2), 258-264.
- Olalude, C. B., Oyediji, F. O., & Adegboyega, A. M. (2015). Physicochemical analysis of *Daucus carota* (carrot) juice for possible industrial applications. *Journal of Applied Chemistry*, 8(8), 110-113. <https://doi.org/10.9790/5736-0882110113>
- Phetrit, R., Chaijan, M., Sorapukdee, S., & Panpipat, W. (2020). Characterisation of Nipa Palm's (*Nypa fruticans* Wurmb.) sap and syrup as functional food ingredients. *Sugar Tech*, 22(1), 191-201. <https://doi.org/10.1007/s12355-019-00756-3>
- Prasad, N., Yang, B., Kong, K. W., Khoo, H. E., Sun, J., Azlan, A., Ismail, A., & Romli, Z. B. (2013). Phytochemicals and antioxidant capacity from *Nypa fruticans* Wurmb. fruit. *Evidence-Based Complementary and Alternative Medicine*, 2013, 1-9. <https://doi.org/10.1155/2013/154606>
- Sharp, D. C., Townsend, M. S., Qian, Y., & Shellhammer, T. H. (2014). Effect of harvest maturity on the chemical composition of Cascade and Willamette hops. *Journal of the American Society of Brewing Chemists*, 72(4), 231-238. <https://doi.org/10.1094/ASBCJ-2014-1002-01>
- Sowndhararajan, K., & Kang, S. C. (2013). Free radical scavenging activity from different extracts of leaves of *Bauhinia vahlii* Wight and Arn. *Saudi Journal of Biological Sciences*, 20(4), 319-325. <https://doi.org/10.1016/j.sjbs.2012.12.005>
- Sukairi, A. H., Sabri, W. M. A. W., Yusop, S. A. T. W., & Asaruddin, M. R. (2019). Phytochemical screening, antidiabetic, and antioxidant properties of *Nypa fruticans* Sap. *Materials Today: Proceedings*, 19, 1738-1744. <https://doi.org/10.1016/j.matpr.2019.11.211>

- Tamunaidu, P., Matsui, N., Okimori, Y., & Saka, S. (2013). Nipa (*Nypa fruticans*) sap as a potential feedstock for ethanol production. *Biomass and Bioenergy*, 52, 96-102. <https://doi.org/10.1016/j.biombioe.2013.03.005>
- Wakili, A., Abdullahi, M. B., & Madara, M. S. (2015). Proximate composition of five commonly used horticultural products in northern Nigeria. *International Journal of Current Microbiology and Applied Sciences*, 4(7), 924-928.
- Yusoff, N. A., Yam, M. F., Beh, H. K., Razak, K. N. A., Widyawati, T., Mahmud, R., Ahmad, M., & Asmawi, M. Z. (2015). Antidiabetic and antioxidant activities of *Nypa fruticans* Wurmb. vinegar sample from Malaysia. *Asian Pacific Journal of Tropical Medicine*, 8, 595-605. <https://doi.org/10.1016/j.apjtm.2015.07.015>
- Zhao, Y., Wang, J., Balleve, O., Luo, H., & Zhang, W. (2012). Antihypertensive effects and mechanisms of chlorogenic acids. *Hypertension Research*, 35(4), 370-374. <https://doi.org/10.1038/hr.2011.19>



Short communication

Comparative Analyses on Synthetic Membranes for Artificial Blood Feeding of *Aedes aegypti* using Digital Thermo Mosquito Blood Feeder (DITMOF)

Mohd Farihan Md Yatim^{1,2}, Aishah Hani Azil^{2*}, Nazarudin Safian³,
Ahmad Firdaus Mohd Salleh² and Mohd Khadri Shahar⁴

¹Centre for Communicable Diseases Research, Institute for Public Health, National Institutes of Health, Ministry of Health, Malaysia, Block B5 & B6, Jalan Setia Murni U13/52, Seksyen U13, Setia Alam, 40170, Shah Alam, Selangor, Malaysia

²Department of Parasitology and Medical Entomology, Faculty of Medicine, Universiti Kebangsaan Malaysia, Jalan Yaacob Latif, Bandar Tun Razak, 56000, Cheras, Kuala Lumpur, Malaysia

³Department of Community Health, Faculty of Medicine, Universiti Kebangsaan Malaysia, Jalan Yaacob Latif, Bandar Tun Razak, 56000, Cheras, Kuala Lumpur, Malaysia

⁴Institute for Medical Research, National Institutes of Health, Ministry of Health, Malaysia, Jalan Setia Murni U13/52, Seksyen U13, Setia Alam, 40170, Shah Alam, Selangor, Malaysia

ABSTRACT

The use of live animal to blood feeding mosquito colony is proven to be expensive and inconvenient. As an alternative, artificial feeding (AF) is used to rear mosquito colony. The use of synthetic membrane in AF provided a more convenient method as compared to natural membrane which require extensive preparation. In this study, three synthetic membranes were compared (Parafilm-M, Polytetrafluoroethylene tape or PTFE tape and collagen sausage casing) to blood feeding *Aedes aegypti*. The membranes were incorporated with our in-house developed device named as Digital Thermo Mosquito Blood Feeder

(DITMOF) to heat cattle blood for mosquito feeding. Results showed that PTFE tape recorded the highest blood feeding rate (95.00% ± 1.67%) with significant mean difference ($p < 0.001$) as compared to both Parafilm-M (72.00% ± 2.60%) and collagen sausage casing (71.50% ± 3.50%). However, there was no difference in term of fecundity for mosquito feed with all three membranes tested ($p=0.292$). In conclusion, PTFE tape

ARTICLE INFO

Article history:

Received: 07 February 2021

Accepted: 01 April 2021

Published: 31 July 2021

DOI: <https://doi.org/10.47836/pjst.29.3.31>

E-mail addresses:

farihanmy@moh.gov.my (Mohd Farihan Md Yatim)

aishah.azil@gmail.com (Aishah Hani Azil)

nazarudin@ppukm.ukm.edu.my (Nazarudin Safian)

afirwise@yahoo.com (Ahmad Firdaus Mohd Salleh)

khadri@moh.gov.my (Mohd Khadri Shahar)

* Corresponding author

should be considered as the preferred membrane to blood feeding *Ae. aegypti*. Furthermore, this artificial blood feeding system, DITMOF successfully feed *Ae. aegypti* conveniently and effectively, thus should be further tested to feed other mosquito species.

Keywords: *Aedes aegypti*, artificial feeding, blood feeding device, collagen sausage casing, DITMOF, Parafilm-M, PTFE tape, synthetic membrane

INTRODUCTION

Mosquito colony in the laboratory is essential for the study of vector-parasite interactions, insecticide susceptibility, mosquito behaviour, attractant or repellent cues and others. Generally, live animals such as rat, mice and guinea pig or even human volunteer are utilized to blood feed the mosquito colony (Ross et al., 2019). This technique known as direct feeding (DF) has certain advantages such as mosquito blood feeding response that is based on natural signals (WHO, 1995). However, rearing mosquito with this technique has been proven to be costly, inconvenient, and ethically questionable (Nasirian & Ladonni, 2006). Besides, the use of laboratory animals without any quality-assured care and treatment may affect the experimental results (Baumans et al., 1993). Systematic allergic reactions among these animals to mosquito saliva were also reported (Peng et al., 2004). As a result, an alternative mosquito blood feeding technique with no dependency on live animal is needed to overcome these problems.

Artificial blood feeding (AF) is a technique whereby mosquito can be fed using the combination of blood feeder device and animal blood or blood meal substitutes (BMS) for eggs development. The first AF device was developed in 1900's (Wade, 1976). In 2000's, many blood feeder devices invented had utilized or modified the water bath to heat the blood to achieve the range of human body temperature (Klun et al., 2005). Besides the water bath, several other different heating elements used were ceramic heating element (Deng et al., 2012), preheated glycerol (Costa-da-Silva et al., 2013), preheated metal plate (Gunathilaka et al., 2017) and preheated water (Siria et al., 2018). Commercialized blood feeder is also available such as Hemotek membrane feeding system (Hemotek, Accrington, United Kingdom). This system uses its own heating element and can feed up to six cages simultaneously. However, due to the demand in mosquito research and control, an advanced blood feeder equipped with modern technology such as microprocessor and sensor with features like automated temperature regulation, feeding time and effective membrane are needed to reduce the labour, operating costs and improve the efficacy of mosquito rearing (Romano et al., 2018).

The use of membrane in AF is to provide a skin-like surface for female mosquitoes to land before using its proboscis to penetrate the membrane for blood meal. Generally, two types of membranes used in AF are natural and synthetic membranes. In previous studies,

natural membranes such as mouse skin and quail skin were used (Novak et al., 1991). However, the disadvantages of these natural membranes are shorter shelf-life and require longer preparation as compared to easily available synthetic membrane. For synthetic membrane in AF, the Parafilm-M was the most widely used (Gunathilaka et al., 2017). Other popular synthetic membranes such as collagen sausage casing (Luo, 2014), latex condom (Novak et al., 1991) and recently, the polytetrafluoroethylene (PTFE) tape or plumber's tape (Siria et al., 2018) were also tested to explore the best effective membrane to feed mosquitoes. Nonetheless, only few studies that specifically compared blood feeding efficacy among these synthetic membranes (Deng et al., 2012; Luo, 2014).

For AF, the most common type of blood used is bovine or cattle (Finlayson et al., 2015). Gunathilaka et al. (2017) reported that there were no significant differences between *Ae. aegypti* mosquitoes fed with bovine and human blood in terms of fecundity, oviposition rate, and fertility. Another alternative blood source is rabbit blood. However, not all animal blood is suitable for mosquito blood feeding for instance sheep blood, whereby lower feeding rate was observed (Paris et al., 2018). Nonetheless, with the development of blood meal substitute (BMS) product such as SkitoSnack (Gonzales et al., 2018), the dependency on animal's blood could be reduced and AF efficiency would be improved. However, this BMS has not been used extensively as the commercial BMS is not yet available.

Previous studies by Deng et al. (2012) and Pothikasikorn et al. (2010) that compared AF with DF technique found that there was no significant difference in terms of fecundity, survival rate, hatchability, and adult mosquito development to development between these two-feeding techniques. Mosquito attraction to host cues and feeding ability on human were also not affected even after AF was performed for eight generations (Ross et al., 2019). Many other studies conducted also utilized mosquitoes that was reared artificially (Paris et al., 2018).

Recently, new mosquito control techniques such as Sterile Insect Technique (SIT) and Incompatible Insect Technique (IIT) that require the release of large number of mosquitoes to suppress the wild strain mosquito populations which could effectively carry dengue viruses (Zhang et al., 2017). These SIT or IIT mosquitoes are usually produced in the mosquito mass rearing facilities whereby millions of mosquitoes are reared. Therefore, these rearing facilities need modern and effective rearing equipment to rear the large-scale mosquitoes efficiently. Nevertheless, only a few new equipment that have been proposed for the use in the mosquito mass rearing facilities (Balestrino et al., 2012). This leads to our invention of DITMOF which is foreseen to have large potential to support such purpose. Nonetheless, this device requires the incorporation of suitable synthetic membrane for mosquito blood feeding. Thus, in this study, we aimed to compare the effectiveness of three types of synthetic membranes heated using DITMOF for blood feeding of *Ae. aegypti*. It is hoped that findings of this study will help to indicate the effective membrane for *Ae. aegypti* AF and overall improve the mosquito rearing efficiency in the laboratories.

MATERIALS AND METHODS

Ethics Statement

Neither humans nor laboratory animals were involved in this study. The procedure of using cattle blood to blood feeding *Ae. aegypti* colony was approved by Animal Ethic Committee, National University of Malaysia with UKMAEC approval number: PARST/PP/2017/AISHAH/22-NOV./885-NOV.-2017-MAC.-2019-AR-CAT2 on 22nd November 2017. The permission to perform this study was granted by Medical Research Committee, Faculty of Medicine, National University of Malaysia with project code number: FF-2017-492 on 21st December 2017.

Mosquitoes and Eggs

Laboratory strain of *Ae. aegypti* eggs batch F1071 was obtained from the Institute for Medical Research (IMR), Ministry of Health, Malaysia. *Aedes aegypti* eggs were soaked in dechlorinated water to induce hatching and larvae were fed with both TetraMin fish food and beef liver powder at 1:1 ratio. The rearing water was replaced daily to prevent any scum formation on the water surface. Pupae were transferred to rearing cage for adult emergence and adults were fed with 10% sugar solution with added 1% Vitamin B complex. Both female and male *Ae. aegypti* mosquitoes were left for 3-5 days in adult rearing cage at 1:1 ratio to ensure mosquito mating. The insectary temperature was maintained at $25 \pm 3^{\circ}\text{C}$, $80\% \pm 10\%$ humidity with natural photoperiod.

Type of Blood and DITMOF Device

Cattle blood used in this study was obtained from the Jasin Abattoir Complex, Department of Veterinary Services, Melaka, Malaysia. The blood was mixed with anticoagulant CPDA-1 at 1:7 ratio (anticoagulant: blood ratio) and was put inside a cooler box with ice packs for transportation before being stored in a chiller at 1 to 6°C . This chilled citrated cattle blood could be used for a maximum 35 days (Rudmann, 2005).

The in-house developed automated mosquito blood feeder, Digital Thermo Mosquito Blood Feeder, or DITMOF (patent pending) was used to heat the cattle blood to be used in the AF of *Ae. aegypti*. DITMOF device is consisted of a digital thermo controller (Shinko BCS1), K thermocouple sensor (VITAR standard thermocouple sensor PS-C-1M), stainless steel casing (128 mm x 128 mm x 198 mm), strip heater (VITAR LBAA26 240V/450W), power plug (UK 13A), blood feeder reservoir (55 mm diameter, 5 mm depth) and external digital thermometer.

Membrane Test and Blood Feeding Rate

Three types of membranes that were selected for evaluation were Parafilm-M (10.2 cm x 38.1 m, Bemis, USA), Polytetrafluoroethylene (PTFE) tape or plumber's tape (RS PRO

White, 12 mm × 12 m × 0.075 mm, Malaysia) and collagen sausage casing (32 mm, The SausageMaker Inc, Buffalo New York, USA). On the day of blood feeding, all three membranes were cut in 9 cm in length and subsequently, each membrane was attached on top of the blood feeder reservoir as shown in Figure 1. Excess membranes at the edge of the blood feeder reservoir were cut off. Stretched PTFE tape and Parafilm-M membranes were self-adhesive thus it can be attached directly on blood feeder reservoir on its own. To prevent Parafilm-M from snapping during blood feeding, it was carefully stretched uniformly and was measured not to exceed more than twice its original size. However, for collagen sausage casing it was boiled under pressure for three minutes, washed twice with tap water to remove any excess oil and the rubber band was used to attach the collagen sausage casing onto the blood feeder reservoir as shown in Figure 1c.

Next, 30 ml of chilled blood in three separate universal bottles (10 ml each) were preheated at 40°C in warm water for 5 minutes. Subsequently, for each blood feeder reservoir attached with Parafilm-M, PTFE tape and collagen sausage casing, 10 ml of preheated blood was transferred into each blood feeder reservoir. Next, to attach or secure the blood feeding reservoir to DITMOF heating surface, each blood feeding reservoir was wrapped with thin layer of Parafilm-M at the bottom. This thin Parafilm-M layer acted as a bonding substance between the blood feeder reservoir and DITMOF heating surface in which it will become sticky when the heat is applied. Constant heating during blood feeding ensures blood feeder reservoir to stick on DITMOF heating surface thus maintaining the desired blood temperature as has been set on the DITMOF digital controller. To ensure constant temperature of DITMOF heating surface during entire feeding time, 30-minute measurement of DITMOF's heating surface using infrared thermometer yielded a constant temperature ranging $\pm 0.1^\circ\text{C}$ after targeted temperature was achieved. However, based on three confirmatory testing at 0, 15 and 30 minutes for each membrane attached to blood feeder reservoir, different temperature range had to be set on DITMOF digital thermo

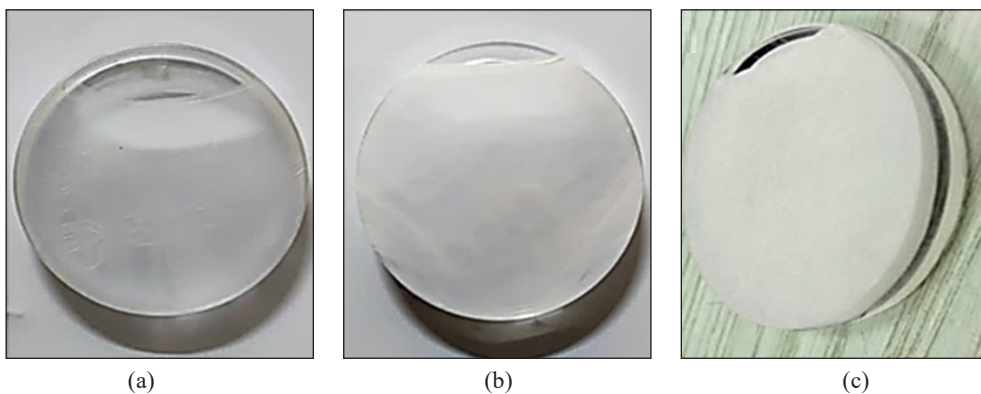


Figure 1. Attachment of membrane to blood feeder reservoir a) Parafilm-M; b) PTFE tape; c) Collagen sausage casing. Rubber band was used to attach collagen sausage casing to blood feeder reservoir.

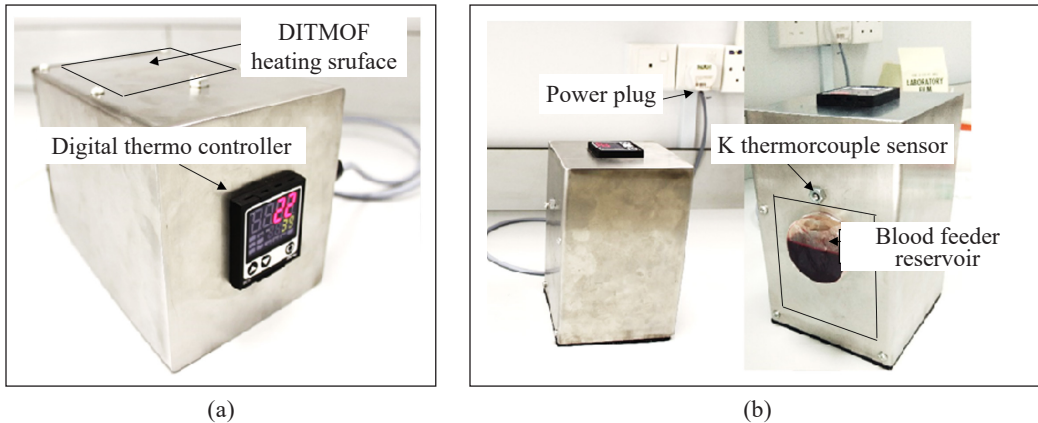


Figure 2. Digital Thermo Mosquito Blood Feeder (DITMOF) in: (a) horizontal position; and (b) vertical position (feeding position)

controller for each membrane. For PTFE tape and collagen sausage casing, temperature had to be set at 54°C while for Parafilm-M it was set at 40°C to ensure that the blood temperature in the blood feeder reservoir could be maintained at 35°C - 37°C range. The mean temperature of blood in Parafilm-M was 36.2°C, PTFE tape was 35.9°C and collagen sausage casing was 35.9°C (ANOVA, $p=0.121$). It was presumed that different temperature settings between these membranes were due to the membrane ability to retain the heat. The DITMOF device and its vertical feeding position are shown in Figure 2.

The mosquitoes used in this test were 3-5 days old mated female *Ae. aegypti* which were previously starved for 24 hours prior to blood feeding (Siria et al., 2018). For each replicate, 20 mosquitoes were put inside the test cage (20 cm × 20 cm × 20 cm). The cage was put side-by-side to DITMOF position for blood feeding process as shown in Figure 3. Total blood feeding time for each replicate was 30 minutes and black cloth was used to cover the test cage throughout the blood feeding period to minimize the interference. During the first one-minute of blood feeding, human breath was expelled near blood feeder reservoir to enhance the mosquito response. Number of mosquitoes landed on membrane after 1-minute human breath expelled was also recorded. At 15 minutes interval, fully engorged females were taken out and the remaining unfed mosquitoes were offered with blood feeding for another 15 minutes. After 30 minutes completed, total number of fully engorged females were calculated and analysed. Fully engorged mosquito was determined by visual inspection of fully distended or stretched mosquito abdomen (Ciota et al., 2011). Blood feeding rate was calculated as number of blood-fed females / numbers of mosquito tested × 100%. This method was repeated for all membranes type with 10 replicates performed for each membrane. The test was conducted at the same time during the day (1400 hours-1600 hours) for 10 consecutive days.

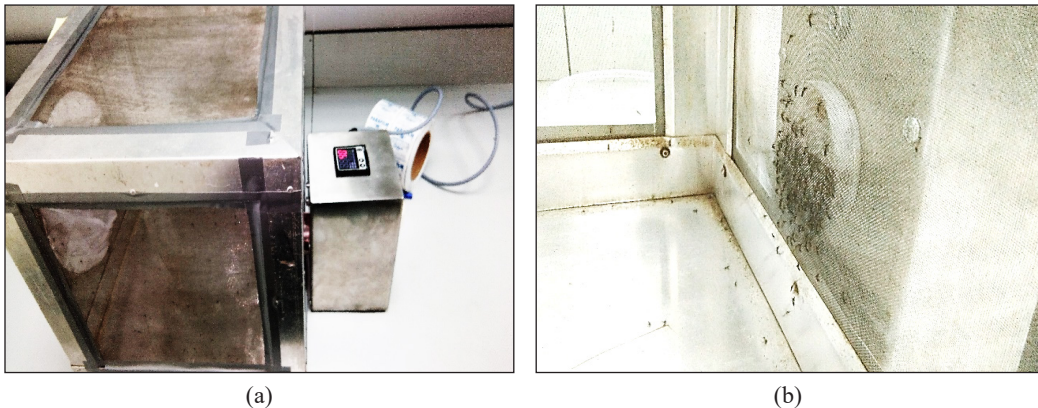


Figure 3. Mosquito artificial blood feeding using DITMOF device: (a) DITMOF and test cage at side-by-side position; and (b) *Ae. aegypti* mosquitoes were having blood meal.

Fecundity Rate

To measure fecundity, 10 mosquitoes three days post blood feeding were used for each replicate. Mosquitoes were put inside rearing cage where black paper cup containing 150 ml dechlorinated adapted for oviposition was added. This black paper cup was added with cone-shape filter paper to provide suitable oviposition sites for *Ae. aegypti*. After 48 hours exposure, total eggs accumulated on filter paper were calculated using stereo microscope. 10 replicates were performed for every membrane. Fecundity in this study was defined as total number of eggs collected per 10 mosquitoes.

Statistical Analysis

To evaluate the number of *Ae. aegypti* landed on blood feeder reservoir, blood feeding rate and fecundity using tested membranes, the parametric one-way analysis of variance (ANOVA) and Bonferroni post-hoc tests were used at significance level of $p < 0.05$, given that the data collected was normally distributed. Data normality testing was performed using the Shapiro-Wilk and Kolmogorov-Smirnov test. All statistical analyses were completed using the SPSS version 24 from IBM.

RESULTS

In terms of the membrane preparation for the AF, both PTFE tape and Parafilm-M were easier to be handled as compared to the collagen sausage casing. The PTFE tape and Parafilm-M are self-adhesive especially when being stretched out and could be easily attached to the blood feeder reservoir. In contrast, the attachment of the collagen sausage casing was trickier as the use of the rubber band could cause damage onto the collagen sausage casing and it could also be easily slipped out from the blood feeder reservoir

especially when it is wet. However, for all three membranes tested, no blood leakage was observed during the whole feeding period using DITMOF device.

The number of mosquitoes landed on the blood feeder reservoir after 1–minute of feeding duration showed that the highest mean was recorded for PTFE tape at 15.20 ± 0.39 , followed by Parafilm-M at 14.30 ± 0.52 and collagen sausage casing at 13.9 ± 0.46 . However, ANOVA analysis showed that there was no significant mean difference of number of landed mosquitoes among tested membrane with p value of 0.140. For blood feeding performance, after the first 15-minutes of blood feeding completed, PTFE tape membrane recorded the highest *Ae. aegypti* blood feeding rate with $90.00\% \pm 2.47\%$, followed by Parafilm-M ($56.00\% \pm 2.21\%$) and collagen sausage casing ($54.50\% \pm 3.11\%$). Analysis of variance (ANOVA) with post-hoc Bonferroni test showed significant difference for the use of PTFE tape as compared to the Parafilm-M and collagen sausage casing with both p-values were <0.001 . However, the difference between Parafilm-M and collagen sausage casing was not significant with a p-value of 1.000. Subsequently, after the full blood feeding test was completed in 30 minutes, the similar pattern was observed. The use of PTFE tape recorded the highest *Ae. aegypti* blood feeding rate with $95.00\% \pm 1.67\%$, followed by the Parafilm-M ($72.00\% \pm 2.60\%$) and collagen sausage casing ($71.50\% \pm 3.50\%$). Only PTFE tape membrane showed a significant difference as compared to both Parafilm-M and collagen sausage casing with p value of <0.001 . The utilization of Parafilm-M and collagen sausage casing were not significantly different to each other with p-value of 1.000. Comparison of the mean mosquito landed after 1–minute of blood feeding duration and the blood feeding rate at 15–and 30–minutes interval for three tested membranes are shown in Table 1.

For fecundity among mosquitoes that had been artificially fed using different type of membranes, the highest mean was recorded using Parafilm-M at 532.10 ± 22.67 followed by PTFE tape at 502.90 ± 19.00 and collagen sausage casing at 487.20 ± 18.25 . However,

Table 1
Comparison of the mean mosquito landed after 1–minute of blood feeding duration and the blood feeding rate at 15- and 30-minutes interval for three tested membranes

Membrane type	Mean mosquitoes landed after 1 minute (n=20) ± SEM	Blood feeding duration	Blood feeding rate (%) ± SEM
Parafilm-M	$14.30^a \pm 0.52$	15 minutes	$56.00^a \pm 2.21$
		30 minutes	$72.00^a \pm 2.60$
PTFE tape	$15.20^a \pm 0.39$	15 minutes	$90.00^b \pm 2.47$
		30 minutes	$95.00^b \pm 1.67$
Collagen sausage casing	$13.90^a \pm 0.46$	15 minutes	$54.50^a \pm 3.11$
		30 minutes	$71.50^a \pm 3.50$

*Values with the same alphabet are not significantly difference at p level 0.05 while values with different alphabets are significantly different.

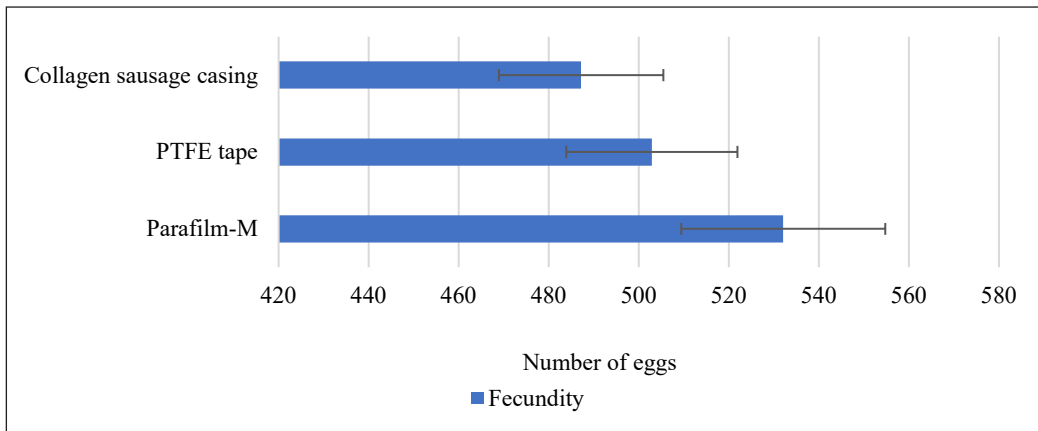


Figure 4. Fecundity of *Ae. aegypti* mosquitoes that had been artificially fed using three tested membranes

there was no significant mean difference among the three tested membranes as determined by one-way ANOVA ($F(2,27) = 1.289, p=0.292$). Figure 4 shows the fecundity of *Ae. aegypti* mosquitoes that were blood fed using the three tested membranes.

DISCUSSION

Choosing the correct type of membrane is essential to develop a mosquito blood feeder that can feed the mosquitoes effectively. In this study, we found that the PTFE tape was the most effective synthetic membrane for *Ae. aegypti* blood feeding. As for the Parafilm-M and collagen sausage casing, acceptable feeding rates (>70%) were observed; with no significant difference seen between both membranes. These findings are in line with Luo (2014) who also compared the blood feeding rate of *Ae. aegypti* using the Parafilm-M and collagen sausage casing.

There is a strong indication that membrane thickness could affect *Ae. aegypti* blood feeding ability (Luo, 2014). The thickness of PTFE tape used in this study was rated at 0.075 mm while the Parafilm-M was thicker at 0.127 mm. The PTFE tape was stretched out for more than twice its size resulting in the final membrane thickness of less than 0.038 mm. For Parafilm-M it was stretched out about twice its size resulting in the final membrane thickness approximately 0.064 mm. This step was performed carefully to prevent over-stretching of Parafilm-M. Over-stretched Parafilm-M could develop weak spot on its surface and increase the risk of rupture especially when heating. At 0.064 mm thickness, it was stretched far from its braking point at 0.025 mm (Luo, 2014). Additionally, other researcher that used Parafilm-M in AF also stretched about twice its original size (Nasirian & Ladonni, 2006). As the boiled collagen sausage casing, the thickness was rated at 0.073 ± 0.004 mm (Luo, 2014). Collagen sausage casing could not be stretched-out; thus, it was categorized as the thickest membrane among the three.

It was also postulated that the membrane pore size influences the blood feeding efficacy of *Ae. aegypti*. Bigger pore sizes enhanced the mosquito proboscis penetration. The type of membrane used would also affect the on piercing and probing of mosquito blood feeding (Novak et al., 1991; Ross et al., 2019). Direct membrane pore measurement was not performed in this study. However, PTFE tape pore size was reported to have an average of 500 nm and this pore size may increase if the tape is stretched out (Van der Linden, 1983). In contrast, the pore size of a similar non-stretchable collagen sausage casing has an average of 48.2 nm (Ledesma et al., 2015) while the Parafilm-M is a non-porous wax-modified polyolefin film.

The blood feeding rates for the 15-minute and 30-minute blood feeding were higher for the PTFE tape as compared to the Parafilm-M and collagen sausage casing. However, there was no significant mean difference of the number of mosquitoes landed on all three membranes at first minute of the blood feeding duration ($p=0.140$). These findings indicated that the attraction of mated female mosquitoes towards all membrane attached to blood feeder reservoirs were almost similar. Nonetheless, mosquito feed on PTFE tape membrane recorded a higher and significant blood feeding rate as compared to the others.

Besides being more effective for *Ae. aegypti* blood feeding, the PTFE tape membrane is also more heat resistant, with the maximum operating temperature rated at 260°C (RSPRO, 2020). For collagen sausage casing, the boiling of this synthetic membrane in water will not change its basic microstructure and thickness (Barbut, 2010). In contrast, the Parafilm-M becomes soft and sticky at 54°C and completely melt at 100°C (AMCOR, 2019). When the heat was used to warm the blood, the Parafilm-M membrane is more prone to disintegrate and cause the blood leakage especially if it was used for a longer period. In these circumstances, the PTFE tape and collagen sausage casing are more suitable to be used as the blood feeding membrane in AF.

In term of fecundity, there was no significant mean difference of eggs produced among all the tested membranes although the slightly higher mean was seen using Parafilm-M. The use of the same cattle blood source as a standard blood for mosquito feeding in this study could contributed to these non-significant differences. There were reports indicate that different blood types using in AF could have effects on fecundity. For example, Gunathilaka et al. (2017) reported that there was higher and significant mean difference of *Ae. aegypti* that were feed using bovine blood compared to chicken blood. However, our study shows that the use three different synthetic membranes tested have minimal effect to mosquito fecundity.

Ae. aegypti mosquitoes used in the testing has successfully been maintained for one year and a half using DITMOF and Parafilm-M membrane combination. Thus, it is suggested that DITMOF as a proven blood feeder device for rearing *Ae. aegypti* mosquito. The use of DITMOF device in the AF provided a more convenient blood feeding process

where constant and precise blood temperature was achieved. In comparison, several other blood feeder devices that are using preheated medium such as glycerol, metal plate or water, require continuous monitoring to maintain a precise and constant feeding temperature (Costa-da-Silva et al., 2013; Gunathilaka et al., 2017; Siria et al., 2018). Furthermore, feeding process using DITMOF does not require modification to the adult cage due to the ready-to-use design and additional feature such as adjustable feeding temperature which could provide a better temperature option for users.

Moreover, up to four blood feeder reservoirs can be attached to DITMOF heating surface at one feeding session to feed many mosquitoes. The DITMOF side-by-side feeding position also minimizes the risk of membrane rupture where less weight and pressure were put on a fragile membrane. This side-by-side feeding setting also ensures that the mosquito blood feeding could be performed in a nose-up vertical position instead of traditional upside-down horizontal position. This nose-up vertical feeding position allows a more normal flow of blood to be achieved and for *Aedes albopictus* species, an increase of 46% blood feeding rate was reported (Lyski et al., 2011). Additionally, mosquito with a heavy abdomen inclines to maintain in nose-up vertical position, thus blood meal offered in upside-down feeding position in most traditional blood feeder device, are less favourable for the blood meal consumption (Bender & Frye, 2009). However, further comparison and tests with current commercial blood feeder should be performed to confirm these advantages in rearing the mosquito colony.

CONCLUSION

In this study, the use of PTFE tape as membrane indicated superior blood feeding performance for *Ae. aegypti* mosquitoes as compared to the Parafilm-M and collagen sausage casing. This membrane should be the preferred synthetic membrane in the AF to feed *Ae. aegypti* mosquitoes. In combination with the effective membrane, the in-house developed automated mosquito blood feeder, DITMOF shows great a potential to be used as a mosquito blood feeder in mass rearing mosquito facilities or small laboratories. Further testing to feed other mosquito species should be conducted using this device. It is hoped that the findings and invention from this current study will help in the enhancement of mosquito production and facilitate the mosquito research and control programmes.

ACKNOWLEDGEMENT

The authors are grateful to the Director-General of Health Malaysia for permission to publish this paper. We also want to thank Dr Azlan Enjah and Mr Abdul Rahim Bin Abdul Karim from Department of Veterinary Services, Melaka for providing cattle blood for the rearing of of *Ae. aegypti* colony, Department of Parasitology & Medical Entomology, Faculty of Medicine, Universiti Kebangsaan Malaysia for providing research facilities

and technical support and Centre for Collaborative Innovation, Universiti Kebangsaan Malaysia for assistance in patent application for the in-house developed mosquito blood feeder, Digital Thermo Mosquito Blood Feeder, DITMOF. This study was financially supported by UKMMC (Universiti Kebangsaan Malaysia Medical Centre) Fundamental Research Grant [FF-2017-492]. Mohd Farihan Md Yatim is from Institute for Public Health and sponsored by Ministry of Health, Malaysia. All figures in this article are authors and co-authors own copy.

REFERENCES

- AMCOR (2019). *PARAFILM® M laboratory film- technical datasheet*. Retrieve April 4, 2019, from <http://www.bemis.com/Bemis/media/Library/pdf/unrestricted/amcor-techdata-parafilm-m-lab.pdf>
- Balestrino, F., Benedict, M., & Gilles, J. (2012). A new larval tray and rack system for improved mosquito mass rearing. *Journal of Medical Entomology*, 49(3), 595-605. <https://doi.org/10.1603/ME11188>
- Barbut, S. (2010). Microstructure of natural, extruded and co-extruded collagen casings before and after heating. *Italian Journal of Food Science*, 22(2), 126-133.
- Baumans, V., Zutphen, L., & Beynen, A. (1993). *Principles of laboratory animal science: A contribution to the humane use and care of animals and to the quality of experimental results*. Elsevier
- Bender, J. A., & Frye, M. A. (2009). Invertebrate solutions for sensing gravity. *Current Biology*, 19(5), 186-190. <https://doi.org/10.1016/j.cub.2008.12.024>
- Ciota, A. T., Styer, L. M., Meola, M. A., & Kramer, L. D. (2011). The costs of infection and resistance as determinants of West Nile virus susceptibility in *Culex* mosquitoes. *BMC Ecology*, 11(1), 1-8. <https://doi.org/10.1186/1472-6785-11-23>
- Costa-da-Silva, A. L., Navarrete, F. R., Salvador, F. S., Karina-Costa, M., Ioshino, R. S., Azevedo, D. S., Rocha, D. R., Romano, C. M., & Capurro, M. L. (2013). Glytube: A conical tube and parafilm M-based method as a simplified device to artificially blood-feed the dengue vector mosquito, *Aedes aegypti*. *PLoS One*, 8(1), Article e53816. <https://doi.org/10.1371/journal.pone.0053816>
- Deng, L., Koou, S., Png, A., Ng, L., & Lam-Phua, S. (2012). A novel mosquito feeding system for routine blood-feeding of *Aedes aegypti* and *Aedes albopictus*. *Tropical Biomedicine*, 29(1), 169-174. <https://doi.org/10.1111/jvec.12101>
- Finlayson, C., Saingamsook, J., & Somboon, P. (2015). A simple and affordable membrane-feeding method for *Aedes aegypti* and *Anopheles minimus* (Diptera: Culicidae). *Acta Tropica*, 152, 245-251. <https://doi.org/10.1016/j.actatropica.2015.09.026>
- Gonzales, K. K., Rodriguez, S. D., Chung, H. N., Kowalski, M., Vulcan, J., Moore, E. L., Li, Y., Willette, S. M., Kandel, Y., Van Voorhies, W. A., Holguin, F. O., Hanley, K. A., & Hansen, I. A. (2018). The effect of SkitoSnack, an artificial blood meal replacement, on *Aedes aegypti* life history traits and gut microbiota. *Scientific Reports*, 8(1), 1-14. <https://doi.org/10.1038/s41598-018-29415-5>
- Gunathilaka, N., Ranathunge, T., Udayanga, L., & Abeyewickreme, W. (2017). Efficacy of blood sources and artificial blood feeding methods in rearing of *Aedes aegypti* (Diptera: Culicidae) for sterile insect technique

- and incompatible insect technique approaches in Sri Lanka. *Hindawi BioMed Research International* 2017, 1-7. <https://doi.org/10.1155/2017/3196924>
- Klun, J. A., Kramer, M., & Debboun, M. (2005). A new in vitro bioassay system for discovery of novel human-use mosquito repellents. *Journal of the American Mosquito Control Association*, 21(1), 64-70.
- Ledesma, E., Rendueles, M., & Díaz, M. (2015). Characterization of natural and synthetic casings and mechanism of BaP penetration in smoked meat products. *Food Control*, 51, 195-205. <https://doi.org/10.1016/j.foodcont.2014.11.025>
- Luo, Y. P. (2014). A novel multiple membrane blood-feeding system for investigating and maintaining *Aedes aegypti* and *Aedes albopictus* mosquitoes. *Journal of Vector Ecology*, 39(2), 271-277. <https://doi.org/10.1111/jvec.12101>
- Lyski, Z. L., Saredy, J. J., Ciano, K. A., Stem, J., & Bowers, D. F. (2011). Blood feeding position increases success of recalcitrant mosquitoes. *Vector-Borne Zoonotic Diseases*, 11(8), 1165-1171. <https://doi.org/10.1089/vbz.2010.0164>
- Nasirian, H., & Ladonni, H. (2006). Artificial bloodfeeding of *Anopheles stephensi* on a membrane apparatus with human whole blood. *Journal of the American Mosquito Control Association*, 22(1), 54-56. [https://doi.org/10.2987/8756-971X\(2006\)22\[54:ABOASO\]2.0.CO;2](https://doi.org/10.2987/8756-971X(2006)22[54:ABOASO]2.0.CO;2)
- Novak, M., Berry, W., & Rowley, W. (1991). Comparison of four membranes for artificially bloodfeeding mosquitoes. *Journal of the American Mosquito Control Association*, 7(2), 327-329.
- Paris, V., Cottingham, E., Ross, P. A., Axford, J. K., & Hoffmann, A. A. (2018). Effects of alternative blood sources on *Wolbachia* infected *Aedes aegypti* females within and across generations. *Insects*, 9(4), Article 140. <https://doi.org/10.3390/insects9040140>
- Peng, Z., Beckett, A. N., Engler, R. J., Hoffman, D. R., Ott, N. L., & Simons, F. E. R. (2004). Immune responses to mosquito saliva in 14 individuals with acute systemic allergic reactions to mosquito bites. *Journal of Allergy and Clinical Immunology*, 114(5), 1189-1194. <https://doi.org/10.1016/j.jaci.2004.08.014>
- Pothikasikorn, J., Boonplueang, R., Suebsaeng, C., Khaengraeng, R., & Chareonviriyaphap, T. (2010). Feeding response of *Aedes aegypti* and *Anopheles dirus* (Diptera: Culicidae) using out-of-date human blood in a membrane feeding apparatus. *Journal of Vector Ecology*, 35(1), 149-155. <https://doi.org/10.1111/j.1948-7134.2010.00071.x>
- Romano, D., Stefanini, C., Canale, A., & Benelli, G. (2018). Artificial blood feeders for mosquitoes and ticks-Where from, where to? *Acta Tropica*, 183, 43-56. <https://doi.org/10.1016/j.actatropica.2018.04.009>
- Ross, P. A., Lau, M. J., & Hoffmann, A. A. (2019). Does membrane feeding compromise the quality of *Aedes aegypti* mosquitoes? *PLoS One*, 14(11), Article e0224268. <https://doi.org/10.1371/journal.pone.0224268>
- RSPRO. (2020). *RS PRO White PTFE Tape 12mm x 12m x 0.075mm*. Retrieve May 9, 2020, from <https://my.rs-online.com/web/p/ptfe-tapes/0512238/>
- Rudmann, S. V. (2005). *Textbook of blood banking and transfusion medicine* (2nd Ed.). Elsevier Saunders.
- Siria, D. J., Batista, E. P., Opiyo, M. A., Melo, E. F., Sumaye, R. D., Ngowo, H. S., Eiras, A. E., & Okumu, F. (2018). Evaluation of a simple polytetrafluoroethylene (PTFE)-based membrane for blood-feeding

of malaria and dengue fever vectors in the laboratory. *Parasites Vectors*, 11(1), Article 236. <https://doi.org/10.1186/s13071-018-2823-7>

Van der Linden, W. (1983). Membrane separation in flow injection analysis: Gas diffusion. *Analytica Chimica Acta*, 151, 359-369. [https://doi.org/10.1016/S0003-2670\(00\)80097-5](https://doi.org/10.1016/S0003-2670(00)80097-5)

Wade, J. O. (1976). A new design of membrane feeder incorporating an electrical blood stirring device. *Annals of Tropical Medicine & Parasitology*, 70(1), 113-120. <https://doi.org/10.1080/00034983.1976.11687102>

WHO. (1995). *Manual on practical entomology in Malaria*. Retrieve April 4, 2020, from <http://www.who.int/iris/handle/10665/42481>.

Zhang, D., Zhang, M., Wu, Y., Gilles, J. R. L., Yamada, H., Wu, Z., Xi, Z., & Zheng, X. (2017). Establishment of a medium-scale mosquito facility: Optimization of the larval mass-rearing unit for *Aedes albopictus* (Diptera: Culicidae). *Parasites & Vectors*, 10(1), 1-9. <https://doi.org/10.1186/s13071-017-2511-z>

The Characteristics of West Season Wind and Wave as well as Their Impacts on Ferry Cruise in The Kalianget-Kangean Cruise Route, Madura, Indonesia

Viv Djanat Prasita*, Lukman Aulia Zati and Supriyatno Widagdo

Department of Oceanography, Hang Tuah Surabaya, Jalan Arif Rahman Hakim 150, Sukolilo Surabaya, Indonesia

ABSTRACT

The wind and wave conditions in the waters of the Kalianget-Kangean cruise route in the west season are relatively high so that these winds and waves can have a dangerous impact on that cruise route. The aim of this research was to analyze the characteristics of wind speed and wave height over a 10 year period (2008-2017), as well as to evaluate the weekly patterns for three months (December 2017-February 2018). These time stamps represent the west season in waters at Kalianget-Kangean route, and to identify the impact of winds and wave on this path. The method used in this research is descriptive statistical analysis to obtain the mean and maximum values of wind speed and wave height. Wind and wave patterns were analyzed by WRPlot and continued with mapping of wind and

wave patterns in the waters of Kalianget-Kangean and its surroundings. The data used was obtained from the Meteorology, Climatology and Geophysics Agency. The results show wind and wave characteristics with two peaks formed regularly between 2008-2017, marking the west and east monsoons. In addition, the wind speed and wave height were generally below the danger threshold, ie <10 knots and <2 m, respectively. However, there are exceptions in the west season, especially at the peak in January, where the forces are strengthened with a steady blowing direction. The

ARTICLE INFO

Article history:

Received: 23 December 2021

Accepted: 16 April 2021

Published: 19 July 2021

DOI: <https://doi.org/10.47836/pjst.29.3.16>

E-mail addresses:

viv.djanat@hangtuah.ac.id (Viv Djanat Prasita)

lukman.zati10@gmail.com (Lukman Aulia Zati)

supriyatno.widagdo@hangtuah.ac.id (Supriyatno Widagdo)

*Corresponding author

maximum wind speed reaches and wave height reaches 29 knots and 6.7 m, respectively. The weekly conditions for both parameters from December 2017 to February 2018 were relatively safe, for sailing. Moreover, January 23-29, 2018 featured extreme conditions estimated as dangerous for cruise due to the respective maximum values of 25 knots and 3.8 m recorded. The channel is comparably safe, except during the western season time in December, January, February, characterized by wind speeds and wave height exceeding 21 knots and 2.5 m, correspondingly.

Keywords: Cruise security, wave height, west monsoon, wind speed

INTRODUCTION

Indonesia's geographical condition comprises thousands of islands, with the sea serving as a noticeable connecting factor. This makes sea transportation, especially inter-island crossings an important aspect in marine resource utility and is expected to drive the wheels of the archipelago's maritime development. Moreover, some of the essential considerations in crossings between islands or countries include the weather-oceanography factors, particularly in the form of wind, current and wave conditions. Also, it is important to assess the physical characteristics of sea surfaces, to provide a safe and comfortable cruise database, especially in busy regular channels (Aji, 2015). This evaluation is required due to the increasingly intensive global climate change, as observed with the relatively erratic weather conditions in Indonesia. Furthermore, the volatility has some negative impacts, including rainy seasons with rainfall above normal; the emergence of strong winds with the potential to become whirlwinds, accompanied by heavy rain and lightning; and high sea waves. These undesirable effects have been observed in Sumenep Regency, in the district at the eastern tip of Madura Island, featuring a rainy season extending from January 2008.

In addition, the wave height in the west season could be between 2 – 4.5 meters (Nugraha et al., 2013). Based on estimates from the Class II Maritime Meteorological Station of Tanjung Perak Surabaya, the wave height in Kangean waters and its surroundings was in the range of 1 meter to 2.25 meters on Friday (1/3/2020) and 1.5 meters to 3.5 meters on Saturday (1/3/2020) so that KMP Dharma Bahari Sumekar I belonging to PT Sumekar, which was scheduled to sail from Kalianget Port to Kangean Island, Sumenep, Madura, East Java, would not operate due to bad weather (Slamet, 2020).

Moreover, Madura waters as a part of the Java Sea Oceanic region are on an ideal path for the ongoing monsoonal processes, known to influence the weather conditions. The west season is monsoonally attributed as the period with the strongest winds.

Conversely, Kangean Island is a great tourist location with coral reefs and natural conditions considered as good (Arisandi et al., 2018). The coral reef area expanding up to 41,849 hectares, with details in the Sapeken District and Sepanjang Island reaching 30,786

and 11,063.7 hectares, respectively, while the mangroves cover about 4,227.8 hectares (Muhsoni, 2015).

Previous study has also shown the high suitability of Kangean island for nautical tourism (Rini et al., 2015). Therefore, it is important to have in-depth knowledge of the weather and climate conditions, being an intrinsic component of the vacation experience, and is required to further motivate tourists (Scotta & Lemieux, 2010). The wind is one of the most important climate parameters, known to provide comfort and capable of generating harmful waves to visitors and the environment. The beaufort wind scale is frequently used as an indicator standard to assess wind and waves (Sandino et al., 2016).

Moreover, this cruise route is important for the movement of the economic wheels of the two regions. Therefore, delays in shipping can affect the socio-economic life of the local community. For the local community, marine resources in the Kangean Sumenep archipelago are a good asset to develop (Faqih, 2014).

Therefore, the objectives of this research were to analyze the wind and wave characteristics over 10 years (2008-2017), patterns for 3 months (December 2017-February 2018) as a representation of the west season and identify dangerous forms in this route.

MATERIALS AND METHODS

The data used in this study include 2 periods, a long period and a short period. Long period data is from 2008 - 2017 to elaborate seasons that have high waves and wind speeds that have the potential to endanger the Kalianget-Kangean route. Short period data was obtained for 3 months, December 2017-February 2018 as representative of the western season which during the 10-year period was the most dangerous season and at the same time became the up-to-date period when this research was conducted. From these data, statistical data processing is carried out in the form of determining the average wind speed and wave height and their maximum value. The minimum value is not used because the hazard aspect only refers to the maximum value.

The materials needed in this research include oceanographic data obtained from the Meteorology Climatology and Geophysics Agency (Badan Meteorologi, Klimatologi, dan Geofisika, 2019). These comprised of information on wind, and waves from January 2008 to February 2018. Furthermore, data processing was performed with various software to create a vectorial map of the research position, and Table 1 shows the visual display of descriptive statistics used.

The wind and current data were downloaded from the Windwaves-05 software. The Windwave 05 software developed by Badan Meteorologi, Klimatologi, dan Geofisika (BMKG), where data were taken from the World Meteorological Organization, and consequently processed with MS Excel to obtain a visual display of descriptive statistics. In addition, the wind and wave rose diagrams were obtained using WRPlot®, while wind and wave map layouts were processed with generic mapping tools (GMT).

Figure 1 shows the research sites situated at part of the Java Sea, and it has a geographical extent of latitude $6^{\circ} 82'49''$ - $7^{\circ}18'30''$ S and longitude $113^{\circ} 95' 17''$ - $115^{\circ} 30'34''$ E.

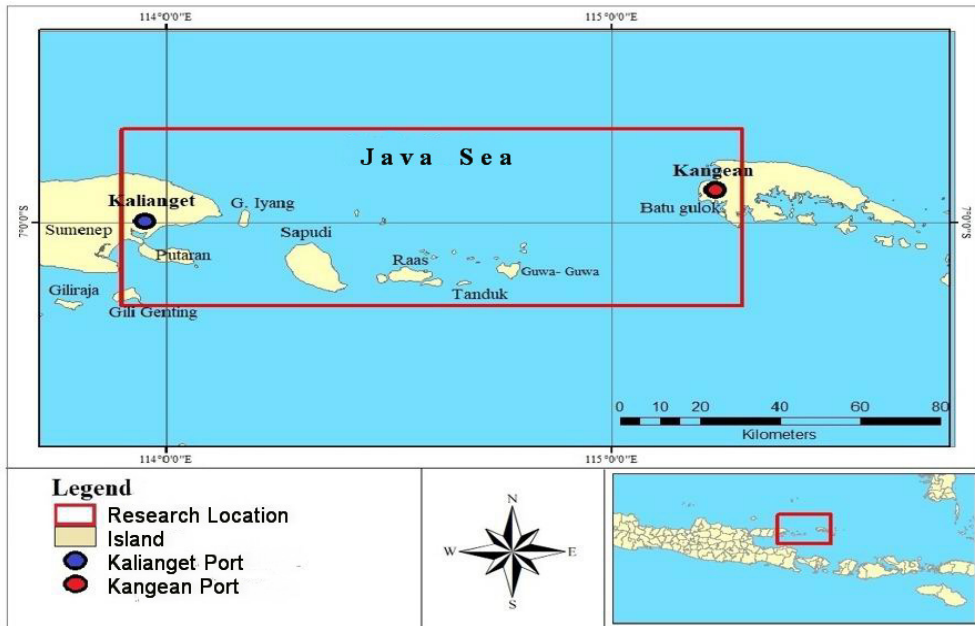


Figure 1. Research location in the Kalianget-Kangean cruise channel

Table 1

Software and usability as a research tool

Software	Function
Google Earth	Make research position
Matlab	Processing data, making charts and rose diagrams
GMT	Make outputs of wind and wave maps
Microsoft excel	Data processing and making chart of descriptive statistical
WRPlot	Processing of wind and wave roses
Windwave-05	Marine meteorological information

The safety of ferry cruise on the Kalianget-Bawean channel is evaluated at the Badan Meteorologi, Klimatologi, dan Geofisika (2019) by analyzing the weekly wind and wave data. This was performed every 6 hours daily, at 00:00, 06:00, 12:00, 18:00 from December 2017, January, and February 2018. The outcome is then processed with Matlab, and further by MS Excel to create a visual display. Subsequently, the information obtained is processed using GMT to create a map layout, to help predict the cruise's safety.

Table 2 shows the comparison of wind speed and wave height results of the subsequent data analysis against wind and wave risk matrix for cruise safety (Badan Meteorologi, Klimatologi, dan Geofisika, 2018). This assessment is issued by BMKG, with the following conditions stipulated for ferries:

Table 2
Wind and wave risk matrix for cruise safety

Level of Risks	Ferry Cruise	
Very Safe (VS)	Wind	< 11 Knot
	Wave	< 1.25 m
Safe (S)	Wind	11 – 15 Knot
	Wave	1.25 – 2.0 m
Less Dangerous (LD)	Wind	15 -21 Knot
	Wave	2.0 – 2.5 m
Dangerous (D)	Wind	>21 Knot
	Wave	>2.5 m

Sources. Badan Meteorologi, Klimatologi, dan Geofisika (2018)

RESULTS AND DISCUSSION

Wind Characteristics 2008-2017

Figure 2 shows the results of 10-year wind patterns (2008-2017) analysis, which indicates the fluctuations of average speed between two peaks and two valleys. This phenomenon signifies the occurrence of an increase during the main season: west and east spaced by the transition period indicated by the valleys between. Furthermore, the average seasonal wind speed denotes slightly higher winds in the east season (June-September) compared to the west (December-March).

The average of <15 knots is considered a safe cruise status throughout the season. However, it is important to prioritize vigilance at the possibility of maximum values measuring nearly 30 knots, which is frequently observed in January through February. Furthermore, a sharp decline to below 20 knots is observed in March and is followed by a steady decrease between April-May. The wind speed tends to increase again at the inception of the east season in May, and peaks in August at >21 knots. This is considered a “dangerous” status for ferry before a subsequent decline to touch the nadir at the end of a Transition Season (November). Therefore, another rise is detected in December, indicating the inception of western season.

The wind pattern analysis in the west season during the strongest speed period in 2008-2017 shows a steady blow from the west. This dominates nearly 40% of the event

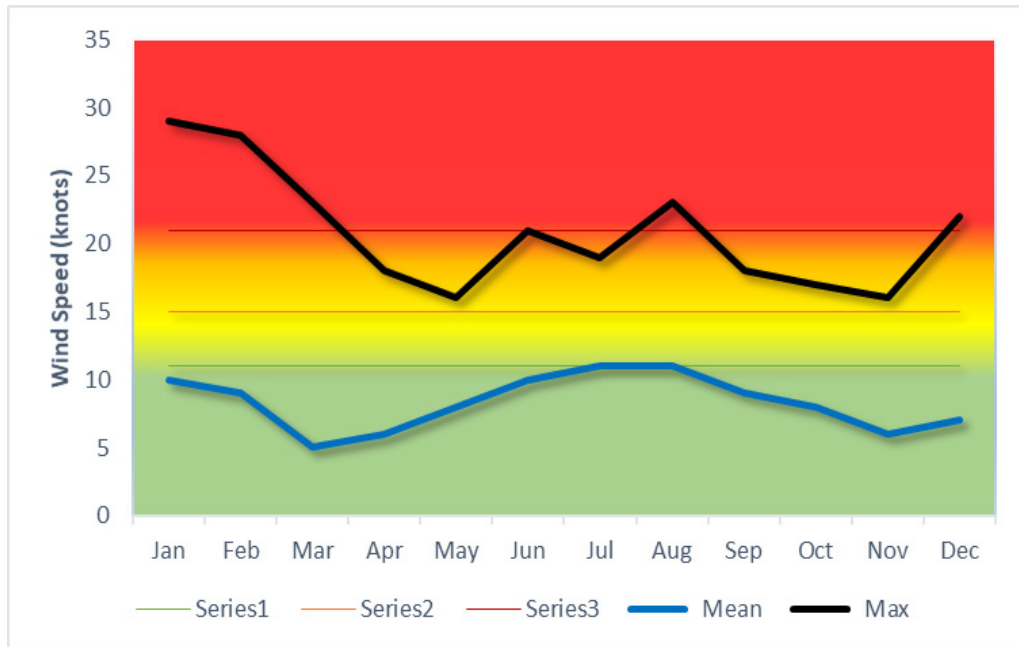


Figure 2. Monthly fluctuations in wind speeds during 2008-2017 confirm the high wind speeds in the west and east monsoons, as well as the weakening wind speeds during the transition periods.

frequency at the inception in December, followed by the 20% contributed by northwest wind. The rest sources blow from all directions at <10%. The dominant wind (38%) blows at 4-8 knots during December, followed by 2-4 knots (33.4%). In addition, the maximum speed recorded was at 20-24 knots, despite the very small frequency (0.5%) (Figure 3: Dec). The peak is reached a month later and is indicated by the strengthened stability of the western wind, as shown in Figure 3. Moreover, January is characterized by ~65% with a maximum of 28-32 knots (0.4%), although the dominant wind blows at speeds of 8-12 knots (23.4%) and 5-8 knots (22.3%). The west season subsequently weakened in February after attaining the peak, despite the persistence of the dominant source from the west. The value at this point was <50%, with a top speed of 24-26 knots (1.7%), although 4-8 knots (29.4%) was dominant (Figure 3: Feb).

Wave Characteristics of 2008-2017

The wave pattern was like the wind between 2008-2017, as evidenced by the two peaks observed, marking the highest values in the west and east season. Figure 4 shows the simultaneous presence of two valleys indicating low waves in the transition periods, observed at the beginning and end of each year. Moreover, the average wave height records

all year round was generally below 2 m (except in July), and cruising along the Kalianget-Kangean channel is considered safe from this perspective. However, the maximum wave height recorded confirms the presence of very significant waves in the west season, which peaked in January at 6.7 m. The highest values recorded in February was slightly reduced at 5 m. Prior to attaining the peak in January, the maximum height recorded in December was 3.90 m. Hence, there is a prohibition for Kalianget-Kangean route delivery in the west season because the greatest wave height value is >2.5 m.

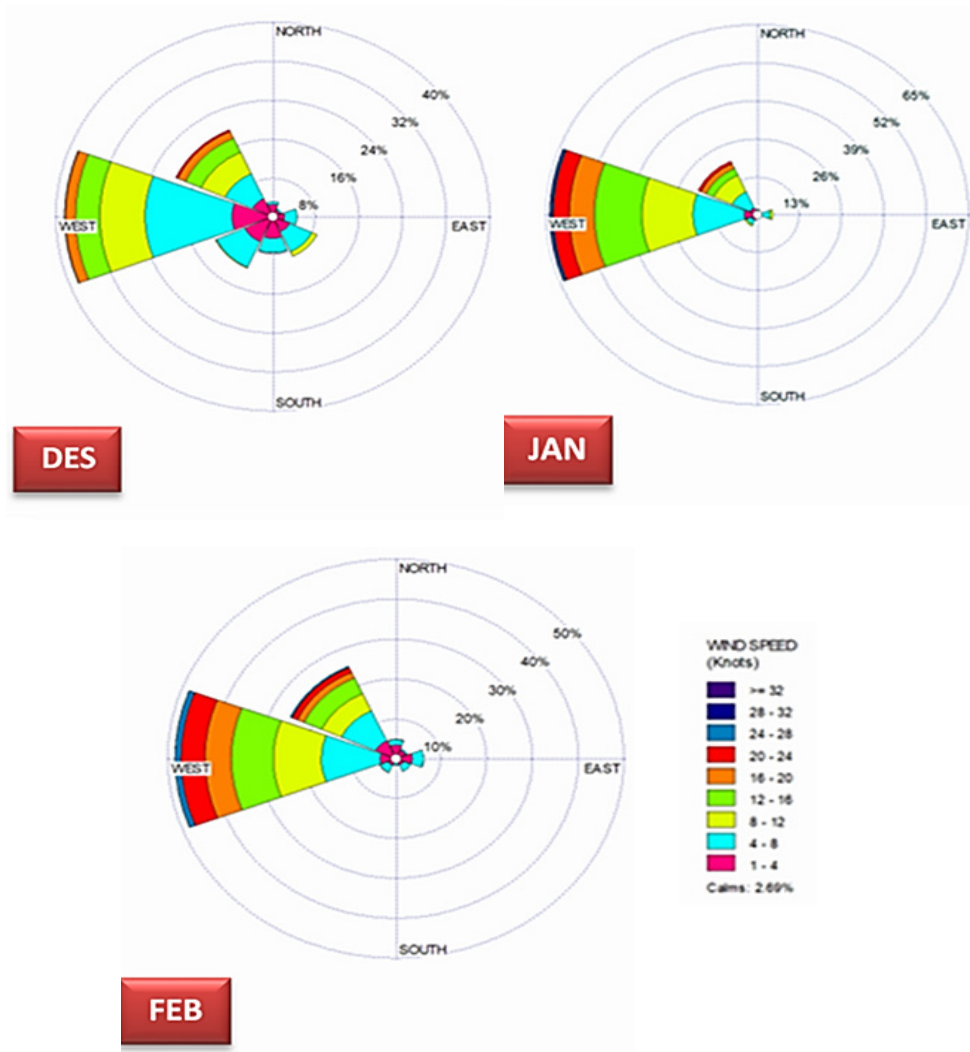


Figure 3. Wind speed patterns during December-February representing the west season 2008-2017 which shows the steady wind from the west

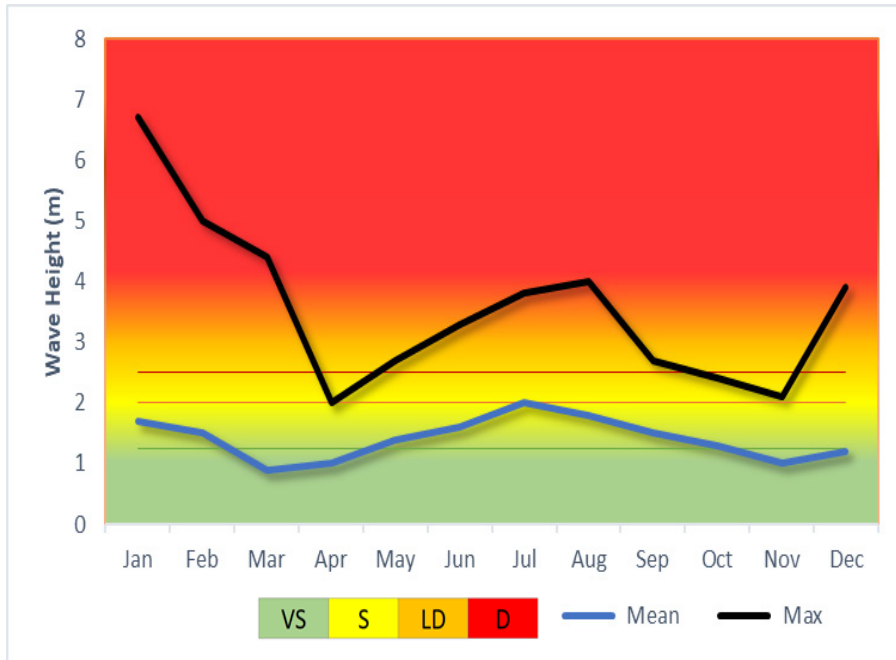


Figure 4. Monthly fluctuation in wave height during 2007-2018 confirms the increased wave height in the west and east seasons interspersed with low waves in the early and late year transition seasons

The transition season at the beginning of a year in March is marked by lower wave heights up to nadir 2.0 m observed in April. Furthermore, the values reported during the eastern season in May increased again and peaked in August, although a maximum of 4 m was attained. The results showed a subsequent decline to 2.1 m in November.

In addition, over 55% of the waves recorded in December were 1-2 m high, and Figure 5 showed the highest value of 3-4 m 2.7%. The predominant movement ensues from the south (<50%) and northwest (>30%) at the end of the year (Figure 5: Dec). Despite the dominance of 1-2 m high waves, the frequency is slightly reduced (47.5%). This relatively lower value is accompanied by an increase in the highest attainable wave to 5-6 m (0.4%) and then 6-7 m (0.3%). The direction of flow is observed to be from the northwest (~45%). Despite the high level recorded from the south, the frequency was observed to be <25%, which is like the western waves. These conditions mark wave maturity in the west season, which peaks in January (Figure 5: Jan), followed by a weaker disposition in Feb, although the data obtained confirm the dominance of northwest waves (<40%). Furthermore, there was a subsequent decline in the maximum height to 4-5 m (3.9%), leading to an increase in the wave region of 1-2 m to 40.7%.

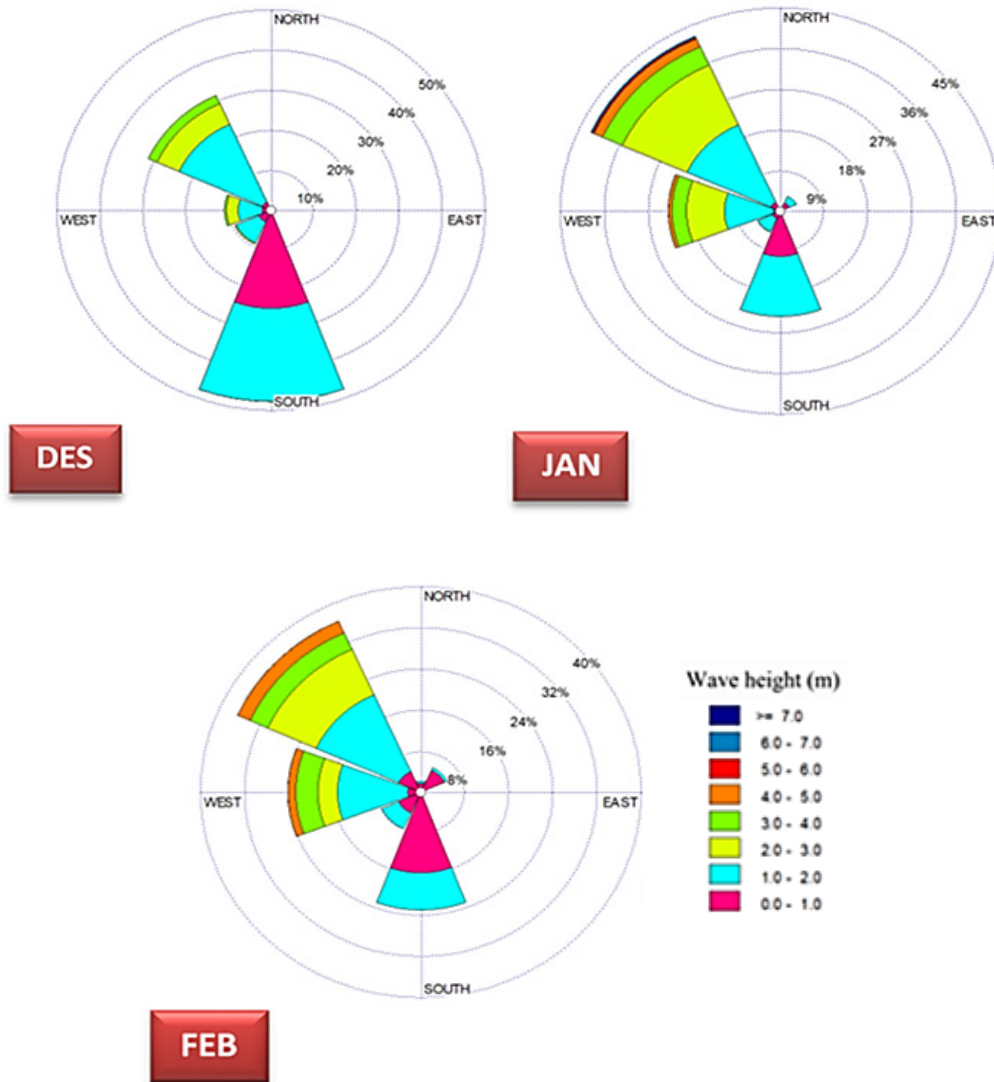


Figure 5. Wave height patterns during December-February representing the west season for the period 2008-2017. In general, the dominance of waves moves from the northwest

Wind Characteristics from December 2017 to January-February 20018

The weekly wind patterns at the peak of the west season from December 2017 to February 26, 2018 were analyzed. Figure 6 indicates the occurrence of two peaks and two valleys on the chart for wind speed. The average velocity fluctuates with a pattern like the maximum wind speed, where the peak of 13 knots was reached during the first fluctuation on December

19-25, although a maximum of 22 knots was also recorded. Furthermore, speeds exceeding 21 knots in this time are considered dangerous for cruise in the Kalianget-Kangean route.

The first peak is followed by more slower winds to attain an average and maximum speed of nadir of 4 m and 7 m respectively on January 2-8, 2018. In addition, these conditions are considered relatively safe. This is followed by further wind reinforcement to maximum values of up to 25 knots and are considered dangerous to sail on January 23-29, 2018. In addition, these huge values > 20 knots were recorded for the next two weeks and was followed by a decline to 11 knots. Hence, the waters were reconsidered as safe for cruise activities.

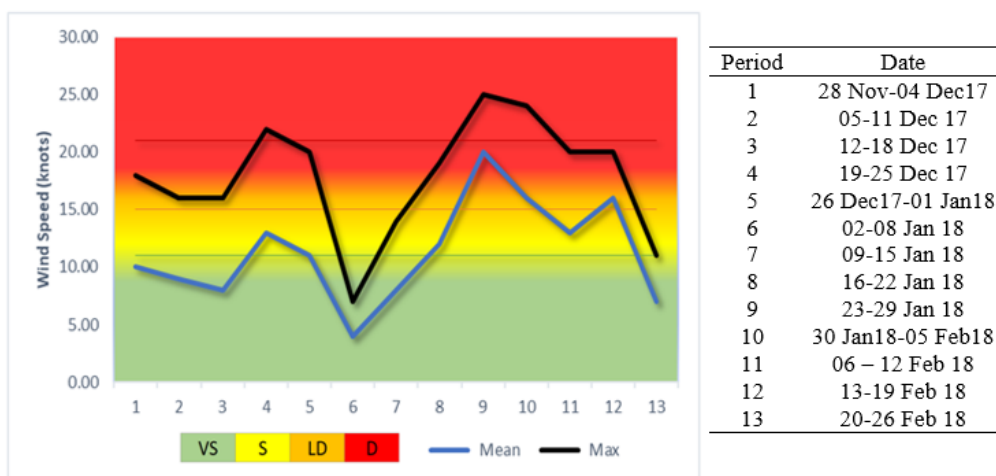


Figure 6. Weekly fluctuations in wind speed during November 2017- February 2018 which represent the peak of the west season

The illustration of various wind conditions and the risk level at the Kalianget-Kangean cruise route was performed by extracting data pertaining to wind patterns on January 4 at 12.00, January 15 at 18.00, January 17 at 17.00 and January 26, 2018 at 03.00. These were respectively shown in Figure 7a through to Figure 7d.

Specifically, a maximum wind speed of 6-8 knots were recorded on January 4, 2018 at 12.00, and the Kalianget waters alongside the surrounding areas of Kangean Island were assessed to be in a very safe and sailable condition (Figure 7a). Figure 7b shows a highest range of 10-15 knots on January 15 at 18:00, and the areas were considered safe for navigation. Figure 7c shows an increase to dangerous levels two days later at 17:00, in the Kalianget-Kangean cruise route to 15-20 knots. This phenomenon was observed particularly in the waters of Sapudi, Raas and Tanduk Islands, as well as around Kangean. Furthermore, all routes were classified as unsafe for navigation on January 26, 2018 at

03.00, due to the maximum speed values measured, which reached 20-25 knots, as shown in Figure 7d.

Wave Characteristics from December 2017 to February 2018

Similar to wind speed, Figure 8 showed the weekly fluctuations in wave height during the 2018 west season, as indicated by two peaks and two valley wave. After the peaks were reached on December 6-11, with average and maximum wave heights of 0.61 m and 1.09 m, respectively, there was a consequent elevation to values exceeding 2.5 m.

Nugraha et al. (2013) also realized that the wave height in the west season could be between 2 – 4.5 meters. This phenomenon was considered dangerous for cruise. Furthermore, 3.3 m was determined as the peak wave height between December 19-25, 2017, while the average values were estimated to be in a safe cruise condition, at 1.8 m (<2 m).

Subsequently, there was a decline in wave height, where the average and maximum values recorded on January 2-8, 2018 were below 1.5 m. Therefore, higher levels, respectively at 2.73 m and 3.84 m were observed on January 23-29, 2018, and further considered as dangerous for cruise. These values were above the 2.50 m threshold were maintained up to the period of 13-19 February 2018. Subsequently, weaker waves emerged to average and maximum values of 0.31 m and 0.70 m, respectively in February 20-26, 2018.

The risk levels are illustrated in relation to the varying wave conditions on the Kalianget-Kangean route by assessing the patterns recorded on 2 January 2018 at 12.00, 15 January 2018 at 21.00, 16 January 2018 at 21.00 and 25 January 2018 at 21.00. These were respectively shown in Figure 9a through to Figure 9d.

The waters at Kalianget and the Kangean archipelago, as well as the surroundings were in a very safe condition for navigation on January 2, 2018 at 12.00. This was due to the wave height of ~0.5 m measured, as observed in Figure 9a. In addition, the recording on January 15, 2018 at 21:00 was determined to be harmless for cruise from Kalianget to Sapudi Island, at <2 m. However, there was an increase to dangerous level (2-2.5 m) on the consequent route to Kangean, as Figure 9b showed values > 2.5 m in the northern waters of this Island. The waves recorded appear weakened at 21.00 on the next day, as shown in Figure 9c. In addition, the conditions were assumed to be very safe for navigation from the waters of Kalianget to Raas Island. The area around Tanduk Island was considered dangerous for sailing, as well as in areas further east approaching Kangean Island. Moreover, there was a drop to <2 m at zones around the Kangean port and is further classified safe. Figure 9d shows the situation from Kalianget harbor to Sapudi Island waters as very safe (<2 m) on January 25, 2018 at 21:00. However, dangerous levels reaching 2.5 m were observed towards eastern, and approaching the waters of Raas Island. In addition, heights > 2.5 m

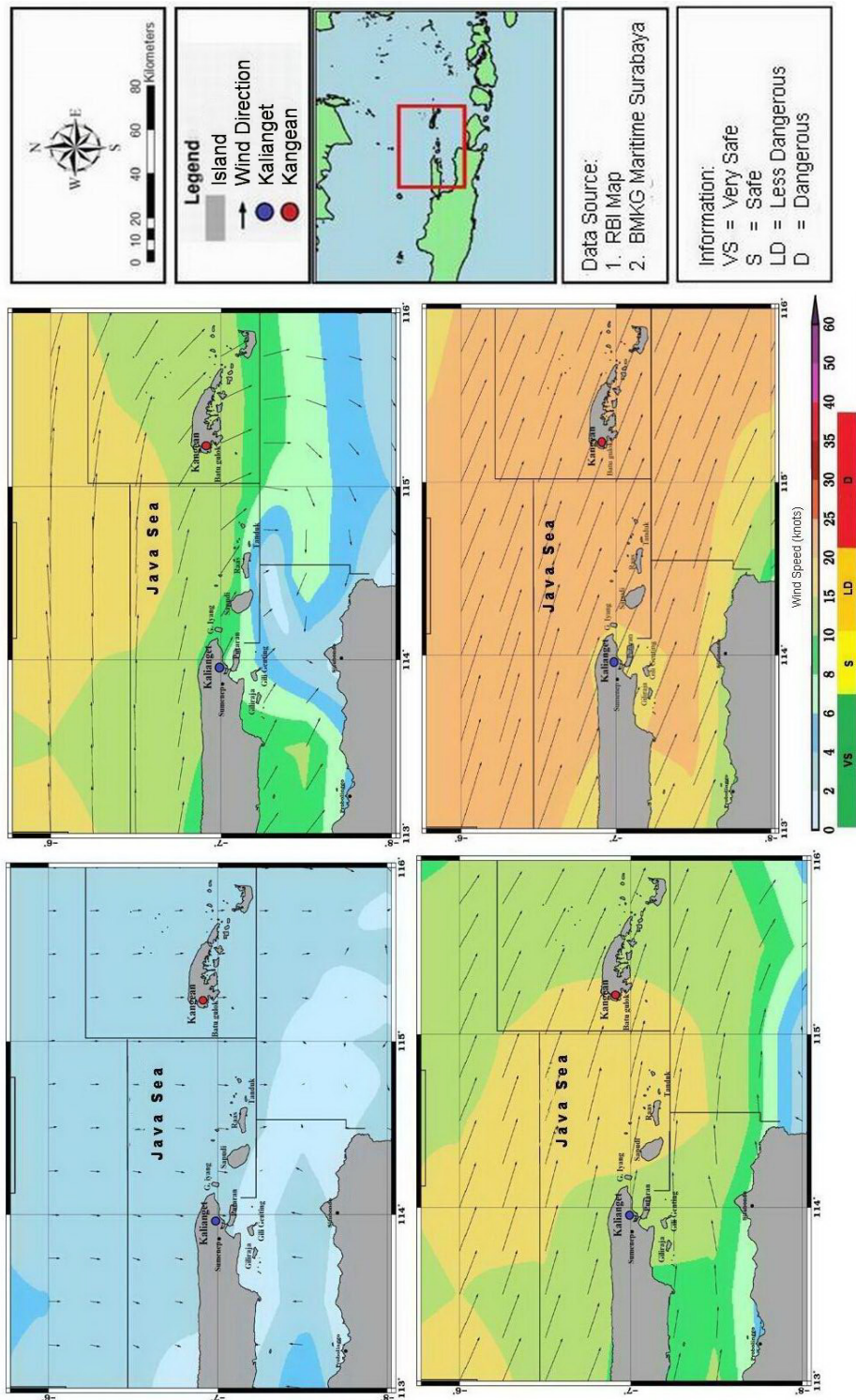


Figure 7. Maximum wind speed patterns in the waters of the Kalianget-Kangean cruise route on: (a) 4 January 2018 at 12.00, (b) 15 January 2018 at 18.00, (c) 17 January 2018 at 17.00, and (d) 26 January 2018 at 03.00.

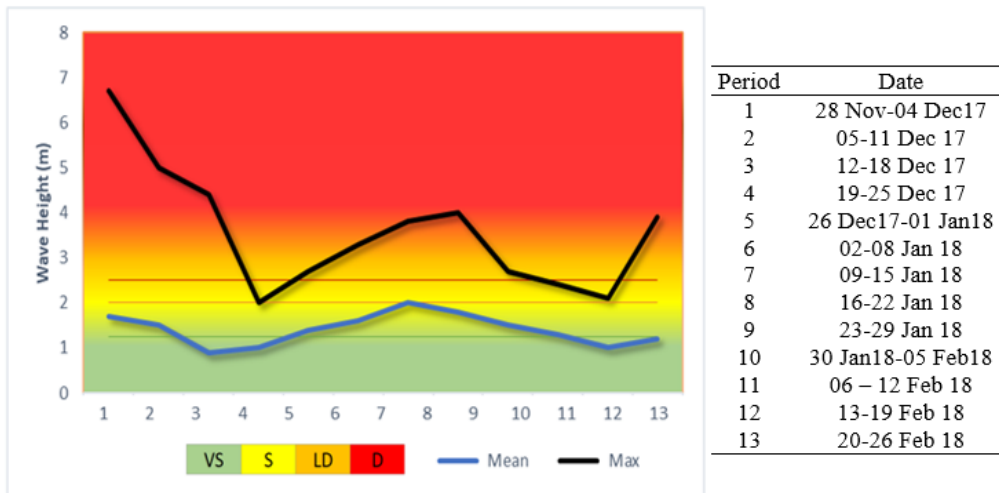


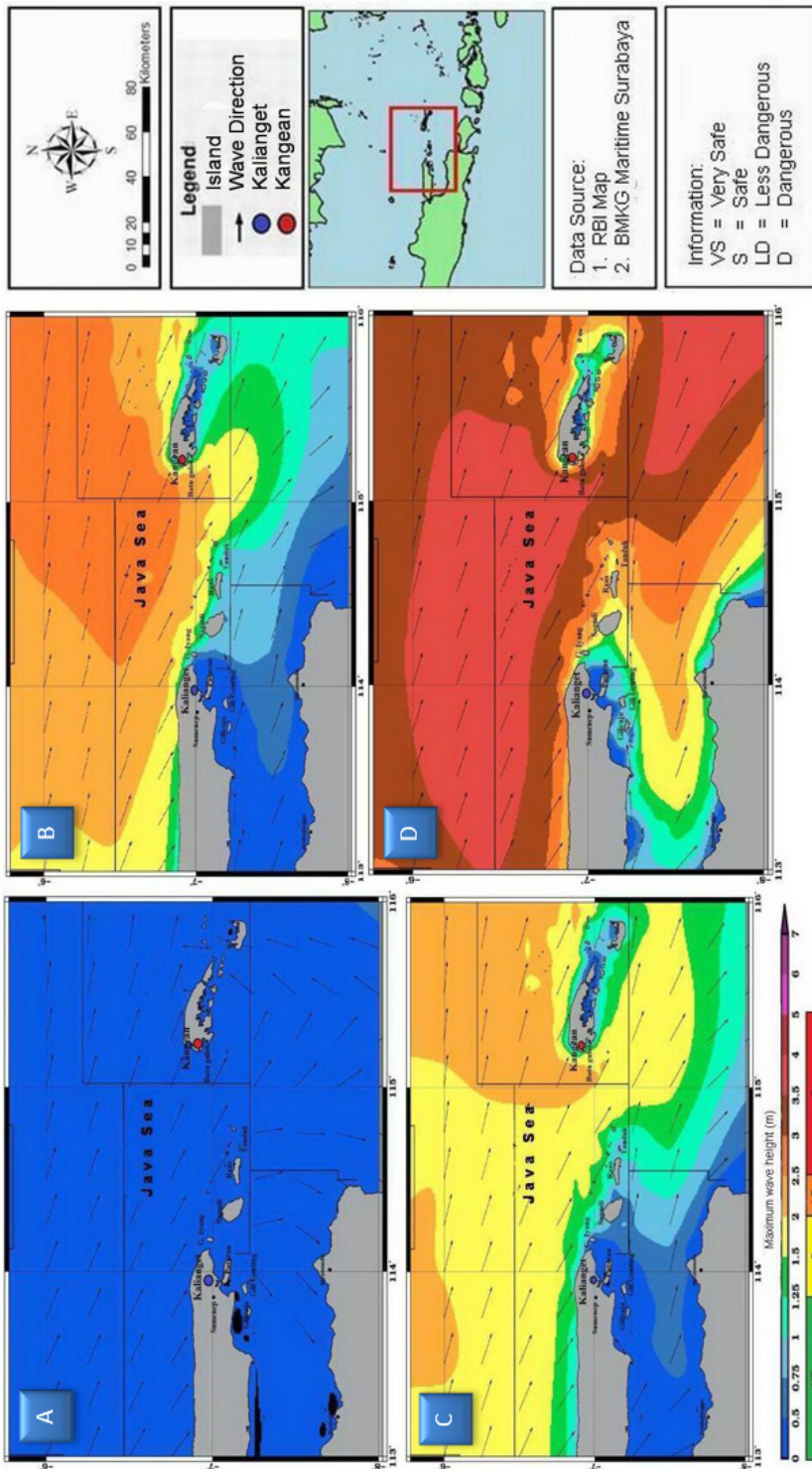
Figure 8. Weekly wave height fluctuations during November 2017-February 2018 which represent the peak of the west season

were observed further east in the sea before the Kangean waters, which potentially reaches 5 m, although the consequent approach towards the Kangean port showed another decline to <2 m.

The wind and wave conditions in waters between Kalianget and Kangean moved steadily from northwest-west. This condition reflects the strong influence of (western) season, particularly at study sites situated at parts of the Java Sea. In addition, the west monsoon is characterized by both resilient blows in the northwest-west direction, as well as strong winds and high waves, in contrast with the monsoon season, which features relatively weak and unstable airstreams.

Wind-generated surface gravity waves occur everywhere in the oceans and play a primordial role in the oceans in the dynamics of the sea-land-atmosphere interface. In particular, sea surface wind waves fluctuate over a time span from a few seconds to several hours (Guillaume, et al. 2011). The waves are a combination of local sea-winds and large waves originating from a distant hurricane. Waves are most commonly caused by wind. Wind-driven waves, or surface waves, are created by the friction between wind and surface water. As wind blows across the surface of the ocean or a lake, the continual disturbance creates a wave crest (National Oceanic and Atmospheric Administration, 2021).

The size of the waves generated by the wind depends on the speed and duration of the wind, as well as the fetch which is the open water rapids where the wind blows. In addition, the depth of the sea also plays a role, because it is difficult to produce large waves in shallow waters. The invasion of the inter-tropical convergence zone (ITCZ) to the north or south due to the asymmetry of the continents of Eurasia and Australia caused a monsoon which



led to a wet (rainy) and dry (drought) period (Yamanaka, 2016). Monsoon, which is the 'Major Regime of Seasonal Wind Reversal,' is influenced by countries in Southeast Asia, including Indonesia as a maritime continent (Khan, 2020). These results also demonstrate the tendency to cause elevation in the wave height of waters between Tanduk and Kangean Islands. Furthermore, this phenomenon is possible through the effect of bathymetry depth as well as the incidence of narrowing on the north-south side of waters investigated. The silting effects around Kalianget and Kangean seaports are debilitating. Hence, the surrounding wave conditions are considered relatively safe for cruise.

Therefore, changes in surface wind speed and wave height may dramatically affect coastal communities (Ranasinghe, 2016), as well as offshore operations (Bitner-Gregersen et al. 2018).

CONCLUSIONS

The wind and wave characteristics between 2008 and 2017 generally form two peaks per annum and are known to mark the main seasons (west and east). Also, two valleys were observed in the middle, which further denotes the transition periods. The wind speed and wave height tend to generally occur below the danger threshold (<10 knots and <2 m). However, there are exceptions in the west season, especially in January, featuring significant peak values during periods of strengthened wind speed and wave height with a steady blow. The maximum levels recorded reached 29 knots and 6.7 m, respectively.

The weekly wind and wave conditions during December 2017 to February 2018 were relatively safe for sailing. Meanwhile, extreme conditions observed in January 23-29, 2018 were characterized by a maximum value of 25 knots and 3.8 m, respectively, and further considered as dangerous.

The Kalianget-Kangean cruise channel is relatively safe, except in the time span of the west season, known to extend from December to February. This period features wind speeds exceeding 21 knots, with wave height reaching 2.5 m, and the route was therefore determined to be dangerous in the west season.

ACKNOWLEDGMENTS

The authors gratefully acknowledge Professor Supartono for his invaluable inspiration. This research was supported by Hang Tuah University, Surabaya, Indonesia.

REFERENCES

- Aji, D. R. (2015). Analisa karakteristik kecepatan angin dan tinggi gelombang menggunakan data satelit altimetri [Analysis of wind speed characteristics and wave height using altimetry satellite data]. *Journal of Geodesy and Geomatics*, 11(1), 75-78. <http://dx.doi.org/10.12962/j24423998.v11i1.1102>
- Arisandi, A., Tamam B., & Fauzan, A. (2018). Coral reef profile of Kangean Island, Sumenep District, Indonesia. *Jurnal Ilmiah Perikanan dan Kelautan*, 10(2), 104-111. <http://dx.doi.org/10.20473/jipk.v10i2.10516>

- Badan Meteorologi, Klimatologi, dan Geofisika. (2019). *Data angin tahunan 2008-2017 Sumenep, Jawa Timur, Indonesia* [Annual wind data 2008-2017 Sumenep, East Java, Indonesia]. Author.
- Badan Meteorologi, Klimatologi, dan Geofisika. (2018). *Saran keselamatan pelayaran* [Recommendation for cruise safety]. Retrieved February 26, 2021, from <http://maritim.bmkg.go.id>
- Bitner-Gregersen, E. M., Vanem E., Gramstad, O., Hørte, T., Aarnes, O. J., Reistad, M., Breivik, Ø., Magnusson, A. K., & Natvig, B. (2018). Climate change and safe design of ship structures. *Ocean Engineering*, *149*, 226-237. <https://doi.org/10.1016/j.oceaneng.2017.12.023>.
- Faqih, A. (2014). *Prospek pengembangan potensi sumberdaya kelautan kepulauan Sumenep Madura* [Prospect of marine resources potential development in Sumenep Madura Islands]. Universitas Brawijaya Press.
- Guillaume, D., Angélique, M., Fabrice, A., Xavier, B., Déborah, I., & Rafael, A. (2011). The contribution of wind-generated waves to coastal sea-level changes. *Surveys in Geophysics*, *40*(6), 1563-1601. <https://doi.org/10.1007/s10712-019-09557-5>
- Khan, M. S. A. (2020). Climate change effect on southeast Asia's monsoon rainfall. *International Journal of Advance Scientific Research and Engineering Trends*, *5*(9), 118-123.
- Muhsoni, F. F. (2015). Pemanfaatan citra satelit LDCM untuk pemetaan kerapatan tajuk mangrove dan terumbu karang [Utilization of LDCM satellite imagery for mapping of mangrove and coral reef canopy density]. In *Prosiding Seminar Perikanan dan Kelautan*, (pp. 601-609). UTM Press.
- National Oceanic and Atmospheric Administration. (2021). *Why does the ocean have waves?* Retrieved February 26, 2021, from <https://oceanservice.noaa.gov/facts/wavesinocean.html>
- Nugraha, W. A., Hidayah, Z., & Insafitri. (2013). *Developing coral reef conservation zones in the Kangean Archipelago, Indonesia*. SEAMO SEARCA.
- Ranasinghe, R. (2016). Assessing climate change impacts on open sandy coasts: A review. *Earth-Science Reviews*, *160*, 320-332. <https://doi.org/10.1016/j.earscirev.2016.07.011>.
- Rini, D. A. S., Pratikto, W. A., & Sambodo, K. (2015). Identifikasi potensi kawasan sumberdaya Pulau Kangean Kabupaten Sumenep Madura sebagai kawasan wisata bahari [Identification of the potential of the Kangean Island resource area in Sumenep Madura Regency as a marine tourism area]. *Indonesian Journal of Marine Science and Technology*, *8*(2), 60-70. <https://doi.org/10.21107/jk.v8i2.814>
- Sandino, L. A., Bejar M., Kondak, K., & Ollero, A. (2016). Multi-sensor data fusion for a tethered unmanned helicopter using a square-root unscented Kalman filter. *Unmanned Systems*, *4*(4), 273-287. <https://doi.org/10.1142/S2301385016500114>
- Scotta, D., & Lemieux, C. (2010). Weather and climate information for tourism. *Procedia Environmental Sciences*, *1*(2010), 146-183. <https://doi.org/10.1016/j.proenv.2010.09.011>
- Slamet, H. D. (2020). Kapal kangean tak beroperasi akibat cuaca buruk [Kangean ship not operating due to bad weather]. *PortalMadura*. Retrieved February 26, 2021, from <https://portalmadura.com/kapal-ke-kangean-tak-beroperasi-akibat-cuaca-buruk-217429/>
- Yamanaka, M. D. (2016). Physical climatology of Indonesian Maritime Continent: An outline to comprehend observational studies. *Atmospheric Research*, *178-179*(2016), 231-259.

Spatial Distribution of Picophytoplankton in Southeastern Coast of Peninsular Malaysia Using Flow Cytometry

Roswati Md Amin¹, Md Suffian Idris^{1*}, Nurul Asmera Mudiman¹, Noor Hazwani Mohd Azmi² and Hing Lee Siang¹

¹Faculty of Science and Marine Environment, Universiti Malaysia Terengganu, 21030 Kuala Nerus, Terengganu, Malaysia

²Institute of Oceanography and Environment, Universiti Malaysia Terengganu, 21030 Kuala Nerus, Terengganu, Malaysia

ABSTRACT

The distribution of picocyanobacteria from two genera, *Synechococcus* and *Prochlorococcus*, and picoeukaryotes in surface water (0.5 m) was investigated by flow cytometry in the southeastern coast of Peninsular Malaysia during the Southwest monsoon in August 2014. During the cruise, *Synechococcus* cells were predominant throughout the study area, contributing as much as 50% to the total picophytoplankton population, whereas picoeukaryotes and *Prochlorococcus* constituted only 31% and 19% of the population, respectively. Spatially, *Synechococcus* and picoeukaryotes were more dominant in coastal waters, while *Prochlorococcus* appeared to be more highly abundant in offshore waters. Furthermore, the percentage contribution of each population to total picophytoplankton also exhibited different spatial distribution patterns along a coastal-offshore gradient. The percentage contribution of *Synechococcus* was spatially constant throughout the study area, while the fraction contributed by picoeukaryotes showed a reduced contribution from coastal to offshore waters. In contrast, *Prochlorococcus* exhibited an increased proportion to total picophytoplankton across

ARTICLE INFO

Article history:

Received: 18 December 2020

Accepted: 24 February 2021

Published: 19 July 2021

DOI: <https://doi.org/10.47836/pjst.29.3.18>

E-mail addresses:

roswati_ma@umt.edu.my (Roswati Md Amin)

suffian@umt.edu.my (Md Suffian Idris)

nurulasma.mudiman@gmail.com (Nurul Asmera Mudiman)

noorhazwanimohdazmi@gmail.com (Noor Hazwani Mohd Azmi)

lshing@umt.edu.my (Hing Lee Siang)

*Corresponding author

a coastal-offshore gradient, suggesting the increasing importance of this population in offshore waters of the study area. As revealed by Canonical Correlation Analysis, the abundance of *Synechococcus* and picoeukaryotes increased significantly with reducing dissolved oxygen levels and pH, and with increasing total chlorophyll. In contrast, temperature was the only factor influencing the abundance of *Prochlorococcus* significantly increased with decreasing water temperature in the study area. Overall, results of the present study provide valuable information on the role of regional environmental factors in the distribution and dominance of picophytoplankton communities that are not only critical for the ocean productivity but also the impact on the carbon cycle in the study area.

Keywords: Picoeukaryotes, picophytoplankton, *Prochlorococcus*, South China Sea, *Synechococcus*

INTRODUCTION

Picophytoplankton, generally known as phytoplankton with a diameter of less than 2 or 3 μm , is the smallest phytoplankton class composed of both prokaryotes and eukaryotes. The eukaryotes (0.8–3 μm) are a taxonomically complex group comprising members of four algal phyla: The Chlorophyta, Haptophyta, Cryptophyta and Heterokontophyta (Vaulot et al., 2008). The prokaryotes are a member of the Cyanobacteria, class Cyanophyceae and order Synechococcales and are subdivided into the genera *Prochlorococcus* (~0.6 μm) and *Synechococcus* (~1 μm). Picophytoplankton has been described as the smallest known autotrophic species; it is of great significance and present in all oceanic provinces. They contribute up to 90% of chlorophyll present in particulate matter < 2.0 μm (Guiry & Guiry, 2016; Miyashita, 2015; Scanlan, 2012).

Synechococcus distribution is ubiquitous from the open ocean to the coastal area in most of the world's oceans (Gin et al., 2003; Li, 1998) while *Prochlorococcus* tends to be abundant in oligotrophic waters (Campbell et al., 1994; Partensky et al., 1999a; Partensky et al., 1999b). Although the abundance of *Prochlorococcus* generally exceeds *Synechococcus* in areas where they co-exist, there are several conditions that allow *Synechococcus* to thrive. These include regions that are permanently or seasonally enriched with nutrients (Partensky et al., 1999a). Meanwhile, *Prochlorococcus* thrives through the euphotic zone of tropical and subtropical oligotrophic oceans (Chisholm et al., 1988). This is due to traits that make them well-adapted to the oligotrophic environment (Biller et al., 2015) such as a small size that facilitates efficient nutrient and enhanced light absorption (Moore et al., 1995). As a result, these traits enable *Prochlorococcus* to thrive at low light intensities (Moore et al., 1995) and in deeper waters (Zwirgmaier et al., 2008). On the other hand, autotrophic picoeukaryotes show enhanced abundance in coastal eutrophic waters, where they can surpass picocyanobacteria in terms of biomass (Pan et al., 2007).

Prokaryotic growth and distribution studies in most oceanic regions indicate that prokaryotes have a significant effect on carbon cycling processes, not only by assimilating photosynthetically derived organic matter but also by serving as a major food resource for heterotrophic flagellates, ciliates (Gasol et al., 1997; Lønborg & Søndergaard, 2009). Several biotic and abiotic factors can interact to affect the picoplankton assemblage composition and cell abundances. Abiotic factors, known to drive bottom-up control include temperature, salinity, as well as availability of light and nutrient. Biotic factors attributed to top-down control, include predation by nano- and microzooplankton, as well as virioplankton lysis (Evans & Brussaard, 2012).

Despite the growing knowledge of picophytoplankton, *Prochlorococcus* and *Synechococcus* and their co-occurrence in ocean and coastal waters, little is known about their abundance and distribution in Malaysian waters. The distribution of picophytoplankton in tropical water has been the subject of past research in the Philippines (Agawin et al., 2003; Zhao et al., 2010), Vietnam, western South China Sea (Chen et al., 2009) and Nansha Island, South China Sea (Yang & Jiao, 2004). However, to date only data on the abundance of *Prochlorococcus* and *Synechococcus* in the Johor Strait, Malaysia is published (Gin et al., 2000; Gin et al., 2003). Latest reports on general phototrophic picoplankton studies are available, i.e., on the diel variation and distribution in mangrove areas of Melaka (Lee et al., 2006) and Klang estuary (Lee et al., 2013). Therefore, this is the first study on the distribution of *Synechococcus*, *Prochlorococcus* and picoeukaryotes, documented by using a flow cytometer, in the southeastern coast of Peninsular Malaysia. This aims to increase our understanding on the structures of phytoplankton assemblages in our areas. Direct analysis using flow cytometry provides information on the abundance and pigment content of the major photosynthetic picophytoplankton groups (Marie et al., 2005).

MATERIALS AND METHODS

Field Sampling and Study Area

Field sampling was conducted in the southeastern coast of Peninsular Malaysia from 18th to 24th August 2014 on board UMT's RV Discovery, covering an area from Pahang to Johor waters (1° 45' - 4° 00' N and 103° 30' - 104° 44' E) (Figure 1). Samplings were performed at 18 stations along 6 coastal-offshore transects from depths between 10 m and 70 m. Each transect (denoted by numbers 1 to 6) consists of three to four measurement stations located between coastal (stations with letter "a") and offshore waters (stations with letter "d").

At each station, hydrographical parameters of the surface water, such as temperature, salinity, pH, and dissolved oxygen (DO) were measured from vertical profile with a CTD (SBE 19 plus, Sea-Bird Electronic Inc., USA). This instrument was calibrated by the manufacturer before the cruise. A known volume of water samples (1 - 5 L depending on particle load) for chlorophyll (Chl) and picophytoplankton abundance were collected using a

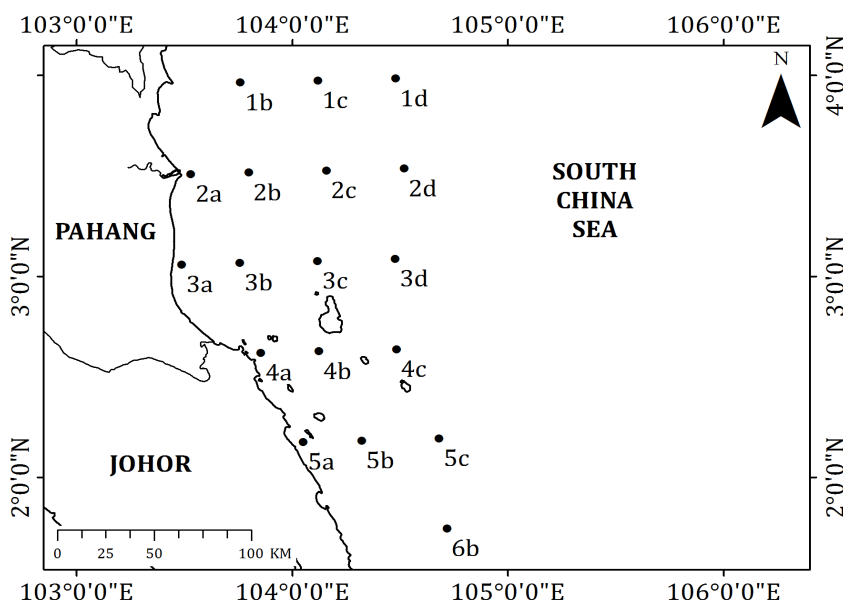


Figure 1. Location of sampling stations in southeastern coast of Peninsular Malaysia

water pump from approximately 0.5 m depth and transferred into a 10 L dark bottle. Water samples were filtered onboard immediately after collection under low vacuum pressure (less than 0.5 atm). For the total chlorophyll (TChl) concentration, only one replication of water sample was collected at each station and samples were directly concentrated onto 0.7- μm pore-size Whatman glass-fibre filters (GF/F). For flow cytometry counts, triplicate 2 mL of water samples were collected with GF/D (2.7 μm) and fixed immediately with 10% cold glutaraldehyde (final concentration 1%). All samples were stored in the dark at -20°C until analysis in the laboratory (Vaulot et al., 1989).

Laboratory Analysis of Chlorophyll Concentration and Flow Cytometry

Chlorophyll concentration was determined spectrophotometrically using a Shimadzu double beam Spectrophotometer (Agilent Technologies). The particulate matter retained on the filters was extracted in 90% acetone before being refrigerated at 4°C for 8 to 24 hours. The chlorophyll absorbances were determined at 750 (background correction), 664, 647 and 630 nm, with 1 cm quartz cuvette. To ensure accurate and consistent results, the spectrophotometer was programmed to take at least five repeated measurements of absorbance and averaged to a single value if the coefficient of variation (cv) was below 50%. Absorbances of each wavelength were referenced against a buffered 90% acetone blank which was inserted after every 4-5 samples. The trichromatic equations of Jeffrey

and Humphrey (1975) were used to convert absorbances to concentrations of chlorophyll. Since this method may include contributions from other pigments (especially phaeophytin), the symbol TChl rather than Chl-a will be used hereafter to represent the chlorophyll concentration.

Cell abundance of *Synechococcus*, *Prochlorococcus* and picoeukaryotes were determined according to Liu et al. (2014) using a BD Accuri™ C6 flow cytometer (Ann Arbor, MI, USA) excited with blue (488 nm) and red (640 nm) emissions of argon lasers, and four fluorescent emission optical filters (FL1-FL4). Prior to analysis, samples were thawed at room temperature and maintained on ice in a dark container until processing. Approximately 100 µL of sample was run under medium flow rate (35 µL min⁻¹), with a threshold set at 800 for chlorophyll (FL3) axis. Forward scatter (FSC; indicative of the cell size and shape), side scatter (SSC; indicative of cell granularity), chlorophyll (Chl; >640 nm, FL3), phycocyanin (PC; 675 ± 12.5 nm, FL4), and phycoerythrin (PE; 585 ± 20 nm, FL2) were recorded for each cell. Picophytoplankton groups were discriminated and specified according to their specific fluorescence properties, based on FL2 (orange fluorescence) vs. FL3 (red fluorescence) and side scatter vs. FL3 signatures (Liu et al., 2014).

Data Analysis

Flow cytometric data were analyzed using the Flowjo software (Treestar, Inc., www.flowjo.com). The Pearson correlation and Canonical Correlation Analysis (CCA) were used to determine the relationship between picophytoplankton groups (*Synechococcus*, *Prochlorococcus* and picoeukaryotes) and environmental factors (TChl, temperature, salinity, pH, and DO). Picophytoplankton abundances were log-transformed prior to CCA analysis. All statistical analyses were performed using R software version 3.6.0 (CCA and CCP packages; <https://cran.r-project.org/web/packages/>).

RESULTS

Hydrographical Parameters

The data range of hydrographic and biogeochemical parameters (surface temperature, salinity, pH, DO, and TChl) during the study period are summarized in Table 1 while Figure 2 shows their spatial distributions. In general, all the hydrographic parameters (temperature, salinity, pH, and DO) varied little from coastal to offshore waters (coefficient of variation, $CV < 1.5\%$) (Table 1). Sea surface temperature varied from 28.47 to 29.65 °C with the mean of 29.01 ± 0.31 °C and no discernible spatial pattern was observed in the horizontal temperature gradient from coastal to offshore waters (Figure 2A). The non-uniform spatial pattern of surface temperature could probably be due to diurnal warming as field observations at each station were made during different daylight hours. As can be seen in Figure 2A, the highest water temperature (~29.4°C) was found

at the coastal stations (stations 2a and 3a) and in the middle of the study area (station 4b) while the lowest temperature ($\sim 28.5^{\circ}\text{C}$) was mainly observed in offshore stations. Isolated, small patches of colder waters were also observed at stations 1b and 4a. In general, the water column was almost isothermal (well-mixed) in coastal waters but showed strong thermal stratification, with mixed layer depth of more than 40 m in offshore waters (Figure 3A). The surface salinity for the entire dataset varied slightly, ranging from 32.34 to 33.11 psu, with the mean value of 32.70 ± 0.22 psu. Spatially, high salinity values (> 33 psu) were observed in coastal waters distributed along the northern regions of the study area. Water masses of low salinity (~ 32.5 psu) flanked on either side by high-salinity waters were also observed in the central part of the study area (Figure 2B). High saline waters were mainly found at stations 2b and 3b, while low saline waters were found at station 5b. Similar to the trend observed in temperature, the vertical salinity at near-shore stations was almost homogeneous (between 32.3 and 33.1 psu) through the whole water column but was well-stratified at offshore stations (Figure 3B). The effects of river discharge and tidal mixing are suggested to be the dominant factors influencing salinity distribution in the study area. Surface pH varied over a small range (8.08 - 8.22), averaging about 8.15 ± 0.04 (Table 1). The distribution of this parameter showed a clear spatial variability, with low pH water masses ($\sim \text{pH } 8.1$) mainly found along the coast and more alkaline waters ($\sim \text{pH } 8.2$) at offshore stations (Figure 2C). Differently from pH, DO displayed patches of oxygen depletions ($\sim 5.7 \text{ mg L}^{-1}$) at coastal stations (stations 4a and 5a) and maximum values ($\sim 6.0 \text{ mg L}^{-1}$) in the middle parts of the study area (stations 4b and 5b) and offshore stations (station 1d) (Figure 2D). Across the study area, measured DO values varied from a minimum of 5.74 to a maximum of 6.07 mg L^{-1} (5.95 ± 0.09). In general, total chlorophyll (TChl) concentrations showed a clear difference in values ($CV = 64.1\%$), with relatively clear waters and low concentrations ($\sim 0.2 \text{ mg m}^{-3}$) at offshore stations and high values ($\sim 0.8 \text{ mg m}^{-3}$) at coastal stations with the highest concentration of TChl ($\sim 1.0 \text{ mg L}^{-1}$) was mainly found at station 3a (Figure 2E). The concentration of TChl for the entire data set varied widely from coastal to offshore stations, ranging from 0.17 to 0.94 mg m^{-3} (mean 0.37 ± 0.24) (Table 1).

The results of correlation analysis using the Pearson correlation coefficient between environmental variables are illustrated in Table 2. Analysis of data showed that pH had a strong positive correlation with DO concentration ($r=0.80$; $p<0.05$). Correlation analysis also revealed that TChl concentration had a strong negative correlation with pH ($r=-0.77$; $p<0.05$) and DO ($r=-0.71$; $p<0.05$) but only a weak positive correlation with temperature ($r=0.47$; $p<0.05$). No significant relation ($p>0.05$) was observed between TChl and salinity. On the hand, a significant weak correlation ($r=0.40$; $p<0.05$) was also found between temperature and salinity.

Table 1

Average (mean \pm standard deviation), range, and coefficient of variation (CV, %) values of surface temperature, salinity, pH, dissolved oxygen (DO) and total chlorophyll (TChl) concentration); of all stations during August 2014 in the southeastern coast of Peninsular Malaysia

Parameter	Temp ($^{\circ}$ C)	Salinity (psu)	pH	DO (mg L^{-1})	TChl (mg m^{-3})
Average	29.01 \pm 0.31	32.70 \pm 0.22	8.15 \pm 0.04	5.95 \pm 0.09	0.37 \pm 0.24
Range	28.47 - 29.65	32.34 - 33.11	8.08 - 8.22	5.74 - 6.07	0.17 - 0.94
CV	1.10 %	0.70 %	0.50 %	1.50 %	64.10 %

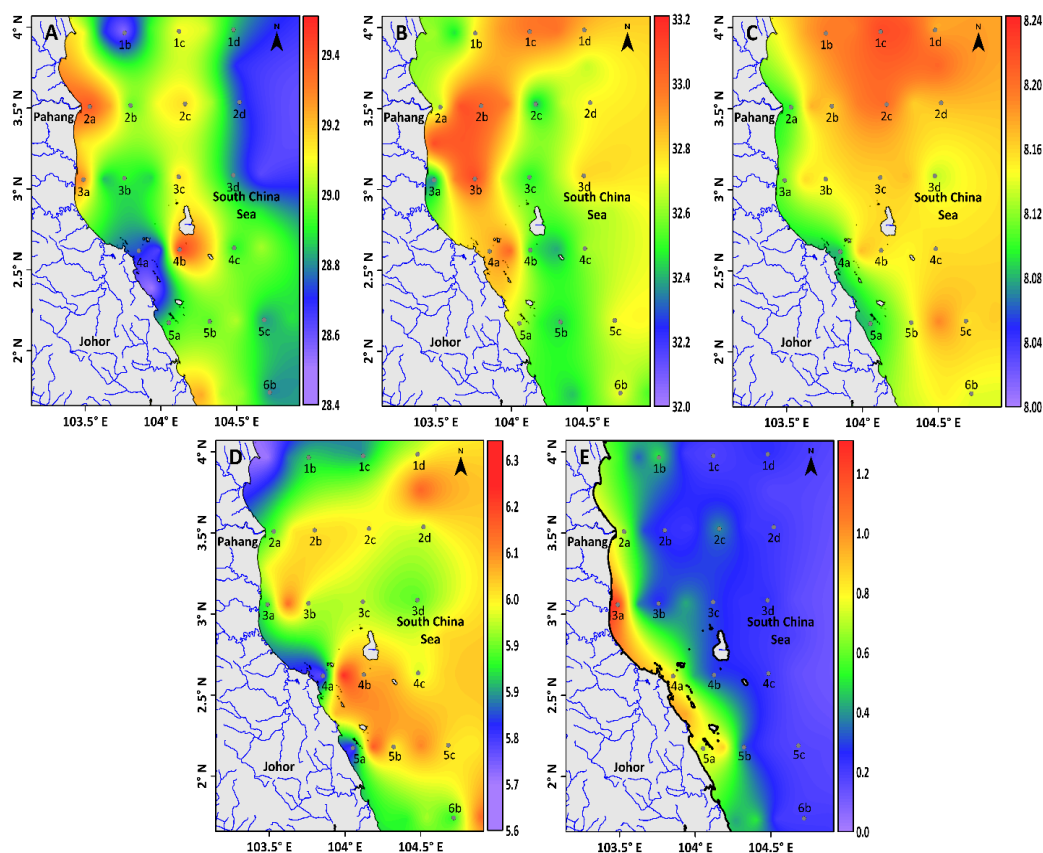


Figure 2. Spatial distributions of sea surface (A) temperature ($^{\circ}$ C), (B) salinity (psu), (C) pH, (D) dissolved oxygen (mg L^{-1}), and (E) TChl (mg m^{-3}) in the southeastern coast of Peninsular Malaysia

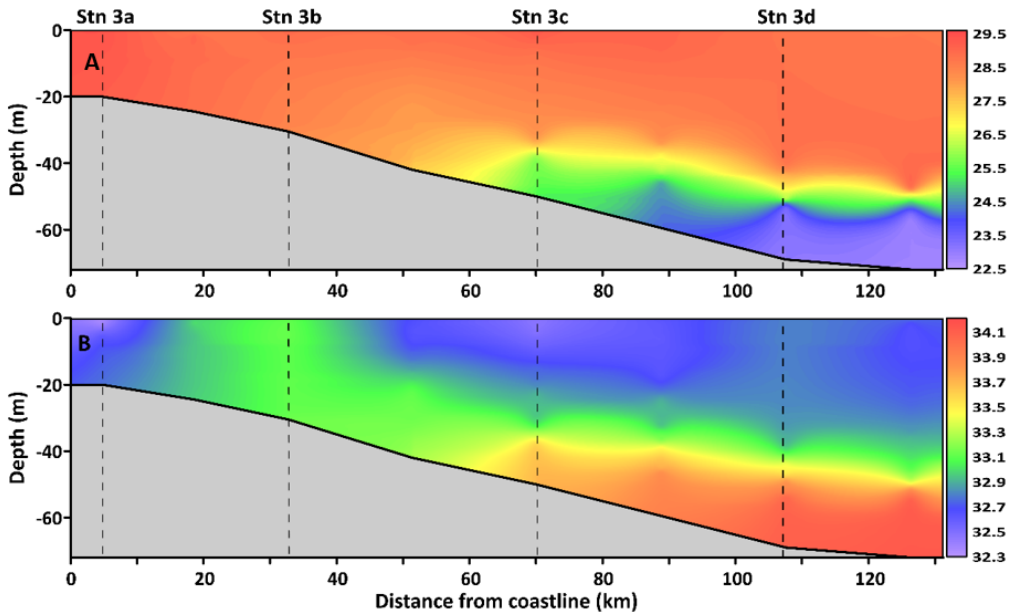


Figure 3. Cross section of water (A) temperature (°C) and (B) salinity (psu) along a transect between stations 3a and 3d. The water column was almost homogeneous at stations 3a and 3b but showed strong vertical stratification at stations 3c and 3d, with mixed layer depth of about 40 m

Table 2

Pearson's correlation coefficient (*r*) amongst physicochemical factors. Significant correlations ($p < 0.05$) are given in bold

Variables	Temperature	Salinity	pH	DO
Temperature				
Salinity	-0.40			
pH	-0.22	0.12		
DO	-0.06	-0.03	0.80	
TChl	0.47	-0.38	-0.77	-0.71

Picophytoplankton Distribution and Abundance

At all sampling stations, all picophytoplankton groups (i.e., *Synechococcus*, *Prochlorococcus* and picoeukaryotes) were identified according to their specific fluorescent properties and light scatter profiles. Overall, *Synechococcus* formed the dominant component of the

picophytoplankton populations, covering about 72% of the surface waters in the study area. This was followed by Picoeukaryotes (6%) while the remaining stations (22%) corresponded to the mixed picophytoplankton population. Although present at most stations, *Prochlorococcus* was not the dominant contributors (< 35%) to the picophytoplankton community at any station.

Table 3 summarizes the data range of total picophytoplankton, and their respective groups and Figure 4 presents the spatial distribution of all picophytoplankton groups during the study period. As with TChl distribution, the population of total picophytoplankton displayed an obvious spatial distribution pattern (CV=41%), averaging about one order of magnitude higher in coastal waters than in more clear offshore waters. The surface abundance of total picophytoplankton was highly variable, ranging from 4.61 to 24.29 x10⁴ cells ml⁻¹ (mean 14.61± 6.01), where the highest cell density was observed at station 5a and the lowest at station 1c. The most dominant picophytoplankton, *Synechococcus*, showed a high variability in density, with an average value of 7.36 ± 3.29 x10⁴ cells ml⁻¹, accounting for 50.3% of the total picophytoplankton abundance. The maximum *Synechococcus* abundance was primarily distributed along the coast and progressively decreased seaward, although relatively high densities (as high as ~8.0 x 10⁴ cells ml⁻¹) were observed to have spread far offshore and moved northeast in the direction of the prevailing wind (Figure 4A). Along the coast, higher surface densities of *Synechococcus* were clearly apparent in the Pahang coastal waters, especially at stations 1b and 2a, than those observed in Johor waters. On the other hand, *Prochlorococcus* was poorly represented in density (<19% of total picophytoplankton), with an average value of 2.59 ± 1.42 x10⁴ cells ml⁻¹. In contrast to *Synechococcus* and picoeukaryotes, the *Prochlorococcus* population (Figure 4B) showed a patchy surface distribution pattern that did not vary spatially from coastal to offshore waters. The highest density of *Prochlorococcus* was clearly observed at two intermediate stations (stations 1b and 6b) while the lowest density was mostly dominated in the middle parts of the study area and at a few coastal stations (stations 2a, 3a, and 5a). It was also shown that there was a slightly increasing trend in *Prochlorococcus* abundances from the middle parts of the study area to the open oceanic waters. Picoeukaryotes was the second most abundant picophytoplankton group in the area, constituting an average of 30.8% of the total picophytoplankton. On average, 4.66 ± 3.33 x10⁴ cells ml⁻¹ of picoeukaryotes was measured in the study area. Similar to *Synechococcus* distribution, the picoeukaryotes assemblage (Figure 4C) was characterized by a strong decreasing density gradient, with maximum values concentrating along the coast and minimum values in the offshore waters. Contrary to what has been observed in *Synechococcus*, the maximum densities of picoeukaryotes were particularly confined to the southern coast of Johor, with the highest value observed at station 5a.

Table 3

Average density (mean \pm standard deviation), range, and coefficient of variation (CV, %) values of total picophytoplankton, *Synechococcus*, *Prochlorococcus* and picoeukaryotes in surface water of southeastern coast of Peninsular Malaysia

Picophytoplankton group	Average Density ($\times 10^4$ cells ml^{-1})	Range	CV
<i>Synechococcus</i>	7.36 ± 3.29	2.13-13.65	45%
<i>Prochlorococcus</i>	2.59 ± 1.42	0.52-5.86	55%
Picoeukaryotes	4.66 ± 3.33	1.37-14.43	71%
Total picophytoplankton	14.61 ± 6.01	4.61-24.29	41%

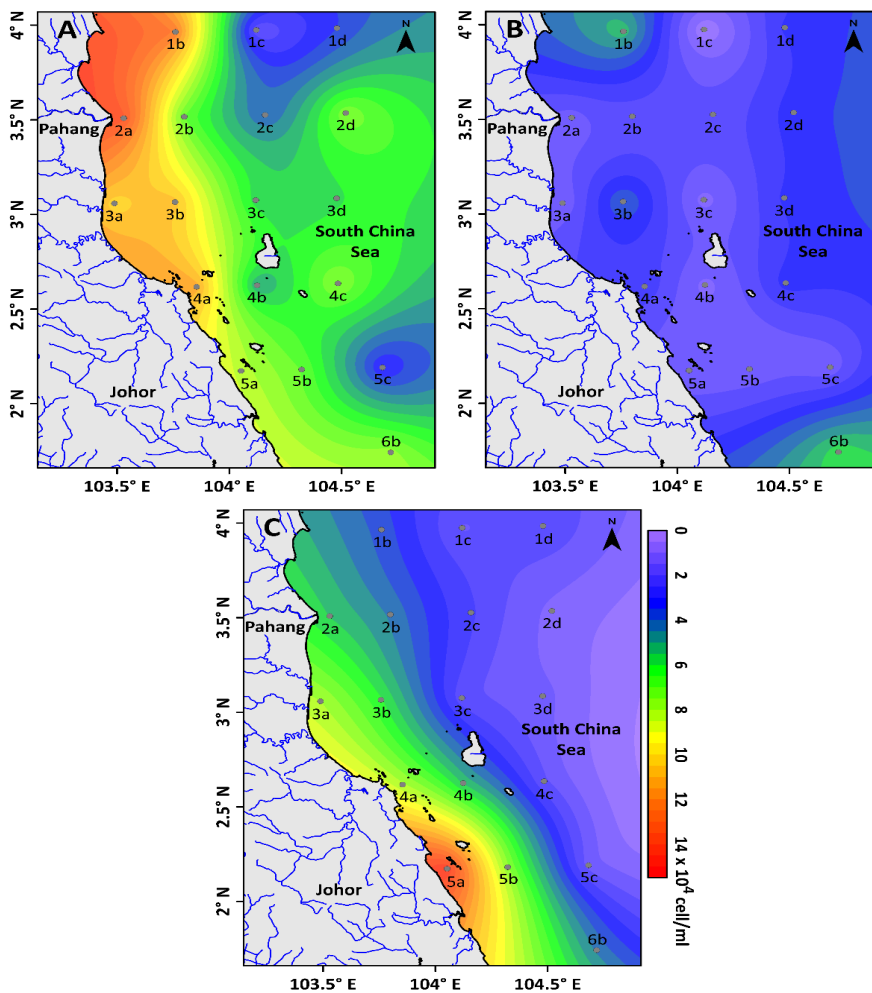


Figure 4. Spatial distributions of surface abundance ($\times 10^4$ cell ml^{-1}) of A) *Synechococcus*, B) *Prochlorococcus* and C) picoeukaryotes in the southeastern coast of Peninsular Malaysia

Differences in the fraction contributed by each picophytoplankton group along the coastal-offshore gradients were also assessed with all data were pooled according to distance from the coastline. The percentage contribution to total picophytoplankton along coastal-offshore stations showed a clear difference between each picophytoplankton assemblage (Figure 5). The relative contribution of *Synechococcus* was slightly high with increasing distance offshore (from 50 to 52%), indicating the strong ability of this assemblage to adapt to a range of environmental conditions. Meanwhile, the relative contribution of picoeukaryotes to total picophytoplankton showed a decreasing linear trend, from ~40% at the coastal stations to ~18% at the offshore stations, suggesting the decreasing importance of this assemblage among picophytoplankton groups with increasing distance offshore. In contrast, the minimum contribution of *Prochlorococcus* was found at the coastal stations (<10%), rather than at the offshore stations (~30%).

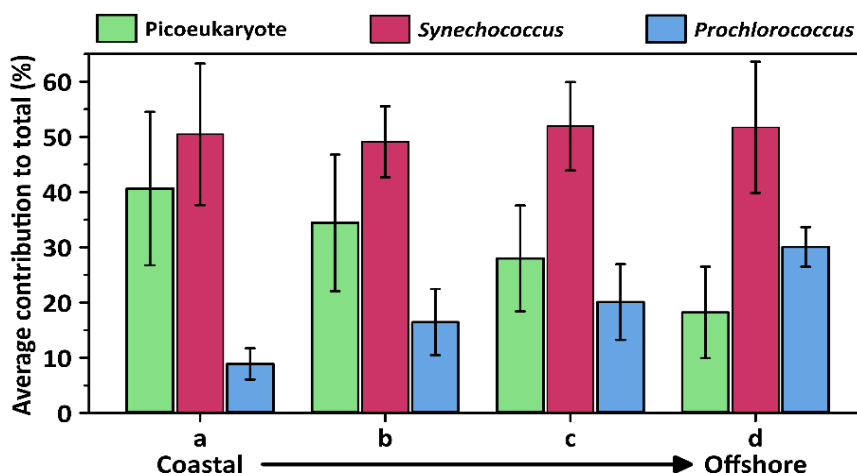


Figure 5. Relative contribution (%) of picoeukaryotes, *Synechococcus* and *Prochlorococcus* assemblages to total picophytoplankton population from coastal (a) to offshore stations (d) in the southeastern coast of Peninsular Malaysia. Error bars represent one standard deviation of the mean

Influence of Environmental Conditions on Picophytoplankton Populations

The correlation between picophytoplankton groups and environmental conditions identified with Canonical Correlation Analysis (CCA) is depicted in Figure 6. The first two axes of CCA (F1 and F2) were significant ($p < 0.03$) as evidenced by the Wilks' Lambda test, explaining 90% of the variability in the picophytoplankton and environmental conditions relationship (55.2% and 34.9% for axes 1 and 2, respectively). Moreover, there were strong correlations between picophytoplankton groups and environmental variables for the first axis ($r = 0.92$, $p < 0.03$) and second axis ($r = 0.73$, $p < 0.03$), indicating a strong influence of environmental factors on the distribution of picophytoplankton population in the study area. The first environmental canonical axis (F1) was most negatively

correlated with TChl ($r = 0.93$) and most positively correlated with pH ($r = 0.88$) and DO ($r = 0.66$), while the second environmental axis (F2) was most negatively associated with temperature ($r = 0.87$) and positively associated with DO ($r = 0.63$) (Figure 6). For the picophytoplankton canonical variable, the first axis (F1) was most negatively correlated with total picophytoplankton ($r = 0.85$), *Synechococcus* ($r = 0.82$) and picoeukaryotes ($r = 0.78$), while the second axis (F2) was most negatively associated with *Prochlorococcus* ($r = 0.89$) and total picophytoplankton ($r = 0.53$) (Figure 6).

Correlations between the abundances of picophytoplankton assemblages and environmental conditions for both canonical axes (F1 & F2) (Figure 6 & Table 4) suggested that different assemblages were influenced by different environmental conditions. For the first canonical axis, total picophytoplankton, *Synechococcus* and picoeukaryotes had a strong positive correlation with TChl ($r = 0.72, 0.70, 0.66$), and negative correlation with pH ($r = -0.85, -0.76, -0.71$) and DO ($r = -0.76, -0.61, -0.64$). This indicates that an increased in TChl and a decrease in pH and DO would favor the development of these assemblages. In the second canonical axis, *Prochlorococcus* was the only assemblage to exhibit a strong negative association with temperature ($r = -0.66$), which indicated that low temperature is the favorable condition for their growth. Similar to the first canonical axis, total picophytoplankton, *Synechococcus* and picoeukaryotes also had a negative correlation with DO, suggesting that this environmental parameter had a significant influence on the abundance and composition of picophytoplankton community.

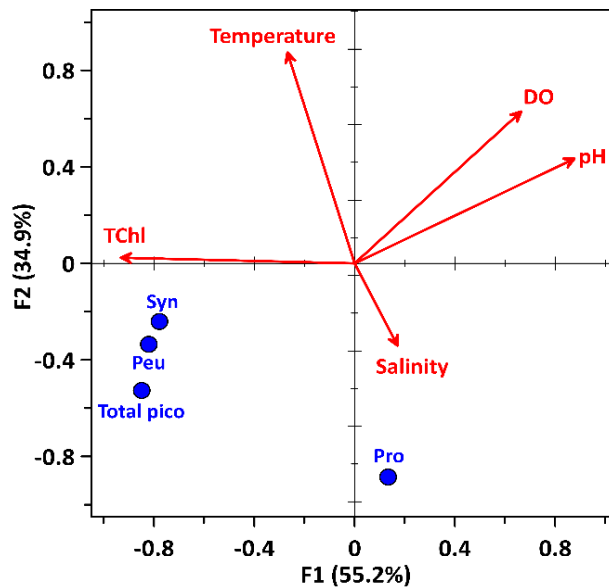


Figure 6. Canonical correlation analysis (CCA) ordination diagram of total (Total pico) and picophytoplankton groups (Syn: *Synechococcus*, Pro: *Prochlorococcus* and Peu: picoeukaryotes) with environmental variables (TChl, temperature, salinity, pH and DO) in the southeastern coast of Peninsular Malaysia. The percentage of the variation in the picophytoplankton groups for each axis (F1 and F2) is indicated in parentheses next to the axis label.

Table 4

Pearson's correlation coefficient (r) between physicochemical factors and total picophytoplankton, *Synechococcus*, *Prochlorococcus* and picoeukaryotes populations. Significant correlations ($p < 0.05$) are given in bold.

Variables	Total picophytoplankton	<i>Synechococcus</i>	<i>Prochlorococcus</i>	Picoeukaryotes
Temperature	-0.13	-0.08	-0.66	0.12
Salinity	0.00	0.02	0.31	-0.15
pH	-0.85	-0.76	-0.17	-0.71
DO	-0.76	-0.61	-0.29	-0.64
TChl	0.72	0.70	-0.13	0.66

DISCUSSION

Environmental conditions in the study area are generally associated with the monsoonal systems which have a great influence on the physical, chemical, and biological processes of the water column (Liu et al., 2002; Liu & Chai 2009; Powley et al., 2017; Wei et al., 2020). The results of this study clearly reveal the typical oligotrophic conditions with low concentrations of total Chlorophyll (TChl) dominated the surface water of the study area. Particularly during the southwest monsoon (SWM), strong vertical stratification due to sea surface heating and weak wind could result in nutrient limitation and low phytoplankton productivity (Zainol & Akhir, 2016; Akhir et al., 2014; Yanagi et al., 2001). High TChl levels along the coast especially at station very close to river mouths (e.g., station 3a) could be attributed to significant freshwater discharge that cause nutrient enrichment in coastal waters (Powley et al., 2017; Wei et al., 2020).

The present study showed that picophytoplankton was represented by *Synechococcus*, followed by picoeukaryotes and *Prochlorococcus*. The observed trend towards an increase of TChl concentration, consistent with an increase in picophytoplankton abundance indicated that these groups of phytoplankton are the dominant contributors to TChl in the study area, except for *Prochlorococcus*. The ubiquity of *Synechococcus* spp. during our study confirms the ability of this genus to adapt to a local coastal–offshore variable environment. *Synechococcus* is known to be ubiquitous in most of the world's oceans (Gin et al., 2003; Li, 1998) and can dominate in subtropical regions with stronger

temperature fluctuations. On the other hand, *Prochlorococcus* is commonly more abundant in oligotrophic waters (Campbell et al., 1994; Partensky et al., 1999a; Partensky et al., 1999b) and ubiquitous in the latitudinal band from 40°N to 40°S (Partensky et al., 1999b) while picoeukaryotes mainly dominated in coastal systems (Mouriño-Carballido et al., 2016). Although the maximum values for *Synechococcus* abundance found in this study are close to those reported in previous studies (Agusti et al., 2019; Chen et al., 2009), *Prochlorococcus* population abundance was found to be two-three orders of magnitude lower than the populations found in the global data set (Agusti et al., 2019; Flombaum et al., 2013). In accordance with our finding, studies reveal that *Synechococcus* accumulated higher than *Prochlorococcus* and picoeukaryotes in tropical and equatorial ocean from surface waters down to the base of thermocline (Partensky et al., 1999a; Mena et al., 2019; Pan et al., 2007). Contrastingly, some studies found *Prochlorococcus* to be more abundant than *Synechococcus* in the North Atlantic, South Pacific, North Indian basins (Buitenhuis et al., 2012), the subtropical and tropical ocean (Agusti et al., 2019; Chen et al., 2009), including south China Sea (Jiang & Sun, 2020; Wei et al., 2020).

These differences could be due to variation in phytoplankton adaptation to several factors such as temperature, photosynthetic active radiation (PAR), light conditions and nutrient, which may have led to the segregation of their maximal distributions across space and through time (Flombaum et al., 2013; Mella-Flores et al., 2012). Laboratory analysis showed that the optimum temperature for *Synechococcus* and *Prochlorococcus* growth was 24°C and 28°C, respectively (Moore et al., 1995). However, the results are most likely strain- or clone- specific as *Prochlorococcus* spp. has been detected at water temperatures of up to 30°C, with maximum integrated concentrations was between 26 and 29°C in the warm equatorial and South Pacific waters, and the Red Sea at the surface (Moore et al., 1995; Partensky et al., 1999b). A previous study in the upper 200 m of the subtropical regions of the Pacific, Atlantic and Indian oceans using a compilation of flowcytometry data indicates that the *Prochlorococcus* distributions were controlled by temperature and PAR(400–700 nm, Flombaum et al., 2013). However, this prediction of increasing abundance with increasing temperature in the subtropical and tropical ocean (Flombaum et al., 2013), is inconsistent with our results for the southeastern coast of Peninsular Malaysia. Our findings showed no clear effect of temperature on *Synechococcus* and picoeukaryotes, but *Prochlorococcus* abundance decreased with increasing temperature suggesting that high temperature negatively affects the *Prochlorococcus* concentration in the study area. This difference could be the result of different ecotype with different temperature optima or thermal sensitivity (Otero-Ferrer et al., 2018). The global model considering interactions between environmental variables predicted a population decline at the surface water with warming (Agusti et al., 2019), indicating that increased surface stratification, higher underwater PAR and Ultraviolet (UVB) penetration should inhibit

the surface populations of picophytoplankton in the water column. According to Agusti et al. (2019) and Wei et al. (2020), *Prochlorococcus* are more sensitive to light intensity and better adapted to absorb blue wavelengths that predominate deeper in the water column. Unfortunately, the abundance of *Prochlorococcus* ecotypes has not been assessed during this study to validate this.

Alternatively, according to Otero-Ferrer et al. (2018), nutrient supply was the main factor that determined the distribution of the picophytoplankton community in highly contrasting marine environments in the Atlantic Ocean. High abundances of *Synechococcus* and picoeukaryotes have been reported under nutrient-rich conditions typical of coastal surface waters affected by mixing or upwellings (Echevarría et al., 2009; Sherr et al., 2005). Previous research suggests that picophytoplankton commonly dominate in waters with concentrations of nutrient $<1 \mu\text{M}$. At higher concentrations, the contribution of picophytoplankton to total biomass and production decreased significantly (Agawin et al., 2000b). According to Liu et al. (1997) and Agawin (2000a), the optimal nutrient concentration for *Synechococcus* growth was $0.25 \mu\text{M}$ nitrogen (N) in the Mediterranean Sea and $0.1\text{--}3 \mu\text{M}$ N in the Arabian Sea. High concentrations of about $> 8 \mu\text{M}$ could inhibit *Synechococcus* growth. However, no data on nutrient concentration was recorded during this study period. A previous study has shown that surface nitrate was observed in a range between $1.6 \mu\text{M}$ (offshore) and $6.4 \mu\text{M}$ (coastal) in the Pahang coast (Shaari et al., 2013). Our results showed that *Synechococcus* are the most successful group among the picophytoplankton in Pahang coastal waters (Station 1a, 2b, Figure 4) where we would expect an influence of the nutrient derived from the riverine and the aquaculture area output to this area, as indicated in Shaari et al. (2013). Nevertheless, several studies could not find a clear relationship between nutrient concentration and cell abundance of picophytoplankton (Flombaum et al., 2013; Guo et al., 2014; Mouriño-Carballido et al., 2016; Wei et al., 2020).

Overall, both physical and biological parameters were likely to have an effect on DO values. Similarly, previous studies conducted in Ireland Estuary and Bengal Bay noticed a positive tight coupling between pH and DO (O'Boyle et al., 2013; Shaik et al., 2017). The significant correlation between pH and phytoplankton (both TChla concentrations and picophytoplankton density) indicated that biological activities had a substantial effect on pH (Shi et al., 2019). In general, when any aquatic environment is governed by autotrophy, CO_2 is eliminated by photosynthesis, resulting in a rise in pH values. In comparison, when heterotrophy is dominant, microbial respiration releases more CO_2 than photosynthetic carbon uptake, thus reduces pH level (Shaik et al., 2017). However, further research is needed to justify this in the study area.

Moreover, several studies have reported that the transition of the picophytoplankton population may also depend on other factors which were not the scope of this study such

as sedimentation (Brussaard et al., 1995), turbulence (Huisman et al., 2004), the balance between growth and grazing and viral lysis (Weinbauer & Höfle, 1998). In term of grazing pressure, zooplankton filter feeders and heterotrophic flagellates are thought to maintain the biomass of its prey and thus changes in picophytoplankton growth rate may significantly alter the resulting biomass of the picophytoplankton subgroups (Calbet et al., 2008; Chen et al., 2009). However, studies have shown that *Synechococcus* tend to be a poor food source for nanoflagellates (Dolan & Šimek, 1999). But in terms of viral lysis, it was reported *Synechococcus* cells could lose 5 to 77% daily in the open ocean (Evans & Brussaard, 2012; Suttle & Chan, 1994; Wang et al., 2011). Thus, we believe that such alternative explanations do not preclude each other, because the ecological pattern of distribution of plankton biomass in a particular area is more likely to be influenced by a combination of some (or many) factors.

CONCLUSION

Our results for the first-time covering the surface distribution of picophytoplankton in the southeastern coast of Peninsular Malaysia. This study revealed a coastal–offshore gradient dominated by *Synechococcus*, followed by picoeukaryotes and *Prochlorococcus*. *Synechococcus* and picoeukaryote abundance was primarily distributed along the coast and progressively decreased seaward, whereas *Prochlorococcus* abundances showed a slight increasing trend from the middle parts of the study area to the open oceanic waters. Our observation of physicochemical factors has enabled us to obtain a better understanding of the factors controlling the picophytoplankton composition. The results of canonical correspondence analysis demonstrate that TChl, pH, DO and temperature would favor the abundance of picophytoplankton assemblages in the study areas. However, the inclusion of accurate nutrient level and functional characteristics – such as size, pigments, biomass and photosynthetic properties – in future phytoplankton studies may be suggested in order to better understand the distribution of picophytoplankton at high spatial and/or temporal resolution, which could lead to a detailed understanding of abundance data from a broader ecological perspective.

ACKNOWLEDGEMENTS

This work was supported by the Ministry of Higher Education Malaysia, under the Fundamental Research Grant Scheme (FRGS) (Vote No. 59246) and Higher Institution Centre of Excellence (HiCoE) Research Grant (Vote No. 66928) Institute of Oceanography and Environment (INOS), Universiti Malaysia Terengganu. Sincere thanks to Ms See Hui Shien from the Biomarketing service for the flow cytometry analysis and RV Discovery's crews for great support onboard.

REFERENCES

- Agawin, N. S. R., Duarte, C. M., & Agustí, S. (2000a). Response of Mediterranean *Synechococcus* growth and loss rates to experimental nutrient inputs. *Marine Ecology Progress Series*, 206, 97-106. <https://doi.org/10.3354/meps206097>
- Agawin, N. S. R., Duarte, C. M., & Agustí, S. (2000b). Nutrient and temperature control of the contribution of picoplankton to phytoplankton biomass and production. *Limnology and Oceanography*, 45(3), 591-600. <https://doi.org/10.4319/lo.2000.45.3.0591>
- Agawin, N. S. R., Duarte, C. M., Agustí, S., & McManus, L. (2003). Abundance, biomass and growth rates of *Synechococcus* sp. in a tropical coastal ecosystem (Philippines, South China Sea). *Estuarine, Coastal and Shelf Science*, 56, 49-502. [https://doi.org/10.1016/S0272-7714\(02\)00200-7](https://doi.org/10.1016/S0272-7714(02)00200-7)
- Agustí, S., Lubián, L. M., Moreno-Ostos, E., Estrada, M., & Duarte, C. M. (2019). Projected changes in photosynthetic picoplankton in a warmer subtropical ocean. *Frontiers in Marine Science*, 5, Article 506. <https://doi.org/10.3389/fmars.2018.00506>
- Akhir, M., Zakaria, N., & Tangang, F. (2014). Intermonsoon variation of physical characteristics and current circulation along the east coast of Peninsular Malaysia. *International Journal of Oceans and Oceanography*, 2014, Article 527587. <https://doi.org/10.1155/2014/527587>
- Biller, S. J., Berube, P. M., Lindell, D., & Chisholm, S. W. (2015). *Prochlorococcus*: The structure and function of collective diversity. *Nature Reviews Microbiology*, 13(1), 13-27. <https://doi.org/10.1038/nrmicro3378>
- Brussaard, C. P., Riegman, R., Noordeloos, A. A., Cadée, G. C., Witte, H., Kop, A. J., Nieuwland, G., Van Duyl, F. C., & Bak, R. P. (1995). Effects of grazing, sedimentation and phytoplankton cell lysis on the structure of a coastal pelagic food web. *Marine Ecology Progress Series*, 123(1), 259-271. <https://doi.org/10.3354/meps123259>
- Buitenhuis, E. T., Li, W. K. W., Vaultot, D., Lomas, M. W., Landry, M. R., Partensky, F., Karl, D. M., Ulloa, O., Campbell, L., Jacquet, S., Lantoiné, F., Chavez, F., Macías, D., Gosselin, M., & McManus, G. B. (2012). Picophytoplankton biomass distribution in the global ocean. *Earth System Science Data*, 4, 37-46. <https://doi.org/10.5194/essd-4-37-2012>
- Calbet, A., Trepát, I., Almeda, R., Saló, V., Saiz, E., Movilla, J. I., Alcaraz, M., Yebra, L., & Simó, R. (2008). Impact of micro- And nanograzers on phytoplankton assessed by standard and size-fractionated dilution grazing experiments. *Aquatic Microbial Ecology*, 50, 145-156. <https://doi.org/10.3354/ame01171>
- Campbell, L., Nolla, H. A., & Vaultot, D. (1994). The importance of *Prochlorococcus* to community structure in the central North Pacific Ocean. *Limnology and Oceanography*, 39(4), 954-961. <https://doi.org/10.4319/lo.1994.39.4.0954>
- Chen, B., Liu, H., Landry, M. R., Dai, M., Huang, B., & Sun, J. (2009). Close coupling between phytoplankton growth and microzooplankton grazing in the western South China Sea. *Limnology and Oceanography*, 54(4), 1084-1097. <https://doi.org/10.4319/lo.2009.54.4.1084>
- Chisholm, S. W., Olson, R. J., Zettler, E. R., Goericke, R., Waterbury, J. B., & Welschmeyer, N. A. (1988). A novel free-living prochlorophyte abundant in the oceanic euphotic zone. *Nature*, 334, 340-343. <https://doi.org/10.1038/334340a0>

- Dolan, J. R., & Šimek, K. (1999). Diel periodicity in *Synechococcus* populations and grazing by heterotrophic nanoflagellates: Analysis of food vacuole contents. *Limnology and Oceanography*, *44*, 1565-1570. <https://doi.org/10.4319/lo.1999.44.6.1565>
- Echevarría, F., Zabala, L., Corzo, A., Navarro, G., Prieto, L., & Macías, D. (2009). Spatial distribution of autotrophic picoplankton in relation to physical forcings: The Gulf of Cádiz, Strait of Gibraltar and Alborán Sea case study. *Journal of Plankton Research*, *10*(24), 9824-9829. <https://doi.org/10.1093/plankt/fbp070>
- Evans, C., & Brussaard, C. P. D. (2012). Viral lysis and microzooplankton grazing of phytoplankton throughout the Southern Ocean. *Limnology and Oceanography*, *54*, 1826-1837. <https://doi.org/10.4319/lo.2012.57.6.1826>
- Flombaum, P., Gallegos, J. L., Gordillo, R. A., Rincón, J., Zabala, L. L., Jiao, N., Karl, D. M., Li, W. K. W., Lomas, M. W., Veneziano, D., Vera, C. S., Vrugt, J. A., & Martiny, A. C. (2013). Present and future global distributions of the marine Cyanobacteria *Prochlorococcus* and *Synechococcus*. *Proceedings of the National Academy of Sciences of the United States of America*, *110*(24), 9824-9829. <https://doi.org/10.1073/pnas.1307701110>
- Gasol, J. M., Del Giorgio, P. A., & Duarte, C. M. (1997). Biomass distribution in marine planktonic communities. *Limnology and Oceanography*, *42*(6), 1353-1363. <https://doi.org/10.4319/lo.1997.42.6.1353>
- Gin, K. Y. H., Lin, X., & Zhang, S. (2000). Dynamics and size structure of phytoplankton in the coastal waters of Singapore. *Journal of Plankton Research*, *22*(8), 1465-1484. <https://doi.org/10.1093/plankt/22.8.1465>
- Gin, K. Y. H., Zhang, S., & Lee, Y. K. (2003). Phytoplankton community structure in Singapore's coastal waters using HPLC pigment analysis and flow cytometry. *Journal of Plankton Research*, *25*(12), 1507-1519. <https://doi.org/10.1093/plankt/fbg112>
- Guiry, M. D., & Guiry, G. M. (2016). *AlgaeBase. World-wide electronic publication*. National University of Ireland. Retrieved November 15, 2020, from https://doi.org/http://www.algaebase.org/search/genus/detail/?genus_id=43474
- Guo, C., Liu, H., Zheng, L., Song, S., Chen, B., & Huang, B. (2014). Seasonal and spatial patterns of picophytoplankton growth, grazing and distribution in the East China Sea. *Biogeosciences*, *11*(7), 1847-1862. <https://doi.org/10.5194/bg-11-1847-2014>
- Huisman, J., Sharples, J., Stroom, J. M., Visser, P. M., Kardinaal, W. E. A., Verspagen, J. M. H., & Sommeijer, B. (2004). Changes in turbulent mixing shift competition for light between phytoplankton species. *Ecology*, *85*(11), 2960-2970. <https://doi.org/10.1890/03-0763>
- Jiang, Z. Y., & Sun, F. L. (2020). Diversity and biogeography of picoplankton communities from the Straits of Malacca to the South China Sea. *Oceanological and Hydrobiological Studies*, *49*(1), 23-33. <https://doi.org/10.1515/ohs-2020-0003>
- Jeffrey, S. W., & Humphrey, G. F. (1975). New spectrophotometric equations for determining chlorophylls a, b, c1 and c2 in higher plants, algae and natural phytoplankton. *Biochimie Und Physiologie Der Pflanzen*, *167*, 191-194. [https://doi.org/10.1016/s0015-3796\(17\)30778-3](https://doi.org/10.1016/s0015-3796(17)30778-3)
- Lee, C. W., Bong, C. W., Ng, C. C., & Alias, S. A. (2006). Factors affecting variability of heterotrophic and phototrophic microorganisms at high water in a mangrove forest at Cape Rachado, Malaysia. *Malaysian Journal of Science*, *25*(2), 55-66.

- Lee, C. W., Lim, J. H., & Heng, P. L. (2013). Investigating the spatial distribution of phototrophic picoplankton in a tropical estuary. *Environmental Monitoring and Assessment*, *185*, 9697-9704. <https://doi.org/10.1007/s10661-013-3283-3>
- Li, W. K. W. (1998). Annual average abundance of heterotrophic bacteria and *Synechococcus* in surface ocean waters. *Limnology and Oceanography*, *43*(7), 1746-1753. <https://doi.org/10.4319/lo.1998.43.7.1746>.
- Liu, G., & Chai, F. (2009). Seasonal and interannual variability of primary and export production in the South China Sea: A three-dimensional physical-biogeochemical model study. *ICES Journal of Marine Science*, *66*(2), 420-431.
- Liu, H., Jing, H., Wong, T. H. C., & Chen, B. (2014). Co-occurrence of phycocyanin- and phycoerythrin-rich *Synechococcus* in subtropical estuarine and coastal waters of Hong Kong. *Environmental Microbiology Reports*, *6*(1), 90-99. <https://doi.org/10.1111/1758-2229.12111>
- Liu, H., Nolla, H. A., & Campbell, L. (1997). *Prochlorococcus* growth rate and contribution to primary production in the equatorial and subtropical North Pacific Ocean. *Aquatic Microbial Ecology*, *12*, 39-47. <https://doi.org/10.3354/ame012039>.
- Liu, K. K., Chao, S. Y., Shaw, P. T., Gong, G. C., Chen, C. C., & Tang, T. Y. (2002). Monsoon-forced chlorophyll distribution and primary production in the South China Sea: Observations and a numerical study. *Deep-Sea Research Part I: Oceanographic Research Paper*, *49*(8), 1387-1412.
- Lønborg, C., & Søndergaard, M. (2009). Microbial availability and degradation of dissolved organic carbon and nitrogen in two coastal areas. *Estuarine, Coastal and Shelf Science*, *81*(4), 513-520. <https://doi.org/10.1016/j.ecss.2008.12.009>
- Marie, D., Simon, N., & Vaulot, D. (2005). Phytoplankton cell counting by flow cytometry. *Algal Culturing Techniques*, *1*, 253-267. <https://doi.org/10.1016/b978-012088426-1/50018-4>
- Mella-Flores, D., Six, C., Ratin, M., Partensky, F., Boutte, C., Le Corguillé, G., Marie, D., Blot, N., Gourvil, P., Kolowrat, C., & Garczarek, L. (2012). *Prochlorococcus* and *Synechococcus* have evolved different adaptive mechanisms to cope with light and uv stress. *Frontiers in Microbiology*, *3*, Article 285. <https://doi.org/10.3389/fmicb.2012.00285>
- Mena, C., Reglero, P., Hidalgo, M., Sintés, E., Santiago, R., Martín, M., Moyà, G., & Balbín, R. (2019). Phytoplankton community structure is driven by stratification in the oligotrophic Mediterranean Sea. *Frontiers in Microbiology*, *10*, Article 1698. <https://doi.org/10.3389/fmicb.2019.01698>
- Miyashita, H. (2015). Diversity of marine phototrophs. In S. K. Kim (Ed.), *Springer handbook of marine biotechnology* (pp. 27-34). Springer. <https://doi.org/10.1007/978-3-642-53971-8>
- Moore, L. R., Goericke, R., & Chisholm, S. W. (1995). Comparative physiology of *Synechococcus* and *Prochlorococcus*: Influence of light and temperature on growth, pigments, fluorescence and absorptive properties. *Marine Ecology Progress Series*, *116*(1), 259-275. <https://doi.org/10.3354/meps116259>
- Mouriño-Carballido, B., Hojas, E., Cermeño, P., Chouciño, P., Fernández-Castro, B., Latasa, M., Maraño, E., Morán, X. A. G., & Vidal, M. (2016). Nutrient supply controls picoplankton community structure during three contrasting seasons in the northwestern Mediterranean Sea. *Marine Ecology Progress Series*, *543*, 1-19. <https://doi.org/10.3354/meps11558>

- Otero-Ferrer, J. L., Cermeño, P., Fernández-Castro, B., Gasol, J. M., Morán, X. A. G., Marañón, E., Moreira-Coello, V., Varela, M., Villamaña, M., & Mourinho-Carballido, B. (2018). Factors controlling the community structure of picoplankton in contrasting marine environments. *Biogeosciences Discussions*, *15*, 6199-6220. <https://doi.org/10.5194/bg-2018-211>
- O'Boyle, S., McDermott, G., Noklegaard, T., & Wilkes, R. (2013). A simple index of trophic status in estuaries and coastal bays based on measurements of pH and dissolved oxygen. *Estuaries and Coasts*, *36*(1), 158-173. <https://doi.org/10.1007/s12237-012-9553-4>
- Pan, L. A., Zhang, J., & Zhang, L. H. (2007). Picophytoplankton, nanophytoplankton, heterotrophic bacteria and viruses in the Changjiang Estuary and adjacent coastal waters. *Journal of Plankton Research*, *29*, 187-197. <https://doi.org/10.1093/plankt/fbm006>
- Partensky, F., Blanchot, J., & Vaulot, D. (1999a). Differential distribution and ecology of *Prochlorococcus* and *Synechococcus* in oceanic waters: A review. *Bulletin de l'Institut océanographique, Monaco*, *19*, 457-475.
- Partensky, F., Hess, W. R., & Vaulot, D. (1999b). *Prochlorococcus*, a Marine photosynthetic prokaryote of global significance. *Microbiology and Molecular Biology Reviews*, *63*(1), 106-127. <https://doi.org/10.1128/membr.63.1.106-127.1999>
- Powley, H. R., Krom, M. D., & Van Cappellen, P. (2017). Understanding the unique biogeochemistry of the Mediterranean Sea: Insights from a coupled phosphorus and nitrogen model. *Global Biogeochemical Cycles*, *31*, 1010-1031. <https://doi.org/10.1002/2017GB005648>
- Scanlan, D. J. (2012). Marine picocyanobacteria. In B. A. Whitton (Ed.), *Ecology of Cyanobacteria II* (pp. 503-533). Springer. https://doi.org/10.1007/978-94-007-3855-3_20
- Shaari, F., Mustapha, M. A., Ali, M. M., & Lihan, T. (2013, November). Chlorophyll-a and nutrient distribution of Pahang coastal waters during southwest monsoon using satellite images. In *AIP Conference Proceedings* (Vol. 1571, No. 1, pp. 493-497). American Institute of Physics. <https://doi.org/10.1063/1.4858703>
- Sherr, E. B., Sherr, B. F., & Wheeler, P. A. (2005). Distribution of coccoid cyanobacteria and small eukaryotic phytoplankton in the upwelling ecosystem off the Oregon coast during 2001 and 2002. *Deep-Sea Research Part II: Topical Studies in Oceanography*, *52*, 317-330. <https://doi.org/10.1016/j.dsr2.2004.09.020>
- Shaik, A. U. R., Biswas, H., & Pal, S. (2017). Increased CO₂ availability promotes growth of a tropical coastal diatom assemblage (Goa coast, Arabian Sea, India). *Diatom Research*, *32*(3), 325-339. <https://doi.org/10.1080/0269249X.2017.1379443>
- Shi, X., Li, S., Li, H., Chen, F., & Wu, Q. (2019). The community structure of picophytoplankton in Lake Fuxian, a deep and oligotrophic mountain lake. *Frontiers in Microbiology*, *10*, Article 2016. <https://doi.org/10.3389/fmicb.2019.02016>
- Suttle, C. A., & Chan, A. M. (1994). Dynamics and distribution of cyanophages and their effect on marine *Synechococcus* spp. *Applied and Environmental Microbiology*, *60*(9), 3167-3174. <https://doi.org/10.1128/aem.60.9.3167-3174.1994>
- Vaulot, D., Eikrem, W., Viprey, M., & Moreau, H. (2008). The diversity of small eukaryotic phytoplankton (< or =3 microm) in marine ecosystems. *FEMS Microbiology Reviews*, *32*(5), 795-820. <https://doi.org/10.1111/j.1574-6976.2008.00121.x>

- Vaulot, D., Courties, C., & Partensky, F. (1989). A simple method to preserve oceanic phytoplankton for flow cytometric analyses through division by the corresponding parameters. *Cytometry*, *10*, 629-635.
- Wang, K., Wommack, K. E., & Chen, F. (2011). Abundance and distribution of *Synechococcus* spp. and cyanophages in the Chesapeake Bay. *Applied and Environmental Microbiology*, *77*(21), 7459-7468. <https://doi.org/10.1128/AEM.00267-11>
- Wei, Y., Huang, D., Zhang, G., Zhao, Y., & Sun, J. (2020). Biogeographic variations of picophytoplankton in three contrasting seas: The Bay of Bengal, South China Sea and western Pacific Ocean. *Aquatic Microbial Ecology*, *84*, 91-103. <https://doi.org/10.3354/ame01928>
- Weinbauer, M. G., & Höfle, M. G. (1998). Significance of viral lysis and flagellate grazing as factors controlling bacterioplankton production in a eutrophic lake. *Applied and Environmental Microbiology*, *64*, 431-438. <https://doi.org/10.1128/aem.64.2.431-438.1998>.
- Yanagi, T., Sachoemar, S. I., Takao, T., & Fujiwara, S. (2001). Seasonal variation of stratification in the gulf of Thailand. *International Journal of Oceans and Oceanography*, *57*, 461-470. <https://doi.org/10.1023/A:1021237721368>.
- Yang, Y., & Jiao, N. (2004). Dynamics of picoplankton in the Nansha Islands area of the South China Sea. *Acta Oceanologica Sinica*, *23*, 493-504.
- Zainol, Z., & Akhir, M. F. (2016). Coastal upwelling in the vicinity of Tioman Island. *Journal of Sustainability Science and Management Special Issue Number 1: The International Seminar on the Straits of Malacca and the South China Sea*, 71-80.
- Zhao, S., Wei, J., Yue, H., & Xiao, T. (2010). Picophytoplankton abundance and community structure in the Philippine Sea, western Pacific. *Chinese Journal of Oceanology and Limnology*, *28*(1), 88-95. <https://doi.org/10.1007/s00343-010-9274-0>
- Zwirgmaier, K., Jardillier, L., Ostrowski, M., Mazard, S., Garczarek, L., Vaulot, D., Not, F., Massana, R., Ulloa, O., & Scanlan, D. J. (2008). Global phylogeography of marine *Synechococcus* and *Prochlorococcus* reveals a distinct partitioning of lineages among oceanic biomes. *Environmental Microbiology*, *10*(1), 147-161. <https://doi.org/10.1111/j.1462-2920.2007.01440.x>



Effects of Vegetation Covers for Outdoor Thermal Improvement: A Case Study at Abubakar Tafawa Balewa University, Bauchi, Nigeria

Kabiru Haruna Abdulkarim^{1,2*}, Azmiah Abd Ghafar³, Lee Yoke Lai³ and Ismail Said³

¹Architecture Program, Faculty of Built Environment and Surveying, Universiti Teknologi Malaysia, 81310, Johor Bahru, Johor, Malaysia

²Architecture Department, School of Environment Technology, Abubakar Tatari Ali Polytechnic, 100989, Bauchi, Nigeria

³Landscape Architecture Program, Faculty of Built Environment and Surveying, Universiti Teknologi Malaysia, 81310, Johor Bahru, Johor, Malaysia

ABSTRACT

Frequent increases in temperature and related consequences have been the trending phenomenon for over ten decades, with a general rise of about 0.74°C. This study evaluates the effects of different percentage covers of tree canopies for outdoor thermal improvement of campus areas in Bauchi, Nigeria. Firstly, the study involves on-site measurement of existing features on the site and the climatic conditions. Secondly, performing simulation for evaluation of the plant-surface-atmosphere interactions with Envi-met Version 4.4.2.

The vegetation effects were evaluated for outdoor air temperature and mean radiant temperature (MRT) reduction. It is found that the maximum air temperature reduction of 3.38°C and 24.24°C of MRT were achieved with up to 45% tree canopy coverage. The mean air temperature and MRT reduction of 0.63°C and 4.80°C were respectively achieved with the same percentage coverage of the canopies. However, it was found that the thermal reduction effects of vegetation do not apply to every hour of the day. In essence, proper planning and implementation of campus

ARTICLE INFO

Article history:

Received: 25 February 2021

Accepted: 21 May 2021

Published: 31 July 2021

DOI: <https://doi.org/10.47836/pjst.29.3.43>

E-mail addresses:

kabiru.haruna-1973@graduate.utm.my (Kabiru Haruna Abdulkarim)

azmiahabdghafar@gmail.com (Azmiah Abd Ghafar)

lylai@utm.my (Lee Yoke Lai)

ismailbinsaid@gmail.com (Ismail Said)

*Corresponding author

outdoor spaces is the key factor in improving its thermal conditions. Thus, adhering to the practical recommendations bring a significant improvement in ameliorating the rise in atmospheric temperature on campus outdoors.

Keywords: Air temperature, campus outdoor, envi-met simulation, hot-and-dry climate, mean radiant temperature, urban climate

INTRODUCTION

A rise in temperature and its related consequences have been the trending phenomenon because of its rapid increase than in previous decades (Brysse et al., 2013; Morakinyo et al., 2016). Between 1906 and 2005 indicates a general rise of 0.74°C with up to 0.13°C increase in some decades (Frédéric et al., 2008). Correspondingly, an increase in global atmospheric temperature to 0.74°C in the past 100 years has been reported by Intergovernmental Panel on Climate Change (Morgan, 2006). Moreover, it has been projected that the global mean atmospheric temperature will increase by 0.3 to 4.8°C by the year 2100, depending on the context parameters and its specific emissions scenario (Centre for Science and Environment, 2018). In urban areas, frequent anthropogenic activities increase the effects of greenhouse in the atmosphere. Consequently, the increase in the greenhouse effect leads to a rise in temperature (Shahzad, 2015). Apart from the increase in the greenhouse effect in the atmosphere, Urban Heat Island manifests in most urban environments, which leads to the rise in atmospheric temperature. The rise in temperature due to the Urban Heat Island in cities deteriorates its microclimates, decreases energy efficiency, and increases the thermal condition of outdoor spaces (Lai et al., 2019).

A study conducted by Hassan et al. (2017) reveals that there were increasing temperature trends from 1982-2014 in most parts of the cities in northern Nigeria with a value of 0.03°C to 0.05°C per decade. Air temperature and MRT are the most common parameters used to assess indoor and outdoor thermal conditions (Al-Mohsen et al., 2020; Lucchi et al., 2017; Yıldırım, 2020). An increase in these two climatic parameters tends to worsen the thermal conditions of a microclimate. Air temperature (Adunola, 2014) and the MRT remain the dominant climatic parameters affecting the outdoor thermal state in the hot and dry regions (Soydan, 2020), especially in Nigeria. In Nigeria, the hot and dry region possesses the highest degree of air temperature and MRT. In the area, the air temperature rises to 42°C in late May of each year. The excessive rise in the temperature emanates from less vegetation in the region that can provide shades over surfaces against direct solar radiation. The vegetated areas are mostly replaced with hard surfaces that absorb more heat and light (Hami et al., 2019; Hertel & Schlink, 2019). This phenomenon frequently happens in urban areas of Nigeria, especially during construction processes.

Shading in urban outdoor environments has been identified as an essential aspect in modifying microclimatic conditions and enhancing thermal comfort, particularly in hot regions (Peeters et al., 2020). Many open and semi-open spaces in university campuses are not adequately planned to respond to microclimate conditions. These aspects hinder university students from having campuses with thermally comfortable outdoor environments (Ghaffarianhoseini et al., 2019). Including vegetation in the planning and implementation of campus outdoor spaces will ameliorate the rise in outdoor temperature. Equally, it improves the well-being and learning capacity of students. Thus, vegetation is one of the fundamental concepts for enhancing the thermal condition of urban microclimates (Morakinyo & Lam, 2016). It plays a significant role in influencing the urban microclimate thermal conditions (Tong et al., 2017; Wong et al., 2007; Wong et al., 2010). There are three aspects to consider in reducing outdoor air temperature and MRT: designing the outdoor spaces, vegetation planning, and implementation (Hami et al., 2019; Yahia et al., 2018; Yahia & Johansson, 2014). The cooling effect of vegetation extends beyond its green area (Lu et al., 2017). The extension depends on the vegetation density and its percentage cover. Generally, foliage has a vital influential role in outdoor and indoor thermal condition improvement (Tong et al., 2017). Tree canopy, in particular, helps in the provision of shade against direct solar radiation. Furthermore, evapotranspiration by leaves is important in reducing the intensity of heat (Dhakal, 2002).

Researchers in passive architecture and urban planning have been trying tremendously in improving outdoor thermal environments in urban centres. They suggested practical solutions to achieve the mitigating effects. Such as increasing the green areas (Abounaga & Mostafa, 2020), proper natural ventilation (Al-Mohsen et al., 2020), provision of shades from natural and built forms (Abaas, 2020; Peeters et al., 2020), and minimization for the use of surfaces that enhance the increase of longwave radiations. However, studies are still needed to add to the body of knowledge regarding improving our microclimates. Authorities and scholars around the globe put less emphasis on climate conditions and thermal improvement of microclimates at regional and urban scales (Dhakal, 2002). Furthermore, most studies on thermal improvement were indoors; few were conducted on the outdoor spaces. Hence, the fewer conducted in urban areas were centred on improving parks, street canyons, office environments, and residential neighbourhoods rather than academic environments. Equally, the research emphasis was less on hot and dry climates than other parts of the globe.

This study investigates the effects of tree canopy coverage in the outdoor thermal environment of a university campus in the city centre of Bauchi. The ENVI-met 3-dimensional non-hydrostatic simulation model was employed to evaluate the outdoor thermal environment. It is widely used to improve urban spaces in various climatic zones and within diverse urban structures (Chatzinikolaou et al., 2018; Perini et al., 2017). The

study investigated the reducing effects of tree canopy cover on the intensity of the outdoor climatic conditions in a campus setting. It equally hypothesized the significant positive effects of tree canopy cover in reducing the intensity of outdoor air temperature and the MRT in the context of urban centres within hot and dry climates (Davtalab et al., 2020).

MATERIALS AND METHOD

The research work was carried out in two stages consecutively to evaluate the effects of different vegetation cover on air temperature and MRT reduction. The stages were field measurement survey and the Envi-met computer simulation.

Study Site

The study was conducted at the Abubakar Tafawa Balewa University in Bauchi town of Northern Nigeria (Figures 1 & 2). The location is categorized as a hot and dry Savanna climate, with less grass and sparse trees. The university has a student enrolment of 14,492 for the 2016/2017 academic session (Office of the University Registrar, 2018). The mean daily maximum temperature of Bauchi town ranges from 27.0°C to 29.0°C between July and August. While 37.6°C in March and April (Sylvester & Abdulquadir, 2015). The mean daily minimum temperature ranges from 22.0°C in December and January to about 24.7°C in April and May. The mean maximum air temperature of Bauchi was higher than the mean maximum air temperature of the country (Eludoyin et al., 2014). The sunshine hours range from 5.1 hours to 8.9 hours. October to February was recorded as the longest sunshine hours in the city of Bauchi. Humidity ranges from 12% in February to about 98% in August. The months for the rainy season are May to September, with the annual precipitation ranges from 600mm to 1300mm (Akande & Adebamowo, 2010). Currently, vegetation covers 9% of the total land area of the study site.

Field Measurements

On-site air temperature data were collected from the study site for twenty-one days, from the 10th to 31st August 2018. The selected study period was to obtain changes in air temperature. HOBO UX100-011 data loggers were placed at the height of 1.5m above the ground (Evola et al., 2017) to capture the climate parameter at the pedestrian level (Ghaffarianhoseini et al., 2019). Ten days of pretest measurement were conducted for the climatic condition parameter before the actual site measurement. The pretest measurement took place from the 1st to 10th day of August 2018. It was carried out to ensure the functionality and reliability of the data loggers. All the data loggers were set at 8:00hrs on the first day. Receptor points were selected for the on-site measurements (Figure 2b) as; i. location without vegetation (T_a NV), ii. location with grasses only (T_a GR), iii. location with trees only (T_a TR), and



Figure 1. The location Bauchi, Nigeria (<https://www.mapsofworld.com/nigeria/maps/nigeria-location-map.jpg>)



Figure 2. (a) The study area, (b) study area with the four receptors on the measurement points as TaNV (location without vegetation), TaGR (location with grasses only), TaTR (location with trees only), and TaTG (location with both trees and grass) (Google map imagery).

iv. location with both trees and grass (T_aTG). The four different receptors were placed to capture all the possible different vegetation scenarios on the site. Both the actual and the pretest measurements were carried out on the same measurement points.

Figure 3 presents the mean daily air temperature changes for the four measurement points, measured against the primary “y” axis. While the line charts depict the daily maximum and daily minimum changes. They were measured against the secondary “y” axis. The measurement shows that the scenario without vegetation has the highest degree of outdoor air temperature to about $38.6^{\circ}C$ on the second day. The combination of trees and grass has the lowest maximum outdoor air temperature of about $35^{\circ}C$ on a corresponding

day. The decrease of air temperature in the latter scenario was from the effects of the existing vegetation on the campus. The shading and evapotranspiration rates significantly influenced the air temperature. Exposure of surfaces to direct solar radiation leads to increased air temperature in the scenario 0% vegetation.

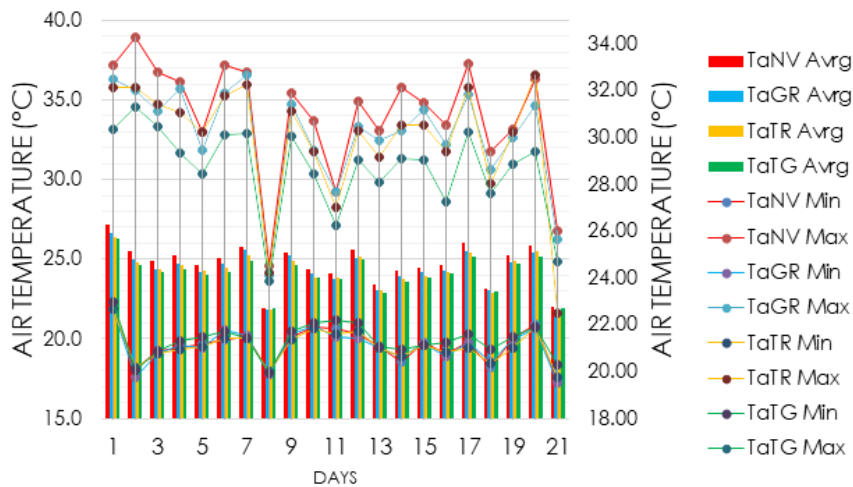


Figure 3. Mean daily changes for the existing air temperature for the 21 measurement days

Envi-met Simulation

Envi-met Version 4.4.2 computer simulation was employed in this study for the simulation of the modelled environment. In the same vein, while performing the simulations, the Envi-met evaluated the heat flux, evaporation, and transpiration flowing from the trees to the atmosphere (Salata et al., 2016). ENVI-met was developed to simulate the relation of surfaces, vegetation, and airflow for local microclimatic conditions. It also evaluates the effects of solar irradiance, humidity, and heat storage in the soil (Shinzato et al., 2019). A grid resolution was used to model the geometry of the study site. The numerical simulations were performed in the summer, on 26th August 2018. As postulated by Tsoka et al., (2018), about 90% of the scientific studies on microclimate analysis used the ENVI-met model during summer. It shows that vegetation significantly influences the thermal condition of microclimates when the temperature is higher (Hami et al., 2019). The simulation day was determined based on the on-site measurements. A day with the highest air temperature and a clear sky (Roth & Lim, 2017) was used for the simulation. The simulation models were run for 24 hours (Tsoka, 2017). The Envi-met computer simulation software Version 4.4.2

was preset as a 10-minute time step. At the end of each domain simulation, hourly time steps were extracted for scenario comparison.

Model Area Geometry

The study site was developed based on physical measurements and google imagery. It has a domain size of 425.00m x 375.00m, designated within 85 x 75 x 15 grids. The grid cell size was 5.00m x 5.00m x 2.00m as dx, dy, and dz, respectively. The height of the total grids for the dz axis is 30m which is more than 2times of the highest building on the site (Ozkeresteci et al., 2003). Priorities were given to the buildings' geometry, vegetation on the site, ground surfaces, and the receptors for the microclimate condition measurements. The overall height of the buildings within the measurement site ranges from 5m to 12m. The ground surfaces were loamy soils and asphalt roads. The vegetation was a combination of grasses and trees, with an average height of 25cm, and 7.5m, respectively. The Leaf Area Density (LAD) for a tree is 1.2, used for the model domain. In the end, four receptors were placed at four places to record the existing climatic conditions. Table 1 shows the input data for model development and simulation initialization process.

Models Domains

Five outdoor models were simulated to evaluate the optimal thermal influence of vegetation coverage on the campus outdoor environment. The five different models were scenario with 0% vegetation cover, as the base model (Figure 4), the scenario with 9% vegetation cover as the existing condition of the study site (Figure 5a), the scenario with 15% vegetation cover (Figure 5b), the scenario with 30% vegetation cover (Figure 5c), and the scenario with 45% vegetation cover (Figure 5d). The numerical model simulations were run for 24hrs from 6:00:00hrs in the early morning. To let the software follow the atmospheric process (Forouzandeh, 2018; Salata et al., 2016).

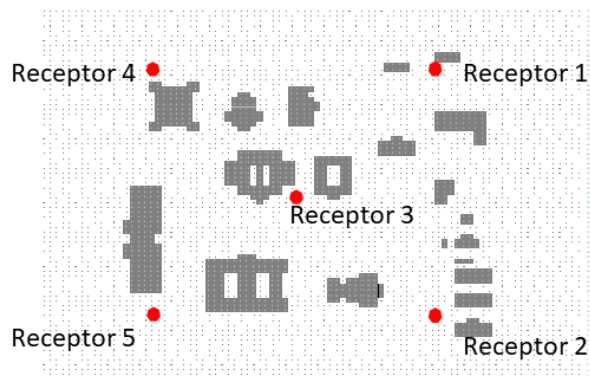


Figure 4. Shows the base model with 0% vegetation cover, with five receptors placed at different places

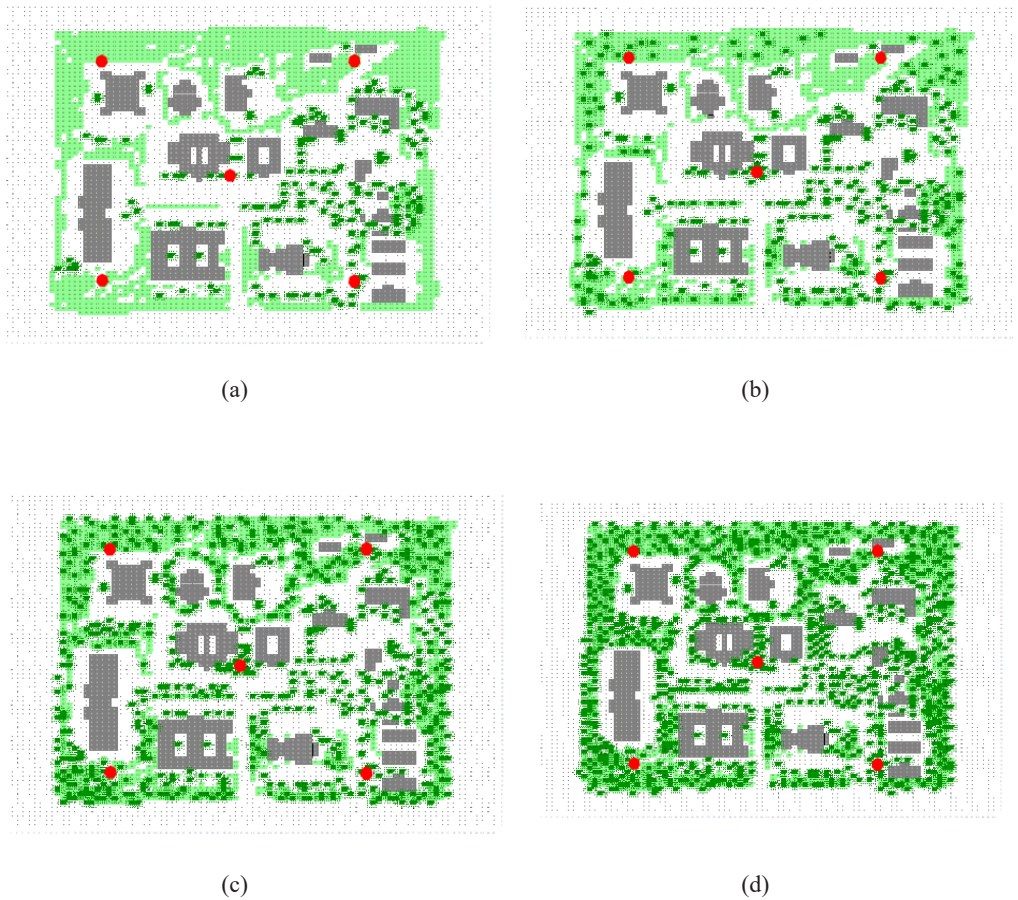


Figure 5. Model domains for different vegetation coverage; (a) the existing condition of site study with 9% of vegetation coverage, (b) Scenario with 15% of vegetation coverage (c) Scenario with 30% of vegetation coverage, and (d) Scenario with 45% of vegetation coverage

Table 1
Envi-met model domain initial input parameters

	ITEMS	INPUT DATA
Study site	Climate type	Hot and dry
	Soil	Loamy soil
	Latitude	10° 16' 45" N
	Longitude	09° 47' 16" E

Table 1 (Continued)

	ITEMS	INPUT DATA
Simulation input data	Simulation day	On 26th August 2018
	Effective simulation time	24hrs
	Domain size	425.00m x 375.00m x 30.00m
	Resolution	5.00m x 5.00m x 2.00m
	Roughness length	0.01
	Minimum Air temperature	18°C at 6:00hrs
	Maximum Air temperature	34°C at 15:00hrs
	Wind speed	3.0m/s
	Wind direction	90°
	Minimum Relative humidity	45% at 15:00hrs
	Maximum Relative humidity	99% at 06:00hrs

RESULTS

Software Validation

The validation process in this study compares the on-site measurements and the computer simulation outputs. Better validation results indicate the reliability and validity of the software in predicting the plant-surface-atmosphere interaction (Forouzandeh, 2018) within the campus microclimate. Equally, the validation process is an essential step in obtaining accurate results for domain simulation (Shinzato et al., 2019).

The on-site measurements were designed to measure the existing microclimate conditions of the study site at the ATBU campus. The air temperature on 26th August 2018 was selected as the parameter for the software validation. It was selected based on the day with the highest maximum air temperature and sky clarity. The measured air temperature values were compared with the obtained ENVI-met simulated results (Figure 6). The coefficient of determination (R^2) ranges from 0.8697 to 0.9323 for the four measurement points. Equally, the Root Mean Squared Error (RMSE) for the four measurement points was 1.59°C, 1.03°C, 1.88°C, and 0.92°C (Figure 6a-6d). The validation results showed that there was a good correlation between the measured values and the simulation results (Yang et al., 2018). The R^2 and the RMSE values suggest that the ENVI-met model can significantly represent the existing condition of the study area. Equally, indicate the software reliability for studying plant-surface-atmosphere interaction in the context of hot and dry climates. Notwithstanding, the ENVI-met underestimated daytime air temperature in all four scenarios, from 09:00hrs to 19:00hrs. Which was due to the anthropogenic heating from vehicles, and other moveable objects that were not accounted for in the simulation (Eniolu et al., 2017).

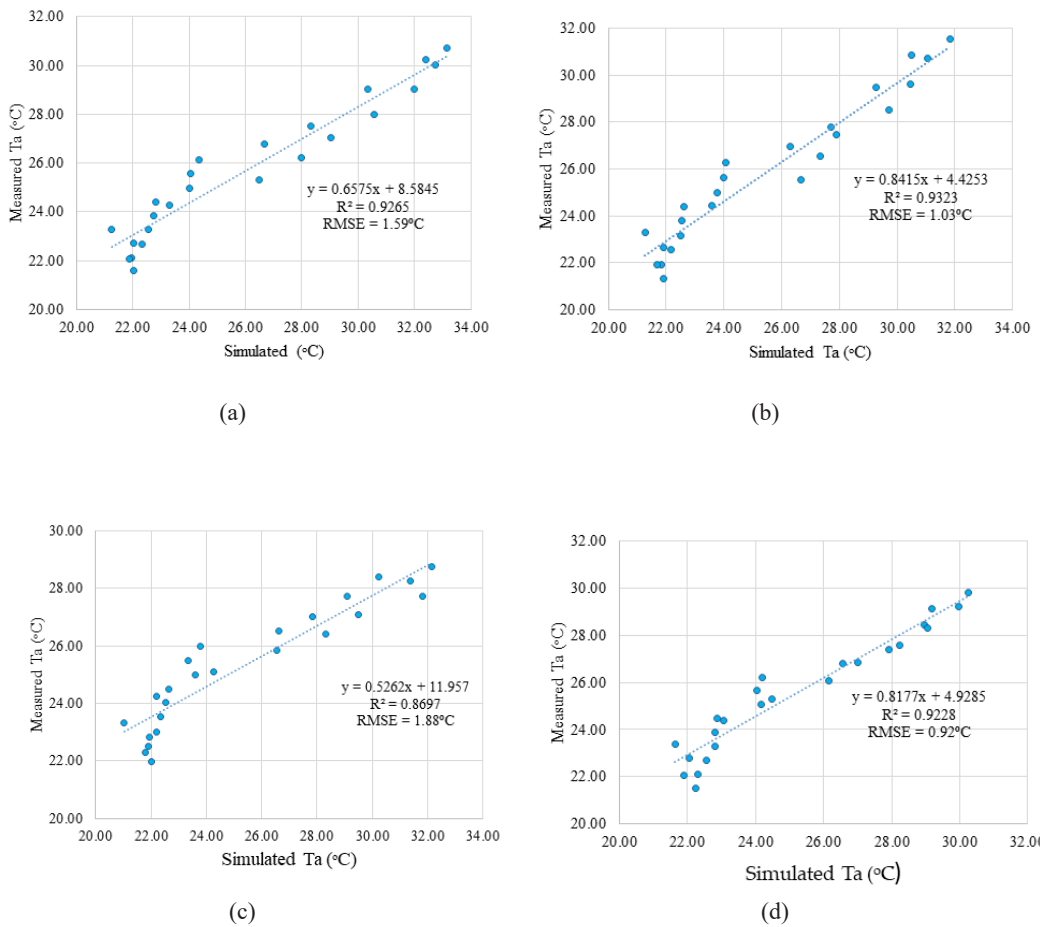
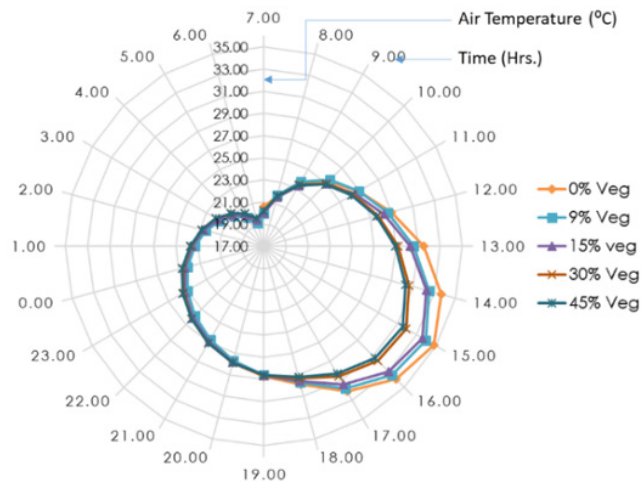


Figure 6. Envi-met software validation output for the four measurement points

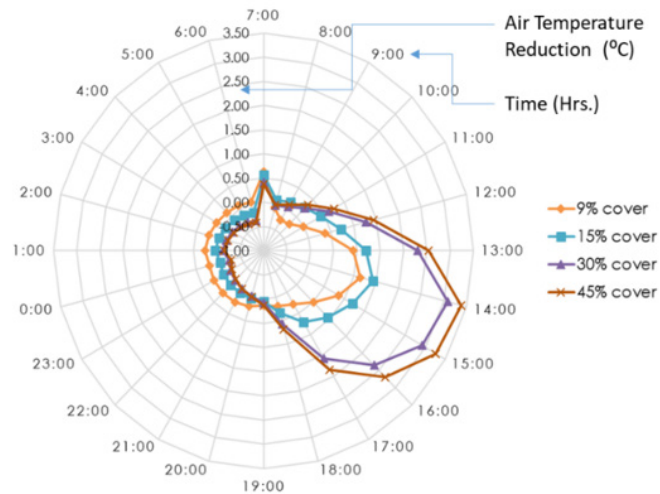
Air Temperature

All four scenarios were compared with the base model to evaluate the total effects of the vegetation covers on the air temperature reduction. The existing situation that has the 9% vegetation cover was with the least reduction effects. The cover reduced the air temperature by a maximum of 1.14°C at 14:00hrs (Figure 8) with a daily average reduction of 0.27°C (Table 2). The 15%, 30%, and 45% tree canopy covers showed a daily average reduction effect of 0.32°C , 0.55°C , and 0.63°C respectively. The simulation results showed that from 8:00hrs to 11:00hrs, the 9% vegetation cover has adverse effects on air temperature reduction. Within the stated period, the air temperature rises above that of the base model domain. Equally, from 21:00hrs to 6:00hrs the next day, any increase of the vegetation

cover negates its influence on air temperature reduction. This is because the thermal effects of tree canopies are based on shading and evapotranspiration (Morakinyo & Lam, 2016). The shading effects occur significantly in the daytime, whereby the shortwave radiations were shaded from reaching surfaces. An increase in the percentage of vegetation coverage decreases the wind speed. Consequently, it traps the heated air within the densely vegetated environment. Thus, it raises the temperature at night time (Figure 7).



(a)



(b)

Figure 7. (a) Air temperature output on the simulation day (b) Outdoor air temperature reduction for different vegetation cover at every hour of the day

Table 2

Effects of different vegetation covers on air temperature reduction

Vegetation Cover	9%	15%	30%	45%
Maximum reduction (°C)	1.14	1.43	3.08	3.38
Minimum reduction (°C)	-0.27	-0.19	-0.37	-0.41
Average reduction (°C)	0.27	0.32	0.55	0.63

Simulation outputs were imported into a Leonardo visualization program. Each output file has a multitude of information that has been translated into different layers in the program. The following layers shown in Figure 8 and 9 are visual output for five scenarios at 15:00hrs of the simulation day. The five scenarios have different vegetation cover. The visualized layer outputs for the models with vegetation cover 0%, 9%, and 15% as presented in Figure 8, 9a, and 9b, respectively, indicate a significant proportion of hotter areas in the respective models. These explain that the less coverage of the vegetation the scenarios lead to an increase in the daytime air temperature. Consequently, the daytime air temperatures rise to a maximum of 37.25°C, 36.94°C, and 36.21°C, for scenarios with the vegetation cover of 0%, 9%, and 15%, respectively. Conversely, models with the vegetation cover 30% and 45% in Figure 9c and 9d indicated a remarkable decrease in air temperature during the day to a maximum of 36.06°C and 35.97°C, respectively. The visualized outputs were dominated by layers of blue and green at 15:00hrs. Therefore, it indicated a more significant improvement for outdoor air temperature reduction in the daytime. It was a result of the percentage increase in the vegetation cover above 30%.

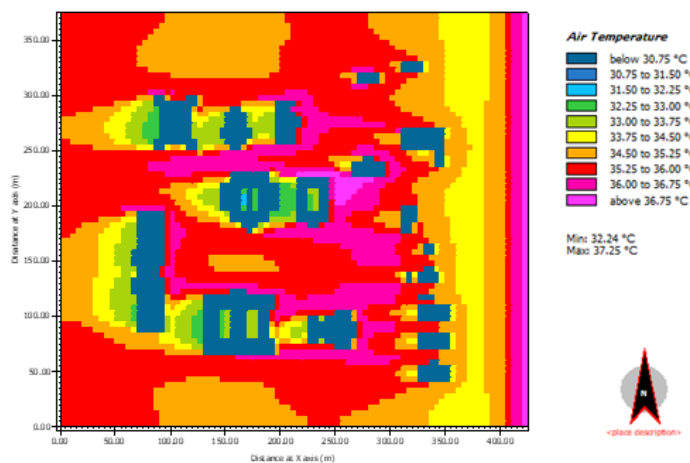
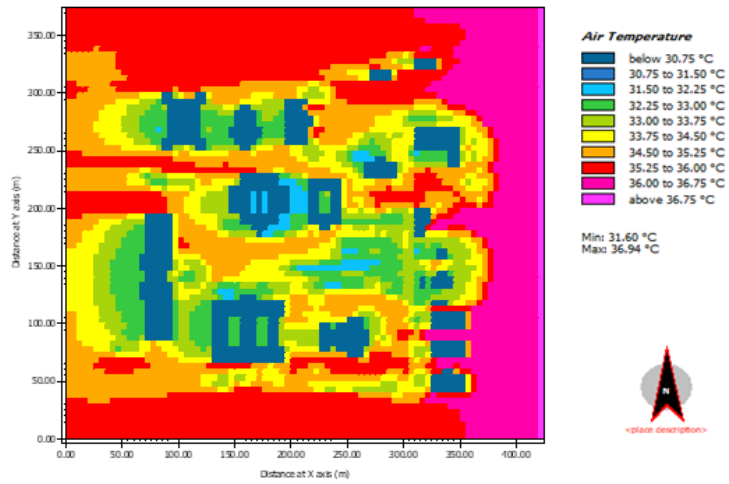
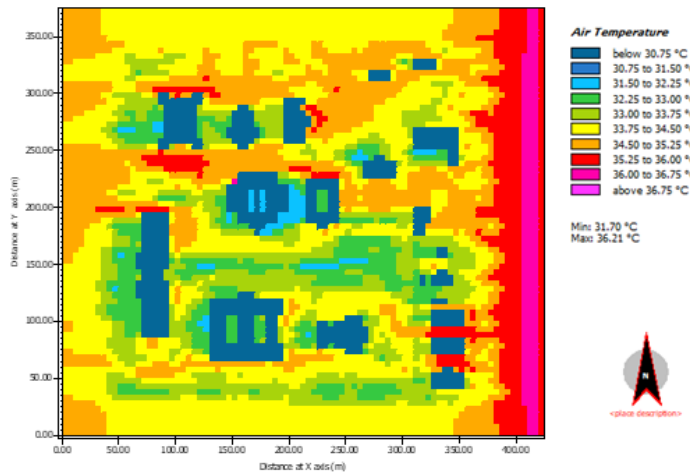


Figure 8. Air temperature visual output for the scenario with 0% vegetation cover at 15:00 hrs

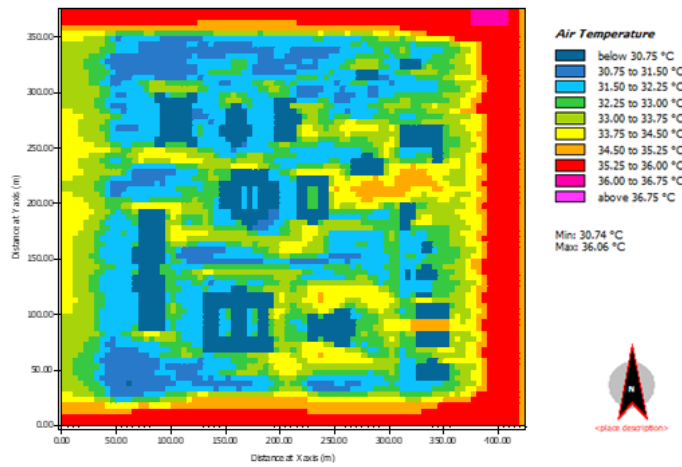
Thermal Effects of Vegetation Cover in Campus Outdoor Environment



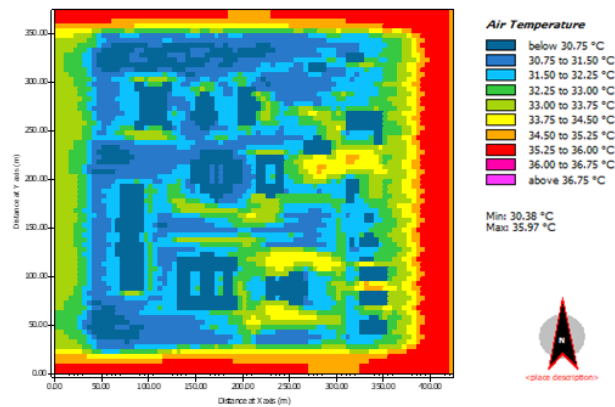
(a)



(b)



(c)



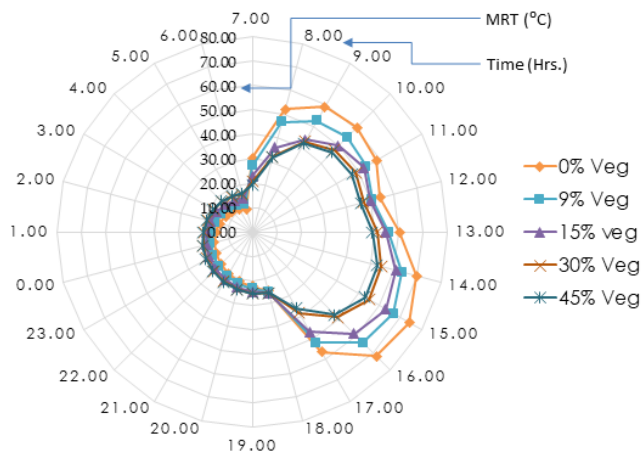
(d)

Figure 9. Air temperature visual output for different vegetation cover at 15:00 hours; (a) Scenario with 9% vegetation cover which is also the current condition of the study site, (b) Scenario with 15% vegetation cover, (c) Scenario with 30% vegetation cover, and (d) Scenario with 45% vegetation cover

Mean Radiant Temperature

In the context of the hot and dry urban climate, MRT changes due to the absence or less vegetation in the region (Soydan, 2020). The need for vegetation on campuses in such areas deemed essential to reduce the intensity of the MRT. For this reason, five different models were simulated to evaluate the effects of varying percentage coverage of tree canopies on MRT reduction. The four vegetated domains (Figure 10b) were compared with the base

model, which has 0% tree canopy cover. The comparison was to ascertain the magnitude of the MRT reduction by different percentage coverage of tree canopies. The results showed that in all the models' domain, the MRT started magnifying its intensity precisely at 7:00hrs with a sudden decline at 17:00hrs. Among all the five simulated domains, the base model resulted in the highest daily maximum MRT of up to 74.27°C at 15:00hrs. Equally, despite its 0% vegetation, the base model resulted in the lowest daily minimum MRT of 9.44°C at 06:00hrs. The results demonstrated higher vegetation coverage lowers the MRT in the daytime. Increase in vegetation coverage resulting in a higher MRT from 18:00hr to 07:00hrs the next day (Figure 10a). Furthermore, all the simulation results showed that the thermal reduction effects on the MRT were more effective at 08:00hrs and 16:00hrs (Figure 10b). The 45% tree canopy cover showed the maximum MRT reduction effect. It reduced the MRT by 24.24°C at 16:00hrs, with a daily average of 4.80°C reduction effects (Figure 9b). The results showed a sudden drop in the MRT reduction at 12:00hrs for all the four vegetated domains. The significance of MRT reduction requires 15% vegetation coverage in the morning time (Figure 9b). In contrast, a minimum of 30% vegetation cover in the afternoon time for significant MRT reduction.



(a)

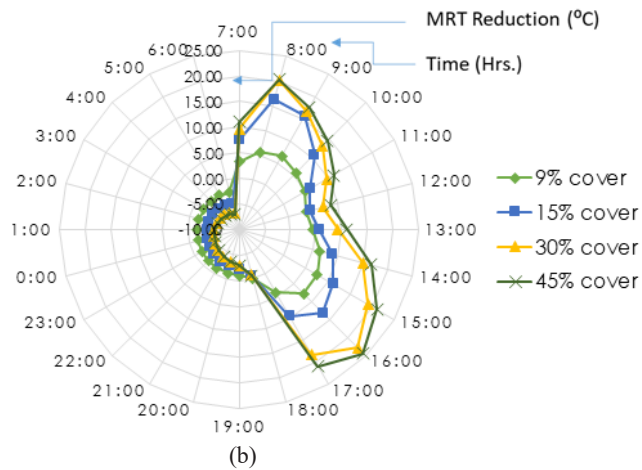


Figure 10. (a) Mean radiant temperature output on the simulation day (b) Effects of different vegetation covers on mean radiant temperature reduction.

Table 3

Average reduction for different vegetation covers on mean radiant temperature

Vegetation Cover	9%	15%	30%	45%
Maximum reduction (°C)	7.79	16.32	22.73	24.24
Minimum reduction (°C)	-2.52	-4.86	-6.59	-6.95
Average reduction (°C)	1.62	2.72	4.23	4.80

All the results for the five scenarios were imported into Leonardo software for visual presentation. Figure 11 is the base model scenario that has 0% canopy cover. Figures 12(a) and 10(b) are scenarios with 9% and 15% vegetation cover, respectively. While Figures 12(c) and 10(d) are the scenarios with 30% and 45% vegetation cover, respectively. The MRT for the five different vegetation cover scenarios was illustrated at 15:00 hrs, whereas the MRT was at the peak point. The visual images showed a significant MRT reduction with the increase in the vegetation cover. The reduction effects were 2.82°C, 4.88°C, 7.53°C, and 8.62°C for scenarios with 9.%, 15.%, 30.%, and 45.% vegetation cover respectively. Thus, it demonstrated no significant difference between the base model and the current situation on campus with 9% vegetation.

Thermal Effects of Vegetation Cover in Campus Outdoor Environment

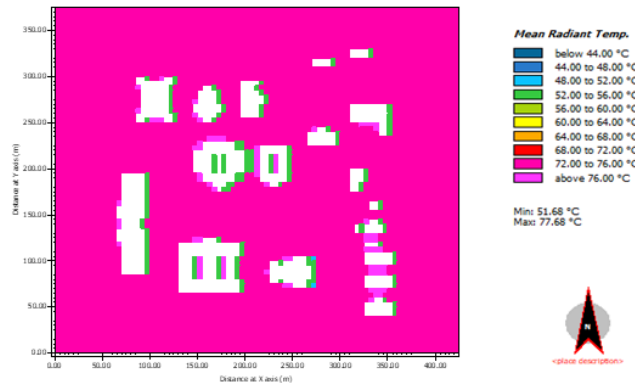
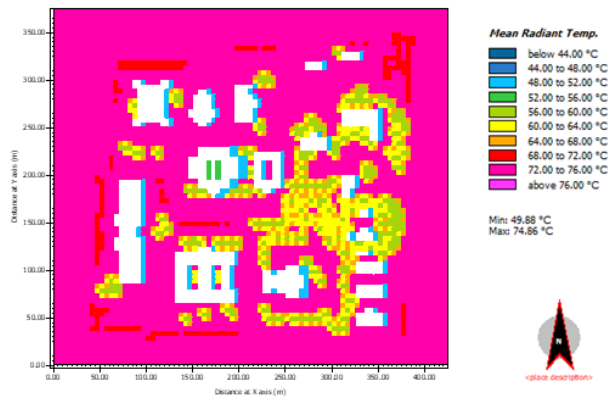
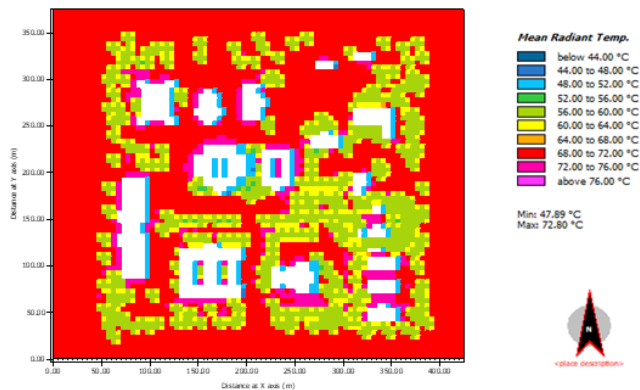


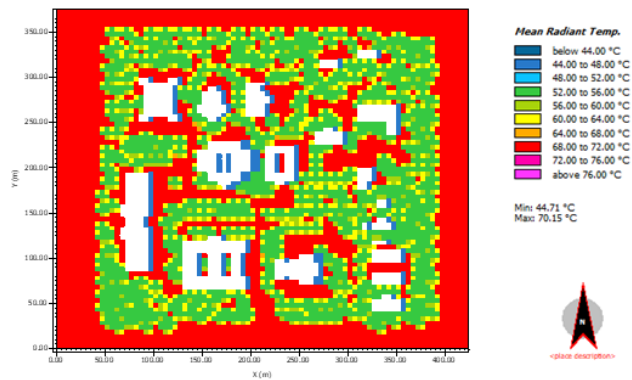
Figure 11. Mean radiant temperature visual output for the scenario with 0% vegetation cover



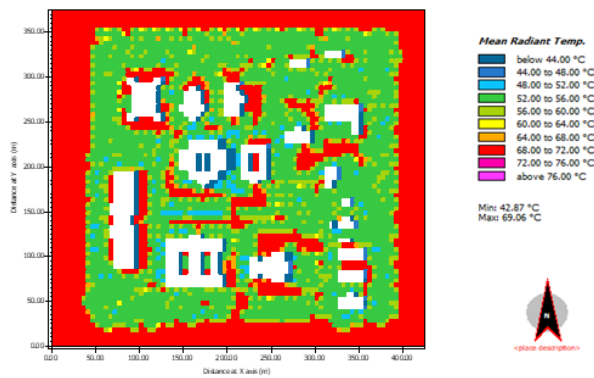
(a)



(b)



(c)



(d)

Figure 12. Mean radiant temperature visual output for; (a) Scenario with 9% vegetation, (b) Scenario with 15% vegetation cover, (c) Scenario with 30% vegetation cover, and (d) Scenario with 45% cover

DISCUSSION

Several anthropogenic and natural features in an urban centre influence the thermal condition of its microclimates (Soydan, 2020). The features lead to higher or lower thermal conditions of the urban environments. Vegetation forms part of the natural features that improve the thermal state of urban microclimates (Davtalab et al., 2020). Five modelled scenarios were simulated for 24hrs in evaluating the improvement capacity of different percentages of vegetation covers within a campus. The initial simulation inputs were based on the field measurements. The simulation outputs showed that the higher the tree canopy cover percentage, the higher the thermal reduction effects in the daytime. The base model

with 0% tree canopy cover has the highest air temperature (Figure 7a) and the MRT (Figure 10a) in the daytime. The scenario with 45% vegetation cover has the lowest maximum air temperature and MRT in the day. The high level intensity of the parameters in the base model was due to the absence of vegetation cover. Lack of shaded areas from tree canopies allows direct solar radiation onto surfaces. The exposed surfaces, in turn, emit more heat to the surrounding atmosphere. The results showed that all the maximum thermal reduction effects are positive, while the minimum thermal reduction effects appeared in a negative value (Table 2 & 3). These indicate that vegetation does not render thermal reduction effects every hour of the day. The thermal reduction effects generally occur in the daytime, where the thermal properties of the climatic parameters are at their peak degrees.

The highest reduction effect of 0.63°C was recorded with the tree canopy covers of 45%. The air temperature amelioration effect obtained in this study was lower than those obtained by Davtalab et al. (2020) and Nasir et al. (2015). Who found that a scenario with dense vegetation was lower by 1.0°C than scenarios without any vegetation. The difference might have been due lack of inclusion of specific percentages of vegetation coverage in the Davtalab et al. (2020). Similarly, Nasir et al. (2015) used up to 80% of vegetation coverage to achieve the 1.0°C temperature reduction. The 24.4% reduction of MRT in this study was achieved only when 45% of the tree canopy coverage was used. The insignificant MRT reduction effect found here agrees well with the study by Spangenberg et al. (2008). Whereby, they equally recorded up to 24.0°C MRT reduction after using dense trees of 10m height. However, the maximum MRT reduction of 24.4% was lower than the 30°C obtained by Taleghani et al. (2016). It was a result of differences in the base model scenarios, as Taleghani's base model receptor was placed directly above the unshaded asphalt concrete road.

CONCLUSION

Air temperature and MRT are important meteorological parameters that determine the thermal condition of campus outdoors in a hot and dry climate. This study evaluated the effects of different coverage of tree canopies on air temperature and MRT reduction in a campus environment in Bauchi, Nigeria. The study concludes that the thermal reduction effects of vegetation do not apply to every hour. The vegetation enhances the thermal condition of the campus microclimates, especially during the daytime. The study has identified the best thermal reduction provided by vegetation cover of 45% is in the daytime. The study suggests up to 45% vegetation cover at places used by students in the daytime. Such locations include academic areas and outdoor recreational areas. In contrast, up to 30% of vegetation cover be placed at places that engage students in the nighttime. In essence, the university authority needs to have proper planning and implementation of the campus outdoor green spaces. The proper planning, implementation and maintenance of the

green space is the key factor in improving the thermal conditions of campus outdoor. Thus, adhering to the practical recommendations will significantly improve the amelioration of the rise in temperature on campus outdoors. The improved campus outdoors will equally improve the students' physical and psychological well-being. Similarly, it will enhance learning capacity due to the students' satisfaction with the thermal environment.

ACKNOWLEDGEMENT

The authors acknowledged the support of Tertiary Education Trust Fund (TETFund) Nigeria as part of its Academic Staff Training and Development (AST&D) interventions. We also appreciate the permissions granted to the authors by the Abubakar Tafawa Balewa University, Bauchi, Nigeria, in the process of data collection. Furthermore, we would like to thank the editors and anonymous referees for the constructive review of this manuscript. Finally, the authors would also like to thank all the people who rendered their supports in one way or the other in ensuring the success of this study.

REFERENCES

- Abaas, Z. R. (2020). Impact of development on Baghdad's urban microclimate and human thermal comfort. *Alexandria Engineering Journal*, 59(1), 275-290. <https://doi.org/10.1016/j.aej.2019.12.040>
- Aboulnaga, M., & Mostafa, M. (2020). Climate change adaptation: Prioritising districts for urban green coverage to mitigate high temperatures and UHIE in developing countries. In *Renewable Energy and Sustainable Buildings* (pp. 825-837). Springer. https://doi.org/10.1007/978-3-030-18488-9_68
- Adunola, A. O. (2014). Evaluation of urban residential thermal comfort in relation to indoor and outdoor air temperatures in Ibadan, Nigeria. *Building and Environment*, 75, 190-205. <https://doi.org/10.1016/j.buildenv.2014.02.007>
- Akande, O. K., & Adebamowo, M. A. (2010, April 9-11). Indoor thermal comfort for residential buildings in hot-dry climate of Nigeria. In *Proceedings of Conference: Adapting to Change: New Thinking on Comfort* (Vol. 911, pp. 133-144). Windsor, UK.
- Al-Mohsen, M. A. S., Ismail, S., & Ismail, I. S. (2020). Improving thermal comfort through natural ventilation and passive solar systems in residential buildings in Iraq: Review paper. *International Conference in Architecture and Civil Engineering*, 59, 207-216. https://doi.org/10.1007/978-981-15-1193-6_24
- Brysse, K., Oreskes, N., O'Reilly, J., & Oppenheimer, M. (2013). Climate change prediction: Erring on the side of least drama? *Global Environmental Change*, 23(1), 327-337. <https://doi.org/10.1016/j.gloenvcha.2012.10.008>
- Centre for Science and Environment. (2018). *CSE analyses the new IPCC special report on global warming of 1.5°C* (Press release). Brill. https://doi.org/10.1163/9789004322714_cclc_2018-0009-002
- Chatzinikolaou, E., Chalkias, C., & Dimopoulou, E. (2018). Urban microclimate improvement using ENVI-MET climate model. *International Archives of the Photogrammetry, Remote Sensing and Spatial Information Sciences - ISPRS Archives*, 42(4), 69-76. <https://doi.org/10.5194/isprs-archives-XLII-4-69-2018>

- Davtalab, J., Deyhimi, S. P., Dessi, V., Hafezi, M. R., & Adib, M. (2020). The impact of green space structure on physiological equivalent temperature index in open space. *Urban Climate*, 31(October 2017), Article 100574. <https://doi.org/10.1016/j.uclim.2019.100574>
- Dhakal, S. (2002). The urban heat environment and urban sustainability. In F. Moavenzadeh, K. Hanaki, & P. Baccini (Eds.), *Future Cities : Dynamics and Sustainability* (pp. 149-172). Springer Science+Business Media. https://doi.org/10.1007/978-94-010-0365-0_8
- Eludoyin, O. M., Adelekan, I. O., Webster, R., & Eludoyin, A. O. (2014). Air temperature, relative humidity, climate regionalization and thermal comfort of Nigeria. *International Journal of Climatology*, 34(6), 2000-2018. <https://doi.org/10.1002/joc.3817>
- Eniolu, T., Kong, L., Lau, K. K., Yuan, C., & Ng, E. (2017). A study on the impact of shadow-cast and tree species on in-canyon and neighborhood 's thermal comfort. *Building and Environment*, 115, 1-17. <https://doi.org/10.1016/j.buildenv.2017.01.005>
- Evola, G., Gagliano, A., Fichera, A., Marletta, L., Martinico, F., Nocera, F., & Pagano, A. (2017). UHI effects and strategies to improve outdoor thermal comfort in dense and old neighbourhoods. *Energy Procedia*, 134, 692-701. <https://doi.org/10.1016/j.egypro.2017.09.589>
- Forouzandeh, A. (2018). Numerical modeling validation for the microclimate thermal condition of semi-closed courtyard spaces between buildings. *Sustainable Cities and Society*, 36(August 2017), 327-345. <https://doi.org/10.1016/j.scs.2017.07.025>
- Frédéric, D., Du, C., Et, S., & Club, W. A. (2008). *Atlas on regional integration in West Africa* (Issue January). Retrieved October 13, 2019, from www.atlas-westafrica.org
- Ghaffarianhoseini, A., Berardi, U., Ghaffarianhoseini, A., & Al-obaidi, K. (2019). Analyzing the thermal comfort conditions of outdoor spaces in a university campus in Kuala Lumpur, Malaysia. *Science of the Total Environment*, 666, 1327-1345. <https://doi.org/10.1016/j.scitotenv.2019.01.284>
- Hami, A., Abdi, B., Zarehaghi, D., & Bin, S. (2019). Assessing the thermal comfort effects of green spaces : A systematic review of methods , parameters , and plants ' attributes. *Sustainable Cities and Society*, 49(May), Article 101634. <https://doi.org/10.1016/j.scs.2019.101634>
- Hassan, S. F., Tantawi, A. M. E., & Hashidu, U. S. (2017). Trends of rainfall and temperature over North-Eastern Nigeria (1949-2014). *IOSR Journal of Environmental Science, Toxicology and Food Technology*, 11(05), 01-09. <https://doi.org/10.9790/2402-1105010109>
- Hertel, D., & Schlink, U. (2019). Decomposition of urban temperatures for targeted climate change adaptation. *Environmental Modelling and Software*, 113, 20-28. <https://doi.org/10.1016/j.envsoft.2018.11.015>
- Lai, D., Liu, W., Gan, T., Liu, K., & Chen, Q. (2019). A review of mitigating strategies to improve the thermal environment and thermal comfort in urban outdoor spaces. *Science of the Total Environment*, 661, 337-353. <https://doi.org/10.1016/j.scitotenv.2019.01.062>
- Lu, J., Li, Q., Zeng, L., Chen, J., Liu, G., Li, Y., Li, W., & Huang, K. (2017). A micro-climatic study on cooling effect of an urban park in a hot and humid climate. *Sustainable Cities and Society*, 32(April), 513-522. <https://doi.org/10.1016/j.scs.2017.04.017>

- Lucchi, E., Becherini, F., Di Tuccio, M. C., Troi, A., Frick, J., Roberti, F., Hermann, C., Fairmington, I., Mezzasalma, G., Pockel , L., & Bernardi, A. (2017). Thermal performance evaluation and comfort assessment of advanced aerogel as blown-in insulation for historic buildings. *Building and Environment*, *122*, 258-268. <https://doi.org/10.1016/j.buildenv.2017.06.019>
- Morakinyo, T. E., Dahanayake, K. W. D. K. C., Adegun, O. B., & Balogun, A. A. (2016). Modelling the effect of tree-shading on summer indoor and outdoor thermal condition of two similar buildings in a Nigerian University. *Energy and Buildings*, *130*, 721-732. <https://doi.org/10.1016/j.enbuild.2016.08.087>
- Morakinyo, T. E., & Lam, Y. F. (2016). Simulation study on the impact of tree-configuration, planting pattern and wind condition on street-canyon's micro-climate and thermal comfort. *Building and Environment*, *103*, 262-275. <https://doi.org/10.1016/j.buildenv.2016.04.025>
- Morgan, M. R. (2006). Climate change 2001. In E. Graham & S. Lee (Eds.), *Weather* (p. 235). Cambridge University Press. <https://doi.org/10.1256/wea.58.04>
- Nasir, R. A., Ahmad, S. S., Zain-Ahmed, A., & Ibrahim, N. (2015). Adapting human comfort in an urban area: The role of tree shades towards urban regeneration. *Procedia - Social and Behavioral Sciences*, *170*, 369-380. <https://doi.org/10.1016/j.sbspro.2015.01.047>
- Ozkeresteci, I., Crewe, K., Brazel, A. J., & Bruse, M. (2003). Use and evaluation of the envi-met model for environmental design and planning: An experiment on linear parks. In *Proceedings of the 21st International Cartographic Conference (ICC)* (pp. 10-16). Document Transformation Technologies. [https://doi.org/ISBN: 0-958-46093-0](https://doi.org/ISBN:0-958-46093-0)
- Peeters, A., Shashua-Bar, L., Meir, S., Shmulevich, R. R., Caspi, Y., Weyl, M., Motzafi-Haller, W., & Angel, N. (2020). A decision support tool for calculating effective shading in urban streets. *Urban Climate*, *34*(April 2019), Article 100672. <https://doi.org/10.1016/j.uclim.2020.100672>
- Perini, K., Chokhachian, A., Dong, S., & Auer, T. (2017). Modeling and simulating urban outdoor comfort: Coupling ENVI-Met and TRNSYS by grasshopper. *Energy and Buildings*, *152*, 373-384. <https://doi.org/10.1016/j.enbuild.2017.07.061>
- Roth, M., & Lim, V. H. (2017). Evaluation of canopy-layer air and mean radiant temperature simulations by a microclimate model over a tropical residential neighbourhood. *Building and Environment*, *112*, 177-189. <https://doi.org/10.1016/j.buildenv.2016.11.026>
- Salata, F., Golasi, I., de Lieto Vollaro, R., & de Lieto Vollaro, A. (2016). Urban microclimate and outdoor thermal comfort. A proper procedure to fit ENVI-met simulation outputs to experimental data. *Sustainable Cities and Society*, *26*, 318-343. <https://doi.org/10.1016/j.scs.2016.07.005>
- Shahzad, U. (2015). Global warming: Causes, effects and solutions. *Durreesamin Journal*, *1*(4), 1-7.
- Shinzato, P., Simon, H., Silva Duarte, D. H., & Bruse, M. (2019). Calibration process and parametrization of tropical plants using ENVI-met V4-Sao Paulo case study. *Architectural Science Review*, *62*(2), 112-125. <https://doi.org/10.1080/00038628.2018.1563522>
- Soydan, O. (2020). Effects of landscape composition and patterns on land surface temperature: Urban heat island case study for Nigde, Turkey. *Urban Climate*, *34*(December 2019), Article 100688. <https://doi.org/10.1016/j.uclim.2020.100688>

- Spangenberg, J., Shinzato, P., Johansson, E., & Duarte, D. (2008). Simulation of the influence of vegetation on microclimate and thermal comfort in the city of São Paulo. *Revista da Sociedade Brasileira de Arborização Urbana*, 3(2), 1-19.
- Sylvester, O., & Abdulquadir, I. (2015). An Assessment of the evidence of climate change in Bauchi, Nigeria. *Journal of Applied Sciences and Environmental Management*, 19(3), 375-381. <https://doi.org/10.4314/jasem.v19i3.5>
- Taleghani, M., Sailor, D., & Ban-Weiss, G. A. (2016). Micrometeorological simulations to predict the impacts of heat mitigation strategies on pedestrian thermal comfort in a Los Angeles neighborhood. *Environmental Research Letters*, 11(2), Article 024003. <https://doi.org/10.1088/1748-9326/11/2/024003>
- Tong, S., Wong, N. H., Tan, C. L., Jusuf, S. K., Ignatius, M., & Tan, E. (2017). Impact of urban morphology on microclimate and thermal comfort in northern China. *Solar Energy*, 155, 212-223. <https://doi.org/10.1016/j.solener.2017.06.027>
- Tsoka, S. (2017). Investigating the relationship between urban spaces morphology and local microclimate: A study for Thessaloniki. *Procedia Environmental Sciences*, 38, 674-681. <https://doi.org/10.1016/j.proenv.2017.03.148>
- Tsoka, S., Tsikaloudaki, A., & Theodosiou, T. (2018). Analyzing the ENVI-met microclimate model's performance and assessing cool materials and urban vegetation applications – A review. *Sustainable Cities and Society*, 43(August), 55-76. <https://doi.org/10.1016/j.scs.2018.08.009>
- Wong, N. H., Tan, A. Y. K., Chen, Y., Sekar, K., Tan, P. Y., Chan, D., Chiang, K., & Wong, N. C. (2010). Thermal evaluation of vertical greenery systems for building walls. *Building and Environment*, 45(3), 663-672. <https://doi.org/10.1016/j.buildenv.2009.08.005>
- Wong, N. H., Yok, T. P., & Yu, C. (2007). Study of thermal performance of extensive rooftop greenery systems in the tropical climate. *Building and Environment*, 42(1), 25-54. <https://doi.org/10.1016/j.buildenv.2005.07.030>
- Yahia, M. W., & Johansson, E. (2014). Landscape interventions in improving thermal comfort in the hot dry city of Damascus, Syria-The example of residential spaces with detached buildings. *Landscape and Urban Planning*, 125, 1-16. <https://doi.org/10.1016/j.landurbplan.2014.01.014>
- Yahia, M. W., Johansson, E., Thorsson, S., Lindberg, F., & Rasmussen, M. I. (2018). Effect of urban design on microclimate and thermal comfort outdoors in warm-humid Dar es Salaam, Tanzania. *International Journal of Biometeorology*, 62(3), 373-385. <https://doi.org/10.1007/s00484-017-1380-7>
- Yang, Y., Zhou, D., Gao, W., Zhang, Z., Chen, W., & Peng, W. (2018). Simulation on the impacts of the street tree pattern on built summer thermal comfort in cold region of China. *Sustainable Cities and Society*, 37, 563-580. <https://doi.org/10.1016/j.scs.2017.09.033>
- Yıldırım, M. (2020). Shading in the outdoor environments of climate-friendly hot and dry historical streets: The passageways of Sanliurfa, Turkey. *Environmental Impact Assessment Review*, 80, Article 106318. <https://doi.org/10.1016/j.eiar.2019.106318>



Evaluating the Steady-state Performance of the Synthetic Coefficient of Variation Chart

Ming Hui Chew¹, Wai Chung Yeong^{2*}, Muzalwana Abdul Talib³, Sok Li Lim⁴ and Khai Wah Khaw⁵

¹*Institute for Advanced Studies, Universiti Malaya, 50603 Kuala Lumpur, Malaysia*

²*Department of Operation and Management Information Systems, Faculty of Business and Accountancy, Universiti Malaya, 50603 Kuala Lumpur, Malaysia*

³*Department of Applied Statistics, Faculty of Economics and Administration, Universiti Malaya, 50603 Kuala Lumpur, Malaysia*

⁴*Institute of Mathematical Sciences, Faculty of Science, Universiti Malaya, 50603 Kuala Lumpur, Malaysia*

⁵*School of Management, Universiti Sains Malaysia, 11800 Penang, Malaysia*

ABSTRACT

The synthetic coefficient of variation (CV) chart is attractive to practitioners as it allows for a second point to fall outside the control limits before deciding whether the process is out-of-control. The existing synthetic CV chart is designed with a head-start feature, which shows an advantage under the zero-state assumption where shifts happen immediately after process monitoring has started. However, this assumption may not be valid as shifts may happen quite some time after process monitoring has started. This is

called the steady-state condition. This paper evaluates the performance of the chart under the steady-state condition. It is shown that the steady-state out-of-control average run length (ARL_1) is substantially larger than the zero-state ARL_1 , hence larger number of samples are needed to detect the out-of-control condition. From the comparison with other CV charts, the steady-state synthetic CV chart does not show better performance, especially for small sample sizes and shift sizes. Hence, the synthetic CV chart is not recommended to be adopted under the steady-state condition, and its

ARTICLE INFO

Article history:

Received: 21 December 2020

Accepted: 1 April 2021

Published: 31 July 2021

DOI: <https://doi.org/10.47836/pjst.29.3.20>

E-mail addresses:

rachelchewjingsi@gmail.com (Ming Hui Chew)

thomas_yeong@yahoo.com (Wai Chung Yeong)

wana_am@um.edu.my (Muzalwana Abdul Talib)

sokli@um.edu.my (Sok Li Lim)

khaiwah@usm.edu.my (Khai Wah Khaw)

*Corresponding author

good performance is only applicable under the zero-state assumption. The results of this paper enable practitioners to be aware that the performance of the synthetic CV chart may be inferior under actual application (when shifts do not happen at the beginning of process monitoring) compared to its zero-state performance.

Keywords: Coefficient of variation; control chart, exponentially weighted moving average, run rules, Shewhart, steady-state, synthetic chart, zero-state

INTRODUCTION

Control charts are useful tools to monitor a process for the presence of assignable cause(s), which results in an out-of-control condition. A lot of studies to improve the performance of control charts and to apply them in various scenarios are available in the literature, some of the recent ones are Khan et al. (2017), Marchant et al. (2018), You (2018), Mim et al. (2019) and Kinat et al. (2020). Similar with most conventional control charts, the charts are designed to monitor shifts in the process mean (μ) and/or standard deviation (σ), usually through \bar{X} and/or R/S charts. However, control charting techniques are extended to various scientific areas, where μ and σ are always not constant and the process is nevertheless considered as in-control. This setting is usual in the context of engineering, healthcare, agriculture, education, and a variety of applications where the process output changes from time to time. For example, to maintain quality control checks on laboratory measurement on the amount of chemical in a patient's blood, the mean amount varies from patient to patient, making it unsuitable to monitor μ .

Conventional μ and/or σ charts cannot be applied to monitor the stability and variability for such processes, since a change in μ and/or σ does not show an out-of-control (OOC) process. For processes with an inconsistent μ and/or σ , it is a better alternative to monitor the CV= $\left(\gamma = \frac{\sigma}{\mu}\right)$ if the ratio of σ to μ is consistent, even though μ and/or σ varies. Yeong et al. (2017) have reviewed several fields where the CV is important. For example, σ is often found to be proportional with μ for certain quality characteristics related to the physical properties of metal alloys or composite materials, for example tool cutting life and several properties of sintered materials (Castagliola et al., 2011). In investments, the CV can measure the volatility compared to the expected return (Curto & Pinto, 2009). For example, Pang et al. (2008) measured the stability of dividend yields of the Hang Seng index through γ .

Kang et al. (2007) was the pioneer who first proposed a Shewhart type chart to monitor the CV. Subsequently, several new CV charts are proposed to improve the performance of CV-type charts, for example the Exponentially Weighted Moving Average (EWMA) CV chart by Castagliola et al. (2011) and the synthetic CV chart by Calzada and Scariano (2013). Recently, Zhang et al. (2018) proposed an improved EWMA CV chart by truncating

negative normalized observations to zero and Mahmood and Abbasi (2021) improved the performance of the Shewhart CV chart under neoteric ranked set sampling.

The synthetic CV chart by Calzada and Scariano (2013) modifies the synthetic chart by Wu and Spedding (2000), who proposed the synthetic chart to monitor the process mean, so that it can monitor the CV. Subsequently, Yeong et al. (2018) proposed the economic and economic-statistical designs of the synthetic CV chart. The synthetic CV chart shows smaller ARL_1 than the Shewhart CV chart in detecting all shifts but shows larger ARL_1 than the EWMA CV chart. The ARL is a commonly used measure of performance for control charts (Montgomery, 2019). There are two types of ARL, i.e., the IC ARL (ARL_0) and OOC ARL (ARL_1). The ARL_0 measures the average number of samples taken until a false alarm occurs, while the ARL_1 measures the average number of samples taken until an OOC condition is detected. A large ARL_0 and a small ARL_1 is preferred. By fixing the ARL_0 as a specific value, a chart shows better performance if it has a small ARL_1 . This is because a chart with a smaller ARL_1 can detect shifts faster.

For a synthetic CV chart, when a sample CV ($\hat{\gamma}$) falls outside the upper and lower control limits (UCL and LCL, respectively), an OOC signal is not immediately produced. Instead, these samples are only known as non-conforming samples, while conforming samples are samples within the limits. The chart will signal depending on the conforming run length (CRL), which counts the number of conforming samples between successive non-conforming samples. When $CRL \leq L$, the process is OOC, conversely it is in-control (IC). Note that L is a threshold set by the practitioner, which determines how close two successive non-conforming samples must be to each other (measured in terms of the number of conforming samples between two successive non-conforming samples), so that an OOC signal will be produced. Since the synthetic CV chart gives an OOC signal when $CRL \leq L$, a smaller value of L indicates that the non-conforming samples must be quite close to each other to produce an OOC signal, while for larger values of L , an OOC signal will still be produced even though the non-conforming samples are quite far from each other. A larger L is usually selected when practitioners are interested to detect a small shift in the process, conversely a smaller L is selected for large shifts. In practice, the value of L is determined to minimize the ARL_1 , subject to constraints in the ARL_0 .

Recently, Rakitzis et al. (2019) gave an overview of recent studies on synthetic-type charts. A thorough review is provided for different types of synthetic chart monitoring the mean, variance and the joint monitoring of the mean and variance. Rakitzis et al. (2019) has stated that the synthetic chart is designed with a head-start feature which leads to misleading conclusion on the actual performance of the synthetic chart. Similarly, the synthetic CV chart by Calzada and Scariano (2013) is also designed based on an enormous head-start. This head-start feature assumes that a non-conforming sample is present at the starting time ($t = 0$). As a result, the first CRL will simply be the number of samples until

the first non-conforming sample is observed. If the first CRL is less than or equals to L , then this head-start feature will provide an advantage to the synthetic CV chart, since fewer samples are required to give an OOC signal as the chart does not have to wait until the second sample to fall outside the control limits before deciding whether the process is IC or OOC. If the process starts in an OOC condition (commonly referred to as the zero-state condition), it is likely that the first non-conforming sample will be encountered not long after process monitoring has started, hence it is likely that the first CRL will be less than or equal to L . Under such conditions, the head-start feature will result in an improvement in the performance of the synthetic CV chart.

However, when the process shifts only happen after the process has been operating for quite some time (commonly referred to as the steady-state condition), it is unlikely for a non-conforming sample to be encountered not long after the starting time. As a result, it is likely that the first CRL will be more than L , and the head-start feature will not result in an advantage anymore. In this paper, the performance of the synthetic CV chart when the head-start advantage has faded away will be studied. This is important so that practitioners can evaluate the performance of the synthetic CV chart without the head-start advantage, which is likely to occur in a steady-state condition.

Davis and Woodall (2002) were the pioneer who propose the steady-state synthetic \bar{X} chart. Recently, Knoth (2016) conducted a thorough study on the synthetic \bar{X} chart by considering two steady-state assumptions, i.e., conditional, and cyclical steady-states. Conditional steady-state assumes that there are no false alarms before the shift, while the cyclical steady-state assumes that a series of false alarms may happen before the shift. Formulae for the conditional and cyclical ARLs are derived. There is a significant difference between the zero-state and steady-state performance of the synthetic \bar{X} chart. For small and moderate shifts, the zero-state synthetic \bar{X} chart performs better than the run rules chart, while for large shifts, it performs better than the EWMA chart. However, the synthetic \bar{X} chart shows the worst steady-state performance compared to the steady-state EWMA and run rules charts (Knoth, 2016).

Teoh et al. (2016) compared the cyclical steady-state performance of the synthetic and EWMA CV charts. However, the methodology to evaluate the cyclical steady-state performance is not given. Furthermore, the conditional steady-state performance is not studied in Teoh et al. (2016). This paper provides the formulae for the conditional and cyclical steady-states, so that practitioners can easily evaluate the steady-state performance of the synthetic CV chart. The methodology to obtain the optimal chart parameters based on the steady-state performance is also provided. Furthermore, this paper also evaluates the impact of different assumptions on initial states towards the ARL, which is not studied in Teoh et al. (2016). The initial state refers to the state prior to the shift in the process. This paper considers two designs. Both designs evaluate the steady-state performance. In

the first design, chart parameters that optimizes the zero-state ARL are adopted, while the second design optimizes the steady-state ARL. These two designs are, then, compared to evaluate whether the second design results in a significant improvement compared to the first design.

MATERIALS AND METHODS

This section starts with a review of the operations of the synthetic CV chart. Subsequently, the zero and steady-state ARL of the synthetic CV chart is discussed.

The synthetic CV chart classifies a sample as non-conforming if the sample CV is either above the upper control limit (UCL) or below the lower control limit (LCL), i.e., $\hat{\gamma} > UCL$ or $\hat{\gamma} < LCL$. By letting “0” denote a conforming sample and “1” denote a non-conforming sample, a series of samples can be illustrated as a sequence of zeros and ones. For example, 10010 shows a series of five samples, where the non-conforming samples are the first and fourth samples. The digits to the right show whether the most recent sample is conforming/non-conforming, while digits to the left shows whether the earlier samples are conforming or non-conforming.

When two successive “1”s are encountered, the number of samples between the successive “1”s are defined as the CRL, where the CRL includes the ending non-conforming sample. For example, the CRL is 4 for string 10001. When $CRL \leq L$, the process is OOC, conversely it is IC. For example, the string 10001 is IC if L is set as 3, while it is OOC if L is set as 4, or any value more than 4.

When two successive non-conforming samples are encountered, the synthetic chart determines whether the process is IC or OOC by counting the number of conforming samples between successive non-conforming samples. However, when the first non-conforming sample is encountered, the CRL will simply be the number of samples until this non-conforming sample is encountered. This is called the head-start feature. For example, CRLs for the initial strings 1, 01, 001 and 0001 are 1, 2, 3 and 4, respectively. If L is set as 3, the first three strings will result in an OOC signal, while the fourth string results in an IC signal.

The head-start feature will result in a faster detection under a zero-state assumption. However, under the steady-state condition (where the process becomes OOC after the process has been operating for some time), the head-start advantage would have faded away. Hence, it is important for practitioners to evaluate the steady-state performance of the synthetic CV chart without the head-start advantage.

Zero-state ARL

Castagliola et al. (2011) has shown that the cumulative distribution function (cdf) of $\hat{\gamma}$ in Equation 1.

$$F_{\hat{\gamma}}(x|n, \gamma) = 1 - F_t\left(\frac{\sqrt{n}}{x} \middle| n-1, \frac{\sqrt{n}}{\gamma}\right) \tag{1}$$

Where $F_t\left(\cdot \middle| n-1, \frac{\sqrt{n}}{\gamma}\right)$ is the non-central t -distribution with $(n-1)$ degrees of freedom and non-centrality parameter $\frac{\sqrt{n}}{\gamma}$, with n being the sample size and γ the CV.

Inverting the cdf in Equation 1 gives Equation 2,

$$F_{\hat{\gamma}}^{-1}(\alpha|n, \gamma) = \frac{\sqrt{n}}{F_t^{-1}\left(1 - \alpha \middle| n-1, \frac{\sqrt{n}}{\gamma}\right)} \tag{2}$$

with $F_t^{-1}\left(\cdot \middle| n-1, \frac{\sqrt{n}}{\gamma}\right)$ being the inverse cdf of the non-central t distribution. From Equation 1 and 2, if $F_{\hat{\gamma}}^{-1}(\alpha|n, \gamma) = x$, then $F_{\hat{\gamma}}(x|n, \gamma) = \alpha$. In other words, $F_{\hat{\gamma}}^{-1}(\alpha|n, \gamma)$ evaluates the value of x such that $P(\hat{\gamma} \leq x) = \alpha$. In control chart design, α is usually related to the false alarm probability, so that the control limits can be determined to obtain a false alarm probability set by the practitioner.

The LCL and UCL can be obtained as Equation 3,

$$LCL = \frac{\sqrt{n}}{F_t^{-1}\left(1 - \frac{p}{2} \middle| n-1, \frac{\sqrt{n}}{\gamma_0}\right)} \tag{3}$$

and Equation 4.

$$UCL = \frac{\sqrt{n}}{F_t^{-1}\left(\frac{p}{2} \middle| n-1, \frac{\sqrt{n}}{\gamma_0}\right)} \tag{4}$$

Where γ_0 is the IC CV and p is the probability the sample CV falls outside the LCL and UCL when the process is IC. Note that p is usually determined to fix the IC run length.

Let A and B be the probabilities a sample is conforming and non-conforming, respectively. A is obtained as Equation 5,

$$\begin{aligned} A &= P(LCL < \hat{\gamma} < UCL) \\ &= F_{\hat{\gamma}}(UCL|n, \gamma) - F_{\hat{\gamma}}(LCL|n, \gamma) \end{aligned} \tag{5}$$

with $F_{\hat{\gamma}}(\cdot)$ defined in Equation 1 and $B = 1 - A$. By merging Equation 1 and 5, A can be computed as Equation 6.

$$A = F_t\left(\frac{\sqrt{n}}{LCL} \middle| n-1, \frac{\sqrt{n}}{\gamma}\right) - F_t\left(\frac{\sqrt{n}}{UCL} \middle| n-1, \frac{\sqrt{n}}{\gamma}\right). \tag{6}$$

To construct the Markov chain, we define the states $0, 1, \dots, L-1$ as the number of “0”s after the most recent 1, and state L as the state with at least L “0”s after the most recent 1. For example, for $L = 3$, the states 0, 1, 2 and 3 represent the initial strings 001, 010, 100 and 000, respectively. The transition probability matrix is constructed as Equation 7,

$$\mathbf{P} = \begin{matrix} 0 \\ 1 \\ 2 \\ \vdots \\ L-2 \\ L-1 \\ L \\ \text{OOC} \end{matrix} \begin{pmatrix} 0 & A & 0 & 0 & \dots & 0 & 0 & B \\ 0 & 0 & A & 0 & \dots & 0 & 0 & B \\ 0 & 0 & 0 & A & \dots & 0 & 0 & B \\ \vdots & \vdots \\ 0 & 0 & 0 & 0 & \dots & A & 0 & B \\ 0 & 0 & 0 & 0 & \dots & 0 & A & B \\ B & 0 & 0 & 0 & \dots & 0 & A & 0 \\ 0 & 0 & 0 & 0 & \dots & 0 & 0 & 1 \end{pmatrix} \quad [7]$$

where OOC is the absorbing OOC state. Note that the states of the Markov chain in Equation 7 are defined differently from most synthetic papers. By referring to the state definitions in Davis and Woodall (2002), states $0, 1, \dots, L-1$ in this paper is equivalent to states $1, 2, \dots, L$ in Davis and Woodall (2002), while state L in this paper is equivalent to state 0 in Davis and Woodall (2002). \mathbf{P} in Equation 7 can be converted to the same form as that in Davis and Woodall (2002) by shifting the row and column for state L to the first row and column, respectively.

The rationale behind adopting slightly different state definitions is to facilitate a more intuitive analysis of the performance for the synthetic CV chart under different initial states. By referring to the state definitions in the preceding paragraph, as the states become larger, the non-conforming sample moves towards the left (except for State L where all the samples are conforming). This shows that the smaller states have a more recent occurrence of the non-conforming sample. By studying the performance of the chart as the states increases, practitioners will be able to easily observe the impact of the non-conforming sample’s position on the performance of the chart.

By removing the last row and column of \mathbf{P} , a transient $(L+1) \times (L+1)$ sub-matrix \mathbf{Q} is obtained. The ARL is computed as Equation 8.

$$\text{ARL} = \mathbf{q}^T (\mathbf{I} - \mathbf{Q})^{-1} \mathbf{1} \quad [8]$$

Where \mathbf{q} is the $(L+1) \times 1$ vector of initial probabilities for the transient states, \mathbf{I} is an $(L+1) \times (L+1)$ identity matrix and $\mathbf{1}$ is an $(L+1) \times 1$ vector of ones. Under the zero-state assumption, $\mathbf{q} = (1, 0, \dots, 0)^T$. In addition, zero-state ARLs for all possible starting states can also be obtained by solving $(\mathbf{I} - \mathbf{Q})\mathbf{l} = \mathbf{1}$, where $\mathbf{l} = (l_0, l_1, \dots, l_L)^T$ are the ARLs for the different starting states. By letting $r = B(1 - A^L)$, Knoth (2016) has defined Equation 9.

$$\mathbf{l}^T = \begin{matrix} 0 & 1 & \dots & L-1 & L \end{matrix} \begin{pmatrix} \frac{1}{r} & \frac{1 + A^L(A^{-1} - 1)}{r} & \dots & \frac{1 + A^L(A^{-(L-1)} - 1)}{r} & \frac{1}{r} + \frac{1}{B} \end{pmatrix}, \quad [9]$$

Where the ARL_0 is computed by letting $\gamma = \gamma_0$ in Equation 6 to obtain the A and B in Equation 9, while the ARL_1 is computed by letting $\gamma = \tau\gamma_0$, with τ being the shift size the practitioner is interested to detect. Note that although notionally different and with different state definitions as mentioned in the preceding paragraph, \mathbf{l}^T in Equation 9 is the same as the ARL vector in Shongwe and Graham (2017; 2019). However, note that Shongwe and Graham (2017; 2019) conducted a study for the synthetic \bar{X} chart, while this paper studies the synthetic CV chart.

Steady-state ARL

The distribution for different initial states before the change point (θ) is studied in this section. The distribution is based on conditional and cyclical assumptions, and it will be utilized in formulating the steady-state ARLs.

To obtain the conditional stationary density, let $\Psi^T = (\pi_0 \ \pi_1 \ \dots \ \pi_{L-1} \ \pi_L)$ be the quasi-stationary density conditioned on no false alarm before θ , where π_i is the state i stationary probabilities, $i = 0, 1, \dots, L$. From Markov chain theory, Ψ^T can be obtained by solving the equations $\mathbf{Q}^T \Psi = \varphi \Psi$ and $\Psi^T \mathbf{1} = 1$, where Ψ^T is obtained as Equation 10.

$$\Psi^T = \begin{pmatrix} 0 & 1 & \dots & L-1 & L \\ s & \frac{A}{\varphi}s & \dots & \left(\frac{A}{\varphi}\right)^{L-1} s & \frac{\varphi}{B}s \end{pmatrix}, \tag{10}$$

Where $s = 1 - \frac{A}{\varphi}$. φ is obtained by solving $\Psi^T \mathbf{1} = 1$ numerically with the starting value $\varphi_0 = 1$.

To obtain the cyclical stationary density, it needs to be considered that the process restarts at the zero-state level after a false alarm. Hence, the matrix \mathbf{Q} is modified by adding the contents of the last column of \mathbf{Q} into the first column of \mathbf{Q} . We refer to this modified matrix as \mathbf{Q}_* . By adopting a similar approach as that for the conditional probability distribution Ψ , the cyclical stationary density is obtained as Equation 11,

$$\Psi_* = \begin{pmatrix} 0 & 1 & \dots & L-1 & L \\ B & AB & \dots & A^{L-1}B & A^L \end{pmatrix}, \tag{11}$$

which is the cyclical stationary distribution for the synthetic chart. The cyclical stationary distribution for the synthetic chart was first discussed and formulated by Machado and Costa (2014). Note that Machado and Costa (2014) investigated the performance for the synthetic \bar{X} chart, while this paper studies the performance of the synthetic CV chart.

From the conditional and cyclical distributions in Equation 10 and 11, the conditional and cyclical steady-state ARLs, denoted as ARL_{cond} and ARL_{cyc} respectively, is obtained

as Equation 12,

$$= \left(\begin{array}{c} \varphi_0 + \frac{1 - \left(\frac{A_0}{\varphi_0}\right)^L}{B_0} \\ 1 - \frac{A_0}{\varphi_0} \end{array} \right) \frac{s_0}{B_\delta} + \left(\begin{array}{c} \varphi_0 + A_\delta^L \frac{1 - \left(\frac{A_0}{A_\delta \varphi_0}\right)^L}{B_0} \\ 1 - \frac{A_0}{A_\delta \varphi_0} \end{array} \right) \frac{s_0}{r_\delta}, \quad [12]$$

and Equation 13.

$$\begin{aligned} \text{ARL}_{\text{cyc}} &= \mathbf{\theta}_{*,0}^T \mathbf{I}_\delta \\ &= \frac{1 + A_0 B_\delta \frac{A_0^L - A_\delta^L}{A_0 - A_\delta}}{r_\delta} \\ &= \frac{1}{B_\delta} + \left(1 - \frac{B_\delta A_0 (1 - A_0^L) - B_0 A_\delta (1 - A_\delta^L)}{A_0 - A_\delta} \right) \frac{1}{r_\delta} \end{aligned} \quad [13]$$

Where the subscripts 0 and δ denote the IC and OOC versions. The longer term in Equation 13 is like that of Wu et al. (2010). Note that Wu et al. (2010) studied the performance for the synthetic \bar{X} chart, while this paper studies the performance of the synthetic CV chart.

RESULTS AND DISCUSSION

This section starts with a study on the performance of the synthetic CV chart under different initial states, and the probability for different initial states under the conditional and cyclical steady-state assumptions. The initial states refer to the state before the process shift. Next, the steady-state performance of the synthetic CV chart is studied based on two designs. Finally, the zero and steady-state performance of the synthetic CV chart is compared with the EWMA, run rules and Shewhart CV charts.

Synthetic CV Chart Under Different Initial States

In this section, the impact of different initial states on the performance of the synthetic CV chart is studied. Unlike the zero-state ARL which assumes that the initial state is zero, the actual initial state can belong to any of the states 0, 1, ..., L . This section investigates the effects on the ARL_1 when the optimal chart parameters that minimize the zero-state ARL_1 is adopted on processes with a non-zero initial state. The probability for different initial states is also obtained. The effects on the ARL_1 and the initial state probabilities are evaluated based on the conditional and cyclical assumptions.

The optimal chart parameters and ARL_1 for $n = 5$ and $\tau \in \{1.10, 1.25, 1.50, 2.00\}$ from Calzada and Scariano (2013) is shown in Table 1. Note that the optimal chart parameters from Calzada and Scariano (2013) is based on the zero-state ARL_1 .

The ARL_1 shown in Table 1 can only be obtained under a zero-state condition or if the initial state is 0. However, under the steady-state assumption, the initial state may not be zero, and the ARL_1 shown in Table 1 may not be obtained. For example, the zero-state ARL_1 for $i = 0, 1, \dots, L$ is 115.39. However, the ARL_1 might not be 115.39 if the initial state is not 0. Hence, this section will look at the actual ARL_1 for different initial states. For an initial state i , $i = 0, 1, \dots, L$, this is achieved by letting the $(i + 1)^{th}$ element of the vector \mathbf{q} be 1, while letting the other elements of \mathbf{q} be zero. Table 2 shows the conditional and cyclical probabilities, as well as the ARL_1 for different initial states, when the optimal chart parameters in Table 1 is adopted, where similar with Table 1, $n = 5$ and $\gamma_0 = 0.05$. Due to space constraints and the consistency in the trends, only results for states 0, 1, $L-1$ and L are shown in Table 2.

The same optimal chart parameters in Table 1 are adopted in Table 2. This is to study the effects of adopting these chart parameters for cases where the initial state is not zero. For example, for $n = 5, \gamma_0 = 0.05$ and $\tau = 1.10$, this paper investigates the impact towards ARL_1 when the optimal chart parameters ($L = 73, LCL = 0.01031, UCL = 0.09943$), obtained to optimize the ARL_1 based on a zero initial state, is implemented on processes with a non-zero initial state, i.e. any initial state from states 1 to 73. This will enable us to study the actual performance of the chart when the initial state is not zero, as shown in Table 2.

Table 1

Optimal chart parameters and ARL_1 of the zero-state synthetic CV chart for $n = 5, \gamma_0 = 0.05$ and $\tau \in \{1.10, 1.25, 1.50, 2.00\}$

τ	L	LCL	UCL	ARL_1
1.10	73	0.01031	0.09943	115.39
1.25	30	0.01142	0.09651	24.02
1.50	12	0.01277	0.09326	5.76
2.00	5	0.01426	0.08993	1.97

By moving vertically down the second last column of Table 2, the ARL_1 increases gradually as the initial state becomes larger. The last column of Table 2 shows the percentage increase from the zero-state ARL_1 . The differences between the ARL_1 for an initial state of zero and an initial state of L can be quite large, especially for small shift sizes of $\tau = 1.10$. For example, when $\tau = 1.10$, the ARL_1 increases by 63.39% from 115.39 when the initial state is zero to 188.53 when the initial state is 73. A similar trend is also shown for other values of τ . This shows that the actual performance will differ from that shown by the zero-state ARL_1 when the state before the change point is not zero.

Table 2

The conditional probability, cyclical probability and ARL_1 for different initial states based on the optimal chart parameters for the zero-state synthetic CV chart

τ	L	LCL	UCL	Initial state	Conditional Probability	Cyclical Probability	ARL_1	Percentage Increase from the Zero-state ARL_1
1.10	73	0.01031	0.09943	0	0.00482	0.00685	115.39	0%
				1	0.00480	0.00680	115.97	0.50%
				⋮	⋮	⋮	⋮	⋮
				72	0.00341	0.00418	186.96	62.02%
				73	0.70264	0.60547	188.53	63.39%
1.25	30	0.01142	0.09651	0	0.00802	0.01019	24.02	0%
				1	0.00796	0.01009	24.28	1.08%
				⋮	⋮	⋮	⋮	⋮
				29	0.00635	0.00757	41.95	74.65%
				30	0.78532	0.73536	43.20	79.85%
1.50	12	0.01277	0.09326	0	0.01335	0.01565	5.76	0%
				1	0.01317	0.01540	5.87	1.91%
				⋮	⋮	⋮	⋮	⋮
				11	0.01151	0.01316	9.96	72.92%
				12	0.85107	0.82757	11.05	91.84%
2.00	5	0.01426	0.08993	0	0.02142	0.02381	1.97	0%
				1	0.02096	0.02324	2.03	3.05%
				⋮	⋮	⋮	⋮	⋮
				4	0.01964	0.02162	2.87	45.69%
				5	0.89740	0.88649	3.89	97.46%

Steady-state Performance

This section evaluates the conditional and cyclical steady-state ARL_1 s. The first design adopts chart parameters that are optimal for the zero-state ARL_1 , while the second design adopts chart parameters that are optimal for the steady-state ARL_1 .

First Design. The optimal chart parameters based on the methodology by Calzada and Scariano (2013), which optimizes the zero-state ARL_1 , is adopted in this design. The value

of p in Equation 3 and 4 is obtained so that the zero-state $ARL_0 = 370.4$. Table 3 shows the zero-state, conditional and cyclical steady-state ARL_1 s based on these optimal chart parameters for $\gamma_0 \in \{0.05, 0.10, 0.20\}$, $n \in \{5, 10, 15\}$ and $\tau \in \{1.10, 1.25, 1.50, 2.00\}$. In parenthesis beside the steady-state ARL_1 s are the percentage increase from the zero-state ARL_1 . The first three columns of Table 3 show the optimal (L, LCL, UCL) which minimizes the zero-state ARL_1 in Equation 8, subject to the constraint $ARL_0 = 370.4$.

Table 3

The conditional and cyclical steady state ARL'_1 when chart parameters which optimizes the zero-state ARL_1 are adopted

$\gamma_0 = 0.05$						
$n = 5$						
τ	L	LCL	UCL	Zero-state ARL_1	Conditional Steady-state ARL'_1	Cyclical Steady- state ARL'_1
1.10	73	0.01031	0.09943	115.39	175.10 (51.75%)	170.37 (47.65%)
1.25	30	0.01142	0.09651	24.02	40.47 (68.48%)	39.81 (65.74%)
1.50	12	0.01277	0.09326	5.76	10.47 (81.77%)	10.37 (80.03%)
2.00	5	0.01426	0.08993	1.97	3.73 (89.34%)	3.71 (88.32%)
$n = 10$						
1.10	57	0.02118	0.08237	78.87	122.40 (55.19%)	119.56 (51.59%)
1.25	17	0.02277	0.07975	11.48	20.03 (74.48%)	19.82 (72.65%)
1.50	6	0.02435	0.07727	2.71	5.05 (86.35%)	5.03 (85.61%)
2.00	3	0.02550	0.07552	1.22	2.35 (92.62%)	2.34 (91.80%)
$n = 15$						
1.10	46	0.02651	0.07554	58.48	92.21 (57.68%)	90.36 (54.51%)
1.25	12	0.02814	0.07304	7.18	12.50 (74.09%)	12.39 (72.56%)
1.50	4	0.02965	0.07109	1.86	3.50 (88.17%)	3.49 (87.63%)
2.00	2	0.03070	0.06968	1.07	2.06 (92.52%)	2.05 (91.59%)
$\gamma_0 = 0.10$						
$n = 5$						
1.10	73	0.02057	0.20079	116.16	176.19 (51.68%)	171.44 (47.59%)
1.25	31	0.02271	0.19499	24.34	41.06 (68.69%)	40.37 (65.86%)
1.50	12	0.02549	0.18805	5.85	10.62 (81.54%)	10.53 (80.00%)
2.00	5	0.02846	0.18120	2.00	3.78 (89.00%)	3.76 (88.00%)

Table 3 (Continued)

$\gamma_0 = 0.05$						
τ	L	LCL	UCL	Zero-state ARL ₁	Conditional Steady-state ARL' ₁	Cyclical Steady-state ARL' ₁
$n = 10$						
1.10	59	0.04217	0.16590	79.77	124.06 (55.52%)	121.08 (51.79%)
1.25	17	0.04544	0.16038	11.71	20.37 (73.95%)	20.15 (72.08%)
1.50	6	0.04859	0.15533	2.76	5.15 (86.59%)	5.12 (85.51%)
2.00	3	0.05090	0.15175	1.24	2.37 (91.13%)	2.37 (91.13%)
$n = 15$						
1.10	46	0.05291	0.15180	59.32	93.43 (57.50%)	91.57 (54.37%)
1.25	12	0.05616	0.14702	7.33	13.04 (77.90%)	12.94 (76.53%)
1.50	4	0.05919	0.14273	1.89	3.56 (88.36%)	3.54 (87.30%)
2.00	2	0.06128	0.13985	1.07	2.07 (93.46%)	2.06 (92.52%)
$\gamma_0 = 0.20$						
$n = 5$						
1.10	73	0.04080	0.41798	119.29	180.34 (51.18%)	175.52 (47.14%)
1.25	32	0.04488	0.40525	25.68	43.19 (68.19%)	42.45 (65.30%)
1.50	12	0.05057	0.38902	6.25	11.28 (80.48%)	11.18 (78.88%)
2.00	5	0.05647	0.37369	2.13	4.01 (88.26%)	3.99 (87.32%)
$n = 10$						
1.10	59	0.08355	0.34021	83.48	129.14 (54.70%)	126.08 (51.03%)
1.25	18	0.08976	0.32867	12.65	21.92 (73.28%)	21.68 (71.38%)
1.50	6	0.09636	0.31705	2.98	5.52 (85.23%)	5.49 (84.23%)
2.00	3	0.10096	0.30929	1.29	2.48 (92.25%)	2.47 (91.47%)

Table 3 (Continued)

$\gamma_0 = 0.05$						
τ	L	LCL	UCL	Zero-state ARL ₁	Conditional Steady-state ARL' ₁	Cyclical Steady- state ARL' ₁
$n = 15$						
1.10	49	0.10461	0.30989	62.78	98.81 (57.39%)	96.73 (54.08%)
1.25	13	0.11098	0.29973	7.97	14.15 (77.54%)	14.02 (75.91%)
1.50	5	0.11617	0.29178	2.02	3.82 (89.11%)	3.80 (88.12%)
2.00	2	0.12164	0.28368	1.10	2.12 (92.73%)	2.11 (91.82%)

From Table 3, the conditional and cyclical ARL₁ is larger than the zero-state ARL₁, especially for small values of τ . For instance, when $\gamma_0 = 0.05$, $n = 5$ and $\tau = 1.10$, under a zero-state assumption, practitioners would assume that the ARL₁ is 115.39. However, if these chart parameters are adopted for the steady-state condition, the ARL₁ increases to 175.10 and 170.37, respectively under conditional and cyclical assumptions. For ease of reference, the steady-state ARL₁s based on optimal chart parameters that minimize the zero-state ARL₁ is referred to as ARL'₁. There is a large difference between the zero-state ARL₁ and ARL'₁ when τ and n is small. As a result, under the steady-state condition, the zero-state ARL₁ gives an incorrect evaluation of the actual performance and will likely lead to a lack of confidence towards the chart.

There is a smaller difference between the zero-state ARL₁ and ARL'₁ for larger values of n and τ , although a higher percentage increase from the zero-state is shown. For example, when $\gamma_0 = 0.05$, $n = 5$ and $\tau = 1.10$, the difference between the zero-state ARL₁ with the conditional and cyclical ARL'₁ s are 59.71 and 54.98, respectively, but when $\gamma_0 = 0.05$, $n = 5$ and $\tau = 2.00$, the corresponding difference reduces to 1.76 and 1.74, respectively, while when $\gamma_0 = 0.05$, $n = 15$ and $\tau = 1.10$, the corresponding difference reduces to 33.73 and 31.88.

There are minimal differences between the conditional and cyclical ARL'₁, with the conditional ARL'₁ being slightly larger than the cyclical ARL'₁. For example, when $\gamma_0 = 0.05$, $n = 5$ and $\tau = 1.10$, the conditional and cyclical steady states ARL'₁ s are 175.10 and 170.37, respectively, with a difference of 2.70%. For larger values of τ , the differences are even smaller. For example, when $\gamma_0 = 0.05$, $n = 5$ and $\tau = 2.00$, the conditional and cyclical steady states ARL'₁ is 3.73 and 3.71, respectively, with a minimal difference of 0.54%.

Second Design. Alternative optimal chart parameters (L , LCL, UCL) are proposed to minimize the conditional and cyclical steady-state ARL₁s, unlike in first design where

they are chosen to minimize the zero-state ARL_1 . The chart parameters can be obtained through the following steps.

1. Specify γ_0 , n and τ .
2. Set $L = 1$.
3. Numerically solve $ARL_0 = 370.4$ to obtain p . This is achieved by using numerical methods in the Scicoslab software to find the value of p to solve $\frac{1}{p(1-(1-p)^L)} = 370.4$.
4. By substituting p in Step 3 into Equation 3 and 4, the LCL and UCL are obtained.
5. Calculate the conditional (cyclical) ARL_1 from Equation 12 (Equation 13) with the current combination of (L, LCL, UCL) .
6. Increase L by 1.
7. Repeat Steps 3 to 6 until the conditional (cyclical) ARL_1 for $L+1$ is larger than the conditional (cyclical) ARL_1 for L .

The (L, LCL, UCL) with the smallest conditional (cyclical) ARL_1 are considered the optimal chart parameters. In Step 3, p is obtained by solving the zero-state ARL_0 , instead of solving the steady-state ARL_0 with $\delta = 0$ in Equation 12 or 13. This is to ensure that both the first and second designs have the same IC run length performance, so that a fair comparison can be made between these two designs.

The optimal chart parameters, conditional and cyclical ARL_1 s when $\gamma_0 \in \{0.05, 0.10, 0.20\}$, $n \in \{5, 10, 15\}$ and $\tau \in \{1.10, 1.25, 1.50, 2.00\}$ are shown in Table 4. In parenthesis beside the ARL_1 s are the percentage improvement compared to the first design in Table 3.

From Table 4, for smaller shift sizes, the conditional and cyclical ARL_1 adopting the optimal chart parameters that minimize the steady-state ARL_1 are smaller than the corresponding ARL'_1 that is based on the optimal parameters that minimize the zero-state ARL_1 . For instance, when $\gamma_0 = 0.05$, $n = 5$ and $\tau = 1.10$, the conditional and cyclical ARL_1 are 175.10 and 170.37, respectively, when the parameters from Table 3 are adopted. However, when the optimal parameters that minimizes the steady-state ARL_1 are adopted, the conditional and cyclical ARL_1 are 161.45 and 160.88, respectively. This shows a percentage improvement of 7.80% and 5.57%, respectively, when the correct optimal parameters are adopted. The reduction on ARL_1 shows that less average number of samples are required to detect the OOC condition. This results in quicker corrective action taken to repair the process and reduces the number of defective products produced due to an OOC process. For large shift sizes, there are minimal or no difference between the ARL_1 in Table 3 and 4.

Table 4

The optimal chart parameters and ARL_1 for the conditional and cyclical steady-state synthetic CV chart

$\gamma_0 = 0.05$								
Conditional Steady State					Cyclical Steady State			
τ	L	LCL	UCL	$n = 5$				
				ARL_1	L	LCL	UCL	ARL_1
1.10	13	0.01264	0.09355	161.45 (7.80%)	14	0.01253	0.09382	160.88 (5.57%)
1.25	14	0.01253	0.09382	39.18 (3.19%)	15	0.01242	0.09407	38.91 (2.26%)
1.50	8	0.01343	0.09174	10.32 (1.43%)	8	0.01343	0.09174	10.26 (1.06%)
2.00	4	0.01467	0.08905	3.72 (0.27%)	4	0.01467	0.08905	3.71 (0%)
τ				$n = 10$				
1.10	14	0.02305	0.07930	114.48 (6.47%)	15	0.02295	0.07846	113.95 (4.69%)
1.25	9	0.02371	0.07826	19.53 (2.50%)	9	0.02371	0.07826	19.42 (2.02%)
1.50	4	0.02501	0.07626	5.02 (0.59%)	5	0.02464	0.07682	5.01 (0.40%)
2.00	3	0.02550	0.07552	2.35 (0%)	3	0.02550	0.07552	2.34 (0%)
τ				$n = 15$				
1.10	13	0.02804	0.07335	86.97 (5.75%)	15	0.02785	0.07361	86.55 (4.22%)
1.25	7	0.02886	0.07219	12.53 (-0.24%)	7	0.02886	0.07219	12.47 (-0.65%)
1.50	3	0.03008	0.07052	3.50 (0%)	3	0.03008	0.07052	3.40 (2.58%)
2.00	2	0.03070	0.06968	2.06 (0%)	2	0.03070	0.06968	2.05 (0%)
				$\gamma_0 = 0.10$				
τ				$n = 5$				
1.10	13	0.02524	0.18865	162.36 (7.85%)	14	0.02501	0.18921	161.78 (5.63%)
1.25	14	0.02501	0.18921	39.66 (3.53%)	15	0.02480	0.18973	39.38 (2.45%)
1.50	8	0.02681	0.18493	10.48 (1.32%)	8	0.02681	0.18493	10.42 (1.04%)
2.00	4	0.02928	0.17940	3.77 (0.26%)	4	0.02928	0.17940	3.76 (0%)

Table 4 (Continued)

$\gamma_0 = 0.05$								
τ	Conditional Steady State				Cyclical Steady State			
	L	LCL	UCL	ARL ₁	L	LCL	UCL	ARL ₁
	$n = 10$							
1.10	14	0.04600	0.15947	115.66 (7.26%)	15	0.04580	0.15980	115.12 (4.92%)
1.25	9	0.04732	0.15734	19.88 (2.41%)	10	0.04700	0.15785	19.78 (1.84%)
1.50	4	0.04992	0.15326	5.12 (0.58%)	5	0.04918	0.15440	5.09 (0.59%)
2.00	3	0.05090	0.15175	2.37 (0%)	3	0.05090	0.15175	2.37 (0%)
	$n = 15$							
1.10	13	0.05596	0.14732	88.12 (5.68%)	15	0.05559	0.14785	87.68 (4.25%)
1.25	7	0.05761	0.14496	12.78 (1.99%)	7	0.05761	0.14496	12.72 (1.70%)
1.50	3	0.06004	0.14155	3.55 (0.28%)	3	0.06004	0.14155	3.54 (0%)
2.00	2	0.06128	0.13985	2.07 (0%)	2	0.06128	0.13985	2.06 (0%)
	$\gamma_0 = 0.20$							
	$n = 5$							
1.10	13	0.05007	0.39038	166.11 (7.89%)	13	0.05007	0.39038	165.54 (5.69%)
1.25	14	0.04961	0.39164	41.67 (3.65%)	15	0.04919	0.39280	41.38 (2.52%)
1.50	8	0.05320	0.38201	11.15 (1.15%)	8	0.05320	0.38201	11.08 (0.89%)
2.00	4	0.05810	0.36966	4.01 (0%)	5	0.05647	0.37369	3.99 (0%)
	$n = 10$							
1.10	13	0.09163	0.32531	120.45 (6.73%)	15	0.09080	0.32680	119.90 (4.90%)
1.25	9	0.09383	0.32143	21.36 (2.55%)	10	0.09319	0.32255	21.24 (2.03%)
1.50	5	0.09754	0.31504	5.49 (0.54%)	5	0.09754	0.31504	5.47 (0.36%)
2.00	3	0.10097	0.30929	2.48 (0%)	3	0.10096	0.30929	2.47 (0%)

The difference between the conditional and cyclical ARL_1 by adopting the optimal chart parameters that minimize the steady-state ARL_1 are smaller compared to the one in Table 3. For example, for $\gamma_0 = 0.05$, $n = 5$ and $\tau = 1.10$, the conditional and cyclical ARL_1 are 161.45 and 160.88 in Table 4 (a difference of 0.35%), but for Table 3, they are 175.10 and 170.37 (a difference of 2.70%). Similar with Knoth (2016), the optimal L in Table 4 is smaller than the optimal L in Table 3, especially for small shift sizes. For example, when $\gamma_0 = 0.05$, $n = 5$ and $\tau = 1.10$, the optimal L in Table 4 is 13 and 14 under the conditional and cyclical assumptions, respectively, while the corresponding optimal L in Table 3 is 73. Meanwhile, a larger LCL and smaller UCL is observed in Table 4, compared with Table 3. For example, when $\gamma_0 = 0.05$, $n = 5$ and $\tau = 1.10$, the optimal (LCL, UCL) in Table 4 is (0.01264, 0.09355) and (0.01253, 0.09832) under the conditional and cyclical assumptions, respectively, while the corresponding optimal (LCL, UCL) in Table 3 is (0.01031, 0.09943). Hence, the range of CV values for a sample to be identified as conforming has been reduced and will likely result in an increase in the occurrence of non-conforming samples. From Equation 5, a larger LCL and smaller UCL will decrease the probability for A , thus increasing the probability of non-conforming samples. For example, when $\gamma_0 = 0.05$, $n = 5$ and $\tau = 1.10$, the probability of a non-conforming sample is 0.02659 and 0.01784 for the conditional and cyclical assumptions in Table 4, respectively, while the corresponding probability of a non-conforming sample in Table 3 is 0.01367.

Although the second design results in better steady-state performance than the first design for small shift sizes, the ARL_1 is still quite large compared with the zero-state ARL_1 . As expected, the zero-state ARL_1 does not give a true picture on the chart's performance under the steady-state condition.

Performance Comparisons

The synthetic CV chart is compared with the run rules, EWMA and Shewhart CV charts in this section. Castagliola et al. (2013) and Castagliola et al. (2011) gave a thorough discussion on the run rules and EWMA CV charts, respectively.

The zero-state ARL_1 of these charts, for $\gamma_0 \in \{0.05, 0.10, 0.20\}$, $n \in \{5, 10, 15\}$ and $\tau \in \{1.1, 1.2, 1.5, 2.0\}$ are shown in Table 5. In parenthesis are the percentage of improvement of the run rules, EWMA and Shewhart CV charts compared to the synthetic CV chart, where a negative percentage shows that the synthetic CV chart performs better. The optimal L in Table 3 is adopted for the synthetic CV chart. For instance, when $n = 5$ and $\gamma_0 = 0.05$, $L = 73, 30, 12$ and 5 for $\tau = 1.10, 1.25, 1.50$ and 2.00 , respectively. Besides that, it is assumed that the initial state for the synthetic CV chart is state 0 since that is the assumption for the zero-state design of the chart.

From Table 5, the zero-state synthetic CV chart outperforms the Shewhart CV chart for all γ_0 , n and τ . This is especially so for small n and τ , where the difference in ARL_1

is quite large. The zero-state synthetic CV chart outperforms the zero-state run rules CV chart for most cases, except when $\tau = 1.10$ for $n = 5$, where the run rules chart slightly outperforms the synthetic chart. The zero-state EWMA chart outperforms the zero-state synthetic chart, except when shift sizes are large.

Although the synthetic CV chart seems to outperform the run rules CV chart in most cases, the comparison is based on a zero-state assumption. Note that the zero-state synthetic CV chart assumes that the initial state is zero. Although a zero initial state results in the best performance, the probability for a zero initial state is very small in a steady-state scenario. For example, from Table 2, when $\gamma_0 = 0.05$, $n = 5$ and $\tau = 1.10$, the conditional and cyclical probability of a zero initial state are 0.00482 and 0.00685, respectively. This shows that there is a less than 1% chance for the occurrence of the zero-initial state. Hence, in Table 6, the conditional and cyclical steady-state ARL_{1s} for synthetic, run rules, EWMA and Shewhart CV charts are compared. In parenthesis are the percentage of improvement of the run rules, EWMA and Shewhart CV charts compared to the synthetic CV chart, where a negative percentage shows that the synthetic CV chart performs better.

By comparing Tables 5 and 6 for the run rules and EWMA charts, negligible differences are shown between the zero-state and steady-state ARL_{1s} , since these two charts does not involve any head-start feature, while the zero-state and steady-state Shewhart CV charts are the same, as no assumptions are required for the initial state. Note that in Table 6, the same L as that in Table 4 is adopted for the synthetic chart. For example, for $n = 5$ and $\gamma_0 = 0.05$, $L = 13, 14, 8$, and 4 for $\tau = 1.10, 1.25, 1.50$ and 2.00, respectively for the conditional steady-state, while $L = 14, 15, 8$ and 4 for $\tau = 1.10, 1.25, 1.50$ and 2.00, respectively during cyclical steady-states.

From Table 6, the run rules CV chart outperforms the synthetic CV chart for all n , γ_0 and τ , especially for small n and τ . However, for large n and τ , the synthetic and run rules CV charts shows comparable steady-state performance, with the run rules CV chart showing slightly better performance. Hence, the synthetic CV chart outperforms the run rules CV chart only for a zero-state assumption and not under the steady-state scenario. In fact, for numerous cases, the synthetic CV chart is not even better than the basic Shewhart CV chart. Since it is more difficult to implement the synthetic CV chart, practitioners would rather implement the Shewhart CV chart. Furthermore, the steady-state EWMA CV chart outperforms the steady-state synthetic CV chart for all n , γ_0 and τ . Hence, the synthetic CV chart does not show good performance under the steady-state scenario.

Table 5
 A comparison of the zero-state ARL_1 of the synthetic, run rules and Shewhart C \bar{V} charts for $\gamma_0 \in \{0.05, 0.10, 0.20\}$, $n \in \{5, 10, 15\}$ and $\tau \in \{1, 1.1, 1.2, 1.5, 2, 2.0\}$

τ	$n = 5$											
	$\gamma_0 = 0.05$				$\gamma_0 = 0.10$				$\gamma_0 = 0.20$			
	Synthetic	Run Rules	EWMA	Shewhart	Synthetic	Run Rules	EWMA	Shewhart	Synthetic	Run Rules	EWMA	Shewhart
1.10	115.39	113.77	55.05	159.86	116.16	113.88	55.21	160.64	119.29	111.57	55.85	163.95
	(1.40%)	(52.29%)	(-38.54%)	(-38.54%)	(1.96%)	(1.96%)	(52.47%)	(-38.29%)	(6.47%)	(6.47%)	(53.18%)	(-37.44%)
1.25	24.02	30.65	15.30	43.55	24.34	30.66	15.37	44.08	25.68	30.82	15.67	44.98
	(-27.60%)	(36.30%)	(-81.31%)	(-81.31%)	(-25.97%)	(-25.97%)	(36.85%)	(-81.10%)	(-20.02%)	(-20.02%)	(38.98%)	(-75.16%)
1.50	5.76	9.01	5.65	10.57	5.85	9.01	5.70	10.76	6.25	9.36	5.91	11.09
	(-56.42%)	(1.91%)	(-83.51%)	(-83.51%)	(-54.02%)	(-54.02%)	(2.56%)	(-83.93%)	(5.44%)	(-49.76%)	(5.44%)	(-77.44%)
2.00	1.97	3.53	2.34	2.89	2.00	3.53	2.37	2.95	2.13	3.72	2.51	3.05
	(-79.19%)	(-18.78%)	(-46.70%)	(-46.70%)	(-76.50%)	(-76.50%)	(-18.50%)	(-47.50%)	(-17.84%)	(-17.84%)	(-17.84%)	(-43.19%)

τ	$n = 10$											
	$\gamma_0 = 0.05$				$\gamma_0 = 0.10$				$\gamma_0 = 0.20$			
	Synthetic	Run Rules	EWMA	Shewhart	Synthetic	Run Rules	EWMA	Shewhart	Synthetic	Run Rules	EWMA	Shewhart
1.10	78.87	90.88	32.08	120.27	79.77	90.60	32.30	121.32	83.48	89.68	33.17	125.69
	(-15.23%)	(59.33%)	(-52.49%)	(-52.49%)	(-13.58%)	(-13.58%)	(59.51%)	(-52.09%)	(-7.43%)	(-7.43%)	(60.27%)	(-50.56%)
1.25	11.48	17.44	8.50	22.94	11.71	17.56	8.57	23.37	12.65	18.07	8.88	24.11
	(-51.92%)	(25.96%)	(-99.83%)	(-99.83%)	(-49.96%)	(-49.96%)	(26.81%)	(-99.57%)	(29.80%)	(29.80%)	(29.80%)	(-90.59%)
1.50	2.71	4.75	3.14	4.78	2.76	4.81	3.18	4.89	2.98	5.05	3.35	5.09
	(-75.28%)	(-15.87%)	(-76.38%)	(-76.38%)	(-74.28%)	(-74.28%)	(-15.22%)	(-77.17%)	(-12.42%)	(-12.42%)	(-12.42%)	(-70.81%)
2.00	1.22	2.36	1.41	1.52	1.24	2.38	1.43	1.55	1.29	2.46	1.51	1.60
	(-93.44%)	(-15.57%)	(-24.59%)	(-24.59%)	(-91.94%)	(-91.94%)	(-15.32%)	(-25.00%)	(-17.05%)	(-17.05%)	(-17.05%)	(-24.03%)

τ	$n = 15$											
	$\gamma_0 = 0.05$				$\gamma_0 = 0.10$				$\gamma_0 = 0.20$			
	Synthetic	Run Rules	EWMA	Shewhart	Synthetic	Run Rules	EWMA	Shewhart	Synthetic	Run Rules	EWMA	Shewhart
1.10	58.48	73.53	23.58	95.85	59.32	73.53	23.78	96.92	62.78	73.56	24.55	101.34
	(-25.74%)	(59.68%)	(-63.90%)	(-63.90%)	(-23.95%)	(-23.95%)	(59.91%)	(-63.39%)	(-17.17%)	(-17.17%)	(60.90%)	(-61.42%)
1.25	7.18	11.65	6.14	14.83	7.33	11.79	6.21	15.16	7.97	12.31	6.46	15.71
	(-62.26%)	(14.48%)	(-106.55%)	(-106.55%)	(-60.85%)	(-60.85%)	(15.28%)	(-106.82%)	(-54.45%)	(-54.45%)	(18.95%)	(-97.11%)
1.50	1.86	3.40	2.29	3.02	1.89	3.45	2.33	3.09	2.02	3.62	2.46	3.22
	(-82.80%)	(-23.12%)	(-62.37%)	(-62.37%)	(-82.54%)	(-82.54%)	(-23.28%)	(-63.49%)	(-23.28%)	(-23.28%)	(-23.28%)	(-59.41%)
2.00	1.07	2.11	1.15	1.19	1.07	2.12	1.16	1.21	1.10	2.16	1.21	1.23
	(-97.20%)	(-7.48%)	(-11.21%)	(-11.21%)	(-98.13%)	(-98.13%)	(-8.41%)	(-13.08%)	(-13.08%)	(-13.08%)	(-10.00%)	(-11.82%)

Table 6
 The conditional and cyclical steady-state ARL_1 of the synthetic, run rules, EWMA and Shewhart CV charts for $\tau \in \{1.1, 1.2, 1.5, 2.0\}$

τ	$n = 5$														
	$\% = 0.05$						$\% = 0.10$								
	Synthetic		Run Rules		EWMA		Shewhart		Synthetic		Run Rules		EWMA		Shewhart
Cond	Cyc	Cond	Cyc	Cond	Cyc	Cond	Cyc	Cond	Cyc	Cond	Cyc	Cond	Cyc	Cond	Cyc
1.10	161.45	160.88	113.02	113.03	52.70	52.77	159.86	162.36	161.78	112.52	112.52	52.89	52.95	160.64	160.64
	(30.00%)	(29.74%)	(67.36%)	(67.20%)	(0.98%)	(0.98%)	(16.81%)	(30.70%)	(30.45%)	(67.42%)	(67.27%)	(1.06%)	(1.06%)	(44.08)	(44.08)
	39.18	38.91	30.28	30.28	14.83	14.83	43.55	39.66	39.38	30.30	30.30	14.90	14.90	44.08	44.08
	(22.72%)	(22.18%)	(62.17%)	(61.89%)	(-11.15%)	(-11.15%)	(-11.15%)	(23.60%)	(23.06%)	(62.43%)	(62.16%)	(-11.14%)	(-11.14%)	10.76	10.76
1.50	10.32	10.26	8.83	8.83	5.52	5.52	10.57	10.48	10.42	8.90	8.90	5.57	5.57	10.76	10.76
	(14.44%)	(13.94%)	(46.51%)	(46.20%)	(-2.42%)	(-2.42%)	(-2.42%)	(15.08%)	(14.59%)	(46.85%)	(46.55%)	(-2.67%)	(-2.67%)	2.95	2.95
	3.72	3.71	3.43	3.43	2.32	2.32	2.89	3.77	3.76	3.47	3.47	2.35	2.35	2.95	2.95
	(7.80%)	(7.55%)	(37.63%)	(37.47%)	(22.31%)	(22.31%)	(22.31%)	(7.96%)	(7.71%)	(37.67%)	(37.50%)	(21.75%)	(21.75%)		
2.00	3.72	3.71	3.43	3.43	2.32	2.32	2.89	3.77	3.76	3.47	3.47	2.35	2.35	2.95	2.95
	(7.80%)	(7.55%)	(37.63%)	(37.47%)	(22.31%)	(22.31%)	(22.31%)	(7.96%)	(7.71%)	(37.67%)	(37.50%)	(21.75%)	(21.75%)		
1.10	114.48	113.95	90.21	90.22	30.73	30.80	120.27	115.66	115.12	89.94	89.94	31.02	31.02	121.32	121.32
	(21.20%)	(20.82%)	(73.16%)	(72.97%)	(-5.06%)	(-5.06%)	(-5.06%)	(22.24%)	(21.87%)	(73.21%)	(73.05%)	(-4.89%)	(-4.89%)	23.37	23.37
	19.53	19.42	17.18	17.18	8.23	8.16	22.94	19.88	19.78	17.30	17.30	8.31	8.24	23.37	23.37
	(12.03%)	(11.53%)	(57.86%)	(57.98%)	(-17.46%)	(-17.46%)	(-17.46%)	(12.98%)	(12.54%)	(58.20%)	(58.34%)	(-17.56%)	(-17.56%)	4.89	4.89
1.50	5.02	5.01	4.63	4.63	3.09	3.09	4.78	5.12	5.09	4.69	4.69	3.13	3.13	4.89	4.89
	(7.77%)	(7.58%)	(38.45%)	(38.32%)	(4.78%)	(4.78%)	(4.78%)	(8.40%)	(7.86%)	(38.87%)	(38.51%)	(4.49%)	(4.49%)	1.55	1.55
	2.29	2.34	2.29	2.29	1.41	1.41	1.52	2.37	2.37	2.30	2.30	1.42	1.43	1.55	1.55
	(2.55%)	(2.14%)	(40.43%)	(39.74%)	(35.32%)	(35.32%)	(35.32%)	(2.95%)	(2.95%)	(40.08%)	(39.66%)	(34.60%)	(34.60%)		
2.00	2.35	2.34	2.29	2.29	1.41	1.41	1.52	2.37	2.37	2.30	2.30	1.42	1.43	1.55	1.55
	(2.55%)	(2.14%)	(40.43%)	(39.74%)	(35.32%)	(35.32%)	(35.32%)	(2.95%)	(2.95%)	(40.08%)	(39.66%)	(34.60%)	(34.60%)		
1.10	86.97	86.55	72.94	72.94	22.65	22.27	95.85	88.12	87.68	72.94	72.94	22.84	22.86	96.92	96.92
	(16.13%)	(15.73%)	(73.96%)	(74.27%)	(-10.21%)	(-10.21%)	(-10.21%)	(17.23%)	(16.81%)	(74.08%)	(74.08%)	(73.93%)	(73.93%)	(-9.99%)	(-9.99%)
	12.53	12.47	11.45	11.45	5.91	5.91	14.83	12.78	12.72	11.58	11.58	6.01	5.97	15.16	15.16
	(8.62%)	(8.18%)	(52.43%)	(52.61%)	(-18.36%)	(-18.36%)	(-18.36%)	(9.39%)	(8.96%)	(52.97%)	(53.07%)	(-18.62%)	(-18.62%)	3.09	3.09
1.50	3.50	3.40	3.31	3.31	2.26	2.26	3.02	3.55	3.54	3.35	3.35	2.30	2.30	3.09	3.09
	(5.43%)	(5.43%)	(35.43%)	(35.53%)	(13.71%)	(13.71%)	(13.71%)	(5.63%)	(5.37%)	(35.21%)	(35.03%)	(12.96%)	(12.96%)	1.21	1.21
	2.04	2.05	2.04	2.04	1.15	1.15	1.19	2.07	2.06	2.05	2.05	1.16	1.16	1.21	1.21
	(0.97%)	(0.49%)	(44.17%)	(43.90%)	(42.23%)	(42.23%)	(42.23%)	(0.97%)	(0.49%)	(43.96%)	(43.69%)	(41.55%)	(41.55%)		
2.00	2.06	2.05	2.04	2.04	1.15	1.15	1.19	2.07	2.06	2.05	2.05	1.16	1.16	1.21	1.21
	(0.97%)	(0.49%)	(44.17%)	(43.90%)	(42.23%)	(42.23%)	(42.23%)	(0.97%)	(0.49%)	(43.96%)	(43.69%)	(41.55%)	(41.55%)		

Table 6 (Continued)

$\gamma_0 = 0.20$							
τ	Synthetic		Run Rules		EWMA		Shewhart
	Cond	Cyc	Cond	Cyc	Cond	Cyc	
1.10	166.11	165.54	110.83 (33.28%)	110.83 (33.05%)	53.60 (67.73%)	52.50 (68.29%)	163.95 (1.30%)
1.25	41.67	41.38	30.45 (26.93%)	30.45 (26.41%)	15.20 (63.52%)	15.12 (63.46%)	44.98 (-7.94%)
1.50	11.15	11.08	9.18 (17.67%)	9.18 (17.15%)	5.77 (48.25%)	5.79 (47.74%)	11.09 (0.54%)
2.00	4.01	3.99	3.61 (9.98%)	3.61 (9.52%)	2.49 (37.91%)	2.49 (37.59%)	3.05 (23.94%)
$n = 10$							
$\gamma_0 = 0.20$							
τ	Synthetic		Run Rules		EWMA		Shewhart
	Cond	Cyc	Cond	Cyc	Cond	Cyc	
1.10	120.45	119.90	89.02 (26.09%)	89.03 (25.75%)	31.86 (73.55%)	31.89 (73.40%)	125.69 (-4.35%)
1.25	21.36	21.24	17.80 (16.67%)	17.80 (16.20%)	8.61 (59.69%)	8.56 (59.70%)	24.11 (-12.87%)
1.50	5.49	5.47	4.93 (10.20%)	4.93 (9.87%)	3.29 (40.07%)	3.29 (39.85%)	5.09 (7.29%)
2.00	2.48	2.47	2.38 (4.03%)	2.38 (3.64%)	1.51 (39.11%)	1.51 (38.87%)	1.60 (35.48%)
$n = 15$							
$\gamma_0 = 0.20$							
τ	Synthetic		Run Rules		EWMA		Shewhart
	Cond	Cyc	Cond	Cyc	Cond	Cyc	
1.10	92.74	92.30	72.97 (21.32%)	72.97 (20.94%)	23.60 (74.55%)	23.62 (74.41%)	101.34 (-9.27%)
1.25	13.81	13.75	12.10 (12.38%)	12.10 (12.00%)	6.27 (54.60%)	6.23 (54.69%)	15.71 (-13.76%)
1.50	3.79	3.78	3.52 (7.12%)	3.52 (6.88%)	2.42 (36.15%)	2.42 (35.98%)	3.22 (15.04%)
2.00	2.12	2.11	2.08 (1.89%)	2.08 (1.42%)	1.21 (42.92%)	1.21 (42.65%)	1.23 (41.98%)

CONCLUSIONS

This paper studies the performance of the synthetic CV chart under the more realistic steady-state condition, where the assignable cause which results in an OOC condition happens after the process has been operating for some time. Under the steady-state condition, the advantage of the head-start feature has faded away. This paper contributes to the literature by highlighting large differences between the steady-state and zero-state performances, especially for small shift sizes and sample sizes. Hence, the zero-state performance is not an accurate representation for the synthetic CV chart's performance. Practitioners should be cautious in evaluating the performance of the synthetic CV chart based on its zero-state performance.

This paper also proposes an alternative design for the synthetic CV chart based on its steady-state performance. The alternative design results in an improvement in the steady-state performance of the synthetic CV chart. The proposed design is useful for practitioners who intend to adopt the synthetic CV chart to monitor a steady-state process, which is more realistic in most practical applications since processes are usually stable in the beginning. The synthetic CV chart does not show better steady-state performance compared to the run rules and Shewhart CV charts for small sample sizes and shift sizes, while comparable performance is shown for large sample sizes and shift sizes. Among the charts under comparison, the EWMA CV chart has the best steady-state performance.

ACKNOWLEDGEMENTS

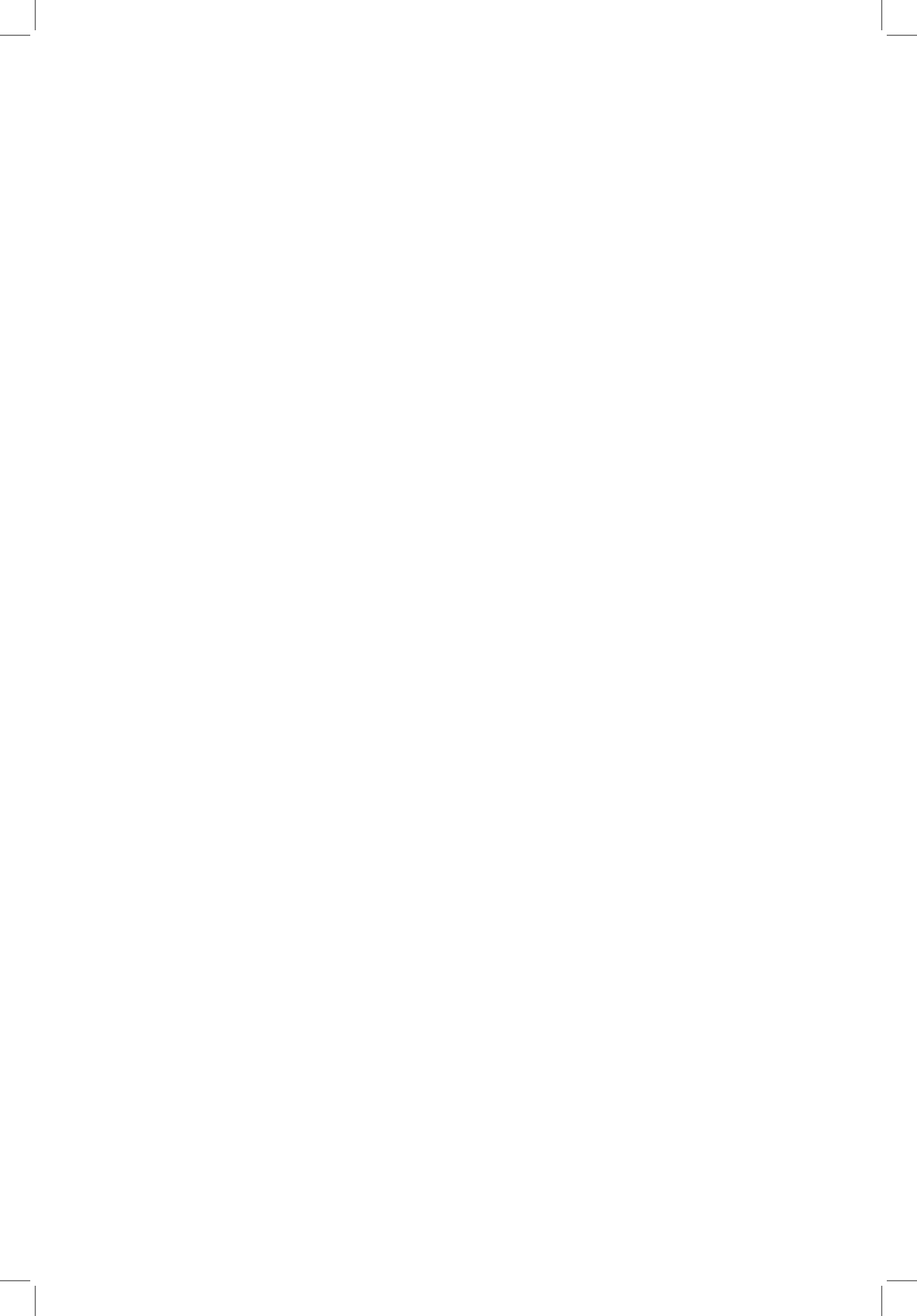
This research is supported by the Ministry of Higher Education Malaysia, Fundamental Research Grant Scheme (FRGS), project code FRGS/1/2018/STG06/UM/02/3 (FP052-2018A) and Research University Grant, number GPF030B-2018.

REFERENCES

- Calzada, M. E., & Scariano, S. M. (2013). A synthetic control chart for the coefficient of variation. *Journal of Statistical Computation and Simulation*, 83(5), 853-867. <https://doi.org/10.1080/00949655.2011.639772>
- Castagliola, P., Achouri, A., Taleb, H., Celano, G., & Psarakis, S. (2013). Monitoring the coefficient of variation using control charts with run rules. *Quality Technology and Quantitative Management*, 10(1), 75-94. <https://doi.org/10.1080/16843703.2013.11673309>
- Castagliola, P., Celano, G., & Psarakis, S. (2011). Monitoring the coefficient of variation using EWMA charts. *Journal of Quality Technology*, 43(3), 249-265. <https://doi.org/10.1080/00224065.2011.11917861>
- Curto, J. D., & Pinto, J. C. (2009). The coefficient of variation asymptotic distribution in the case of non-iid random variables. *Journal of Applied Statistics*, 36(1), 21-32. <https://doi.org/10.1080/02664760802382491>
- Davis, R. B., & Woodall, W. H. (2002). Evaluating and improving the synthetic control chart. *Journal of Quality Technology*, 34(2), 200-208. <https://doi.org/10.1080/00224065.2002.11980146>

- Kang, C. W., Lee, M. S., Seong, Y. J., & Hawkins, D. M. (2007). A control chart for the coefficient of variation. *Journal of Quality Technology*, 39(2), 151-158. <https://doi.org/10.1080/00224065.2007.11917682>
- Khan, Z., Razali, R. B., Daud, H., Nor, N. M., & Fotuhi-Firuzabad, M. (2017). The control chart technique for the detection of the problem of bad data in state estimation power system. *Pertanika Journal of Science & Technology*, 25(3), 825-834.
- Kinat, S., Amin, M., & Mahmood, T. (2020). GLM-based control charts for the inverse Gaussian distributed response variable. *Quality and Reliability Engineering International*, 36(2), 765-783. <https://doi.org/10.1002/qre.2603>
- Knoth, S. (2016). The case against the use of the synthetic control charts. *Journal of Quality Technology*, 48(2), 178-195. <https://doi.org/10.1080/00224065.2016.11918158>
- Machado, M. A. G., & Costa, A. F. B. (2014). Some comments regarding the synthetic chart. *Communications in Statistics - Theory and Methods*, 43(14), 2897-2906. <https://doi.org/10.1080/03610926.2012.683128>
- Mahmood, T., & Abbasi, S. A. (2021). Efficient monitoring of coefficient of variation with an application to chemical reactor process. *Quality and Reliability Engineering International*, 37(3), 1135-1149. <https://doi.org/10.1002/qre.2785>
- Marchant, C., Leiva, V., Cysneiros, F. J. A., & Liu, S. (2018). Robust multivariate control charts based on Birnbaum-Saunders distributions. *Journal of Statistical Computation and Simulation*, 88(1), 182-202. <https://doi.org/10.1080/00949655.2017.1381699>
- Mim, F. N., Saha, S., Khoo, M. B. C., & Khatun, M. (2019). A side-sensitive modified group runs control chart with auxiliary information to detect process mean shifts. *Pertanika Journal of Science & Technology*, 27(2), 847-866.
- Montgomery, D. C. (2019). *Introduction to statistical quality control*. John Wiley and Sons Inc.
- Pang, W. K., Yu, B. W., Troutt, M. D., & Shui, H. H. (2008). A simulation-based approach to the study of coefficient of variation of dividend yields. *European Journal of Operational Research*, 189(2), 559-569. <https://doi.org/10.1016/j.ejor.2007.05.032>
- Rakitzis, A. C., Chakraborti, S., Shongwe, S. C., Graham, M. A., & Khoo, M. B. C. (2019). An overview of synthetic-type control charts: Techniques and methodology. *Quality and Reliability Engineering International*, 35(7), 2081-2096. <https://doi.org/10.1002/qre.2491>
- Shongwe, S. C., & Graham, M. A. (2017). A letter to the editor about "Machado, MAG and Costa AFB (2014), some comments regarding the synthetic chart. *Communications in Statistics---Theory and Methods*, 43(14), 2897-2906". *Communications in Statistics - Theory and Methods*, 46(21), 10476-10480. <https://doi.org/10.1080/03610926.2016.1236958>
- Shongwe, S. C., & Graham, M. A. (2019). Some theoretical comments regarding the run-length properties of the synthetic and runs-rules \bar{X} monitoring schemes—part 2: Steady-state. *Quality Technology & Quantitative Management*, 16(2), 190-199. <https://doi.org/10.1080/16843703.2017.1389141>
- Teoh, W. L., Khoo, M. B. C., Yeong, W. C., & Teh, S. Y. (2016). A comparison between the performances of synthetic and EWMA charts for monitoring the coefficient of variation. *Journal of Scientific Research and Development*, 3(1), 16-20.

- Wu, Z., & Spedding, T. A. (2000). A synthetic control chart for detecting small shifts in the process mean. *Journal of Quality Technology*, 32(1), 32-38. <https://doi.org/10.1080/00224065.2000.11979969>
- Wu, Z., Ou, Y., Castagliola, P., & Khoo, M. B. C. (2010). A combined synthetic & X chart for monitoring the process mean. *International Journal of Production Research*, 48(24), 7423-7436. <https://doi.org/10.1080/00207540903496681>
- Yeong, W. C., Khoo, M. B. C., Tham, L. K., Teoh, W. L., & Rahim, M. A. (2017). Monitoring the coefficient of variation using a variable sampling interval EWMA chart. *Journal of Quality Technology*, 49(4), 380-401. <https://doi.org/10.1080/00224065.2017.11918004>
- Yeong, W. C., Lim, S. L., Khoo, M. B. C., Chuah, M. E., & Lim, A. J. X. (2018). The economic and economic-statistical designs of the synthetic chart for the coefficient of variation. *Journal of Testing and Evaluation*, 46(3), 1175-1195. <https://doi.org/10.1520/JTE20160500>
- You, H. W. (2018). Design of the side sensitive group runs chart with estimated parameters based on expected average run length. *Pertanika Journal of Science & Technology*, 26(3), 847-866.
- Zhang, J., Li, Z., & Wang, Z. (2018). Control chart for monitoring the coefficient of variation with an exponentially weighted moving average procedure. *Quality and Reliability Engineering International*, 34(2), 188-202. <https://doi.org/10.1002/qre.2247>



Assessing the Impacts of Competition and Dispersal on a Multiple Interactions Type Model

Murtala Bello Aliyu^{1,2*}, Mohd Hafiz Mohd^{1,3} and Mohd Salmi Md. Noorani³

¹*School of Mathematical Sciences, Universiti Sains Malaysia, 11800 USM, Penang, Malaysia*

²*Department of Mathematics, Nigerian Defence Academy, Afaka, PMB 2019, Kaduna, Nigeria*

³*Department of Mathematical Sciences, Faculty of Science and Technology, Universiti Kebangsaan Malaysia, 43600 UKM, Bangi, Selangor, Malaysia*

ABSTRACT

Multiple interactions (e.g., mutualist-resource-competitor-exploiter interactions) type models are known to exhibit oscillatory behaviour as a result of their complexity. This large-amplitude oscillation often de-stabilises multispecies communities and increases the chances of species extinction. What mechanisms help species in a complex ecological system to persist? Some studies show that dispersal can stabilise an ecological community and permit multi-species coexistence. However, previous empirical and theoretical studies often focused on one- or two-species systems, and in real life, we have more than two-species coexisting together in nature. Here, we employ a (four-species) multiple interactions type model to investigate how competition interacts with other biotic factors and dispersal to shape multi-species communities. Our results reveal that dispersal has (de-)stabilising effects on the formation of multi-species communities, and this phenomenon shapes coexistence mechanisms of interacting species. These contrasting effects of dispersal can best be illustrated through its combined influences with the competition. To do this, we employ numerical simulation and bifurcation analysis techniques to track the stable and unstable

attractors of the system. Results show the presence of Hopf bifurcations, transcritical bifurcations, period-doubling bifurcations and limit point bifurcations of cycles as we vary the competitive strength in the system. Furthermore, our bifurcation analysis findings show that stable coexistence of multiple species is possible for some threshold values of ecologically-relevant parameters in this complex system. Overall,

ARTICLE INFO

Article history:

Received: 11 October 2020

Accepted: 30 April 2021

Published: 31 July 2021

DOI: <https://doi.org/10.47836/pjst.29.3.04>

E-mail addresses:

murtalabelloaliyu@gmail.com (Murtala Bello Aliyu)

mohdhafizmohd@usm.my (Mohd Hafiz Mohd)

msn@ukm.edu.my (Mohd Salmi Md. Noorani)

* Corresponding author

we discover that the stability and coexistence mechanisms of multiple species depend greatly on the interplay between competition, other biotic components and dispersal in multi-species ecological systems.

Keywords: Hopf bifurcation, limit cycle, limit point bifurcation, period-doubling bifurcation, stability, transcritical bifurcation.

INTRODUCTION

Competition for the scarce resource is a renowned interaction that often occurs in an ecological system (Gause, 1932). The Lotka-Volterra competition model is a well-known competition model (Grover et al., 1997; Mohd, 2019). The result from this model analysis shows that two or more species can only coexist if and only if the intraspecific competition is greater than interspecific competition (Gotelli, 2008; Mittelbach & McGill, 2019). In contrast, if the interspecific competition is greater than the intraspecific competition, this scenario leads to the exclusion of species from the system (“principle of competitive exclusion”) (Hardin, 1960). However, this situation contrast with real-world phenomena as many species coexist in nature and this observation is being postulated as the “paradox of phytoplankton” (Hutchinson, 1961). This paradox describes the situation in which a limited range of resources supports a great diversity of species. To re-address this problem, we hypothesise that there could be some essential mechanisms like dispersal and different forces of biotic interactions that lead to the coexistence of complex ecological systems (Tubay et al. 2013; Kakishima et al., 2015). Therefore, an important question is, how do we generalise a simple coexistence mechanism inferred by classical ecological theories to multi-species communities? One possible way to do this is through the use of multiple interactions type modelling framework and the incorporation of spatial diffusion mechanism into such a system to model the effects of local dispersal of multiple species.

In general, research on simple ecological communities attempted to integrate different modules of interaction into a multi-species system (Kondoh, 2008) and demonstrated that a mixed type of interaction is more plausible in modelling natural ecosystems. The complex interspecific interactions between multiple species are typical features of ecological ecosystems, and those interactions are in the form of predation, parasitism, competition, and mutualism. Some studies have suggested that ecological communities (Kondoh & Mougi, 2015; Mougi & Kondoh, 2012; Mougi & Kondoh, 2014; Mougi, 2016) have a synergistic effect between interaction type and species diversity. Some simulation studies involving multiple interacting species illustrate complex dynamical behaviours such as oscillations and chaotic dynamics (Shabunin et al., 2005). Another modelling work involving a four-species system demonstrates that dispersal plays an important role in shaping the population dynamics of multi-species communities (Kouvaris et al., 2011). It has also been discovered that distinct dispersal mechanisms, coupled with species interactions, can determine the

occurrence of the different amplitude of oscillations in community structures (Shabunin & Provata, 2013).

Dispersal in multi-species communities can stabilise population dynamics, reduces local extinction of species and support recolonisation of species (Crowley, 1981; Briggs & Hoopes, 2004; Lampert & Hasting, 2016). Dispersal is an essential concept in conservation biology and spatial ecology (Hanski, 1998; Crooks & Sanjayan, 2006; Kindlmann & Burel, 2008; Kool et al., 2013). Dispersal helps species migrate into a new community and adapt to the changes in such community (Bullock et al., 2002, Aliyu & Mohd, 2021). Several demographic, evolutionary and ecological processes drive dispersal evolution. For instance kin competition (Gandon & Rousset, 1999; Bach et al., 2006; Poethke et al., 2007), inbreeding avoidance (Gandon, 1999; Perrin & Goudet, 2001), density-dependent factor (Poethke & Hovestadt, 2002; Hovestadt et al., 2010), spatio-temporal habitat variability (Travis, 2001; Poethke et al., 2003) have been reported to affect dispersal positively by their synchronising effects. Synchronising effect is a term used to describe the interactions that exist between extrinsic environmental variation and population dynamics. Several empirical and theoretical studies have illustrated how antagonistic interactions and environmental factors shape the evolution of species dispersal (Mondor et al., 2005; Green, 2009; Poethke et al., 2010; Chaianunporn & Hovestadt, 2015; Amarasekare, 2016). Strong oscillation is a direct consequence of antagonistic interactions in multi-species communities, and this has led to spatio-temporal variation in the species fitness (Green, 2009; Chaianunporn & Hovestadt, 2012). Weak dispersal strength has a synchronisation effect on large amplitude population cycles across space; a phenomenon called phase-locking (Bjørnstad, 2000; Vasseur & Fox, 2009; Vogwill et al., 2009). There is little possibility for dispersal-induced stabilisation when the population cycles in the system undergo spatial synchronisation (Yaari et al., 2012).

Numerous empirical and theoretical studies have reported how dispersal effects reduce species population variability and subsequently, extinction rate (Vogwill et al., 2009; Abbott, 2011). However, there are divergent views on the impact of dispersal on the stability of the multi-species community. Increase in spatial synchrony (i.e. variation in time-dependent characteristics or abundance of different geographical populations) is a product of stabilising effects of dispersal on a local population (Kendall et al., 2000). In some other studies, these synchronisation effects distort species stability and persistence (Feyrer et al., 2015; Gouhier et al., 2010). Thus, Hudson and Cattadori (1999) describe dispersal as a sword with double-edge: dispersal can reduce species variability through its stabilising effects or increase them through synchronisation effects. Some experimental studies report that dispersal effects could either be destabilising, stabilising or no effects on multi-species communities (Dey & Joshi, 2006; Steiner et al., 2013; Mohd et al., 2017). Given these controversies, it becomes imperative to assess the impacts of competition and

dispersal on multi-species coexistence. Specifically, it remains unexplored the effects of competition and dispersal on multiple interactions type model.

To address this problem, we extend the ecological model by adding the diffusion term; this incorporation leads to a system of partial differential equations (PDE) (Mitani & Mougi, 2017). We investigate numerically how competition and dispersal shape multi-species structures, stability and their coexistence mechanisms. From the numerical simulation results, we identify several observations as a result of the interplay between competition and dispersal in this multiple interactions type system. Finally, we discuss the ecological implications of our findings for the conservation of the natural ecosystem.

MATERIAL AND METHODS

Model Description and Theoretical Analysis

We propose a system of PDE for the densities $X(x, t)$, $W(x, t)$, $Y(x, t)$ and $Z(x, t)$ in one-dimension ($0 \leq x \leq 1$) (Equation 1) (Mitani & Mougi, 2017; Mohd et al., 2017):

$$\begin{aligned}\frac{\partial X}{\partial t} &= X \left(r_k - X - \beta W - \alpha Y + \frac{uZ}{h_Z + Z} \right) + D_X \frac{\partial^2 X}{\partial x^2} \\ \frac{\partial W}{\partial t} &= W(r_W - W - \alpha X) + D_W \frac{\partial^2 W}{\partial x^2} \\ \frac{\partial Y}{\partial t} &= Y(g\alpha X - d) + D_Y \frac{\partial^2 Y}{\partial x^2} \\ \frac{\partial Z}{\partial t} &= Z \left(r_Z - Z + \frac{vX}{h_X + X} \right) + D_Z \frac{\partial^2 Z}{\partial x^2}\end{aligned}\quad [1]$$

where X , W , Y , Z represent the population densities of resource, competitor, exploiter, and mutualist species, respectively. The parameter r_k is the rate at which the resource species grows; r_w is the rate at which the competitor species grows; r_z is the rate at which the mutualist species grows; α and β represent the strength of competition (i.e., resource and competitor species, respectively); a represents capture rate (i.e., the rate at which the exploiter species capture the prey). The term g represents the conversion efficiency; d represents exploiter species death; u and v represent the benefits from the mutualistic interactions (i.e., mutualistic strength of the resource and mutualist species, respectively); h_X and h_Z represent the half-saturation constant of resource and mutualist species, respectively (i.e., density at which half the average intake of prey is achieved, irrespective of the prey population available). It is assumed that the self-regulation mechanism of mutualist species (net effect of a mutualist on the other mutualist species) is unity for theoretical simplicity. Equation (1) is a spatial extension of the multiple interactions type

model (Mitani & Mougi, 2017). In the absence of dispersal ($D_x=D_w=D_y=D_z=0$), the ecological system becomes a system of ordinary differential equations (ODE). The steady states of the ODE system can be computed analytically by letting the time-derivative equal zero which gives:

1. Extinction equilibrium: $E_0(0, 0, 0, 0)$,
2. Extinction of resource species equilibrium: $E_1(0, r_w, \frac{1}{a}(-\beta W^* + (\frac{uZ^*}{h_z + Z^*})), r_z)$,
3. Extinction of competitor species equilibrium: $E_2(\frac{d}{ga}, 0, \frac{1}{a}(r_k - X^* + (\frac{uZ^*}{h_z + Z^*})), r_z + (\frac{vX^*}{h_x + X^*}))$,
4. Extinction of exploiter species equilibrium: $E_3(\frac{d}{ga}, r_w - \alpha X^*, 0, r_z + (\frac{vX^*}{h_x + X^*}))$,
5. Extinction of mutualist species equilibrium: $E_4(\frac{d}{ga}, r_w - \alpha X^*, \frac{1}{a}(r_k - X^* - \beta W^*), 0)$,
6. Four-species coexistence equilibrium: $E_5(\frac{d}{ga}, r_w - \alpha X^*, \frac{1}{a}(r_k - \frac{d}{ga} - r_w\beta - \frac{d\alpha\beta}{ga} + \frac{uM^*}{Q^*}), \frac{r_z + vd}{Q^*})$.

where $M^* = r_z(gahX + d) + vd$ and $Q^* = gahX + d$.

We can analyse the stability of each steady state by using Jacobian matrix to calculate their respective eigenvalues, which is given by:

$$J = \begin{bmatrix} r_k - 2X^* - \beta W^* - \alpha Y^* + \frac{uZ^*}{h_z + Z^*} & -\beta X^* & -\alpha Y^* & X^* \left(\frac{u}{h_z + Z^*} - \frac{uZ^*}{(h_z + Z^*)^2} \right) \\ -\alpha W^* & r_w - 2W^* - \alpha X^* & 0 & 0 \\ gaY^* & 0 & gaX^* - d & 0 \\ Z^* \left(\frac{v}{h_x + X^*} - \frac{vX^*}{(h_x + X^*)^2} \right) & 0 & 0 & r_z - 2Z^* + \frac{vX^*}{h_x + X^*} \end{bmatrix}$$

We note that if all the real parts of the eigenvalues are negative, it follows that the steady state is stable. For example, the extinction equilibrium $E_0(0, 0, 0, 0)$ has the following eigenvalues: $\lambda_1=r_k, \lambda_2=r_w, \lambda_3=-d$, and $\lambda_4=r_z$. Since some eigenvalues are positive and λ_3 is negative, it follows that $E_0(0, 0, 0, 0)$ is unstable equilibrium (i.e., saddle type). The eigenvalues of the remaining steady states can be calculated using same techniques.

When the effect of local dispersal is considered ($D_x=D_w=D_y=D_z>0$) and the diffusion term is added into the system, the model (1) now becomes a system of PDE, which is a spatial extension of the multiple interactions type model (Mitani & Mougi, 2017). The term $D_i(i = X, W, Y, Z)$ represents the dispersal strength along spatial domain (x). We assume equal dispersal strength for all the interacting species ($D_x=D_w=D_y=D_z=0.005$). Also, we apply zero-flux boundary conditions for each of the interacting species (Equation 2) (i.e., no movement is allowed across the boundaries):

$$D_x \frac{\partial X(0, t)}{\partial x} = D_x \frac{\partial X(1, t)}{\partial x}$$

[2]

$$D_W \frac{\partial W(0, t)}{\partial x} = D_W \frac{\partial W(1, t)}{\partial x}$$

$$D_Y \frac{\partial Y(0, t)}{\partial x} = D_Y \frac{\partial Y(1, t)}{\partial x}$$

$$D_Z \frac{\partial Z(0, t)}{\partial x} = D_Z \frac{\partial Z(1, t)}{\partial x}$$

To solve Equation 1 with the boundary conditions as in Equations 2, we use the method of line. This numerical approach is implemented in XPPAUT, which provides a good platform for solving PDE systems in one spatial variable x (Mohd, 2019). The spatial domain is divided into meshes of $M + 1$ equivalent points of $x_i = ih$ for $i = 0, 1, \dots, M$ ($0 \leq x \leq 1$). The central difference approximation is then employed to replace the spatial derivative in model (1). In this numerical method, the zero-flux boundary conditions are encoded into the scheme using finite difference approximation. The resulting transformation results in a $4(N+1)$ ODE scheme, one for each species at spatial location x_i . The regular ODE solver, `cvode`, is used for solving the resulting ODE system for $t = 1000$ (i.e., until steady-state). The size of the mesh used in the numerical simulation is $h = 0.09$. We have also used AUTO to continue the steady-state, in which case we tracked the stable, unstable and bifurcation points that arise as the parameters change in this ecological system (Omaiye & Mohd, 2018). It is also verified that the numerical results are insensitive to changes in grid spacing (i.e., by increasing and decreasing the number of finite difference points). Since the PDE model (1) is nonlinear, we conducted local stability analysis whereby the system is linearised about the steady states via numerical techniques. To do this, the Jacobian matrix and the spectrum of eigenvalues are calculated numerically using `fsolve` and `eig` functions in MATLAB. Note that the steady state is stable if all the real parts of the eigenvalues are negative (and otherwise unstable). Further discussion on this topic (i.e., numerical stability analysis of PDE system) can be found in the modelling work of Mohd (2018). The parameter values used in the numerical simulation are defined in Table 1, which are motivated by the ecological studies of (Mitani & Mougi, 2017; Mohd et al., 2017; Mohd et al., 2018).

RESULT

The effects of dispersal on this multiple interactions type system is illustrated in Figures 1-4. We observe that dispersal influence the coexistence mechanisms of this multi-species ecological system. The interacting species disperse from areas of high competition to low competition to avoid going extinct due to the complexity of interactions in the community. In the later section, it is observed that steady state phenomena and oscillatory dynamics

Table 1
Symbols, their definitions and the parameter values used for the numerical simulations

Symbol	Definition	Parameter value
r_k	The intrinsic growth rate of resource species	1
r_w	The intrinsic growth rate of competitor species	1
r_z	The intrinsic growth rate of the mutualist species	1
u	Maximum benefit of the mutualistic interaction	3
v	Maximum benefit of the mutualistic interaction	2
a	Capture rate	1.8
g	Conversion efficiency of the exploiter species	0.25
d	Death rate of the exploiter	0.05
h_x	Half saturation constant of the hyperbolic functional response	1
h_z	Half saturation constant of the hyperbolic functional response	1
β	Competitive strength of the competitor species	0.7
a	Competitive strength of the resource species	0.2
$D_X=D_W=D_Y=D_Z$	Dispersal strength	0.005

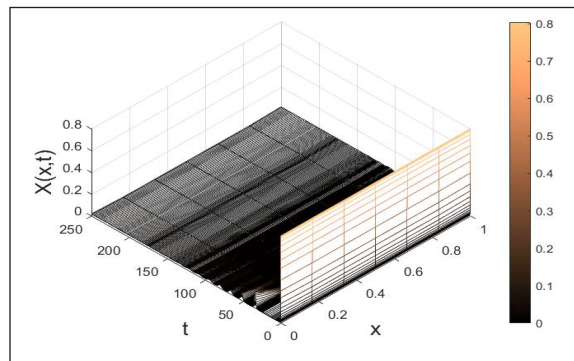


Figure 1. The effects of dispersal on the resource species using model (1) with $D_X=D_W=D_Y=D_Z=0.005$. Initial species density $X(x, t=0) = 0.9$, $W(x, t=0) = 0.3$, $Y(x, t=0) = 0.2$, $Z(x, t=0) = 0.8$. The diagram is plotted using MATLAB ode15s solver and the parameter values as in Table 1.

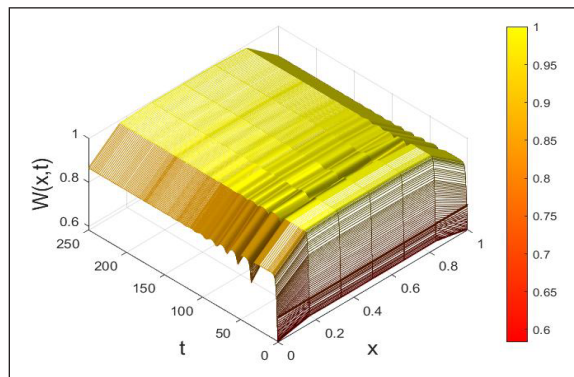


Figure 2. The effects of dispersal on the competitor species using model (1) with $D_X=D_W=D_Y=D_Z=0.005$. Initial species density $X(x, t=0) = 0.9$, $W(x, t=0) = 0.3$, $Y(x, t=0) = 0.2$, $Z(x, t=0) = 0.8$. The diagram is plotted using MATLAB ode15s solver and the parameter values as in Table 1.

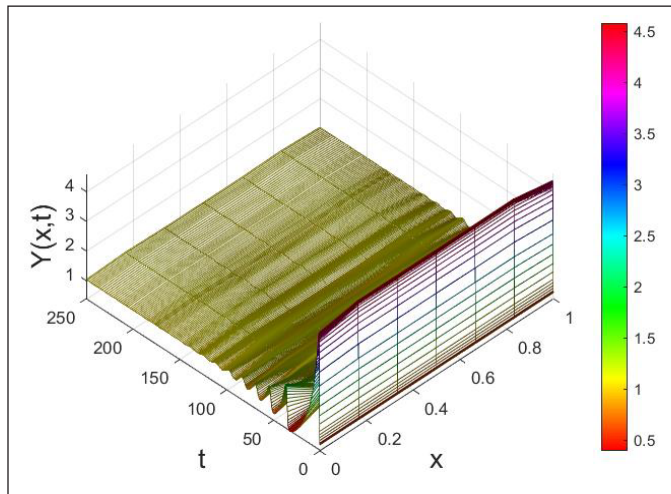


Figure 3. The effects of dispersal on the exploiter species using model (1) with $D_X=D_W=D_Y=D_Z=0.005$. Initial species density $X(x, t=0) = 0.9$, $W(x, t=0) = 0.3$, $Y(x, t=0) = 0.2$, $Z(x, t=0) = 0.8$. The diagram is plotted using MATLAB ode15s solver and the parameter values as in Table 1.

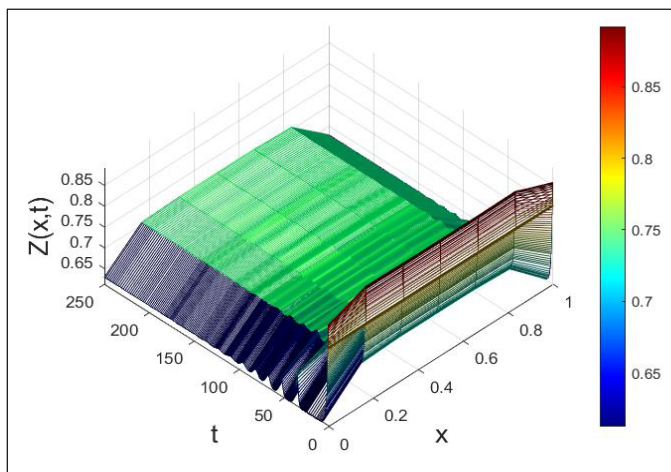


Figure 4. The effects of dispersal on the mutualist species using model (1) with $D_X=D_W=D_Y=D_Z=0.005$. Initial species density $X(x, t=0) = 0.9$, $W(x, t=0) = 0.3$, $Y(x, t=0) = 0.2$, $Z(x, t=0) = 0.8$. The diagram is plotted using MATLAB ode15s solver and the parameter values as in Table 1.

are the plausible behaviour of this multi-species system with dispersal. This findings are parallel to some theoretical studies which report that dispersal strength influences species coexistence outcomes (i.e., steady state or population oscillation) (Goldwyn & Hastings, 2008; Williams & Hastings, 2013; Anderson & Hayes, 2018; Bassett et al., 2017; Chow et al., 2018). To have a good understanding of how species competitive strength affects the community stability and species coexistence mechanisms, we conduct co-dimension one bifurcation analysis using β and α as our bifurcation parameters in the following sections.

The Dynamics of the Ode Model in the Absence of Dispersal ($D = 0$)

Since our goal is to better understand how competitive interactions shape community dynamics in multiple interactions type model, we perform co-dimension one bifurcation analysis using parameter β , i.e., the strength of competitor species. Bifurcation analysis provide a good techniques for studying different dynamics of nonlinear PDE (Mohd, 2018). As an example, Figure 5 illustrates the population density of prey species (X) as parameter β is changed with other parameter values are given in Table 1. There occur several critical values in this co-dimension one bifurcation diagram corresponding to supercritical Hopf bifurcation (i.e., HB) and transcritical bifurcations (i.e., $BP1$ and $BP2$). We notice the existence of some branches of steady states, particularly unstable (black curves) and stable (red curves) steady states. As the competitive strength β increases, the emergence of distinct outcomes of species interactions are observed: (i) four-species steady-state (i.e., when $\beta < HB$); (ii) bistable outcomes between three- and two-species steady states (i.e., when $BP2 < \beta < BP1$); (iii) two-species steady states (i.e., when $\beta > BP1$). When $HB < \beta < BP2$, oscillatory behaviour (green dots) emerges with population fluctuations in this four-species system are observed; in this case, stable limit

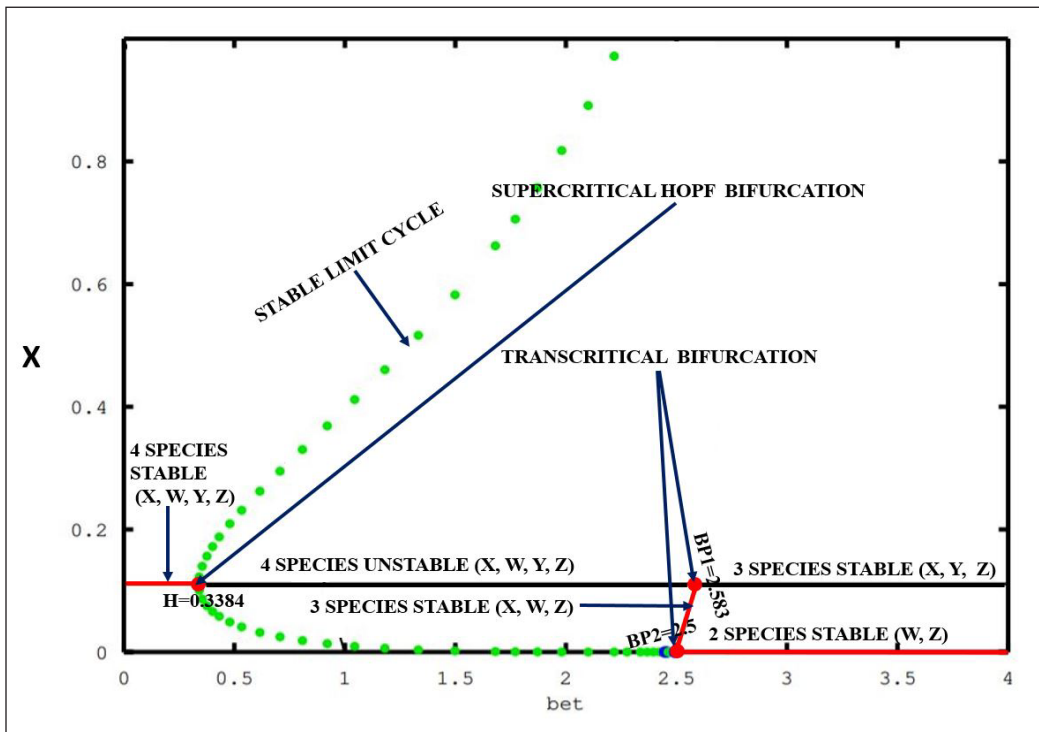


Figure 5. Co-dimension one bifurcation analysis as the density of species X varies against β in the model (1) without dispersal ($D = 0$). This bifurcation diagram shows different dynamics that occur in the ODE system. Initial population densities: $X(x; t = 0) = 0.9$, $W(x; t = 0) = 0.7$, $Y(x; t = 0) = 0.6$, $Z(x; t = 0) = 0.8$. The diagram is plotted using XPPAUT package and the parameter values as in Table 1

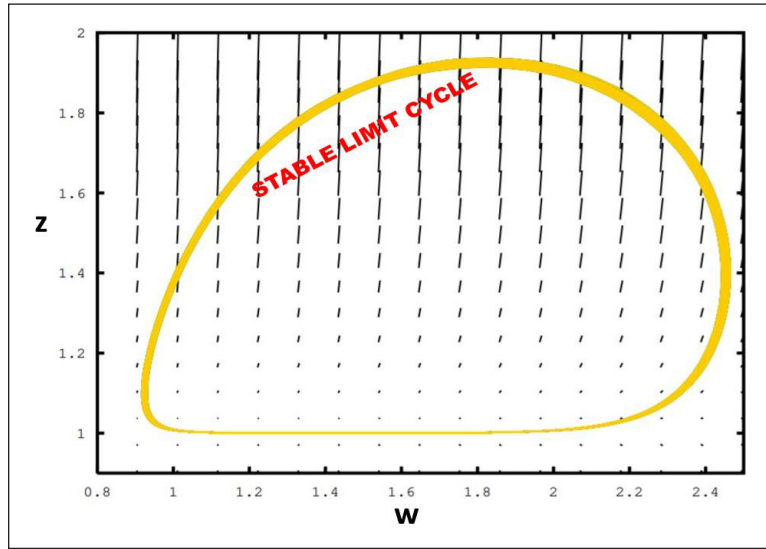


Figure 6. Stable limit cycle of model (1) with $D=0$. Initial species density $X(x, t=0) = 0.9$, $W(x, t=0) = 0.3$, $Y(x, t=0) = 0.2$, $Z(x, t=0) = 0.8$. The diagram is plotted using XPPAUT and the parameter values as in Table 1.

cycles (Figure 6) appear with all steady states of the system become unstable. Due to this reason, the trajectories do not converge to any steady-state as it converges to a stable limit cycle from positive initial densities. Based on these observations, we realise that Hopf bifurcation is the best-known mechanism that mediates oscillatory dynamics in this ecological system. These bifurcation changes in dynamics and their consequences on species coexistence outcomes has been observed in several other studies (Liu & Huang, 2018; Gyllenberg et al., 2019; Mohd, 2019; Wei et al. 2020).

Joint Effects of Competition and Dispersal in the Multiple Interactions Type PDE Model

To explain the differences observed in the number of species that persist as shown by Figure 7, we perform co-dimension one bifurcation analysis of the PDE model (1) and the result is depicted in Figure 7. This bifurcation diagram shows the density of resource species (X) as β varies. There occurs several threshold values of β , which correspond to transcritical bifurcation points (i.e., $BP1$, $BP2$ and $BP3$). As we cross these critical points, different presence-absence of species are seen: (i) four-species coexistence (i.e., when $\beta < BP3$); (ii) three-species coexistence with species Y absent (i.e., when $BP3 < \beta < BP2$); (iii) two-species coexistence with species X and Y absent (i.e., when $BP2 < \beta < BP1$); (iv) single-species steady-state with only species Z present (i.e., when $\beta > BP1$). We realise that transcritical bifurcation plays an important factor in determining survival (and exclusion) of different interacting species in this multi-species PDE system. It is also discovered that the strength of multiple interactions type arising from distinct ecological populations such as resource,

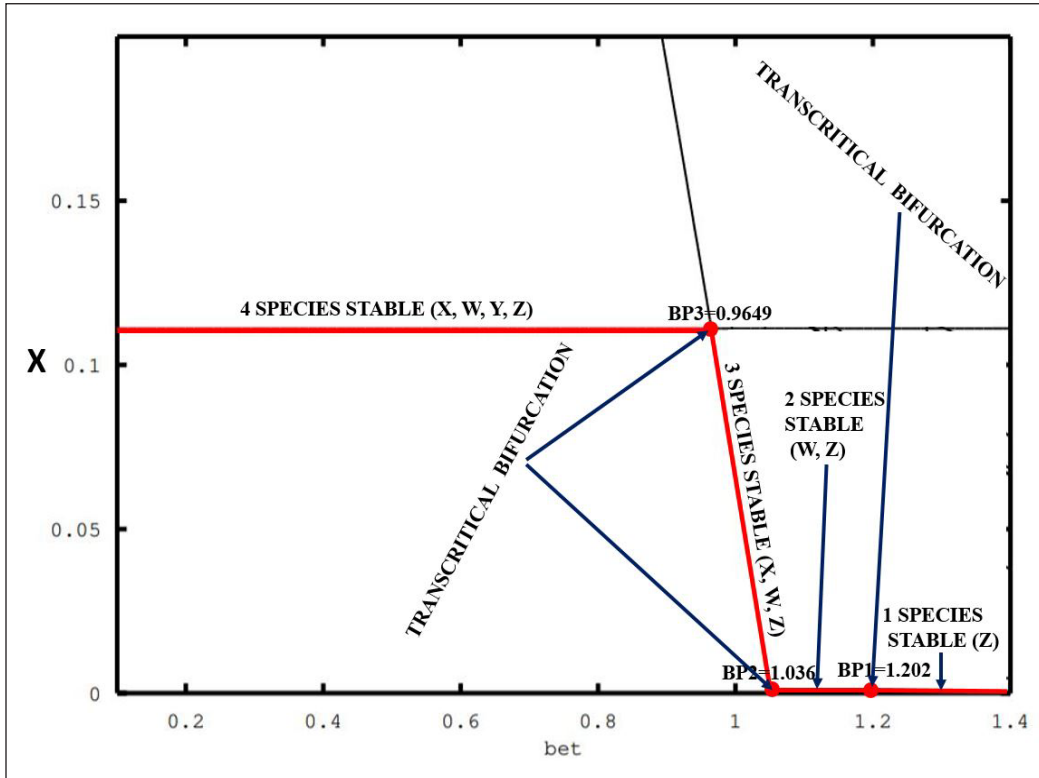


Figure 7. Co-dimension one bifurcation analysis as the density of species X varies against β in the model (1) with dispersal ($D_X=D_W=D_Y=D_Z=0.005$). This bifurcation diagram shows different dynamics that occur in the ODE system. Initial population densities: $X(x; t=0)=0.9$, $W(x; t=0)=0.7$, $Y(x; t=0)=0.6$, $Z(x; t=0)=0.8$. The diagram is plotted using XPPAUT package and the parameter values as in Table 1

competitor and exploiter species is amplified in the presence of dispersal, which can weaken the chance of species survival in the system.

Closer examination of our bifurcation analysis results without dispersal (Figure 5) and with dispersal (Figure 7) illustrates some intriguing observations. We found that the inclusion of dispersal into this ecological system promotes more outcomes with four-species coexistence steady state. Without dispersal, we observe that oscillatory dynamics are more pronounced in this multiple interactions type model with species populations oscillate between some maximum and minimum densities. However, one of the concerns with this kind of oscillatory dynamics is that some populations of species would fluctuate to a very low abundance; in the presence of external factors (e.g., stochasticity), this situation would increase the likelihood of extinction and could result in de-stabilisation of multi-species communities (Mohd, 2019). This vulnerability is softened by incorporation of dispersal into the model: multi-species coexistence outcomes are more likely to occur due to the positive effects of dispersal in rescuing some weaker species from going extinct. This observation is consistent with the reports in some theoretical studies that dispersal can

induce stability and synchrony in complex systems (Fussell et al., 2019; Verma & Gupta, 2020; Mohd & Noorani, 2020).

We also investigate the impacts of competition exerted by the resource species, α , on this multi-species ecosystem. Figure 8 shows the food web dynamics with respect to the density of resource species (X) as α is varied in the case of no-dispersal ($D = 0$). In general, this ecological system exhibits rich bifurcation structures that are of ecological importance. There occurs numerous threshold values of α , which determine different outcomes of the model; in particular, two supercritical Hopf bifurcations ($H1$ and $H2$), transcritical bifurcation (BP), period-doubling bifurcations ($PD1$, $PD2$ and $PD3$) and limit point bifurcations of cycles ($LPC1$ to $LPC10$). It is observed that multi-species coexistence is possible as $\alpha < H1$ or $H2 < \alpha < BP$. When the competitive strength of the resource species is intense ($\alpha > BP$), exclusion of species occurs with the weaker competing species (W) is being displaced in the long run due to competitive asymmetry. In the case of moderate competitive strength (i.e., in between $H1$ and $H2$), we realise some stimulating complex dynamics in this multiple interactions type system: stable (green dots) and unstable (blue dots) limit cycles and period-doublings. We

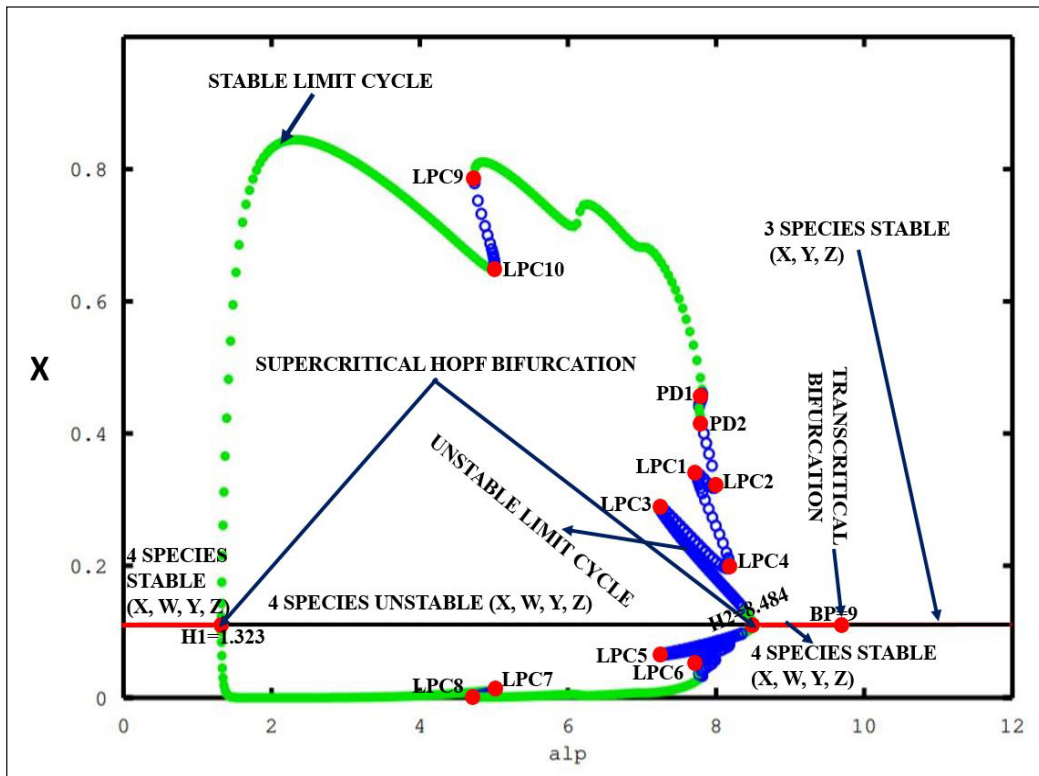


Figure 8. Co-dimension one bifurcation analysis as the density of species X varies against α in the model (1) without dispersal ($D = 0$). This bifurcation diagram shows different dynamics that occur in the PDE system. Initial population densities: $X(x; t = 0) = 0.9$, $W(x; t = 0) = 0.7$, $Y(x; t = 0) = 0.6$, $Z(x; t = 0) = 0.8$. The diagram is plotted using XPPAUT package and the parameter values as in Table 1.

observe that the stable limit cycles give birth to unstable limit cycles and period-doubling bifurcations and, in some cases, this situation could trigger more complex dynamics. The complex dynamics associated with period-doubling has been observed in some theoretical studies (Selvam & Dhineshabu, 2020; Bashkirtseva et al., 2019; Gupta & Yadav, 2020; Namba et al., 2018; Baek, 2018).

In the presence of dispersal, the system exhibit qualitatively similar bifurcation structures (Figure 9) to no-dispersal scenario (Figure 8), as α is varied. This bifurcation diagram shows that starting from low (or high) α values do not result in sustained oscillation patterns but only lead to attraction towards four- or three-species coexistence steady state. Stable limit cycles of different amplitudes occur from supercritical Hopf bifurcation points ($H1$ and $H2$) as the value of α changes to moderate competitive strength. There occurs several period-doubling bifurcations ($PD1$, $PD2$ and $PD3$) and limit point bifurcations of cycles ($LPC1$ to $LPC6$), which can engender complex dynamical behaviour in this ecological system such as aperiodic oscillations (Figure 10). It is also noted that when $\alpha > BP$, competing species (W) is being displaced and thus only three-species coexistence outcome is possible in this situation.

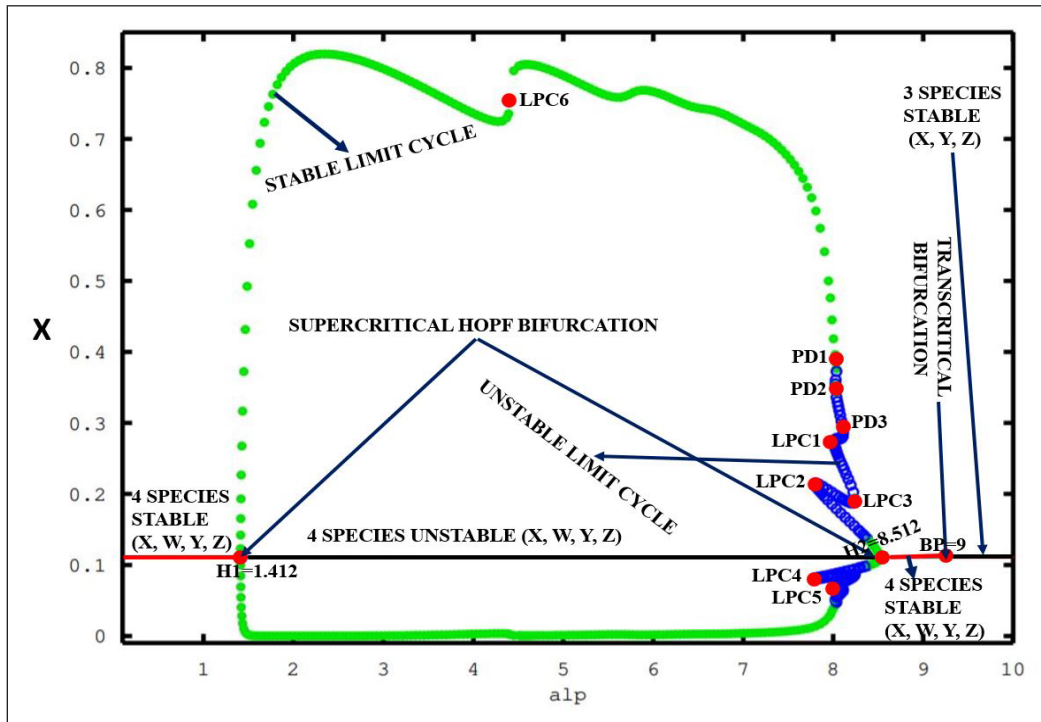


Figure 9. Co-dimension one bifurcation analysis as the density of species X varies against α in the model (1) with the inclusion of dispersal ($D_X = D_W = D_Y = D_Z = 0.005$). This bifurcation diagram shows different dynamics that occur in the PDE system. Initial population densities: $X(x; t = 0) = 0:9$, $W(x; t = 0) = 0:7$, $Y(x; t = 0) = 0:6$, $Z(x; t = 0) = 0:8$. The diagram is plotted using XPPAUT package and the parameter values as in Table 1.

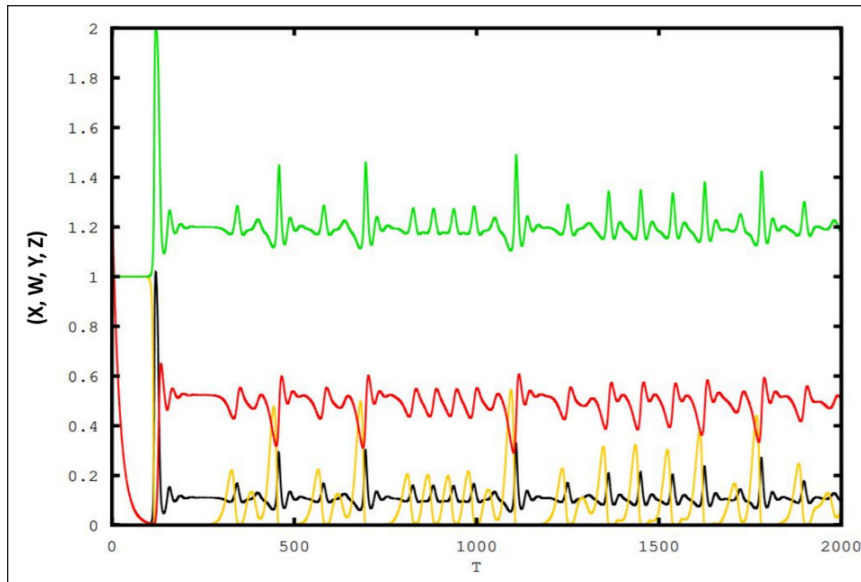


Figure 10. Time series for model (1) in the presence of dispersal ($D_X=D_W=D_Y=D_Z = 0.005$) with $\alpha = 8:1$. Initial population densities: $X(x; t = 0) = 0.9$, $W(x; t = 0) = 0.7$, $Y(x; t = 0) = 0.6$, $Z(x; t = 0) = 0.8$. X (yellow), W (black), Y (red) and Z (green). The results remains the same for different choices of initial conditions. The diagram is plotted using XPPAUT package and the parameter values in Table 1.

DISCUSSION

The ecological theories have emphasised the crucial impacts of competition and dispersal in shaping the dynamics of the multi-species system. Thus, a better understanding of their joint effects on the multi-species community assemblies is an important aspect in devising effective species conservation strategies and in maintaining the biodiversity of species. To address these issues, we extended previous multiple interactions type studies (Mitani & Mougi, 2017) by incorporating a spatial dispersal (i.e., diffusion) term into the system to examine the combined influences of distinct biotic factors and dispersal on community dynamics. In the presence of mutualist-resource-exploiter interactions, our numerical results show that competition and dispersal affect the stability and coexistence of species in the community. The interplay of dispersal with competition shows some intriguing dynamics that are essential for the formation of multi-species ecosystems. An interesting observation from our findings is that the combined influences between competition and dispersal result in different species composition (presence-absence) in this ecological community. Further comparing our results with and without dispersal in this modelling framework shows that there is a qualitative change in the overall dynamics of the ecological system as a result of dispersal and different biotic interactions between multiple species. This finding is in parallel with previous ecological studies (Mohd et al., 2016; Lee et al., 2020), which demonstrated that dispersal has different effects on the outcomes of species interactions.

Our results in this work extend the insights of some experimental studies (Holyoak, 2000), which used small-scale mesocosm techniques to verify the effects of the paradox of enrichment and dispersal on the persistence of prey-predator species. We discover that large population oscillations are also possible in a multiple interaction type system with dispersal. Our analysis shows the presence of stable and unstable limit cycles (through Hopf bifurcations) together with the emergence of period-doubling bifurcations as the plausible mechanisms that can induce fluctuating populations. These population cycles occur as a result of the interactions between competition and other biotic factors (e.g., mutualist-resource-exploiter interactions) in both systems with and without dispersal. This point of view re-enforces some theoretical results that other mechanisms might cause population cycles outside the conventional paradox of enrichment (Turchin, 2003; Rozhnova et al., 2013; Barraquand et al., 2017). The findings in this work demonstrate that the interplay of multiple interactions type and dispersal mediate population cycles as a result of their complexity.

In general, understanding the stability and coexistence mechanisms in multi-species ecosystems is a challenging task, and this issue has been studied from different contexts previously: for instance, regarding the influences of ecological and temporal process (Chesson, 2018; Leibold & Chase, 2017), the impacts of several limiting resources (Barabás et al., 2018) and the effects of multiple interactions type on multi-species community dynamics (Loreau, 2010; Carrara et al., 2015). Our work adds further insights to these previous studies, and we show that it is possible to maintain species diversity and multi-species coexistence in the presence of dispersal and mutualist-resource-competitor-exploiter interactions as long as the interspecific interactions strength is within certain threshold values. This line of thought also agrees with previous studies (Allesina & Tang, 2012; Becks et al., 2012; Mougi, 2012; Fussman & Gonzalez, 2013; Koch et al., 2014; Vellend, 2020). Our numerical simulation results have also demonstrated the importance of interaction strength in the overall stability of a multi-species ecological system. These findings further suggest that weak competition strength is a pre-requisite for species stability, coexistence and persistence. This result has shed some light on past empirical and theoretical studies (Kokkoris et al., 1999; Barabás et al., 2016; Gellner & McCann, 2016). The weak competition strength plays a critical role in maintaining the population oscillation (McCann et al., 1998). Another point to note is that diversity in species interactions strength affects the stability and composition of the community and this agrees with other theoretical results (Landi et al., 2018; Karakoç et al., 2020).

From the dynamical systems viewpoints, our bifurcation analysis results emphasise the importance of numerical continuation studies in comprehending the overall dynamics of the complex ecological system and the stability properties of different attractors. The bifurcation results show the dynamics that occur in the system and the threshold values at which they occur. It further illustrates the presence of transcritical bifurcations in the

ODE and PDE systems under consideration, as we vary competitive strength; the direct effects of this bifurcation can be seen in the species composition (presence-absence) as the magnitude of competitive strength changes, due to the exchange of stability between distinct steady states (Mohd, 2016). Other fascinating dynamical behaviours such as multi-species coexistence, stable and unstable limit cycles and aperiodic oscillations also emerge owing to the occurrences of Hopf bifurcations, limit point bifurcations of cycles and period-doubling bifurcations. In general, the presence of Hopf bifurcations gives birth to sustained oscillations that are uniform in space and periodic in time (Upadhyay et al., 2015; Upadhyay & Roy, 2016; Moustafa et al., 2020). The presence of period-doubling bifurcation may lead to the possibility of chaotic dynamics in some ecological systems (Ladeira & de Oliveira, 2019; Nath & Das, 2020).

As a conclusion, our results demonstrate the crucial roles of competition and dispersal play in multiple interactions type models on the stability and coexistence of complex ecological systems. We show that dispersal has (de-)stabilising effects on the multi-species systems and that the interplay between dispersal and several biotic factors have significant consequences on the community dynamics. In this paper, we have made some simplification by assuming a symmetric dispersal strength ($D_X = D_W = D_Y = D_Z = 0.005$) in multiple interactions type model; in reality, not all species disperse with the same dispersal strength and some species are more mobile (or immobile) than the others. As demonstrated by some previous theoretical studies (Zhou, 2016; He & Ni, 2013), the asymmetrical dispersal strength among species is another vital force that can shape multi-species community dynamics. For future work, we will consider this open problem and examine how the unequal dispersal strategies can determine the survival of species in this multiple interactions type system.

ACKNOWLEDGEMENT

This research is supported by the Universiti Sains Malaysia (USM) Fundamental Research Grant Scheme (FRGS) No. 203/PMATHS/6711645. The second author also wants to thank Ministry of Higher Education Malaysia for the financial support under the MOHE Postdoctoral Training Award that gives him the opportunity to do research in Universiti Kebangsaan Malaysia.

REFERENCES

- Abbott, K. C. (2011). A dispersal-induced paradox: Synchrony and stability in stochastic metapopulations. *Ecology Letters*, 14(11), 1158-1169. <https://doi.org/10.1111/j.1461-0248.2011.01670.x>
- Aliyu, M. B., & Mohd, M. H. (2021). Combined impacts of predation, mutualism and dispersal on the dynamics of a four-species ecological system. *Pertanika Journal of Science & Technology*, 29(1), 239-244. <https://doi.org/10.47836/pjst.29.1.13>

- Allesina, S., & Tang, S. (2012). Stability criteria for complex ecosystems. *Nature*, *483*(7388), 205-208. <https://doi.org/10.1038/nature10832>
- Amarasekare, P. (2016). Evolution of dispersal in a multi-trophic community context. *Oikos*, *125*(4), 514-525. <https://doi.org/10.1111/oik.02258>
- Anderson, K. E., & Hayes, S. M. (2018). The effects of dispersal and river spatial structure on asynchrony in consumer–resource metacommunities. *Freshwater biology*, *63*(1), 100-113. <https://doi.org/10.1111/fwb.12998>
- Bach, L. A., Thomsen, R., Pertoldi, C., & Loeschcke, V. (2006). Kin competition and the evolution of dispersal in an individual-based model. *Ecological Modelling*, *192*(3-4), 658-666. <https://doi.org/10.1016/j.ecolmodel.2005.07.026>
- Baek, H. (2018). Complex dynamics of a discrete-time predator-prey system with ivlev functional response. *Mathematical Problems in Engineering*, *2018*, Article 8635937. <https://doi.org/10.1155/2018/8635937>
- Barabás, G., D'Andrea, R., & Stump, S. M. (2018). Chesson's coexistence theory. *Ecological Monographs*, *88*(3), 277-303. <https://doi.org/10.1002/ecm.1302>
- Barabás, G., J. Michalska-Smith, M., & Allesina, S. (2016). The effect of intra-and interspecific competition on coexistence in multispecies communities. *The American Naturalist*, *188*(1), E1-E12. <https://doi.org/10.1086/686901>
- Barraquand, F., Louca, S., Abbott, K. C., Cobbold, C. A., Cordoleani, F., DeAngelis, D. L., & Murray, D. L. (2017). Moving forward in circles: Challenges and opportunities in modelling population cycles. *Ecology Letters*, *20*(8), 1074-1092. <https://doi.org/10.1111/ele.12789>
- Bashkirtseva, I., Ryashko, L., & Ryazanova, T. (2019). Stochastic variability and transitions to chaos in a hierarchical three-species population model. *Chaos, Solitons & Fractals*, *119*, 276-283. <https://doi.org/10.1016/j.chaos.2018.12.035>
- Bassett, A., Krause, A. L., & Van Gorder, R. A. (2017). Continuous dispersal in a model of predator–prey–subsidy population dynamics. *Ecological Modelling*, *354*, 115-122. <https://doi.org/10.1016/j.ecolmodel.2017.02.017>
- Becks, L., Ellner, S. P., Jones, L. E., & Hairston Jr, N. G. (2012). The functional genomics of an eco-evolutionary feedback loop: Linking gene expression, trait evolution, and community dynamics. *Ecology Letters*, *15*(5), 492-501. <https://doi.org/10.1111/j.1461-0248.2012.01763.x>
- Bjørnstad, O. N. (2000). Cycles and synchrony: two historical ‘experiments’ and one experience. *Journal of Animal Ecology*, *69*(5), 869-873. <https://doi.org/10.1046/j.1365-2656.2000.00444.x>
- Briggs, C. J., & Hoopes, M. F. (2004). Stabilizing effects in spatial parasitoid–host and predator–prey models: A review. *Theoretical Population Biology*, *65*(3), 299-315. <https://doi.org/10.1016/j.tpb.2003.11.001>
- Bullock, J. M., Kenward, R. E., & Hails, R. S. (Eds.). (2002). *Dispersal ecology: 42nd symposium of the British ecological society* (Vol. 42). Cambridge University Press.
- Carrara, F., Giometto, A., Seymour, M., Rinaldo, A., & Altermatt, F. (2015). Inferring species interactions in ecological communities: A comparison of methods at different levels of complexity. *Methods in Ecology and Evolution*, *6*(8), 895-906. <https://doi.org/10.1111/2041-210X.12363>

- Chaianunporn, T., & Hovestadt, T. (2012). Evolution of dispersal in metacommunities of interacting species. *Journal of Evolutionary Biology*, 25(12), 2511-2525. <https://doi.org/10.1111/j.1420-9101.2012.02620.x>
- Chaianunporn, T., & Hovestadt, T. (2015). Evolutionary responses to climate change in parasitic systems. *Global Change Biology*, 21(8), 2905-2916. <https://doi.org/10.1111/gcb.12944>
- Chesson, P. (2018). Updates on mechanisms of maintenance of species diversity. *Journal of Ecology*, 106(5), 1773-1794. <https://doi.org/10.1111/1365-2745.13035>
- Chow, Y., Jang, S. R. J., & Yeh, N. S. (2018). Dynamics of a population in two patches with dispersal. *Journal of Difference Equations and Applications*, 24(4), 543-563. <https://doi.org/10.1080/10236198.2018.1428962>
- Crooks, K. R., & Sanjayan, M. (Eds.). (2006). *Connectivity conservation* (Vol. 14). Cambridge University Press.
- Crowley, P. H. (1981). Dispersal and the stability of predator-prey interactions. *The American Naturalist*, 118(5), 673-701. <https://doi.org/10.1086/283861>
- Dey, S., & Joshi, A. (2006). Stability via asynchrony in *Drosophila* metapopulations with low migration rates. *Science*, 312(5772), 434-436. <https://doi.org/10.1126/science.1125317>
- Feyrer, F., Hobbs, J., Acuna, S., Mahardja, B., Grimaldo, L., Baerwald, M., Johnson, R. C., & Teh, S. (2015). Metapopulation structure of a semi-anadromous fish in a dynamic environment. *Canadian Journal of Fisheries and Aquatic Sciences*, 72(5), 709-721. <https://doi.org/10.1139/cjfas-2014-0433>
- Fussell, E. F., Krause, A. L., & Van Gorder, R. A. (2019). Hybrid approach to modeling spatial dynamics of systems with generalist predators. *Journal of Theoretical Biology*, 462, 26-47. <https://doi.org/10.1016/j.jtbi.2018.10.054>
- Fussmann, G. F., & Gonzalez, A. (2013). Evolutionary rescue can maintain an oscillating community undergoing environmental change. *Interface Focus*, 3(6), Article 20130036. <https://doi.org/10.1098/rsfs.2013.0036>
- Gandon, S. (1999). Kin competition, the cost of inbreeding and the evolution of dispersal. *Journal of Theoretical Biology*, 200(4), 345-364. <https://doi.org/10.1006/jtbi.1999.0994>
- Gandon, S., & Rousset, F. (1999). Evolution of stepping-stone dispersal rates. *Proceedings of the Royal Society of London. Series B: Biological Sciences*, 266(1437), 2507-2513. <https://doi.org/10.1098/rspb.1999.0953>
- Gause, G. F. (1932). Experimental studies on the struggle for existence: I. Mixed population of two species of yeast. *Journal of Experimental Biology*, 9(4), 389-402.
- Gellner, G., & McCann, K. S. (2016). Consistent role of weak and strong interactions in high- and low-diversity trophic food webs. *Nature Communications*, 7(1), 1-7. <https://doi.org/10.1038/ncomms11180>
- Goldwyn, E. E., & Hastings, A. (2008). When can dispersal synchronize populations? *Theoretical Population Biology*, 73(3), 395-402. <https://doi.org/10.1016/j.tpb.2007.11.012>
- Gotelli, N. J. (2008). *A primer of ecology*. Sunderland. Sinauer Associates.
- Gouhier, T. C., Guichard, F., & Gonzalez, A. (2010). Synchrony and stability of food webs in metacommunities. *The American Naturalist*, 175(2), E16-E34. <https://doi.org/10.1086/649579>
- Green, D. M. (2009). Coevolution of dispersal in a parasitoid-host system. *Population Ecology*, 51(2), 253-260. <https://doi.org/10.1007/s10144-008-0131-3>

- Grover, J. P., Hudziak, J., & Grover, J. D. (1997). *Resource competition* (Vol. 19). Springer Science & Business Media
- Gupta, R. P., & Yadav, D. K. (2020). Complex dynamical behavior of a three species prey–predator system with nonlinear harvesting. *International Journal of Bifurcation and Chaos*, 30(13), Article 2050195. <https://doi.org/10.1142/S0218127420501953>
- Gyllenberg, M., Jiang, J., Niu, L., & Yan, P. (2019). On the dynamics of multi-species Ricker models admitting a carrying simplex. *Journal of Difference Equations and Applications*, 25(11), 1489-1530. <https://doi.org/10.1080/10236198.2019.1663182>
- Hanski, I. (1998). Metapopulation dynamics. *Nature*, 396(6706), 41-49. <https://doi.org/10.1038/23876>
- Hardin, G. (1960). The competitive exclusion principle. *Science*, 131(3409), 1292-1297.
- He, X., & Ni, W. M. (2013). The effects of diffusion and spatial variation in Lotka–Volterra competition–diffusion system I: Heterogeneity vs. homogeneity. *Journal of Differential Equations*, 254(2), 528-546. <https://doi.org/10.1016/j.jde.2012.08.032>
- Holyoak, M. (2000). Effects of nutrient enrichment on predator–prey metapopulation dynamics. *Journal of Animal Ecology*, 69(6), 985-997. <https://doi.org/10.1111/j.1365-2656.2000.00453.x>
- Hovestadt, T., Kubisch, A., & Poethke, H. J. (2010). Information processing in models for density-dependent emigration: a comparison. *Ecological Modelling*, 221(3), 405-410. <https://doi.org/10.1016/j.ecolmodel.2009.11.005>
- Hudson, P. J., & Cattadori, I. (1999). The Moran effect: A cause of population synchrony. *Trends in Ecology and Evolution*, 14(1), 1-2. [https://doi.org/10.1016/S0169-5347\(98\)00000-0](https://doi.org/10.1016/S0169-5347(98)00000-0)
- Hutchinson, G. E. (1961). The paradox of the plankton. *The American Naturalist*, 95(882), 137-145. <https://doi.org/10.1086/282171>
- Kakishima, S., Morita, S., Yoshida, K., Ishida, A., Hayashi, S., Asami, T., Ito, H., Miller III, D. G., Uehara, T., Mori, S., & Hasegawa, E. (2015). The contribution of seed dispersers to tree species diversity in tropical rainforests. *Royal Society Open Science*, 2(10), Article 150330. <https://doi.org/10.1098/rsos.150330>
- Karakoç, C., Clark, A. T., & Chatzinotas, A. (2020). Diversity and coexistence are influenced by time-dependent species interactions in a predator–prey system. *Ecology Letters*, 23(6), 983-993. <https://doi.org/10.1111/ele.13500>
- Kendall, B. E., Bjørnstad, O. N., Bascompte, J., Keitt, T. H., & Fagan, W. F. (2000). Dispersal, environmental correlation, and spatial synchrony in population dynamics. *The American Naturalist*, 155(5), 628-636. <https://doi.org/10.1086/303350>
- Kindlmann, P., & Burel, F. (2008). Connectivity measures: A review. *Landscape ecology*, 23(8), 879-890. <https://doi.org/10.1007/s10980-008-9245-4>
- Koch, H., Frickel, J., Valiadi, M., & Becks, L. (2014). Why rapid, adaptive evolution matters for community dynamics. *Frontiers in Ecology and Evolution*, 2, Article 17. <https://doi.org/10.3389/fevo.2014.00017>
- Kokkoris, G. D., Troumbis, A. Y., & Lawton, J. H. (1999). Patterns of species interaction strength in assembled theoretical competition communities. *Ecology Letters*, 2(2), 70-74. <https://doi.org/10.1046/j.1461-0248.1999.22058.x>

- Kondoh, M. (2008). Building trophic modules into a persistent food web. *Proceedings of the National Academy of Sciences*, 105(43), 16631-16635. <https://doi.org/10.1073/pnas.0805870105>
- Kondoh, M., & Mougi, A. (2015). Interaction-type diversity hypothesis and interaction strength: The condition for the positive complexity-stability effect to arise. *Population Ecology*, 57(1), 21-27. <https://doi.org/10.1007/s10144-014-0475-9>
- Kool, J. T., Moilanen, A., & Treml, E. A. (2013). Population connectivity: Recent advances and new perspectives. *Landscape Ecology*, 28(2), 165-185. <https://doi.org/10.1007/s10980-012-9819-z>
- Kouvaris, N., Kugiumtzis, D., & Provata, A. (2011). Species mobility induces synchronization in chaotic population dynamics. *Physical Review E*, 84(3), Article 036211.
- Ladeira, D. G., & de Oliveira, M. M. (2019). Chaotic coexistence in a resource–consumer model. *Journal of Biological Systems*, 27(02), 167-184. <https://doi.org/10.1142/S0218339019500086>
- Lampert, A., & Hastings, A. (2016). Stability and distribution of predator–prey systems: Local and regional mechanisms and patterns. *Ecology letters*, 19(3), 279-288. <https://doi.org/10.1111/ele.12565>
- Landi, P., Minoarivelo, H. O., Brännström, Å., Hui, C., & Dieckmann, U. (2018). Complexity and stability of ecological networks: A review of the theory. *Population Ecology*, 60(4), 319-345. <https://doi.org/10.1007/s10144-018-0628-3>
- Lee, A. M., Sæther, B. E., & Engen, S. (2020). Spatial covariation of competing species in a fluctuating environment. *Ecology*, 101(1), Article e02901. <https://doi.org/10.1002/ecy.2901>
- Leibold, M. A., & Chase, J. M. (2017). *Metacommunity ecology* (Vol. 59). Princeton University Press.
- Liu, X., & Huang, Q. (2018). The dynamics of a harvested predator–prey system with Holling type IV functional response. *Biosystems*, 169, 26-39. <https://doi.org/10.1016/j.biosystems.2018.05.005>
- Loreau, M. (2010). Linking biodiversity and ecosystems: Towards a unifying ecological theory. *Philosophical Transactions of the Royal Society B: Biological Sciences*, 365(1537), 49-60. <https://doi.org/10.1098/rstb.2009.0155>
- McCann, K., Hastings, A., & Huxel, G. R. (1998). Weak trophic interactions and the balance of nature. *Nature*, 395(6704), 794-798. <https://doi.org/10.1038/27427>
- Mitani, N., & Mougi, A. (2017). Population cycles emerging through multiple interaction types. *Royal Society Open Science*, 4(9), Article 170536. <https://doi.org/10.1098/rsos.170536>
- Mittelbach, G. G., & McGill, B. J. (2019). *Community ecology*. Oxford University Press.
- Mohd, M. H. (2018). Numerical bifurcation and stability analyses of partial differential equations with applications to competitive system in ecology. In *SEAMS School on Dynamical Systems and Bifurcation Analysis* (pp. 117-132). Springer. https://doi.org/10.1007/978-981-32-9832-3_7
- Mohd, M. H. (2019). Diversity in interaction strength promotes rich dynamical behaviours in a three-species ecological system. *Applied Mathematics and Computation*, 353, 243-253. <https://doi.org/10.1016/j.amc.2019.02.007>
- Mohd, M. H. B. (2016). *Modelling the presence-absence of multiple species* (Doctoral dissertation). University of Canterbury. <http://dx.doi.org/10.26021/1670>

- Mohd, M. H., & Noorani, M. S. M. (2020). Local dispersal, trophic interactions and handling times mediate contrasting effects in prey-predator dynamics. *Chaos, Solitons & Fractals*, 142, Article 110497. <https://doi.org/10.1016/j.chaos.2020.110497>
- Mohd, M. H., Murray, R., Plank, M. J., & Godsoe, W. (2016). Effects of dispersal and stochasticity on the presence-absence of multiple species. *Ecological Modelling*, 342, 49-59. <https://doi.org/10.1016/j.ecolmodel.2016.09.026>
- Mohd, M. H., Murray, R., Plank, M. J., & Godsoe, W. (2017). Effects of biotic interactions and dispersal on the presence-absence of multiple species. *Chaos, Solitons & Fractals*, 99, 185-194. <https://doi.org/10.1016/j.chaos.2017.04.012>
- Mohd, M. H., Murray, R., Plank, M. J., & Godsoe, W. (2018). Effects of different dispersal patterns on the presence-absence of multiple species. *Communications in Nonlinear Science and Numerical Simulation*, 56, 115-130. <https://doi.org/10.1016/j.cnsns.2017.07.029>
- Mondor, E. B., Rosenheim, J. A., & Addicott, J. F. (2005). Predator-induced transgenerational phenotypic plasticity in the cotton aphid. *Oecologia*, 142(1), 104-108. <https://doi.org/10.1007/s00442-004-1710-4>
- Mougi, A. (2012). Unusual predator-prey dynamics under reciprocal phenotypic plasticity. *Journal of theoretical biology*, 305, 96-102. <https://doi.org/10.1016/j.jtbi.2012.04.012>
- Mougi, A. (2016). Stability of an adaptive hybrid community. *Scientific reports*, 6, Article 28181. <https://doi.org/10.1038/srep28181>
- Mougi, A., & Kondoh, M. (2012). Diversity of interaction types and ecological community stability. *Science*, 337(6092), 349-351. <https://doi.org/10.1126/science.1220529>
- Mougi, A., & Kondoh, M. (2014). Adaptation in a hybrid world with multiple interaction types: A new mechanism for species coexistence. *Ecological Research*, 29(2), 113-119. <https://doi.org/10.1007/s11284-013-1111-4>
- Moustafa, M., Mohd, M. H., Ismail, A. I., & Abdullah, F. A. (2020). Dynamical analysis of a fractional-order eco-epidemiological model with disease in prey population. *Advances in Difference Equations*, 2020(1), Article 48. <https://doi.org/10.1186/s13662-020-2522-5>
- Namba, T., Takeuchi, Y., & Banerjee, M. (2018). Stabilizing effect of intra-specific competition on prey-predator dynamics with intraguild predation. *Mathematical Modelling of Natural Phenomena*, 13(3), Article 29. <https://doi.org/10.1051/mmnp/2018033>
- Nath, B., & Das, K. P. (2020). Harvesting in tri-trophic food chain stabilises the chaotic dynamics-conclusion drawn from Hastings and Powell model. *International Journal of Dynamical Systems and Differential Equations*, 10(2), 95-115. <https://doi.org/10.1504/IJDSDE.2020.106025>
- Omaiye, O. J., & Mohd, M. H. (2018). Computational dynamical systems using XPPAUT. In *SEAMS School on Dynamical Systems and Bifurcation Analysis* (pp. 175-203). Springer. https://doi.org/10.1007/978-981-32-9832-3_10
- Perrin, N., & Goudet, J. (2001). Inbreeding, kinship, and the evolution of natal dispersal. *Dispersal*, 123-142.

- Poethke, H. J., & Hovestadt, T. (2002). Evolution of density–and patch–size–dependent dispersal rates. *Proceedings of the Royal Society of London. Series B: Biological Sciences*, 269(1491), 637-645. <https://doi.org/10.1098/rspb.2001.1936>
- Poethke, H. J., Hovestadt, T., & Mitesser, O. (2003). Local extinction and the evolution of dispersal rates: Causes and correlations. *The American Naturalist*, 161(4), 631-640. <https://doi.org/10.1086/368224>
- Poethke, H. J., Pfenning, B., & Hovestadt, T. (2007). The relative contribution of individual and kin selection to the evolution of density-dependent dispersal rates. *Evolutionary Ecology Research*, 9(1), 41-50.
- Poethke, H. J., Weisser, W. W., & Hovestadt, T. (2010). Predator-induced dispersal and the evolution of conditional dispersal in correlated environments. *The American Naturalist*, 175(5), 577-586. <https://doi.org/10.1086/651595>
- Rozhnova, G., Metcalf, C. J. E., & Grenfell, B. T. (2013). Characterizing the dynamics of rubella relative to measles: the role of stochasticity. *Journal of The Royal Society Interface*, 10(88), Article 20130643. <https://doi.org/10.1098/rsif.2013.0643>
- Selvam, A. G. M., & Dhineshababu, R. (2020). Bifurcation and chaos in a discrete fractional order prey-predator system involving infection in prey. In *Mathematical Models of Infectious Diseases and Social Issues* (pp. 95-119). IGI Global.
- Shabunin, A. V., Efimov, A., Tsekouras, G. A., & Provata, A. (2005). Scaling, cluster dynamics and complex oscillations in a multispecies Lattice Lotka–Volterra Model. *Physica A: Statistical Mechanics and its Applications*, 347, 117-136. <https://doi.org/10.1016/j.physa.2004.09.021>
- Shabunin, A., & Provata, A. (2013). Lattice limit cycle dynamics: Influence of long-distance reactive and diffusive mixing. *The European Physical Journal Special Topics*, 222(10), 2547-2557. <https://doi.org/10.1140/epjst/e2013-02036-5>
- Steiner, C. F., Stockwell, R. D., Kalaimani, V., & Aqel, Z. (2013). Population synchrony and stability in environmentally forced metacommunities. *Oikos*, 122(8), 1195-1206. <https://doi.org/10.1111/j.1600-0706.2012.20936.x>
- Travis, J. M. (2001). The color of noise and the evolution of dispersal. *Ecological Research*, 16(1), 157-163. <https://doi.org/10.1046/j.1440-1703.2001.00381.x>
- Tubay, J. M., Ito, H., Uehara, T., Kakishima, S., Morita, S., Togashi, T., Tainaka, K., Niraula, M. P., Casareto, B. E., Suzuki, Y. & Yoshimura, J. (2013). The paradox of enrichment in phytoplankton by induced competitive interactions. *Scientific Reports*, 3(1), 1-8. <https://doi.org/10.1038/srep02835>
- Turchin, P. (2003). *Complex population dynamics: A theoretical/empirical synthesis* (Vol. 35). Princeton University Press.
- Upadhyay, R. K., & Roy, P. (2016). Disease spread and its effect on population dynamics in heterogeneous environment. *International Journal of Bifurcation and Chaos*, 26(01), Article 1650004. <https://doi.org/10.1142/S0218127416500048>
- Upadhyay, R. K., Roy, P., & Datta, J. (2015). Complex dynamics of ecological systems under nonlinear harvesting: Hopf bifurcation and Turing instability. *Nonlinear Dynamics*, 79(4), 2251-2270. <https://doi.org/10.1007/s11071-014-1808-0>

- Vasseur, D. A., & Fox, J. W. (2009). Phase-locking and environmental fluctuations generate synchrony in a predator–prey community. *Nature*, *460*(7258), 1007-1010. <https://doi.org/10.1038/nature08208>
- Vellend, M. (2020). *The theory of ecological communities (MPB-57)*. Princeton University Press.
- Verma, T., & Gupta, A. K. (2020). Mean-field dispersal induced synchrony and stability in an epidemic model under patchy environment. *Physica A: Statistical Mechanics and its Applications*, *541*, Article 123300. <https://doi.org/10.1016/j.physa.2019.123300>
- Vogwill, T., Fenton, A., & Brockhurst, M. A. (2009). Dispersal and natural enemies interact to drive spatial synchrony and decrease stability in patchy populations. *Ecology Letters*, *12*(11), 1194-1200. <https://doi.org/10.1111/j.1461-0248.2009.01374.x>
- Wei, Z., Xia, Y., & Zhang, T. (2020). Stability and bifurcation analysis of an amensalism model with weak Allee effect. *Qualitative Theory of Dynamical Systems*, *19*(1), Article 23. <https://doi.org/10.1007/s12346-020-00341-0>
- Williams, P. D., & Hastings, A. (2013). Stochastic dispersal and population persistence in marine organisms. *The American Naturalist*, *182*(2), 271-282.
- Yaari, G., Ben-Zion, Y., Shnerb, N. M., & Vasseur, D. A. (2012). Consistent scaling of persistence time in metapopulations. *Ecology*, *93*(5), 1214-1227. <https://doi.org/10.1890/11-1077.1>
- Zhou, P. (2016). On a Lotka-Volterra competition system: diffusion vs advection. *Calculus of Variations and Partial Differential Equations*, *55*(6), 137. <https://doi.org/10.1007/s00526-016-1082-8>



Modelling Benign Ovarian Cyst Risk Factors and Symptoms via Log-Linear Model

Siti Zulaikha Mohd Jamaludin¹, Mohd Tahir Ismail¹, Mohd Shareduwan Mohd Kasihmuddin¹, Mohd. Asyraf Mansor², Siti Noor Farwina Mohamad Anwar Antony^{1*} and Adnin Adawiyah Makhul³

¹*School of Mathematical Sciences, Universiti Sains Malaysia, 11800, Penang, Malaysia*

²*School of Distance Education, Universiti Sains Malaysia, 11800, Penang, Malaysia*

³*Pusat Penyelidikan Klinikal, Hospital Sultan Ismail, Taman Mount Austin, 81100 Johor Bahru, Johor, Malaysia*

ABSTRACT

Ovarian cancer among women is known as “The Silent Killer”. It is caused by the malignant ovarian cyst, which can spread to other organs if it is not treated at an early stage. Some are benign ovarian cyst which can be treated through medical procedures such as laparoscopic and laparotomy. The type of medical procedure that the patients have to undergo depends on the size of cyst. A few risk factors that can cause benign ovarian cyst are age, pregnancy, menopause and menstrual cycle. Apart from that, there are a few symptoms of benign ovarian cyst which are fever, nausea and abdominal pain, abdominal distension, dysmenorrhea and intermenstrual bleeding. The association between these 12 discrete categorical data variables (factors, symptoms, treatment and size) are measured using the log-linear analysis in this study. According to the analysis, the patients who have large benign ovarian cyst need laparoscopic procedure, while those with smaller cyst need

either laparotomy procedure or they do not have to undergo any surgery at all. Among all of the factors, menopause gives the highest risk factor of benign ovarian cyst, followed by age, pregnancy and menstrual cycle. Meanwhile, the interaction between nausea, abdominal pain and intermenstrual bleeding give the highest symptom rate to the benign ovarian cyst.

Keywords: Abdominal pain, benign ovarian cyst, fever, log-linear analysis, menopause, pregnancy

ARTICLE INFO

Article history:

Received: 02 February 2021

Accepted: 24 May 2021

Published: 31 July 2021

DOI: <https://doi.org/10.47836/pjst.29.3.26>

E-mail addresses:

szulaikha.szmj@usm.my (Siti Zulaikha Mohd Jamaludin)

m.tahir@usm.my (Mohd Tahir Ismail)

shareduwan@usm.my (Mohd Shareduwan Mohd Kasihmuddin)

asyrafiman@usm.my (Mohd. Asyraf Mansor)

farwina@usm.my (Siti Noor Farwina Mohamad Anwar Antony)

adninadawiyah@gmail.com (Adnin Adawiyah Makhul)

* Corresponding author

INTRODUCTION

Around the world, ovarian cyst causes the most hospitalizations and surgical procedures among women (Farahani & Datta, 2016). It can cause cancer and has been coined as a “The Silent Killer”, as it can lead to more deaths than any other gynaecological cancers (Ahmad & Arslan, 2015; Al-Azri et al., 2018). A cyst is a pocket or fluid-filled sac that forms in female sex cell-producing organs called ovaries. Normally, the size of a cyst would be smaller than 1 centimeter in diameter, which is it could be as small as a pea. However, the size of the cyst can also be as large as an orange which may need to be removed (Shiota et al., 2012; Jha et al., 2019). The ovarian cyst is categorized into three main types: malignant, functional and benign. Benign cases can be defined as the cyst that consists of is non-cancerous cells and is not harmful to the body (Telli et al., 2013). Sanersak et al. (2006) found that majority of the ovarian cyst cases are benign ovarian cyst. It has been reported that around 70% of the total ovarian cyst masses are benign ovarian cyst, 24% are functional cyst and 6% are malignant cyst (Rofe et al., 2013).

In gynaecology, a benign ovarian cyst is regularly viewed with the most precise surgical excision (Mohamed et al., 2016). Most of the ovarian cyst patients need to go through primary surgical procedure either laparoscopic or laparotomy (Wu et al., 2013). Cyst with 5 diameter centimetres can be removed with recent advances in minimal surgery procedure known as laparoscopy. Hizkiyahu et al. (2019) considered laparoscopic as minimal surgery due to less pain, shorter duration of hospitalization, lower infection rates and shorter recovery period. However, in some cases, the patient can recover without any surgical treatment throughout their annual ultrasound scan (Akkoyun & Gülen, 2012). The use of medications can help to control the cyst’s growth and lower the pain especially when the cysts are small in size. According to Medeiros et al. (2009), if the cyst has a diameter that is larger than 6 centimetres and it is considered cancerous, then laparotomy surgery will be proposed. However, there are cases where the large size of ovarian cyst can be removed via laparoscopic (Hizkiyahu et al., 2019).

The occurrence of ovarian cyst among female is associated with numerous symptoms and risk factors. Over the years, medical practitioners such as doctors and specialists have relied on the late symptoms or factors to give an accurate diagnosis. According to Udomsinklul et al. (2020), potential symptoms such as abdominal pain, breast tenderness, abnormal bleeding, dysmenorrhea, nausea or vomiting and abdominal bloating lead to benign ovarian cyst. However, the symptoms of ovarian cyst vary according to the risk factors (Mandai et al., 2012). Mukhopadhyay et al. (2016) and Gameraddin et al. (2018) evaluated the risk factors of benign ovarian cyst using chi-square analysis. They found that the potential risk factors associated with benign ovarian cyst were age, menstrual cycle, pregnancy, and menopause stage. Therefore, all these potential risk factors and symptoms could help doctors to predict the size of ovarian cyst and decide on the type of treatment

a patient might need. A specific data-adaptive model is required to extract the relationship of these factors that contribute to ovarian cyst. Thus, this study employs the log-linear model due to the effective feature selection mechanism to analyze specific symptoms and risk factors that contribute to benign ovarian cyst.

Numerous studies have employed the log-linear model to capture the behaviour of the medical data. Milewska et al. (2018) proposed log-linear analysis to estimate the chance of pregnancy among couples who implemented Assisted Reproductive Technology (ART) insemination. The proposed model provided a promising interaction extraction that predicts the chance of achieving a clinical pregnancy. In another context, Vilsen et al. (2019) utilized log-linear analysis to predict Lithium-ion resistance. In this model, log-linear is modelled as a function of State of the Art Charge (SOC) for lithium battery. The model was fitted to the extracted internal resistance and was reported to be consistent with the conventional internal resistance. The log-linear approach is also beneficial in the field of macroeconomics. Eggertsson and Singh (2019) utilize log-linear as a prediction model for the Keynesian model. Although their work revealed some limitations in log-linear model, the proposed exact non-linear model revealed the same predictions capability as in several policies such as government spending and tax multipliers. In a recent development, the log-linear model has been used to estimate the progression of the COVID-19 infection in Tamil Nadu (Bhaskar et al., 2020). Two separate log-linear models were fitted to model the growth phase before the peak and the decay phase after the peak. As a result, both models revealed the effectiveness of control measures by the government. It is to be noted that the common contribution of all the above studies emphasize the log-linear model as a good prediction model in various perspectives. Unfortunately, the application of log-linear with logic mining in predicting specific cancer disease is not properly studied. The closest model that is associated with cancer disease is the primary liver cancer where the log-linear capture and recapture model has been utilized to estimate a more correct incidence of underreporting for hepatocellular carcinoma (Törner et al., 2017). In addition, there is a work by Jamaludin et al. (2020), emphasizing the logistic regression and log-linear analysis in benign ovarian cyst. However, there is no recent effort to diagnose patients with benign ovarian cyst using log-linear model and logic mining approach. Moreover, the standard prediction model such as machine learning approach may become infeasible in terms of risk factors selection; thus, we proposed the standalone log-linear model to cope with the benign ovarian cyst detection task on risk factors and symptoms, separately. From the log-linear model, assumptions can be obtained for possible prediction among all the contributing attributes.

Hence, the objectives of this paper are as follows:

1. To measure the association between the types of operation and the size of a benign ovarian cyst.
2. To build a suitable model for risk factors and symptoms of a benign ovarian cyst.

The remaining part of this paper is as follows: Section 1 explores the uses of log-linear model in studies of benign ovarian cyst; Section 2 explains the material and method in detail; Section 3 discusses the result and discussion thoroughly and Section 4 gives the concluding remarks.

MATERIALS AND METHOD

General Overview of Log-linear Analysis

Log-linear analysis is a multi-dimensional data analysis model that is commonly known as a log-linear model (Zhu et al., 2006). According to McCullagh and Nelder (1989), the log-linear model is defined by assuming a Poisson distribution (with mean μ). This method is favoured when all variables of interest are presented on a qualitative scale and discrete in nature, while their relationships are presented in the form of a contingency table. It is to be noted that, the significance testing of main and interaction effects can be conducted using either the Wald test or the likelihood ratio test (Wiedermann & von Eye, 2020). According to Cox and Hinkley (1979), the Wald test and the likelihood ratio test are asymptotically equivalent as the sample size approaches infinity. An exception for small sample size where the likelihood ratio test may be preferred (Agresti, 2003).

Formulation of Log-linear Model

Analytically, the log-linear model is defined as an expression of expected frequencies (μ_{ij}) in the form of a function of parameters that represent the characteristics of discrete variables and the interactions taking place between them. According to Milewska et al. (2018), log-linear will choose the model with the lowest possible number of parameters. The model that is usually applied in the log-linear analysis is a saturated model, which includes model components. Model components are the number of main effects and interactions in the model. A saturated model always best represents the data and is the least parsimonious as every component is included. In this perspective, log-linear is also characterized by a good fit to data (Agresti, 2003). Consider two discrete variables A and J with their empirical frequencies n_{ij} in a contingency table with I row and J columns. According to Agresti (2003), the additive model for A and B is given as Equation (1):

$$\ln(\mu_{ij}) = \lambda + \lambda_i^A + \lambda_j^B + \lambda_{ij}^{AB} \quad (1)$$

where μ_{ij} is an expected values with regards to variable A and B . The symbol λ_i^A and λ_j^B represent the effect of i -th category of variable A and j -th category of variable B , respectively. Meanwhile, the symbol λ_{ij}^{AB} represents the effect of both i -th category of

variable A and j -th category of variable B . It is to be noted that, logarithmic mean μ for all cells is given as Equation (2):

$$\lambda = \frac{1}{IJ} \sum_{i=1}^I \sum_{j=1}^J \ln \mu_{ij} \quad (2)$$

It is worth mentioning that the parameters of any log-linear model must satisfy the following Equation (3):

$$\sum_{i=1}^I \lambda_i^A = \sum_{j=1}^J \lambda_j^B = \sum_{i=1}^I \lambda_{ij}^{AB} = \sum_{j=1}^J \lambda_{ij}^{AB} = 0 \quad (3)$$

where $\mu_{ij} > 0$. The log-linear model is utilized in this paper due to the nature of the categorical data. The categorical data analyzed by the log-linear model can provide us the information on association among the variables of the dataset. Log-linear is also a useful technique for modelling the count of μ_{ij} in the tables of categorical data with three and more dimension. Since more than two variables involve in this study, log-linear is considered practical for the medical dataset where the associations between discrete categorical data are to be analysed.

Data Analysis Setup

A cross-sectional study was conducted in which the data was collected based on 201 patients who were detected with ovarian cyst from January 2016 to December 2016 in Hospital Sultan Ismail, Johor Bahru, Malaysia. However, the inclusion criteria in this study identified 108 patients, who were diagnosed with benign ovarian cyst. The exclusion criteria eliminated 93 patients who were not diagnosed with benign ovarian cyst. The data was analysed by using IBM SPSS Statistic Version 24 in Windows 10 with computer specifications Intel CORE i5 processor, RAM 16GB. Each data simulation was conducted in single simulation rather than parallel simulation. Single simulation was chosen due to parallel simulation can lead to bad sector which will affect the final result (Kasihmuddin et al., 2019). In this study, we employed 95% confidence interval in the simulation where the value is ideally selected based on previous study by Milewska et al. (2018). This dataset has no missing entries and must be represented in the form of binary. In addition, log-linear model adopted unlimited ways of interaction among the risk factors and symptoms of benign ovarian cyst.

Benign Ovarian Cyst Dataset

They were 12 factors of interest used in this study: size of benign ovarian cyst, type of operation, risk factors and symptoms. For the risk factors, we emphasized several factors such as age, pregnancy, menopause and menstrual cycle. Meanwhile, as of factors for symptoms, we emphasized on fever, nausea, abdominal pain, abdominal distension, dysmenorrhea and intermenstrual bleeding. These variables were selected because the previous literature (Ahmad & Arslan, 2015; Al-Azri et al., 2018) utilizes the same variables. All these variables are important to be assessed statistically based on the clinical reports, which are obtained from the Hospital Sultan Ismail, Johor Bahru, Malaysia for the year 2016. This study is an extension of the study by Jamaludin et al. (2020) where all the variables interest in this study is critically analyzed by using log-linear analysis described in the previous section. Table 1 describes the information of the dataset used in this study.

Table 1
Summary of dataset for risk factor

Factor	Variable	Description	Scale	Unit
	size	Size of benign ovarian cyst	Nominal	0 = Small 1 = Large
	operation	Type of operation	Nominal	0 = No operation 1 = Laparotomy 2 = Laparoscopic
	age	Age of patient	Nominal	0 = 41 years old and above 1 = 40 years old and below (Zhu et al., 2019)
Risk Factor	pregnancy	The patient is pregnant or not	Nominal	0 = Yes 1 = No
	menopause	The menopause stage of patient	Nominal	0 = Yes 1 = No
	menscycle	The normality of menstrual cycle of patient	Nominal	0 = Not normal 1 = Normal
Symptom	fever	Symptoms of fever absent or not	Nominal	0 = Yes 1 = No
	nausea	Symptom of nausea is absent or not	Nominal	0 = Yes 1 = No
	abdopain	The patient have abdominal pain or not	Nominal	0 = No 1 = Yes
	abdodisten	Symptom of abdominal distension is absent or not	Nominal	0 = Yes 1 = No
	dysmenorrhoea	Symptoms of dysmenorrhoea is absent or not	Nominal	0 = Yes 1 = No
	bleeding	The patient have intermenstrual bleeding or	Nominal	0 = Yes 1 = No

RESULT AND DISCUSSION

This section presents results of log-linear analysis for two key components of the datasets which are risk factors and symptoms. Both analysis are made based on K-way effects, partial association and odds ratio. In order to visualize the datasets discussed in the previous session, this study proposed mosaic plot to demonstrate the composition of the type of treatment with respect to the size of the benign ovarian cyst. In terms of the frequency of the treatment, contingency table has been proposed to reveal the total number of patients that should undergo treatment. Note that the chi-square test will be utilized to test the independence of the variables in contingency table. By analysing the partial association and odds ratio for each risk factors and symptoms, the study can determine the association of the variables for main effects and interaction. This information is required to build a suitable model from the log-linear assumption for risk factors and symptoms of a benign ovarian cyst.

Mosaic Plot

According to Figure 1, the red section refers to the patients with large benign ovarian cyst, while the green section refers to the patients with small benign ovarian cyst. Based on Figure 1, most of the patient with small benign ovarian cyst have to undergo laparoscopic procedure or they do not have to undergo any operation procedure. Meanwhile, patients with large benign ovarian cyst will undergo laparotomy procedure.

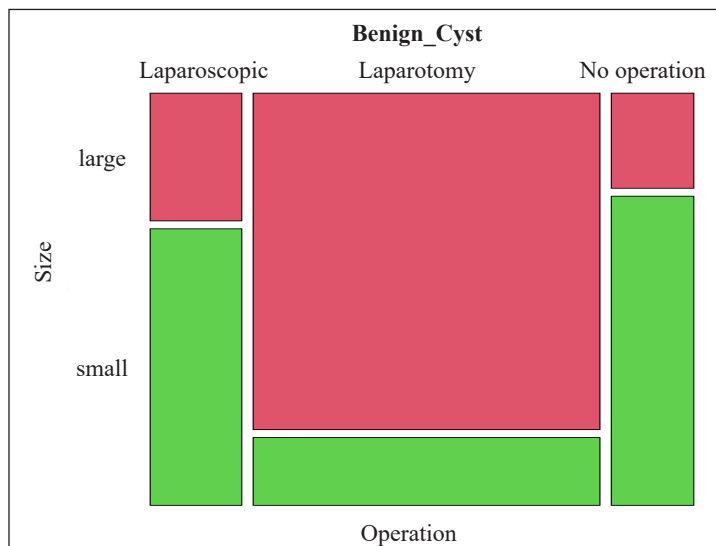


Figure 1. Mosaic plot of type of treatment by size of benign ovarian cyst

Contingency Table

From cross tabulation in Table 2, patients with small cyst had about 31.6% tendency of having laparoscopic surgery and about 34.2% for not having any operation or laparotomy surgery. For patient with large benign ovarian cyst, the probability to undergo laparoscopic was quite large which was 46.7% and only 11.0% of patient does not have to undergo any operation.

Table 2
Contingency table of type of treatment by size of benign cyst

Size		Type of Treatment			TOTAL
		No Operation	Laparoscopic	Laparotomy	
Small	Count	13	12	13	38
	% within Size	34.2	31.6	34.2	100.0
Large	Count	4	60	6	70
	% within Size	11.0	46.7	12.3	100.0
TOTAL	Count	17	72	19	108
	% within Size	15.7	66.7	17.6	100.0

Chi-Square Test

Based on the Table 3, the Chi-square value was 34.214 and the significance value was less than 0.05. It was concluded that there was an association between the size of benign ovarian cyst and the type of treatment. In other words, if the patient had a large size of cyst, they would have to undergo laparotomy surgery.

Table 3
Table of Chi-Square test of association

	Value	Exact Sig.
Pearson Chi-Square	34.214	0.000

Log-linear Analysis for Risk Factors

There are four variables in consideration when conducting log-linear analysis for demographic data which are age, pregnancy, menopause and menstrual cycle.

K-way Effects. The K-way effect was used to analysed which components of the model can be removed.

Table 4 manifests the K-way effects component, where the possible effect components obtained by the model can be filtered. Based on the first row ($K = 1$) with degree freedom of 4, the main effect terms for both likelihood-ratio and Pearson test are statistically significant at 0.05 level of significance. This implies that the main effect terms are included in this model. The significant p -value for the two-way effect ($K = 2$) indicates that two-factors

Table 4
K-Way effects component of the model for risk factor

K	df	Likelihood Ratio		Pearson	
		χ^2	<i>p</i> -value	χ^2	<i>p</i> -value
1	4	108.507	0.000	172.975	0.000
2	6	64.440	0.000	107.633	0.000
3	4	5.327	0.255	5.350	0.253
4	1	0.206	0.650	0.116	0.733

interaction would be included in the model. In conclusion, a good fitted model for risk factor can have up to two interaction terms, as supported by the work of Fatin et al. (2020).

Partial Association. Although the two-way interactions significantly affect the model, the specific two-way interaction among the risk factors need to be determined statistically via log-linear model.

Table 5 manifested the partial association obtained by assessing all risk factor variables. Consequently, based on Table 5, the Pearson χ^2 test were reported to be statistically significant for several interactions such as age*pregnancy and age*menopause. This is due to the optimal *p*-value for these two interactions ($p \leq 0.05$). Furthermore, the similar *p*-value have been reported in other parameters ($p \leq 0.05$) such as the age, pregnancy and menopause that statistically justify the significance of the effects.

Table 5
Table of partial association for risk factor

Effect	df	Partial χ^2	<i>p</i> -value
age*pregnancy*menopause	1	.080	.777
age*pregnancy*menscycle	1	1.256	.262
age*menopause*menscycle	1	.004	.949
pregnancy*menopause*menscycle	1	3.695	.055
age*pregnancy	1	25.032	.000
age*menopause	1	11.904	.001
pregnancy*menopause	1	.366	.545
age*menscycle	1	.517	.472
pregnancy*menscycle	1	.536	.464
menopause*menscycle	1	1.234	.267
age	1	35.303	.000
pregnancy	1	49.245	.000
menopause	1	20.233	.000
menscycle	1	3.725	.054

General Log-linear. Table 6 shows the summary of parameter estimate of variables that significantly effects the model. Note that, the parameters in Table 6 will be estimated by using z -score instead of χ^2 test. This is due to the usefulness of z -score in comparing the effect of variables (Field, 2013). High magnitude of z -score indicates that the effect of the parameters is more significant compared to low value of z -score. Based on Table 6, menopause ($z = 4.626$) is the most important effect in the model and followed by age, pregnancy, menscycle and age*menopause.

Note that, the obtained log-linear model that evaluate the risk factors for benign ovarian cyst is given as Equation (4):

$$\ln \mu_{hijk} = \lambda + \lambda_{A(k)} + \lambda_{B(l)} + \lambda_{C(m)} + \lambda_{D(n)} + \lambda_{AC(km)} \quad (4)$$

where,

A : Age (0 = 41 years old and above, 1 = 40 years old and below); B : Pregnancy (0 = yes, 1 = no); C : Menopause (0 = yes, 1 = no); D : Menstrual cycle (0 = not normal, 1 = normal).

Table 6
Summary of parameter estimate for risk factor

Parameter	Estimate	Std. Error	z	p-value	95% Confidence Interval	
					Lower Bound	Upper Bound
Constant	3.795	.150	25.319	.000	3.502	4.089
[age = 0]	-2.879	.650	-4.430	.000	-4.153	-1.605
[pregnancy = 0]	-2.879	.650	-4.430	.000	-4.153	-1.605
[menopause = 0]	-2.091	.452	-4.626	.000	-2.977	-1.205
[menscycle = 0]	-0.638	.255	-2.504	.012	-1.138	-.139
[age = 0] * [menopause = 0]	2.091	1.002	2.086	.037	.127	4.055

Odds Ratio. Odds ratios are used to determine the association of the variables for main effects and two interaction, since the the model for risk factor is obtained with two-way effect.

According to Table 7, patients with the age of 41 and older has a higher odds of benign ovarian cyst by 0.06 times compared to 40 years old and below. Similar odds ratio is reported for patient that is pregnant compared to non-pregnant women. As for other parameters such as menopause and menscycle, the odds ratio for benign ovarian cyst with age 40 years old is 0.12 and 0.52 respectively. Meanwhile, that the odds of benign ovarian cyst patients with age 41 years old and above and menopause are 8.09 times higher than the odds of patients with age 40 years old and below and not menopause.

Table 7
Summary of odds ratio for risk factor

Parameter	Estimate	Odds Ratio
[age = 0]	-2.879	0.0562
[pregnancy = 0]	-2.879	0.0562
[menopause = 0]	-2.091	0.1237
[mencycle = 0]	-0.638	0.5283
[age = 0] * [menopause = 0]	2.091	8.0930

Log-linear Analysis for Symptoms

There are six variables in conducting log-linear analysis for symptoms data which are fever, nausea, abdominal pain, abdominal distension, dysmenorrhea and intermenstrual bleeding.

K-way Effects. The K-way effect was used to analyze which components of the model can be removed.

Table 8
K-Way Effects Component of the Model for Symptom

K	df	Likelihood Ratio		Pearson	
		χ^2	p-value	χ^2	p-value
1	6	197.876	.000	471.381	.000
2	15	127.358	.000	263.375	.000
3	20	58.437	.000	55.269	.000
4	15	0.664	.917	0.345	.988
5	6	0.000	.960	0.000	.993
6	1	0.000	1.000	0.000	1.000

Based on Table 8, for the case $K = 1$, the main effect terms for both likelihood-ratio and Pearson χ^2 test are statistically significant at 0.05 level of significant. This implies that the main effect terms are included in this model. The significant p -value for the two-way effects ($K = 2$) and three-way effects ($K = 3$) indicate that both two-factors and three-factors interaction would be included in the model. In conclusion, a good fitted model can have up to three interaction terms.

Partial Association. As mentioned in Table 8, removing all three-way interactions significantly affects the model. Table 9 shows the partial association among all symptom variables.

Table 9
Table of partial association for symptom

Effect	df	Partial χ^2	<i>p</i> -value
fever*abdopain*dysmenorrhea	1	6.113	.013
nausea*abdopain*bleeding	1	37.073	.000
nausea*abdodisten	1	17.661	.000
abdopain*dysmenorrhea	1	25.022	.000
abdodisten*bleeding	1	14.379	.000
dysmenorrhea*bleeding	1	14.598	.000
fever	1	83.085	.000
nausea	1	18.458	.000
abdopain	1	9.625	.002
abdodisten	1	12.233	.000
dysmenorrhea	1	46.220	.000
bleeding	1	28.255	.000

Pearson χ^2 as shown in Table 9 indicated that test of partial association for symptoms were significant for several interactions such as nausea*abdopain*bleeding, nausea*abdodisten, and dysmenorrhea*bleeding interactions since the *p*-value for these two and three-interactions were less than 0.05. The main effects of fever, nausea, abdominal pain, abdominal distension, dysmenorrhea and intermenstrual bleeding were significant.

General Log-linear. The summary of parameter estimate of variables that significantly effects the model can be viewed in Table 10. It can be concluded that the nausea*abdopain*bleeding ($z = 4.178$) was the most important effect in the model and followed by nausea*bleeding, nausea, fever, nausea*abdopain, dysmenorrhea, bleeding, abdopain*bleeding, abdopain, nausea*abdopain*dysmenorrhea, fever*nausea, abdopain*dysmenorrhea and fever*nausea*abdopain.

Hence, the final log-linear model for symptom of benign ovarian cyst is defined as Equation (5):

$$\begin{aligned} \ln \mu_{opqst} = & \lambda + \lambda_{E(o)} + \lambda_{F(p)} + \lambda_{G(q)} + \lambda_{I(s)} + \lambda_{J(t)} \\ & + \lambda_{FJ(pt)} + \lambda_{FG(pq)} + \lambda_{GJ(qt)} + \lambda_{EF(op)} + \lambda_{GI(qs)} \quad (5) \\ & + \lambda_{FGJ(pqt)} + \lambda_{EFG(opq)} + \lambda_{FGI(pqs)} + \lambda_{EFG(opq)} \end{aligned}$$

where,

E: Fever (0 = yes, 1 = no); *F*: Nausea (0 = yes, 1 = no); *G*: Abdominal pain (0 = no, 1 = yes); *I*: Dysmenorrhea (0 = yes, 1 = no); *J*: Intermenstrual bleeding (0 = yes, 1 = no).

Table 10
Summary of parameter estimate for symptom

Parameter	Estimate	Std. Error	z	p-value	95% Confidence Interval	
					Lower Bound	Upper Bound
Constant	3.068	.216	14.226	.000	2.645	3.491
[fever = 0]	-2.663	.844	-3.153	.002	-4.318	-1.007
[abdpain = 0]	-3.761	1.431	-2.629	.009	-6.565	-.957
[dysmenorrhea = 0]	-1.815	.576	-3.149	.002	-2.945	-.686
[bleeding = 0]	-1.815	.576	-3.149	.002	-2.945	-.686
[fever = 0] * [nausea = 0]	2.663	1.230	2.165	.030	.252	5.074
[nausea = 0] * [abdpain = 0]	5.096	1.597	3.190	.001	1.965	8.227
[nausea = 0] * [bleeding = 0]	3.250	.910	3.573	.000	1.467	5.033
[abdpain = 0] * [dysmenorrhea = 0]	3.425	1.653	2.072	.038	.185	6.664
[abdpain = 0] * [bleeding = 0]	4.760	1.561	3.049	.002	1.700	7.820
[fever = 0] * [nausea = 0] * [abdpain = 0]	-5.607	2.760	-2.031	.042	-11.017	-.197
[nausea = 0] * [abdpain = 0] * [dysmenorrhea = 0]	-4.760	2.138	-2.226	.026	-8.950	-.569
[nausea = 0] * [abdpain = 0] * [bleeding = 0]	-8.041	1.925	-4.178	.000	-11.813	-4.268

Odds Ratio. Odds ratios are used to determine the association of the variables for main effects, two interaction and three interaction since the best model obtained is the model with three-way effect.

The summary of odds ratio as shown in Table 11 indicates that the odds of benign ovarian cyst patients who have fever are 0.07 times higher than the odds of patients who not have fever. This odds ratio also indicates that the odds of benign ovarian cyst patients who have no abdominal pain symptom are 0.02 times higher than the odds of patients who have abdominal pain. Other than that, the odds ratio indicates that the odds of benign ovarian cyst patients who experience dysmenorrhea and intermenstrual bleeding are 0.16 times higher than the odds of patients who did not experience it. It also indicate the odds of benign ovarian cyst patients who have fever and nausea are 14.33 times higher than the odds of patients who did not experience any fever and nausea. Lastly, the odds ratio able to indicate that the odds of benign ovarian cyst patients who have fever, abdominal pain and intermenstrual bleeding are 0.0003 times higher than the odds of patients who not have fever, abdominal pain and intermenstrual bleeding.

A study done by Al-Azri et al. (2018) which explored knowledge, risk factors, symptoms and time taken to seek early medications for ovarian cancer has agreed that abdominal pain and dysmenorrhea are the important factors for an ovarian cancer. Another interesting note, the finding of this study has a good agreement with the previous study of

Table 11
Summary of odds ratio for symptom

Parameter	Estimate	Odds Ratio
[fever = 0]	-2.663	0.0674
[abdominal pain = 0]	-3.761	0.0233
[dysmenorrhea = 0]	-1.815	0.1628
[bleeding = 0]	-1.815	0.1628
[fever = 0] * [nausea = 0]	2.663	14.3392
[nausea = 0] * [abdominal pain = 0]	5.096	163.3671
[nausea = 0] * [bleeding = 0]	3.250	25.7903
[abdominal pain = 0] * [dysmenorrhea = 0]	3.425	30.7226
[abdominal pain = 0] * [bleeding = 0]	4.760	116.7459
[fever = 0] * [nausea = 0] * [abdominal pain = 0]	-5.607	3.672×10^{-3}
[nausea = 0] * [abdominal pain = 0] * [dysmenorrhea = 0]	-4.760	8.566×10^{-3}
[nausea = 0] * [abdominal pain = 0] * [bleeding = 0]	-8.041	3.22×10^{-4}

Udumsinkul et al. (2020) where they implemented logistic regression to identify risk factors for endometriotic-cyst associated with ovarian cancer. In a good agreement by Huang et al. (2017), the most common symptom of ovarian torsion was pelvic pain and nausea. Although the mentioned studies supported our findings, the result from this study cannot be compared with the mentioned study due to properties of the datasets. Robust comparison can be made if all the dataset has been taken from the same hospital (Jamaludin et al., 2020).

CONCLUSION

Among 108 patients who were diagnosed benign ovarian cyst, about 38% and 70% of patients were diagnosed with benign ovarian cyst of small and large sizes, respectively. The contingency table was presented to measure the association between types of operation and the size of benign ovarian cyst. The results found that patients who had large size of benign ovarian cyst has to undergo laparoscopic surgery, while patients who had small size has to undergo either no operation or laparotomy surgery. Analyzing the odds ratio from each symptoms and risk factors are required to build a suitable model for risk factors and symptoms of a benign ovarian cyst. From log-linear analysis, it is concluded that menopause was the most dominant risk factor of benign ovarian cyst. Whereas, interaction effect of nausea, abdominal pain and intermenstrual bleeding were the most important effect for symptoms of benign ovarian cyst. By considering more criteria of risk factors and symptoms, our proposed model could generate a more generalized rule for classification that have been highlighted in several studies. Therefore, it can be concluded that this study achieved all its objectives.

The limitations of this study can be seen in the cross-sectional design, in which the data was collected at one time. Furthermore, this study employed the retrospective observational study where the data was extracted and limited from the patient's history. In addition, there was a possibility of sampling bias, where the data of patients might be redundant, so the system of patient's database should be enhanced via better technology. The documentation of the patient's history may not be too accurate since this study utilized the secondary data. The secondary data is limited and prone to the possible errors and bias of the data entries. The aforementioned limitation might originate from the medical practitioners during data collection and interpretation. Moreover, the accuracy of the symptoms or risks factors possessed by the patients can be limited in secondary data.

For future work, the simulation would include more patients that have other gynecologic problems since different problems may bring different risk factors and symptoms. This perspective will improve the accuracy of diagnosis and provide holistic findings that will benefit the medical practitioners. Moreover, a larger sample size (more than 1000) is required to investigate the more significant risk factors and symptoms of benign ovarian cyst (Jamaludin et al., 2020). By considering more criteria of risk factors and symptoms, our proposed model can generate more generalized rule for classification task that has been highlighted in several studies such as Zamri et al. (2020) and Alway et al. (2020).

ACKNOWLEDGEMENT

The authors would like to express special dedication to all of the researchers from AI Research Development Group (AIRDG) for the continuous support. This research was funded by Univeriti Sains Malaysia (USM), grant number 304/PMATHS/6315390.

REFERENCES

- Ahmad, G., & Arslan, M. (2015). Unique expression of 35 KDa protein in serum and cystic fluid of women with malignant ovarian cyst substantiates its role in disease progression. *Asian Pacific Journal of Reproduction*, 4(4), 298-304. <https://doi.org/10.1016/j.apjr.2015.07.007>
- Al-Azri, M., Al-Saidi, M., Eman, A. M., & Panchatcharam, S. M. (2018). Awareness of risk factors, symptoms and time to seek medical help of ovarian cancer amongst Omani women attending teaching hospital in Muscat Governorate, Oman. *Asian Pacific journal of cancer prevention: APJCP*, 19(7), Article 1833. <https://doi.org/10.22034/APJCP.2018.19.7.1833>
- Alway, A., Zamri, N. E., Kasihmuddin, M. S. M., Mansor, A., & Sathasivam, S. (2020). Palm oil trend analysis via logic mining with discrete Hopfield neural network. *Pertanika Journal of Science & Technology*, 28(3), 967-981.
- Agresti, A. (2003). *Categorical data analysis* (Vol. 482). John Wiley & Sons.

- Akkoyun, İ., & Gülen, S. (2012). Laparoscopic cystectomy for the treatment of benign ovarian cyst in children: An analysis of 21 cases. *Journal of Pediatric and Adolescent Gynecology*, 25(6), 364-366. <https://doi.org/10.1016/j.jpjg.2012.06.007>
- Bhaskar, A., Ponnuraja, C., Srinivasan, R., & Padmanaban, S. (2020). Distribution and growth rate of COVID-19 outbreak in Tamil Nadu: A log-linear regression approach. *Indian Journal of Public Health*, 64(6), 188-191. https://doi.org/10.4103/ijph.IJPH_502_20
- Cox, D. R., & Hinkley, D. V. (1979). *Theoretical statistics*. CRC Press.
- Eggertsson, G. B., & Singh, S. R. (2019). Log-linear approximation versus an exact solution at the ZLB in the New Keynesian Model. *Journal of Economic Dynamics and Control*, 105, 21-43. <https://doi.org/10.1016/j.jedc.2018.09.011>
- Farahani, L., & Datta, S. (2016). Benign ovarian cyst. *Obstetrics, Gynaecology & Reproductive Medicine*, 26(9), 271-275. <https://doi.org/10.1016/j.ogrm.2016.06.003>
- Fatin N. S. A., Norlida, M. N., & Siti, Z. M. J. (2020). The application of log-linear model to selected poison patients. *ASM Science Journal*, 13, 1-7. [https://doi.org/10.32802/asmscj.2020.sm26\(1.21\)](https://doi.org/10.32802/asmscj.2020.sm26(1.21))
- Field, A. (2013). *Discovering statistics using IBM SPSS statistics*. SAGE.
- Gameraddin, M. B., & Bashab, N. K. (2018). Characterisation of benign ovarian lesions among Sudanese women undergoing pelvic ultrasound scans: The impact of parity and age. *Journal of Clinical & Diagnostic Research*, 12(5), 6-10. <https://doi.org/10.7860/JCDR/2018/35107.11459>
- Hizkiyahu, R., Yahav, L., Yakovi, S., Davidesko, S., Abecassis, A., & Weintraub, A. Y. (2019). Short-and long-term outcomes of intraoperative spillage during laparoscopic removal of benign ovarian cyst. *Surgical Endoscopy*, 34(9), 3883-3887. <https://doi.org/10.1007/s00464-019-07154-6>
- Huang, C., Hong, M. K., & Ding, D. C. (2017). A review of ovary torsion. *Tzu-chi Medical Journal*, 29(3), 143-147. https://doi.org/10.4103/tcmj.tcmj_55_17
- Jamaludin, S. Z. M., Makhul, A. A., Kasihmuddin, M. S. M., Kustiani, A., Rahim, S. A., & Ismail, M. T. (2020). Modeling symptoms and risk factors towards size of benign ovarian cyst. *Proceedings of The 27th National Symposium On Mathematical Sciences (SKSM27), Malaysia*, 2266(1), Article 090010. <https://doi.org/10.1063/5.0018108>
- Jha, P., Shekhar, M., Goldstein, R., Morgan, T., & Poder, L. (2019). Size threshold for follow-up of postmenopausal adnexal cyst: 1 cm versus 3 cm. *Abdominal Radiology*, 45, 3213-3217. <https://doi.org/10.1007/s00261-019-02176-z>
- Kasihmuddin, M. S. M., Mansor, M., Basir, M. F. M., & Sathasivam, S. (2019). Discrete mutation Hopfield neural network in propositional satisfiability. *Mathematics*, 7(11), Article 1133. <https://doi.org/10.3390/math7111133>
- Mandai, M., Suzuki, A., Matsumura, N., Baba, T., Yamaguchi, K., Hamanishi, J., Yoshioka, Y., Kosaka, K., & Konishi, I. (2012). Clinical management of ovarian endometriotic cyst (chocolate cyst): Diagnosis, medical treatment, and minimally invasive surgery. *Current Obstetrics and Gynecology Reports*, 1(1), 16-24. <https://doi.org/10.1007/s13669-011-0002-3>

- McCullagh, P., & Nelder, J. A. (1989). Binary data. In *Generalized linear models* (pp. 98-148). Springer. <http://dx.doi.org/10.1007/978-1-4899-3242-6>
- Medeiros, L. R., Rosa, D. D., Bozzetti, M. C., Fachel, J. M., Furness, S., Garry, R., Rosa, M. I., & Stein, A. T. (2009). *Laparoscopy versus laparotomy for benign ovarian tumour*. John Wiley & Sons, Ltd. <https://doi.org/10.1002/14651858.CD004751.pub3>
- Milewska, A. J., Citko, D., Jankowska, D., Milewski, R., Konończuk, K., Więsak, T., Morgan, A., & Milewski, R. (2018). The use of log-linear analysis for pregnancy prediction. *Studies in Logic, Grammar and Rhetoric*, 56(1), 7-18. <https://doi.org/10.2478/slgr-2018-0037>
- Mohamed, A. A., Al-Hussaini, T. K., Fathalla, M. M., El Shamy, T. T., Abdelaal, I. I., & Amer, S. A. (2016). The impact of excision of benign nonendometriotic ovarian cyst on ovarian reserve: A systematic review. *American journal of obstetrics and gynecology*, 215(2), 169-176. <https://doi.org/10.1016/j.ajog.2016.03.045>
- Mukhopadhyay, A., Shinde, A., & Naik, R. (2016). Ovarian cyst and cancer in pregnancy. *Best Practice & Research Clinical Obstetrics & Gynaecology*, 33, 58-72. <https://doi.org/10.1016/j.bpobgyn.2015.10.015>
- Rofe, G., Auslender, R., & Dirnfeld, M. (2013). Benign ovarian cyst in reproductive-age women undergoing assisted reproductive technology treatment. *Open Journal of Obstetrics and Gynecology*, 3(7A), Article 36929. <https://doi.org/10.4236/ojog.2013.37A1005>
- Sanersak, S., Wattanakumtornkul, S., & Korsakul, C. (2006). Comparison of low-dose monophasic oral contraceptive pills and expectant management in treatment of functional ovarian cyst. *Journal-Medical Association of Thailand*, 89(6), 741-747.
- Shiota, M., Kotani, Y., Umemoto, M., Tobiume, T., & Hoshiai, H. (2012). Study of the correlation between tumor size and cyst rupture in laparotomy and laparoscopy for benign ovarian tumor: Is 10 cm the limit for laparoscopy? *Journal of Obstetrics and Gynaecology Research*, 38(3), 531-534. <https://doi.org/10.1111/j.1447-0756.2011.01748.x>
- Telli, E., Oge, T., Ozalp, S. S., & Yalcin, O. T. (2013). Giant peritoneal inclusion cyst mimicking ovarian cyst. *Asian Pacific Journal of Reproduction*, 2(4), 333-334. [https://doi.org/10.1016/S2305-0500\(13\)60174-8](https://doi.org/10.1016/S2305-0500(13)60174-8)
- Törner, A., Stokkeland, K., Svensson, Å., Dickman, P. W., Hultcrantz, R., Montgomery, S., & Duberg, A. S. (2017). The underreporting of hepatocellular carcinoma to the cancer register and a log-linear model to estimate a more correct incidence. *Hepatology*, 65(3), 885-892. <https://doi.org/10.1002/hep.28775>
- Udomsinklul, P., Triratanachart, S., & Oranratanaphan, S. (2020). Risk factors for endometriotic-cyst associated ovarian cancer: A case controlled study. *Taiwanese Journal of Obstetrics and Gynecology*, 59(2), 269-274. <https://doi.org/10.1016/j.tjog.2020.01.016>
- Vilsen, S. B., Kaer, S. K., & Stroe, D. L. (2019). Predicting Lithium-ion battery resistance degradation using a log-linear model. In *2019 IEEE Energy Conversion Congress and Exposition (ECCE)* (pp. 1136-1143). IEEE Conference Publication. <https://doi.org/10.1109/ECCE.2019.8912770>
- Wiedermann, W., & von Eye, A. (2020). Log-linear models to evaluate direction of effect in binary variables. *Statistical Papers*, 61(1), 317-346. <https://doi.org/10.1007/s00362-017-0936-2>

- Wu, M. P., Wu, C. J., Long, C. Y., Ho, C. H., Huang, K. H., Chu, C. C., & Chou, C. Y. (2013). Surgical trends for benign ovarian tumors among hospitals of different accreditation levels: An 11-year nationwide population-based descriptive study in Taiwan. *Taiwanese Journal of Obstetrics and Gynecology*, *52*(4), 498-504. <https://doi.org/10.1016/j.tjog.2013.10.008>
- Zamri, N. E., Mansor, M., Kasihmuddin, M. S. M., Alway, A., Jamaludin, S. Z. M., & Alzaemi, S. A. (2020). Amazon employees resources access data extraction via clonal selection algorithm and logic mining approach. *Entropy*, *22*(6), Article 596. <https://doi.org/10.3390/e22060596>
- Zhu, B., Walter, S. D., Rosenbaum, P. L., Russell, D. J., & Raina, P. (2006). Structural equation and log-linear modeling: a comparison of methods in the analysis of a study on caregivers' health. *BMC Medical Research Methodology*, *6*(1), 1-14. <https://doi.org/10.1186/1471-2288-6-49>
- Zhu, D., Chung, H. F., Dobson, A. J., Pandeya, N., Giles, G. G., Bruinsma, F., Brunner, E., Kuh, D., Hardy, R., Avis, N. E., Gold, E. B., Derby, C. A., Matthews, K. A., Cade, J. E., Greenwood, D. C., Demakakos, P., Brown, D. E., Sievert, L. L., Anderson, D., ... & Mishra, G. D. (2019). Age at natural menopause and risk of incident cardiovascular disease: A pooled analysis of individual patient data. *The Lancet Public Health*, *4*(11), e553-e564. [https://doi.org/10.1016/S2468-2667\(19\)30155-0](https://doi.org/10.1016/S2468-2667(19)30155-0)

***In silico* Study of Potential Non-oxime Reactivator for Sarin-inhibited Human Acetylcholinesterase**

Rauda A. Mohamed^{1,2}, Keat Khim Ong^{2,4}, Norhana Abdul Halim³, Noor Azilah Mohd Kasim^{2,4}, Siti Aminah Mohd Noor^{2,3}, Victor Feizal Knight², Rabbani Muhamad¹ and Wan Md Zin Wan Yunus^{1,2*}

¹Centre for Tropicalization, National Defence University of Malaysia, Kuala Lumpur, 57000, Malaysia

²Centre for Chemical Defense, National Defence University of Malaysia, Kuala Lumpur, 57000, Malaysia

³Centre for Defence Foundation Studies, National Defence University of Malaysia, Kuala Lumpur, 57000, Malaysia

⁴Faculty of Defence Science and Technology, National Defence University of Malaysia, Kuala Lumpur, 57000, Malaysia

ABSTRACT

The search for new compounds other than oxime as potential reactivator that is effective upon organophosphate poisoning treatments is desired. The less efficacy of oxime treatment has been the core factor. Fourteen compounds have been screened via *in silico* approach for their potential as sarin-inhibited human acetylcholinesterase poisoning antidotes. The selection of the compounds to be synthesized based on this computational screening,

reduces the time and cost needed. To perform the docking study of sarin-inhibited acetylcholinesterase and reactivator-sarin inhibited acetylcholinesterase complexations, a bioinformatics tool was used. Estimation of the nucleophilic attack distance and binding energy of fourteen potential compounds with sarin inhibited acetylcholinesterase complexes to determine their antidote capacities was carried out using Autodock. A commercially available antidote, 2-PAM was used for the comparison. The best docked-pose was further examined with molecular dynamics

ARTICLE INFO

Article history:

Received: 18 December 2020

Accepted: 24 February 2021

Published: 19 July 2021

DOI: <https://doi.org/10.47836/pjst.29.3.19>

E-mail addresses:

raudamohamed@gmail.com (Rauda A. Mohamed)

ongkhim@upnm.edu.my (Keat Khim Ong)

norhana@upnm.edu.my (Norhana Abdul Halim)

azilah@upnm.edu.my (Noor Azilah Mohd Kasim)

aminah@upnm.edu.my (Siti Aminah Mohd Noor)

victor.feizal@upnm.edu.my (Victor Feizal Knight)

rabbani_muhamad@yahoo.com (Rabbani Muhamad)

wanmdzin@upnm.edu.my (Wan Md Zin Wan Yunus)

*Corresponding author

simulation. Apart from being lipophilic, a compound with a carboxylic acid, (*R*)-Boc-nipecotoc acid is shown to exhibit 6.29 kcal/mol binding energy with 8.778 Å distance of nucleophilic attack. The stability and flexibility of the sarin-inhibited acetylcholinesterase, complexed with (*R*)-Boc-nipecotoc acid suggests this compound should be tested experimentally as a new, promising antidote for sarin-inhibited acetylcholinesterase poisoning.

Keywords: Antidote, docking, *in silico*, inhibition, organophosphate, oxime, reactivator, simulation

INTRODUCTION

Acetylcholinesterase (AChE) is a serine hydrolase which hydrolyzes acetylcholine. Acetylcholine exhibits neurotransmitter functions to transfer signals from the nerve to the muscle cell. It is located at the synaptic cleft and the hydrolysis products of this reaction are choline and acetic acid. The accumulation of acetylcholine causes continuity of signaling and leads to neurotoxicity, which results in muscle paralysis, seizures and finally, death. Organophosphorus (OP) is one of the inhibitors that inhibit the hydrolysis of acetylcholine from occurring, thus resulting in the accumulation of acetylcholine. OP poisonings usually happen either from dietary, household erroneous handling, accidental or/and occupational exposure and these incidents are increasing (Baker, 1990). Apart from that, the use of OP as chemical weapons is also alarming, such as the assassination of Kim Jong-Nam in Malaysian airport.

The binding site of AChE acts as a charge relay system and consists of three distinct residues which are Ser203, Glu334 and His447. AChE comprises two dissimilar pockets in the binding site domain which are esteric site and anionic site. Fourteen conserved aromatic amino acids are lined along with these domains (Ranjan et al., 2015). An OP toxicity effect on the central nervous system is initiated through the non-reversible phosphorylation of esterase when it interacts with Ser203 in the AChE molecule. Ser203 together with Trp86 are the critical residues in inactivation and act to guard the inhibitor on the bottleneck of the binding gorge (Patil et al., 2018). OP is substrate analogue to acetylcholine and hence, a similar route is used to enter the active site of AChE and covalently bind to –OH group of Ser203 for the inhibition mechanism. The hydroxy moiety of Ser203 attacks the phosphoryl group and caused the leaving group of the OP to leave (Namba et al., 1971).

Dephosphorylation of AChE can be carried out by a highly nucleophilic atom. The mechanism of action is based on the nucleophilic attack of the nucleophile towards the phosphorus atom of the phosphorylated organophosphate-AChE (Figure 1) (Matos et al, 2011). Among this highly nucleophilic atom, oximes were found in the literature as the best reactivator for OP-AChE poisoning. For years, HI6 and 2-PAM have been the leading

oximes due to their competency to reactivate OP-inhibited AChE (Ajami & Rebek, 2013; Mercey et al., 2012a; Kuca et al., 2013). However, there are limitations of these oximes due to their quaternary nitrogen charge, which lead to the inefficiency to penetrate the blood-brain barrier (de Souza et al., 2020; Radic et al., 2013; Radic et al., 2012; Sit et al., 2011; Kovarik et al., 2013; Tang et al., 2013). Subsequently, several attempts have been performed to find potential non-ionic oximes.

There were reported studies on the designation and synthesis of non-ionic oxime reactivators which successfully enhanced brain permeability (Mercey et al., 2012b; de Koning et al., 2011). Unfortunately, most of the compounds were hard to synthesis due to their complex structure especially in large quantities which is crucial for *in vivo* evaluation. Furthermore, the non-charge oximes reduce the reactivity function of the oxime and muddling in the design process of effective oxime-based reactivators. Hence, the finding of a new antidote should be expanding towards the non-oxime group. Katz et al. (2015) has discovered compounds from large bioactive libraries and approved drugs as a potential antidote as tested by *in vitro* screening. None of these reported potential compounds possessed the oxime structural motive. Bhattacharjee et al. (2015) claimed that the active compounds possess a slight structural resemblance, while Katz et al. (2018) reported the screening compounds to have common structural features such as basic moieties (pyridine, imidazole and piperazine) or Mannich phenol (*i.e.*, phenols representing a benzylic amine in the α -position). Specifically, 4-Amino-2((diethylamino)methyl)phenol (ADOC) shows promising potential to reactivate paraoxon-ethyl (PXE) and DIFP-inhibited AChE (Katz et al., 2018).

Our study aims to screen the interaction of charged and uncharged nitrogen from a different group of compounds towards sarin-inhibited AChE. This present study also utilized MD simulation (MDS) to reveal the interactions of the different subdomains of the AChE's active site towards the compound. These compounds have never been investigated as potential reactivators.

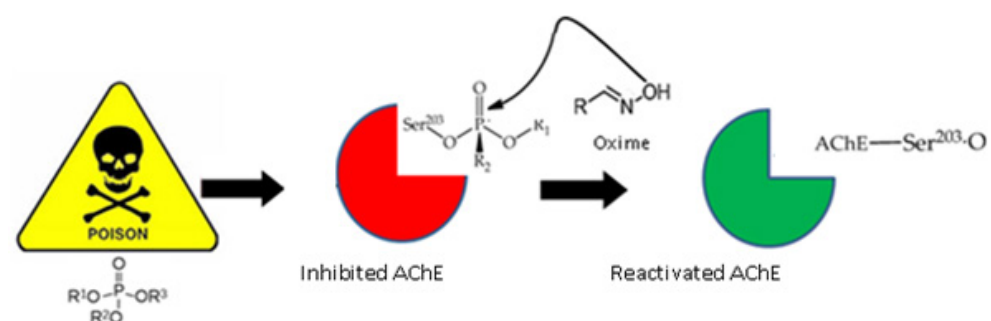


Figure 1. Reactivation mechanism of oxime towards OP inhibited-AChE

MATERIALS AND METHODS

A 3D model structure of human AChE (*hAChE*) in apo form and a complex structure of sarin-inhibited *hAChE* were downloaded from the RCSB-Protein Data Bank under the code 4EY4 and 5FPQ respectively. The X-ray diffractions of the 3D structure for both proteins have a resolution of around 2.16-2.40 Å. Structural files of sarin and reactivators were obtained from the PubChem library (<https://pubchem.ncbi.nlm.nih.gov/>) (Kim et al., 2016). The docking process was carried out by AutoDock 4.2.5.1 (Morris et al., 1998) tool with some modification on the commands to suits covalent bonding. Both docking and MD simulation were performed and analyzed using YASARA software version 12.5.7 (YASARA Biosciences GmbH, Austria) (Krieger et al., 2002).

Docking Studies

Validation of the Autodock 4.2.5.1 Tool to Perform Covalent Docking. The preparation of apo-formed *hAChE* (4EY4) structure prior to docking involved the removal of chain B, crystal associated heteroatoms and water molecules. To perform covalent docking, serine-sarin adduct has to be flexible by editing the command on dockrun_mcr (flexres: Ser 203). This is followed by energy minimization for both the receptor and ligand. The entire residue Ser 203 and ligand were selected before the files were separately saved as a .job file by clicking 'Edit > Select'. The other parameters (the simulation cell was placed around the active sites to target docking at the most important region and the pH-dependent bond orders and hydrogen atoms) were automatically set. Docking analysis using Autodock was performed (Kryger et al., 2000). Both the complex docked-structure of sarin-inhibited *hAChE* and the deposited crystal structure of sarin-inhibited *hAChE* (5FPQ) were superposed using MUSTANG algorithm (Konagurthu et al., 2006) alignment to validate the docking protocol. In order to further compare the interactions of the docked-sarin AChE with the literature from the crystal structure of sarin-inhibited *hAChE*, important intramolecular interactions were highlighted as well.

Docking of Reactivators towards Sarin-inhibited *hAChE*. The 3D deposited crystal structure of sarin-inhibited *hAChE* was further modified by removing crystal associated heteroatoms and water molecules. As mention previously, in order to perform covalent docking, serine-sarin adduct has to be flexible by editing the command on dockrun_mcr (flexres: SGB 203). This is followed by energy minimization for both the receptor and ligand. The entire residue Ser 203 and ligand were selected before the files were separately saved as a .job file by clicking 'Edit > Select'. Docking analysis using Autodock was performed for the *hAChE* complex structure with these selected compounds: salicylamidoxime, hydroxybenzohydrazide, 6-hydroxypicolinohydrazide, pyridine-2-carbohydrazide, picolinohydroxamic acid, 3-pyridinecarbohydroxamic acid, 2-acetylpyridine, pyrimidine,

acetic acid, salicylic acid, pidolic acid, boc-nipeptic acid and indole butyric acid with 2-PAM as a commercial antidote to screen for the potential reactivators. The structure of sarin and the screened compounds (Figure 2), which have been retrieved from (<https://pubchem.ncbi.nlm.nih.gov/>) represent various functional groups with cationic or uncharged properties such as oxime, hydrazide, pyridine, pyrimidine, carboxylic acid and hydroxamic acid.

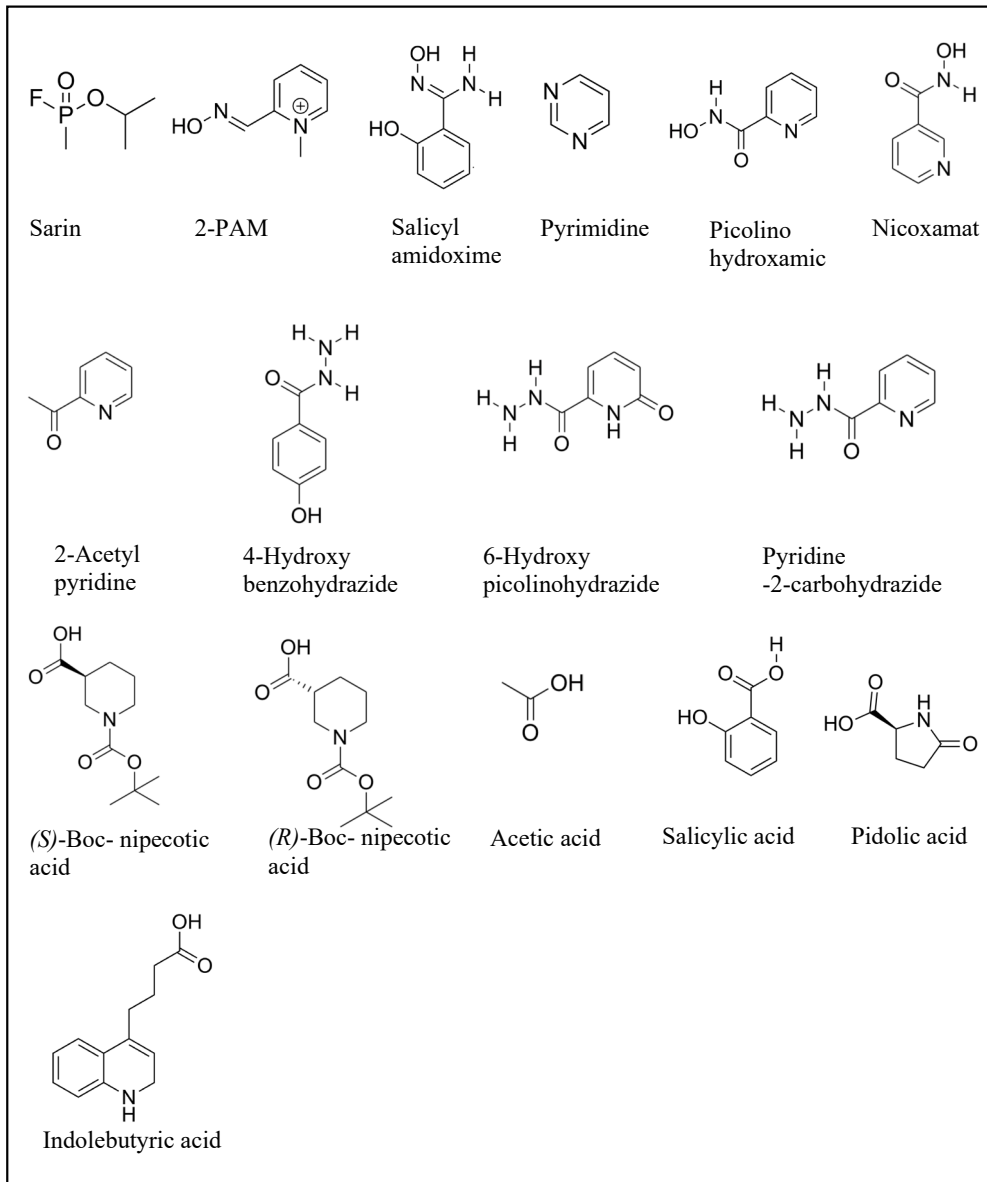


Figure 2. The structures of sarin and the screened compounds for sarin-inhibited hAChE reactivation

The binding energy of the sarin-inhibited *hAChE* complex with the compounds was estimated and compared. The binding energy is obtained by calculating the energy at the infinite distance between the selected object and the rest of the simulation system (the unbound state) and subtracting the energy of the simulation system (the bound state) (Chen et al., 2015). The reactivators, which have higher binding energy with the sarin-inhibited *hAChE* complex, were selected as potential antidotes. In some other docking programs, binding energy with negative value represents better binding, for example, AutoDock. This is because these programs do not report 'binding energies' but the energy required to disassemble a compound into separate components which usually positive.

LogP Calculation to Predict the Selected Compounds Lipophilicity

For compounds with good binding and reactivation potential (based on their nucleophilic attack distance), LogP determination was carried out using Molinspiration (<http://www.molinspiration.com/cgi-bin/properties>) to determine their lipophilicity.

Molecular Dynamics Simulation (MDS)

Simulation of molecular dynamics was performed for the sarin-inhibited *hAChE* and sarin-inhibited *hAChE* complex with the selected potential reactivator. The pose with high energy value and shorter distances O-P was selected. The simulation protocol started with the covalent geometry corrected and the unwanted water molecules were removed. Optimization of the hydrogen-bond network, and thereafter a cubic simulation cell was created in the periodic boundary state, where the protein of each complex was parameterized by the force field of AMBER03 (Duan et al., 2003). The pH of the system was maintained at 7.4 to mimic the physiological conditions. MDS has been performed for 20 ns and the resulting trajectories were studied for different analyses. This final system setup was used for the production run and simulation snapshot coordinates were saved every 30 ps.

Analysis of MDS Trajectories

The analyses of the trajectories were performed from replicates of three different simulations run at different initial velocities. All the MDS results were characterized using a preinstalled macro within the YASARA suite including total energy, Root Mean Square Deviation (RMSD), Root Mean Square Fluctuations (RMSF) and Solvent Accessible Surface Area (SASA). RMSD value is the average distance between the atoms estimation during simulation, which suggests structural changes (Ishak et al., 2017). The local variations as well as the residue movement differences could be computed by the RMSF. Both RMSD and RMSF calculate the stability and flexibility of a residue in the enzyme-complex at a given simulated time. Besides, the quality of the complex structure could also determine by the RMSD value (Bagaria et al., 2012). SASA represents the accessibility surface area

of a biomolecule towards solvent. All visual structure analysis and figure design were performed using YASARA and POVray (<http://www.povray.org>) (Krieger & Vriend, 2014).

RESULTS AND DISCUSSION

Validation of the Autodock 4.2.5.1 Tool to Perform Covalent Docking

The molecular surface of sarin-docked *hAChE* is shown in Figure 3. Superposition of sarin-docked-*hAChE* with the deposited crystal structure of sarin-inhibited *hAChE* (Figure 4) presented 0.3 Å RMSD value is with 99.81% sequence identity. The residues of the active sites were fully conserved. These two structures show low variation positions to validate the docking protocol used since the RMSD value falls in the acceptable range of below 1 Å. This validation is important to support the reliability of the output for reactivators docked-inhibited AChE study. Several important interactions of the docked-sarin AChE were in agreement with the reported literature on the crystal structure of sarin-inhibited *hAChE*. Thus, these important intramolecular interactions were highlighted in detail as well.

When the sarin molecule enters into the active sites gorge of the AChE, the sarin-inhibited *hAChE* complex is formed. The aromatic hydrophobic residues lining along the gorge, as shown by Asp74, helps to orient the sarin molecule into the active sites in a

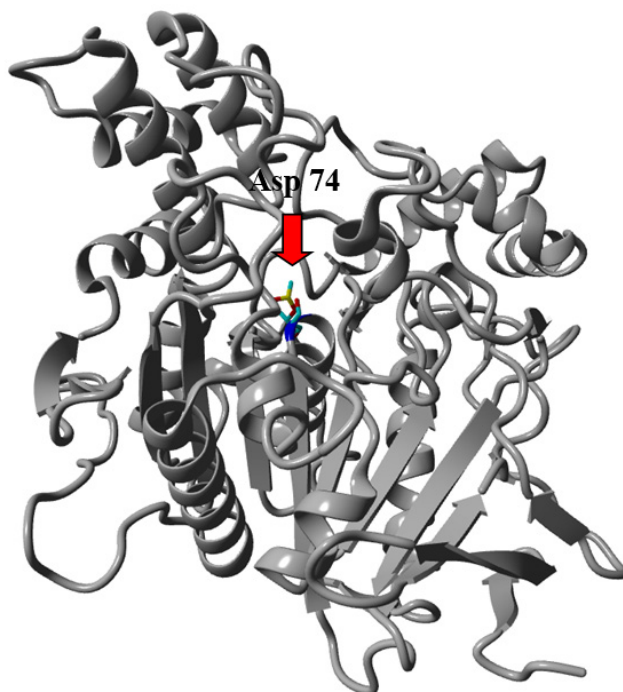


Figure 3. Molecular surface of sarin-docked inhibited *hAChE*. The red arrow shows the gorge entrance of the binding pocket. Sarin (multicolor) is attracted to the binding pocket by the interaction of polar hydrophobic residues around the gorge entrance

reactive position (Wlodek et al., 2000). *hAChE* residue in the catalytic triad, Ser203, will attack the phosphoryl group from sarin. This nucleophilic attack involves the oxygen atom of Ser203 (Qiao et al., 2014). The bond between phosphorus and fluorine becomes weaker as the partial bond forms between the oxygen in serine and the phosphorus in sarin. This molecular configuration is known as a pentacoordinate intermediate. Fluorine acts as a leaving group once the bond between the serine and sarin is fully formed. The ability of the AChE to hydrolyze acetylcholine is entirely disabled because of the stability of the sarin adduct. Table 1 presents the distance, interaction and binding energy of sarin-inhibited AChE. These output values are given by the YASARA integrated Autodock scoring function. The binding energy of sarin towards *hAChE* with stated contacting residues was calculated as 3.63 kcal/mol.

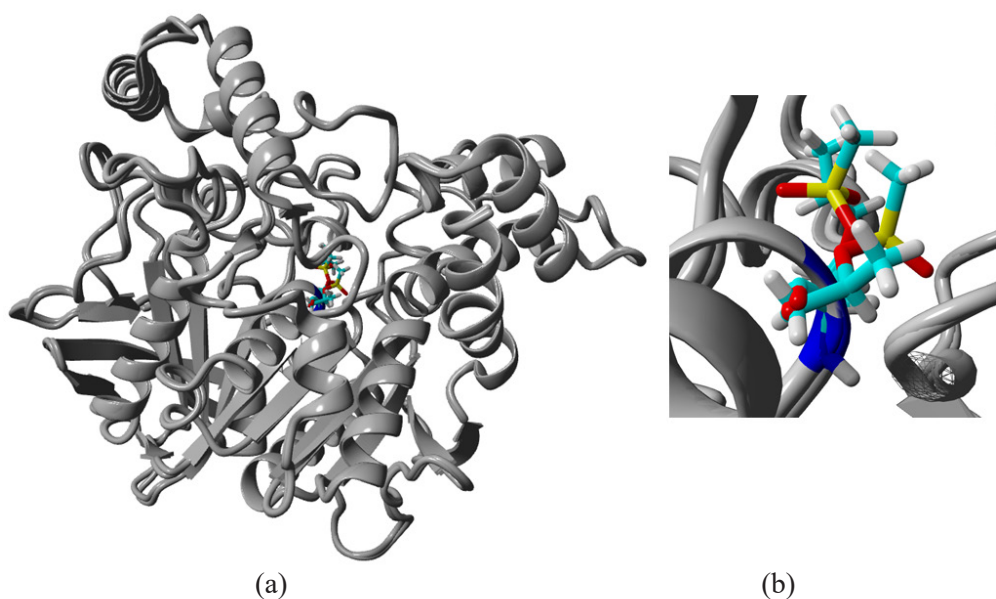


Figure 4. (a) Superposition of sarin-inhibited *hAChE* with the deposited crystal structure of sarin-inhibited *hAChE*, (b) a zoomed-in figure of the superposition, multicolor denotes sarin

Sarin is categorized as a classical nerve agent in which its structure, bearing a dimethoxy or diethoxy group attached to a phosphorylated AChE consequence in a complex that can be easily reactivated (Lotti, 2010). This fact supports the low binding energy value of sarin towards *hAChE*. Ser203, Gly121 and Gly122 are the AChE residues that create a hydrogen bond towards sarin with a distance of approximately 1.03-2.04 Å. Residues involved in the sarin-inhibited *hAChE* complex are shown in Figure 5. Gly121 and 122 form hydrogen bonds with the oxygen from the sarin molecule (shown by the yellow dotted line). Ser203,

Table 1

Distance, interaction and binding energy of sarin-inhibited hAChE

Distance O-P (Å)	H-bond interactions	Binding energy (kcal/mol)	Peripheral site interactions
0.98	Ser203, Gly121, Gly122	3.63	Gly122, Glu202, Ser203, Ala204, Gly205, Ala206, Ala207, Gln228, Ser229, Gly230, Ala231, Trp236, Phe295, Phe297, Phe338, Val407, His447.

Glu334 and His447 are the active site's residues for the catalytic machinery of *hAChE*. The nucleophilic oxygen from Ser203 attacks the phosphoryl group of sarin, forming the bonding with a distance of 3.206 Å, which is a new forming bond between Ser203 and sarin. Trp86 interacts with sarin for the maximum π -cation interaction on the anionic subsite of the AChE apart from Ser203 (Patil et al., 2018). This residue is also reported to guard the inhibitor at the bottleneck on the binding gorge. The role of Trp86, Tyr124 and Ser203 is to hold sarin in its binding cavity (Zhang et al., 2016; Abou-Donia et al., 2016). Intramolecular π - π interaction of Phe297 with other *hAChE* residues is also detected, whereby this interaction is significant in terms of most of the OP-AChE interaction. The sarin AChE complex is stabilized by hydrophobic interactions.

Docking Study of the Selected Compounds towards Sarin-inhibited *hAChE*

The AChE has two important sites for the reactivation to occur, known as the PAS and the esteric site. These residues, Trp86, Tyr124, Phe297, Tyr337 and Tyr341, are the major contributors for the hydrophobic interaction and ligand stabilization in the peripheral site area (de Almeida et al., 2016). Table 2 presents the distance, interaction and binding energy of the reactivators towards sarin-inhibited AChE compared to commercially available 2-PAM. These values were calculated by the YASARA integrated Autodock scoring function. Larger molecules give higher binding energy despite their compound charge, which highly due to the H-bonds formed with the amino acids and their interaction energies (Schaeffer, 2008). (*R*)-Boc-nipecotinic acid is among the compound with a larger structure and exhibits high binding energy (6.29 kcal/mol) with the shortest nucleophilic O—P distance.

The detailed interaction of this compound is further discussed below. Another factor that contributes to the binding energy value, is the charged or uncharged oxime group which affects its affinity for the complex *hAChE*/sarin (Colovic et al., 2013). The binding energy of salicylamidoxime is lower as compared to 2-PAM. This might occur due to the charged quaternary group of the oxime interacts with the anionic center of AChE (Musilek et al., 2007). For non-oxime reactivator, which has been reported by Cadieux et al. (2016),

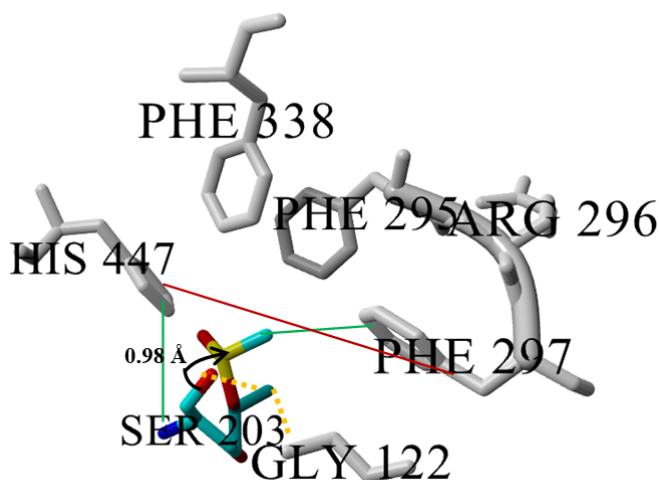


Figure 5. Residues involved in the sarin-inhibited *hAChE* complex interactions. Multicolored represents sarin, while gray color denotes *hAChE*. The arrow represents the nucleophilic attack distance from Ser203 towards the phosphorus atom of sarin, the yellow dotted line represents hydrogen bonding while red and green lines denote π - π and hydrophobic interactions, respectively

the alkylation or acylation of the amine (aniline) affects binding affinity, whereby the para position of the amine concerning the hydroxyl group is preferred. The presence or position of the hydroxyl group is also crucial for reactivation (Cadieux et al., 2016). Additionally, the existence or position of another amine (benzylic amine) highly influences the binding affinity compared to reactivation. Compounds under the hydrazide group display moderate binding energies with shorter nucleophilic distances except for pyridine-2-carbohydrazide which has a longer distance towards O-P. This is due to the absence of the hydroxyl group (strong nucleophile) in its benzene ring.

Hydroxamic acid group consists of two compounds that only differs at their N position; meta and ortho have a distinct nucleophilic distance with slightly higher binding energy recorded for nicoxamat with ortho position. The substituent position does affecting the reactivation activity due to electron cloud distribution (de Koning et al., 2018; Bregente & Yunes, 1997). Interestingly, compounds in carboxylic acids show high binding energy especially for (*R*)-Boc-nipecotic acid, (*S*)-Boc-nipecotic acid and indolebutyric acid due to the presence of the amine group in their benzene ring. Both Boc-nipecotic acid have amine and hydroxyl group in the para position which is favored, the binding energy and nucleophilic attack distance values are promising (Cadieux et al., 2016). (*R*) isomer shows a slightly lower binding energy value compared to the (*S*) isomer which might due to the further position of this isomer towards the anionic subsite. This subsite is responsible for the binding of the reactivator to steer towards AChE's active site. Nevertheless, the (*R*)

Table 2

Distance, interaction and binding energy of the reactivators towards sarin-inhibited hAChE compared to commercially available 2-PAM

Reactivators	Distance O ... OP (Å)	H-bond interactions	Binding energy (kcal/ mol)	Peripheral site interactions
4-hydroxybenzohydrazide	4.346	Tyr124, Arg296	5.93	Tyr72, Asp74, Tyr124, Trp286, Tyr341
2-acetylpyridine	9.800	Tyr124, Arg296	4.21	Tyr124, Trp286, Tyr341
Salicylamidoxime	15.95	Tyr124, Arg296	5.54	Trp86, Gly120 Gly121, Tyr124, Ser203, His447, Gly448
2-PAM	7.426	Tyr124, Arg296	6.69	Trp86, Gly120, Gly121, Ser203 Tyr337, His447, Gly448
Salicylic acid	8.825	Tyr124, Arg296	5.13	Trp86, Gly120, Gly121, Ser203, Tyr337, His447, Gly448
6-hydroxypicolinohydrazide	6.868	Tyr124, Arg296	5.51	Trp86, Gly120, Gly121, Tyr124, Ser203, Tyr337, His447, Gly448
Acetic acid	21.133	-	3.95	-
(R)Boc-nipecotnic acid	8.778	Phe295, Tyr341	6.29	Tyr124, SGB203 Trp286, Leu289, Arg296, Phe297, Tyr337, Phe338, Tyr341
(S)Boc-nipecotnic acid	10.958	Tyr124, Arg296	6.91	Tyr72, Tyr124, Trp286, Tyr337, Tyr341
Nicoxamat	9.748	Tyr 124, Arg296	5.21	Tyr72, Tyr124, Ser203, Trp286, Phe338, Tyr341

Table 2 (Continued)

Reactivators	Distance O...OP (Å)	H-bond interactions	Binding energy (kcal/ mol)	Peripheral site interactions
Indolebutyric acid	15.837	Tyr124, Arg296	5.98	Tyr72, Asp74, Gly121, Gly122, Tyr124 Ser203, Trp286, Tyr337, Phe338, Tyr341
Picolinohydroxamic acid	15.002	Tyr124, Arg296	4.92	Trp86, Gly120, Gly121, Ser203, Tyr337, His447, Gly448
Pidolic acid	9.950	Tyr124, Arg296	4.51	Tyr124, Trp286, Tyr341
Pyridine-2-carbohydrazide	19.422	Tyr124, Arg296	4.84	Trp86, Gly120, Gly121, Gly122, Tyr124, Ser203, Tyr337, His447, Gly448
Pyrimidine	9.856	Arg296	2.58	Trp286, Tyr341

and (*S*) configuration of this compound seems to highly affect the nucleophilic distance which shows the nucleophile from (*R*) position directing towards the OP.

Indolebutyric acid which has a hydroxyl group located far from its benzene ring, shows a longer nucleophilic distance. Salicylic acid shows lower binding energy and shorter nucleophilic distance because of the absence of the N atom and the presence of the hydroxyl group respectively. Pidolic and acetic acid, which have no benzene ring, recorded low binding energy. Both pyridine and pyrimidine show lower binding energies, although they exhibit an amine group, which might due to the smaller size of the structures. Based on the nucleophilic attack distances of all the tested compounds, 4-hydroxybenzohydrazide, 6-hydroxypicolinohydrazide and (*R*)-Boc-nipecotic acid show higher reactivation potential. Nevertheless, since lipophilicity is another important factor to be considered, Log*P* values for 4-hydroxybenzohydrazide, 6-hydroxypicolinohydrazide and (*R*)-Boc-nipecotic acid were recorded as -0.16, -1.19 and 1.40 respectively. This explains our preference towards (*R*)-Boc-nipecotic acid. Molecular surface view of the docking of (*R*)-Boc-nipecotic acid towards sarin-inhibited *h*AChE is shown in Figure 6. Asp74 appears at the gorge entrance which helps to steer the molecule into the active sites in the reactive orientation. Asp74

which is located at the PAS of human AChE is recorded as the first step in the catalytic pathway and affects the binding energy (Mallender et al., 2000).

Some experimental results highlight this finding, whereby the quaternary nitrogen or the charge oxime is crucial for the affinity towards the OP/AChE complex (Shafferman et al., 1992; Barak et al., 1994; Mallender et al., 2000; Ordentlich et al., 2004; Johnson & Moore, 2006; Artursson et al., 2009). de Souza et al. (2020) described that based on the binding energies of 2-PAM and HI-6 towards AChE-OP, a higher affinity of HI-6 towards the AChE-OP complex is seen. This highlights the contribution of the two quaternary N atoms in electrostatic effects which granted twice more affinity compared to 2-PAM. Meanwhile, in this study, binding energies of 2-PAM and (*R*)-Boc-nipepotic acid towards sarin-inhibited *h*AChE showed a small difference in their binding energies values since both tested reactivators have only one N atom in their structure.

In order to reactivate the AChE-OP complex, a reactivator should exhibit good affinity and reactivity. Good affinity derived from these physicochemical features such as; electrostatic effects, hydrophobic interactions and steric compatibility, while reactivity derived from the nucleophilicity of the oxime or non-oxime moiety (de Souza et al., 2020). Hence, the structure and the position of the reactivator also affect the reactivation potential. (*R*)-Boc-nipepotic acid is seen to interact with PAS residues (Tyr124, Trp286, Phe297, Tyr337 and Tyr341) from the *h*AChE. These residues are essential in the binding of the reactivators, thus exposing them to the anionic subsite where electrostatic interaction occurs. Figure 7 shows the hydrogen bonding of Phe295 and Tyr341 towards (*R*)-Boc-nipepotic acid. The distance is around 2.08-2.12 Å. Nucleophilic attack of the hydroxyl group from (*R*)-Boc-nipepotic acid towards the sarin-inhibited *h*AChE complex occurs with a distance of 8.778 Å (Figure 8).

Hence, the sarin adduct from the oxygen of the active site serine is removed and reactivate the *h*AChE. The affinity for the whole system increases when the affinity between the reactivators and the P-site area increases, and causes stabilization (de Almeida et al., 2016).

Figure 9 shows the interaction of OH from Tyr124 at the anionic site with nitrogen from (*R*)-Boc-nipepotic acid with a distance of 3.603 Å (electrostatic interaction). Aromatic rings of Tyr124 flank the indole group of Trp286 and together they interact with charged groups of ligand (Johnson & Moore, 2006). Moreover, the indole ring of Trp286 can make different interaction modes towards the ligand, such as aromatic-aromatic, stacking and π -cation depending on the nature of the ligand. Hydrophobic interactions of *h*AChE residues towards (*R*)-Boc-nipepotic acid is also detected for complex stabilization. Apart from these interactions, (*R*)-Boc-nipepotic acid might also introduce as a carboxylic acid moiety source, which can be attached to various oximes that have been successfully proven as a potential antidote. A study carried out by de Koning et al. (2017), which reported the

insertion of various linker lengths of carboxylic acid to the pyridinium and imidazole oximes, has successfully reactivated sarin-inhibited AChE.

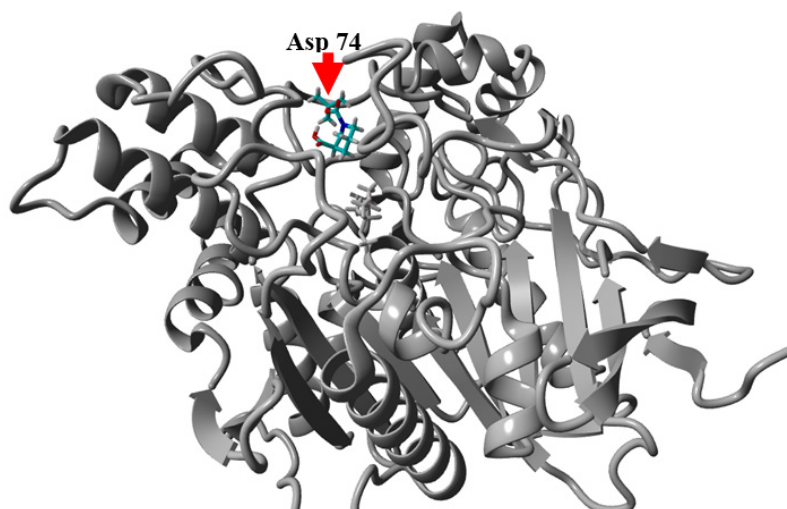


Figure 6. Docking of (R)-Boc-nipecotic acid towards sarin-inhibited hAChE. The red arrow shows the gorge entrance of the binding pocket. Multicolor represents (R)-Boc-nipecotic acid and gray represents inhibited hAChE

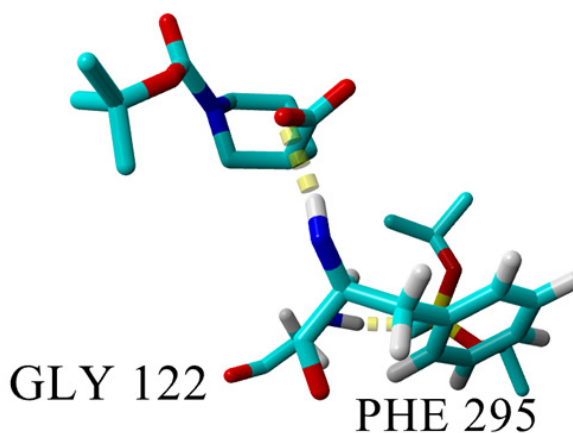


Figure 7. Hydrogen bonding of Phe295 and Tyr341 towards (R)-Boc-nipecotic acid (indicated by the yellow dotted line)

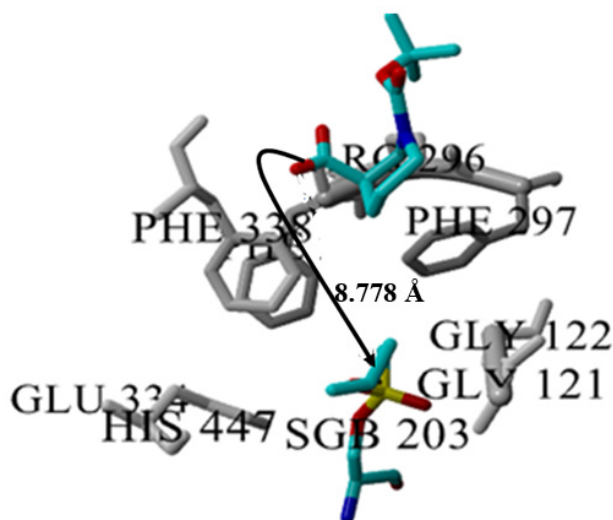


Figure 8. Nucleophilic attack of OH from (*R*)-Boc-nipepic acid towards phosphorus atom (from sarin- Ser203 adduct). The bonding distance is 8.778 Å

MDS Analysis of *hAChE*-sarin and *hAChE*-sarin/(*R*)-Boc-nipepic Acid

The best pose for *hAChE*-sarin/(*R*)-Boc-nipepic acid complex was further investigated by MDS. The energy plot for the complex *hAChE*-sarin with and without reactivator (*R*)-Boc-nipepic acid during 20 ns of MDS is presented in Figure 10. The results indicated that both *hAChE*-sarin and *hAChE*-sarin/(*R*)-Boc-nipepic acid docking complexes showed initial energy around -1.390000×10^6 kJ/mol, fluctuated up to 1.35 ns and afterward the complex *hAChE*-sarin/(*R*)-Boc-nipepic acid stabilized at an energy range of -1.376385×10^6 kJ/mol. This energy level is slightly higher compared to the energy level of *hAChE*-sarin complex before docking with (*R*)-Boc-nipepic acid, which stabilized at an energy range of -1.381719×10^6 kJ/mol. The lower the energy, the higher the stability (Yellapu et al., 2015). The small increment in the energy levels of the *hAChE*-sarin/(*R*)-Boc-nipepic acid indicates the stability of this complex after reactivation occurs.

RMSD plot for the complexes *hAChE*-sarin with and without (*R*)-Boc-nipepic acid during 20 ns of MDS is presented (Figure 11) to analyze the stability and affinity of the system. There is a slight variation in the RMSD value of *hAChE*-sarin complex before and after docking with (*R*)-Boc-nipepic acid. Even though the RMSD fluctuated at the initial stage, after 1.35 ns, the *hAChE*-sarin/(*R*)-Boc-nipepic acid complex stabilized within the same RMSD range as that of *hAChE*-sarin complex at a value below 2.00 Å. It is therefore appears from the MDS, that complex *hAChE*-sarin/(*R*)-Boc-nipepic acid is stable, thus indicating the selective reactivating mode of (*R*)-Boc-nipepic acid against *hAChE*-sarin.

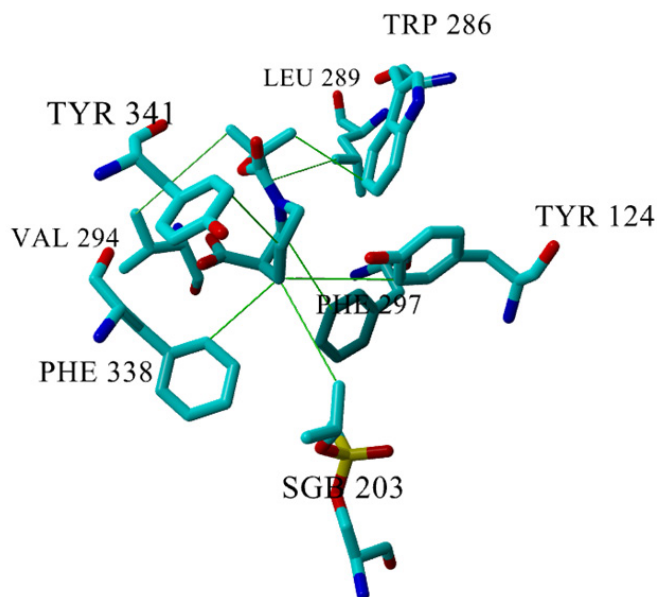


Figure 9. The interactions of OH from Tyr124 at the anionic site with nitrogen from (*R*)-Boc-nipecotic acid (multicolor) with a distance of 3.603 Å (electrostatic interaction). Hydrophobic interactions of contacting residues towards (*R*)-Boc-nipecotic acid (indicated by the green line)

This is also consistent with the variable docking scores. The RMSD value for *hAChE*-sarin/*(R)*-Boc-nipecotic acid complex has deviated from sarin-inhibited *hAChE* complex at around 0.236 Å which represents low position variation. The digression could be related to the affinity and the interactions performed with the enzymes, which also presented by the higher binding energy of *hAChE*-sarin/*(R)*-Boc-nipecotic acid complex as compared to the *hAChE*-sarin. *hAChE*-sarin/*(R)*-Boc-nipecotic acid complex exhibits larger position variation at the early stage of the simulation. However, at the later stage of the simulation, the values were restricted to the range of 1.612 Å and 1.739 Å, which can be regarded as stable, given its degree of freedom and frame size. This behavior can be described by the larger volume of the interaction site of (*R*)-Boc-nipecotic acid inside the complex *AChE*-sarin. For a better understanding of the structural variations and the conformation flexibility of both complexes, RMSFs of C α on the protein backbone were assessed to analyze the variations of every *AChE* amino acid residue towards the simulation time.

According to Baweja et al. (2017) and Ishak et al. (2017), residues within protein structures show low RMSF values, while loop regions and residues located on the protein surface show higher RMSF values. Some high peaks were detected around amino acid residues 72–98, 250–280 and 330–360 for structure *hAChE*-sarin complex compared to *hAChE*-sarin/*(R)*-Boc-nipecotic acid structure, which shows no peak. This can be seen

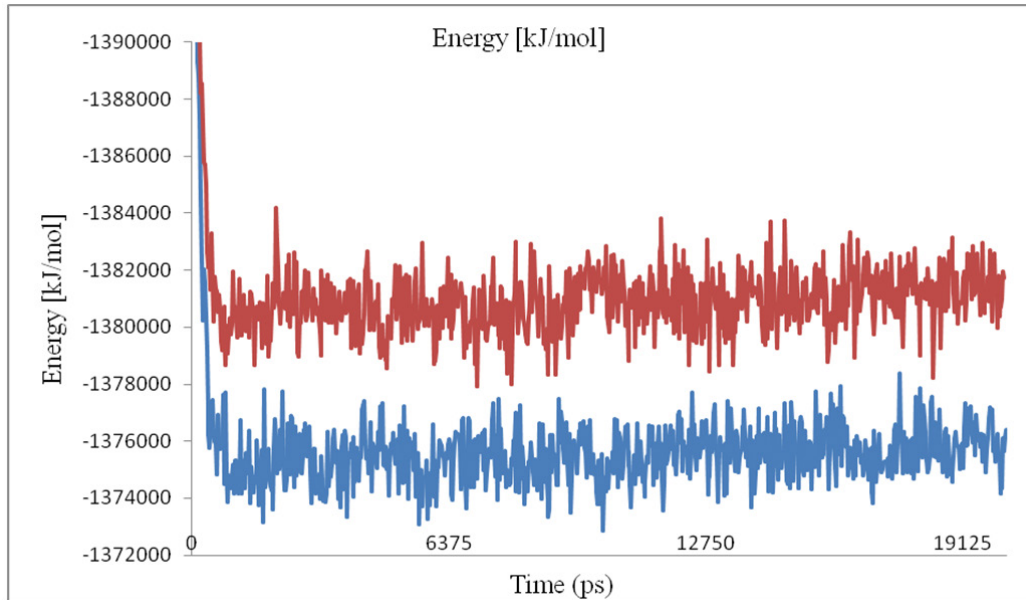


Figure 10. Energy plot for the complex *hAChE*-sarin without (red) and with (*R*)-Boc-nipecotic acid (blue) during 20 ns of MDS

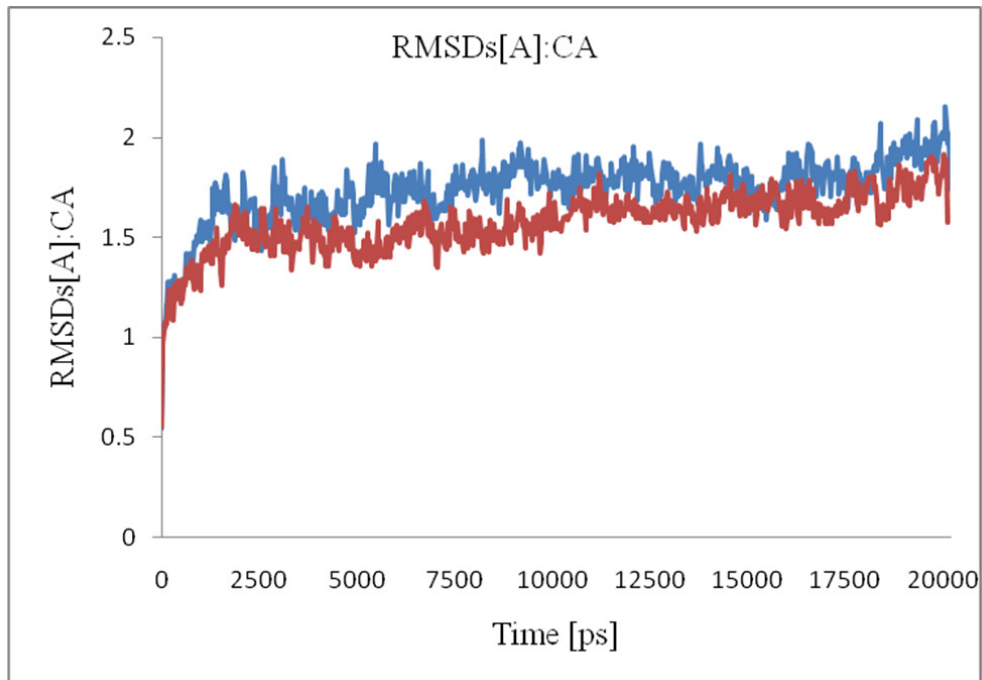


Figure 11. RMSD plot for the complexes *hAChE*-sarin without (red) and with (*R*)-Boc-nipecotic acid (blue) during 20 ns of MDS

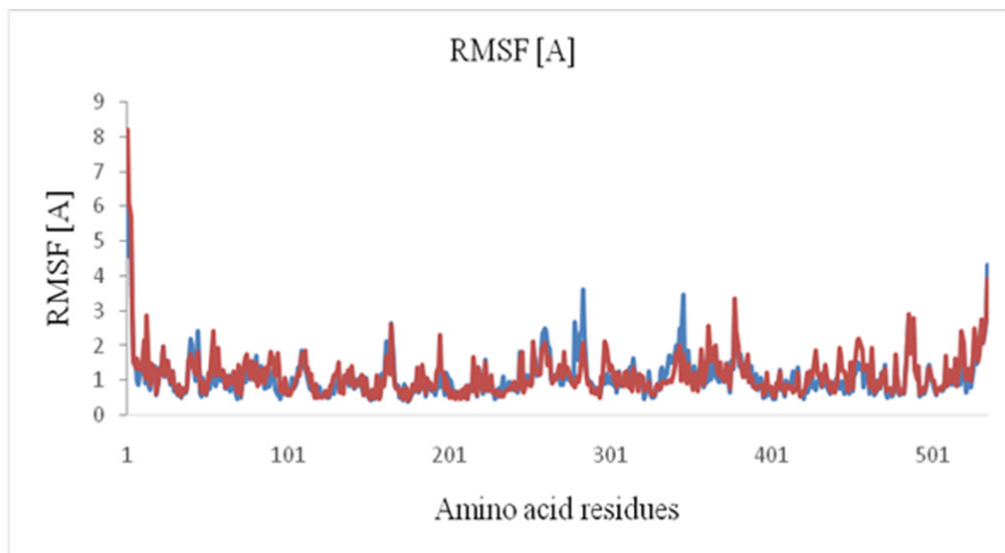


Figure 12. RMSF plot for the complexes *hAChE*-sarin without (blue) and with (*R*)-Boc-nipecotic acid (red) during 20 ns of mds

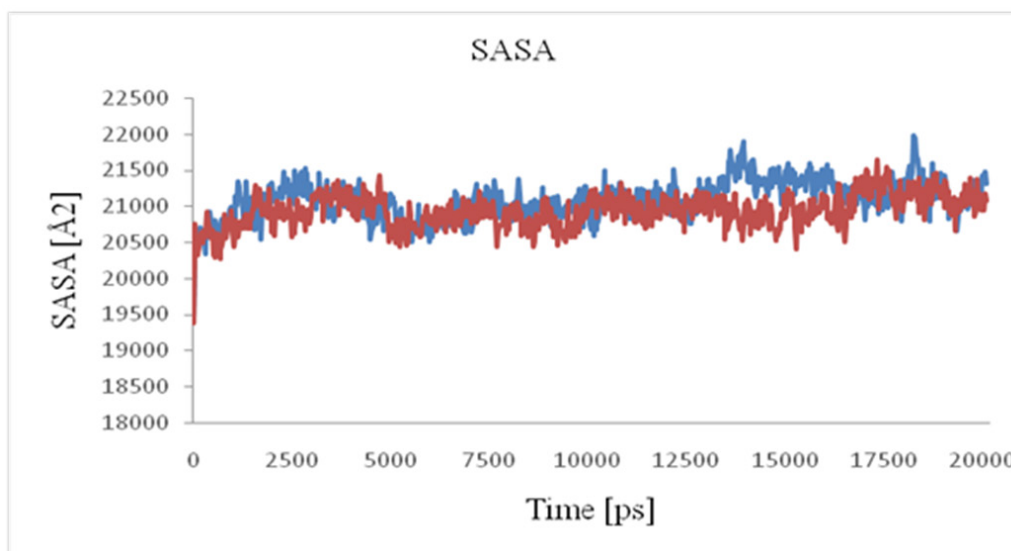


Figure 13. SASA plots for the complexes *hAChE*-sarin without (blue) and with (*R*)-Boc-nipecotic (red) acid during 20 ns of MDS

from the RMSF plot for the complexes *hAChE*-sarin with and without reactivator (*R*)-Boc-nipecotinic acid during 20 ns of MDS (Figure 12). Since the interacting PAS residues responsible for the reactivation mechanism are located within these residues, it strengthens the possible interaction occurred between (*R*)-Boc-nipecotinic acid with these residues. Ser203 shows no peak for the *hAChE*-sarin complex since this residue is responsible for the nucleophilic attack.

Previously, literature that reported on the MDS of sarin-AChE complex, shows that sarin-AChE presents greater position variation from the starting system configuration (de Souza et al., 2020). Sarin can affect the whole protein structure due to its interaction with the AChE active site's. This led to a greater volume of the interaction site, directly affecting the interactions between amino acids and oximes. Referring to SASA plots for the complexes *hAChE*-sarin with and without reactivator (*R*)-Boc-nipecotinic acid during 20 ns of MDS (Figure 13), SASA values of both *hAChE*-sarin and *hAChE*-sarin/(*R*)-Boc-nipecotinic acid complexes fluctuate at a range of 19500–21000 Å² until 1.35 ns. Following that, both complexes show a similar SASA pattern of up to 12.5 ns. However, after that, the pattern slightly changes for *hAChE*-sarin whereby its SASA value increased compared to *hAChE*-sarin/(*R*)-Boc-nipecotinic acid complex. This might represent the beginning point of the reactivation process. Higher scores mean that more molecules are sticking out into the water. Lower scores mean that more molecules are buried in the protein (Mukherjee & Bahadur, 2018).

Hence, it shows that the increment of the SASA value for *hAChE*-sarin complex is due to no interaction or reactivation occurring. After the reactivation, the protein accessible surface area is smaller since the protein became compact due to the H bond between (*R*)-Boc-nipecotinic acid and *hAChE*-sarin complex thus explained the lower SASA value of *hAChE*-sarin/(*R*)-Boc-nipecotinic acid complex after 12.5 ns. As described in the docking part previously, there are hydrogen bond forms between the (*R*)-Boc-nipecotinic acid towards *hAChE*-sarin complex residues involving Phe295 and Tyr341.

CONCLUSIONS

This study provides information to determine the potential reactivators for sarin-inhibited AChE based on the possible distance of the nucleophilic attack of O from the reactivator towards P from the sarin. (*R*)-Boc-nipecotinic acid shows shorter nucleophilic attack distance and high binding affinity implying that this compound could be an alternative antidote towards sarin inhibited-*hAChE*. Despite the commercial charged oxime, 2-PAM, which might present better nucleophilicity towards sarin-inhibited AChE, the uncharged (*R*)-Boc-nipecotinic acid is presumed to penetrate the blood-brain barrier and worth to be proven experimentally. It is hoped that these data should be beneficial in assessing new antidote candidates for nerve agent poisoning.

ACKNOWLEDGMENTS

This research was supported by the Ministry of Education under Grant UPNM/2018/CHEMDEF/ST/01. The authors acknowledge Prof. Madya Dr. Adam Leow Thean Chor from the Department of Cell and Molecular Biology, Faculty of Biotechnology and Biomolecular Sciences Universiti Putra Malaysia for the YASARA software.

REFERENCES

- Abou-Donia, M. B., Siracuse, B., Gupta, N., & Sokol, A. S. (2016). Sarin (GB, O isopropyl methylphosphonofluoridate) neurotoxicity: Critical review. *Critical Reviews in Toxicology*, *46*(10), 845-875. <https://doi.org/10.1080/10408444.2016.1220916>
- Ajami, D., & Rebek, J. (2013). Chemical approaches for detection and destruction of nerve agents. *Organic and Biomolecular Chemistry*, *11*(24), 3936-3942. <https://doi.org/10.1039/c3ob40324f>
- Artursson, E., Akfur, C., Hornberg, A., Worek, F., & Ekstrom, F. (2009). Reactivation of tabun-hAChE investigated by structurally analogous oximes and mutagenesis. *Toxicology*, *265*(3), 108-114. <https://doi.org/10.1016/j.tox.2009.09.002>
- Bagaria, A., Jaravine, V., Huang, Y. J., Montelione, G. T., & Guntert, P. (2012). Protein structure validation by generalized linear model root-mean-square deviation prediction. *Protein Science*, *21*(2), 229-238. <https://doi.org/10.1002/pro.2007>
- Baker, S. R. (1990). The effects of pesticides on human health. In C. F. Wilkinson (Ed.), *Advances in modern environmental toxicology* (pp. 35-130). Princeton Scientific Publication.
- Barak, D., Kronman, C., Ordentlich, A., Ariel, N., Bromberg, A., Marcus, D., Lazara, A., Velan, B., & Shafferman, A. (1994). Acetylcholinesterase peripheral anionic site degeneracy conferred by amino acid arrays sharing a common core. *Journal of Biological Chemistry*, *269*(9), 6296-6305. [https://doi.org/10.1016/S0021-9258\(17\)37371-4](https://doi.org/10.1016/S0021-9258(17)37371-4)
- Baweja, M., Singh, P. K., Sadaf, A., Tiwari, R., Nain, L., Khare, S. K., & Shukla, P. (2017). Cost effective characterization process and molecular dynamic simulation of detergent compatible alkaline protease from *Bacillus pumilus* strain MP27. *Process Biochemistry*, *58*, 199-203. <https://doi.org/10.1016/j.procbio.2017.04.024>
- Bhattacharjee, A. K., Marek, E., Le, H. T., Ratcliffe, R., DeMar, J. C., Pervitsky, D., & Gordon, R. K. (2015). Discovery of non-oxime reactivators using an *in silico* pharmacophore model of reactivators for DFP-inhibited acetylcholinesterase. *European Journal of Medicinal Chemistry*, *90*, 209-220. <https://doi.org/10.1016/j.ejmech.2014.11.013>
- Brighente, I. M. C., & Yunes, R. A. (1997). The general mechanisms of attack of nitrogen nucleophiles on carbonyl compounds. Facts that determine the change of the rate-pH profiles. *Journal of the Brazilian Chemical Society*, *8*(5), 549-553. <https://doi.org/10.1590/S0103-50531997000500018>
- Cadieux, C. L., Wang, H., Zhang, Y., Koenig, J. A., Shih, T. M., McDonough, J., Koh, J., & Cerasoli, D. (2016). Probing the activity of a non-oxime reactivator for acetylcholinesterase inhibited by organophosphorus nerve agents. *Chemico-Biological Interactions*, *259*(Pt B), 133-141. <https://doi.org/10.1016/j.cbi.2016.04.002>

- Chen, D. E., Willick, D. L., Ruckel, J. B., & Floriano, W. B. (2015). Principal component analysis of binding energies for single-point mutants of hT2R16 bound to an agonist correlate with experimental mutant cell response. *Journal of Computational Biology*, 22(1), 37-53. <https://doi.org/10.1089/cmb.2014.0192>
- Colovic, M. B., Krstic, D. Z., Lazarevic-Pasti, T. D., Bondzic, A. M., & Vasic, V. M. (2013). Acetylcholinesterase inhibitors: Pharmacology and toxicology. *Current Neuropharmacology*, 11(3), 315-335. <https://doi.org/10.2174/1570159x11311030006>
- de Almeida, J. S. F. D., Guizado, T. R. C., Guimarães, A. P., Ramalho, T. C., Gonçalves, A. S., de Koning, M. C., & França, T. C. C. (2016). Docking and molecular dynamics studies of peripheral site ligand-oximes as reactivators of sarin-inhibited human acetylcholinesterase. *Journal of Biomolecular Structure and Dynamics*, 34(12), 1-11. <https://doi.org/10.1080/07391102.2015.1124807>
- de Koning, M. C., Horn, G., Worek, F., & Grol, M. V. (2018). Discovery of a potent non-oxime reactivator of nerve agent inhibited human acetylcholinesterase. *European Journal of Medicinal Chemistry*, 157, 151-160. <https://doi.org/10.1016/j.ejmech.2018.08.016>
- de Koning, M. C., Joosen, M. J. A., Worek, F., Nachon, F., van Grol, M., Klaassen, S. D., Alkema, D. P. W., Wille, T., & de Bruijn, H. M. (2017). Application of the Ugi multicomponent reaction in the synthesis of reactivators of nerve agent inhibited Acetylcholinesterase. *Journal of Medicinal Chemistry*, 60(22), 9376-9392. <https://doi.org/10.1021/acs.jmedchem.7b01083>
- de Koning, M. C., van Grol, M., & Noort, D. (2011). Peripheral site ligand conjugation to a non-quaternary oxime enhances reactivation of nerve agent-inhibited human acetylcholinesterase. *Toxicology Letters*, 206(1), 54-59. <https://doi.org/10.1016/j.toxlet.2011.04.004>
- de Souza, F. R., Garcia, D. R., Cuya, T., Pimentel, A. S., Gonçalves, A. S., de Alencastro, R. B., & França, T. C. C. (2020). Molecular modeling study of uncharged oximes compared to HI-6 and 2-PAM inside human AChE sarin and VX conjugates. *American Chemical Society Omega*, 5(9), 4490-4500. <https://doi.org/10.1021/acsomega.9b03737>
- Duan, Y., Wu, C., Chowdhury, S., Lee, M. C., Xiong, G., Zhang, W., Yang, R., Cieplak, P., Luo, R., Lee, T., Caldwell, J., Wang, J., & Kollman, P. (2003). A point-charge force field for molecular mechanics simulations of proteins based on condensed-phase quantum mechanical calculations. *Journal of Computational Chemistry*, 24(16), 1999-2012. <https://doi.org/10.1002/jcc.10349>
- Ishak, S. N. H., Aris, S. N. A. M., Halim, K. B. A., Ali, M. S. M., Leow, T. C., Kamarudin, N. H. A., Masomian, M., & Rahman, R. N. Z. R. A. (2017). Molecular dynamic simulation of space and earth-grown crystal structures of thermostable T1 lipase *Geobacillus zalihae* revealed a better structure. *Molecules*, 22(10), Article 1574. <https://doi.org/10.3390/molecules22101574>
- Johnson, G., & Moore, S. (2006). The peripheral anionic site of acetylcholinesterase: structure, functions and potential role in rational drug design. *Current Pharmaceutical Design*, 12(2), 217-225. <https://doi.org/10.2174/138161206775193127>
- Katz, F. S., Pecic, S., Schneider, L., Zhu, Z., Hastings-Robinson, A., Luzac, M., Macdonald, J., Landry, D. W., & Stojanovic, M. N. (2018). New therapeutic approaches and novel alternatives for organophosphate toxicity. *Toxicology Letters*, 291, 1-10. <https://doi.org/10.1016/j.toxlet.2018.03.028>

- Katz, F. S., Pecic, S., Tran, T. H., Trakht, I., Schneider, L., Zhu, Z., Ton-That, L., Luzac, M., Zlatanovic, V., Damera, S., Macdonald, J., Landry, D. W., Tong, L., & Stojanovic, M. N. (2015). Discovery of new classes of compounds that reactivate acetylcholinesterase inhibited by organophosphates. *ChemBioChem*, *16*(15), 2205-2215. <https://doi.org/10.1002/cbic.201500348>
- Kim, S., Thiessen, P. A., Bolton, E. E., Chen, J., Fu, G., Gindulyte, A., Han, L., He, J., He, S., Shoemaker, B. A., Wang, J., Yu, B., Zhang, J., & Bryant, S. H. (2016). PubChem substance and compound databases. *Nucleic Acids Research*, *44*(D1), D1202-D1213. <https://doi.org/10.1093/nar/gkv951>
- Konagurthu, A. S., Whisstock, J. C., Stuckey, P. J., & Lesk, A. M. (2006). MUSTANG: A multiple structural alignment algorithm. *Proteins: Structure, Function, and Bioinformatics*, *64*(3), 559-574. <https://doi.org/10.1002/prot.20921>
- Kovarik, Z., MačEk, N., Sit, R. K., Radić, Z., Fokin, V. V., Sharpless, K., & Taylor, P. (2013). Centrally acting oximes in reactivation of tabun-phosphoramidated AChE. *Chemico-Biological Interactions*, *203*(1), 77-80. <https://doi.org/10.1016/j.cbi.2012.08.019>
- Krieger, E., Koraimann, G., & Vriend, G. (2002). Increasing the precision of comparative models with YASARA NOVA—A self-parameterizing force field. *Proteins*, *47*(3), 393-402. <https://doi.org/10.1002/prot.10104>
- Krieger, E., & Vriend, G. (2014). YASARA View - molecular graphics for all devices - from smartphones to workstations. *Bioinformatics*, *30*(20), 2981-2982. <https://doi.org/10.1093/bioinformatics/btu426>
- Kryger, G., Harel, M., Giles, K., Toker, L., Velan, B., Lazar, A., Kronman, C., Barak, D., Ariel, N., Shafferman, A., Silman, I., & Sussman, J. L. (2000). Structures of recombinant native and E202Q mutant human acetylcholinesterase complexed with the snake-venom toxin fasciculon-II. *Acta Crystallographica Section D: Biological Crystallography*, *56*(11), 1385-1394. <https://doi.org/10.1107/S0907444900010659>
- Kuca, K., Musilek, K., Jun, D., Karasova, J., Soukup, O., Pejchal, J., & Hrabanova, M. (2013). Structure-activity relationship for the reactivators of acetylcholinesterase inhibited by nerve agent VX. *Medicinal Chemistry*, *9*(5), 689-693. <https://doi.org/10.2174/1573406411309050008>
- Lotti, M. (2010). Clinical toxicology of anticholinesterase agents in humans. In R. Krieger (Ed.), *Hayes' Handbook of Pesticide Toxicology* (pp. 1543-1589). Elsevier Inc.
- Mallender, W. D., Szegletes, T., & Rosenberry, T. L. (2000). Acetylthiocholine binds to Asp74 at the peripheral site of human acetylcholinesterase as the first step in the catalytic pathway. *Biochemistry*, *39*(26), 7753-7763. <https://doi.org/10.1021/bi000210o>
- Matos, K. S., Mancini, D. T., da Cunha, E. F. F., Kuca, K., Franca, T. C. C., & Ramalho, T. C. (2011). Molecular aspects of the reactivation process of acetylcholinesterase inhibited by cyclosarin. *Journal of Brazilian Chemistry Society*, *22*(10), 1999-2004.
- Mercey, G., Renou, J., Verdelet, T., Kliachyna, M., Baati, R., Gillon, E., Arboleas, M., Loiodice, M., Nachon, F., Jean, L., & Renard, P. Y. (2012a). Phenyltetrahydroisoquinoline-pyridinaldoxime conjugates as efficient uncharged reactivators for the dephosphorylation of inhibited human acetylcholinesterase. *Journal of Medicinal Chemistry*, *55*(23), 10791-10795. <https://doi.org/10.1021/jm3015519>
- Mercey, G., Verdelet, T., Renou, J., Kliachyna, M., Baati, R., Nachon, F., Jean, L., & Renard, P. Y. (2012b). Reactivators of acetylcholinesterase inhibited by organophosphorus nerve agents. *Accounts of Chemical Research*, *45*(5), 756-766. <https://doi.org/10.1021/ar2002864>

- Morris, G. M., Goodsell, D. S., Halliday, R. S., Huey, R., Hart, W. E., Belew, R. K., & Olson, A. J. (1998). Automated docking using a Lamarckian genetic algorithm and an empirical binding free energy function. *Journal of Computational Chemistry*, 19(14), 1639-1662. doi: [https://doi.org/10.1002/\(SICI\)1096-987X\(19981115\)19:14<1639::AID-JCC10>3.0.CO;2-B](https://doi.org/10.1002/(SICI)1096-987X(19981115)19:14<1639::AID-JCC10>3.0.CO;2-B)
- Mukherjee, S., & Bahadur, R. P. (2018). An account of solvent accessibility in protein-RNA recognition. *Scientific Reports*, 8(1), 1-13. doi: <https://doi.org/10.1038/s41598-018-28373-2>
- Musilek, K., Jun, D., Cabal, J., Kassa, J., Gunn-Moore, F., & Kuca, K. (2007). Design of a potent reactivator of tabun-inhibited acetylcholinesterases-synthesis and evaluation of (E)-1-(4-carbamoylpyridinium)-4-(4-hydroxyiminomethylpyridinium)-but-2-ene dibromide (K203). *Journal of Medicinal Chemistry*, 50(22), 5514-5518. doi: <https://doi.org/10.1021/jm070653r>
- Namba, T., Nolte, C. T., Jackrel, J., & Grob, D. (1971). Poisoning due to organophosphate insecticides. Acute and chronic manifestations. *The American Journal of Medicine*, 50(4), 475-492. doi: [https://doi.org/10.1016/0002-9343\(71\)90337-8](https://doi.org/10.1016/0002-9343(71)90337-8)
- Ordentlich, A., Barak, D., Sod-Moriah, G., Kaplan, D., Mizrahi, D., Segall, Y., Kronman, C., Karton, Y., Lazar, A., Marcus, D., Velan, B., & Shafferman, A. (2004). Stereoselectivity toward VX is determined by interactions with residues of the acyl pocket as well as of the peripheral anionic site of AChE. *Biochemistry*, 43(35), 11255-11265. doi: <https://doi.org/10.1021/bi0490946>
- Patil, N., Ranjan, A., Chauhan, A., & Jindal, T. (2018). Mechanistic of organophosphate mediated inhibition of human acetylcholinesterase by molecular docking. *JSM Bioinformatics, Genomics and Proteomics*, 3(2), 1032-1040.
- Qiao, Y., Han, K., & Zhan, C. G. (2014). Reaction pathways and free energy profiles for cholinesterase-catalyzed hydrolysis of 6-monoacetylmorphine. *Organic and Biomolecular Chemistry*, 12(14), 2214-2227. doi: <https://doi.org/10.1039/c3ob42464b>
- Radić, Z., Sit, R. K., Garcia, E., Zhang, L., Berend, S., Kovarik, Z., Amitai, G., Fokin, V. V., Sharpless, K. B., & Taylor, P. (2013). Mechanism of interaction of novel uncharged, centrally active reactivators with OP-hAChE conjugates. *Chemico-Biological Interactions*, 203(1), 67-71. doi: <https://doi.org/10.1016/j.cbi.2012.08.014>
- Radić, Z., Sit, R. K., Kovarik, Z., Berend, S., Garcia, E., Zhang, L., Amitai, G., Green, C., Radic, B., Fokin, V. V., Sharpless K. B., & Taylor, P. (2012). Refinement of structural leads for centrally acting oxime reactivators of phosphorylated cholinesterases. *Journal of Biological Chemistry*, 287(15), 11798-11809. doi: <https://doi.org/10.1074/jbc.M111.333732>
- Ranjan, A., Kumar, A., Gulati, K., Thakur, S., & Jindal, T. (2015). Role of aromatic amino acids in stabilizing organophosphate and human acetylcholinesterase complex. *Journal of Current Pharma Research*, 5(4), 1632-1639. doi: <https://doi.org/10.33786/JCPR.2015.V05I04.006>
- Schaeffer, L. (2008). The role of functional groups in drug-receptor interactions. In C.G. Wermuth, P. Raboisson, D. Aldous, & D. Rognan (Eds.), *The practice of medicinal chemistry* (pp. 359-378). Elsevier Incorporation. doi: <https://doi.org/10.1016/B978-0-12-417205-0.00014-6>
- Shafferman, A., Velan, B., Ordentlich, A., Kronman, C., Grosfeld, H., Leitner, M., Flashner, Y., Cohen, S., Barak, D., & Ariel, N. (1992). Substrate inhibition of acetylcholinesterase: Residues affecting signal

- transduction from the surface to the catalytic center. *European Molecular Biology Organization Journal*, 11(10), 3561-3568. <https://doi.org/10.1002/j.1460-2075.1992.tb05439.x>
- Sit, R. K., Radić, Z., Gerardi, V., Zhang, L., Garcia, E., Katalinić, M., Amitai, G., Kovarik, Z., Fokin, V. V., Sharpless, K. B., & Taylor, P. (2011). New structural scaffolds for centrally acting oxime reactivators of phosphylated cholinesterases. *Journal of Biological Chemistry*, 286(22), 19422-19430. <https://doi.org/10.1074/jbc.M111.230656>
- Tang, M., Zhou, Y., Xu, W., Li, S., Wang, L., Wei, D., & Qiao, Z. (2013). A novel drug candidate for Alzheimer's disease treatment: Gx-50 derived from *Zanthoxylum bungeanum*. *Journal of Alzheimer's Disease*, 34(1), 203-213. <https://doi.org/10.3233/JAD-121831>
- Wlodek, S. T., Shen, T., & McCammon, J. A. (2000). Electrostatic steering of substrate to acetylcholinesterase: Analysis of field fluctuations. *Biopolymers*, 53(3), 265-271. [https://doi.org/10.1002/\(SICI\)1097-0282\(200003\)53:3<265::AID-BIP6>3.0.CO;2-N](https://doi.org/10.1002/(SICI)1097-0282(200003)53:3<265::AID-BIP6>3.0.CO;2-N)
- Yellapu, N., Gopal, J., Thulasibabu, R., Gunasekaran, K., & Jambulingam, P. (2015). Screening and identification of inhibitors against glutathione synthetase, a potential drug target of *Plasmodium falciparum*. *Combinatorial Chemistry & High Throughput Screening*, 18, 492-504.
- Zhang, Y., Zhang, S., Xu, G., Yan, H., Pu, Y., & Zuo, Z. (2016). The discovery of new acetylcholinesterase inhibitors derived from pharmacophore modeling, virtual screening, docking simulation and bioassays. *Molecular BioSystems*, 12(12), 3734-3742. <https://doi.org/10.1039/C6MB00661B>

REFEREES FOR THE PERTANIKA JOURNAL OF SCIENCE & TECHNOLOGY

VOL. 29 (3) JUL. 2021

The Editorial Board of Pertanika Journal of Science & Technology wishes to thank the following:

Abd Rahman Abdul Rahim
(UTM, Malaysia)

Azeana Zahari
(UM, Malaysia)

Hasmaliza Mohamad
(USM, Malaysia)

Abdul Hafiz Ab Majid
(USM, Malaysia)

Azmah Hanim Mohamed Ariff
(UPM, Malaysia)

Hasnuri Mat Hassan
(USM, Malaysia)

Abdul Rahim Abdullah
(UTeM, Malaysia)

Badaruddin Mohamed
(USM, Malaysia)

Hazril Sherney Basher
(USM, Malaysia)

Abdullah Muhammed
(UPM, Malaysia)

Bambang Karsono
(UNIMAS, Malaysia)

Idham Khalil
(UMT, Malaysia)

Adeyi Abel Adekanmi
(ABUAD, Nigeria)

Chandran Somasundram
(UM, Malaysia)

Jabir Idan Intidhar
(University of Babylon, Iran)

Ahmad Zhafran Ahmad
Mazlan
(USM, Malaysia)

Che Maznah Mat Isa
(UiTM, Malaysia)

Jamaluddin Abdullah
(USM, Malaysia)

Ahmed Jalal Khan Chowdhury
(IIUM, Malaysia)

Chuah Cheng Hock
(UM, Malaysia)

Jayaraj Vijaya Kumaran
(UMK, Malaysia)

Aida Mustapha
(UTHM, Malaysia)

Dayang Norulfairuz Abang
Zaidel
(UTM, Malaysia)

Joel Than Chia Ming
*(Swinburne University of Technology,
Malaysia)*

Aisyah Hartini Jahidin
(UM, Malaysia)

Dian Darina Indah Daruis
(UPNM, Malaysia)

Johan Afendi Ibrahim
(UUM, Malaysia)

Amir Izzwan Zamri
(UMT, Malaysia)

Douglas Law
(UMK, Malaysia)

Khairil Anas Md Rezali
(UPM, Malaysia)

Amir Rizaan Rahiman
(UPM, Malaysia)

Dzati Athiar Ramli
(USM, Malaysia)

Khairul Anuar Shariff
(USM, Malaysia)

Ana Sakura Zainal Abidin
(UNIMAS, Malaysia)

Emedya Murniwaty Samsudin
(UTHM, Malaysia)

Khairul Hamimah Abas
(UTM, Malaysia)

Anasyida Abu Seman
(USM, Malaysia)

Eris Elianddy Supeni
(UPM, Malaysia)

Lee Teang Shui
(UPM, Malaysia)

Anuar Mikdad Muad
(UKM, Malaysia)
Aweng Eh Rak
(UMK, Malaysia)

Fadhilah Mat Yamin
(UUM, Malaysia)

Lim Soh Fong
(UNIMAS, Malaysia)

Ayu Haslija Abu Bakar
(UCSI University, Malaysia)

Hadya S Hawedi
(Al-Asmariya University, Libya)

Mastura Jaafar
(USM, Malaysia)

Mazran Ismail
(USM, Malaysia)

Mohamad Yusof Maskat <i>(UKM, Malaysia)</i>	Nik Noordini Nik Abd Malik <i>(UTM, Malaysia)</i>	Rabiah Abdul Kadir <i>(UKM, Malaysia)</i>
Mohamed Abd Rahman <i>(IIUM, Malaysia)</i>	Nik Norsyahariati Nik Daud <i>(UPM, Malaysia)</i>	Rafeah Wahid <i>(UNIMAS, Malaysia)</i>
Mohammad Razip Selamat <i>(USM, Malaysia)</i>	Nik Raihan Nik Yusoff <i>(UMK, Malaysia)</i>	Ravi Prakash <i>(Amity University, India)</i>
Mohan Reddy Moola <i>(Curtin University, Malaysia)</i>	Noor Aziah Mohd Ariffin <i>(IIUM, Malaysia)</i>	Raviraj H Havaladar <i>(KLESCET, India)</i>
Mohd Asyraf Mansor <i>(USM, Malaysia)</i>	Nor Zalina Harun <i>(UKM, Malaysia)</i>	Riza Wirawan <i>(ITB, Indonesia)</i>
Mohd Azan Mohammed Sapardi <i>(IIUM, Malaysia)</i>	Norashikin Mohd Fauzi <i>(UMK, Malaysia)</i>	Rizafizah Othaman <i>(UKM, Malaysia)</i>
Mohd Fadzil Mohd Akhir <i>(UMT, Malaysia)</i>	Norashiqin Misni <i>(UPM, Malaysia)</i>	Roslaini Abd Majid <i>(UPM, Malaysia)</i>
Mohd Khair Hassan <i>(UPM, Malaysia)</i>	Norlaila Mohd Zanuri <i>(USM, Malaysia)</i>	Sapto Purnomo Putro <i>(Diponegoro University, Indonesia)</i>
Mohd Razif Harun <i>(UPM, Malaysia)</i>	Normah Maan <i>(UTM, Malaysia)</i>	Sarina Sulaiman <i>(IIUM, Malaysia)</i>
Mostafa Abdulghafoor Mohammed <i>(UPB, Romania)</i>	Nur Aainaa Hasbullah <i>(UMS, Malaysia)</i>	Sazlina Md Salleh <i>(USM, Malaysia)</i>
Muhammad Abbas Ahmad Zaini <i>(UTM, Malaysia)</i>	Nur Anisah Mohamed Rahman <i>(UM, Malaysia)</i>	Sharifah Akmam Syed Zakaria <i>(USM, Malaysia)</i>
Muhammad Nassir Hanapi <i>(UTM, Malaysia)</i>	Nur Fadhilah Ibrahim <i>(UMT, Malaysia)</i>	Siti Noor Linda Taib <i>(UNIMAS, Malaysia)</i>
Muhammad Nur Salihin Yusoff <i>(USM, Malaysia)</i>	Nur Fatihah Fauzi <i>(UiTM, Malaysia)</i>	Siti Nurul Ain Mat Jamil <i>(UPM, Malaysia)</i>
Muzalwana Abdul Talib <i>(UM, Malaysia)</i>	Nurul Izzaty Hassan <i>(UKM, Malaysia)</i>	Sreetheran Maruthaveeran <i>(UPM, Malaysia)</i>
Nasri Sulaiman <i>(UPM, Malaysia)</i>	Ooi Lu Ean <i>(USM, Malaysia)</i>	Suhaidi Shafie <i>(UPM, Malaysia)</i>
Neeraj Dineshchandra Sharma <i>(GDEC, India)</i>	Perumal Kumar <i>(Curtin University, Malaysia)</i>	Syahrul Imran Abu Bakar <i>(UiTM, Malaysia)</i>
Ng Peh Sang <i>(UTAR, Malaysia)</i>	Peter David Kulyakwave <i>(CAAS, China)</i>	Tan Ping Ping <i>(UNIMAS, Malaysia)</i>
		Tan Tien Ping <i>(USM, Malaysia)</i>

Tang Suk Peng
(USM, Malaysia)

Tay Chia Chay
(UiTM, Malaysia)

Tuan Zaharinie Tuan Zahari
(UM, Malaysia)

Vivien Jong
(UiTM, Malaysia)

Wan Mohd Rauhan Wan
Hussin
(UMT, Malaysia)

Wan Norafikah Othman
(UiTM, Malaysia)

Wuriti Sridhar
(KL University, India)

Yasmin Mustapha Kamil
(UPM, Malaysia)

Yugal Kumar
(JUIT, India)

Zaiton Haron
(UTM, Malaysia)

Zakiyah Zain
(UUM, Malaysia)

Zulfa Hanan
(UPM, Malaysia)

ABUAD – Afe Babalola University
GDEC – GIDC Degree Engineering College
IIUM – International Islamic University Malaysia
ITB – Bandung Institute of Technology
JUIT – Jaypee University of Information Technology
KL University – Koneeru Lakshmaiah University
KLESCET – KLE DR. M. S. Sheshgiri College of Engineering and Technology
UiTM – Universiti Teknologi MARA
UKM – Universiti Kebangsaan Malaysia
UM – Universiti Malaya
UMK – Universiti Malaysia Kelantan
UMS – Universiti Malaysia Sabah

UMT – Universiti Malaysia Terengganu
UNIMAS – Universiti Malaysia Sarawak
UPB – Politehnica University of Bucharest
UPI – Universitas Pendidikan Indonesia
UPM – Universiti Putra Malaysia
UPNM – Universiti Pertahanan Nasional Malaysia
USM – Universiti Sains Malaysia
UTAR – Universiti Tunku Abdul Rahman
UTeM – Universiti Teknikal Malaysia Melaka
UTHM – Universiti Tun Hussein Onn Malaysia
UTM – Universiti Teknologi Malaysia
UUM – Universiti Utara Malaysia

While every effort has been made to include a complete list of referees for the period stated above, however if any name(s) have been omitted unintentionally or spelt incorrectly, please notify the Chief Executive Editor, *Pertanika* Journals at executive_editor.pertanika@upm.edu.my

Any inclusion or exclusion of name(s) on this page does not commit the *Pertanika* Editorial Office, nor the UPM Press or the University to provide any liability for whatsoever reason.



Pertanika Journal of Science & Technology

Our goal is to bring high-quality research to the widest possible audience

INSTRUCTIONS TO AUTHORS

(REGULAR ISSUE)

(Manuscript Preparation & Submission Guide)

Revised: November 2020

Please read the *Pertanika* guidelines and follow these instructions carefully. The Chief Executive Editor reserves the right to return manuscripts that are not prepared in accordance with these guidelines.

MANUSCRIPT PREPARATION Manuscript Types

Pertanika accepts submission of mainly 4 types of manuscripts

- that have not been published elsewhere (including proceedings)
- that are not currently being submitted to other journals

1. Regular article

Regular article is a full-length original empirical investigation, consisting of introduction, methods, results, and discussion. Original research work should present new and significant findings that contribute to the advancement of the research area. *Analysis and Discussion* must be supported with relevant references.

Size: Generally, each manuscript is **not to exceed 6000 words** (excluding the abstract, references, tables, and/or figures), a maximum of **80 references**, and **an abstract of less than 250 words**.

2. Review article

A review article reports a critical evaluation of materials about current research that has already been published by organising, integrating, and evaluating previously published materials. It summarises the status of knowledge and outlines future directions of research within the journal scope. A review article should aim to provide systemic overviews, evaluations, and interpretations of research in a given field. Re-analyses as meta-analysis and systemic reviews are encouraged.

Size: Generally, it is expected **not to exceed 6000 words** (excluding the abstract, references, tables, and/or figures), a maximum of **80 references**, and **an abstract of less than 250 words**.

3. Short communications

Each article should be timely and brief. It is suitable for the publication of significant technical advances and maybe used to:

- (a) reports new developments, significant advances and novel aspects of experimental and theoretical methods and techniques which are relevant for scientific investigations within the journal scope;
- (b) reports/discuss on significant matters of policy and perspective related to the science of the journal, including 'personal' commentary;
- (c) disseminates information and data on topical events of significant scientific and/or social interest within the scope of the journal.

Size: It is limited to **3000 words** and have a maximum of **3 figures and/or tables, from 8 to 20 references, and an abstract length not exceeding 100 words**. The information must be in short but complete form and it is not intended to publish preliminary results or to be a reduced version of a regular paper.

4. Others

Brief reports, case studies, comments, concept papers, letters to the editor, and replies on previously published articles may be considered.

Language Accuracy

Pertanika emphasises on the linguistic accuracy of every manuscript published. Articles can be written in **English** or **Bahasa Malaysia** and they must be competently written and presented in clear and concise grammatical English/Bahasa Malaysia. Contributors are strongly advised to have the manuscript checked by a colleague with ample experience in writing English manuscripts or a competent English language editor. For articles in Bahasa Malaysia, the title, abstract and keywords should be written in both English and Bahasa Malaysia.

Author(s) **may be required to provide a certificate** confirming that their manuscripts have been adequately edited. **All editing costs must be borne by the authors.**

Linguistically hopeless manuscripts will be rejected straightaway (e.g., when the language is so poor that one cannot be sure of what the authors are really trying to say). This process, taken by authors before submission, will greatly facilitate reviewing, and thus, publication.

MANUSCRIPT FORMAT

The paper should be submitted in **one-column format** with 1.5 line spacing throughout. Authors are advised to use Times New Roman 12-point font and *MS Word* format.

1. Manuscript Structure

The manuscripts, in general, should be organised in the following order:

Page 1: Running title

This page should **only** contain the running title of your paper. The running title is an abbreviated title used as the running head on every page of the manuscript. The running title **should not exceed 60 characters, counting letters and spaces.**

Page 2: Author(s) and Corresponding author's information

General information: This page should contain the **full title** of your paper **not exceeding 25 words**, with the name of all the authors, institutions and corresponding author's name, institution and full address (Street address, telephone number (including extension), handphone number, and e-mail address) for editorial correspondence. **The corresponding author must be clearly indicated with a superscripted asterisk symbol (*).**

Authors' name: The names of the authors should be named **in full without academic titles**. For Asian (Chinese, Korean, Japanese, Vietnamese), please write first name and middle name before surname (family name). The last name in the sequence is considered the surname.

Authors' addresses: Multiple authors with different addresses must indicate their respective addresses separately by superscript numbers.

Tables/figures list: A list of the number of **black and white/colour figures and tables** should also be indicated on this page. See **"5. Figures & Photographs"** for details.

Example (page 2):

Fast and Robust Diagnostic Technique for the Detection of High Leverage Points

Habshah Midi^{1,2*}, Hasan Talib Hendi¹, Jayanthi Arasan² and Hassan Uraibi³

¹*Institute for Mathematical Research, Universiti Putra Malaysia, 43400 UPM, Serdang, Selangor, Malaysia*

²*Department of Mathematics, Faculty of Science, Universiti Putra Malaysia, 43400 UPM, Serdang, Selangor, Malaysia*

³*Department of Statistics, University of Al-Qadisiyah, 88 -Al-Qadisiyah -Al-Diwaniyah, Iraq*

E-mail addresses

habshah@upm.edu.my (Habshah Midi)

h.applied.t88@gmail.com (Hasan Talib Hendi)

jayanthi@upm.edu.my (Jayanthi Arasan)

hssn.sami1@gmail.com (Hassan Uraibi)

*Corresponding author

List of Table/Figure: Table 1.

Figure 1.

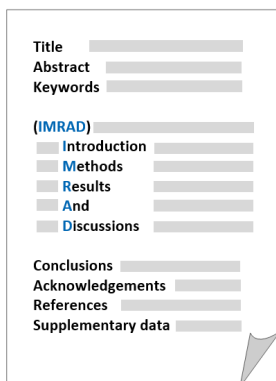
Page 3: Abstract

This page should **repeat** the **full title** of your paper with only the **Abstract**, usually in one paragraph and **Keywords**.

Keywords: *Not more than 8 keywords in alphabetical order must be provided to describe the content of the manuscript.*

Page 4: Text

A regular paper should be prepared with the headings *Introduction, Materials and Methods, Results and Discussions, Conclusions, Acknowledgements, References, and Supplementary data* (if any) in this order. The literature review may be part of or separated from the *Introduction*.



MAKE YOUR ARTICLES AS CONCISE AS POSSIBLE

Most scientific papers are prepared according to a format called IMRAD. The term represents the first letters of the words Introduction, Materials and Methods, Results, And, Discussion. It indicates a pattern or format rather than a complete list of headings or components of research papers; the missing parts of a paper are: Title, Authors, Keywords, Abstract, Conclusions, and References. Additionally, some papers include Acknowledgments and Appendices.

The Introduction explains the scope and objective of the study in the light of current knowledge on the subject; the Materials and Methods describes how the study was conducted; the Results section reports what was found in the study; and the Discussion section explains meaning and significance of the results and provides suggestions for future directions of research. The manuscript must be prepared according to the Journal's instructions to authors.

2. Levels of Heading

Level of heading	Format
1 st	LEFT, BOLD, UPPERCASE
2 nd	Flush left, Bold, Capitalise each word
3 rd	Bold, Capitalise each word, ending with .
4 th	Bold italic, Capitalise each word, ending with .

3. Equations and Formulae

These must be set up clearly and should be typed double-spaced. Numbers identifying equations should be in square brackets and placed on the right margin of the text.

4. Tables

- All tables should be prepared in a form consistent with recent issues of *Pertanika* and should be numbered consecutively with Roman numerals (Table 1, Table 2).
- A brief title should be provided, which should be shown at the top of each table (APA format):

Example:

Table 1

PVY infected Nicotiana tabacum plants optical density in ELISA

- Explanatory material should be given in the table legends and footnotes.
- Each table should be prepared on a new page, embedded in the manuscript.
- Authors are advised to keep backup files of all tables.

**** Please submit all tables in Microsoft word format only, because tables submitted as image data cannot be edited for publication and are usually in low-resolution.**

5. Figures & Photographs

- Submit an original figure or photograph.
- Line drawings must be clear, with a high black and white contrast.
- Each figure or photograph should be prepared on a new page, embedded in the manuscript for reviewing to keep the file of the manuscript under 5 MB.
- These should be numbered consecutively with Roman numerals (Figure 1, Figure 2).
- Provide a brief title, which should be shown at the bottom of each table (**APA format**):

Example: Figure 1. PVY-infected in vitro callus of Nicotiana tabacum

- If a figure has been previously published, acknowledge the original source, and submit written permission from the copyright holder to reproduce the material.
- Authors are advised to keep backup files of all figures.

**** Figures or photographs must also be submitted separately as TIFF or JPEG, because figures or photographs submitted in low-resolution embedded in the manuscript cannot be accepted for publication. For electronic figures, create your figures using applications that are capable of preparing high-resolution TIFF files.**

6. Acknowledgement

Any individuals and entities who have contributed to the research should be acknowledged appropriately.

7. References

References begin on their own page and are listed in alphabetical order by the first author's last name. Only references cited within the text should be included. All references should be in 12-point font and double-spaced. If a Digital Object Identifier (DOI) is listed on a print or electronic source, it is required to include the DOI in the reference list. Use Crossref to find a DOI using author and title information.

NOTE: When formatting your references, please follow the **APA-reference style** (7th edition) (refer to the examples). Ensure that the references are strictly in the journal's prescribed style, failing which your article will **not be accepted for peer-review**. You may refer to the *Publication Manual of the American Psychological Association* (<https://apastyle.apa.org/>) for further details.

Examples of reference style are given below:

Books		
	Insertion in text	In reference list
Book/E-Book with 1-2 authors	<p>Information prominent' (the author's name is within parentheses):</p> <p>... (Staron, 2020)</p> <p>... (Darus & Rasdi, 2019)</p> <p>... Or</p> <p>'Author prominent' (the author's name is outside the parentheses):</p> <p>(Starron, 2020)...</p> <p>Darus and Rasdi (2019) ...</p>	<p>Staron, M. (2020). <i>Action research in software engineering</i>. Springer International Publishing. https://doi.org/10.1007/978-3-030-32610-4</p> <p>Darus, A., & Rasdi, I. (2019). <i>Introduction to occupational health a workbook</i>. UPM Press.</p>
Book/E-Book with 3 or more authors	<p><i>For all in-text references, list only the first author's family name and followed by 'et al.'</i></p> <p>Information prominent' (the author's name is within parentheses):</p> <p>... (Yusof et al., 2020)</p> <p>... Or</p> <p>'Author prominent' (the author's name is outside the parentheses):</p> <p>Yusof et al. (2020) ...</p>	<p>Yusof, N. A., Azmi, U. Z. M., Ariffin, N., & Rahman, S. F. A. (2020). <i>Biosensors and chemical sensors: A practical approach</i>. UPM Press.</p>
Book/E-Book with more than 20 authors		<p>For books with more than 20 authors, please follow the guidelines for journal articles with more than 20 authors.</p>
Chapter in an edited Book/E-Book	<p>Inform ation pr ominent' (the author 's name is within parentheses):</p> <p>... (Mainzer, 2020) ...</p> <p>... (Tang et al., 2020) ...</p> <p>Or</p> <p>'Author prominent' (the author's name is outside the parentheses):</p> <p>Mainzer (2020) ...</p> <p>Tang et al. (2020) ...</p>	<p>Mainzer, K. (2020). Logical thinking becomes automatic. In K. Mainzer (Ed.), <i>Artificial intelligence-When do machines take over?</i> (pp. 15-45). Springer. https://doi.org/10.1007/978-3-662-59717-0_3</p> <p>Tang, W., Khavarian, M., Yousefi, A., & Cui, H. (2020). Properties of self-compacting concrete with recycled concrete aggregates. In R. Siddique (Ed.), <i>Self-Compacting Concrete: Materials, Properties, and Applications</i> (pp. 219-248). Woodhead Publishing. https://doi.org/10.1016/B978-0-12-817369-5.00009-X</p>

	Insertion in text	In reference list
Editor	<p>Information prominent' (the author's name is within parentheses): ... (Kesharwani, 2020) (Lanza et al., 2020) ... Or 'Author prominent' (the author's name is outside the parentheses): Kesharwani (2020) ... Lanza et al. (2020) ...</p>	<p>Kesharwani, P. (Ed.). (2020). <i>Nanotechnology based approaches for tuberculosis treatment</i>. Academic Press.</p> <p>Lanza, R., Langer, R., Vacanti, J. P., & Atala, A. (Eds.). (2020). <i>Principles of tissue engineering</i>. Academic press. https://doi.org/10.1016/C2018-0-03818-9</p>
Several works by the same author in the same year	<p>Information prominent' (the author's name is within parentheses): ... (Aggarwal & Aggarwal, 2020a, 2020b) ... Or 'Author prominent' (the author's name is outside the parentheses): Aggarwal & Aggarwal (2020a, 2020b) ...</p>	<p>Aggarwal, P., & Aggarwal, Y. (2020a). Strength properties of SCC. In R. Siddique (Ed.), <i>Self-Compacting Concrete: Materials, Properties, and Applications</i> (p. 83-115). Woodhead Publishing. doi: https://doi.org/10.1016/B978-0-12-817369-5.00004-0</p> <p>Aggarwal, P., & Aggarwal, Y. (2020b). Carbonation and corrosion of SCC. In R. Siddique (Ed.), <i>Self-Compacting Concrete: Materials, Properties, and Applications</i> (p. 147-193). Woodhead Publishing. doi: https://doi.org/10.1016/B978-0-12-817369-5.00007-6</p>
Journals		
Journal article with 1-2 authors	<p>Information prominent' (the author's name is within parentheses): ... (Laan & Fox, 2019) ... Or 'Author prominent' (the author's name is outside the parentheses): Laan and Fox (2019) ...</p>	<p>Laan, E., & Fox, J. W. (2019). An experimental test of the effects of dispersal and the paradox of enrichment on metapopulation persistence. <i>Oikos</i>, 129(1), 49-58. https://doi.org/10.1111/oik.06552</p>
Journal article with 3 or more authors	<p><i>For all in-text references, list only the first author's family name and followed by 'et al.'</i> Information prominent' (the author's name is within parentheses): ... (Midi et al., 2020) (Shagufta et al., 2017) ... Or 'Author prominent' (the author's name is outside the parentheses): Midi et al. (2020) ... Shagufta et al. (2017) ...</p>	<p>Midi, H., Hendi, H. T., Arasan, J., & Uraibi, H. (2020). Fast and Robust Diagnostic Technique for the Detection of High Leverage Points. <i>Pertanika Journal of Science & Technology</i>, 28(4), 1203-1220.</p> <p>Shagufta, B., Sivakumar, M., Kumar, S., Agarwal, R. K., Bhilegaonkar, K. N., Kumar, A., & Dubal, Z. B. (2017). Antimicrobial resistance and typing of Salmonella isolated from street vended foods and associated environment. <i>Journal of Food Science and Technology</i>, 54(8), 2532-2539. doi: https://doi.org/10.1007/s13197-017-2698-1</p>
Journal article with more than 20	<p>Information prominent' (the author's name is within parentheses): ... (Wiskunde et al., 2019) ... Or 'Author prominent' (the author's name is outside the parentheses): Wiskunde et al. (2019) ...</p>	<p>Wiskunde, B., Arslan, M., Fischer, P., Nowak, L., Van den Berg, O., Coetzee, L., Juárez, U., Riyaziyyat, E., Wang, C., Zhang, I., Li, P., Yang, R., Kumar, B., Xu, A., Martinez, R., McIntosh, V., Ibáñez, L. M., Mäkinen, G., Virtanen, E., ... Kovács, A. (2019). Indie pop rocks mathematics: Twenty One Pilots, Nicolas Bourbaki, and the empty set. <i>Journal of Improbable Mathematics</i>, 27(1), 1935-1968. https://doi.org/10.0000/3mp7y-537</p>
Journal article with an article number	<p>Information prominent' (the author's name is within parentheses): ... (Roe et al., 2020) ... Or 'Author prominent' (the author's name is outside the parentheses): Roe et al. (2020) ...</p>	<p>Roe, E. T., Bies, A. J., Montgomery, R. D., Watterson, W. J., Parris, B., Boydston, C. R., Sereno, M. E., & Taylor, R. P. (2020). Fractal solar panels: Optimizing aesthetic and electrical performances. <i>Plos One</i>, 15(3), Article e0229945. https://doi.org/10.1371/journal.pone.0229945</p>
Journal article with missing information	<p>Information prominent' (the author's name is within parentheses): ... (Alfirevic et al., 2017) (Hayat et al., 2020) (Fan et al., 2020) ...</p>	<p>Missing volume number Alfirevic, Z., Stampalija, T., & Dowswell, T. (2017). Fetal and umbilical Doppler ultrasound in high-risk pregnancies (review). <i>Cochrane Database of Systematic Reviews</i>, (6), 1-163. https://doi.org/10.1002/14651858.CD007529.pub4. Copyright</p>

	Insertion in text	In reference list
Journal article with missing information	Or 'Author prominent' (the author's name is outside the parentheses): Alfirevic et al. (2017) ... Hayat et al. (2020) ... Fan et al. (2020) ...	Missing issue number Hayat, A., Shaishta, N., Mane, S. K. B., Hayat, A., Khan, J., Rehman, A. U., & Li, T. (2020). Molecular engineering of polymeric carbon nitride based Donor-Acceptor conjugated copolymers for enhanced photocatalytic full water splitting. <i>Journal of colloid and interface science</i> , 560, 743-754. https://doi.org/10.1016/j.jcis.2019.10.088 Missing page or article number Fan, R. G., Wang, Y. B., Luo, M., Zhang, Y. Q., & Zhu, C. P. (2020). SEIR-Based COVID-19 Transmission Model and Inflection Point Prediction Analysis. <i>Dianzi Keji Daxue Xuebao/Journal of the University of Electronic Science and Technology of China</i> , 49(3). https://doi.org/10.12178/1001-0548.9_2020029
Several works by the same author in the same year	Information prominent' (the author's name is within parentheses): ... (Chee et al., 2019a, 2019b) ... Or 'Author prominent' (the author's name is outside the parentheses): Chee et al. (2019a, 2019b) ...	Chee, S. S., Jawaid, M., Sultan, M. T. H., Alothman, O. Y., & Abdullah, L. C. (2019a). Accelerated weathering and soil burial effects on colour, biodegradability and thermal properties of bamboo/kenaf/epoxy hybrid composites. <i>Polymer Testing</i> , 79, Article 106054. https://doi.org/10.1016/j.polymeresting.2019.106054 Chee, S. S., Jawaid, M., Sultan, M. T. H., Alothman, O. Y., & Abdullah, L. C. (2019b). Evaluation of the hybridization effect on the thermal and thermo-oxidative stability of bamboo/kenaf/epoxy hybrid composites. <i>Journal of Thermal Analysis and Calorimetry</i> , 137(1), 55-63. https://doi.org/10.1007/s10973-018-7918-z
Newspaper		
Newspaper article – with an author	... (Shamshuddin, 2019) ... Or ... Shamshuddin (2019) ...	Shamshuddin, J. (2019, September 23). Lynas plant waste residue can be used to boost oil palm growth? <i>New Straits Times</i> . https://www.nst.com.my/opinion/letters/2019/09/523930/lynas-plant-waste-residue-can-be-used-boost-oil-palm-growth
Newspaper article – without an author	("Zoonotic viruses," 2017). OR "Zoonotic viruses" (2017) ... Use a shortened title (or full title if it is short) in Headline Case enclosed in double quotation marks.	Zoonotic viruses like swine flu are ticking time bombs, say experts. (2020, July 4). <i>New Straits Times</i> , 3.
Dissertation/Thesis		
Published Dissertation or Thesis References	... (Rivera, 2016) ... Or ... Rivera (2016) ...	Rivera, C. (2016). <i>Disaster risk management and climate change adaptation in urban contexts: Integration and challenges</i> [Doctoral dissertation, Lund University]. Lund University Publications. https://lup.lub.lu.se/search/ws/files/5471705/8570923.pdf
Unpublished Dissertation or Thesis References	... (Brooks, 2014) ... Or ... Brooks (2014) ...	Brooks, J. D. (2015). <i>Bamboo as a strengthening agent in concrete beams for medium height structures</i> [Unpublished Doctoral dissertation]. The University of Washington.
Conference/Seminar Papers		
Conference proceedings published in a journal	... (Duckworth et al., 2019) ... Or Duckworth et al. (2019) ...	Duckworth, A. L., Quirk, A., Gallop, R., Hoyle, R. H., Kelly, D. R., & Matthews, M. D. (2019). Cognitive and noncognitive predictors of success. <i>Proceedings of the National Academy of Sciences, USA</i> , 116(47), 23499-23504. https://doi.org/10.1073/pnas.1910510116
Conference proceedings published as a book chapter	... (Bedenel et al., 2019) ... Or Bedenel et al. (2019) ...	Bedenel, A. L., Jourdan, L., & Biernacki, C. (2019). Probability estimation by an adapted genetic algorithm in web insurance. In R. Battiti, M. Brunato, I. Kotsireas, & P. Pardalos (Eds.), <i>Lecture notes in computer science: Vol. 11353. Learning and intelligent optimization</i> (pp. 225-240). Springer. https://doi.org/10.1007/978-3-030-05348-2_21

	Insertion in text	In reference list
Online	... (Gu et al., 2018) ... Or Gu et al. (2018) ...	Gu, X., Yu, J., Han, Y., Han, M., & Wei, L. (2019, July 12-14). <i>Vehicle lane change decision model based on random forest</i> . [Paper presentation]. 2019 IEEE International Conference on Power, Intelligent Computing and Systems (ICPICS), Shenyang, China. https://doi.org/10.1109/ICPICS47731.2019.8942520
Government Publications		
Government as author	First in-text reference: Spell out the full name with the abbreviation of the body. ... National Cancer Institute (2019) ... Or ... (National Cancer Institute, 2019) ... Subsequent in-text reference: ... NCI (2019) ... Or ... (NCI, 2019) ...	National Cancer Institute. (2019). <i>Taking time: Support for people with cancer</i> (NIH Publication No. 18-2059). U.S. Department of Health and Human Services, National Institutes of Health. https://www.cancer.gov/publications/patient-education/takingtime.pdf

8. General Guidelines

Abbreviations: Define alphabetically, other than abbreviations that can be used without definition. Words or phrases that are abbreviated in the *Introduction* and following text should be written out in full the first time that they appear in the text, with each abbreviated form in parenthesis. Include the common name or scientific name, or both, of animal and plant materials.

Authors' Affiliation: The primary affiliation for each author should be the institution where the majority of their work was done. If an author has subsequently moved to another institution, the current address may also be stated in the footer.

Co-Authors: The commonly accepted guideline for authorship is that one must have substantially contributed to the development of the paper and share accountability for the results. Researchers should decide who will be an author and what order they will be listed depending upon their order of importance to the study. Other contributions should be cited in the manuscript's *Acknowledgements*.

Similarity Index: All articles received must undergo the initial screening for originality before being sent for peer review. *Pertanika* does not accept any article with a similarity index exceeding **20%**.

Copyright Permissions: Authors should seek necessary permissions for quotations, artwork, boxes or tables taken from other publications or other freely available sources on the Internet before submission to *Pertanika*. The *Acknowledgement* must be given to the original source in the illustration legend, in a table footnote, or at the end of the quotation.

Footnotes: Current addresses of authors if different from heading may be inserted here.

Page Numbering: Every page of the manuscript, including the title page, references, and tables should be numbered.

Spelling: The journal uses American or British spelling and authors may follow the latest edition of the Oxford Advanced Learner's Dictionary for British spellings. Each manuscript should follow one type of spelling only.

SUBMISSION OF MANUSCRIPTS

All submissions must be made electronically using the **ScholarOne™ online submission system**, a web-based portal by Clarivate Analytics. For more information, go to our web page and click "**Online Submission (ScholarOne™)**".

Submission Checklist

1. MANUSCRIPT:

Ensure your manuscript has followed the *Pertanika* style particularly the first-4-pages as explained earlier. The article should be written in a good academic style and provide an accurate and succinct description of the contents ensuring that grammar and spelling errors have been corrected before submission. It should also not exceed the suggested length.

2. DECLARATION FORM:

Author has to sign a declaration form. In signing the form, authors declare that the work submitted for publication is original, previously unpublished, and not under consideration for any publication elsewhere.

Author has to agree to pay the publishing fee once the paper is accepted for publication in Pertanika.

3. COVER LETTER:

In Step 6 of the ScholarOne system, author is asked to upload a cover letter in *Pertanika* format. Please ignore this instruction and replace the cover letter with the **Declaration Form**.

Note:

COPYRIGHT FORM: Author will be asked to sign a copyright form when the paper is accepted. In signing the form, it is assumed that authors have obtained permission to use any copyrighted or previously published material. All authors must read and agree to the conditions outlined in the form and must sign the form or agree that the corresponding author can sign on their behalf. Articles cannot be published until a signed form (original pen-to-paper signature) has been received.

Visit our Journal's website for more details at <http://www.pertanika.upm.edu.my/>.

ACCESS TO PUBLISHED MATERIALS

Under the journal's open access initiative, authors can choose to download free material (via PDF link) from any of the journal issues from *Pertanika*'s website. Under "**Browse Journals**" you will see a link, "*Regular Issue*", "*Special Issue*" or "*Archives*". Here you will get access to all current and back-issues from 1978 onwards. No hard copy of journals or offprints are printed.

Visit our Journal's website at:

http://www.pertanika.upm.edu.my/regular_issues.php for "Regular Issue"

http://www.pertanika.upm.edu.my/cspecial_issues.php for "Special Issue"

http://www.pertanika.upm.edu.my/journal_archives.php for "Archives"

PUBLICATION CHARGE

Upon acceptance of a manuscript, a processing fee of RM 750 / USD 250 will be imposed on authors; RM 750 for any corresponding author affiliated to an institution in Malaysia; USD 250 for any corresponding author affiliated to an institution outside Malaysia. Payment must be made online at <https://paygate.upm.edu.my/action.do?do=>

Any queries may be directed to the **Chief Executive Editor's** office via email to executive_editor.pertanika@upm.edu.my

Modelling Benign Ovarian Cyst Risk Factors and Symptoms via Log-Linear Model 2199

Siti Zulaikha Mohd Jamaludin, Mohd Tahir Ismail, Mohd Shareduwan Mohd Kasihmuddin, Mohd. Asyraf Mansor, Siti Noor Farwina Mohamad Anwar Antony and Adnin Adawiyah Makhul

Chemical Sciences

In silico Study of Potential Non-oxime Reactivator for Sarin-inhibited Human Acetylcholinesterase 2217

Rauda A. Mohamed, Keat Khim Ong, Norhana Abdul Halim, Noor Azilah Mohd Kasim, Siti Aminah Mohd Noor, Victor Feizal Knight, Rabbani Muhamad and Wan Md Zin Wan Yunus

Detection of COVID-19 from Chest X-ray and CT Scan Images using Improved Stacked Sparse Autoencoder <i>Syahril Ramadhan Saufi, Muhd Danial Abu Hasan, Zair Asrar Ahmad, Mohd Salman Leong and Lim Meng Hee</i>	2045
<i>Short communication</i>	
Determination of Antioxidant Compounds, Proximate Compositions and Assessment of Free Radical Scavenging Activities of <i>Nypa Fruticans</i> Wurmmb. Sap <i>Siti Fatimah Roqiah Yahaya, Niza Samsuddin, Suhana Mamat, Rozita Hod, Nor Zamzila Abdullah, Nor Azlina A. Rahman and Siti Zaiton Mat So'Ad</i>	2061
<i>Short communication</i>	
Comparative Analyses on Synthetic Membranes for Artificial Blood Feeding of <i>Aedes aegypti</i> using Digital Thermo Mosquito Blood Feeder (DITMOF) <i>Mohd Farihan Md Yatim, Aishah Hani Azil, Nazarudin Safian, Ahmad Firdaus Mohd Salleh and Mohd Khadri Shahar</i>	2073
Earth Sciences	
The Characteristics of West Season Wind and Wave as well as Their Impacts on Ferry Cruise in The Kalianget-Kangean Cruise Route, Madura, Indonesia <i>Viv Djanat Prasita, Lukman Aulia Zati and Supriyatno Widagdo</i>	2087
Spatial Distribution of Picophytoplankton in Southeastern Coast of Peninsular Malaysia Using Flow Cytometry <i>Roswati Md Amin, Md Suffian Idris, Nurul Asmera Mudiman, Noor Hazwani Mohd Azmi and Hing Lee Siang</i>	2103
Effects of vegetation covers for outdoor thermal improvement: A Case Study at Abubakar Tafawa Balewa University, Bauchi, Nigeria <i>Kabiru Haruna Abdulkarim, Azmiah Abd Ghafar, Lee Yoke Lai and Ismail Said</i>	2125
Mathematical Sciences	
Evaluating the Steady-state Performance of the Synthetic Coefficient of Variation Chart <i>Ming Hui Chew, Wai Chung Yeong, Muzalwana Abdul Talib, Sok Li Lim and Khai Wah Khaw</i>	2149
Assessing the Impacts of Competition and Dispersal on a Multiple Interactions Type Model <i>Murtala Bello Aliyu, Mohd Hafiz Mohd and Mohd Salmi Md. Noorani</i>	2175

<i>Review article</i>	
A Comprehensive Review of Automated Essay Scoring (AES) Research and Development <i>Chun Then Lim, Chih How Bong, Wee Sian Wong and Nung Kion Lee</i>	1875
PRIB-CDS: An Energy Efficient Low Duty Cycle Broadcasting Scheme for Wireless Sensor Network <i>Anubhama Ramasamy and Rajendran Thangavel</i>	1901
Speech Emotion Recognition Using Deep Learning LSTM for Tamil Language <i>Bennilo Fernandes and Kasiprasad Mannepalli</i>	1915
An Analysis of Emotional Speech Recognition for Tamil Language Using Deep Learning Gate Recurrent Unit <i>Bennilo Fernandes and Kasiprasad Mannepalli</i>	1937
Performance Evaluation of Heuristics and Meta-Heuristics Traffic Control Strategies Using the <i>UTNSim</i> Traffic Simulator <i>Ng Kok Mun and Mamun Ibne Reaz</i>	1963
Material Sciences	
Effect of Stick - Slip Phenomena between Human Skin and UHMW Polyethylene <i>Emad Kamil Hussein, Kussay Ahmed Subhi and Tayser Sumer Gaaz</i>	1979
Development of Mini CNC Machine Design and Building for Making Ceramic Cup and Bowl Prototype <i>Anantakul Intarapadung</i>	1991
Synthesis and Characterization of Composite Materials with Enhanced Thermo-Mechanical Properties for Unmanned Aerial Vehicles (Uavs) and Aerospace Technologies <i>Zahid Iqbal Khan, Zurina Mohamad, Abdul Razak Rahmat and Unsia Habib</i>	2003
Electromechanical Characteristics of Core Free Folded Dielectric Electro-active Polymer Soft Actuator <i>Abdul Malek Abdul Wahab, Muhamad Azhan Anuar and Muhamad Sukri Hadi</i>	2017
Medical and Health Sciences	
Methylmercury Detection in Maternal Blood Samples by Liquid Chromatography with Inductively Coupled Plasma Mass Spectrometry <i>Amirah Abedinlah1, Saliza Mohd Elias, Sarva Mangala Praveena, Suhaili Abu Bakar, Zulida Rejali and Juliana Jalaludin</i>	2027

Behavior for Sandwich Plate with Functionally Graded Porous Metal Core 1655
Emad Kadum Njim, Sadeq H. Bakhy and Muhannad Al-Waily

Design of Soymilk Product Development from Grobogan Soybean Variety 1683
in Indonesia
Andita Sayekti, Atris Suyantohadi, Mirwan Ushada and David Yudianto

Engineering Sciences

Review article

Contact and Non-contact Heart Beat Rate Measurement Techniques: 1707
Challenges and Issues
Wei Leong Khong, Muralindran Mariappan and Chee Siang Chong

Application of Cubature Information Filter for Underwater Target Path 1733
Estimation
Guduru Naga Divya and Sanagapallea Koteswara Rao

Effect of Extraction Time and Temperature on Total Flavanoid Contents 1751
of Petai Belalang (*Leucaena leucocephala*) Seed Pretreated by Enzymatic
Hydrolysis
*Nor Hanimah Hamidi, Nurul Athirah Mohd Alwi, Haishwari
Tarmalingam, Siti Sabirah Ani Kutty and Siti Nur Nadzmiah
Mohd Nor*

Empirical Model of Ground-Borne Vibration Induced by Freight Railway 1763
Traffic
*Mohd Khairul Afzan Mohd Lazi, Muhammad Akram Adnan and
Norliana Sulaiman*

Development of Mini CNC Machine Design and Building for Making 1787
Ceramic Cup and Bowl Prototype
Anantakul Intarapadung

Magnetohydrodynamic Flow and Heat Transfer Over an Exponentially 1811
Stretching/Shrinking Sheet in Ferrofluids
Nurfazila Rasli and Norshafira Ramli

Development of a Fluidized Bed Dryer for Drying of a Sago Bagasse 1831
Nur Tantiyani Ali Othman and Ivan Adler Harry

Information, Computer and Communication Technologies

Review article

Text Messaging Platforms in Mental Health Computerised-based Therapy: 1847
A Review
Teh Faradilla Abdul Rahman and Norshita Mat Nayan

Treat-ability of <i>Manihot esculenta</i> Peel Extract as Coagulant Aid for Stabilised Leachate <i>Siti Nor Aishah Mohd-Salleh, Nur Shaylinda Mohd-Zin, Norzila Othman, Yashni Gopalakrishnan and Norshila Abu-Bakar</i>	1503
Sequestration of Pb(II) from Aqueous Environment by Palm Kernel Shell Activated Carbon: Isotherm and Kinetic Analyses <i>Ekemini Monday Isokise, Abdul Halim Abdullah and Tan Yen Ping</i>	1517
Rhodamine 6g Removal from Aqueous Solution with Coconut Shell-Derived Nanomagnetic Adsorbent Composite (Cs-Nmac): Isotherm and Kinetic Studies <i>Palsan Sannasi Abdullah, Lim Kai Wen, Huda Awang and Siti Nuurul Huda Mohammad Azmin</i>	1535
Length-weight Relationship and Relative Condition Factor of Two Dominant Species (<i>Cyclocheilichthys apogon</i> and <i>Notopterus notopterus</i>) at Subang Lake, Selangor, Malaysia <i>Xeai Li Chai, Rohasliney Hashim, Muhammad Nur Aiman Rahmat, Mohamad Hamizan Kamaludin, Nur Ain Habullah and Izharuddin Shah Kamaruddin</i>	1557
Applied Sciences and Technologies	
<i>Review article</i>	
Revisiting Solar Photovoltaic Roadmap of Tropical Malaysia: Past, Present and Future <i>Hedzlin Zainuddin, Hazman Raziq Salikin, Sulaiman Shaari, Mohamad Zhafran Hussin and Ardin Manja</i>	1567
Environmental Assessment of Groundwater Quality for Irrigation Purposes: A Case Study of Hillah City In Iraq <i>Zaid Abed Al-Ridah, Ahmed Samir Naje, Daaa Fliah Hassan and Hussein Ali Mahdi Al-Zubaid</i>	1579
Designing the Ergonomic Press and Molding Machine of Cassava Chips for Sustainable Development in SMEs <i>Silviana, Andy Hardianto, Naif Fuhaid and Dadang Hermawan</i>	1595
Numerical Simulations and Experimental Validation on LBW Bead Profiles of Ti-6Al-4V Alloy <i>Harish Mooli, Srinivasa Rao Seeram, Satyanarayana Goteti and Nageswara Rao Boggarapu</i>	1609
Thermal Comfort Performance of Naturally Ventilated Royal Malaysian Police (RMP) Lockup in Hot and Humid Climate of Malaysia <i>Bismiazan Abd. Razak, Mohd. Farid Mohamed, Wardah Fatimah Mohammad Yusoff and Mohd. Khairul Azhar Mat Sulaiman</i>	1627

Content

Foreword <i>Mohammad Jawaid</i>	i
Environmental Sciences	
<i>Review article</i>	
Wastewater from Washed Rice Water as Plant Nutrient Source: Current Understanding and Knowledge Gaps <i>Nabayi Abba, Christopher Teh Boon Sung, Tan Ngai Paing and Ali Tan Kee Zuan</i>	1347
Measurement of Thermal Comfort in Urban Public Spaces Semarang, Indonesia <i>Rina Kurniati, Wakhidah Kurniawati, Diah Intan Kusumo Dewi and Mega Febrina Kusumo Astuti</i>	1371
Efficient Solid Waste Management in Prai Industrial Area through GIS using Dijkstra and Travelling Salesman Problem Algorithms <i>Gaeithry Manoharam, Mohd. Tahir Ismail, Ismail Ahmad Abir and Majid Khan Majahar Ali</i>	1397
Traffic Noise Level Assessment in the Residential Area around Different Road Functions in Malang City, East Java, Indonesia <i>Ngudi Tjahjono, Imam Hanafi, Latipun Latipun and Suyadi Suyadi</i>	1419
Factors in Adopting Green Information Technology: A Qualitative Study in Malaysia <i>Siti Aishah Ramli, Boon Cheong Chew and Adi Saptari</i>	1431
Magnesium-Palm Kernel Shell Biochar Composite for Effective Methylene Blue Removal: Optimization via Response Surface Methodology <i>Nur Hanani Hasana, Rafeah Wahi, Yusralina Yusof and Nabisab Mujawar Mubarak</i>	1451
Evaluation and Application of New-Semarang Coastal Resources Management <i>Alin Fithor, Slamet Budi Prayitno, Frida Purwanti and Agus Indarjo</i>	1475
Immobilized Microalgae using Alginate for Wastewater Treatment <i>Amanatuzzakiah Abdul Halim and Wan Nor Atikah Wan Haron</i>	1489



Pertanika Editorial Office, Journal Division
Putra Science Park
1st Floor, IDEA Tower II
UPM-MTDC Technology Centre
Universiti Putra Malaysia
43400 UPM Serdang
Selangor Darul Ehsan
Malaysia

<http://www.pertanika.upm.edu.my/>
E-mail: executive_editor.pertanika@upm.edu.my
Tel: +603 9769 1622

PENERBIT
UPM
UNIVERSITI PUTRA MALAYSIA
PRESS

<http://penerbit.upm.edu.my>
E-mail: penerbit@upm.edu.my
Tel: +603 9769 8851

